



AFRL-SR-BL-TR-98-

0209

Wilmington, Virginia

# CONFERENCE DIGEST

Henry P. Freund

Editor

## TWENTY SECOND INTERNATIONAL CONFERENCE ON INFRARED AND MILLIMETER WAVES

Sponsored by

TECHNICAL CO-SPONSOR:

IEEE NUCLEAR AND PLASMA  
SCIENCES SOCIETY



NAVAL RESEARCH LABORATORY  
UNIVERSITY OF MARYLAND  
US DEPARTMENT OF ENERGY  
AIR FORCE OFFICE OF SCIENTIFIC RESEARCH

**NORTHROP GRUMMAN**

DISTRIBUTION STATEMENT A

Approved for public release  
Distribution Unlimited



Science Applications International Corporation  
An Employee-Owned Company

DTIC QUALITY ASSURANCE

19980225 058

REPORT DOCUMENTATION PAGE			Form Approved OMB No. 0704-0188	
<small>Public reporting burden for this collection of information is estimated to average 1 hour per response, including the time for reviewing instructions, searching existing data sources, gathering and maintaining the data needed, and completing and reviewing the collection of information. Send comments regarding this burden estimate or any other aspect of this collection of information, including suggestions for reducing this burden, to Washington Headquarters Services, Directorate for Information Operations and Reports, 1215 Jefferson Davis Highway, Suite 1204, Arlington, VA 22202-4302, and to the Office of Management and Budget, Paperwork Reduction Project (0704-0188), Washington, DC 20503.</small>				
1. AGENCY USE ONLY (Leave blank)		2. REPORT DATE		3. REPORT TYPE AND DATES COVERED Final 01 Apr 97 to 31 Dec 97
4. TITLE AND SUBTITLE  22ND International Conference on Infrared and Millimeter Waves			5. FUNDING NUMBERS  61102F 2301/ES	
6. AUTHOR(S)  DR. GRANATSTEIN				
7. PERFORMING ORGANIZATION NAME(S) AND ADDRESS(ES) University of Maryland Institute for Plasma Research University of Maryland, College Park College Park, MD 20742-3511			8. PERFORMING ORGANIZATION REPORT NUMBER  F49620-97-1-0226	
9. SPONSORING/MONITORING AGENCY NAME(S) AND ADDRESS(ES) AFOSR/NE 110 Duncan Ave Room B115 Bolling AFB DC 20332-8050			10. SPONSORING/MONITORING AGENCY REPORT NUMBER  F49620-97-1-0226	
11. SUPPLEMENTARY NOTES				
12a. DISTRIBUTION/AVAILABILITY STATEMENT  APPROVAL FOR PUBLIC RELEASE: DISTRIBUTION UNLIMITED			12b. DISTRIBUTION CODE	
13. ABSTRACT (Maximum 200 words)  The 22nd International Conference on Infrared and Millimeter Waves was successfully held on 20-25 July 97 in Wintergreen, Virginia. AFOSR funding was used to cover part of the printing/Publishing costs associated with this conference.				
14. SUBJECT TERMS			15. NUMBER OF PAGES	
			16. PRICE CODE	
17. SECURITY CLASSIFICATION OF REPORT UNCLASSIFIED	18. SECURITY CLASSIFICATION OF THIS PAGE UNCLASSIFIED	19. SECURITY CLASSIFICATION OF ABSTRACT UNCLASSIFIED	20. LIMITATION OF ABSTRACT  UL	

Extra copies of this Digest may be obtained from the members of the Conference Organizing Committee. There will be a charge for these copies payable by check to the International Conference on Infrared and Millimeter Waves. Please contact one of the following Committee Members for price and availability:

Robert H. Jackson  
Code 6840  
Naval Research Laboratory  
Washington, DC 20375  
Phone: (202) 767-  
FAX: (202) 767-1280  
e-mail: jackson@mmace.nrl.navy.mil

Victor L. Granatstein  
Institute for Plasma Research  
University of Maryland  
College Park, MD 20742  
Phone: (301) 405-4956  
FAX: (301) 314-9437  
e-mail: vlg@lpf.umd.edu

Gregory Nusinovich  
Institute for Plasma Research  
University of Maryland  
College Park, MD 20742  
Phone: (301) 405-4917  
FAX: (301) 314-9437  
e-mail: gregoryn@glue.umd.edu

Henry P. Freund  
Science Applications International Corp.  
McLean, VA 22102  
Phone: (202) 767-0034  
FAX: (202) 767-1280  
e-mail: freund@mmace.nrl.navy.mil

# ACKNOWLEDGMENTS

Grateful thanks are due to everyone who have made this digest and conference possible. First and foremost is Dr. Monica Blank, without whose help this digest might never have been completed in time. Thanks are also due to Jim McDonald whose assistance in translating incoming digest contributions and figures into formats that our computers could read was also invaluable. We would also like to acknowledge the important assistance provided by Stephanie Law, Margaret Hess, Kathleen Santangelo, Carol Bellamy, and Charlene Isham for organizational help.



## **Greetings from the Program Committee Chairman**

Welcome to the 22nd meeting of the International Conference on Infrared and Millimeter Waves. About 240 papers were submitted to the Conference from 22 countries, which indicates the international character of the research in the field of infrared and millimeter waves. One of our goals was to emphasize applications of infrared and millimeter wave devices since very often novel (or even potential) applications may cause new trends in the development of the devices. Therefore we included in the Conference Program a number of plenary talks devoted to this issue. Plenary talks will start every morning and afternoon sessions. These talks will be followed by three parallel sessions containing invited and contributed presentations.

I would like to acknowledge the help of the Program Committee members in preparation of the Program. Especially invaluable was the strong contribution made by Dr. James Wiltse.

All of us who were involved in the preparation of the Conference wish all participants a productive and enjoyable visit to Wintergreen Resort for the 22nd International Conference. We are thankful to the authors and speakers for their extensive efforts to provide the latest research results.

Gregory Nusinovich

Program Committee Chairman

# ORGANIZING COMMITTEE

## General Chairman

K. J. Button

## Organizing Committee

R. H. Jackson, Chair  
H. P. Freund, Digest Editor  
R. W. McMillan, Exhibition  
M. R. Jackson, Social Program

## Program Committee

G. S. Nusinovich, Chair  
K. Evenson  
H. Fetterman  
K. Kreischer  
F. Skiff  
J. Wiltse

## International Advisory Committee

V. L. Granatstein, Chair	
T. Antonsen	M. von Ortenberg
C. Armstrong	R. Parker
R. Barker	T. Parker
A. V. Gaponov-Grekhov	K. Sakai
T. V. George	Liu Shenggang
A. Hadni	R. Temkin
T. Itoh	M. Thumm
M. Kimmit	M. Q. Tran
K. Mizuno	

# **The 23rd International Conference on Infrared and Millimeter Waves**

**September 7-11, 1998.**

**University of Essex  
Wivenhoe Park, Colchester, Essex, CO4 3SQ, United Kingdom.**

The twenty third conference in this series will be held at the University of Essex in Colchester. Colchester is Britain's oldest recorded town with a rich and colourful past. It is situated in Essex about 60 miles north-east of London (about 50 minutes by train) in an attractive area near the coast surrounded by river estuaries, and it is close to the River Stour and the border with the county of Suffolk, a delightful area associated with the landscape artist John Constable. The university is modern, with a purpose built lecture theatre block which can accommodate all parallel sessions in one building. Ample residential accommodation is available on campus within a few minutes walk of the lecture theatre block with a range of prices and facilities that should suit everyone.

The conference will cover progress in all areas of infrared and millimeter waves, including the following topics, with special emphasis on new fields of research. Sources: lasers, free electron lasers, gyrotrons, synchrotrons, frequency mixing, calibration and standards. Detectors: receivers, mixers, amplifiers, thermal and photon detectors, Schottky diodes, Josephson and SIS devices, imaging arrays, FET amplifiers. Guided propagation and components: waveguides and other structures, Gaussian beams, integrated devices, optical fibres. Spectroscopic techniques: interferometric, laser and heterodyne spectroscopy. Spectroscopy of solids, liquids and gases. Astronomy and atmospheric physics: techniques, results and interpretation. Applications in biology and medicine. Plasma interactions and diagnostics. Technical and industrial applications: imaging, remote sensing, non-destructive testing.

## **General Chairman**

K.J. Button,  
2095 North A1A Highway  
Indialantic, Florida 32903-2514  
USA

## **Conference Chairman**

T.J. Parker  
Department of Physics  
University of Essex  
Wivenhoe Park  
Colchester CO4 3SQ  
UK  
Tel: +44 1206 872827  
Fax: +44 1206 873598  
e-mail: partj@essex.ac.uk

## **Program Chairman**

J.R. Birch  
JB Research  
Clifton Terrace  
Cliftonville, Dorking  
Surrey RH4 2JG  
UK  
Tel: +44 1306 884668  
Fax: +44 1306 740579

# **TECHNICAL EXHIBIT**

## **List of Exhibitors**

- **QMC Instruments**
- **Graseby Specac**

**Robert W.  
McMillan  
Rome Lab  
Exhibit Manager**

# **The Kenneth J. Button Prize**

“... in recognition of outstanding  
contributions to  
the science of the electromagnetic  
spectrum.”

1996 Medal

**Professor Mikhail I. Petelin**

Institute of Applied Physics  
Russian Academy of Sciences

1997 Medal

**Professor Paul L. Richards**

Department of Physics  
University of California, Berkeley

The Kenneth J. Button Medal in Far Infrared Physics is awarded in recognition of outstanding contributions to the science of the electromagnetic spectrum. The prize is awarded annually by The Institute of Physics at that year's International Conference on Infrared and Millimeter Waves. The 1996 and 1997 prizes will be awarded to Profs. Petelin and Richards respectively at the 22nd International Conference in Wintergreen, Virginia, USA on 22 July 1997. The award consists of a £1,400 prize and a bronze medal. Nominations for the 1998 Button Medal, including candidates qualifications, should be sent to:

The Institute of Physics  
Attn: Clive Jones, Senior Manager  
76 Portland Place  
London W1N 4AA  
UK

**CONFERENCE PROGRAM**  
**The 22nd International Conference on**  
**Infrared and Millimeter Waves**  
**20-25 July 1997**

Monday AM	Plenary Talk: R. Roy, "Mm-Wave Material Processing"		
	FELs	Quasioptics	Radars & Antennas
Monday PM	Plenary Talk: D. Whittum, "Mm-Wave Drivers for Linear Colliders"		
	CRMs	Waveguides I	Atmospheric Studies
Tuesday AM	Plenary Talk: P.L. Richards, "FIR & Mm-Wave Detectors for Astrophysics"		
	Plenary Talk: M.I. Petelin, "Relativism in Microwave Electronics"		
	Gyrotrons I	Waveguides II	Solid State Devices I
Tuesday PM	Plenary Talk: A. Wong, "Global Communication Network Using Geo-Stationary Stratosphere Platforms"		
	Gyrotrons II	Numerical Methods I	Solid State Devices II
Wednesday AM	Plenary Talk: M. Kimmit, "Tunable THz Sources"		
	Gyrotrons III	Vacuum Sources I	Lasers
Wednesday PM	Trip to Monticello		
Thursday AM	Plenary Talk: A. Hadni, "Infrared Spectroscopy of High Tc Superconductors"		
	Gyrotrons IV	Solid State Sources II	Spectroscopy
Thursday PM	Plenary Talk: J. Mead, "Mm-Wave Radars for Atmospheric Sensing"		
	Gyrotrons V	Applications	Solid State Devices III
Friday AM	Plenary Talk: B. Lax, "Quantum Interpretation of Mm- and Submm-Wave Sources"		
	Relativistic Sources	Biological Applications	Numerical Methods II

**MORNING:**

Plenary Sessions: 8:15 A.M. - 9:30 A.M.  
Regular Session: 9:45 A.M. - 12:30 P.M.

**LUNCH BREAK:** 12:30 P.M. - 3:30 P.M.

**AFTERNOON:**

Plenary Sessions: 3:30 P.M. - 4:30 P.M.  
Regular Sessions: 4:30 P.M. - 7:00 P.M.

## SESSION M1 - Free Electron Lasers

Monday, A.M.

July 21

**M1.1 FIRST EXPERIMENTAL DEMONSTRATION OF THE REGENERATIVE AMPLIFIER FEL (RAFEL) - *(Invited)***  
R. Sheffield, Los Alamos National Laboratory, USA

**M1.2 FIRST EXPERIMENTS OF THE FOM FUSION FEM**  
T. Verhoeven, FOM, Netherlands

**M1.3 RECENT RESULTS FROM THE COMPACT INFRARED FREE ELECTRON LASER**  
H. Bluem, I.S. Lehrman, J. Krishnaswamy, R.A. Hartley, R.H. Austin  
Northrop-Grumman Corp. and Princeton University, USA

**M1.4 OPERATION OF A KA-BAND CHI WIGGLER UBITRON AMPLIFIER**  
J.M. Taccetti, R.H. Jackson, H.P. Freund, D.E. Pershing, V.L. Granatstein,  
Naval Research Laboratory, USA

**M1.5 A TUNABLE FIR GRATING-BASED FEL**  
J. Urata, M. Kimmitt, A. Naumov, C. Platt, J. Walsh  
Dartmouth College, USA

**M1.6 THE CERENKOV FEL, A VERSATILE SOURCE FOR MM- AND SUBMM WAVELENGTH RADIATION**  
P.J.M. Van der Slot, J. Wieland, J. Couperus, W.J. Witteman,  
Netherlands Center for Laser Research, Netherlands

**M1.7 THE INFLUENCE OF THE VELOCITY DISTRIBUTION ON THE PERFORMANCE OF A CERENKOV FEL**  
P.J.M. Van der Slot, J. Wieland, J. Couperus, W.J. Witteman,  
Netherlands Center for Laser Research, Netherlands

**M1.8 PRELIMINARY DESIGN OF A W-BAND FREE-ELECTRON LASER AMPLIFIER**  
H.P. Freund, B.G. Danly, R.H. Jackson, B. Levush  
Naval Research Laboratory, USA

**M1.9 A Ka-BAND BRAGG FREE ELECTRON MASER OSCILLATOR**  
A.D.R. Phelps, A. W. Cross, D.A. Jaroszynski, C.G. Whyte, W. He, N.S. Ginzburg, N. Yu. Peskov,  
University of Strathclyde, Scotland, UK; IAP, Russia

**M1.10 FREE ELECTRON LASER WITH CROSSED MAGNETIC AND VORTEX ELECTRIC UNDULATED FIELDS OF PUMPING**  
V.V. Kulish, O.B. Krutko, A.G. Kailuyk  
Sumy University, Ukraine

## SESSION M2 - Quasioptics

Monday, A.M.

July 21

### **M2.1 COLD TEST OF GYROTRON OUTPUT WAVE BEAM SPLITTER AND COMBINER**

Y. Mitsunaka, Y. Hirata, K. Hayashi, Y. Itoh, K. Sakamoto, A. Kasugai, K. Takahasi, T. Imai  
Toshiba Corp. and JAERI, Japan

### **M2.2 LOW POWER PERFORMANCE TESTS ON HIGHLY OVERSIZED WAVEGUIDE COMPONENTS OF HIGH POWER GYROTRONS**

O. Braz, A. Arnold, H.-R. Kunkel, M. Thumm  
EURATOM-FZK, Germany

### **M2.3 EXPERIMENTAL RESULTS OF GYROTRON-OUTPUT MATCHING WITH THE HE<sub>11</sub> MODE**

Y. Hirata, Y. Mitsunaka, M. Komuro, K. Hayashi, S. Sasaki, Y. Kanai, S. Kubo, T. Shimozuma, M. Satoh, Y. Takita, K. Ohkubo, T. Watari  
Toshiba Corp., Japan

### **M2.4 DESIGN OF A QUASI-OPTICAL MODE CONVERTER FOR A COAXIAL 165 GHz, TE<sub>31,17</sub> GYROTRON**

G. Michel, M. Thumm, D. Wagner  
EURATOM-FZK, Germany

### **M2.5 DESIGN OF A MODE CONVERTING TRANSMISSION LINE FOR A 28 GHz TE<sub>02</sub>-MODE GYROTRON**

J. Shafii, R.J. Vernon, J.N. Talmadge, D.T. Anderson  
University of Wisconsin-Madison, USA

### **M2.6 A TE<sub>22-6</sub> TO TEM<sub>00</sub> MODE CONVERTER WITH NONPERIODIC INNER DEFORMATIONS**

A. Möbius, O. Braz,  
EURATOM-FZK, Germany

### **M2.7 COMPACT AND EFFICIENT TRANSMISSION LINE FOR TECHNOLOGICAL GYROTRON**

G.G. Denisov, S.V. Kuzikov,  
D.V. Vinogradov, A.V. Chirkov, IAP, Russia

### **M2.8 EXPERIMENTAL RESULTS ON A COAXIAL TEM-CIRCULAR TE<sub>16,2</sub> MODE TRANSDUCER**

F. Volgyi, G. Reiter, G. Veszely, T. Berceli, Budapest Technical University, Hungary

### **M2.9 ANALYSIS OF A CO-AXIAL COUPLER FOR A 35 GHz GYRO-KLYSTRON**

A.H. McCurdy, J.J. Choi, W.M. Manheimer  
Univ. Southern California and Naval Research Laboratory, USA



## SESSION M3 - Radars and Antennas

Monday, A.M.

July 21

### **M3.1 GYROKLYSTRON BASED 35 GHz RADAR - (Invited)**

A. Tolkachev  
Research Institute of Radiophysics, Russia

### **M3.2 MILLIMETER-WAVE RADARS TRACKING APPROACHING SEA SKIMMING TARGETS - (Invited)**

D. Lohrmann, NRL,  
USA

### **M3.3 TRANSMITTERS BASED ON MAGNETRONS WITH COLD SECONDARY-EMISSION CATHODE**

V.D. Naumenko, K. Schünemann, V. Ye.Semenuta, D.M. Vavriv, V.A. Volkov  
Technische Universität Hamburg-Harburg, Germany

### **M3.4 MILLIMETER WAVE PHASE CONJUGATION USING ARTIFICIAL NONLINEAR SURFACES**

Y. Chang, H.R. Fetterman, I.L. Newberg  
UCLA and Hughes Aircraft Co., USA

### **M3.5 MULTIPLE-FREQUENCY FRESNEL ZONE PLATE ANTENNAS**

J.C. Wiltse  
Georgia Tech Research Institute, USA

### **M3.6 THz RADIATION FROM LARGE APERTURE ANTENNA**

G. Mouret, J. Burie, D. Boucher, D. Lippens  
Institut d'Electronique et de Microelectronique du Nord  
Université du Littoral, France

### **M3.7 SIXTEEN-ELEMENT LINEAR ARRAY OF Ge:Ga FAR-INFRARED PHOTO-CONDUCTOR**

M. Fujiwara, N. Horomoto,  
Communications Research Laboratory, Japan

### **M3.8 ACCURATE ANALYSIS OF FUNDAMENTAL WAVE PHENOMENA IN THE PRINTED ANTENNAS**

N.Yu. Bliznyuk, A.I. Nosich  
IRE, Ukraine

### **M3.9 ABOUT PLASMA HEATING BY HIGH FREQUENCY FIELDS**

N.A. Khizhnyak, E.A. Yatsenko, N.M. Yatsenko  
Kharkov State University, Ukraine

## SESSION M4 - CRMs

Monday, P.M.

July 21

**M4.1 CARMs AND RELATIVISTIC GYROTRONS AS EFFECTIVE SOURCES OF MILLIMETER AND SUBMILLIMETER WAVES - (Invited)**

V.L. Bratman,  
IAP, Russia

**M4.2 THEORY OF THE ANOMALOUS DOPPLER CRM-AMPLIFIER WITH TAPERED PARAMETERS**

G. Nusinovich, M. Korol, E. Jerby,  
University of Maryland, USA; Tel Aviv University, Israel

**M4.3 CONCEPT OF A KA-BAND FREE ELECTRON MASER OSCILLATOR WITH A TWO-DIMENSIONAL BRAGG CAVITY**

N.S. Ginzburg, N. Yu. Peskov, I.V. Konoplev, A.S. Sergeev, G.R.M. Robb,  
A.D.R. Phelps, A.W. Cross  
IAP, Russia; University of Strathclyde, Scotland, UK.

**M4.4 CYCLOTRON-RESONANCE MASER ARRAY-CONCEPT, THEORY, AND EXPERIMENTS**

E. Jerby, M. Korol, Li Lei  
Tel Aviv University, Israel

**M4.5 RADIATION BURSTS FROM A SLOW-WAVE CRM WITH A FERRO-ELECTRIC CATHODE**

R. Drori, D. Shur, E. Herby, G. Rosenman, R. Advani, and R. Temkin  
Tel Aviv University, Israel; MIT, USA

**M4.6 DEVELOPMENT OF AN EFFICIENT MILLIMETER-WAVE HARMONIC AMPLIFIER**

J.E. Velazco, P. Ceperley  
MicrowaveTechnologies, Inc. and George Mason University, USA

**M4.7 SECOND AND THIRD HARMONIC OSCILLATIONS IN A QUADRUPOLE PERIODIC TEM-GUIDE CYCLOTRON-RESONANCE MASER**

Y. Leibovich, E. Jerby  
Tel Aviv University, Israel

**M4.8 THERMIONIC CATHODE CYCLOTRON AUTO-RESONANCE MASER (CARM) EXPERIMENTS**

A.R. Young, W. He, S.J. Cooke, A.W. Cross, A.D.R. Phelps  
University of Strathclyde, Scotland, UK.

## SESSION M5 - Waveguides I

Monday, P.M.

July 21

### **M5.1 A QUASI-OPTICAL RESONANT RING FOR HIGH POWER MILLIMETER-WAVE TESTING**

T.S. Bigelow

Oak Ridge National Laboratory, USA

### **M5.2 CALCULATIONS AND EXPERIMENTS ON MULTI-BEAM WAVEGUIDES**

L. Empacher, G. Gantenbein, W. Kasperek

Institut für Plasmaforschung, Germany

### **M5.3 MEASUREMENT LIMITATIONS ON PHASE PATTERN DETERMINATION FROM SEVERAL AMPLITUDE PATTERN MEASUREMENTS**

R.J. Vernon

University of Wisconsin-Madison, USA

### **M5.4 PHASE RETRIEVAL FROM GYROTRON NEAR-FIELD INTENSITY MEASUREMENTS**

D.R. Denison, T. Kimura, M.A. Shapiro, R.J. Temkin

MIT, USA

### **M5.5 GAUSSIAN BEAM PROPAGATION VERSUS HUYGENS METHOD IN NO-PARAXIAL CONDITIONS**

R. Gonzalo, P. Turullols, C. del Rio, M. Sorolla

Public University of Navarra, Spain

### **M5.6 GROOVE DIPLEXER FOR MILLIMETER WAVE APPLICATIONS**

A.S. Aydinlik, A.A. Vertiy, S.P. Gavrilov, S.R. Samedov

TÜB\_TAK, Marmara Research Center, Turkey

### **M5.7 WAVEGUIDE MODEL OF QUASI-OPTIC RESONATOR WITH SMALL-DIMENSION CORNER-ECHELETTE MIRROR**

O.I. Belous, A.I. Fisun, A.A. Kirilenko, V.I. Tkachenko

IRE, Ukraine

### **M5.8 MODELING OF RADAR SCATTERING CONDITIONS INSIDE A CIRCULAR HOLLOW DIELECTRIC WAVEGUIDE**

V.K. Kiseliyov, T.M. Kushta

IRE, Ukraine

### **M5.9 EXTINCTION AND BACKSCATTERING FOR A WAVEGUIDE INHOMOGENEITY**

V.K. Kiseliyov, T.M. Kushta

RE, Ukraine

## SESSION M6 - Atmospheric Studies

Monday, P.M.

July 21

**M6.1 FAR INFRARED SPECTROSCOPY OF THE EARTH'S STRATOSPHERE: BALLOON-BASED MEASUREMENTS OF COMPREHENSIVE HOX, NOX, AND CIOX FREE RADICAL CHEMISTRIES - (Invited)**

K. Chance, Smithsonian Astrophysical Observatory, USA

**M6.2 PUMPED PHONONS IN ATMOSPHERIC AEROSOLS**

H. A. Gebbie  
Imperial College, London, UK

**M6.3 INFRARED DIFFERENCE FREQUENCY GENERATION AND APPLICATIONS TO THE TRACE GASES MONITORING IN THE ATMOSPHERE**

W. Chen, J. Burie, D. Boucher  
Université du Littoral, France

**M6.4 LIQUID WATER FADE MARGIN REQUIREMENTS FOR INFRARED AND MILLIMETER WAVE RUNWAY IMAGING SENSORS IN FOG**

R.E. Marshall, D.A. de Wolf, C. Kontogeorgakis  
Research Triangle Institute, Virginia Polytechnic Institute and State University, USA

**M6.5 SUPER-RESOLUTION IN PASSIVE MILLIMETER WAVE RADIO-VISION**

Y.A.Pirogov, M.F. Attia, V.V. Gladun, A.I. Dubina, D.A. Tischenko, E.N. Terentiev,  
Moscow State University, Russia

**M6.6 ON POSSIBILITY OF REDUCTION OF MUTUAL INFLUENCE OF CLOUDY ATMOSPHERE TO PROBLEM OF RADIOMAPPING**

N.V. Ruzhentsev, Yu. A. Kuzmenko  
Radio Astronomy Institute, Ukraine

**M6.7 THE ALGORITHM OF RADIO IMAGES QUALITY IMPROVEMENT AT MM WAVES**

N.V. Ruzhentsev, Yu. A. Kuzmenko, V.P. Churilov  
Radio Astronomy Institute, Ukraine

## SESSION T1 - Gyrotrons I

Tuesday, A.M.

July 22

### **T1.1 LONG PULSE OPERATION OF 110 GHz, 1 MW GYROTRON**

V.E. Myasnikov, M.V. Agapova, V.V. Alikae, A.A. Bogdashov, A.A. Borschegovsky, G.G. Denisov, V.A. Flyagin, A. Sh. Fix, V.I. Ilyin, V.N. Ilyin, V.A. Khmara, D.V. Khmara, A.N. Kostyna, V.O. Nichiporenko, L.G. Popov, V.E. Zapevalov  
GYCOM, Russia

### **T1.2 STATUS OF THE 118 GHz, 0.5 MW QUASI-CW GYROTRON FOR THE TORE SUPRA AND TCV TOKAMAKS**

E. Giguët, Ph. Thouvenin, C. Tran, M. Pain, P. Garin, M.Q. Tran, S. Alberti, M. Thumm  
EUROATOM, France, Switzerland, and Germany

### **T1.3 DEVELOPMENT OF HIGH POWER 170GHz GYROTRON**

K. Sakamoto, A. Kasugai, K. Takahashi, M. Tsuneoka, Yu. Ikeda, T. Imai, T. Kariya, Y. Okazaki, K. Hayashi, Y. Mitsunaka, Y. Hirata  
JAERI and Toshiba Co., Japan

### **T1.4 DEVELOPMENT OF 1 MW OUTPUT POWER LEVEL GYROTRON FOR ITER**

V.E. Zapevalov, V.V. Alikae, G.G. Denisov, V.A. Flyagin, A. Sh. Fix, A. N. Kuftin, V.I. Kurbatov, V.E. Myasnikov  
GYCOM, Russia

### **T1.5 FREQUENCY MODULATION OF A SUB-MILLIMETER WAVE GYROTRON FU IV**

T. Idehara, T. Tatsukawa, I. Ogawa, M. Pereyaslavets, N. Nishida, K. Yoshida  
Fukui University, Japan

### **T1.6 INVESTIGATION OF COAXIAL GYROTRONS AT IAP RAS**

V.A. Flyagin, V.I. Khizhnyak, A.N. Kuftin, V.N. Manuilov, A.B. Pavelyev, V.G. Pavelyev, V.E. Zapevalov  
IAP, Russia

### **T1.7 OPERATION OF A COAXIAL GYROTRON WITH A DUAL RF-BEAM OUTPUT**

B. Piosczyk, O. Braz, G. Dammertz, C.T. Iatrou, S. Kern, M. Kuntze, G. Michel, A. Mobius, M. Thumm, V.A. Flyagin, V.I. Khizhnyak, A.B. Pavelyev, V.E. Zapevalov  
EUROATOM-FZK, Germany; IAP, Russia

### **T1.8 140 GHz CONFOCAL CAVITY GYROTRON EXPERIMENT**

W. Hu, M.A. Shapiro, K.E. Kreischer, and R.J. Temkin  
MIT, USA

### **T1.9 A HIGH-POWER 32 GHz PULSED GYROTRON**

J.J. Barroso, P.J. Castro, A.A. Pimenta, V.A. Spassov, R.A. Correa, T. Idehara, I. Ogawa  
INPE, Brazil; Fukui University, Japan

## SESSION T2 - Waveguides II

Tuesday, A.M.

July 22

- T2.1 THEORETICAL ANALYSIS OF COMPLETE MODE OF RECTANGULAR GROOVE WAVEGUIDE**  
Y.-Z. Xu, H.-S. Yang,  
Southeast University, PRC
- T2.2 EIGENMODES IN GYROTRON CORRUGATED COAXIAL CAVITY**  
R.A. Correa, J.J. Barroso, P.J. Castro  
INPE, Brazil
- T2.3 THE DISPERSION EQUATION OF THE HALF-CIRCULAR HELICAL-GROOVE STRUCTURE**  
G. Yu, W. Wang, Y. Wei, S. Liu  
University of Science and Technology of China, PRC
- T2.4 BROADSIDE COUPLED DIELECTRIC IMAGE GUIDE AT MILLIMETER WAVE FREQUENCIES**  
A.K. Rostogi, S. Mishra  
Dept. of Physics, Government MVAM, India
- T2.5 ENHANCEMENT OF THE QUALITY FACTOR OF SHIELDED DIELECTRIC RESONATOR BY GROOVING OF INSIDE SHIELD WALL**  
Y.A. Pirogov, E.V. Miriuriyeva  
Moscow State University, Russia
- T2.6 DISPERSION CHARACTERISTICS OF COPLANAR WAVEGUIDE WITH THICK METAL COATING**  
A.K. Rastogi  
Dept. of Physics, Government MVAM, India
- T2.7 ELECTROMAGNETIC VIBRATION IN SEMI-OPENED WAVEGUIDE JUNCTION WITH ANISOTROPIC DIELECTRIC**  
O.M. Lazarjev, A.A. Zvyagintsev, A.V. Strizhachenko  
Kharkov State University, Ukraine
- T2.8 EIGEN-MODES CLASSIFICATION OF CROSS-SHAPED WAVEGUIDE SPLITTERS**  
A.G. Yushchenko, S.F. Shibalkin  
National Technical University of Ukraine, Ukraine
- T2.9 WAVE RESISTANCE AND ATTENUATION OF THE CROSS-SHAPED PARTIALLY FILLED WAVEGUIDE**  
M.E. Ilchenko, A.G. Yushchenko, A.F. Zorkin  
National Technical University of Ukraine, Ukraine
- T2.10 THE PHYSICAL PECULIARITIES OF WAVE PROPAGATION IN COUPLED CYLINDRICAL SLOT LINES**  
A. Svezhentsev  
IRE, Ukraine
- T2.11 FREE OSCILLATIONS SPECTRUM IN RESONATOR ON EVANESCENT WAVEGUIDE WITH TWO-LAYER MAGNETO-DIELECTRIC**  
R.I. Belous, Yu. G. Makeev, A.P. Motornenko  
IRE, Ukraine

## SESSION T3 - Solid State Devices I

Tuesday, A.M.

July 22

### **T3.1 SUB-MILLIMETER-WAVE MIXERS**

I. Galin  
Aerojet, USA

### **T3.2 A NOVEL MICROMACHINED 1.6 THz MIXER**

S.T.G. Wootton, S.R. Davies, N.G. Cronin  
University of Bath, UK

### **T3.3 A SUBHARMONIC SCHOTTKY DIODE MIXER AT 650 GHz: MEASUREMENTS ON SCALED MODELS**

V.S. Möttönen, J.T. Louhi, P.V. Piironen, J. Zhang, A.O. Lehto, A.V. Räisänen  
Helsinki University of Technology, Finland

### **T3.4 AN OPTICALLY CONTROLLED MODULATOR USING A METAL STRIP GRATING ON A SILICON PLATE FOR MILLIMETER AND SUBMILLIMETER WAVELENGTHS**

J. Bae, T. Fujii, T. Uno, F. Takei, K. Maezaki, K. Mizuno  
Tohoku University, Japan

### **T3.5 MICROMACHINING TECHNOLOGY FOR TERAHERTZ APPLICATIONS**

S.R.Davies, H. Kazemi, J.G. Partridge, S.T.G. Wootton, N.J. Cronin  
University of Bath, UK

### **T3.6 MIXING AND RECTIFICATION PROPERTIES OF POINT CONTACTS**

S.K. Masalmeh, J. Korving  
Huygens Laboratory, Netherlands

### **T3.7 A TUNABLE ANTENNA-COUPLED INTERSUBBAND TERAHERTZ (TACIT) DETECTOR**

C. Cates, G. Briceno, J.B. Williams, M.S. Sherwin, K. Campman, A.C. Gossard  
University of California at Santa Barbara, USA

### **T3.8 COMPLEX PROPAGATION RESULTS IN 3-D OF THE GENERIC ARBITRARY BILATERAL FINLINES**

H.C.C. Fernandes, J.A.S. Neto  
Federal University of Rio Grande do Norte, Brazil

## SESSION T4 - Gyrotrons II

Tuesday, P.M.

July 22

- T4.1 DEVELOPMENT OF OUTPUT WINDOWS FOR HIGH-POWER LONG-PULSE GYROTRONS - (*Invited*)**  
M. Thumm  
FZK, Germany
- T4.2 DIELECTRIC LOSS MEASUREMENTS IN CVD DIAMOND WINDOWS FOR GYROTRONS**  
R. Heidinger, R. Schwab, R. Spörl, M. Thumm  
FZK, Germany
- T4.3 HIGH-POWER MILLIMETER-WAVE TRANSMISSION THROUGH CVD DIAMOND**  
M. Thumm, O. Braz, T. Imai, A. Kasugai, K. Sakamoto, K. Takahashi, M. Tsuneoka  
FZK, Germany; JAERI, Japan
- T4.4 A FORCED GAS-COOLED SINGLE DISK WINDOW FOR HIGH POWER CW MILLIMETER WAVES**  
T. Shimozuma, S. Morimoto, M. Sato, Y. Takita, S. Itoh, S. Kubo, H. Idei, K. Ohkubo, T. Watari,  
NIFS and Kanazawa Institute of Technology, Japan
- T4.5 D-BAND FREQUENCY STEP-TUNING OF A 1 MW GYROTRON USING A BREWSTER OUTPUT WINDOW**  
O. Braz, G. Dammertz, M. Kuntze, M. Thumm  
FZK, Germany
- T4.6 DIELECTRIC LOSS MEASUREMENTS WITH A CONFOCAL FABRY-PEROT RESONATOR**  
J.M. Dutta, C.R. Jones  
North Carolina Central University, USA
- T4.7 INFLUENCE OF WINDOW REFLECTIONS ON GYROTRON OPERATION**  
G. Dammertz, O. Braz, M. Kuntze, B. Piosczyk, M. Thumm  
FZK, Germany
- T4.8 ENHANCED FACE COOLED GYROTRON OUTPUT WINDOW**  
G.S. Haldeman  
MIT, USA
- T4.9 NUMERICAL SIMULATION OF PROCESSES OF MODE INTERACTION IN POWERFUL GYROTRONS**  
M.A. Moiseev, V.E. Zapevalov, N.A. Zavolskiy  
IAP, Russia
- T4.10 SCATTERING MATRIX DESCRIPTION OF COMPLETE GYROTRON OSCILLATORS**  
D. Wagner, G. Gantenbein, W. Kasperek, M. Thumm, T. Idehara  
FZK, Germany and Fukui University, Japan



## SESSION T5 - Numerical Methods I

Tuesday, P.M.

July 22

**T5.1 RIGOROUS ANALYSIS OF SLOTTED-CIRCULAR COAXIAL WAVEGUIDES USED IN SOME RF VACUUM ELECTRONIC DEVICES**

J.-Y. Raguin, K. Schünemann,  
Technische Universität Hamburg-Harburg, Germany

**T5.2 EIGENMODES OF MICROWAVE CAVITIES CONTAINING HIGH-LOSS DIELECTRIC MATERIALS**

S.J. Cooke, B. Levush  
NRL, USA

**T5.3 MAGY: A SELF-CONSISTENT CODE FOR MODELING ELECTRON BEAM DEVICES**

M. Botton, T.M. Antonsen, B. Levush  
University of Maryland and NRL, USA

**T5.4 STABLE NUMERICAL SOLUTION OF SOURCE DRIVEN EVANESCENT EQUATIONS, APPLICATION TO BEAM-RF WAVE SIMULATION**

R.H. Jackson  
NRL, USA

**T5.5 NOVEL APPLICATION OF MODAL EXPANSION METHOD TO TIME-DOMAIN ANALYSIS OF GYROTRONS**

J. Jelonnek, K. Schünemann  
Technische Universität Hamburg-Harburg, Germany

**T5.6 2D DYADIC GREEN'S FUNCTION FOR HOMOGENEOUS FERRITE MICROSTRIP CIRCULATOR WITH SOFT WALLS**

C.M. Krowne  
NRL, USA

**T5.7 ANALYSIS OF TWO-DIMENSIONAL DIELECTRIC GRATINGS FOR THE DESIGN OF DICHROIC STRUCTURES**

I.T. Lima, Jr, A.J. Giarola  
State University of Campinas, Brazil

**T5.8 HOMOGENEOUS FERRITE MICROSTRIP CIRCULATOR 3D DYADIC GREEN'S FUNCTION WITH AND WITHOUT PERIMETER INTERFACIAL WALLS**

C.M. Krowne  
NRL, USA

## SESSION T6 - Solid State Devices II

Tuesday, P.M.

July 22

- T6.1 FAR INFRARED INVESTIGATION OF MAGNETIC RESONANCES IN CONDUCTING MAGNETIC THIN FILMS, e.g. Cr AND RARE EARTH METALS, AND INSULATING THIN FILMS, e.g. NiO**  
S.R.P. Smith, T.J. Parker, S.A. Feiven  
University of Essex, UK
- T6.2 A COMPLETE FREQUENCY-FIELD CHART FOR THE ANTI-FERROMAGNETIC RESONANCE IN MnF<sub>2</sub>**  
M. Hagiwara, K. Katsumata, H. Yamaguchi, I. Yamada, M. Gross, P. Goy,  
RIKEN, Japan
- T6.3 TERAHERTZ RADIATION FROM COHERENT PHONONS EXCITED IN SEMICONDUCTORS**  
M. Tani, H. Abe, R. Fukasawa, S. Matsuura, K. Sakai, S. Nakashima  
Kansai Advanced Research Center and Osaka University, Japan
- T6.4 TRANSITION FROM SEMI-CLASSICAL TO QUANTUM MECHANICAL LIMIT OF TERAHERTZ TUNNEL IONIZATION OF DEEP IMPURITIES**  
S.D. Ganichev, I.N. Yassievich, E. Ziemann, Th. Gleim, W. Prettl  
Universität Regensburg, Germany; Ioffe Institute, Russia
- T6.5 TERAHERTZ MIXING WITH HIGH-T<sub>c</sub> SUPERCONDUCTORS**  
W. Prettl  
Universität Regensburg, Germany
- T6.6 FAR IR TRANSMISSION SPECTRA OF HIGH-T<sub>c</sub> SUPERCONDUCTOR FILMS OF YBCO**  
M. Tazawa, X. Gerbaux, A. Hadni  
National Industrial Research Institute of Nagoya, Japan  
Université de Nancy, France
- T6.7 COUPLED SUPERCONDUCTIVITY IN OPENED AND CLOSED MICROSTRIP WITH VARIOUS SEMICONDUCTOR SUBSTRATS**  
H.C.C. Fernandes, G.A.B. Lima  
Federal University of Rio Grande do Norte, Brazil
- T6.8 HOST AND IMPURITY MAGNETIC EXCITATIONS IN RARE-EARTH CUPRATE CRYSTALS**  
V. Eremenko  
Institute for Low Temperature Physics and Engineering, Ukraine
- T6.9 IMPURITY ESR-ABSORPTION ANISOTROPY IN DIAMAGNETIC MgO CRYSTAL**  
V. Pishko  
Institute for Low Temperature Physics and Engineering, Ukraine
- T6.10 FERROELECTRIC FILMS INVESTIGATIONS**  
M.E. Ilchenko, Yu. M. Poplavko, A.G. Yushchenko, L.P. Pereverzeva, Yu. V. Prokopenko  
National Technical University of Ukraine, Ukraine

## SESSION W1 - Gyrotrons III

Wednesday, A.M.

July 23

### **W1.1 IMPLICATION OF DC SPACE CHARGE INDUCED VELOCITY SPREAD ON GYROTRON GUN PERFORMANCE**

C. Liu, T.M. Antonsen Jr.  
University of Maryland, USA

### **W1.2 MEASUREMENT AND INTERPRETATION OF ELECTRON ENERGY SPECTRA IN GYROTRONS**

V. Bratman, M. Glyavin, A. Goldenberg, A. Savilov, N. Venediktov, V. Zapevalov  
IAP, Russia

### **W1.3 STUDY OF HELICAL ELECTRON BEAM PROPERTIES FOR POWERFUL GYROTRONS**

A.N. Kuftin, V.K. Lygin, V.N. Manuilov, Sh.E. Tsimring, V.E. Zapevalov  
IAP, Russia

### **W1.4 A NEW ALGORITHM FOR TRACING BACK-SCATTERED ELECTRONS**

A. Singh, S. Rajapatirana, V.L. Granatstein  
University of Maryland, USA

### **W1.5 EXPERIMENTAL AND SIMULATION STUDY OF THE THERMAL CHARACTERISTICS OF A MIG-TYPE ELECTRON GUN FOR A 32 GHz, 100 kW GYROTRON**

H. Patire, Jr., J.J. Barroso  
INPE, Brazil

### **W1.6 THE FIRST EXPERIMENTS ON AN 84 GHz GYROTRON WITH A SINGLE STAGE DEPRESSED COLLECTOR**

T. Shimosuma, M. Sato, Y. Takita, S. Itoh, S. Kubo, H. Idei, K. Ohkubo, T. Watari, T.S. Chu, K. Felch, C.M. Loring, Jr.  
NIFS, Japan, CPI, USA

### **W1.7 DEVELOPMENT OF A MULTI-STAGE DEPRESSED COLLECTOR FOR 1 MW CW GYROTRONS**

R. L. Ives, Y.M. Mizuhara, R.S. Schumacher, A. Singh, S. Rajapatirana, V.L. Granatstein  
Calabazas Creek Research and University of Maryland, USA

### **W1.8 DESIGN OF MAGNETRON INJECTION GUN FOR HIGH AVERAGE POWER 94 GHz GYRO-AMPLIFIERS**

K. Nguyen, B. Danly, B. Levush, M. Blank, D. True, K. Felch, P. Borchard  
NRL, Litton, and CPI, USA

### **W1.9 ELECTRON GUN DEVELOPMENT FOR HIGH POWER LOW VELOCITY-SPREAD AXIS-ENCIRCLING BEAM**

D. Gallagher, J. Richards, F. Scafuri, C. Armstrong  
Northrop-Grumman, USA

### **W1.10 PSEUDOSPARK CATHODE, ELECTRON BEAM AND MICROWAVE PRODUCTION, THEORY AND EXPERIMENT**

H. Yin, A.D.R. Phelps, W. Ho, C.R.M. Robb, P. Aitken, B.W.J. McNeil, A.W. Cross, C.G. Whyte  
University of Strathclyde, Scotland, UK

## SESSION W2 - Vacuum Sources

Wednesday, A.M.

July 23

### **W2.1 MILLIMETER POWER MODULE PERFORMANCE REVIEW**

G. Lednum, T. Ninnis, T. Schoemehl, N. Chiang, J. Shumaker, R. Kopeck, P. Ballagh  
Litton Systems, USA

### **W2.2 THEORY OF THE CLINOTRON**

K. Schünemann, D.M. Vavriv, K. Yemelyanov  
Technische Universität Hamburg-Harburg, Germany

### **W2.3 EXPERIMENTS OF SPACE HARMONIC PENIOTRON**

K. Yokoo  
Research Institute of Electrical Communication, Tohoku University, Japan

### **W2.4 THEORY OF ELECTRON BEAM-WAVE INTERACTION IN WAVEGUIDE FILLED WITH PLASMA IN AXIAL MAGNETIC FIELD**

S. Liu, et al.  
University of Electronic Science and Technology of China, PRC

### **W2.5 EFFECTIVE MILLIMETRIC NOISE SOURCES WITH CONTROLLED CHARACTERISTICS**

V.A. Rakityansky,  
IRE, Ukraine

### **W2.6 DESIGNING OF MM-WAVE LNA**

I. Sunduchkov, K. Sunduchkov, B. Shelkovnikov  
Saturn and National Technical University, Ukraine

### **W2.7 MILLIMETER WAVE COLD-CATHODE COAXIAL TWT**

V.D. Yeremka, M.O. Khorunzhiy  
IRE, Ukraine

### **W2.8 RIGOROUS THEORY OF THE ELECTRON BEAM-ELECTROMAGNETIC WAVES INTERACTION IN PERIODIC STRUCTURES**

I.L. Verbitskii  
Kharkov State Pedagogical University, Ukraine

### **W2.9 STUDY OF ELECTRON-WAVE INTERACTION IN THE TWO OPEN-RESONATOR ELECTRODYNAMICAL SYSTEM**

Y.A. Myasin, V.V. Evdokimov, S.G. Tchigarev, M.B. Tseytlin, T.A. Mazur, A. Yu. Ilyin  
IREE, Russia

### **W2.10 PHASE-LOCKING MICROWAVE OSCILLATOR WITH PROFILED DC MAGNETIC FIELD**

E. Odarenko, A. Shmat'ko  
Kharkov State University, Ukraine

### **W2.11 MILLIMETER AND SUBMILLIMETER CW CLINOTRONS**

S. Churilova, Ye. Lysenko  
Institute of Radio Astronomy, Ukraine

### **W2.12 MILLIMETER WAVE PENIOMAGNETRON**

V.D. Yeremka  
IRE, Ukraine

### **W2.13 INFLUENCE OF NON-RESONANCE STANDING WAVE FIELD COMPONENTS ON THE PERFORMANCE CHARACTERISTICS OF MMW AUTORESONANCE PENIOTRON-OSCILLATOR**

V.D. Yeremka  
IRE, Ukraine

## SESSION W3 - Lasers

Wednesday, A.M.

July 23

### **W3.1 HYDRAZINE, THE FORGOTTEN FIR LASING GAS - (Invited)**

E.C.C. Vasconcellos  
Universidade Estadual de Campinas, Brazil

### **W3.2 FAR-INFRARED LASER MAGNETIC RESONANCE - (Invited)**

K.E. Evenson and J. M. Brown  
NIST, USA and Oxford University, UK

### **W3.3 OPTICALLY PUMPED FAR INFRARED MOLECULAR LASERS: MOLECULAR AND EXPERIMENTAL ASPECTS**

I. Mukhopadhyay, S. Singh  
Centre for Advanced Technology, India

### **W3.4 NEW OPTICALLY PUMPED FIR LASER LINES FROM CD3OH**

E.M. Telles, L.R. Zink, K.M.  
Evenson, NIST, USA

### **W3.5 CROSS-SATURATED GAINS AND DISPERSION OF OPTICALLY PUMPED FAR-INFRARED LASER MEDIA IN A RING CAVITY**

N. Sokabe, M. Hasegawa, S. Yamakawa, N. Togawa, Y. Horiuchi  
Osaka City University and Nara National Institute of Technology, Japan

### **W3.6 NEW FAR-INFRARED LASER LINES FROM N<sub>2</sub>O LASER PUMPED HYDRAZINE AND FREQUENCY MEASUREMENTS**

E.C.C. Vasconcellos, M. Tachikawa, L.R. Zink, K.M. Evenson  
Universidade Estadual de Campinas, Brazil

### **W3.7 ACTIVE MODE LOCKING OF A *p*-Ge HOT HOLE LASER**

J.N. Hovenier, A.V. Muravjov, S.G. Pavlov, V.N. Shastin, R.C. Strijbos, W.  
Th. Wenckebach  
Delft University of Technology, Netherlands; Institute for Physics of  
Microstructures, Russia

### **W3.8 PROBLEMS IN REALISING A LONG PULSE, HIGH DUTY CYCLE *p*-Ge LANDAU LEVEL FAR-IR LASER**

P.D. Coleman, D. Cronin  
University of Illinois, USA

### **W3.9 ACCURATE FREQUENCY MEASUREMENTS OF OPTICALLY PUMPED FIR LASER LINES**

E.M. Telles, L.R. Zink, K.M. Evenson  
NIST, USA

### **W3.10 TRANSITIONAL PROCESSES IN HCN-LASER PLASMA**

Yu.Yu. Kamenev  
IRE, Ukraine

## SESSION Th1 - Gyrotrons IV

Thursday, A.M.

July 24

### **Th1.1 EXPERIMENTAL STUDY OF A HIGH POWER W-BAND GYRO-KLYSTRON AMPLIFIER - (Invited)**

M. Blank, B.G. Danly, P.E. Latham, B. Levush  
NRL, USA

### **Th1.2 DEVELOPMENT OF A W-BAND GYROKLYSTRON FOR RADAR APPLICATIONS**

B. Danly, M. Blank, J. Calame, S. Cooke, B. Levush, W. Manheimer, A. McCurdy, K. Nguyen, D. Pershing, J. Petillo, R. Parker, T. Hargreaves, A. Theiss, R. True, K. Felch, T.S. Chu, H. Jory, P. Borchard, W. Lawson, T. Antonsen -- NRL, Litton, CPI and University of Maryland, USA

### **Th1.3 EXPERIMENTS ON HIGH POWER 35 GHz GYROKLYSTRON AMPLIFIERS**

J.J. Choi, A.H. McCurdy, R.H. Kyser, F. Wood, B.G. Danly, B. Levush, R.K. Parker  
NRL, USA

### **Th1.4 INPUT COUPLER DESIGN FOR THE NRL/INDUSTRIAL 94 GHz GYROKLYSTRON AMPLIFIER**

D. Pershing, K. Nguyen, J. Petillo, M. Blank, J. Calame, T. Hargreaves, B. Danly  
NRL and Litton, USA

### **Th1.5 PHASE AND AMPLITUDE NOISE STUDY OF THE NRL GYRO-KLYSTRON AMPLIFIER**

G.S. Nusinovich, M. Garven, O. Dumbrajs, B.G. Danly  
University of Maryland and NRL, USA; Helsinki University of Technology, Finland

### **Th1.6 PHASE STABILITY AND NOISE MEASUREMENTS OF GYRO-KLYSTRON AMPLIFIERS**

M. Garven, B.G. Danly, M. Blank, M.J. Siegert  
NRL and University of Maryland, USA

### **Th1.7 OPERATION OF TWO- AND THREE-CAVITY FIRST HARMONIC COAXIAL X-BAND GYROKLYSTRONS**

W. Lawson, J.P. Calame, M. Castle, J. Cheng, V.L. Granatstein, B. Hogan, M. Reiser and G.P. Saraph  
University of Maryland, USA

### **Th1.8 SCALING LAW FOR BALLISTIC BUNCHING IN MULTICAVITY HARMONIC GYROKLYSTRONS**

G.S. Nusinovich, G.P. Saraph, V.L. Granatstein  
University of Maryland, USA

### **Th1.9 HFSS SIMULATIONS OF AN ADVANCED CONCEPT GYRO-KLYSTRON**

G.P. Saraph, J.P. Anderson, W. Lawson  
University of Maryland, USA

### **Th1.10 THEORY OF MULTI-BEAM STAGGER TUNED GYROKLYSTRONS**

G.S. Nusinovich, B. Levush, B. Danly  
University of Maryland and NRL, USA

### **Th1.11 FREQUENCY TUNABILITY AND PHASE STABILITY OF RELATIVISTIC GYROKLYSTRON AMPLIFIERS**

G.P. Saraph -- University of Maryland, USA

## SESSION Th2 - Solid State Sources

Thursday, A.M.

July 24

### **Th2.1 A HORN ANTENNA COUPLED QUASI-OPTICAL OSCILLATOR WITH GUNN DIODES AT MILLIMETER WAVELENGTHS**

J. Bae, T. Uno, H. Mazaki, T. Fujii, F. Takei, K. Mizuno  
Tohoku University and RIKEN, Japan

### **Th2.2 DESIGN OF NEW MILLIMETER WAVE SOURCES USING ELECTRICALLY THICK MONOLITHIC SUBSTRATE MODE RESONANT COMBINERS**

D.W. Griffin, A.A. Sayyah  
University of Adelaide, Australia

### **Th2.3 MODELING OF InGaN-GaN MODULATION-DOPED FIELD-EFFECT TRANSISTORS FOR 60 GHz OPERATION**

S.K. Islam, F.C. Jain  
University of North Florida and University of Connecticut, USA

### **Th2.4 A HIGH-POWER, MILLIMETER-WAVE BALANCED DOUBLER**

D. Porterfield, T. Crowe, R. Bradley, N. Erickson  
University of Virginia; National Radio-Astronomy Observatory; and Five College Radio-Astronomy Observatory, USA

### **Th2.5 A FREQUENCY DOUBLER FOR 200 GHz WITH A PLANAR SCHOTTKY VARACTOR**

J.T. Louhi, A.V. Räisänen, Helsinki  
University of Technology, Finland

### **Th2.6 A 300 GHz INTEGRATED QUASIOPTICAL SCHOTTKY FREQUENCY MULTIPLIER**

M. Shaalan -- Technical University of Darmstadt, Germany

### **Th2.7 NOVEL FABRICATION PROCESS FOR HIGHLY RELIABLE REFRACTORY metal/n-GaAs SCHOTTKY DIODES**

B.K. Sarpong, T.W. Crowe, W.L. Bishop, P.J. Koh  
University of Virginia, USA

### **Th2.8 GENERATION OF SUBMILLIMETER-WAVE PULSES OF VARIABLE DURATION USING OPTICALLY EXCITED SILICON PLATES**

H. Minamide, T. Nozokido, K. Mizuno  
Tohoku Univeristy and RIKEN, Japan

### **Th2.9 GaAs SCHOTTKY DIODES FOR THz APPLICATIONS**

P. Gleeson, J. Pike, P. Maaskant, W.M. Kelly, A. Simon, C.I. Lin, H.L. Hartnagel  
National Microelectronics Research Center, Ireland; Institut fur Hochfrequenztechnik, Germany

### **Th2.10 AUTO-MODULATION AND AUTO-THERMOSTABILIZATION OF OUTPUT POWER LEVEL IN MILLIMETER WAVE IMPATT-DIODE**

Y.A. Pirogov, V.V. Gladun  
Moscow State University, Russia

### **Th2.11 MILLIMETER WAVE EVANESCENT MODE GUNN OSCILLATOR IN SUSPENDED STRIPLINE CONFIGURATION**

A.K. Poddar, S.K. Koul, B. Bhat  
Indian Insitute of Technology, India

### **Th2.12 ACTIVE CONFORMABLE MICROSTRIP ANTENNA ARRAY**

J.X. Ge, Y.X. Li  
Beijing University of Aeronautics and Astronautics, PRC

## SESSION Th3 - Spectroscopy

Thursday, A.M.

July 24

### **Th3.1 INFRARED MEGAGAUSS-SPECTROSCOPY: A CHALLENGE IN SOLID STATE PHYSICS - (*Invited*)**

N. Puhlmann

Humboldt-University, Germany

### **Th3.2 DETERMINATION OF THE ANISOTROPY OF THE EFFECTIVE MASSES OF ELECTRONS AND HOLES IN DOPED GaN EPI-LAYERS BY FAR INFRARED SPECTROSCOPY - (*Invited*)**

G. Mirjalili, R.A. Levett, T.J. Parker, T.S. Cheng, C.T. Foxon

University of Essex and University of Nottingham, UK; University of Yazd, Iran

### **Th3.3 A COMPACT COHERENT THz SOURCE BY PHOTOMIXING OF DIODE-LASERS IN A PHOTOCONDUCTIVE ANTENNA FOR HIGH-RESOLUTION SPECTROSCOPY**

S. Matsuura, M. Tani, H. Abe, K. Sakai, S. Saito, H. Ozeki

Kansai Advanced Research Center and Institute for Molecular Science, Japan

### **Th3.4 TUNABLE FAR-INFRARED SPECTROSCOPY IN THE 6 TO 8 THz REGION**

H. Odashima, M. Tachikawa, L.R. Zink, K.M. Evenson

Toyama University, Japan; NIST, Boulder, CO, USA



## SESSION Th4 - Gyro-amplifiers

Thursday, P.M.

July 24

### **Th4.1 GYRO-TRAVELING-WAVE-TUBES - (Invited)**

K.R. Chu  
National Tsing Hua University, Taiwan

### **Th4.2 STUDY OF X-BAND THREE-STAGE GYROTWYSTRON AMPLIFIER**

E.V. Zasytkin, B. Levush, M. Blank, E.V. Sokolov, I.I. Antakov  
IAP, Russia; NRL, USA

### **Th4.3 LINEAR THEORY OF THE GYRO-TWYSTRON WITH STAGGER-TUNED PREBUNCHING CAVITIES**

G.S. Nusinovich, V.K. Tripathi, W. Chen  
University of Maryland, USA

### **Th4.4 A HIGH PERFORMANCE, FREQUENCY DOUBLING, INVERTED GYROTWYSTRON**

H. Guo, S.H. Chen, V.L. Granatstein, J. Rodgers, G. Nusinovich, M. Walter, W.J. Chen  
University of Maryland, USA

### **Th4.5 THEORY OF THE INVERTED GYRO-TWYSTRON**

G. Nusinovich, M. Walter, V.L. Granatstein  
University of Maryland, USA

### **Th4.6 GYRO-TWT WITH A HELICAL OPERATING WAVEGUIDE: NEW POSSIBILITIES TO ENHANCE EFFICIENCY AND FREQUENCY BANDWIDTH**

G.G. Denisov, V.L. Bratman, A.D.R. Phelps, S.V. Samsonov  
IAP, Russia; University of Strathclyde, Scotland, UK

### **Th4.7 DESIGN OF AN EFFICIENT BROADBAND 250 kW Ka-BAND GHz AMPLIFIER**

W. Lawson, M.R. Arjona, G.P. Saraph  
University of Maryland, USA

### **Th4.8 STUDY OF TRANSIENT EFFECTS IN INJECTION LOCKED GYROTRONS**

J. Jelonnek, K. Schünemann  
Technical University of Hamburg-Harburg, Germany

### **Th4.9 THE CYCLOTRON RESONANCE MASER INTERACTION IN A LONG NONUNIFORM SYSTEM: APPLICATION TO THE GYROTRON BEAM TUNNEL**

J.L. Vomvouridis, I.G. Tigelis  
National Technical University of Athens, and University of Athens, Greece

### **Th4.10 DENSITY AND ENERGY MODULATION OF A GYROTRON ELECTRON BEAM IN A PERIODICALLY CORRUGATED BEAM TUNNEL**

A. Lazaros, J.L. Vomvouridis  
National Technical University of Athens, Greece

### **Th4.11 HIGH-FREQUENCY NON-CYLINDRICAL MODES IN A DIELECTRICALLY LOADED CORRUGATED GYROTRON BEAM TUNNEL**

S. Tzima, I.G. Tigelis, J.L. Vomvouridis  
University of Athens and National Technical University of Athens, Greece

## SESSION Th5 - Applications

Thursday, P.M.

July 24

### **Th5.1 THE MICROWAVE SINTERING OF CERAMICS: NEW INSIGHTS, MODELS, AND APPLICATIONS BASED ON REALISTIC CERAMIC MICRO STRUCTURES - (*Invited*)**

J.P. Calame, Y. Carmel, D. Gershon, E. Pert  
University of Maryland, USA

### **Th5.2 MILLIMETER-WAVE SINTERING OF CERAMIC COMPACTS**

A.W. Fliflet, R.W. Bruce, R.P. Fischer, A.K. Kinkead, D. Lewis, III, B.A. Bender, G.-M. Chow, R.J. Rayne, L.K. Kurihara, P.E. Schoen  
NRL, USA

### **Th5.3 INITIAL TESTING OF A CW QUASI-OPTICAL GYROTRON FOR MATERIALS PROCESSING**

R.P. Fischer, A.W. Fliflet  
NRL, USA

### **Th5.4 SCANNING NEAR-FIELD MILLIMETER-WAVE MICROSCOPY USING A METAL SLIT AS A SCANNING PROBE**

T. Nozokido, J. Bae, T. Fujii, M. Ito, K. Mizuno  
RIKEN and Tohoku University, Japan

### **Th5.5 TOMOGRAPHY SYSTEM AT MILLIMETER WAVEBAND**

A. Vertiy, S. Gavrilov, D.S. Arman, S.R. Samedov  
Marmara Research Center, Turkey; IRE, Ukraine

### **Th5.6 APPLICATION OF F-BAND GYROTRON FOR SUPERCONDUCTING MAGNETIC FUSION**

S. Ahn, R. Temkin  
NRL and MIT, USA

### **Th5.7 THE INFLUENCE OF IONIZATION AND STRICTION NONLINEARITIES ON THE SURFACE WAVES SELF-INTERACTION IN MICROWAVE GAS DISCHARGE PLASMAS**

K.N. Ostrikov  
Kharkov State University and Kharkov Fire Safety Institute, Ukraine

## SESSION Th6 - Solid State Devices III

Thursday, P.M.

July 24

**Th6.1 DIRECT TRANSFORMATION OF THE VIDEOPULSE INTO  
RADIOPULSE ON TRANSMISSION LINES ON THE BASIS OF  
MULTILAYER HETEROSTRUCTURES**

A.M. Belyantsev, A.B. Kozyrev  
Institute for Physics of Microstructures, Russia

**Th6.2 HIGH-FREQUENCY PROPERTIES OF THE DOUBLE LAYER  
ELECTRON SYSTEM**

I.E. Aronov, Yu. O. Averkov, N.N. Beletskii  
IRE, Ukraine

**Th6.3 COLLECTIVE MODES OF SEMI-CONDUCTOR SUPERLATTICE  
IN A HIGH MAGNETIC FIELD**

I.E. Aronov, N.N. Beletskii, J.V. Bludov  
IRE, Ukraine

**Th6.4 CHARACTERIZATION OF THE FREQUENCY MEASUREMENT  
TECHNIQUE FOR MICROWAVE SIGNALS BASED ON HISTO-  
GRAM ANALYSIS OF THE CURRENT-VOLTAGE CURVE OF THE  
JOSEPHSON JUNCTION**

N.V. Kovalenko  
FONON, Ukraine

**Th6.5 SURFACE MAGNETOPLASMA WAVES IN A SEMICONDUCTOR-  
SEMICONDUCTOR STRUCTURE WITH A NON-UNIFORM TRAN-  
SIENT LAYER**

N.A. Azarenkov, A.V. Gapon, K.N. Ostrikov  
Kharkov State University and Kharkov Fire Safety Institute, Ukraine

**Th6.6 THE USE OF AUTOCORRELATION FUNCTION OF THE JOSEPH-  
SON JUNCTION RESPONSE SIGNAL FOR MICROWAVE SIGNAL  
SPECTROMETRY**

V.V. Kamychine  
FONON, Ukraine

## SESSION F1 - Relativistic Sources

Friday, A.M.

July 25

- F1.1 GENERATION OF ULTRASHORT MILLIMETER-WAVE PULSES BASED ON SUPERRADIANCE - (Invited)**  
N.S. Ginzburg, A.D.R. Phelps, M.I. Yalandin,  
IAP, Russia; Univ. of Strathclyde, Scotland, UK; Inst. of Electrophysics, Russia
- F1.2 DEVELOPMENT OF A 50 MW MAGNICON AMPLIFIER AT 11.4 GHz**  
S.H. Gold, A.W. Fliflet, A.K. Kinkead, B. Hafizi, O.A. Nezhevenko, V.P. Yakovlev, J.L. Hirshfield, R. True  
NRL, Icarus Research, Omega-P and Litton, USA
- F1.3 OSCILLATION OF TE<sub>11</sub> MODE FROM A HIGH POWER BACKWARD WAVE OSCILLATOR**  
K. Minami, K. Tanaka, X.D. Zheng, Y. Carmel, T.M. Antonsen, Jr., A.N. Vlasov, V.L. Granatstein  
Niigata University, Japan; University of Maryland, USA
- F1.4 COHERENT TRANSITION RADIATION PRODUCED BY A 1.2 MeV ELECTRON BEAM**  
C.R. Jones, J.M. Dutta, H. Kosai, S.V. Benson  
North Carolina Central University and TJNAF, USA
- F1.5 THE ANGULAR DISTRIBUTION OF POWER PRODUCED BY SMITH-PURCELL RADIATION**  
J.H. Brownell, G. Doucas, M.F. Kimmitt, J.H. Mulvey, M. Omori, J.E. Walsh  
Dartmouth College, USA; University of Oxford and University of Essex, England
- F1.6 HIGH POWER MICROWAVE EMISSION OF LARGE AND SMALL ORBIT RECTANGULAR CROSS SECTION GYROTRONS**  
J.M. Hochman, R.M. Gilgenbach, R.L. Jaynes, J.I. Rintamaki, Y.Y. Lau, T.A. Spencer  
University of Michigan, USA
- F1.7 HIERARCHIC THEORY OF OSCILLATIONS AND WAVES AND ITS APPLICATION FOR PROBLEMS OF RELATIVISTIC ELECTRONICS**  
V. V. Kulish, O.B. Krutko  
Sumy University, Ukraine
- F1.8 APPLICATION OF THE THEORY OF HIERARCHIC OSCILLATIONS AND WAVES FOR INVESTIGATION OF NON-LINEAR PROCESSES IN THE GYRO-RESONANCE SYSTEMS**  
V.V. Kulish, O.B. Krutko, A.G. Kailuyk  
Sumy University, Ukraine
- F1.9 EFFECT OF RELATIVISTIC ELECTRON BEAM COOLING IN THE ACCELERATING SYSTEM WITH CROSSED MAGNETIC AND VORTEX ELECTRIC UNDULATED FIELD**  
V.V. Kulish, P.B. Kosel, O.B. Krutko, I.V. Gubanov  
Sumy University, Ukraine
- F1.10 NONLINEAR THEORY OF THE RELATIVISTIC OROTRON**  
E. Odarenko, V. Chursin, A. Shmat'ko  
Kharkov State University, Ukraine
- F1.11 TRANSITION RADIATION OF CHARGE IN MEDIA WITH POTENTIAL**  
V.L. Falko, S.I. Khankina, V.M. Yakovenko  
IRE, Ukraine

## SESSION F2 - Biological Applications

Friday, A.M.

July 25

### **F2.1 BIOLOGICAL EFFECT OF COHERENT RADIATION OF HYPER-HIGH FREQUENCY WHEN IRRADIATING ACUPUNCTURAL ZONES**

V.K. Kiseliyov, E.M. Kuleshov, Yu. E. Kamenev, V.I. Makolinet, O.P. Timoshenko, B.N. Shevtsov  
IRE and Institute of Orthopedics and Traumatology, Ukraine

### **F2.2 THE POSSIBILITY OF EMPLOYING LASER RADIATION OF HYPERHIGH FREQUENCY IN ORTHOPEDICS AND TRAUMATOLOGY**

V.K. Kiseliyov, E.M. Kuleshov, Yu. E. Kamenev, V.I. Makolinet, O.P. Timoshenko, C.D. Shevchenko  
IRE and Institute of Orthopedics and Traumatology, Ukraine

### **F2.3 LOW-ENERGETIC PICOSECOND PULSE ELECTROMAGNETIC FIELDS OF EHF INTERACTIONS WITH TISSUE: ANALYTICAL DESCRIPTIONS OF ULTRASHORT OPTICAL PULSE PROPAGATION IN AN HETEROGENEOUSLY BROADENED BIOMEDIUM**

Y.V. Chovnjuk  
Kiev State Technical University of Construction and Architecture, Ukraine

### **F2.4 NOISE INDUCED TRANSITIONS IN TISSUE INTERACTIONS WITH WEAK ELECTROMAGNETIC FIELDS OF EXTRA HIGH FREQUENCY (EHF)**

Y.V. Chovnjuk,  
Kiev State Technical University of Construction and Architecture, Ukraine

### **F2.5 INFORMATIONAL-ENTROPY CONCEPTIONS IN ANALYSIS AND MODELLING OF THE MAIN PROBLEMS OF THE INTERACTION BETWEEN MILLIMETER WAVES AND TISSUE: STOCHASTIC DIFFERENTIAL EQUATIONS, MARKOVIAN AND DIFFUSIONAL PROCESSES, AND THEIR TRAJECTORIES**

Y.V. Chovnjuk, L.I. Turchaninova  
Kiev State Technical University of Construction and Architecture, Ukraine

### **F2.6 PHENOMENOLOGICAL ANALYSIS OF MILLIMETER WAVE INTERACTION AND ABSORPTION BY THE BIO-OBJECTS WITH CHIRAL PROPERTIES: MODELS FOR THE COMPLEX DIELECTRICAL PERMITTIVITY AND VOLUME MODEL'S POLARIZATION**

Y.V. Chovnjuk, I.A. Ivanchenko, L.V. Sveshnikova  
Kiev State Technical University of Construction and Architecture, and Scientific Research Center (VIDHUK), Ukraine

## SESSION F3 - Numerical Methods II

Friday, A.M.

July 25

### **F3.1 A GENERALIZED FDTD COMPUTATION METHOD**

Z. Zhang, L. He  
Southeast University, PRC

### **F3.2 THE TTL METHOD APPLIED TO THE FINLINE COUPLER**

H.C.C. Fernandes, S.A.P. Silva, L.C. de Freitas, Jr.  
Federal University of Rio Grande do Norte, Brazil

### **F3.3 ANALYSIS OF ELECTROMAGNETIC WAVES SCATTERING BY A DIELECTRIC CYLINDER IN RECTANGULAR WAVEGUIDE**

V. Kalesinskas, A. Konstantinov, V. Shugurov  
Vilnius University, Lithuania

### **F3.4 GENERALIZED FOURIER SERIESEXPANSION METHOD FOR DETERMINING VCO OF ELLIPTICAL OPTICAL WAVEGUIDES**

Y.H. Wang, X. Zhang  
Shanghai Transmission Lines Research Institute, PRC

### **F3.5 CAD-ORIENTED NUMERICAL ANALYSIS OF SURFACE-WAVE FILTERS**

S.V. Boriskina, A.I. Nosich  
Kharkov State University and IRE, Ukrainian Academy of Sciences, Ukraine

# Organization of the Digest

The bulk of the papers received for the conference are published in what follows in sequence as they will be delivered at the conference. However, there are exceptions which were necessitated by authors either not submitting digest papers, submitting papers which were too long, or submitting papers too late to be included in the regular sequence. In the case of authors who failed to submit a digest contribution or whose contribution was too long, it was decided to print the abstracts immediately following the regular digest contributions. In these cases, it was possible to include the abstracts in the index. However, in several cases, the digest contributions were received too late for that and it was decided to print these papers in a special section which follows the index.

## Material Processing with Microwave Radiation

R. Roy, P. D. Gigl, and D. Agrawal  
Materials Research Laboratory  
The Pennsylvania State University  
University Park, Pennsylvania 16802

Innovative processing of materials continues to be the key to new developments in this field since one of the fundamental ways to approach new, better, faster, or greener material is through new processing methods. What else is materials processing other than the dynamic control of energy within a system? One such method, which injects energy directly into the materials that are being reacted and/or sintered, is the application of microwave radiation as an energy source. This is the topic of this presentation.

Of course, this energy is not new. But, like any "newly" discovered innovation, it is more the result of coming of age rather than being new. Microwave processing has been adapted to materials processing since the end of the second world war. However, the last decade has seen it become a new force in materials processing since the equipment became readily available because of the development of the home microwave oven. This introduced cheap and accessible equipment to the experimentalist. The communication industry has also been beneficial as well as detrimental to this development. Helpful in the sense that useful equipment and knowledge was made available but detrimental because of the limitation of governmental regulations as to wavelength and bandwidth allowed for industrial usage and therefore equipment availability.

The microwave processing of materials other than food is relatively new, especially for high temperature processing. The uniqueness of microwave energy is that it is absorbed directly by the specific absorbing sites within the material in the process. For example, drying of materials is accomplished by inputting the energy directly to the water molecule and forming the vapor without having to heat the rest of the material. This is a very efficient method of energy transfer. The result is that energy is instantaneously supplied to the point of use. However, in many other cases, the desired or unexpected reaction is also initiated quickly and efficiently which forces new reaction pathways to be taken or finer microstructures to be formed and improved materials, which were impossible by conventional methods, are synthesized.

This direct input of energy requires some unusual experimental parameters to be formulated and applied, not only with respect to processing conditions but also with respect to the process materials and experimental design. Precautions must now be taken so as not to conduct or radiate the internally generated heat to the environment before the useful reactions occur. Also, container or insulating materials have the added requirement of being reflective or absorptive as appropriate.

Over the last decade, Penn State has studied the microwave processing of a wide variety of ceramic materials. As with so many other process discoveries, serendipity, good observation, and action started the ball rolling with respect to new developments. In this case, the catastrophic conclusion of a simple microwave drying step of an AlOOH gel triggered the question as to what was really happening to this "microwave transparent" material. At about the same time, the observation that Corning "Centura"-ware shattered violently and became red hot in a matter of minutes when heating food in a home microwave oven resulted in the same question. The follow up analysis of both observations indicated that the material was actually an effective absorber.

In the latter case, the synthetic nepheline phase in the Corning -ware coupled with the microwave energy. In the former case, the aluminum oxyhydroxide phase developed a hot spot during the drying operation and thermal runaway occurred as the material reacted and changed into other inorganic phases. The beaker melted as well as the bottom of the oven. The surprise was the attainment of high temperatures in "white ceramics," nominally microwave transparent materials. However, this was not dropped as just another experimental observation and avoided in the future but was embraced as an opportunity and used as a basis of research into the effects of microwave processing in this new field.

The actual materials studied are listed in Table 1. These include alumina and silica materials, complex ceramic phases which were shown to sinter into visibly transparent bodies, zeolite synthesis, low pressure plasma synthesis of diamond, hydrothermal microwave induced synthesis of oxides and silicates even metal powders were synthesized.

Other topics in ceramic processing that have been investigated are the manipulation of the starting materials to improve the sintering of oxides. In this case,  $\text{TiO}_2$  was pre-reduced to form a defective material that is a very good absorber of microwaves. This was then reacted at low temperatures ( $300^\circ\text{C}$  to  $700^\circ\text{C}$ ) in a matter of minutes to form  $\text{BaTiO}_3$ , "PZT," and "BMT." These normally require temperatures in the area of  $900^\circ\text{C}$  to  $1400^\circ\text{C}$  to react. Lower process temperatures are an ongoing goal in the synthesis of materials for all of the obvious reasons and is no exception with microwave processing of materials. But other benefits are also available. For example, the problem of PbO vaporization in the formation of PZT is reduced by the lower temperatures and, since the reaction is so efficient, nearly all the Pb is taken into the PZT and excessive Pb material is not needed.



The next step for materials synthesis was the sintering of electrically conductive materials such as cemented tungsten carbide, again a material that should not be able to be heated with microwave energy. Metals and conductive phases are reflective to microwave energy. However, when in the powder form, surface resistive heating occurs and other mechanisms may play a part in this process. The bottom line is that it does happen and is very effective in obtaining materials with improved properties.

These are some of the results of only one research facility in this new area of materials synthesis and only the surface of this field has been uncovered. Much more will occur in the years to come. This is not to say that now this will be an easy

experimental or commercial endeavor. As the above examples have shown, the material in question has to be considered an integral active part of the whole system and not just a passive player that is bathed in radiant or thermal conductive energy. Technique is very important and an understanding of the interaction of microwave energy with all parts of the system is needed before useful results will be obtained.

This understanding is being obtained and reported on much more frequently today. Even meetings on the uses of microwave energy such as this one and a recent international congress, First World Congress on Microwave Processing, are becoming more frequent and dedicated to this topic. The future looks very promising for this materials processing field.

Table 1. Materials Studied in Microwave Processing Area at Penn State's MRL.

1984-85	Microwave sintering of alumina and silica and melting of silica gel and platinum capsule which contained alumina gel.
1986-96	Diamond synthesis in plasma (a) CVD process; in plasma: 100 papers (b) LPSSS process with and without plasma: 12 papers
1986-96	Ceramic powder making (mullite, $\text{Al}_2\text{O}_3$ , etc.) including cement Porous ceramics, especially apatite Dense ceramics Transparent ceramics, especially apatite, mullite Highly absorbing materials, zeolites, and clays
1991-97	Microwave <i>hydrothermal</i> synthesis of metals, ferrites, electroceramics, $\text{BaTiO}_3$ , PZT, silica gels
1993-97	Microwave synthesis of commercial ceramics
1995	Alumina abrasive grain sintering
1995	Sintering tungsten carbide tools
1995	Diamond-metal-carbide composites

## First experiments of the FOM Fusion FEM

A.G.A. Verhoeven, W.A. Bongers, V.L. Bratman\*, M. Caplan\*\*, G.G. Denisov\*, G. van Dijk, P.J. Eecen  
B.S.Q. Elzendoorn, C.A.J. van der Geer, S.W.T. de Kroon, P. Manintveld, A. Poelman, J. Pluygers  
P.R. Prins, M.Yu. Shmelyov\*, P.H.M. Smeets, A.B. Sterk, W.H. Urbanus, M. Valentini, M.J. van der Wiel

FOM-Instituut voor Plasmafysica 'Rijnhuizen', Association EURATOM-FOM, tel.: (31)30-6096999  
fax: (31)30-6031204, e-mail: verhoeven@rijnh.nl, P.O. Box 1207, 3430 BE Nieuwegein, the Netherlands

\*Institute of Applied Physics, Nizhny Novgorod, Russia

\*\*Lawrence Livermore National Laboratories, Livermore, CA, USA

### Abstract

A free electron maser is being built as a mm-wave source for applications on future fusion research devices such as ITER. A unique feature of the Dutch Fusion FEM is the possibility to tune the frequency over the entire range from 130 to 260 GHz at an output power exceeding 1 MW.

In the first phase of the project, a so-called inverse set-up is used. The electron gun is mounted inside the high-voltage terminal. The entire beam line, including the accelerating structure up to 2 MV level and the transport through the undulator was tested successfully with extremely low loss current, lower than 0.05 %.

### A. Introduction to the FEM project

The FEM uses a 12 A thermionic electron gun and a 2 MeV electrostatic accelerator. The undulator and mm-wave system are located inside a terminal at 2 MV level. The terminal is placed inside a steel vessel of 11 m length and a diameter of 2.6 m, filled with SF<sub>6</sub> at 7 bar. After interaction with the mm-waves in the undulator, the energy of the electron beam is recovered by means of a decelerator and a multi-stage depressed collector. This enables to achieve a system efficiency of 50 % [1].

For long-pulse generation a low loss-current is essential. Therefore, the electron beam line is entirely straight from gun to collector. This is done to minimise the current loss to a value lower than 20 mA [2]. The mm waves are directed sideways from the electron beam. This is achieved by means of a stepped waveguide, a symmetrical step in the transverse dimension of a low-loss HE<sub>11</sub> waveguide, just behind the undulator. Furthermore, an adjustable reflector enables adjustment of the feedback power [3,4].

### B. Inverse set-up

The first experiments are done in the inverse set-up [1], see figure 1. Here, the electron gun is mounted inside the high-voltage terminal. The undulator and waveguide systems are outside the pressure vessel at earth potential for easy adjustments and fine tuning of the entire system. As a consequence, the decelerator and depressed collector cannot be used yet, which means that the FEM pulse duration is limited to 20  $\mu$ s. In October 1996, an important milestone was reached in the Fusion-FEM project. An electron beam of 3 A was accelerated up to 1.70 MeV and transported through the

undulator with current loss of less than 2 mA. The energy range achieved, allows generation of mm-waves at frequencies ranging from 130 - 190 GHz.

First experiments on transport through the undulator were performed at 1.55 MeV, with a 3 A electron beam and a pulse length of 20  $\mu$ s. The crucial test concerned the loss currents in the waveguide structure, see figure 1. This structure consists of a set of two separate mirrors at the beginning of a 50 $\times$ 20 mm<sup>2</sup> waveguide (together forming the reflector of the eventual mm-wave cavity) and the undulator waveguide. The latter has a cross section of 15 $\times$ 20 mm<sup>2</sup>.

In figure 2, the loss current on the undulator waveguide is shown. The total loss on the mirrors of the reflector, the reflector waveguide and the undulator waveguide is less than 1 mA. In the present experiments the beam current was limited to 3 A, instead of the nominal current of 12 A. Due to vacuum problems, the electron gun was operated in a rather poor vacuum, halfway the 10<sup>-7</sup> mbar range. Consequently, the cathode was poisoned, i.e., the work function of the cathode material had increased. A beam current of 3 A was extracted, at a reduced anode voltage, giving the same perveance and therefore a self-similar beam to the nominal 12 A beam. The peaks at the beginning and end of the beam, as seen in figure 2, appear when the gate electrode of the gun is being switched from -12 kV (beam off) to 4.4 kV (beam on). Now, the beam has a higher emittance, which results in some beam loss.

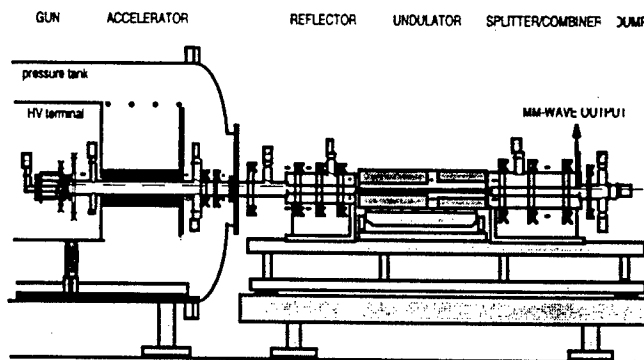


Fig. 1 Lay-out of the Fusion-FEM in the so-called inverse set-up. The electron gun is mounted in the high-voltage terminal, which is now at -2 MV. The undulator, mm-wave system and most of the electron beam line are outside the tank at earth potential for easy accessibility.

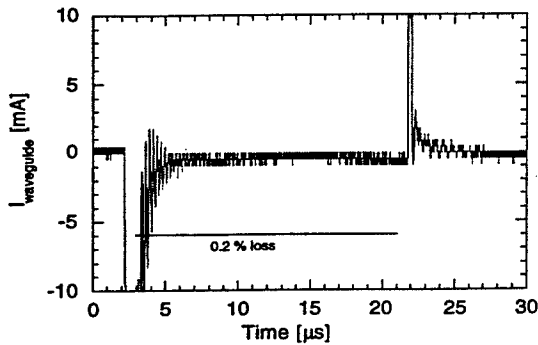


Fig. 2 Loss current on the undulator waveguide, for a beam current of 3 A and a beam energy of 1.53 MeV. Note that the loss current is much lower than the allowable 0.2 % beam loss.

The height of these peaks is very sensitive to beam alignment. The peaks are a superposition of the loss current (negative) and the capacitive currents (negative or positive). The loss current, measured on the various waveguides and apertures appeared to be an important diagnostic tool to properly align the electron beam.

Electron-beam trajectories have been simulated using the multi-particle tracking code GPT [5]. For comparison, beam envelopes have been calculated with a code based on the Herrmann optical theory [2]. This code calculates the beam envelope which contains 99.9% of the beam current. Both beam-simulation codes showed good agreement with the experimental results.

Figure 3 shows that there is only little difference between the envelopes for 3 A and 12 A beams. This is a result of the fact that the beam envelope is largely determined by the beam emittance and the betatron oscillations in the undulator rather than by the space charge fields.

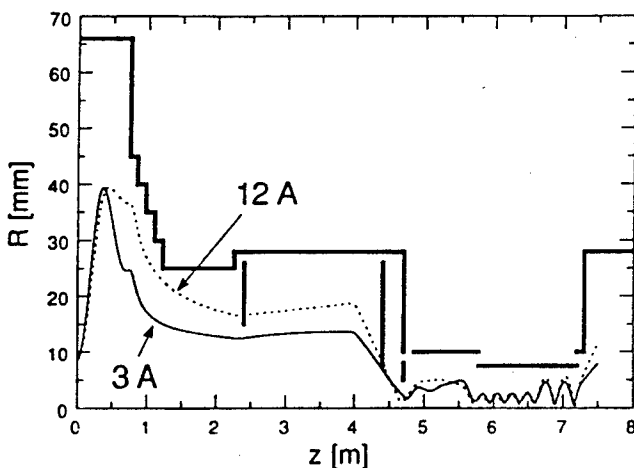


Fig. 3 Beam envelope as simulated with the Herrmann optical theory, for a 3 A and a 12 A electron beam as indicated. The thick lines are the beam-pipe dimensions and apertures, respectively.

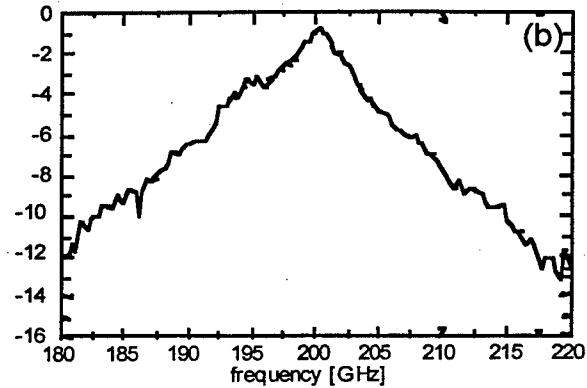


Fig. 4 The frequency characteristic (in dB) of the entirely installed cavity. A low-power signal was coupled into the mm-wave output, and the reflected power was measured. The total loss at the peak (200 GHz) was 0.9 dB. This value agrees with the sum of the losses of the individually measured components.

Based on these simulations, and on the good agreement between the simulations and the experimental results, it is expected that a 12 A beam can be transported with losses well below 20 mA, as required.

#### C. Millimeter-wave System

After installation of all the mm-wave parts of the FEM a total cavity test has been done to check the tuning of all parts after mounting, see figure 4.

#### D. Conclusions

The target for the loss current was 20 mA at 12 A beam current, i.e., 99.8 % transmission. Now a beam transmission of better than 99.9 % at 3 A beam current is achieved. The simulation codes, which include space-charge effects and predict the size of the beam at various positions, was benchmarked against the experiment. The codes predict that transmission of a 12 A beam will lead to a marginally higher current loss. First generation of mm-wave power at 1 MW level and pulses of 20  $\mu$ s duration are foreseen for Summer 1997.

#### E. Acknowledgements

This work was performed as part of the research programme of the association agreement of EURATOM and FOM with financial support from NWO and EURATOM.

#### F. References

- [1] W.H. Urbanus, *et al.*, April 97, Proc. 10th Workshop on ECE and ECRH, EC10, World Scientific, Editors: A.J.H. Donne and A.G.A. Verhoeven.
- [2] M. Valentini, *et al.*, *ibid.*
- [3] W.A. Bongers, *et al.*, *ibid.*
- [4] G.G. Denisov, *et al.*, Proc. 21th Int. Conf on IR & MMWs 1996, Berlin, BF3.
- [5] S. B. van der Geer, M. J. de Loos, GPT Manual, Pulsar Physics, Utrecht (1996).

## Recent Results from the Compact Infrared Free Electron Laser

Hans P. Bluem, Ira S. Lehrman, Jayaram Krishnaswamy, Richard A. Hartley, and Robert H. Austin<sup>†</sup>

Northrop Grumman Advanced Systems and Technology Organization,  
4 Independence Way, Princeton, NJ 08540

<sup>†</sup>Princeton University Physics Department,  
Jadwin Hall, Princeton, NJ 08544

### Abstract

The Compact Infrared Free Electron Laser (CIRFEL) is part of a program to develop FEL's for use by researchers in the materials, medical, and physical sciences. The CIRFEL has lased from 12.5 to 20.5 microns with 5 psec pulses in excess of 5 micro-Joules/pulse. Much progress has been made towards the CIRFEL becoming a useful research tool. We will discuss the operational status, stability issues, and experimental results of the CIRFEL.

### Introduction

The Compact Infrared Free Electron Laser (CIRFEL) was built as part of a joint collaboration between Northrop Grumman and Princeton University to develop FEL's for use by researchers in the material, medical, and physical sciences and to provide a platform for the development of future FEL systems. The design and layout of the CIRFEL have been well documented elsewhere[1,2] so only its primary features will be touched on. The CIRFEL utilizes an RF, photo-cathode electron gun to achieve high brightness, short electron bunches in a train of 5 $\mu$ s duration. These electron bunches are accelerated through a compact accelerating structure ( $\sim 0.31$ m) to 9-12MeV and directed into the 13.6mm period, 73 period permanent magnet undulator to produce a train of short ( $\sim 5$ ps with 7ns separation), intense pulses of IR. The parameters of the CIRFEL are summarized in Table 1.

	Achieved	Planned
Energy	9-12.2 MeV	7-14 MeV
Beam Charge	2 nC	2 nC
Energy Spread	<0.2%	0.1%
Macropulse Length	6 $\mu$ sec	10 $\mu$ sec
Repetition Rate	5 Hz	10 Hz
FEL Wavelength	12.5-20 $\mu$ m	8-20 $\mu$ m
FEL Micropulse Energy	$\sim 5$ $\mu$ J	50-80 $\mu$ J
Wiggler Period	13.6 mm	10 mm
Aw	0.2	0.24

Table 1. CIRFEL performance parameters achieved to date and planned for the future.

The electron energy is presently limited by arcing in both the gun and the booster. The macropulse length is also limited by this problem. The beam charge goal of 2nC/micropulse has been met, but routine operation at this level is still elusive. The energy spread measurement is

emittance limited at the present time, so better performance is unmeasurable. The repetition rate is limited by the DC power supply, but a new one is in hand and plans are to install it in the near future, allowing operation at 10Hz. A new wiggler is also in hand and is planned to be installed in the near future. This wiggler, along with new FEL cavity mirrors, will allow for a dramatic improvement in FEL output power.

### Progress

The CIFEL first lased on May 15, 1996[3]. Since that time all efforts have been devoted to achieving stable, reliable lasing. Work has been focussed on measuring and correcting the shot-to-shot stability of the photo-cathode laser and RF systems. The goal is to achieve 0.2% wavelength stability (0.1% energy stability) and 10% amplitude stability of the FEL's IR output pulse. The wavelength (energy) stability goal is a very challenging number to achieve. These numbers correspond to an RF input power stability of better than 0.14% (less than a 0.007dB change) and a charge stability of better than 1.5% at 1nC (or 2mA), assuming equal contributions.

Previously, the RF power stability was measured to be about 0.25%. Most of the variation could be traced to noise introduced in the low-level RF chain. A slight redesign of the RF signal chain eliminated this noise source. This, along with a tune-up of the 500W amplifier, reduced the RF power shot-to-shot jitter to  $\sim 0.15\%$  or better over a minute of time or less. There is however a long term drift of the RF power associated with temperature which needs to be corrected. These improvements in the RF stability have also enabled the Feed-Forward system[4] to flatten the RF pulse with unprecedented accuracy. The RF pulse amplitude can now be flattened reliably to within  $\pm 0.025\%$  and the phase corrected to better than  $\pm 0.25^\circ$ .

The charge stability should be exclusively due to the stability of the UV photo-cathode laser. However, we may have seen some evidence of shot-to-shot variations in the quantum efficiency of the photo-cathode itself under certain circumstances. This seems to occur only at high emissions. The photo-cathode laser was initially measured to have  $\pm 10\%$  amplitude variations. A number of things were done to improve the shot-to-shot stability of the laser. Baffling was installed along the entire path of the laser beam to eliminate beam steering due to air currents. This produced a very noticeable improvement. All of the optics have also been realigned. In addition, the original KDP second and fourth

harmonic generation crystals have been replaced with BBO crystals to improve the conversion efficiency and decrease the sensitivity with temperature. These efforts have reduced the laser variations to around 4% from pulse to pulse. This corresponds to current variations in the range of 1.5 to 3mA. This is very close to our goal (and sometimes exceeds it). As with the RF system, we have longer term drifts in the laser system due to temperature effects. We also have experienced long term drifts in cathode emission characteristics while operating the FEL.

### Present Status

The CIRFEL has been lasing for about a year. In that year, great strides have been made toward making it into a reliable research tool. One can typically be lasing within minutes of turning the beam on. Energy variation between pulses has been measured to be ~0.1-0.2% on a reliable basis. This measurement was taken using an OTR screen in the accromat and measuring the beam movement. The resolution limit of this measurement is about 0.1% due to the minimum beam size achievable on this screen. The actual wavelength stability is also a difficult measurement due to the width of the spectrum and our current measurement method. Where most of the measurements have been made (16-17 $\mu$ m) the spectrum is about 0.1 $\mu$ m wide, limiting our measurement resolution to about 0.05 $\mu$ m or about 0.3%. The amplitude stability of the IR output has been measured to be better than 10%. An output energy of about 1 $\mu$ J/micropulse (or 200kW/micropulse) can be reliably achieved, although energies up to 5 $\mu$ J/micropulse have been measured. Lasing can be maintained for more than two hours, although the wavelength will drift during that time unless corrective measures are taken. We expect the first experiment utilizing the IR laser light to take place in the very near future.

### Future

We have a replacement wiggler in hand. This wiggler has a shorter period and fewer periods, allowing us to shorten the resonator cavity from three electron bunches to two electron bunches. The new wiggler will allow access to shorter wavelengths and will provide substantially higher output powers. A spectrometer is in the design stage to allow more accurate energy spread measurements. And, we are addressing the long term drift issues to minimize operator intervention and to more accurately hold the wavelength steady for extended periods of time.

### References

[1] "Design and Operation of the Compact Infrared Free Electron Laser (CIRFEL)," I. S. Lehrman, *et al.*, Electron-Beam Sources and Charged-Particle Optics, Proceedings of the SPIE, Eric Munro and Henry Freund, Eds., 2522 (1995) 451.

[2] "Status of the Grumman Compact Infrared FEL," I. S. Lehrman, *et al.*, Nucl. Inst. Meth., A358 (1995) ABS 5.

[3] "First Lasing of the Compact Infrared Free Electron Laser," I. S. Lehrman, *et al.*, to be published Nucl. Inst. Meth.

[4] "Feed Forward Control: An Implementation at CIRFEL," R. Hartley, *et al.*, Nucl. Inst. Meth, A375 (1996) ABS 22.

# Progress on a Ka-Band CHI Wiggler Ubitron Amplifier

J.M. Taccetti, R.H. Jackson, H.P. Freund, D.E. Pershing, and V.L. Granatstein

Naval Research Laboratory  
Washington, DC 20375-5347, USA

## Abstract

A summary of the progress on the construction of a CHI wiggler ubitron amplifier experiment is provided. Details on the final wiggler design are presented, along with the methods used to arrive at an adiabatic entrance configuration.

## Introduction

Free electron lasers, while attractive as sources of high power, high frequency radiation, suffer from the high voltages presently utilized for operation, causing them to be impractical for many applications. The Coaxial Hybrid Iron (CHI) wiggler [1-5] configuration overcomes this obstacle by allowing the use of short periods and gap spacings while maintaining excellent beam focusing properties and high magnetic fields. This reduces the overall system size while maintaining the ability to operate at high frequencies and power levels.

The 35 GHz ubitron amplifier experiment will demonstrate the operation of this wiggler configuration and allow a study of its predicted potential for generating high wiggler magnetic fields at short periods with excellent beam focusing and transport properties.

## Design Parameters

The ubitron amplifier will operate at a center frequency of 35 GHz, with a (simulated) bandwidth of approximately 25 %. A modified SLAC klystron electron gun will provide the 10 A, 100 kV annular beam, at a repetition rate of 1-100 Hz (pulse width of 1  $\mu$ s). The design parameters are summarized in Table 1. Input power is fed into the amplifier through a novel coupler which converts the TE<sub>01</sub> coaxial mode in an outer coaxial guide to a TE<sub>01</sub> coaxial mode in the inner coaxial guide where it joins the annular beam [6]. The bandwidth of this input coupler is comparable to that of the interaction and allows for wideband operation of the device.

## Wiggler Design

An entrance section to the wiggler was designed, wherein the wiggler field increases adiabatically towards its final

Table 1: Parameters of the experimental design.

Wiggler period, $\lambda_w$	6.4 mm
Beam voltage	100 kV
Beam current	10 A
Beam radius	0.56 cm
Beam thickness	0.10 cm
Applied field	7.7 kG
Center frequency	35 GHz
Interaction mode	TE <sub>01</sub> coaxial
Input power	100 W
Peak efficiency	6.75 %
Gain(saturated)	28 dB

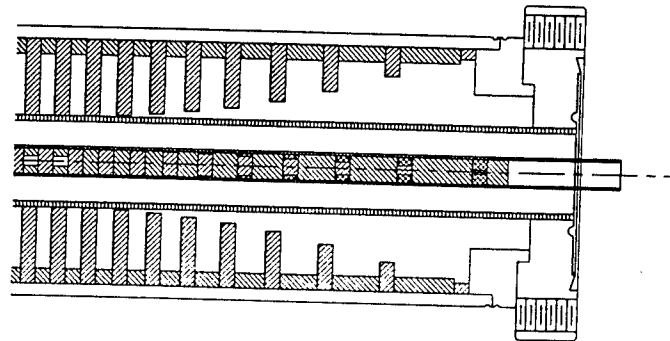


Figure 1: Closeup of the wiggler entry section. Ferromagnetic pieces are hatched with lines running from lower left to upper right.

value at the interaction section. A closeup schematic of the wiggler entrance is shown in Fig. 1. In the figure, the ferromagnetic pieces are surrounded by a stainless steel shell, used for indexing purposes only, which attaches to the flanges through another stainless steel disk. By indexing on the outer shell, the non-ferromagnetic spacers may then be made from lighter rings of larger inner radius than the ferromagnetic pieces. The vacuum jacket is formed by the outer waveguide, which is welded to the flanges at either end. The inner pieces are completely enclosed in their own vacuum jacket, a stainless tube which forms the inner waveguide, also shown in the figure.

The entry tapered field section consists of the first ten periods at each end of the wiggler, with the tenth being

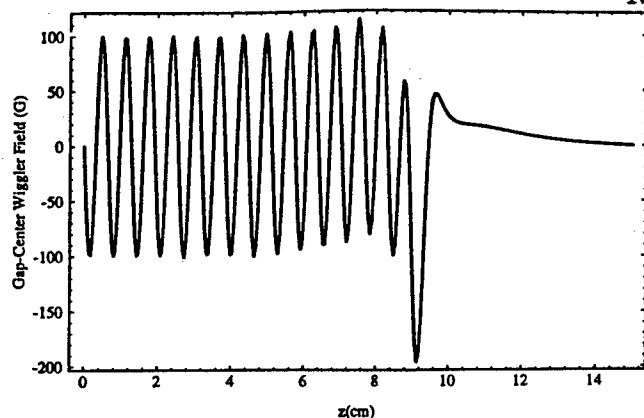


Figure 2: Wiggler field for untapered CHI.

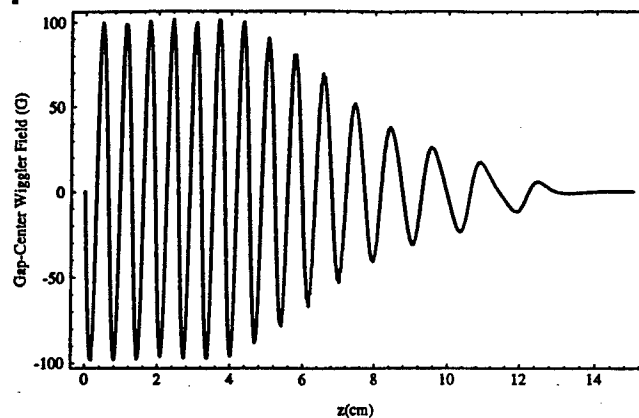


Figure 3: Wiggler field for tapered CHI.

a standard size period. In order to obtain a slowly increasing field amplitude as the beam enters the interaction region, variations are necessary in both the ferromagnetic pole shapes and the period (the poles remain the same width, but their spacing varies). For the outer poles, the peak radial field at gap-center (of standard-sized poles) decreases as the inner radius is increased. A similar result is observed as the outer radius of the inner poles is reduced. The reasoning behind the varied spacing comes from the fact that increasing the inner radius of the outer poles also increases their sphere of influence along the axis (analogous to increasing the radius of a coil). A careful empirical study of these two effects in both the inner and outer poles gives us the necessary radii to obtain a desired field magnitude. The inner and outer poles are placed as a pair a distance away from the next period equal to the sum of the  $\Delta z_{outer}$  from the outer poles of each of these periods, where  $\Delta z_{outer}$  is the distance between the maximum and the center null of the gap-center  $B_w$  of the outer poles. (The fields are similar to those of a coil.)

Figures 2 and 3 are plots of the wiggler field (simulated) for an untapered and a tapered configuration, respectively. The untapered one consists of fifteen uniform periods, while in the tapered case the first nine periods are modified as previously discussed. (The applied field in these cases was only 1.74 kG.) Successful simulations were performed in which the beam enters the tapered interaction region with minimum perturbation.

### Summary

The final wiggler design should prove to be very flexible in case of any necessary changes. The experiment is presently in the final stages of assembly and will be online shortly.

### Acknowledgement

This work was supported in part by the Office of Naval Research and the Naval Research Laboratory through a

contract with the University of Maryland.

### References

- [1] J. Feinstein. U.S. Patent No. 4,876,687.
- [2] H. Freund, R. Jackson, D. Pershing, and J. Taccetti. *Phys. Plasmas*, 1:1046, 1994.
- [3] R. H. Jackson, H. P. Freund, D. E. Pershing, and J. M. Taccetti. U.S. Patent No. 5,499,255.
- [4] R. H. Jackson, H. P. Freund, D. E. Pershing, and J. M. Taccetti. *Nucl. Instrum. Methods*, A341:454, 1994.
- [5] J. Taccetti, R. Jackson, H. Freund, D. Pershing, M. Blank, and V. Granatstein. *Nucl. Instrum. Methods*, A358:193, 1995.
- [6] J. Taccetti, R. Jackson, H. Freund, D. Pershing, and V. Granatstein. Submitted for publication at the 1996 International Free Electron Laser Conference.

## A Tunable FIR Grating-Based FEL

John Urata, Maurice Kimmitt\*, Andrei Naumov, Christopher Platt, and John Walsh  
*Department of Physics and Astronomy, Dartmouth College, Hanover, NH 03755-3528*

A new grating-based free-electron laser is operating in the 500  $\mu\text{m}$  wavelength range. It is driven by a scanning electron microscope e-beam and the necessary feedback comes from the grating. The performance and future prospects will be discussed.

When an electron beam passes close to the surface of a metal diffraction grating, radiation is produced with a wavelength

$$\lambda = \frac{l}{|n|} \left( \frac{1}{\beta} - \sin \theta \right) \quad (1)$$

where  $l$  is the grating period,  $\beta \equiv v/c$  is the electron's relativistic velocity,  $\theta$  is the angle of emission measured from a direction normal to the surface of the grating, and  $n$  is the spectral order. Since light produced in this manner was first observed by Smith and Purcell [1], it has come to be known as Smith-Purcell radiation.

Smith-Purcell radiation from millimeter to optical wavelengths has been observed by various investigators [2-6]. In the millimeter wave region, the stimulated component of the emission process has been successfully used as the basis for continuously tunable oscillators. Various feedback schemes have been employed [7,8]. It would be desirable to produce similar, compact sources at far-infrared (FIR) wavelengths (30-1000  $\mu\text{m}$ ), a spectral regime of growing interest. However, difficulty has been encountered in scaling these devices down to operate at these wavelengths. This paper reports on a grating-based free-electron laser that operates in the FIR. It was found that no external feedback elements were necessary to produce stimulated emission; the necessary feedback is provided by the grating itself.

This device is based on a scanning electron microscope (SEM). A schematic of the SEM is shown in Fig. 1. After several modifications were made to the SEM, the machine was capable of generating a continuous, cylindrical beam (tungsten cathode) with an energy of 30-40 keV, a waist diameter  $\geq 20 \mu\text{m}$ , and a total current  $\leq 750 \mu\text{A}$ . The rectangular profile of the gratings was chosen, using the theory of van den Berg [9], to maximize the power of first order spontaneous radiation ( $n = -1$ ) emitted in the normal direction ( $\theta = 0$ ). The gratings ranged in period from 128 to 308  $\mu\text{m}$ .

The beam waist was placed at the midpoint of the grating, and using the SEM's scanning coils, the beam was swept perpendicular to the surface of the grating at

200 Hz to temporally modulate the emitted radiation for lock-in amplification. The beam current was monitored with a carbon Faraday cup.

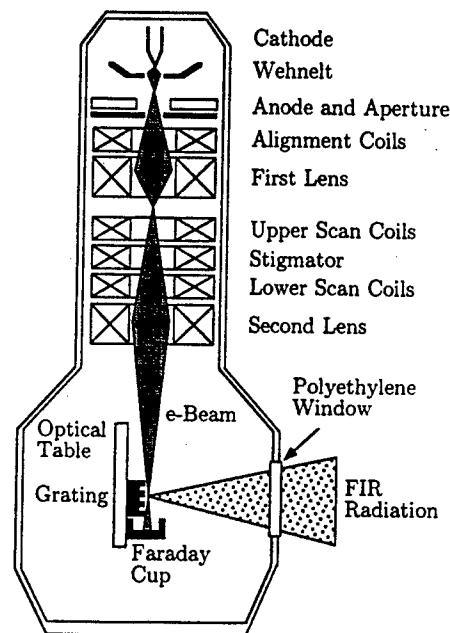


FIG. 1. Schematic of the modified SEM.

The radiation was directed out of the SEM by means of a polyethylene window, focused into a Czerny-Turner monochromator, and detected using a helium-cooled, silicon composite bolometer. The wavelengths corresponding to the peak signals through the monochromator are in excellent agreement with those predicted by Eq. (1), as is shown in Fig. 2. In addition, using a wire grid mesh, the light was found to be entirely polarized, as expected from an elementary application of Maxwell's equations to the beam-grating system.

In order to make power measurements the light leaving the SEM was focused directly into the bolometer by means of a TPX lens. The time averaged power incident on the detector was recorded as a function of beam current. As can be seen in Fig. 3, for relatively low currents the power increases linearly with the beam current as expected for purely spontaneous emission. However, when the beam current surpasses a certain threshold, the detected power evolves from a linear to a superlinear current dependence. There was no discernible difference in the light's polarization or wavelength between the two regimes.



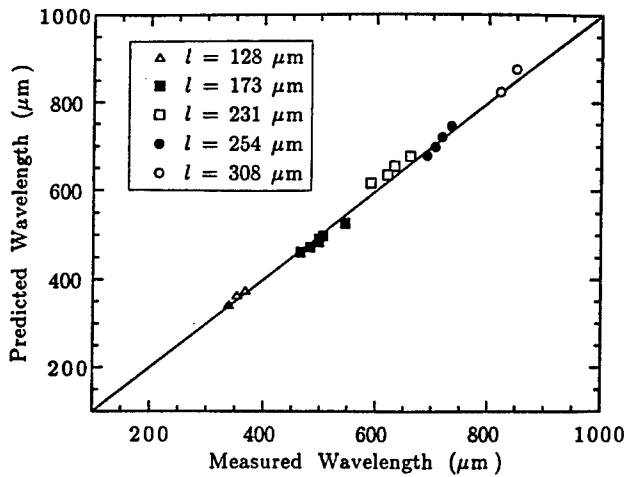


FIG. 2. Theoretically predicted vs. experimentally measured wavelength for gratings of various periods run at beam energies between 30-40 keV (Error bars are approximately the same size as the data points).

The transition from a linear to a superlinear dependence of the power on the beam current indicates the onset of a stimulated process. There are no external feedback elements; the grating itself acts as a resonator.

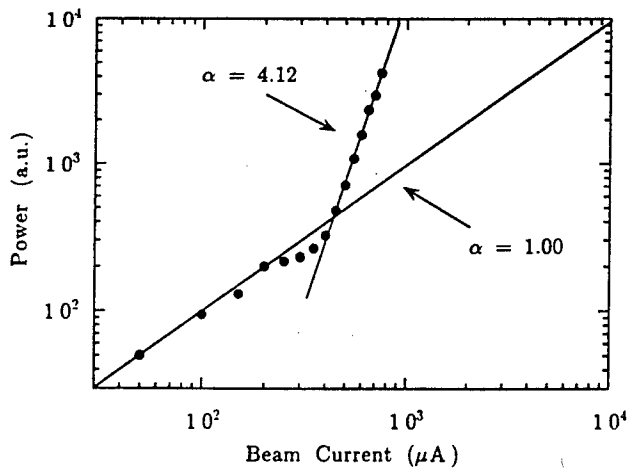


FIG. 3. Detected power vs. electron beam current using the  $l = 173 \mu\text{m}$  grating at 35 keV ( $\lambda = 490 \mu\text{m}$ ). The beam waist diameter is approximately  $24 \mu\text{m}$ . Fits were made of the form  $y = Ax^\alpha$ .

The largest peak power measured was 10 nW at  $500 \mu\text{m}$  and  $750 \mu\text{A}$ . The bandwidth was  $38 \mu\text{m}$ , which can be obtained using Eq. (1) and the collected solid angle of 0.038 sr. The effective emitting area is not known precisely, but using a value derived from the projected area of the beam, the spectral radiance is at least an order of magnitude greater than that of a 5000 K blackbody.

It must be emphasized that in our present experiment the current densities available were only sufficient to raise the output by about an order of magnitude above the spontaneous emission level. The current density could

be increased by switching to, for instance, a lanthanum hexaboride cathode which produces a beam approximately ten times brighter than tungsten. With higher current densities significantly greater output powers are expected as well as shorter wavelength operation. Eventually, an extremely compact version of this device could be constructed using field emitter array cathodes which could produce high current density, low emittance, ribbon beams [10].

The authors would like to thank Vanderbilt University for the loan of the bolometer. The support of ARO Contract DAAH04-95-1-0640 and Vermont Photonics, Inc. is gratefully acknowledged.

\* Also affiliated with the Department of Physics, University of Essex, Colchester C04 3SQ, England.

- [1] S. J. Smith and E. M. Purcell, *Phys. Rev.* **92**, 1069 (1953).
- [2] A. Gover, P. Dvorkis, and U. Elisha, *J. Opt. Soc. Am. B* **1**, 723 (1984).
- [3] I. Shih *et al.*, *Opt. Lett.* **15**, 559 (1990).
- [4] G. Doucas *et al.*, *Phys. Rev. Lett.* **69**, 1761 (1992).
- [5] K. J. Woods *et al.*, *Phys. Rev. Lett.* **74**, 3808 (1995).
- [6] K. Ishi *et al.*, *Phys. Rev. E* **51**, R5212 (1995).
- [7] *Infrared and Millimeter Waves*, edited by K. J. Button (Academic Press, New York, 1979), see the chapters on the Ledatron (Vol.1) and the Orottron (Vol. 7).
- [8] J. Killoran, F. Hacker, and J.E. Walsh, *IEEE Trans. Plasma Sci.* **22**, 530 (1994).
- [9] P. M. van den Berg and T. H. Tan, *J. Opt. Soc. Am.* **64**, 325 (1974).
- [10] C. M. Tang, M. Goldstein, T. A. Swyden, and J. E. Walsh, *Nucl. Instrum. Methods* **358**, 7 (1995).

# The Cerenkov FEL, a versatile source for mm- and sub mm wavelength radiation

P.J.M. van der Slot<sup>a</sup>, J. Wieland<sup>b</sup>, J. Couperus<sup>a</sup>, W.J. Witteman<sup>a,b</sup>

<sup>a</sup>Nederlands Centrum voor Laser Research, P.O. Box 2662, 7500 AE Enschede, The Netherlands

<sup>b</sup>Department of Applied Physics, University of Twente, P.O. Box 217, 7500 AE Enschede, The Netherlands

## Abstract

A Cerenkov FEL is under construction at NCLR in collaboration with the Quantum Electronics group of the University of Twente. The system described here will operate from about 0.6 to 6 mm wavelengths at average power levels from tens of Watts up to about 1 kW.

## Introduction

Free electron lasers (FEL) form a class of radiation sources which are both tunable and capable of delivering high output powers. Tuning characteristics of undulator based FEL's imply that an increase in electron beam energy results in an decrease in radiation wavelength. Therefore, huge expensive accelerators are needed to obtain short wavelength radiation. In this paper we describe a Cerenkov FEL (CFEL), which has opposite tuning characteristics. This allows the generation of mm- and submm radiation with a relatively compact and cheap device.

A Cerenkov FEL basically consists of a dielectrically lined waveguide and an electron gun. The dielectrically lined waveguide plays the role of the undulator.

## Physical principles

Consider a cylindrical waveguide with inner radius  $r_i$  lined with a dielectric material of thickness  $d_e$ . Apart from 'normal' modes, this waveguide can support modes with a phase velocity less than the speed of light in vacuum. These modes

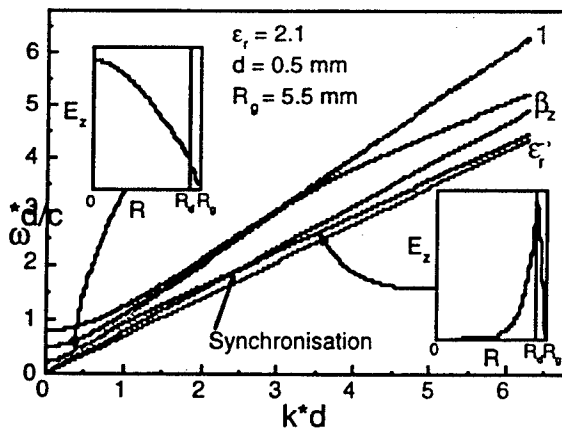


Fig. 1. Dispersion relation for the three lowest  $TM_{0n}$  modes. The inserts show the radial dependence of the axial component of the electric field for a  $TM_{01}$  mode at two different frequencies corresponding to a phase velocity greater and less than the velocity of light respectively.

essentially propagate through the dielectric and have an evanescent part in the vacuum. Due to this evanescent part, an electron beam moving in the vacuum can have an overlap with the radiation field. As the electron beam may become synchronous to such a mode, macroscopic energy exchange between electron beam and radiation field is now possible through interaction of the electrons with the z-component of the electric field. In fig. 1 we have plotted the dispersion relation for the three lowest  $TM_{0n}$  modes together with the light line in vacuum ( $\omega/(ck)=1$ ), the light line of a dielectric medium ( $\omega/(ck)=\epsilon_r^{1/2}$ ) and the beamline ( $\omega=c\beta k$ ). The operating frequency is given by the intersection of the beam line with the mode dispersion relation. It is easily seen that the frequency increases with decreasing beam energy. From fig. 1 it becomes clear that interaction is only possible if the electron beam energy is above a threshold value  $\gamma_T^2 = \epsilon_r/(\epsilon_r - 1)$  because the phase velocity of the wave is always above  $c/\epsilon_r^{1/2}$ . From the radial profile of the axial electric field, also given in Fig. 1, one can see that good coupling can only occur if the electrons move close to the dielectric liner. A hollow beam will be more efficient than a solid beam as it has a better overlap with the evanescent electric field.

## Non-linear simulations

To estimate the performance of the CFEL, non-linear calculations were performed using a three-dimensional model [1]. The parameters used in the simulation reflect the design parameters of the CFEL given in Table 1. A strong axial magnetic field for beam guiding purposes has been incorporated in this model. Fig. 2 shows the saturated output power as a function of frequency for two different electron beam energies. These curves were obtained by calculating the maximum amplification of a single-frequency 100 W input field. The radiation field is restricted to a few  $TM_{0n}$  modes. The  $TM_{01}$  mode however, is the only mode which has appreciable interaction with the electron beam. Remarkable is the

Parameter	Value	Unit
Beam energy (ripple < 0.5%)	250-500	KeV
Beam current $I$	30-100	A
Outer beam radius $R_b$	5	mm
Thickness beam $dr$	<1	mm
Waveguide radius $r_i$	6	mm
Thickness dielectric material $d_e$	0.2-0.5	mm
Dielectric constant $\epsilon_r$	2-9	
Axial magnetic field $B_0$	0-2.75	T
Longit. momentum spread $\delta p/p_i$	<1%	
Electron pulse duration $\tau$	10	$\mu$ s
Repetition rate $f_{rep}$	$\leq 10$	Hz
Interaction length $l$	30	cm

Table 1. Design parameters of the Cerenkov FEL.

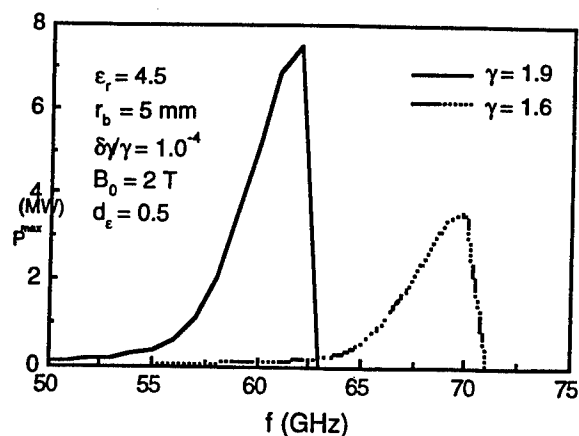


Fig. 2. Saturated power for two different values of  $\gamma$ . All other parameters are fixed.

asymmetry of the curves. According to these calculations, output powers of several MW are realizable. Combined with a 10  $\mu$ s pulse and a 10 Hz repetition rate, average output powers of the order of 1 KW should be possible. The saturation power decreases with increasing frequency ( $\sim$  decreasing beam energy). Further calculations (not presented here) indicate that the saturation output power depends sensitively on the electron beam thickness. It was found that the maximum power dropped with a factor of 4 in going from an annular beam with  $d_b = 0.5$  mm to a solid electron beam while keeping the total beam current constant. The maximum power also depends rather sensitively on the longitudinal momentum and energy spread of the electron beam.

Therefore, it was necessary to develop an electron gun which produces a thin walled, cold electron beam.

### Thermionic electron gun

A thermionic electron gun powered by a modulator was designed to deliver an annular electron beam for the CFEL [2,3]. A Lanthanum hexaboride thermoemitter was chosen in view of its good reproducibility, high repetition rate and well developed technology. As the emissive power of LaB<sub>6</sub> is not high enough to produce a high current beam of the desired dimensions, a rather large cathode surface is necessary in combination with a high degree of magnetic compression ( $\approx 10$ ). In fig. 3 a simplified electrode configuration is presented along with the magnetic field produced by a superconducting magnet. Numerical simulations have been performed to estimate the amount of transverse momentum that electrons acquire during the compression. It can be shown that the magnetic field can be tuned in such a way that electrons emitted from a certain radial position on the cathode will have zero transverse momentum in the interaction region. Electrons emitted from other radial positions will have a non-zero transverse momentum component [4]. In Fig.3 electrons emitted from the outer edge of the emitter have zero transverse momentum in the interaction region. The transverse momentum of this electron is shown in Fig. 3 as the dotted line. Preliminary experiments with the electron gun indicate that its emissive power agrees with the design value.

Measurements of the modulator output voltage give that the energy spread of the electron beam is less than 0.5%.

### Acknowledgements

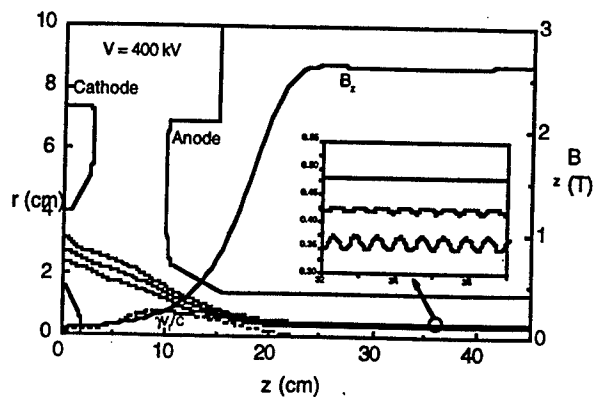


Fig. 3. Schematic configuration of the electrodes along with the magnetic field required for beam compression and guiding. Shown are three electron orbits, for electrons emitted at the inside of the emitter ring, the outside and center.

The development of the electron gun has been supported by a grant from the Netherlands Organization for Scientific Research (NWO).

### References

- [1] H.P. Freund et.al. Phys. Fluids B 2 (1990) 2506
- [2] A.V. Agafonov et.al. Proc. 10<sup>th</sup> Int. Conf. on High Power Particle Beams, 1994, San-Diego, USA, Vol 2, p522.
- [3] P.J.M. van der Slot et.al. Nucl. Instr. and Meth. A 358 (1995) 100.
- [4] P.J.M. van der Slot et.al. This digest.

# The influence of the velocity distribution on the performance of a Cerenkov FEL

P.J.M. van der Slot<sup>a</sup>, J. Wieland<sup>b</sup>, J. Couperus<sup>a</sup>, W.J. Witteman<sup>a,b</sup>

<sup>a</sup>Nederlands Centrum voor Laser Research, P.O. Box 2662, 7500 AE Enschede, The Netherlands

<sup>b</sup>Department of Applied Physics, University of Twente, P.O. Box 217, 7500 AE Enschede, The Netherlands

## Abstract

A thermionic electron gun can be used to provide the electron beam for a Cerenkov Free-Electron Laser (CFEL). However, for high beam currents of approximately 100 A or more beam compression is usually required. Under certain conditions one can show that the longitudinal velocity distribution produced is approximately parabolic and can be controlled by the magnetic field. A 3D numerical code has been used to check the influence of this type of distribution on the performance of the CFEL.

## Electron beam produced by a thermionic gun

A thermionic electron gun producing an annular electron beam will be considered as it is optimised for use in a Cerenkov FEL (e.g. [1,2]). Operating at high beam currents requires the emission area to be much larger than the desired beam cross-section in the interaction region, i.e., the region where the waveguide is lined with a dielectric material. In the gun considered both the accelerating electric field and a magnetic field produced by a set of coils are used to compress the electron beam from its initial dimensions at the cathode surface to a final outer beam diameter in the interaction region. Fig. 1 shows an example of such a gun. During the compression the electrons will obtain a small transverse velocity component and will therefore perform a Larmor motion around the magnetic field lines. The radius of the Larmor motion, and thus the transverse velocity component, depends on the

geometry of the gun and the strength of the magnetic field at the emitter surface. By placing an additional coil with opposite current near the cathode one can tune the magnetic field to become tangential to the velocity of an electron emitted from a fixed radial position at the cathode. When this happens the velocity remains tangential to the magnetic field line for that particular electron and it will have zero transverse velocity in the interaction region. Fig. 1 shows the situation where the magnetic field is tuned to obtain zero transverse velocity for electrons emitted from the outer edge of the ring shaped emitter. Single particle trajectories are numerically calculated for the geometry shown in fig. 1. These calculations show that in the interaction region the transverse momentum is nearly linear with the displacement from  $r_z$ ,  $p_{\perp} = \gamma m c k_p (r - r_z)$ , where  $r_z$  is the radial position within the beam for which the transverse momentum is zero and  $k_p$  is a constant independent of the magnetic field when it is optimised for a specific value of  $r_z$ . One easily finds that the corresponding longitudinal velocity distribution is approximately parabolic of shape as a function of the radial position and that the maximum  $v_z$  is determined by the position of  $r_z$ . Note that the beam has the lowest spread in axial velocity for  $r_z$  in the middle of the beam. Also the average axial velocity,  $\langle v_z \rangle$ , is now a function of  $r_z$ . Again taking  $r_z$  in the middle of the beam results in the highest value for  $\langle v_z \rangle$  while it reaches a smallest value near the edges of the annular beam.

## Performance of the Cerenkov FEL

In order to investigate the influence of this type of velocity distribution on the performance of the CFEL, in particular the influence of  $r_z$ , a non-linear model of the CFEL [3] was adjusted. Normally a Gaussian distribution is used for the energies of the electrons and the velocity components are initialised assuming a certain emittance for the beam. This

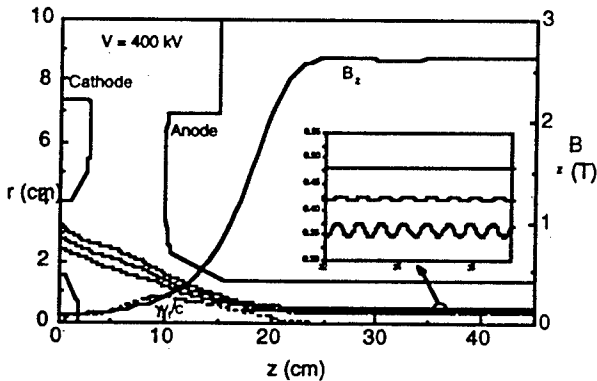


Fig. 1. Schematic view of electron gun. The electrodes are shown together with the radial position of electrons emitted from the two edges of the emitter and the centre. The magnetic field and the transverse velocity  $\gamma v_{\perp}/c$  for an electron emitted from the edge of the emitter are also shown.

Parameter	Value	Unit
Beam energy $\gamma$	1.45	
Beam current $I$	100	A
Outer beam radius $R_b$	5	mm
Thickness beam $dr$	0.5	mm
Gap between beam and dielectric $d$	0.5	mm
Thickness dielectric material $d_e$	0.5	mm
Dielectric constant $\epsilon_r$	4.5	
Axial magnetic field $B_0$	2.0	T
Input power $P_{in}$	100	W

Table 1. Main parameters of CFEL

method is not suitable for the parabolic type of axial velocity distribution where a correlation exists between initial radial position and axial velocity. Therefore the following method is

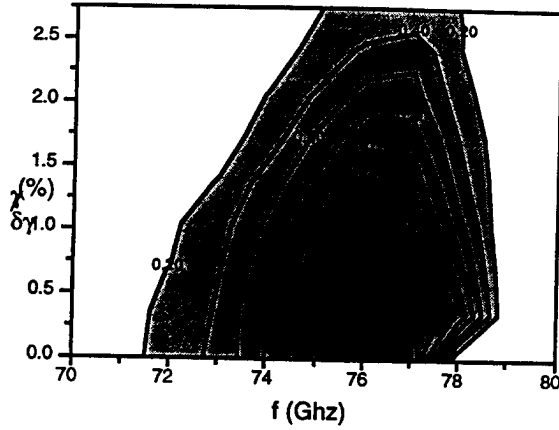


Fig. 2. Saturated power in MW as a function of energy spread and frequency.

used. After the electrons are distributed over the cross section of the beam a transverse momentum is allocated according to its radial position. A random angle distribution is used to calculate the two transverse components from  $p_{\perp}$ . The longitudinal velocity is calculated from  $p_{\perp}$  and the energy of the electron. Compared to a real electron beam emitted from the cathode, this method of initialisation effectively changes the centre of the Larmor motion of the electrons and the outer beam radius will be larger by about the Larmor radius in the model.

The main parameters used in the simulation are summarised in table 1. First the result for the normal initialisation will be given. Fig. 2 shows the saturated power as a function of the frequency and the energy spread in the beam. Here a very small normalised emittance is used (0.1 mm mrad), so that all electrons have approximately only an axial velocity component, its value being determined by the energy of the electron. The maximum power is about 1.9 MW at 77 GHz. Note that the interaction length was allowed to increase until saturation was obtained and that the frequency has been increased with 1 GHz steps. As the average axial velocity remains the same (as only the spread is increased), one finds no

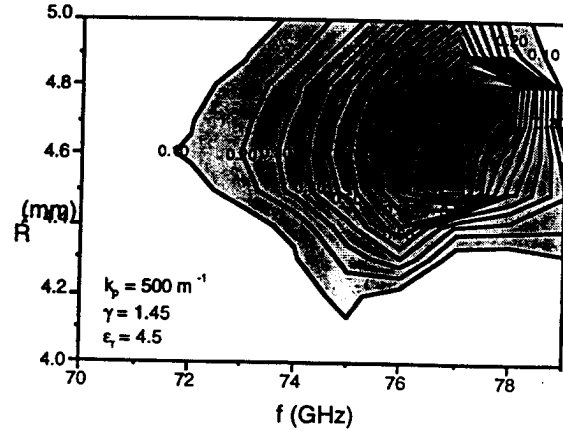


Fig. 4. Saturated power in MW as a function of  $r_z$  and frequency for a parabolic longitudinal velocity distribution. shift in frequency for which maximum saturated power is obtained.

For the same parameters the parabolic distribution is investigated. Here the electron beam is considered to be mono-energetic. All velocity spread is due to the beam compression by the electric and magnetic field in the gun. Two values of the constant  $k_p$  are considered,  $200 \text{ m}^{-1}$  and  $500 \text{ m}^{-1}$ . The shift in frequency for maximum power is clearly visible in fig. 3 and is due to the dependence of  $\langle v_z \rangle$  on  $r_z$ . It is also clear that the maximum power of about 2.4 MW at 78 GHz is obtained for  $r_z$  near the outer edge of the electron beam. This is due to the velocity distribution and the radial dependence of the  $\text{TM}_{01}$  mode of the radiation field. An increase in  $k_p$  (fig. 4) has several effects. First it results in a higher (axial) velocity spread in the beam and consequently the saturated power decreases (1.3 MW maximum for fig. 4). Also the value of  $r_z$  for which maximum power is obtained shifts towards the centre of the beam. Note that the saturated power drops faster for  $r_z$  moving from the centre towards the inner edge compared to moving to the outer edge. With increasing  $k_p$  the increase in velocity spread when  $r_z$  moves away from the centre of the beam counteracts the increase in gain due to radial dependence of the radiation field eventually resulting in lower saturated powers for  $r_z$  moving towards the edge of the beam.

## References

- [1] A.V. Agafonov et.al. Proc. 10<sup>th</sup> Int. Conf. on High Power Particle Beams, 1994, San-Diego, USA, Vol 2, p522.
- [2] P.J.M. van der Slot et.al. Nucl. Instr. and Meth. A 358 (1995) 100.
- [3] H.P. Freund et.al. Phys. Fluids B 2 (1990) 2506

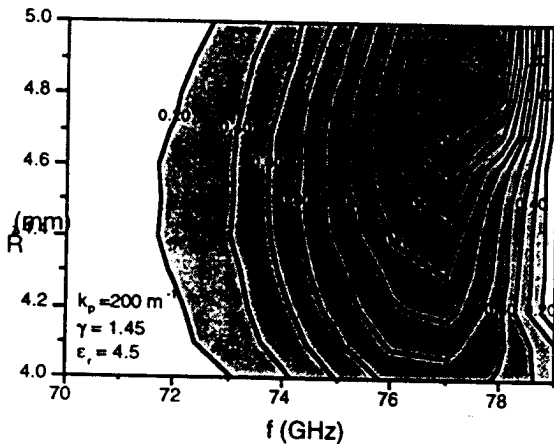


Fig. 3. Saturated power in MW as a function of  $r_z$  and frequency for a parabolic longitudinal velocity distribution.

# Preliminary Design of a W-Band Free-Electron Laser Amplifier

H.P. Freund<sup>†</sup>, B.G. Danly, R.H. Jackson, and B. Levush

Naval Research Laboratory  
4555 Overlook Avenue, Washington, DC. 20373

## Abstract

Theoretical analysis of a W-band free-electron laser amplifier has begun for a helical wiggler/cylindrical waveguide configuration using the ARACHNE simulation code [1]. ARACHNE is a three-dimensional slow-time-scale free-electron laser simulation code which integrates equations for the evolution of the amplitudes and phases of an arbitrary number of TE and TM modes in a cylindrical waveguide in the presence of an electron beam propagating through the waveguide in the presence of a helical wiggler and an axial guide magnetic field. Preliminary studies indicate that an efficiency of 5-10% with a bandwidth of 10 GHz is possible in the W-band using a 320 kV/50 A electron beam and a wiggler with a magnitude of 2.5 kG and a period of 0.88 cm.

## Mathematical Formulation

The basic formulation relies upon the nonlinear, three-dimensional, slow-time-scale simulation code ARACHNE [ref. 1, chap. 5] which describes the interaction between an electron beam and the TE and TM modes in a cylindrical waveguide as mediated by the presence of a helically symmetric wiggler field and an axial guide magnetic field. ARACHNE is a single-frequency, steady-state amplifier model in which the equations describing the evolution of the amplitudes and phases of each TE and TM mode included in the simulation is integrated simultaneously with the Lorentz force equations for an ensemble of electrons.

Maxwell's equations for the field are averaged over a wave period in order to (1) eliminate the fast time scale from the simulation, and (2) reduce the number of electrons in the simulation to a beamlet which is injected over one wave period. However, it is important to point out that no orbit average is performed for the electron trajectories. For frequencies near resonance these equations are implicitly slowly-varying. The advantage of this procedure is that a greater wealth of physical phenomena are included in the simulation. For example, ARACHNE models the injection of the beam into the wiggler. This will be seen to be important because substantial beam loss can occur during this process.

## Numerical Simulations

We are interested in W-Band operation with a center frequency of 94 GHz, and with the minimum beam voltage that is practical for operation at the fundamental. To this end, we assume a helical wiggler with a period of 0.88 cm with amplitudes of up to 3.0 kG which is possible using a superconducting design [2]. A 94 GHz fundamental resonance is possible for beam voltages of 300-400 kV using a wiggler with this period.

In simulating such a device, we assume a TE<sub>11</sub> mode interaction in a waveguide with a 0.3 cm inner radius. We also assume an initial beam radius [i.e., prior to injection into the wiggler] of 0.2 cm and a beam current of 50 A. This results in a current density of 398 A/cm<sup>2</sup>. Under the assumption of an ideal beam in which the normalized emittance vanishes, we plot the efficiency at 94 GHz versus beam voltage for wiggler field amplitudes of  $B_w = 1.5, 1.75, 2.0, 2.5,$  and 3.0 kG in Fig. 1. It is evident that the efficiency peaks at values between 14-15% for  $B_w \approx 2.0-2.5$  kG and for beam voltages of 320-340 kV.

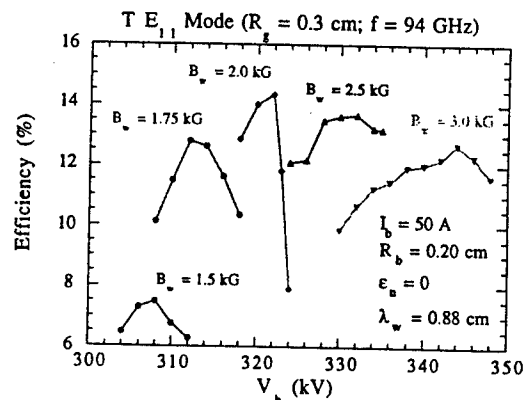


Fig. 1 Plots of the efficiency versus beam voltage.

Since the interaction occurs over a broader range of voltages for  $B_w = 2.5$  kG, we now study the instantaneous bandwidth for voltages of 320 and 330 kV. These results are shown in Fig. 2. It is clear that both the peak efficiency ( $\approx 13.9\%$ ) and the FWHM bandwidth (92.8-101.4 GHz) is greater at the higher voltage.

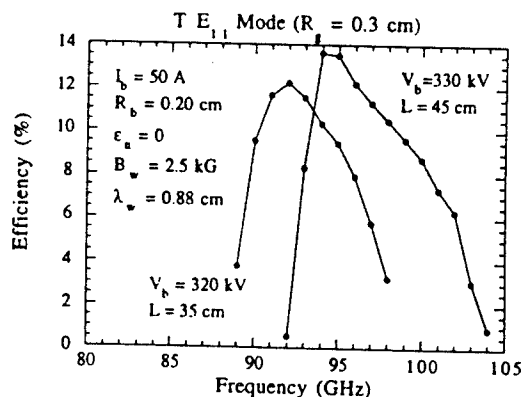


Fig. 2 Instantaneous bandwidth for  $B_w = 2.5$  kG.

We now consider the effect of increases in the normalized emittance on the efficiency and bandwidth at 330 kV. This is illustrated in Fig. 3 where we plot the efficiency versus frequency for normalized emittances of 0,  $20\pi$  mm-mrad,  $28\pi$  mm-mrad, and  $45\pi$  mm-mrad. It is clear from the figure that the peak efficiency falls off from 13.8% for an ideal beam to about 6% for a normalized emittance of  $45\pi$  mm-mrad and the center frequency falls from 97.1 GHz to 93.7 GHz; however, the bandwidth remains relatively constant.

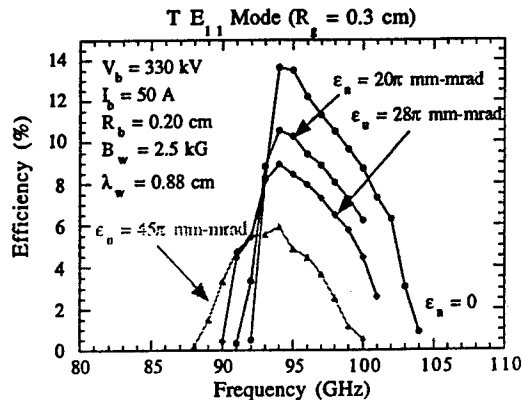


Fig. 3 Variation in the efficiency with emittance.

One prime issue in the development of a W-Band FEL amplifier with a high duty cycle is the extent of beam transmission. At high average powers, the loss of even a small fraction of the beam can result in a catastrophic burn of the waveguide. To this end, we study the beam transmission for each of the emittances used in Fig. 3 for an interaction at 94 GHz, and plot the results in Fig. 4. Recall that we model beam injection, and for this purpose we assume that the wiggler field amplitude increases adiabatically over 10 wiggler periods (8.8 cm) from the entrance to the wiggler. It is clear that no beam loss occurs for an ideal beam. As the emittance increases to  $20\pi$  mm-mrad, the beam loss increases to only about 1% of the beam, and most of this loss occurs during beam injection. As the emittance increases still further, beam loss increases rapidly up to almost 40% for an emittance of  $45\pi$  mm-mrad. Once again, however, most of this beam loss occurs during the injection process.

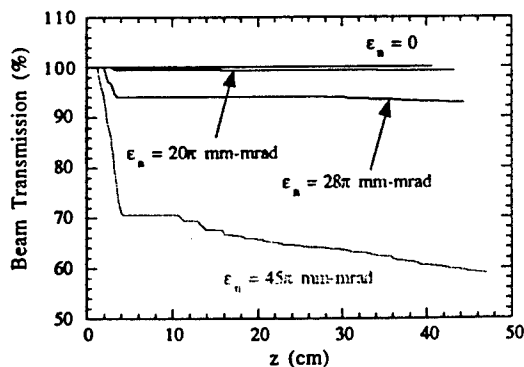


Fig. 4 Beam propagation versus emittance.

The key to minimizing beam loss, therefore, appears to be twofold. In the first place, the emittance should be kept below  $20\pi$  mm-mrad for the chosen parameters. To this end, it should be noted that a gun design has been reported recently for use in a free-electron maser for fusion heating applications with an emittance of  $10\text{--}30\pi$  mm-mrad [3]; hence this target does appear to be achievable. In the second place, beam injection must be carefully considered. No axial guide field was used in the present sample cases, and we expect that the additional focusing will result in improved beam transmission during injection. In addition, the proper shaping of the adiabatic region might also improve beam transmission during injection.

## Summary and Discussion

Design calculations have been presented here for a W-Band free-electron laser amplifier. The helical wiggler parameters of 0.88 cm period and 2.5 kG peak on-axis field amplitude are within the state-of-the-art for superconducting wiggler design, and permit operation in W-Band using beam voltages of 300–400 kV. Assuming a current density of  $\leq 400$  A/cm<sup>2</sup> and an emittance of  $20\pi$  mm-mrad or less, which is also with the state-of-the-art, efficiencies of 10–14% are possible with an instantaneous bandwidth of about 9%. This yields peak powers of 1.6–2.3 MW, which results in average powers in the range of 16–230 kW for duty factors ranging from 1–10%.

## Acknowledgments

This work was supported by the Office of Naval Research. The computational work was supported in part by grants of High Performance Computing (HPC) time from the Department of Defense HPC Shared Resource Centers CEWES and NAVO.

## References

- †Permanent Address: Science Applications International Corp. McLean, VA 22102, USA.
- [1] H.P. Freund and T.M. Antonsen, Jr., *Principles of Free-electron Lasers* (Chapman & Hall, London, 1996) 2nd edition.
- [2] G. Ingold et al., Nucl. Instrum. Meth. **A375**, 451 (1996).
- [3] M. Caplan et al., Nucl. Instrum. Meth. **A375**, 91, (1996).

# A Ka-band Bragg Free Electron Maser Oscillator with Axial Guide Magnetic Field

A.D.R. Phelps, A.W. Cross, D.A. Jaroszynski, W. He,  
C. Whyte, N.S. Ginzburg\* and N.Yu. Peskov\*

University of Strathclyde, Glasgow, G4 0NG, UK

\*Institute of Applied Physics RAS, 603600 Nizhny Novgorod, Russia

## Abstract

The narrow-band FEM-oscillator with Bragg resonator operated in reversed guide field regime was realized on the base of high-current accelerator University of Strathclyde formed 300 keV, 50 A, 100 ns electron beam. At the frequency 32 GHz the radiation with the power 500 kW and efficiency 5% was registered. The FEM parameters under which the generation was observed were in good agreement with numerical simulation as well as measured radiation frequencies coincided with the results of "cold" microwave experiments.

## Introduction

One of the promising sources of powerful coherent Ka-band radiation are Free Electron Masers (FEM) with a guide magnetic field. The high efficiency operation of such FEMs have been demonstrated for, the so-called, reversed guide field regime both for amplifier [1, 2] and oscillator [3] schemes. In oscillators, the use of Bragg resonator [4] permits one to realize a narrow-band width of radiation spectrum [3-5]. Results of experimental study of a Ka-band FEM-oscillator operated in reversed guide field regime on the base of high-current accelerator University of Strathclyde are discussed in the report.

## Experimental set-up

An experimental study of the FEM was performed on an explosive emission accelerator (fig.1) University of Strathclyde which generated electron energies of ~300 keV and up to 50 A beam current pulse of duration 100 ns. An operating transverse velocity of electrons was induced by a helical wiggler with period 2.3 cm and amplitude of transverse magnetic field on the axis of up to 0.3 T. The wiggler field was slowly up-tapered over the initial five periods, providing an adiabatic entrance for the electron beam, the regular section of the wiggler contained 15 periods. The wiggler was immersed in a uniform axial magnetic field generated by a dc-solenoid. The strength of this field can be varied up to 0.3 T. Also, it was possible to vary the direction of the guide field.

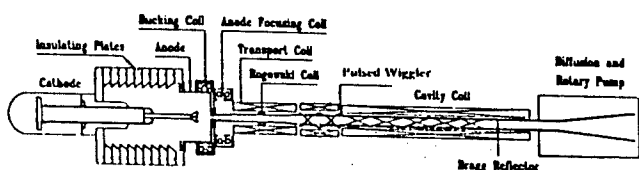


Fig.1 Scheme of the experiment

## Advantages of FEM operation in reversed guide field regimes

A reversed guide field regime was chosen for operation of the FEM. In such a regime the direction of the rotation of the electrons in the uniform axial guide field is opposite to its rotation in the wiggler field (marked by "-" sign further). An advantage of the reverse guide magnetic field regime, operating far from the cyclotron resonance, is the ability to form a high-quality helical electron beam with low spread of parameters, if an adiabatic entrance for the electrons is used.

Computer simulation of the e-beam/e.m.wave interaction confirms this conclusion. In this simulation a 3-D code was used for particle motion in the wiggler and solenoid fields which were obtained from "cold" measurements with the RF-field structure found from simulation of the "cold" Bragg resonator. It was discovered that for a FEM with axial guide field operating in reversed guide field regimes the sensitivity to the initial spread of beam parameters was very small. Even for an electron beam with a rather large initial "parasitic" transverse velocity (approximately 50% of operating transverse velocity  $\beta_{\text{oper}}$ ) a decline of FEM efficiency averaged over all the fractions (fig.2) was not more than 1% of the efficiency in comparison to a FEM when driven by an ideal electron beam (zero abscise in fig.2). The simulations carried out therefore prove the capability of high-efficiency FEM operation and was corroborated in previous experiments of a FEM with reversed guide field [1-3].

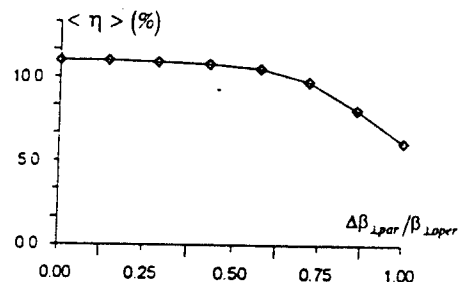


Fig.2 Efficiency of the FEM operating in reversed guide field regime versus initial parasitic transverse velocity in the driving beam  $\Delta\beta_{\text{Lpar}}$  (computer simulation)

## Microwave system of the FEM

The microwave cavity consisted of two Bragg reflectors separated by a central 10 cm long, 15 mm inner diameter uniform cylindrical waveguide. The Bragg reflectors were constructed by machining 0.3 mm deep and 5.6 mm period



corrugations on the inner wall of the waveguide. The cavity was optimized for oscillation of the lowest order  $TE_{1,1}$  cylindrical cavity mode. The frequency of operation for optimum reflection of the backward  $TM_{1,1}$  wave was designed and measured in "cold" microwave experiments to be near 32.5 GHz. The band-width of effective reflection in this zone as well as positions of longitudinal modes of the resonator were shown in fig.3.

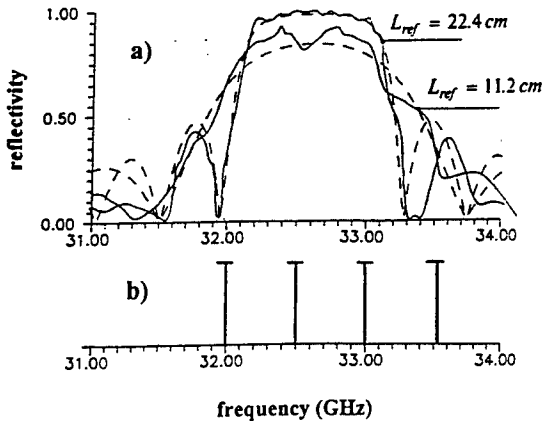


**Fig.3** (a) Reflection coefficient of Bragg mirrors having different lengths versus frequency (solid line corresponds to the "cold" microwave measurements, dotted line corresponds to the calculations). (b) Positions of longitudinal modes of the Bragg resonator (11 cm + 15 cm + 11 cm) utilized in the experiment

### Experimental results

An electron beam transportation through the electron-optical FEM system and the formation of a helical electron beam was achieved for both conventional forward and reverse guide magnetic fields. A witness plate electron beam diagnostic consisting of a beam sensitive Mylar sheet inserted in the beam transport region was used to measure the beam, position, size and shape for both the forward and reversed guide fields. Comparison of the beam 'spots' on the witness plate clearly showed a more uniform electron beam was obtained for the reversed guide field regime.

Radiation with the designed structure of the  $TE_{1,1}$  wave was observed in "hot" experiments when a reversed guide field configuration was utilized. The typical oscilloscope traces of diode voltage, beam current and RF-signal are shown in fig.4. In the experiments the microwave output pulses were detected by a rectifying crystal detector and RF-power was registered by a calibrated thermocouple calorimeter. The frequency of radiation was measured by means of a set of cut-off meshes and was in good agreement with calculations and was also consistent with results obtained from "cold" microwave experiments.

It should be noted, that two operation regimes were registered in the experiments. When the wiggler field of 0.1 T and axial guide field of -0.2 T was applied, the generation of the  $TE_{1,1}$  mode with the frequency of 11 GHz corresponding to the cut-off frequency of the microwave system was observed (without the Bragg resonator). The increasing of wiggler field lead to decreasing of output power.

The critical wiggler field under which the radiation disappeared was 0.11 T. This can be explained by the decreasing of the axial velocity of the electrons resulting in a shift of the crossing point with the dispersion curves of the  $TE_{1,1}$  mode out off its cut-off frequency and decreasing the Q-factor of the near-cut-off mode.

The maximum radiation power in designed Doppler frequency up-shift regime on the  $TE_{1,1}$  mode with the frequency near 32.5 GHz was observed under the wiggler field of 0.13 T in the 10% band of its changing. With the Bragg resonator configuration of 11 cm length of both collector-side and output-side reflectors and 15 cm length of regular waveguide section an output power of 500 kW corresponding to electron efficiency of about 5% was measured when an electron beam current of 30 A was utilized.

The results of the experiments confirm a possibility of using a high-current relativistic electron beam (without any electron beam reduction) for generation of powerful microwave generation in FEM with reversed guide field configuration. However, the measured electron efficiency was less than theoretically predicted and optimization of the Bragg cavity parameters will be done.

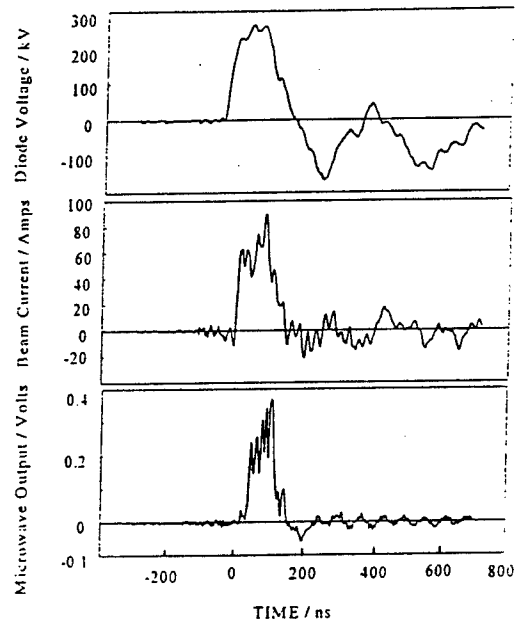


**Fig.4** The applied accelerating potential, beam current and mm-wave output. All displayed on the same absolute time axis

### References

1. Kaminsky A.A., Kaminsky A.K., Rubin S.B. Particle Accelerators, 1990, vol.33, p.189.
2. Conde M.E., Bekefi G. Phys. Rev. Lett., 1991, vol.67 (22), p.3082.
3. Kaminsky A.K., Kaminsky A.A., Sarantsev V.P., Sedykh S.N., Sergeev A.P., Ginzburg N.S., Peskov N.Y., Sergeev A.S. Nucl. Instr. and Meth. in Phys. Research, 1996, vol.A375, p.215.
4. Bratman V.L., Ginzburg N.S., Denisov G.G., Petelin M.I. IEEE J. Quant. Electr., 1983, vol.QE-19, p.282.
5. Chu T.S., Hartemann F.V., Danly B.G., Temkin R.J. Phys. Rev. Letters, 1994, vol.72, p.2391.

# COLD TEST OF GYROTRON OUTPUT WAVE-BEAM SPLITTER AND COMBINER

Y. Mitsunaka, Y. Hirata, K. Hayashi, Y. Itoh

Energy and Mechanical Research Laboratories,  
Research and Development Center, Toshiba Corporation,  
4-1 Ukishima-Cho, Kawasaki-ku, Kawasaki 210, Japan

K. Sakamoto, A. Kasugai, K. Takahashi and T. Imai

Naka Fusion Establishment, Japan Atomic Energy Research Institute,  
801-1 Mukouyama, Naka-machi, Ibaraki 311-01, Japan

## Abstract

A millimeter wave-beam splitter and a combiner, both of which comprise phase-correction mirrors, were fabricated and tested. The splitter is applied in a high power gyrotron to reduce the output power density at the window, and the combiner is used to combine the two wave-beams into one for transmission. For a 110-GHz, TE<sub>22,6</sub> mode input, the power profiles measured at the splitter and combiner output positions were in good agreement with calculations.

## Introduction

Future experimental fusion devices such as ITER or LHD require 1-MW, CW gyrotron tubes at operating frequencies of about 170 GHz. The design of their output windows is a crucial problem in realizing such tubes, whose heat load is so high that conventional face-cooled sapphire double disk windows can hardly endure to pass a 1-MW, CW beam. The window heat load can be reduced by dividing the output wave power in the tubes and by transmitting the divided power through plural windows.

We proposed a scheme whereby a given wave-beam is shaped into the desired profile using multiple phase-correction mirrors [1]. A wave-beam splitting and combining technique was also presented in that paper. The present paper presents a design of a millimeter wave-beam splitter and a combiner for the 170GHz TE<sub>31,8</sub> mode wave, and the result of cold test carried out for a millimeter wave-beam splitter and a combiner for the 110GHz TE<sub>22,6</sub> mode wave.

## Design (for 170GHz)

A millimeter wave-beam splitter and a combiner were designed for the TE<sub>31,8</sub> mode at a frequency of 170 GHz, which is suitable for a 1MW CW gyrotron. Fig. 1 shows a schematic diagram of the millimeter wave-beam splitter and the combiner. The splitter inside a gyrotron tube comprises

seven mirrors. Oscillated wave of 170 GHz TE<sub>31,8</sub> mode was transformed into a wave-beam by a dimple mode converter [2], and focused by a parabola mirror M1. Four phase-correction mirrors M2-M5 split the wave-beam into two flattened circular beams at the position of two output windows of a gyrotron. Mirror M6 is a flat mirror. Mirror M7 is a parabola mirror which adjusts wave-beam size. The combiner outside the tube comprises four mirrors. Mirror M8 is a parabola mirror which adjusts wave-beam size. Three phase-correction mirrors M9-M11 combine the two flattened circular wave-beams into one beam at the position of a corrugated waveguide.

Fig. 2 shows the calculated power distributions at the position of the splitter output end where two output windows will be placed. Fig. 3 shows the calculated power distributions at the position of the combiner output end where a corrugated waveguide will be placed. Contour lines are drawn every 1/10 of the peak power density in the linear scale. Peak power density at the position of the windows was calculated to be 0.18 times that of one Gaussian beam of 35mm spot size. Transmission efficiencies at the position of the windows and the corrugated waveguide were calculated to be 89.3 % and 82.3 % respectively. The HE<sub>11</sub> mode purity was calculated to be 99.2 %. Thus the 170GHz TE<sub>31,8</sub> mode wave can be split into two flattened circular beams and combined into one HE<sub>11</sub>-like beam.

## Cold test results (for 110GHz)

A millimeter wave-beam splitter and a combiner were designed and manufactured for the TE<sub>22,6</sub> mode at a frequency of 110 GHz, which is suitable for the existing cold test stand. The mirror size and arrangement were designed to be the same as those for 170GHz wave, so that a part of the equipment (base, mirror holders, parabola mirrors) could be used for 170GHz cold test. Wave-beam profile at the position of the splitter output end and the combiner output end were detected by a crystal detector swept by a computer controlled X-Y table.

Fig. 4 and Fig. 5 show the calculated and measured power distributions at the position of the splitter output end. Fig. 6 shows the calculated and measured power distribution at the combiner output end. Measured wave profiles were in good agreement with calculations, and no spurious wave-beam was observed around the mirrors. The TE<sub>22,6</sub> mode wave was thus efficiently transformed into a pair of circular beams and then combined to one beam.

## Conclusions

A millimeter wave-beam splitter and a combiner were tested for the TE<sub>22,6</sub> mode at a frequency of 110 GHz. Measured wave profiles at the positions of output end of the splitter and the combiner were in good agreement with calculations. Thus it is shown that a millimeter wave-beam can be split into two flattened wave-beams and combined into one beam.

By dividing and flattening the output power with this splitter, the heat load of gyrotron output windows can be reduced, and by combining the two output beams, the cost of transmission lines can be reduced.

## References

- [1]Y. Hirata, Y. Mitsunaka, K. Hayashi, Y. Itoh, "Wave-Beam Shaping Using Multiple Phase-Correction Mirrors", IEEE Tans. MTT, Vol.45, No.1, Jan. 1997, pp. 72-77
- [2]G. G. Denisov, et al., "110 GHz gyrotron with a built-in high-efficiency converter", Int. J. Electronics, 1992, vol. 72, nos. 5 and 6, 1079-1091.

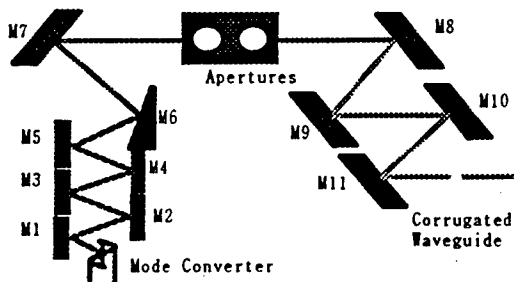


Fig. 1 Schematic diagram of millimeter wave-beam splitter and combiner

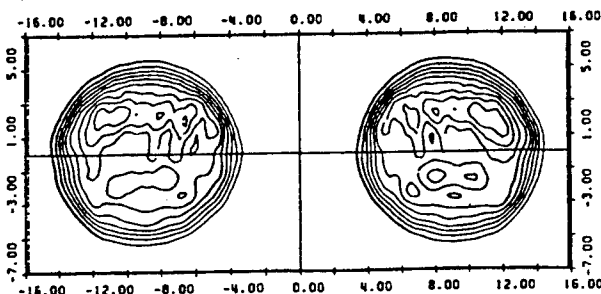


Fig. 2 Calculated power distributions at the position of the two windows for the 170 GHz wave

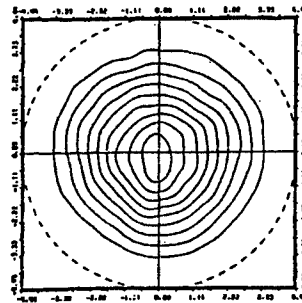


Fig. 3 Calculated power distributions at the position of the corrugated waveguide for the 170 GHz wave

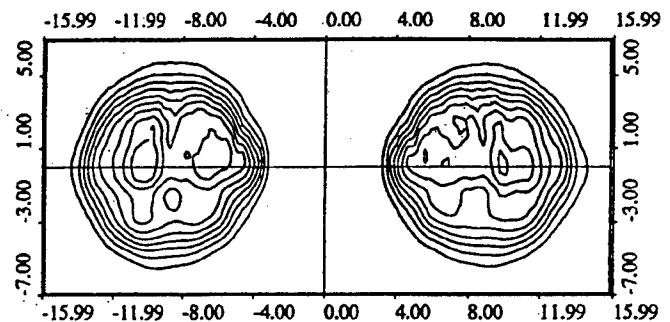


Fig. 4 Calculated power distributions at the position of the splitter output end for the 110 GHz wave

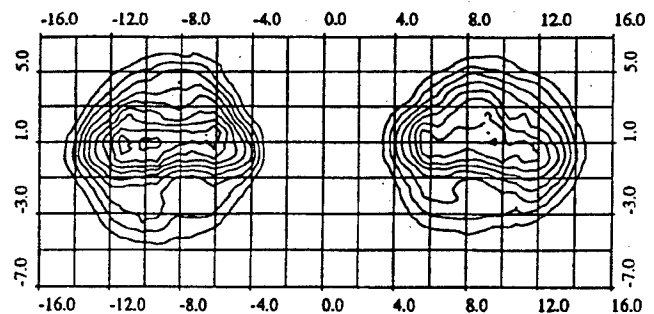


Fig. 5 Measured power distributions at the position of the splitter output end for the 110 GHz wave

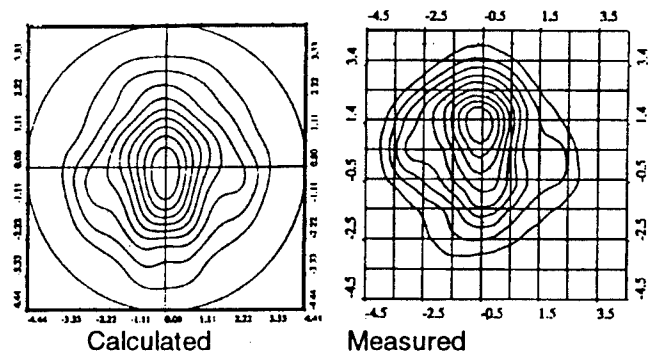


Fig. 6 Power distributions at the position of the combiner output end for the 110 GHz wave

## Low Power Performance Tests on Highly Oversized Waveguide Components of High Power Gyrotrons

O. Braz <sup>1) 2)</sup>, A. Arnold <sup>1) 2)</sup>, H. - R. Kunkel <sup>1)</sup>, M. Thumm <sup>1) 2)</sup>

<sup>1)</sup> Forschungszentrum Karlsruhe (FZK), ITP, Association EURATOM-FZK,  
Postfach 3640, D-76021 Karlsruhe, Germany

<sup>2)</sup> and Universität Karlsruhe, Institut für Höchstfrequenztechnik und Elektronik,  
Kaiserstr. 12, D-76128 Karlsruhe, Germany

### Abstract

To generate and transport high power micro- and millimeter-waves, highly oversized waveguide components have to be used. For the verification of their performance in cold-test measurements, analyzing systems covering a large dynamic range ( $> 100$  dB) are needed. This paper describes the realization of a new vector network analyzer ( $f = 110$  GHz to 170 GHz) covering the requirements mentioned above. The analyzing system will be applied to measurements on a low power  $TE_{76,2}$  mode generator and a  $TE_{28,16}$  - to  $-TE_{476,2}$  mode converter for a 1.5 MW, 140 GHz coaxial cavity gyrotron.

### Introduction

High power gyrotrons are nowadays usually equipped with a quasi-optical mode converter system. By converting the operating high order TE cavity mode into a defined free-space distribution the influence of the required vacuum barrier window on the gyrotron's oscillation behavior can be reduced. For low-loss energy transportation either in corrugated  $HE_{11}$ -waveguides or in quasi-optical mirror lines a fundamental Gaussian beam is preferred. To decrease the Ohmic loading on the cavity wall and to maximize the achievable millimeter-wave power it is necessary to operate at extremely high-order modes. To separate the problem for the most efficient power output coupling from the demand for a high beam quality, currently the use of phase-correcting mirrors outside the gyrotron is under investigation. This results in increasing requirements on the used test facilities. For cold test measurements the gyrotron cavity mode can be excited by mode generators applying quasi-optical techniques [1], [2]. With respect to the achievable mode purity this high-order modes together with the high frequencies (170 GHz planned for ITER plasma heating) lead to extreme requirements on the mechanical precision in fabricating the mode generator. One possibility to overcome these mechanical restrictions is a more complicated design. In our case we prefer a detailed analysis of the excited mode spectrum. By knowing the magnitude and phase of the disturbing competitors their influence on the measured field patterns can be removed by calculation. A standard method for analyzing the wavenumber spectrum are k-spectrometer measurements [3]. Due to the low coupling characteristics of this device, analyzing systems covering a large dynamic range are needed.

### The D-Band vector network analyzer

Figure 1 shows a schematic drawing of the new homemade D-band vector network analyzer. At the desired frequency range from 110 GHz to 170 GHz powerful narrow-band signal sources are of special interest. Therefore a backward-wave oscillator (BWO) has been frequency stabilized by installing a phase locked loop (PLL) circuit. By this way the BWO's output frequency (8 MHz bandwidth unstabilized) could be phase locked to a 10 MHz quartz reference with a line width of less than 10 Hz! In order to achieve a narrow bandwidth and by this way an extremely low noise level ( $-130$  dBm) a multi-stage super-het receiver was built. To be able to determine the phase shift caused by the device under test (DUT) the required frequencies for down conversion are also derived from the quartz reference. By using the stabilized BWO for the transmitting part of the vector network analyzer its dynamic range is extended to more than 110 dB.

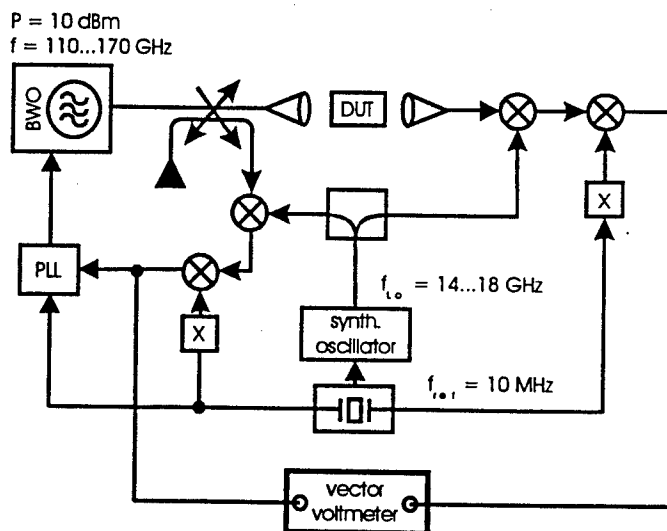


Fig. 1: Schematic drawing of the vector network analyzer.

Figure 2 shows a typical vector k-spectrometer measurement performed on a  $TE_{476,2}$  low power-mode generator. One has to take into account that the coupling attenuation (generator losses and k-spectrometer coupling) has been approximately 85 dB. As it can be seen in the lower part of the figure for each mode also the phase information could be determined.

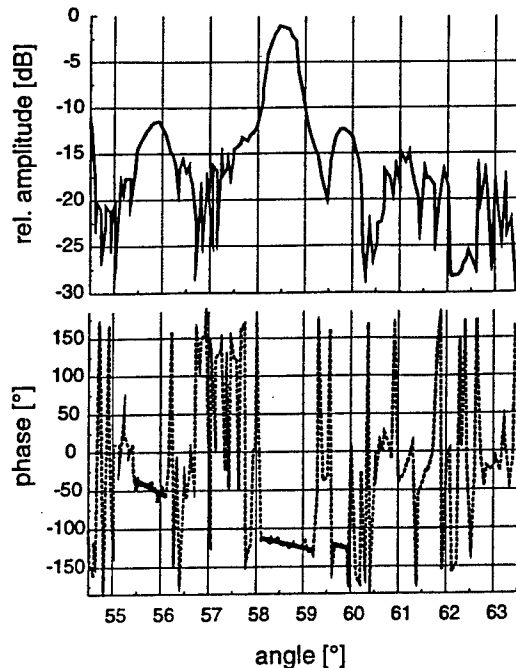


Fig. 2: Vector k-spectrometer measurement of  $TE_{76,2}$  generator.

### Measurements on the $TE_{76,2}$ mode generator

For testing the dual-beam output coupling system for the RF power of the FZK 140 GHz, 1.5 MW coaxial gyrotron [4] a low-power mode generator for a rotating  $TE_{76,2}$  mode has been built up. The wavenumber spectrum of this generator is shown in Figure 3. In contrast to the measurement shown in Figure 2 a more careful alignment had been performed.

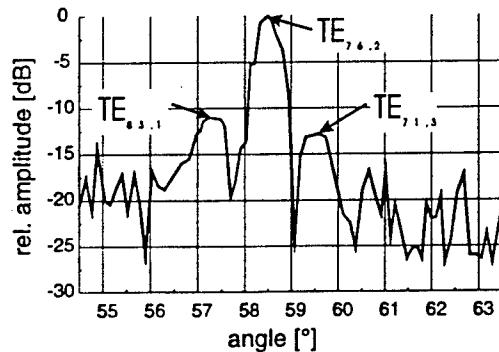


Fig. 3: k-spectrometer measurement of  $TE_{76,2}$  generator.

As it can be seen the main content of RF power is radiated under an angle of  $58.3^\circ$  to the axis of the k-spectrometer waveguide. This angle corresponds to the  $TE_{76,2}$  mode propagating at 140 GHz in a 70 mm diameter waveguide. Unfortunately the spectrum shows two undesired competitors at  $57.4^\circ$  and  $58.8^\circ$  which have been identified to be the  $TE_{83,1}$  and  $TE_{71,3}$  mode respectively. Taking the different k-spectrometer coupling attenuation factors into account the suppressions of the modes  $TE_{83,1}$  and  $TE_{71,3}$  have been determined to be 16 dB and 11.5 dB. By rotating the k-spectrometer around its waveguide axis the content of the counter rotating  $TE_{76,2}$  mode was determined to be 4 %.

The overall mode purity of the desired  $TE_{76,2}$  mode is approximately 88 %.

### The $TE_{28,16}$ - to - $TE_{76,2}$ mode converter

In the coaxial gyrotron the needed  $TE_{76,2}$  mode for the dual beam output is achieved by conversion from the  $TE_{28,16}$  gyrotron cavity mode [5]. To check the proper behavior of the required converter (104 axial slots in the waveguide wall) the system was operated in the reverse way. This means that the  $TE_{76,2}$  mode was fed into the converter. The measured field pattern at the converter output (input) is shown in Figure 4. It is obvious that the pattern shows a rather high content of the desired  $TE_{28,16}$  mode. This is in agreement with k-spectrometer measurements which also had been performed.

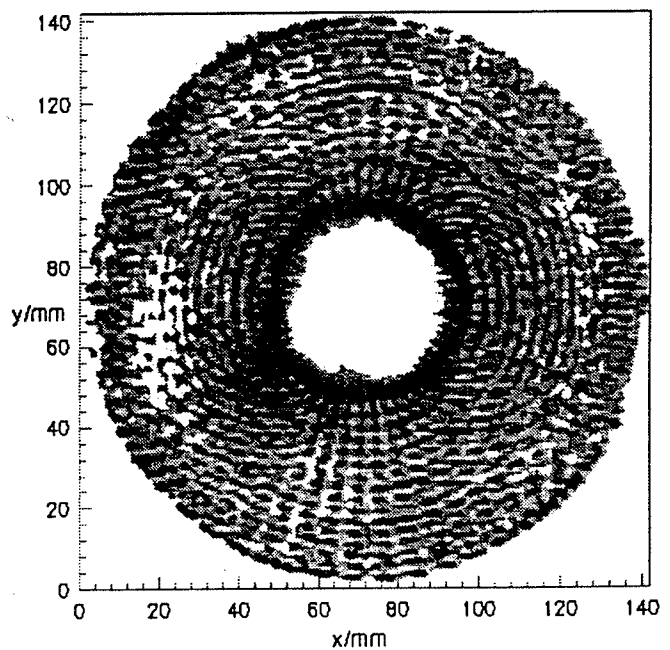


Fig. 4: Measured field pattern of  $TE_{28,16}$  mode.

### References

- [1] Pereyaslavets, M., Braz, O., Kern, S., Losert, M., Möbius, A., Thumm, M., 1997, *Int. J. Electronics*, **82**, 107-115.
- [2] Braz, O., Arnold, A., Losert, M., Möbius, A., Pereyaslavets, M., Thumm, M., 1996, *Conf. Proceedings 21th Int. Conf. on Infrared and Millimeter Waves*, Berlin, ATh6.
- [3] Kasparek, W., Müller, G. A., 1988, *Int. J. Electronics*, **64**, 5-20.
- [4] Piosczyk, B., et al., accepted for *IEEE Trans. Plasma Science*, June 1997.
- [5] Thumm, M., et al., 1996, *Conf. Proceedings 21th Int. Conf. on Infrared and Millimeter Waves*, Berlin, AM6.

## EXPERIMENTAL RESULTS OF GYROTRON-OUTPUT MATCHING WITH THE HE11 MODE

Y. Hirata, \*Y. Mitsunaka, M. Komuro, K. Hayashi, S. Sasaki(1), Y. Kanai(1),  
S. Kubo(2), T. Shimozuma(2), M. Sato(2), Y. Takita(2), K. Ohkubo(2), T. Watari(2)

Energy and Mechanical Research Laboratories, Toshiba Corporation,  
4-1 Ukishima-cho, Kawasaki-ku, Kawasaki 210, Japan

(1) Keihin Product Operations, Toshiba Corporation

(2) National Institute for Fusion Science

### Abstract

The flattened output wave of a 168-GHz gyrotron was reshaped into the HE11 mode using an external matching box (MBOX) comprising phase-correction mirrors. The power and phase profiles of the wave were determined before and after the MBOX from power profile measurement at multi cross sections. The power levels of the gyrotron operation were 250 kW. From the power and phase profiles of the wave at the MBOX end, the HE11 mode purity was estimated to discuss the coupling efficiency of the gyrotron output with the transmission line.

### Introduction

Current electron cyclotron heating systems for nuclear fusion devices use, as a wave source, high power gyrotrons with frequencies around 170 GHz. In the present research of high power gyrotrons, the focus is mainly on the gyrotron internal mode converter and mirror system that transform the cavity-generated wave into a flat wave beam in order to reduce the local power density of the wave at the window [1, 2, 3].

The wave power, generated by a gyrotron, is conveyed to a fusion device which is typically placed at a distance of about 100 m. The gyrotron output, therefore, must be highly coupled with corrugated waveguides which are the main component of the transmission line. In order for the flattened output to highly couple with corrugated waveguides, a matching box (MBOX) comprising plural phase-correction mirrors is placed outside the gyrotron to reconvert the flattened output into the HE11 mode, a basic transmitting mode in corrugated waveguides [4].

This paper deals with experimental results of 168-GHz gyrotron internal and external mirror systems. Both the power and phase profiles of the gyrotron-generated wave were determined at the gyrotron window and the MBOX end from power profile measurement at multi cross sections combined

with iterative calculations [5]. To improve accuracy in the determination of the phase profile, furthermore, the waves with the measured power- and calculated phase-profiles at the four positions were averaged.

In the following sections we will describe the power and phase profile measurement of the gyrotron output wave at the gyrotron window and MBOX end positions, including the averaging process which improves the accuracy of the wave measurement. We will also discuss HE 11 mode purity of the reconverted wave.

### Wave measurement at the gyrotron window

Fig. 1 shows a schematic of the gyrotron system comprising a gyrotron and a matching box (denoted as MBOX). The gyrotron cavity generates a wave in the TE<sub>31,8</sub> mode at a frequency of 168 GHz. The wave is, then, radiated by the internal single-helical mode converter, and is transformed into a flat wave beam with a diameter of 120 mm by the internal mirror system comprising flat and shaping mirrors. The flattened output is directed into the MBOX placed outside the gyrotron. The shaping-mirrors of the MBOX are designed to convert the ideally-flat wave beam into the HE11 mode, a basic transmitting mode in corrugated waveguides. To the end of the MBOX is attached a corrugated waveguide with an inner diameter of 88.9 mm, which guides the wave to the transmission line. The flattened output of the gyrotron is, thus, transformed into the HE11 mode, and is directed into the transmission line.

Power profile measurement was first done at the gyrotron window. A paper screen was placed perpendicular to the wave-beam axis. The power density profile of the wave is measured by a thermo-camera as the profile of temperature rise in the screen. At four distances from the gyrotron window with an interval of 200 mm, the power profiles of the gyrotron output wave were measured. The power levels of the wave beam were between 250 - 300 kW. The phase profiles at the four cross sections were reconstructed by iterative calculations according to Ref. [5]. In addition to the referenced procedure, we try to average

these four waves in order to improve accuracy in the phase reconstruction. The waves with measured power- and reconstructed phase-profiles at the second, third, and fourth cross sections are transmitted to the first cross section, respectively, and are averaged there. Mathematically, averaging can be done at any cross section to result in a single wave. The square overlap integrals (see Ref. [5]) of the resulting single wave and the measured power profiles at the corresponding distances were all greater than 99.5%. It should be noted that averaging the waves measured and calculated at more than four cross sections will improve accuracy in the phase profile measurement even more.

While several peakings exist, the power profile of the obtained wave is rather flat. Concerning the phase, the phase in the window equivalent area ( $\phi 140$  mm) shows a small variation with a standard deviation of  $\pi/8$ .

### Wave measurement at the MBOX end

The gyrotron output wave was directed into the MBOX, which converts the output into the HE11 mode at the MBOX end. Here, wave profile measurement was also done using a thermo-camera at four cross sections with an interval of 200 mm. The resulting wave beam, after phase-reconstruction and averaging, is shown in Fig. 2 (power profile) and Fig. 3 (phase profile), where the profiles are displayed within a 88.9-mm-diameter circle. The square overlap integrals of the resulting wave and the measured power profiles at the corresponding positions were 97 - 99%. This wave contained an HE11 mode purity of 87%.

The wave power at the MBOX end was also measured via a 1-m-long, 88.9-mm-diameter corrugated waveguide placed between the MBOX and the dummy load. The measured power transmission efficiency of the MBOX was 87%. The measurement shows that 76% of the gyrotron output was directed into the corrugated waveguide as the HE11 mode.

### Conclusions

Both the power and phase profiles of a 168-GHz gyrotron output wave were examined. The wave measurement was conducted at the gyrotron window and the MBOX end. A well-flattened wave beam was obtained at the window position. Moreover, the wave profile measured at the MBOX end contained an HE11 mode purity of 87%; the measured power transmission efficiency of the MBOX was 87%. Thus, 76% of the gyrotron output was coupled with the corrugated waveguide in the HE11 mode.

### References

- [1] G. G. Denisov, V. A. Flyagin and V. E. Zapevalov, Conf. Digest of 20th Int. Conf on Infrared and Millimeter

Waves, 1995, pp. 197-198.

- [2] K. Sakamoto, A. Kasugai, M. Tsuneoka, et al., Conf. Digest of 20th Int. Conf. on Infrared and Millimeter Waves, 1995, pp. 269-270.
- [3] K. Felch, P. Borchard, T. S. Chu, et al., Conf. Digest of 20th Int. Conf. on Infrared and Millimeter Waves, 1995, pp. 191-192.
- [4] Y. Hirata, Y. Mitsunaka, K. Hayashi, and Y. Itoh, IEEE Trans. Microwave Theory Tech., Vol. 45 (1997), pp. 72-77.
- [5] A. V. Chirkov, G. G. Denisov and N. L. Aleksandrov, Optics Comm., Vol. 115 (1995), pp. 449-452.

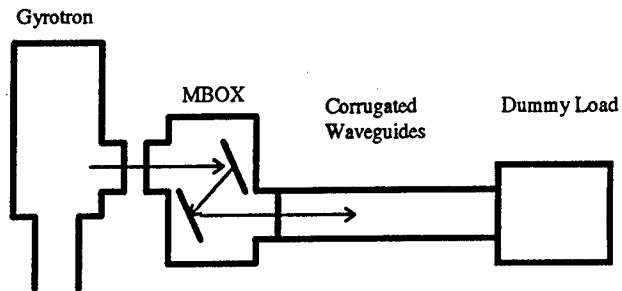


Fig. 1 Experimental setup.

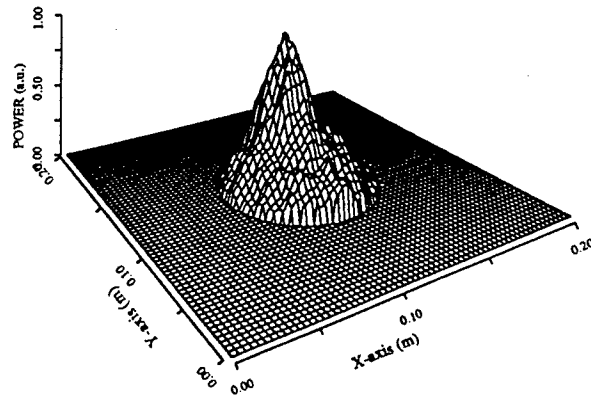


Fig.2 Power profile at MBOX end.

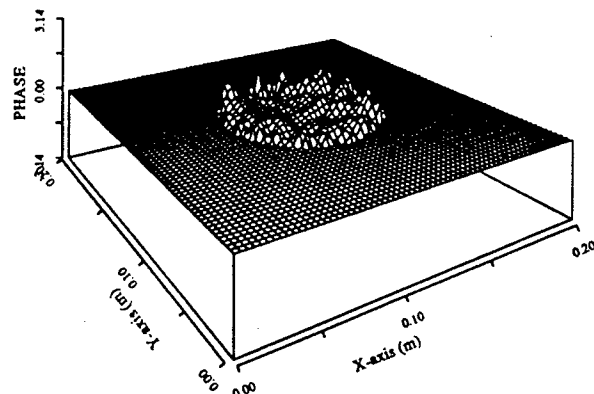


Fig. 3 Phase profile at MBOX end.

## Design of a Quasi-Optical Mode Converter for a Coaxial 165 GHz $TE_{31,17}$ Gyrotron

G. Michel\*, M. Thumm\*, D. Wagner†

\*) Forschungszentrum Karlsruhe, ITP, Association EURATOM-FZK,  
P.O.Box 3640, 76021 Karlsruhe, Germany  
and Universität Karlsruhe, IHE, Kaiserstr. 12,  
76128 Karlsruhe, Germany

†) Universität Stuttgart, Institut für Plasmaforschung,  
Pfaffenwaldring 31, 70569 Stuttgart, Germany

### Abstract

The design of a quasi optical mode converter for the extreme volume mode  $TE_{31,17}$  is described. It is the operating mode of a 1.5 MW, 165 GHz coaxial cavity gyrotron to be built. The goal is to launch the operating mode directly in order to keep the converter short and the conversion losses and ohmic losses low. Due to the large azimuthal angle of this mode, the design is based on a hybrid geometrical optical and physical optical technique.

### Choice of the Converter Principle

The common principle for launching a gaussian like beam from a waveguide cut is the dimple wall converter. It provokes a resonant [1] eigenmode change in the waveguide before launching the beam. For the  $TE_{31,17}$  mode this can be easily achieved for a pentagram like ray structure ( $\Delta m = 5$ ) which is well suited for a double beam launcher.

For a single beam launcher, the large spread angle ( $2\theta = 140^\circ$ ) cannot be transformed into a small one with a short converter and the mode  $TE_{31,17}$  as the main mode. Since a dimple wall launcher has only little advantage in this case, an ordinary Vlasov launcher is used and the transformation of the strongly divergent beam into a paraxial one is done by means of specific mirrors. This transformation requires either a few weakly curved mirrors [2] or one strongly curved mirror.

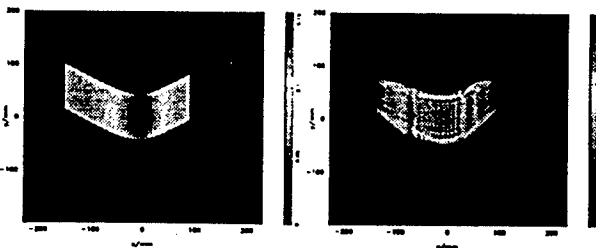


Figure 1: GO (left) and PO (right) Output of the Vlasov Launcher

In the gyrotron vacuum vessel space is limited, therefore the second solution is chosen. The strongly curved mirror, however, cannot be considered as a phase corrector in the sense of a thin lens and must be designed by means of geometrical optics. Here the Vlasov converter has the advantage that it can be easily analysed with geometrical optics. Figure 1 shows the output of the Vlasov converter calculated with the Bessel function and

physical optics and with geometrical optics in the input plane of the quasi parabolic mirror.

The good agreement (except from the fine structure) comes from the high Fresnel number ( $N \approx 140$ ). Because of the strong curvature and the large longitudinal extent of the mirror, it should not be considered as a phase corrector and it corresponds rather to a thick lens.

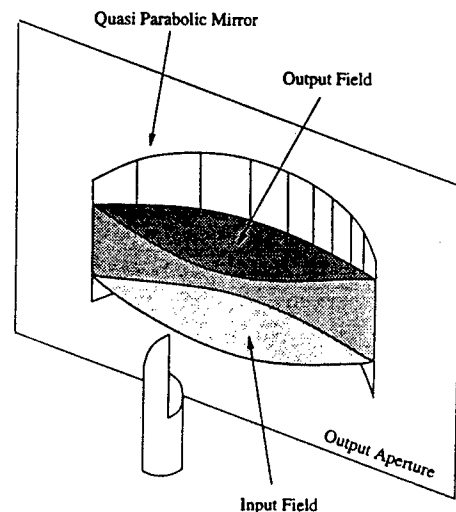


Figure 2: Output Aperture of the Quasi Parabolic Mirror

Therefore the output of the mirror is calculated with geometrical optics in the same aperture as the input (Figure 2). From here, we have a paraxial beam and can continue with physical optics. Figure 3 shows the final setup. A second ("turning") mirror directs the beam out of the gyrotron window.

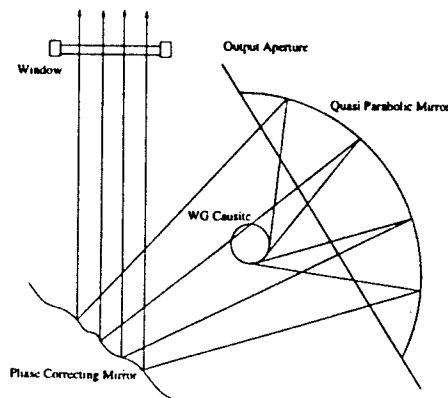


Figure 3: Setup of the Quasi Optical Mode Converter



## Design of the Second Mirror

The turning mirror is designed by means of the well known error reduction algorithm [3]. For technical reasons, the gyrotron window is off axis. Therefore it must be turned around two axes. Since the beam has a large transverse extent and a large tilt angle, it is desirable to use the field in the mirror plane for the synthesis instead of the perpendicular lens approximation. This is achieved with a new propagation formula which allows the source as well as the target aperture to be rotated around all three axes. For the forward transform we get in spectral domain

$$\hat{U}(\hat{f}^1, \hat{f}^2, d) = \frac{1}{\hat{f}^3} \hat{U}(\bar{a}_k^1 \bar{b}_j^k \hat{f}^j, \bar{a}_k^2 \bar{b}_j^k \hat{f}^j, 0) \beta(-\bar{a}_k^3 \bar{b}_j^k \hat{f}^j) e^{j2\pi d \bar{b}_j^3 \hat{f}^j} \quad (1)$$

and for the backward transform

$$\bar{U}(\hat{f}^1, \hat{f}^2, 0) = \frac{1}{\hat{f}^3} \hat{U}(\bar{b}_k^1 \bar{a}_j^k \hat{f}^j, \bar{b}_k^2 \bar{a}_j^k \hat{f}^j, d) \beta(-\bar{b}_k^3 \bar{a}_j^k \hat{f}^j) e^{-j2\pi d \bar{a}_j^3 \hat{f}^j}. \quad (2)$$

Here,  $\bar{a}$  and  $\bar{b}$  are the turning dyads of the source and the target aperture,  $\beta$  is the ramp function,  $d$  is the distance between the apertures and  $\hat{f}^3 = -\sqrt{\lambda^{-2} - (\hat{f}^1)^2 - (\hat{f}^2)^2}$ . A detailed derivation of the formulae is given in [4].

In addition, (1) allows to define the target distribution on a tilted mirror. Applications in general antenna engineering or optics suggest themselves.

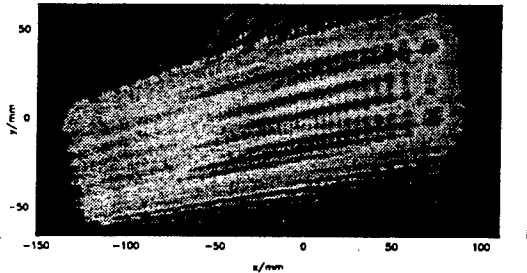


Figure 3: Input Field on the 2nd Mirror

The design goal for the second mirror is a homogeneous field distribution on the window on the one hand and a high gaussian content at some distance after the window on the other hand. Since the input field (see Figure 3) is already relatively homogeneous, both goals can be achieved with this mirror (Figure 4). At the position with the highest gaussian amplitude content, another phase correcting mirror will be placed.

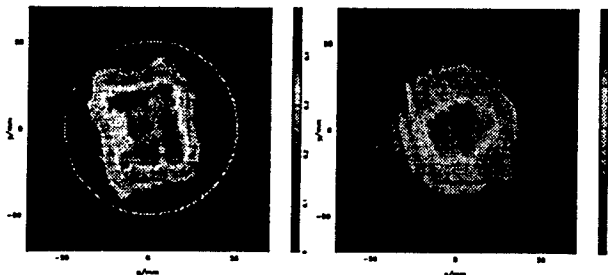


Figure 4: Field Distribution on the Window (left) and 40cm behind the Window (right)

Because of mechanical tolerances and the geometrical optical approximation on the first mirror, the real field distribution will not be as gaussian as in Figure 4. Therefore after the manufacture of the gyrotron the beam will be reconstructed by means of the error reduction algorithm [3] using (1) for oblique view angle correction. Then a pair of two phase correcting mirrors will be placed at the position with the highest gaussian content in order to match the beam to a standard transmission line with elliptical mirrors or a corrugated waveguide.

The actual problem in the design of phase correcting mirrors is the unwrapping of the phase corrector in order to get a smooth mirror surface. However, in most cases this is an ill-posed problem and an exact unwrapping without phase jumps is not possible.

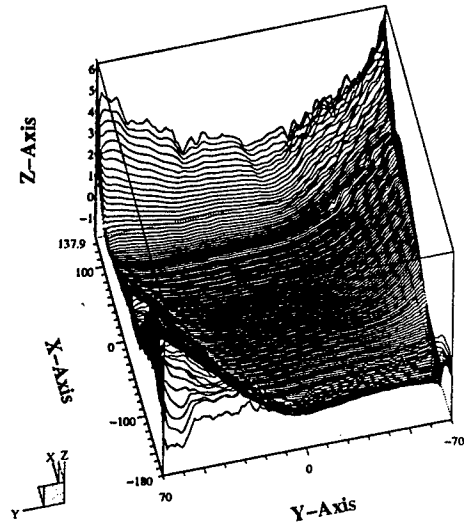


Figure 5: Contour of the Second Mirror

To overcome this problem, a new pathless algorithm was developed which always produces a smooth surface (Figure 5). For ill-posed problems it yields a least squares solution (as a side effect, this is good for compensating noise) and for well-posed problems it yields the exact unwrapped phase corrector. Hence, the algorithm is also interesting for interferometry. A detailed description is published in [4].

## References

- [1] G. G. Denisov, S. V. Kuzikov, *Eigenmodes Evolution Due to Changing the Shape of the Waveguide Cross-Section*, Int. J. of IR and MM-Waves, Vol. 18 (1997), No. 3
- [2] Y. Hirata et. al., *Wave Beam Shaping Using Multiple Phase-Correction Mirrors*, IEEE Trans. on Microwave Theory and Techniques, Vol. 45 (1997), No. 1
- [3] B. Z. Katzenelenbaum, V. V. Semenov, *Synthesis of the Phase Correctors forming a given Field*, Radiotekhnika i Elektronika 12/1967, p.244
- [4] G. Michel, E. Sanchez, *Investigations on Transmission Lines with Nonquadratic Mirrors*, 10<sup>th</sup> Joint Workshop on ECE and ECRH, 6-11 April 1997, Ameland, The Netherlands

# Design of a Mode Converting Transmission Line for a 28 GHz $TE_{02}$ -Mode Gyrotron for the HSX Stellarator

J. Shafii, R.J. Vernon, J.N. Talmadge, D.T. Anderson

Department of Electrical and Computer Engineering  
University of Wisconsin-Madison, Madison, WI 53706

## Abstract

A waveguide mode conversion and transmission system is being developed at the University of Wisconsin Torsatron/Stellarator Laboratory for a 200 kW gyrotron for use with the Helically Symmetric Experiment (HSX) stellarator. This paper reports on the specific system components. Although the system discussed here and some of the components have been presented previously in the literature, some new design considerations will be discussed. In particular, some new aspects of the design of a  $TE_{01}$ -to- $TE_{11}$  mode converter will be presented.

## Introduction

The HSX device represents a hybrid of the tokamak and stellarator concepts, combining the good single particle confinement and neoclassical transport of the tokamak with the external poloidal field generation in the stellarator [1]. To test the neoclassical properties of HSX and its alternate configurations in the low collisionary regime, the plasma will be heated with a 200 kW gyrotron at 28 GHz to create a hot electron plasma at low to moderate densities.

## Transmission Line

To obtain a symmetric, narrow Gaussian beam, for efficient plasma heating, the following mode conversion sequence is used:  $TE_{02} \rightarrow TE_{01} \rightarrow TE_{11} \rightarrow HE_{11}$  [2], [3]. The actual layout of the transmission line is illustrated in Fig. 1. The gyrotron's output is a circular waveguide 2.5 inches in diameter. However, this waveguide size is tapered down to 1.875 inches. The line will not be evacuated, however, it will be purged with gas.

The  $TE_{02}$ -to- $TE_{01}$  mode converter is a three cycle quasi periodic component [4] with a total length of 43 cm and a computed mode purity above 99%. The maximum angle between the wall and the waveguide axis is 8 degrees.

The  $TE_{01}$ -to- $TE_{11}$  mode converter is a three-cycle quasi-periodic component. A mode converter was initially designed with a 99% efficiency where only the following eight modes were included as is normally done in the literature [3]:  $TE_{01}$ ,  $TE_{02}$ ,  $TE_{11}$ ,  $TE_{12}$ ,  $TE_{21}$ ,  $TE_{22}$ ,  $TM_{11}$ , and  $TM_{21}$ . However by calculating the term  $\kappa_j / (\beta_i - \beta_j)$ , where  $\kappa_j$  and  $\beta_i - \beta_j$  are respectively the coupling and the phase constant difference between  $i$  and  $j$  modes, we realized

that  $TM_{12}$  and  $TM_{22}$  are also strongly coupled. The mode purity dropped to 78% when these two modes were included in the coupled mode equations in addition to the eight modes mentioned earlier. The power coupled into the  $TM_{22}$  mode is mainly transferred from the  $TM_{12}$  mode. In the design process we thus have to include all ten modes above. The strong effect of the  $TM_{12}$  and  $TM_{22}$  modes is due to the relatively large waveguide curvature which is unavoidable in the design of shorter mode converters. A mode converter was designed with a mode purity of 99.2% with all ten modes included. The mode purity dropped only to 97.7% when we included 25 more modes (all propagating TE and TM modes with azimuthal index up to 5; not including the  $TM_{0n}$  modes since they are not coupled). The total length of the mode converter is 120 cm. The maximum angle between the wall and the waveguide axis is 2 degrees and the smallest radius of curvature is 50 cm. These values guarantee that the device is within the validity of the coupled mode equations which are accurate only for slowly-varying cross sections. Although the input and output ports are parallel to the guide axis, there is about 0.6 cm vertical misalignment between them. The calculated power in the  $TE_{11}$  mode and the unwanted modes with appreciable power along the mode converter are plotted in Fig. 2.

The slot depth profile of the  $TE_{11}$ -to- $HE_{11}$  mode converter follows a 4th order polynomial function [5]. The length of the mode converter is 22.3 cm which is about half a beat-wavelength between the  $TE_{11}$  and  $TM_{11}$  modes. The slot and tooth widths are 3 mm. The mode compositions of the  $TE_{11}$  and  $TM_{11}$  modes at the output are 87% and 12% respectively. The input reflection is -39 dB, the side lobe level is -25 dB, and the maximum cross polarization is -32 dB.

The conversion efficiency of these components drops for randomly generated smooth perturbation to the designed profiles simulating possible machining errors. The conversion efficiency of the  $TE_{01}$ -to- $TE_{11}$  mode converter dropped 2% for such a smoothed random error perturbation with a maximum deviation of 5 mils. The conversion efficiency dropped only 0.1% for the  $TE_{02}$ -to- $TE_{01}$  converter. The  $TE_{01}$ -to- $TE_{11}$  converter is more sensitive to machining errors since here the coupling coefficients depend on the second derivative of wall profile while for the  $TE_{02}$ -to- $TE_{01}$  converter the coupling coefficient is only proportional to the first derivative. The conversion efficiency of the  $TE_{11}$ -to- $HE_{11}$  converter dropped about 1% for randomly changing the depth and width of the corrugations and teeth with a maximum deviation of 5 mils, while the input reflection increased to -27 dB.

A reflector antenna will be used to focus the beam on the center of plasma. The wall profiles of the smooth-wall mode converters were optimized for highest efficiency by using an optimization code developed at the University of Wisconsin [6]. Computer-aided optimization of the corrugated-wall converter was achieved by a scattering matrix code provided by Dan Hoppe (now at Hughes Space and Communication Co.) [7]. The mode converters are being fabricated and will be tested at low power using a radiation pattern measurement technique.

### Acknowledgment

This work is supported by the U.S. Department of Energy under grant DE-FG02-93ER54222 and DE-FG02-85ER52122.

### References

- [1] D.T. Anderson, F.S.B. Anderson, J.L. Shohet, and J.N. Talmadge, HSY: A Helically Symmetric Toroidal Experiment, Torsatron/Stellarator Laboratory, University of Wisconsin-Madison, 1995.
- [2] J.L. Doane, Int. J. Electronics, Vol. 53, No. 6, pp. 573-585, 1982.
- [3] M. Thumm, Int. J. Electronics, Vol. 57, No. 6, pp. 1225-1246, 1984.
- [4] M.J. Buckley and R.J. Vernon, IEEE-MTT, Vol. 38, No. 6, pp. 712-721, 1990.
- [5] M. Thumm, A. Jacobs, and M.S. Ayza, IEEE-MTT, Vol. 39, No. 2, pp. 301-309, 1991.
- [6] S.W. Pan and Y.H. Hu, A Fortran Code for Solving Least Square Optimization Problem with General Inequality Constraints and Equality Constraints, University of Wisconsin-Madison, 1992.
- [7] D. Hoppe, Scattering Matrix Program for Circular Waveguide Junctions, JPL, 1986.

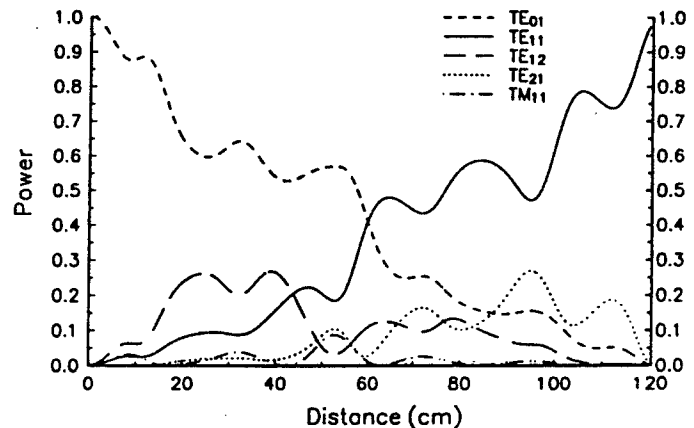


Fig. 2. Calculated power in desired mode and unwanted modes with appreciable power along the  $TE_{01}$ -to- $TE_{11}$  mode converter.

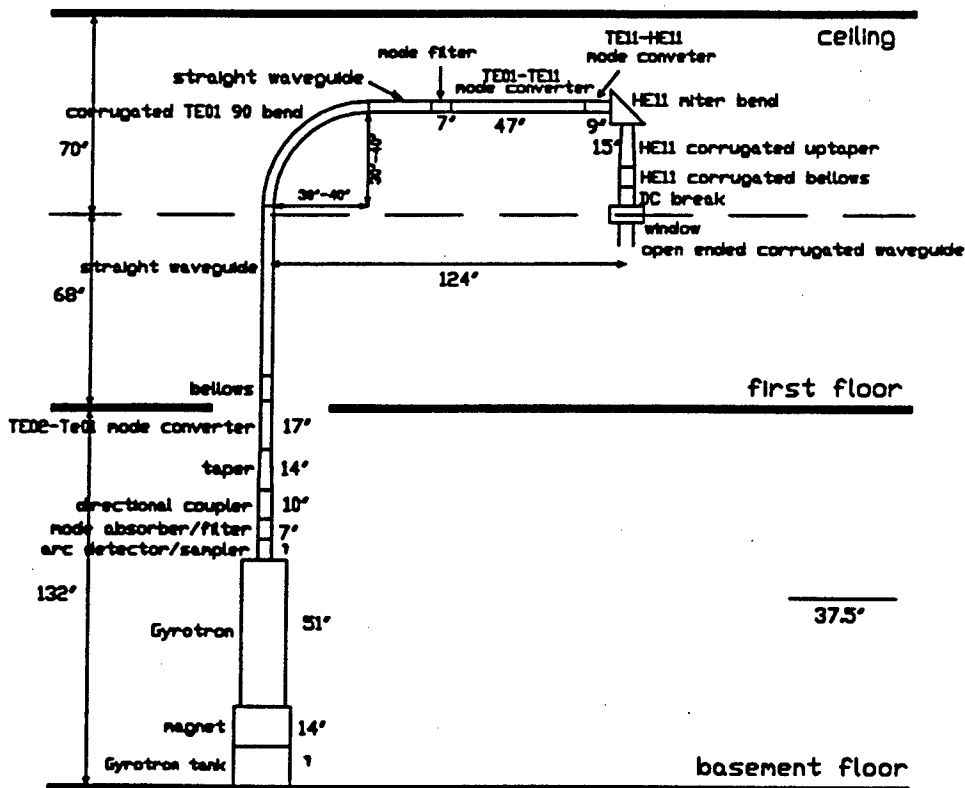


Fig. 1. schematic diagram of a 28 GHz transmission line for TSL at UW-Madison

# A $TE_{22,6}$ to $TEM_{0,0}$ Mode Converter with Non-periodic Inner Deformations

A. Möbius\*, O. Braz†

\*) Innovative Microwave Technology GmbH, Luisenstrasse 23,  
D-76344 Eggenstein, Germany, e-mail: arnold@itpgyro1.fzk.de

†) Forschungszentrum Karlsruhe, ITP, Association EURATOM-FZK,  
P.O.Box 3640, 76021 Karlsruhe, Germany  
and Universität Karlsruhe, IHE, Kaiserstr. 12, 76128 Karlsruhe, Germany

## Abstract

Helically cut quasi-optical aperture antennas with feed waveguide deformations based on the in-waveguide-mirror approach have been improved. The focusing in azimuthal and axial direction is no longer separated but combined. The design and analysis principles are discussed. An experiment is under preparation.

## Introduction

In recent years progress has been made to improve the conversion efficiency of the high order rotating gyrotron cavity mode into the fundamental  $TEM_{0,0}$  free space Gaussian beam [1], [2], [6] with the typical arrangement of a helically cut aperture antenna serving as launcher and a series of typically two or three reflectors. [1], [2] treat the improvement of the field distribution inside the launcher, whereas in [6] the beam radiated from the simple helically cut launcher is profile shaped by means of reflectors of non quadratic shape.

Most developed and experimentally verified is the dimpled wall in-waveguide conversion principle proposed in [1] also known as Denisov type converter, which for example has been successfully applied in a 118 GHz  $TE_{22,6}$  mode gyrotron [3]. This type of converter requires an input mode which is represented by g.o. rays that have an integer number of reflections as they complete one turn which strongly limits the choice of the cavity modes. However, as gyrotrons are required to deliver higher power at raising frequencies the need occurs to also increase the indices of the operating cavity mode where any limitation in the choice of this mode due to converter requirements is undesired.

To overcome these problems a different approach has been presented first in [2]. The deformation of the segments is calculated by means of the g.o. representation of rotating  $TE_{mn}$  modes. For a first proof of principle experiment a converter based on this idea has been designed, fabricated and tested. The input mode was the  $TE_{22,6}$  mode at 140 GHz. The focusing in axial and azimuthal direction has been separated. The azimuthal focusing has been performed by means of two segments followed by a focusing section in axial direction. Numerical simulations showed that the axial focusing section partially spoiled the azimuthal focusing. In cold test experiments this lead to an overall efficiency down to about 85%. After being integrated into the  $TE_{22,6}$  mode tube [4] a hot test showed a significantly lower output power than it has been the case for the same tube with a simple Vlasov converter. Several attempts were made

to explain this unexpected result. The answer was found when in a PHD Thesis a self-consistent mode competition program has been written [5]. It was stated that a reflection of 4 % of the power of the counter rotating mode excited spuriously in the cavity will lead to this drop of efficiency of the interaction in the cavity. By means of a k-spectrometer and modifying the mode generator this amount of reflection of the power of the counter rotating mode has been verified experimentally. It has been due to the fact that this launcher was optimized for the co-rotating mode exclusively. The knowledge of this behavior lead to the additional requirement of low back reflection into the cavity for both the rotating and the counter-rotating mode.

## Theory

A rotating  $TE_{mn}$  mode propagating in a circular waveguide of radius  $R_w$  can be represented by means of g. o. rays forming a caustic at the radius

$$R_c = \frac{m}{X_{mn}} R_w$$

with  $X_{mn}$  being the eigenvalue of the mode. This representation allows a circular waveguide to be considered as a series of mirror segments of parallelogram shape of the transverse size  $2R_w\phi$  with

$$\phi = \cos^{-1} \frac{m}{X_{mn}}$$

and the height

$$L_c = 2\pi R_w \tan \theta \frac{\sin \phi}{\phi}$$

For a helically cut antenna the field distribution of the last of these segments serves as current sheet of the aperture. To be able to launch a side-lobe free Gaussian beam, the aperture distribution has to be tailored such that it is Gaussian like. This is achieved by deforming the waveguide such that the density of the g.o. rays representing the rotating mode is modified from initially constant to Gaussian like. More about the theory, the method of caustic transformation, the equations as well as the design procedure can be found in [2].

## Design

To calculate the deformations the focusing in axial and azimuthal direction is separated. To obtain segments that simultaneously perform focusing in both directions on first glance

would make it necessary to simply multiply the deformation depths. The problem however is that the focusing in azimuthal direction leads to having first a section with a mirror bent inwards and then an outward bent mirror whereas for the axial direction this has to be reverse first an outwards bent mirror followed by an inwards bent section. The combination can not be achieved by simply multiplying.

The way out is the following: The two segments focusing in azimuthal direction are interchanged. This no longer leads to maxima at the center but at the sides of the segments. Since the segments are joined there will be no edge diffraction. To have simultaneously focusing in axial and azimuthal direction the deformations in both directions now can be multiplied. The first segment is bent outwards, the second segment is bent inwards. This leads to simple deformations, where no smoothing due to fabrication needs is necessary. Since the deformations are smooth, also the boundary lines of the segments are not deformed. This has been different for the first experiment. Since there was no multiplication of the axial and azimuthal deformation there have been sharp edges that only were smoothed due to fabrication needs. The smoothed but remaining edges were the main reason for the reflected power of the counter-rotating mode.

## Analysis

The validity of the g.o. design has to be checked. This has to be done by numerical methods. Among the several possible methods solving the Stratton - Chu equation is most convenient. This is due to the drawbacks of other methods as there are:

Modal analysis: The perturbations are non-periodic. To perform a modal analysis a harmonic analysis of the deformations has to be made, leading to an increased effort.

Finite element methods: The size of the deformed section, is too big for these numerical calculations.

Multiple Multipoles: This method most likely is appropriate as well, however some uncertainty lies in the proper choice of the multipoles.

Implementing the Stratton Chu Formula leads to difficulties of the proper choice of the surface serving as current sheet. In particular it is not allowed to use one of the mirror segments as the current sheet and the following segment as the surface of interest. This is due to the fact that the reflectors are joined which has the consequence that the denominator of the Greens Function will be close to zero at the junction of the surfaces. For that reason for each individual point of interest the current sheet has to be matched such that the distance of its center to the point of interest is not altered. We still have the problem that the power is radiated tangential to the current sheet surface, i.e. the distances between the point of interest and the points on the aperture vary considerably leading to numerical instabilities. For that reason the contribution of the respective points on the current sheet has to be artificially weighted. It has to be maximum where the contribution is assumed to be maximum, i.e. the area of stationary phase. With increasing distance from this area the contribution has to be artificially reduced.

For the practical implementation this optimum artificial decay has to be found. It has to be done by calculating a known converter. In our case a Denisov type converter has been chosen where the focusing can be calculated by both methods, the Stratton - Chu formula and the coupling mode theory.

A  $TE_{22,6}$  Denisov type converter that has been experimentally tested with however much weaker deformations than the g.o. designed converter has been analyzed by means of coupling mode theory and compared to the field distribution calculated by means of the Stratton Chu Formula. It turns out that the maxima calculated by both programs have the same location. In both cases these maxima are located between the maxima of the deformation. These calculations were used as gauge to calculate the behavior of the new converter. If the artificial weighting function is chosen to be Gaussian, this helps to find the standard deviation.

## Experiment

The launcher for the experiment has four deformed inner segments. The deformations are considerably stronger than for the Denisov type converter. The launcher is currently under fabrication. Experimental results can not be shown yet.

## References

- [1] D. V. Vinogradov, G. G. Denisov, M. I. Petelin, 1993, Proc. X School seminar on wave diffraction and Propagation, pp 96-128 in Russian
- [2] A. Möbius and J. Pretterebner, 1991, *Avoidance of edge diffraction by feed waveguide deformation*, Dig. 16th Int. Conf. on Infrared and Millimeter Waves, in Proc. Soc. Photo-Opt. Instrum. Eng., 1514, pp 209-210.
- [3] E. Giguët, A. Dubrovin, J.M. Krieg, Ph. Thouvenin, C. Tran, P. Garin, M. Pain, S. Alberti, M.Q. Tran, D.R. Whaley, E. Borie, O. Braz, A. Möbius, B. Piosczyk, M. Thumm, A. Wien, 1995, *Operation of a 118 GHz 0.5 MW Gyrotron with Cryogenic Window, Design and long Pulse experiments*, Dig. 20th Int. Conf. on Infrared and Millimeter Waves, Orlando, pp 339-340.
- [4] M. Thumm, O. Braz, G. Dammertz, C.T. Iatrou, M. Kuntze, B. Piosczyk, G. Soudee, 1995, *Operation of an Advanced Step tunable 1MW Gyrotron at Frequencies between 118 GHz and 162 GHz*, Dig. 20th Int. Conf. on Infrared and Millimeter Waves, Orlando, pp 199-200.
- [5] S. Kern, 1996, *Numerische Simulation der Gyrotron Wechselwirkung in koaxialen Resonatoren*, PhD. Thesis University of Karlsruhe, FZK Report, FZKA 5837
- [6] A.A. Bogdashov, A.V. Chirkov, G.G. Denisov, D.D. Vinogradov, A.N. Kuftin, V.I. Malygin, V.E. Zapevalov, 1995, *Mirror Synthesis for Gyrotron Quasi-optical Mode converters*, Int. J. of Inf. and Millimeter Waves, Vol. 16, No. 4, pp 735 - 744.

G.G.Denisov, S.V.Kuzikov, D.V.Vinogradov, A.V.Chirkov

Institute of Applied Physics, Russian Academy of Sciences

46 Ulyanov St., Nizhny Novgorod, 603600, Russia

## Abstract

A new compact and efficient transmission line from a technological gyrotron to a microwave furnace has been developed. It is based on an improved quasi-optical converter of the gyrotron operating mode into a paraxial wave beam. Results of measurements are discussed.

## Main requirements

Gyrotrons for technological purposes produce CW microwave radiation with moderate power 5-15 kW at frequencies about 30 GHz. Such gyrotrons typically operate at the second harmonic of cyclotron radiation. Their operating modes are relatively low (e.g.  $TE_{02}$ ) and the gyrotrons are not equipped with an internal mode converter of the operating mode into a paraxial wave beam. Due to this the gyrotrons are rather sensitive to reflections from a following transmission line. The distance from a technological gyrotron to a microwave furnace is typically several meters and includes one or two bends. The coefficient of reflection from the furnace is about tens of per cent and vary depending on baking samples. The furnace input cross-section is significantly larger than the half of wavelength (e.g. 30-40 mm) and the radiation reflected from the furnace consists of many modes.

General requirements to a technological transmission line are as follows:

- High transmission coefficient: desired value of the transmission coefficient is higher than 90%. The loss of microwaves reduces total setup efficiency and brings more difficulties to transmission line cooling.
- Elements which allow transmission of the forward wave (from a gyrotron to a furnace) and strong attenuation of the backward wave have to be included in the transmission line.
- Simple design and performance.

## Scheme of the transmission line

The scheme chosen for investigation consists of a quasi-optical mode converter of the gyrotron operating mode into a paraxial wave beam and a section of mirror line (several mirrors). The last mirror focuses the wave beam on the input hole of the furnace. The line is screened by a water cooled-absorber. The mirror line transmits with low losses one (or

few) of its eigenwaves. A circular waveguide with diameter 40 mm (typical diameter of furnace input hole) allows transmission of about 40 waves at the 30 GHz frequency. This means that the radiation reflected from the furnace and consisted of many modes (stray reflected radiation) is strongly attenuated in the mirror line. From that point of view the furnace input can not be made as a single-mode waveguide. This principle implies operation of the mirror line with a low mode (the lower the better) which has a very narrow spatial wave number spectrum. The mirror line has to support this spectrum only. Reflected radiation with a wide wave number spectrum does not pass the line.

## Results of measurements and calculations

The line tested was composed of the following parts: quasi-optical mode converter consisted of a special irregular wave guide section with a non-symmetrical end cut and a parabolic mirror; two mirrors with 920 mm distance in between. Three versions of the mode converter were tested and compared: conventional quasi-optical converter [1], the converter with an elliptical guide section [2,3] which pre-shapes the wave in the azimuthal direction before its radiation from the cut; the new-type irregular waveguide section which makes a proper mixture of the modes  $TE_{02}$ ,  $TE_{13}$ ,  $TE_{22}$  and forms after the parabolic mirror a paraxial wave beam practically without side lobes.

The main results of "cold" tests performed are: in the first case the total transmission coefficient is  $80 \pm 3\%$ , in the second version it is  $89 \pm 3\%$ , the third line shows rather high transmission  $94 \pm 2\%$ . Results of measurements agree with calculations. The improved versions of the mode converter are compact and quite simple in manufacturing.

## References

1. S.N.Vlasov, I.M.Orlova. Quasi-optical mode converter of waves of a circular wave guide into a paraxial wave beam. *Radiofizika* (Russian). 1974, V.17, No.1, pp.148-154.
2. G.G.Denisov, M.I.Petelin, D.V.Vinogradov. *Int.Conf. on Infrared and Millimeter Waves*. Pasadena, Dec. 14-17, 1992. *Conference Proceedings*, pp.124-125
3. G.G.Denisov, A.N.Kuftin, V.I.Malygin, N.P.Venediktov, D.V.Vinogradov. *Int.J.Electronics*, 1992, v.XI, pp.783-786.
4. G.G.Denisov, S.V.Kuzikov, D.V.Vinogradov. *Int. Conf. on Infrared and Millimeter Waves*. Berlin, July 14-19, 1996. *Conference Proceedings*, BF5.

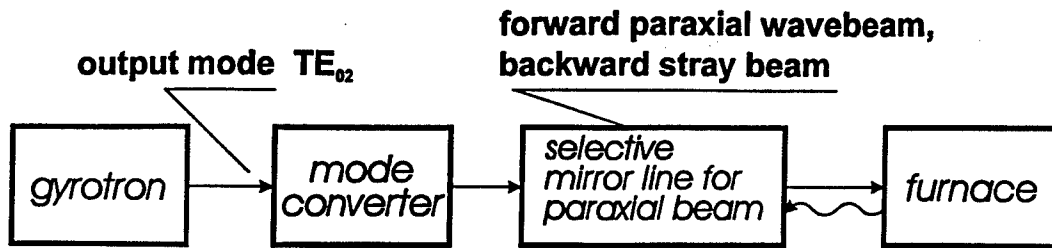


**Fig. 1:** General scheme of technological setup

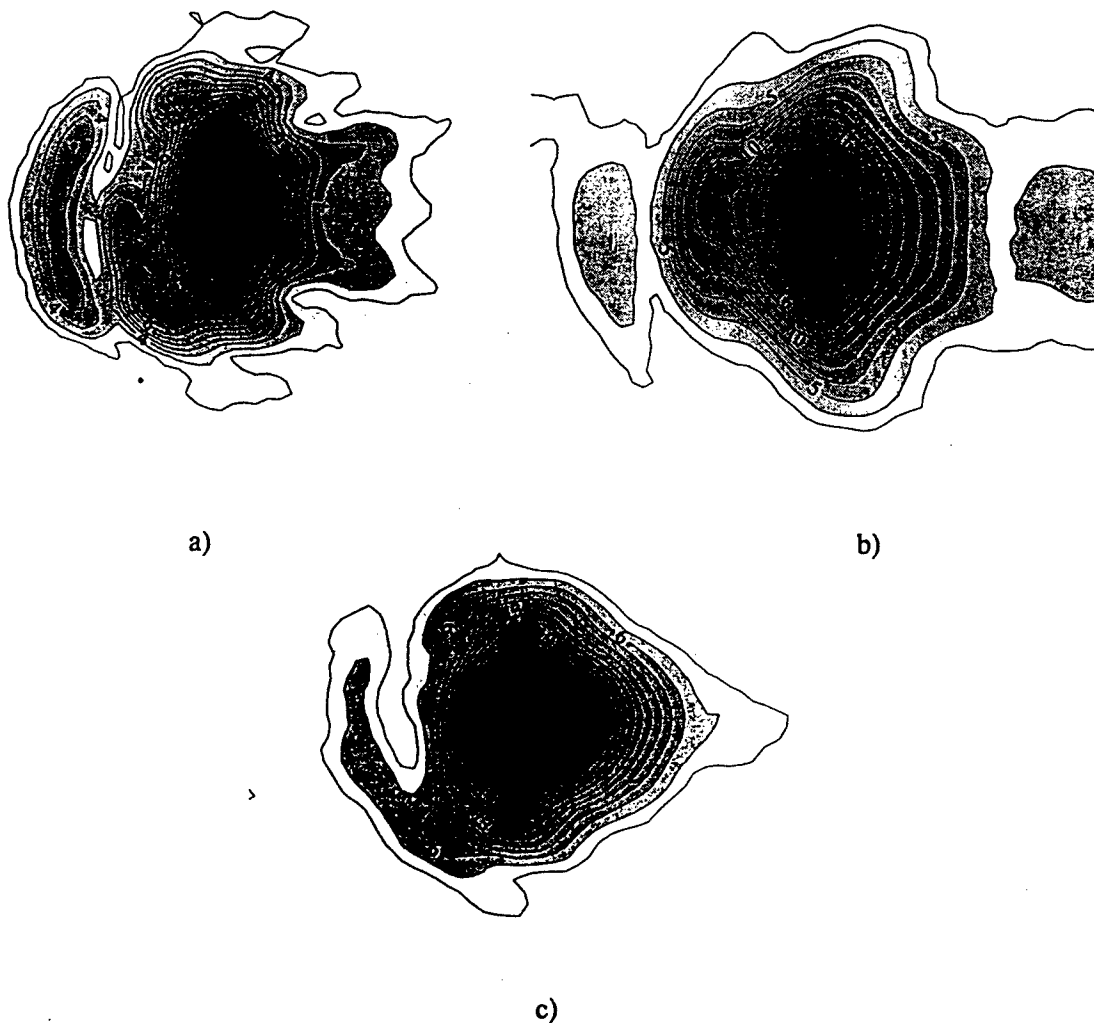


**Fig. 2.** Measured amplitude distributions of paraxial wavebeam at the input of mirror line when: conventional quasi-parabolic converter is used (a); additional elliptical wave guide section is placed before the wave guide cut (b); short dimpled mode converter is used at the gyrotron output (c)

# Experimental Results on a Coaxial TEM-Circular $TE_{16,2}$ Mode Transducer

F. Volgyi, Gy. Reiter, Gy. Veszely and T. Berceli

Budapest Technical University, Department of Microwave Telecommunications  
Goldmann t.3. Budapest, 1111. Hungary

## Abstract

A mode transducer was developed consisting of a microstrip-slot antenna system and iris-coupled resonators [1]. Measurements were made on the transducer controlling its mode purity. The results prove the correctness of the construction ideas.

## Construction

The transducer consists of a microstrip-slot antenna system with coaxial input. This antenna is of 16 identical parts and simulates the transverse distribution of the radial electric field of the  $TE_{16,2}$  mode [1]. The antenna radiates into an overmoded circular waveguide. Supposing the total symmetry in azimuthal direction only the  $TE_{16k,n}$  and  $TM_{16k,n}$  modes are excited, where  $k,n$  are integers. Those unwanted modes which are able to propagate in the given waveguide can be filtered out by resonator(s), which are resonant for the  $TE_{16,2}$  mode. The resonators are coupled to each other by irises. If we apply the irises of Fig. 1. then according to the orthogonality realitions no mode coupling occurs between the modes of the same azimuthal index.

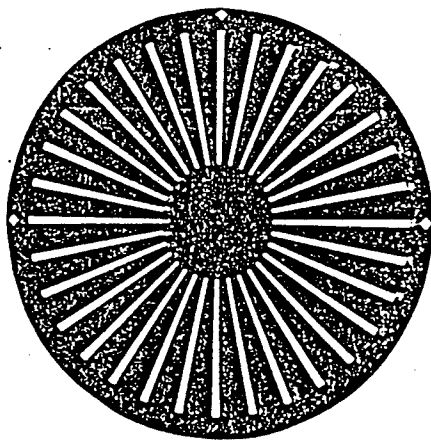


Fig. 1. The iris

For the sake of variability the device was built from separate parts. Two identical antennas serve for transmission and reception. The circular resonators can be fitted together from rings of halfwave length. Three identical pieces of rings make possible the device to be built up from one, two or three resonators.

## The network model

Using the results of [2] the network model of the transducer can be constructed (Fig. 2). The voltage generator on the left

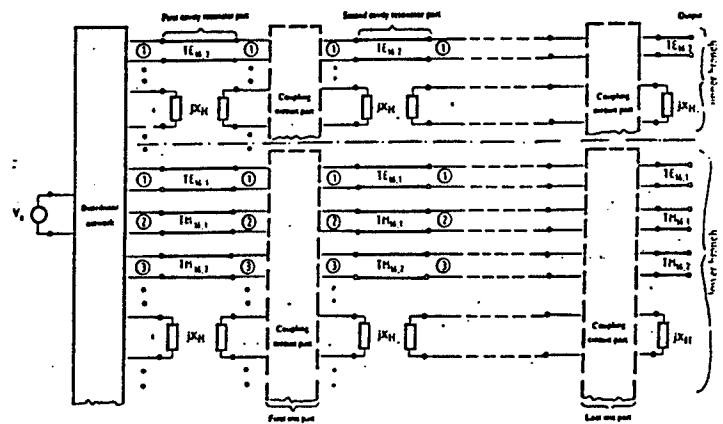


Fig. 2. Network model of the transducer

side is coupled to the coaxial input. The distributor network symbolizes the mode-converter effect of the microstrip-slot antenna: it transforms the voltage into the different transmission lines, corresponding to the propagating modes. The concentrated reactances correspond to the cut-off modes. The coupling circuit parts model the mode-coupling effect of the irises. As we saw there are no mode-coupling between modes of the same first index, therefore the upper part (belonging to the  $TE_{16,2}$  mode) is independent from the lower part.

## Measurements

Based on the network model of the converter transmission and reflexion measurements were made on the closed device using a HP network analyzer. The result of a transmission measurement is given in Fig. 3. The dot-dashed line is obtained, when the two antenna is faced only. Among some unidentified peaks the modes of the 16th azimuthal index can be seen clearly. After this three coupled resonators are formed using three rings and two irises. The resonators are resonant for the  $TE_{16,2}$  mode. The measured result is represented by the curves filled by black. All of the unwanted modes are suppressed more or less.



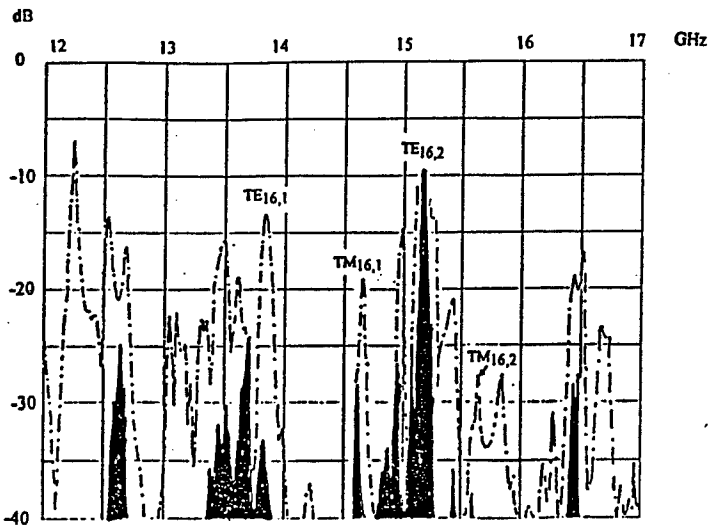


Fig.3. Transmission measurements without and with resonators

Fig.4. shows the transmission characteristics of the  $TE_{16,2}$  mode and the reflection coefficient of the antenna in a narrower frequency band. The regular resonance-curve shape proves the purity of the mode to be transmitted. The antenna is matched on several frequencies as can be seen from the reflection curve. The return loss is 6,17dB from which the mismatch loss is 1,2dB on the mid-band.

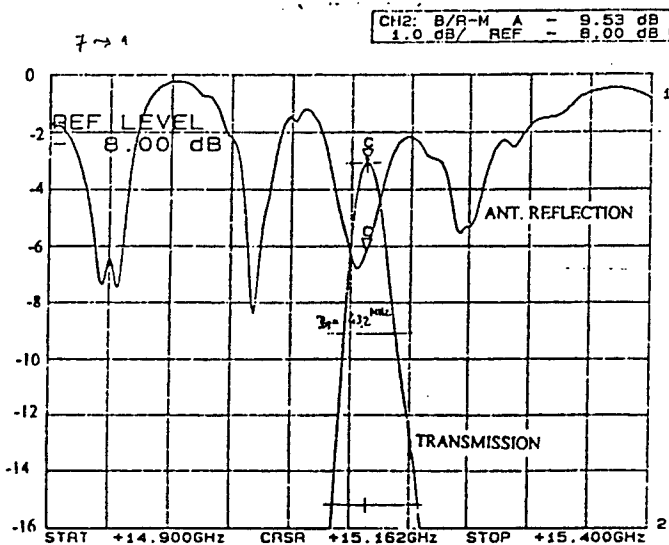


Fig.4. Transmission in the main mode and reflection from the antenna

From the measurements 4.6dB transmission loss was given. Subtracting the mismatch loss remains 3,4dB. As the calculated loss of the microstrip feeding network (dielectric+copper) equal to 1.25dB the remainder is 2.15dB. The components of this are: the loss of the SMA connector,

the loss of the coaxial-microstrip transition, radiation losses of the microstrip feeding network, the losses of the back cavity, misalignment error in the circular waveguide consisting of several parts, the dielectric loss at the slots, finite conductivity of the irises, poor contacts.

## Conclusions

The fundamental idea, i.e. to simulate the field of the useful mode by a microstrip-slot antenna and to filter out the unwanted modes by a waveguide-cavity filter is proved to be realizable. Using the network model a network-like measurement was carried out on the closed device.

The adjustment of the optimal coupling between the cavities requires additional experiments. It is desirable to identify the unknown peaks in Fig.3..

It is possible to optimize the position and dimension of the slots. An objective is to maximize the ratio of the amplitude of the wanted mode and of the sum of the amplitudes of the unwanted modes. Such calculation was carried out but no experiments were made yet.

Finally it should be mentioned that the construction of a transducer working on 40GHz is begun..

## Acknowledgement

This work was supported by the US-Hungarian Joint Fund. We would like to thank Dr. R. Temkin of the MIT Plasma Fusion Center for the helpful discussions.

## References

- [1] G. Reiter et al., "A coaxial TEM-circular  $TE_{16,2}$  mode transducer for cold test of gyrotron output converters", 21th Int. Conf. on Infrared and Millimeter Waves, Berlin, (1996) AT4
- [2] G. Reiter, "Solution of field equations for strongly coupled cavity systems", Electromagnetic Wave Theory. Proc. of Symposium held in Delft, the Netherlands, Sept. 1965. pp.357-367

# Analysis of a Coaxial Coupler for a 35 GHz Gyroklystron

Alan H. McCurdy,<sup>†</sup> Jin J. Choi, and Wallace M. Manheimer<sup>‡</sup>

Code 6840  
Naval Research Laboratory  
Washington, D.C. 20375, USA

## Abstract

Analytic theory, CAD design, and experimental cold-test are described for an input coupler for the NRL 35 GHz gyrokystron experiment. Electron beam effects can be included in the analysis. This work is supported by the Office of Naval Research.

## Introduction

Code 6840 at the Naval Research Laboratory is actively investigating gyrokystron amplifiers for radar applications. Emphasis is on broadband operation (1% bandwidth) and high average power capability (10 % duty factor) at 35 GHz and 94 GHz. A coaxial input coupler geometry is used for both of these experimental efforts. Here we report cold test and design results for the 35 GHz experiment.

The design goals for the input coupler are: 1) broad bandwidth - implying a low external quality factor ( $Q_e$ ), 2) resonant frequency at 35 GHz, 3) good coupling of input power, 4) high degree of mode purity in the  $TE_{011}$  cylindrical mode. A cross-section of the coupler is shown in Fig. 1. The input guide is fundamental  $TE_{10}$  rectangular and couples via an open aperture to the  $TE_{411}$  coaxial cavity mode. This cavity is coupled to the central cylindrical cavity by four rectangular apertures. Large radius drift tubes connect to the cavity ends.

The following will discuss matching the input coupler, cold-test and HFSS simulations of the input coupler, and an alternative coupler theory based on mode matching.

## Results

### A. Matching the Input Coupler

Broadband operation of the input coupler, without excessive Ohmic loss, requires  $Q_e \ll Q_o$  where  $Q_o$  is the Ohmic quality factor. Since there is no other power loss mechanism internal to the cavity (beam loading is minimal) then the coupling coefficient is high  $\beta = Q_o/Q_e \gg 1$  and a poor match is obtained. Adding internal Ohmic loss improves the match but wastes power in Ohmic heating that would otherwise be wasted in reflection. A passive, lossless external matching circuit may be used to improve the match without collapsing the bandwidth. Circuit theory developed some time ago [1] reveals the optimum match possible  $S_{11}^o$  for a given bandwidth  $\Delta\omega^o$

$$\ln \left[ \frac{1}{S_{11}^o} \right] \leq \frac{\pi \Delta\omega_{loss}}{\Delta\omega^o}$$

where  $\Delta\omega_{loss}$  is the bandwidth of the cavity due only to Ohmic loss. It can be seen from this relation that there is a

clear trade-off between bandwidth and reflection coefficient, with a decrease in bandwidth resulting from an improvement in match. Thus the matching improvement by even an optimized external circuit is minimal for our coupler.

### B. Simulations used in Coupler Design

The coupler was entirely designed using the HFSS code in conjunction with cold test. The code performed well, predicting the resonant frequency to within 70 MHz (with all corrections taken into account) and loaded quality factor to within 25 %. There was some uncertainty in the conductivity to be used due to unknown surface roughness effects. A conductivity value for 304 stainless steel of  $5.8 \times 10^5$  S/m was used, which is about half the value typically reported in the literature. The computer resources to perform this design were enormous suggesting further design work should include a simplified description of the coupler. This is accomplished by employing various analytical techniques to match the incoming rectangular mode to the coaxial modes and through the apertures to the cylindrical cavity modes and finally into the drift tubes to cutoff waveguide modes. This mode matching theory (MMT) requires considerable effort in setup time, but allows a lot of information to be obtained with little investment in computer time. For example, obtaining the stored energy in the coupler structure as a function of frequency is a very time-consuming calculation for HFSS (30 min per frequency), but can be computed in seconds using the MMT description.

### C. A MMT Solution

Figure 1 indicates how each part of the coupler geometry was modeled in the MMT. A single  $TE_{10}$  rectangular mode is used in the feed waveguide. Mode matching in an E-plane tee geometry allows S-parameters to be found for the junction with the coaxial cavity. This cavity is now treated as a

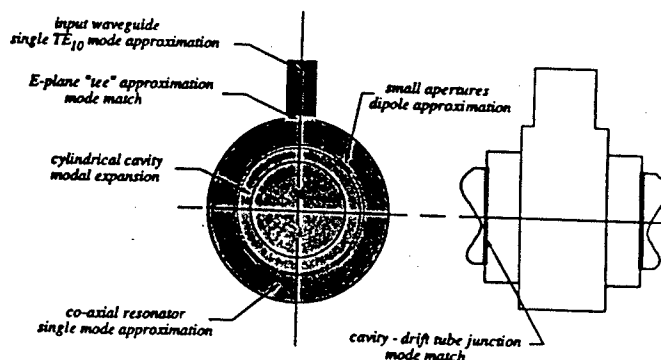


Figure 1. Input coupler schematic.

circular guide which propagates one mode (in the azimuthal direction). This traveling wave then scatters off the various apertures connecting to the central cavity. More feed guides may be added by simply including the S-parameters of the equivalent tees. The wave amplitude and phase can change across each aperture (equivalent to keeping many azimuthal coaxial cavity modes). The apertures are treated via the dipole approximation because they are so small and well separated from the guide walls in current designs. Improved mode matching models could be included later. Three dipole moments are included: two magnetic moments in the plane of the apertures, and one electric moment perpendicular to the aperture. The central cavity field is expanded in a complete set of short-circuit modes with the irrotational portion of the magnetic field included to match to the large apertures connecting to the drift tubes. The cavity fields are matched to the cutoff drift modes using mode matching.

The field solution is obtained by eliminating the drift tube fields in favor of the cavity fields, then eliminating the cavity fields in favor of the dipole moments. The circular guide fields are written in terms of the input field and the radiated fields from the dipole apertures [2]. Note that because of the circular nature of the coaxial structure fields incident on the apertures include both the input field and recirculating radiated fields from all the apertures. The solution is found by performing a few matrix inversions where the matrix order is equal to the number of apertures. The known dipole moments can then be used to find the fields in any part of the structure. Because the matrix sizes do not depend on the number of cavity modes or drift tube modes, the computation time is insensitive to the number of modes included. These modes appear as sums in the matrix elements.

#### D. Comparison between Theory and Experiment

Comparison of results obtained in cold test, from HFSS and the MMT are shown in the table below. The agreement is quite good except for the resonant frequency predicted by the MMT. This is because the drift tubes were not included in the calculation. Predictions from other codes indicate that the drift tube loading is about - 500 MHz, making the resonant frequencies very close.

	Cold Test	HFSS	MMT
$Q_o$	1484	1600	1601
$Q_e$	187	232	194
$Q_L$	166	203	173
$f_o$	34.88 GHz	35.047	35.57

Mode purity in the central cavity is another critical design goal. Figure 2, from an MMT calculation, shows that the competing modes are  $TE_{411}$  and  $TM_{111}$ . The  $TE_{011}$  purity at resonance is over 99 %. This degree of mode purity is comparable to what is predicted by HFSS. However the presence of the  $TM_{111}$  mode was not observed in HFSS due to the rapid variation of amplitude with frequency.

Figure 3 shows the energy stored in the coaxial and cylindrical portions of the input coupler for an input power of 1 W. Results are shown from MMT and HFSS. The shift in resonance of 500 MHz is seen again in the MMT results. However, the energy ratio between the two regions is quite close for the two calculations. At  $TE_{011}$  resonance, most of

the energy is stored in the central cavity, where it can interact with the electron beam.

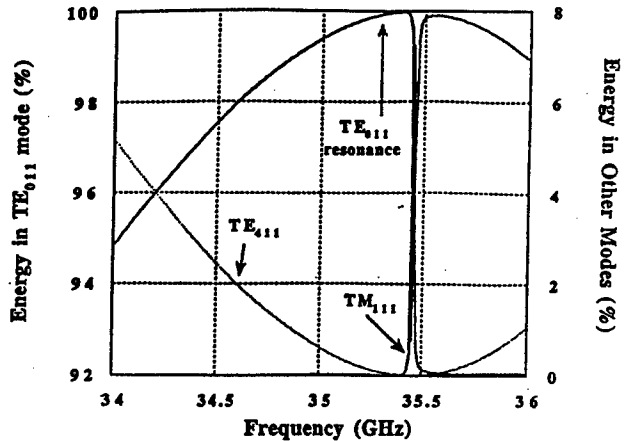


Figure 2. Mode purity in central cavity.

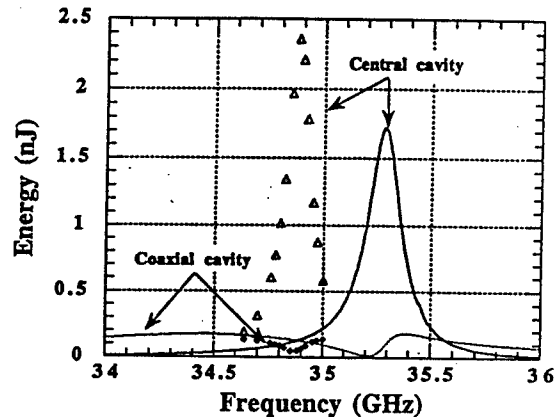


Figure 3. Energy stored in coupler (points from HFSS, curves from MMT).

#### E. Inclusion of the Electron Beam

Free currents inside the cavity structure are included as volume integrals of  $\mathbf{J} \cdot \mathbf{E}_n$ . In the upstream drift tube the beam current drives evanescent modes in the waveguide. The relation between the guide modal amplitudes and the driving beam current can be found by application of the Lorentz Reciprocity Theorem. This produces a perturbed current density at the entrance to the cavity. Assuming a linear interaction, the cavity fields produce a modification to the current density which adds to that of the input drift tube. The same occurs for the output drift tube. The beam dynamics can be described in any of the usual ways: single particle, guiding center, Vlasov etc. and all the slow-time scale assumptions can be profitably employed.

<sup>†</sup> permanent address: University of Southern California, Los Angeles, CA 90089.

<sup>‡</sup> Code 6707, Naval Research Laboratory.

[1] R. M. Fano, J. Franklin Inst. 249, 57 (1950).

[2] R. E. Collin, Foundations for Microwave Engineering, (McGraw-Hill, Inc., New York), 1992.

# Gyroklystron-based 35 GHz radar for observation of space objects

Alexei A. Tolkachev

JSC "Radiophysika", 10, Geroev Panfilovtsev St.  
Moscow 123363, Russia

## Abstract

The paper considers the possibilities of using the mm-wave range for creation of radar stations for observing space objects of the man-made and natural origin. High capabilities of the radars in the indicated range allow solution of a number of technical problems associated with the space object observation that can not be solved by the existing radars of the lower frequency ranges. The special attention is concentrated on the problems of providing generation and amplification of powerful microwave signals.

## Introduction

The state of development of the system-technical engineering solutions and element base for creation of the powerful radar stations of a longer wavelength part of the mm-wave range and on-board radars of a shorter wavelength part of the mm-wave range providing the capability of electrical beam steering opens a number of new possibilities in the area of detecting and tracking objects in the circumterrestrial space. These possibilities are based on the high power concentration, high resolution, and high accuracy of the coordinate measurement inherent for the radars of the range in question.

The problems where the capabilities of the mm-wave radars can be used are, [1]:

- density distribution measurement and cataloguing of the space debris of more than 1 cm dimensions for providing the safety of inhabited and other satellites at the heights of 500÷1000 km.;
- provision of monitoring of functioning space vehicles in the Earth geostationary orbit;
- accuracy forecast of the time and place of falling large man-made and natural space objects onto the Earth;
- radar research of the Moon surface.

The solution of the indicated and other problems can be performed with using a large earth radar operating in a longer wavelength part of the K<sub>a</sub> band. Such a radar is being under development in Russia and has been described in a number of papers [2], [3], and [4].

A number of other problems associated mainly with observation of space debris of 1÷3 mm dimensions require using the W-band. The preliminary analysis shows that the radar in the indicated band are expedient to be realized in the on-board variant. In this case, the radar will not require generation of high power and its transmitter can be

realized on the basis of the traditional devices like a klystron or a TWT available at present.

Some points concerning with generation and amplification of powerful microwave signals of the K<sub>a</sub> band for a large stationary earth radar station are considered below.

## Requirements to energetic characteristics of radar

One of the technical problems associated with detecting and tracking objects in space is provision of the necessary energy characteristics. The radar energetic possibilities are described by using the concept of "pulse potential" (measured in square meters) which characterizes the possibility of observation of an object with a specified radar cross-section at some distance. The "pulse potential" is more convenient to be described in decibels referred to a square meter. For tracking an object with radar cross-section  $\sigma$  at a distance  $R$ , it is necessary to provide the ratio of a signal to noise  $q^2 = s/n$ , then we get

$$\Pi = q^2 \frac{R^4}{\sigma}$$

For the radar with transmitting-receiving antenna, the value of "pulse potential" may be determined by approximate expression:

$$\Pi \cong \frac{E \cdot S^2 \cdot \eta}{\lambda^2 \cdot T} \cdot 6 \cdot 10^{21},$$

where:

$E$  – energy of primary signal, J;

$S$  – area of aperture, m<sup>2</sup>;

$\eta$  – loss factor in a radar;

$\lambda$  – wavelength, m;

$T$  – noise temperature of a receiver, K.

For tracking some space objects, it is necessary to provide "pulse potential" of about 290 dB and higher, that requires considerable power of transmitter and large antenna aperture. For example, a millimeter-wave band radar installed at the Kwajalein Atoll, USA, has a reflector antenna of about 14 m in diameter and a transmitter forming a primary signal with the energy of about 5 J in a pulse. The "pulse potential" of the radar channel operating at frequency of 35 GHz is approximately equal to 265 dB [5].

The use of the radars with large full-rotary reflector antenna puts before developers a number of complex problem associated both with the necessity of maintaining the reflector shape with high accuracy when operating and with providing the space survey by a narrow beam when detecting an object and control of the antenna when tracking the object. High power primary signal transmission to the rotating antenna also requires application of the methods that are unordinary for the traditional radiolocation [5], [6].

A modification of the structure for a millimeter-wave band antenna of module type and electric beam steering free of the shortcomings indicated has been considered in [7]. The antenna is an active transmitting-receiving phased array with a small (about one degree) sector of scan, that, from our viewpoint, meets the requirements arising when carrying out a number of operations in space.

The main characteristics of the radar are shown in Table 1.

Table 1. Main radar characteristics

Central frequency, GHz	34
Pulse potential, dB/m <sup>2</sup>	290
Pulse potential with coherent accumulation, dB/m <sup>2</sup>	310
Antenna diameter, m	18
Peak power, kW	20
The electric scan sector, min	50
Distance error, m	2
Angle error, sec	6

One of the main difficulties in creation of the radar in question is the providing of the powerful microwave signal amplification with using the devices arranged in the antenna body. The possibility of using the tubes of the traditional klystrons or TWT for the indicated purposes is considered as the basic variant. In this case, the tubes are arranged in individual modules of the antenna body. The total number of the powerful output amplifiers amounts to 600÷1200 units.

Such large number of powerful elements in the radar antenna is undesirable because it leads to:

- the increase of the radar cost;
- the reduction of its reliability;
- complication of operation.

The possibility of using the gyroklystrons in the station of such a class was first indicated in [8]. However, it was supposed there to use the device with the stationary cryogenic superconducting solenoids. Such a solution is very bulky and complex from the viewpoint of the power canalization to the full-rotary antenna. Besides, it will be associated inevitably with considerable additional loss. Although, the experience of such a work with much less number of the devices is available.

At the same time in development of the gyroklystrons, the necessary prerequisites to creation of the powerful Ka band gyroklystron amplifiers packaged with the permanent magnets on the second harmonic have been created in

Russia. The preliminary analysis allows to expect creation of the gyrodevices with the following characteristics.

Table 2. Main characteristics of gyroklystrons

Central frequency, GHz	34
Peak power, kW	300-350
Factor amplification, dB	30-40
Weight, kg	~200

The use of such devices will reduce the total number of the output amplifiers down to 50÷100 that will considerably enhance the operating characteristics of the radar and will reduce its cost.

## References

1. A. A. Tolkachev, V. A. Trushin, and V. V. Vejtsel. On the possibility of using powerful millimeter wave band radars for tracking objects in circumterrestrial space. China International Conference on Radar Beiging, oct. 1996.
2. A. A. Tolkachev, V. P. Botavin, A. A. Kuzmin, A. P. Pytsyk, and V. A. Trushin. Radar means for detection and tracking of orbital debris. Scientific Conference of the Russian Academy of Sciences "Technogeneous space debris: problems and directions of research", Moscow, February 24-28, 1992 (in Russian).
3. V. V. Denisenko, B. A. Levitan, A. A. Tolkachev, A. V. Shishlov and other. About possibility of millimeter radar use for space debris control. AMSE Int. Conf. "Signals and systems", Geneva (Switzerland), June 17-19, 1992.
4. V. V. Denisenko, B. A. Levitan, A. A. Tolkachev, A. V. Shishlov and other. "SUMMIT Radar Ground Station for EHF observation of small space objects", Know-How News, N 3, Moscow, 1993 (in Russian).
5. M. D. Abouzahra, R. K. Avent. The 100-kW Millimeter-Wave Radar at the Kwajalein Atoll. IEEE AP-Magazine, vol.36, No.2, April 1994.
6. V. V. Denisenko, L. V. Tretjakov, and A. V. Cherednik. TE<sub>01</sub> Circular Waveguide Transmission Lines of Complex Path. 9th Microwave Conf. "MICON-91", Proceeding, v.1, p.267, Rydzyna-Poland, May 20-24, 1991.
7. A. A. Tolkachev, et al. High Gain Antenna Systems for Millimeter Wave Radars with Combined Electronical and Mechanical Beam Steering. IEEE Int. Symp. on Phased Array Systems and Technology. 15-18 October, 1996, Boston, Massachusetts, p.266-271.
8. A. V. Gaponov-Grekhov, V. L. Granatstein. Applications of High-Power Microwaves, Boston; London: Artech House, 1994.

## Millimeter Wave Radars Tracking Approaching Sea Skimming Targets

Dieter R. Lohrmann

Naval Research Laboratory

### Abstract

Using millimeter waves for tracking sea skimming targets, improved tracking accuracy is expected in comparison to use of microwaves. The reason is that for equal antenna aperture, the narrower mm wave beam helps to discriminate against reflections from the sea. Further, a rough sea surface breaks up specular reflections at mm waves much more than at microwaves.

To some extent, Doppler radars tracking fast approaching targets can discriminate against the low Doppler returns of rain clutter. At 95 Ghz, targets with greater than 0.1 square meters of radar cross section are expected to be detectable at up to 3 km range even in medium rain, provided that at least 10 dB of excess signal to noise is available in clear weather.

75 cm diameter is about 3 degrees at 10 Ghz, and 0.3 degrees at 95 Ghz.

### 1. *The Problem*

Tracking targets flying low above the sea surface by radar has been a long standing problem due to reflections from the sea surface. These reflections may be specular, diffuse or both. The largest elevation tracking errors are due to specular reflections.

Figure 1 shows the scenario. The path reflected by the sea creates a virtual image of the target below the surface. The depth of the image is approximately equal to the height of the target above the sea surface.

If both target and image are in the radar antenna beam, then the radar tracks the point on the surface between the target and its image, when the target and image return signals arrive at the radar in phase. The resulting elevation error is commonly called "bias". If the signals are close to opposite phase, the phase front of the arriving signal is warped, causing errors which can amount to many beamwidths of the radar.

### 2. *Discrimination against sea reflections by narrow antenna beam*

For equal antenna aperture, the antenna beam of a millimeter wave radar is much narrower than that of a microwave radar. For example, the 3 dB beam width of an antenna of

The narrower beam width of the millimeter wave radar tends to discriminate against the specular reflection. For instance, with a height of both radar and target of 10 m above the sea surface, at a range of 3 km, the image is in the first null of the sum pattern of the 95 Ghz radar, whereas both target and image are still in the beam of the X-band radar.

As the target approaches, the angle between the line of sight to target and to the image increases. If the boresite of the radar would be kept on the target during the approach, eventually, the image return would fall into the first sidelobe minimum of the sum pattern of the monopulse antenna. At that point, the return from the image is still strong in the difference pattern, because the difference pattern is wider than the sum pattern. Therefore, at that point, the bias error is not reduced much.

As the target approaches closer, the image falls into the first null of the difference pattern. The minimum of the bias error and the minimum of the elevation error occurs at that point. Figure 2 shows the elevation error due to bias vs. range. The height of radar and target above the sea surface was 10 m, the radars frequency 95 Ghz and the antenna aperture 75 cm. The sea surface was assumed to be smooth. At a range above 3 km, the bias is equal to the target height. During multipath maxima, the radar

tracks the point on the sea surface between target and image. Below 3 km range the radar tracks either the target or the image with high accuracy. The minimum of the tracking elevation error occurs at approximately 2600 m. Given range and elevation angle, one can discriminate between image and target, because the target usually does not fly below the surface of the Ocean.

### 3. Reduction of specular sea reflections by wave action

As was seen, specular reflections from the sea may cause elevation tracking errors. Fortunately, sea waves break up specular reflections at millimeter waves much more than they do at microwaves [1], [2]. This was verified recently by multipath measurements [3] [4] [5]. Figure 3 (from [4]) shows measured values of reflection coefficient vs. rms sea wave height, grazing angle and electrical wave length. The solid curves (triangles) show values derived theoretically by Ament [1], the curves with circles show values by a theory modified by Miller and Brown [2] to fit measured results more closely. Using the Miller and Brown theory, the reflection coefficient vs. wave height with grazing angle as parameter was plotted in figure 4 for 10 GHz and in figure 5 for 95 GHz. It is seen that for a grazing angle of 0.5 degrees, a wave height of 0.05 m rms (smooth sease) already reduces the specular reflections by 10 dB at 95 Ghz, whereas at 10 Ghz, this occurs at 0.5 m wave height (rough seas).

Historically, sea wave heights were given in H3 values. Since H3 is a poorly defined parameter, it should be replaced by rms values in the future. Table 1 relates rms wave height to "Sea State", as given in [6].

With increasing sea state, the specular reflection coefficient decreases, but the diffuse reflection coefficient increases. see figure 6. Since these reflections come from all ranges on the sea surface, the phase angles of the returns are randomly distributed between zero and two pi. Because these contributions tend to average out, diffuse reflections are expected to cause very little elevation tracking error [7].

### 4. Influence of rain

Common wisdom has it that "mm waves don't work in rain". But neither does infrared, for that matter. For medium rain (4mm/hour) the path attenuation is about 3 dB/km one way at 95 GHz, or 18 dB two ways at 3 km range. To burn thru 18 dB additional path attenuation is not difficult, using a high powered radar, but the rain clutter return tends to hide the target. However, a fast approaching target (typically 300 m/s or greater) creates a much greater Doppler shift than the rain drops. Assuming that a clutter suppression by Doppler filtering is achievable, a target with -10 dBsm cross section will produce a signal to clutter ratio of 23 dB, which is amply sufficient for accurate tracking.

TABLE 1 (from [6])

Sea State Number	Wave Height rms (m)	Description
1	0 - 0.06	smooth
2	0.06 - 0.2	slight
3	0.2 - 0.34	moderate
4	0.34 - 0.52	rough
5	0.52 - 0.79	very rough

[1] Ament, "Toward a theory of reflection by a rough surface", Proc. IRE 1953 41 pp. 142-146

[2] Miller, Brown and Vegh, "New derivation for the rough surface reflection coefficient...", IEEE Proceedings Vol. 131 Pt. H No. 2. April 1984

[3] Beard "Coherent and incoherent scattering of microwaves....", IRE Transactions 1961 AP-9 pp 470-483

[4] NATO Defense Research Group AC/243 Panel 3/RSG8 "Millimetre wave propagation joint data analysis of the measurement campaign 1990

[5] Naval Surface Warfare Center Report NSWC TR 89-219, "Target Acquisition for ship defense: MIKE/TALONS propagation tests June 1989

[6] Naval Research Laboratory Report 8177

[7] Naval Research Memo Report  
NRL/MR/5747--93-7194

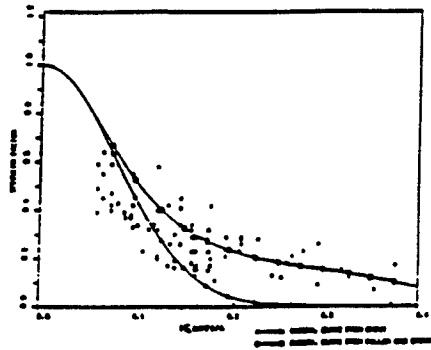
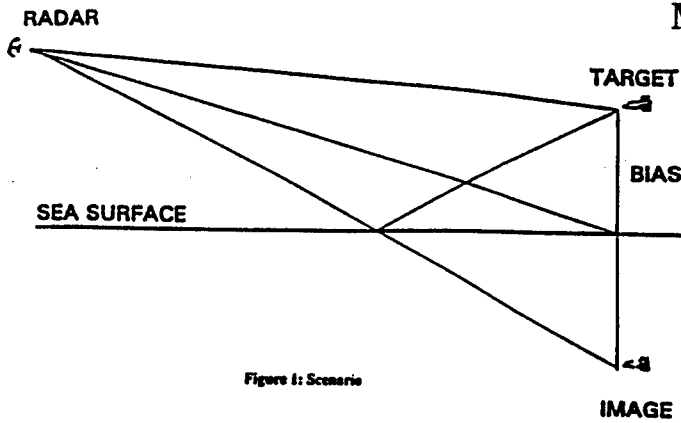


Figure 3: Specular reflection coefficient, theoretical and measured values at 95 GHz

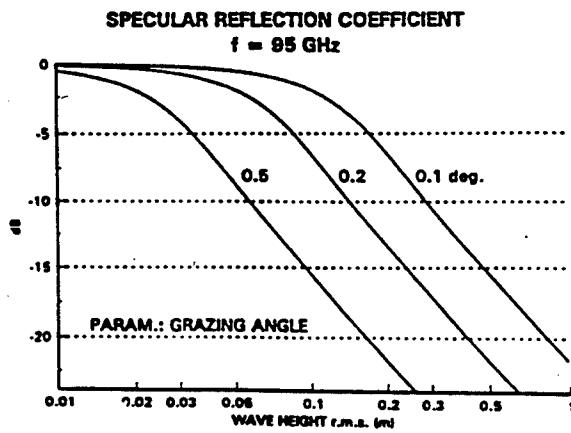


Figure 5: Specular reflection coefficient at 95 GHz

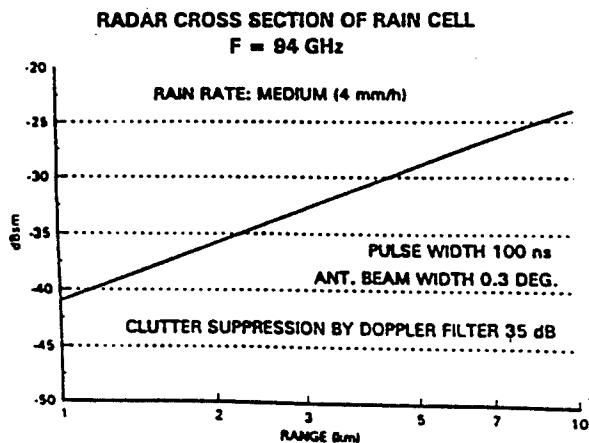


Figure 7: Radar Cross section of rain cell at 94 GHz vs. range with 35 dB clutter suppression by Doppler filter

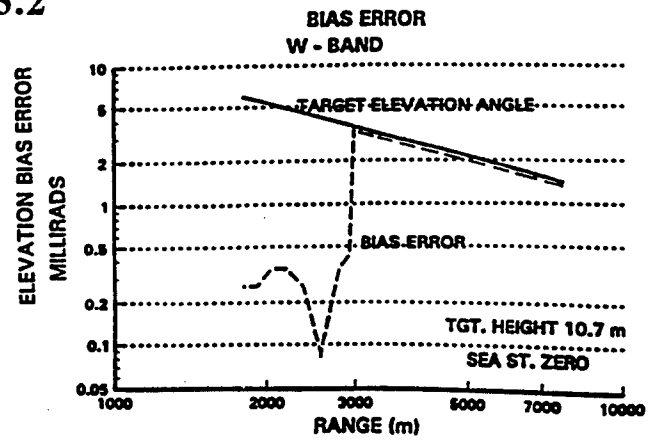


Figure 2: Bias error vs. range

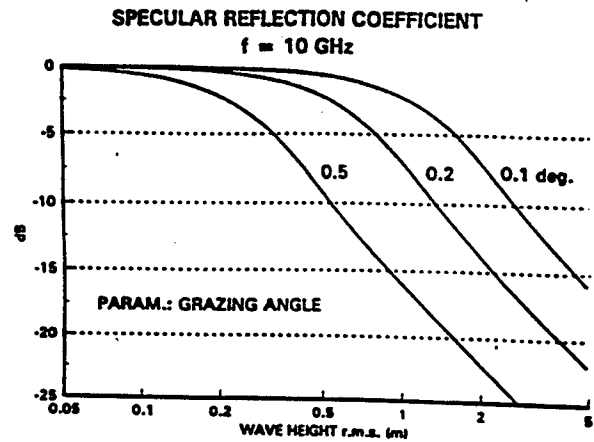


Figure 4: Specular reflection coefficient vs. sea wave height with grazing angle as parameter at 10 GHz

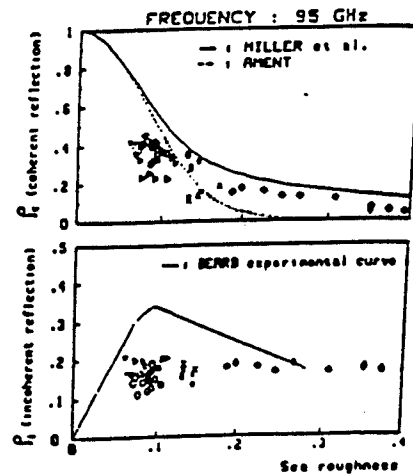


Figure 6: Specular and diffuse reflection coefficient at 95 GHz



## Transmitters Based on Magnetrons with Cold Secondary-Emission Cathode

V.D. Naumenko<sup>1</sup>, K. Schünemann<sup>2</sup>,  
V. Ye. Semenuta<sup>1</sup>, D.M. Vavriv<sup>1</sup>, and V.A. Volkov<sup>1</sup>

1) Radio Astronomy Institute of Ukrainian Academy of Sciences,  
4 Chervonopraporna St., 310002 Kharkov, Ukraine

2) Technical University Hamburg-Harburg, Arbeitsbereich Hochfrequenztechnik,  
Wallgraben 55, D-21071 Hamburg, Germany

### Abstract

We report here the recent results on the development of 95 and 140 GHz transmitters employing magnetrons with cold secondary-emission cathode and a solid-state modulator. Design and fabrication of transmitters with 1 and 5 kW peak output power suitable for radar applications are discussed.

### Introduction

Recent advances in magnetrons with cold secondary-emission cathode [1,2] along with potentials of modern solid-state modulators have opened a promising way for the development of efficient, reliable, and cost-effective transmitters with output peak power of several kilowatts at frequencies around 100 GHz and higher. Such magnetrons have been developed at the Institute of Radio Astronomy of Ukrainian Academy of Sciences as an alternative to the conventional magnetrons using thermal cathodes. The magnetrons with cold secondary-emission cathode are superior to the conventional magnetrons using thermal cathodes in such parameters as lifetime, pulse and average output power. Our recent efforts have been directed to reducing their physical dimensions and weight, and to decreasing the anode voltage in order to make the magnetrons suitable for airborne radar systems. Besides, we developed a new compact 9 and 15 kV solid-state modulators to drive these magnetrons. These activities have resulted in the development of compact 95 GHz transmitters with output peak power of 1 and 5 kW, and the average power of 1- and 5 W, respectively. The same power level has also been achieved in the 140 GHz transmitters. In this presentation, we discuss design and fabrication of the transmitters and give the performance descriptions.

### Magnetron with cold secondary-emission cathode

Spatial-harmonic magnetrons with cold secondary-emission cathode have been used as high power

oscillators in the transmitters developed. There are two principal differences between these magnetrons and the conventional ones. Firstly, in order to improve their life time and reliability and to make them capable to work at high duty factor, a cold secondary-emission cathode is used instead of a conventional L-cathode. The secondary emission is initiated by an auxiliary thermal cathode placed outside the interaction space as shown in fig.1. Secondly, to reduce the values of anode voltage and dc magnetic field, an interaction of the secondary electrons with the first backward space-harmonic of the  $\pi/2$  cavity mode is realized.

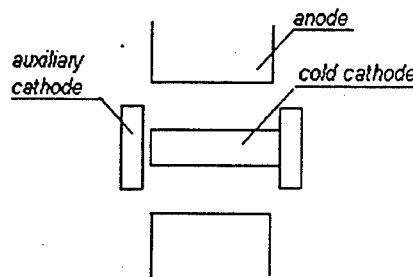


Fig. 1. Schematic representation of the magnetron with cold secondary-emission cathode

Wave-length	Peak output power (kW)	Average power (W)	Peak anode voltage (kV)	Weight (kg)
3	20	20	18	2.0
3	13	10	16.5	2.0
3	5	5	15	1.7
3	5	40	12	2.0
3	1	1	6.5	0.3
2	5	5	15	1.7
2	1	1	9	0.8

Table 1. Specifications of the 95 and 140 GHz magnetrons

These approaches resulted in the development of a series of 95 and 140 GHz magnetrons with the parameters summarized in table 1. Their life-time is around 1000 hours. The 5 and 1 kW magnetrons have been used for the transmitter development.

### Modulator

Due to a difference in the anode voltage and the prime power required for the 5 and 1 kW magnetrons, two types of modulators have been developed. The modulator for the 1 kW magnetrons has been designed as a direct drive unit. A series of standard 12 MOSFET stacks has been used as power key. Specifications of this modulator are:

peak anode voltage(max) - 9 kV  
average power(max) - 100 W  
pulse duration- 40-100 ns  
volume -1200 cm<sup>3</sup>  
weight -1.5 kg  
efficiency -80%  
DC supply voltage -24V

For the 5 kW magnetrons, a high voltage modulator with transformer coupling and a thyristor stack as power key has been designed. The modulator parameters are:

peak anode voltage(max) - 15 kV  
average power(max)- 200 W  
pulse duration- 50-200 ns  
volume -2500 cm<sup>3</sup>  
weight -3 kg  
efficiency -70%  
DC supply voltage -24V

To obtain these modulator parameters the following solutions have been introduced: (i) The synchronization from an external clock of all DC-AC-DC converters of the modulator has been realized at a frequency equal to the pulse repetition frequency in order to decrease interferences. (ii) A delay line has been used the energy storage device in a full discharge mode operation. (iii) The pulse charge of the delay line has been realized from a low voltage supply by using an intermediate inductive storage element. (iv) A special design of the pulse transformer of the modulator has been developed to decrease pulse distortion.

### Performance of the transmitters

Operating parameters of the developed and produced 95 and 140 GHz transmitters are summarized in table 2 and 3. The transmitters are built as single compact units with a forced-air cooling system incorporated in them. A further increase of both peak and average power is

possible by applying of other types of magnetrons developed.

	T95-5	T95-1
Peak output power, kW	5	1
Average power (max), W	5	1
Pulse duration, ns	40-100	50-200
Duty cycle (max)	1000	1000
Volume, cm <sup>3</sup>	3500	2000
Weight, kg	4.5	2.5
DC supply voltage, V	24	24
Watt consumption (max)	100	50

Table 2. Parameters of the 95 GHz transmitter

	T140-5	T140-5
Peak output power, kW	5	1
Average power(max), W	5	1
Pulse duration, ns	40-100	50-200
Duty circle (max)	1000	1000
Volume, cm <sup>3</sup>	4500	3500
Weight, kg	5.5	5
DC supply voltage, V	24	24
Watt consumption (max)	100	50

Table 3. Parameters of the 140 GHz transmitter

### Conclusion

Recent advances in design and realization of both magnetrons with cold secondary-emission cathode and solid-state modulators enabled the development of 95 and 140 GHz transmitters, which possess attractive operating characteristics and which can find wide applications in practical systems.

### Acknowledgement

This work is supported in part by EC under contract ERBIC15CT960816. D. V. acknowledges support from Technical University Hamburg-Harburg.

### References

1. V. Naumenko, A. Suvorov, and A. Sirov, "Tunable Magnetron of a Two-Millimeter-Wavelength Band", *Microwave and Opt. Techn. Let.*, vol. 12, no. 3, pp.129-131 (1996).
2. V.Naumenko and D.Vavriv, "Millimeter Wave Magnetrons with Secondary Emission Cathode: Theory and Experiments", *Proc. of the 21st Int. Conf. on Infrared and Millimeter Waves*, Berlin, Germany, 1996.

# Millimeter Wave Phase Conjugation Using Artificial Nonlinear Surfaces

Yian Chang and Harold R. Fetterman

Electrical Engineering Department  
University of California, Los Angeles, CA 90095

Irwin L. Newberg and Steve K. Panaretos

Hughes Aircraft Co.  
PO Box 92426, Los Angeles, CA 90009-2426

## Abstract

A new type of artificial nonlinear surface has been developed using antenna coupled mixers with optical interconnects for millimeter wave phase conjugation. A prototype linear array surface has demonstrated two-dimensional free space phase conjugation at 10 GHz.

## Introduction

Since its first demonstration, optical phase conjugation has been studied intensively. Most of this interest can be traced to potential applications in imaging processing and in dynamic compensation for distortion. This technique utilizes the nonlinear susceptibility of a medium to reverse the phase factor of an incoming wave. The phase-conjugate wave propagates backward and has the same wavefronts as that of the incoming wave. This unique property of phase-conjugate waves is useful in applications requiring automatic pointing and tracking, phase aberration corrections, phase-conjugate resonators, and many other devices. To date, most of the phase conjugation development has been concentrated in the optical (visible and IR) regime. Efforts to extend this technique to microwave and millimeter wave (MMW) have encountered severe difficulties due to the small nonlinearity of materials and the low power density at these wavelengths. In the search for alternative media suitable for the use in MMW nonlinear optics, artificial media were found to have much larger nonlinearities than that of crystals. Using shaped microparticle suspensions, microwave phase conjugation has been demonstrated in a waveguide environment using a degenerate four-wave mixing (DFWM) technique. [1] In this study, the basic concept is to replace the weak nonlinearity of electron distribution in a crystal with the strong nonlinear V-I response of a P-N junction. Using an array of antenna coupled mixers with optical interconnects as an artificial nonlinear surface, we have demonstrated two-dimensional free space phase conjugation at 10 GHz.

## Concepts

It has been proven theoretically that if a wave is conjugate to another at a certain plane, they will conjugate to each other

everywhere. In other words, phase conjugation can be achieved using a strong nonlinear surface instead of a block of weak nonlinear crystal. To realize this theory, we turn to the nonlinear V-I characteristic of diodes. Microwave circuits that combine antennas and microwave mixers can effectively replace the nonlinear dipoles of a medium. The idea is to "sample" the incident wave at different positions of the wavefront and then generate phase-conjugate currents using microwave mixers. These currents will then excite a phase-conjugate field at each sampling point. The combined field of all elements will be the phase-conjugate wave of the incident beam. This sampling concept was proposed in the 60's, but due to the lack of modern semiconductor and optical technologies, researchers did not have a practical way to realize the concept. [2] To understand how the conjugate signal can be generated at each element using microwave circuitry, let's consider the incident electric field at the  $j^{\text{th}}$  element:

$$E = A(r_j)e^{i(\alpha x - \varphi_j)} + c.c.$$

where

$$\varphi_j = \mathbf{k} \cdot \mathbf{r}_j + \varphi(r_j)$$

The signal picked up by the antenna and then sent to the RF port of the mixer can be written as:

$$V_{j1} \propto A(r_j)e^{i(\alpha x - \varphi_j)} + c.c.$$

Now consider a  $2\omega$  signal delivered to the LO port of the mixer given by:

$$V_{j2} = Ce^{2i\alpha x} + c.c.$$

This  $2\omega$  pump signal has to be delivered to all elements at the same amplitude and phase; otherwise the mixed output will contain a term other than  $V_{j1}$  that depends on  $j$ . If this happens, the sum of the excited field at each element will be distorted and will not form the conjugate beam. Optical interconnection is the crucial technology implemented to carry this  $2\omega$  microwave pump signal in phase to all mixing elements because of its low loss, light weight and small size compared to the microwave counterpart. Using difference frequency generation in a mixer, the IF output current can be written as:

$$I_c \propto e^{2i\alpha x} \cdot e^{-i(\alpha x - \varphi_j)} = e^{i(\alpha x + \varphi_j)}$$

This current component has the conjugate phase  $+\phi_j$  instead of the input phase  $-\phi_j$ . Therefore when it is delivered to the antenna, it will excite the conjugate field at  $r_j$ :

$$E_C(r_j) \propto A(r_j)e^{i(\alpha+\phi_j)} + c.c.$$

When the sampling spacing is less than  $\frac{\lambda}{2}$ , the combined field  $E_C = \sum_j E_C(r_j)$  forms the phase-conjugate wave on the sampling surface and therefore everywhere. Computer simulation has shown that the quality of the conjugate wave is limited by the size of the conjugation surface, not the element spacing, as long as the interelement spacing is less than  $\frac{\lambda}{2}$ .

### Demonstration

To demonstrate the above-mentioned concepts, we have built an 8-element one-dimensional array with optical interconnects to deliver the  $2\omega$  pump signals. Figure 1 shows the configuration of each element.

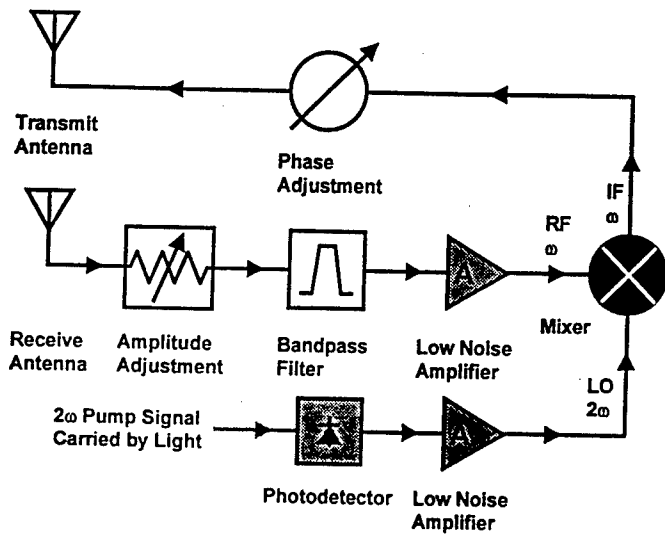


Figure 1. The configuration of a phase-conjugate element used in this study.

Since we plan to demonstrate two-dimensional free space phase conjugation using a one-dimensional array, we have chosen to separate the transmit and the receive antennas for simplicity. This means the sampling of the incident field and the excitation of the conjugate field happen at the same  $(x, y)$  coordinates but slightly different  $z$  coordinate. This small shift in the  $z$  direction will only disturb the electric field distribution on the  $z = 0$  plane to a negligible level.

In this demonstration, the RF frequency is set at 10.24 GHz. A diode-pumped Nd:YAG laser is used as the light source. The optical wavelength is at 1319 nm, with a linewidth  $\leq 5$  KHz. The laser light is directed into a Mach-Zehnder optical modular using a polarization preservation fiber and is

modulated by the  $2\omega$  (20.48 GHz) signal. The  $2\omega$  pump signal is delivered to each element using optical fibers. It is then extracted by a photodetector to be used as the LO signal for mixing. The amplitudes of all phase-conjugate elements are matched to within  $\pm 2\%$ . The phases are matched to within  $\pm 0.2$  ps (0.2%). The conjugate electric field of two transmitting horns is measured and shown in Figure 2.

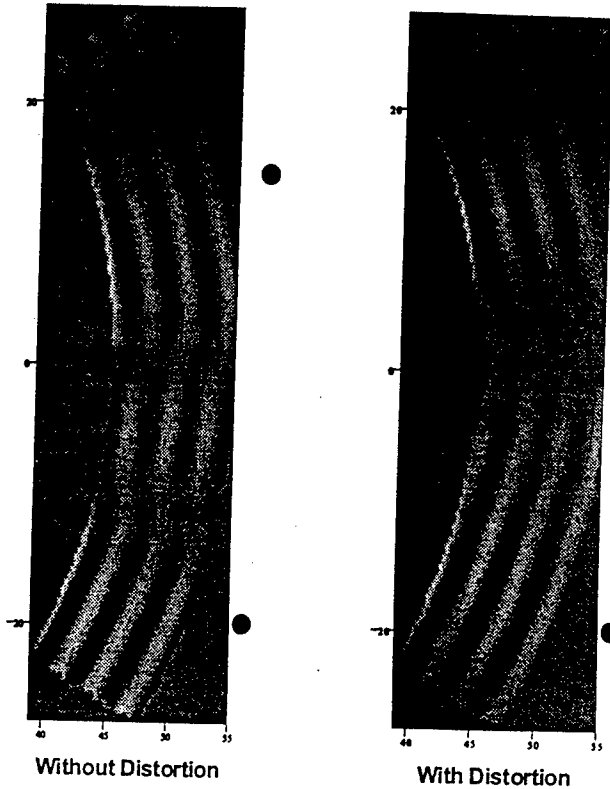


Figure 2. The contour plots of the phase-conjugate electric field of two sources at  $+15^\circ$  and  $-20^\circ$ . They demonstrate multiple-source retrodirectivity and automatic phase correction when a distorting medium is inserted in front of the conjugator. The four black dots represent the transmitting horns and brighter color represent higher field in the plots. Reflections, down by about 10 dB, also appear adjacent to the conjugate signals.

### Conclusions

We have demonstrated two-dimensional phase conjugation at 10.24 GHz with diffraction limited results using an optically injected artificial nonlinear microwave array. By extending this linear array into a two-dimensional surface, complete wavefront reconstruction can be realized at microwave and millimeter wave frequencies.

- [1] R. Shih, H. R. Fetterman, et al., "Microwave phase conjugation in a liquid suspension of elongated microparticles," *Phys. Rev. Lett.*, vol. 65, no. 5, pp. 579-582, 1990.
- [2] C. C. Cutler, R. Kompfner, and L. C. Tillotson, "A self-steering array repeater," *Bell Syst. Tech. J.*, vol. 42, pp. 2013-2032, 1963.

## Multiple-Frequency Fresnel Zone Plate Antennas

James C. Wiltse

Georgia Tech Research Institute  
215 Hillsboro Trace, Spartanburg, SC 29301

### Abstract

Fresnel zone plate (FZP) antennas are normally designed for a particular center frequency. However, it is possible to so design the zone plate that it will function well at 2 or 3 widely-spaced frequency bands, providing narrow beamwidth and high gain. The theory for this approach will be described, and examples will be given of a FZP designed for such combined operation.

### Background and Analysis

The phase-correcting Fresnel zone plate (FZP) antenna is a stepped planar lens [1-4]. The response of the zone plate is frequency dependent, and the intensity at the focal point exhibits a periodic behavior with frequency. The theory for this response was derived in the earlier papers [1,2]. It was also pointed out that a zone plate corrected to a quarter wavelength (quarter-period) at a particular frequency behaves as a half-wave plate at twice that frequency. Thus, with appropriate design, one might develop an FZP optimized for two or more frequency bands.

The simplest zone plate is one where alternate concentric zones are opaque (semi-opaque FZP), but this design is very inefficient. The phase-correcting FZP utilizes all zones, introducing phase delay in alternate zones that approximates the correct delay. A half-wave correcting FZP has a 6 dB higher intensity at the focus than the semi-opaque zone plate, while a quarter-wave correcting FZP has an additional 3 dB higher intensity at the focus compared to a half-wave plate [3,4].

The design equations for a phase-correcting zone plate (FZP) involve the depth of cut ( $d$ ) and the zone outer radii ( $r_n$ ), as follows:

$$d = \frac{\lambda}{P(\sqrt{\epsilon} - 1)}$$

$$r_n = \left[ \frac{2nf\lambda}{P} + \left( \frac{n\lambda}{P} \right)^2 \right]^{1/2}$$

where  $\lambda$  = wavelength in cm,  $P$  = degree of phase correction,  $\epsilon$  = dielectric constant,  $n$  = number of the zone,  $f$  = focal length. At 30 GHz ( $\lambda = 1$  cm), for a focal length of 50 cm and a quarter-wave correction ( $P = 4$ ), we obtain:

$$d = \frac{1}{4(\sqrt{\epsilon} - 1)}$$

$$r_1 = 5.00625 \text{ cm}$$

If we make the calculations for 60 GHz ( $\lambda = 0.5$  cm,  $P = 2$ ,  $f = 50$  cm) the values of  $d$  and  $r_1$  are equal to those above. A check of  $r_2$  values show them also to be equal to each other. Thus, a zone plate designed as above will have high gain and narrow beamwidths at frequency bands around 30 and 60 GHz, and low gain at intermediate frequency ranges. If the design were for an eighth-wave correction at 15 GHz, then performance would be excellent at bands around 15, 30, and 60 GHz.

A more unusual design dealing with bands at 30 and 90 GHz (3:1 ratio) is also possible. For the 30 GHz case, assume  $P = 6$  and the focal length is 50 cm. Then:

$$d = \frac{1}{6(\sqrt{\epsilon}-1)}$$

$$r_1 = \left\{ \frac{100}{6} + \frac{1}{36} \right\}^{1/2} = 4.0859$$

At 90 GHz ( $\lambda = 1/3$  cm and  $P = 2$ ):

$$d = \frac{1}{6(\sqrt{\epsilon}-1)}, \quad r_1 = 4.0859$$

The two  $d$  values are equal, as are the  $r_1$  values. This FZP will therefore provide narrow beamwidths and high gain at 30 and 90 GHz. But, also, assuming that the same aperture is being used at both frequencies, the higher one will have an additional gain factor, because the aperture diameter in wavelengths is 3 times larger (gain is proportional to diameter squared). Thus, a gain factor of 9 (9.5 dB) is added and the higher frequency should have several dB larger gain. (The actual amount will depend on the amplitude taper across the aperture.) Surprisingly, we obtain a design that is excellent at both bands.

## Conclusions

Multiple-frequency band designs for FZPs are possible. Two different examples have been described.

## References

1. J. C. Wiltse, "The Fresnel zone-plate lens", *Proceedings S.P.I.E.*, 544, Arlington, Virginia, pp. 41-47, April 9-10, 1985.
2. D.N. Black and J.C. Wiltse, "Millimeter-wave characteristics of phase-correcting Fresnel zone plates", *IEEE Transactions on Microwave Theory and Techniques*, MTT-35, pp. 1122-1129, December, 1987.
3. J.E. Garrett and J.C. Wiltse, "Fresnel zone plate antennas at millimeter wavelengths", *International Journal of Infrared and Millimeter Waves*, 12, pp. 195-220, March, 1991.
4. L.C.J. Baggen and M.H.A.J. Herben, "Design procedure for a Fresnel-zone plate antenna," *International Journal of Infrared and Millimeter Waves*, 14, pp. 1341-1352, June, 1993.

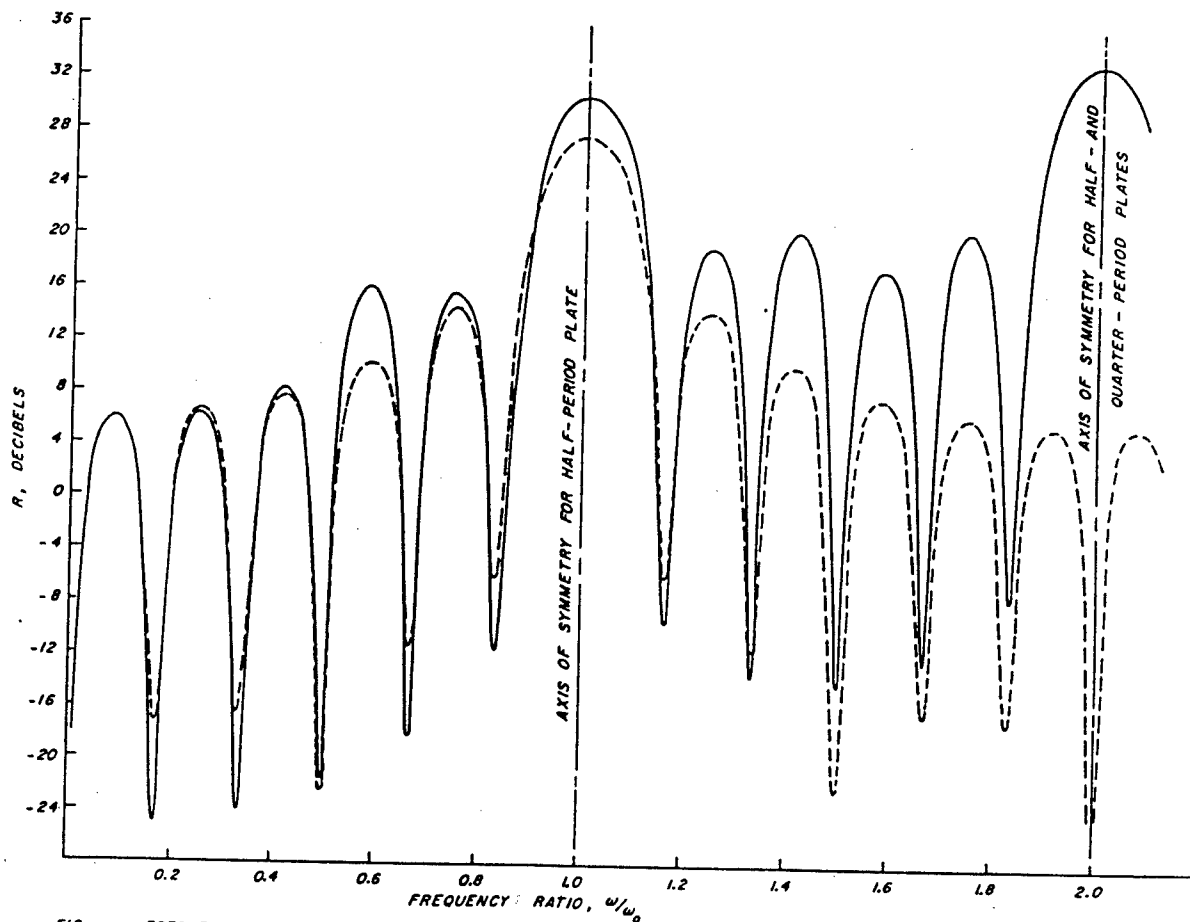


FIG. - FREQUENCY CHARACTERISTICS OF ZONE PLATES WITH  $f = 50 \lambda$ . QUARTER-PERIOD PLATE OF 24 ZONES, HALF-PERIOD PLATE OF 12 ZONES.

# Terahertz radiation from large aperture photoconducting GaAs antenna

G. Mouret\*, W. Chen and D. Boucher  
Laboratoire de PhysicoChimie de l'Atmosphère  
Université du Littoral,  
145 Route du Pertuis d'Amont  
59140 Dunkerque, France.

R. Bocquet  
Laboratoire de Spectroscopie Hertzienne  
Université des Sciences et Technologies de Lille  
59655 Villeneuve d'Ascq Cedex, France.

P. Mounaix, D. Théron and D. Lippens  
Institut d'Electronique et de Microélectronique du Nord  
Avenue Pioncaré, B.P. 69, 59652 Villeneuve d'Ascq Cedex, France.

\*E-mail: mouret@HPLAMER.univ-littoral.fr

**Abstract:** Coherent Terahertz radiation from GaAs photoconducting antennas was demonstrated. To this aim, we combine for the first time, to our knowledge, a large aperture (3.5mm) GaAs:Cr photoconducting antenna for the transmitter and a small gap (25  $\mu\text{m}$ ) transmission lines printed on low-temperature grown (LTG) GaAs epilayers for the receiver. Correlation measurements by electro-optic sampling techniques show sub-picosecond pulses (FWHM 750fs) governed by carrier life time in LTG GaAs.

**Introduction:** Pulsed electromagnetic radiation with terahertz bandwidth but relatively limited power have been produced over the past by means of femtosecond optical pulses incident notably upon Hertzian dipoles, strip lines and spiral antennas [1]. For many applications however high peak power is required thus motivating the development of large aperture antenna which accept high optical power and high applied voltage [2] [3]. We present an experiment which use a high repetition rate regenerative amplifier (up to 300kHz) which permit to report an alternative approach for producing high peak power electromagnetic pulses which combines a large aperture emitter antenna and a small gap striplines detector antenna. In addition, we have used non stoichiometric low temperature grown GaAs which offer great potential as extremely fast photoconducting detectors.

**Material Growth:** Low-temperature grown (LTG) GaAs epilayers were used for implementing the detecting antenna. Unlike GaAs materials grown at substrate temperature of about 600°C, LT-GaAs contains a high concentration of deep defects which promote carrier recombination while maintaining a good crystal quality. Optically generated carriers thus recombine at rates order of magnitudes faster than for higher grown materials. The film structure consisted of a 0,13 microns thick GaAs buffer layer grown at 600°C and a 1microns-thick LT GaAs grown at 200°C under normal AS-stabilized conditions. All layers were grown nominally

undoped. Besides, no post-growth anneal was performed in order to have the faster decay time [4].

**Experimental Setup:** Femtosecond laser pulses were obtained from a Coherent Titanium:Sapphire MIRA laser, pumped by a 25 W argon laser, tune to 800 nm and subsequently amplified by a regenerative amplifier REGA. The 800 nm wavelength was chosen because it was approximately 100meV above the gap of normal GaAs avoiding satellite valley conduction. At the output, the optical pulse duration was 200 fs, with 4.5  $\mu\text{J}$  energy and 200 kHz repetition rate. This optical beam was split into two beams (Figure 1). One beam with 98% of the net intensity was delivered from the front side to the transmitting antenna with approximately a diameter excitation spot equal to the antenna gap. This corresponds to an optical fluence of about 0.04mJ/cm<sup>2</sup> [2]. The second beam which contains the remainder of optical intensity was focused to the receiver to gate the detector. In addition, a delay line permits a path adjustment between the pump and probe beams. For collimating the THz pulses radiating from GaAs:Cr substrate, we positioned on the back side of the samples an elliptic mirror whereas a paraboloidal reflector was used to focus the Terahertz radiation on the detector.

**Results:** By means of pump-probe femtosecond time arrangement the measurement of the photocurrent is a convolution of the radiated field and of the conductivity of the detector, but generally the response of the receiver can be eliminated by making comparative measurements. Figure 2 shows the variation of the detected under these conditions versus time. A sharp peak in THz waveform can be seen with a Full Width at Half Maximum (FWHM) of 750 fs followed by replica which result directly from the reflection of the radiation at semiconductor-air interfaces. The delay between each pulse is about 8.3ps. It can be checked that this time corresponds to  $2w/v$ , where  $w$  and  $v$  are the GaAs substrate thickness and  $v$  the speed of electromagnetic field in the semiconductor medium. In addition, the relative amplitude between the pulses is  $\approx 0,35$ .

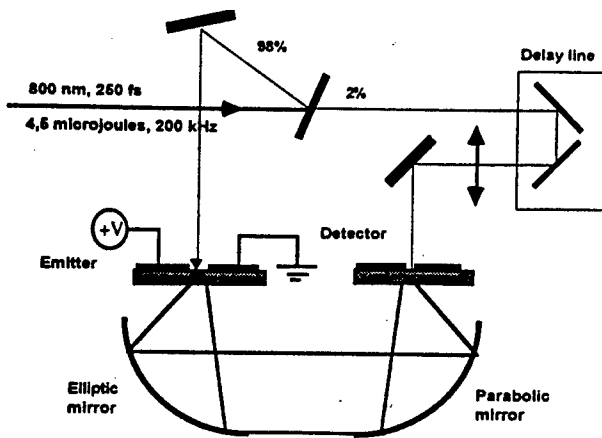


Figure 1: Pump-probe femtosecond experimental setup combining a large aperture Cr-doped GaAs emitter antenna and a stripline LTG:GaAs detector antenna

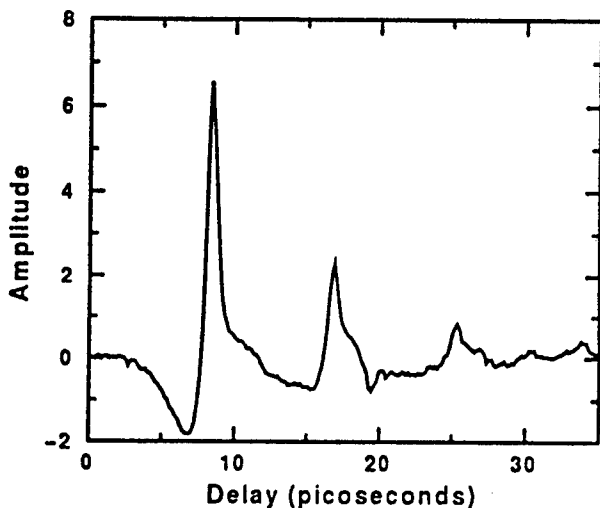


Figure 2: Temporal response of the EM field convolved with transient photoconductivity

The fresnel formulas for reflection at a plane interface on the basis of energy conservation gives an expected ratio  $[(n-1)/(n+1)]^2$  of 0.3 assuming an index of refraction  $n=3.3$ , in good agreement with experiment. Due to this multiple reflection mechanism, the corresponding Fourier transform, depicted in Figure 3, shows multi-peaked variation versus frequency. In order to estimate the radiated spectrum free of these reflections, we also performed the Fourier transform of a single pulse, whose frequency transform is plotted in dotted lines. The maximum amplitude was centered around 140 GHz with radiated signal up to 1.5 THz. These results

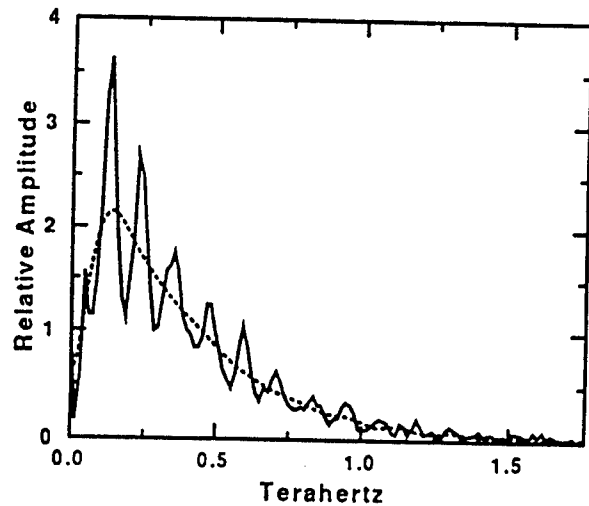


Figure 3: Spectral response obtained by Fourier transform of the temporal shape (solid lines) and of the truncated signal (dashed lines)

demonstrating short pulses are agreement with the theory of large aperture antennas [2]. Indeed, it can be shown that the radiated field is related to the first derivative of the current density in the biased photoconductor and hence do not depends, for the positive part of  $E_T(t)$ , on the rather long carrier lifetime in GaAs S-I substrate. In contrast, it is imperative to use LT GaAs with short duration of photo-conductivity for observing the submillimeter radiation by electro-optic sampling. In the present experiment, maximum biased field was 1.5KV/cm, we expect further improvement in this experiment by increasing this threshold voltage.

#### References

- [1] See as example Auston D.H.: "Ultrafast Optoelectronics", in Topics III Applied Physics Ultrashort laser Pulses and applications, Editor Kaiser W., 1992, 80, pp183-233
- [2] Benicewicz P.K., Roberts J.P., and Taylor A.J.: "Scaling of terahertz radiation from large aperture biased photoconductors". J. Opt. Soc. Am. B, 1994, 11, (12), pp 2533-2546
- [3] You D., Jones R.R., Bucksbaum P.H., D.R. Dyckaa: "Generation of high power sub-single cycle 500-fs electromagnetic pulses", Opt. Lett. 18, (4), 1993, pp 290-292
- [4] Harmon E.S., Melloch M.R., Woodall J.M., Nolte D.D., Otsuka N. and Xhang C.L.: "Carrier lifetime versus anneal in low temperature growth GaAs", Appl. Phys. Lett. 63, (16), pp2248-2250



## Sixteen-Element linear Array of Ge:Ga Far-infrared Photoconductor

\*M. Fujiwara and N. Hiromoto

Communications Research Laboratory, Ministry of Posts and Telecommunications  
4-2-1 Nukuikita-Machi, Koganei-Shi, Tokyo 184, Japan

### Abstract

We have fabricated a 16-element unstressed Ge:Ga far-infrared photoconductor array with monolithic structure. The detector has a longitudinal configuration, and the sensitive area of one pixel is  $0.5 \times 0.5 \text{ mm}^2$ . The spacing between pixels is 0.05 mm, and the length between electrodes is 0.5 mm. The responsivity and the noise equivalent power (NEP) of the linear array detector in the first fabrication of the development achieved 7.6 A/W and  $2.1 \times 10^{-16} \text{ W/Hz}^{1/2}$  respectively for 15 Hz chopped light at an operating temperature of 2.0 K and at a bias field of 1.6 V/cm.

### Introduction

Gallium-doped germanium (Ge:Ga) extrinsic semiconductors have been used as sensitive far-infrared detectors with a cutoff wavelength at 110  $\mu\text{m}$ , especially for applications in astronomy and far-infrared spectroscopy.<sup>[1],[2]</sup> Development of arrays of doped-Ge photoconductors is now an important target for research fields to take far-infrared two-dimensional images.<sup>[3],[4]</sup> In order to fabricate a two-dimensional Ge:Ga photoconductor array, it is necessary to make a transparent electrode for placing the detectors in a "longitudinal" configuration in which the electric field is applied parallel to the photon influx. This configuration is more suitable for constructing a two-dimensional format than the transverse configuration in which the applied electric field and the resulting current flow are transverse to the incident photon influx. In this paper, we report on the performances of the 16-element unstressed Ge:Ga linear array in the first fabrication of the development as well as the loss of far-

infrared radiation through the transparent electrode.

### Characteristics of transparent electrode

The transparent electrode must be good in two characteristics which are transmission of far-infrared radiation and ohmic contact. The transparent electrode was made by implanting  $\text{B}^+$  ions on one surface of a Ge:Ga wafer. The Ga concentration of this wafer was  $2 \times 10^{14} \text{ cm}^{-3}$ .  $\text{B}^+$  ions were implanted at a density of  $5 \times 10^{13} \text{ ions/cm}^2$  at 40 keV and the Ge:Ga wafers were heated to 320°C for 1 h in an atmosphere of  $\text{N}_2$ . The far-infrared transmissions of the ion-implanted Ge:Ga specimens were measured at a temperature of approximately 4.2 K by use of a Fourier spectrometer and a Si bolometer. We measured the transmission of far-infrared radiation through Ge:Ga with and without  $\text{B}^+$  ion-implantation and undoped Ge wafers in comparison. The thickness of specimens were 1 and 0.5 mm for each sample. We estimated the far-infrared absorption of the  $\text{B}^+$  layer by comparing the transmission before and after ion-implantation. Fig. 1 shows the transmittance of Ge:Ga wafer as a function of wave number. In the 40-130  $\text{cm}^{-1}$  spectral region, the transmittance of the Ge:Ga wafers with the  $\text{B}^+$  ion layer decreased. It is considered that the ion-implanted layer reduces the number of signal photons due to free carrier absorption. Strong absorption lines at 68 and 74  $\text{cm}^{-1}$  can be consistent with lines labeled D and C by Haller and Hansen, which are transitions from the ground state level to higher energy states of gallium acceptor.<sup>[5],[6]</sup> The transmission of far-infrared radiation through the ion-implanted layer at a wavelength of 100- $\mu\text{m}$  was about 84%.

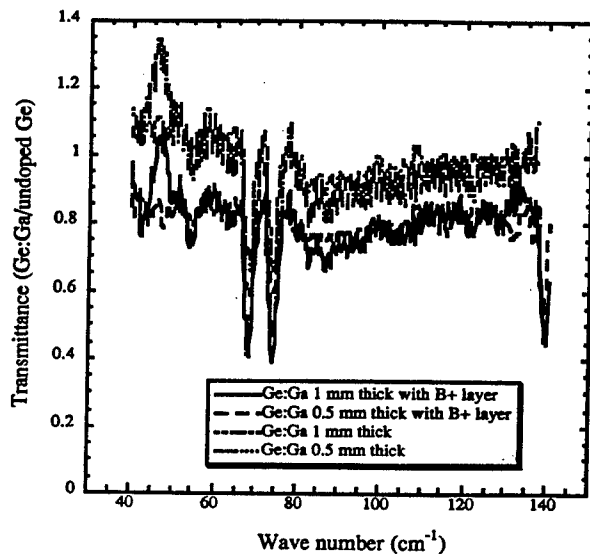


Fig. 1 Transmittance of far-infrared radiation of Ge:Ga wafers with and without transparent ion-implanted layer

### Fabrication of linear array

We chose a 0.5 mm-thick wafer for the first fabrication of the array detector. After ion-implantation of the transparent electrode,  $B^+$  ions were implanted on the back metal electrode at a dose density of  $1 \times 10^{14}$  ions/cm<sup>2</sup> at 40 keV and  $2 \times 10^{14}$  ions/cm<sup>2</sup> at 60 keV. This condition was the same as that for the single-element photoconductors with two metallic ohmic electrodes.<sup>[7],[8]</sup> Following a 5-min annealing in  $N_2$  atmosphere at 320°C, a 5000-Å-thick Au on 500-Å Cr layer was evaporated onto the ion implanted surfaces. To bond gold wires, to increase conductance on the front surface, and to optically separate the pixels, a metal pattern was deposited on the transparent electrode as shown in the upper half of Fig. 2. Fig. 2 also details the pattern of the back metal electrode of the detector array. A linear array was fixed with silver epoxy on a metallic pattern on a magnesium oxide plate. In the process of removing excess metal on the front electrode, the transparent electrode on the window was regrettably damaged, however, the ion implanted layer remained under the metallized surface. The ditches 50  $\mu$ m in width and 10-

$\mu$ m deep were dugged on the back metal surface by wet etching for the purpose of separating pixels.

### Performance of linear array

We measured the responsivity and NEP of four detectors in the 16-element array. Typical performance of the detectors is as follows: the responsivity and NEP are 7.6 A/W and  $2.1 \times 10^{-16}$  W/Hz<sup>1/2</sup>, respectively, for 15 Hz chopped light at an operating temperature of 2.0 K and at a bias field of 1.6 V/cm. From the test of putting photon influx on to one element, it was estimated that the crosstalk between neighboring pixels was 8~14%. We supposed that main part of the crosstalk occurred in the read-out circuits.

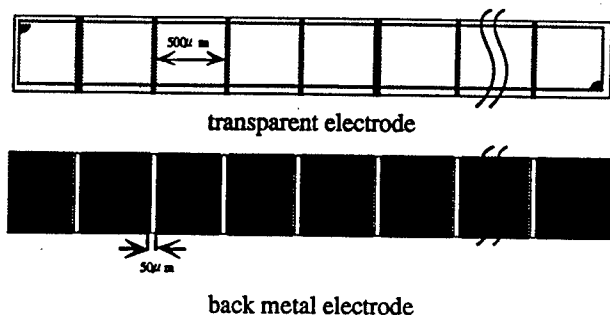


Fig. 2 Detail of 16-element linear array format

### References

- [1] M. F. Kessler: Opt. Eng. 33 (1994) 10.
- [2] H. Shibai *et al.*: Astrophys J. 428 (1994) 354.
- [3] J. W. Beeman *et al.*: Infrared Phys. 35 (1994) 827.
- [4] E. F. Erickson *et al.*: Proc. ESA Sympo. on Submillimetre and Far-Infrared Space Instrumentation (ESA SP-388, 1996) p. 41.
- [5] E. E. Haller *et al.*: Solid St. Commun. 15 (1974) 687.
- [6] J. Leotin *et al.*: Infrared Phys. 3 (1988) 165.
- [7] N. Hiromoto *et al.*: Jpn. J. Appl. Phys. 29 (1990) 1739.
- [8] N. Hiromoto *et al.*: Jpn. J. Appl. Phys. 35 (1996) 1676.

## Accurate Analysis of Fundamental Wave Phenomena in the Printed Antennas

Natalia Yu. Bliznyuk and Alexander I. Nosich

Institute of Radiophysics and Electronics,  
National Academy of Sciences, Kharkov, Ukraine

**Abstract** - The fundamental antenna effects of a circular metallic patch antenna on dielectric substrate, backed by a perfectly-conducting ground plane are investigated. The solution is numerically accurate in the resonant range due to a sophisticated method used. Applications to millimeter wave antennas are discussed.

### 1. The basic properties of the fields excited by VED and HMD in a homogeneous dielectric substrate

To analyze the basic properties of a canonical substrate (Fig. 1, without patch) fed by coaxial line or elementary slot, the problems of the Hertzian vertical electrical dipole (VED) and horizontal magnetic dipole (HMD) are solved exactly. Although similar problems were considered in some works [1,2], it appears that the mentioned characteristics have been studied only in the case of a horizontal electric dipole.

The Poynting theorem in a complex form (real part, which defines the power) is used to investigate the fundamental effects of similar structures.

The field-potential components for the infinitesimal dipoles are derived by using Sommerfeld's method in the form of the Fourier-Bessel integrals. After that, a contour integration is used in order to compute the surface wave power in the transverse magnetic (TM) surface waves excited by VED, and in the transverse electric (TE) and hybrid surface waves of HMD. The space-wave radiation pattern is obtained by application of the saddle-point method.

Some typical results are presented in Fig. 2 and Fig.3. They show the radiation efficiency versus the substrate thickness for different media. In each case, the maximum radiation efficiency is obtained either at the cutoff frequency of a surface mode (a threshold phenomenon,) or at the frequency of an interference peak. As it is seen, the radiation efficiency in the case of HMD excitation is greater and decreases more slowly than in VED excitation case with larger  $h/\lambda_0$ .

### 2. Accurate analysis of fundamental wave phenomena in the circular-patch antenna.

Metallic patches printed on dielectric substrates are widely used in antenna applications. From theoretical point of view, such a patch of circular geometry is canonical one for a wide class of patch antennas on layered substrates. The known literature contains the numerous analyses of various

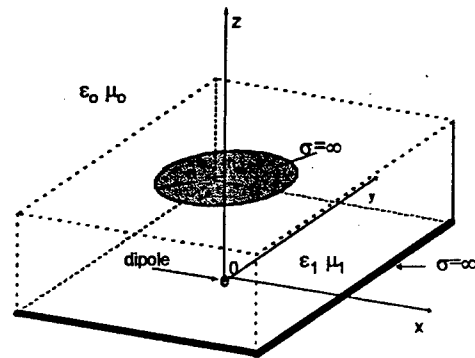


Figure 1. Geometry of the problem

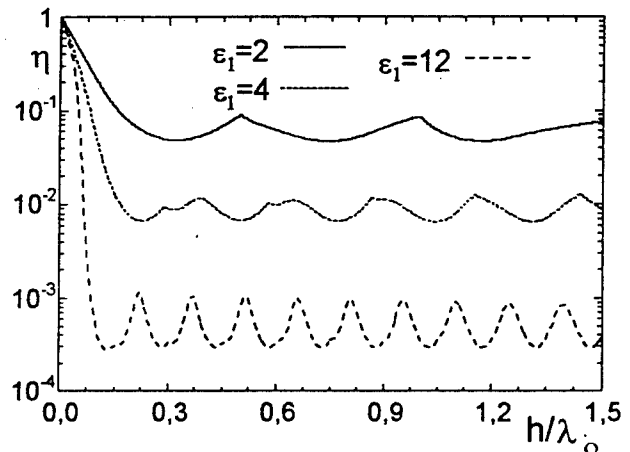


Figure 2. The radiation efficiency (VED)

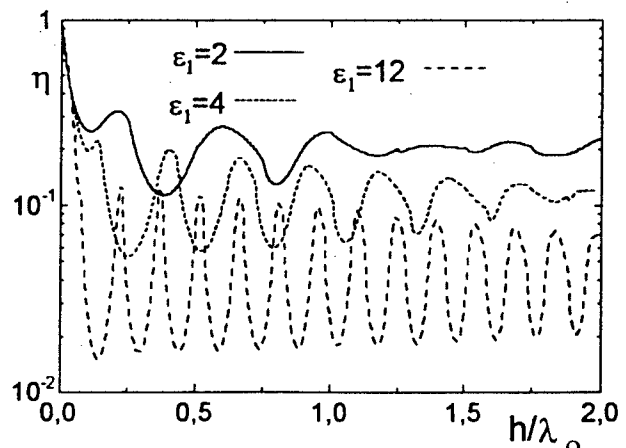


Figure 3. The radiation efficiency (HMD)

radiating patches done by approximate circuit theory methods and by direct application of the Method of Moments (MoM) [3]. Our solution of the diffraction problem by a circular metallic patch (see Fig. 1) is based on the Method of Regularization (MoR) approach exploiting the analytical inversion of the static part of the corresponding full-wave integral equations. Numerical algorithm based on MoR outperforms conventional moment-method algorithms, and has controlled accuracy due to a much smaller matrix size and few, if any, numerical integrations for filling the matrix.

As an example of a printed antenna, we consider a circular patch excited by a symmetrical VED source. The problem solution consists of the following steps. First, dual integral equations are to be derived based on the different boundary conditions on the patch and on the substrate-free-space interface and using the Fourier-Bessel transform. Due to the presence of the metal ground plane and the dielectric layer, the integrand functions are determined by the Green's function of the stratified medium. In terms of the normalized coordinate  $r$ :

$$\begin{cases} \int_0^\infty \alpha(\kappa) \beta(\kappa) J_1(\kappa r) d\kappa = \int_0^\infty F_o(\kappa) J_1(\kappa r) \kappa^2 d\kappa & (r \leq 1) \\ \int_0^\infty \alpha(\kappa) J_1(\kappa r) d\kappa = 0 & (r > 1) \end{cases}$$

where  $\alpha(\kappa)$  is an unknown function,  $\beta(\kappa)$  is a function depending on the media parameters. Right hand part integrand  $F_o(\kappa)$  is determined by the excitation, e.g. by the location of the VED source.

The weight function  $\beta(\kappa)$  has a number of poles correspond to the surface-wave and leaky-wave modes of the substrate, respectively.

Further we expanded of the unknown function like follows:

$$\alpha(\kappa) = \sum_{n=0}^{\infty} C_n \psi_n(\kappa),$$

where the expansion functions

$$\psi_n = \sqrt{4n+5} J_{2n+5/2}(\kappa) \frac{1}{\sqrt{\kappa}},$$

so that they are proportional to the spherical Bessel functions.

Such a choice of the basis functions allows to invert the static (singular) part of the dual integral equations analytically and provides satisfying the edge condition on the patch rim. Furthermore, the second equation in the set is satisfied identically [4].

Extracting the static (singular) part of the dual integral equations is done by introducing the function  $\Omega(\kappa)$ , such that

$$\beta(\kappa) = \kappa(1 - \Omega(\kappa)),$$

where

$$\Omega(\kappa) = \frac{\gamma_1 \gamma_2}{\kappa(\gamma_2 \varepsilon_1 + \gamma_1 \varepsilon_2 \tanh(\gamma_2 h))},$$

$$\gamma_j = \sqrt{\kappa^2 - (ak_j)^2}.$$

Further, using the property of orthogonality of the Bessel functions [4], the infinite matrix equation of the Fredholm 2-kind in transform domain is obtained:

$$C_k - \sum_{n=0}^{\infty} C_n \int_0^\infty \psi_k(\kappa) \psi_n(\kappa) \Omega(\kappa) d\kappa = \int_0^\infty \psi_k(\kappa) F_o(\kappa) d\kappa$$

The matrix elements here have rapidly decaying kernels and is efficiently computed by a simple numerical procedure. Note that analytical inversion of a part of original operator essentially exploits the circular shape of the patch.

Next is the numerical investigation of the far field radiation patterns, near field structure, surface modes, and other values of interest such as radiation efficiency and directivity. This results will be presented in the conference.

#### References

1. N. G. Alexopoulos, P. B. Katehi, D.B. Rutledge, "Substrate Optimization for Integrated Circuit Antennas," *IEEE Trans. Microwave Theory Tech.*, Vol. MTT-31, No. 7, 1983, pp. 550-557.
2. J. R. Mosig, R. C. Hall, F. E. Gardiol, Numerical analysis of microstrip patch antennas, in J. R. James and P. S. Hall (Eds.), *Handbook of Microstrip Antennas*, London: Peter Peregrinus, 1989, pp. 391-453.
3. A. K. Skrivervik, J. R. Mosig, (1990), "Impedance Matrix of Multiport Microstrip Discontinuities Including Radiation Effects," *Arch. Elektr. Übertragungstechnik*, 44(6): pp. 453-461.
4. M. Abramovitz, I. A. Stegun, Eds., *Handbook of mathematical functions*, Washington, DC: NBS, Ch. 10, 11, 1964.

## Millimeter-Wave Drivers for Future Linear Colliders

David H. Whittum

ARDB, SLAC, Stanford University,  
POB 4349, Stanford CA, 94309

## Abstract

The challenges for high-gradient mm-wave driven colliders are reviewed. Requirements on power sources are examined, and a particular tube is considered for illustration. Research topics relevant to a compact 1 GeV linac are noted throughout.

## Introduction

High-energy physics is an experimental science whose reach is limited by its instruments, accelerators[1]. While theorists look toward the 5 TeV frontier[2], the highest energy linear collider, the Stanford Linear Collider (SLC) operates at 0.05 TeV[3]. This disparity reflects the status and the cost of the technology required to meet the collider scalings[4], relations that determine the useful event rate and the accelerator size and power consumption in terms of a couple dozen major machine parameters. It is an open question how or whether a 5 TeV center-of-mass energy machine could be built. There is no technical solution at present for such a machine, but if one could be found, *without* innovation in rf technology, it would be somewhere between 30 and 300 km long[5].

To escape this trend toward great lengths, a high-gradient accelerator is required. For example, a 5 TeV collider fitting on the existing SLAC site, would require a gradient of 1 GeV/m or more. Yet it is impossible to conceive of an electron collider operating with such a gradient relying on known collider technology. Innovations are required. This is why accelerator physicists are interested in the subject.

In this work, we look beyond what can be engineered today, and ask what manner of basic research, in high power microwave systems might be fruitful for the machines of the future.

## Problems of High Gradient

For the linac proper one must account for *trapping*, *breakdown*, and *pulsed heating*. These phenomena are represented quantitatively in Fig. 1. Trapping refers to the acceleration from rest of field-emitted electrons in the structure; trapping fraction is a function of the product  $G\lambda$  of the gradient  $G$  and the rf wavelength  $\lambda$ , and may be computed using the binding field expression[6].

Breakdown is a phenomenological problem at present, but it does exhibit a clear pulse length dependence. The curve in Fig. 1 is an extrapolation for pulse length equal to the natural fill-time of a travelling wave structure with attenuation parameter  $\tau=1$ [7]. Pulsed

heating refers to the deposition of heat, by Ohmic loss, in the conducting structure, in a single pulse. For a pulsed temperature rise  $\Delta T$ , the corresponding gradient is given by,

$$G\left(\frac{\text{GeV}}{\text{m}}\right) = 0.25\left(\frac{\Delta T}{40^\circ\text{K}}\right)^{1/2}\left(\frac{f}{91.4\text{GHz}}\right)^{1/4}$$

for idealized rectangular pillbox cells, in a constant gradient structure with attenuation parameter  $\tau=1$ , and pulse length equal to a fill time.

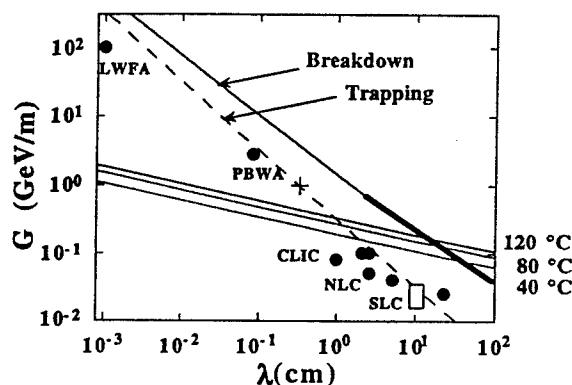


Figure: 1 Current state of the art in high-gradient accelerator research.

Also seen in Fig. 1 are gradients achieved at present, including results for Laser Wakefield Accelerator (LWFA), Plasma Beat-Wave Accelerator (PBWA)[8], and several 0.5 TeV collider concepts[9]. The block marked "SLC" extends from 20 MV/m as for a typical structure, to 40 MV/m as for certain higher gradient structures on the linac.

These scalings imply that *high-gradient* requires *short-wavelength*. For a 1 GeV/m linac, interest begins in the *W-Band*, 75-110 GHz. We have added a cross-mark in Fig. 1 as a helpful landmark, corresponding to 1 GeV/m. The corresponding frequency is close to 91.4 GHz (3.3 mm), the 32nd harmonic of the SLC fundamental frequency, 2.856 GHz.

The curves of pulsed temperature rise, in Fig. 1, make clear that such a linac will suffer severe pulsed heating, and the *conventional* travelling wave structure we have taken as our paradigm, will surely fail short of 1 GeV/m. To be sure, it is yet an open question exactly what cyclic pulsed temperature rise a structure can withstand and this is the subject of ongoing research on materials under conditions of high-power pulsed rf[10,11].

In addition, based on experience at longer wavelengths, one would expect to find serious problems

with field emission[7]. Even with a very low field enhancement factor of 5, a gradient of 1 GeV/m would produce explosive electron emission. At the same time, there is experimental evidence that field emission is inhibited on short, ns time-scales[12], and this is encouraging insofar as the natural fill time for a W-Band structure is on the order of 10ns, and contemplated exposure times are below 1ns.

### Structures

The scalings for accelerating structures determine the essential considerations for the rf drivers. For copper accelerators, optimized for  $[R/Q]$ , the scaling for wall quality factor,  $Q \propto f^{1/2}$  implies a  $Q$  of 2500 at W-Band, and a field decrement time  $T \sim 10$ ns. Achieving the theoretical  $Q$  at W-Band is not taken to be a straightforward matter, as the skin-depth  $\delta \sim 0.2 \mu\text{m}$  and thus surface finish is an issue[13]. Theoretically one may obtain  $[R/Q] \sim 220 \Omega$  per cell, but in practice, with realistic beam-passing apertures,  $[R/Q] \sim 90 \Omega$  is typical. The corresponding shunt impedance per unit length is  $220 \text{ M}\Omega/\text{m}$ .

The more serious constraint here is the fabrication tolerance due to random cell-to-cell frequency errors. For a structure of length  $L$ , with group velocity  $\beta_g c$ , operated at free-space wavelength  $\lambda$ , these are characterized by

$$\delta \approx \frac{1}{2} \frac{\delta \omega^2}{\omega^2} \frac{\theta}{\beta_g},$$

with  $\theta$  the design phase-advance per cell, and  $\delta \omega / \omega$  the fractional frequency detuning error of one cell. The loss in no-load voltage for a Gaussian distribution in  $\delta$  with rms  $\sigma_\delta$  is

$$\frac{\delta V_{NL}}{V_{NL}} \approx -\frac{1}{2} (N+1) \sigma_\delta^2,$$

with  $N$  the number of cells. This scaling implies a fabrication tolerance at the level of  $2 \mu\text{m}$  for a W-Band structure operating within 95% of optimal no-load gradient. Fabrication of such structures at the level of  $3.5 \mu\text{m}$  is now an accomplished fact[14]. A related, but less significant constraint is the tolerance on uniform errors. For a uniform fractional deviation  $\delta \omega / \omega$  from synchronism, the loss in voltage is given by

$$\frac{\delta V_{NL}}{V_{NL}} \approx -\frac{1}{6} \left( 2\pi \frac{L_s}{\lambda} \frac{\delta \omega}{\omega} \frac{1}{\beta_g} \right)^2.$$

This corresponds to a  $\pm 10 \text{ MHz}$  detuning at the 5% level in voltage.

After fabrication, perhaps the most significant objection to short wavelength structures has been wakefields. Wakefields, it has been demonstrated[15] can be dealt with in a constructive fashion, making use of the structure itself as a beam-position monitor, and permitting, in principle, precision structure alignment. The most significant consequences of wakefields at W-

Band are a limit to the charge per bunch, to 60pC or less, and the problem of magnetic lattice fabrication[16].

One additional problem arises in planar structures: quadrupole field components[17]. These would likely require dedicated quadrupole-mode structures to compensate their effect on the beam.

Given the inextricable relation between energy storage and bandwidth in a passive structure, together with the high-bandwidth implied by the short pulse needed to control pulsed heating, active elements are of great interest at W-Band. A high-power microwave switch permits resonant energy storage in a large volume, holding down fields and pulsed heating. "Q-switching" then permits fields to be discharged in a short, sub-ns time interval, lowering the pulsed heating. As to the choice of photoconductor, diamond looks promising. The thermal conductivity of diamond is 4-5 times that of copper,  $\kappa \sim 1500-2000 \text{ W}/^\circ\text{K}\cdot\text{m}$ . The bandgap is 5.4eV, so that excitation by 220nm wavelengths or shorter is required. Experience with diamond as a photo-conductor indicates that fields of order 100MV/m-1000MV/m can be held off on a  $\mu\text{s}$  time scale[18].

### Tube Requirements

There are two known, and quite different routes to a power source for a high-gradient mm-wave linac. The first is the class of concepts known as two-beam accelerators[19]. For these concepts one has no particular concern about generating adequate peak power in the appropriate pulse length. Induction linac driven FELs have produced 2GW at wavelengths from 1cm to 2mm[20,21]. Instead research areas of interest concern the more subtle issues of drive-beam stability and phase stability, issues that can be adequately addressed only by the construction and operation of a prototype facility. In fact, facilities exist that have some affinity for such work, for example, The LELIA accelerator, operated at the Centre d'Etudes Scientifiques et Techniques d'Aquitaine (CESTA), generates a 1 kA, 2.2 MeV beam with an 80 nsec (FWHM) pulse length[19].

The second route to high peak power at W-Band is through a modulator-driven amplifier, a "tube". As far as accelerators are concerned, the present state of the art in W-Band tubes is quite similar to that of S-Band tubes in the pre-Mark III days[22]. Commercial amplifiers at W-Band provide at most 3-5 kW[23]. Gyroklystron tube research has resulted in 67 kW power levels [24]. A planar ubitron has been operated at 250 kW[25]. Regardless of the kind of driver, to reach 1 GeV/m, one needs power levels in the range of 200 MW, for pulse lengths of order 10 ns. Two-beam concepts would generate 200MW directly in a 10ns pulse. Tubes on the other hand would be matched to a typical modulator pulse length of  $1 \mu\text{s}$  and would generate lower peak powers, but would require pulse compression.

For tubes, a useful research goal, matched to the linac requirements would include 5MW over a  $1 \mu\text{s}$  pulse, and an active pulse compression system. As for the tube itself, there are at present four identified lines of research and development: (a) sheet beam klystron (b) sheet beam ubitron (c) gyro-TWT and (d) gyroklystron. Of these, the gyroklystron is perhaps the most advanced [24]. A low-

voltage sheet beam klystron, would open up many new possibilities for powering an accelerator [27]. Most prominent among these is the possibility of an integrated power source, as opposed to one high-voltage source followed by power splitting to multiple structures. Given the problems of attenuation (1dB/ft) in a fundamental mode waveguide network, and the complications of transport and mode-conversion in overmoded guide, a source module integrated with the structure is an attractive proposition. Power levels in excess of 100kW and pulse lengths of order a microsecond have been considered for low-voltage (50kV) tubes.

### Planar Ubitron

For illustration, let us consider a particular concept for a 5MW, 1 $\mu$ s tube: a planar ubitron. To save development time and cost, it is desirable to fashion a tube that could run on an existing modulator. This sets the beam voltage in the 500kV range, let us say 480kV. To characterize performance, we employ a dispersion relation including waveguide corrections, space-charge, emittance, energy-spread, and low-energy corrections. To reach a saturation power of 5MW without tapering the wiggler, requires then a beam current of 295A, corresponding to 0.9 $\mu$ perv. The wiggler wavelength should be on the order of 1cm and 1.16 cm appears optimum. One hopes eventually to arrive at a tube adequate as a collider power source, and for this reason, the design should be consistent with the use of permanent magnets, even if the first series of tubes makes use of electromagnets. This constrains the wiggler gap to a small value, 0.4cm. Focusing in the vertical is provided by the wiggler itself. One long quadrupole can be employed to focus in the horizontal, at the expense of some vertical focusing. This magnet layout is similar to that employed for the 30 MW X-Band FEL at KEK[28]. With these parameters, the peak wiggler field on-axis, at optimal gain is 5.1kG, well within the 7kG Halbach limit for NdFeB with Vanadium Permendur. These wiggler parameters are less demanding than those produced by Cheng, *et al.* [25]. Without tapering, the signal saturates in 60cm, with 1kW input.

The gun for such a tube has never been designed, and thus is a prominent research problem. It is likewise prominent in the sheet-beam klystron line of development. Needless to say, long-lived cathodes with much higher loading would be quite helpful for such devices. Leaving a 50% beam-clearance in height and width, the current density in the wiggler is then 750A/cm<sup>2</sup> [15]. At 10A/cm<sup>2</sup> at the cathode, this would require 75x convergence, *i.e.*, convergence in both planes, and therefore, 3D gun design, a challenging problem. If we ask for a very ambitious cathode loading of 100 A/cm<sup>2</sup>, the required convergence is  $\times 7.5$ , and the gun design could approach that of a section of a cylindrical diode; in this case avoidance of large fields and gun arcing will be a concern.

To inhibit tube oscillation, a high power driver would be quite helpful. With 1kW input, and gain of 37dB, the tube becomes unstable against oscillations at a VSWR of 1.03 at the output. This highlights the fact that there are actually two categories of tube development

required, the high-power amplifier and the driver itself. Commercial drivers are not only too expensive, they are close to inadequate.

Other features to be investigated for this tube are: (a) beam transport (b) beam collection (c) output coupling and (d) the gun. Beam transport is being modelled with a three-dimensional particle in-cell simulation. Beam collection in the first tube, at low repetition rate (10Hz) could simply amount to the dispersal of the beam on the vertical waveguide walls, after the wiggler exit, over the natural 5cm space-charge spreading length of the beam. Output coupling from TE<sub>01</sub> in overmoded guide, and the matter of a window will be important problems for the output assembly.

It should be emphasized that the immediate purpose of a 5MW tube would not be the powering of an accelerator. Such a tube would be first an invaluable research instrument for studies of field emission, breakdown, and structure damage. It would permit studies of pulse compression in the pulse length range of interest. It would also permit tests of structures at intermediate gradients (100MV/m), without pulse compression. Eventually, however, such a tube could be extended by wiggler tapering to the 20MW level. At such a power level and with an active pulse compression network, and active structures, it is conceivable to power a 1 GeV, 1 meter linac with eight tubes.

### Conclusions

The challenges for a high-gradient mm-wave linac are immense, and this is what makes the field interesting in the first place, to physicists. It has been forty years since the advent of the first 1 GeV linac[5], 220 ft long, powered by 21 home-built klystrons, putting out 20MW--30dB more than anyone thought a klystron could put out a decade before[18]. Perhaps the next wave of power tube development will occur at W-Band.

### Acknowledgments

I am indebted to Perry B. Wilson for his encouragement and many helpful conversations. This work has benefited from numerous conversations with Ping J. Chou, Al Menegat, Glenn Scheitrum, Mike Seidel, Robert H. Siemann, Daryl Sprehn and Xiaoxi Xu. Supported by DOE Contract DE-AC03-76SF00515.

### References

- [1] Robert N. Cahn and Gerson Goldhaber, *The Experimental Foundations of Particle Physics* (Cambridge University Press, Cambridge, 1989)
- [2] *Proceedings of the 1996 DPB/DPF Workshop on New Directions for High Energy Physics* (AIP, New York, to be published).
- [3] J. T. Seeman, "Stanford Linear Collider" *Ann. Rev. Nucl. Part. Sci.* **41** (1991) pp.389-428.
- [4] R. B. Palmer, "Prospects for High Energy e+e- Linear Colliders", *Ann. Rev. Nucl. Part. Sci.* **40** (1990) pp.529-592.
- [5] D. Whittum and R. H. Siemann, "Neutral Beam Collisions at 5 TeV", *Proc. 1997 Particle Accelerator Conference* (AIP, to be published).
- [6] M. Chodorow, et al., "Stanford High-Energy Linear Electron Accelerator (Mark III)" *Rev. Sci. Instrum.* **26** (1955) pp. 134-204.
- [7] A.E. Vlieks, et al., "Breakdown Phenomena in High-Power Klystrons", SLAC-PUB-4546, presented at the XIIIth International Symposium on Discharges and Electrical Insulation in Vacuum (Paris, June, 1988); G. A. Loew and J. W. Wang, "RF Breakdown Studies in Room Temperature Electron Linac Structures", SLAC-PUB-4647, (ibid).
- [8] D. H. Whittum and H. Henke, "High-Gradient Cavity Beat-Wave Accelerator at W-Band", *Proc. 1997 Particle Accelerator Conference* (IEEE, to be published).
- [9] *International Linear Collider Technical Review Committee Report*, G. A. Loew and T. Weiland, eds, (July 1995) SLAC-R-95-471.
- [10] D. Pritzkau, et al., "Experimental Study of Pulsed Heating of Electromagnetic Cavities", *1997 Particle Accelerator Conference* (to be published).
- [11] O. A. Nezhevenko, "On the Limitations of Accelerating Gradient in Linear Colliders Due to Pulse Heating", *1997 Particle Accelerator Conference* (to be published).
- [12] F. Villa and A. Luccio, "Test of a High-Gradient Low-Emittance Electron Gun", June 1996 (*Laser and Particle Beams*, to be published).
- [13] F. A. Benson, et al., "Rectangular-waveguide attenuation at millimetre wavelengths", *Proc. IEEE* **110** (1963) pp. 1008-1014.
- [14] P.J. Chou, et al., "Design and Fabrication of a Traveling-Wave Muffin-Tin Accelerating Structure at 91 GHz", *1997 Particle Accelerator Conference* (to be published).
- [15] M. Seidel, et al., "Microwave Analysis of the Damped Detuned Structure", *Proceedings of the XVIII International Linac Conference* (CERN, Geneva, to be published).
- [16] M. Hill, "A Study of a Planar Six-Wire quadrupole Magnet Design", *TET-Note-96/08*, Technische Universität Berlin.
- [17] H. Henke, "mm-Wave Linac and Wiggler Structures", *Proceedings of the IV European Particle Accelerator Conference* (1994).
- [18] Chi H. Lee, *Picosecond Optoelectronic Devices* (Academic Press, New York, 1984)
- [19] S.M. Lidia, D. H. Whittum and J. T. Donohue, "W-Band Free Electron Lasers for High Gradient Structure Research", *1997 Particle Accelerator Conference* (to be published).
- [20] A. L. Thoop, et. al., "Experimental Results of a High-Gain Microwave FEL Operating at 140GHz", *Nuc. Instr. & Methods in Phys. Res. A* **272**, 15 (1988).
- [21] S. L. Allen, et. al., "Generation of High Power 140 GHz Microwaves with an FEL for the MTX Experiment", *Proceedings of the 1993 Particle Accelerator Conference* (Washington, D.C., 1993), 1551.
- [22] G. Caryotakis, "High Power Microwave Tubes: In the Laboratory and On-Line", *IEEE Transactions on Plasma Science* **22** (1994) pp. 683-691.
- [23] *MMW Power Klystrons for Remote Sensing and Communications*, Communications and Power Industries (CPI), 45 River Dr., Georgetown, Ontario, Canada L7G2J4.
- [24] M. Blank, et. al., "Experimental Investigation of a W-Band Gyroklystron Amplifier", *Proc. 1997 Particle Accelerator Conference* (AIP, to be published).
- [25] S. Cheng, et al., "A High-Power Millimeter-Wave Sheet Beam Free-Electron Laser Amplifier", *IEEE Trans. Plasma Sci.* **24** (1996) pp. 750-757.
- [26] J. Gardelle, et al., *Phys. Rev. Lett.* **76**, 4532 (1996).
- [27] D. Yu and P. B. Wilson, "Sheet-beam klystron rf cavities", *Proc. 1993 IEEE Part. Acc. Conf.* (IEEE, New York, 1993) pp. 2681-2683.
- [28] D. H. Whittum, K. Ebihara, S. Hiramatsu, J. Kishiro, T. Monaka, T. Ozaki, and K. Takayama, "Experimental Studies of Microwave Amplification in the Ion-Focused Regime", *IEEE Trans. Plasma Sci.* **21**, 136 (1993).



## CARMs and Relativistic Gyrotrons as Effective Sources of Millimeter and Submillimeter Waves

V.L. Bratman, Yu.K. Kalynov, M.M. Ofitserov,  
S.V. Samsonov, and A.V. Savilov

Institute of Applied Physics, Russian Academy of Sciences,  
46 Ulyanov St., Nizhny Novgorod, 603600 Russia

### Abstract

In a number of cases, relativistic gyrotrons and Cyclotron Autoresonance Masers (CARMs) look easier for production of high power at the millimeter and especially submillimeter waves than usual subrelativistic gyrotrons and FELs. Due to the improvement of the electron beam quality the efficiency of the CARM was recently significantly increased and practically achieved the theoretically predicted value. The technique of the beam formation allowed also the realization of the Large Orbit Gyrotron where selective excitation of the 1st-5th cyclotron harmonics at the wavelengths from 14 mm down to 4 mm with the output power of 300 - 100 kW was obtained using a 300-keV, 30-A, 20-ns electron beam. Simulations and experiments predict the possibility for the realization of relatively low-voltage pulse sources with the power  $10^4$ - $10^6$  W in the whole submillimeter wavelength range.

### Introduction

Successful realization of FELs has almost no effect on the position of subrelativistic gyrotrons at mm/sbmm wavelengths. The gyrotrons provide the radiation power up to 1 MW in quasi-CW regime at shorter millimeter waves [1], as well as about 100 kW with pulse duration of tens of microseconds at the wavelengths of 0.5 mm [2]. It is difficult for novel sources to compete with so developed devices. However, novel relativistic devices significantly excel the subrelativistic gyrotrons in a number of characteristics even in the first experiments, and this superiority could become more significant in future. First of all, one could expect the achievement of higher frequency and pulse power, as well as of fast broadband frequency tuning. Among a lot of possible types of shorter-wavelength relativistic devices, basically FELs are being investigated at present. But at mm/sbmm waves other types of the devices, such as CARMs and relativistic gyrotrons, can have important advantages as compared with both subrelativistic gyrotrons and FELs.

### Cyclotron Autoresonance Masers

The CARM with high Doppler frequency up-shift [3,4] was realized in many successful experiments at IAP and other laboratories [5-18]. All our experiments were carried out using high-current electron accelerators with explosive-emission injectors, which provided the current pulses tens nanoseconds long and the electron energy of 0.5 - 1.2 MeV. One of the best results was the amplifier at the wavelength of 8 mm with power of 10 MW and amplification of 30 dB realized in collaboration with the High-Current Electronics Institute [11,14]. The highest power (30-50 MW) and the frequency up-shift (about 8) were obtained in the collaboration with the Joint Nuclear Research Institute, at their LIA [15].

CARMs realized at IAP and in collaboration with other  
Institutions

$\lambda$ mm	Mode	P MW	$\eta$ %	Ampl dB	$\tau$ ns	Institution, year
2-4	TE <sub>1,1</sub> TE <sub>4,1</sub> TE <sub>2,1</sub>	6-15	2-4		5 0	IAP IAP+Lebedev Phys. Inst., 1982
8	TE <sub>5,1</sub>	30	10		1 5	IAP, 1993
4 6	TE <sub>1,1</sub>	50 30	8 10		3 0	IAP+JINR (LIA), 1991
8	TE <sub>1,1</sub>	13	26		1 5	IAP, 1995
8	TE <sub>1,1</sub>	10	4	30	2 0	IAP+HCEI, 1986

Some CARMs realized in other laboratories.

$\lambda$ mm	Mode	P MW	$\eta$ %	Ampl dB	$\tau$ ns	Institution , year
20	TE <sub>1,1</sub>	7	1.5		100 0	U. of Michigan 1989, 1992
1.2		50	3		20	LLNL, 1990, LIA
10	TE <sub>1,1</sub>	0.1	2		100 0	MIT, 1992 Thermocathode
21	TE <sub>2,1</sub>	0.5	4		100	U. of Strathclyde 1995, 2nd harm.
8	TE <sub>1,1</sub>	12	7	32	15	MIT, 1989

Among experiments performed in other laboratories one has to mention the amplifier realized at MIT [13]. Its output parameters are close to the parameters of our amplifier, but the efficiency is higher. At MIT the first CARM with the thermocathode was also realized [12]. The CARM with the shortest wavelength (1.2 mm) was studied at Livermore [6]. The CARM at the second cyclotron harmonic was realized at the MIT [12] and the University of Strathclyde [16]. Thus, a lot of experiments demonstrate high-frequency properties of the CARMs. However, in these experiments efficiency is only 1-10%, i.e. several times smaller than the efficiency calculated for the ideal electron beam. In order to demonstrate the possibility of achievement of high efficiency in CARM, a special experiment at relatively long wavelength was carried out at the high-current direct-action "Sinus-6" accelerator with a field-emission injector (Fig.1) [17]. The accelerator provided electron energy of 300-600 keV, total current of 3-8 kA and pulse duration of 20 ns. The selection of the "most rectilinear" particles by a narrow anode outlet, similar to that realized earlier for the FEL [19] was used. For

the operating beam having passed through the outlet, the diameter was 2.5 mm, the current was 100 A at the electron energy 500 keV and the 10 ns flat-top of a voltage pulse. The beam quality was also improved by the use of the correcting coil [20]. The initially rectilinear beam was pumped by the kicker in the form of a rectangular current frame sloping to the z-axis, producing practically homogeneous transverse magnetic field near the beam and, therefore, providing a weak sensitivity to spread in the particle position. Sensitivity to the velocity spread was reduced using a short cavity, where electrons underwent only 4-5 gyrorotations. To prevent excitation of parasitic modes, the operating mode was chosen to be the lowest transverse  $TE_{1,1}$  mode of a cylindrical cavity in the regime of grazing dispersion characteristics of the beam and wave. The cavity was made up of the operating waveguide section 7.8 mm in diameter and 60 mm long, bounded by a cutoff waveguide on the cathode side and by a Bragg reflector on the collector side.

According to the simulations, the maximum efficiency for an ideal beam amounted to 30%. In the experiment the maximum power at the wavelength of  $(7.9 \pm 0.1)$  mm amounted to  $(13 \pm 2)$  MW for the guiding magnetic field of 1.2 T and the transverse electron velocity of  $\beta_{\perp} = 0.55$ . The corresponding electronic efficiency reached  $(26 \pm 5)\%$ . Thus, the use of an electron beam with small velocity spread raises CARM efficiency at least to the level of efficiency of the FEL.

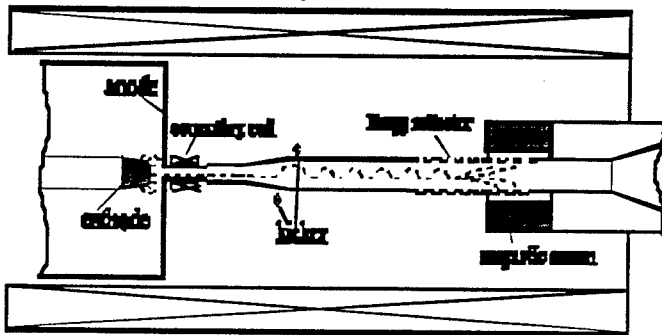


Fig.1. The schematic of the high-efficiency CARM.

### High-Harmonic Relativistic Gyrotrons

Basing on achievements of subrelativistic gyrotrons and the theory of relativistic gyrotrons [21,22] we are trying to develop a powerful submillimeter gyrotron operating at moderately relativistic electron energies 200-300 keV instead of 3-6 MeV for the FELs. Already at the mentioned energy, coupling of the electron beam having a large pitch-factor with cavity modes at higher harmonics is practically as strong as at the fundamental. Using high pulsed magnetic fields up to 20-30 T and providing selective excitation of the separate modes at the 5-10th harmonics it would be possible to obtain coherent radiation with broadband frequency step-tuning down to 0.1 mm.

As a first step to a sbmm gyrotron, we started our experiments at millimeter waves with known [22] Large Orbit Gyrotron (LOG). In a LOG a thin electron beam encircles the axis of an axisymmetric cylindrical cavity. Due to the symmetry the significant mode separation takes place; namely, only rotating  $TE_{s,p,q}$  modes, having the azimuthal index equal to the number of the resonant harmonic, can be excited. At small velocity spread this provides selective excitation of a single harmonic. According to the theory [21], the efficiency at the higher

harmonic, can amount to at least a few percent, which is sufficient for a number of applications. The increase of the electron-wave coupling for high transverse electron velocities and of diffraction  $Q$  of the given gyrotron cavity with the increase of the harmonic number lead to a significantly smaller difference in the operating currents of the harmonics as compared with the subrelativistic situation. For example, for electron energy 300 keV, pitch factor  $g=1.5$ , and cavity length corresponding to 4-5 electron rotations, the 1st-5th harmonics have practically the same starting currents (Fig.2). It is important to emphasize that the frequency non-equidistance of the first  $TE_{s,p,1}$  modes is sufficiently large; thus, having the electron beam with small velocity spread one can expect selective excitation of the above harmonics.

In order to check the theory predictions, we studied a LOG at the "Sinus-6" accelerator. The current passing into the cavity and electron energy were 30 A and 300 keV at pulse duration 20 ns. Like the CARM, the selected, rectilinear, 1.5 mm in diameter, electron beam from the central part of the explosive emission cathode, was used. After pumping in the kicker, electrons with the pitch factor  $g=1.3-1.5$  enter a traditional gyrotron cavity with diameter 8.2 mm and length of its cylindrical part of 42 mm bounded by the input and output conical taperings. When decreasing the magnetic field from 1.2 T down to 0.7 T, we clearly observed successive excitation of the  $TE_{s,1}$  modes at the harmonics  $s=1-5$ , which was confirmed by measurements of the radiation frequency. The maximum signal was registered at the 3rd cyclotron harmonic when the wavelength of the radiation was equal to 6.1 mm at the output power about of 300 kW. The radiation power at the 5th harmonic, when  $\lambda = 4.0$  mm, was more than 100 kW.

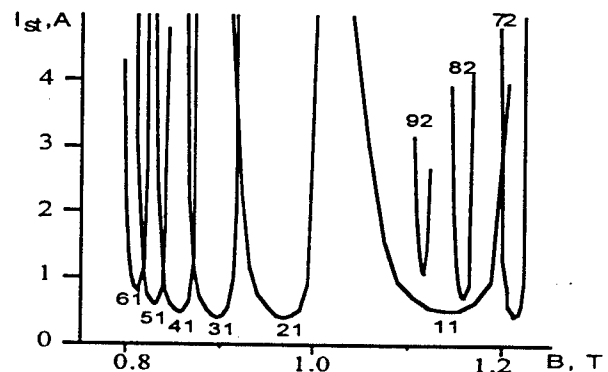


Fig.2. Starting currents of higher harmonics in LOG.

### Efficiency enhancement

One of the ways to decrease sensitivity to the beam quality and to increase efficiency in CARMs and relativistic gyrotrons is the use of the regime of trapping and adiabatic deceleration of electrons [23-25], being analogous to that which has been successfully realized in FELs [26]. For the CRM, in this regime the prolonged synchronous interaction between the wave and the main part of electrons is provided by tapering of the guiding magnetic field. The most particles are trapped by the potential well, formed by the wave, and their energies oscillate around the resonant energy,  $\gamma = \gamma_r$ . This energy corresponds to the exact electron-wave resonance, and decreases with the coordinate due to profiling of the magnetic field. The averaged electron energy decreases with the coordinate in proportion to the resonant energy (Fig.3).

$\langle \gamma(z) \rangle \approx K \gamma_r(z)$ , where  $K$  is share of trapped particles. It is important that one needs to provide an arbitrary slow law of the magnetic field decrease. For the gyrotron the same profile of the magnetic field provides trapping for various harmonics (while the resonant fields are certainly different for different harmonics because of the non-equidistant spectrum of the cavity modes). In the regime of trapping the sensitivity to the spread in electron velocity is smaller than in the usual regime of electron bunching, while the interaction region length is significantly larger [25]. Actually, the electron efficiency is basically defined by the trapping coefficient at the beginning of the interaction region. Then, moving through this region, the trapped particles with various pitch-factors practically identically lose their energies with the decrease of the resonant energy.

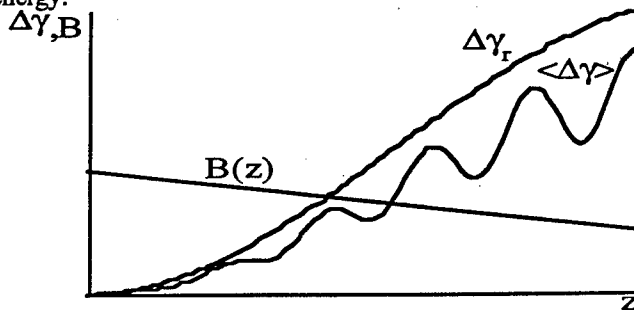


Fig.3. Electron energy extraction during the process of the adiabatic deceleration of the trapped particles.

Another way of the efficiency increase, which can be used in CARMs and gyrotrons operating in the CW or long-pulse regimes [27], is the depressed collector method and recovery by the power supply of the electron energy, which is saved by particles at the output of the electron-wave interaction region. This method has been utilized in the subrelativistic gyrotron and the FEL. But for the CARM and the relativistic gyrotron, energy recovery can have higher priority in their competition with the very efficient subrelativistic gyrotron. The simplest scheme with the single-step depressed collector, can provide a significant recovery efficiency for CARMs and higher-harmonic gyrotron. For the gyrotron, recovery efficiency decreases with the increase of the harmonic number. But in this case the recovery can be even more important than at the fundamental. It could be very attractive to combine the both above methods of the efficiency increase. The regime of trapping provides the increase not only in electron efficiency, but also in the recovery efficiency, which is induced by smaller RF amplitude and, therefore, smaller spread in output electron energy [27]. For instance, in the CARM operating in the regime of trapping, the total efficiency is higher than in the regime of bunching and can be about 50%. Thus, at shorter waves, CARMs and relativistic high-harmonic gyrotrons can be effective and competitive with both subrelativistic gyrotrons and FELs.

### Acknowledgements

This research was supported by the Russian Interdisciplinary Scientific and Technological Program "Physics of Microwaves" and the Russian Foundation for Fundamental Research, Grant No. 96-02-18971.

1. V.E.Myasnikov et al., Proc. of 21st Int. Conf. on Infrared and Millimeter Waves, ATh1 (Berlin, 1996).

2. V.A.Flyagin et al., Int. J. IR & MM Waves 4, 629 (1983).
3. M.I.Petelin, Radiophys. Quant. Electron. 17, 686 (1974).
4. V.L.Bratman et al., Optics Commun. 30, 409 (1979).
5. I.E.Botvinnik et al., Pis'ma v Zh. Eksper. Teoret. Fiz. 35, 418 (1982).
6. M.Caplan et al., LLNL, Livermore, CA, UCRL-55689-90.
7. G.G.Choi et al., Int. J. Electronics 72, 1045 (1992).
8. A.W.Fliflet et al., Nucl. Instr. Meth. Phys. Res. A285, 233 (1989).
9. V.L.Bratman and G.G.Denisov, Int. J. Electronics 72, 969 (1992).
10. S.Alberti et al., Phys. Rev. Lett. 71, 2018 (1993).
11. V.L.Bratman et al., Digest of 6th All-Union Symp. on High-Current Electronics, part 3, 6 (Novosibirsk, 1986).
12. K.D.Pendergast et al., Int. J. Electronics 72, 983 (1992).
13. G.Bekefi et al., Appl. Phys. Lett. 54, 1302 (1989).
14. V.L.Bratman et al., Relativistic HF Electronics 6, 206 (IAP, Gorky, 1990).
15. V.L.Bratman V.L. et al., Int. J. IR and MM Waves 13, 1857 (1992).
16. S.J.Cooke et al., Phys. Rev. Lett. 77, 4836 (1996).
17. V.L.Bratman et al., Phys. Rev. Lett. 75, 3102 (1995).
18. J.G.Wang et al., IEEE Trans. on Plasma Sci. 17, 906 (1989); J.J.Choi et al., Int. J. Electron. 72, 1045 (1992).
19. M.E.Conde and G.Bekefi, IEEE Trans. Plasma Sci. 20, 240 (1992).
20. S.V.Samsonov, Int. J. IR and MM Waves 16, 753 (1995).
21. V.L.Bratman et al., Pis'ma v Zh. Tekhn. Fiz. 3, 961 (1977).
22. D.B.McDermott et al, Phys. Fluids 26, 1936 (1983).
23. N.S.Ginzburg, Izv. Vuzov - Radiofiz. 30, 1181 (1987).
24. G.S.Nusinovich, Phys. Fluids B. 4, 1989 (1992).
25. V.L.Bratman et al., Relativistic HF Electronics 7, 22 (IAP, N.Novgorod, 1992).
26. T.J.Orzechowski et al., Phys. Rev. Lett. 57, 2172 (1986).
27. V.L.Bratman et al., Int. J. IR and MM Waves 16, 459 (1995); Phys. of Plasmas 4, No.6 (1997).

## Theory of anomalous Doppler CRM-amplifier with tapered parameters

G. S. Nusinovich<sup>(1)</sup>, M. Korol<sup>(2)</sup>, and E. Jerby<sup>(2)</sup>

(1) Institute for Plasma Research, University of Maryland, College Park, MD 20742, USA.

(2) Faculty of Engineering, Tel Aviv University, Ramat Aviv, 69978, Tel Aviv, Israel.

### Abstract

The theory of a slow-wave CRM-amplifier driven by an initially linear electron beam is developed. In such a device, the electrons radiate electromagnetic waves under the anomalous Doppler effect. We consider the system with the waveguide parameters tapered in such a way that the profiling of the axial wavenumber provides the cyclotron resonance between the wave and decelerating electrons. The efficiency of the device may asymptotically approach 100%. The use of the microstrip waveguide is discussed.

Slow-wave cyclotron resonance masers (CRMs) can operate when the axial phase velocity of the electromagnetic (EM) wave is smaller than the axial velocity of electrons. This condition corresponds to the EM wave radiation under the anomalous Doppler effect when radiating electrons lose their axial momentum and gain the orbital momentum. The coherent EM radiation in such a case can be generated even by initially linear electron beams which can be easily produced by Pierce-type electron guns.

Anomalous Doppler CRMs with constant parameters were studied earlier [1,2] and it was shown that the maximum efficiency can be realized when electrons make only one gyroorbit in the interaction region. The corresponding value of the external magnetic field should be very small while the amplitude of the EM wave should be very large. The latter, definitely, can not be realized in devices operating at moderate voltages.

To realize the cyclotron resonance interaction between electrons and the EM wave of a reasonable amplitude during many cycles, we suggest to taper the interaction parameters of the anomalous Doppler CRM in the way similar to that used in free-electron lasers, traveling-wave tubes, and conventional CRMs. In this paper we develop the theory of anomalous Doppler CRM-amplifiers in which the waveguide parameters are tapered in such a way that the variation in the axial wavenumber of the wave allows us to maintain the cyclotron resonance between the wave and decelerating electrons during many gyrocycles.

Stripline waveguides were used successfully in slow-wave FEL [3] and CRM [4] experiments at Tel Aviv University with uniform transverse cross-sections of the dielectric-loaded stripline. The advantage of these striplines comparing to (only) dielectrically loaded waveguides is the protection of the dielectric by the metallic strip from electron bombardment. In comparison with periodic slow-wave structures these lines

have the advantage of operation at quasi-TEM waves. This, first, provides the linear dispersion, thus making a wide bandwidth operation possible, and second, eliminates parasitic Cherenkov interaction with other spatial harmonics which is possible in periodic structures. The CRM experiment [4] is being modified now to a tapered-stripline slow-wave CRM, and this paper presents a theoretical model for its analysis.

The tapered stripline concept is based on the requirement to taper the axial wavenumber  $k_z$  in order to maintain the cyclotron resonance between the wave and electrons with the variable axial velocity,  $v_z$ , and the gyrofrequency,  $\Omega$ . For anomalous Doppler CRMs this condition can be written as

$$h = 1/\beta_z + \mu/p_z. \quad (1)$$

Here  $h$  is the axial wavenumber normalized to  $\omega/c$  ( $c$  is the speed of light),  $\beta_z = v_z/c$ ,  $\mu$  is the ratio of the initial gyrofrequency to  $\omega$ , and  $p_z$  is the electron axial momentum normalized to  $\gamma_0 m_0 c$  ( $\gamma_0$  is the electron initial energy normalized to  $m_0 c^2$ ). As follows from equations for the electron energy and axial momentum given elsewhere [5], when the axial wavenumber obeys Eq. (1) the normalized electron axial momentum relates to the electron energy as

$$p_z^2 = \beta_{z0}^2 - 2h_0\beta_{z0}\bar{\omega} + \bar{\omega}^2. \quad (2)$$

Here  $\bar{\omega} = (\gamma_0 - \gamma)/\gamma_0$  is the variation in electron energy normalized to its initial value (subscript '0' denotes all values at the entrance). Eq. (2) is the counterpart of the known autoresonance integral [5] valid for CRMs with non-tapered parameters. The normalized orbital momentum of an electron moving initially along a linear trajectory, as follows from Eq. (2) and the general relation between the electron energy and momentum  $\gamma^2 = 1 + (p_\perp^2 + p_z^2)/\gamma_0^2$ , relates to  $\bar{\omega}$  as

$$p_\perp^2 = 2(h_0\beta_{z0} - 1)\bar{\omega}. \quad (3)$$

For electrons having a non-zero initial orbital momentum the corresponding dependence is given in [6].

The phase of electron gyration with respect to the phase of the wave is constant when not only Eq. (1) is fulfilled but also this phase has a certain value. For this value of the phase the equation for the electron energy can be written as (c.f. [1])

$$\frac{d\bar{\omega}}{dz} = A \sqrt{\frac{2(h_0\beta_{z0} - 1)\bar{\omega}}{\beta_{z0}^2 - 2h_0\beta_{z0}\bar{\omega} + \bar{\omega}^2}}. \quad (4)$$

In Eq. (4)  $A$  is the normalized amplitude of the wave which obeys the following equation

$$\frac{dA}{dz} = I \sqrt{\frac{2(h_0\beta_{z0} - 1)\omega}{\beta_{z0}^2 - 2h_0\beta_{z0}\omega + \omega^2}} \quad (5)$$

Eqs. (4) and (5) are written with the account for given above equations for  $p_z$  and  $p_\perp$ . In Eq. (5)  $I$  is the normalized beam current parameter which is also proportional to the coupling impedance of electrons to the wave. Equations (4) and (5) being combined give the energy conservation law

$$A^2 - A_0^2 = 2I\omega. \quad (6)$$

Using Eq. (6) and introducing new normalized axial coordinate  $\zeta = A_0 z$  and beam current parameter  $I_0 = 2I / A_0^2$  one can rewrite Eq. (4) as

$$\frac{d\omega}{d\zeta} = \sqrt{(1 + I_0\omega) \frac{2(h_0\beta_{z0} - 1)\omega}{\beta_{z0}^2 - 2h_0\beta_{z0}\omega + \omega^2}} \quad (7)$$

This equation contains only three parameters ( $I_0$ ,  $\beta_{z0}$  and  $h_0$ ) and allows one to study the efficiency

$$\eta = \omega / (1 - \gamma_0^{-1}) \quad (8)$$

as the function of these parameters. The corresponding profiling of the axial wavenumber, as follows from Eq. (1), in these variables and parameters is given by

$$h = (h_0\beta_{z0} - \omega) / p_z. \quad (9)$$

Since the EM wave is amplified due to the axial deceleration of electrons, the maximum efficiency corresponds to the point where  $p_z = 0$ . As follows from Eq. (7) and the cyclotron resonance condition  $h_0\beta_{z0} = 1 + \mu$  [c.f. Eq. (1)],

$$\eta_{\max} = \frac{1}{\gamma_0 - 1} \left\{ \gamma_0(1 + \mu) - \sqrt{\gamma_0^2[(1 + \mu)^2 - 1] + 1} \right\}. \quad (10)$$

Eq. (10) gives us the maximum efficiency at finite magnetic field. In the case of the vanishingly small external magnetic field ( $\mu \rightarrow 0$ )  $\eta_{\max} \rightarrow 1$ .

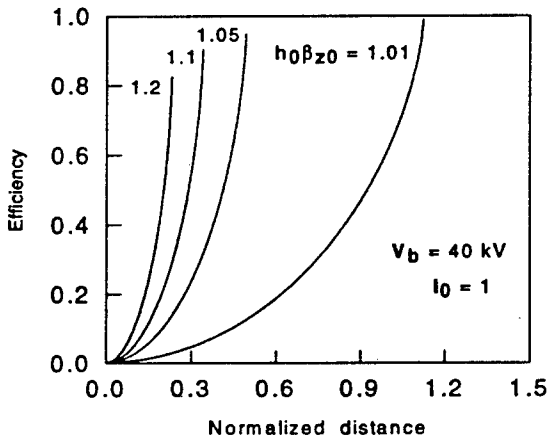


Fig. 1

parameter  $I_0 = 1$  and several values of  $h_0\beta_{z0}$ . Fig. 2 shows corresponding axial dependencies of the normalized axial wavenumber  $h$ . Note that when the initial wave amplitude is small the distance corresponding to the significant deceleration of electrons (see Fig. 1) can be much larger than a wavelength.

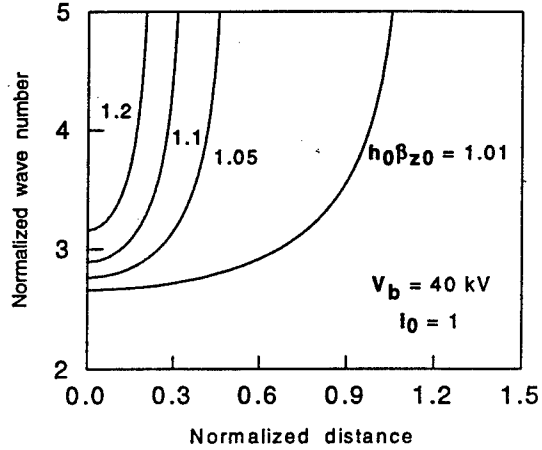


Fig. 2

In the slow-wave CRM experiment [4], the fundamental mode of such waveguide is a quasi-TEM mode with axial wavenumber  $h = \sqrt{\epsilon_{\text{eff}}}$ , where  $\epsilon_{\text{eff}}$ , the effective permittivity of the microstrip waveguide depends of the relative permittivity of dielectric material and the waveguide transverse geometry. The strip width is varied along the waveguide axis, and causes changes in  $\epsilon_{\text{eff}}$  and consequently in  $h$ . This variation satisfies the resonance condition (1) and consequently provides the theoretical conditions for high efficiency of the anomalous Doppler cyclotron interaction.

This work has been sponsored by the Binational Science Foundation BSF (grant #95-00438), the Israeli Academy of Sciences (grant #724/94-3), and DoD MURI program (AFOSR grant #F4962001528306).

## References

- [1] N. S. Ginzburg, *Radiophys. Quantum Electron.*, **22** (1979) 323.
- [2] T. N. Kho and A. T. Lin, *Phys. Rev. A*, **38** (1988) 2883.
- [3] M. Einat, E. Jerby, and A. Shahadi, *Nucl. Instrum. Methods Phys. Res. A*, **375** (1996) 21.
- [4] M. Einat and E. Jerby, to be published in *Phys. Rev. E*.
- [5] V. L. Bratman et al., *Int. J. Electron.*, **51** (1981) 541.
- [6] G. S. Nusinovich, *Phys. Fluids B*, **4** (1992) 1989.

Results are illustrated by Figs. 1 and 2. Fig. 1 shows the efficiency as the function of the normalized axial coordinate for a 40-kV electron beam with the normalized current

## Concept of a Ka-band Free Electron Maser Oscillator with a Two-dimensional Bragg Cavity

N.S.Ginzburg, N.Yu.Peskov, I.V.Konoplev, A.S.Sergeev,  
G.R.M.Robb\*, A.D.R.Phelps\* and A.W.Cross\*

Institute of Applied Physics RAS, 603600 Nizhny Novgorod, Russia

\*University of Strathclyde, Glasgow, G4 ONG, UK

### Abstract

An operability of novel two-dimensional distributed feedback mechanism in a FEM driven by hollow relativistic electron beam was studied theoretically. A prospect of experimental realization of such a FEM on the base of high-current accelerator University of Strathclyde is discussed

### Introduction

In recent years many successful experiments [1-4] have been carried out on Free Electron Masers (FEMs) which utilise Bragg resonators [1]. Such resonators are constructed by machining single periodic corrugations (1-D Bragg resonators) on the inner wall of the waveguide. However, in all previous experiments the diameter of the microwave systems used ( $D$ ) does not exceed the wavelength of the radiation ( $\lambda$ ) by more than  $D/\lambda \approx 2$  to 4.

In order to increase the power of microwave oscillators one should increase the power of the electron beam driving the system. For mildly relativistic beams this can be achieved by increasing the beam current. To prevent RF breakdown the transverse size of the system must be increased with increasing the operating current. However this will lead to the oversized microwave system losing mode selectivity.

An attractive solution is to increase the beam current together with the transverse size of the system enabling the current density per unit transverse size to remain constant while simultaneously maintaining mode selectivity. This can be achieved with the proposed use of a 2-D Bragg resonator [5, 6] to provide additional mode selection over the transverse coordinate. Theoretical analysis has demonstrated the capability of obtaining powerful spatial-coherent radiation in this system when diameter of the beam was tens to hundreds of times greater than the wavelength of the emitted radiation [7].

In this report a theoretical evaluation for a project to investigate a 8 mm FEM with a coaxial 2-D Bragg resonator based on a high-current accelerator currently in operation at Strathclyde University is presented.

### Eigenmodes of the coaxial 2-D Bragg resonator

The coaxial 2-D Bragg resonator can be made in the form of two metal cylinders (fig.1) which are corrugated on the inner wall as

$$a = a_1 \left( \cos(\bar{h} R \varphi - \bar{h} z) + \cos(\bar{h} R \varphi + \bar{h} z) \right) \quad (1)$$

where  $\bar{h} = \sqrt{2}\pi/d$ ,  $d$  is a corrugation period and  $a_1$  is corrugation depth. This corrugation provides mutual scattering of four partial waves propagating in the  $\pm z$  and in

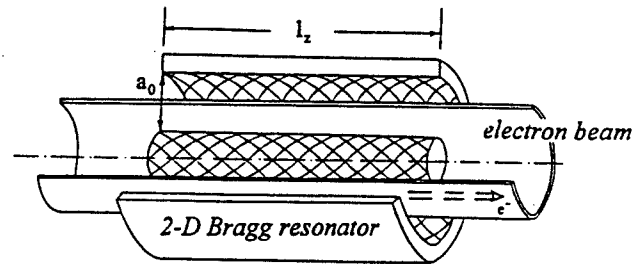


Fig.1 Scheme of FEM-oscillator with coaxial 2-D Bragg resonator and hollow electron beam

the azimuthal  $\pm\varphi$  directions. The additional azimuthal electromagnetic energy fluxes arising in this resonator should synchronise radiation from a large hollow electron beam.

Eigenfrequencies of the modes are situated near the Bragg resonance frequency  $\bar{\omega} = \bar{h}c$  as well as near the frequencies  $\bar{\omega} = \bar{h}c(1 \pm 2\alpha)$  ( $\alpha$  is a wave coupling coefficient [5]). The Q-factor of the mode with  $n$  variation along  $z$  coordinate and  $m$  variation along azimuth is given by relations:

$$Q_{m,n} = \frac{4\alpha^2 \bar{h}^3 l_z R^2}{m^2} + Q_{ohm} \quad \text{near } \bar{\omega} = \bar{h}c, \quad (2)$$

$$Q_{m,n} = \frac{\alpha^2 \bar{h}^3 l_z^3}{\pi^2 n^2} + Q_{ohm} \quad \text{near } \bar{\omega} = \bar{h}c(1 \pm 2\alpha),$$

where  $Q_{ohm}$  is a Ohmic losses of the modes in the resonator. The maximum Q-factor has an eigenmode of frequency equal to the resonant Bragg frequency. It is important to note that this mode is azimuthally symmetric ( $m = 0$ ) and can provide equal energy extraction for all parts of the electron beam.

### Simulation of interaction of hollow magnetic guided electron beam with wiggler and RF-field

In the design of a FEM a mildly relativistic (electron energy 0.8 - 1.0 MeV) high-current ( $\sim 0.5 - 1.5$  kA) hollow electron beam (of diameter  $\sim 3 - 5$  cm) will be used to drive the oscillator. An operational transverse velocity of  $\beta_{\perp} \approx 0.2$  in the magnetic guided beam will be produced by a helical wiggler which has a slowly up-tapered entrance. Fig.2 presents the results of computer simulation of the interaction between the electromagnetic wave and the electron beam

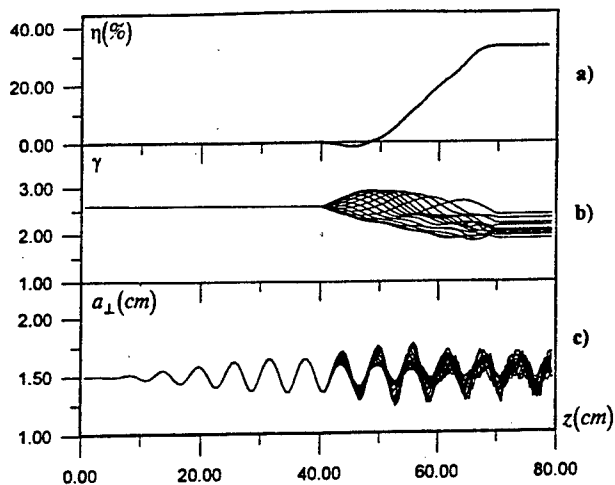


**Fig.2** Dependence on longitudinal coordinate  $z$ : (a) electron efficiency, (b) energy of electrons with different initial phases and (c) their displacement from the axis for the project FEM parameters

moving in the wiggler and axial guide magnetic field. In this simulation the RF field structure was considered to be the eigenmode which had the highest Q-factor eigenmode of the "cold" resonator. This simulations predicted high-efficiency operation of the FEL for the parameters discussed below. The short interaction length of 5 - 6 wiggler periods reduced a sensitivity of the FEM to the initial spread of beam parameters.

### Simulation of excitation of the coaxial 2-D Bragg resonator by a hollow electron beam

Dynamics of FEM operation with a two-dimensional coaxial Bragg resonator was studied theoretically. Time domain analysis taking into consideration the dispersion properties of the Bragg reflectors was used. The numerical simulation of excitation of a FEM by a hollow relativistic electron beam and oscillation build-up demonstrated an establishment of stationary generation regime under parameters close to experimental one (fig.3). In this stationary regime spatial profiles of partial waves are close to the profiles of the highest Q-factor azimuthal symmetrical mode of the cold resonator. The frequency of this mode as well as the oscillating frequency coincides with the Bragg frequency.

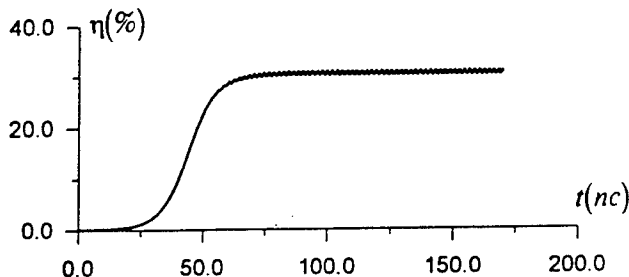


**Fig.3** Establishment stationary regime of oscillations in FEM with 2-D coaxial Bragg resonator for the project parameters: electron efficiency versus time

The transient process in the coaxial 2-D Bragg resonator may be divided into two stages. The first stage is relatively short where during several passes of the partial waves over the resonator an azimuthally symmetrical distribution of the waves amplitudes are formed (the amplitudes of all harmonics besides  $m = 0$  fall practically to zero). The second stage is much longer when storage of the electromagnetic energy in resonator occurs. At the end of this stage stationary generation of the radiation is achieved.

It should be noted, that for a moderate gain parameter  $C \approx 0.01$  establishment of the stationary regime was observed in the computer simulation up to the diameter of the system  $D/\lambda \approx 500$  [7]. Thus, the possibility of using 2-D Bragg resonator for generation of spatial-coherent radiation in FELs driven by high-current large size hollow electron beam has been proved.

### A Project of the Strathclyde FEM with 2-D Bragg resonator

Theoretical evaluation for a project to investigate a 8 mm FEM with a 2-D Bragg resonator based on a high-current accelerator currently in operation at Strathclyde University is presented. An 0.8 MeV / 1 kA / 200 ns hollow electron beam of 3 cm diameter will be used to drive the FEM. An electron-optical FEM system will consist of a 6 cm period wiggler producing up to 1 kG transverse field and a pulsed solenoid producing a guide axial magnetic field of up to 10 kG. The coaxial 2-D Bragg resonator of 2 cm inner cylinder diameter and 4 cm outer cylinder diameter with double periodic corrugations of period 6 mm and depth 0.6 mm will provide an effective interaction between the beam and RF field. This project will experimentally confirm operation of a novel Bragg resonator which will provide spatial coherent single-mode generation when the ratio of  $D/\lambda$  is equal to 10 to 12.

### References

1. Bratman V.L., Denisov G.G., Ginzburg N.S., Petelin M.I., IEEE J. Quant. Electr. QE-19 (1983) 282.
2. Chu T.S., Hartemann F.V., Danly B.G., Temkin R.J., Phys. Rev. Lett. 72 (1994) 2391.
3. Mima K., Imasaki K., Kuruma S., Akiba T. e.a., Nucl. Instr. Meth. in Phys. Research A285 (1991) 47.
4. Kaminsky A.K., Ginzburg N.S., Kaminsky A.A., Peskov N.Yu. e.a., Nucl. Instr. Meth. in Phys. Research A375 (1996) 215.
5. Ginzburg N.S., Peskov N.Yu., Sergeev A.S., Opt. comm. 96 (1993) 254.
6. Arzhannikov A.V., Ginzburg N.S., Nikolaev V.S., Peskov N.Yu. e.a., 14-th Int. FEL Conf., Kobe, Japan, 1992, p.214.
7. Ginzburg N.S., Peskov N.Yu., Phelps A.D.R., Robb G.R.M., Sergeev A.S., Digest of 20th Int. Conf. on Infrared and Millim. Waves, Orlando, USA, 1995, p.56.

# Cyclotron-resonance maser arrays - concept, theory, and experiments

E. Jerby\*, M. Korol, Li Lei, V. Dikhtiar, R. Milo, and I. Mastovsky<sup>1</sup>  
Faculty of Engineering, Tel Aviv University, Ramat Aviv 69978, Israel.

## Abstract

The cyclotron-resonance-maser array (CRM-A) has been proposed as a high-power microwave source operating at low voltages. Several conceptual schemes of CRM-A and preliminary studies, including a linear model of a 2D CRM-A and experimental results of a two-beam CRM device, are presented. The feasibility of a practical high-power CRM-A is discussed.

Generation of high-power microwaves (HPM) is a subject of a great importance in modern science and technology. Cyclotron-resonance masers (CRMs) are known as promising generators of HPM radiation. Possible schemes of compact HPM devices in the megawatt power range are of interest for various applications [1]. The cyclotron-resonance maser array (CRM-A) is proposed as a compact high-power microwave source operating at low voltages. This article describes the CRM-A concept, and its development status in our laboratory.

The CRM-A concept stems from the periodic-waveguide cyclotron (PWC) studies [2]. The PWC combines properties of fast- and slow-wave CRM interactions, whereas the metallic periodicity acts as an artificial dielectric. The evolution of the CRM-A concept is depicted in Fig. 1.

In view of the experimental results of the PWC oscillator experiments [2] (>25% efficiency at 10 kV), a further increase in the radiation power could be achieved either by increasing the electron energy or current, or by increasing the dimension of the array, from 1 to 2 dimensions as illustrated in Fig. 1. This approach keeps the high perveance and low-voltage for each electron beam. Many low-current electron-beams radiate then microwaves in a multi-channel 2D periodic metallic structure. Each channel resembles the 1D PWC, but their radiation beams are partially coupled by the structure.

The use of many low-current, low-energy electron beams instead of a single high-current, high-energy beam reduces space-charge effects, and therefore increases the output power and efficiency. The CRM-A scheme simplifies elements of the experimental setup (electron gun, collector section, output window, etc.) and results in a compact low-cost device. The 2D periodic-waveguide acts as a mode selector yielding single-mode operation at high frequencies.

The 3D CRM-A shown in Fig. 3c might have an attractive feature as an active phased-array antenna incorporated in the

CRM-A device itself. The output radiation could be emitted directly from the exit aperture of the 3D CRM-A, as a planar antenna. The wide cross-section of the output aperture may alleviate output-window problems, which limit conventional gyrotrons. A one step further may lead to far-field steering of the radiation as in phased-array antennas, by applying a voltages gradient on the cathode-array which may result in a phase shear in the output aperture. Focusing, steering, and splitting of the radiation pattern in the far-field can be conceived as well.

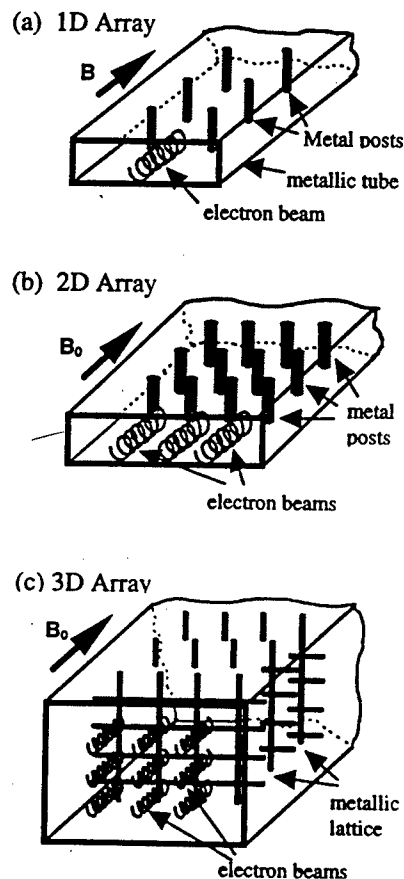


Fig. 1 : The evolution of the CRMA concept.

Preliminary theoretical studies of the 2D CRM-A are presented in Ref. [3]. Each mode of the em-wave in the 2D periodic structure is expressed as an infinite set of spatial harmonics. A linear analysis results in a matrix dispersion relation, in a form of a matrix Pierce-equation, as follows

\* Correspondence- e-mail: jerby@taunivm.tau.ac.il

Fax: (+) 972 3 642 3508

<sup>1</sup> Permanent address: PSFC, MIT, Cambridge, MA 02139



$$\tilde{\mathbf{A}}(\hat{s}) = \left[ \hat{s} \hat{\mathbf{U}} - \hat{\mathbf{\Theta}}_k \right]^2 - \mathbf{C}_k(\hat{s}) \hat{\mathbf{\Theta}}_{pk}^2 \mathbf{Q}_k(\hat{s}) \Bigg]^{-1} \left[ \hat{s} \hat{\mathbf{U}} - \hat{\mathbf{\Theta}}_k \right]^2 \mathbf{A}_0, \quad (1)$$

where the diagonal coupling-matrix is defined as

$$\mathbf{Q}_k(\hat{s}) = \beta_{ez} [\hat{s} \hat{\mathbf{U}} - \hat{\mathbf{\Theta}}_k] [\hat{\mathbf{Z}}_k - \beta_{ez} \hat{\mathbf{U}}] + \frac{1}{2} \beta_{e\perp}^2 [\hat{k}_0 \hat{\mathbf{Z}}_k - s \hat{\mathbf{U}} - \hat{\mathbf{\beta}}_k]. \quad (2)$$

In Eqs. (1) and (2), the vectors  $\tilde{\mathbf{A}}$  and  $\mathbf{A}_0$  contain the output and input mode amplitudes, respectively,  $\hat{\mathbf{U}}$  is a unit matrix,  $\beta_{ez}$  and  $\beta_{e\perp}$  are axial and transverse electron velocities, respectively,  $\hat{\mathbf{\beta}}_k$ , and  $\hat{\mathbf{Z}}_k$  are diagonal matrices for the resonant  $k$ -th wavenumbers and their corresponding harmonic impedance, respectively, and  $\hat{\mathbf{\Theta}}_k$  is a diagonal tuning matrix.

The diagonal space-charge matrix  $\hat{\mathbf{\Theta}}_{pk}$  describes the coupling between electron beams and resonant harmonics. The power-flow matrix  $\mathbf{C}_k$  represents the distribution of the em power among the different modes and spatial harmonics.

As a step toward the realization of a full scale CRM-A, a two electron-beam experiment has been conducted [4] in a 2D structure shown in Fig. 1b. An array of  $4 \times 24$  elements was used. The parameters of this experiment are:

electron energy	4.0 - 7.5 keV
e-beam current	~ 0.1 A
solenoid field	2.7 - 3.8 kG
tube cross-section	48 X 25 mm <sup>2</sup>
length	48 cm

A typical output of the two-beam 2D CRM-A experiment is shown in Fig. 2. The radiation frequency is 6.8 GHz. The experimental results agree with the theoretical model. Fast- and slow-wave interactions are observed in different magnetic fields.

Currently, a four-beam 3D CRM-A setup is under construction in our laboratory. The interaction region is contained in circular waveguide (30 cm long, 7.5cm diameter) periodically loaded with alternating horizontal and vertical posts. This arrangement forms a 4-channel structure. The structure sustains slow and fast wave interactions with a circular EM polarization, as well as a single mode operation in high modes. The power is supplied by a Marx-generator reconnected to operate at lower voltage (< 50 KV) and higher (total) current. The fundamental mode frequency is in the range of 2-3 GHz. Different accelerating voltages would be applied to the electron beams, in order to form velocity and

phase shears throughout the output cross section and to demonstrate a far-field steering.

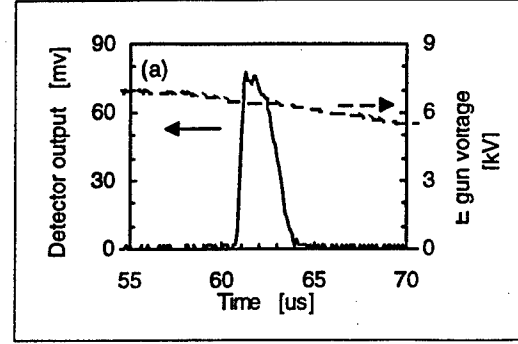


Fig. 2: A typical RF output of a two-beam 2D CRM-A.

The CRM-A concept may lead to new schemes of HPM sources. It alleviates problems of space charge, and results in a compact and low-voltage device. First steps in theory and experiments have been made. A 20-beam 3D CRM-A experiment is planned as the next step in this program. The ultimate goal of this study would be to realize a  $20 \times 20$  beam CRM-A at 10 KV (1A current per beam) and to reach 1 MW output power.

## References

1. A.V. Gaponov-Grekhov and V. L. Granatstein, *Applications of High-Power Microwaves*, Artech House, Norwood MA, 1994, and references therein.
2. E. Jerby, and G. Bekefi, "Cyclotron maser oscillator experiments in a periodic waveguide," *Physical Review E*, **48**, 4637-4641 (1993); see also E. Jerby, A. Shahadi, V. Grinberg, V. Dichtiar, E. Agmon, H. Golombek, V. Trebich, M. Bensal, and G. Bekefi, "Cyclotron maser oscillator experiments in a periodically loaded waveguide", *IEEE J. Quantum Electron*, Vol. 31, pp. 970-979, 1995.
3. M. Korol and E. Jerby, "Linear analysis of a multi-beam cyclotron resonance maser array," *Physical Review E* (May 1997).
4. Li Lei and E. Jerby, "Spectral measurements of cyclotron resonance maser array with two electron beams," to be published.

## Radiation bursts from a ferroelectric-cathode based tube

R. Drori, D. Shur, E. Jerby\*, and G. Rosenman,

Faculty of Engineering, Tel Aviv University, Ramat Aviv, 69978, Tel Aviv, Israel.

R. Advani, and R. Temkin

Plasma Fusion Center, Massachusetts Institute of Technology, Cambridge MA02139, USA.

### Abstract

A ferroelectric cathode emits electrons into a slow-wave tube immersed in a 1.7 kG axial magnetic field. The cathode, based on a (Pb, La)(Zr,Ti)O<sub>3</sub> ceramic, is subjected to a ~2 kV pulse (~0.3  $\mu$ s pulse width). An electron current of ~0.4 A is measured at the end of the 0.5 m tube. A helix slows down the em wave to 0.13c. Radiation bursts are observed through a bandpass filter in the range 2-4 GHz. The detected power is ~1 W. The appearance of the radiation bursts is clear and repetitive.

Extensive studies of cathodes using different PLZT ceramic compositions have been conducted by several research groups [1]. Typical current densities provided by these cathodes were up to 100 A/cm<sup>2</sup>. Recently, it has been shown that the total electron current emitted by such cathodes may be as high as 1 kA [2]. In the majority of the cases, this rather strong electron emission was ascribed to fast spontaneous polarization switching of ferroelectric ceramics [3]. The strong electron emission has also been observed without any polarization switching from PLZT 12/65/35 ceramic [1]. This composition does not possess a macroscopic spontaneous polarization at room temperature [4], hence characterized as a nonswitchable composition. It has been shown that the electrons are emitted from a plasma of surface flashover caused by high voltage stress applied to the PLZT ceramic in a nanosecond time scale [1].

Recently, this nonswitchable PLZT 12/65/35 ceramic composition has been studied in our laboratory as a possible emitter for free-electron RF generators [5]. A schematic of the experimental e-gun is shown in Fig. 1 [6]. The ceramic plate has a rectangular shape (1x1 cm<sup>2</sup>) and a thickness of 1 mm. A conductive silver paint contact ( $\varnothing$ 6 mm) is deposited on the rear surface of the ceramic sample (rear contact). A brass washer is glued to the emitting surface by the same type of silver paint as a ring electrode. Its external diameter, internal diameter and thickness are 6 mm, 3.4 mm and 0.2 mm, respectively. A stainless steel grid (52  $\mu$ m wire diam., 460  $\mu$ m period) is mounted directly on the front of the brass washer providing a volume for free plasma expansion (plasma expander). A similar grid, placed 3 mm ahead, is grounded

and used as an anode for the emitted electrons. A negative trigger voltage pulse (0.1-0.4  $\mu$ s width), applied between the grounded rear contact and the ring electrode, excites a process of plasma generation.

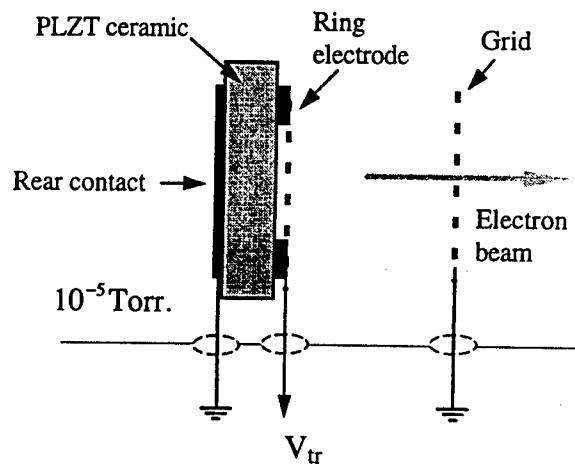


Fig. 1. Schematic of the PLZT ceramic e-gun.

Comparing to a scheme in which the negative voltage is applied to the rear contact, this e-gun (Fig. 1) has a narrower electron energy spectrum (~10% energy spread), a higher electron current density, and a better perveance [6].

In the experiment presented here, the PLZT ceramic e-gun is employed in a slow-wave cyclotron tube with a helix [7]. The experimental setup is illustrated in Fig. 2. The 0.5 m long helix slows down the wave velocity to 0.13c. The helix radius and pitch are 5.5 mm and 5 mm, respectively. An axial magnetic field of ~1.7 kG (4.8 GHz cyclotron frequency) is induced along the tube by an external solenoid. The electrons are collected at the end of the drift tube by a collimated Faraday cup. The e-beam current is measured by a 50  $\Omega$  resistor. Backward microwave signals are sampled at the port of the helix located near the e-gun, whereas the far port is shorted. The signals are detected by a calibrated diode detector through a 2-4 GHz bandpass filter.

\* Correspondence - e-mail: jerby@taunivm.tau.ac.il

In view of the state of art and the possible trends, a further research on PLZT ceramic cathodes is needed in order to integrate them in advanced microwave sources.

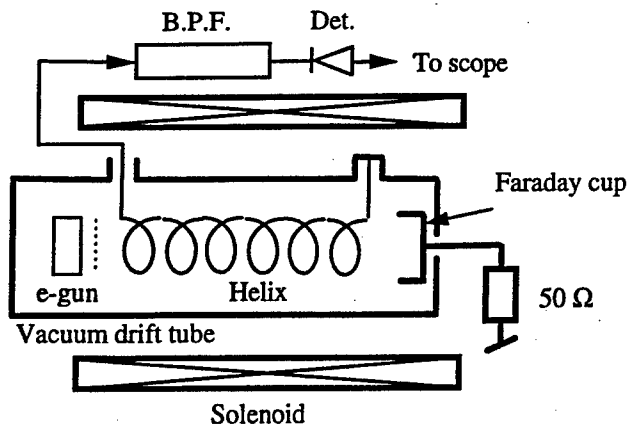


Fig. 2: The experimental device.

The device is operated at a vacuum of  $\sim 10^{-5}$  Torr. Current pulses of 0.3-0.5A are observed with a delay of  $\sim 100$  ns after the leading edge of the 2 kV voltage pulses. The voltage pulse widths are 150-400 ns. Radiation bursts are observed near the trailing edge of the current pulses, as shown in Fig. 3. The detected power is  $\sim 1$  W. The appearance of the bursts is clear and repetitive. The mechanism of the observed radiation in this experiment could be a backward cyclotron emission.

To the best of our knowledge, this is a first report on an em emission from a device based on a ferroelectric cathode. The use of this cathode may reduce the size and cost of microwave tubes, since it eases the vacuum requirements and does not require any heating. A limitation of this cathode, at the present development stage, is that it may operate only in a repetitive mode. We consider to utilize this type of cathodes in devices that tolerate the energy spread by a small Doppler shift. These include free-electron RF generators [5] and CRM-arrays [8]. The latter is a new conceptual device, for which the low-cost and simple installation of a large array of PLZT cathodes is a critical factor in its development process.

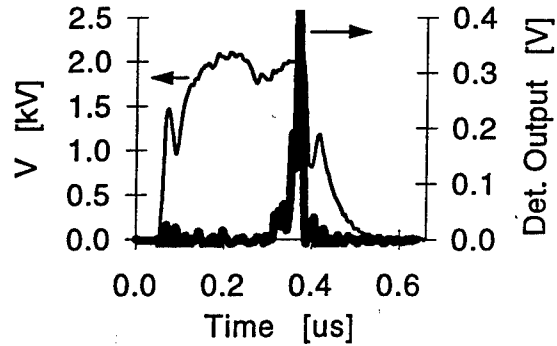


Fig. 3: Typical radiation burst and voltage pulses

#### References

1. D. Shur, G. Rosenman, Ya. E. Krasik, and V. D. Kugel, *J. Appl. Phys.*, **79**, (1996) 3669 and references therein.
2. R. Advani and R. Temkin, to be published.
3. G. Rosenman, V. A. Okhapkin, Yu. L. Chepelev, and V. Ya. Shur, *Sov. Phys.-JETP's Letts.*, **39**, (1984) 477.
4. G. H. Haertling, *Ferroelectrics*, **75**, (1987) 25.
5. R. Drori, E. Jerby, and A. Shahadi, "Free-electron maser operation at 1 GHz / 1 keV regime," *Nuclear Instrum. and Methods*, Vol. A375, pp. 186-189, 1996.
6. D. Shur, G. Rosenman, R. Drori, E. Jerby, Ya. E. Krasik, R. Advani, and R. Temkin, in preparation.
7. H.S. Uhm and J. Y. Choe, *Phys. Fluids*, **26**, (1983) 3418.
8. E. Jerby, M. Korol, Li Lei, V. Dikhtiar, R. Milo, and I. Mastovsky, "CRM arrays - concept, theory and experiments," in these proceedings.

# Development of An Efficient Millimeter Wave Harmonic Amplifier

Jose E. Velazco

Microwave Technologies Incorporated,  
5716 Edgewater Oak Court, Burke, VA 22015, USA

Peter H. Ceperley

George Mason University,  
4400 University Drive, Fairfax, VA 22030, USA

## Abstract

In this paper we present the design considerations of a novel high efficiency millimeter wave harmonic amplifier (HARA). Due to its novel mechanism, the HARA is compact, lightweight and does not require an external focusing system. It is capable of producing frequency multiplication in the millimeter wave regime with high efficiency and gain.

## Introduction

In past years there has been increased interest in the development of compact, lightweight microwave devices capable of delivering hundreds of kilowatts of millimeter wave radiation at high efficiencies. Potential uses of these devices include communications and millimeter high-resolution radar for mobile and airborne applications. Microwave Technologies Incorporated (MTI) is currently developing an efficient harmonic amplifier jointly with George Mason University for operation in the Ka frequency-band.

A simplified schematic of the HARA amplifier is shown in Fig. 1. It is a compact, lightweight microwave device that provides both microwave signal amplification and frequency multiplication. The basic device is composed of an electron gun, an input cavity, drift region, and an output

cavity. A thin cylindrical electron beam (~1mm in diameter) is produced by the electron gun. The beam is injected into the input cavity, which is driven by the input signal. The electrons, as they traverse the cavity, see a transverse magnetic field that oscillates and rotates azimuthally at the drive frequency  $\omega$  [1-3]. Upon interacting with this field the electrons are gradually deflected (circularly-scanned) by the rf magnetic field. In the drift region, due to the finite amount of transverse velocity that the beam carries, electrons gradually drift away from the axis as they stream towards the output cavity. A snapshot of the electron beam in this region resembles a growing helix. The length of the drift region is selected so as to obtain a suitable beam radial displacement for optimum energy transfer in the output cavity. As electrons enter the cavity, they set up a rotating  $TM_{m,10}$  mode inside the cavity ( $m$  is the azimuthal index of the mode). The excited output mode operates at a frequency that is  $m$  times the drive frequency. The output beam-wave interaction is short and synchronous allowing for the efficient generation of coherent millimeter wave radiation [2]. Another advantage of this type of interaction is that, due to the beam-wave synchrony, the output cavity operates at the design mode with no mode competition and with high electronic efficiency. Table I lists a set of parameters for the HARA design discussed in this paper.

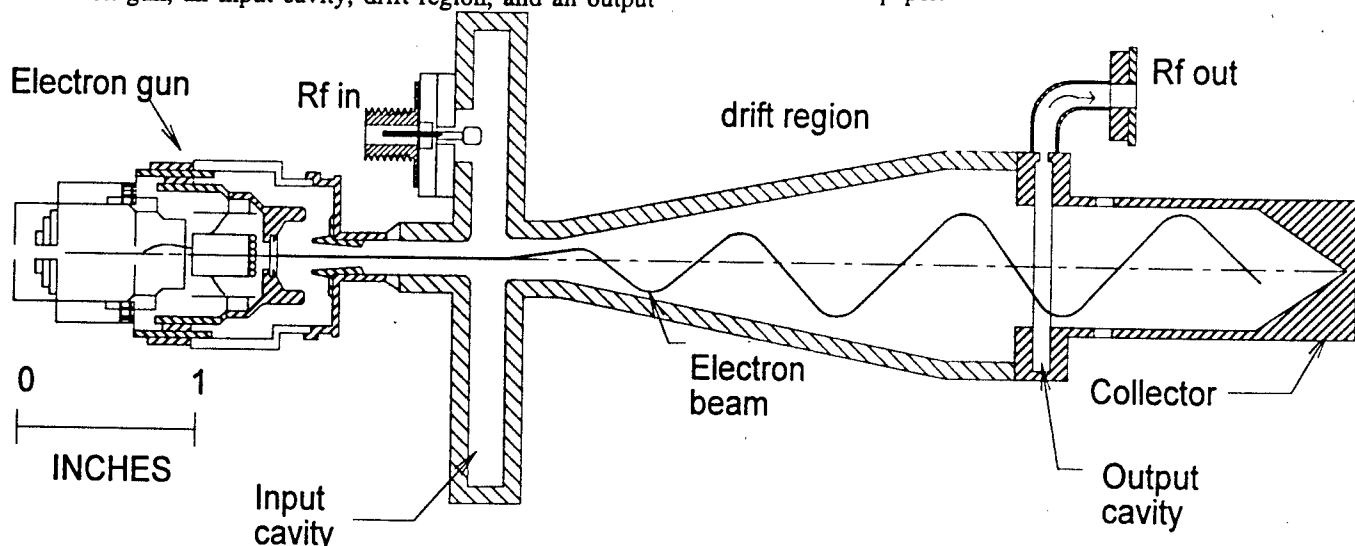


Figure 1: Schematic of HARA amplifier

**Table I: HARA System Parameters**

Parameter	Units	Value
Beam Energy	keV	60
Beam Current	A	3
Beam radius	mm	0.5
Drive Frequency	GHz	5.85
Drive power	kW	3.5
Drift length	cm	5
Beam radial displacement	cm	1
Output Frequency	GHz	35.1
Output Power	kW	120
Gain	dB	20
Efficiency	%	70

### Computer Simulations

We have performed three-dimensional fully self-consistent particle- in-cell studies of the HARA mechanism on the computer code SOS [4]. Figure 2 illustrates the electron beam dynamics along the drift region for parameters listed in Table I. In the simulation the beam has been previously modulated in the input cavity and at injection into the drift region carries a transverse to longitudinal velocity ratio of 0.1. Vector plots of the rf magnetic field excited by the rotating beam inside the output cavity are shown in Fig. 3a. These plots represent the field pattern of the design mode ( $TM_{610}$ ). The corresponding frequency spectrum for these fields is shown in Fig. 3b. Note that single frequency operation is obtained at 35 GHz.

### Acknowledgments

This work was supported by the Ballistic Missile Defense Organization and by the Virginia's Center for Innovative Technology.

### References

1. J. Velazco, PhD Dissertation, Spring 1994, George Mason University.
2. J. Velazco and P. Ceperley, IEEE Trans. Microwave Theory Tech. MTT-41 (1993).
3. P. Ceperley and J. Velazco, Rev. Sci. Instr. 66 (1) 256-260, Jan 1995.
4. SOS/MAGIC User's Manual. Mission Research Corporation, Newington Virginia.

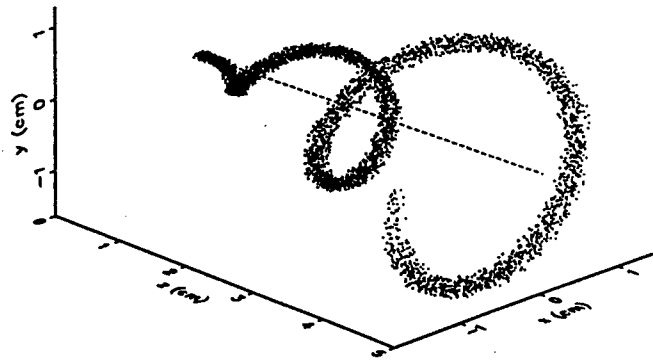
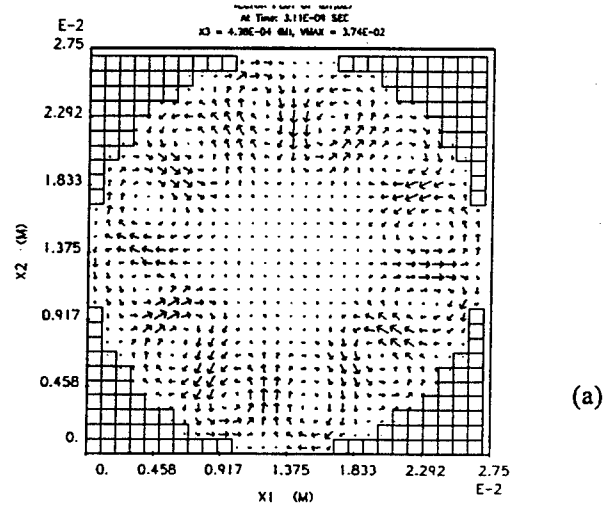
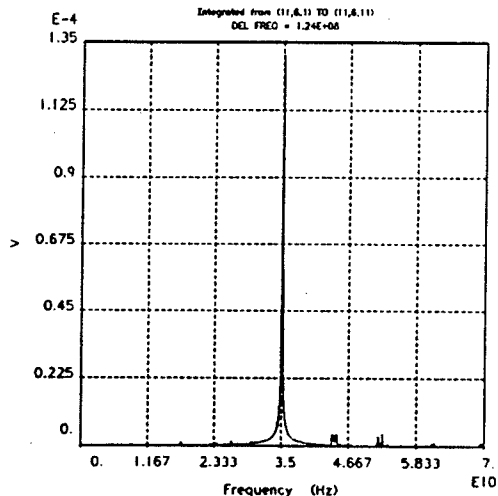


**Figure 2:** Electron beam dynamics along the drift region calculated in 3D code SOS. Parameters are listed in Table I.



(a)



(b)

**Figure 3:** a) Vector plots of rf magnetic field inside the output cavity and b) frequency spectrum of the excited mode obtained on 3D-PIC code SOS. Parameters are listed in Table I.

## Harmonic oscillations in a cyclotron-resonance maser with a periodic quadropole TEM-guide

Y. Leibovich, E. Jerby\*, and A. Shahadi

Faculty of Engineering, Tel Aviv University, Ramat Aviv 69978, Israel

### Abstract

A quadropole TEM-guide is used in a compact cyclotron-resonance maser (CRM) experiment. The CRM oscillates near the fundamental cyclotron frequency ( $\sim 2.4$  GHz) and its second and third harmonics ( $\sim 4.8$  GHz and  $\sim 7.2$  GHz, respectively). Circularly polarized waves are detected in the cavity. The feasibility of operation at higher frequencies is discussed.

Cyclotron-resonance interactions with slow waves, as well as high (spatial and temporal) harmonics, have been studied intensively in the CRM literature (see for instance Refs. [1-6]). In our laboratory, we study low-voltage CRMs in periodic rectangular waveguides [7,8], and in stripline [9,10] schemes. The CRM oscillator scheme presented here combines a periodic structure [7] with a non-dispersive (TEM-mode) transmission line [9].

Periodic-waveguide CRMs may operate with fast or slow harmonics [1-4]. They have been studied in amplifier and oscillator schemes. The CRM interaction is feasible at the first frequency pass-band of the periodic-waveguide, and at higher pass-bands as well. An opposite approach leads to the concept of the non-dispersive TEM-mode CRM [9]. This device has a wide frequency band-width, and it requires a large initial rotation of the electron beam.

The periodic quadropole-TEM-guide used in our CRM experiment is shown schematically in Fig. 1. The waveguide consists of a transmission-line with four parallel conductors, and a periodic array of 8 disks along them. The transverse quadropole modes enable interaction with high (temporal) harmonics of the cyclotron frequency, whereas the array of disks introduces a longitudinal periodicity (6.2 cm period) and consequently spatial harmonics and slow-waves.

The experimental setup (except for the waveguide shown in Fig. 1) is similar to that of Ref. [7]. The CRM tube consists of a Pierce electron-gun with a thermionic cathode (Spectra-Mat Std200). A solenoid and a kicker-coil induce the magnetic-field profile needed for the CRM interaction ( $\sim 1$  kG on-axis).

Synchronized pulsers feed the electron-gun and the magnetic coils. The pulse-width of the  $\sim 10$  kV electron-gun pulse is  $\sim 1$  ms, and the electron current is  $\sim 0.2$  A. Two partial mirrors are placed at both ends of the waveguide. The RF power is sampled out by four symmetric probes (coupled to each metal wire) at the end of the interaction region.

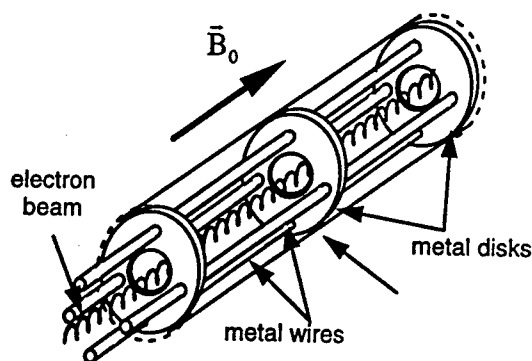


Fig. 1: A section of the CRM waveguide.

The detected RF output is attenuated and divided to two arms. One is terminated by power detectors, and the other by a HP5372A Frequency-Time Domain Analyzer (which measures frequency variations in a single pulse). In addition, the RF sample is filtered by three bandpass filters which cover the cyclotron harmonic frequency bands. The four RF-probe outputs are combined in  $0^\circ$ ,  $\pm 90^\circ$ , and  $\pm 180^\circ$  phases. This enables detection of a circular polarization inside the CRM tube.

Fig. 2. shows typical pulses of the detector output and the electron-gun voltage. The detected power is  $\sim 2$  W. A simultaneous frequency measurement shows a sweep in the range of 2.3-2.5 GHz during the pulse, while the axial magnetic field is  $B_0 \sim 1$  kG (i.e. the cyclotron frequency is  $\sim 2.8$  GHz). The  $\sim 0.4$  GHz Doppler down-shift indicates a CRM interaction with a backward-wave.

\* e-mail: jerby@taunivm.tau.ac.il Fax: + 972 3 642 3508

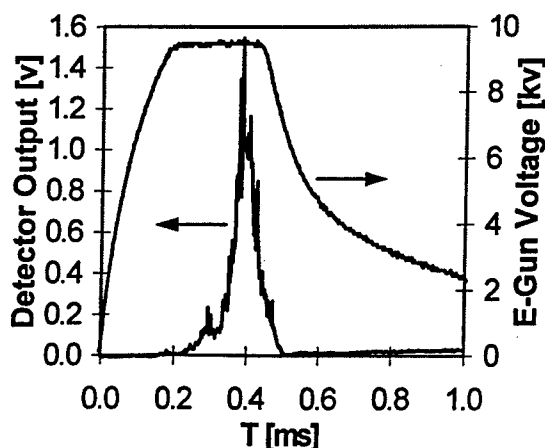


Fig. 2: Typical detector and e-gun traces.

Fig. 3 shows spectral measurements accumulated in many runs (in the same operating conditions) through three bandpass filters (2-4 GHz, 4.5-5.5 GHz, and 6.8-9.0 GHz). The results show clearly three harmonics around the center frequencies: ~2.4 GHz, ~4.8 GHz, and ~7.3 GHz. These CRM harmonics match the frequency passbands of the periodic waveguide. Polarization measurements show that the wave inside the cavity is circularly polarized.

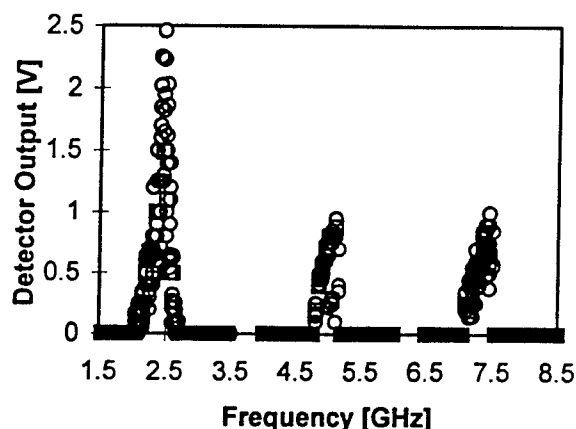


Fig. 3: Spectral measurements of the CRM harmonics.

This experiment leads to further improvements of the periodic quadropole TEM-guide CRM, such as a better coupling of the RF power, and detailed studies of the higher harmonics generation in this scheme, toward the development of a compact CRM harmonic oscillator in the millimeter-wave regime.

## References

1. K. R. Chu, P. Sprangle, and V. L. Granatstein, "Theory of a dielectric loaded cyclotron traveling wave amplifier," *Bull. Amer. Phys. Soc.*, Vol. 23, p. 748, 1978.
2. B. I. Ivanov, D. V. Gorozhanin, and V. A. Miroshnichenko, "Observation of amplification by the anomalous Doppler effect," *Sov. Tech. Phys. Lett.*, Vol. 5, pp. 464-465, 1979.
3. K. R. Chu, A. K. Ganguly, V. L. Granatstein, J. L. Hirshfield, S. Y. Park, and J. M. Baird, "Theory of a slow wave cyclotron amplifier," *Int. J. Electron.*, Vol. 51, pp. 493-502, 1981.
4. H. S. Uhm and J. Y. Choe, "Gyrotron amplifier in a helix loaded waveguide," *Phys. Fluids*, Vol. 26, pp. 3418-3425, 1983.
5. D. V. Kisel', G. S. Korablev, V. G. Pavel'yev, M. I. Petelin and Sh. Ye. Tsimring, "An experimental study of a gyrotron operating at the second harmonic of the cyclotron frequency, with optimized distribution of the high-frequency field," *Radio Eng. Electron. Phys.*, Vol. 19, pp. 95-100, 1974.
6. D. S. Furuno, D. B. McDermott, H. Cao, C. S. Kou, N. C. Luhmann Jr., P. Vitello, and K. Ko, "A four cavity, high harmonic gyrokystron amplifier," *Int. J. Electron.*, Vol. 65, pp. 429-435, 1988.
7. E. Jerby, A. Shahadi, V. Grinberg, V. Dikhtiar, M. Sheinin, E. Agmon, H. Golombek, V. Trebich, M. Bensal, and G. Bekefi, "Cyclotron maser oscillator experiments in a periodically loaded waveguide," *IEEE J. Quantum Electron.*, Vol. 31, pp. 970-979, 1995.
8. M. Korol and E. Jerby, "Linear analysis of a multi-beam cyclotron resonance maser array," *Physical Review E*, May 1997.
9. E. Jerby, A. Shahadi, R. Drori, M. Korol, M. Einat, I. Ruvinsky, M. Sheinin, V. Dikhtiar, V. Grinberg, M. Bensal, T. Harhel, Y. Baron, A. Fruchtmann, V. L. Granatstein, and G. Bekefi, "Cyclotron resonance maser experiment in a non-dispersive waveguide," *IEEE Trans. Plasma Science*, Vol. 24, pp. 816-824, 1996.
10. M. Einat and E. Jerby, "Anomalous and normal Doppler effects in a dielectric-loaded stripline cyclotron resonance masers," submitted to *Physical Review E*.

## Thermionic Cathode CARM Experiments

A.R. Young, S.J. Cooke, W. He, A.W. Cross and A.D.R. Phelps

*Department of Physics and Applied Physics,  
University of Strathclyde, Glasgow G4 0NG, U.K.*

### Abstract

The development of fully relativistic computer codes at the University of Strathclyde has provided an insight into the mechanisms of the Cyclotron Autoresonance Maser (CARM) and assisted in the development and improvement of its component parts. The codes have been used to extensively model the electron gun and this has led to an efficient, high quality, thermionic electron beam source.

### Introduction

The CARM is a high power source of microwaves. Use of the CARM instability means the electron beam and the RF field stay in resonance as the electron beam loses energy to the field which indicates a high potential efficiency for the device. Also the cyclotron frequency of the device is Doppler upshifted, given by the equation

$$\omega = 2\gamma_1^2 \omega_c$$

This frequency gain can be quite significant and reduces the magnetic field required for a given frequency.

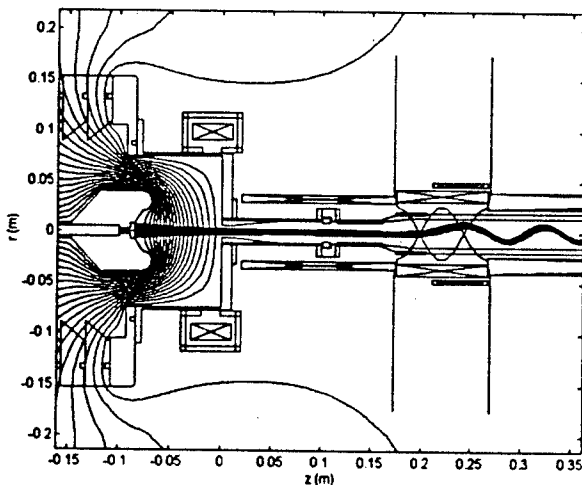


Fig. 1 Schematic diagram of CARM electron Optical system with Cold Cathode

It has been shown [1] that the efficiency of the CARM, like other microwave devices that have a large Doppler frequency upshift, is dependent on the quality of the electron beam. Such a beam can be formed using a Pierce like cathode producing a thin rectilinear electron beam and a short pumping system (kicker) which introduces a rotational velocity to the electrons.

### Electron Beam Source

The University of Strathclyde CARM experiment uses a cold explosive field emission cathode which operates in the space charge limited regime, to produce a high current (~50A), high quality, but short (~100ns) beam. Due to gap closure, it was difficult to increase the duration of the electron beam from such a source. The pulsed power system used delivers a 300kV pulse, which was approximately 100ns in duration.

The CARM was operated using the second harmonic of the cyclotron frequency. An interaction efficiency of 3.9% was measured at a frequency of 14.27 GHz, using an 80 ns pulsed, 14 A electron beam of energy 300keV, to produce a coherent microwave power of 170kW. Emission occurred at 3.7 times the relativistic cyclotron frequency, due to the large Doppler frequency increase and second harmonic interaction.

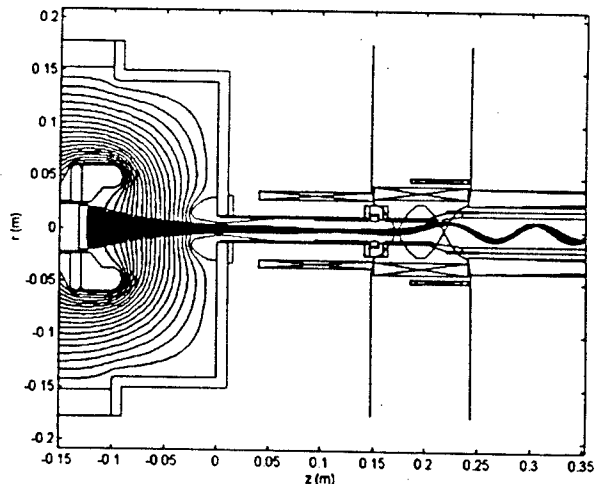


Fig. 2 Schematic diagram of CARM electron-optical system with Thermionic Cathode



Table 1 Results of Computer Modelling of CARM Cathodes

Cathode	Original Pierce Cold	Modified Pierce Cold	Thermionic
Operating Voltage	300kV	450kV	500kV
Diode Current	60 A	40 A	30 A
Beam Current	60 A	40 A	30 A
Emission Current Density	44 → 82 A/cm <sup>2</sup>	23 → 30 A/cm <sup>2</sup>	2.3 → 2.7 A/cm <sup>2</sup>
Parallel Velocity / c	0.683 ± 0.026	0.8452 ± 0.0005	0.8618 ± 0.0003
Perpendicular Velocity / c	0.042 ± 0.019	0.0389 ± 0.0117	0.0302 ± 0.0086
Pulse Duration	100ns	100ns	>1μs

An alternative power supply has been developed which is capable of producing a 800kV pulse with a longer duration, which will be operated at a potential of 500kV. This will allow operation of the CARM at the fundamental frequency, but requires a redesign of the existing cold cathode diode system to operate at this voltage (fig 1).

### Modelling of Beam Source

The computer models developed at the University of Strathclyde are fully relativistic electron trajectory codes that can calculate (1) the space-charge limited emission current, (2) the current density profile of the e-beam, (3) the diode and beam currents, and (4) the velocity profile of the e-beam.

The first electron-optical system built for the Strathclyde University CARM used no beam focusing and lost a large amount of the beam due to scraping by the anode. This was corroborated by the computer models[2,3] and the codes were used to design Pierce electrodes which significantly reduced the scraping of the beam, and produced a better quality beam which has led to more efficient operation of the CARM, Fig 3.

The new voltage pulse system with its greater potential, has required some modifications to be made to the existing diode to still produce a high quality beam with little scraping of the beam. The main modifications in the design of the higher voltage cold cathode are the necessary increase in the anode

cathode spacing and the addition of a semicircular rim to the Pierce like electrodes to reduce field enhancement at the edge of the electrodes. The results of the computer model are shown in table 1, along side the results of the original Pierce diode.

As the new power supply is capable of producing a longer pulse and to take advantage of this a thermionic cathode has been developed. The most significant modification to the diode geometry in the design of the thermionic cathode is the convergence of the beam. This was made necessary by the fact that a high current density is required at the anode aperture and the achievement of such a current emission density from a thermionic cathode would be almost impossible, and would most certainly give a very short lifetime cathode.

### Acknowledgements

An EPSRC/CASE award with EEV and a research agreement with the DRA supported this research. We would like to thank D. Wilcox of EEV and D.M. Parkes, and S.N. Spark of the DRA for their advice and assistance with this project.

### References

1. V.L. Bratman, G.G. Denisov, M.M. Ofitserov, M.I. Petelin, S.V. Samsonov, "Concept of a submillimeter wavelength CARM.", Nucl. Instr. And Meth. A. 358, 135-138, 1995.
2. S.J. Cooke, S.N. Spark, W. He, A.D.R. Phelps, "100Hz PRF CARM experiment", in Eighteenth International Conference on Infrared and Millimeter Waves, James R. Birch, Terence J. Parker, Editors, Proc. SPIE 2104, pp. 462-463, 1993
3. S.J. Cooke, S.N. Spark, A.W. Cross, W. He and A.D.R. Phelps, "Fast Pulsed CARM Oscillator Experiments", Nineteenth International Conference on Infrared and Millimeter Waves, 427-428, 1994.

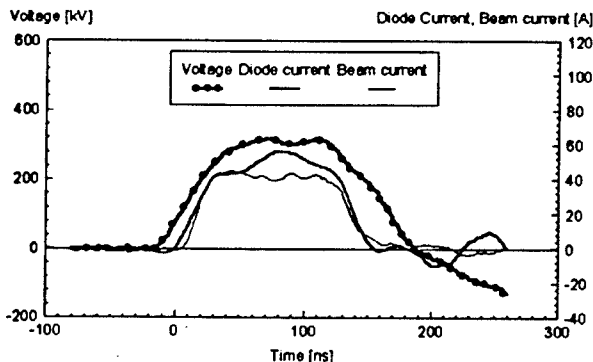


Fig 3. Diode and beam current and voltage pulse for original Pierce diode

# A quasi-optical Resonant Ring for high power millimeter-wave testing

T.S. Bigelow

Oak Ridge National Laboratory

P.O. Box 2009, MS 8071, Oak Ridge, TN 37831-8071

## ABSTRACT

A quasi-optical resonant ring is being developed for testing of millimeter wave components, windows and low-loss materials at very high power levels using medium power level sources[1]. The resonant ring generates a traveling wave resonance of uniform amplitude along the waveguide that is ideal for testing components and materials. Both smooth-wall TE<sub>01</sub> mode and a corrugated-wall HE<sub>11</sub> mode versions have been constructed. These units use highly oversized waveguide and four miter bends to form a quasi-optical resonant ring. A perforated plate miter bend serves as the input directional coupler. A water-cooled tube array is being designed for a coupler capable high-power cw operation. A theoretical power gain of >10 is possible using the 63.5 mm HE<sub>11</sub> version at 53 GHz. Low power measurements have been performed to confirm the operation and >1.5 MW high power tests using a 200 kW gyrotron are expected in the near future.

## INTRODUCTION

Gyrotrons of >1-MW cw power in the 110- to 160-GHz frequency range with HE<sub>11</sub> output beams are being developed for electron cyclotron heating (ECH) of plasmas. Windows are required for gyrotrons and for waveguide transmission systems at the plasma device to provide vacuum isolation and containment. Windows are difficult to build for these systems because the window dielectric losses increase with frequency and the centrally peaked output power beam concentrates the power deposition near the center. Development and testing of a window independent of gyrotron development is desirable since window failure on a cw gyrotron usually means an expensive reprocessing of the entire tube or possibly even total loss. Testing new window designs to equivalent power levels using an off-line facility provides significant savings in tube development costs.

The resonant ring technique [2] has been successful in the past for testing single-mode, rectangular waveguide windows above the power level available from existing sources. The resonant ring is preferred for window and other component testing because it provides traveling waves as opposed to the standing waves that exist in typical resonant cavities. A waveguide resonant ring is formed using four bends and a phase shifter for adjusting the total path length to equal an integral number of guide wavelengths. Power is coupled into the ring with a high directivity directional coupler having an optimized coupling value. A resonant ring can be easily adjusted to have low input reflection to the source provided the components under test have low reflection coefficients. At resonance and with optimum coupling, the uncoupled source power straight through the coupler is canceled exactly by the power coupled back out of the ring so that all the power enters the ring. The buildup of power level in the ring is limited only by losses in the ring components which can be quite low. A ring path loss of 0.45 dB results in a power level gain of 10.

## A QUASI-OPTICAL RESONANT RING

Low-loss TE<sub>01</sub> mode in smooth-wall waveguide or the HE<sub>11</sub> mode in a corrugated waveguide are the common transmission modes used in highly oversized ECH waveguide systems. Typical waveguide diameters used for ECH range from 30 to 90 mm for a 1-MW transmission system [3]. A quasi-optical resonant ring can be formed using four miter bends with a small adjustable gap or bellows in two legs as shown in Fig. 1.

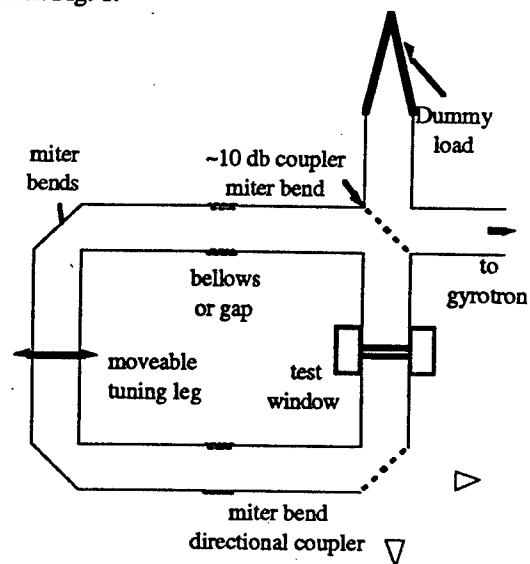


Figure 1. quasi-optical resonant ring configuration

The gap spacing is adjusted for resonance at the operating frequency and, if kept small, has very low loss. Power is coupled into the ring at one of the miter bends that is set up as a cross-guide directional coupler. A dummy load is placed on the other arm of the coupler to absorb uncoupled power. A quasi-optical directional coupler can take the form of a parallel wire grating, a perforated plate, a dielectric sheet for the HE<sub>11</sub> mode and a perforated plate or dielectric sheet for the TE<sub>01</sub> mode. A water-cooled wire grating is being designed for HE<sub>11</sub> high-power cw operation. The wires must be sized and spaced to avoid grating lobe effects. Cooling of a dielectric sheet can be accomplished by using a double sheet with a liquid dielectric cooling layer flowing between.

Modeling of the resonant ring for power gain follows the conventional resonant ring approach [2] with additional loss terms for mode conversion at the miter bends. The electric field ratio from the input to the ring side of the directional coupler is given by

$$\left| \frac{E_{\text{ring}}}{E_{\text{in}}} \right| = \frac{1}{\sqrt{C} - \sqrt{C-1} e^{-\alpha}} \quad (\text{eq. 1})$$

where C is the directional coupling factor and  $\alpha$  is the total ring loss including miter bend mode conversion loss, resistive

loss, and window loss. The maximum possible power gain also equals the optimum directional coupler value and is given by

$$C_{\text{opt}} = \frac{1}{1 - e^{-2\alpha}} = \left( \frac{P_{\text{ring}}}{P_{\text{in}}} \right)_{\text{max}} \quad (\text{eq. 2})$$

which is equal to the reciprocal of the total ring loss including resistive and mode conversion loss at the miter bends.

An 88.9-mm-diameter corrugated-waveguide resonant ring operating at 110 GHz in the  $\text{HE}_{11}$  mode with 2 gaps, 3 miter bends, 1 miter bend cross coupler (assume an additional 1% loss), and a window with 1% loss will have a total loss of ~6% and a ring power gain of 16. If a 200-kW gyrotron is used, the equivalent power in the ring would be 3.2 MW. At 53 GHz with 63.5-mm waveguide, losses would be ~13.5% and the maximum power gain would be 7.5. The 53 GHz, 200-kW cw Varian gyrotrons currently operating at ORNL could produce ~1.5 MW in a 63.5 mm ring waveguide.

In most cases, the total ring loss is dominated by mode conversion loss which can be minimized by using larger diameter waveguide. Pairs of miter bends can be configured to reduce mode conversion loss by separating them by a half beat wavelength[4]. At this spacing, mode conversion to the next higher order mode at a bend, is canceled by mode conversion from the previous bend.

### Low Power Measurements

Low power measurements have been performed on a  $\text{TE}_{01}$  smooth-wall resonant ring constructed from 63.5 mm diameter waveguide, a perforated plate directional coupler and a second perforated plate directional coupler to monitor ring gain. A high mode purity  $\text{TE}_{01}$  swept-frequency source from 50-75 GHz was used with a scalar network analyzer to display

ring gain. Since a swept frequency source is used, there is no need for tuning the ring path length to a particular resonance. To establish a reference level, one of the miter bend plates downstream from the monitoring directional coupler is removed so that the ring is "spoiled". As indicated in figure 2, a signal increase of nearly 13 dB (20x) over the reference level is measured at four resonances in the frequency range shown. Also shown is a calculated ring gain based on (eq 1) adjusted to have lower net loss so that the peaks line up. For this frequency range, the calculated gain with full miter bend loss is 7.5 which is very close to that found at a slightly higher frequency. The ~50 GHz range for this figure is very close to the  $\text{TE}_{01-02}$  beat wavelength for two legs of the ring. The significantly wider width for the measured resonances may be caused by FM noise from the BWO sweep oscillator.

Further low and high power tests on the  $\text{TE}_{01}$  and  $\text{HE}_{11}$  resonant rings are planned.

### Acknowledgments

Research is sponsored by Thoughtventions, Ultd., as part of a SBIR program with the Department of Energy and by DOE under contract number DE-AC05-96OR22464.

### References

- [1] T.S. Bigelow, Proceedings 19th Conf. Infrared & Millimeter Waves (1994)
- [2] L.J. Milosevic and R. Vautey, "Traveling Wave Resonators," IEEE Trans. MTT, Vol. 6, pp.136-143 (1958)
- [3] W. Helne et al., "Study on ECW Transmission Lines for NET/ITER," Report EUR-FU/80/90-99, October 1990
- [4] E.A.J. Marcatilli, "Miter Elbow for Circular Electric Mode," in Proc. on Symp. on Quasi-optics, Polytechnic Press, New York (1964)

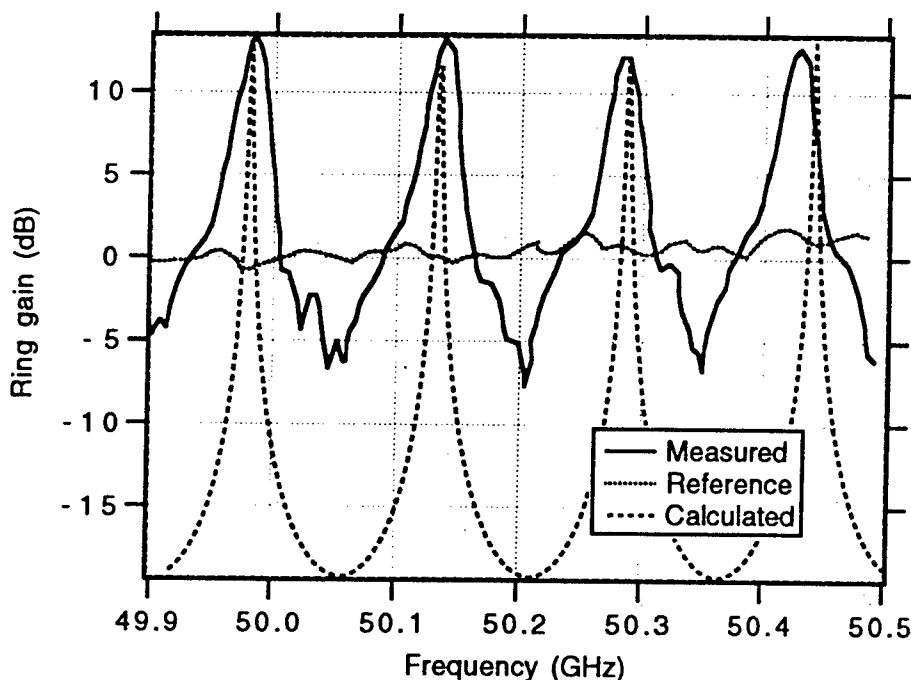


Figure 2 Measured and calculated ring gain for a  $\text{TE}_{01}$  mode quasi-optical resonant ring

## Calculations and Experiments on Multi-Beam Waveguides

L. Empacher, G. Gantenbein, W. Kasperek

Institut für Plasmaforschung, Universität Stuttgart, Pfaffenwaldring 31,  
D-70569 Stuttgart, Germany

### Abstract

Design issues for multi-beam waveguide transmission of mm-wave power are discussed. Diffraction calculations are carried out and have been confirmed by experimental results. A control-system for the alignment of the mirrors based on auto-collimation of the beam is presented.

### Introduction

ECRH is planned as a principal heating system for the next device in the stellarator line of IPP Garching, the superconducting HELIAS-type experiment WENDELSTEIN 7-X. The main part of this system includes 10 gyrotrons with a power of 1 MW each operating at a frequency of 140 GHz and two multi-beam waveguides (MBWG) as transmission lines, each combining 5 beams at 140 GHz, 1 beam at 70 GHz and a spare beam channel on common mirrors.

At present, a test-facility is constructed at IPF Stuttgart to get experience on the performance of the transmission system and to test components. In parallel, the detailed design is underway concentrating on the following issues: Diffraction calculations for multi-beam waveguides, first experiments on a small scale, investigations on multi-mode transmission, control-system for alignment of the mirrors.

### Calculations and measurements for multi-beam waveguides

In beam waveguides, the mirror surfaces are designed to achieve an iterative correction of the phasefronts. Mode conversion losses are very small for high-power designs due to the low curvature of the mirrors [1]. In the confocal multi-beam waveguide [2], the design of the mirrors must offer a low-loss propagation of all (on-axis and off-axis) beams and a correct imaging from the input to the output plane. In Fig. 1, a simple MBWG with 2 mirrors in Z-configuration is sketched. Note, that for a compact design the beams overlap on the mirrors, so that no optimization of partial mirror surfaces is possible. For single mirrors, losses of off-axis beams were calculated [3], however, for multi-mirror configurations single-mirror losses cannot be simply added due to phasing effects between the higher-order modes.

Therefore, 3-dim. diffraction calculations for multi-beam waveguides consisting of four mirrors have been performed. The mirrors are ellipsoids designed for an axial 140 GHz beam with the geometry of the W7-X system (waist radius of input beam  $w_0 = 50$  mm, mirror size  $0.74 \times 1.1$  m, focal lengths 5 m, ring-arrangement). Fig. 2 shows calculated power distributions of an off-axis 140 GHz gaussian beam. Although there is some slight astigmatism after two mirrors the distribution of the input beams is correctly reproduced at the output.

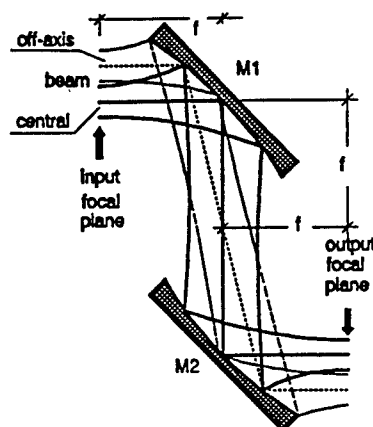


Fig. 1: Sketch of a 2-mirror unit of a confocal MBWG. Shown is the central beam (solid) and one off-axis beam.

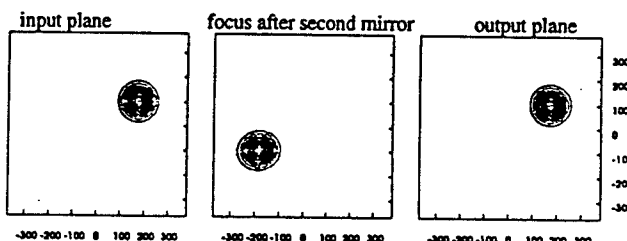


Fig. 2: Power distributions for the MBWG design for W7-X at the input plane, after 2 mirrors and at the output plane.

To check the calculations and to illustrate the behaviour of off-axis beams, a small-scale 4-mirror MBWG was constructed. Mirrors with strong curvature ( $f=120$  mm,  $w_0 = 4.5$  mm, mirror size  $160 \times 230$  mm) were chosen to get strong mode conversion effects. Calculations of amplitude and phase distributions for co- and cross-polarization were performed and compared with corresponding measurements. Generally, good agreement is found. In Fig. 3, various power distributions calculated and measured at the output plane after four mirrors are shown. Whereas a central beam (Fig. 3a) still suffers only a small deformation, a beam shifted by  $f/4$  in the plane of incidence (x-direction) is slightly deformed (Fig. 3b). However, the measurements show that the deformation is smaller compared to the focal planes after one and two mirrors. Similar behaviour is found for beams which are shifted perpendicular to the plane of incidence by  $f/4$  (y-direction). The cross-polarization is low, in spite of the extreme curvatures of the mirrors. The beams shifted in the y-direction also suffer a rotation of the polarization, which however is cancelled after four mirrors.

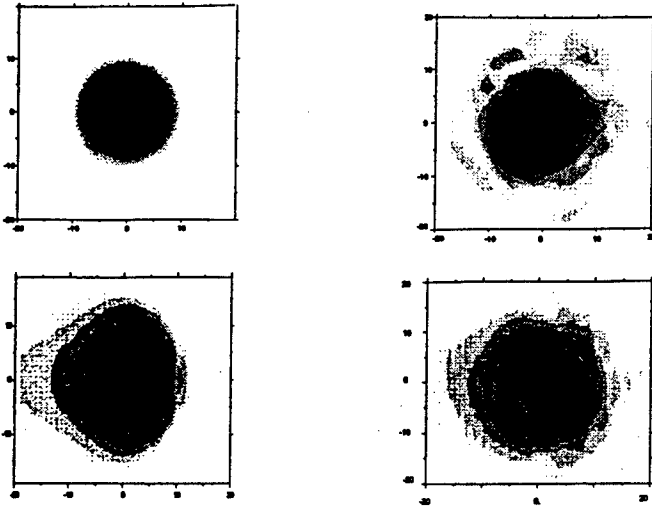


Fig. 3: Amplitude patterns for a 140 GHz MBWG with parameters showing mode conversion ( $f=120$  mm,  $w_0=4.5$  mm), calculated (left) and measured (right) after 4 mirrors, above: central beam, below: beam shifted by  $x=30$  mm.

### Alignment Control

An essential issue for highly oversized closed and open (beam) waveguides is the alignment. The following auto-collimation scheme can be used for this task: Shallow diffraction gratings in first order Littrow mount [4], i.e. with a distance of the grooves  $d = \lambda_r / (2 \sin \alpha)$  are machined on the surfaces the alignment of which has to be checked. Here,  $\alpha$  is the local angle of incidence and  $\lambda_r$  the wavelength of the test source. The gratings then reflect a small amount of an incident test radiation back into itself. The test beam should have a sufficiently high frequency to avoid grating reflection for the operating frequency. By coupling this beam into the line under test and detecting the reflected power with a directional coupler, the transmission efficiency up to the reflecting device can be monitored (see Fig. 4).

Spatial resolution, i.e. discrimination of the reflecting elements can be obtained by sweeping the test source with a constant speed  $dv/dt$ . The spatial resolution  $\Delta z$  is then determined by the sweeping range  $\Delta v$  according to  $\Delta z = c/2\Delta v$  and the location  $z$  is determined by a frequency  $\nu_F = dv/dt \cdot 2z/c$  which is measured if the reflected signal is mixed with the forward signal [5]. Thus with an appropriate spectrum analyzer, an alignment check can be performed simultaneously for all components. A proof-of-principle experiment for this scheme was performed using a simple beam waveguide including three mirrors with a grating structure designed for 140 GHz at an angle of incidence of  $45^\circ$ . The reflected signal was measured between 135 to 145 GHz, and, due to the lack of a sweeper with a constant sweep speed, the Fourier transformation of the mixing signal was generated. Fig. 5 confirms the above scheme: For the perfectly aligned mirror (dotted line), three peaks are seen in the spectrum together with a reference stemming from the teflon surface of a lens horn. In case of a misaligned ( $1^\circ$ ) first mirror (solid line), the following signals are smaller, and a shift is seen owing to the changed reflection points.

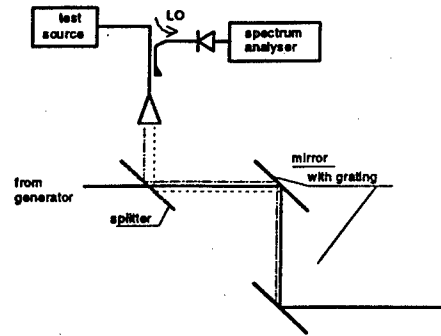


Fig. 4: Sketch of a remotely controlled alignment system

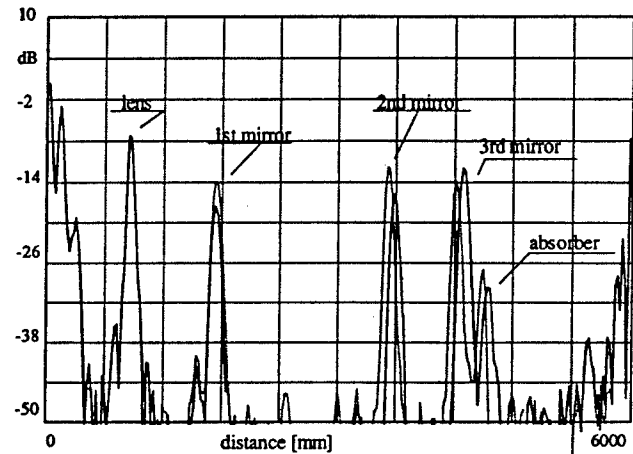


Fig. 5: Reflected spectrum from 3 grating mirrors. Dotted line: correct alignment, solid line: 1st mirror misaligned.

### Conclusions

Calculations and measurements yield a very low mode conversion loss for the multi-beam waveguide transmission for the ECRH system on W7-X and show that even more beams can be combined on a single mirror system without remarkable loss of performance.

Auto-collimating gratings machined on reflecting components allow the remote control of alignment, failure detection of components as well as calibration of movable antennas.

### References

- [1] J.A. Murphy, Int. J. of Infrared and Millimeter Waves, 8, 1165 (1987)
- [2] L. Empacher et al, to be published in: Proc. of the Symp. on Fusion Technology 1996, in Fusion Technology, (Elsevier, Amsterdam, 1997).
- [3] C. Dragone, IEEE Trans. Antennas and Propagation, AP-30, 331 (1982).
- [4] R. Petit (ed.), Electromagnetic theory of gratings (Springer, Berlin, 1980).
- [5] R.J. Smith et al., Digest of the 18th Conf. on IR and mm waves, Essex, SPIE Proc. Vol. 2104, 248 (1993).

# Measurement Limitations on Phase Pattern Determination from Several Amplitude Pattern Measurements

B. M. Harper and R. J. Vernon

Department of Electrical and Computer Engineering  
University of Wisconsin - Madison  
Madison, WI 53706

## Abstract

It is difficult to directly measure the phase pattern of millimeter wave beams. It is possible to obtain the phase pattern associated with a propagating beam from amplitude pattern measurements over several surfaces. An iterative, diffraction-based technique for obtaining the phase pattern associated with a propagating beam has been developed. In this paper we discuss the effects of several limitations of the physical measurements on the quality of the reconstructed phase pattern.

## Phase Pattern Determination

There are several applications where it is desirable or necessary to measure the phase of millimeter wave beams. It is very difficult to directly measure the phase of such beams. Since the amplitude and phase of a propagating beam are uniquely coupled, it is possible to obtain the phase information associated with a propagating beam from amplitude measurements over several surfaces. We have taken amplitude data over several surfaces and reconstructed the phase information in the beam from these measurements using a technique which will be described later. However, the accuracy of this information for a given set of measured amplitude data is not clear. Therefore, it is desirable to determine some guidelines for how accurate amplitude data must be in order to adequately specify the phase information.

Specifically, a few of the experimental considerations which may limit the recovered phase information are the dynamic range of the measured signal, random noise, drift in the measured signal strength, and size and separation of measurement surfaces. These experimental sources of error will be considered in theoretical simulations and/or empirical measurements.

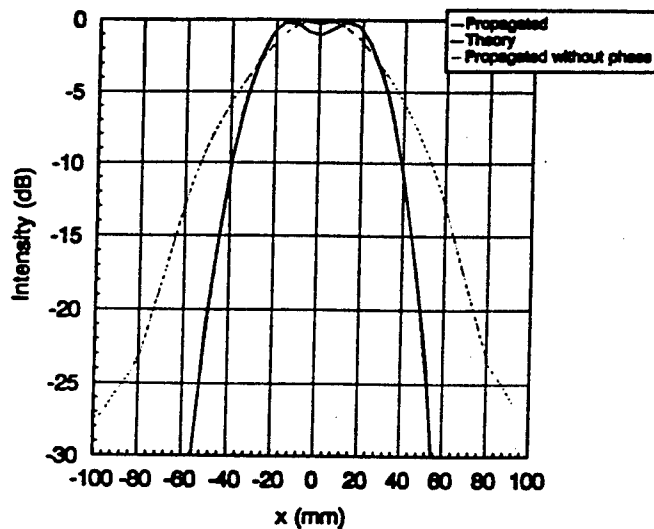
As mentioned above we have the capability to reconstruct the phase of a propagating millimeter wave beam from amplitude measurements over several surfaces. We usually take planar cross sections of a beam as it propagates. This data is then used to recover the phase information associated with the beam. The technique involves writing the measured amplitudes in terms of currents and using numerical integration to propagate the data from one plane to another. For a beam which is well behaved, the phase pattern can often be obtained by using data from only two planes as long as there is a reasonable first guess at the phase pattern at one of the planes. Using the amplitude data and an approximate phase pattern for one of the planes, the

beam is propagated using numerical integration to the second plane. The difference in the phases of the propagated beam and that of the measured data at the second plane suggests the phase necessary to apply to the amplitude on that plane. This phase pattern is applied to the amplitude at the second plane, and then this beam is propagated back to the first plane. The phase patterns are compared at the first plane suggesting a better phase distribution there. The process is then repeated until the solution converges, usually in only a few iterations. The amplitude and applied associated phase are unique to the beam and only the "correct" applied phase will produce the proper distributions when propagated to the other planes.

The theoretical amplitude distribution of a 110 GHz, propagating, flat-top beam is considered over several planes up to two meters apart. We define a flat-top beam as a beam with a relatively flat profile near the center which tapers quickly near the edges of an aperture. The flat-top beam used here was generated using a weighted combination of the first three Laguerre-Gaussian modes. As the beam propagates it begins to lose its flat-top appearance when it approaches 100 cm from its theoretical waist. For a beam waist radius  $w_0$  of 2.0 cm used in this calculation, the characteristic length for Gaussian modes is  $z_0 = 46$  cm. The characteristic length is the distance from the waist in which half of the relative phase shift between modes will occur and is given by  $k_0 w_0^2 / 2$ . Most of the relative phase shift will have occurred for planes that are 100 cm apart. The theoretical data at  $z = 15$  cm and  $z = 115$  cm from the position of the waist were used to reconstruct the phase information of the beam. For this simulation the initial approximation of the beam's phase pattern was set to zero everywhere on the  $z = 15$  cm plane. The reconstructed phase information was applied to the amplitude data at each plane. The amplitudes and applied phases were then propagated using numerical integration to the other planes. The theoretical power density profile at the  $z = 15$  cm plane along with the power density profile of the propagated beam from the  $z = 115$  cm plane are shown in Fig. 1. The data at the  $z = 115$  cm plane was first propagated using a phase distribution set to zero everywhere and then using the reconstructed phase. Both are shown in Fig. 1. The theoretical power profile at a third plane at  $z = 200$  cm along with the power profile of the propagated beam from the  $z = 15$  cm plane with the reconstructed phase and with no phase are shown in Fig. 2. The curves at both planes have very good agreement.

However, this simulation only demonstrates that the phase reconstruction technique itself is sound when using perfect data with none of the limitations involved in taking

physical measurements. As various limitations on the "accuracy" of the initial beam are applied, the corresponding phase pattern obtained will no longer be accurate either. How accurate does the measured data need to be to recover a reasonable picture of the beam's phase pattern? This question will be addressed in this presentation.



1. Power density profiles at the  $z = 15$  cm plane (plane #1). Theoretical data at plane #1 and theoretical data at the  $z = 115$  cm plane (plane #2) propagated to plane #1. The data at plane #2 was first propagated with the phase pattern set to zero and then with the reconstructed phase applied.

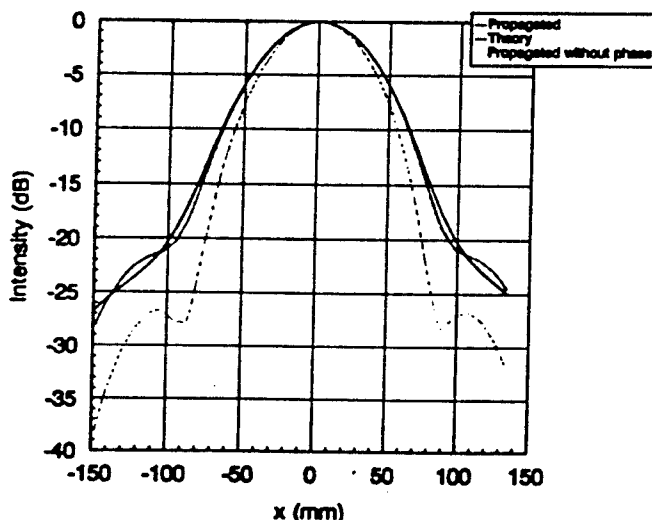


Fig. 2. Power density profiles at the  $z = 200$  cm plane (plane #3). Theoretical data at plane #3 and theoretical data at the  $z = 15$  cm plane (plane #1) propagated to plane #3. The data at plane #1 was first propagated with the phase pattern set to zero and then with the reconstructed phase applied. The phase was reconstructed using data from plane #1 at  $z = 15$  cm and plane #2 at  $z = 115$  cm.

One important potential limitation is the separation between the measured surfaces. For a 110 GHz system with a characteristic length of  $z_0 = 46$  cm, separations of 10 cm to 100 cm between the planes were used. The phase pattern was reconstructed using planes 10 cm apart, the first plane 15 cm from the waist and the second plane 25 cm from the waist. The phase pattern was then applied to the theoretical data at the first plane. This amplitude and phase distribution was then propagated using numerical integration to a third plane 200 cm from the waist. The power density distribution of the propagated beam and theoretical power density at the third plane are shown in Fig. 3.

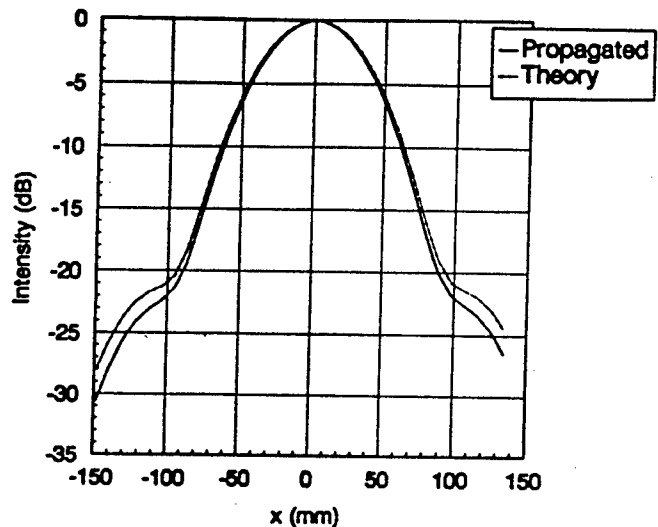


Fig. 3. Power density profiles at the  $z = 200$  cm plane (plane #3). Theoretical data at plane #3 and theoretical data at the  $z = 15$  cm plane (plane #1) propagated to plane #3. The phase pattern was obtained using data from plane #1 at  $z = 15$  cm from the waist and plane #2 at  $z = 25$  cm from the waist.

The phase reconstruction is very good, even with the planes only 10 cm apart. Again, this reconstruction uses perfect amplitude data but over finite planes. It might be expected that these conditions would still produce good results. However, even with perfect amplitude data, the reconstruction technique still requires a reasonable first approximation for the phase pattern at one of the planes.

Another measurement limitation is the dynamic range of the signal and random noise. A noise generator and a limited dynamic range have also been incorporated into other theoretical simulation. In addition a small ramp in amplitude has been added to simulate a drift in the physical signal's power. The reconstruction technique does a reasonable job of producing the phase pattern for data with even 1% errors in power.

\*This work was supported by the US Dept. of Energy under contract DE-F02-85ER52122.

# Phase Retrieval from Gyrotron Near-Field Intensity Measurements

D.R. Denison, T. Kimura, M.A. Shapiro, R.J. Temkin

Plasma Science and Fusion Center  
Massachusetts Institute of Technology  
167 Albany St., Cambridge, MA, 02139, USA

## Abstract

We present several applications of phase retrieval to gyrotron electric field intensity measurements. The phase of a microwave beam is determined from the intensity measurements and is then used to analyze a matching optics unit. We also propose a new approach to mode converter design using phase retrieval techniques.

## 1 Introduction

The difficulty of measuring the phase of a high-frequency electromagnetic field has lead to an extensive treatment of the problem of retrieving phase (or field reconstruction) from a given set of intensity measurements. The literature on this inverse problem is extensive and covers many applications; for brevity we refer the interested reader to some representative papers [1-4]. In the current treatment we employ a modified Gerchberg-Saxton iterative algorithm presented in [1], and we also use the formulation given by [2]. These methods are applicable to near-field measurements as long as the reactive fields are negligible. The following sections illustrate several uses for the phase retrieval algorithm in the context of gyrotron mode converter analysis and design.

## 2 Phase Retrieval Example

We use the phase retrieval algorithm to analyze a set of measurements from cold tests of a gyrotron internal mode converter to demonstrate that we can reconstruct the beam phase and amplitude at a gyrotron window. The measurements of electric field intensity were performed at Communications and Power Industries (CPI), Palo Alto, CA, on a mode converter designed to transform a 110 GHz,  $TE_{22,6}$  gyrotron cavity mode into a quasi-Gaussian beam. Measurements were made over two planes: one at the gyrotron window and one located 25.4 cm (10.0 in) from the window.

Ideally, the reconstructed intensity from the iterative phase retrieval algorithm should approach the initial (measured) intensity distribution. Figure 1 compares

the measured and reconstructed intensity profiles on the window plane after 200 iterations, and shows very good agreement. Figure 2 shows the reconstructed phase over the window plane, and we note a slight tilt in the phase across the plane. The design phase profile is flat, and this analysis shows that the beam will not evolve as predicted in the design.

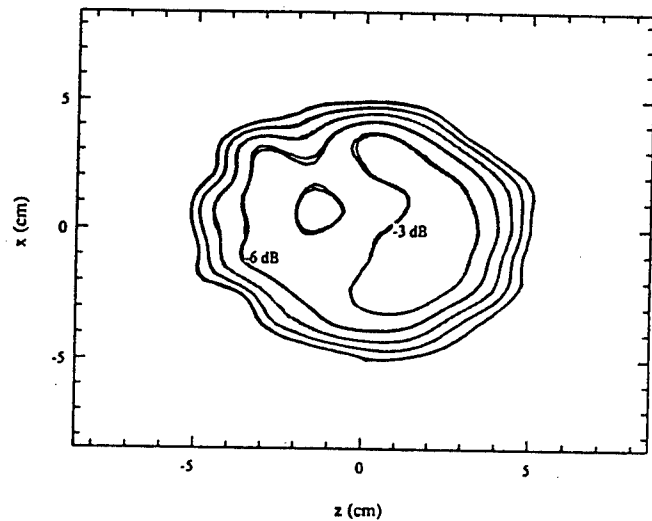


Figure 1. Electric field intensity at gyrotron window, measured and reconstructed.  $z$  is parallel to the gyrotron axis.

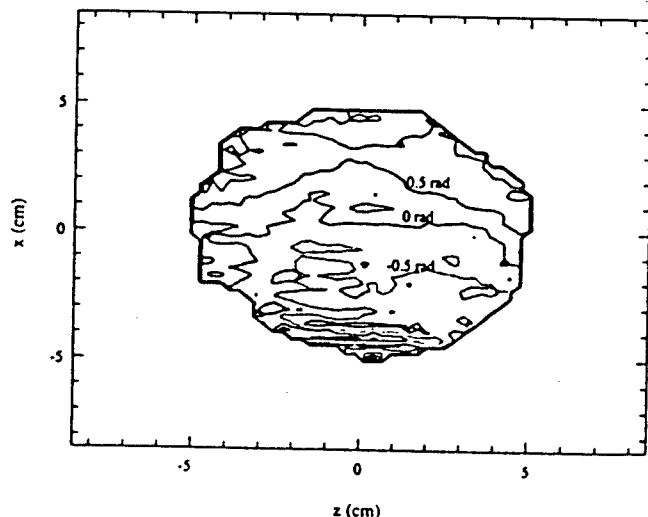


Figure 2. Phase at gyrotron window.



### 3 Analysis of Matching Optics Unit

The Matching Optics Unit (MOU) matches the microwave beam from a gyrotron to a waveguide suitable for high-power microwave transmission. A MOU was designed by CPI to focus the ideal, uniform field from the gyrotron into a 3.2 cm (1.25 in) corrugated waveguide. Figure 3 shows the focussed beam at the output of the CPI MOU with the MOU excited by the ideal gyrotron microwave beam. The reconstructed fields from Section 2 were used to simulate the behavior of the MOU under experimental conditions, and Figure 4 shows the results of the simulation. Clearly, the non-uniform propagation of the beam expected from Section 2 causes a sidelobe to form and propagate through the system.

### 4 Design of Microwave Structures from Measurements

The previous sections reveal that the actual fields from a microwave system may differ substantially from the theoretical fields. Therefore, basing subsequent systems on the theoretical fields may (and indeed often does) lead to unpredicted and possibly unacceptable behavior of the system. One alternative to this situation is to design the overall microwave structure in stages, where each stage is based on *measurements* of the field intensity from the previous stage. We use the phase retrieval algorithm at each stage to derive the full field profile and design the next stage based on simulations using the reconstructed fields. We are currently designing an internal mode converter for a high-power gyrotron based on the above principles.

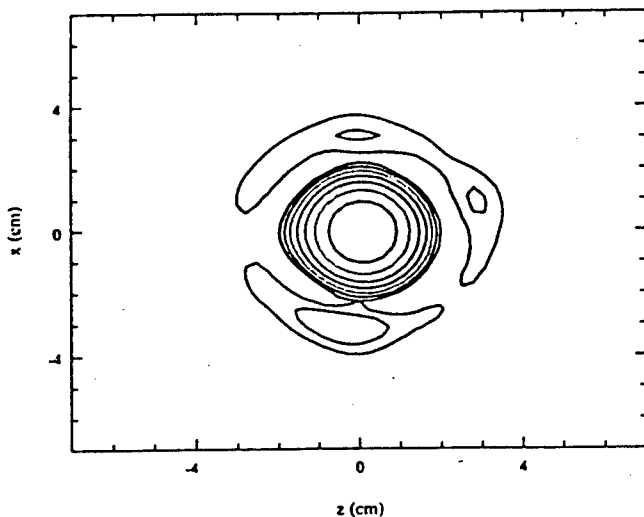


Figure 3. Ideal field intensity pattern at MOU output. Curves are at 3 dB intervals.

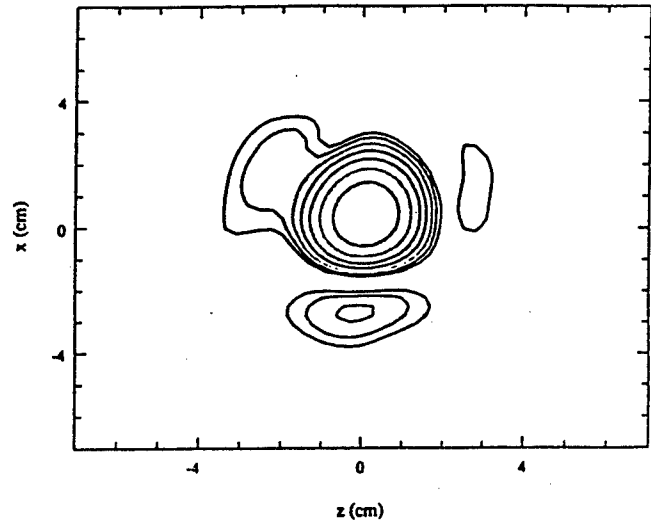


Figure 4. Field intensity at MOU output computed from reconstructed fields. Curves are at 3 dB intervals. The sidelobe is at -15 dB.

### 5 Conclusion

We have presented several applications of phase retrieval to experimental measurements. We determined the microwave beam phase profile on a gyrotron window based on intensity-only measurements of the electric field, and we used these results to analyze a MOU. We propose a new scheme for designing external as well as internal mode converters that accounts for non-ideal mode converter performance by using measured fields at each stage of mode converter design.

The authors gratefully acknowledge Dr. Sam Chu at CPI for his help with the cold test measurements and the design of the MOU.

### 6 References

- [1] Anderson, A.P. and S. Sali, 'New Possibilities for Phaseless Microwave Diagnostics. Part 1: Error Reduction Techniques,' *IEE Proc.*, vol. 132, Pt. H, No. 5, pp 291-298, 1985.
- [2] Chirkov, A.V., G.G. Denisov, N.L. Aleksandrov, '3D Wavebeam Field Reconstruction from Intensity Measurements in a Few Cross Sections,' *Opt. Comm.*, vol. 115, pp 449-452, 1995.
- [3] Katsenelenbaum, B.Z. and V.V. Semenov, 'Synthesis of Phase Correctors Shaping a Specified Field,' *Rad. Eng. & Elec. Phys.*, vol. 12, pp 223-230, 1967.
- [4] Fienup, J.R., 'Phase Retrieval Algorithms: A Comparison,' *Appl. Opt.*, vol. 21, no. 15, pp 2758-2769, 1982.

# "GAUSSIAN BEAM PROPAGATION VERSUS HUYGENS METHOD IN NON-PARAXIAL CONDITIONS"

*Ramón Gonzalo, Pedro Turullols, Carlos del Río and Mario Sorolla*  
*Microwave and Millimeter Group. Public University of Navarra*  
*Campus Arrosadía. E-31006 Pamplona, Spain*  
*e.m.:ramon@upna.es*

## Abstract

In this paper, we present a study about the difference between Gaussian beam propagation and Huygens method to obtain the radiation pattern in the case of non-paraxial conditions.

We fix a way to determine the error in the Gaussian beam propagation, in this way, we could know if the approximation is good enough.

The computational results show that it is not possible to use the Gaussian propagation equation when we are working with Gaussian beams in non-paraxial conditions.

## Introduction

There are many applications, as for instance systems using a quasi-optical transmission line between the source and the load (high power heating, material processing and ceramic sintering), in which free space eigenmodes must be used [1], [2]. These ones are the preferred choice when high efficiency, maximum matching and low losses on the mirror system are required.

If the wave equation in free space is solved using paraxial condition, the gaussian beams are obtained as result. The exact expression can be found in [3].

Anyway, this solution is only an approximation to the real solution of the wave equation in free space.

By the way, the designers use the gaussian beams as free space solution obtaining easily the transmission lines features like position and size of the mirrors. Nevertheless, this will only be valid in the case of paraxial conditions.

In [4] and [5], an analysis between using the exact expression for the far field pattern of a gaussian amplitude distribution with constant phase, and the paraxial approximation under the form of the paraxial expressions for the gaussian modes is presented. There, a value of  $k\omega_0 > 6$  is chosen to fix the paraxial condition. This value, shown in [5], is corresponds to an 2-Dimensional error of 3%.

In this paper, we present a paraxiality analysis using the Huygens method versus Gaussian propagation. We show graphically the difference between both methods and fix new error values. In this way, a correct design of the transmission line could be done.

## Huygens Method versus Gaussian Propagation

The Huygens method consists on performing the direct integration of the electromagnetic field equations of the source over any surface, obtaining the real solution of the far field radiation pattern in three dimensions. In this case, the field distribution at the source is following a Gaussian profile.

The equations used to compute radiation pattern with this technique can be found in [6].

On the other hand, using the formulas shown in [3], we obtain directly the approximation of the gaussian beam radiation. In particular, the equations describing the gaussian expansion are the following :

$$\text{for } z \gg z_0 = \frac{k\omega_0^2}{2} \quad \varpi(z) = \omega_0 \sqrt{1 + \left(\frac{2z}{k\omega_0^2}\right)^2} \approx \frac{2z}{k\omega_0}$$

$k$  being the wave number and  $\omega_0$  the beam waist of the gaussian beam.

In this equation we can see that with lower values of  $k\omega_0$  the asymptotic slope will be increased, so the paraxial solution will not be an adequate approximation.

After this, to compare the two previous techniques we define the following error equation over the surface radiation.

$$\varepsilon = \frac{\sum_i |Huy(x, y, z)_i|^2 - |\Psi_{0,0}(x, y, z)_i|^2}{\sum_i |Huy(x, y, z)_i|^2}$$

where  $|Huy(x, y, z)_i|$  is the radiation pattern over each point of the radiation surface obtained with the Huygens method and  $|\Psi_{0,0}(x, y, z)_i|$  is the gaussian expansion .

## Results

To determine if the paraxial condition is satisfied, we will calculate the theoretical error ( $\varepsilon$ ) for different values of  $k\omega_0$ . This one can be observed in figure 1. For instance, in the case of  $k\omega_0=6$ , an error of 6.9% is obtained. Using this figure, and fixing the maximum error that we can get, the paraxial condition can be found.

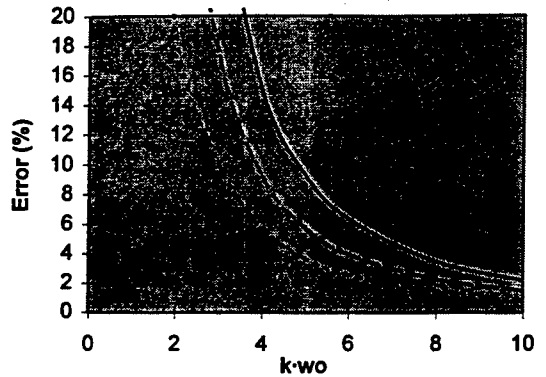


Figure 1 : 3-dimensional error ( $\epsilon$ ) for different  $k\omega_0$  values.

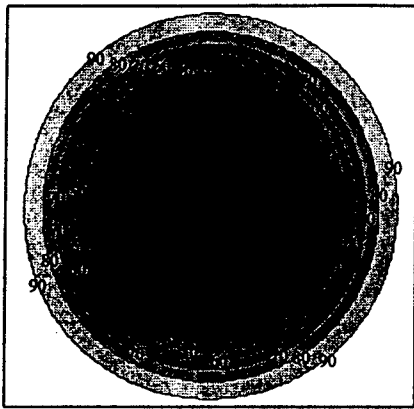


Figure 4: Surface error (%) between the Huygens and Gaussian propagation methods (figures 3 and 4 respectively) in the case of  $k\omega_0=4$ .

In particular, we show some results for  $k\omega_0=4$ . In figure 2 and 3, we can see the Huygens and Gaussian propagation radiation pattern respectively. Furthermore, in figure 4, we analyse the error surface between the two methods. The total error is 14.8%, so we can consider that the paraxial condition is not satisfied.

### Conclusions

A comparison between the Huygens and Gaussian propagation methods to obtain the radiation pattern has been proposed and analysed.

Graphical with different error values in function of the  $k\omega_0$  values has been obtained. In this way, paraxial condition can be extracted for this graphic.

### References

[1] Del Río, C., Gonzalo, R., Sorolla, M., Möbius, A. y Thumm, M. "High Order Mode Beam Waveguide for Technological Medium Power Millimetre Wave Applications". 20th Int. Conf. on Infrared and Millimetre Waves. Conference digest Orlando (EEUU)1995, pp 519-520.

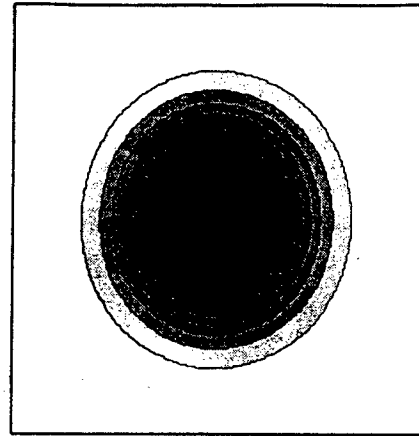


Figure 2: Radiation pattern obtained with Gaussian propagation with  $k\omega_0=4$ .

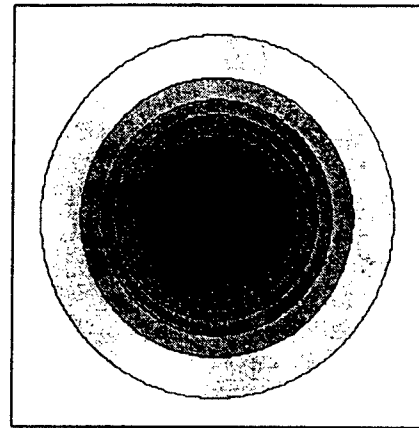


Figure 3: Radiation pattern obtained with Huygens method for  $k\omega_0=4$ .

- [2] Möbius, A., Del Río, C., Sorolla, M. and Thumm, M. "A hollow cone gaussian beam quasi-optical transmission line for a gyrotron technological system" Conference Digest of the 21th Int. Conf. on Infrared and Millimeter Waves. Berlin, Germany, July 1996.
- [3] Wencker, G. "Rekursionsformeln und Entwicklungen der Strukturformeln Gaußscher Strahlen". A.E.U. Band 23, 1969, pp 521-523.
- [4] Martin, D.H. and Bowen, J.W. "Long-Wave Optics". IEEE Transactions on Microwave theory and techniques, Vol. 41, n° 10, October 1993, pp 1676-1690.
- [5] Del Río, C., Gonzalo, R., Sorolla. "Paraxiality considerations of High Order Gaussian Modes". 21th Int. Conf. on Infrared and Millimeter Waves. Conference digest Berlin 1996, pp Bth6.

[6] Stratton, J.A. "Electromagnetic Theory". McGraw-Hill Book Company, 1941.

# Modeling of Radar Scattering Conditions inside a Circular Hollow Dielectric Waveguide

V.K. Kiseliyov and T.M. Kushta

Institute of Radiophysics and Electronics  
Ukrainian National Academy of Sciences  
12 Akademika Proskury St., 310085 Kharkov, Ukraine  
fax: +38-(0572)-441105, tel.: +38-(0572)-448335,  
E-mail:kiseliyov@ire.kharkov.ua

## Abstract

A new ray representation of electromagnetic field inside a quasi-optical structure in the form of a circular hollow dielectric waveguide which confirms a possibility for unusual application of such waveguides - the design in their terms of a off-beat microanechoic chamber for electromagnetic modeling in the near millimeter and submillimeter wave regions is suggested.

## I. Introduction

Scale modeling of the scattering characteristics of various physical objects in the near millimeter and submillimeter wave regions has important application in meteorological physics, radiolocation, astronomy, flaw detection, and other fields. Owing to the well-known principle of electrodynamic similarity, the scattering by real objects of large and very large physical size can be analyzed in laboratory frames using the scaled-down models at shorter wavelengths. On the other hand, inverse scale modeling advances our understanding of the scattering of light and infrared waves by variously shaped single microparticles and sets of them through the scaled-up physical models fabricated of appropriate materials.

A new relatively simple and available laboratory-scale method for studies of the scattering by physical objects in the near-millimeter and submillimeter wave regions has been suggested by the authors [1]. In our method, the investigated object or its scaled model is placed inside a quasi-optical structure - a hollow dielectric waveguide (HDW) of circular cross section which serves several functions: it forms a quasiplane incident wave within the scattering area where test object is placed, performs the low-loss and low-distortion transmission of the scattered wave carrying the test object information to the receiver, effectively filters unwanted modes arising at the scattering on the test object in the region of the receiver, and insulates the scattering area against the ambient conditions containing parasitic sources; that is act as a key component of the microanechoic chamber.

In this paper, we intend to theoretically substantiate the proposed method for measuring RCS inside a circular HDW. Using geometrical optical ray representation of guided

modes and "virtual" waveguide concept as the base, we shall justify the principle of measuring the scattering characteristics of an object when it is inserted in the above quasi-optical structure.

## II. Representation of Electromagnetic Field in a Circular HDW

A quasi-optical guiding structure of the HDW type is a circular channel of large radius  $a$  when compared to the wavelength  $\lambda$ . The walls may be dielectric, or layered dielectric, or metal coated by dielectric layer; the internal surface may be smooth or profiled, for example, corrugated. The electromagnetic field in such a waveguide are described through the modal fields [2]-[4] and also with the use of geometrical optics [5], [6] so that each HDW mode is equivalent to the defined ray family.

In circular HDW with  $\epsilon_1 < 4.08 \epsilon_0$ , where  $\epsilon_1$  and  $\epsilon_0$  are the permittivities of the waveguide walls and filling medium, respectively (normally  $\epsilon_0 = 1$ ), the fundamental mode (whose attenuation is lowest) is  $HE_{11}$ . Its electromagnetic field is defined [7] as

$$\mathbf{E} = E_{0,1}(r) \exp(i h_{0,1} z) \mathbf{i}_y, \quad (1)$$

$$\mathbf{H} = -(\epsilon_0 / \mu_0)^{1/2} E_{0,1}(r) \exp(i h_{0,1} z) \mathbf{i}_x,$$

where  $\mu_0$  is the permeability of the filling medium;  $\mathbf{i}_x$ ,  $\mathbf{i}_y$ , and  $\mathbf{i}_z$  are the unit vectors of a Cartesian coordinate system whose  $z$  axis is coincident with the HDW axis;  $h_{0,1}$  is the propagation constant of the  $HE_{11}$  mode;  $E_{0,1}(r) = J_0(u_{0,1} r/a)$ , where  $J_0$  is the zeroth-order Bessel function;  $a$  is the waveguide channel radius, and  $u_{0,1}$  is the first root of the equation  $J_0(u_{0,1}) = 0$ .

In the traditional geometrical optics representation [5], the ray family corresponding to  $HE_{11}$  mode is meridian, that is each ray intersects with the HDW axis between the reflection points, and the waveguide axis is found to be the caustic of this ray family. Near caustics, the traditional ray model is known to face problems, and the geometrical optics approach fails when the object is on the HDW axis or near so. To overcome this limitation, a different ray representation of the fundamental  $HE_{11}$  mode is proposed.

With the well-known relation  $1 = J_0(x) + 2 \sum_{k=1}^{\infty} J_{2k}(x)$  of Bessel functions, the radial distribution of the  $HE_{11}$  mode field is transformed to given

$$E_{0,1}(r) = 1 - 2 \sum_{k=1}^{\infty} J_{2k}(u_{2k1} r / \rho_{2k}). \quad (2)$$

Here the modal parameter  $u_{2k1}$  is the first root of the equation  $J_{2k}(u_{2k1}) = 0$ , and

$$\rho_{2k} = u_{2k1} a / u_{01}. \quad (3)$$

The first term of expansion (2) evidently represents a plane homogeneous wave propagating along the  $z$  axis; the second and subsequent terms correspond to radial distributions of the fields of modes  $LP_{21}$ ,  $LP_{41}$ , etc. [7]. Each of these modes may be thought of as excited in its "virtual" waveguide of radius  $\rho_{2k}$  given by (3).

Owing to the dual definition of the HDW field, any term of the right-hand of (2) giving the modal field has its ray analogue. In this case, each ray family which corresponds to the certain term in series (2) has its caustic as a cylindrical surface of the radius

$$R_{2k} = \frac{2a k}{u_{01}}, \quad k = 0, 1, 2 \dots \quad (4)$$

The given approach considers the field of the fundamental mode  $HE_{11}$  as a superposition of the fields of the homogeneous plane wave and the modes  $LP_{21}$ ,  $LP_{41}$ , etc. Each of these modes may be seen to be excited in its "virtual" waveguide of radius  $\rho_{2k}$  and each is defined as a family of oblique rays [6] whose caustic is a cylindrical surface centered at the HDW axis.

On the basis of the correspondence of each term of series (2) to the definite ray family, it is possible to divide the space around the axis of a circular HDW into a series of the characteristic areas centered at the HDW axis and shown in Fig.1 with different cross-hatching. In the first area, only rays corresponding to the plane homogeneous wave exist (Fig.1,a). The second area is for the rays corresponding to the plane

homogeneous wave plus oblique rays related to the  $LP_{21}$  mode (Fig.1,b). The third one is for the rays associated with plane homogeneous wave plus the oblique rays related to  $LP_{21}$  mode and  $LP_{41}$  mode (Fig.1,c), and so on.

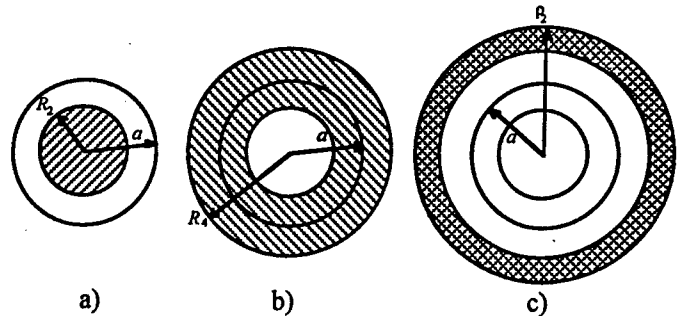


Fig.1.

Thus inside a circular HDW, the new ray model reveals a spatial cylindrical region of radius  $R_2 \approx 0.8 a$  (Fig.1,a) where only a family of rays parallel to the HDW axis and corresponding to the restricted plane homogeneous wave exists. This in turn confirms that the scattering and diffraction by an object when illuminated with a plane homogeneous wave in free space can be physically modeled inside a suitable HDW [1].

### III. CONCLUSION

The capabilities of a quasi-optical structure of the HDW type in measuring scattering characteristics of physical objects or their scaled models in the near millimeter and submillimeter wave regions have been shown.

### REFERENCES

1. V.K. Kiselyev and T.M. Kushta, "Method for radar cross section measurements in millimeter and submillimeter wave regions," *International J. Infrared Millimeter Waves*, vol.16, no.6, pp.1159-1165, June 1995.
2. E.A.J. Marcatili and R.A. Schmeltzer, "Hollow metallic and dielectric waveguides for long distance optical transmission and lasers," *Bell System Tech. J.*, vol.43, pp.1783-1809, July 1964.
3. C. Dragone, "High-frequency behavior of waveguides with finite surface impedances," *Bell System Tech. J.*, vol.60, no.1, pp.89-115, January 1981.
4. Yu.N. Kazantsev and O.A. Kharlashkin, "Circular waveguides with hollow dielectric channel," *Radio Eng. Electron. Physics*, English translation, vol.29, no.8, pp.78-88, Aug. 1984.
5. M.J. Adams, *An introduction to optical waveguides*. Chichester: John Wiley and Sons, 1981.
6. A.W. Snyder and J.D. Love, *Optical waveguide theory*. London: Chapman and Hall, 1983.
7. J.J. Degnan, "Waveguide laser mode patterns in the near and far field," *Applied Optics*, vol.12, no.5, pp.1026-1030, May 1973.

# Extinction and Backscattering for a Waveguide Inhomogeneity

V.K. Kiseliov and T.M. Kushta

Institute of Radiophysics and Electronics  
Ukrainian National Academy of Sciences  
12 Akademika Proskury St., 310085 Kharkov, Ukraine  
fax: +38-(0572)-441105, tel.: +38-(0572)-448335,  
E-mail:kiseliov@ire.kharkov.ua

## Abstract

A correspondence was established between the free-space scattering characteristics (extinction and backscattering) of a physical object and those of same object put in a hollow dielectric waveguide. This enables to formulate, among other things, an analogue of optical theorem for such waveguide scattering.

## I. Introduction

In a new technique [1], suggested by the authors to investigate scattering characteristics of physical objects in the near millimeter and submillimeter wave regions, the object under study (or its scale model) is put into a quasi-optical structure in the form of a circular hollow dielectric waveguide (HDW) [2]-[4] so as to measure the scattering parameters of the waveguide fundamental mode  $HE_{11}$  which is certainly related to the wanted scattering characteristics of the investigated object. To ensure the technique, we have to test it on a reference scatterer whose scattering characteristics are well known and can be exactly calculated. One such object is a sphere. Therefore a sphere placed inside a circular HDW is the first we have investigated both theoretically [5] and experimentally [1]. The obtained results agree well with those predicted by Mie theory through a wide range of values of diffraction parameter  $kb = 2\pi b/\lambda$ , where  $b$  is the sphere radius and  $\lambda$  is the wavelength, including resonance area.

In this paper, we intend to establish the relation between the free-space scattering characteristics of a physical object (extinction and backscattering) and those of the same object put in a HDW.

## II. Relation between Scattering Characteristics in Free Space and inside a HDW

Essential characteristics of the free-space plane-wave scattering are extinction cross section  $C_{ext}$  and backscattering cross section  $C_b$ . With the far-field consideration, the extinction cross section is defined in particular as follows [6]

$$C_{ext} = \frac{4\pi}{k^2} \operatorname{Re} \left\{ \left( \mathbf{X} \cdot \mathbf{i}_x \right)_{\theta=0} \right\}, \quad (1)$$

where  $\mathbf{X}$  is the vector of the forward-scattering field amplitude ( $\theta = 0$ ).

Expression (1) is a special formulation of optical theorem. It means that the extinction depends only on the scattered field amplitude in the forward direction without respect of that the scattering occurs everywhere round the scatterer which, in addition, absorbs some electromagnetic power.

The backscattering cross section which is similar to radar cross section (RCS) is defined as [6]

$$C_b = \frac{4\pi}{k^2} \left| \mathbf{X}(180^\circ) \right|^2, \quad (2)$$

where  $\mathbf{X}(180^\circ)$  is the vector of the backward-scattering field amplitude ( $\theta = 180^\circ$ ).

Now we shall define the analogous parameters characterizing the object scattering in a HDW in terms of the waveguide characteristic values. Let an object be placed inside a regular waveguide near its axis chosen to be the  $z$  axis of a Cartesian system as shown in Fig.1. By cross section  $S_1$  and  $S_2$  we separate a waveguide irregularity portion containing the scatterer. Whatever the field within the separated volume  $V$ , the fields at section  $S_1$  and  $S_2$  are the superpositions of the propagating modes fields. So to the right of the irregularity, the scattered field is

$$\begin{aligned} \mathbf{E}^{sc} &= \sum_{m=1}^{\infty} c_m \mathbf{E}_m, \\ \mathbf{H}^{sc} &= \sum_{m=1}^{\infty} c_m \mathbf{H}_m \end{aligned} \quad (\text{for } z > z_2),$$

(3) and to the left

$$\begin{aligned} \mathbf{E}^{sc} &= \sum_{m=1}^{\infty} c_{-m} \mathbf{E}_{-m}, \\ \mathbf{H}^{sc} &= \sum_{m=1}^{\infty} c_{-m} \mathbf{H}_{-m} \end{aligned} \quad (\text{for } z < z_1). \quad (4)$$

The complex amplitudes  $c_m$  and  $c_{-m}$  of these modes are easy to find using Lorenz lemma. A surface  $S$  to enclose

volume  $V$  is chosen as shown in Fig.1, where  $\mathbf{i}_n$  is a normal to surface  $S$ ,  $S_3$  is the scatterer surface, and  $S_0$  is the internal cylindrical surface of the waveguide channel. Since  $V$  is free from current sources, we arrive at the equation

$$\int_{S_0+S_1+S_2+S_3} \{ [\mathbf{E}^{sc} \mathbf{H}_m] - [\mathbf{E}_m \mathbf{H}^{sc}] \} \mathbf{i}_n dS = 0. \quad (5)$$

Since impedance boundary conditions are fulfilled at the HDW internal channel surface [3], [4], the surface integral over  $S_0$  vanishes.

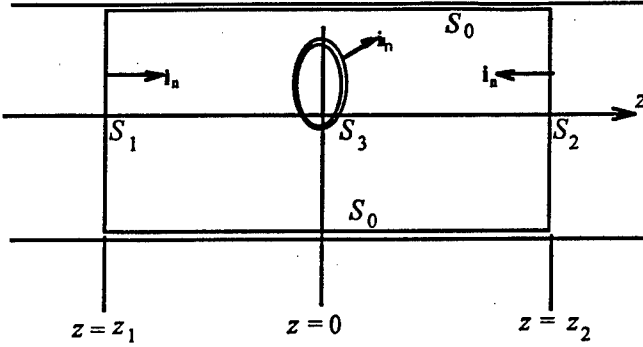


Fig.1

Applying the orthogonality property of guided modes of a HDW one obtains the unknown amplitudes

$$c_{\pm m} = \frac{1}{N_m} \int_{S_3} \{ [\mathbf{E}_{\pm m}^* \mathbf{H}^{sc}] + [\mathbf{E}^{sc} \mathbf{H}_{\pm m}^*] \} \mathbf{i}_n dS. \quad (6)$$

of modes occurring in the object scattering inside the HDW. Here  $N_m$  is the norm of the  $m$ th mode. For simplicity, the waveguide losses are not considered. Comparing (6) with the customary definition of extinction cross section in free space [6] yields the waveguide analog of the extinction cross section

$$C_{ext}^w = \frac{N_l \operatorname{Re} c_{+l}}{2 I_{inc}},$$

(7)

in terms of waveguide parameters. Here  $I_{inc}$  is the maximum intensity of the  $l$ th mode incident on the object,  $c_{+l}$  is the transmission coefficient of this mode. Expression (7) offers the waveguide analog to optical theorem (1) for free space. Besides, expression (7) suggests: if within the volume of a scatterer inserted in a HDW the incident mode behaves as a quasipplane wave and all the repeated reflections from the scatterer surface and waveguide walls are minimized, then using the transmission coefficient of the incident mode, one obtains the scatterer extinction in free space.

Formula (7) correlates the HDW mode transmission coefficient and the plane-wave forward-scattering amplitude in free space as follows

$$X(0^\circ) = \frac{k^2 N_l c_{+l}}{2\pi I_{inc}}.$$

(8)

Using (8), we arrive at a similar relation between the free space backward-scattering amplitude and the waveguide mode reflection coefficient in the form

$$X(180^\circ) = \frac{k^2 N_l c_{-l}}{2\pi I_{inc}}.$$

(9)

Substituting (9) into (2) gives the waveguide backscattering cross section

$$C_b^w = \frac{k^2 N_l^2 |c_{-l}|^2}{\pi I_{inc}^2}.$$

(10)

Formulae (7) and (10) correlate the scattering processes occurring inside a HDW and in free space. Under the proper conditions stated above, these processes are identical.

### III. Conclusion

The presented consideration physically justifies the method of electrodynamic modeling of such scattering characteristics as extinction and backscattering cross sections in the field of HDW fundamental mode under the deduced limits on the scatterer relative size and providing effective filtering from spurious modes and elimination of parasitic repeated reflections from the scatterer surface and HDW channel walls.

### REFERENCES

1. V.K. Kiselyev and T.M. Kushta, "Method for radar cross section measurements in millimeter and submillimeter wave regions," *International J. Infrared Millimeter Waves*, vol.16, no.6, pp.1159-1165, June 1995.
2. E.A.J. Marcatili and R.A. Schmeltzer, "Hollow metallic and dielectric waveguides for long distance optical transmission and lasers," *Bell System Tech. J.*, vol.43, pp.1783-1809, July 1964.
3. C. Dragone, "High-frequency behavior of waveguides with finite surface impedances," *Bell System Tech. J.*, vol.60, no.1, pp.89-115, January 1981.
4. Yu.N. Kazantsev and O.A. Kharlashkin, "Circular waveguides with hollow dielectric channel," *Radio Eng. Electron. Physics*, English translation, vol.29, no.8, pp.78-88, Aug. 1984.
5. V.K. Kiseliyov and T.M. Kushta, "A Spherical Scatterer inside a Circular Hollow Dielectric Waveguide," *International J. Infrared Millimeter Waves*, vol.18, no.1, January 1997.
6. C.F. Bohren, D.R. Huffman, *Absorption and scattering of light by small particles*. New York: John Wiley and Sons, 1986.

## Far Infrared Spectroscopy of the Earth's Stratosphere: Balloon-Based Measurements of Comprehensive HO<sub>x</sub>, NO<sub>x</sub>, and Cl<sub>x</sub> Free Radical Chemistries

Kelly Chance

Harvard-Smithsonian Center for Astrophysics  
60 Garden Street, Cambridge, MA 02138, USA

### Abstract

The Smithsonian Astrophysical Observatory (SAO) far infrared balloon-borne Fourier transform spectrometer, FIRS-2, measures concentration profiles of trace gases in the earth's stratosphere. Measurements are made from altitudes of 36-39 km in the limb geometry using thermal emission from 80 - 1000+ cm<sup>-1</sup>. OH, HO<sub>2</sub>, H<sub>2</sub>O, H<sub>2</sub>O<sub>2</sub>, O<sup>3</sup>P (thermospheric), O<sub>2</sub>, O<sub>3</sub>, HCl, HF, HBr, ClONO<sub>2</sub>, HOCl, CO, CO<sub>2</sub>, N<sub>2</sub>O, NO<sub>2</sub>, N<sub>2</sub>O<sub>5</sub>, HNO<sub>3</sub>, and HCN are currently measured as functions of altitude and time. ClO is measured on some flights using the Jet Propulsion Laboratory Balloon Microwave Limb Sounder, BMLS, or Submillimeterwave Limb Sounder, SLS, flown on the same gondola. This talk briefly describes the instrument and the atmospheric measurements and concentrates on the development of underlying spectroscopy for the prediction and analysis of spectroscopic features, and on conclusions that may be drawn regarding atmospheric photochemistry. Other examples of current problems in the application of spectroscopy to atmospheric measurements will also be briefly described, including the spectroscopic measurement of stratospheric OH from space.

### Introduction

Catalytic destruction of ozone from the HO<sub>x</sub>, Cl<sub>x</sub>, and NO<sub>x</sub> reaction cycles is a central feature of the chemistry of the earth's ozone layer. However, it has been difficult to obtain simultaneous measurements of these radical species and their reservoirs over a range of altitudes. Using balloon-based spectroscopy of the atmospheric thermal emission, we are now able to make simultaneous measurements of HO<sub>x</sub>, Cl<sub>x</sub>, and NO<sub>x</sub> species throughout the middle atmosphere. These observations represent the most comprehensive description yet obtained of the distribution of free radicals and photochemically-related gases involved in catalytic destruction of ozone.

The strength of this type of measurement is the simultaneous observation of a large number of individual species, covering a large range of altitudes in the stratosphere and, for some flights, the full diurnal cycle. The completeness of the data sets provides a basis for examining our understanding of processes that regulate the partitioning of free radicals in the stratosphere. FIRS-2 measurement applications include the following.

- Atmospheric modeling: FIRS-2 determines details of stratospheric photochemistry, improving predictive capability of models.
- Global warming studies: FIRS-2 determines details of the atmospheric radiative properties of greenhouse gases, especially CO<sub>2</sub>.
- Industrial processes: FIRS-2 measures effects of chlorofluorocarbons and halons on the ozone layer.
- Agricultural processes: FIRS-2 measures gaseous by-products of agriculture; nitrous oxide, bromine species resulting from methyl bromide use.

Until this year, the FIRS-2 concentrated on measurements in the regions 80-210 cm<sup>-1</sup> and 350-700 cm<sup>-1</sup>. The major reason for the lack of fuller coverage was the response of the Mylar beam splitter used in the FTS. Beginning with the April, 1997 balloon flight we are employing new coated beam splitter technology to provide both higher efficiency over much of the previously-measured regions and extended coverage (80-1000+ cm<sup>-1</sup>), where the highest measurable wavenumber is now limited by detector efficiency. This improvement should provide for better measurements of, at least, stratospheric NO<sub>2</sub>, ClONO<sub>2</sub> and N<sub>2</sub>O<sub>5</sub>, add CH<sub>4</sub> and several of the CFCs to our measurements suite, and might permit us to measure ClO and NO<sub>3</sub>.

### Balloon Flights

FIRS-2 has now had 10 successful stratospheric balloon flights, from 1987 through 1997. Launches were from Palestine, TX; Ft. Sumner, NM; Daggett, CA; and Ft. Wainwright, AK. Float altitudes are from 36 to 39 km and flight durations from 6 to 24+ hours, depending on the specific mission and complement of atmospheric measuring instruments on board. FIRS-2 is flown on balloon gondolas provided by the NASA Jet Propulsion Laboratory, JPL. Balloon flights with FIRS-2 have included the BMLS, the SLS, an in situ ultraviolet ozone sensor, and the Far Infrared Limb Observing Spectrometer, FILOS (all from JPL), an ultraviolet/visible flux measuring instrument developed by the Max Planck Institute for Chemistry, Atmospheric Chemistry Division, in conjunction with the SAO, and an in situ particle (aerosol) instrument supplied by Nagoya University, Japan.



Flights include validation and correlative measurements for the Upper Atmosphere Research Satellite, UARS (NASA) and the Japanese Advanced Earth Observing Satellite, ADEOS "MIDORI" (NASDA). We also participated in the second NASA Airborne Arctic Stratospheric Experiment, AASE II, where we obtained 140 hours of measurement data on board the NASA DC-8 airborne laboratory, flying into the north polar region and as far south as the equator, during January-March 1992.

### Spectroscopic Development

Precise values for line positions, intensities and pressure broadening coefficients are needed for quantitative analysis of the atmospheric measurements in order to derive atmospheric concentrations. An ongoing laboratory spectroscopy program to support atmospheric measurements is conducted at the National Institute of Standards and Technology, NIST, Boulder. It includes collaboration among NIST, SAO, the University of Oregon, NASA Langley Research Center, and several other institutions. Laboratory measurements are made using the TuFIR method of laser mixing spectroscopy, which provides tunable far infrared radiation of extremely high spectral purity. Measurements include line positions, pressure broadening widths, and relative line intensities. Molecules measured to date include OH, HO<sub>2</sub>, H<sub>2</sub>O, H<sub>2</sub>O<sub>2</sub>, O<sub>2</sub>, O<sub>3</sub>, HCl, HF, HI, and CO.

SAO maintains a publicly-available spectroscopic database for analysis of atmospheric spectra. It includes data available from the HITRAN and the JPL Spectral Line Catalog, plus additional measurements and calculations. Past versions have covered the 10-800 cm<sup>-1</sup> range. Because of our recent extended FIRS-2 spectral coverage, we are currently revising it to include higher frequencies and additional species.

### Conclusions from FIRS-2 Measurements

- We have made the first simultaneous measurement

of HO<sub>x</sub>, Cl<sub>x</sub>, and NO<sub>x</sub> species throughout the middle atmosphere. The relative contributions to ozone destruction from the HO<sub>x</sub>, NO<sub>x</sub>, and Cl<sub>x</sub> catalytic cycles are determined from 20-40 km.

- Comprehensive budgets of NO<sub>y</sub>, and Cl<sub>y</sub> are measured.
- Chlorine budget studies suggest that a small channel exists for production of HCl from ClO + OH and/or ClO + HO<sub>2</sub>, diminishing the effectiveness of the Cl<sub>x</sub> catalytic cycle in the upper stratosphere.
- O<sub>3</sub> formation and loss rates in the upper stratosphere are now shown to be in balance; under-prediction of stratospheric O<sub>3</sub> above 35 km was a long-standing problem.
- OH near 40 km has been under-predicted.
- HBr measurements provide constraint on bromine budget, Br<sub>x</sub> chemistry (in particular, it provides limits to the effectiveness of BrO + HO<sub>2</sub>).
- Closely-coupled chemical relationships in the upper stratosphere have been tested, e.g.

$$[HOCl] = k_1[HO_2][ClO]/(j_{HOCl} + k_2[OH])$$

$$[H_2O_2] = k_3[HO_2]^2/(j_{H_2O_2} + k_4[OH])$$

### Acknowledgements

The FIRS-2 work depends heavily on the contributions of my SAO colleagues, Drs. W. Traub, D. Johnson, and K. Jucks. We are grateful for invaluable support from the Jet Propulsion Laboratory Atmospheric Ballooning Group and the National Scientific Balloon Facility. The research at SAO is supported by NASA grants NSG-5175 and NAGW-1292.

## Pumped Phonons in Atmospheric Aerosols

H. A. Gebbie, P. F. Miller & S. Abend

Department of Chemistry, Imperial College of Science, Technology & Medicine,

South Kensington, London, SW7 2AY, UK

### Abstract

The explanation of what was called anomalous absorption can be found in aerosols in which a pumped phonon mechanism proposed by Fröhlich is operating [1]. Here we present atmospheric and laboratory spectra which show the salient features of the mechanism of enhanced low wavenumber strengths and creation of giant dipoles.

Many anomalous absorption spectra have been reported from measurements in the atmosphere and in the laboratory [2, 3]. For some of these the value of temperature dependence of absorption was also measured since this can help to identify the effective species. These species at one time were thought to be dimeric. This had to be rejected due to the measured temperature dependence being too steep. The fact that the latent heat of evaporation of water is twice the measured binding energy suggested a possible explanation [4] in terms of droplets of small radius, which it was tenuously argued might have transition dipoles. This failed since they were not large enough to be stable at high relative humidity [5]. These efforts however were made before it was shown that anomalies came from non equilibrium conditions created by photon pumping [6]. This implied nonlinearity which clarified many results by showing that emission as well as absorption was to be expected. Further experiments [7, 8] gave results which pointed to aerosols being responsible notably by showing that observations required diffusion coefficients appropriate to them rather than to molecules. This gave impetus to examining Fröhlich's insights about a pumped phonon model (PPM) since this gave the prospect of aerosol sized entities having dipole moments.

Fröhlich's mechanism required that the pumped entities be in isolation and this is met by aerosols which at sea level densities are separated by  $10^4$  times their radii. They can be pumped by photons to acquire giant dipoles which Fröhlich described as being in the manner of a ferroelectric. Their interaction with radiation is greatly enhanced and this explains their ability to be strong absorbers and emitters in the atmosphere as is shown in figure 1. Both spectra show additional structure in absorption and emission from aerosols and the steep rise in emission for wavenumbers less than  $5\text{cm}^{-1}$  in both spectra is notable.

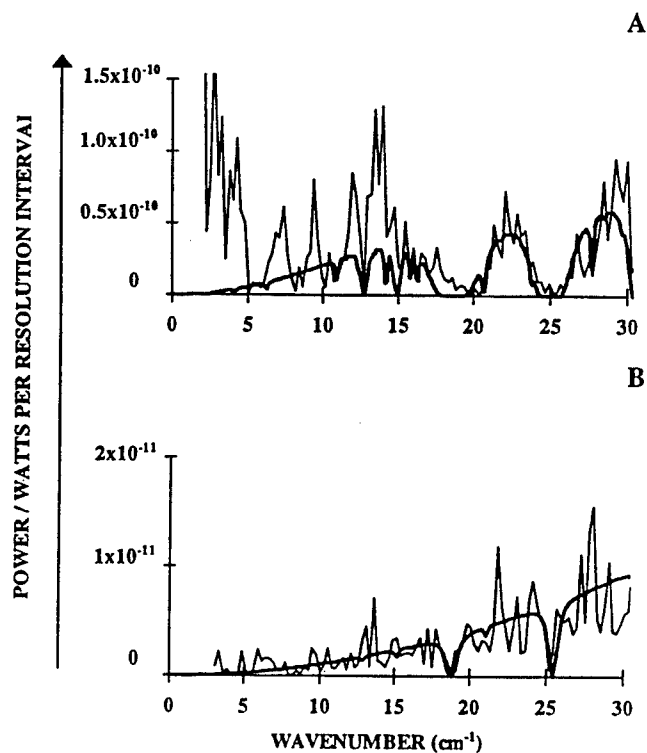


Figure 1

Measured atmospheric spectra with an instrumental resolution of  $0.2\text{cm}^{-1}$  are compared with models of their sources and expected molecular absorption as shown by the thick line. In figure 1A the source was the sun as seen above the HFS Jungfraujoch (altitude 3.5km). In 1B the source was an MB mercury lamp seen through 7.5m path in the laboratory.

In figure 2 a derivation is given from laboratory measurements of the effective dipole moments of aerosols. Their absorption at about  $50\text{cm}^{-1}$  is seen to be comparable with that of a water rotation line at  $47\text{cm}^{-1}$  which has a transition dipole of 1.1 debyes in an air sample containing  $10^{17}\text{cm}^{-3}$  water molecules. If the aerosol concentration [9] is taken as  $10^4\text{cm}^{-3}$  then to order magnitude a transition moment of the order of  $10^6$  debyes can be inferred. A similar value for the dipole moments of aerosols in the upper troposphere can be deduced from a spectrum given in reference [10].

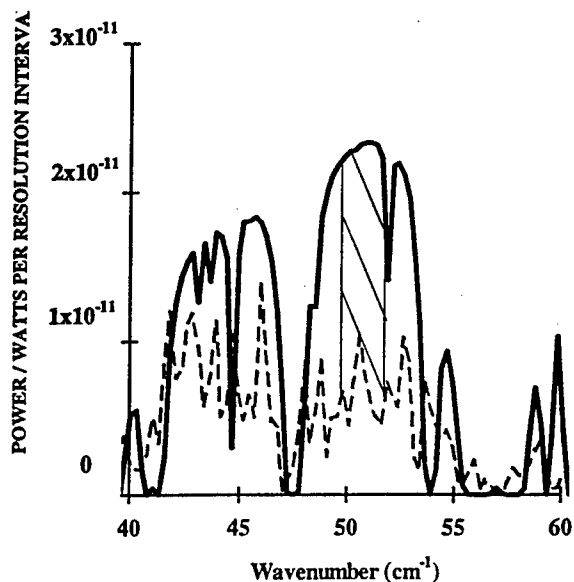


Figure 2

The conditions were as in figure 1B. The model (thick line) shows a transparent region a few wavenumbers wide in the region of  $50\text{cm}^{-1}$  in which measured absorption can be attributed to aerosols. Its area is comparable with that of the water monomer line centred on the  $47\text{cm}^{-1}$  and from this, as discussed in the text, a value of the order of a million debyes for the dipole moment of a single aerosol can be deduced.

The PPM model explains not only the great strength of the anomalies but why their emission increases rapidly with decreasing wavenumber. This is shown by both spectra in figure 1 which are representative of many such measurements. It also prompted a laboratory study [1] in which low wavenumber behaviour was emphasised including the use of monochromatic pumping sources in this wavenumber range. These gave emission spectra with power levels several orders of magnitude higher than those recorded with continuum pumping. Finding that the spectral dependence of the increment at low wavenumbers had the same form at low and high emission strengths suggested that it was a basic property and gave further support to the relevance of the Bose Einstein Condensation mechanism.

In all of the atmospheric and most of the laboratory spectra considered here what is observed is dominated by maser action [11]. The wavenumber range to which this applies depends on the background spectrum available for amplification and is usually that of the pump radiation with any structure becoming conspicuous only when there is adequate instrumental resolution. Maser action is not intrinsic to the PPM but comes from cooperative behaviour between aerosols giving amplification and gain narrowing of their emission lines.

Some valuable evidence for solar pumping at millimetre wavelengths comes from combining the results from two independent aircraft experiments. Nolt et. al. [12] recorded sky emission at 12.5km altitude with only 6 microns of precipitable water overhead. As expected no emission from water lines at  $6.1\text{cm}^{-1}$  and  $10.7\text{cm}^{-1}$  was seen but a feature at about  $8\text{cm}^{-1}$  was well established without however making a distinction between daytime and night-time data. Baluteau et. al. [13] from measurements at the same altitude show a feature at about  $8\text{cm}^{-1}$  which they always observed in daylight but never at night.

Operationally pumped aerosols with their temperature and humidity as important parameters will have to be considered as significant atmospheric absorbers and emitters of millimetre waves.

### Acknowledgements

Support from DRA and MOD is gratefully acknowledged.

### References

1. P.F. Miller and H.A. Gebbie, , *Int. J. IR & MM Waves*, 17(10), 1573 (1996)
2. H.A. Gebbie, *Phys. Rev.*, 107, 1194 (1957)
3. H.A. Gebbie, *Infrared Phys.*, 24, 429 (1984)
4. H.A. Gebbie, *Nature*, 269, 422 (1982)
5. W. Byers Brown and H.A. Gebbie, *Infrared Phys.*, 33, 359 (1992)
6. P. Dias Lalcaca, N.J.C. Packham and H.A. Gebbie, *Infrared Phys.*, 24(5), 437 (1984)
7. P.F. Miller and H.A. Gebbie, *Infrared Phys.*, 34, 23 (1993)
8. P.F. Miller and H.A. Gebbie, *Infrared Phys.*, 34, 143 (1993)
9. H.R. Pruppacher and J.D. Klett, '*Microphysics of Clouds and Precipitation*', D. Reidel, Dordrecht (1978)
10. W.G. Mankin, J.A. Eddy, R.M. MacQueen, R.H. Lee and C.W. Querfield, *Nature Phys. Science*, 245, 8 (1973)
11. H.A. Gebbie and N. Apsley, *Infrared Phys.*, 28, 337 (1988)
12. I.G. Nolt, J.V. Radostitz, R.J. Donnelly and L.P. Stearns, *NOAA Tech. Rpt. ERL406-APCL 44*. May 1979
13. J.P. Baluteau, E. Bussoletti and N. Epchtein, *Nature*, 244, 562 (1973)

## **Infrared Difference Frequency Generation and Application to Trace Gases Monitoring in the Atmosphere**

W. CHEN, J. BURIE, and D. BOUCHER  
Laboratoire de Physicochimie de l'Atmosphère  
Université du Littoral  
145, Route du Pertuis d'Amont, 59140 Dunkerque, France  
e-mail: chen@pca3.univ-littoral.fr

Paper No. #178

As compared with infrared diode laser which requires usually cryogenic temperature operation, room-temperature difference-frequency generation (DFG) based infrared source becomes recently attractive and alternative not only for high-resolution molecular spectroscopy application, but also environmental monitoring application [1-2].

In our continuous-wave DFG experiment, two orthogonally polarized optical laser beams were combined by use of a polarization prism and collinearly focused by a  $f=350$  mm lens into an  $\text{AgGaS}_2$  crystal operated at room temperature. A germanium filter was used to separate generated infrared light from the laser beams. The infrared radiation, continuously tunable from 3.8 to 6.5  $\mu\text{m}$  under type I  $90^\circ$  noncritical phase-matching condition, was detected by a liquid-nitrogen-cooled  $\text{HgCdTe}$  infrared detector. Configuration of two Ti:Sapphire solid-state lasers was used to cover the 3.8-4.5  $\mu\text{m}$  region [3], and DCM dye and Ti:Sapphire lasers configuration used for the 4.6-6.5  $\mu\text{m}$  spectral domain [4]. By pumping the crystal with about 300 mW total laser power, the generated infrared power was in the range of several tens of microwatts.

Significant improvement in optical coupling system has been achieved based on Gaussian beam optical design consideration. Laser beam waists focused inside the crystal were frequency-independently overlapped. Compromise between maximum laser intensities and maximal laser beam interaction coupling in the crystal was taken into account to optimize optical parametric frequency down-conversion efficiency.

This improvement leads to an increase in generated infrared power roughly three times higher than that generated using a conventional optical design system.

Monitoring of water vapor [5] and carbon dioxide (CO<sub>2</sub>) traces in air has been performed using spectroscopic detection over the 0.5-m open laboratory path between the crystal and the detector. A new numerical treatment processing approach has been developed for atmospheric sensing application in order to extract spectral signals drowned in a background structure due to phase-mismatching and etalon interference fringes effects.

#### References

- [1] P. Canarelli, Z. Benko, R. F. Curl, and F. K. Tittel, "Continuous-wave infrared laser spectrometer based on difference frequency generation in AgGaS<sub>2</sub> for high-resolution spectroscopy", *J. Opt. Soc. Am.*, **B9**, 197, (1992)
- [2] Th. Töpfer, K. P. Petrov, Y. Mine, R. F. Curl, and F. K. Tittel, "Room temperature mid-infrared laser sensor for trace gas detection", submitted to *Appl. Opt.* (January 1997)
- [3] in preparation
- [4] W. Chen, J. Burie, and D. Boucher, "Midinfrared cw difference-frequency generation using a synchronous scanning technique for continuous tuning of the full spectral region from 4.7 to 6.5  $\mu\text{m}$ ", *Rev. Sci. Instrum.*, **67**, 3411, (1996)
- [5] J. Burie, C. Przygodzki, H. Delbarre, W. Chen, and D. Boucher, "Difference-frequency mixing based infrared generation and application to the water vapor trace monitoring near 1844  $\text{cm}^{-1}$ ", submitted to *J. Phys. III* (April 1997)

# Liquid Water Fade Margin Requirements for Infrared and Millimeter Wave Runaway Imaging Sensors in Fog

Robert E. Marshall

Research Triangle Institute

One Enterprise Parkway, Hampton, VA 23666, USA

marshall@rti.org

David deWolf and Christos Kontogeorgakis

Bradley Department of Electrical Engineering

Virginia Polytechnic Institute and State University

## Abstract

Particle size distribution at each 10 meters in the vertical for an advection and a radiation fog are analyzed to determine liquid water loss for millimeter and infrared wavelengths along a 3 degree glideslope. Fog drops size distributions in both fog layers are well fitted to a gamma distribution. The radiation fog imposes minimal fade margin requirements on millimeter wave imaging systems, however, one way fog attenuation along the glideslope for the advection fog is in the 1 to 6 dB range for the millimeter wave spectrum. Infrared fade margin requirements for both fog layers are two orders of magnitude greater than for millimeter waves.

## Introduction

Infrared and millimeter wave runway imaging sensors have recently been proposed as means for landing and taxiing aircraft in fog, [1, 2]. Fade margin may be defined as the excess clear air system signal to noise ratio required to insure adequate image quality when the path between the imaging sensor and the scene is populated with liquid or frozen water. This paper focuses on IR and millimeter wave fade margin requirements for a shallow radiation fog and a deep advection fog [3].

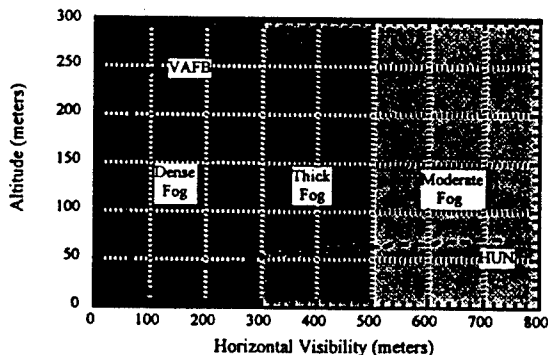


Figure 1: Horizontal visibility as a function of height in the Vandenberg, AFB and Huntington, WV fog layers.

Figure 1 represents the horizontal visibility for the radiation fog recorded at Huntington, WV (HUN) and the advection fog documented at Vandenberg, AFB, CA (VAFB). A forward scattering spectrometer, liquid water content (LWC), and temperature sensor were on board a Gulfstream II aircraft as it landed in fog along a 3 degree glideslope. Fog particle size data analyzed in this paper were averaged at each ten meters in the vertical over six landings at VAFB and two landings at HUN. 3-5 $\mu$ m and 8.6mm imaging sensors were on board to facilitate landing in the low visibility fog layers. Only the 8.6mm system obtained a runway image suitable for landing in either fog layer.

Figure 2 is a schematic representation of a runway and a 3 degree glideslope immersed in fog. IR and millimeter wave fade margin predictions are calculated from the current aircraft position along the glideslope to the touchdown point. Fade margin is then displayed in dB as a function of aircraft height above the runway.

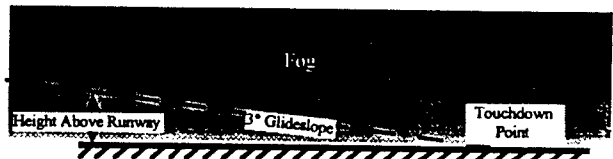


Figure 2: Geometry used to calculate fade margin

## Fog Layer Modeling

The particle size data taken for both fog layers were collected in 3 $\mu$ m bins from diameters of 2  $\mu$ m to 47  $\mu$ m and well fit to a gamma size distribution given in Equation 1.

$$n(z,D) = \alpha(z) D^4 \exp(-\beta D) \quad (1)$$

$n$   $\equiv$  fog drop number concentration

$z$   $\equiv$  vertical distance from surface

$D$   $\equiv$  fog drop diameter

$\alpha$   $\equiv$  vertical fit parameter

A regression analysis for  $\beta$  from (1) in both the VAFB and HUN fogs found a weak dependence on  $z$  with values of  $0.445 \pm 0.015$  and  $0.463 \pm 0.06$  respectively. The vertical fit parameters  $\alpha$  from (1) are given in Equations 2 and 3.

$$\text{VAFB: } \alpha(z) \approx 2.377 \times 10^4 + 5026.9 z - 19.614 z^2 \quad (2)$$

$$\text{HUN: } \alpha(z) \approx 24710 z^{1.3} \exp(-0.066z) \quad (3)$$

Equation 4 predicts the attenuation due to fog in dB along a slant path of angle  $\theta$ .

$$S_i(z) = 8.686 \frac{2\pi}{k \sin \theta} \int_0^z d\zeta \int n(\zeta, D) f(k, D, \mu) dD \quad (4)$$

$k \equiv$  wave number

$f(k, d, U) \equiv$  imaginary part of forward scattering Mie coefficient

$\mu \equiv$  refractive index of fog drop

Calculations of the Mie coefficient are accomplished by means of a subroutine adapted from Bohren and Huffman[4]. A significant difficulty at the IR wavelengths is the prediction of the refractive index of water drops and we have used the piecewise expressions of Ray [5] to do so. Combining (1), (2), and (3) with (4) and adding a factor of 1/30 to convert to a 1  $\mu\text{m}$  bin and a 1 meter vertical resolution yields Equations 5 and 6 for slant path attenuation in the VAFB and HUN fog layers respectively.

$$S_i(z) = \frac{8.686}{30} (2.377 \times 10^4 z + 5.027 \times 10^3 z^2 - 19.614 z^3) \frac{2\pi}{k \sin \theta} \int D^4 e^{-\beta D} f(k, D, \mu) dD \quad \text{VAFB} \quad (5)$$

Figure 3 represents the one way fade margin predictions from (5) for the VAFB fog. The fade margin requirements at 8.6 mm (35 GHz) and 6.8 mm (44 GHz) are of little system engineering concern, however, the 5.4dB fade margin prediction at 3.2 mm (95 GHz) must be considered when evaluating an imaging sensor design. The far infrared shows slight improvement over the near infrared but the IR fade margin requirements are two orders of magnitude above those predicted for millimeter waves.

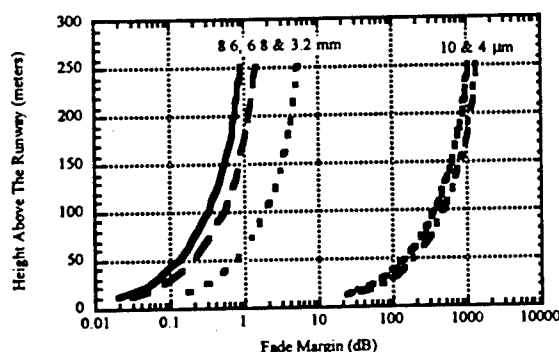


Figure 3: Millimeter wave and IR fade margin predictions for the VAFB fog.

$$S_i(z) = \frac{8.686}{30} (2.471 \times 10^4 z^{4/3} e^{-0.066z}) \frac{2\pi}{k \sin \theta} \int D^4 e^{-\beta D} f(k, D, \mu) dD \quad \text{HUN} \quad (6)$$

The one way fade margin predictions for HUN are given in Figure 4 and indicate a negligible impact on millimeter wave imaging systems but significant losses at the IR wavelengths.

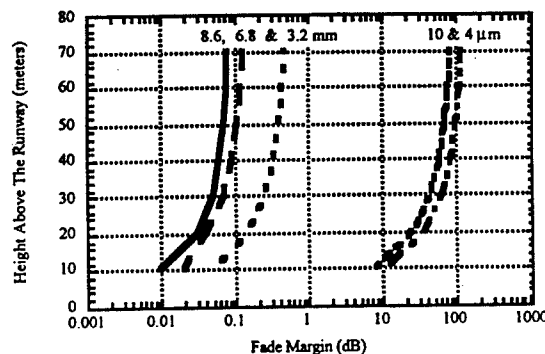


Figure 4: Millimeter wave and IR fade margin predictions for the HUN fog.

## Conclusions

Liquid water fade margin requirements for millimeter wave runway imaging sensors become more significant as wavelength decreases and the depth and LWC of the fog layer increases. Infrared runway imaging sensors will experience severe liquid water losses even in shallow radiation fog.

## References

- [1] Burgess, M. A. et al, "Synthetic Vision Technology Demonstration" Final Report DOT/FAA/RD-93/40, I, Synthetic Vision Program Office, Federal Aviation Administration, Washington, D. C., 1993
- [2] Burgess, M. A. and R. D. Hayes, "Synthetic Vision- A View in the Fog", IEEE 11th Digital Avionics System Conference, Seattle, Washington, October 5-8, 1992.
- [3] Zak, J. A., "Drop Size Distributions and Related Properties of Fog for Five Locations Measured from Aircraft", NASA Contractor Report 4585, DOT/FAA/CT-94/02, April, 1994.
- [4] Bohren C.F. and D. R. Huffman, *Absorption and Scattering of Light Particles*, J. Wiley & Sons, New York, 1983.
- [5] Ray P., *Broadband Complex Refractive Indices of Ice and Water*, Appl. Optics 11, pp. 1836-1844, 1972.

This work was funded under NASA contract NAS1-18925

## Far Infrared and Millimeter Waves Detectors for Astrophysics

P.L. Richards

Department of Physics, University of California  
and Materials Sciences Division, Lawrence Berkeley National Laboratory  
Berkeley, California 94720, U.S.A.

## Abstract

Important astrophysical experiments at far infrared and millimeter wavelengths require receivers of extremely high sensitivity. These requirements have driven the development of sensitive direct detectors and heterodyne mixers over the past 30 years. This development will be reviewed with attention to the kinds of astrophysics being done and to the physical principles of receiver operation. Direct detectors discussed will include the Ge:Ga photoconductive detectors, composite bolometers with metal film absorbers and doped semi-conducting thermistors and the voltage-biased superconducting bolometer which shows promise for future applications. The evolution of heterodyne mixers from the Schottky barrier diode to the SIS quasiparticle mixer to hot electron bolometric mixers will also be described.

## A. Introduction

Most of the electromagnetic energy in the universe falls in the range from far infrared to millimeter wavelengths. The dominant contribution is the cosmic microwave background (CMB) which has the spectrum of a 2.73K blackbody with a peak at  $\sim 2$  mm. This radiation was in thermodynamic equilibrium with the matter in the universe at a time when that matter was a hot ionized plasma. As the universe expanded and cooled, electrons and protons combined to form hydrogen and the plasma disappeared. The background radiation that we see today has been propagating freely through the essentially transparent universe since that time and has been Doppler shifted to microwave frequencies. It contains detailed information about the state of the universe at the time of recombination when the plasma disappeared. Studies of the spectrum and anisotropy of this radiation have strongly driven the development of bolometric direct detectors at millimeter and submillimeter wavelengths.

Galaxies like the Milky Way contain large quantities of dust which is heated by starlight to temperatures of order 20 K. The thermal radiation from this warm dust provides the second strongest contribution to the electromagnetic energy density of the universe. It is stronger than the microwave background inside galaxies,

but much weaker in the vast regions of intergalactic space. The spectrum of dust emission is that of a 20 K blackbody modified by a small emissivity which varies as frequency squared. Consequently, the peak occurs at  $\sim 100$   $\mu$ m. The need to study this galactic dust emission has driven the development of the gallium doped germanium photoconductor and the stressed gallium doped germanium photoconductor which provide very high sensitivity at far infrared wavelengths from 50 to 200  $\mu$ m. It has also driven the development of bolometers for far infrared wavelengths.

The second important galactic contribution to the far infrared and millimeter wave energy of the universe comes from galactic gas clouds. The temperature of this gas is similar to that of the dust. Its emissivity can be much larger than the dust, but only at the frequencies of atomic and molecular transitions. Consequently, the far infrared and millimeter wave spectra of galaxies are composed of a thermal dust continuum on which atomic and molecular emission lines are superimposed. Observations of these lines can produce a wealth of detailed information about the physics and chemistry of galactic gas. These scientific opportunities have driven the development of high frequency Schottky diode mixers, SIS quasiparticle heterodyne mixers, and hot electron bolometric mixers. Direct detectors such as the stressed germanium photoconductor have played an important role at far infrared wavelengths.

Two types of receiver are used in the far infrared millimeter wave band. For low frequencies and narrow bandwidths, the best sensitivity is obtained by using a device technically known as a phase conserving linear photon amplifier. Examples of importance for astrophysics include high electron mobility transistor (HEMT) amplifiers and heterodyne mixers (which produce more photons at the intermediate frequency than are absorbed at the signal frequency). Since the phase is conserved, there is a quantum uncertainty of  $\pm 1$  in the number of photons in the receiver on a time scale equal to the inverse of the bandwidth. At higher frequencies and for experiments which can make use of wider bandwidths,



this quantum noise becomes a severe limitation. Better sensitivity is obtained using direct detectors such as photoconductors and bolometers. Since direct detectors do not conserve phase there is no quantum noise. In practice for the ~20% bandwidths used for photometry, the crossover between these approaches occurs at mm wavelengths. For a resolution of  $10^{-5}$ , used for spectroscopy, the crossover is near  $10\mu\text{m}$ . Direct detectors can in principle count individual photons. The photon rate for sources at far infrared to millimeter wavelengths, however, is typically far too high. The ideal direct detector, therefore, is limited only by random fluctuations in the rate of arrival of signal photons at the detector.

Astronomical receivers do not have information about the phase of the radiation source. Consequently, they all incorporate direct detection at some stage. For example, a heterodyne downconverter is followed by a diode detector or a correlator. In a photoconductive or bolometric receiver the direct detection is at the front end. It is an unfortunate fact that each type of receiver is supported by a community whose terminology is not always compatible with other receiver types. The word detector is used to describe very different devices which convert electromagnetic wave energy to a steady state output. Examples include "lock-in or homodyne detector", "heterodyne detector", "HEMT detector", "photon detector", etc. Given this wide range of usages in our wavelength range, it is best to use the more explicit term direct detector when describing the conversion of incident power or photon rate to output voltage or current. A heterodyne downconverter produces a difference frequency which results from the product of the incident electric field with that from a local oscillator. There is no confusion about the meaning of linear amplifier. In each case, the name is for a function, not for a device. In some cases, the same device can be used for more than one function.

Linear photon amplifiers are given a variety of names, some of which are misleading. The name coherent receiver is frequently used to emphasize that such systems often have narrow frequency bandwidths and respond only to one spatial electromagnetic mode. The usefulness of this distinction is blurred, however, because modern photon amplifiers can have quite wide fractional bandwidths and direct detectors are often used with narrow band filters and with diffraction limited optical systems which limit the throughput to a single spatial mode.

The sensitivity of infrared receivers with moderate and broad bandwidths is often limited by background radiation arising from sources other than the signal. For example the background can cause excess noise in photoconductors. Also, the responsivity of bolometers must be reduced to avoid saturation by this background. In all cases, the

photon noise from the background is superimposed on the signal. A primary goal in all astronomical observations is to reduce the excess backgrounds to an absolute minimum. This is done by observing from mountain top, aircraft, balloon, and space platforms, sometimes with cooled optics. This paper will focus primarily on the performance of astronomical detectors at the lowest achievable backgrounds.

## B. Direct Detectors

The far infrared photoconductive detectors developed for the Space Infrared Telescope Facility (SIRTF) are the most advanced yet developed for low background conditions. These devices are called photon detectors because the current from a carrier excited into a band is measured before the carrier is thermalized. SIRTF is a pointed NASA infrared space instrument with a superfluid He cooled telescope which is scheduled for flight in 2002. One primary goal of SIRTF will be to do deep infrared surveys using direct photon detectors on wavelength bands centered at 12, 30, 70 and  $160\mu\text{m}$ . The number and size of detectors is selected to obtain the highest resolution on the sky consistent with the 85 cm primary mirror diameter, and to simultaneously produce maps with the same sky coverage in each band which are limited only by unavoidable astrophysical backgrounds. In the far infrared, for example, the noise level will be low enough that the maps will be limited by confusion arising from multiple sources in each pixel.

The  $70\mu\text{m}$  band on SIRTF uses Ge:Ga chips produced at Berkeley. The  $32 \times 32$  square array of these detectors has been designed, assembled and tested at the Steward Observatory in Arizona. The  $160\mu\text{m}$  band uses Ge:Ga detector chips under uniaxial stress in a  $2 \times 20$  detector close backed array. Important features of these arrays include the optimally doped very low compensation Ge, ion implanted contacts, and a readout that makes use of low temperature charge integration amplifiers and a silicon multiplexer. Performance characteristics [1] are very good. In the two bands, dark currents are approximately 100 and 300 e/s, detective quantum efficiencies are 10 and 5% and the read noise is  $\sim 30e$ . In a typical 10s observation the rms noise is  $\sim 100e$ , giving NEP of 4 and  $24 \times 10^{-18} \text{ W}/\sqrt{\text{Hz}}$ .

As originally conceived, SIRTF was to include a four bolometer array for a band at  $300\mu\text{m}$  and a single bolometer at  $700\mu\text{m}$ . In order to achieve the sensitivity required to reach the confusion limit in these bands, it was necessary to cool the detectors to 100 mK. An adiabatic demagnetization refrigerator was developed at Berkeley and many space qualification issues successfully addressed [2] before the SIRTF project was descope and the long wavelength bands were removed to reduce costs.

Many astrophysical projects would profit from sensitive photon detectors at longer wavelengths than 200  $\mu\text{m}$ . A number of semiconductor systems have low enough excitation energy to be candidates. None, however, have the material quality necessary to achieve astronomically interesting performance in low backgrounds. Current work on Ge BIB detectors and on ultrapure GaAs appears promising for the future. Long wavelength photon detectors require low temperatures to avoid thermally generated dark current. The temperature for the SIRT 160  $\mu\text{m}$  band is  $\sim 1.5\text{K}$ . Photon detectors for a  $\sim 500\text{ }\mu\text{m}$  band, therefore would require cooling to 500 mK, and would have no cooling advantage over  $^3\text{He}$  cooled bolometers.

The most sensitive direct detectors for wavelengths longer than 200  $\mu\text{m}$  are bolometers cooled to 300 mK with  $^3\text{He}$  or to 100 mK by an adiabatic demagnetization or a dilution refrigerator [3]. A bolometer is a thermal detector in which the energy of the absorbed photon is thermalized before the resulting temperature rise is detected by a thermistor. Bolometers have been highly developed for measurements of the anisotropy of the cosmic microwave background. They frequently use neutron transmutation doped germanium thermistors from Berkeley mounted on a dielectric substrate which is coated with a metal film absorber. In the microwave background application where backgrounds are low and bandwidths of 20% can be used, such bolometric receivers provide the highest available sensitivity for wavelengths out to 1 cm (30 GHz) where their sensitivity is equal to that of cooled HEMT receivers. Of particular interest is the spider web bolometer developed at Caltech. In this case, the dielectric substrate is a metalized  $\text{Si}_3\text{N}_4$  membrane in the shape of an orb spider web with 98% open space. The holes are small compared to the wavelength so the millimeter wave absorptivity can be comparable to that for a continuous metal film. The cross section for cosmic rays, however, is very small. Using multilayer metal mesh bandpass filters, such bolometers can achieve photon noise limited performance on the microwave background photons alone [4].

A large number of millimeter and submillimeter wave experiments have been done to extract the important cosmological information that is available from the microwave background radiation. The FIRAS experiment on the Cosmic Background Explorer Satellite used a composite bolometer and a polarizing interferometer to make an extraordinarily precise measurement of the CMB spectrum. The DMR experiment on COBE demonstrated that fluctuations exist in the CMB on angular scales near  $10^\circ$ . Balloon-based bolometric experiments and ground based experiments using HEMT receivers have detected fluctuations in the microwave background on

angular scales down to  $0.1^\circ$ . A new generation of experiments is coming on line. The most powerful combine bolometric arrays with long duration ballooning from Antarctica and HEMT-based radio interferometers sited in the Canary Islands, Chile and Antarctica. The spider bolometers operated at 100 mK on the MAXIMA experiment, for example, have  $\text{NEP} < 2 \times 10^{-17} \text{ W}/\sqrt{\text{Hz}}$  at wavelengths of 2 mm.

A recent report by the National Academy of Sciences has recommended that the highest scientific priority in astrophysics be given to the determination of the geometry, size, and material content of the universe from studies of the CMB. NASA has selected the Midex mission MAP, which will be launched in 2001. It uses HEMT amplifiers to survey the anisotropy of the cosmic microwave background. The European Space Agency has selected the PLANCK Explorer spacecraft as a mid-size mission for CMB anisotropy studies using both HEMTs and bolometers. The baseline design includes spider bolometers with neutron transmutation doped germanium thermistors cooled to 100 mK by a dilution refrigerator. The target date for the PLANCK explorer is 2005.

When using low background bolometers, there is often a tradeoff between sensitivity and the required speed. A new technical development promises to increase the speed of bolometers with no sacrifice in sensitivity. Superconducting transition edge bolometers have been discussed since the 1940's but rarely used because bias current must be maintained low to prevent thermal instability. The new approach [5] is to bias the bolometers with a constant voltage and read out the current with a SQUID amplifier. The electro-thermal feedback is then negative and can have an effective gain of several hundred. The bolometer thus operates as a null detector with feedback holding the temperature constant. A far infrared or millimeter wave bolometer with a voltage-biased superconducting thermistor has a number of advantages over bolometers using doped semiconducting thermistors. The speed of response is increased by a factor equal to the effective feedback gain, which can be several hundred. The detector is very linear with a current responsivity equal to the inverse of the bias voltage. The thermistors can be produced by thin film deposition and optical lithography. SQUID amplifiers can operate at low temperatures close to the bolometer, and have very low power dissipation. Their noise is well understood and is low enough for bolometer applications both in the white noise and inverse frequency noise regimes. It may prove possible to make multiplexers using superconducting switching techniques.

### C. Heterodyne Mixers

Heterodyne downconverters using Schottky barrier diodes in waveguide structures have played an important role in

radio astronomy at ever decreasing wavelengths. Receivers based on these mixers were highly developed at millimeter wavelengths for molecular line radio astronomy. The superconductor-insulator-superconductor (SIS) quasiparticle heterodyne mixer has largely replaced the Schottky diode for wavelengths near 1 mm. It provides lower noise, a lithographed planar construction, and a smaller local oscillator power requirement. Receivers based on SIS mixers with both waveguide and planar antenna configurations give double sideband noise temperature approximately 10 times the quantum limit  $T_N = h\nu/k$  for frequencies up to the bandgap of the superconducting niobium used for the tunnel junction [6]. Efforts are being made to extend the range of SIS mixers using superconductors with larger bandgaps. Much attention has been given recently to a hot electron bolometric heterodyne downconverter. The device is a very small thin film superconducting microbridge which is designed to cool very rapidly by hot particle diffusion from the bridge into the surrounding metal film. The response speed is fast enough to make heterodyne downconverters with gigahertz of bandwidth. At the present state of development, the noise in receivers made with hot electron bolometric mixers is ~20 times the quantum limit, so these devices do not supplant the SIS mixer. They are very promising, however, for frequencies above the limits set by the superconducting energy gap.

Millimeter and submillimeter wavelength heterodyne receivers are used for molecular line astronomy through atmospheric windows from high ground-based sites and from airborne observatories such as the NASA's KAO and the forthcoming SOPHIA. NASA has considered space observatories for this type of astronomy including the Large Deployable Reflector and the Submillimeter Explorer, but neither has been selected. The European Space Agency has selected the FIRST cornerstone mission with a launch target of 2005. This mission is designed around bolometers for continuum observations and large numbers of heterodyne downconverters for molecular line studies.

## Acknowledgments

Much of the work on the detectors described here has been done by persons who at one time or another have been students, postdocs or collaborators of the author. Stimulating interactions with them are gratefully acknowledged. This work was supported in part by the Director, Office of Energy Research, Office of Basic Energy Sciences, Materials Sciences Division of the U. S. Department of Energy under Contract No. DE-AC03-76SF00098.

## References

1. E.T. Young, M. Scutero, G.H. Rieke, E.E. Haller, and J.W. Beeman, "High Performance Ge:Ga Arrays for the Far Infrared", in Infrared Detector and Instrumentation, A.M. Fowler editor, SPIE Proc. 1946, 376 (1993).
2. C. Hagmann and P.L. Richards, "Adiabatic Demagnetization Refrigerators for Small Laboratory Experiments and Space Astronomy," Cryogenics 35, 303 (1995).
3. P.L. Richards, "Bolometers for Infrared and Millimeter Waves," J. Appl. Phys. 76, 1 (1994).
4. A.E. Lange, S.E. Church, P.D. Mauskopf, V. Hristov, J.J. Bock, H.M. DelCastillo, J. Beeman, P.A.R. Ade, and M.J. Griffin, "Bolometric Detector Systems for IR and mm-Wave Space Astronomy," Proc. 30th ESLAB Symposium ESA SP-388, 105 (1996).
5. A.T. Lee, P.L. Richards, S.-W. Nam, B. Cabrera, and K.D. Irwin, "A Superconducting Bolometer with Strong Electrothermal Feedback," Appl. Phys. Lett. 69, 1801 (1996).
6. M. Bin, M.C. Gaidis, J. Zmuidzinas, T.G. Phillips, and H. LeDuc, "Quasi-Optical SIS Mixers with Normal Metal Tuning Structures," IEEE Trans. on Appl. Superconductivity (1997) in press.
7. B.S. Karasik, M.C. Gaidis, W.R. McGrath, B. Bumble, and H. LeDuc, "A Low-Noise 2.5 THz Superconductive Nb Hot-Electron Mixer," IEEE Trans. on Appl. Superconductivity (1997) in press.

## RELATIVISM IN MICROWAVE ELECTRONICS

(plenary talk)

M.I. Petelin

Institute of Applied Physics, Russian Academy of Sciences,  
Nizhniy Novgorod, Russia

In the philosophy (assumed to be the science of all sciences) the relativism recommends that all values should be measured relative to other ones. In the physics the relativism recommends to measure observable values relative to reference ones being most natural for a concrete situation. In the classical electronics the most natural reference values are the electron charge  $e$ , the electron mass  $m$  and the light velocity  $c$ ; their combinations producing the \*absolute electron voltage\*  $U_e = mc^2/e = 0.5$  MV, the \*absolute electron current\*  $I_e = mc^3/e = 17$  kA and the \*absolute electron power\*  $P_e = I_e U_e = 8.5$  GW. In the classical microwave electronics, if the operating voltage  $U$  of a radiation source is small compared with  $U_e$ , the electron velocity  $v$  is small compared with the light velocity ( $v \ll c$ ). In this non-relativistic domain, where the microwave electronics dwelled monopolically for a half a century, the now famous klystron, magnetron, TWT and their close relatives were conceived. That golden age of the classical microwave electronics was interrupted with advent of quantum masers (later lasers) and solid state sources (transistors et al), and now the classical electron devices make sense, only if producing sufficiently high powers accessible only at relatively high operating voltages. When, with the rise of voltage, the velocity of electrons becomes commensurable with that of the light, their dynamics becomes governed by relativistic laws accompanied with a number of favorable consequences. One of them, namely the gyro-frequency dependence on the electron energy, is used in the cyclotron resonance masers, providing the prevalence of stimulated radiation over absorption. Now the most efficient version of the cyclotron resonance masers, namely the gyrotron, delivers relatively high powers at millimeter and submillimeter waves. Another favorable effect at the relatively high electron energies is the relativistic-Doppler up-conversion of the radiation frequency, which at  $U \gg U_e$  is  $(U/U_e)^2$  times higher relative to the frequency of electron oscillations in the focusing macroscopic field. Due to this effect, the classical generators of coherent electromagnetic radiation have penetrated into relatively high frequencies: up to the UV band. As for the microwaves being more traditional for the classical Cherenkov electronics, here, due to relativistic effects, the power  $P$  of coherent radiation sources has become commensurable with the  $P_e$  (in the pulse regime), the operating currents  $I$  being commensurable with the  $I_e$ . It is important that the growth of  $P/P_e$  is being provided with growth of not only  $U/U_e$ , but of another independent parameter as well, namely of the relative cross dimension  $R/\lambda$  of the microwave interaction space, where  $\lambda$  is the free space wave length and  $R$  is, e.g., the inner radius of the device. Note, however, that the interaction space expansion is possible, only if, using proper methods of mode selection, the output radiation is kept coherent, because most of consumers do not need non-coherent one. From the last viewpoint it seems likely that one of the first officially registered relativists, Protagoras, was not quite wrong with his dictum: \*Man is the measure of all things\*.

## Long-pulse operation of 110-GHz 1-MW Gyrotron

V.E. Myasnikov, M.V. Agapova, V.V. Alikaev, A.A. Bogdashov, A.A. Borschegovsky, G.G. Denisov, V.A. Flyagin, A.Sh. Fix, V.I. Ilyin, V.N. Ilyin, V.A. Khmara, D.V. Khmara, A.N. Kostyna, V.O. Nichiporenko, L.G. Popov, V.E. Zapevalov

GYCOM Ltd., 46 Ulianov St., Nizhny Novgorod, 603600, RUSSIA

### Abstract

110 GHz gyrotron with an output power of 1 MW was developed and its parameters were measured at pulse duration range from 1 s to 10 s. Gyrotron has a traditional configuration with built-in converter of operating mode  $TE_{19,5}$  to wave beam of optimized power density distribution over the output window surface. A boron nitride single disk was used for the gyrotron output window. Maximal window temperature was limited at the level of 950 °C. The gyrotron collector was equipped with additional solenoid scanning an electron beam along the collector.

The gyrotron output power was of 900 kW at 2 s pulses, of 500 kW at 5 s pulses and of 350 kW at 10 s pulses.

The gyrotron was produced within the frame of the contract between Gycom Ltd. and CCFM, Canada.

### Gyrotron design

The gyrotron design in its main subunits is similar to that one used for the gyrotron which was developed before [1] and shipped to GA, San Diego, USA.

The electron-optical system is designed for a beam voltage of 80 kV and a beam current up to 40 A. The electron velocity spread is less than 20 %. The impregnated metal-porous emitter with the maximal current density of not more than 4 A/cm<sup>2</sup> is used. Measured value of the emission current inhomogeneity is discovered to be within  $\pm 10$  %. The calculated velocity ratio is of 1.3 in the operating regimes.

Cavity specific losses of the  $TE_{19,5}$  operating mode are about 2 kW/cm<sup>2</sup> at 1 MW output power. Cavity cooling system allow to have losses value up to 3 kW/cm<sup>2</sup> at inner wall maximal temperature not more than 250 °C.

The built-in converter of the operating mode in the wave beam includes a visor of the optimized shape and three mirrors. The last mirror has a nonquadric shape. It forms the output radiation with the relatively uniform distribution over the output window. The calculated  $TEM_{00}$  mode contents is of 85-89 % with internal 6-7% and external 5-6% diffraction losses.

The gyrotron collector has the average diameter of 240 mm and the length of about 800 mm. Due to the use of the additional sweeping current solenoid the electron beam is spread over the surface of about 5000 cm<sup>2</sup> at the average heat load of 0.5 kW/cm<sup>2</sup> and the inner surface maximal temperature of 260 °C. The water flow rate in the collector cooling circuit is of 1200 l/min at the pressure of 3 bar.

The collector and the cavity heat transfer constants are less than 1.5 s.

The gyrotron potential capability to operate with the longer pulses is limited basically with the output window features. For the BN disc of 130 mm diameter, which was used for output window in this tube,  $\tan \delta \sim 1.1 \cdot 10^{-3}$ , window losses total value is about 4%. The window maximal temperature in any case has not to exceed the level of 950 °C because the higher temperature can lead at the normal conditions to non-reversible changes of the output window parameters. To check the window temperature surface distribution and its maximal value the special diagnostic equipment and measuring method were developed.

### Testing Results

The results of the two gyrotrons long-pulse testing are presented below. Gyrotron output power during the test was absorbed by the brick load. Output power was calculated from the measured values of the window absorbed power and the window losses coefficient.

Table 1. Gyrotron fundamental parameters at 2 s and 5 s pulse length.

Pulse duration, s	2	5
Frequency, GHz	109.76	109.92
Total output power, MW	0.83	0.37
RF power in the $TEM_{00}$ mode, MW	0.7	0.32
Efficiency, %	37	30
Beam voltage, kV	69.5	60
Beam current, A	27.3	18.1

The gyrotron output power as a function of beam voltage at pulse duration of 2 s is shown in the Fig. 1.

For one of the two tested gyrotrons the regimes of its operation at longer pulses (up to 10 s) were investigated, as it was done before for 140 GHz gyrotron [2]. During this experiments maximal window temperature was checked and window temperature surface distribution was measured by

means of the infrared camera. In the Fig. 2 gyrotron output power is plotted against pulse duration at window different maximal temperatures. The admissible limit of  $900^{\circ}\text{C}$  for the window maximal temperature was set in this experiment. Measured values of the output power at maximal window temperature of  $(850-870)^{\circ}\text{C}$  were: 850 kW with 2 s pulse, 520 kW with 5 s pulse, 410 kW with 7 s pulse and 350 kW with 10 s pulse.

The test of the gyrotron matching to the quasioptical line was carried out. This line consisted of the mirror optics unit, power measuring unit (included the polarizer) and the piece of a corrugated waveguide of 88.9 mm diameter and 1 m length. At the waveguide end the output power accounts for 700 kW in the 2 s pulse. In the power measuring unit both forward and reflected power signals are monitored.

### Summary

The megawatt power level gyrotrons with the single disc BN window were tested in the long-pulse regimes at pulse duration from 2 s to 10 s. Typically gyrotrons generate from 850 kW to 900 kW output power at pulse duration of 2 s. In the 10 s pulse 340 kW output power was achieved. For the output power of 500 kW the pulse length of 5 s was admissible.

The gyrotrons were produced in the frame of the contract between Gycom Ltd., Russia and CCFM, Canada.

### References

- [1]. M.V. Agapova et al. "Long-pulse 110 GHz / 1 MW gyrotron." 20<sup>th</sup> International Conference on Infrared and Millimeter Waves. December, 1995, Orlando.
- [2]. V.E. Mjasnikov et al. "Megawatt power long-pulse 140 GHz gyrotron" 21<sup>st</sup> International Conference on Infrared and Millimeter Waves. July, 1996, Berlin.

Fig. 1 Gyrotron output power as a function of a beam voltage reducing.

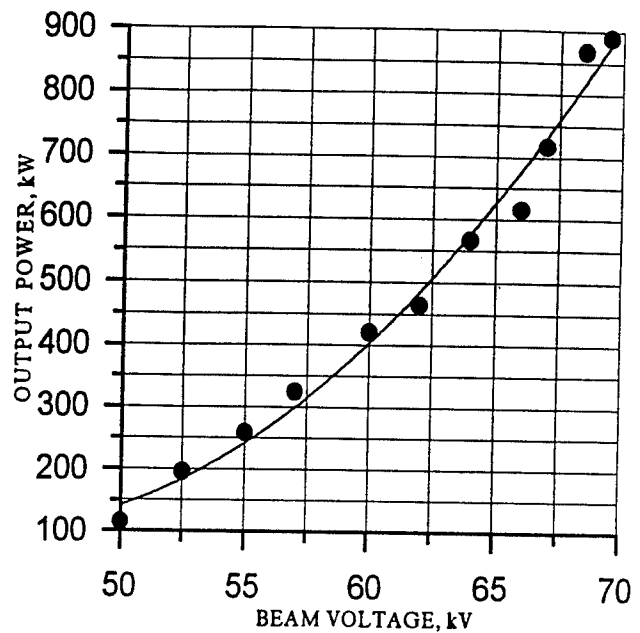
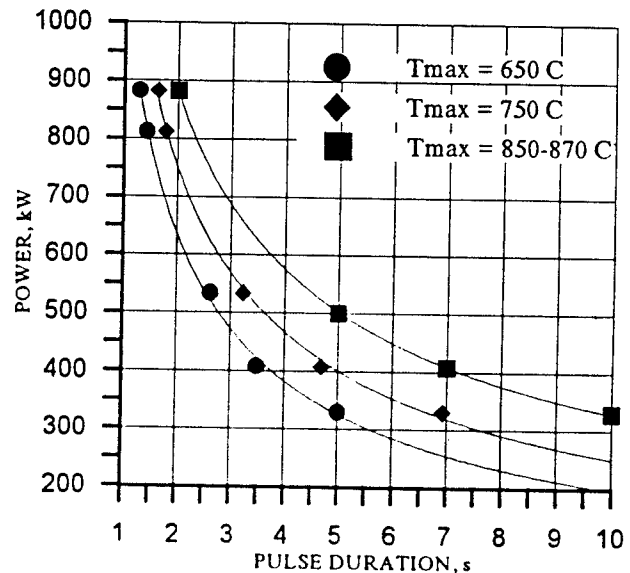


Fig. 2 Gyrotron output power versus pulse duration at the various maximal window temperature.



# STATUS OF THE 118 GHz - 0.5 MW - QUASI CW GYROTRON FOR TORE SUPRA AND TCV TOKAMAKS

E. GIGUET, Ph. THOUVENIN, C. TRAN

Thomson Tubes Electroniques - 2, rue Latécoère - 78141 Vélizy - France

P. GARIN, M. PAIN

Association Euratom - CEA, Département de Recherches sur la Fusion Contrôlée  
13108 Saint Paul lez Durance - France

S. ALBERTI, M.Q. TRAN

Centre de Recherches en Physique des Plasmas, Association Euratom - Confédération Suisse  
Ecole Polytechnique Fédérale de Lausanne - 21, Av. des Bains - CH-1007 Lausanne - Switzerland

M. THUMM

Forschungszentrum Karlsruhe, Association Euratom - FZK  
Institut für Technische Physik - P.O. Box 3640 - D-76021 Karlsruhe - Germany

## Abstract

In the frame of a collaboration between CEA - Cadarache, CRPP - Lausanne, FZK - Karlsruhe and TTE - Vélizy, a 0.5 MW-118 GHz-210 s gyrotron is under development for ECRH experiments on Tore Supra (Association Euratom-CEA) and TCV (Association Euratom-Confédération Suisse) Tokamaks. The cavity mode,  $TE_{22,6}$ , is converted into a Gaussian beam extracted out of the tube through a cryogenically cooled sapphire window and then coupled through a matching optics unit into a 63.5 mm diameter evacuated corrugated waveguide. The prototype, presently under modification, has delivered hundreds of 0.5 MW - 5s pulses into a matched load with the desired design parameters.

## Design and experimental set-up

A detailed description of the gyrotron design is presented in references <sup>[1], [2]</sup>. It is composed of a triode-type electron gun, an improved beam tunnel, a high-mode-purity low-ohmic-loss cavity with an optimized non linear output taper, a highly efficient internal quasi-optical mode converter made of a rippled-wall waveguide launcher followed by three mirrors <sup>[3]</sup>, a large collector making use of a beam sweeping magnet, and a horizontal RF output through a liquid nitrogen edge-cooled single-disk sapphire window<sup>[4]</sup>. The vacuum is controlled through four ion pumps located inside the tube and using the fringing field generated by the superconducting magnet.

A matching optics unit (MOU) system is connected to the gyrotron output window. It consists of a vacuum vessel including two flat and moveable mirrors allowing for corrections of minor errors in the extracted RF beam direction of propagation and a focusing mirror which launches the beam with an optimized profile into a 63.5 mm diameter

evacuated corrugated waveguide. The RF power is then dissipated and measured in a metallic water load. The schematic of the gyrotron and its MOU is shown in Fig. 1.

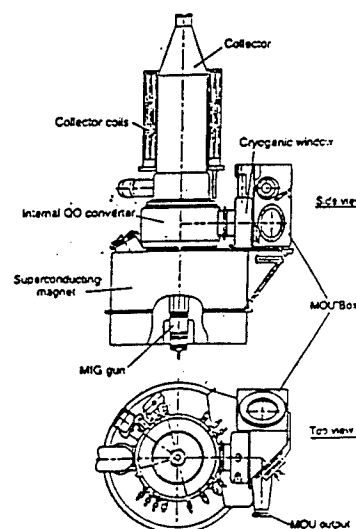


Figure 1: Gyrotron and MOU schematic view

## Long pulse experimental results

All power measurements were made in the water load. The MOU mirrors were aligned using burn patterns placed at different locations. The mode purity was then evaluated, in short pulse, by means of infrared measurements performed in different planes and for different lengths of corrugated waveguide. The  $HE_{11}$  mode content is higher than 96%. The pulse duration was extended to 5 s for the nominal power of 0.5 MW measured in the load without any need for conditioning (one single day to go from 2 to 5 s with ion pumps currents lower than 20  $\mu$ A).

The operating parameters were: cathode voltage,  $V_k = 81.5$  kV; beam current,  $I_b = 21.3$  A; anode voltage,  $V_a = 25.8$  kV, cavity magnetic field,  $B_0 = 4.59$  T. This leads to a global efficiency of 29 %, and of 28 % in the  $HE_{11}$  mode. Taking into account the RF losses measured and estimated in the components located between the gyrotron window and the load (MOU walls and mirrors, transmission line) on one side and inside the tube (beam tunnel, cavity, quasi-optical mode converter, mirror box, window) on the other side, the power levels are:

- Power extracted through the window: 0.535 MW;
- Power generated in the cavity: more than 0.6 MW, value leading to an interaction efficiency close to 35 %.

The variations of RF power and efficiency with respect to the cathode voltage,  $V_k$  are shown on Fig. 2. The gyrotron operates in stable regime between 0.2 and 0.5 MW by modulating  $V_k$ .

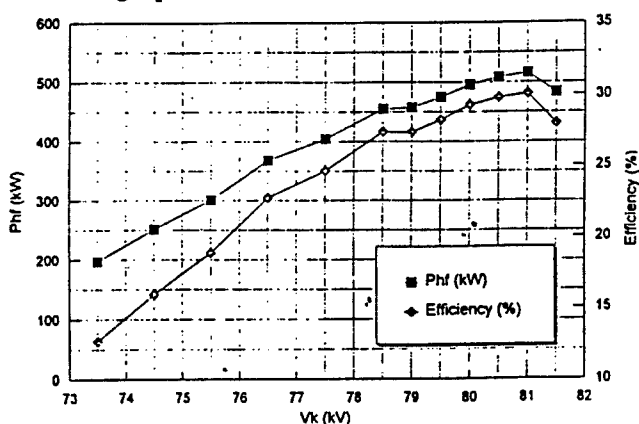


Figure 2: Dependence of RF power and efficiency on  $V_k$

On the other side, Fig. 3 shows that the RF power modulation is much more limited by acting on the anode voltage  $V_a$ .

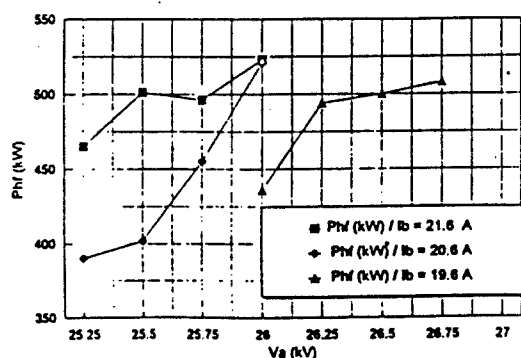


Figure 3: Dependence of RF power on  $V_a$

The temperature variations and RF losses were monitored on the most thermally loaded components: beam tunnel, cavity, rippled-wall waveguide launcher, mirrors and collector. It appeared that all of them reached equilibrium state at reasonable values within 4 s. The same observation also applied for vacuum: the ion pumps currents never exceeded 20  $\mu$ A during the pulses, and went back to their static values within a few seconds.

Pulses were not enlarged above 5 s because of limitations on some major tube accessories such as HV modulator and water load.

Despite extra losses due to absorption of the tail of the Gaussian beam in stainless steel walls, the cryogenic window and thermosiphon system have proven to perfectly work up to 0.5 MW - 5s.

Figure 4 shows a histogram of pulses above 1 s successfully passed with this gyrotron. Among the two hundreds 5 s pulses, more than 90 were obtained within the same afternoon with a duty cycle of 2.5 %: the success rate was of 92%.

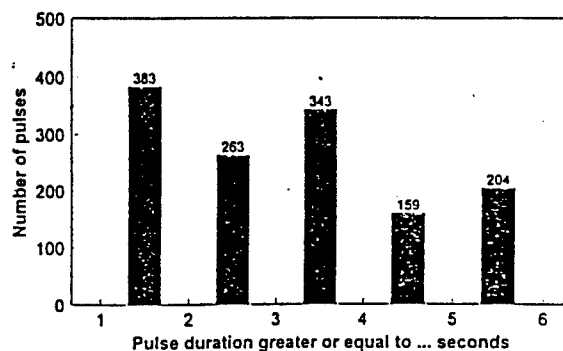


Figure 4: Number of pulses versus pulse duration

This cycling test revealed a brazing weakness in the cooling circuit common to the cavity and the rippled-wall launcher which has been analyzed and corrected.

## Conclusion

The 118 GHz gyrotron has proven its capability to repetitively generate more than 0.5 MW on pulses up to 5s, with respect to the specified parameters. A new prototype is at present under tests with the aim to reach pulses up to 210s.

The 118 GHz gyrotron development is performed within the frame of a joint development between the Associations Euratom-CEA, Euratom-Confédération Suisse and Thomson Tubes Electroniques. The work performed at the CRPP is partially supported by the Fonds National Suisse pour la Recherche Scientifique.

## References

- [1] E. Giguet et al. "Operation of a 118 GHz-0.5 MW gyrotron with cryogenic window: design and long pulse experiments", 20<sup>th</sup> Int. Conf. IR&MM Waves, Orlando, 1995, pp339-340
- [2] S. Alberti et al. "Long pulse operation of a 0.5 MW-118 GHz gyrotron with cryogenic window", 21<sup>st</sup> Int. Conf. IR&MM Waves, Berlin, 1996
- [3] O. Braz et al. "Cold tests and high power measurements on an advanced quasi-optical mode converter for a 118 GHz gyrotron", 20<sup>th</sup> Int. Conf. IR&MM Waves, Orlando, 1995, pp281-282
- [4] P. Garin et al. "Cryogenically-cooled window: a new step towards CW operation", 20<sup>th</sup> Int. Conf. IR&MM Waves, Orlando, 1995, pp271-272



# DEVELOPMENT OF HIGH POWER 170GHz GYROTRON FOR ITER

K.Sakamoto, A.Kasugai, M.Tsuneoka, K.Takahashi, Yu.Ikeda and T.Imai

Dep. of Fusion Engineering, Japan Atomic Energy Research Institute, Naka-machi, Ibaraki-ken, Japan, 311-01

T.Kariya, K.Hayashi(a), Y.Mitsunaka(a), Y.Hirata(a), Y.Ito(a) and Y.Okazaki

Electron Tube Division, Toshiba Co., Ohtawara-shi, Tochigi, Japan 329-2

(a) Energy and Mechanical Research Laboratories, Toshiba Co., Ukishima, Kawasaki-shi, Japan 210

## Abstract

The present status of 170GHz gyrotron development for ITER is reported. In the short pulse operation, the maximum power of 750kW was obtained at 85kV/40A. The efficiency is 22%. In the depressed collector operation, 500kW/36%/50ms was obtained. The maximum efficiency of 40% was obtained at PRF=470kW whereas the power decrease by the electron trapping was observed. Pulse extension was done up to 10s at PRF=175kW. The power was limited by the window temperature. For further pulse extension and power increase, the new materials are inevitable for the output window.

The cavity length was extended from  $L_{eff}/\lambda=10.0$  to  $L_{eff}/\lambda=10.9$  to obtain the efficient oscillation at the pitch factor of  $\alpha \sim 0.9$ . Q-value of the cavity is  $\sim 2450$ . The expected efficiency is  $>25\%$  and the efficiency enhancement factor by the depressed collector  $\eta_{DC}$  is greater than 2. And the thermocouple was installed to measure the temperature at the input end of the in-waveguide mode converter, where the unexpected large heat deposition was observed[3].

## 1. Introduction

For an electron cyclotron heating and current drive of ITER(International Thermonuclear Experimental Reactor), a 170GHz, 1MW, CW gyrotron with high efficiency is required[1]. The development of ITER relevant gyrotron is undergoing as the R&D Task under EDA (Engineering Design Activities). In JAERI (Japan Atomic Energy Research Institute), the development of the 170GHz gyrotron is carried on in cooperation with Toshiba Co. In 1995, short pulse 170GHz gyrotron was tested and confirmed a stable 1MW oscillation with high order volume modes( $TE_{31,8}$ , etc.)[2]. In 1996, the gyrotron with depressed collector was fabricated and 525kW/0.6s and 230kW/2.2s were demonstrated[3]. For these gyrotron, the oscillation was performed with a low pitch factor operation( $\sim 1.0$ ) using a high-Q cavity ( $Q \sim 2100$ ). The output power was limited mainly by the temperature increase of the output window (double disk sapphire). In 1997, some modifications were done on the gyrotron based on the result obtained in 1996. In this report, the present status of the modified 170GHz gyrotron is described.

## 2. Design and configuration

The conceptional view of the gyrotron is shown in Fig.1. The basic design of the gyrotron is the same as that of the previous gyrotron[3]. The modified sections are the window and the cavity. The window material was replaced from sapphire to silicon nitride produced by Kyocera(SN287). The silicon nitride has a comparable loss tangent with sapphire, smaller dielectric constant ( $\epsilon=7.9$ ), higher thermal conductivity (59W/mK) and is stronger against a thermal shock[4]. The silicon nitride disks, 161mm in diameter and thickness of 3.45mm, are used as a double disk window and are cooled by FC-75.

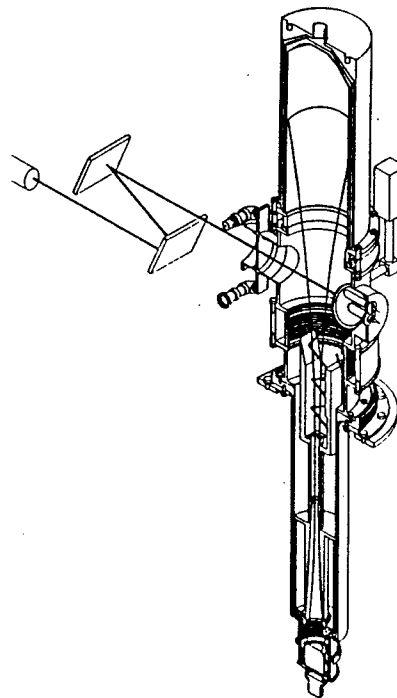


Fig.1 Conceptional view of 170GHz ITER gyrotron

## 3. Experimental Results

Fig.2 is the beam current  $I_c$  dependence of the output power and the efficiency at the short pulse operation, where the beam current of more than 40A is available. The output power of 750kW was obtained at  $I_c=40A$ , the beam voltage of 85kV. The efficiency is 22%. Fig.3 is a result of the depressed collector operation. The power without depressed collector is 500kW at the beam voltage of 85kV and the beam current of 28A, where the efficiency is 36%( $\eta_{CD}=1.7$ ). The maximum efficiency of 40% was obtained at the

depressed voltage of 43kV( $\eta_{CD}=2$ ), whereas the power decreased to 470kW due to the influence of the trapped electron. The pulse extension was carried out without collector voltage depression at first. In Fig.4, the increase of window peak temperature is shown for  $P_{RF}=210\text{kW}$ , 175kW. At  $P_{RF}=175\text{kW}$ , the window temperature stabilized at  $\Delta T=120\text{deg.C}$  and 10s operation was attained. Here, the 10 s is limited by the capacity of the power supply system. However, for  $P_{RF}=210\text{kW}$ , so called thermal runaway was observed, and the operation was stopped at 4s for safety. Next, the collector voltage depression was applied for long pulse operation. At  $P_{RF}=170\text{kW}$ , very stable 10s operation was also attained, and that the outgassing was extremely small ( $\sim 2\mu\text{A}$  of ion pump current). The efficiency was  $\sim 30\%$ . At  $P_{RF}=500\text{kW}$ , the maximum pulse duration was 0.7s, which is limited by the increase of the window temperature (efficiency was  $\sim 34\%$  with the depressed collector). For further pulse extension/power enhancement, materials of lower loss tangent are required. During the experiment, no large temperature increase was detected by the thermocouple at the mode converter, and the power distribution on the window was constant. In table 1, the major results are summarized.

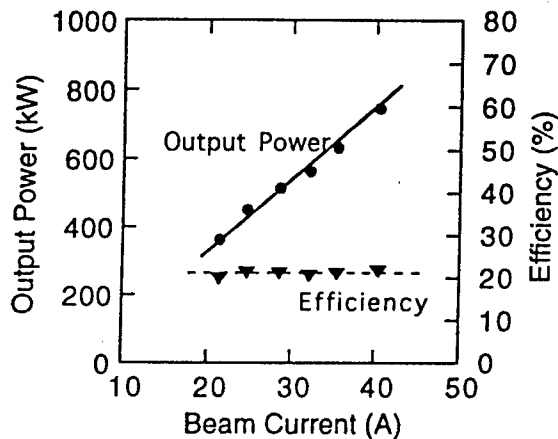


Fig.2 Output power, efficiency vs. beam current. Pulse duration is 0.4ms, and the beam voltage is  $\sim 85\text{kV}$ .

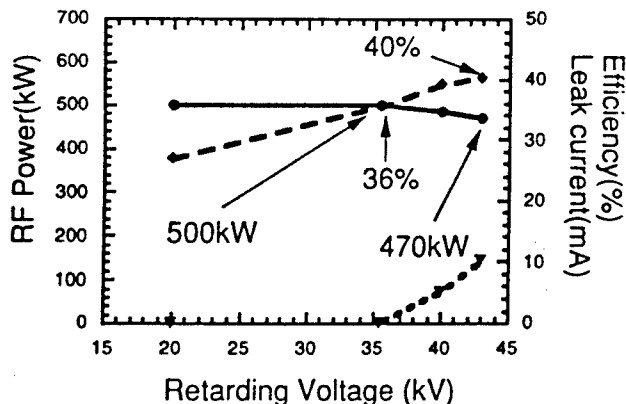


Fig.3 Output power, efficiency, leak current vs. retarding voltage of depressed collector operation. Pulse duration is 50ms, beam voltage of 85kV, beam current of 28A.

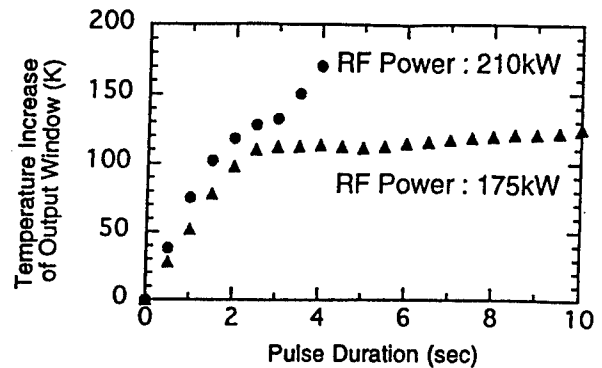


Fig.4 Temperature increase of output window vs. pulse duration for  $P_{RF}=210\text{kW}$ , 175kW.

Table 1 Major performance of 170GHz gyrotron

Power	pulse dur.	eff.	Limit of pulse dur.
750kW	0.4ms	22%	P/S
500kW	50ms	36%(D/C)	
470kW	50ms	40%(D/C)	
520kW	0.7s	34%(D/C)	Window
340kW	2s	20%	Window
210kW	4s	18%	Window
170kW	10s	30%(D/C)	P/S

(P/S:Power supply, D/C:Depressed Collector)

#### 4. Discussion and plan

The pulse duration and the high power operation is limited mainly by the temperature increase of the output window. For further pulse extension, the application of the diamond window, which has low loss tangent and extremely high thermal conductivity[5], will be tried. The oscillation efficiency increased from 19% to 22% by changing the cavity. However, the efficiency and the efficiency enhancement factor are still lower than expected. To increase the oscillation efficiency, the MIG and the electron beam system will be improved. The 1MW, long pulse oscillation will be tried from 1998 using a 1MW/CW relevant power supply system.

#### Acknowledgment

The window material, Silicon Nitride, was proposed to use on the gyrotron by NIFS (National Laboratory of Fusion Science) and we acknowledge Drs.T.Shimozuma, M.Sato and K.Ohkubo for collaborative work on the Silicon Nitride.

#### References

- [1]M.Makowski, Digest of the 21th Int.Conf.on IR&MM waves, AW1, ISBN 3-00-000800-4(1996).
- [2]K.Sakamoto et al., J.Phys.Soc.of Japan, vol.65, no.2 (1996).
- [3] K.Sakamoto, et al., Digest of the 21th Int.Conf.on IR&MM waves, AT2, ISBN 3-00-000800-4(1996).
- [4] T.Shimozuma, M.Sato, private communication.
- [5]O.Bratz, A.Kasugai, et al., this conference.

## Development of 1MW Output Power Level Gyrotron for ITER

V.E.Zapevalov, V.V.Alikaev, G.G.Denisov, V.A.Flyagin, A.Sh.Fix  
A.N.Kuftin, V.I.Kurbatov, V.E.Myasnikov

Institute of Applied Physics RAS, 46 Ulyanov Street, 603600, Nizhny Novgorod, Russia;  
GYCOM Ltd., 46 Ulyanov Street, 603600, Nizhny Novgorod, Russia;  
INF RRC Kurchatov Institute, Moscow, Russia

### Abstract

The report reviews some problems of high power gyrotron and their possible solutions, results of calculation and experimental study of gyrotrons for fusion operating at the 1 MW power level in a wide frequency range. The design versions of the 170 GHz/1 MW gyrotron for ITER are discussed. ITER related 110 GHz and 140 GHz gyrotrons also are investigated.

### Introduction

Electron-cyclotron heating and current control in planned ITER plasma set-ups require gyrotrons with the level of CW power up to 1 MW and frequencies 170 GHz. In the framework of the international ITER project, the program for design of a 170 GHz gyrotron with output power 1 MW for operation in the continuous regime was implemented. From the preliminary analyses possible operating modes have been chosen (Table 1) and the general design concept of the gyrotron has been developed [1]. Finally basing on the analysis of technical limitations TE<sub>28,7</sub> operating modes have been chosen for experimental-industrial tube and TE<sub>25,10</sub> for the test tube which give us the possibility to check different scientific and technical solution during the time of elaboration of the industrial tube with criomagnet and auxiliary equipment. The TE<sub>25,10</sub> test tube can use the existing criomagnet with room temperature boor diameter 140 mm. The TE<sub>28,7</sub> experimental-industrial tube need the new criomagnet with room temperature boor diameter 180 mm

### Gyrotron Design

The 170 GHz gyrotron has the same principal design concept as the earlier developed 140 GHz/0.5 MW/3 s and 110 GHz/1 MW/2 s gyrotron. Magnetic system of the tube includes a main superconducting solenoid, a cathode coil for fine adjustment of electron beam parameters.

All the gyrotrons uses the magnetron injection guns (diode and triode versions), which forms a quasi-laminar helical beam [2]. In result of numerical simulation for operating modes, the shapes of gun electrodes were optimized and dependencies velocity spread  $\delta v_{\perp}$  (I) and ratio oscillatory energy to the total one-  $t_{\perp}$  (I) on the beam current are received. Simulations were performed taking into account initial velocities (EPOS-V [3]). For experiments a method of a retarding field [4-5] was used. The measurements were carried out for guns with  $R_c = 45.2$  mm and  $R_c = 41.5$  mm in a scale down

regime on automated installation [6], as at presence of influence electrons, caught in adiabatic trap between the cathode and magnetic mirror, and at exception such electrons. The received dependencies  $\delta v_{\perp}$  and  $t_{\perp}$  are compared with results of numerical simulation and good correlation are observed. The reliable technology and equipment for fabrication and test of the gyrotron's gun emitters and electron-optical system has been developed.

Table 1: Main parameters of 170 GHz/1 MW/CW gyrotrons

Operating mode	TE <sub>28,7</sub>	TE <sub>31,8</sub>	TE <sub>25,10</sub>
Accelerating voltage, kV	80	80	80
Maximum beam current, A	45	45	45
Voltage depression at resonator center (at 40 A), kV	5.12	5.29	6.95
Resonator radius, mm	15.86	17.9	17.77
Mean beam radius in resonator, mm	8.26	9.13	7.4
Resonator Q-factor	1000	1100	1100
Specific density of losses in resonator at 1MW output, kW/cm <sup>2</sup>	2.5	2.1	1.9
Radius of the cathode R <sub>c</sub> , mm	45.2, (47.5)	50, (51)	41.5
Electrical field on the cathode E <sub>c</sub> , kV/mm	6.3, (5.6)	6.3, (5.8)	5.8
Pitch-factor	1.25	1.25	1.25
Calculated maximum (electron) efficiency	0.4	0.4	0.4
Structure of output radiation	narrowly-directed wave beam		

Stable single-mode generation in an oversized resonator at sufficiently high efficiency and the megawatt level of output power becomes an extremely complicated problem as the operating frequency grows [1,4]. An essential circumstance here is, that this problem has to be solved within a number of limitations. The most difficult is the limitation on density of

ohmic losses in resonator walls - energy removal is limited by possibilities of the cooling system, which are, as a rule, not higher than 2–3 kW/cm<sup>2</sup>. Effects of beam potential depression and mode interaction as well as methods of mode selection are investigated also.

The converter separates RF radiation from the worked-out electron beam, transforms a complicated cavity mode to a paraxial wave beam with an optimised structure and allows one to minimise harmful action of possible reflections of RF power back to the gyrotron. The converter includes a specially shaped waveguide end and several mirrors which are profiled to provide:

- low diffraction losses inside the tube (below 5% of the total power is possible, in some cases);
- the optimal RF power distribution over an output window;
- matching of the output wave beam to a transmission line (90...95% efficiency is possible).

The technology for fabrication of the gyrotron's electrodynamic system elements with complex curvilinear surfaces on lathes with numerical control has been developed.

The problem of the output window is the main difficulty that hinders creation of 1 MW CW gyrotrons. The main variant of the output window for 1 MW CW gyrotrons at frequencies up to 170 GHz is considered now a high-purity and doped silicon window. Some other materials, e.g., sapphire cryogenic window, diamond are under investigation as well.

The three following versions of collectors for powerful CW gyrotrons seem to be the most promising now:

- collector with non-adiabatic pumping of gyration movement of electrons;
- collector with dynamic scanning along it by means of additional coils generating magnetic field of the saw-teeth form;
- CPD - collector.

The collector for experimental-industrial tube has been designed for the CW regime of operation to withstand up to 3 MW electron beam power when the RF oscillation breaks. It is now the traditional type with sweeping of the electron beam along the axis. For sweeping, a special collector coil is used, which is fed with saw-shaped current producing an alternative magnetic field in the collector region. Both the collector profile and distribution of the magnetic field in the collector are optimized to provide a temperature increase below an admissible one and as homogeneous thermal load as possible.

### Short-pulse Gyrotron Prototypes

Experimental investigation of short pulse prototype of the 170 GHz gyrotron were made on the automated set-up and dependencies of gyrotron parameters on the beam current, accelerating voltage and magnetic field is analyzed. The output power level 1 MW was achieved at the TE<sub>28,7</sub> and TE<sub>25,10</sub> operating modes in design regime with efficiency 32% and 34%, correspondingly. The maximum output power near 1.3 MW with efficiency 32% was achieved at the TE<sub>25,10</sub> operating mode. The same TE<sub>25,10</sub> gyrotron has been operated also with a single-stage depressed collector. Measurements of the RF-output power in dependence on the retarding collector

voltage were provided. Output power of 1MW/50 mks was obtained at the beam parameters of 80 kV/40 A. The improved efficiency with single-stage depressed collector was near 60%. Calculation and experimental data are in a good correlation.

### ITER Related 110 and 140 GHz Gyrotrons

110 GHz high power experimental gyrotron using the TE<sub>19,5</sub> mode has been operated with a single-stage depressed collector. Measurements on a CPD with respect to the body current and the RF-output power in dependence of the retarding collector voltage was provided. Output power of 1MW/50 mks is obtained at the beam parameters of 80 kV/30 A. The efficiency is 40% and the improved efficiency with single-stage depressed collector is 65%.

140 GHz industrial gyrotrons with output power about 1 MW in 1.5 s pulses and output power 650 kW in 2.5 s, 270 kW in 5 s, 150 kW in 9.3 s pulses were developed for electron cyclotron resonance heating (ECRH) of plasmas generated in the Tokamak ASDEX- Upgrade at IPP-Garching. The gyrotron efficiency is over 40 % at operating regimes. The gyrotrons are designed to operate in stray magnetic field with their total horizontal component up to 6·10<sup>-4</sup> T.

Industrial 140 GHz frequency range CPD gyrotron using the TE<sub>22,6</sub> mode has been operated with a single-stage depressed collector with output power about 810 kW in 1 s is obtained at the beam parameters of 72 kV/31.5 A. The gyrotron efficiency without CPD is 32% and the improved efficiency with single-stage depressed collector is over 50% at operating regimes.

### Conclusion

The possibility to make 170 GHz/1 MW gyrotron for ITER is proved by calculations and experiments. Calculation results and experimental data for the ITER related gyrotrons and prototype 170 GHz/1 MW gyrotron for ITER are in a good correlation. Successfully tested short pulse prototype is a reliable basement for elaboration of an industrial tube operating in the full-scale regime.

### References

1. Denisov G.G., Flyagin V.A., Zapevalov V.E. Conf. Proc. 20 Int. Conf. on IR & MM waves. Orlando, USA. 197 (1995)
2. A.N.Kuftin, et al. Int. J. Electronics, 72, 1145 (1992).
3. V.K.Lygin. Int. J. of Infrared and Millimeter waves, 16, 363 (1995).
4. V.A.Flyagin, A.L.Goldenberg, V.E.Zapevalov., Conf. Proc. 18 Int. Conf. on IR & MM waves, Colchester, United Kingdom, 581 (1993).
5. A.L.Goldenberg and E.G.Avdoshin. Izvestiya Vysshikh Uch. Zavedenii, Radiofizika, 16, 1605 (1973).
6. A.N.Andronov, et al. Conf. Proc. 20 Int. Conf. on IR & MM waves. Orlando, USA. 141 (1995)

## Frequency modulation of a submillimeter wave gyrotron, Gyrotron FU IV

T. Idehara, T. Tatsukawa, I. Ogawa, M. Pereyaslavets, N. Nishida and K. Yoshida

*Faculty of Engineering, Fukui University, Bunkyo 3-9-1, Fukui 910, Japan*

### Abstract

Frequency modulation of submillimeter wave gyrotron, Gyrotron FU IV is presented. A modulation of beam electrons results in the modulation of electron cyclotron frequency, which, in turn, modulates the frequency of gyrotron output. The modulation width  $\Delta f$  of several ten MHz has been achieved by using the gyrotron.

### 1. Introduction

The development of gyrotrons are proceeding in two directions, that is, developments of high power, millimeter wave gyrotrons and medium power, submillimeter wave gyrotrons. As well known, the development of the latter is going in Fukui University. Gyrotron FU Series<sup>1)</sup> has achieved frequency tunability in wide range in a millimeter to submillimeter wavelength region (38 to 850 GHz), amplitude modulation of the output<sup>2)</sup> and rapid frequency step-switching.<sup>3)</sup> Gyrotrons included in the series have been applied to plasma scattering measurement<sup>4)</sup> and ESR experiment<sup>5)</sup> as radiation sources. In future, we are intending to develop further their applications to wider fields.

Modulations of amplitude and frequency of the output, as well as their high stabilities which will be achieved by cw operation, are useful and necessary for the applications of such high frequency gyrotrons as radiation sources. We have succeeded in the first experiment of the frequency modulation by modulating the electron beam energy. In this paper, the results and some considerations are described.

### 2. Experimental arrangements and procedures

Gyrotron FU IV<sup>1)</sup> was used for the experiment. The typical operation parameters are as follows, the beam energy  $eV_c = 30$  to 40 keV, the beam current  $I_b = 0.1$  to 1 A, the magnetic field intensity  $B_0 = 8$  to 12 T, the output frequency  $f = 100$  to 640 GHz and the output power  $P_0 = 0.1$  to 1 kW. In the frequency modulation experiment, the beam energy is modulated by the potential modulation of the body, which includes the cavity and divided electrically from the beam collector by the insulator (ceramic).

The output power is transmitted by circular waveguides and emitted to the horn antenna. The frequency is measured by heterodyne detection system consisting of a sweep oscillator, a frequency counter, a harmonic mixer and a modulation domain analyzer. Fig.1 shows the block diagram. Time and frequency resolutions of the detection system are  $10 \mu\text{sec}$  and 10 kHz respectively.

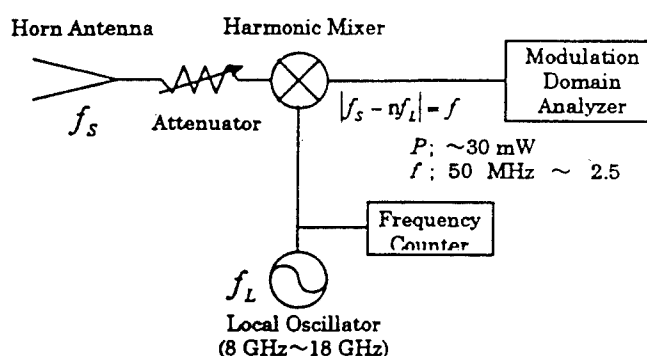


Fig.1 Block diagram of a frequency measurement system

### 3. Experimental results and considerations

Fig.2 shows a typical result of frequency modulation experiment. The upper trace shows the po-

tentail modulation of the body and the lower trace the variation of the output frequency. A peak-to-peak value of the potential modulation is 250 V, a modulation frequency is 60 Hz and the width  $\Delta f$  of frequency modulation is 18.8 MHz. The gyrotron operates in cw mode. At the phase of higher beam energy, the measured frequency of the output is lower, which corresponds to the variation of electron cyclotron frequency, qualitatively.

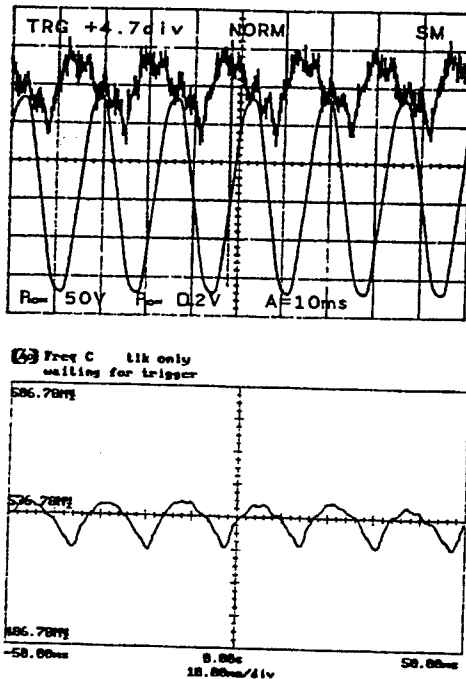


Fig.2 Result of frequency modulation measurement. Upper trace: potential modulation applied to the body of the gyrotron. Lower trace: variation of output frequency. Modulation frequency is 60 Hz.

Fig.3 shows the result for high frequency modulation around 1.46 kHz. In this case, the gyrotron operates pulsively. The base line of measured frequency increases in time, because of the sag in high voltage pulse applied to the gun cathode. The width  $\Delta f$  of frequency modulation is 4.4 MHz.

The calculated modulation width  $\Delta f_c$  of electron cyclotron frequency is much larger than  $\Delta f$ . The result may come from the restriction of high  $Q$ -cavity to the flexibility of operation frequency in it. The detailed consideration is under way.

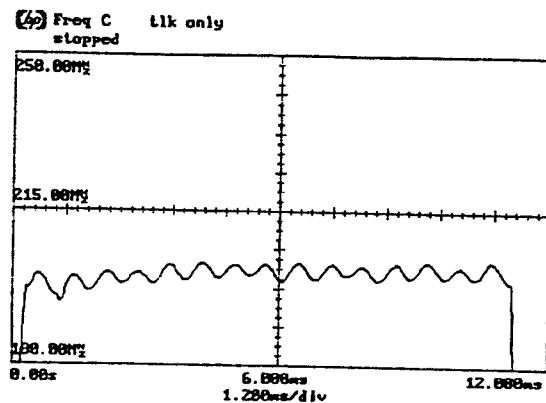


Fig.3 Variation of output frequency. Modulation frequency is 1.46 kHz.

## References

- 1) T.Idehara, T.Tatsukawa, I.Ogawa, Y.Shimizu, K.Kurahashi, N.Nishida and K.Yoshida, Digest of 21st Int. Conf. on Infrared and Millimeter Waves, Berlin, Germany, July 1996.
- 2) T.Idehara, Y.Shimizu, S.Makino, K.Ichikawa, T.Tatsukawa, I.Ogawa and G.F.Brand, Phys. Plasmas 1, 461-463 (1994).
- 3) T.Idehara, Y.Shimizu, S.Makino, K.Ichikawa, T.Tatsukawa, I.Ogawa and G.F.Brand, Phys. Plasmas 1, 1774-1776 (1994).
- 4) I.Ogawa, T.Idehara, H.Ibe, K.Kawahata and W.Kasperek, Int. J. Infrared and Millimeter Waves 15, 1587-1602 (1994).
- 5) T.Tatsukawa, T.Maeda, H.Sasai, T.Idehara, M.Mekata, T.Saito and T.Kanemaki, Int. J. Infrared and Millimeter Waves 16, 293-305 (1995).

## Investigation of Coaxial Gyrotrons at IAP RAS

V.A. Flyagin, V.I. Khizhnyak, A.N. Kuftin, V.N. Manuilov, A.B. Pavelyev, V.G. Pavelyev, V.E. Zapevalov

Institute of Applied Physics, Russian Academy of Sciences,  
46 Ulyanov Street, 603600 Nizhny Novgorod, Russia

### Abstract

Some latest results of experimental testing of the 140 GHz/ 1.5 MW coaxial gyrotron (Russian version of the joint Russian-German coaxial gyrotron) with a lower level of ohmic losses in the cavity are presented. The experience of investigations of coaxial gyrotrons carried out at the IAP is briefly summarized.

### Introduction

Conventional gyrotron's output power is limited due to ohmic losses, mode competition and limiting beam current. All these problems can be essentially reduced by the use of coaxial cavities. Due to effective mode selection and insignificant beam voltage depression such cavities provide the stable very high volume modes excitation and the effective operation with extremely low ohmic losses. As a result of numerous theoretical estimates and experiments performed at the IAP before the end of eighties it was found that the most advantage can be achieved in coaxial cavities with a fully metallic and corrugated inner rod. Moreover, selective properties of the system can be improved still more by means of the additional corrugation of the cavity outer wall. Further more detail researches of the gyrotrons with such cavities was continued in the collaboration with the FZK gyrotron group (Karlsruhe, Germany). Now the jointly developed 140 GHz/ 1.5 MW coaxial gyrotron is under investigations. In this report some experimental results concerning the Russian version of this gyrotron are presented.

### 140 GHz/ 1.5 MW coaxial gyrotron

#### A. Design parameters

The design of Russian version of the 140 GHz/1.5 MW coaxial gyrotron is practically the same as for FZK one [1]. Some differences are conditioned mainly by superconducting magnets properties. In this gyrotron the inverse electron gun with a system of the inner rod alignment and the coaxial cavity with a tapered and corrugated inner rod were used. The main design parameters of the tube are summarized in Table 1.

Table 1: Design parameters of the coaxial gyrotron

operating mode	TE <sub>28,16</sub>
operating frequency, $f$ (GHz)	140
accelerating voltage, $U_b$ (kV)	90
maximum operating beam current, $I_b$ (A)	50
beam radius in the cavity, $R_b$ (mm)	10
rf output power, $P_{out}$ (MW)	1.5
efficiency, $\eta$ (%)	> 30
peak wall loading (for real copper), $p_0$ (kW/cm <sup>2</sup> )	≤ 1.3

The peak ohmic losses at the inner conductor are calculated to be less than 15% of the peak cavity wall losses.

At the first stage it was planned to study the operation of the electron gun and coaxial cavities in the gyrotron with an axial rf output. Then the output section has to be replaced by the two-step quasi-optical (q.o.) converter with a dual-beam rf output (similar to [1]).

#### B. Experiments with an axial rf output gyrotron.

The measurements were performed with 50  $\mu$ sec HV pulses. At first the cavity with a smooth cylindrical outer wall and the conical impedance inner rod was tested (the impedance surface was formed by 60 narrow longitudinal slots as it is shown in Fig. 1).

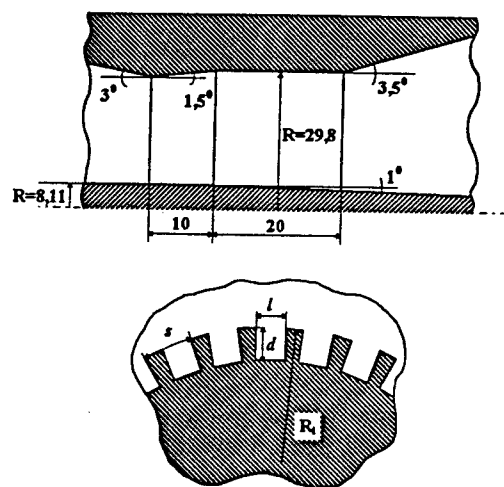


Fig. 1 The cavity profile and a cross-section of the inner rod ( $l \approx 0.5$  mm;  $d \approx 0.52$  mm;  $s \approx 0.83$  mm).

In the first series of experiments a maximum output power of operating mode TE<sub>28,16</sub> about 1.35 MW with an efficiency of about 29% has been achieved at the beam voltage  $U_b = 95$  kV. At the design voltage  $U_b = 90$  kV measured values were some lower:  $P_{out} \approx 1.25$  MW,  $\eta \approx 28\%$ . (Practically the same results were obtained on the similar FZK tube). Then, during the check-up of geometry of the electron gun, enough strong misalignment of components of the gun has been found. Some correction of the gun allowed to increase an output power and efficiency of the gyrotron and approach them to the theoretically expected values. Measured dependencies of operating mode output parameters on the beam current are shown in Fig. 2. The stable oscillations of the operating mode have been observed over the wide range of the magnetic field that testified about the high efficient mode selection over

radial indices. In order to extend still more the range of a single-mode operation and to enhance the efficiency of the gyrotron, at the second step the cavity with a smooth outer wall was replaced for corrugated one (see Fig. 3).

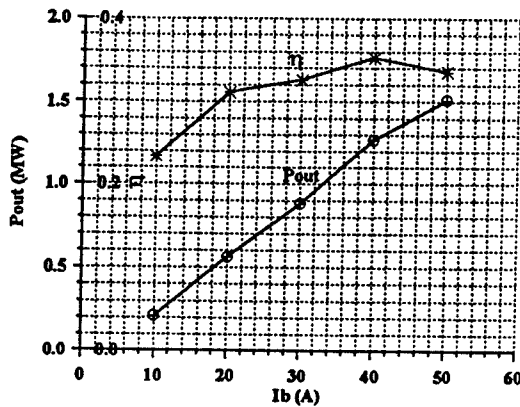


Fig. 2 RF output power and output efficiency versus electron beam current (operating mode  $TE_{28,16}$ ;  $U_b = 90$  kV).

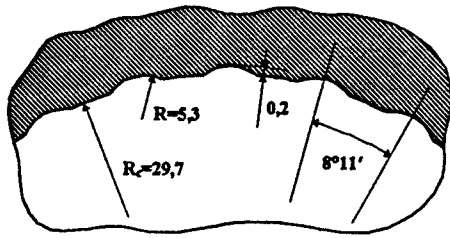


Fig. 3 The cavity with corrugated outer wall.

The suppression of parasitic modes with neighbouring (as compared with operating mode) azimuthal indices in such systems can be achieved due to effective transformation of these modes to strongly disturbed low-Q ones. The experimental tube cavity output was equipped also with a corrugated waveguide mode converter ( $TE_{28,16} - TE_{76,2}$ ) which was planned to be used further as the part of the two-step q.o. mode converter. Measured output power in the wide region of the magnetic field for this case is presented by Fig. 4.

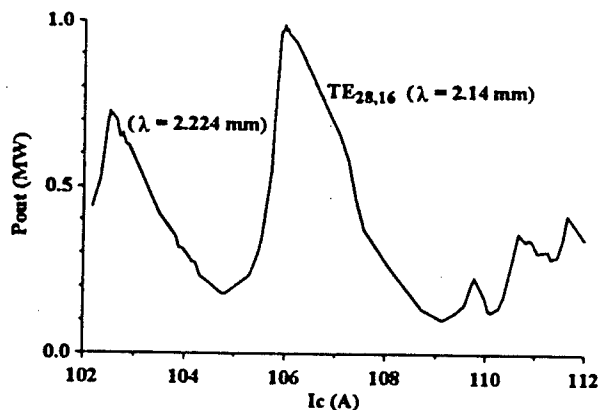


Fig. 4 RF output power versus superconducting magnet current ( $U_b = 95$  kV;  $I_b \leq 35$  A; corrugated cavity outer wall; corrugated waveguide mode converter).

This graph indicates a very effective mode selection realized in the corrugated cavity. Unfortunately the output power and the gyrotron efficiency (Fig. 5) were found to be some lower than in preceding experiments. Up to now the reason are not yet quite clear.

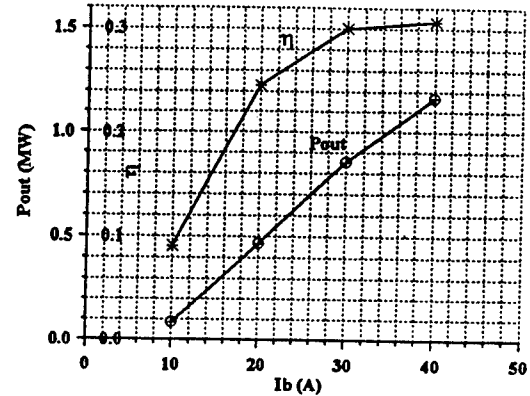


Fig. 5 RF output power and output efficiency versus electron beam current (operating mode  $TE_{28,16}$ ;  $U_b = 95$  kV; corrugated cavity outer wall; corrugated waveguide mode converter)

Analysis of the thermal image of the output radiation (by infrared camera) has shown that rf power radiated out mainly in the form of several modes  $TE_{76,1} - TE_{76,6}$ . So complicated structure can be explained by the transformation in the output window of the axial gyrotron. One can hope that this problem will be solved in the tube with a q.o. mode converter. Now a such version of the gyrotron (with double beam output) is under investigation.

## Conclusions

Theoretical and experimental investigations of coaxial gyrotrons at the IAP testify that these systems can be used for generation of a power rf radiation at the frequencies above 170 GHz. Electrodynamics parts of all experimentally tested coaxial tubes operated quite satisfactory. A high efficiency of the mode selection, an extremely low level of ohmic losses in coaxial cavities make them very attractive as resonant systems of supermegawatt short wavelength CW gyrotrons. But up to now the main problem which can prevent from a wide use of coaxial gyrotrons is related with development of an adequate electron gun and inner rod supporting system for such gyrotrons. Present inverse electron guns seem to be enough convenient for laboratory investigations. But their relatively complicated construction makes it problematical to use these guns in industrial coaxial gyrotrons. Probably this problem can be solved by some improvement of existing inverse electron guns or by the use of conventional guns with supporting of the inner conductor from collector side.

## References

- [1]. B. Piosczyk, et al., accepted for IEEE Trans. Plasma Science, June, 1997.



# OPERATION OF A COAXIAL GYROTRON WITH A DUAL RF-BEAM OUTPUT

B. Piosczyk, O. Braz<sup>+</sup>, G. Dammertz, C.T. Iatrou<sup>++</sup>, S. Kern<sup>+</sup>, M. Kuntze, G. Michel<sup>+</sup>,  
A. Möbius<sup>+++</sup>, M. Thumm<sup>+</sup>,

Forschungszentrum Karlsruhe, Association EURATOM-FZK, ITP, Postfach 3640, D-76021 Karlsruhe, Germany

<sup>+</sup> also Universität Karlsruhe, Institut für Höchstfrequenztechnik und Elektronik, <sup>++</sup> National Technical University of Athens, Greece,

<sup>+++</sup> IMT GmbH, Luisenstr. 23, D-76344 Eggenstein, Germany; e-mail: piosczyk@itpgyro1.fzk.de

V.A. Flyagin, V.I. Khishnyak, A.B. Pavelyev, V.E. Zapevalov,

Institute of Applied Physics, Russian Academy of Sciences, Nizhny Novgorod, 603600, Russia

## Abstract

A 140 GHz,  $TE_{28,16}$  - coaxial cavity gyrotron with dual rf-beam output and single-stage depressed collector (SDC) has been operated for the first time. A maximum rf output power of about 875 kW with an output efficiency of 19 % (27 % with SDC) has been achieved. About 15 % of the output power has been measured to be captured within the gyrotron tube. In comparison to results of numerical simulations the generated rf-power is only about 62% of the expected value, nearly independent of the operating parameters. There are some indications that captured stray radiation may be a main reason for the power deficit.

## Introduction

A 1.5 MW coaxial cavity gyrotron operated at 140 GHz in the  $TE_{28,16}$  mode and at 165 GHz in the  $TE_{31,17}$  mode is under development at FZK. In a first step a gyrotron with an axial waveguide output has been designed, built and tested with very promising results [1]. An rf-output power close to 1.2 MW with an efficiency of about 27 % has been achieved, in good agreement with numerical simulations. At present, a tube design with a radial rf-output is under investigation. The rf power is split into two parts and coupled out through two rf output windows.

## Design parameters and experimental set-up

A schematic layout of the gyrotron with the dual rf-beam output is shown in Fig. 1. The superconducting (sc) magnet, the electron gun, the beam tunnel and the cavity are as in the experiment with axial rf output[1]. The components are arranged in an easily demountable way with no special cooling. The beam tunnel consists of copper without any rf absorber material. For the resonator a cavity with a cylindrical outer wall and a radially tapered and corrugated inner rod is used. The gyrotron is equipped with a single-stage depressed collector. The two rf-output windows with a diameter of 100 mm are made of 6.0 mm fused silica with optimum transmission for the  $TEM_{00}$  wave at 140 GHz. For observation of the stray radiation captured in the gyrotron tube an additional window is placed at  $90^\circ$  to the direction of the rf output beams. The quasi-optical (q.o.) converter system is based on a two-step mode conversion scheme,

$$TE_{28,16} \Rightarrow TE_{+7,6,2} \Rightarrow TEM_{00}.$$

The double-cut q.o. converter uses an improved dimpled wall double-beam launcher and generates two diametrically opposed narrowly-directed output wave beams[2]. It should

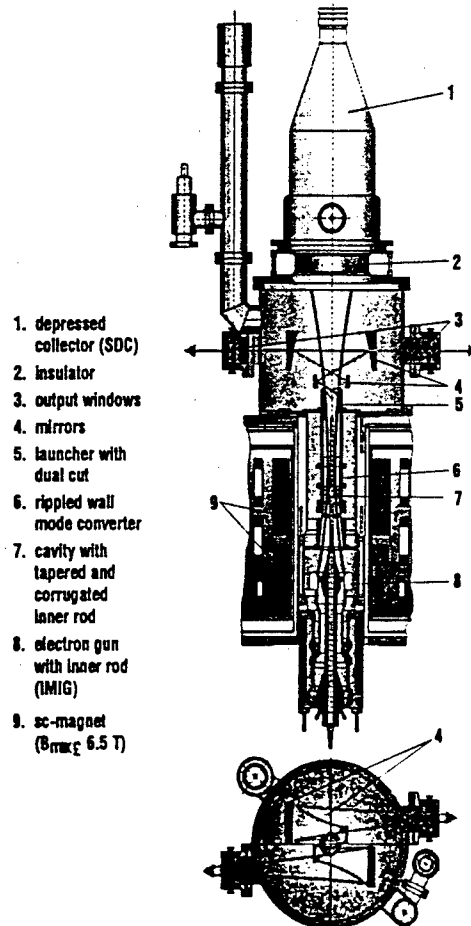


Fig. 1: The coaxial gyrotron with dual rf-beam output.

be pointed out, however, that the two step mode conversion scheme works properly only for the design mode and that therefore, frequency step tuning is excluded. The conversion of the  $TE_{28,16}$  cavity mode to the  $TE_{+7,6,2}$  whispering gallery mode (WGM) is achieved by introduction of longitudinal corrugations into the linear part of the output taper ( $1.5^\circ$ ) consisting of 104 slots with corrugation depth of only about 0.1mm.

## Experimental performance and results

The measurements have been performed with pulses up to a few msec. However, most data have been taken with pulses around 0.5 msec. In addition to the rf-power  $P_{out}$  through the two output windows, the power  $P_{stray}$  radiated through the additional window was measured calorimetrically.  $P_{stray}$  is

taken as a measure for the amount of stray radiation captured in the gyrotron tube. With a contiguous filter bank a signal of the generated rf-power has been observed simultaneously in different frequency channels giving information whether there was single or multi-mode oscillation in the cavity. The distribution of the rf-power radiated out of the windows was detected with an infrared camera. The generated HV-pulse had a rise time of about 200  $\mu$ sec followed by a stable plateau without any voltage overshooting.

#### The gun and the electron beam :

Stable operation at the design parameters ( $U_c=90$  kV,  $I_b=50$  A) has been achieved only with the magnetic field configuration in the gun region delivering an  $\alpha$ -value of about 1.1 at  $U_c=90$  kV. With the magnetic configuration corresponding to an  $\alpha$ -value of about 1.4 at 90 kV the electron beam becomes noisy during the pulse above a certain voltage value. This beam instability occurred also in the magnetic configuration with the lower  $\alpha$ -value at voltages far below 90 kV when either the neighbouring modes TE<sub>27,16</sub> and TE<sub>29,16</sub> or the TE<sub>28,16</sub>-design mode rotating in the wrong direction were generated. In these modes the amount of captured stray radiation is relatively higher than in the design mode since the modes are not adapted to the rf-output system. As an example the operation was stable at  $U_c=90$  kV with  $I_b=50$  A and  $\alpha=1.1$  when operated in the TE<sub>28,16</sub> mode. By reversing the direction of the magnetic field the wrong rotating TE<sub>28,16</sub> mode is generated causing beam instabilities above  $U_c \approx 82$  kV with  $I_b=50$  A and  $\alpha=0.95$ . The amount of the captured stray radiation is about 3 times higher in this case. This observation is taken as an indication that the captured rf radiation may stimulate beam instabilities.

#### RF-operation :

The measurements have been performed with an approximately constant magnetic compression corresponding to a beam radius of 10.0 mm. The frequency of the TE<sub>28,16</sub> mode was measured to be 139.9 GHz. The distribution of the rf-power radiated out of the windows has been found to be in good agreement with the results of cold measurements and of numerical calculations. This seems to prove the proper working of the launcher with the double cut and the mirrors. A single-stage depressed collector was used successfully up to a retarding voltage  $U_{col} = -27$  kV, limited only by its HV-voltage performance.

The measured value of  $P_{stray}$  in the TE<sub>28,16</sub> mode was found to be proportional to  $P_{out}$ . For absolute calibration of the amount of the captured stray radiation it was assumed that the power generated in the cavity is equal for both rotations when operated at the same parameters with reversed magnetic field. Thus for the design mode  $P_{stray}$  has been determined to be:  $P_{stray} \approx 0.15 \cdot P_{out}$ .

The stray radiation has its origin both in diffraction losses of the launcher which are estimated to be  $\geq 6\%$  and in imperfect TE<sub>28,16</sub> to TE<sub>27,16</sub> conversion. The depth of the grooves of the converter has been measured to be smaller than the design resulting in a conversion of only 93%. The unconverted part (7%) of the cavity mode contributes to the stray radiation.

The rf - power through each window was measured to be the same within the experimental accuracy ( $\pm 5\%$ ). The experimentally observed single-mode operating range is in good agreement with results of numerical calculations performed with a multimode code taking into account the diode start-up. A maximum rf-output power of 875 kW with an output efficiency of 19 % (27 % with SDC) has been achieved at  $U_c=88.2$  kV,  $I_b=52$  A and  $B_{cav}=5.63$  T. The measured rf-power versus the beam current  $I_b$  is shown in Fig. 2. The cathode voltage was optimized for maximum output power. In the figure the rf-losses in the walls and the windows  $P_{\Omega}$  (estimated to 13%), the stray radiation  $P_{stray}$  and the calculated rf-power generated in the cavity  $P_{cav}$  are also given. For the calculations the operating parameters and a velocity spread  $\delta\beta_{rms} = 6\%$  have been taken. Also if the rf-losses  $P_{\Omega}$  and  $P_{stray}$  are taken into account, a deficit of rf-power of about  $(0.35-0.4) \cdot P_{cav}$  remains, approximately independent of the operating parameters ( $I_b$ ,  $U_c$ ,  $B_{cav}$ ) as is shown by the stars in Fig. 2.

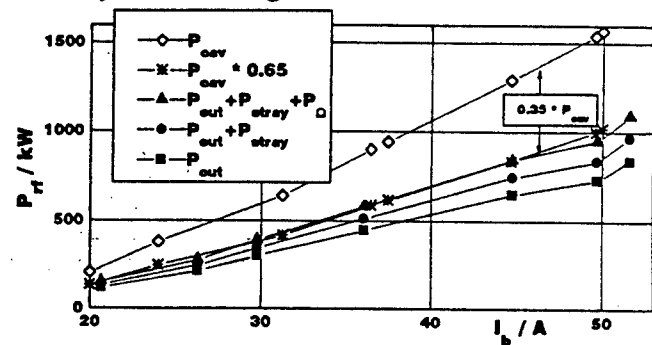


Fig. 2: Rf-power vs. beam current  $I_b$  for the TE<sub>28,16</sub>-mode.

#### Conclusions

The single-mode operating range is in good agreement with numerical simulations. This confirms the influence of the voltage overshooting and the window reflections on single-mode oscillation as observed in the measurements with the axial version of the tube[1]. The efficiency of the rf-output system with the two-step conversion scheme is only about 85 %. The generated rf power ( $P_{\Omega} + P_{stray} + P_{out}$ ) is still less than 2/3 of the theoretically expected value  $P_{cav}$ . The corresponding results in the axial version of the gyrotron showed good agreement between experiment and calculations. The occurrence of beam instabilities enhanced by the captured stray radiation indicates that the observed operation with reduced efficient may be related to a distortion of the beam properties within the full-metal beam tunnel due to beam instabilities, which above a certain level, completely destabilize the beam. An experiment with a modified beam tunnel employing rf-absorbing material and an improved in-waveguide mode converter is under preparation.

#### References

- [1] B. Piosczyk, et al., accepted for IEEE Trans. Plasma Science, June, 1997
- [2] M. Thumm et al., 21. Int. Conf. Infrared and Millimeter Waves, Berlin, 1996, paper AM6, ISBN 3-00-000800-4.

# 140 GHz Confocal Cavity Gyrotron Experiment

W.Hu, M.A.Shapiro, K.E.Kreischer, and R.J.Temkin

Plasma Science and Fusion Center, Massachusetts Institute of Technology,  
Cambridge, MA 02139, USA

**Abstract.** We designed and experimentally demonstrated the operation of a novel quasi-optical gyrotron oscillator. The core of the device is an overmoded confocal cavity which can effectively suppress undesired modes, and therefore has extremely low mode density. Stable single-mode, single-frequency operation at 140 GHz has been achieved with peak RF output power exceeding 30 kW. The results and experience obtained on this tube will benefit further development of confocal gyro-TWT amplifiers.

**1. Introduction.** Conventional high-power millimeter-wave gyrotron oscillators and gyro-amplifiers utilize cylindrical cavities and waveguides. Some researchers have studied gyrotrons based on slotted, almost cylindrical, cavities [1,2]. The novel quasi-optical concept we propose uses structures made of two cylindrical mirrors forming a confocal cavity (mirror curvature radii are equal to the distance between mirrors) as shown in Fig. 1. It has the quality of having a low mode density. By properly choosing the mirror width, one can selectively choose a desired mode with little loss while spurious modes are suppressed through diffraction. Such qualities are extremely important in the development of gyro-TWT amplifiers in which mode competition is a severe problem. As a precursor to the amplifier experiment, a gyrotron oscillator with a confocal cavity was designed to study the characteristics of confocal structures.

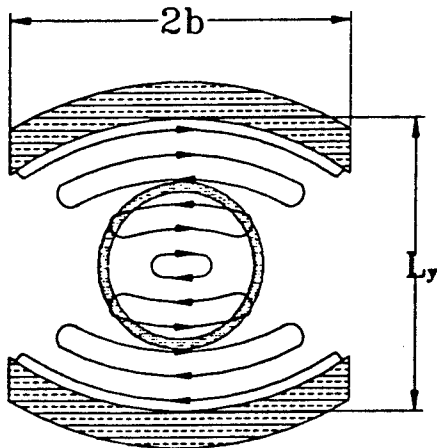


Fig. 1. Transverse geometry of confocal waveguide, with E-field lines and annular electron beam.

**2. Gyrotron Design.** We theoretically modeled the confocal cavity and gyrotron. The resulting design parameters for the gyrotron oscillator are given in Table I.

Table I. Design parameters.

Frequency (GHz)	140
Confocal cavity mode	$TE_{061}$
Beam voltage (kV)	60
Beam current (A)	5
Electron velocity ratio $\alpha$	1...1.2
Efficiency (%)	10
Magnetic field (kG)	54
Beam compression	25
Perpendicular velocity spread (%)	10
Beam radius (mm)	1.8
Mirror width $2b$ (mm)	6.2
Distance between mirrors $L_y$ (mm)	6.7
Cavity axial length (mm)	17
Diffraction Q-factor	1300

A triode magnetron-injection gun is used as the beam source and a gun coil and 60 kG magnet are utilized for electron beam formation. Like conventional gyrotron cavities, the confocal cavity is an open-ended cavity with three sections: a  $5^\circ$  down taper, a straight section and a  $5^\circ$  up taper for output. The cavity is embedded in a cylindrical tube which also serves as the beam dump and the output waveguide. The RF beam is then radiated into free space through a quartz window at the end of the tube.

The favorable qualities of the confocal cavity over conventional cavities result from its distinct gaussian-like field distribution. However, the lack of azimuthal symmetry reduces the form factor, and as a result, sacrifices some efficiency. To analyze how this affects the starting current of

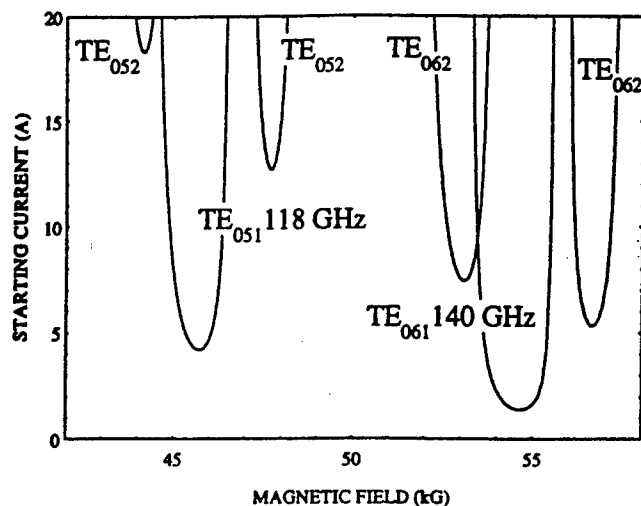


Fig. 2. Gyrotron starting current.

the gyrotron, we use the generalized theory [1,4]. For a velocity ratio of  $\alpha=1.0$  and no velocity spread, Fig. 2 shows the starting current versus the magnetic field for operation in the  $TE_{061}$  and  $TE_{051}$  modes. Spurious modes like the  $TE_{161}$  and  $TE_{151}$  modes have low diffraction Q-factors and therefore cannot be excited in the cavity.

**3. Experimental Results.** The designed  $TE_{061}$  mode is observed at 136 GHz. A peak power of 30 kW is achieved in stable operation, with a pulse width of 3  $\mu$ s and up to 10% efficiency. By sweeping the magnetic field, we revealed the neighboring mode of  $TE_{051}$  at 114 GHz. Both modes have substantial RF power output as shown in Fig. 3. The result is in a good agreement with the small signal theory (Fig. 2.). The data plotted in Fig. 3, taken at 58-63 kV and 5.5 A, was optimized with gun magnet coil and beam voltage to maximize power. The small levels of parasitic output at magnetic fields of 47 to 51 kG are not yet conclusively identified.

The dependence of power and efficiency on beam current at voltage of 63 kV and frequency of 136 GHz is measured and shown in Fig. 4 with a velocity ratio  $\alpha$  close to 1. The measured starting currents for the  $TE_{061}$  and  $TE_{051}$  modes are 0.3A and 0.8A respectively.

Simulations using EGUN predict a perpendicular velocity spread of 20%. The relatively high velocity spread is expected because the magnetic field profile is not suitably optimized for this experiment. Nonetheless, an efficiency over 10% is observed at  $\alpha$  larger than 1. We plan to redo these experiments using a different magnet which in theory provides a much lower velocity spread, higher  $\alpha$  values, and higher efficiency.

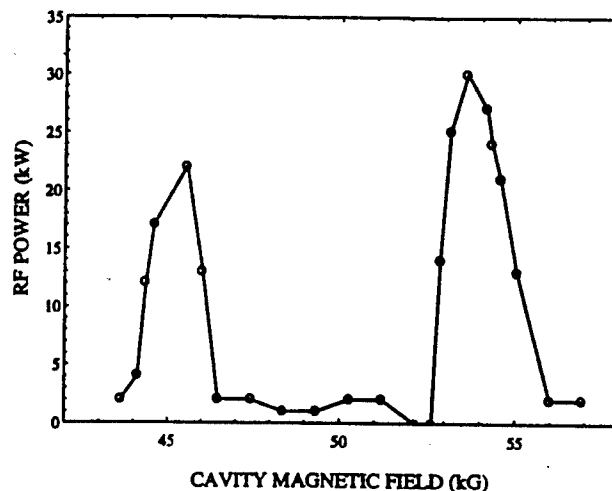


Fig. 3. Measured gyrotron power vs. magnetic field.

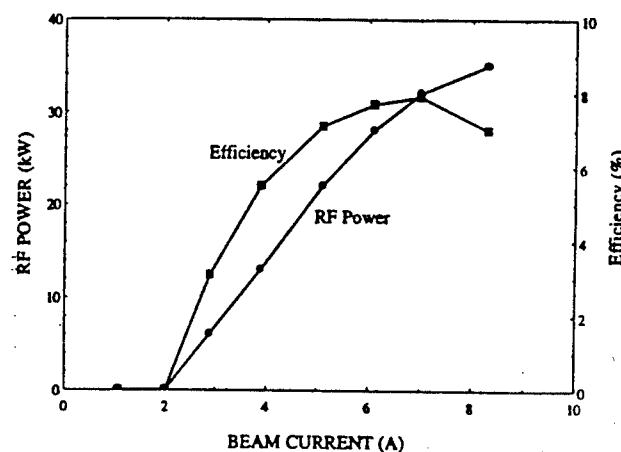


Fig. 4. Measured gyrotron power and efficiency vs. current.

**Conclusion.** The confocal gyrotron oscillator experiment demonstrates the feasibility of the operation of a fully mode-selective gyrotron. As shown in Fig. 3: confocal cavity is characterized by the distinct feature of low mode density and high mode selectivity. This demonstrated feature of the confocal cavity makes it particularly suitable for further applications in gyro-TWT amplifiers.

#### References.

1. A.V.Gaponov et al. Int. Journal of Electronics, 1981, Vol. 51, No. 4, pp. 277-302.
2. I.I.Antakov et al. Elektron. Tekhn., Ser.1, Elektronika SVCh, 1975, Vol. 8, pp. 20-23.
3. W.Hu, K.E.Kreischer, M.A.Shapiro, and R.J.Temkin. 21st Int. Conference on Infrared and Millimeter Waves, Berlin, July 14-19, 1996, paper AT3.
4. A.G.Luchinin and G.S.Nusinovich. Int. Journal of Electronics, 1984, Vol. 57, No. 6, pp. 827-834.

## OPERATION OF A 32 GHz GYROTRON

J.J. Barroso, P.J. Castro, A.A. Pimenta, V.A. Spassov, and R.A. Corrêa  
Laboratório Associado de Plasma - INPE  
12201-970 São José dos Campos, SP, Brasil

T. Idehara, and I. Ogawa  
Faculty of Engineering, Fukui University  
Fukui 910, Japan

**Abstract** - The design and operation of a 32 GHz pulsed gyrotron are reported. The device is step-tuned between the  $TE_{1,2}$  (24.16 GHz) and  $TE_{0,2}$  (31.78 GHz) modes with cathode voltages ranging from 30 to 40 kV and beam currents up to 3.0 A. In the  $TE_{2,2}$  resonator mode an output peak power of 6 kW was obtained with an 18% measured efficiency.

### 1. Introduction

The design and operating characteristics of a 32 GHz gyrotron developed at INPE are presented. The experiments have been carried out at short pulse length ( $\sim 15 \mu s$ ) and low duty cycle (0.025%) which greatly alleviate problems associated with heating of the tube. However, the design of both the resonant cavity and collector is consistent with technological constraints posed by long pulse and high average power devices.

### 2. Design of Experiment

A 15  $\mu s$  pulselength annular electron beam is generated by a temperature-limited MIG-gun with a triode configuration and cathode radius of 2.5 cm. The beam couples to the second radial maximum of  $TE_{m,2}$  modes in the resonator which consists of a standard, tapered cavity machined from brass with tolerances of  $\pm 0.1$  mm, having input and output linear tapers of  $1^\circ$  and  $5^\circ$ , respectively. The straight mid-section is 4.95 cm long and 2.10 cm in diameter which provides a diffractive Q factor of the order of 1000 for TE modes operating in the range 29-32 GHz. The collector is a copper tube of 6.3 cm internal diameter. The active length of 13 cm was determined from the study of the deposited energy pattern by the spent beam on the inner collector surface [1]. By means of the collector coil, the electron trajectories can be controlled to some extent to restrain the energy flux density to a maximum tolerable value of 2 kW/cm<sup>2</sup> in CW operation. The cavity magnetic field is provided by 20 conventional water-cooled solenoids fed by a current of 900 A. This system produces a magnetic field strength up to 1.3 T with a spatial homogeneity of  $\pm 0.1\%$  over the cavity interaction region.

### 3. Experimental Results

Frequency measurements were made using a direct reading frequency meter to within a 0.15% accuracy. Measured data are presented in Table 1 which also includes frequencies calculated from self-consistent theory using the design cavity radius of 10.57 mm.

For the absolute output power measurement, a fast response calorimeter with a thermal sensitivity of  $0.1^\circ C/W \cdot min$  was built and tested. The calorimeter comprises a quartz cone which is made sufficiently long so as to provide an effective broad band impedance matching. The chosen absorbing fluid is water, since ordinary water is almost ideal both as dissipating medium and calorimetric fluid. Power measurement results are given in Table 1, where the highest average power of 0.63 W, that corresponds to a 6 kW output peak power, was achieved by the  $TE_{2,2}$  mode. A typical oscillogram for this mode is shown in Fig. 1, where it is seen that microwave is present only during the flat top of the current pulse.

Beam velocity measurements on the beam were made using a coaxial capacitive probe [2], which consists of an electrically isolated cylinder 20 mm long placed just before the cavity.

### 4. Discussion and Conclusions

First we note from Table 1 that the measured efficiencies are lower than the expected values, which are on the order of 30%. There are a variety of reasons that account for the low efficiencies measured. These include: beam alignment, electron velocity dispersion, and mirroring effects. Alignment of the beam guiding centre is a critical requirement to minimize beam interception at the cavity entrance and ensure high-efficiency operation. This is supported by the fact that the lowest efficiency so far obtained corresponds to the  $TE_{0,2}$  mode, which - due to its azimuthally symmetric field structure - requires a well centered beam to be strongly coupled to electron beam. Nevertheless, an 18% efficiency was obtained with the  $TE_{2,2}$  mode, which is less sensitive to beam misalignment. The low efficiencies are also ascribable to electron velocity dispersion, and it

Table 1: Summary of the results ( $V_k$ : cathode voltage;  $\bar{P}_{beam}$ : average beam input power;  $\bar{P}_o$ : measured output power;  $\eta$ : efficiency;  $\beta_\perp, \beta_\parallel$ : transverse and axial electron velocities normalized to the speed of light;  $\alpha$ : velocity pitch ratio)

TE mode	Frequency [GHz]		$V_k$ [kV]	$I_{beam}$ [A]	$P_{beam}$ [W]	$P_o$ [W]	$\eta$ [%]	Capacitive Probe		
	measured	calculated						$\beta_\perp$	$\beta_\parallel$	$\alpha$
1,2		24.1594	30.0	1.2	3.6	0.58	16.0	0.31	0.10	3.0
5,1	29.09	29.0437	37.0	2.6	9.6	0.46	4.8	0.31	0.18	1.7
2,2	30.38	30.3528	34.0	1.0	3.4	0.63	18.5	0.32	0.11	2.9
0,2	31.78	31.7475	40.0	2.8	11.2	0.32	2.8	0.34	0.15	2.3

is likely that the actual velocity dispersion on the beam should be much larger than the 5% value predicted by numerical simulation [1]. The third major reason explaining the low efficiencies is attributed to the beam mirroring that occurred as the beam propagated down the drift tube. This was strongly made evident by our beam velocity measurements using the capacitive probe, which gave electron velocity ratios  $\alpha = v_\perp/v_\parallel$  as high as 3.0 (Table 1). To illustrate this point, Fig. 2 shows the phase space for the electron beam with control parameters (magnetic field and cathode voltage) set at the TE<sub>2,2</sub>-mode operating conditions. We can see that for  $z \geq 40.0$  cm and after a time span of 13.0 ns, a strong mirroring process takes place with 35% of the beam electrons returning to the gun region. This is an undesirable effect as the back bombardment of the electrons on the cathode surface reduces the life of the emitter, which in our device consists of a coating mixture of (Ba Sr)CO<sub>3</sub> sprayed onto a nickel base.

The corresponding signal detected by the capacitive probe (installed at  $z = 50.0$  cm) is displayed in Fig. 3, where it is apparent in the voltage pulse a sharp peak that rapidly decreases to approach a constant value. This suggests that a stationary state was reached by the beam. We conjecture that accumulation of reflected electrons in the near cathode region leads to a depression of the electric field on the emitter; this effect decreases the electron transverse velocity and enables the trapped particles to escape towards the cavity.

In the next experiments, considerations will involve beam alignment and reduction of the pitch ratio parameter to the optimum value of  $\alpha \simeq 1.5$  as indicated by numerical simulation. A way to reduce  $\alpha$  is to enlarge the gap spacing between the first and second anodes [3], which leads to an increase in the electron axial velocity as the beam propagates past the first anode.

## References

- [1] J.J. Barroso, A. Montes, and R.A. Corrêa, *Int. J. Infrared Millimeter Waves*, vol. 11(2): 251-274, 1990.
- [2] W.C. Guss, T.L. Grimm, K.E. Kreischer, J.T. Polevoy, and R.J. Temkin, *J. Appl. Phys.*, 69(7): 3789-3795, 1990.
- [3] H. Patire Jr., and J.J. Barroso, these Proceedings.

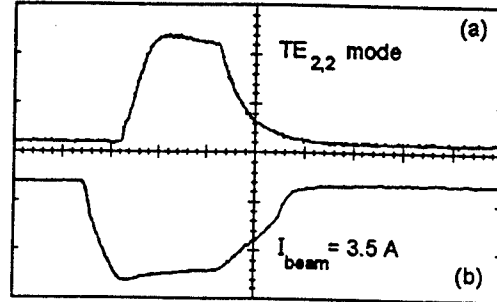


Fig. 1 - (a) RF pulse and (b) beam current waveform

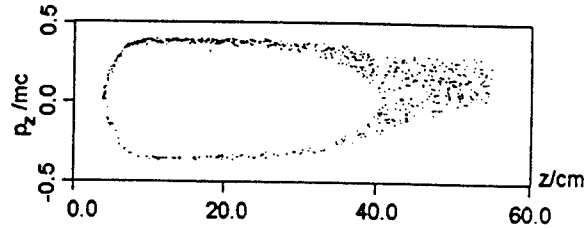


Fig. 2 - Phase space for beam electrons

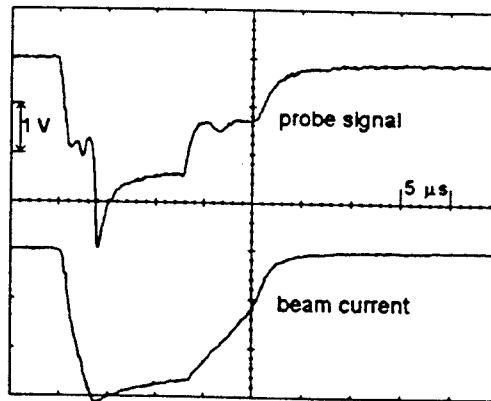


Fig. 3 - Probe and beam current signals

# Theoretical Analysis of Complete Mode of Rectangular Groove Waveguide

Yaozhong Xu, Yong Liu, Hongsheng Yang

Department of Electronic Engineering, National Key Laboratory of Millimeter Waves  
Southeast University, Nanjing 210096, P.R.China

## Abstract

In this paper we present a method to analyze the complete modes of rectangular groove waveguide. By this method we have derived the characteristic equations of that waveguide

## 1. Introduction

When the frequency is higher than 100Ghz, traditional waveguides suffer from the difficulties such as smaller size, higher loss, and lower power handling, etc. Groove waveguide has attractive features, which has been analyzed by many authors.<sup>[1][5]</sup> One of these is rectangular groove waveguide which can be easily transformed to common rectangular waveguide and has potentially widely applicational prospect. In order to use it we need more informations about its mode characteristic.

## 2. Theoretical Analysis

The cross section of the guide has the form and the dimensions shown if Fig.1. There are two symmetry planes. One is horizontal plane( $x=0$ ), and the other is perpendicular plane ( $y=0$ ). They can be treated as electric wall or magnetic wall respectively. The cross section of the guide is divided into two regions, A and B. Because of the symmetry, we consider the half plane( $x \geq 0$ ).

In the following, we derive the field components' expressions and the characteristic equations of TE and TM modes in the case of  $x=0$  plane being an electric wall and  $y=0$  plane being a magnetic wall only. The field components and characteristic equations of TE and TM modes in other cases

can be derived in a similar way.

### (1) TE modes

Considered  $x=0$  plane being an electric wall,  $y=0$  plane being a magnetic wall and other boundary conditions,  $H_z$  components of TE modes can be expressed as

$$H_{xA} = k_c^2 \sum_{n=0}^{\infty} e_n \sin(k_{yAn} y) \cos(k_{xA_n} x) \quad (1)$$

in region A, and

$$H_{xB} = k_c^2 \sum_{m=0}^{\infty} d_m \sin(k_{yBm} y) \exp[-k_{xBm}(x-b/2)] \quad (2)$$

in region B, where

$$k_{yAn} = \frac{2n+1}{a} \pi, k_{yBm} = \frac{2m+1}{c} \pi, \quad (3)$$

$$k_c^2 = k_{yAn}^2 + k_{xA_n}^2 = k_{yBm}^2 - k_{xBm}^2$$

The remaining field components can be derived from the above equations. The boundary conditions between region A and B are given by the following expressions.

$$H_{xA} = H_{xB} \quad (x=b/2, -c/2 \leq y \leq c/2) \quad (4)$$

$$E_{yA} = \begin{cases} E_{yB} & (x=b/2, -c/2 \leq y \leq c/2) \\ 0 & (x=b/2, c/2 \leq |y| \leq a/2) \end{cases} \quad (5)$$

By making use of boundary conditions the following equation is obtained

$$e_s W_{xA_s} \sin(W_{xA_s} \frac{B}{2}) = \sum_{n=0}^{\infty} e_n \sum_{m=0}^{\infty} W_{xBm} \cos(W_{xA_n} \frac{B}{2}) \quad (6)$$

$$\frac{B(m,n)}{A(m,m)} \cdot \frac{B(m,s)}{C(s,s)} \quad (s=0,1,2,3\dots)$$

where

$$W_{yAn} = k_{yAn} \cdot a = (\frac{2n+1}{a} \pi) \cdot a$$

$$W_{yBm} = k_{yBm} \cdot a = (\frac{2m+1}{c} \pi) \cdot a$$

$$W_{xA_n} = k_{xA_n} \cdot a, W_{xBm} = k_{xBm} \cdot a$$

$$A(m,n) = \int_{-\frac{c}{2}}^{\frac{c}{2}} \sin(\frac{2m+1}{c} \pi y) \sin(\frac{2n+1}{c} \pi y) dy$$

$$B(m,n) = \int_{-\frac{c}{2}}^{\frac{c}{2}} \sin(\frac{2m+1}{c} \pi y) \sin(\frac{2n+1}{a} \pi y) dy$$

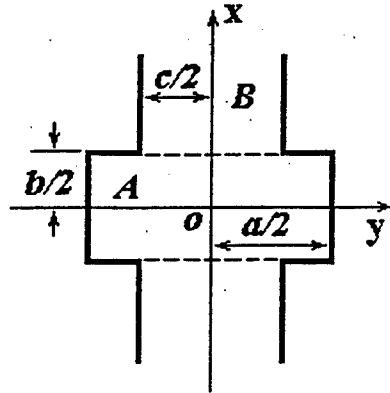


Fig. 1. The cross section of the rectangular groove waveguide

$$C(s,s) = \int_{-\frac{c}{2}}^{\frac{c}{2}} \sin\left(\frac{2s+1}{a}\pi y\right) \sin\left(\frac{2s+1}{a}\pi y\right) dy$$

It can be simplified as

$$[A][T]=0 \quad (7)$$

where

$$[T]=[e_0, e_1, e_2, \dots]^T$$

The each element of the matrix [A] can be expressed as

$$a_{sm} = W_{\alpha As} \cdot \sin\left(W_{\alpha As} \frac{B_a}{2}\right) \cdot \delta_{sm} - \sum_{n=0}^{\infty} W_{\alpha Bm} \cdot \cos\left(W_{\alpha As} \frac{B_a}{2}\right) \frac{B(m,n)}{A(m,n)} \frac{B(m,s)}{C(s,s)} \quad (8)$$

where  $\delta_{sm}$  is the Kronecker delta.

The characteristic equation of TE modes is

$$\det[A]=0 \quad (9)$$

According to our calculation, Fig.2 shows the relation between  $\lambda/2a$  of the dominant mode  $TE_{11}^{(1)}$  and the normalized plate spacing  $c/a$ . The varying tendency of the curve coincides with the theoretical result of rectangular groove given by A.A.Oliner<sup>[2]</sup>.

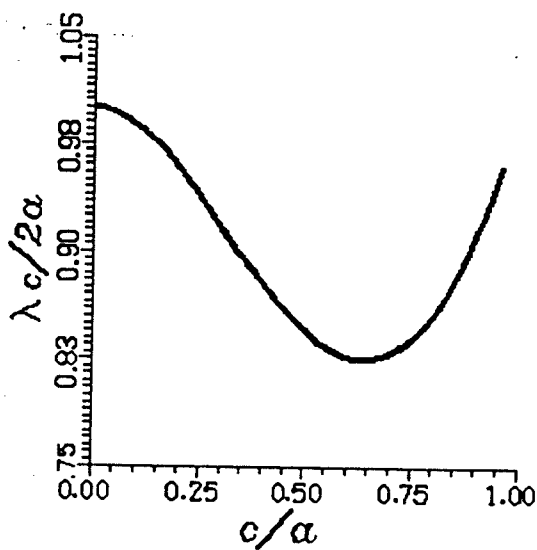


Fig. 2.  $\lambda/2a \sim c/2a$

## (2) TM modes

The longitudinal field components of TM mode in region A and B are expressed as follows

$$E_{xA} = k_c^2 \sum_{n=0}^{\infty} e_n \cos(k_{yAn} y) \sin(k_{xA n} x) \quad (10)$$

in region A, and

$$E_{xB} = k_c^2 \sum_{n=0}^{\infty} d_n \cos(k_{yBn} y) \exp[-k_{xBn} (x - b/2)] \quad (11)$$

in region B.

We have the boundary conditions

$$E_{xA} = \begin{cases} E_{xB} & (x = b/2, -c/2 \leq y \leq c/2) \\ 0 & (x = b/2, c/2 \leq |y| \leq a/2) \end{cases} \quad (12)$$

$$H_{yA} = H_{yB} \quad (x = b/2, -c/2 \leq y \leq c/2) \quad (13)$$

$$e_s \sin\left(W_{\alpha As} \frac{B_a}{2}\right) = - \sum_{n=0}^{\infty} e_n W_{\alpha An} \cos\left(W_{\alpha An} \frac{B_a}{2}\right) \sum_{m=0}^{\infty} \frac{1}{W_{\alpha Bm}} \frac{O(m,n)}{P(m,m)} \frac{O(m,s)}{Q(s,s)} \quad (s=0,1,2,\dots) \quad (14)$$

where

$$P(m,m) = \int_{-\frac{c}{2}}^{\frac{c}{2}} \cos\left(\frac{2m+1}{c}\pi y\right) \cos\left(\frac{2m+1}{c}\pi y\right) dy$$

$$O(m,n) = \int_{-\frac{c}{2}}^{\frac{c}{2}} \cos\left(\frac{2m+1}{c}\pi y\right) \cos\left(\frac{2n+1}{a}\pi y\right) dy$$

$$Q(s,s) = \int_{-\frac{a}{2}}^{\frac{a}{2}} \cos\left(\frac{2s+1}{a}\pi y\right) \cos\left(\frac{2s+1}{a}\pi y\right) dy$$

It can be simplified as

$$[A][T]=0 \quad (15)$$

where

$$[T]=[e_0, e_1, e_2, \dots]^T$$

The each element of [A] is

$$a_{sm} = \sin\left(W_{\alpha As} \frac{B}{f}\right) \cdot \delta_{sm} + W_{\alpha An} \cos\left(W_{\alpha An} \frac{B}{f}\right) \sum_{n=0}^{\infty} \frac{1}{W_{\alpha Bm}} \frac{O(m,n)}{P(m,m)} \frac{O(m,s)}{Q(s,s)} \quad (16)$$

The characteristic equation of TM modes is

$$\det[A]=0 \quad (17)$$

## 3 Conclusion

Under the case of  $x=0$  plane being an electric wall and  $y=0$  plane being a magnetic wall, the characteristic equations of TE and TM modes are given. Using the similar way we can derive the characteristic equations of TE and TM modes in other seven cases. So we can obtain the complete modes from all of the characteristic equations.

## References

- [1] Yat Man Choi and D.J.Harris, "Groove guide for short millimetric waveguide systems", *Infrared and Millimeter Waves*, Vol.11, pp. 99~140.
- [2] A.A.Oliner and Paolo Lampariello, "The dominant mode properties of open groove guide: an improved solution", *IEEE Trans. Microwave Theory Tech.*, Vol. MTT-33, No.9, 1985, pp. 755~764.
- [3] T.Nakahara and N.Kurauchi, "Transmission modes in the grooved guide", *J. Inst. Electron., Commun. Eng. Jap.*, Vol.47, No. 7, pp. 43~51, July 1964.
- [4] Y.M.Choi and D. J. Harris, "The theoretical and experimental characteristic of single V-groove guide for X-band and 100GHz operation", *IEEE Trans. MTT*, Vol. MTT-36, No. 4, 1988, pp. 715~722.
- [5] Hongsheng Yang, Jianglei Ma and Zhongzuo Lu, "Circular groove guide for short millimeter and submillimeter waves", *IEEE Trans. Microwave Theory Tech.*, Vol. MTT-43, No.2, 1995, pp. 324~330.



# Eigenmodes in gyrotron corrugated coaxial cavity

R.A. Corrêa, J.J. Barroso, and P.J. Castro  
Laboratório Associado de Plasma - INPE  
12201-970, São José dos Campos, SP, Brazil

**Abstract**—A systematic study of corrugated coaxial gyrotron cavities is done by examining the role played by the corrugation parameters on the dependence of the transverse eigenvalue  $\chi_{mp}$  with respect to the coaxial parameter  $C$ . An explicit expression for slope function  $d\chi_{mp}/dC$  is then obtained which provides added insight into the selective properties of corrugated coaxial cavities. A cold experiment to verify the values of resonant frequency and total  $Q$  factor is performed where measured and calculated results are in close agreement.

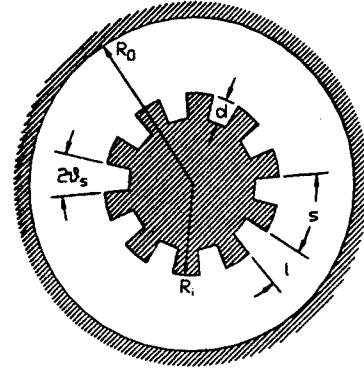


Figure 1: Cross section of the corrugated coaxial cavity

## I. Calculation of the Eigenvalues

Let us consider a corrugated cylindrical cavity with geometry as shown in Fig. 1, where the coaxial insert is a longitudinally slotted cylinder. Instead of using space harmonics [1] in the formulation of the electromagnetic field problem, we shall proceed with a simpler method, usually referred to as the surface-impedance approach [2]. The method relies on the assumption that the ratio between the tangential  $\vec{E}$  and  $\vec{H}$  fields can be expressed as an impedance-type boundary condition and that such a ratio must be given unambiguously in terms of the geometry of the corrugated wall. Under the condition that the slot width is less than a half wavelength of the operating mode, which means that the field variation along a slot interval is negligible, the corrugations may be represented by a homogeneous reactive surface at  $r = R_i$  (Fig.1).

The characteristic equation for the transverse wavenumber is obtained on applying continuity conditions to the surface reactance at  $r = R_i$ , so that

$$\frac{J'_m(x) Y'_m(y) - J'_m(y) Y'_m(x)}{J_m(y) Y'_m(x) - J'_m(x) Y_m(y)} = w \quad (1)$$

and

$$w = \frac{l J_1(y) Y_1(y_d) - Y_1(y) J_1(y_d)}{s J_0(y) Y_1(y_d) - Y_0(y) J_1(y_d)} \quad (2)$$

where the transverse eigenvalues  $\chi_{mp} = k_{\perp} R_0 \equiv x$ ,  $y \equiv \chi_{mp}/C$  with  $C = R_0/R_i$  and  $y_d = y(1 - d/R_i)$ ;  $J_m$  and  $Y_m$  are, respectively, Bessel functions of the first and second kinds with primes denoting differentiation with respect to the argument.

To investigate the effect on the  $\chi(C)$  curve shape of varying the corrugation parameters, we shall look at the extremes of the eigenvalue curves, by expressing the derivative of  $\chi_{m,p}$  with respect to  $C$  in the form

$$\frac{d\chi_{mp}}{dC} = \frac{-yf(y)}{(x^2 - m^2) \left[ \frac{wJ_m(y) + J'_m(y)}{CJ'_m(x)} \right]^2 - f(y)} \quad (3)$$

where

$$f(y) = y^2 w^2 \left(1 - \frac{s}{l}\right) + y^2 \left(1 - \frac{s}{l}\right) + \frac{l}{s} y_d^2 G^2(y_d) - m^2 \quad (4)$$

with

$$y_d G(y_d) = \frac{4/\pi}{J_1(y_d) Y_0(y) - Y_0(y) J_1(y_d)} \quad (5)$$

As can be shown, the denominator of the right-hand side of (3) is always positive. Hence, the sign of the derivative  $d\chi/dC$  is opposite to the sign of  $f(y)$ , and further the condition for obtaining an extremum of  $\chi(C)$  is given by  $f(y) = 0$ . To illustrate this point, we show in Fig. 2 the function  $yf(y)$  corresponding to the corrugation parameters  $d/R_i = 0.4$ ,  $l/s = 0.2$  and azimuthal number  $m = 6$ . Examining this plot we can anticipate the behavior of the eigenvalue curves for the family of modes  $TE_{6,p}$  with radial number  $p > 1$ . As the variable  $y$  is the ratio of eigenvalue  $\chi$  to the parameter  $C$ , the first zero at  $A = 0$ , implies that the eigenvalue curves tend asymptotically to  $C \rightarrow \infty$  with zero  $d\chi/dC$  slope. This limit corresponds to the hollow cylindrical resonator. Since  $yf(y) < 0$  in the range  $A < y < B$ , the slope  $d\chi/dC$  is positive in this range with  $B = 6.31$  corresponding to the first local minimum on the  $\chi(C)$  curve. From  $B$  to  $C$  the derivative  $d\chi/dC$  is negative and  $C = 11.29$  should correspond to a local maximum. Further,  $D = 12.51$  gives a minimum,  $E = 19.17$  is a maximum and so on. For this case we may infer, therefore, without solving the characteristic equation (1), that the function

$\chi(C)$  has an oscillatory behavior with alternating minima and maxima, but with the oscillation period shortening as  $y$  increases. On the other hand, the function  $yf(y)$  displays a different behavior when the following corrugation parameters  $d/R_i = 0.20$  and  $l/s = 0.40$  are considered. In this case (Fig. 3), there exists only one minimum; after reaching this minimum at  $y = 5.79$  the curves  $\chi_{6,p}(C)$  with  $p > 1$  should exhibit negative slope.

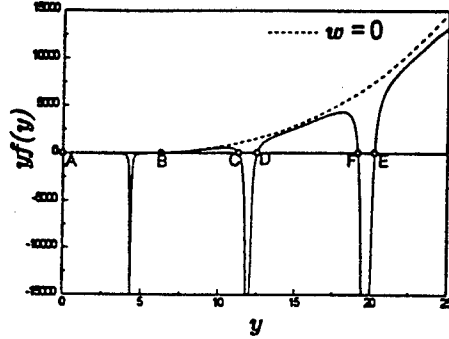


Figure 2: Function  $yf(y)$  with  $d/R_i > l/s$

We can obtain still more information about the eigenvalue curves by noting in Figs. 2 and 3 that the function  $yf(y)$  diverges as  $|w| \rightarrow \infty$ . Upon using the asymptotic forms of Bessel and Neumann functions for large arguments in (2) we have  $w = (l/s) \tan(yd/R_i)$  and (3) reduces to

$$\frac{d\chi_{mp}}{dC} = \frac{\chi_{mp}}{C} \frac{-\left(1 - \frac{d/R_i}{l/s}\right)}{\frac{x^2 - m^2}{x^2} \frac{J_m^2(y)}{J_m^2(x)} - \left(1 - \frac{d/R_i}{l/s}\right)} \quad (6)$$

as  $|w| \rightarrow \infty$ . Recalling that the denominator of the right-hand side of (6) is positive, we see for  $(d/r_i)/(l/s) > 1$  that the derivative  $d\chi/dC$  is positive and, accordingly,  $yf(y)$  diverges to minus infinity as shown in Fig. 2; the converse occurs for  $(d/R_i)/(l/s) < 1$  and, as  $|w| \rightarrow \infty$ , the limiting value of  $yf(y)$  is  $+\infty$  as indicated in Fig. 3.

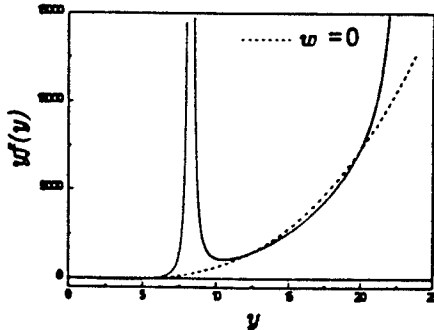


Figure 3: Function  $yf(y)$  with  $d/R_i < l/s$

By contrast, for  $d/R_i = l/s = 0.4$  we see in Fig. 4 that the  $TE_{6,4}$ -mode curve broadens and flattens over a relatively large range of the parameter  $C$ . In this particular case, the singular points of  $f(y)$  are associated with a zero derivative  $d\chi/dC$  as indicated by (6); therefore, all the  $\chi(C)$  curves have zero slope when crossing the line  $y = y_{s,1}$  corresponding to the first singular point at  $y_{s,1} \simeq 1.25\pi$ , which explains the flatness of the main por-

tion  $y_B \geq y \geq y_{s,1}$  of the curves. For  $y \gg 1$ , the singular points of  $f(y)$ , or the poles of  $w$ , are approximated by  $y_{s,p} = (2p-1)\pi/(2d/R_i)$ , and it is apparent that the upper curves  $\chi_{6,4}$  and  $\chi_{6,3}$  exhibit secondary plateaus in the neighborhood of the intersection points on the lines  $y = y_{s,2} = 3.75\pi$  and  $y = y_{s,3} = 6.25\pi$ . We see also in Fig. 4 that the  $y_{s,1}$  line does not intercept the  $TE_{6,1}$ -mode curve. Such a lowest order mode with circumferential variations is very insensitive to the presence of the corrugated rod and has a unique feature in exhibiting transverse eigenvalues lower than the azimuthal number  $m=6$ . This yields that the tangent to the curve (6,1) through the point  $T$  coincides with the line joining this point and the origin at  $C = 0$  since, according to (6),  $d\chi/dC = \chi/C$  for  $m = \chi$ . We note that the function  $yf(y)$  has only a zero at the point  $C = 0$ , so that the function  $\chi(C)$  when  $p = 1$  has neither minimum nor maximum. It is important to observe in Fig. 4 that differently from the smooth wall case for which the eigenvalue increases without limit as  $C \rightarrow 1$ , a noticeable effect is that the eigenvalue for the corrugated cavity is limited as  $C \rightarrow 1$ . This limiting value can be easily estimated and it is given by  $\chi_{mp} = (p-1)\pi/(d/R_i)$  where  $p$  is an integer denoting the radial mode number.

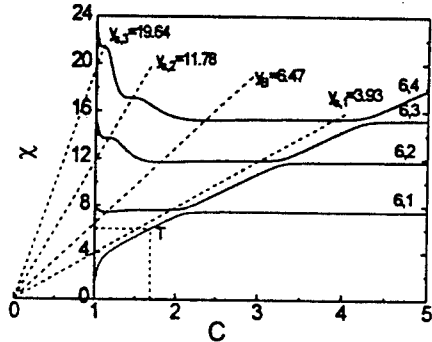


Figure 4:  $\chi(C)$ -curves for  $TE_{6,p}$  modes with  $d/R_i = l/s$

## II. Conclusions

The potentialities of a corrugated coaxial cavity configuration with longitudinal corrugations on the inner conductor has been investigated in the case of small corrugation periodicity. A judicious study of the characteristic and influence of the parameters of the corrugations in the eigenvalues curves  $\chi(C)$  was carried out. The use of corrugations enables the change of the slope of the curves  $\chi(C)$ , and the choice of the values of the quality  $Q_T$  factors associated with the frequency spectrum of the coaxial cavities with tapered inner rod. It is suggested the use of this geometry for overmoded cavities of high power and frequency gyrotrons in order to reduce the problems of mode competition in gyrotron cavities. A cold experiment was carried out and good agreement between measured and calculated values for resonant frequency and  $Q_T$  values was found.

## References

- [1] R.E. Collin, *Foundations for Microwave Engineering*, Tokyo: McGraw-Hill Kogakusha, 1966, Chap. 8
- [2] T.A. Senior and J. Volakis, *Proc. IEEE*, 79(10), 1991

# ELECTROMAGNETIC VIBRATION IN SEMI-OPENED WAVEGUIDE JUNCTION WITH ANISOTROPIC DIELECTRIC

*Prof. Lazaryev O.M., Prof. Zvyagintsev A.A., Prof. Strizhachenko A.V.  
Microwave Physics Department, Kharkov State University, Svoboda sq.4,  
Kharkov, 310077, Ukraine.*

This work is the continuation of the whole series works [1,2] devoted to investigation of semi-opened waveguide junctions and their utilizing for dielectrics and ferrites electromagnetic characteristics measurement on SHF.

## RESULTS

The rectangular waveguide junction loaded with anisotropic dielectric have been considered in this work. For choozen anisotropy (single-axis crystal with  $\hat{\epsilon} = \{\epsilon_x, \epsilon_y, \epsilon_z\}$ ) and  $H_{mno}$ - and  $E_{mnc}$  modes (the indecies show the number of semi-variants of field along x,y and z axes correspondingly) common wave equation break up into two equations:

a) for H-modes:

$$\frac{\partial^2 E_z}{\partial x^2} + \frac{\partial^2 E_z}{\partial y^2} + k_0^2 \epsilon_z E_z = 0, \quad (1)$$

b) for E-modes:

$$\frac{1}{\epsilon_y} \frac{\partial^2 H_z}{\partial x^2} + \frac{1}{\epsilon_x} \frac{\partial^2 H_z}{\partial y^2} + k_0^2 H_z = 0, \quad (2)$$

where  $k_0 = 2\pi/\lambda$  -wave length.

After the decision of correspondent electromagnetic problem two infinite system of the linear algebraic equations of second kind (SLAE) have been obtained:

a)  $H_{mnc}$ -oscillations:

$$A_n - \frac{16\pi^4}{a^3 b^3} \sum_{k=1}^{\infty} \sum_{m=1}^{\infty} A_k \frac{n k m^2 \left[ \gamma_{ma}^I \operatorname{th} \left( \gamma_{ma}^I \frac{b}{a} \right) + \gamma_m^{III} \operatorname{cth} \left( \gamma_m^{III} \frac{c-b}{2} \right) \right]^{-1}}{\left[ \gamma_{ma}^{I2} + \left( \frac{m\pi}{b} \right)^2 \right] \left[ \gamma_{kb}^{I2} + \left( \frac{m\pi}{a} \right)^2 \right] \left[ \operatorname{th} \left( \gamma_{nb}^I \frac{a}{2} \right) \gamma_{nb}^I + \gamma_n^{II} \right]} = 0, \quad (3)$$

$$\gamma_{nb}^I = \left[ \left( \frac{m\pi}{b} \right)^2 - k_0^2 \epsilon_z \right]^{1/2}; \quad \gamma_{ma}^I = \left[ \left( \frac{m\pi}{a} \right)^2 - k_0^2 \epsilon_z \right]^{1/2};$$

where following designations have been introduced:

$$\gamma_n^{II} = \left[ \left( \frac{m\pi}{b} \right)^2 - k_0^2 \right]^{1/2}; \quad \gamma_m^{III} = \left[ \left( \frac{m\pi}{a} \right)^2 - k_0^2 \right]^{1/2} -$$

-transmission (fade) constant if waveguides are cut-off on resonant frequencies; the upper indecies are corresponding to waveguides A and B with transverse sizes 2b and 2a; I -the central region (junction region) loaded with anisotropic

$$A_n - \frac{16\pi^2}{a^2 b^2} \sum_{k=1}^{\infty} \sum_{m=1}^{\infty} A_k \frac{nm\gamma_{ma}^I \gamma_{kb}^I \left[ \gamma_{nb}^I \operatorname{th} \left( \gamma_{nb}^I \frac{a}{2} \right) + \epsilon_y \gamma_n^{II} \right]^{-1}}{\left[ \gamma_{ma}^I + \left( \frac{m\pi}{b} \right)^2 \right] \left[ \gamma_{kb}^I + \left( \frac{m\pi}{a} \right)^2 \right] \left[ \gamma_{ma}^I \operatorname{th} \left( \gamma_{ma}^I \frac{b}{2} \right) + \epsilon_x \gamma_m^{III} \operatorname{th} \left( \gamma_m^{III} \frac{c-b}{2} \right) \right]} = 0$$

$$\gamma_{nb}^I = \left[ \left( \frac{m\pi}{b} \right)^2 \frac{\epsilon_y}{\epsilon_x} - k_0^2 \epsilon_y \right]^{1/2}, \gamma_{ma}^I = \left[ \left( \frac{m\pi}{a} \right)^2 \frac{\epsilon_x}{\epsilon_y} - k_0^2 \epsilon_x \right]^{1/2},$$

$$\gamma_n^{II} = \left[ \left( \frac{m\pi}{b} \right)^2 - k_0^2 \right]^{1/2}, \gamma_m^{III} = \left[ \left( \frac{m\pi}{a} \right)^2 - k_0^2 \right]^{1/2}. \quad (4)$$

Waveguides II and III always must be cut-off for eigen modes and the region I may be cut-off or not. In last case  $\gamma_{nb}^I$  and  $\gamma_{ma}^I$  become imaginary.

The next designations in (4) correspond to introduced designations in equation (3).

The resonant frequencies may be determine from the condition of the equality to zero the determinant of equation system (3,4). The effective algorithm for solving of SLAE (3), (4) by PC IBM have been carried out.

It can be seen from the (1)-(4) that the expression for  $H_{mnc}$ -oscillations has only  $\epsilon_z$ , and the expression for  $E_{mnc}$ -oscillations has  $\epsilon_x$  and  $\epsilon_y$ .

This is permit to create set for determination of each components of dielectric permittivity tensor  $\hat{\epsilon}$ . The measurement set includes standart VSWR as P2-65, standart SHF waveguide tract and frequency meter. The set is automatic (frequency meter connected with PC AT 386/387), due to this the time of single measurement of  $\hat{\epsilon}$  with accuracy

## CONCLUSIONS

On the basis of the theoretical analysis carried out, a method and the measurement complete set for electromagnetic characteristics of materials measuring are developed. They have non-destructive nature and permit follows:

- to measure local parameters of isotropic and anisotropic dielectrics;
- to define the direction of permittivity ellipsoid axis of anisotropic crystals.

## REFERENCES

1. Zvyagintsev A.A., Strizhachenko A.V., Furman D.F. Natural Electromagnetic Modes In Cylindrical Waveguide Junction And Their Use For Non-destructive Microwave Measurements Of Materials Electromagnetic Characteristics. -International Journal of Infrared and Millimeter Waves, 1995, vol.16,N5.
2. Strighachenko A.V., Zvyagintsev A.A. Non-destructive Microvave Measurements of Electromagnetic Characteristics of Anisotropic Dielectrics. International Conference of Millimeter and Submillimeter Waves and Application III, 1984, Denver USA, pp.101-102.

## Eigenmodes Classification of The Cross-Shaped Waveguide Splitters

A.G. Yushchenko, S.F. Shibalkin, M.E. Ilchenko

*National Technical University of Ukraine "Kiev Polytechnic Institute",  
Prospect Peremogy 37, Kiev, 252056, Ukraine,  
Fax: +38-044-274-59-32; E-mail: yush@polytech.kiev.ua*

### Abstract

Eigen modes classification of the equal-arm cross-shaped waveguide splitters has been suggested in this work. It's based on the field topology graphical investigations and shows the agreement with symmetric field space principal.

### Introduction

Comprehension the resonance phenomenon physics of waveguide splitters made possible a rigid calculations of their eigen [1,2] and quasi-eigen [3] spectrums. It has been stimulated a splitters practical utilization as a basis of both magnetodielectric bar test fixture [4,5] and transmission lines design [6,7]. Nevertheless, some mistakes were made during field classification. The higher order modes have been described as modes having different number of field variations along axis X and Y [1,6]. A necessity even mode classification also was arisen.

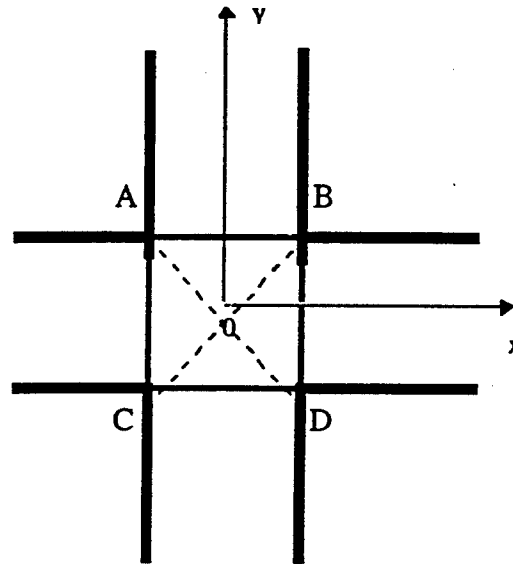


*Fig. Cross- section of equal-arm  
waveguide splitter with  
dielectric bar*

### Eigenmodes classification

Figure shows the cross section of equal-arm cross-shaped transmission line [7,8] with dielectric bar [6]. A critical frequencies of the line correspond a resonance frequencies applicable rectangular waveguide. For example, the line  $EH_{11}$  -wave corresponds the rectangular waveguide splitter  $H_{110}$ -eigenmode.

The odd and even wave field topology investigations, have made by us, allow to conclude that a equal number of field variations is settled at the waveguide arms, i.e. along X and Y axis. The waves, having a equal number of variations in waveguide arms compare by the number variations along the diagonals AD and BC (Fig); and we have here "electric" or "magnetic" walls, simultaneously. That is why we have proposed a mode classification which seems to us more comfortable in this case.

For example, according to the new classification  $EH_{mn}^+$ -wave will be in agreement with the following field structure:

(+) - along the diagonals AD and BC are electric walls and (n) is the electric field variations number along their;  
(m) are variations number along X and Y in waveguide arms.

Similarly, for the  $HE_{mn}^-$ -wave we have:

(-) - along the diagonals AD and BC are magnetic walls and (n) is a magnetic field variations along their.

The obtained results consistent with general symmetry principal according to which an each of the symmetry plans of electrodynamics system must be an electric or magnetic walls [9].

## References

- [1] Korobkin V.A., Osintsev V.V., "Electromagnetic Field Eigenmode of Dielectric Parallelepiped in Waveguide Splitter", *Radiotekhnica i Elektronika*, vol.30, n. 3, pp.417-421, 1985.
- [2] Korobkin V.A., Obolyaninova E.V., Osintsev V.V., "Electromagnetic Field Eigenmode of Dielectric Resonators placed in Flat Waveguide Splitter", *Radiotekhnica i Elektronika*, v. 34, n.8, pp.1770-1773.
- [3] Korobkin V.A., Shibalkin S.F., Yushchenko A.G., "Coupled Quasi-eigen- modes of Waveguide Splitters", *Radiotekhnica i Elektronika*, vol.39, n.7, pp.1107-1112, 1994.
- [4] Korobkin V.A., Osintsev V.V., "Eigenmode of Cross-Shaped Rectangular Waveguide Splitter with Magnetodielectric Filling", *Zhurnal Tekhnicheskoy Fizique*, vol.55, n.10, pp.1907-1911, 1985.
- [5] Yushchenko A.G., Ilchenko M.E., Shibalkin S.F. at all., "The Nondestructive Microwave Test of Extended Dielectric Structures Parameters by the Method of Waveguide Junctions", *Proc. "ISRAMT-95"*, Kiev, Sept.11-16, 1995, pp.707-710.
- [6] Korobkin V.A., Osintsev V.V., "Eigen Electromagnetic Waves of Rectangular Dielectric Bar Placed in Semi-open Cross-shaped Screen", *V Trudakh Vsesouznogo Seminar "Volny i Difraktsia"*, Moscow: Phizhicheskoe Obshchestvo, vol.3, pp.20-22, 1990.
- [7] Yushchenko A.G., Shibalkin S.F., "Electrodynamic Modeling of Waveguide Properties Semi-open Transmission Lanes Based on Flat Waveguide Splitters", *Infrared and Millimeter Waves*, vol.15, no.7, pp.1523-1552, 1994.
- [8] Yushchenko A.G., Shibalkin S.F., Obolyaninova E.V., "Waveguide Properties of Cross-Shaped Section Semi-open Transmission Line", *Proc. of the Third Intern. Symposium on Antennas and EM Theory (ISAE'93)*, Sept.6-9, 1993, Najing, China, pp.323-326.
- [9] Silin R.A., Sazonov V.P., "Slow-wave Systems", *Izdatelstvo: Sovetskoe Radio*, 1966.

# Wave Resistance and Attenuation of the Cross - Shaped Partially Filled Waveguide

M.E. Ilchenko, A.G. Yushchenko, A.F. Zorkin

National Technical University of Ukraine "Kiev Polytechnic Institute"

Prospect Peremogy 37, Kiev, 252056, Ukraine,

Fax: +38-044-274-59-32; E-mail: yush@polytech.kiev.ua

## Abstract

The wave resistance and attenuation expressions of the line principal  $LME_{10}$ -wave have been obtained. Their frequency dependence, based on obtained expressions, were analyzed.

thoroughly engineered filters with band width  $\Delta f \approx (5 - 15) \%$  to show promising of this structure investigations as a millimeter transmission line with working  $LME_{10}$ -wave.

## Introduction

The interest to the cross-shaped waveguide is due to necessity for CAD theoretical base establishment of band pass filters [1], having high electrical parameters [2]. By the method of partial regions a problem of the hybrid  $LME$  and  $LEM$  waves propagation have been solved. The first ones are transformed to the  $LM$  and the second ones - to the  $LE$  waves during limiting passes to the rectangular waveguide. The coupling quantity of this wave is proportional to the projections value  $(a_2 - a_1)$  {Fig.} and for the practically using waveguide it can be neglected  $\{[(a_2 - a_1) / a_2] \leq 5\% \}$ .

A small insertion losses  $\alpha_0 \approx (0.2 - 0.5) dB$  of the

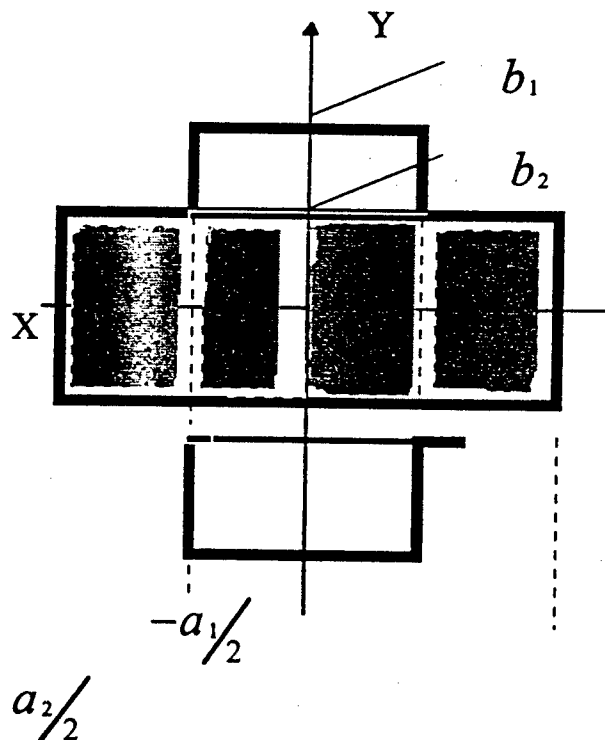


Fig. Cross-Shaped Partially Filled Waveguide Cross Section

The expressions for wave resistance  $R_w$  and attenuation  $\alpha$  of  $LME_{10}$  wave were obtained on the assumption that projections are small. The calculations were performed according to the follow formulae:

$$\alpha = \frac{P_\sigma + P_\varepsilon}{2P_z},$$

where  $P_\sigma$  and  $P_\varepsilon$  are the apportioned losses power in the waveguide walls and dielectric, respectively;  $P_z$  is the moving wave power.

$$R_w = \frac{U_m^2}{2P_z},$$

where

$$U = 2 \left\{ \int_0^{b_2} E_y^{(2)}(0, y) dy + \int_{b_2}^{b_1} E_y^{(1)}(0, y) dy \right\}$$

the electric field  $E_y$ , upper indices are indicated to the partially region number {Fig}.

## Short Conclusions

The numerical calculations based on the received formulae were performed. They have shown that cross shaped waveguide losses value when  $b_1 \approx b_2$  agree with losses of the rectangular waveguide with dielectric filling and tend to the H-guide losses when  $b_1 \gg b_2$ . At the first case they are maximal and the second case they are less that one order when a high -Q dielectric is used. Both  $R_w$

and  $\alpha$  are changed heavily with small wedge ( $b_1 - b_2$ ) and practically aren't changed with  $b_1 \gg b_2$ .

The explanation for this is that the electromagnetic field in wedge has a attenuated behavior.

## References

- [1] Yushchenko A.G., Popov V.V., Shibalkin S.F. at all. *Patent of Russian Federation N2040080 /21.06.1991/*.
- [2] Ilchenko M.E., Yushchenko A.G., Popov V.V., Shibalkin S.F., *Conf. Digest, "Intern. Conference on Millimeter and Submillimeter Waves and Applications"*, January 10-14, 1994, San Diego, v.2250, pp.571-572.



# The Physical Peculiarities of Wave Propagation in Coupled Cylindrical Slot Lines.

Alexander Svezhentsev

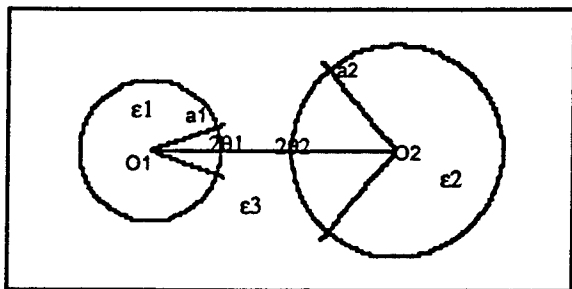
Institute of Radiophysics & Electronics  
National Academy of Sciences of Ukraine  
12, Ac. Proskura st., Kharkov 85, 310085, Ukraine

## Abstract

Physical peculiarities of the wave propagation in coupled cylindrical slot are first studied in the context of a rigorous electromagnetic theory. The mode analysis is given. Dispersion characteristics of the waves are examined for different geometry and constitutive parameters. For the lines possessing symmetry, the wave spectrum splitting is considered. The phenomenon of the waves mutual transformation is found.

## Introduction and Problem Formulation

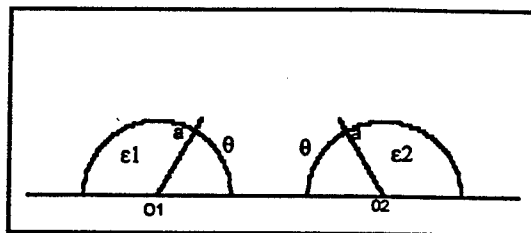
It is well known that structures built around electro-dynamically coupled open waveguides are actively engaged in microwave engineering for directional couplers, filters, antennas, etc.



The wave propagation problem for a pair of cylindrical slot lines (Fig.1) has already been rigorously solved [1]. The present work is first that offers numerical characteristics of the waves in a structure. By now, the spectral problem of single slot/strip lines is rather complete, and spectral characteristics, field structure have received their study [2-3].

It has been shown [1] that the eigenwave problem for a pair of cylindrical slot lines (CSIL) is reduced to the solution of the dispersion equation of the kind  $\det[I-A(h)]=0$ , where  $A(h)$  is kernel operator function in the form of a 4x4 block matrix constituted from infinite matrices;  $I$  is unit operator;  $h$  is propagation constant; the eigenwave fields depend on  $z$  and time as  $\exp(ihz-i\omega t)$ . The block structure and 4x4 dimension of the matrix point to the interaction between these two CSILs and to the coupling of the E- and H- waves in the considered metal-dielectric waveguides. In this case, the diagonal cells  $A(h)$  describe the single CSILs, and the nondiagonal ones account for their interaction. If the considered structure has planes of symmetry (their number does not exceed two), the

order of the examined systems of equations may be reduced. The considered boundary value problem is solved by the Riemann-Hilbert problem technique using the additional theorem for cylindrical function. The present work offers dispersions characteristics of the surface and leaky waves for some modifications of coupled CSILs, and it also analyses effect arising due to the mutual interaction of single lines.



## Discussion and conclusions

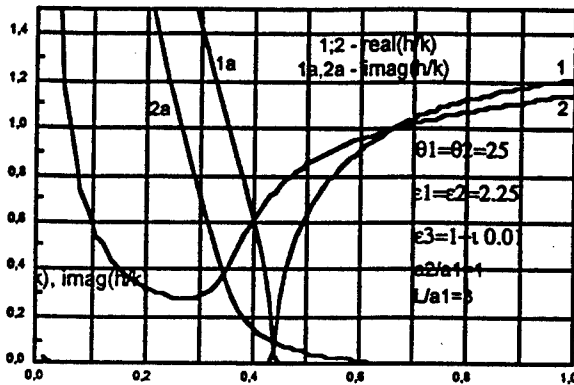
The reduced dispersion equation is numerically solved using an algorithm based on the Newton's method. The surface and complex waves whose spectral numbers belong to the principal sheet of the Riemann surface arising due to the Hankel function multivalueness [1] will be considered. It is possible to show that the wave spectrum of two coupled CSILs in the case of the narrow slots ( $\theta_1, \theta_2 \ll 1$ ) and  $kL > 1$  ( $k = 2\pi/\lambda$ ,  $\lambda$  - free space wavelength,  $L$  - the distance between the waveguide centra) consist of: quasi-  $E_{mn}^{(1)\pm}, E_{pq}^{(2)\pm}, H_{mn}^{(1)\pm}, H_{pq}^{(2)\pm}$

waves of the inner waveguides;  $XE_{mn}^{(1)\pm}, XE_{pq}^{(2)\pm}, XH_{mn}^{(1)\pm},$

$XH_{pq}^{(2)\pm}$  waves of the outside region; two quasi- $T_0$  waves; four quasi- $T_1$  waves; and quasi- $H_{00}^{(1)}, H_{00}^{(2)}$  waves (+(-) sign corresponds to the orthogonal families of waves, 1 and 2 show waveguide).

First we consider coupled CSILs lying on a metal base (Fig.2) and having the two planes of symmetry: the vertical and the horizontal ones. It is distinguished the wave family corresponding to the electric wall presence at the horizontal plane

of symmetry. In such a structure with the narrow slots, the lowest modes are the slot waves  $H_{00}^+$  and  $H_{00}^-$  which arise due to the spectrum splitting and possess different symmetry about the vertical plane of symmetry: the wave  $H_{00}^+$  arises if there is a magnetic wall at the vertical plane of symmetry,  $H_{00}^-$  arises if there is an electric wall. Dispersion characteristics of the slot waves  $H_{00}^+$  and  $H_{00}^-$  are shown in Fig.3 with curves 1

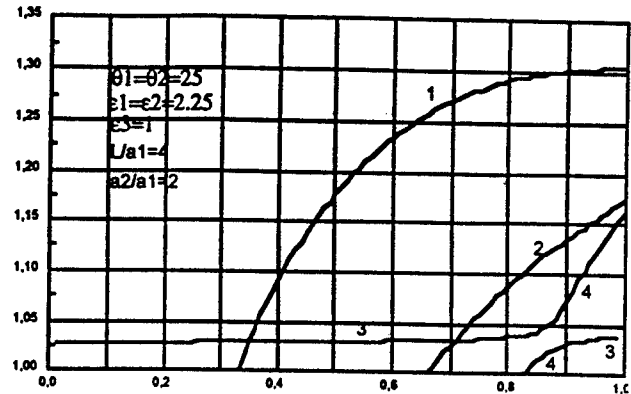


and 2, respectively; the external medium loss is  $\text{Imag}(\epsilon_3) = 0.01$ . In this case both of the slot waves exhibit a close transition normalised frequency  $ka_1 = ka_n$ , where  $ka_n$  is the frequency when  $\text{real}(h/k) = 1$  ( $k = 2\pi/\lambda$ , where  $\lambda$  is free space wavelength). It is well known that the field behaviour in the external region depends on the transverse wavenumber which in this case is  $\chi^2 = ka_1^2(\epsilon_3 - h^2)$ . If  $ka_1 > ka_n$ , then  $\text{real}(\chi) > 0$  and  $\text{Imag}(\chi) > 0$  for both of the slot waves. So their fields exponentially decrease with distance from the structure in a transverse direction, and two slow waves ( $\text{real}(h/k) > 1$ ) are observed. If  $ka_1 < ka_n$ , then for the wave  $H_{00}^+$   $\text{real}(\chi) > 0$  and  $\text{Imag}(\chi) > 0$  are initially valid. But at  $ka_1 = 0.22$   $H_{00}^+$  is transformed to the leaky wave outgoing from the structure ( $\text{real}(\chi) > 0$  and  $\text{Imag}(\chi) < 0$ ). The field of this wave increases with distance from the structure in a transverse direction. For  $H_{00}^-$  ( $\text{real}(\chi) > 0$  and  $\text{Imag}(\chi) < 0$ ) for every  $ka_1 < ka_n$ , and  $H_{00}^-$  is a leaky wave outgoing from the structure. It is seen from Fig.3 that there is the region of  $ka$  values, namely,  $0.45 < ka < 0.65$ , in which the losses of the leaky  $H_{00}^+$  wave are very small. It means that the leaky  $H_{00}^+$  wave of open coupled structure in the above-mentioned region is similar to a fast wave in the closed waveguide. The further behaviour of the  $\text{real}(h/k)$ ,  $\text{imag}(h/k)$  for the  $H_{00}^+$  wave under  $ka < 0.42$  confirms this fact, showing that  $\text{imag}(h/k) \gg \text{real}(h/k)$ .

Now we shall consider a pair of CSILs with the horizontal plane of symmetry (Fig.1). In this case, the CSILs have different diameters. Dispersion characteristics (Fig.4) of such a structure correspond to the orthogonal wave families which belong to different classes of symmetry about the plane of symmetry, namely, to  $H_z^+/E_z^-$  and  $H_z^-/E_z^+$  (+/-) sign indicates the evenness (oddness) of the  $z$ -component of the field about the plane of symmetry). Slot waves 1 and 2 supported, respec-

tively, by CSILs 2 and 1 belong to the family  $H_z^+/E_z^-$ , the rest waves belong to the family  $H_z^-/E_z^+$ . The slot wave associated with CSIL 2 has evidently greater normalised propagation constant  $h/k$ . Wave 3-4 (this notation indicates the subsequent change of the wave type as  $ka_1$  varies) is the principal one having no cut-off and it represents a slot-perturbed quasi-T wave of a two-conductor line.

As seen from Fig.4 there is a region where quasi-T wave 3-4 "interacts" with wave 4-3. The field structure investigation shows that this is a region of the wave mutation: the quasi-T



wave whose field is essentially concentrated in the external region transforms into the wave of the internal region of CSIL 2. The similar effects were found [4] for the waves in a single CSIL. It has been shown [5] that the "interaction" region contains the so-called Morse critical point.

Thus physical peculiarities of the wave propagation in coupled cylindrical slot lines have been first numerically investigated through a rigorous approach. The obtained results have both theoretical and practical value.

## References

- [1]. A.Svezhentsev The Waves in Coupled Cylindrical Slot and Strip Lines. Doklady of National Academy of Sciences of Ukraine, Ser.A, 1996, 5, p.p.71-76.
- [2]. A.I.Nosich and A.Ye.Svezhentsev. Accurate Computation of Mode Characteristics for Open- Layered circular Cylindrical Microstrip and Slot Lines. Microwave and Optical Technology Letters, vol.4, N 7, June, 1991, pp.274-277.
- [3]. A.I.Nosich and A.Ye.Svezhentsev. Principal and Higher Order Modes of Microstrip and Slot Lines on a Cylindrical Substrate. Electromagnetics, 1993, vol.13, N 1, pp.85-94.
- [4]. A.Svezhentsev. The Coupling Effect for Slow Waves in the Partially Screened Circular Dielectric Rod. Doklady of Ukrainian Academy of Sciences, ser.A, N 7, 1986, pp.58-62.
- [5]. A.Ye.Svezhentsev. Coupling Effects for Complex Waves in Multilayer Cylindrical Strip and Slot Lines. In Proc. of the 1992 International Symposium on Antennas and Propagation, Sapporo, 1992, vol.4, pp.1285-1288.

## A Novel Micromachined 1.6 THz Mixer

Simon T.G. Wootton, Steven R. Davies and Nigel J. Cronin.

School of Physics, University of Bath, Claverton Down, Bath, BA2 7AY. United Kingdom.

### Abstract

The latest developments towards the fabrication of a fully micromachined 1.6THz mixer are presented. The structure consists of a Schottky diode contacted by an electroplated low parasitic capacitance post integrated into an air-filled micromachined rectangular waveguide.

### Introduction

In this paper, work towards the fabrication of a 1.6 THz mixer structure is presented. In contrast to the standard approach of employing a machined mixer block with a whisker contacted Schottky diode, we have used semiconductor processing techniques to allow the fabrication of an integrated structure using a number of standard processing stages. The advantages of this approach are that these structures will be of a higher tolerance than those produced by conventional machining methods and should therefore yield better performance and consistency.

These devices have possible applications for detectors in space-borne astronomy and remote sensing instrumentation. The possibilities of integrating other types of device into these micromachined waveguides make it theoretically possible to create integrated downconverters and detectors. These systems would be of a low mass and size and would be of a high dimensional tolerance. Such devices would therefore be appropriate for use in satellite systems.

### Fabrication

Figure 1 shows a sectional view of the prototype detector/mixer structure displaying its important features. The waveguide is typically 17.5 microns tall and 140 microns wide (quarter height waveguide).

The waveguide is fabricated from nickel electroplated onto an evaporated seed layer of gold. This ensures that the entire inner surface of the waveguide is fabricated from pure gold. The high conductivity and non-oxidising properties of gold ensure optimal performance of the waveguide. The gold layer is of a thickness of several skin depths.

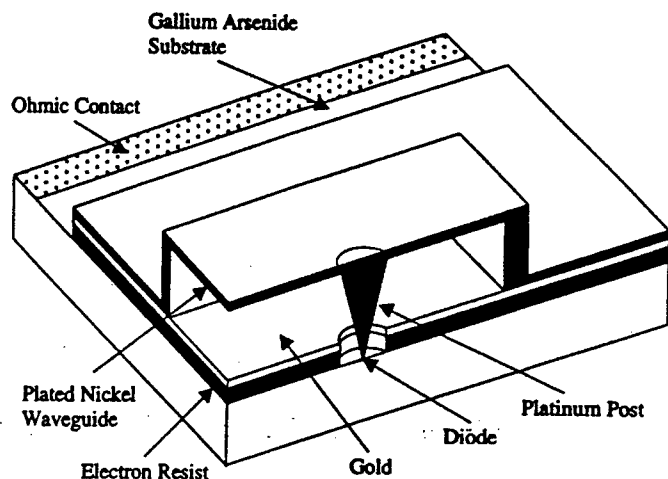


Fig. 1: Sectional diagram of prototype structure.

The structure is fabricated using the following process:

1. Deposit and anneal ohmic contacts onto the surface of the Gallium Arsenide.
2. Fabricate diode and platinum post by electroplating upon the substrate through a window defined in a thick layer of photoresist that was spun directly onto the gallium arsenide surface. This technique results in structures of up to 20 microns in height with base (and device) diameter of less than a micron. The resist layer is then removed.
3. Spin and bake a PMMA based electron resist onto the sample.
4. Evaporate a layer of gold onto the sample in such a way that the top of the platinum structure shadows its base, leaving an unmetallised area around the diode.
5. Expose electron resist from around the diode in a scanning electron microscope and develop the resist away. Figure 2 shows a scanning electron micrograph of the structure after this stage.



Fig. 2: Electron micrograph of a free-standing platinum structure surrounded by an electrically isolated gold layer.

6. Spin photoresist to thickness of 17.5 microns, expose and develop waveguide shape so that it is aligned to the platinum structure
7. Deposit a seed layer of gold onto the photoresist waveguide former using thermal evaporation from a number of angles.
8. Plate waveguide with nickel and remove photoresist leaving an air-filled rectangular waveguide with an integrated Schottky diode.

Figure 3 shows a scanning electron micrograph of a length of rectangular waveguide made by this method. This guide is 140 microns wide and approximately 17.5 microns tall. Further fabrication details are given in [1].

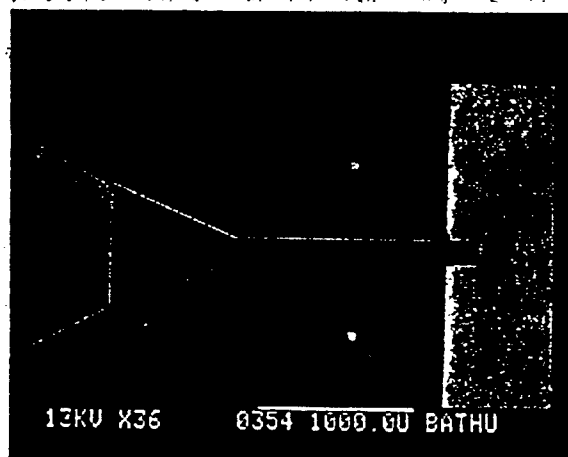


Fig. 3: Electron micrograph of a 1.6 THz integrated waveguide and linearly tapered antenna.

The waveguide has an integrated feedhorn structure of the type proposed by Bowen et al. [2] and the other end of the waveguide has been left open for the purposes of characterisation. In the proposed detector design, this open end is replaced by a fixed backshort and the guide is positioned so that the diode is situated one quarter of a guide wavelength (63 microns) from the backshort and situated on the plane of symmetry of the waveguide. Interesting work has been done on micromachined sliding backshorts, for example, [3]. It may be possible to include a sliding backshort into our waveguide structures thus producing tuneable mixers.

### Conclusions

It has been demonstrated that the technology exists to produce diodes of a sub-micron base diameter with integrated platinum mounting structures as tall as 17.5 microns. This mounting structure has a greater mechanical stability than conventional whisker-contacts, making it attractive for space-borne applications. The tapered platinum post should result in a low parasitic capacitance environment for the diode, hence better mixing performance. Such a structure has been successfully mounted into a waveguide and experiments are underway to characterise the performance of these micromachined devices. We therefore expect to be able to assess the performance of these devices in the near future.

### Acknowledgements

This research is supported by EPSRC (the United Kingdom Engineering and Physical Sciences Research Council) as part of the TINTIN research programme. We would also like to thank Matra Marconi Space UK Ltd. for their support of this project and for financing a CASE studentship.

### References

- [1] Treen A.S. and Cronin N.J., "Terahertz Metal-Pipe Waveguides", 18th International Conf. on Infrared and Millimeter Waves, 1993, SPIE vol. 2104, pp. 470-471.
- [2] Bowen J.W., Karatzas L.S., Towilson B.M., Cronin N.J., Brown D.A., Wootton S.T.G., Agbor N.E., et al., "Micromachined Integrated Components for Terahertz Frequencies", 30th ESLAB Symp. on Sub-mm and Far-IR Space Instrumentation, 1996, ESA SP-388, pp. 183-186.
- [3] Lubecke V.M., McGrath W.R. and Rutledge D.B., "Sliding Backshorts for Planar Circuits", Int. J. of Infrared and Millimeter Waves, 1991, 12, pp.1387-1397.

# A Subharmonic Schottky Diode Mixer at 650 GHz: Measurements on Scaled Models

Ville S. Möttönen, Jiang Zhang, Jyrki T. Louhi,  
Petri V. Piironen, Arto O. Lehto and Antti V. Räisänen

Helsinki University of Technology, P.O.Box 3000, FIN-02015 HUT, Finland

## Abstract

Preliminary design of a 650 GHz subharmonically pumped planar Schottky-diode mixer has been carried out. The mixer design is based on the use of scaled models. Before the implementation of the final mixer, 2.5/5 GHz and 5/10 GHz scaled models as well as a 216 GHz mixer are designed and tested.

## 1. Introduction

Technology for the next century remote sensing applications is currently being developed by the European Space Agency (ESA). In many space based receiver applications technology requiring no cryogenic cooling is preferred. Schottky-diode mixers have the property to work well at either cryogenic or room temperature. The use of planar diodes allows easy space qualification with convenient receiver design and assembly. The development for the replacement of whisker contacted Schottky honeycomb diodes by planar devices has been going on for a number of years. We are in the process of designing 216 GHz and 650 GHz subharmonic waveguide mixers based on a quasi-vertical antiparallel diode pair configuration [1].

## 2. Waveguide Mount Description

The mixer employs a modified split-waveguide mount design [2], which has been successfully applied to a subharmonically pumped planar Schottky-diode mixer [3]. The primary modification compared to the original design is reduction of the number of sliding backshorts and the use of a bent LO waveguide. Figure 1 shows a schematic of the mixer mount. The RF signal is coupled into a  $215\ \mu\text{m} \times 430\ \mu\text{m}$  (dimensions are for the 650 GHz mixer, dimensions of the 216 GHz mixer are obtained by scaling) waveguide by a diagonal feedhorn and into the shielded microstrip channel by a waveguide to microstrip transition. The RF transition utilizes a microstrip line, which extends across and beyond the input RF waveguide allowing grounding. The LO signal is fed through the bent  $425\ \mu\text{m} \times 850\ \mu\text{m}$  waveguide, the waveguide to microstrip transition and a quartz microstrip LO filter to the antiparallel quasi-vertical Schottky-diode pair. The width and height of the shielded microstrip channel are  $120\ \mu\text{m}$  and  $100\ \mu\text{m}$ . The quartz substrate is  $110\ \mu\text{m}$  wide and  $50\ \mu\text{m}$  thick. The IF signal leaves the mixer through an IF filter followed by an SMA connector. The IF channel microstrip line is bonded to the main strip between the waveguides.

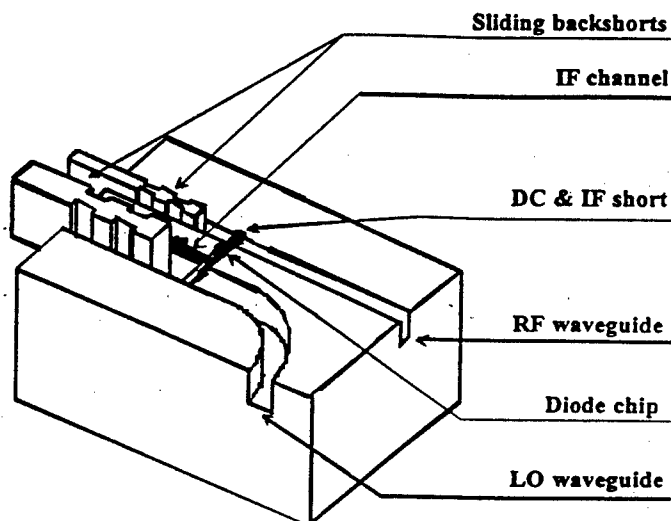


Figure 1. Schematic drawing showing one half of the subharmonic mixer mount (diagonal feedhorn not shown).

## 3. Mixer Diodes

The subharmonic mixers at 216 GHz and at 650 GHz will utilize a quasi-vertical planar Schottky-diode pair in an antiparallel configuration (APD). The diodes are being manufactured by Technische Hochschule Darmstadt (THD). The chip will be attached onto the quartz substrate by using flip-chip technique. The anode diameter is  $0.8\ \mu\text{m}$  on a  $70\ \text{nm}$  thick epilayer with doping concentration of  $3 \cdot 10^{17}\ \text{cm}^{-3}$ . The diode series resistance is  $16\ \Omega$ , ideality factor 1.1, saturation current lower than  $1 \cdot 10^{-16}\ \text{A}$  and a zero bias junction capacitance  $1.2\ \text{fF}$ . The thickness of the remaining semi-insulating GaAs substrate is reduced to  $10\text{--}15\ \mu\text{m}$  in order to lower the contribution to the parasitic capacitance. This diode chip will be used in both mixers (216 GHz and 650 GHz). If there is a need for further reduction of the parasitics, the GaAs substrate will be entirely removed after soldering the diode onto the microstrip.

## 4. Transition and Filter Design

The waveguide to microstrip transitions and the IF and LO filters were designed using the 2.5/5 GHz scaled model. EM-simulations were also carried out in order to verify de-embedding impedances at discrete frequencies and to find out transmission line impedances in the shielded microstrip channel. Hewlett Packard's High Frequency Structure Simulator (HFSS) and an FDTD analysis program in APLAC (a tool for circuit simulation developed by Helsinki University

of Technology and Nokia Corporation) were used for EM-simulations.

For the LO transition, a 50  $\Omega$  transmission line was used. The width of the 50  $\Omega$  line was determined by HFSS. The transition was optimized by changing the length of the transmission line over the LO waveguide and the backshort position. The first step in optimizing the RF transition was to change the width of the transmission line across the RF waveguide. Further optimization was done by changing the width of the transmission line beyond the RF waveguide. In this way, wideband transitions were obtained. A bandstop filter, which employs bent  $\lambda_p/4$  stubs, is used for RF and LO rejection. The lengths and the number of the stubs were optimized to obtain the desired rejection at stopband. With this filter structure, high rejection is easily obtained over a wide band. The entire mixer structure is shown in Figure 2.

### 5. Scaled Mixer at 10 GHz

A 10 GHz mixer has been designed and preliminary measurements have been done. GaAs beam-lead Schottky diodes have been implemented in the mixer. Diode parameters are given in Table 1 with corresponding impedance values at 10 GHz. The diodes were chosen so that the impedance values of the parameters would match as well as possible to those of the 650 GHz mixer diode. The diodes were placed onto the microstrip in antiparallel configuration. Harmonic balance analysis in Hewlett Packard's Microwave Design System (MDS) was used in order to find out the diode de-embedding impedances for minimum conversion loss. After determination of the de-embedding impedances, a mixer circuit was designed. Two bonding wires were used in order to connect the IF channel to the coaxial connector and to the main strip. The diodes were placed near the RF transition in order to minimize signal losses. The measured conversion loss versus the scaled IF frequency is shown in Figure 3. According to the preliminary measurements, a scaled IF bandwidth of more than 40 GHz is achievable. In the simulation of the 10 GHz mixer, the LO power was 10 dBm. Measured LO and RF return losses were over 11 dB and over 13 dB at 10 dBm LO power.

Table 1. Parameters of the beamlead diode.

Series resistance	$R_s$	10 $\Omega$
Zero junction capacitance	$C_{j0}$	0.13 pF (122 $\Omega$ )
Parasitic capacitance (package)	$C_p$	0.14 pF (114 $\Omega$ )
Parasitic inductance (package)	$L_p$	0.6 nH (38 $\Omega$ )
Ideality factor	$\eta$	1.18
Saturation current	$I_s$	$4.46 \cdot 10^{-13}$ A

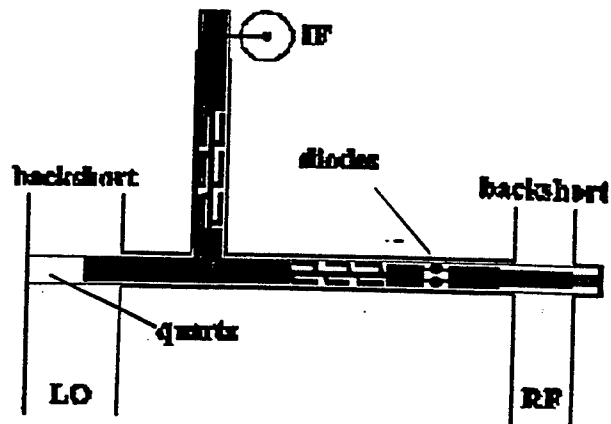


Figure 2. Mixer circuit.

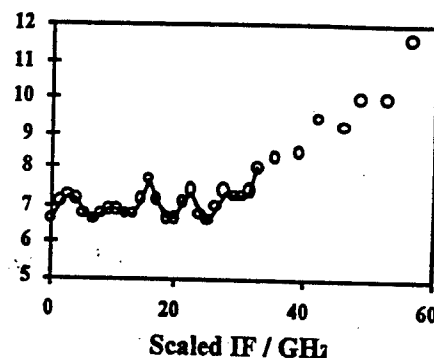


Figure 3. Conversion loss vs scaled IF frequency.

### 6. Conclusion

Preliminary design of a subharmonic mixer at millimeter and submillimeter frequencies has been carried out by simulations and scaled model measurements. According to the scaled model measurements, a broadband low-conversion-loss subharmonic mixer at 650 GHz can be achieved. This compact mixer structure can be scaled even for higher frequencies.

### References

- [1] A. Simon, A. Grüb, V. Krozer, K. Beilenhoff, H. L. Hartnagel, "Planar THz Schottky diode based on a quasi vertical structure", *Proc. Fourth Int. Symp. on Terahertz Technology*, LA, USA, pp. 392-403, 1993.
- [2] A. V. Räisänen, D. Choudhury, R. J. Dengler, J. E. Oswald, P. H. Siegel, "A novel split-waveguide mount design for millimeter- and submillimeter-wave frequency multipliers and harmonic mixers", *IEEE Microwave and Guided Wave Letters*, vol. 3, no. 10, pp. 369-371, 1993.
- [3] A. V. Räisänen, R. J. Dengler, I. Mehdi, J. E. Oswald, D. Choudhury, P. H. Siegel, "Subharmonic mixer with planar Schottky diodes in a novel split-block at 200 - 240 GHz", *IEEE MTT-S Digest*, pp. 775-777, 1994.

## An Optically Controlled Modulator Using a Metal Strip Grating on a Silicon Plate for Millimeter and Submillimeter Wavelengths

Jongsuck Bae<sup>†‡</sup>, Tetsu Fujii<sup>†</sup>, Takanori Uno<sup>†</sup>, Fumikazu Takei<sup>†</sup>, Kojun Maezaki<sup>†</sup>, and Koji Mizuno<sup>†‡</sup>

<sup>†</sup>*Research Institute of Electrical Communication, Tohoku University,  
2-1-1 Katahira, Aoba-ku, Sendai 980-77, Japan*

<sup>‡</sup>*Photodynamics Research Center, The Institute of Physical and Chemical Research,  
19-1399 Aza-Koeji, Nagamachi, Aoba-ku, Sendai 980, Japan*

### Abstract

An optically controlled modulator which has a metal strip grating on a low doped silicon plate and an external electric field applied between the strips, has been developed as a quasi-optical high-speed modulator for millimeter and submillimeter wavelengths. The experiments performed at frequencies around 56 GHz have shown that the maximum modulation frequency in the inductive metal strip modulator can be increased from 4 kHz to 37 kHz by applying only 13 volts to the strips.

### Introduction

An optically controlled modulator using a metal strip grating on a silicon plate has been developed as a quasi-optical component for millimeter and submillimeter wavelengths [1]. In the metal strip (MS) modulator, laser light excites free carriers in silicon at gaps between the metal strips and changes an effective refractive index  $n$  of the silicon plate (Fig. 1). Since the transmission property of the metal strip grating strongly depends on  $n$  [2], the transmittance and reflectance of the MS-modulator are largely changed with the laser illumination. An external electric field applied to the metal strip gaps quickly sweeps out the free carriers from the silicon plate, and consequently increases the time-response speed of the modulator. In principle, a modulation frequency of the order of GHz is available for the MS-modulator even with a low doped silicon plate ( $\rho \sim 10 \text{ k}\Omega\text{-cm}$ ). This is because the maximum modulation frequency is limited not by a low inherent relaxation rate of free carriers in low doped silicon [3], but by a higher ratio of a saturation velocity of the carriers in silicon to the gap width. In this paper, the theoretical and experimental results obtained at millimeter wavelengths are reported to show the feasibility of the MS-modulator.

### Experimental Setup

Figure 1 shows the experimental setup of a MS-modulator with a silicon tuning plate. The MS-modulator has a strip grating with a pitch of 1.7 mm and a gap width of 0.87 mm. The thickness of the low doped silicon plate is 1 mm. The modulator is placed between the transmitting and receiving horns and illuminated by a laser diode. The laser has a wavelength of 880 nm, a pulse energy of 2  $\mu\text{J}$ , and a pulse width of 100 nsec. The DC and pulsed metal strip voltages,  $V_g$ , were used and changed from zero to 15 V. The silicon tuning plate was used to maximize the transmittance of the MS-modulator.

Due to the configuration of the experimental setup, only transmittances of the modulator were measured. In the experiments, both inductive and capacitive metal strip configurations were used, and a silicon plate without metal strips was tested for comparison.

### Experimental Results

Figure 2 shows the measured time responses of the inductive metal strip (IMS) modulator for  $V_g = 0, 1.7, 4.3$ , and 13 V in DC at 57 GHz. In Fig. 3, the minimum dip indicates that the transmittance of the modulator has decreased by 6.8 %. When  $V_g$  increases from zero to 13 V, the recovery time  $t_r$  (for 10%-90% variation) decreases from 114  $\mu\text{sec}$  to 12  $\mu\text{sec}$ . In the response curve for  $V_g = 0 \text{ V}$ , the long recovery time results from slow relaxation of the free carriers in the low doped silicon plate. The experimental results show that the maximum modulation frequency ( $=0.44/t_r$ ) of the modulator can be increased from 4 kHz to 37 kHz by applying  $V_g$  of only 13 V to the metal strips.

For an optically controlled semiconductor modulator, modulation efficiency and a time response speed generally have a trade-off relationship [3]. Therefore, a faster the response speed results in a lower the modulation efficiency. Actually, it is seen from the results shown in Fig. 2 that the peak modulation degree for  $V_g = 13 \text{ V}$  has decreased by 13 % compared to that for  $V_g = 0 \text{ V}$ .

Figure 3 shows the measured maximum modulation degree,  $M$ , and recovery time,  $t_r$ , in the capacitive metal strip (CMS) modulator for pulsed metal strip voltages,  $V_g$ , at 57 GHz. For comparison, the results measured for DC strip voltages are also indicated in the same figure. The pulse voltages have a square wave form, an amplitude of  $V_g$ , and a duration of 80  $\mu\text{sec}$ , and were applied to the strips 1  $\mu\text{sec}$  after the laser pulse.

Figure 3 shows that the DC and pulse strip voltages have a similar effect to decrease the recovery time for the CMS-modulator. For the DC strip voltages, the modulation degree decreases when  $V_g$  increases and is 0.7 at  $V_g = 8 \text{ V}$ . In contrast, the modulation degrees for the pulse strip voltages are almost constant for  $V_g$  up to 8 V. These experimental results show that the MS-modulator can overcome the trade-off between the modulation efficiency and time response speed by using a voltage pulse synchronized with the laser pulse.

Figure 4 compares the peak modulation degrees,  $M$ , for the IMS-, CMS-, and silicon (Si)-modulators measured at between 52 GHz and 60 GHz. The theoretical calculations for  $M$  were done using a simple transmission line model, assuming a

lumped resistance for an optically generated plasma layer in the modulators. The theoretical modulation degrees are also indicated in Fig. 4. The experimental results show that the modulation degree for the IMS-modulator is about three times greater than that for the Si-modulator at around 57 GHz, which is caused by a resonant effect occurring in the metal strip grating [4].

### Conclusion

Two important features of the metal strip modulator have been demonstrated in the millimeter wave frequency region: increased modulation efficiency compared to a silicon modulator without the metal strips, and externally controllable time-response speed of modulation. These results show that the metal strip modulator is a potential high-speed modulator at millimeter and submillimeter wavelengths.

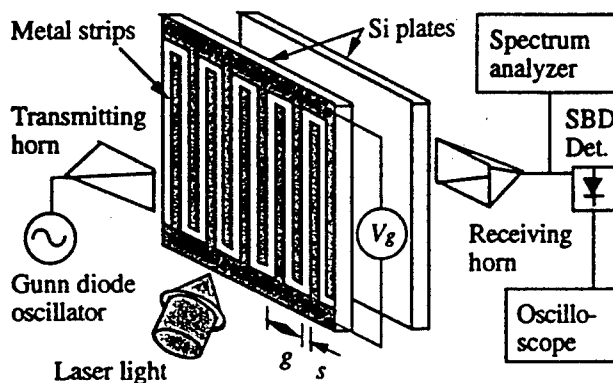


Fig. 1 Experimental configuration of the MS-modulator.

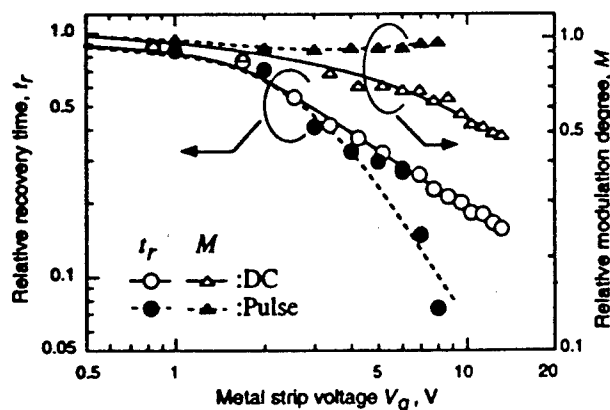


Fig. 3 Measured normalized maximum modulation degree  $M$  and recovery time  $t_r$  for the CMS-modulator as a function of the metal strip voltage  $V_g$  in DC and pulse at 57 GHz.

### Acknowledgments

The authors would like to express our gratitude to Professor D. B. Rutledge at Caltech and Dr. J. C. Chiao at Bellcore co. for providing us the calculation program of the metal strip grating. This work was partially supported by a Grant-in-Aid of Scientific Research from the Ministry of Education, Science, Sports and Culture of Japan.

### References

- [1] J. Bae, *et al.*, Digest of 1996 IEEE MTT-S Int. Microwave Symp., San Francisco, pp. 1239-1242, 1996.
- [2] J. Bae, *et al.*, Int. J. Infrared and Millimeter Waves, vol. 16, no. 2, pp. 377-390, 1995.
- [3] C. H. Lee, *et al.*, IEEE J. Quantum Electronics., vol. QE-16, no. 3, 1990.
- [4] R. C. Compton, *et al.*, Appl. Opt., vol. 23, no. 18, 1984.

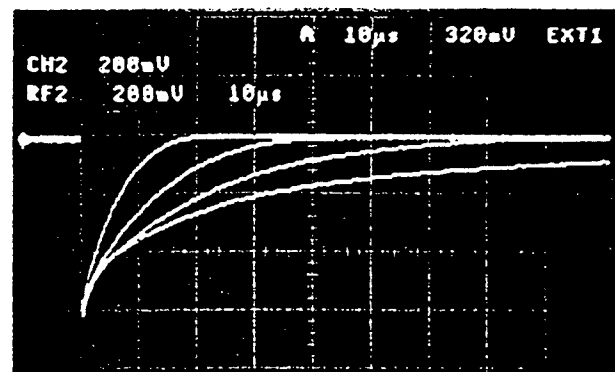


Fig. 2 Oscilloscope traces of the ac-components of the transmission signals for the IMS-modulator measured for different metal strip voltages  $V_g$  of 0, 1.7, 4.3, and 13 V at 57 GHz. The lowest trace is for  $V_g = 0$  V.

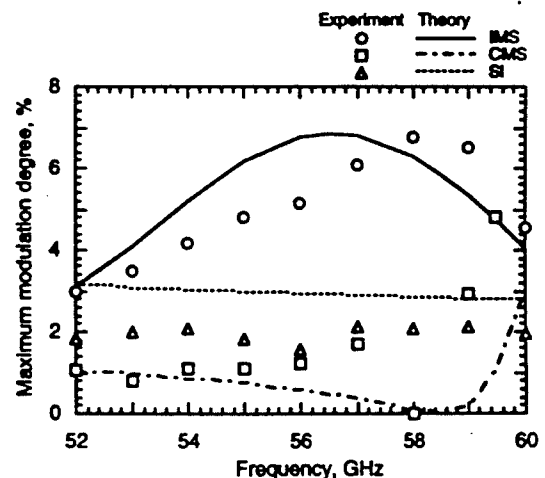


Fig. 4 Comparison of the maximum modulation degrees of the IMS-, CMS-, and Si-modulators as a function of frequency.



# Mixing and Rectification Properties of Point Contacts

S. K. Masalmeh and J. Korving

Huygens Laboratory, Rijksuniversiteit Leiden  
Niels Bohrweg 2, 2333 CA, Leiden, The Netherlands

May 13, 1997

## Abstract

We have studied the  $I$ - $V$  characteristics of metal-insulator-metal (MIM) diodes and metal (MC) contacts at low and at laser frequency. For both configurations the characteristics appear to be independent of frequency. The MC contacts are usually slightly more effective as mixers than MIM diodes with the exception of W - W contacts.

## Introduction

Metal-insulator-metal diodes have been used frequently as mixers and detectors as well as harmonic generators of submillimeter, infrared and visible laser radiation [?]. The fast and nonlinear response of these diodes have been attributed to electron tunneling in the insulating layer. Electron tunneling through a thin insulating layer between two metals has been studied theoretically and experimentally since 1930 starting with the work of Frenkel [?].

MIM diodes consist of three essential parts: 1) an ultra fine metal tip prepared by electrochemical etching (tip diameter about 100 nm) which is called whisker, 2) a metal base, usually a monocrystal and 3) a barrier region located between the whisker tip and the base. The barrier region is an oxide layer which grows naturally on the base after being exposed to air. Various aspects of MIM diodes have been investigated both theoretically and experimentally (see e.g. [?, ?] and references therein). In contrast to the turbulent development of MIM diodes as experimentally interesting physical tools, the understanding of their physical nature is still quite modest. It is surprising to see that when the scarce attempts to come to a quantitative comparison between theory and experiment are reviewed, one must conclude that the results are often inconclusive and at times even contradictory. In the course of our experiments we found that it is quite well possible that this situation has occurred because throughout the MIM literature the presence of MC contacts has been ignored. In this respect it is worth noting that in our experience about 50% of the contacts realized in practice are of the MC type. For metal contacts, in the absence of an insulating layer, one can observe qualitatively the same features as in MIM diodes concerning laser frequency mixing. The main ex-

perimental difference is that the resistance increases with bias voltage, whereas in MIM diodes it decreases.

## Results

Point contacts like MIM diodes are notably unstable. Furthermore, the main properties of the junctions as the contact area, the thickness of the oxide layer or the potential parameters of the barrier, are only approximately known. This makes it extremely difficult to perform systematic and reliable measurements of the  $I$ - $V$  characteristic of the diode and its response to laser radiation. Therefore, it is essential to use a measuring circuit which 1) is simple enough to give accurate and reliable results without much calibration work, 2) is fast enough to measure the  $I$ - $V$  curve and the mixing properties before any change due to instability can occur, 3) does not introduce any spurious nonlinearity due to the electronic elements used in the circuit and 4) makes it possible to measure the required properties at low and high frequency simultaneously. The latter may shed light on a possible correlation between the characteristics of a contact at low and at high frequency. These experimental requirements were fulfilled for the measurements described below (see also ref. [?]).

In the experiment we focused on the study of the nonlinearity in the  $I$ - $V$  characteristic as a source of information of the fundamental properties of the junctions. Therefore we measured the nonlinearity at low and at laser frequencies. This has been done by simultaneously measuring the second harmonic of a low frequency (600 Hz) signal, the amplitude of the mixing signal at the beat frequency of two  $CO_2$  lasers operated at slightly different frequency, the dc (rectified) voltage of the laser signal and the resistance of the junction. These quantities have been measured as a function of bias. To investigate the influence of the work functions on the mixing properties, we used combinations of metals with a sufficiently large variety in work function. The whisker material was always tungsten, whereas the base was chosen from crystals of W, Ni, Co and Ta. All measurements have been carried out under atmospheric conditions.

The results of the experiments can be summarized as follows. For MIM diodes, where the resistance  $R$  decreases

with bias voltage, we find that the low frequency nonlinearity defined as

$$\beta = - \frac{d \ln R}{dV}$$

is proportional to the mixing and rectification signals of the lasers for all contacts. For MC contacts we find a similar result, except that here the resistance increases with bias voltage. The variation of e.g. the mixing signal at low bias can hardly be distinguished for the two configurations. The main difference between the two is that the nonlinearity of MIM diodes shows a maximum at around 0.2 V bias, whereas for MC contacts the nonlinearity tends to increase monotonously in the range investigated. Furthermore, it should be noted that the rectified signal for MIM diodes and MC contacts have different signs. Another interesting difference is that W-W contacts hardly show a nonlinear behavior in MC contacts but perform very good as MIM diodes. In terms of contact stability and the value of  $\beta$  at maximum, MIM diodes made up of W-W are superior to the other metal combinations, whereas for MC contacts this role is taken over by W-Ni junctions. As a rule, the resistance of MIM diodes is higher than that of MC contacts for obvious reasons. Nevertheless, both types can be found with a resistance in the order of 100  $\Omega$ , which shows that a low resistance is not a commensurate with a MC contact and that in general a junction may even be regarded as a parallel circuit of MIM and MC contacts.

For MC contacts the nonlinear response originates for a large part from heating of the contact by the bias voltage. This has been clearly demonstrated by measurements reported in ref. [?]. Theoretical studies of electric contacts by Holm [?] show a reasonable qualitative and quantitative agreement with our experimental results. The very weak nonlinear signal for W-W contacts can, however, not be explained. The response time of these contacts can be estimated from the heat capacity per volume and the thermal conductivity of the metals and the diameter,  $a$ , of the contact. With  $\tau \approx (C_p a^2)/k$ ,  $\tau$  ranges from  $10^{-15}$  to  $10^{-16}$  s. For MIM diodes a comparison with theory is much more complicated. In tunneling theory the contact is modeled as a potential barrier between the whisker tip and the metal base, through which the electron transport can take place. The nonlinearity of the  $I$ - $V$  characteristic is explained in terms of the work function difference of the contacted metals, their separation and the applied bias voltage. The diode resistance is expected to decrease monotonously as the bias voltage increases. The amplitude of the mixing signal should vary with the combinations of contacted materials, depending on the difference of their work functions. In the experiment we did not observe an influence of the (vacuum) work functions on the shape and symmetry of the nonlinearity as a function of bias voltage, which should be expected according to the theoretical description [?]. It suggests that the potential barrier is mainly determined by the oxide layer on the metal surface. Further, the maximum in the nonlinearity can not be reproduced from theory for any set of reasonable potential parameters. This situ-

ation changes when one takes into account the heating of the contact by the bias voltage, analogous to the situation in MC contacts. When this effect is included, a good agreement can be found between theory and experiment. The response time of these junctions has been estimated (for diodes of similar metals) from  $\hbar/(E_F \Psi)^{1/2} \approx 10^{-16}$  s [?], where  $E_F$  is the Fermi energy and  $\Psi$  is the work function of the contacted metals. In practice the response time is determined by the RC time of the diode:  $10^{-13}$  to  $10^{-14}$  s. The theory describing electron transport in MC junctions is quite different from the tunneling theory as commonly in use for MIM diodes (for a review see ref. [?]). Therefore, serious errors in the interpretation can be made when it is not *a priori* clear what type of contact has been studied. This problem can only be avoided when the measurements combine low frequency (for the resistance) as well as high frequency (mixing) experiments. Preferably these should be carried out simultaneously as one type of contact may change to the other during an experiment.

## References

- [1] D. A. Jennings, K. M. Evenson and D. J. E. Knight, *Proc. IEEE* 74, 168 (1986).
- [2] J. Frenkel, *Phys. Rev.* 36, 1604 (1930).
- [3] H. D. Riccius and K. J. Siemsen, *Appl. Phys. A* 35, 67 (1984).
- [4] K. J. Siemsen and H. D. Riccius, *Appl. Phys. A* 35, 177 (1984).
- [5] a) S. K. Masalmeh, H. K. E. Stadermann and J. Koring, *Physica B* 218, 56 (1996).  
b) S. K. Masalmeh, Thesis, University of Leiden, 1997.
- [6] B. I. Verkin, I. K. Yanson, I. O. Kulik, O. I. Shklyarevski, A. A. Lysykh and Yu. G. Naydyuk, *Solid State Commun.* 30, 215, (1979).
- [7] R. Holm, *Electric Contacts Handbook*, Springer Verlag, Berlin, Germany (1958).
- [8] J. G. Simmons, *J. Appl. Phys.* 43, 2581 (1963).
- [9] T. E. Hartman, *J. Appl. Phys.* 33, 3427 (1962).
- [10] A. M. Duif, A. G. M. Jansen and P. Wyder, *J. Phys.: Condens. Matter* 1, 3157 (1989).

## A Tunable Antenna-Coupled Intersubband Terahertz (TACIT) Detector

Carey Cates, Gabriel Briceño, Jon B. Williams, Mark S. Sherwin

Physics Department and Center for Terahertz Science and Technology,  
University of California, Santa Barbara, CA 93106, USA

Kevin D. Maranowski, Ken Campman, Art C. Gossard

Materials Department, University of California, Santa Barbara, CA 93106, USA

### Abstract

Detectors based on intersubband transitions in quantum wells have great potential for use between one and several Terahertz. We propose a tunable, antenna-coupled, intersubband Terahertz (TACIT) detector that is both sensitive and fast, with a speed limited only by the intersubband relaxation rate (1ns at  $T=10K$ ,  $<10ps$  at  $T=50K$ ). The detector is sensitive over a narrow range of frequencies, and the frequency of peak absorption can be tuned by applying a bias voltage to the device.

### Discussion

Intersubband transitions in quantum wells have enabled the development of sensitive quantum well infrared photoconductors (QWIPs) at wavelengths shorter than 20 microns. The potential of quantum well-based detectors at wavelengths of order  $100\ \mu m$  (3 Terahertz) has not been realized. We propose a novel tunable antenna-coupled intersubband Terahertz (TACIT) detector.

TACIT detectors can be patterned from a variety of quantum well heterostructures. One prototype TACIT detector is patterned from the GaAs/AlGaAs asymmetric double square quantum well structure grown by molecular beam epitaxy (MBE) shown in Fig. 1. The asymmetry of the double quantum well separates the otherwise-degenerate ground subband energy level into two closely-spaced energy levels, with the next energy level sufficiently higher in energy that the system can be safely modeled as a two-level system.

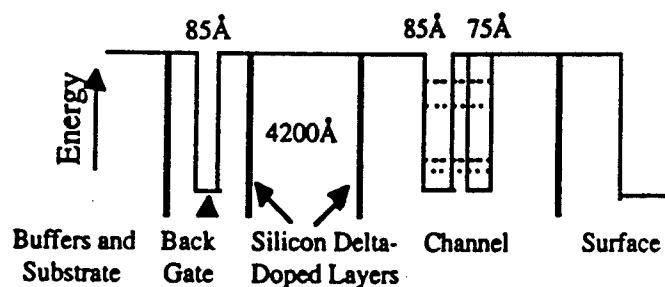


Fig. 1 Schematic of one GaAs/Al<sub>0.3</sub>Ga<sub>0.7</sub>As heterostructure used for a prototype TACIT detector. The dotted lines are a sketch of the subband energy levels.

Terahertz-frequency light incident on the detector excites electrons in the channel quantum well structure from

the first to the second subband. The device is sensitive to a narrow band of frequencies centered on the depolarization-shifted and DC Stark-shifted intersubband transition frequency. Fig. 2 shows the frequency-dependent absorption measured for the asymmetric double quantum well depicted in Fig. 1.

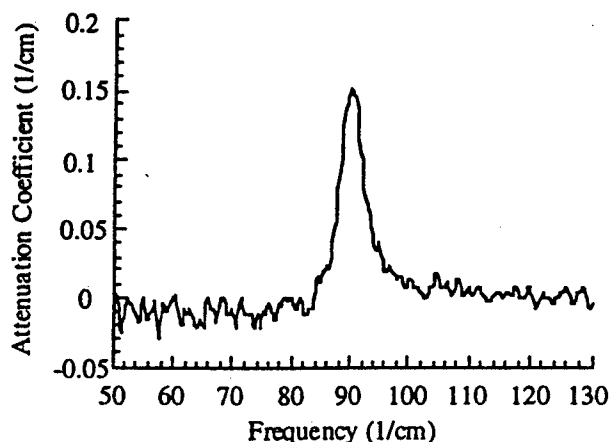


Fig. 2 Attenuation measured as a function of frequency for the heterostructure shown in Fig. 1

The heterostructure also has another quantum well below the channel for a back gate. The intersubband absorption frequency can be tuned by applying a bias voltage between the front and back gate contacts of the device. The bias voltage tilts the quantum wells and changes the subband energy spacing. In this manner, the frequency of maximum absorption for one heterostructure could be changed by a factor of 1.6 with a bias voltage of order 1V, shown in Fig. 3. Other structures are tunable over different ranges, such as 1.2-4.2THz demonstrated by Hopkins et. al. in a logarithmic well.[4]

A planar metal antenna pattern on the surface of the device couples the Terahertz radiation into the device. One leaf of the antenna makes contact to the back gate, and the other leaf serves as a Schottky front gate. Two ohmic contacts to the channel quantum wells allow a current to be passed through the active region.

When Terahertz radiation is incident on the device, the planar metal antenna couples the oscillating electric field from free space to the heterostructure, with the field polarization perpendicular to the plane of the quantum wells.

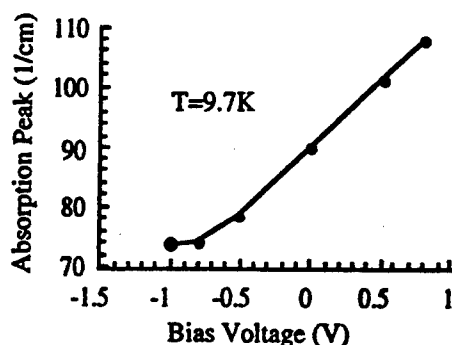


Fig. 3 The frequency of peak absorption can be tuned by applying a bias voltage to the detector heterostructure.

Electrons in the channel quantum wells absorb the far infrared radiation, exciting them from the first to the second energy level. The channel electrons then have an increased temperature, which changes their mobility and hence the resistance of the channel. A current is applied to the active area through the source and drain contacts, and the change in resistance is detected in the source-drain voltage.

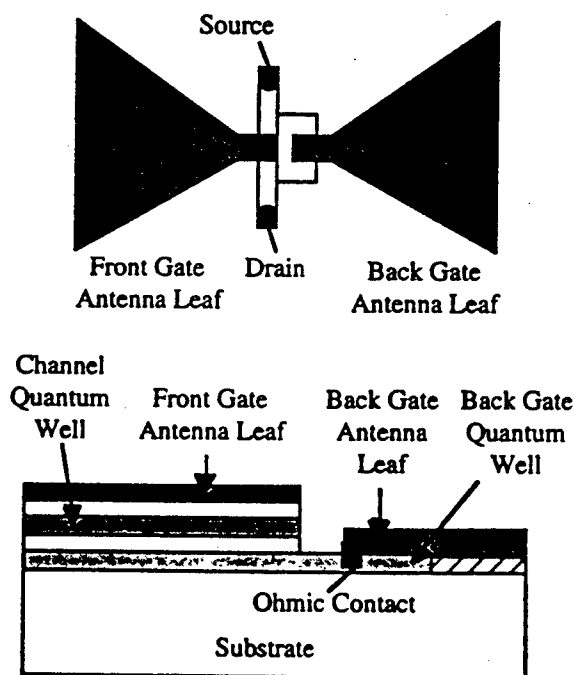


Fig. 4 Top-down and cut-away views of a TACIT detector. Ohmic contacts electrically connect the back gate antenna leaf with the back gate quantum well, and the source and drain contacts to the channel quantum wells.

The speed of the TACIT detector is limited only by the excited subband lifetime, or energy relaxation rate, which is about 1 nanosecond at a temperature of 10K and less than 10 picoseconds at  $T=50K$ . [2] The detector sensitivity can be computed by modeling the device as a hot electron bolometer. In such a model, a TACIT detector could theoretically be made to have background limited performance (BLIP) with a noise-

equivalent power (NEP) of  $2 \times 10^{-16} \text{ W/Hz}^{1/2}$  operating at 10K at frequencies below a corner frequency of 2.6THz. Such a device would have feasible device parameters, such as an electron sheet density of  $3 \times 10^{10} \text{ cm}^{-2}$  and an active area size of  $10 \mu\text{m}^2$ . For comparison, composite bolometers have been reported [3] with NEP's of order  $10^{-16} \text{ W/Hz}^{1/2}$  at 300mK but with a time constant of 11ms. TACIT detectors can have a much faster response than composite bolometers. Also, TACIT detectors are also easily tunable, which allows them to be used in a wider array of applications, including to record spectra without the use of a big bulky spectrometer in certain situations. TACIT detectors are expected to compare favorably with the superconducting hot electron bolometers in speed and sensitivity. A diffusion-cooled superconducting hot electron bolometer with a  $0.04 \mu\text{m}^2$  active area has been demonstrated in a waveguide mixer to have a receiver noise temperature of 650K and a 1.7GHz intermediate frequency (IF) bandwidth. [4] With the addition of a suitable local oscillator, the TACIT detector can also be operated as a mixer with a multi-GHz IF bandwidth expected at  $T=50K$ .

Currently, prototype TACIT detectors are being made, with an electron sheet density of order  $1 \times 10^{11} \text{ cm}^{-2}$  and an  $100 \mu\text{m}^2$  active area.

This work has been supported by the NSF Science and Technology Center for Quantized Electronic Structures (QUEST) DMR 91-20007, NSF DMR 9623874, AFOSR91-0214, NPSC (CC), and the Ford Foundation (GB).

1. P. F. Hopkins et. al., Appl. Phys. Lett. 64 (3), 348-50 (1994)
2. J. N. Heyman et. al., Phys. Rev. Lett. 74 (14), 2682-5 (1995)
3. D. C. Alsop et. al, Applied Optics 31 (31), 6610-15 (1992)
4. A. Sklare et. al., Appl. Phys. Lett. 68 (11), 1558-60 (1996)

## Dielectric loss measurements in CVD diamond windows for gyrotrons

R. Heidinger\*, R. Schwab\*, R. Spörl\*, M. Thumm\*\*

Forschungszentrum Karlsruhe, Association FZK-Euratom

\* Institut für Materialforschung I, \*\* Institut für Technische Physik,  
Postfach 3640, D-76021 Karlsruhe, Germany

### Abstract

Large sized CVD diamond discs (close to 4" diameter and 2 mm thickness) were studied in open resonator systems for dielectric parameter measurements at 15-20 GHz, 32-42 GHz and 145 GHz. Distinct differences in the dielectric loss tangent were found depending on the contribution of the growth and nucleation face as well as on the disc area seen by the mm-wave beam. On average,  $\tan\delta$  reaches the  $10^{-4}$  level at 145 GHz.

### The role of CVD diamond for high power gyrotron windows

Plasma heating and current drive in the next generation fusion devices (ITER, Wendelstein-X) by electron cyclotron wave (ECW) systems call for gyrotrons which provide mm-waves (90-180 GHz) in continuous wave operation at a Megawatt level. As a critical issue, it became evident that the gyrotron output windows were the limiting components unless cryogenic cooling schemes provided for the existing window materials the required combination of low dielectric losses and of high resistance against thermal crack formation [1]. In parallel with the development of cryogenically-cooled sapphire windows, alternative concepts which conceived specially developed materials in conventional cooling scenarios were pointed out and pursued from a materials point of view [2]. Outstanding potentials are found in high resistivity silicon and CVD diamond because of their homopolar structure [3]. While the loss mechanisms in silicon are related to intrinsic and extrinsic free charge carriers, no dominating mechanism is *per se* evident in diamond. The advent of large diamond discs through the CVD processes [4,5] and the identification of low loss grades [6-8] have stimulated the high power window development opening the path to first actual size test windows.

### Experimental set-up

The established open resonator method is used to determine the dielectric properties at mm-wave frequencies covering three different frequency ranges by three individual (quasi-) hemispherical Fabry-Perot resonator installations. The dielectric loss tangent ( $\tan\delta$ ) is obtained by Q-factor measurements using Gaussian  $TEM_{00q}$  modes. For spatially varying losses, the apparent value arises from an integration of the loss over the disc plane weighted by the lateral beam profile and over the disc axis weighted by the field distribution in the material (contribution of the faces). The effective lateral beam diameter was determined to be 6 mm for a specially optimised 145 GHz set-up [9] and about 25 mm for a 35 GHz resonator.

### Characteristics of 4" test windows

Two discs - 'JAERI' (lapped, uniform white) and 'FZK' (lapped, grey with dark shadows) - were studied in different production states (extension (a), (b)). State (b) was achieved from state (a) by subsequently removing material mainly from the nucleation faces. In contrast to the 'FZK' disc the loss tangent values for the 'JAERI' disc were in general lowered by the thickness reduction (Tab.1). The orientation effect in the 'FZK' disc was strongly superimposed by bulk losses. But in every disc and state,  $\tan\delta$  at 35 GHz and 145 GHz values for 'growth face oriented into the resonator' are lower than for the other orientation. Different loss mechanisms seem to be relevant at 15 GHz. In a third disc - 'EVALUATION' (0.6 mm thick, polished to optical grade), a low  $\tan\delta$ , at 145 GHz was determined:  $0.5 \cdot 10^{-4}$ .

		$\tan\delta [10^{-4}]$		
		15 GHz	35 GHz	145 GHz
JAERI(a) t = 2.41 mm	growth	14	4	1.8
	nucleation	3	4.5	1.8
JAERI(b) t = 2.24 mm	growth	12	2	1.3
	nucleation	0.9	2.8	1.7
FZK(a) t = 2.74 mm	growth	-	13	5
	nucleation	-	16	7
FZK(b) t = 2.15 mm	growth	-	12	5
	nucleation	-	16	7

Tab. 1 Results from  $\tan\delta$  measurements at the centre of the discs. ('nucleation' and 'growth' indicate the face that was oriented into the resonator during the test).

### Mapping of dielectric loss

To analyse the radial homogeneity of the dielectric loss in large discs spatially resolved measurements were performed at 35 and 145 GHz. As an example the results from the inhomogeneous 'FZK' disc are shown in Fig.1. The level of the losses goes along with the colour of the disc. With an additional line scan along the y-direction in 1 mm steps the results from the mapping were reproduced (Fig.2a). With two succeeding TEM-modes the inhomogeneity of loss tangent along the x-direction was verified (Fig.2b). Also an inhomogeneous  $\tan\delta$  distribution ( $0.6 - 1.6 \cdot 10^{-4}$ ) was found in the uniform white 'JAERI' disc and verified with infrared mapping of the temperature rise in the disc exposed to high power mm-waves (170 GHz, 170 kW, 100 ms) [10]. The  $\tan\delta$  values in 'EVALUATION' disc did not go beyond the  $0.8 \cdot 10^{-4}$  level.

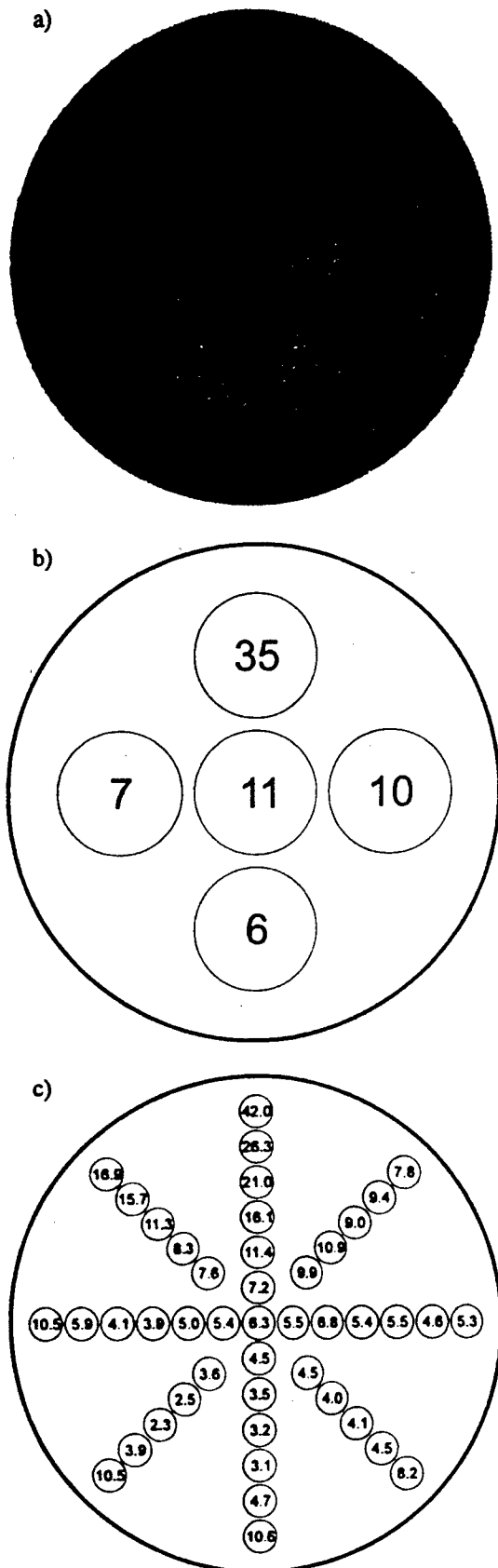


Fig. 1 Picture of 'FZK' disc a) and results of spatially resolved measurement of  $\tan\delta$  [ $10^{-4}$ ] at 15 GHz b) and 145 GHz c) The circles indicate the area seen by the

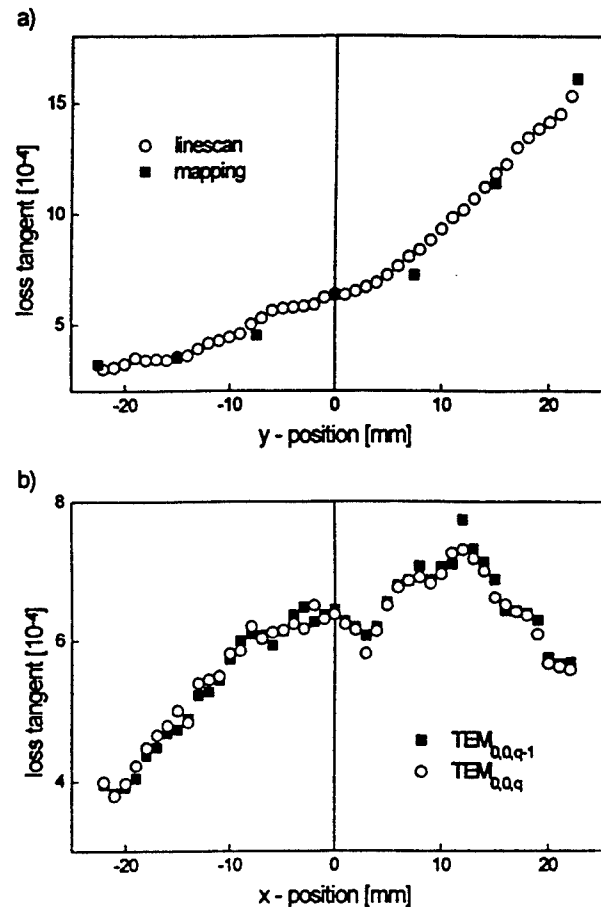


Fig. 2 Line scan of  $\tan\delta$  along the a) x-direction and b) y-direction in 'FZK' disc at 145 GHz

### Acknowledgement

This work has been performed in the framework of the Nuclear Fusion Project of the Forschungszentrum Karlsruhe and is supported by the European Communities within the European Fusion Technology Programme.

### References

- [1] R.Heidinger, J.Nucl.Mater., 179-181(1991),pp64-69
- [2] L.Rebuffi, Conf.Dig.16.IR+MMWaves,SPIE Vol.1576(1991),pp441-442
- [3] R.Heidinger, Proc.4.Russian-German Meeting on ERCH + Gyrotrons, Nizhny Novogorod, 10-17/5/92
- [4] R.S.Sussmann, Conf.Dig.MicroMat'97, Berlin, 16-18/4/97, p67
- [5] P.Koidl, C.Wild, E.Wörner, Conf.Dig.MicroMat'97, Berlin, 16-18/4/97, p74
- [6] G.Lu, L.K.Bigelow, Diamond and Related Mater., 1(1992), pp134-136
- [7] R.S.Sussmann et al., Diamond and Related Mater., 3(1994), pp303-312
- [8] R.Heidinger, Conf.Dig.19.IR+MMWaves, JSAP Cat.AP9411228(1994), pp277-278
- [9] R.Schwab, R.Heidinger, Proc.MIOP'97, Sindelfingen, 22-24/4/97, pp106-110
- [10] O.Braz, M.Thumm, A.Kasugai, K.Sakamoto, K.Takahashi, M.Tsuneoka, T.Imai, paper no.6, this conference

# High-Power Millimeter-Wave Transmission through CVD Diamond

O. Braz<sup>1)</sup>, M. Thumm<sup>1)</sup>, A. Kasugai<sup>2)</sup>, K. Sakamoto<sup>2)</sup>,  
K. Takahashi<sup>2)</sup>, M. Tsuneoka<sup>2)</sup>, T. Imai<sup>2)</sup>

<sup>1)</sup> Forschungszentrum Karlsruhe (FZK), Association EURATOM-FZK,  
Institut für Technische Physik, Postfach 3640, D-76021 Karlsruhe, Germany

<sup>2)</sup> Japan Atomic Energy Research Institute (JAERI),  
Naka Fusion Research Establishment, Naka-machi, Ibaraki 311-01 Japan

## Abstract

In order to check the usability of large-size CVD (Chemical Vapor Deposition) diamond disks for high power millimeter wave vacuum barrier windows at room temperature ( $T=293$  K) a first series of experiments, using a 170 GHz, 0.4 MW, 0.2 sec. JAERI/ Toshiba gyrotron [1], have been performed. The dielectric loss tangent at a frequency of 170 GHz has been determined to be  $\tan(\delta) = 1.3 \cdot 10^{-4}$ . This value is 6.5 times higher than values which already have been measured in smaller size samples. By comparing the experimental results to numerical simulations the thermal conductivity was estimated to be about  $k = 1800$  W/mK.

## Introduction

ECH is one of the major candidates for plasma heating, non-inductive current drive, start-up and profile control of the plasma current in fusion reactors such as ITER. Gyrotron oscillators operating at a frequency of 170 GHz are foreseen as highly efficient ECH power sources for ITER. An output power of at least 1 MW per unit is needed for economical use of such heating systems. The requirement of CW operation results in extremely high demands on the material properties of the vacuum barrier windows at gyrotrons and plasma torus. One answer to this problem is to use a single-disk edge-cooled sapphire window at cryogenic temperatures (liquid Nitrogen at 77 K or liquid Neon at 30 K). To avoid the necessity of a cryogenic coolant, research interests currently concentrate on materials which allow operation at room temperature with simple water cooling.

A very promising material is synthetic diamond which nowadays can be manufactured in samples of up to 110 mm diameter (thickness, approx. 2mm) [2], [3]. Diamond is an attractive material due to its low loss tangent, high thermal conductivity, outstanding mechanical properties and modest permittivity. Finite element calculations show that such a diamond window assembly using a water edge-cooling would be capable to withstand a CW power transmission of 2 MW at 170 GHz.

In a first collaborative experiment between JAERI and the FZK (as part of the ECH window collaboration between Japan and EU within an ITER-Task) the excellent material properties of diamond have been demonstrated.

## Experimental Setup

Fig. 1(a) shows a schematic drawing of the high power experimental setup. The unbrazed window disk has been placed in the output beam of a 170 GHz JAERI/Toshiba gyrotron. For transportation of the RF power from the gyrotron to the test facility a non-evacuated corrugated  $HE_{11}$  waveguide with a diameter of 88.9 mm was used. In order to increase the power density and to reduce the spot size on the target disk the waveguide was tapered down to a diameter of 31.75 mm. Finally the RF power was radiated as a Gaussian beam through the window disk. To determine the loss tangent at different locations the disk could be moved to several positions. The transmitted RF power was measured using a calorimetric load. In Fig. 1(b) a detailed drawing of the diamond disk setup is given.

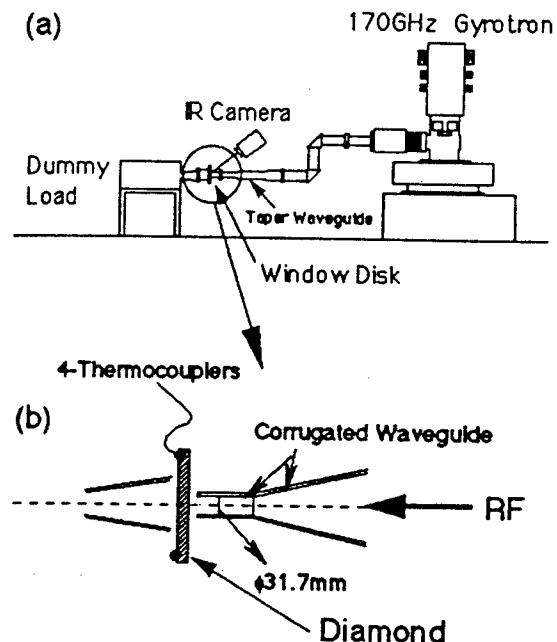


Fig. 1: (a) Schematic drawing of the experimental setup, (b) detailed drawing of the window configuration.

For this experiment a 96 mm diameter, 2.23 mm ( $6 \lambda_{\text{diamond}}/2$ ) thick diamond disk manufactured by DeBeers (UK) has been used. To monitor the increase and the rise time of the disk's edge temperature, caused by the passing through of the RF power, four sheath of non-grounded type thermocouples with

The full width at half maximum (FWHM) of the RF beam at the position of the window disk has been determined to be 23 mm, which is small enough to illuminate different sections of the CVD diamond disk.

Millimeter waves at a frequency of 170 GHz, a power level of 160 - 170 kW and 50 - 105 ms pulse duration have been injected to a large-size CVD diamond disk. The measured linear dependence of the disk's temperature increase on the pulse duration indicate that cooling effects are negligible in the observed time period. The loss tangent ( $\tan \delta$ ) of the CVD diamond has been determined by the following formula:

The thermal conductivity of the CVD diamond disk has been estimated by comparing numerical simulations with the measured increase of the disk's edge temperature. To simulate this time behavior the following equation has been used:

where  $T$  is the window temperature expressed as  $T(r, t)$  ( $r$ : radius,  $t$ : time),  $\rho$  ( $3.54 \cdot 10^3 \text{ kg/m}^3$ ) is the mass density,  $C$  ( $7.42 \cdot 10^2 T^{1.556} \text{ J/(kg K)}$ ) in the range of  $300 \text{ K} < T < 500 \text{ K}$ ) is the specific heat [2] and  $K$  is the thermal conductivity.  $Q$  is the rate of heat generation represented as

where  $c_0$  is the velocity of light,  $\rho$  is the mass density,  $D$  is the disk diameter,  $C_p$  is the specific heat,  $f$  is the frequency of the incident RF,  $\epsilon'$  is the permittivity,  $\Delta T$  is the disk's temperature increase,  $P_{RF}$  is the incident RF power level and  $\Delta t$  is the pulse duration. Transmitting the RF beam through several positions of the disk gave slightly different temperature increases. This indicates an inhomogeneous distribution of the loss tangent across the CVD diamond disk.

where,  $\epsilon_0$  is the dielectric constant in vacuum and  $E(r,t)$  is the electric field strength of the incident RF. Assuming an azimuthally symmetric distribution of the heat deposition Equation (2) is solved using a one dimensional (radial direction) finite element method. For the simulated temperature increase shown in Figure 3, a loss tangent of  $\tan(\delta) = 1.3 \cdot 10^{-4}$ , an RF power of 165 kW and a pulse duration of 57 ms have been used.

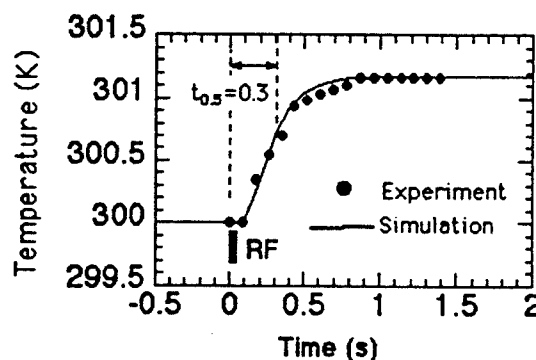


**Fig. 3: Time behavior of the disk's edge temperature increase.**

The best agreement between measurement and simulation has been found by taking a thermal conductivity of 1800 W/mK into account. A value which also has been measured at a smaller sample by applying the photoacoustical method at FZK.

## References

- [1] K. Sakamoto, et. al., 20<sup>th</sup>, Int. Conf. Infrared and Millimeter Waves, Orlando, USA (1996) 269.
- [2] R. Heidinger, Proc. 19th Int. Conf. Infrared and Millimeter Waves, Sendai, Japan (1994) 277.
- [3] R. S. Sussmann, et. al., Diamond and Related Materials, 3, (1994) 303.



## A Forced Gas-Cooled Single Disk Window for High Power CW Millimeter Waves

T. Shimozuma, S. Morimoto<sup>1</sup>, M. Sato, Y. Takita, S. Ito,  
S. Kubo, H. Idei, K. Ohkubo and T. Watari

National Institute for Fusion Science  
322-6, Oroshi-cho, Toki-shi, Gifu, 509-52, Japan  
1) Kanazawa Institute of Technology  
7-1, Oogigaoka, Nonoichi, Minamikyoku, Kanazawa-city, 921, Japan

### Abstract

Silicon nitride composite was high power tested with a surface cooling by impinging gas nitrogen jets on the single-disk surface. With gas cooling of 465l/min., 130kW CW power of HE<sub>11</sub> mode could be transmitted through the window with a diameter of 88.9mm. The peak window temperature was completely saturated on 123.6 °C. Without gas-cooling it did not saturate and reached 323 °C during 30 seconds pulse. A possibility of 1MW CW single disk Brewster windows with a forced gas-cooling is discussed.

### Introduction

A vacuum barrier window is one of the most critical component to realize high power CW (Continuous Wave) gyrotrons. Many efforts to accomplish 1 MW CW windows have been made all over the world. Single-disk windows have a merit of simple structures which assure higher reliability than complicated multiple-disk designs. By means of the gas-cooling, the surface-cooled single-disk window with a low loss and tough material might be possible to persist in CW power transmission.

A new sintered silicon nitride composite (SN-287) has been developed by Kyocera corporation in Japan. It has higher thermal shock resistance, higher flexural strength and better thermal conductivity than sapphire. The loss tangent is comparable to sapphire[1]. Table 1 presents the physical, electrical and mechanical characteristics of the silicon nitride.

We fabricated a single-disk window, which had an 88.9 mm effective diameter, with a surface-cooling mechanism by obliquely impinging gas jets on the disk. It was tested in the 150 kW, HE<sub>11</sub>, 84 GHz transmission line where the power flux density exceeded 8 kW/cm<sup>2</sup> on the center of the window.

In this report, we describe the high power test results of the forced gas-cooled single-disk window with the silicon nitride composite, and discuss a possibility of MW CW transmission through a larger area Brewster window with forced gas-cooling.

### Forced gas-cooled single-disk window and experimental set-up

Using the low loss silicon nitride composite, we assembled a forced gas-cooled single-disk window with an edge-water cooling. Figure 1 shows the structure of the gas-cooled single-disk window for high power testings. A circular

	unit	Silicon Nitride Composite
Density	g/cm <sup>3</sup>	3.4
Modulus of Elasticity	GPa	318
Poisson Ratio		0.28
Linear Expansion Coeff.	x 10 <sup>-6</sup> /K	2.4
Thermal Conductivity	W/mK	59
Specific Heat Capacity	J/gK	0.63
Dielectric Constant		7.9
Loss Tangent	x10 <sup>-4</sup>	1 (30-40GHz, R.T.) 1 -1.5 (84GHz, R.T.) 2.4 (140-145GHz, R.T.)
Dielectric Strength	x10 <sup>4</sup> kV/m	1.85
Bending Strength	MPa	800
Compressive Strength	MPa	5000 - 6000
Thermal Shock Resistance		>750 deg.C (Melting solder)
Metallizing/Brazing		Possible
Possible size		φ 400mm

Table 1 Physical, electrical and mechanical characteristics of a silicon nitride composite

disk of the silicon nitride composite with a diameter of 150mm and a thickness of about 2mm is held between two stainless steel flanges and sealed by O-rings. In this window structure, the whole surface of one side is forced gas-cooled by means of gas erupting nozzles perforated on the inner wall of the flange and the disk edge of another side is water-cooled. The typical diameter of the holes is 1mm and the number is 24. The nozzle section is exchangeable to check the effect of the size, the number of the holes, and its configuration. The effective diameter of the window is 88.9mm and can be connected to a corrugated waveguide with the same inner diameter. Working gases used for testings were dry nitrogen and dry air.

For the high power transmission/absorption testings through the window, we used a high power test-stand. The power source is an 84GHz gyrotron which has an ability of 500kW-2sec., 400kW-10.5sec., 200kW-30sec., and 100kW-30min. operations. Normal operation for the window testings was conducted at 100-200kW power level. The output from the gyrotron which has a flattened RF profile with a peaking factor of about 4.5 is coupled to an HE<sub>11</sub> mode in a corrugated waveguide by two focusing mirrors and transmitted over about 3.4m through two miter bends.

The millimeter-wave power introduced into the corrugated waveguide is transmitted through the window under test, coupled into a dummy load by another set of two mirrors in a matching mirror box. Transmitted power through the window was measured by this dummy load. Temperature profiles and the peak temperature of the window were monitored by an IR camera through a port equipped on the matching mirror box. The readings of the IR temperature were

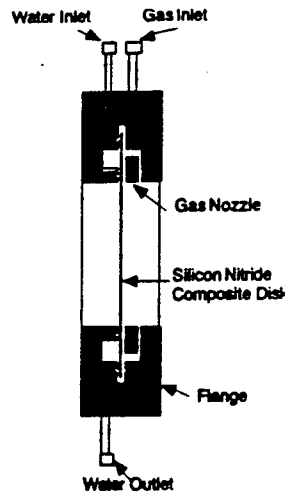


Figure 1 Structure of the forced gas-cooled single-disk window of a silicon nitride composite

directly calibrated by a Pt thermometer in advance. The cooling gas was supplied from a gas cylinder and its flow rate was measured by a float type area flow meter.

### Experimental results

At first we used a 2.53mm thickness disk which corresponded to twice of the wavelength in the disk. The gyrotron was operated at a high repetition rate of 10Hz and 150kW power level. Average input power to the window was changed by increasing the pulse width up to 30msec, corresponding to 30% duty.

The power removed by heat conduction in the disk and maximum temperature on the disk are plotted as a function of the gas flow rate for 30% duty and around 150kW peak power injection in Fig. 2. Both have the same dependence on the gas flow rate. The effect of gas-cooling is significant in the range of 100 liter/min. flow.

In order to demonstrate a possibility of a high power CW transmission, we performed 30 seconds injection with 130kW power. In this case we used the disk of 1.9mm thickness which corresponded to one and half of the wavelength. This disk has a lower loss tangent value than the disk of 2.53mm thickness. Figure 3 shows the time evolution of the peak temperature on the disk with and without gas-cooling. Without gas-cooling it continued to increase during the pulse, because of the inferiority of the thermal conductivity. At the end of the 30sec. pulse the maximum temperature reached as high as 323 °C. On the other hand, with forced gas-surface-cooling of 465 liter/min., the peak temperature completely saturated during the pulse. The saturated temperature is 123.6°C. This fact means that this type of the window can withstand a 130kW CW power transmission of HE<sub>11</sub> mode through the waveguide with 88.9mm in diameter.

The local heat transfer coefficient of the forced gas-cooling can be estimated by means of evaluating the decay time of the peak temperature on the disk after turning off of a millimeter-wave injection. The maximum value of the heat transfer coefficient is achieved 0.1 W/cm<sup>2</sup>K for a gas flow rate of about 400l/min.

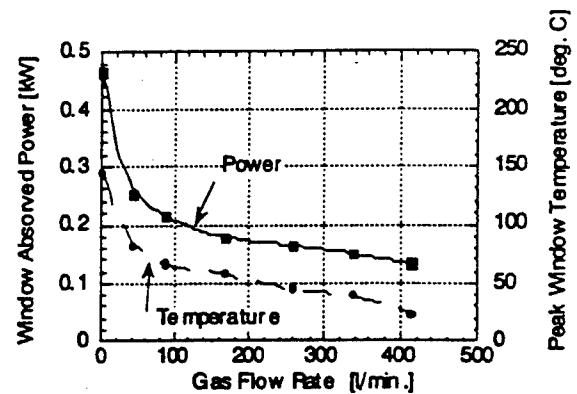


Figure 2 Dependence of peak window temperature and absorbed power in the window on gas flow rate.

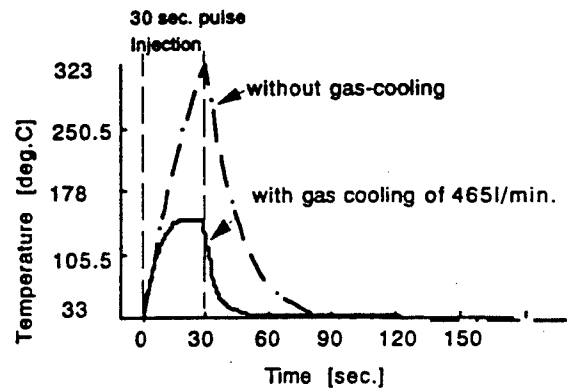


Figure 3 Time evolution of the peak temperature on the disk during 130kW, 30sec. injection without and with gas-cooling.

### Brewster window

From a viewpoint of high power windows, the Brewster window has a lot of merits. In addition to its frequency independence, it has an effectively large area, and the power density of an injected RF beam can be reduced by several times. Its elliptical shape also has less internal stresses and smaller deformation than a circular shape with the same surface area.

For the silicon nitride composite with a permittivity of 7.92, the Brewster angle  $\theta_B$  is 70.44°. When an elliptical disk is installed in a circular waveguide, the disk has an ellipticity of approximately three. Let's estimate the size of a 1MW CW window with this material and with the forced gas-cooling. Since a 130kW CW transmission is possible from the experimental results, 7.7 times of the disk area is required for 1MW, if the peaking factor of the incident wave are kept constant (about 3.7 for HE<sub>11</sub> mode). This means that the size of 140 × 420 mm<sup>2</sup> will be required. The thickness of the disk will be about 3.5 mm, if the maximum tensile stress is suppressed below 100MPa, when the maximum deformation is expected to be 0.3mm.

### Reference

- [1] T. Shimozuma, M. Sato, et al., Conference Digest of the 20th International Conference on Infrared and Millimeter Waves, Orlando, Florida, December 11-14, 1995 T8.3, pp273-274

## D-Band Frequency Step-Tuning of a 1 MW Gyrotron using a Brewster Output Window

O. Braz <sup>1) 2)</sup>, G. Dammertz <sup>1)</sup>, M. Kuntze <sup>1)</sup>, M. Thumm <sup>1) 2)</sup>

<sup>1)</sup> Forschungszentrum Karlsruhe (FZK), ITP, Association EURATOM-FZK,  
Postfach 3640, D-76021 Karlsruhe, Germany

<sup>2)</sup> and Universität Karlsruhe, Institut für Höchstfrequenztechnik und Elektronik,  
Kaiserstr. 12, D-76128 Karlsruhe, Germany

### Abstract

In order to demonstrate the usability of gyrotron oscillators as frequency step tunable high power millimeter-wave sources, experiments on a 1 MW, 140 GHz TE<sub>22,6</sub> gyrotron with a built in quasi-optical (q. o.) mode converter have been performed. By varying the tube's operating parameters a series of oscillations in a frequency range from 114.1 to 166 GHz have been excited. To avoid window reflections the gyrotron has been equipped with a Brewster window. The achieved output power level between 0.85 and 1.05 MW is compared to measurements done with the same gyrotron using a conventional single-disk window. These experiments showed that even by using a q. o. mode converter the influence of window reflections on the gyrotron oscillation behavior cannot be removed completely.

### Introduction

Electron Cyclotron Resonance Heating (ECRH) is one of the major candidates for plasma heating, non-inductive current drive, profile control and start-up of the plasma current in the next generation of fusion plasma machines such as the ITER tokamak. To meet these requirements with a maximum of efficiency it will be necessary to heat at different positions of the fusion plasma. This can be achieved either by radiating fixed frequency mm-wave power via a movable antenna (mirror) into the plasma or by applying different frequencies at fixed launching angle. Since the tokamak's magnetic field is decreasing from the inner to the outer torus wall also the electron cyclotron resonance frequency is decreasing. In order to reduce the ECRH system's costs it is desirable to provide these frequencies by using only one type of mm-wave source, such as a stepwise frequency-tunable gyrotron oscillator.

### The TE<sub>22,6</sub> Gyrotron

The gyrotron consists of a diode-type magnetron injection gun with a LaB<sub>6</sub>-emitter. The beam tunnel is equipped with alternating staggered copper and highly RF-absorbing ceramic rings in order to suppress oscillations in this region. The operating mode has been chosen to be the TE<sub>22,6</sub> mode [1] with a designed output power of 1 MW at a beam current of 40 A and a beam voltage of 80 kV (see Table I). The collector employs an insulation gap allowing a retarding voltage in order to study the efficiency improvement by beam energy recovery in a single-stage depressed collector.

<u>gun</u>		<u>cavity</u>	
cathode voltage	80 kV	output power	1 MW
beam current	40 A	efficiency $\eta$	30%
emitter current	3.6 A/cm <sup>2</sup>	magnetic field	5.49 T
density		Ohmic loss density	3.5 kW/cm <sup>2</sup>
emitter radius	45.2 mm	velocity ratio $\alpha$	1.4
cathode angle	21.48°	beam radius	7.93 mm
magnetic field	0.187 T	beam thickness	0.53 mm
		compression ratio	36
		cavity radius	15.57 mm
		cavity length	15 mm
		input taper angle	3°
		output taper angle	2.5°
		diffractive Q	1000

Table I: Design values of the TE<sub>22,6</sub> gyrotron

In a gyrotron the frequency can be step-wise varied by changing the operating TE-cavity mode via variation of the cavity magnetic field. Due to the helical-cut antenna of the applied q. o. mode converter (Denisov-type) [2] the different modes, which have to be launched into a linearly polarized "Gaussian" beam profile, must have the same rotation. Since the reflections at the window plate only can vanish if the oblique incident beam is linearly polarized it is important to notice that the excited TE mode as well as its launched beam pattern do not show any mentionable part of a longitudinal electric field (cross polarization).

### Window Design and High Power Measurements

Due to the power supply available at FZK, currently the possible pulse length for the high power experiments is limited to several milliseconds. Owing to the low dielectric losses of the common window materials this results in negligible thermal restrictions. Therefore no special attention had to be paid to the window's cooling system and the thermal conductivity of the window material itself. For this reason a fused silica quartz glass with guaranteed isotropic material properties has been used.

#### • conventional single disk window:

In order to decrease the window reflections at least for a few frequencies a conventional single disk was mounted perpendicular to the RF beam as an output window. By choosing the window's thickness to be  $d = 6 \cdot \lambda_n = 6.58$  mm at the gyrotron design frequency of 140 GHz the transmission characteristics

for 117 GHz, 128 GHz, 140 GHz, 152 GHz and 163 GHz are optimized. Figure 1 shows the calculated dependency for the window reflection and the measured gyrotron output power versus the applied cavity magnetic fields, respectively the frequency. One has to keep in mind that only oscillations at discrete frequencies can be excited in a gyrotron cavity. However it is obvious that only modes located at frequencies with low window reflections are coupled out with power levels up to 1 MW.

#### • Brewster window

In a second step the gyrotron had been equipped with a Brewster window. In order to achieve a simple window design and due to the negligible thermal demands the quartz plate was glued to the metal housing without any additional cooling system. The angle between the incident beam and the normal to the window plate was chosen according to Snell's law of refraction for vanishing reflections in case of parallel polarization:

$$\Theta_{Brew} = \arctan\left(\sqrt{\frac{\epsilon_2}{\epsilon_1}}\right) = 62.87^\circ$$

where  $\epsilon_2 = 3.81$  is the permittivity of quartz glass and  $\epsilon_1 = 1$  is that of air or vacuum. The dependency of the reflection coefficient versus frequency and the angle of incidence are shown in Figure 2. It is interesting to notice that the reflections in a stripe from  $55^\circ$  to  $70^\circ$  are below 5 % independent from frequency. Figure 2 b) shows the excellent agreement between the calculated and measured reflection curve for a frequency of 140 GHz. Since all rays are reflected under the same angle as they fall onto the plate surface it is extremely unlikely that any mentionable part is scattered back into the gyrotron. The significant influence on the mode spectrum of the measured output power can be seen in Figure 1. Practically all modes are coupled out with the same intensity. Only at frequencies where the azimuthal indices are changing the power levels are slightly reduced ( $m=5$  to 6 at 132 GHz and  $m=6$  to 7 at 151 GHz).

- without reflections (Brewster window)
- with reflections (conventional window)

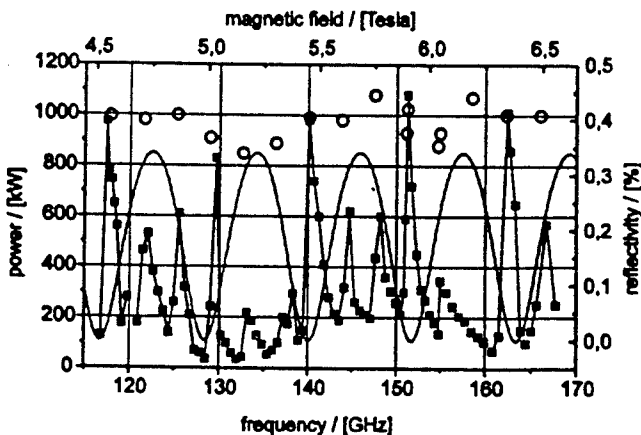


Fig. 1: Calorimetrically measured output power and calculated reflectivity of the conventional window versus magnetic field and frequency, respectively.

### Comparison between the two Window Designs

To be able to compare the inside the gyrotron's cavity excited RF power levels for corresponding modes in the two concepts the values measured with the single disk window can be corrected by the window's reflection. Only for vanishing window reflections the same results were achieved. Whereas modes located at high reflections are coupled out even less than what have been expected by the correction. These results indicate that even by using a q. o. mode converter window reflection cannot be neglected.

For minimal reflections in the conventional design the window plate has a resonant thickness with respect to the wavelength inside the material. This of course results in a local maximum of absorption given by the following formula:

$$A \approx \frac{\pi \cdot f \cdot d \cdot \tan(\delta) \cdot (1 + \epsilon_r')}{c_0}$$

where  $f$  is the resonance frequency,  $d$  is the plate's thickness and  $c_0$  is the velocity of light in vacuum. For a plate mounted under the Brewster angle each ray is passing the window material only once, which results in the following equation:

$$A \approx \frac{2 \cdot \pi \cdot f \cdot \sqrt{\epsilon_r'} \cdot \tan(\delta)}{c_0} \cdot \frac{d}{\sin(\Theta_{Brewster})}$$

From this equations it is obvious that the amount of power absorbed in the conventional window compared to that in a Brewster window of similar thickness is increasing stronger with the permittivity. In addition the RF spot size on the window is increased due to the oblique incidence. Which results in a lower peak temperature and less critical thermal stress conditions.

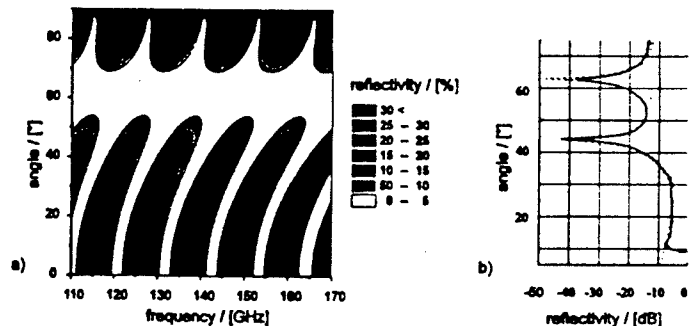


Fig. 2: a) Reflectivity of 7 mm thick fused quartz plate versus frequency and angle of incidence.  
b) Measured reflectivity at a frequency of 140 GHz

### References

- [1] Gantenbein, G., et al., Int. J. Electronics 72 (1995), pp. 771-787.
- [2] Möbius, A., Thumm, A., Gyrotron output launchers and output tapers in Gyrotron Oscillators, C. Edgecombe, ed., Taylor & Francis, London, 1993, Chapter 7, pp. 179-222.

## Influence of window reflections on gyrotron operation

G. Dammertz, O. Braz<sup>1</sup>, M. Kuntze, B. Piosczyk, M. Thumm<sup>1</sup>

Forschungszentrum Karlsruhe, Association EURATOM-FZK, ITP, P.O.Box 3640, D-76021 Karlsruhe, Germany

<sup>1</sup>also Universität Karlsruhe, Inst. für Höchstfrequenztechnik und Elektronik, Kaiserstr. 12, D-76128 Karlsruhe, Germany

### Abstract

A  $TE_{22,6}$  gyrotron with a dimple-type quasi-optical launcher has been built at the Forschungszentrum Karlsruhe. The highest output power for the  $TE_{22,6}$ -mode at 140 GHz was measured to be almost 1.2 MW at an output efficiency of 26% (45% with single-stage depressed collector). The highest efficiency was 27% at an output power of 0.9 MW. The oscillation behaviour was investigated for different modes in a large frequency range extending from 117 GHz to 166 GHz. With a Brewster window the measured output power of about 1 MW was almost independent of the excited modes. A similar measurement has also been performed with a conventional window perpendicular to the rf-beam. This measurement showed a strong dependence of output power on the frequency, even if the output power is corrected according to the reflections. A strong influence also was found with a double-disk window, for which the reflection coefficient could be changed continuously.

### Introduction

Electron Cyclotron Resonance Heating is one of the major candidates for plasma heating, non-inductive current drive, profile control and start-up of the plasma current in the next generation of fusion plasma machines such as the ITER tokamak.

To meet these requirements with high efficiency it is necessary to heat the plasma at different positions. This can be achieved by radiating waves of different frequencies into the plasma. Due to the different magnetic fields at different positions, the location of rf-absorption can be chosen by the appropriate frequency.

The output-wave of a gyrotron is assumed to be a linearly polarized Gaussian beam. In this case a window can be installed with the Brewster angle. For this the reflections are zero independent of frequency.

### Experimental set-up

The layout of the gyrotron is described in earlier papers<sup>1,2</sup>. The  $TE_{22,6}$  gyrotron consists of a diode-type magnetron injection gun with a  $LaB_6$  emitter. The velocity ratio  $\alpha$  can be modified from 1.1 to 1.7 by the change of the magnetic field gradient in the gun region. The beam tunnel is equipped with alternating staggered copper and highly rf-absorbing ceramic rings (aluminum nitride and 40% silicon carbide). The operating mode has been chosen to be the  $TE_{22,6}$  mode with an output power of 1 MW at a beam current of 40 A and a beam voltage of 80 kV.

The peak value of the Ohmic-loss density is 3.5 kW/cm<sup>2</sup> for an output power of 1 MW and a surface temperature of 300°C. A factor of 1.3 is included for surface roughness, and rf-losses of 15% are assumed between generated power and output power.

The Brewster angle  $\Theta$  for a disk with the permittivity  $\epsilon$  is calculated in air according to  $\tan(\Theta) = \sqrt{\epsilon}$ . For a quartz disk ( $\epsilon=3.81$ ) the angle is calculated to be 62.9°. In order to achieve a simple window design, the quartz plate was glued to the metal housing without any additional cooling system. This is possible because of the short pulse length (0.5 ms) and the low duty cycle. The thickness of the disk was 7 mm. The window housing had a diameter of 100 mm.

For cw-operation such a window might be realized using a diamond disk<sup>2</sup> fabricated by chemical vapor deposition.

Due to the large angle of the window it seems to be extremely unlikely that a considerable part of the rf-wave is scattered back to the cavity. However it might be that the reflected power is not totally absorbed in the mirror box of the gyrotron. After a few reflections in the box a small part of the reflected power can enter the launcher and pass to the cavity.

To compare the behavior of the gyrotron with the Brewster window to a conventional gyrotron, we installed a single-disk quartz window perpendicular to the rf-beam. To minimize the reflection at certain frequencies (117 GHz, 128 GHz, 152 GHz and 163 GHz), the thickness was chosen to 6.58 mm. This corresponds to six wavelengths inside the material at the frequency of 140 GHz.

To be able to change the reflection coefficient continuously in order to measure the behavior of the gyrotron with respect to reflections, a double-disk sapphire window was installed. With the disk thickness of 1.73 mm the disks are transparent for a frequency of 140 GHz. By changing the disk distance, the reflections can be varied from 0 to 90%.

### Experiment

With the Brewster window installed it was possible to excite the gyrotron at frequencies of different azimuthal modes at almost the same output level of 1 MW (black bars of figure 1). The spacing of these modes is about 3.7 GHz. However it can be seen that at about 132 GHz and at 154 GHz the output power is reduced slightly. These are those frequencies where the radial number of modes changes. At these points the frequency distance is very small (about the bandwidth of the cavity) and interference might occur. The light bars of figure 1 show the same measurement with a

conventional single-disk window (only the beam voltage was optimized). Of course, one has to correct these values as part of the power is reflected. The corrected power  $P_c = P_{out} (1-r^2)$  is shown by the gray bars.

Even for the corrected power the values are strongly reduced compared to the power measured with the Brewster window. At 122 GHz the reduction is about 20% though the power reflection coefficient is about 35%. The same reflection coefficient is calculated for 136 GHz, but here the reduction in output power is about 70%. The same is true for 155 GHz.

Though we did not expect a severe amount of reflected power inside the cavity the influence is very strong. This is especially true at those frequencies for which the radial dependence changes from one series to the other. The reason might be the same as mentioned before: the frequency spacing between the two modes is rather small (less than 200 MHz). But also for other modes the reduction in (corrected) output power is significant, up to about 40 % for window reflections of 35%.

To prove this statement, another window - a double disk sapphire window with adjustable disk spacing - was installed. As expected, at 140 GHz no power dependence was found. For two other frequencies, the measurements are given in figure 2 and 3.

At 147.5 GHz, far away from other modes, a significant influence of the reflections on the corrected output power was found. The reduction of the measured output power was about a factor of two compared to what has been expected, if one corrects for the calculated reflections (figure 2).

A much stronger influence of the reflections was found at the frequency of 136.37 GHz. Theoretically the distance of frequency between the  $TE_{21,6}$  and the  $TE_{24,5}$  mode is less than 100 MHz and the actual coupling coefficients are almost the same. Even window reflections of only a few percent reduce the output power from 500 kW to less than 100 kW. As already mentioned the reason could be seen in the fact that there are two modes very near in frequency.

### Conclusion

A Brewster window is the ideal window for a step-tunable gyrotron. Many modes with a frequency spacing of 3.7 GHz could be excited at almost the same output level of 1 MW. A decrease of about 20% in output power was found at frequencies at which the radial mode index changes from one to the next. The reason is seen in the fact that the frequencies of the different modes are very near (comparable to the bandwidth of the cavity). For these modes even very small reflections seem to have a strong influence on the oscillation behavior of the cavity.

### References

1. G. Dammertz et al., 3rd International Workshop on Strong Microwaves in Plasmas, Moscow - St. Petersburg, Russia, August 7-14, 1996, to be published
2. O. Braz et al., this issue
3. M. Thumm et al, ITER final report, ID No.25, FZKA-report No.5808,1996

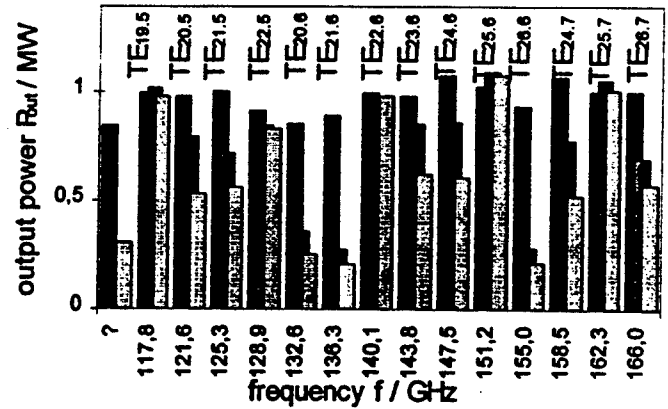


Fig. 1: Output power for different modes, a) with Brewster window (dark), b) measured power (light) and c) corrected power (gray) with a single-disk window

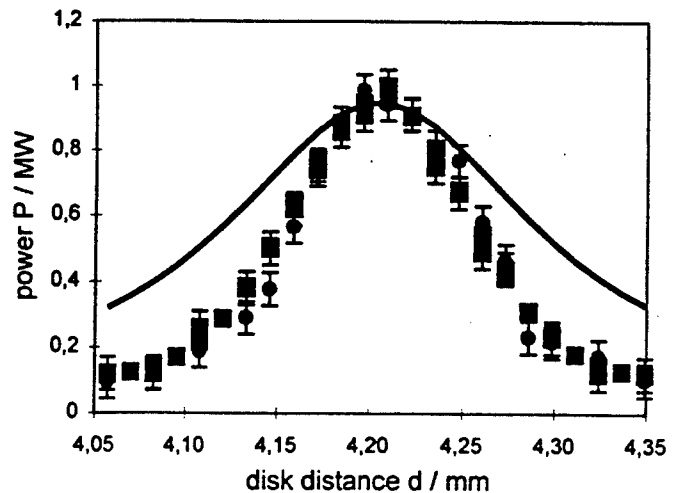


Fig. 2: Output power versus disk distance for 147.5 GHz. The solid line shows the expected power (corrected for reflections) assuming a generated power of 0.9 MW.

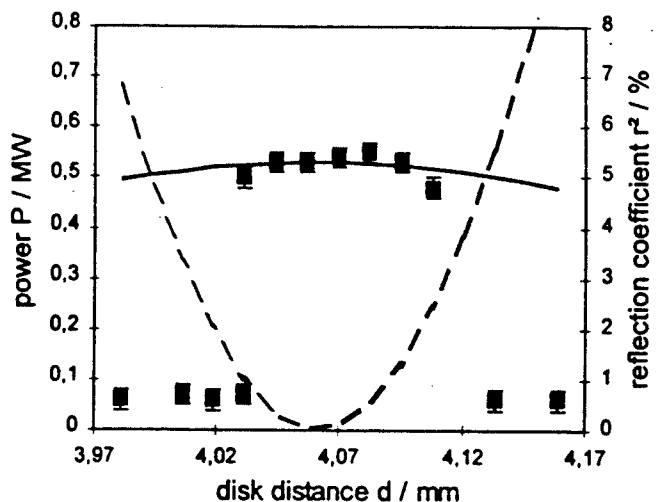


Fig. 3: Output power versus disk distance for 136.6 GHz. The solid line shows values according to  $P=0.53 (1-r^2)$ . The dashed line represents the power reflection.

# Enhanced Face Cooled Gyrotron Output Windows

George S. Haldeman  
MIT Plasma Science and Fusion Center  
NW-16-180, Cambridge, MA, USA

## Abstract

A new gyrotron window configuration is proposed as a modification of existing, double disk, face cooled windows. The design uses curved, rather than flat, elements to reduce the effect of pressure stresses and proposes a pressure recovering diffuser to increase effective flow rates for a given average coolant pressure. Results indicate that these enhanced face cooled windows can theoretically operate at microwave power levels up to 7 MW and should be able to reach practical levels in excess of 2 MW using single crystal sapphire at 110 GHz.

## Overview

Gyrotron oscillators with CW power levels greater than 1 MW at frequencies greater than 100 GHz are presently required to support ongoing plasma heating experiments for fusion research. These gyrotron tubes will require an output window to isolate the tube vacuum environment, and double disk, face cooled windows made of single crystal sapphire are the highest power designs currently in use. Unfortunately, these windows have only achieved power levels up to about 500 kW for conditions approaching CW operation. A number of alternative window designs have been proposed, and are almost exclusively utilizing advanced materials with simple edge cooled designs to extend window performance. Although these new materials are promising, the widespread use of quasi-optical techniques to separate and manipulate the millimeter wave output in Gaussian like beams provides the opportunity to consider alternative configurations.

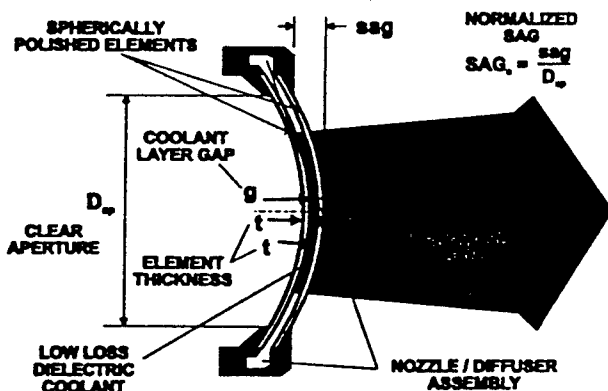


Figure 1  
Nominal Design Parameters

## Analysis

One of these alternatives is shown in Figure 1. The design consists of two uniform thickness spherical elements monocentrically mounted in an optimized nozzle diffuser

assembly. Microwave beam energy is transmitted through the elements and absorbed heat is removed by low loss fluorinert coolant which flows longitudinally through the intermediate layer and across the microwave beam. The window thickness, clear aperture, normalized surface sag, and coolant channel gap, specify the design geometry. The microwave intensity profile and properties for the flowing coolant layer and window elements must also be specified in order to analyze the design.

### A. Stress Limited Power

Absorbed microwave power is deposited throughout the element, and must be removed by conduction to the coolant layer boundary, and then by convection into the moving bulk fluid. In order to drive this heat conduction, temperature gradients with subsequent uneven thermal expansion are induced in the element creating strains and balancing stresses. The circulating fluid, required for cooling, causes an additional loading due to its pressure and also results in stresses and strains throughout the element. For small strains, and constant normalized temperature and pressure profiles, resulting stresses can be linearly related to the input beam power and average coolant pressure giving,

$$\vec{\sigma}_{tot}(\vec{r}) = W\vec{\sigma}_T(\vec{r}) + p_{avg}\vec{\sigma}_p(\vec{r})$$

where the  $\sigma$  vectors represent the stress state due to the thermal, pressure, and combined loads but include dimensional scaling factors as necessary,  $W$  is the input microwave beam power, and  $p_{avg}$  is the average pressure used to characterize the pressure profile. With this expression and given fixed profiles, the beam power required to reach the ultimate tensile or compressive stress in the material can be easily calculated for each point in the element. The minimum of these calculated values will be the stress limited power.

### B. Boiling Limited Power

Although the bulk temperature and flow properties are normally assumed to be constant, edge fluid must have the same temperature as the wall it is touching. As a result, it is possible for the wall temperature to exceed the local boiling point of the coolant, causing a phase change in this edge fluid, and ultimately failure due to thermal stresses as described above. Since the heat conduction problem that must be solved to obtain temperature profiles is also linear, the wall temperature profile (relative to the reference bulk fluid temperature) will also be linearly related to the beam power. The resulting relation can be easily inverted giving,

$$W_{boil} = [T_{boil}(p(\vec{r})) - T_{bulk}]H_{eff}(\vec{r})$$

where  $W_{\text{boil}}$  is the beam power that will cause boiling,  $T_{\text{boil}}(p)$  is the coolant boiling point, functionally dependent on the local pressure,  $T_{\text{bulk}}$  is the bulk fluid temperature, and  $H_{\text{eff}}(r)$  is an effective coupling constant which includes the spatial effects of the power deposition profile and convective cooling. When evaluated at all the points on the element surface, the minimum calculated value of this expression will give the boiling limited power.

### C. Cooling Optimization

Both stress and boiling limited performance are closely related to the level of convective cooling, which in turn, is closely related to the pressure profile within the coolant layer. The relationship is generally complex, but the trends are straightforward. Increasing pressure gradients increase flow and convective cooling, thereby reducing wall temperatures and at least some thermal stresses. Increasing average pressure increases the pressure stresses, thereby reducing allowable thermal stresses while at the same time increasing the boiling point all along the flow path. The trend towards increased cooling generally dominates the boiling point effect, and optimum cooling usually occurs near the maximum possible pressure gradient for a given average pressure. As a result, a fundamental tradeoff between allowable pressure stresses and enhanced cooling is created. The curved elements dramatically change the balance of this tradeoff by reducing the relative magnitude of pressure stresses. Since the maximum pressure gradient is usually assumed to be limited by a fixed exit pressure, the optimized diffuser will allow further improvement by increasing these gradients to that presented by the true limit, exit cavitation.

## Results

Clearly, to achieve improved performance, one must show that curvature induced reductions in pressure stresses and resulting increases in cooling or decreases in thickness more than offset any corresponding increase in thermal stress. Unfortunately, the complex thermal loading precludes any simple analytic solutions, and the problem must be solved numerically. Consequently, a straightforward numerical model which relied on simplification to axial symmetry and an effective 1D duct and heat conduction approximation[1] was developed from the basic shell equations[2] with included thermal loading[3]. The model was benchmarked against a standard finite element code with good agreement, and for the sake of brevity it will not be described further here.

Table 1

NOMINAL FLAT ELEMENT DESIGN PARAMETERS					
Material	Al <sub>2</sub> O <sub>3</sub> , sc		Coolant	FC-75	
Young's Modulus	340 GPa		Bulk Coolant Temp	295 K	
Thermal Conductivity	38 W/m/K		Pressure	1.89 atm	
Thermal Expansion	8.2 E-6 /K		Frequency	110 GHz	
Tensile Failure	350 MPa		Clear Aperture	100 mm	
Compressive Failure	438 MPa		Thickness	1.75 mm	
Surface Sag	0.0 mm		Coolant Duct Gap	0.75 mm	

Stress and boiling limited power were calculated for candidate designs, with curvature, thickness, and average pressure varied about the values for a nominal flat window design[4], shown in Table 1. The results supported the conclusion that reduced pressure stresses had enhanced performance, with curvature increases simultaneous with either pressure increases or thickness decreases producing dramatic beam power improvements. Although curvature and thickness variations showed theoretical maximum power levels up to 7 MW, minimum fabrication limits on thickness meant coolant pressure variations at a fixed minimum thickness would be more practical.

Table 2 shows a direct performance comparison of various point designs. The experimental[4] and analytic values for the reference flat window, flat window performance using cavitation optimized cooling, and a nominal curved window design are all shown. Although results indicate that better performance could be obtained with thinner elements or more curvature, the curved design presented here is a conservative transition from the existing flat window and should be producible and easily integrated into existing gyrotron designs. The resulting 2 MW maximum power can, thus, be taken as a realistic estimate of achievable performance for these enhanced face cooled designs.

Table 2  
POINT DESIGN COMPARISON: 4" APERTURE, 110 GHZ

AVG. PRESS (atm)	THICK (mm)	SAG (mm)	OPTIMIZED DIFFUSER?	RESULT	POWER (MW)
1.89	1.75	0	N	EXP	0.45
1.89	1.75	0	N	ANA	0.44
1.89	1.75	0	Y	ANA	0.67
1.89	1.75	0.005	Y	ANA	2.15

## Conclusions

These results are encouraging, and indicate that an enhanced face cooled window design could meet existing gyrotron window requirements with established single crystal sapphire material technology. More detailed analysis is required to investigate true limits but the conservative point design indicates that gains of at least 4x compared with existing flat windows should be possible.

## References

1. P.M. Borchard, *Thermal and Mechanical Analysis of High Power Microwave Windows*, M.E Thesis, Cambridge, MA, 1995.
2. S. Timoshenko and S. Woinowsky-Kreiger, *Theory of Plates and Shells* (McGraw-Hill, New York, 1959, 2<sup>nd</sup> Ed.), pp 533-547.
3. R.M. Rivelto, *Theory and Analysis of Flight Structures* (McGraw-Hill, New York, 1969), pp51-56.
4. K. Felch, et al, "Long-Pulse and CW Tests of a 110-GHz Gyrotron with an Internal, Quasi-Optical Converter," IEEE Trans. Plasma Sci., vol. 24, pp 558-569 (1996).



# Numerical Simulation of Processes of Mode Interaction in Powerful Gyrotrons

M.A. Moiseev, L.L. Nemirovskaya, V.E. Zapevalov, N.A. Zavolsky

Institute of Applied Physics, Russian Academy of Sciences  
46 Ulyanov Street, 603600, Nizhny Novgorod, Russia

## Abstract

The paper presents improved method and results of numerical simulation of processes of mode interaction in powerful gyrotrons, calculations of the main parameters of the different operating modes for the 110-170 GHz/1MW gyrotrons. Processes of the start-up in optimized gyrotron cavity and mode interaction are discussed.

## Introduction

In powerful gyrotrons as the cavity radius (in wavelength) grows the spectrum of eigenfrequencies becomes more dense, mode competition becomes more acute. Therefore it becomes harder to set up the operating mode when the gyrotron is started. Additionally as a rule admissible deviations of gyrotron parameters from the optimal ones in the stationary regime decrease and the electron beam potential depression effects actions increase.

In this paper we considered three versions of 1MW/CW gyrotrons with operating modes TE<sub>19.5</sub> (110 GHz) and TE<sub>28.7</sub>, TE<sub>31.8</sub> (170 GHz), accelerating voltage 80 kV, beam current  $I \approx 40$  A [1,2].

## Method of calculations

Relativistic gyrotron equations obtained at the assumption of unfixed RF field structure and suitable for any accelerating voltage  $U_0$  [3] are used. For non-stationary multimode oscillation case to study mode interaction process gyrotron equations were generalized [4] and integrated by using of Laplace transformation [5]. Electron velocity spread was represented with the Gaussian distribution function over rotational velocities  $f_0(v_\perp) = f_{0,max} \exp[-4(v_\perp/v_{10}-1)^2/(\delta v_\perp)^2]$ , which at moderate currents corresponds to the calculated and experimental data [1,2]. The cavity RF ohmic losses ( $1/Q_{ohm}$ ) are assumed to be twice exceeded simulated those for ideal copper. It is agreed with the results of measurements  $Q_{ohm}$  for mm-wave gyrotron cavities. The dependence of parameters of an electron beam on  $U_0$  at the front of a pulse was defined from adiabatic theory of the gyrotron electron guns, when an anode voltage is proportional to  $U_0$ .

## Cavity optimisation and mode interaction

At the optimal value of the magnetic field  $B_0$  the RF field longitudinal structure  $f(z)$  is very close to field structure of "cold" cavity (without electron beam). Therefore some important gyrotron characteristics can be determined in a fixed field structure approximation. The Fig.1 shows results of simulation of gyrotron with operating mode TE<sub>19.5</sub> and optimized cavity profile [6]. In the nonoptimal regimes and on the bottom branches of curves  $\eta(B_0)$ ,  $P_{ohm}(B_0)$  the distinctions of exact and approached settlement results grow

owing to unfixing field structure. It can essentially affect interaction of modes.

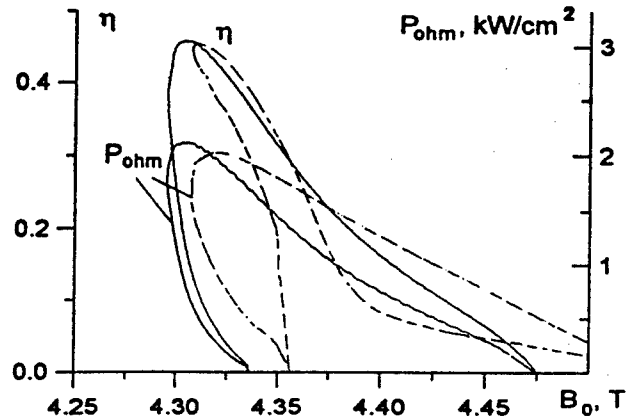


Fig.1. Dependencies of efficiency  $\eta$  and Ohmic loss  $P_{ohm}$ , of the TE<sub>19.5</sub> mode on the value of the magnetic field in the cavity,  $B_0$ , (solid curves - fixed structure, dashed - unfixed one,  $U_0=80$  kV,  $g=v_{10}/v_{20}=1.4$ ,  $I=30$  A,  $\delta v_\perp=0$ ).

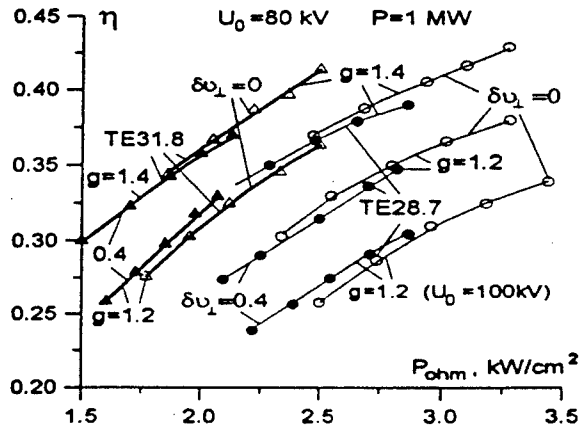


Fig.2. Efficiency  $\eta$  versus specific Ohmic power losses.

The cavity profile was smoothed in input and output [6]. Its diffraction  $Q$ -factor is near to minimum diffraction one. The optimization of a cavity profile was produced. Fig.2 shows opportunities of optimization of the 170 GHz gyrotron cavity. Increasing of  $U_0$  from 80 kV up to 100 kV gives 5% decreasing of the efficiency. Smoother profiles deteriorate mode selection over their longitudinal indexes.

In the gyrotron operating at the TE<sub>19.5</sub> mode the most dangerous is the parasitic mode, TE<sub>18.5</sub>, with the starting current close to the minimum ( $I_{st} \approx 0.2 I_{opt}$ ). In the fixed field structure approximation stationary oscillations of TE<sub>18.5</sub> mode are stable. Fig.3 shows the plane of relative amplitudes of the fields of the operating and parasitic modes  $f_{m,19.5}$  and  $f_{m,18.5}$  ( $f_m$  is maximum value of function  $f(z)$ ) with phase trajectories at

different starting conditions and optimal value of the magnetic field. The simulation with unfixed field structure give us qualitatively different results (Fig.4). Parasitic  $TE_{18.5}$  mode oscillations are unstable. Instead of them double mode two-frequency oscillations are established.

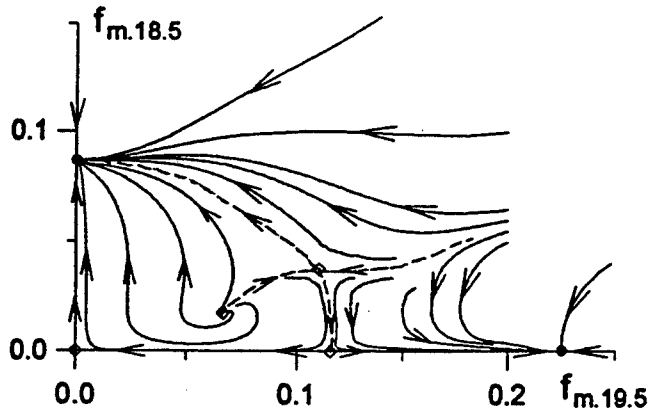


Fig.3. Phase plane of the operating  $TE_{19.5}$  mode and parasitic  $TE_{18.5}$  mode (fixed field structure).

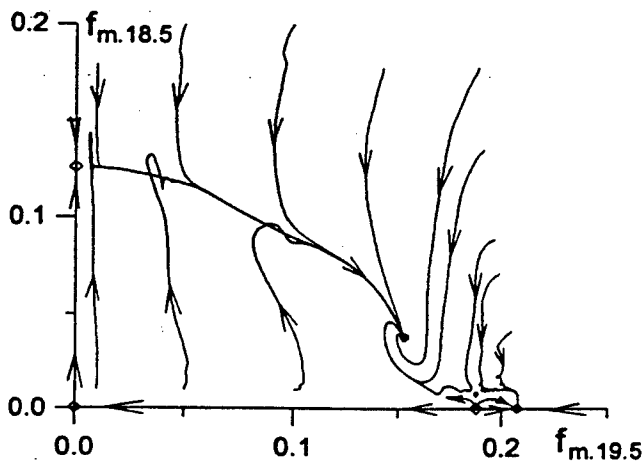


Fig.4. Plane of relative amplitudes of the operating  $TE_{19.5}$  mode and parasitic  $TE_{18.5}$  mode with unfixed field structure.

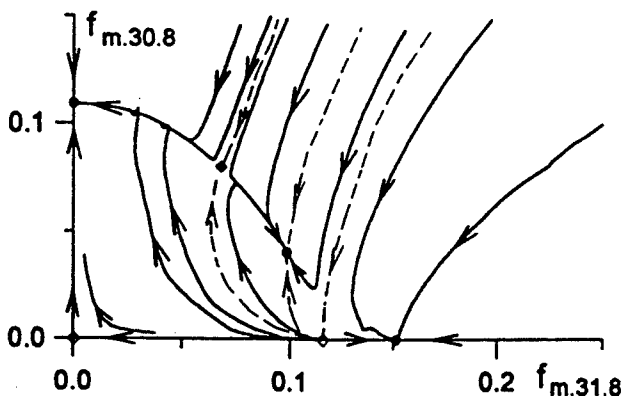


Fig.5. Plane of relative amplitudes of the operating  $TE_{31.8}$  mode and parasitic  $TE_{30.8}$  mode with unfixed field structure.

The accuracy of the fixed structure field approximation grows with reduction of operating beam current and detuning of working and parasitic modes cut off frequencies. In the gyrotron with a working mode  $TE_{31.8}$  the stationary oscillations of a parasitic mode  $TE_{30.8}$  are stable as with fixed,

and nonfixed field structure (Fig. 5). Similar results have been obtained also for the  $TE_{28.7}$  operating mode.

Stationary single-mode oscillations of operating modes stay stable when other parasitic modes are taken into account. In this case the simulations with fixed and unfixed field structure qualitatively the same.

#### Operating mode start-up

The parasitic mode ( $TE_{20.5}$  or  $TE_{29.7}$ ,  $TE_{32.8}$ ) is excited at the front of accelerating voltage pulse. Then it is broken and the operating mode ( $TE_{19.5}$  or  $TE_{28.7}$ ,  $TE_{31.8}$ ) is raised. The stationary oscillations of the operating mode are stable. At the radius of an electron beam  $R_0$  less than the optimum on the 0.2 mm instead of an operating mode ( $TE_{28.7}$  or  $TE_{31.8}$ ) a parasitic one ( $TE_{25.8}$  or  $TE_{28.9}$ ) can be established. To improve of the gyrotron operation stability it is useful to enhance the beam radius  $R_0$  in comparison with the optimum one. The deviation  $U_0$  from stationary value 80 kV at the flat of a pulse should be less than 1%.

#### Ion compensation of the space charge

The potential depression at the cavity in the beginning of the voltage pulse is near 5 kV for a current 40 A. Then space charge of an electron beam is compensated by positive ions [7]. It leads to decreasing frequency at 0.04% (owing to reduction of cyclotron frequency on 1%), and the efficiency maximum on 3% (due to reduction of the pitch-factor on 0.1). The compensation effect can explain the distinction of the dependencies  $\eta(B_0)$  for short pulse (up to 0.01 s) and long pulse (more than 0.1 s) gyrotrons.

#### Conclusions

The parameters of the cavity were optimized with the purpose to increase the gyrotron efficiency and to reduce thermal load of the cavity. An opportunity of achievement of the efficiency 32-42 % is shown at the cavity RF ohmic losses power  $P_{ohm}$  less than 2-2.5 kW/cm<sup>2</sup>. The mode competition is considered. At the starting regime of gyrotrons, a single-frequency, single-mode operation is established. It is shown the effect of ion compensation on electron beam space charge at long pulse duration is essential.

#### References

- [1] Denisov G.G., Flyagin V.A., Zapevalov V.E. Conf. Proc., 20 Int. Conf. on IR and MM Waves, Orlando, USA, 1995, p.197.
- [2] Glyavin M.Yu., Zapevalov V.E. Izv. Vuzov. Radiofizika, 1996, V.39, No.9, pp.1176-1181.
- [3] Bratman V.L., et al. Int. J. Electronics, 1981, V.51, No.4, pp.541-567.
- [4] Zavolsky N.A., Nusinovich G.S., Pavelyev A.B. In: Gyrotrons (Gorky, IAP, 1989), pp.84-112.
- [5] Ginzburg N.S., Nusinovich G.S., Zavolsky N.A. Int. J. Electronics, 1986, V.61, No.6, pp.881-894.
- [6] Zapevalov V.E., et al. Izv. Vuzov. Radiofizika, 1994, V.37, No.3, pp.381-386.
- [7] Varentsov V.A., Tsimring Sh.E. J. T. Phys., 1983, V.53, No.2, pp.264-269.

# SCATTERING MATRIX DESCRIPTION OF COMPLETE GYROTRON OSCILLATORS

D.Wagner, G.Gantenbein, W.Kasperek

*Institut für Plasmaforschung, Pfaffenwaldring 31, D-70569 Stuttgart, Germany*

M.Thumm

*Forschungszentrum Karlsruhe, Institut für Technische Physik*

*and Universität Karlsruhe, Institut für Höchstfrequenztechnik und Elektronik,*

*P.O.Box 3640, D-76021 Karlsruhe, Germany*

T.Idehara

*Department of Applied Physics, Faculty of Engineering*

*Fukui University, Fukui 910, Japan*

## Abstract

Complete gyrotron oscillators in axial arrangement including cavity, uptapers, pumping sections, collector waveguide and window are numerically simulated using a scattering matrix resonator code. The output mode purity and the influence of window reflections on the performance of the step-tunable, very high frequency gyrotron FU IV A at Fukui University are analyzed.

## Introduction

The Gyrotron FU IV A at Fukui University is a stepwise tunable medium power very high frequency gyrotron. The field intensity of its magnet can be increased up to 17 T and therefore frequency tunabilities up to 424 GHz by fundamental operations, up to 873 GHz by second harmonic operations have been demonstrated and up to 1.324 THz by third harmonic operations are expected [1]. In order to keep the starting currents low especially for higher harmonics the cavity must have a high quality factor  $Q_D$ . To avoid conversion of the cavity mode to spurious modes and also to shorten the interaction length the FU IV A cavity has an optimized design including nonlinear tapers together with a rounded iris at the output [2]. However, due to the axial output of the gyrotron and the large operating frequency range, mode conversion in the output section following the cavity and reflections at the output window have to be taken into account.

## Scattering Matrix Formalism

To determine the resonance frequencies, quality factors and mode compositions of the cavity a scattering matrix formalism (SM-code) is used [2]. Here the resonator is divided into a large number of diameter steps, each of them represented by a scattering matrix. Starting from the center of the resonator they are combined into two overall scattering matrices, one for the rear ( $\underline{S}_A$ ) and one for the front part of the resonator ( $\underline{S}_B$ ). After solving the eigenvalue problem:

$$\underline{S}_{22A} \cdot \underline{S}_{11B} \underline{a} = \Lambda \underline{a} \quad (1)$$

( $\underline{S}_{22A}$ ,  $\underline{S}_{11B}$  ... input and output reflection,  $\underline{a}$  ... eigenmode

vector,  $\Lambda$  ... eigenvalue) the amplitude profile of each mode in the resonator can be calculated by a backcascading process. The total quality factor including ohmic losses and mode conversion is:

$$Q_{tot} = \frac{k_0^2 \sum_{n=1}^N |A_n|^2 \cdot \frac{l_n}{k_{zn}}}{|B|^2} \quad (2)$$

( $k_0$  is the free space wavenumber,  $A_n$  is the modal vector in section  $n$ ,  $B$  contains the radiated modal amplitudes at both ends of the resonator,  $l_n$  is the length of section  $n$ ,  $k_{zn}$  is the longitudinal wave number in section  $n$ ). By neglecting the attenuation due to ohmic losses Eq.(2) gives in the diffractive quality factor  $Q_D$ .

## Calculations

The cavity and the output window are optimized for the  $TE_{1,9}$  mode at second harmonic. A resonance calculation using the optimized cavity [2] reveals a resonance frequency of 873.72 GHz with an output mode purity of 99.37% and a quality factor of  $Q_D=118737$ . The FU IVA multilayer output window consists of a sapphire plate ( $\epsilon_r=9.40$ ) between two quartz discs ( $\epsilon_r=3.83$ ) in order to achieve a larger bandwidth of the transmission. The calculated reflection of the window with the geometry shown in Fig.1 is plotted in Fig.2. The reflection shows a minimum close to the resonance frequency of the  $TE_{1,9}$  mode. The complete gyrotron geometry including output tapers straight sections and output window is shown in Fig.3. The output mode suffers from conversion into spurious modes in the linear output tapers following the cavity. Fig.4 shows the calculated modal powers along the length of the second linear taper, taking into account an input of 100%  $TE_{1,9}$ . The resonance calculation using the SM-Code can be performed taking into account the complete gyrotron geometry including the pumping sections (slots) and the window. The output section reduces drastically the mode purity. The quality factor is also varied due to the reflection from the window which acts as an additional feedback to the cavity and leads to an increase or decrease of  $Q_D$  depending on the amount

and phase of the reflected resonant mode. This is especially interesting for modes with high reflection coefficients at the window. Table 1 shows a comparison of output mode purities and quality factors for different modes at different harmonics for the calculation with the cavity only and with the complete geometry.

### Conclusions

A gyrotron with axial output acts like a complex resonator due to feedback from the output window to the cavity. Therefore the complete geometry has to be taken into account in order to get correct values for output mode purity and quality factors which also effects the calculation of starting currents. The output mode purity can be significantly improved by applying nonlinear tapers also in the output section following the cavity.

### References

- [1] T.Idehara, Y.Shimizu, K.Ichikawa, S.Makino, K. Shibutani, K. Kurahashi, T.Tatsukawa, I.Ogawa, Y.Okazaki, T. Okamoto, Development of a medium power, submillimeter wave gyrotron using a 17 T superconducting magnet, Phys. Plasmas, 2, 1995, 3246.
- [2] D.Wagner, G.Gantenbein, W.Kasperek, M.Thumm, Improved gyrotron cavity with high quality factor, Int.J. of Infrared and Millimeter Waves, 16, 1995, 1481.

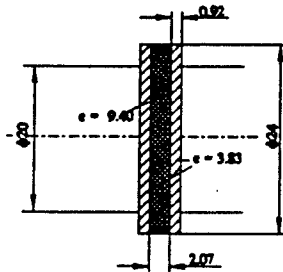


Fig.1 Geometry of the FU IV A gyrotron output window

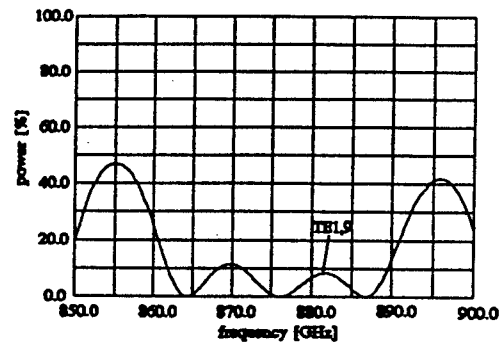


Fig.2 Calculated window reflection of the  $TE_{1,9}$  mode

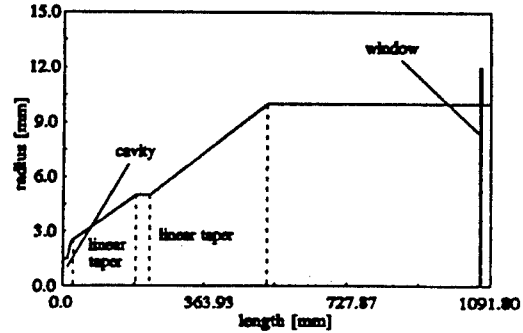


Fig.3 Geometry of the complete FU IV A gyrotron

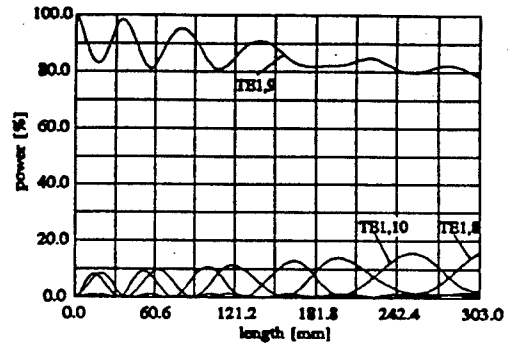


Fig.4 Mode conversion in the linear  $\phi 10 \rightarrow \phi 20$ mm taper

mode	$f_{res}$ [GHz]	cavity		complete tube		
		$Q_D$	$\eta$ [%]	$Q_D$	$\eta$ [%]	$R_w$ [%]
$TE_{7,1}$	273.53	1326	99.99	2205	90.25	7.44
$TE_{8,1}$	307.47	1624	99.99	14234	69.27	27.78
$TE_{3,3}$	361.45	3349	99.73	6094	88.38	23.36
$TE_{6,2}$	373.80	3430	99.96	3294	94.91	4.21
$TE_{9,3}$	604.92	19219	99.88	18545	88.65	13.80
$TE_{3,6}$	757.53	57875	99.56	48315	82.22	17.63
$TE_{3,7}$	768.38	61248	99.53	43589	71.08	39.57
$TE_{1,9}$	873.72	118737	99.37	165884	70.67	3.33
$TE_{2,10}$	1022.25	301240	98.73	951200	43.58	45.50
$TE_{9,7}$	1034.28	338571	98.67	269579	74.73	10.73

Tab.1 Calculated resonance frequencies ( $f_{res}$ ), diffractive quality factors ( $Q_D$ ) and output mode purities ( $\eta$ ) for both the FU IV A cavity and the complete gyrotron as well as window reflection coefficients ( $R_w$ ).

# Rigorous Analysis of Slotted-Circular Coaxial Waveguides Used in Some RF Vacuum Electronic Devices

J.-Y. Raguin and K. Schünemann

Technische Universität Hamburg-Harburg  
Arbeitsbereich Hochfrequenztechnik, D-21071 Hamburg, Germany

## Abstract

Coaxial waveguides coupled to longitudinal slots are used in some RF vacuum electronic devices such as magnetrons, crossed field amplifiers and gyrotrons. The Generalized Spectral Domain (GSD) method provides a fast, accurate and numerically efficient mean to calculate the cut-off wavenumbers of the eigenmodes of such composite coaxial waveguides. Plots of the field lines of a few modes for typical structures are presented.

## Introduction

The traditional method used to calculate the field characteristics of coaxial waveguides with longitudinal slots on the inner or outer conductor is based on the mode-matching procedure. This technique is used with diverse degrees of approximation to design crossed-field devices such as the magnetrons and the crossed-field amplifiers [1]. It has also been applied to study some peculiar RF structures of harmonic gyrotrons [2]-[3].

However, this approach is not well suited for an accurate determination of the fields amplitudes in particular in the vicinity of the common surfaces of the slots and of the coaxial waveguide. This issue would be particularly critical for any attempt to model the electron dynamics in a magnetron with a field theoretical approach.

The Generalized Spectral Domain method (GSM), which has been used in [4] to study composite hollow waveguides, is extended here to analyse rigorously azimuthally periodic slotted-circular coaxial waveguides. This method provides an efficient way to find the cut-off frequencies of such RF structures and to investigate their transverse modal field distributions.

## Description of the Method

The GSD method applied to a composite waveguide consists in short-circuiting the coupling surfaces and in replacing the tangential electric field at their boundary by two surface magnetic currents on both sides of the short-circuit. The continuity of the tangential electric field across each boundary is ensured by imposing that the two surface magnetic currents, which are to be computed, are equal in magnitude but opposite in direction.

The projection of the electromagnetic field of the isolated waveguides on their respective eigenmodes leads to relations between the expansion coefficients and the surface magnetic cur-

rents. A characteristic set of equations of the type:

$$[Y]V = 0,$$

is obtained by expanding the surface magnetic currents on a set of basis functions (moment method) which satisfies the edge condition and by testing the continuity of the tangential magnetic excitation on the same set (Galerkin's procedure). In the above relation,  $V$  is the column voltage vector which elements are the expansion coefficients of the surface magnetic currents.  $[Y]$  is the matrix admittance which terms are functions of the cut-off wavenumbers  $k_c$  of the composite waveguide. These searched cut-off wavenumbers singularize the admittance matrix. The field distribution of the eigenmodes of the waveguide are determined with the calculated voltage eigenvectors  $V$ .

In principle, as long as the translational symmetry in the longitudinal direction is preserved, the above described procedure can be applied to any composite waveguide structure, regardless of the shape of the cross-sections of the waveguides taken separately. However, for azimuthally periodic slotted-circular coaxial waveguides, the procedure can significantly be simplified. According to Floquet's theorem and taking into account the re-entrancy condition, the phase difference of the electromagnetic field between adjacent slots is  $2\pi p/N$ .  $N$  is the number of slots and, in the nomenclature of magnetron mode identification [1], the integer  $p$  is the mode number. This phase relation reduces the numerical implementation of the GSD method to one single slot.

For the  $TE$  modes, which are of practical interest, and for an azimuthally periodic coaxial waveguide with  $N$  slots cut in the outer conductor, the continuity of the axial magnetic excitation across a slot is tested by considering the set of functions:

$$H_{z,n}^w(r, \phi) = N_n^w Q_{p,n} (k_{h,n}^w r, k_{h,n}^w r_i) e^{j p n \phi},$$

for the coaxial waveguide, and:

$$H_{z,m}^s(r, \phi) = N_m^s Q_{p,m} (k_{h,m}^s r, k_{h,m}^s (r_o + h))$$

$$\cos \left[ \frac{m\pi}{\theta} \left( \phi - \frac{\theta}{2} \right) \right],$$

for the slot, where  $-\theta/2 \leq \phi \leq \theta/2$  and:

$$Q_\nu(x, y) = J_\nu(x) Y'_\nu(y) - J'_\nu(x) Y_\nu(y).$$

The other parameters are defined as follows:  $N_n^w$  and  $N_m^s$  are normalization factors,  $k_{h,n}^w$  and  $k_{h,m}^s$  are the cut-off wavenumbers for the  $TE$  modes of the coaxial and slot waveguides respectively,  $\theta$  is the angle subtended by each gap space between

slots of the outer conductor,  $r_i$  and  $r_o$  are the radii of the inner conductor and of the outer conductor respectively,  $h$  is the depth of each slot. For each spatial harmonic indexed by integers  $n = 0, \pm 1, \pm 2, \dots$ , the azimuthal wave numbers  $p_n$  are related to the mode numbers  $p$  by the relations  $p_n = p + nN$ . The axial magnetic surface current is projected on the basis functions:

$$\frac{N_l^c \cos(\frac{l\pi}{\theta}\phi)}{\sqrt{(\frac{\theta}{2})^2 - \phi^2}}, \quad l = 0, 2, 4, \dots,$$

and:

$$\frac{N_l^s \sin(\frac{l\pi}{\theta}\phi)}{\sqrt{(\frac{\theta}{2})^2 - \phi^2}}, \quad l = 1, 3, 5, \dots,$$

where the coefficients  $N_l^c$  and  $N_l^s$  are normalization factors. These functions satisfy the edge condition for an edge angle of  $\pi/2$ .

### Application to Magnetron-Like Structures

The GSD method is applied to the well-known A6 magnetron developed by A. Palevsky and G. Bekefi at MIT in 1979 [5]. This magnetron consists of an anode of radius  $r_o$  of 2.11 cm and of a cathode of radius  $r_i$  equal to 1.58 cm. The six vanes cut in the anode block have a depth  $h$  of 4.11 cm. These slots have an opening  $\theta$  of  $20^\circ$ . The discrete set of cut-off frequencies plotted on the dispersion diagrams of Fig. 1 for the two first passbands shows that our calculations are in agreement within 3 % with those presented in [5].

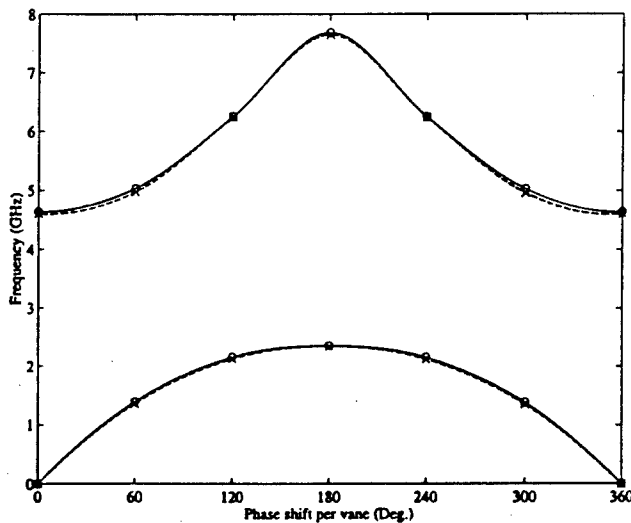


Fig. 1: Dispersion diagrams for the A6 magnetron structure. (x): calculations of [5] (o): our calculations,

We finally illustrate the robustness of the GSD method for slotted-circular coaxial waveguides by applying it to a structure with sixteen slots cut in the outer conductor. The ratio of the inner conductor to the outer conductor  $r_i/r_o$  is 0.6. The ratio  $h/r_o$  is 0.5. The vanes have an opening of  $13.5^\circ$ . Fig.2 shows the electric field lines of the mode belonging to the first passband with a phase shift per vane of  $\pi$ . The reduction of the slot depth would lead to the mode pattern of the whispering-gallery mode  $TE_{81}$

for a coaxial waveguide. Fig.3 shows the modal field distribution of the mode belonging to the second passband with field in phase from vane to vane.

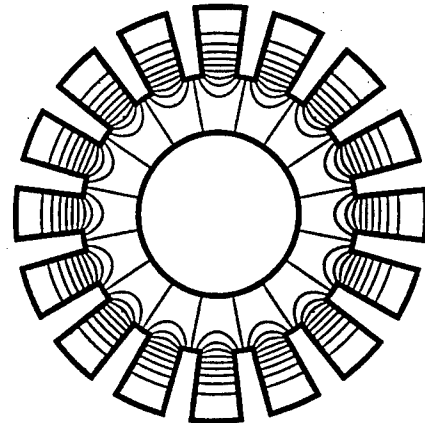


Fig. 2: Electric field lines of the  $TE_{81}$ -like mode

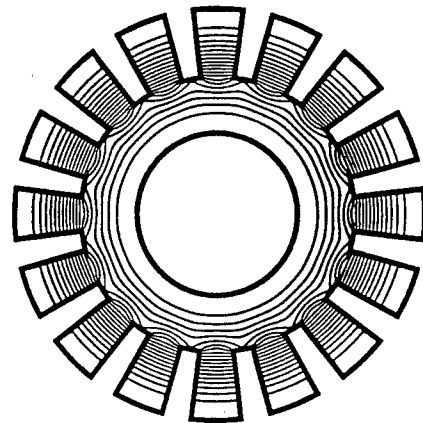


Fig. 3: Electric field lines of the  $TE_{01}$ -like mode

### Acknowledgements

The authors are indebted to the Deutsche Forschungsgemeinschaft for financial support. One of them (J.-Y. R.) would like to thank Mr. C. Rieckmann and Mr. J. Jelonnek from Technische Universität Hamburg-Harburg for many useful discussions.

### References

- [1] *Microwave Magnetrons*, edited by G. B. Collins, McGraw-Hill, New York, 1948.
- [2] H. Li, et. al., *Int. J. Electronics*, vol. 65, pp. 409-418, 1988.
- [3] H. Li, et. al., *Int. J. Electronics*, vol. 70, pp. 213-219, 1991.
- [4] A. S. Omar, et. al., *IEEE Trans. Microwave Theory Tech.*, vol. 42, pp. 2139-2148, 1994.
- [5] A. Palevsky and G. Bekefi, *Phys. Fluids*, vol. 22, pp. 986-996, 1979

# EIGENMODES OF MICROWAVE CAVITIES CONTAINING HIGH-LOSS DIELECTRIC MATERIALS

S. J. Cooke, University of Maryland, College Park, MD 20742 and  
B. Levush, Vacuum Electronics Branch, Code 6840, NRL, Washington DC 20375

## Abstract

The numerical determination of the electromagnetic field eigenmodes of a microwave cavity containing regions of high-loss dielectric material has proved problematic to numerical techniques [1]. The Jacobi-Davidson algorithm [2] is shown to extract a set of eigenmodes, even for degenerate eigenvalues and low ohmic-Q cavity modes. Examples using 2D and 3D electromagnetic operators are presented.

## 1 INTRODUCTION

In electromagnetics, identifying modes of cavity structures is equivalent to a matrix eigenproblem, obtained for example by finite difference, finite element or finite integration methods. The ease with which such problems may be solved depends on the mesh size, but also is strongly dependent upon the distribution of the eigenvalues and whether they are real or complex.

Methods for eigenvalue and eigenvector computation for large, linear systems of equations frequently require self-adjoint (Hermitian) matrices. Inclusion of highly lossy materials makes the related eigensystem non-Hermitian, and more rigorous techniques must be used.

## 2 EIGENVALUE FORMULATION

Two electromagnetic eigenproblems will be considered:

1. Simple electromagnetic planar circuits for which an exact two-dimensional representation can be found in terms of a single field component.

The class includes rectangular waveguides with H-plane bends and junctions or symmetric TE modes of cylindrically symmetric cavities. Such circuits have no structure in the third coordinate, but may include regions of dielectric material. The following eigenvalue form is obtained

$$\{\nabla_{\perp}^2 + \omega^2 \epsilon(r_{\perp}) \mu_0\} E_y(r_{\perp}) = 0$$

The cavity frequencies,  $\omega$ , and mode structures,  $E_y(r_{\perp})$ , are found as solutions of this eigensystem.

2. A 3-dimensional electromagnetic operator derived using the finite integration method [3].

The eigenvalue form derived from Maxwell's equations is (in normalised units) the vector equation [1]

$$\text{curl } \mu^{-1} \text{curl } \mathbf{E} - \text{grad div } \epsilon \mathbf{E} = \omega^2 \epsilon \mathbf{E}$$

where the discretised components of  $\mathbf{E}$  form the eigenvector, and  $\omega^2$  is the eigenvalue.

The finite integration method defines field components using the Yee cell arrangement for which the differential operators take a particularly simple form, and takes account of the permittivity and permeability of each cell.

## 2.1 Lossy materials

Regions of complex permittivity, representing Ohmic loss, make the discretised eigensystems non-Hermitian, and therefore critically change the characteristics of the solution. Solutions for such systems may often be found using methods derived for Hermitian systems, provided that losses are small and eigenvalues almost real. If highly lossy materials are to be modelled successfully, a more rigorous approach is necessary.

## 3 NON-HERMITIAN EIGENSYSTEMS

A generalised linear matrix eigensystem can be written in the form

$$\mathbf{A}\mathbf{x} = \lambda\mathbf{B}\mathbf{x} \quad (1)$$

The column vector  $\mathbf{x}$  satisfying (1) is an eigenvector of the system  $\{\mathbf{A}, \mathbf{B}\}$ , with corresponding eigenvalue,  $\lambda$ . For matrices which are not Hermitian, it is possible to formulate a second, related eigenproblem as follows.

$$\bar{\mathbf{y}}\mathbf{A} = \lambda\bar{\mathbf{y}}\mathbf{B} \text{ or } \bar{\mathbf{A}}\mathbf{y} = \bar{\mathbf{B}}\mathbf{y}\bar{\lambda} \quad (2)$$

where  $\bar{\mathbf{y}}$  is a row vector. The vector  $\bar{\mathbf{y}}$  satisfying (2) is a left-eigenvector of the system  $\{\mathbf{A}, \mathbf{B}\}$ , with corresponding eigenvalue,  $\lambda$ . For a given generalised eigensystem described by  $\{\mathbf{A}, \mathbf{B}\}$ , pairs of left- and right-eigenvectors have equal eigenvalues, though the eigenvectors are not necessarily equal. The left and right eigenvectors possess a mutual orthogonality relationship, such that each left (right) eigenvector with corresponding eigenvalue  $\lambda$  is orthogonal to each right (left) eigenvector of a different eigenvalue.

## 4 THE JACOBI-DAVIDSON METHOD

The iterative Jacobi-Davidson technique is applicable to eigenproblems of the generalised form (1). Here, it has been extended to operate with independent left and right subspaces, so that the left and right eigenvectors may be represented effectively for non-Hermitian problems. In the standard method, a single subspace is used, for which the theory is well described by Sleijpen *et al.* [4]. At each iteration, the subspace is updated by obtaining an estimate of the correction to each approximate eigenvector using Jacobi's orthogonal component correction (JOCC) method. For systems which are not self-adjoint, however, the subspaces spanned by the eigenvectors corresponding to a given set of eigenvalues will be different and separate subspaces should be maintained. This has been suggested in connection with the original Davidson method [5].

The modified Jacobi-Davidson method for non-Hermitian systems obtains separate subspace corrections

using JOCC steps on the left and right eigenvector residuals in a single procedure.

## 5 EXAMPLE GEOMETRIES

### 5.1 2D geometries

Two-dimensional (planar circuit) permit accurate solutions to be obtained for realistic structures with a moderate number of unknowns, typically  $10^4$  to  $10^5$ . Two examples are given here.

1. The first example consists of a  $2\text{mm} \times 2\text{mm}$  square column of lossy dielectric material ( $\epsilon_r = 10 - 2i$ ) located centrally in a  $20\text{mm} \times 20\text{mm}$  square cavity, discretised on a  $100 \times 100$  cell grid. The following table shows the real and imaginary components of the complex eigenfrequency and the cavity- $Q$  for the first eight cavity eigenmodes. Degenerate eigenvalues converged to the limit of numerical round-off error.

Mode	Complex Freq./GHz		Q
1	6.2145185	0.48687	6.38
2/3	13.8931731	0.807264	8.60
4	16.6253632	0.370592	22.43
5/6	19.8161824	0.636433	15.56
7	20.5588852	0.485044	21.19
8	23.1571167	0.394130	29.37

2. Figure 1 shows an eigenmode of a cavity in a cylindrical geometry, loaded with a lossy ceramic ring. The permittivity of the ceramic was  $\epsilon_r = 12.24$ , with loss tangent 0.3. Localised modes in the ceramic having  $Q < 4$  were also observed.

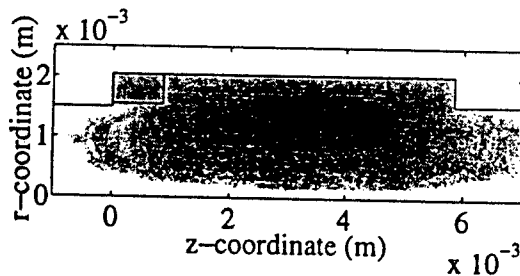


Figure 1: Gyrokystron cavity mode at 93.37GHz

The following table shows good agreement for two similar cavities between eigenmodes determined by (a) this calculation and (b) a scattering matrix calculation:

Mode:	TE <sub>011</sub>	TE <sub>012</sub>	TE <sub>012</sub>	TE <sub>012</sub>
(a) f	93.377	103.095	92.867	102.517
Q	174.198	51.941	187.077	53.654
(b) f	93.491	103.396	92.929	102.736
Q	168.767	46.864	169.635	47.045

These values are also in excellent agreement with experimental cold-test data.

### 5.2 3D geometries

With three-dimensional geometries, problem size increases since there are three components in each cell, and many

more cells are necessary to represent a volume. Two problems illustrate the effectiveness of this method for finding eigenmodes.

1. A perfectly cubic cavity with a symmetric discretisation provides an excellent test for separation of degenerate eigenvalues. This method successfully identified the six-fold eigenvalue degeneracies of this structure, correct to round-off error (approx  $10^{-14}$ ).

2. The final test example follows Schmitt *et al.* [1] and consists of a cavity  $20\text{mm} \times 20\text{mm} \times 10\text{mm}$  with a lossy dielectric block ( $\epsilon_r = 10 - 2i$ )  $7\text{mm} \times 7\text{mm} \times 8\text{mm}$  located centrally on the square cavity floor. The following results were obtained using a  $40 \times 40 \times 10$  cell mesh with approximately  $4.8 \times 10^4$  unknowns:

Mode	Freq./GHz		Q	Freq./GHz [1]	
1	6.1384	0.2810	10.92	6.161	0.278
2/3	9.0865	0.7790	5.83	9.091	0.780
4/5	11.316	0.7583	7.46	11.39	0.759
6	11.416	1.0386	5.49	11.42	1.104
7	13.250	1.1593	5.71	13.25	1.161
8	13.618	0.8746	7.78	13.66	0.870
9/10	13.667	0.8750	7.81	13.78	0.860

The method used here is, however, better applicable to such non-Hermitian systems, and converges uniformly even for loss tangents greater than one.

## 6 CONCLUSION

The Jacobi-Davidson method successfully identifies eigenmodes of complex cavities containing highly absorbing materials. Additionally, there is no requirement for estimation of extreme eigenvalues, and the solution may be seeded for iterative refinement. The method has been shown to be an attractive algorithm to aid the design of microwave cavities containing highly absorbing materials.

This work was supported by the Office of Naval Research. The computational work was supported in part by a grant of HPC time from the DoD HPC Center NAVO.

## 7 REFERENCES

- [1] D. Schmitt, R. Schuhmann, and T. Weiland. The complex subspace iteration for the computation of eigenmodes in lossy cavities. *Int. J. Num. Model.: Electronic Networks, Devices and Fields*, 8:385-398, 1995.
- [2] A. Booten and H.A. van der Vorst. Cracking large-scale eigenvalue problems, part I: Algorithms. *Computers in Physics*, 10(3):239-242, May/June 1996.
- [3] M. Bartsch *et al.* Solution of Maxwell's equations. *Computer Physics Communications*, 72:22-39, 1992.
- [4] G.L.G. Sleijpen and H.A. van der Vorst. A Jacobi-Davidson iteration method for linear eigenvalue problems. *SIAM J. Matrix Anal. Appl.*, 17(2):401-425, 1996.
- [5] E.R. Davidson. Super-matrix methods. *Comp. Phys. Commun.*, 53:49-60, 1989.



# MAGY: A Quasi Three Dimensional Self-Consistent Code for Modeling Electron Beam Devices

M. Botton\*, T. M. Antonsen

Institute for Plasma Research, University of Maryland  
College Park, MD 20742

and

B. Levush

Naval Research Laboratory  
Washington D.C. 20375

## Abstract

A new MAGY code is being developed for numerical modeling of electron beam devices. The code includes a time dependent quasi-three-dimensional description of the fields and electrons. The fields and the particles trajectories are calculated self consistently for an arbitrary profile of the circular waveguide (including discontinuities). The time scale for updating the electromagnetic fields is the cavity fill time. The code requires relatively modest computing resources.

## Introduction

In this work we present the recent development of a new MAGY code. In this version, as in the preceding one [1], we utilize the reduced description of the system, namely, the modal decomposition of the fields into the transverse electric (TE) and transverse magnetic (TM) modes of the waveguide. The complex amplitudes of the modes satisfy the transmission line equations where there is coupling among the modes due to the variation of the wall radius. We assume that all the electrons traverse the interaction region in a fraction of the cavity fill time, and that the Larmor radius is much smaller than the cavity length scale. Therefore, the beam dynamics is described by launching ensembles of particles each time step, computing their trajectories and deducing the current sources for the electromagnetic fields. Since the computed fields are used as the driving force of the electrons, we obtain a self-consistent description of the system. In what follow we briefly describe the code and bring examples of its operation.

## Description

Our derivation of the transmission line equations for the TM amplitudes  $I'_k, V'_k$  and TE amplitudes  $I''_k, V''_k$  follows Reiter [2]:

$$\frac{2}{c} \frac{\partial I'_k}{\partial t} = \Gamma'_k I'_k - \frac{\partial V'_k}{\partial z} + K'_k V'_k + M_k V''_k - \alpha''_k I'_k - \beta_k I''_k - J'_{Tk}$$

$$ik_0 V'_k = \frac{\partial I'_k}{\partial z} + K'_k I'_k + J'_{Tk}$$

$$\frac{2}{c} \frac{\partial V''_k}{\partial t} = \Gamma''_k V''_k - \frac{\partial I''_k}{\partial z} - K''_k I''_k - M_k I'_k - \alpha''_k V''_k - J''_{Tk}$$

$$ik_0 I''_k = \frac{\partial V''_k}{\partial z} - K''_k V''_k + \alpha''_{kL} I''_L + \beta_k I'_k$$

where  $J'_{Tk}, J''_{Tk}, J''_{Tk}$  are the projection of the electronic current on the electromagnetic modes. Unlike the smooth waveguide, in the variable radius waveguide the modes are coupled. There are three different coupling mechanisms. The first cause is the variation of the wall radius ( $K'_k$  for the TM-TM coupling,  $K''_k$  for the TE-TE coupling, and  $M_k$  for TE-TM). The second cause of coupling is the finite conductivity of the walls ( $\alpha''_k, \alpha''_{kL}, \alpha''_{kL}$ , and  $\beta_k$ ). The last is the coupling of the modes through the force term in the equations of motion (see below). The electron trajectories are computed using the following form of the equations of motion:

$$\frac{d p_x}{d z} = \Re \left\{ \frac{(p_x - i p_y)^{p-1}}{p_x} \gamma W_{V1} \right\} - \frac{p_y}{p_x} \left( \frac{\gamma k_0}{p} - \frac{\Omega_0}{c} \right) + \frac{p_x}{2} \frac{\partial \ln B_0}{\partial z}$$

$$\frac{d p_y}{d z} = \Im \left\{ \frac{(p_x - i p_y)^{p-1}}{p_x} \gamma W_{V1} \right\} + \frac{p_x}{p_x} \left( \frac{\gamma k_0}{p} - \frac{\Omega_0}{c} \right) + \frac{p_y}{2} \frac{\partial \ln B_0}{\partial z}$$

$$\frac{d p_z}{d z} = \Re \left\{ \frac{(p_x - i p_y)^p}{p_x} \gamma Q_1 + \frac{4\pi}{i\omega} \frac{1}{\beta_z} J_z \right\} - \frac{p_x^2 + p_y^2}{2 p_x} \frac{\partial \ln B_0}{\partial z}$$

$$p_x + i p_y = \gamma \beta_z \exp\{i\psi\} \quad , \quad p_z = \gamma \beta_z$$

$$W_{V1} = W_V - \beta_z W_I$$

$$W_V = \sum (V'_{in} F'_{Lin} + V''_{in} F''_{Lin}) \quad , \quad W_I = \sum (I'_{in} F'_{Lin} + I''_{in} F''_{Lin})$$

$$Q_1 = \sum (I'_{in} F'_{Lin} + I''_{in} F''_{Lin})$$

Here  $p_x + i p_y$  is the transverse momentum of the electron,  $p_z$  the longitudinal momentum,  $W_{V1}$  and  $Q_1$  are the coupling terms of the fields to the electrons. These equations include coupling between TE and TM modes, inclusion of modes above cutoff, and arbitrary profile of the axial magnetic field.

## Results

As an example we analyze the two cavity gyro-klystron device. The geometry of the cavity is described in Fig. 1a (dotted line). In the calculations we use 5 TE modes (TE<sub>01</sub> -

$TE_{05}$ ). For the computation of the resonance frequency of the input cavity and output cavities, we assign initial Gaussian profile to the  $TE_{01}$  and follow the time development of the field. After the transient time, the decay rate of the amplitude represents the  $Q$  of the cavity and the slow time variation describes the frequency shift. For the input cavity we simulated the diffractive  $Q$  by an equivalent surface conductivity. We obtain a resonance frequency of 34.7855GHz. This resonance is 97MHz lower than the measured resonance frequency. When we use only one TE

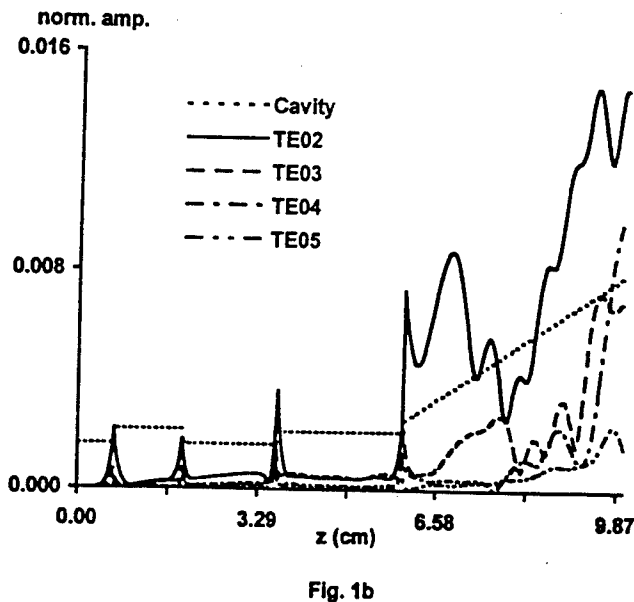
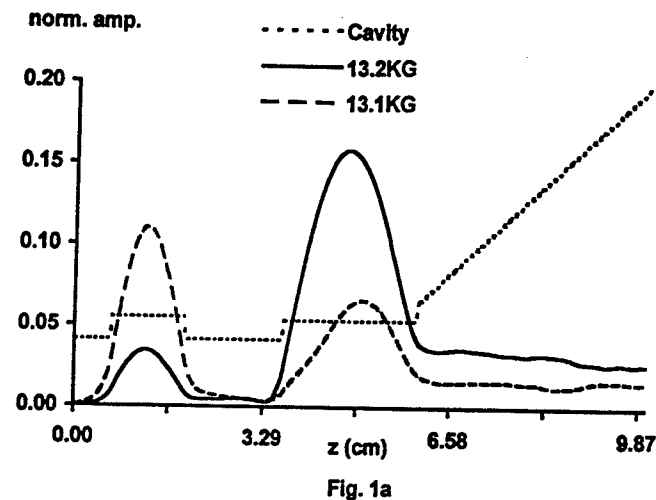


Figure 1 : The externally driven two cavity Gyro-Klystron. a. The fundamental mode for two values of the axial magnetic field. B. The high order modes.

mode the disagreement is larger (282MHz). For the output cavity we obtain a  $Q$  value of about 200 and a resonance frequency of 34.845GHz which is 33.5MHz lower than the measured frequency (34.8785GHz). In our opinion, the discrepancy between the calculated and measured resonance

frequencies is mainly due to the inaccuracy of the coupling matrices we currently use at the point of discontinuity. A better representation of the mode coupling is currently being developed. For the analysis of the system with the electron we excite the  $TE_{01}$  mode at the input cavity (the current model of excitation does not represent the exact coaxial-cavity excitation used in the experiment). We then allow the system to reach steady state. The influence of intensity of the axial magnetic field on the interaction is depicted in Fig. 1a (solid line for 13.2kGauss and dashed line for 13.1kGauss). The change in the magnetic field clearly affect the efficiency of the system. The amplitude of the high order modes is described in Fig. 1b. As all the modes are far below cutoff, they are not propagating in the system, however, at the location of the discontinuities they are excited and may affect the efficiency of interaction.

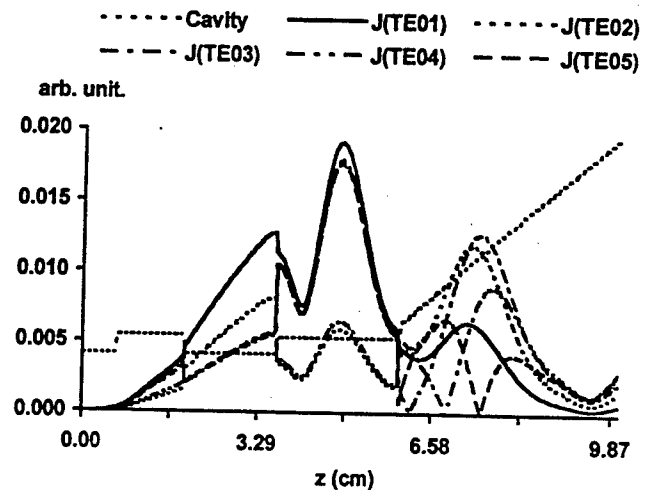


Figure 2: The projection of the electronic current density on the first five TE modes.

Fig. 2 describes the projection of the electronic current on the five TE modes. It is evident that all the terms are of the same order of magnitude. This effect stems from the fact that the current is highly localized in the transverse coordinates and thus the number of eigen modes needed for the description is high.

In conclusion, we presented the new MAGY code and demonstrated a few of its capabilities. Future work will address the improvement of the accuracy of the coupling terms at the discontinuity and the description of interaction between the electrons and multiple harmonics (e.g. the Gyro-TWT).

## References

- [1] Cai S. C., Antonsen T. M., Jr, Saraph G., and Levush B., *Int. J. Electronics*, 72,759-777, 1992.
- [2] Reiter G., *Convention on Long Distance Transmission by WaveGuide*, 54-57, 1959.

**Acknowledgments:** Work supported by AFOSR and NRL.

\* On leave from Rafael, Haifa, Israel.

# Stable Numerical Solution of Source Driven Evanescent Equations

Robert H. Jackson

Vacuum Electronics, Code 6840  
Naval Research Laboratory  
Washington, D.C. 20375-5347, USA

## Abstract

A simulation methodology for beam-rf interactions which bridges the cost/accuracy gap between PIC and "envelope" techniques is presented. The method utilizes a field expansion in eigenfunctions of the transverse Laplacian along with an algorithm for stable numerical solution of inhomogeneous evanescent differential equations. The resulting computational system provides the user with considerable flexibility in adjusting simulation fidelity versus costs.

## Introduction

Present beam-RF simulation techniques fall into roughly two categories, particle-in-cell (PIC) [1,2] and "envelope." The PIC methods tend toward full-physics/geometry, and the "envelope" methods are parametric and assume *a priori* knowledge of the solution. The gulf between these two approaches can be considerable making both ill matched to many applications. One problem with envelope-type methods is the inconsistent treatment of certain fields, *e.g.* ac and dc space charge fields. This is a consequence of the evanescent nature of some ODEs resulting from the "envelope" assumptions. A numerically stable means of integrating such ODEs would permit treatment of all fields on a computationally equal footing. This paper will present an algorithm which permits stable and accurate integration of the evanescent ODEs.

The overall simulation strategy is based on expansion of all fields in series of orthonormal eigenfunctions of the transverse Laplacian. Traveling wave amplifier problems are addressed in an axial-evolution format in which all fields and sources are self-consistently solved in a transverse plane as the plane is shifted axially. Both propagating and evanescent modes can be included in simulations.

## The Basic Equations

The electromagnetic equations in the form of the inhomogeneous Helmholtz equations for the vector and scalar potential (cgs units and Lorentz gauge) will be employed. The goal is to solve these equations, along with the Newton-Lorentz source equations for  $J$  and  $\rho$ , self-consistently for a *time-harmonic traveling wave amplifier*. Meaning that the beam-rf interaction is primarily a function of axial distance and all fields have a harmonic time dependence based on some fundamental frequency, *i.e.*  $f(t) = \sum f_n e^{in\omega t}$ . The resulting equations are shown below rearranged in axial evolution format.

$$\frac{\partial^2 \bar{A}_n}{\partial z^2} = -\nabla_{\perp}^2 \bar{A}_n - \frac{n^2 \omega^2}{c^2} \bar{A}_n - \frac{4\pi}{c} \bar{J}_n \quad (1)$$

$$\frac{\partial^2 \Phi_n}{\partial z^2} = -\nabla_{\perp}^2 \Phi_n - \frac{n^2 \omega^2}{c^2} \Phi_n - 4\pi \rho_n \quad (2)$$

The source terms are determined from:

$$\bar{J}_n = \langle J | e^{in\omega t} \rangle = \frac{1}{\tau} \int_0^{\tau} J e^{in\omega t} dt \quad (3)$$

$$\rho_n = \langle \rho | e^{in\omega t} \rangle = \frac{1}{\tau} \int_0^{\tau} \rho e^{in\omega t} dt \quad (4)$$

Unfortunately, as written, these equations are von Neumann unstable for grid-based solution in the axial direction. The underlying reason is the evanescent nature of many of the wavelengths supported by the transverse grid, *i.e.* the large  $k_{\perp}$ 's inherent in numerically computing the transverse Laplacian on a grid.

## Reduction to Canonical Form

In order to solve the above equations in an axial evolution format a method is needed for handling the evanescent elements. The approach chosen here is expansion of all fields and sources in eigenfunctions,  $\Psi_{ij}$ , of the *transverse* Laplacian operator.

$$\bar{A}_n = \sum_{i,j=1}^{\infty} \bar{a}_{ij}^{(n)} \Psi_{ij} \quad (5)$$

$$\Phi_n = \sum_{i,j=1}^{\infty} \phi_{ij}^{(n)} \Psi_{ij} \quad (6)$$

For the case presented here, only eigenfunctions independent of the axial coordinate and satisfying the transverse boundary conditions of the original PDE will be considered.

$$\nabla_{\perp}^2 \Psi_{ij} = \lambda_{ij} \Psi_{ij} \quad (7)$$

$$\langle \Psi_{ij} | \Psi_{kl} \rangle = \delta_{ik} \delta_{jl} \quad (8)$$

Where  $\langle | \rangle$  represents the spatial inner product over the transverse dimensions of the problem space,  $\lambda_{ij}$  is the transverse Laplacian eigenvalue (usually negative) associated with  $\Psi_{ij}$  and  $\delta_{ij}$  is the usual Kronecker delta.

Substituting Eqs. (5) and (6) into Eqs. (1) and (2) yields a system of (independent) second order ordinary differential equations in  $z$  for the eigenfunction expansion amplitudes.

$$\frac{d^2 \bar{a}_{ij}^{(n)}}{dz^2} = -(\lambda_{ij} + \frac{n^2 \omega^2}{c^2}) \bar{a}_{ij}^{(n)} - \frac{4\pi}{c} \langle \bar{J}_n | \Psi_{ij} \rangle \quad (9)$$

$$\frac{d^2 \phi_{ij}^{(n)}}{dz^2} = -(\lambda_{ij} + \frac{n^2 \omega^2}{c^2}) \phi_{ij}^{(n)} - 4\pi \langle \rho_n | \Psi_{ij} \rangle \quad (10)$$

These equations can be cast into the following canonical form:

$$f'' = \gamma f - s(z) \quad (11)$$

Note that for this case  $\gamma$  is a constant which can be positive or negative and that the driving term,  $s(z)$ , has an indirect dependence on *all* of the eigen-amplitudes through the Newton-Lorentz equations of motion. The general solution [3] to this inhomogeneous ODE can be written as:

$$f = e^{-\sqrt{\gamma}z} g(z) + e^{\sqrt{\gamma}z} h(z) \quad (12)$$

Where  $g(z)$  and  $h(z)$  are determined by:

$$g' = \frac{1}{2\sqrt{\gamma}} e^{\sqrt{\gamma}z} s(z) \quad h' = -\frac{1}{2\sqrt{\gamma}} e^{-\sqrt{\gamma}z} s(z) \quad (13)$$

Depending on the sign of  $\gamma$ , the solutions are decaying and growing exponentials, or backward and forward propagating sinusoidal waves.

### Stable Numerical Solution

Given the equations above, the solution seems straightforward. However, there are two factors which radically alter this view: 1)  $s(z)$  is a co-evolving, nonlinear function of the eigen-amplitudes, and 2) standard numerical techniques are not "stable" for the evanescent form of Eq. (12), see Fig [1]. However, neglect of the evanescent modes would reduce transverse resolution and eliminate the self-consistent inclusion of dc space charge fields.

To achieve a stable numerical solution, the above solution equations, (12) and (13), are modified as shown below ignoring the growing exponential term [4].

$$f = e^{-\kappa z} g(z) \quad (14)$$

$$g' = \frac{1}{\kappa} e^{\kappa z} s(z) \quad (15)$$

Note that explicit evanescent forms of (12) and (13) are used for these equations. This reduces the second order ODE to a first order quadrature and only *explicitly* includes one of the original initial conditions. Taking the second derivative of this solution results in:

$$f'' = \kappa^2 f - s + \frac{s'}{\kappa} \quad (16)$$

This is close to the canonical ODE, Eq. (11), and hints at a modification for achieving an exact solution. If the source term,  $s(z)$ , is redefined to include  $s'/\kappa$ , then differentiating twice results in the canonical ODE plus  $s''/\kappa^2$ . Continued modification of the source term results in an infinite sum of derivatives divided by powers of  $\kappa$ .

$$s \rightarrow \sum_{m=0}^{\infty} \frac{s^{(m)}}{\kappa^m} \quad (17)$$

Assuming convergence, substituting (17) into (15) we obtain the pair of equations below. Differentiation of  $f(z)$  twice shows that it is indeed a solution to the canonical ODE with the original driving term,  $s(z)$ .

$$f = e^{-\kappa z} g(z) \quad (18)$$

$$g' = \frac{1}{\kappa} e^{\kappa z} \sum_{m=0}^{\infty} \frac{s^{(m)}}{\kappa^m} \quad (19)$$

This formal approach gives some hope of achieving a numerically stable solution. However, requiring a large number of derivatives is hardly encouraging. The driving sources of primary interest here will have sinusoidal dependencies on the axial coordinate. Assume a source term

given by  $\cos(kz)$ . Substituting into Eq. (19), performing the derivatives and analyzing the resulting sums gives:

$$g' = \frac{1}{\kappa} e^{\kappa z} \frac{\kappa^2}{\kappa^2 + k^2} \left[ \cos(kz) - \frac{k}{\kappa} \sin(kz) \right] \quad (20)$$

The form of Eq. (20) suggest one further modification which will be useful in cases with multi-component driving terms. Noting that for the simple driving function under consideration, the  $\cos$  and  $\sin$  terms are the source and its first derivative, the relation can be recast as shown below.

$$g' = \frac{1}{\kappa} e^{\kappa z} \frac{\kappa^2}{\kappa^2 + k^2} \left[ s + \frac{s'}{\kappa} \right] \quad (21)$$

Does this work? Fig. [1] compares numerical solutions of Eqs. (12) & (13), Eqs. (14) & (15), and Eqs. (18) & (21) with the analytic solution of the original ODE. The impact of the exponentially growing component can be clearly seen in the plot of the Eqs. (12) & (13) solution. The solution computed from Eqs. (14) & (15) is stable, but has amplitude and phase differences relative to the analytic. As Fig. [1] shows the modified source solution, Eqs. (18) & (21), is both stable and accurate.

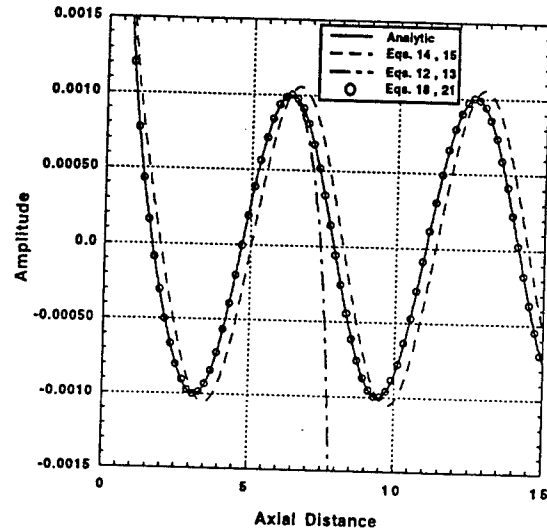


Fig. 1 Comparison of numeric and analytic solutions of the source driven evanescent ODE. Solutions were computed with 4th order Runge-Kutta,  $k = 1$ ,  $\kappa = 3$ ,  $f_0 = s_0 = 0.01$ .

### References

- [1] R. W. Hockney and J. W. Eastwood, *Computer Simulation Using Particles*, McGraw-Hill, 1981.
- [2] C. K. Birdsall and A. B. Langdon, *Plasma Physics via Computer Simulation*, McGraw-Hill, 1985.
- [3] Daniel Zwillinger, *Handbook of Differential Equations*, Academic Press, 1989.
- [4] R. H. Jackson, "Stable Numerical Solution of Source Driven Evanescent Equations, Application to Beam-RF Wave Simulation," in preparation.

# Novel Application of Modal Expansion Method to Time-Domain Analysis of Gyrotrons

J. Jelonnek and K. Schünemann

Technische Universität Hamburg-Harburg  
Arbeitsbereich Hochfrequenztechnik, D-21071 Hamburg, Germany

## Abstract

The modal analysis which uses both the resonant and the irrotational modes of the equivalent short-circuited gyrotron cavity had been derived for time-harmonic electromagnetic fields. Applying it to time-domain analysis of gyrotrons via a Fourier transform leads to a generally rigorous but numerically inefficient analysis. In this contribution, the modal analysis is directly formulated in time-domain. The aperture-coupled cavity is analyzed by using rigorous boundary conditions. Moreover, poorly convergent series in the formulation are replaced by analytic expressions. Thus, a system of coupled first-order differential equations with constant coefficients for determining the mode amplitudes is derived which is easily computed with excellent accuracy and an order-of-magnitude reduction in memory size and cpu time.

## Application of Modal Analysis to Time-Domain

Depending on the bandwidth and on the demand for frequency resolution, it is necessary to compute some thousands of spectral terms if we want to apply the method presented in [1] to gyrotron analysis. Thus a huge amount of computing resources is needed to guarantee a minimum of accuracy. Alternatively, it is possible to derive the modal analysis directly in time-domain. This has been shown in [2] and [4]. Following [2] and [4], one arrives at a system of coupled first-order differential equations with constant coefficients for determining the eigenfunction amplitudes of the closed cavity. Obviously, these equations are in principle more accurate and also much simpler to compute than the direct application of a Fourier transform. Nevertheless, the specific form of a gyrotron cavity as shown in Fig. 1 leads to two severe problems for an application of the modal analysis. It is first the open boundary condition of the gyrotron cavity which needs an accurate description in time-domain, and it is second the axial inhomogeneity of the cavity which leads to a coupling of the transverse waveguide modes and hence to a large number of eigenfunctions which must be taken into account.

## Introduction

ACCURATE and numerically efficient computation of the excited electromagnetic field inside gyrotron cavities is an important problem. In [1] it is proposed to expand the electromagnetic field in terms of the solenoidal and the irrotational eigenfunctions of the corresponding short-circuited cavity [2]. Application to time-domain is done via a Fourier transform. In [3] the Fourier transform has been replaced by a convolution method. Complex impulse responses have been defined which represent the response of the cavity in time-domain. Although this method significantly improves the analysis, large computation time and memory size restricts its efficient application. At this place, we will propose a novel solution which increases accuracy and reduces the demand on computing resources simultaneously.

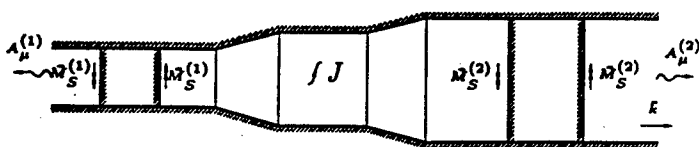


Fig. 1: Longitudinal section of gyrotron cavity. Short-circuit boundary conditions are shown. Surface magnetic currents  $\vec{M}_S$  are introduced at either side of each aperture.

## Open Boundary Conditions

In [2] the open apertures of the gyrotron cavity are replaced by electric walls (Fig. 1). Surface magnetic currents which are equal in amplitude and opposite in sign are introduced at both sides of each electric wall. Using Galerkin's method, it is possible to expand the surface magnetic currents into the waveguide modes of the connecting waveguides. In frequency-domain, the surface magnetic currents are calculated from a multiplication of the mode amplitudes of the magnetic field with the corresponding wave impedance [1]. In time-domain, we can determine the surface magnetic currents if we apply the convolution method which has been proposed by [5]. The convolution method gives accurate results in a broad frequency range which is only limited by the Nyquist theorem, i. e. by the step size of the used time step. Moreover, the accuracy of the convolution method is increased if we use analytic expressions for the impulse responses of the wave impedances [5]. Finally, it is possible to adopt the convolution method to the calculation of mismatched waveguides which are connected to the apertures of the cavity.

## Improvement of the Numerical Accuracy

In a transmission line resonator, the waveguide modes are decoupled. Hence, every eigenfunction consists only of one waveguide mode. In an inhomogeneous gyrotron cavity, all waveguide modes of the same radial index are coupled. Therefore, each eigenfunction of the inhomogeneous gyrotron cavity consists of a sum of relevant waveguide modes [1]. Consequently, the number of eigenfunctions which has to be taken into account increases by a factor which is given by the number of the relevant modes. This restricts the direct application of the presented modal analysis. To overcome this convergence problem, we propose to apply a method to time-domain which has been presented in [6]. As a result, it is possible to reduce the number of necessary eigenfunctions significantly.

## Numerical Results

The application of the modal analysis to time-domain is demonstrated for a cavity which mainly consists of a hollow waveguide which is short-circuited at one side and matched at the other. An electric current with sinusoidal time-dependence is placed in the center of the cavity. The current is switched on at time  $t = 0$ . Moreover, it is assumed that the transversal shape of the current is equivalent to the shape of a  $TE$ -waveguide mode. The cavity is shown in Fig. 2.

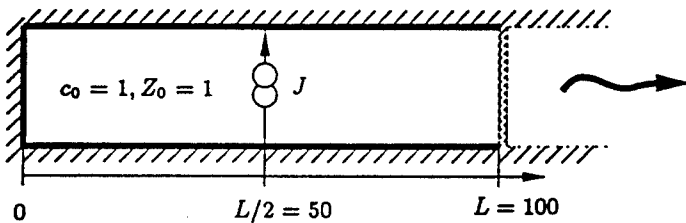


Fig. 2: Cavity used for examination of transient responses (all values have been normalized)  
 $k_0 = 1$  (operating frequency),  $k_c = 0.9$  (cutoff frequency)

Figs. 3a and 3b show the calculated transient response of the excited mode amplitude for the electric field at the matched output port. Fig. 3a compares the calculated transient response with the analytical solution. Fig. 3b shows the convergence of the transient response which depends on the number of eigenfunctions. Both figures demonstrate on one hand an excellent agreement with the analytical solution and on the other hand a fast convergence of the results.

## Conclusions

In this contribution, we have proposed an easy to compute and generally applicable system of differential equations for an accurate time-domain analysis of electromagnetic fields inside gyrotron cavities. We solved the problem of an accurate description of the open boundary conditions as well as the convergence problem which exists in the case of gyrotron cavities.

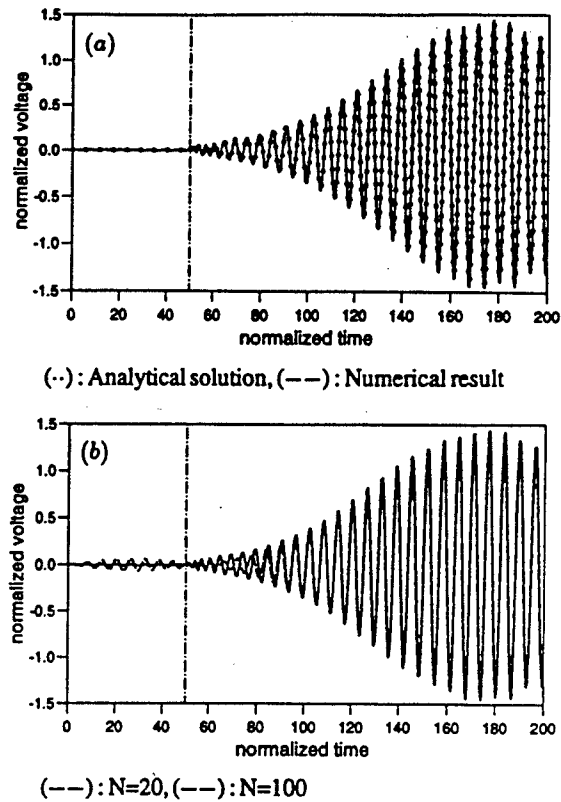


Fig. 3 : Transients of the excited mode amplitude for the electric field at the output port of the cavity.

(a) : Comparison with analytical solution  
 (b) : Use of different numbers  $N$  of eigenfunctions

## Acknowledgement

The authors are indebted to the Deutsche Forschungsgemeinschaft for financial support.

## References

- [1] Jöstingmeier A., Rieckmann C., Omar A. S., *Proc. IEEE MTT-S Symp. (Orlando)*, 1995, pp. 821-824.
- [2] Kurokawa K., *IRE Trans. on Microwave Theory and Techniques*, April 1958, pp. 178-187.
- [3] Jelonnek J., Schünemann K., *Proc. 20th Int. Conf. Infrared Millimeter Waves (Orlando)*, 1995, pp. 32-33.
- [4] Van Bladel J., Washington: Hemisphere, 1985.
- [5] Moglie F., Rozzi T., Marozzi P., Schiavoni A., *IEEE Microwave and Guided Wave Letters*, vol. 2, no. 12, 1992, pp. 475-477.
- [6] Jelonnek J., Schünemann K., *Proc. 21st Int. Conf. Infrared Millimeter Waves (Berlin)*, 1996, pp. AM-7.

## 2D Dyadic Green's Function for Homogeneous Ferrite Microstrip Circulator with Soft Walls

Clifford M. Krowne

Code 6850.3, Microwave Technology Branch, Electronics Science & Technology Division, Naval Research Laboratory, Washington, DC 20375-5347

### Abstract

We treat here the situation of imperfect nonport boundaries of the circulator device, providing the modified dyadic Green's function elements for both internal and external locations in relation to the perimeter.

### Introduction

Ferrite planar circulators are often built with circular symmetry, and they are electrically thin enough to warrant a model based upon a 2D approach. Furthermore, the use of a canonical structure can provide guidance on design for structures with non-canonical geometry. It has already been shown that s-parameter and field results may be obtained numerically with great efficiency using a 2D microstrip dyadic Green's function which is based upon judicious treatment of the source point singularity and mode-matching [1]. Such an approach avoids explicit use of the completeness theorem for the homogeneous part of the problem, a tremendous advantage since the final dyadic Green's function has one less infinite summation.

But in the previous 2D model [2], it is assumed that the non-port boundaries are magnetic walls, confining energy exchange to only the ports. This seems like a reasonable assumption, given that the actual device may only have magnetized material in the circular region, and that the surface current perpendicular to the perimeter on the microstrip goes to zero at the boundary (This particle current being zero does not mean displacement current is null, thereby allowing a finite  $H_\phi$  value.). Convincing experimental evidence for this supposition is certainly found in the literature, and this is also indicated by recent theoretical and experimental data reviewed [3].

Nevertheless, in order to find out the actual effect in switching from a hard impenetrable magnetic wall to an external dielectric material with dielectric constant  $\epsilon_d$ , and also thereby achieving the capability of varying the permittivity of the external dielectric, we develop here a new dyadic Green's function satisfactory to accomplish the task. The permeability  $\mu_d$  is also allowed to differ from the free space value.

We restrict ourselves to the 2D homogeneous circulator case because it approximates many actual operating devices, readily allows explicitly developed compact Green's functions, and enables the modifications to the hard wall device to become evident. Figure 1 shows a cross-sectional diagram of a 3 - port device.

### Fields and Constraints

Applying the radiation condition as  $r \rightarrow \infty$ , leads to

the selection of the modified Bessel function of the second kind  $K_n(k_d r)$  for use in the external field construction,  $r > R$ :

$$E_z^d = \sum_{n=-\infty}^{\infty} a_{ne}^d K_n(k_d r) e^{in\phi} \quad (1a)$$

$$H_\phi^d = \frac{1}{i\omega\mu_d} \sum_{n=-\infty}^{\infty} a_{ne}^d k_d K_n'(k_d r) e^{in\phi} \quad (1b)$$

Requiring continuity of the perpendicular electric field at  $r = R$ ,

$$f E_z^e(R, \phi) = E_z^d(R, \phi) \quad (2)$$

we find

$$a_{ne}^d = f \frac{J_n(k_e R)}{K_n(k_d R)} a_{n0} \quad k_d = \omega \sqrt{\epsilon_d \mu_d} \quad (3), (4)$$

$f$  attempts in an approximate way to allow for a consistent fringing in the 2D model, which has some inherent degree of 3D nature.

The forcing function for the Green's function is applied at  $(r', \phi')$ ,  $r = R$ , through the equality

$$H_\phi^{\text{Per}}(R, \phi) = H_{\phi'A} \delta(\phi - \phi') \Delta\phi' + H_\phi^d(R, \phi \neq \phi') \quad (5)$$

The perimeter azimuthal magnetic field can be represented by a 1D Fourier expansion,

$$H_\phi^{\text{Per}}(R, \phi) = \sum_{n=-\infty}^{\infty} A_n e^{in\phi} \quad (6)$$

$$A_n = \frac{1}{2\pi} \int_{-\pi}^{\pi} H_\phi^{\text{Per}}(R, \phi) e^{-in\phi} d\phi \quad (7)$$

Azimuthal magnetic field in the circulator disk, as  $r \rightarrow R$  from the inside, is given by

$$H_\phi^e(R, \phi) = \frac{1}{i\omega\mu_e} \sum_{n=-\infty}^{\infty} a_{ne} \left[ k_e J_n'(k_e R) - \frac{nK}{\mu R} J_n(k_e R) \right] e^{in\phi} \quad (8)$$

Equating the fields in (6) and (8),

$$H_\phi^e(R, \phi) = H_\phi^{\text{Per}}(R, \phi) \quad (9)$$

or

$$a_{n0} \frac{1}{i\omega\mu_e} \left[ k_e J_n'(k_e R) - \frac{nK}{\mu R} J_n(k_e R) \right] = \frac{1}{2\pi} \int_{-\pi}^{\pi} \left[ H_{\phi'A} \delta(\phi - \phi') \Delta\phi' + H_\phi^d(R, \phi \neq \phi') \right] e^{-in\phi} d\phi \quad (10)$$

Inserting (1) into (7),  $r \rightarrow R$  from the outside, utilizing azimuthal orthogonality, yields

$$a_{n0} \left\{ \frac{1}{i\omega\mu_e} \left[ k_e J'_n(k_e R) - \frac{nK}{\mu} \frac{1}{R} J_n(k_e R) \right] - \frac{f}{i\omega\mu_d} \frac{J_n(k_d R)}{K_n(k_d R)} k_d K'_n(k_d R) \right\} = \frac{1}{2\pi} H_{\phi A} \Delta\phi' e^{-in\phi} \quad (11)$$

### Dyadic Green's Function Within Circulator Puck

With the solution of  $a_{n0}$  from (11) in terms of the forcing field  $H_{\phi A}$ , the elements of the dyadic Green's function for  $r < R$  may be written down as

$$G_{EH}^{zz}(r, \phi; R, \phi') = [i\omega/(2\pi)] \times \sum_{n=-\infty}^{\infty} \frac{J_n(k_e r) e^{in(\phi - \phi')}}{J'_n(k_e R) - \frac{nK}{\mu} \frac{1}{R} J_n(k_e R) - f \frac{k_d}{\mu_d} \frac{J_n(k_e R)}{K_n(k_d R)} K'_n(k_d R)} \quad (12)$$

$$G_{EH}^{zz}(r, \phi; R, \phi') = \frac{1}{2\pi} \sum_{n=-\infty}^{\infty} \frac{\left[ J'_n(k_e r) - \frac{nK}{\mu} \frac{1}{k_e r} J_n(k_e r) \right] e^{in(\phi - \phi')}}{J'_n(k_e R) - \frac{nK}{\mu} \frac{1}{k_e R} J_n(k_e R) - f \frac{\mu_e k_d}{\mu_d k_e} \frac{J_n(k_e R)}{K_n(k_d R)} K'_n(k_d R)} \quad (13)$$

$$G_{EH}^{zz}(r, \phi; R, \phi') = \frac{i}{2\pi} \sum_{n=-\infty}^{\infty} \frac{\left[ \frac{n}{k_e r} J_n(k_e r) - \frac{K}{\mu} J'_n(k_e r) \right] e^{in(\phi - \phi')}}{J'_n(k_e R) - \frac{nK}{\mu} \frac{1}{k_e R} J_n(k_e R) - f \frac{\mu_e k_d}{\mu_d k_e} \frac{J_n(k_e R)}{K_n(k_d R)} K'_n(k_d R)} \quad (14)$$

### Dyadic Green's Function Outside Circulator Puck

For  $r > R$ , the dyadic Green's function elements are

$$G_{EH}^{zz}(r, \phi; R, \phi') = [i\omega f/(2\pi)] \times \sum_{n=-\infty}^{\infty} \frac{[J_n(k_e R)/K_n(k_d R)] K_n(k_d r) e^{in(\phi - \phi')}}{\frac{1}{\mu_e} \left[ k_e J'_n(k_e R) - \frac{nK}{\mu} \frac{1}{R} J_n(k_e R) \right] - f \frac{k_d}{\mu_d} \frac{J_n(k_e R)}{K_n(k_d R)} K'_n(k_d R)} \quad (15)$$

$$G_{EH}^{zz}(r, \phi; R, \phi') = (\mu_e/\mu_d)(k_d/k_e)f \times \frac{1}{2\pi} \sum_{n=-\infty}^{\infty} \frac{[J_n(k_e R)/K_n(k_d R)] K'_n(k_d r) e^{in(\phi - \phi')}}{J'_n(k_e R) - \frac{nK}{\mu} \frac{1}{k_e R} J_n(k_e R) - f \frac{\mu_e k_d}{\mu_d k_e} \frac{J_n(k_e R)}{K_n(k_d R)} K'_n(k_d R)} \quad (16)$$

$$G_{EH}^{zz}(r, \phi; R, \phi') = -n(\mu_e/\mu_d)k_e(f/r) \times \frac{i}{2\pi} \sum_{n=-\infty}^{\infty} \frac{[J_n(k_e R)/K_n(k_d R)] K_n(k_d r) e^{in(\phi - \phi')}}{J'_n(k_e R) - \frac{nK}{\mu} \frac{1}{k_e R} J_n(k_e R) - f \frac{\mu_e k_d}{\mu_d k_e} \frac{J_n(k_e R)}{K_n(k_d R)} K'_n(k_d R)} \quad (17)$$

Factor  $f$

Factor  $f$  is estimated as  $f = f_w f_p$ .  $f_w$  weights the parameter dependence expressed in  $f_p$ . Closed form formulas, based upon self-consistent static solutions, exist for microstrip capacitive (electric) end effect [4]. Stretching the microstrip end so as to connect one corner to the other, constructs the circulator perimeter, and allows us to roughly obtain  $f_p$ .

$$f_p = \frac{C_T - C}{C} = \frac{C_f}{C} = \frac{h}{A\epsilon_d} G_f \quad (18)$$

Assign  $A = \pi R^2$  and  $W = 2\pi R$ , and place them in (14) and in the equivalent additional radial length  $\Delta l_f$  expression which relates to the fringing capacitance  $C_f$ :

$$\frac{\Delta l_f}{h} = \frac{C_f}{W} \frac{c Z_m W/h}{\sqrt{\epsilon_{rde}}} \quad (19)$$

$c$  is the speed of light in vacuum,  $h$  the substrate thickness,  $Z_m$  the microstrip impedance based upon  $\epsilon_d$  dielectric loading causing an effective dielectric constant  $\epsilon_{rde}$ . We replace  $\epsilon_{rde}$  by  $\epsilon_d$  under the  $W/h \gg 1$  limit. The left-and-side of (19) is given by [5], [6]

$$\frac{\Delta l_f}{h} = 0.412 \frac{\epsilon_{rde} + 0.300}{\epsilon_{rde} - 0.258} \frac{W/h + 0.264}{W/h + 0.800} \quad (20)$$

Using (19) and (20) in (18), the final formula for  $f$  is (noting that the "r" subscript denotes relative value)

$$f_p = \frac{0.824h}{R\sqrt{\epsilon_{rd}}} \frac{\epsilon_{rd} + 0.300}{\epsilon_{rd} - 0.258} \frac{R/h + 0.042}{R/h + 0.127} \times [1 + (h/R) \{0.2217 + 0.106 \ln(2\pi R/h + 1.444)\}] \quad (21)$$

Cover location  $h' \gg h$  in deriving (21).

### References

- [1] C. M. Krowne and R. E. Neidert, "Inhomogeneous Ferrite Microstrip Circulator: Theory and Numerical Calculations Using A Recursive Green's Function," 25th European Microwave Conference Dig., pp. 414 - 420, 4 - 7 September 1995, Bologna, Italy.
- [2] C. M. Krowne and R. E. Neidert, "Theory and Numerical Calculations For Radially Inhomogeneous Circular Ferrite Circulators," IEEE Trans. Microwave Theory & Tech., Vol. 44, no. 3, pp. 419 - 431, March 1996.
- [3] H. S. Newman, D. C. Webb, C. M. Krowne, "Design and Realization of Millimeter-Wave Microstrip Circulators," Intern. Conf. Millimeter Submillimeter Waves Appl. III, SPIE Proceedings, Vol. 2842, pp. 181 - 191, 1996.
- [4] K. C. Gupta, R. Garg, and I. J. Bahl, Microstrip Lines and Slotlines, Artech House: Dedham, MA., 1979.
- [5] E.O Hammerstad and F. Bekkadal, Microstrip Handbook, ELAB report STF 44 A74169, The University of Trondheim, The Norwegian Institute of Technology, 1975.
- [6] R. Garg and I. J. Bahl, "Microstrip Discontinuities," Intern. J. Electronics, Vol. 45, pp. 81 - 87, July 1978.

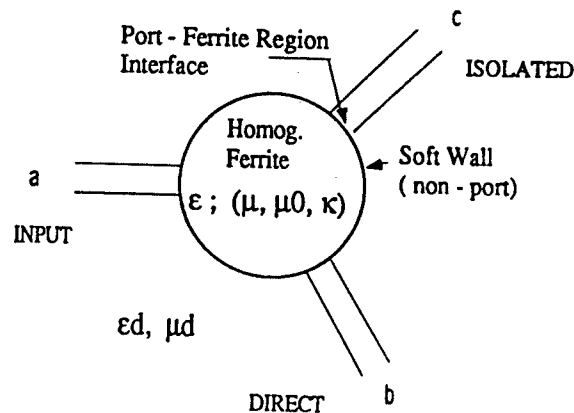


Figure 1



# Homogeneous Ferrite Microstrip Circulator 3D Dyadic Green's Function with and without Perimeter Interfacial Walls

Clifford M. Krowne

Code 6850.3, Microwave Technology Branch, Electronics Science & Technology Division, Naval Research Laboratory, Washington, DC 20375-5347

## Abstract

Modified dyadic Green's function elements for both internal and external locations in relation to the circulator perimeter are given when the puck is allowed to transmit fields into the external medium.

## Introduction

Although the theoretical work has been completed for a 3D model of the ferrite circulator, it has been done for the relatively general case of an inhomogeneous device puck. Here we would like to present the considerably simplified case for only a disk which is homogeneous. The motivation for this is two fold. One is a historical parallel with the developments for the original planar work which in the earlier years found sufficient accuracy using a uniform ferrite region in a 2D model. The other is the more streamlined formulas and more transparent formulation.

The other part of what we want to do here is to allow for either perfect magnetic walls as before, containing the fields within the nonreciprocal region, or for imperfect walls leading to field extension into the area external to the device ferrite material. In the previous inhomogeneous 3D microstrip model [1], it is assumed that the non-port boundaries are magnetic walls, confining energy flow to only the ports. This may be a reasonable assumption in view of the thin dimensions in the  $z$  - direction compared to the extent on the lateral surface. But by its very nature, a 3D model could allow accurate description of field extension beyond the circulator perimeter and fringing fields, depending upon how general and complex the formulation.

Formulation below is fully 3D outside the puck (see Fig. 1), but does not allow for consideration of geometry beyond the thickness of the puck  $h$ . Thus all components of the electromagnetic field exist in coordinate space, including in the dielectric material characterized by dielectric constant  $\epsilon_d$  and permeability  $\mu_d$ . Sensitivity of the dyadic Green's functions to varying  $\epsilon_d$  and  $\mu_d$  is now possible.

## 3D Fields and Constraints

Applying the radiation condition gives for the perpendicular electric field external ( $r > R$ ) to the device perimeter

$$E_z^d(r, \phi, z) = \sum_{j=0}^{\infty} \sum_{n=-\infty}^{\infty} a_{nej}^d \cos(k_{zj}z) K_n(\sigma_{dj}r) e^{in\phi} \quad (1)$$

The same magnetic field component has a sinusoidal factor with an "h" subscript index. Here the characteristic equation

for the radial separation constant  $\sigma_{dj}$  is given in the outside region by

$$\sigma_{dj} = \sqrt{k_d^2 - k_{zj}^2} \quad k_d = \omega \sqrt{\epsilon_d \mu_d} \quad (2)$$

with  $k_{zj} = j\pi/h$ ,  $j = (0 \text{ or } 1), 2, \dots$ . Requiring continuity of the perpendicular electric field at  $r = R$ ,

$$f E_z^c(R, \phi) = E_z^d(R, \phi) \quad (3)$$

entails using the field inside the puck [2]

$$E_z^c = \sum_{j=0}^{\infty} \sum_{n=-\infty}^{\infty} \cos(k_{zj}z) [a_{n0j}^1 J_n(\sigma_{1j}R) + a_{n0j}^2 J_n(\sigma_{2j}R)] e^{in\phi} \quad (4)$$

We find that

$$a_{nej}^d = f \frac{J_n(\sigma_{1j}R)}{K_n(\sigma_{dj}R)} a_{n0j}^1 + f \frac{J_n(\sigma_{2j}R)}{K_n(\sigma_{dj}R)} a_{n0j}^2 \quad (5)$$

Factor  $f$  is chosen so as to correct for the actual vertical fringing seen in a 3D circulator and not treated by the model adopted here for simplicity reasons. The approach here does account for external field extension by assuming to first approximation that the  $j$ th perpendicular mode spectrum inside the puck holds outside also.  $f$  used here modifies the inhomogeneous formulas found in [3], and enables the effect of the external environment to be turned off (set  $f = 0$ ), or left on ( $f \neq 0$ ). Null  $f$  value must be done with some thought in the formulas to follow, but it can be demonstrated that the limit exactly returns the problem to the hard wall 3D case.

Requiring continuity of the azimuthal electric field at  $r = R$ ,

$$f E_\phi^c(R, \phi) = E_\phi^d(R, \phi) \quad (6)$$

entails use of the inside and outside device field representations given by respectively

$$E_\phi^c = \sum_{j=1}^{\infty} \sum_{n=-\infty}^{\infty} i \sin(k_{zj}z) \left[ a_{n0j}^1 \frac{-inr_j}{b_j R} \lambda_{2j} J_n(\sigma_{1j}R) + \frac{\sigma_{1j}}{b_j} (i\omega\mu_0 + s_j \lambda_{2j}) J_n'(\sigma_{1j}R) \right] + a_{n0j}^2 \left[ \frac{-inr_j}{b_j R} \lambda_{1j} J_n(\sigma_{2j}R) + \frac{\sigma_{2j}}{b_j} (i\omega\mu_0 + s_j \lambda_{1j}) J_n'(\sigma_{2j}R) \right] e^{in\phi} \quad (7)$$

$$E_\phi^d = \sum_{j=1}^{\infty} \sum_{n=-\infty}^{\infty} \sin(k_{zj}z) \left[ -s_j a_{nhj}^d \sigma_{dj} K_n'(\sigma_{dj}R) + \frac{ip_{jn}}{R} a_{nef}^d K_n(\sigma_{dj}R) \right] e^{in\phi} \quad (8)$$

Thus it is seen that

$$a_{nhj}^d = f \frac{h d_z A_{nj}^1}{K_n(\sigma_{dj}R)} a_{n0j}^1 + f \frac{h d_z A_{nj}^2}{K_n(\sigma_{dj}R)} a_{n0j}^2 \quad (9)$$

$$h d_z A_{nj}^1 = i \left[ \frac{-in}{R} \left( \frac{r_j}{b_j} \lambda_{2j} + p_j \right) J_n(\sigma_{1j}R) + \frac{\sigma_{1j}}{b_j} (i\omega\mu_0 + s_j \lambda_{2j}) J_n'(\sigma_{1j}R) \right]$$

$$\times \frac{1}{(-s_j)\sigma_{dj}} \frac{K_n(\sigma_{dj}R)}{K'_n(\sigma_{dj}R)} \quad (10)$$

$${}^{hd}A_{nj}^2 = i \left\{ \frac{-in}{R} \left( \frac{\bar{r}_j}{b_j} \lambda_{1j} + p_j \right) J_n(\sigma_{2j}R) + \frac{\sigma_{2j}}{b_j} (i\omega\mu_0 + s_j\lambda_{1j}) J'_n(\sigma_{2j}R) \right\}$$

$$\times \frac{1}{(-s_j)\sigma_{dj}} \frac{K_n(\sigma_{dj}R)}{K'_n(\sigma_{dj}R)} \quad (11)$$

The azimuthal and perpendicular magnetic field forcing functions for the Green's function are applied respectively, at  $(r', \phi')$ ,  $r = R$ , through the equalities

$$H_\phi^{p\omega}(R, \phi) = H_\phi^{p\omega}(z)\delta(\phi - \phi')\Delta\phi' + H_\phi^d(R, \phi \neq \phi')/f \quad (12)$$

$$H_z^{p\omega}(R, \phi) = H_z^{p\omega}(z)\delta(\phi - \phi')\Delta\phi' + H_z^d(R, \phi \neq \phi')/f \quad (13)$$

which result in two equations connecting the driving fields to the system under consideration:

$$\left\{ \frac{-in}{b_j R} \left( ik_z \frac{\mu_0}{\mu} - p_j \lambda_{2j} \right) J_n(\sigma_{1j}R) + \frac{q_j}{b_j} \lambda_{2j} \sigma_{1j} J'_n(\sigma_{1j}R) - \frac{{}^{hd}A_{nj}^1}{f} \right\} a_{n0j}^1$$

$$+ \left\{ \frac{-in}{b_j R} \left( ik_z \frac{\mu_0}{\mu} - p_j \lambda_{1j} \right) J_n(\sigma_{2j}R) + \frac{q_j}{b_j} \lambda_{1j} \sigma_{2j} J'_n(\sigma_{2j}R) - \frac{{}^{hd}A_{nj}^2}{f} \right\} a_{n0j}^2$$

$$= \frac{1}{2\pi} H_\phi^{p\omega} \Delta\phi' e^{-in\phi'} \quad (14)$$

$$\left[ \frac{c_j - \lambda_{2j}}{b_j} J_n(\sigma_{1j}R) - \frac{{}^{hd}A_{nj}^1}{f} \right] a_{n0j}^1 + \left[ \frac{c_j - \lambda_{1j}}{b_j} J_n(\sigma_{2j}R) - \frac{{}^{hd}A_{nj}^2}{f} \right] a_{n0j}^2$$

$$= \frac{1}{2\pi} H_z^{p\omega} \Delta\phi' e^{-in\phi'} \quad (15)$$

where

$${}^{hd}A_{nj}^1 = \frac{inp_j}{(-s_j)\sigma_{dj}R} \frac{K_n(\sigma_{dj}R)}{K'_n(\sigma_{dj}R)} \left[ \frac{-in}{R} \left( \frac{\bar{r}_j}{b_j} \lambda_{2j} + p_j \right) J_n(\sigma_{1j}R) \right.$$

$$\left. + \frac{\sigma_{1j}}{b_j} (i\omega\mu_0 + s_j\lambda_{2j}) J'_n(\sigma_{1j}R) \right] - u_j \sigma_{dj} \frac{K'_n(\sigma_{dj}R)}{K_n(\sigma_{dj}R)} J_n(\sigma_{1j}R) \quad (16)$$

$${}^{hd}A_{nj}^2 = \frac{inp_j}{(-s_j)\sigma_{dj}R} \frac{K_n(\sigma_{dj}R)}{K'_n(\sigma_{dj}R)} \left[ \frac{-in}{R} \left( \frac{\bar{r}_j}{b_j} \lambda_{1j} + p_j \right) J_n(\sigma_{2j}R) \right.$$

$$\left. + \frac{\sigma_{2j}}{b_j} (i\omega\mu_0 + s_j\lambda_{1j}) J'_n(\sigma_{2j}R) \right] - u_j \sigma_{dj} \frac{K'_n(\sigma_{dj}R)}{K_n(\sigma_{dj}R)} J_n(\sigma_{2j}R) \quad (17)$$

### 3D Dyadic Green's Function

From (14) and (15), a few of the elements of the dyadic Green's function are given below for  $r < R$  and  $r > R$ , the third subscript index indicating the location ("c" puck or "d" outside):

$$G_{EHc}^{\phi} = \frac{1}{2\pi} \sum_{j=0}^{\infty} \sum_{n=-\infty}^{\infty} K_{zj}^{\phi} \cos(k_{zj}z) \frac{1}{D_A \bar{B}_j} \left[ \bar{B}_{nj}^2 J_n(\sigma_{1j}R) \right.$$

$$\left. - \bar{B}_{nje}^1 J_n(\sigma_{2j}R) \right] e^{in(\phi - \phi')} \quad (18)$$

$$G_{EHd}^z = \frac{1}{2\pi} \sum_{j=1}^{\infty} \sum_{n=-\infty}^{\infty} i f K_{zj}^z \sin(k_{zj}z) \frac{1}{D_A \bar{B}_j} \left[ {}^{hd}A_{nj}^2 \bar{A}_{nj}^1 - {}^{hd}A_{nj}^1 \bar{A}_{nj}^2 \right]$$

$$\times \frac{K_n(\sigma_{dj}R)}{K_n(\sigma_{dj}R)} e^{in(\phi - \phi')} \quad (19)$$

$$G_{EHd}^{r\phi} = \frac{1}{2\pi} \sum_{j=1}^{\infty} \sum_{n=-\infty}^{\infty} i f K_{zj}^{\phi} \sin(k_{zj}z) \left\{ \frac{ins_j}{r D_A \bar{B}_j} \left[ {}^{hd}A_{nj}^1 \bar{B}_{nj}^2 \right. \right.$$

$$\left. - {}^{hd}A_{nj}^2 \bar{B}_{nj}^1 \right] \frac{K'_n(\sigma_{dj}R)}{K_n(\sigma_{dj}R)} + \frac{inp_j}{r D_A \bar{B}_j} \left[ {}^{hd}A_{nj}^1 \bar{B}_{nj}^2 - {}^{hd}A_{nj}^2 \bar{B}_{nj}^1 \right]$$

$$\times \frac{K_n(\sigma_{dj}R)}{K_n(\sigma_{dj}R)} \left. \right\} e^{in(\phi - \phi')} \quad (20)$$

Leading K factors in (18) - (20) are determined by the choice of forcing z - dependence given as  $g(z)$  or  $h(z)$ .

$$K_{zj}^{\phi} = \frac{2}{h} \int_0^h \cos(k_{zj}z) g(z) dz \quad (21)$$

$$K_{zj}^z = \frac{2}{h} \int_0^h \sin(k_{zj}z) h(z) dz \quad (22)$$

### References

- [1] C. M. Krowne, "3D Dyadic Green's Function for Radially Inhomogeneous Circular Ferrite Circulator," IEEE Micro. Th. Tech. Symp. Dig., San Francisco, CA, pp.121-124, June 18, 1996.
- [2] C. M. Krowne, "Theory of the Recursive Dyadic Green's Function for Inhomogeneous Ferrite Canonically Shaped Microstrip Circulators," in Advances in Imaging and Electron Physics, Ed. Peter W. Hawkes, Academic Press, 1996.
- [3] C. M. Krowne, "Ferrite Microstrip Circulator 3D Dyadic Green's Function with Perimeter Interfacial Walls and Internal Inhomogeneity," Microwave Optical Tech. Letts., July 1997.

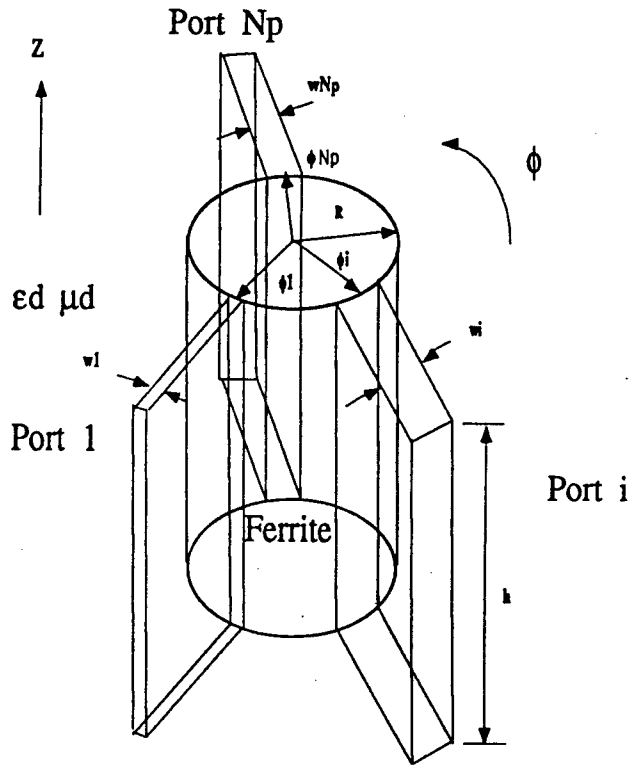


Figure 1

Electric walls exist (due to the top disk microstrip and bottom ground plane) at  $z = 0, h$  with  $r < R$ . For  $r > R$ , ferrite fills the region with diagonal tensor permeability elements  $\mu_r, \mu_\phi, \mu_0$  and off diagonal elements composed of  $ik_z$ . Microstrip lines enter the puck at port locations, and are taken to be of limited extent so as not to disrupt the external field structure.

# Far infrared investigation of magnetic resonance in conducting magnetic thin films, e.g. Cr and the rare earth metals, and insulating thin films, e.g., NiO.

S A Feiven, T J Parker and S R P Smith

Department of Physics, University of Essex, Wivenhoe Park, Colchester CO4 3SQ, UK

## Abstract

We show how careful design of the sample structure to optimise impedance matching can be used to achieve a large enhancement in the efficiency of far infrared coupling to magnetic resonance phenomena in insulating thin film magnetic media, e.g. NiO. In conducting thin film magnetic media, e.g. Cr and the rare earth metals, additional enhancement is obtained by using a grating structure to eliminate the plasma reflectivity.

### A. Introduction

Thin film technology has long been used in the fabrication of magnetic storage devices. However, the investigation of nano-structured magnetic systems is relatively speaking in its infancy, and it is anticipated that these systems will show new magnetic phenomena that can be custom-designed for new technological applications. Current scientific work on layered magnetic structures mainly involves metallic magnetic systems, with GMR as one of the most dramatic developments, but study of insulating layered magnets is relatively less advanced, despite the fact that such structures can also be expected to have important applications in areas such as magnetic storage devices, field sensing, microwave, millimetre wave, and terahertz signal processing and IR imaging.

The overall aims of this work are (i) to establish FIR spectroscopic techniques for studying magnetic resonance phenomena in conducting magnetic thin films and multilayers, and (ii) to establish the feasibility of FIR spectroscopic techniques for investigating the magnetic properties of insulating ferrimagnetic and antiferromagnetic thin films and multilayers. Recent detailed theoretical modelling at Essex has demonstrated that, in both conducting and insulating thin film systems, strongly enhanced coupling to the magnetic response can be achieved over a narrow range of spectroscopic design parameters.

### B. Method and Results

We are presently investigating the following systems by FIR spectroscopy; in each case spectroscopic investigations are guided by detailed phenomenological theoretical modelling:

(i) Metallic magnets (Cr and rare earth metals). Magnetic resonance measurements on conducting media have always presented severe problems because of the high metallic reflectivity. For measurements on Ni, Dy and Tb, Sievers [1] made far infrared transmission lines by rolling alternate thin layers of metal and polyethylene sheet into coils. By using a variation of this approach, we have recently [2] demonstrated theoretically that magnetic resonances are in principle observable by FIR spectroscopy on suitably structured planar metallic systems where, in a simple reflection experiment on an unstructured sample, the plasma reflectivity would mask the magnetic resonance. Our calculations [2] were based on a grating structure, in which the plasma reflectivity is eliminated by polarising the electromagnetic E-field normal to the gratings. Such gratings need to be thick ( $\sim 10 \mu\text{m}$ ), with a period  $\sim 1 \mu\text{m}$ , and are very difficult to fabricate. However, we have since demonstrated by extensive modelling that even greater enhancement of the coupling to the magnetic response is achievable using reflection from a thin grating ( $\sim 1 \mu\text{m}$ ) placed at the base of a Si prism (in effect, an ATR experiment, though without an air gap). At large angles of incidence, close in effect to the Brewster angle for a Si/metal interface, variations in the permeability  $\mu(\omega)$  become significant, and can produce a pronounced magnetic resonance feature with reflectivity changes of order 10% at the resonant frequency,  $\omega_m$ . Thus a combination of a grating structure to eliminate the plasma reflectivity and careful design to optimise impedance matching produces an enhancement of more than 2 orders of magnitude in the coupling efficiency. This discovery opens the way to study most metallic thin film magnetic structures. In addition to transition metal structures, such as Cr, we propose to study rare earth magnetic structures.

The advantages which can be achieved are illustrated in Fig. 1, where we compare calculations on five different structures with a nominal resonance frequency  $\omega_m = 38 \text{ cm}^{-1}$ . We first consider calculations on continuous Cr films, Fig. 1(a). Curve A shows the reflectivity,  $R$ , from a Cr film with a thickness which exceeds the penetration depth ( $\sim 0.3 \mu\text{m}$ ), with the FIR beam incident at normal incidence ( $0^\circ$ ) from vacuum; as expected,  $R \sim 1$  throughout. Curve B shows the reflectivity in s-polarisation at  $85^\circ$  angle of incidence, and curve C shows the calculated reflectivity with the FIR beam incident at an angle of  $85^\circ$  from Si, i.e., an ATR experiment with the Cr sample pressed against the base of a Si prism. In B and C, the experiments will be relatively difficult to set up because of the large angle of incidence, but the expected enhancements are large. In Fig. 1(b) we show calculations on Cr gratings. Curve D, which has been shifted up by 0.2 for clarity, shows the reflectivity from a grating  $10 \mu\text{m}$  thick deposited on a semi-infinite Si substrate with the FIR beam incident at  $60^\circ$  from vacuum; an easily measurable signal is calculated, but  $10 \mu\text{m}$  thick Cr films are very difficult to deposit, so the experiment is not compatible with current thin film technology. Finally, in curve E, the reflectivity of a Cr grating of thickness  $1 \mu\text{m}$  on a  $2 \text{ mm}$  thick quartz substrate with the radiation incident at  $60^\circ$  from a Si prism is shown. The most important advance in curve E is the additional enhancement in coupling efficiency achieved by impedance matching which allows the grating thickness to be reduced to  $1 \mu\text{m}$ . This makes the grating structure practically realisable; we have already used prisms with  $55^\circ$  angle of incidence in ATR measurements on surface magnetic polaritons in  $\text{FeF}_2$  [3,4], so all of the experimental conditions corresponding to curve E can be physically achieved without difficulty. Moreover, we have been careful to use realistic, rather than optimistic, parameters to model the magnetic resonance; for example, the linewidth may be less than the assumed value of  $0.3 \text{ cm}^{-1}$ .

(ii) NiO. This is widely used for biasing in magnetic tapes, and  $\text{CoO}/\text{NiO}$  structures and  $\text{Fe}_3\text{O}_4/\text{NiO}$  structures have been widely studied, though not by FIR spectroscopy. As in the case of thin metal films described above, modelling has demonstrated that by careful design of the experiment, i.e., choice of substrate, prism material, FIR beam polarisation and angle of incidence, the optimum conditions for impedance matching at the magnetic resonance can be identified, and enhancement of the coupling efficiency of at least an order of magnitude compared with a simple reflection measurement can be achieved.

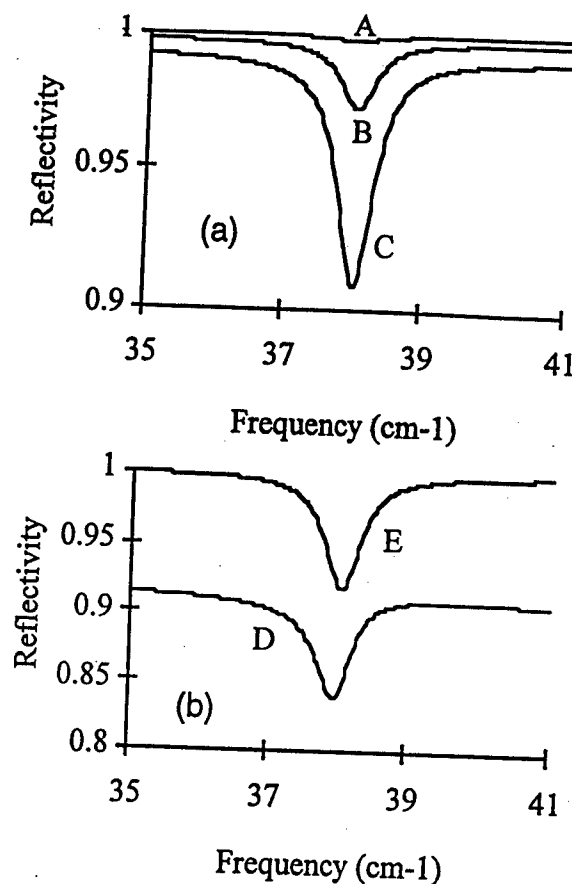


Fig. 1. Reflectivity of (a) Cr film and (b) Cr grating (see text).

#### C. Acknowledgements

This work has been supported by EPSRC under Grant Nos. GR/G54139 and GR/J90831. SAF is supported by an EPSRC studentship.

#### D. References

1. A J Sievers, J. Appl. Phys., **41**, 980 (1970).
2. R E Camley, T J Parker and S R P Smith, Phys. Rev. B, **53**, 5481, (1996).
3. M R F Jensen, T J Parker, Kamsul Abraha, and D R Tilley, Phys. Rev. Letts., **75**, 3756 (1995).
4. M R F Jensen, S A Feiven, T J Parker, and R E Camley, Phys. Rev. B, **55**, 2745 (1997).

# A Complete Frequency-Field Chart for the Antiferromagnetic Resonance in $\text{MnF}_2$

M. Hagiwara<sup>1)</sup>, K. Katsumata<sup>1)</sup>, H. Yamaguchi<sup>1)</sup>, M. Tokunaga<sup>1)</sup>, I. Yamada<sup>2)</sup>, M. Gross<sup>3)</sup> and P. Goy<sup>4)</sup>

<sup>1)</sup>The Institute of Physical and Chemical Research (RIKEN), Wako, Saitama 351-01, Japan

<sup>2)</sup>Department of Physics, Faculty of Science, Chiba University, Yayoi-cho, Inage-ku, Chiba 263, Japan

<sup>3)</sup>Laboratoire Kastler-Brossel, Département de Physique de l'Ecole Normale Supérieure, 24 rue Lhomond, 75231 Paris Cedex 05, France

<sup>4)</sup>AB Millimetre, 52 rue Lhomond, 75005 Paris, France

## Abstract

Antiferromagnetic resonance (AFMR) measurements on a well characterized single crystal sample of  $\text{MnF}_2$  have been performed using various kinds of millimeter and submillimeter sources up to 570 GHz and a superconducting magnet up to 20 T. All the AFMR modes predicted from the theory have been observed. We report a complete frequency-field chart for these AFMR modes.

Recent development of millimeter and submillimeter apparatus has made electron spin resonance (ESR) measurements over wide frequencies easier. It is now possible to have centimeter, millimeter and submillimeter waves ranging from ~1 GHz to ~800 GHz using e.g. klystrons, Gunn-oscillators, Carcinotrons (trademark name for backward-wave oscillators of Thomson Co.) and a millimeter vector network analyzer, and up to ~7 THz using a far-infrared laser. In particular, the millimeter-submillimeter vector network analyzer developed during the last decade has the capability to cover wide frequency ranges and detect not only the amplitude but also the phase of signal. In addition, stable high magnetic fields up to 20 T are now available with a superconducting magnet.

In the Institute of Physical and Chemical Research (RIKEN), we are building an ESR spectrometer with wide frequency and field ranges. In order to test this system, we have measured ESR of a prototypical example of antiferromagnets with uniaxial anisotropy, manganese fluoride ( $\text{MnF}_2$ ) which has been studied extensively [1]. In our previous paper [2], we reported the results of antiferromagnetic resonance (AFMR) measurements on  $\text{MnF}_2$  for the frequencies up to 300 GHz. We observed all the AFMR modes predicted by the theory [3, 4]. In the present study, we have extended the measurement up to 570 GHz and completed the frequency-field chart.

The crystal structure of  $\text{MnF}_2$  belongs to the tetragonal space group  $D_{4h}^{14}$  with two molecules per unit cell. The lattice constants at room temperature are  $a=4.8734 \text{ \AA}$  and  $c=3.3103 \text{ \AA}$  [5]. From the neutron scattering study below the Néel temperature ( $T_N=67.34 \text{ K}$ ) [6], the magnetic structure of  $\text{MnF}_2$  was determined. In the ordered phase, the spins at body center sites point antiparallel to those at the corner sites with the spin easy axis parallel to the  $c$  axis. The main origin of the magnetic anisotropy comes from the dipole-dipole interaction. Single crystals of  $\text{MnF}_2$  were grown by the Bridgman method as written in our previous paper [2]. A thin disc (~0.4 mm thickness) of  $\text{MnF}_2$  with the plane perpendicular to the  $c$  axis was cut from a large crystal.

The ESR spectrometer consists of two main parts (a magnet and a microwave source) and measuring instruments. The microwaves below about 300 GHz are generated from klystrons, Gunn-oscillators and Carcinotrons. Above 300 GHz, we use a millimeter vector network analyzer (MVNA-8-350, AB Millimetre, France) which offers the 8-770 GHz frequency coverage capability with extensions ESA-1 and ESA-2. The magnetic field is produced by a superconducting magnet produced by Oxford Instruments, U. K.. The magnetic field can be swept up to 18 T at 4.2 K and up to 20 T at 2.2 K. A dewar (variable temperature insert) is used to change the temperature of the sample space from 1.6 K to 200 K. The temperature of the sample is measured by a calibrated carbon glass thermometer placed close to it.

Figure 1 summarizes all the AFMR data obtained at 1.8 K or 5 K in the frequency (GHz) vs. magnetic field (T) plane. In the following, we analyze the experimental results shown in figure 1. If the exchange field ( $H_E$ ) is much larger than the anisotropy field ( $H_A$ ), the AFMR frequencies of a uniaxial antiferromagnet are given by equations (1)-(3) below [4,7,8]. In  $\text{MnF}_2$ ,  $H_E \sim 53 \text{ T}$  and  $H_A \sim 0.82 \text{ T}$  so that  $H_E \gg H_A$  [9].

$$h\nu / g\mu_B = \sqrt{2K_u / \chi_{\perp} + (\chi_{\parallel} H / 2\chi_{\perp})^2} \pm H(1 - \chi_{\parallel} / 2\chi_{\perp}) \quad (H \parallel c, H < H_{SF}), \quad (1)$$

$$h\nu / g\mu_B = \sqrt{H^2 - 2K_u / \chi_{\perp}} \quad (H \parallel c, H > H_{SF}), \quad (2)$$

and

$$h\nu / g\mu_B = \sqrt{H^2 + 2K_u / \chi_{\perp}} \quad (H \perp c), \quad (3)$$

where,  $h$  is Planck's constant,  $\nu$  ESR frequency,  $g$  the  $g$ -value,  $\mu_B$  the Bohr magneton,  $K_u$  the anisotropy constant,  $\chi_{\parallel}$  and  $\chi_{\perp}$  magnetic susceptibilities parallel and perpendicular to the  $c$  axis, respectively, and  $H_{SF}$  the critical field for spin flop. At low temperatures ( $T \ll T_N$ ),  $\chi_{\parallel}$  is much smaller than  $\chi_{\perp}$  [2], thus, equation (1) becomes

$$h\nu / g\mu_B = \sqrt{2K_u / \chi_{\perp}} \pm H. \quad (4)$$

The two full straight lines below 9.27 T in figure 1 represent equation (4), the full curve above 9.27 T equation (2) and the broken line equation (3) with  $\sqrt{2K_u / \chi_{\perp}} = 9.27 \text{ T}$ . This value of the zero field gap frequency (259.7 GHz) is very close to that reported before ( $261.4 \pm 1.5 \text{ GHz}$  at 0 K) [9]. The vertical straight line at 9.27 T represents the critical field

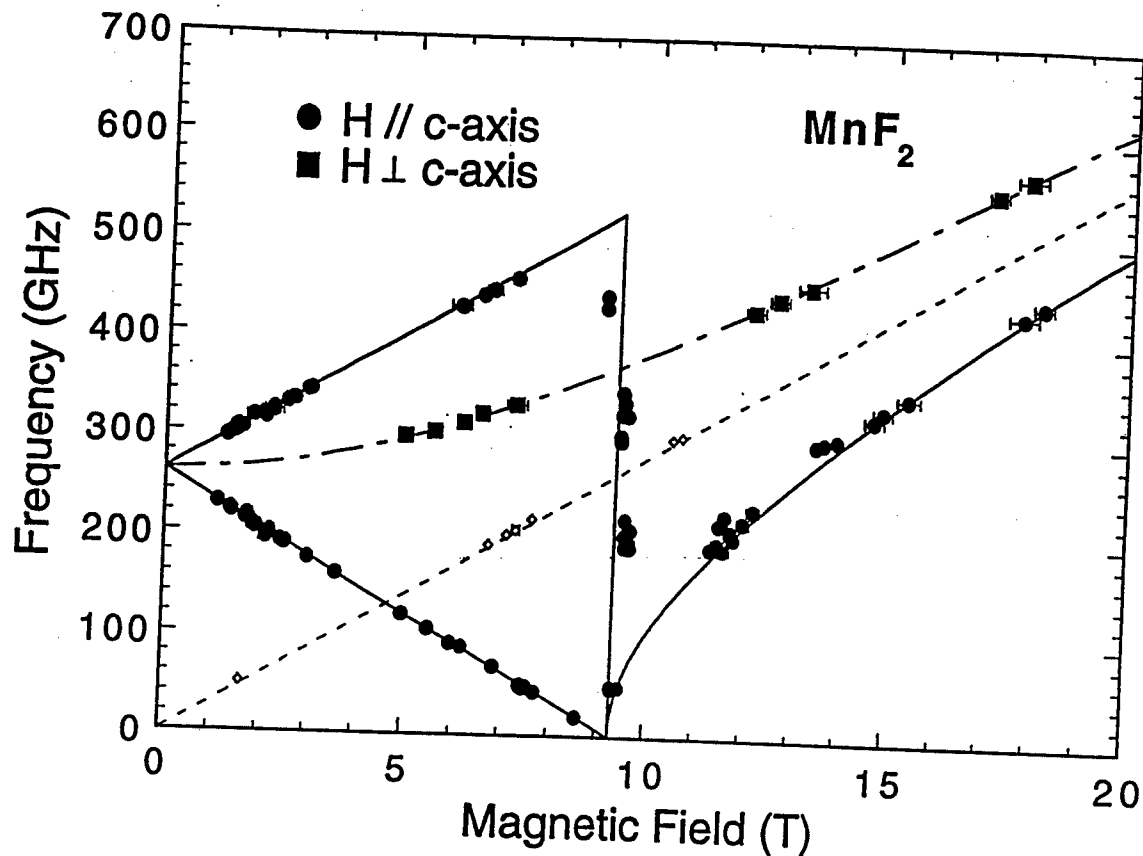


Figure 1. Frequency versus external magnetic field relations of the AFMR signals in  $\text{MnF}_2$ . The full straight lines, the full curve and the broken line are the theoretical ones discussed in the text. The dotted line is the paramagnetic resonance line with  $g=2.00$ .

resonance mode. We see in figure 1 a good agreement between theory and experiment including higher frequency region. In the present experiment, we complete the frequency-field chart for all the AFMR modes in  $\text{MnF}_2$ .

In conclusion, we have made ESR measurements on a well characterized single crystal of  $\text{MnF}_2$  using a wide-frequency and high-field spectrometer installed in RIKEN. We have completed the frequency-field chart for the AFMR modes.

### Acknowledgments

This work was supported by the "MR Science Research Program" from RIKEN.

### References

- [1] K. Katsumata, *Landolt-Börnstein III* 27j1 1-135 (Springer-Verlag, Berlin) (1994) p.1-135 and references therein
- [2] M. Hagiwara, K. Katsumata, I. Yamada and H. Suzuki, *J. Phys.: Condens. Matter.* 8 (1996) 7349.
- [3] T. Nagamiya, *Prog. Theor. Phys.* 6 (1951) 342.
- [4] F. Keffer and C. Kittel, *Phys. Rev.* 85 (1952) 329.
- [5] M. Griffel and J. W. Stout, *J. Am. Chem. Soc.* 72 (1950) 4351.
- [6] R. A. Erickson, *Phys. Rev.* 90 (1953) 779.
- [7] T. Nagamiya, K. Yosida and R. Kubo, *Adv. Phys.* 4 (1955) 1.

[8] S. Foner, *Phys. Rev.* 107 (1957) 683; *Magnetism* 1, ed. Rado G T and Suhl H (New York; Academic) (1963) 383.

[9] F. M. Johnson and A. H. Nethercot, Jr., *Phys. Rev.* 114 (1959) 705.

# Terahertz Radiation from Coherent Phonons Excited in Semiconductors

M. Tani, R. Fukasawa, H. Abe, S. Matsuura, K. Sakai and S. Nakashima<sup>1</sup>

Kansai Advanced Research Center, Communications Research Laboratory  
Ministry of Posts and Telecommunications, Japan

<sup>1</sup>Department of Applied Physics, Graduate School of Engineering  
Osaka University, Japan

## Abstract

Terahertz radiation emitted by coherent phonons excited in Te, PbTe and CdTe is investigated. Coherent radiation originating from the IR-active LO phonon mode was observed with each sample, while radiation from TO phonons was not observed. The mechanism of the emission from coherent phonons is discussed.

## 1. Introduction

Coherent phonons excited in semiconductors or semimetals have been studied extensively by means of transient reflectivity or transmittance measurements. In such measurements, only the Raman active phonon modes were observed. On the other hand, no observation has been reported for the only infrared (IR) active phonon modes. This indicates that Raman activity of the coherent phonon is essential for the transient reflectivity/transmittance signals. Recently, emission of terahertz (THz) radiation from the IR-active coherent longitudinal optical (LO) phonons excited in polar semiconductors, such as GaAs, was predicted theoretically[1], and coherent THz radiation corresponding to an only IR-active LO phonon ( $A_2$ -mode) in Te was observed by Dekorsy *et al.* [2, 3] with a photoconductive sampling detector. The measurement of radiation from coherent phonons, which is complementary to the conventional pump-probe photo-reflectance/transmittance measurements, opens up a new way to study the dynamics of the coherent phonons. In this work we investigated the THz radiation emitted from Te (hexagonal), PbTe (NaCl-like) and CdTe (zinc-blende), whose crystal structures are different from each other, to get more information on the emission mechanism of THz radiation from the coherent phonons excited in semiconductors by using an ultrafast photoconductive detector based on a low-temperature-grown (LTG) GaAs [4, 5].

## 2. Experiment

The experimental setup is illustrated in Fig. 1. A mode-locked Ti:sapphire laser, whose pulse width, wavelength and repetition rate are respectively about 70 fs, 800 nm and 82 MHz, was used to excite the coherent

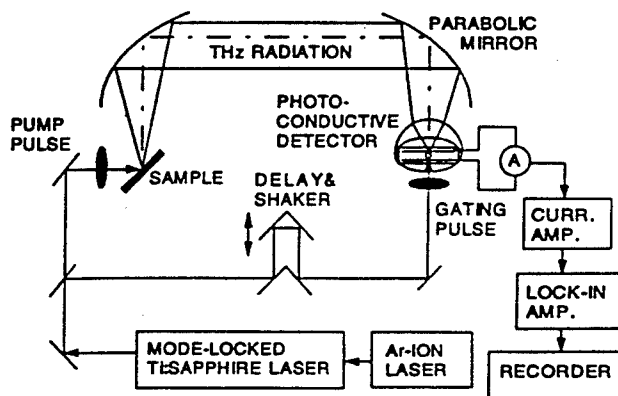


Fig 1. Schematic view of the experimental setup for the detection of terahertz radiation from coherent phonons in semiconductors.

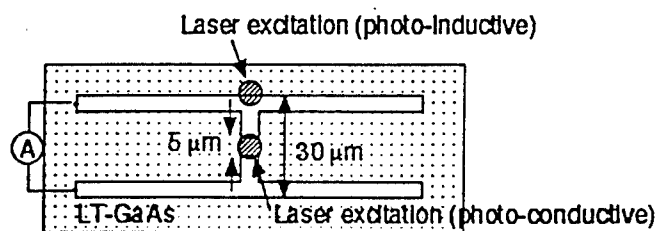


Fig 2. Structure of the photoconductive dipole antenna. For the photo-inductive detection, the laser was directed at the edge of the antenna.

phonons at the sample surfaces and also to gate the photoconductive sampling detector. Laser pulses with an averaged power of 200 mW were irradiated onto the sample surface at an incident angle of  $45^\circ$  and focused to a diameter of about 1 mm. The radiation from the sample surface in the direction of the optical reflection was collected and focused onto the detector by a pair of parabolic mirrors. The time-resolved waveform of the radiation was obtained by measuring the DC photocurrent in the photoconductive detector, which is biased with the electric field of the incident radiation and gated by the gating laser pulses, varying the time-delay between the pump and gating pulses. The detector was a photoconductive dipole antenna with a length of 30  $\mu\text{m}$ , fabricated on LTG-GaAs (Fig. 2). To

increase the responsivity at higher frequencies we carried out the differential detection using a shaker on the optical delay line. In addition, for the detection of the high frequency coherent radiation from CdTe ( $\sim 5$  THz) we carried out photo-inductive sampling [6] by irradiating the edge of the photoconductive dipole antenna (See Fig. 2). With this detection configuration we achieved a reasonable detector responsivity at frequencies beyond 5 THz.

### 3. Results and Discussion

Figures 3 shows the waveforms of radiation from mono-crystalline Te (c-axis perpendicular to the surface), PbTe (100) and CdTe (100) surfaces. The insets in the figure show the Fourier-transformed amplitude spectrum of the each waveform.

In Fig. 3(a), the oscillatory component in the waveform is attributed to the LO phonon of the  $A_2$ -mode (2.8 THz) in Te, as specified by Dekorsy *et al.* [2]

In Fig. 3(b), strongly damped oscillations are observed and attributed to the LO phonon in PbTe (3.4 THz), although the spectral peak (3.1 THz) is slightly shifted to the lower frequency side. This spectral shift may be due to the strong damping of the oscillations and the strong degradation of the detector responsivity for higher frequencies.

In Fig. 3(c), fast oscillations after a strong radiation burst are observed and attributed to the LO phonon in CdTe (5.1 THz). Although the radiation from the coherent phonons appears to be weak, the actual radiation amplitude is estimated to be comparable to that of the first radiation burst by considering the low responsivity of the detector at 5 THz compared to that at 1 THz.

The absence of coherent THz radiation from the transverse optical (TO) phonon modes is understood when we consider the TO phonon property that it does not create a macroscopic electric polarization ( $\text{div} \mathbf{E} = 0$ ), while an LO phonon does. However, we observe spectral dips or minima at the TO phonon frequencies (2.6, 0.9 and 4.2 THz for the TO phonons in Te( $A_2$ -mode), PbTe and CdTe, respectively). This cannot be explained by the absence of radiation from TO phonons alone, nor by the absorption of the radiation, since the absorption in the thin radiation volume is negligible. To explain the spectral dips at TO phonon frequencies we considered the emission efficiency of radiation into free space and into the dielectric (substrate). It is known that for a dipole antenna on a thick dielectric substrate (with its polarization parallel to the surface) the ratio of the radiation power emitted into the dielectric ( $P_d$ ) to that emitted into free space ( $P_a$ ) is scaled approximately as  $\epsilon^{3/2} (\approx P_d/P_a)$ , where  $\epsilon$  is the dielectric constant of the substrate. When we consider the coherent LO phonons excited in a semiconductor as distributed infinitesimal (Hertzian) dipoles on the sample surface (with its polarization normal to the surface), we can calculate the emission efficiency of the radiation into free space ( $P_f/(P_f+P_d)$ ) over the frequencies with the frequency-dependent dielectric constant  $\epsilon(\omega)$ . The

calculated results showed that due to the large value of  $\epsilon$  peaked at the TO phonon frequency the efficiency of emission into free space is greatly reduced, while, due to the small value of  $\epsilon$  at the LO frequency (without the damping  $\epsilon(\omega_{LO}) = 0$ ), the emission efficiency has a maximum at the LO phonon frequency. Thus, the change in the emission efficiency of radiation into free space due to  $\epsilon(\omega)$  explains well the observed spectral dip at the TO phonon frequency and the enhanced spectral amplitude of the coherent radiation by the LO phonons. The details of the discussion will be presented at the conference.

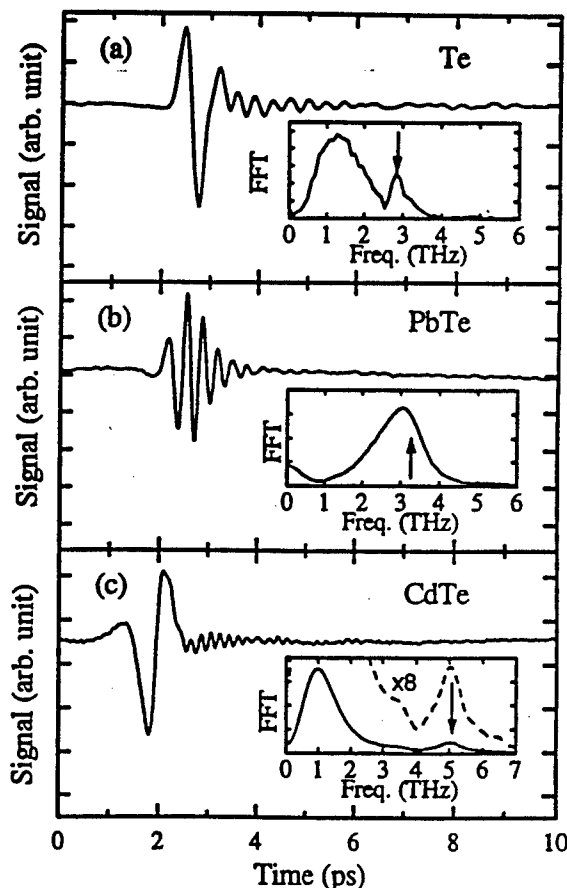


Fig 3. Waveforms of THz radiation emitted from (a) Te, (b) PbTe and (c) CdTe surfaces. The insets show the FFT spectrum of the each waveform. The arrows indicate the corresponding LO phonon frequencies.

### References

- [1] A. V. Kuznetsov and C. J. Stanton, Phys. Rev. B, 51, 7555 (1995).
- [2] T. Dekorsy, *et al.*, Phys. Rev. Lett. 74, 738 (1995).
- [3] T. Dekorsy, *et al.*, Phys. Rev. B 53, 4005 (1996).
- [4] M. Tani, *et al.*, Jpn. J. Appl. Phys. 33, 4807 (1994).
- [5] M. Tani, *et al.*, to be published in Appl. Opt.
- [6] R. H. Jacobsen *et al.*, J. Appl. Phys. 80, 4214 (1996).



# Transition from Semi-Classical to Quantum Mechanical Limit of Terahertz Tunnel Ionization of Deep Impurities

S. D. Ganichev<sup>1,2</sup>, I. N. Yassievich<sup>2</sup>, E. Ziemann<sup>1</sup>, Th. Gleim<sup>1</sup> and W. Prettl<sup>1</sup>

<sup>1</sup>Institut für Experimentelle und Angewandte Physik, Universität Regensburg,  
D 93040 Regensburg, Germany

<sup>2</sup>A. F. Ioffe Physicotechnical Institute, Russian Academy of the Sciences,  
St. Petersburg, 194021, Russia

## Abstract

Tunnel ionization of deep impurities in high frequency electromagnetic fields and multi-photon ionization are two limiting cases of the same nonlinear optical process. The transition between these limits has been observed for the first time with deep impurities in semiconductors subjected to high power laser radiation in the terahertz range with quantum energies being much smaller than the impurity binding energy.

## Introduction

Application of quantum mechanical or classical consideration of the electromagnetic radiation field depends on the relation between the period of radiation and characteristic times of processes involved. L.V. Keldysh [1] has shown that multi-photon ionization in high-frequency fields and tunnel ionization in dc and low-frequency fields are two limiting cases of just the same nonlinear optical process.

As long as  $\Omega\tau \ll 1$ , where  $\Omega$  is the frequency of the radiation field and  $\tau$  is the tunneling time, an electron instantaneously follows the electric field and the tunneling probability is independent of  $\Omega$ . This has been experimentally proved by ionization of deep impurities in semiconductors subjected to far-infrared radiation with photon energies much smaller than the binding energy of the impurities [2-4]. The emission probability of carriers was found to be independent of the radiation frequency in a wide range of frequencies and temperatures. In a substantial range of the electric radiation field strength the emission process could be attributed to phonon assisted tunneling [2-5]. In this case, with very general assumptions, the tunneling time  $\tau$  can be shown to be solely determined by the temperature,  $\tau = \hbar/(2k_B T)$ .

Thermal emission of carriers from deep impurity bound states into the continuum is usually accomplished by thermal activation of the system in the adiabatic bound state potential and tunneling of the bound defect configuration into the ionized configuration. The tunneling trajectory can be split into two parts through the barriers formed by the ground and ionized state potentials corresponding to tunneling times  $\tau_1$  and  $\tau_2$ . This gives a total tunneling time  $\tau = \tau_1 \pm \tau_2$ , where the plus and minus sign depends on the configuration of the adiabatic potentials [3,4].

An electric field enhances defect tunneling due to electron tunneling through the barrier formed by the impurity potential and the potential of the electric field. This corresponds to a lowering of the adiabatic potential of the ionized state. Thus tunneling emission of carriers in an electric field is controlled by  $\tau_2 = \hbar/(2k_B T) \pm \tau_1$ , where  $\tau_1$  is of the order of the period of the impurity vibration [5]. The ionization probability, being independent of the radiation frequency, increases with rising peak electric field strength,  $E$ , like  $\exp(E^2/E_c^2)$  with a characteristic field  $E_c = ((3m^* \hbar)/(\tau_2^3 e^2))^{1/2}$  decreasing with falling temperature.

Here we report on the first observation of frequency dependence of the ionization probability which can be ascribed to the onset of the transition from tunnel ionization to multi-photon ionization in high frequency electromagnetic fields.

## Results and Discussion

The investigation has been carried out on Ge:Hg in the temperature range between 40 K and 90 K where the 90 meV deep impurities are occupied in thermal equilibrium. The radiation source used was a pulsed far-infrared molecular laser optically pumped by a TEA-CO<sub>2</sub> laser. Using NH<sub>3</sub> as active gas, 40 ns pulses with a peak power of 100 kW have been obtained at wavelengths of 35  $\mu$ m, 76  $\mu$ m, 90  $\mu$ m, 148  $\mu$ m, and 280  $\mu$ m.

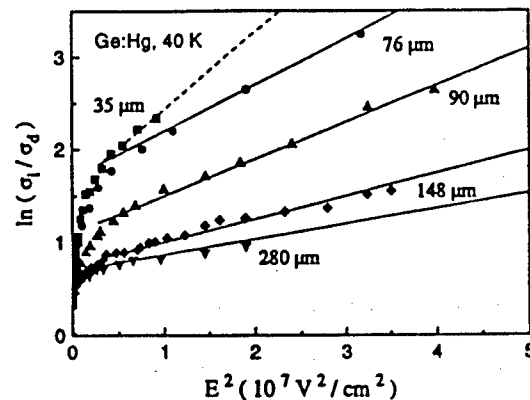


Fig. 1

Fig.1 shows the dependence of  $\ln(\sigma_i/\sigma_d)$  on the square of the amplitude of the optical electric field for Ge:Hg

for different wavelengths and  $T = 40\text{ K}$ . Here  $\sigma_d$  and  $\sigma_i$  are the dark and irradiation induced conductivities of the sample, respectively. Fig. 1 shows that there is a range of electric field strength where the probability of photoexcitation  $e(E)/e(0) = \sigma_i/\sigma_d$  depends on the electric field as  $\exp(E^2/E_c^{*2})$  with a characteristic field strength  $E_c^*$ , like in the case of  $\Omega\tau_2 \ll 1$ . The magnitude of  $E_c^*$ , however, depends strongly on the wavelength in the presented spectral range between  $35\text{ }\mu\text{m}$  and  $280\text{ }\mu\text{m}$ . Thus, in contrast to the case of higher temperatures and in turn smaller  $\tau_2$ , when the ionization probability  $e(E)/e(0)$  does not depend on the frequency [4], at low temperatures or higher frequencies the  $e(E)/e(0)$  is frequency dependent. The ionization probability increases with rising  $\Omega\tau_2$ . For the following discussion we introduce  $\tau_2^*$  defined by  $E_c^* = ((3m^*\hbar)/(e^2\tau_2^{*3}))^{1/2}$ . In the limit  $\Omega\tau_2 \ll 1$ ,  $\tau_2^*$  approaches  $\tau_2$ .

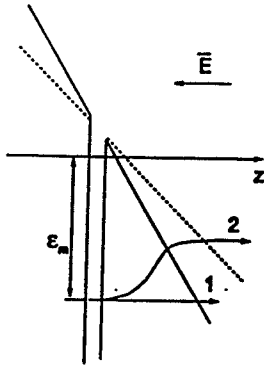


Fig. 2

The situations for electron tunneling out of the potential well of a deep impurity are sketched in Fig. 2 for the limiting case  $\Omega\tau_2 \ll 1$  (trajectory 1) and for  $\Omega\tau_2 > 1$  (trajectory 2). As thermal population decreases, but the tunneling probability through the triangular potential well increases with rising energy, there is an optimum energy  $\epsilon_m$  of highest electron emission rate. In the case of  $\Omega\tau_2 \ll 1$ , due to the exponential dependence of the tunneling probability on the electric field strength, an electron will tunnel through the barrier in a time much shorter than  $\Omega^{-1}$  when the slope of the potential generated by the electric field is largest (trajectory 1 in Fig. 2). This process is fast compared to the radiation period. If  $\Omega\tau_2 > 1$  the electron tunnels through an oscillating barrier which decreases the tunneling probability. On the other hand, during tunneling the electron can absorb energy from the radiation field leaving the triangular barrier at a higher energy,  $\epsilon > \epsilon_m$  (trajectory 2 in Fig. 2). By this the effective width of the barrier is reduced and, thus, the tunneling probability enhanced. The electron emission rate increases because at higher frequencies a smaller number of photons are needed for optical excitation. With increasing radiation frequency this process proceeds into multi-photon ionization of the impurity. Generally, multi-photon transitions override the

reduction of tunneling probability by the oscillation of the barrier leading to an increase of electron emission rate with increasing  $\Omega\tau_2$ .

The ionization probability can be calculated assuming a classical electric field  $\vec{E} = E \cos(\Omega t)$  yielding the exponential dependence of the emission probability  $e(E)$  on  $E^2$  given above with

$$\tau^{*3} = \frac{3}{4} \frac{1}{\Omega^3} (\sinh(2\Omega\tau_2) - 2\Omega\tau_2)$$

where  $\tau_2$  is the tunneling time in the limit of zero frequency.

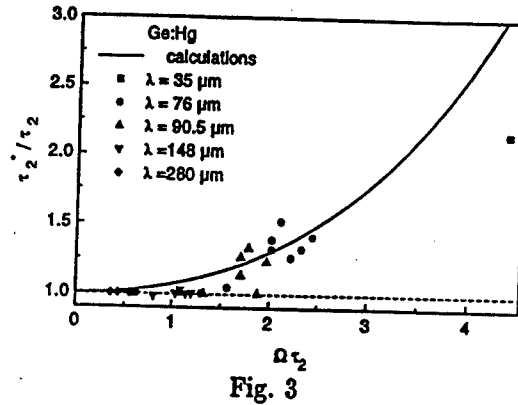


Fig. 3

In Fig. 3  $\tau_2^*/\tau_2$  is plotted as a function of  $\Omega\tau_2$  calculated after this equation and compared to experimental results obtained from measured values of  $E_c^*$  for various wavelengths. Experiment and theory are in good agreement showing that  $\tau_2^*/\tau_2$  approaches unity for  $\Omega\tau_2 < 1$  which means that tunnel ionization is frequency independent. At larger values of  $\Omega\tau_2$ ,  $\tau_2^*/\tau_2$  increases corresponding to enhanced ionization probability.

### Acknowledgements

Financial support by the Deutsche Forschungsgemeinschaft and valuable discussions with V.I. Perel are gratefully acknowledged.

### References

- [1] L. V. Keldysh, Sov. Phys. JETP 20, 1307 (1965).
- [2] S.D. Ganichev, W. Prettl, and P.G. Huggard. Phys. Rev. Lett. 71, 3882 (1993).
- [3] S.D. Ganichev, J. Diener, I.N. Yassievich, W. Prettl, B.K. Meyer and K.W. Benz, Phys. Rev. Lett. 75, 1590 (1995).
- [4] S.D. Ganichev, I.N. Yassievich, and W. Prettl. Semicond. Sci. and Techn. 11, 679 (1996).
- [5] V.N. Abakumov, V.I. Perel, and I.N. Yassievich, *Nonradiative Recombination in Semiconductors*, edited by V.M. Agranovich and A.A. Maradudin, Modern Problems in Condensed Matter Sciences Vol. 33 (North Holland, Amsterdam, 1991).

## Tunable Terahertz Sources

Maurice F. Kimmitt

Department of Physics, University of Essex, Colchester CO4 3SQ, UK

### Abstract

The present status of tunable sources in the frequency range 0.3-10THz (1000-30 $\mu$ m) is reviewed. Future prospects are discussed with specific emphasis on the requirement for CW narrow linewidth sources of sufficient power to be used as local oscillators in heterodyne spectroscopy.

### 1. Introduction

Dye lasers, optical parametric oscillators and diode lasers are convenient tunable CW sources for the ultraviolet, visible and much of the infrared region. With alloy semiconductors such as PbSnTe modest powers, but quite sufficient for high resolution spectroscopy, are available out to just beyond 30 $\mu$ m. A wide range of both electron beam and solid state sources cover the microwave and millimeter range and some of these, for example, backward wave oscillators, resonant tunnel diodes and Josephson oscillators extend the frequency range to about 1THz (300 $\mu$ m). Free electron lasers (FELs) cover the entire spectrum from the visible to millimeter wavelengths but these are pulsed sources and have the added disadvantage that the experimenter must travel to one or more of the FEL facilities.

It is therefore not surprising that most infrared and far-infrared spectroscopy is still performed with conventional spectroscopic instruments. Fourier transform Michelson interferometers will, for example, give resolving powers of better than  $10^4$  at 100 $\mu$ m and Fabry-Perot instruments can improve this to above  $10^5$ . A resolving power of  $10^5$  at 100 $\mu$ m corresponds to a linewidth of 30MHz. The usual spectroscopic source is a mercury arc but at long wavelengths the average power produced by synchrotron sources such as the National Synchrotron Light Source at Brookhaven is one to two orders of magnitude greater [1].

An attractive alternative to conventional spectroscopy is to employ a fixed frequency local oscillator (LO) source in a heterodyne system. Optically pumped far-infrared lasers (OPFIRs) provide many CW lines in the terahertz region at power levels  $>1$ mW and linewidths of 100kHz or less. When such a line is mixed with another source the frequency range over which mixing will occur is dependent on the bandwidth of the mixer. Using Schottky diodes heterodyne spectroscopy can tune over a few 10s of GHz corresponding to about  $\pm 1\mu$ m at 100 $\mu$ m. Although this range is small the potential

resolution, with a 100kHz bandwidth LO is  $3 \times 10^7$ . This form of spectroscopy has been very successful in observing narrow line rotational emissions in both astronomy and pollution monitoring [2] [3].

A further alternative, but in practice rather inefficient, method of performing high resolution far-infrared spectroscopy is to use the demodulation of a mode-locked femtosecond pulse train by means of a subpicosecond response time photoconductive 'switch'. The frequency domain spectrum is given by the Fourier transform of the envelope of the time domain optical pulse train convoluted with the time response of the photoconductive process. Using an extremely stable mode-locked Ti:Sapphire laser and a low temperature grown GaAs (LTG-GaAs) switch a resolution of  $\sim 100$ kHz has been obtained at 880 $\mu$ m [4]. This type of source may be extendable to significantly higher frequencies by exciting oscillations in semiconductor superlattices but the power levels may be too low to be useful.

However, for convenient high resolution spectroscopy a narrow line tunable CW source is needed. Ideally this should be compact and rugged enough to operate in hostile environments and have sufficient power to be used as an LO in heterodyne systems. Sources can be conveniently divided into two categories: fundamental or relying on some frequency conversion process.

### 2. Fundamental oscillators

Traditionally sources in the millimeter wave region were divided into electron beam and solid state oscillators, but with the advent of lasers a more logical separation is into 'transit time' and 'energy transition' devices. This alerts one immediately to the main problem of extending solid state microwave-type sources to higher frequencies; the frequency of operation is determined by the time taken for current carriers (usually electrons) to transit the device. Therefore for solid state oscillators fast carriers are needed in short length structures. Furthermore, it is also necessary to retain negative resistance to provide a transferred electron effect, and this again sets a requirement that the source must be small, as any stray resistance, capacitance or inductance will cause the negative resistance to be overcome by positive terms as the frequency is increased. An almost inevitable consequence of small devices is low power output.

With conventional electron beam devices there are somewhat different problems but with a similar outcome. The basic problems are: (1) as the dimensions of the structure are scaled in proportion to the wavelength, machining problems multiply and there is increasing heat dissipation due to unwanted interaction between the electrons and the structure; (2) the rf current losses increase because of the decrease in skin depth and the increasing significance of machining imperfections. The beam current required for oscillation is therefore increased causing further heating problems.

In both solid state transit time oscillators and conventional electron beam devices the upper frequency limit is about 1THz and one suspects that progress to higher frequencies will be limited. For this reason there is increasing research on laser sources and electron beam structures using optical type cavities (eg Smith-Purcell sources) for the 1-10THz region. The following sections consider some of the more useful fundamental sources beginning with electron beam devices.

### 3. Backward Wave Oscillators (BWOs)

The BWO (carcinotron) is the only commercially available CW electron beam source to oscillate at frequencies above 1THz. Its advantages are that it combines a broad tunable bandwidth of  $\pm 10-15\%$  around the centre frequency and produces relatively high power. Linewidths of 1MHz are readily obtainable and, with good stabilization, 100kHz is feasible. The output power varies from close to 1W at 300GHz to less than 1mW at the highest operating frequency of about 1.2THz. The main disadvantages are cost and a limited lifetime.

### 4. Gyrotron

The extension of gyrotron frequencies to above 300THz requires very large magnets. However, gyrotrons do produce significant output on harmonics of their fundamental frequency although usually in rather high modes. There is a requirement for a high power terahertz source in plasma scattering experiments and at least one laboratory is developing CW gyrotrons with magnetic fields up to 17T [5]. However, one can only envisage these as specialist devices.

### 5. Free Electron Lasers (FELs)

FEL facilities exist which can provide high-power pulsed output at any infrared wavelength. For THz frequencies the most useful are at the FOM Institute at Rijnhuizen in the Netherlands [6] and at the University of California at Santa Barbara (UCSB) [7]. FELIX-1 and -2 at FOM cover the range 5-110 $\mu$ m and have a macropulse lasting  $\sim 10\mu$ s with peak power of a few kW and a repetition rate of 10s of Hz. The macropulse consists of micropulses each a few ps long,

separated by 1ns and with peak powers in the MW region. UCSB has two FELs covering 62-313 $\mu$ m and 340 $\mu$ m-2.5mn. The output is in pulses lasting  $\sim 20\mu$ s at a repetition rate up to 4Hz and with no micropulse structure. Output power varies with wavelength and is in the 2-20kW range. Other long wavelength FEL facilities are available at ENEA, Frascati, Italy and Stanford University, USA.

### 6. Smith-Purcell Sources

If an electron beam passes close to a periodic structure, such as a ruled metallic diffraction grating, the electrons induce surface charge oscillations. In 1953 Smith and Purcell produced visible light using 300keV electrons and a grating period of 1.67 $\mu$ m [8]. Their output was spontaneous emission but at longer wavelengths, with high beam current density and suitable optical feedback, oscillation can occur. The emission process is analogous to an FEL with the grating replacing the undulator or, alternatively, one can liken it to a BWO but with an optical rather than a waveguide cavity. In the late 1960s to 1970s groups in Russia, Japan and the USA achieved considerable success in producing millimeter wave sources with Smith-Purcell radiation using names such as orotron and ledatron to describe their structures. Tuning over a 30% range was achieved by varying the electron beam energy.

In recent years Walsh, at Dartmouth College, USA, with collaborators both there and at various other laboratories has been studying both spontaneous and oscillating radiation from Smith-Purcell sources at THz frequencies. His most recent experiment uses a continuous beam of 20-40keV electrons in a 'converted' scanning electron microscope. With this not only has spontaneous radiation been observed [9] but, with the highest current densities available from the tungsten cathode at present used, significant gain has been achieved at frequencies above 1THz, with a beam voltage of 25kV. Using improved cathode materials a useful, relatively compact CW tunable source seems eminently plausible. With 40keV electrons output up to several THz should not be a problem.

### 7. Resonant Tunnel Diodes

The progress of semiconductor manufacturing has led to the production of devices where the properties depend on structures with dimensions smaller than the typical free path of carriers within the device. Resonant tunnelling is a particularly interesting transport process occurring in one of these 'low-dimension' heterostructures and has led to the construction of room temperature oscillators with frequencies approaching 1THz.

For the construction of a high frequency oscillator the most useful structure is the double barrier resonant tunnel diode

(DBRTD). As its name implies, two barrier layers of a semiconductor material are embedded within another semiconductor which has a smaller energy gap. In simplistic terms the two barrier layers act as a 'Fabry-Perot cavity for electrons'. The properties of electrons travelling through the device can be described in terms of a wave with frequency and wavelength related to energy and momentum. When a voltage is applied to the structure this increases the energy of the electrons and at a certain potential a multiple of their wavelength exactly matches the gap between the barrier layers (the resonant condition), producing maximum current flow. At slightly higher or lower potential the current is reduced, thus providing the negative resistance effect required for oscillation. A further increase of voltage then leads to another resonant condition. With InAs-AlSb DBRTD devices a power of  $0.5\mu\text{W}$  has been produced at the highest oscillation frequency of 712GHz [10].

### 8. P-Germanium Lasers

This is a relative newcomer among far-infrared sources. It has two disadvantages in that it requires cooling to below  $\sim 15\text{K}$  and is at present a pulsed source. Its great advantage is that it is tunable between  $70\text{--}300\mu\text{m}$ , a region not at present covered by any other fundamental tunable source.

Although the inversion process is quite complex it is relatively easy to describe qualitatively. By simultaneously applying high electric and magnetic fields to low-doped uncompensated p-Ge an inversion of population is produced between the light and heavy hole bands. The electric field raises the energy of the holes. When they reach the optical phonon energy scattering occurs and the holes are distributed into both the light and heavy hole bands. The magnetic field then 'traps' the light holes into an energy level less than the optical phonon energy and in the pure material there is very little scattering. This ensures a long lifetime for the light holes. However, the heavy holes continue to be scattered and therefore have a short lifetime. Because the light and heavy hole bands are not parallel, lasing occurs over a wide range of photon energies.

Initially experimenters used large germanium rods, typically with cross-sections of  $7\times 7\text{mm}^2$  and lengths of  $35\text{--}50\text{mm}$ . These were cooled by immersion in liquid helium, to avoid light hole scattering. The required magnetic field of  $0.3\text{--}2.0\text{T}$  was provided with a superconducting solenoid. Electrical input powers were of the order of  $10^5\text{W}$  with FIR output powers of  $\sim 10\text{W}$ , indicating a conversion efficiency of  $\sim 10^{-4}$ . Not surprisingly, heating effects in the crystal restricted operation to short pulses; when the temperature rose above  $\sim 18\text{K}$  oscillation ceased. With these large crystals the  $10\text{W}$  output was typically in  $1\mu\text{s}$  long pulses at a  $10\text{Hz}$  repetition rate. Recently attempts have been made to improve the duty cycle of these lasers and, by using very small p-Ge rods,

Bründermann et al [11] have achieved repetition rates  $> 1\text{kHz}$  with pulse lengths of  $\sim 2.5\mu\text{s}$ . Output powers are in the mW range. Their goal is to obtain CW power of  $1\text{mW}$  with input power of  $10\text{W}$ . The low temperature required could then be achieved with a Stirling cycle cooling engine. Very recently operation of a p-Ge laser in a closed cycle refrigerator has been demonstrated [12]. Mixing experiments using an OPFIRL as the local oscillator show that the linewidth of the p-Ge laser is  $1\text{MHz}$  or less.

### 9. Josephson Oscillators

Oscillators based on the Josephson effect have existed for many years. Apart from the necessity of cooling to liquid helium temperature, the main problem has been low output power at the nanowatt level. Recent work on long overlap junctions called flux-flow oscillators (FFOs) has produced output close to  $1\mu\text{W}$  and there have been various reports of arrays of both conventional junctions and FFOs. For example, Han et al [13] used 500 junctions in a linear array to produce  $47\mu\text{W}$  at  $394\text{GHz}$  and  $10\mu\text{W}$  at  $500\text{GHz}$ . The minimum linewidth of these sources appears to be about  $200\text{kHz}$ .

Semiconductor-Insulator-Semiconductor (SIS) mixers are used in very low noise heterodyne systems at frequencies up to  $1\text{THz}$  and a particular advantage of using Josephson devices for both LO and mixer is the convenience of integrating them in a single structure.

### 10. Frequency Converters

Conventional three-wave mixing and parametric systems have been used to produce pulsed output in the THz region. For example, a parametric oscillator using  $\text{LiNbO}_3$  pumped with a Q-switched ruby laser operated from  $150\text{--}700\mu\text{m}$  [14]. Such systems have been largely unsuccessful in producing useful CW output in the THz region. However, a variety of alternative methods have been employed to provide tunable output for conventional high resolution spectroscopy and, in some instances, with sufficient power to act as LOs in heterodyne systems. The following sections are a brief description of the present state-of-the-art.

### 11. Harmonic Generation

For fifty years the generation of harmonic radiation using microwave and millimeter wave sources and non-linear devices has been a convenient way of producing THz radiation. Most systems now use Gunn oscillators and metal-GaAs point contact Schottky diodes and the best result reported used two tripler stages and a  $70\text{mW}$  CW Gunn diode at  $110\text{GHz}$  to produce an output of  $60\mu\text{W}$  at  $1\text{THz}$ . Only a fairly limited tuning range was available because the efficiency of the tripler stages falls rapidly away from the designed centre frequency.

## 12. Mixing and Sideband Generation in Diodes [15]

In the Introduction it was pointed out that heterodyne spectroscopy could be performed using a fixed frequency LO source and a Schottky diode. Heterodyne systems are also used to generate tunable radiation by mixing a tunable microwave source with a fixed frequency laser, either a fundamental FIR laser or an OPFIRL. The sidebands produced in this way are at relatively low power, typically  $10^{-5}$ - $10^{-7}$ W, but have linewidths of  $\sim 100$ kHz, allowing very high resolution spectroscopy.

An alternative system which provides less output power but even higher resolving power is to mix the output of two CO<sub>2</sub> lasers in a MIM diode. By using one high pressure CO<sub>2</sub> laser which is tunable within a rotational line and mixing it with a different rotational line from a fixed frequency CO<sub>2</sub> laser a limited long wavelength tuning range can be obtained. For greater tuning two fixed frequency CO<sub>2</sub> lasers can be mixed with a microwave source producing a frequency of  $\nu_{\text{CO}_2(1)} - \nu_{\text{CO}_2(2)} \pm \nu_{\text{mw}}$ . With such systems tuning has been obtained over virtually the entire range of 0.3-6THz, with a linewidth of only 35kHz, thus providing a resolving power of more than  $10^8$  at the higher frequencies.

## 13 Optical Heterodyne Conversion

Photomixing of two lasers in resistive elements was used in the 1960s to generate microwave radiation [16]. Recent optical heterodyne research has been led by Brown, at MIT's Lincoln Laboratory, and uses low-temperature-grown GaAs as the photomixer [17]. This material has a photoconductive lifetime of  $< 1$ ps, good mobility and a high electrical breakdown field. Initial experiments employed one fixed frequency and one tunable Ti:Al<sub>2</sub>O<sub>3</sub> laser but later these were replaced by diode lasers. CW photomixing has been achieved over the entire range from 20GHz-3.8THz (1.5cm-80 $\mu$ m). Powers are small, eg 1 $\mu$ W at 300 $\mu$ m, but at least a 5% power conversion efficiency is predicted between the 0.8 $\mu$ m pump wavelength and an output wavelength of 1000 $\mu$ m. Linewidth measurements suggest that 100kHz is an achievable goal and sources of this type will be very useful tunable THz sources, with sufficient power to act as the LO in some heterodyne systems.

## 14. Conclusion and Future Developments

Although much research is still required, Smith-Purcell devices or p-Ge lasers seem the most promising sources of tunable radiation with significant power at frequencies above 1THz. The advantages of Smith-Purcell sources are that, like FELs, there is no fundamental restriction to the operating frequency, CW operation has been demonstrated and they are room-temperature devices. Even at this early stage of their

development the output power is orders of magnitude higher than that from a mercury arc and it should soon be a compact competitor to synchrotrons as a long wavelength source for spectroscopy. We hope that further research will lead to a narrow linewidth electron beam source for frequencies above 1THz, where BWOs do not operate.

The p-Ge laser seems relatively close to becoming a valuable source in the difficult region of 1-4THz. A compact tunable source is needed in this frequency range as an LO in high resolution spectroscopic systems for pollution monitoring. The next generation of mixers for these frequencies seems likely to be helium-cooled electron bolometers requiring LO powers of 10s of  $\mu$ W. A compact structure of p-Ge laser and bolometer can be envisaged.

It does not seem likely that conventional diode lasers will be produced for frequencies much below 10THz, as there has been negligible progress in the past twenty years. Quantum semiconductor structures [18] probably offer the best hope for designing solid-state tunable lasers in the gap between diode lasers and the shortest wavelength of the p-Ge laser.

## 15. References

- [1] G P Williams *Rev Sci Instrum* **63**, 1536 (1992)
- [2] H P Röser *Infrared Phys* **32**, 385 (1991)
- [3] R Titz et al *Infrared Phys Technol* **36**, 883 (1995)
- [4] T M Goyett et al *Appl Phys Lett* **67** 3810 (1995)
- [5] T Idehara et al *Proc of 21st Int Conf on IR and MM Waves* (ISBN 3-00-000800-4) Berlin (1996)
- [6] C Pellegrini et al *Nucl Instr and Meth A* **331**, 235 (1993)
- [7] G Ramian *Nucl Instr and Meth A* **318**, 225 (1992)
- [8] S J Smith and E M Purcell *Phys Rev* **92**, 1069 (1953)
- [9] M Goldstein, J E Walsh, M F Kimmitt, C L Platt and J Urata *Appl Phys Lett* (in the press)
- [10] E R Brown et al *Appl Phys Lett* **58**, 2291 (1991)
- [11] E Bründermann et al *Appl Phys Lett* **68**, 2075 (1996)
- [12] E Bründermann and H P Röser *Infrared Phys Technol* (accepted for publication)
- [13] S Han, B Bi, W Zheng and J E Lukens *Appl Phys Lett* **64**, 1424 (1994)
- [14] M A Piestrup, R N Fleming and R H Pantell *Appl Phys Lett* **26**, 418 (1975)
- [15] G A Blake et al *Rev Sci Instrum* **62**, 1693 (1991)
- [16] J R Fontana and R H Pantell *Proc IRE* **50**, 1796 (1962)
- [17] E R Brown, K A McIntosh, K B Nichols and C L Dennis *Appl Phys Lett* **66**, 285 (1995)
- [18] J Faist et al *Science* **264**, 553 (1994)

# Implication of DC Space Charge Induced Velocity Spread on Gyrotron Gun Performance

C.B. Liu and T.M. Antonsen Jr.

Institute for Plasma Research, University of Maryland, College Park, MD 20742, USA

**Abstract** The confinement of mirror trapped electrons under the influence of DC space charge and their effect on the velocity distribution in a Magnetron Injection Gun are studied analytically and numerically.

An important issue in the design of magnetron injection guns (MIG's) is the spread in transverse velocities of the beam emerging from the gun. A major cause of velocity spread is the presence of a spatially inhomogeneous, steady, self electric field which preferentially accelerates and decelerates electrons depending on their gyro-phase [1,2]. A consequence of the spread in velocities is that electrons with high transverse momenta can be reflected at the magnetic field maximum and travel back and forth between it and the cathode. These trapped electrons can further degrade the quality of the electron beam [3].

Previously, we investigated the limitation of the life time of such trapped electrons due to pitch angle scattering by the spatially inhomogeneous electric field [4]. It was found that the lifetime of most electrons was limited to a score of bounces by this effect. However, some electrons become very deeply trapped due to pitch angle scattering and these electron have extremely long lifetimes. Absent other mechanisms to remove deeply trapped electrons, they would soon come to dominate the space charge in the gun.

In this paper we investigate two aspects of the role of trapped electrons in a MIG gun. First, the limitation in the confinement time of trapped electrons due to azimuthally nonsymmetric fields is studied. We find that even a small azimuthal asymmetry in the beam density provides sufficiently large radial  $E \times B$  drift velocity to carry electrons to the modulation anode after about 50 - 100 bounces. This is illustrated in Fig. 1 where the bounce points of an electron in the transverse plane at the axial position of the mod-anode of a MIG corresponding to that used in the MIT 170 GHz gyrotron [5] are presented. In the figure, the solid circle represents the mod-anode,

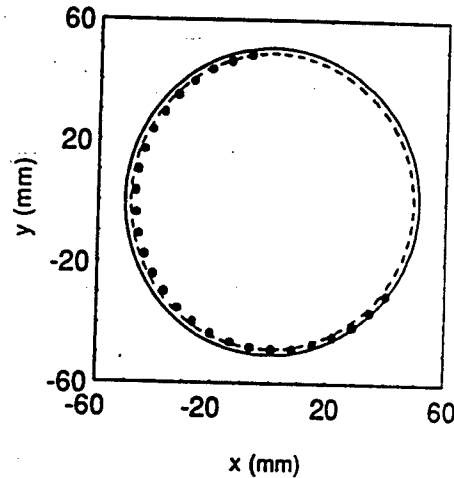


Fig.1 The azimuthal drift and radial excursion of bouncing electrons.

and dashed circle represents the radial position of the electrons emitted from the cathode. Ideally, trapped electrons will drift only azimuthally along the dashed circle. However, any azimuthal inhomogeneity in the current will cause radial excursions to occur. Calculation shows that trapped electrons will gain radial displacements large enough to hit the mod-anode after several dozens of bounces even if a small inhomogeneity is assumed. The positions of bouncing electrons after 10 bounces are given by the solid dots in Fig.1, initially these electrons uniformly distributed along the dashed circle. A detailed calculation of this loss effect is presented in a forthcoming paper.

A simulation of the resulting velocity distribution when orbit losses and pitch angle scattering are combined is displayed in Fig.2. The beam distribution function in the gun consists of a group of electrons near the mean perpendicular energy,  $E_{\perp 0} = \mu_0 B/2$ , along with a high perpendicular energy "tail" of electrons. Some of these tail electrons escape the gun by hitting the mod anode, while the others pitch angle scatter and leave through the cavity.

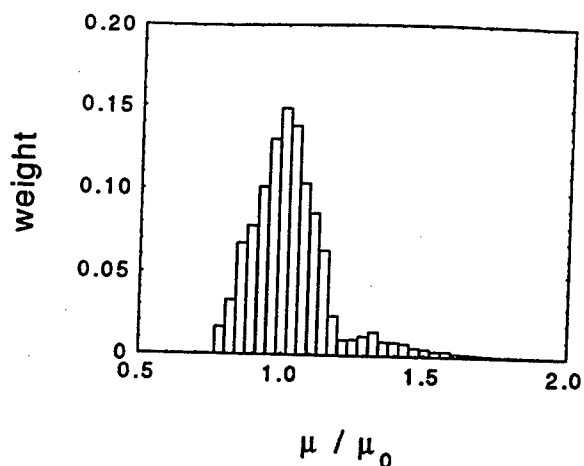


Fig.2 The equilibrium distribution in  $\mu$ , where the initial fraction of reflection is 4.97%.

The number of reflected electrons depends on the mean perpendicular energy, the perpendicular energy spread, and the cavity magnetic field. In the second part of our study we investigate the effect of the space charge of reflected electrons on the properties of the forward beam. To do this, we inject electrons from the cavity and calculate the motion of both forward and injected electrons simultaneously. Here, we let the number of trapped electrons be a parameter and combine our pitch angle scattering model with the particle simulation code EGUN. A typical trajectory plot showing forward and trapped electrons appears in Fig. 3.

The resulting mean perpendicular velocity and the rms spread in the forward beam versus the trapped to forward current ratio is shown in Fig.4. As is clear from the figures, the velocity spread increases with the injected current, and the mean perpendicular momentum decreases. However, for the present design [5] beam properties are essentially unmodified unless the reflected current exceeds the forward current. The dependence of mean perpendicular energy on trapped current ratio is such that reflection process is self limiting [6].

In conclusion, deeply trapped electrons are removed in the presence of asymmetric fields, by striking the mod-anode. Within the present model where all field are steady, a large fraction of trapped electrons is required to modify the beam properties.

This work was supported by the USDOE and ONR.

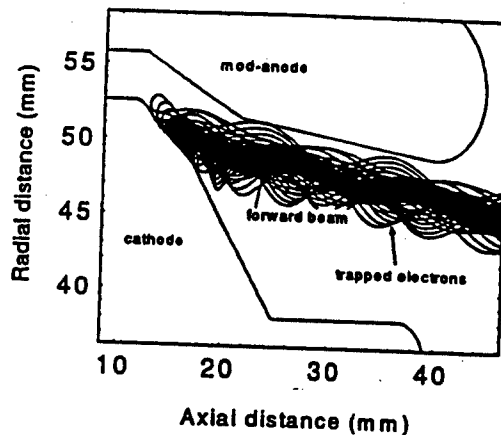


Fig.3 A trajectory plot of forward and trapped electrons in the cathode region.

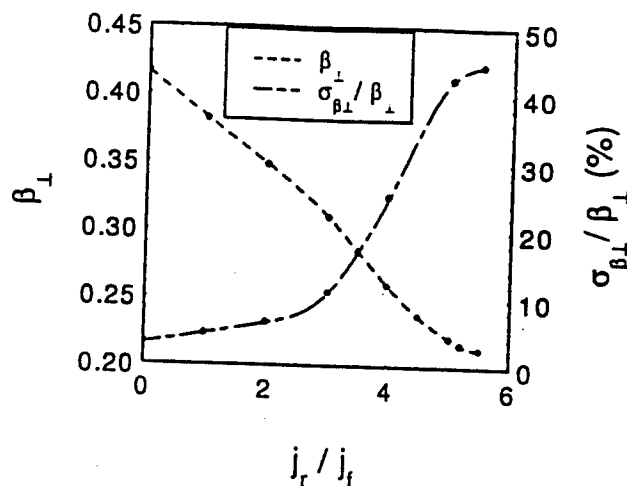


Fig.4 The mean  $\langle \beta_{\perp} \rangle$  and the rms spread  $\sigma_{\beta_{\perp}}$  of the forward beam versus  $j_r/j_f$ .

- [1] J. Neilson, M. Caplan, N. Lopez, and K. Felch, IEDM Tech. Digest, 184-187 (1985).
- [2] C. B. Liu, T. M. Antonsen and B. Levush, IEEE Trans. Plasma Sci. **24**, 982-991 (1996).
- [3] S. E. Tsimring and V. E. Zapevalov, Int. J. Electronics **81**, 199-205 (1996).
- [4] C. B. Liu and T. Antonsen, 21 Int. Conf. IRMW, paper AM12 (1996).
- [5] B.G. Danly, T. Kimura, K.E. Kreischer and R.J. Temkin, 20 Int. Conf. IRMW, paper MA4.
- [6] G.F. Brand, P.W. Fekete, K. Hong, T. Idehara, and T. Tatsukawa, Int. J. IRMW **12**, 89-99 (1991).



## Measurement and Interpretation of Electron Energy Spectra in Gyrotrons

V.L. Bratman, M.Yu. Glyavin, A.L. Goldenberg, A.N. Kuftin,  
A.V. Saviolov, N.P. Venediktov, and V.E. Zapevalov

Institute of Applied Physics RAS, GYCOM Ltd.  
46 Ulyanov St., Nizhny Novgorod, 603600, Russia

### Abstract

In an experimental gyrotron, especially adapted for measurement of the energy spread in the electron beam, energy spectra are obtained and compared with theoretical estimations. It is shown that even without the RF oscillations, the spread caused by space-charge effects (negative-mass instability) can amount several per cent.

### Introduction

The well-known advantage of the gyrotron is its weak sensitivity to the spread in electron pitch factor. At the same time, due to the dependence of the cyclotron frequency on the relativistic electron energy, the gyrotron is sensitive to a spread in electron energy. Such a spread can be caused in particular by the excitation of parasitic fields, as well as by development of space-charge instabilities in dense beams in the region of the beam formation. Possibly, these reasons can explain some difference between experimental and calculated efficiency in powerful gyrotrons. This work is devoted to measurement of the energy spread in the gyrotron electron beam and to the theoretical explanation of its origin. As the source of the spread, the known space-charge (negative-mass) instability is considered. This instability can provide the convective amplification of perturbations in electron density during the process of the beam formation and motion from the cathode to the cavity. Simultaneously, the spread in electron energy also grows [1-3].

### Experiment

For the measurement of the energy spectrum, the modified analyzer [4], based on the method of the decelerating voltage, is used. The analyser is situated far from the gyrotron cavity, where the guiding magnetic field is very small and, therefore, the longitudinal component of the electron velocity is much larger than the transverse one. About of 1% of the electron current only passes into the analyzer. This allows the measurements of the spread in total electron velocity at operating values of the voltage (tens kV). The dependence of the electron current from the analyzer collector on the decelerating voltage  $I(U)$  is measured, and similar to the velocity spread, the energy spread is characterised by the value  $\delta\epsilon = (U_{01} - U_{09})/U_0$ , where  $U_0$  is the accelerating voltage,  $U_{0,9}$  and  $U_{01}$  are decelerating voltages corresponding to electron currents  $0.9I_{\max}$  and  $0.1I_{\max}$ .

Because the goal of the experiment is the measurement of the initial (before the cavity) energy spread, the excitation of the cavity should be avoided. Otherwise, RF fields could give some additional spread. Thus, the measurements were performed only in the modelling regime, when the electron current, the accelerating voltage and the magnetic field are reduced in accordance with the following relations

$$I_m = I_{op} / k^{3/2}, U_m = U_{op} / k, B_m = B_{op} / \sqrt{k}. \quad (1)$$

where  $k$  is the scale coefficient (in the experiment  $k=10$ ). In this case the unperturbed electron trajectories in the modelling and operating regimes are the same. The parameters of the gyrotron are given in the following table.

	Operating regime	Modelling regime
Frequency, GHz	83	-
Power, MW	1	-
Pulse duration, $\mu$ s	100	100
Voltage, kV	70	7
Maximal current, A	40	1.3
Magnetic field, kGs	30	10

According to the measurements, at a rather high magnetic field  $B \geq 10$  kGs, when practically no electrons are reflected from the magnetic mirror, the energy spectrum is symmetrical (Fig.1, dashed curve). It means that the spread is caused by the energy exchange between electrons. At smaller magnetic fields,  $B < 10$  kGs, due to accumulation of reflected electrons and excitation of parasitic oscillations, there are an additional broadening of the distribution function and a shift of the mean energy (Fig.1, solid curve). The energy spread increases with increase of the current and decrease of the magnetic field (Fig.2). In the modelling regime, corresponding to the operating electron current (near 40A), the spread amounts 4-6% in the region of the analyzer.

### Interpretation of the Experimental Results

One of possible effects, causing the spread in electron energy in the region of the electron beam formation, is the Negative-Mass Instability (NMI), which is induced by the effective attraction of rotating electrons due to the relativistic dependence of the cyclotron frequency on the electron energy and the Coulomb interaction of the charged particles. This leads to the growth of perturbations in electron density and, simultaneously, of the spread in electron energy in the beam in a non-oscillating tube between the cathode and the cavity.

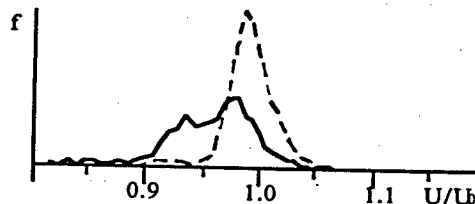


Fig.1. Measured distribution functions over electron energy at small (solid) and large (dashed) magnetic fields.

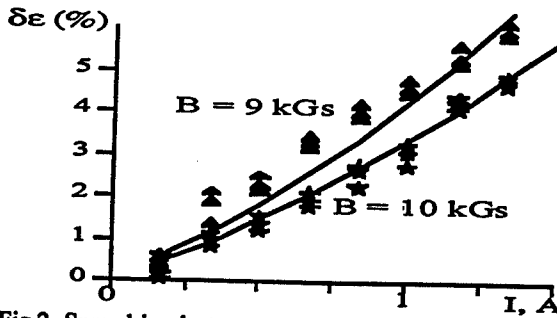


Fig.2. Spread in electron energy versus electron current: experimental results and numerical calculations.

At the linear stage of the instability, the perturbations at different cyclotron harmonics grow independently one on another. For the homogeneous magnetic field, the dispersion in electron energy,  $D$ , (which for the case of the Gaussian distribution is connected with the measured spread as  $\delta\epsilon = 256D$ ) grows with the coordinate,  $z$ , as it follows

$$D_{lin}(z) = \frac{mc^2}{\sqrt{2}eU_0 g_c} \sum_{n=1}^{+\infty} \vartheta_n \Gamma_n \text{sh}(\Gamma_n z / r_c), \quad (2)$$

with the increment  $\Gamma_n = g_c \cdot \sqrt{s L_n}$  [3,2]. Here  $\vartheta_n$  is the level of initial perturbations of the electron density at the  $n$ -th cyclotron harmonic,  $g_c$  is the pitch factor close to the cathode,  $L_n = \frac{4n^2}{\pi(4n^2 - 1)}$ ,  $s = \frac{eI}{mc^3 R_c \pi v_{zc}}$  is the current

parameter,  $r_c$  and  $R_c$  are the Larmor and beam radii close to the cathode. For the ideal beam, the increments  $\Gamma_n$  practically do not depend on the harmonic number. However, the account for initial spreads in velocities and in guiding centres of the electron rotation leads to the fast decrease of the increment with the increase of the harmonic number [2]. Therefore, the fundamental harmonic is the most important. As it follows from Eq.(2), at the fixed voltage the spread increases with the increase of electron current and the decrease of the magnetic field:

$$D_{lin} = A_1 \frac{\sqrt{I}}{B} \text{sh}(A_2 \sqrt{I} z) \approx \frac{A_1}{B} \left( A_2 I z + \frac{A_2^3}{6} I^2 z^3 \right)$$

in the good accordance with the experimental results (Fig.2). At the transition from the modelling to operating regimes, the spread increases:

$$D_{lin}^{(op)}(z) = C_1 k^{-1/2} \text{sh}(C_2 \sqrt{k} z) = D_{lin}^{(m)}(z) + (k-1) C_1 C_2^3 z^3 / 6$$

However, at a rather small distance from the cathode,  $z$ , energy spreads in the both regimes practically coincide.

In the real situation, the magnetic field varies with the coordinate. In this case for the linear stage of NMI the profiling of the magnetic field leads to dependence of the increment on the coordinate due to the two reasons: the variation of "unperturbed" characteristics of the beam (space-charge density, cyclotron frequency, pitch-factor), and the evolution of the spatial structure of the electron density perturbations [5]. The maximal growth of NMI takes place in the region of the maximal magnetic field (Fig.3). As for the maximal possible level of the spread in the saturation stage of NMI, it practically does not depend on the magnetic field profile [5]:

$$D_{sat} \approx \sqrt{s} mc^2 / 2eU_0.$$

(3)

Let us notice, that at the transition from the modelling to the operating regime, the saturated spread decreases,

$$D_{sat}^{(op)} = D_{sat}^{(m)} / \sqrt{k}.$$

For the studied gyrotron, Eq.(3) gives the saturated spread in the modelling regime  $\delta\epsilon \approx 25\%$ , being significantly larger than the measured spread. Therefore, the NMI development has the linear character. In this case the spread depends on the initial level of the perturbations,  $\vartheta_1$ , which can be found by the comparison of numerical calculations and experimental results, and it proves to be independent on the value of the magnetic field (Fig.2). Knowing the value of  $\vartheta_1$ , one can calculate the dependence of the spread on the coordinate (Fig.3) and, therefore, to find the spread at the input of the gyrotron cavity. For the experimental gyrotron, in the both modelling and operating regimes the spread is relatively small:  $\delta\epsilon \approx 1 - 2\%$ . However, the increase of the length of the electron drift from the cathode to the cavity can lead to the increase of the spread up to the saturation value ( $\delta\epsilon = 6 - 8\%$  for the operating regime). Such spread can induce the decrease in gyrotron efficiency about of 5% [6]. The same result can be provided by the increase of the operating frequency, because even at the same length between the cathode and the cavity, the effective length (measured in the reverse NMI increment,  $r_c / \Gamma$ ) increases due to the decrease of the Larmor radius (Fig.3).

Thus, in powerful short-wavelength gyrotrons with long regions of the electron beam formation, negative-mass instability can provide spread in electron energy which decrease the electron efficiency significantly.

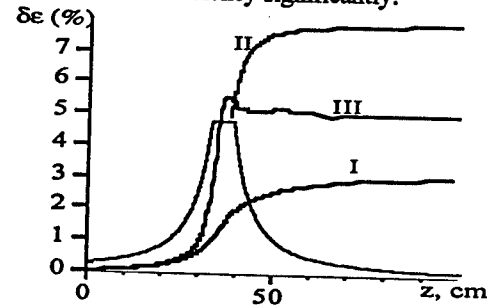


Fig.3. Calculated energy spread and magnetic field approximation versus the coordinate:  $I=1A$ , modelling regime (I);  $I=30A$ , operating regime (II);  $I=30A$ , operating regime for the gyrotron when its frequency is enhanced to 166 GHz (III).

- [1] V.L.Bratman, A.L.Goldenberg, A.V.Savilov. Abstracts of 11th Int. Conf. on High Power Particle Beams (Prague, 1996), P-1-44.
- [2] V.L.Bratman, A.V.Savilov. Phys. Plasmas, 2 (1995) 557.
- [3] V.L.Bratman. Zh. Tekhn. Fiziki, 46 (1976) 2030.
- [4] A.L.Goldenberg. Digest of 19th Int. Conf. on IR and MM Waves (Sendai, 1994) 349.
- [5] A.V.Savilov. Phys. Plasmas, 4 (1997) No.6.
- [6] S.Y.Cai, T.M.Antonsen, Jr., G.Saraph and B.Levush. Int. J. Electron., 72 (1992) 759.

# Study of Helical Electron Beam Properties for Powerful Gyrotrons

A.N.Kuftin, V.K.Lygin, V.N.Manuilov, Sh.E.Tsimring, V.E.Zapevalov

Institute of Applied Physics, Russian Academy of Sciences  
46 Ulyanov Street, 603600, Nizhny Novgorod, Russia

## Abstract

The report presents the results of the numerical simulation and experimental study of the helical electron beam (HEB) formed in magnetron-injection gun of mm waves powerful gyrotron. The dependence of HEB parameters on the beam current is analyzed. The evolution of the transverse velocity distribution functions is traced at the variation of the beam current.

## Introduction

For the creating of powerful high efficiency gyrotrons one of the main problem is the formation of high quality helical electron beams with required parameters. For example achievement of 1MW output power of 70-170 GHz gyrotron with an operating voltage  $U = 80$  kV and the efficiency  $\approx 35\%$  or more is required to a beam with a current  $I \approx 40$  A and a pitch-factor  $g \approx 1.25$  or higher ( $g = v_{\perp}/v_z$ ,  $v_{\perp}$ ,  $v_z$  - oscillatory and longitudinal velocity in operating space). Thus a magnetron-injection gun (MIG) should provide formation of a beam with such parameters.

According to results of numerical simulation and experimental data all possible beam types, forming by magnetron-injection guns (MIGs) have different properties [1,2]. The most promising type for the short millimeter wavelength gyrotrons is the boundary type (intermediate between beams with laminar electron trajectories and regular intersecting ones). The advantage of the specified beam type is very attractive when the operating frequency grows.

Below method and results of investigations of the possible versions of guns for powerful gyrotrons are presented, comparison of calculated and measured parameters of some types of the beam are discussed.

## Improved method of trajectory analysis

To make the detail analysis of the physical processes taking place in the beams with various topology and to find optimize shape of electrodes in MIG, it is necessary to use the improved method of trajectory analysis, in which the trajectory integration up to the operating space and finding the electron distribution function over oscillatory velocities  $f(v_{\perp})$  in various planes is possible. In this case the beam parameters variation may be traced not only vs. beam current, voltage or magnetic field, but in the different positions along the beam, also. The numerical simulations were carried out basing on the model without reflected electrons. Therefore if

some electron is reflected, the integration of corresponding trajectory is stopped. According to experimental data [1] there is significant influence on the beam properties of electrons, reflected from the magnetic mirror and then locked in the adiabatic trap. It may cause essential differences in parameters calculated by static code and measured one. So, a technique taking into account influence of trapped electrons within the framework of non-stationary model was developed also. The definition of parameters of the beam in this method (against [3]) based on a finding of distribution function  $f(v_{\perp})$  from the trajectory analysis.

## Experimental set-up

The experimental study of MIGs of powerful gyrotrons which form intense HEBs of various topologies was performed in the automated set-up using the retarding field method [4] in the scale down regime which conserve trajectory of the electrons. The refined automation experimental set-up permits to define the HEBs characteristics ( $t_{\perp}$ ,  $\delta v_{\perp}$ ,  $f(v_{\perp})$ , etc.). Here  $t_{\perp}$  - ratio of the oscillatory energy to the total one and  $\delta v_{\perp}$  - velocity spread. The application of this system allows to increase the accuracy and the quality of measurements, to obtain and process a large volume of the experimental data for a short period of time. The measurements of electron beam properties can be performed as well at presence of electrons, caught in adiabatic trap between the cathode and magnetic mirror, as at exception such electrons. So the experimental set-up allows to investigate the perturbation of the HEBs properties due to the presence of the caught electrons (CE).

## Results of numerical simulation and experiments

The results of a new numerical simulation procedure and experimental data for the basic types of beams with various topologies are presented. For each beam type the dependences  $t_{\perp}$  and  $\delta v_{\perp}$  on the beam current were received, including results in the model with zero initial velocities. It was found, that there are the small differences between the data obtained from numerical simulation on full formation length and the ones find out from calculation in the cathode region only. The received distinctions are caused by different value of the beam potential, used at the finding  $t_{\perp}$  and  $\delta v_{\perp}$ . According to results of the trajectory analysis, the value of the potential depression in the beam is rather close to the theoretical estimations [5]. Evolution of  $f(v_{\perp})$  for each beam type

along the formation region and when the current grows was traced.

Numerical simulation was performed for powerful gyrotrons in the wide frequency range (70-170 GHz). The allowable value of the cathode radius for a chosen operating mode is defined by the value of an acceptable electrical field on the cathode  $E_c$ , which, as a rule, is necessary not above than 6 kV/mm. Width of the emitter is selected with the account of extreme allowable density of an emission current (usually it is not recommended to exceed 3 A/cm<sup>2</sup>). At selection of an optimum configuration of electrodes the value of velocity spread  $\delta v_{\perp}$  was not allowed above than 30%. The specified restrictions were accepted in attention at account of particular guns for gyrotrons with different operating modes. Then from numerical simulation dependencies  $\delta v_{\perp}(I)$  and  $t_1(I)$  for each gun were received. Calculations were performed as using model with zero initial velocities (EPOSr [6]) as taking into account initial velocities (EPOS-V [2]). Evolution of transverse velocity distribution function  $f(v_{\perp})$  is traced with a beam current growth. The sensitivity of the beam parameters to influence of thermal deformations of a gun and possible technological errors is investigated. The transformation of  $f(v_{\perp})$  can serve one of attributes of loss of beam stability [2]. In considered guns infringement unimodality of oscillatory velocity distribution function was not registered at currents of a beam, even exceeding design value of the current ( $I=40$ A). The specified circumstance allows to hope, that offered MIG will provide formation of a stable beam with acceptable parameters.

In particular, for a 170GHz gyrotron some versions of the gun for different operating modes were designed. For the TE<sub>31,8</sub> mode of in the considering limitations on an electrical field  $E_c$ , optimum radius of the cathode is  $R_c \approx 51$ mm. Thus electrical field on the cathode is  $E_c \approx 5.8$  kV/mm. For gyrotron with an operating mode TE<sub>28,7</sub> two versions of guns with different radiuses of cathode were designed. In the first version a gun with  $R_c = 45.2$ mm was used. The necessary  $g$  value need an increased electrical field on the cathode  $E_c \approx 6.3$  kV/mm. In the second variant the reduction  $E_c$  to 5.5-5.7 kV/mm was reached by using of the cathode with increased average emitter radius ( $R_c = 47.5$ mm). Finally for the operating TE<sub>25,10</sub> mode  $R_c = 41.5$  mm was chosen. For all gun variants dependencies  $\delta v_{\perp}(I)$  and  $t_1(I)$  and evolution  $f(v_{\perp})$  were investigated at presence of the disturbing factors also.

The measurements were carried out for guns with  $R_c = 45.2$ mm and  $R_c = 41.5$ mm in a scale down regime as at presence of electrons, caught in adiabatic trap between the cathode and magnetic mirror, and at exception such electrons. Fig.1 show measured dependencies  $f(v_{\perp})$  at exception CE for the gun with  $R_c = 45.2$ mm.

The received dependencies  $\delta v_{\perp}$  and  $t_1$  are compared with results of numerical simulation and good correlation is observed.

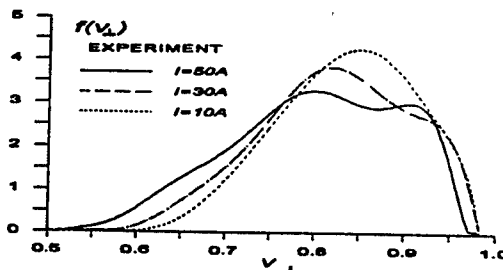


Fig.1. Measured dependencies  $f(v_{\perp})$ .

### Preliminary results of non-stationary simulation

In order to decrease the calculation time, the numerical simulation of non-stationary processes in HEB formation systems with taking into account the CE was performed for the 25 GHz gyrotron operating on the second cyclotron harmonic. The MIG with laminar flow was investigated. The behavior of the distribution function  $f(v_{\perp})$  as well as  $t_1$  and  $\delta v_{\perp}$  parameters as current time functions are presented. The value of emitter electric field depression caused by CE and the distribution of the CE space charge were studied. The energy of electrons bombarded the cathode and the zone of bombardment are found. The comparison of dependencies  $\delta v_{\perp}(I)$  and  $t_1(I)$  calculating from stationary and non-stationary models are presented.

### Conclusion

Methods of numerical simulation and experimental research of HEB were developed. HEBs properties including the electron distribution functions over transverse velocities were studied numerically and experimentally in various regimes. In result of numerical simulation and series of experiments an electron gun, ensuring formation of an electron beam with parameters, necessary for 170 GHz/1MW gyrotron, is created.

### Reference

- [1]. Kuftin A.N., Lygin V.K., Tsimring Sh.E., Zapevalov V.E. Int. J. Electronics, v. 72, nos. 5 and 6, p.1145, 1992.
- [2]. Lygin V.K. Int. J. of Infrared and MM waves, v. 16, n.2, p.363, 1995.
- [3]. Raisky B.V. and Tsimring Sh.E. IEEE Trans. on Plasma science, v.24, n.3, june 1996, pp.992-999.
- [4]. Avdoshin E.G. and Gol'denberg A.L. Izvestiya Vysshikh Uchebnykh Zavedenii, Radiofizika, 16(10), p.1605, 1973.
- [5]. Tsimring Sh.E. Int. J. of Infrared and MM waves, v. 14, n.4, p.817, 1993.
- [6]. Lygin V.K., Manuilov V.N., Tsimring Sh.E. Elektron. tekhnika, ser.1, Elektronika SVCH, n.7, p.38, 1987.
- [7]. Flyagin V.A., Goldenberg A.L., and Zapevalov V.E. Conference Digest, 18 Int. Conference on IR & MM Waves, 6 - 10 September, University of Essex, Colchester, U.K., v.2104, pp.581-584, 1993.

## A New Algorithm for Tracing Back-scattered Electrons

Amarjit Singh, Sanjaya Rajapatirana and Victor L. Granatstein  
Institute for Plasma Research, University of Maryland, College Park, MD, 20770

### Abstract

An algorithm has been designed to give a good representation of experimental/simulation data in the modeling of back-scattered electrons in vacuum devices, while limiting the number of trajectories to be traced. Monte-Carlo techniques are applied for allocating the type of process, the energy and the emergent angle of each ray. Insertion of ad-hoc parameters is avoided.

### Introduction

Primary electrons striking the surface of an electrode, generate backscattered electrons. They fall into the categories of a) true secondaries, b) inelastically scattered primaries and c) elastically scattered primaries. The coefficient of total backscatter and the coefficients for individual processes depend upon the energy and incident angle of the primaries, as well as the nature of the electrode material and its surface. In starting the trajectories of back-scattered electrons, the statistics of energy and the angular spread have to be taken into account.

In modelling backscatter, a number of backscattered rays per primary ray would normally be needed in order to simulate the variety of energy and angles of emergence. With multiple generations of backscatter, the number of rays to be traced can rapidly increase to unmanageable proportions. How to retain the representative nature of the model while keeping the number of backscattered rays within reasonable limits is a significant problem.

While some devices such as photo-multipliers and CFA's turn the phenomenon of backscatter into use, in other cases such as design of depressed collectors, the effects of backscatter need to be minimized. The returning electrons would absorb back some energy from the electrostatic field and thus reduce the collector efficiency. It is necessary to trace the trajectories of backscattered electrons in order to evaluate the decrease in collector efficiency or of rf efficiency caused by any electrons returning to the interaction region.

In devices such as CFA's the coefficient of back-scatter needs to be very precisely defined, as any error can multiply in multiple generations of back-scatter. On the other hand in the case of depressed collector design the angles of emergence of the back-scattered rays acquire greater importance. The number of generations are fewer but where the back-scattered rays end up is of significance. Consequently the approximations to be used may well be different for the two kinds of applications. In this paper

consideration has been given to improved representation of the angle of emergence and the energy of the back-scattered electrons, keeping in view the needs of depressed collector design.

It is common practice in the design of computer codes for tracing the trajectories of back-scattered electrons to specify in advance the number and the parameters of the backscattered rays to be generated by each primary ray. (e.g., Ref. 1,2). Such a restriction is avoided in the new algorithm.

An outline of the new algorithm and its features is presented.

### The algorithm

- \* Evaluate for each primary ray, the angle of incidence. Taking that and its energy into account evaluate the total coefficient of backscatter. We have used the formulas developed by J.R.M. Vaughan, Ref. [3,4], which take into account the above parameters as well as the nature of the electrode and its surface.

- \* Evaluate the total backscatter current for each ray. Reorder them in increasing values and truncate the ones with the smallest current totalling upto a specifiable small percentage 'P' of the total primary current.

- \* Divide each backscattered ray into sub-rays whose number is proportional to the current in that ray. This mimics the natural process but increases the number of sub-rays at this stage in a ratio 'm'. The value of 'm' can be chosen larger or smaller depending upon the degree of accuracy required in the statistical modelling of the process. It may be mentioned here that the number of rays is brought down again in a subsequent step when the sub-rays are coalesced to form composite rays. The sub-rays all have equal current. This introduces a quantization error. This and the effect of truncation in the previous step are taken into account in the next step, which is renormalization.

- \* Renormalize the total current in the sub-rays to equal original total of back-scattered current.

- \* Using Monte Carlo techniques allocate to each sub-ray a process of back-scatter using probability ratios derived from experimental/simulation data. Using the same technique associate with each sub-ray an energy value and an emergent angle.

- \* Put sub-rays into bins which have indices according to energy and angle for locations on the collector surface divided into strips of specified width. This width decides the resolution, which can be kept coarse in the initial stages of a design and increased in later stages.

- \* Sum the current in bins and truncate the ones with the smallest current totalling upto a specified small percentage of the total primary current. Renormalize the current.

- \* Formulate the backscattered rays according to the remaining

bins, their associated locations and the accumulated current in each. This process of going back from sub-rays to composite rays, together with the truncation in the previous steps would keep down the number of rays to be followed in trajectory tracing. We have observed that this process can more than compensate for the increase which took place when going from rays to sub-rays.

\* Simulate the trajectories of the ensemble of primary and secondary rays, using a ray tracing code (eg. EGUN [Ref 5]). Iterate for a specified number of generations or till all the new rays have fallen below a threshold value of a cumulative total. Tracing the entire ensemble each time would avoid error in solution that could otherwise be caused, as the space charge of the secondaries influences that of the primaries and vice-versa.

### The Flow Chart

A flow chart of the algorithm is shown in Fig. 1. Diagnostics are added so that the user has the option of watching the progress of the simulation. At each step graphs are generated so that the range of values of current for individual rays, their incident angles, and coefficients of back-scatter can be monitored. This would be of particular value in the initial stages of a new project. Examples of graphs obtained at various steps will be presented. The code is being developed with a Graphic User Interface. Buttons are provided for choosing various steps of the process one by one, or doing them in sequence automatically.

### Conclusions

An algorithm has been presented which follows a natural course of mimicing the process of backscatter. At each stage the most significant rays and processes are retained. The coarse or fine-grained nature of the simulation can be adjusted as required. In the initial stages estimates that are quickly obtained for comparing various alternatives may be adequate. A flexibility to zoom-in for more and more precise simulation is a built-in feature of the algorithm.

### References

1. D.J. Ferretti, "Development of a dynamic secondary emission model for use in MDC simulations", Technical Report AFTER-19, University of Utah, (1986).
2. J. Petillo, "EGNSEC2, Report and Users Guide for Secondary Modifications to EGUN", SAIC, (1988).
3. J.R.M. Vaughan, "A new formula for secondary emission yield", IEEE Trans. ED- 36, pp 1963-1967, (1989);
4. J.R.M. Vaughan, "Secondary emission formulas", IEEE Trans. ED-40, p. 830, (1993)
5. W.B. Herrmannsfeldt and G.A. Herrmannsfeldt, User Manual for EGUN, (1993), and addendum (1996)

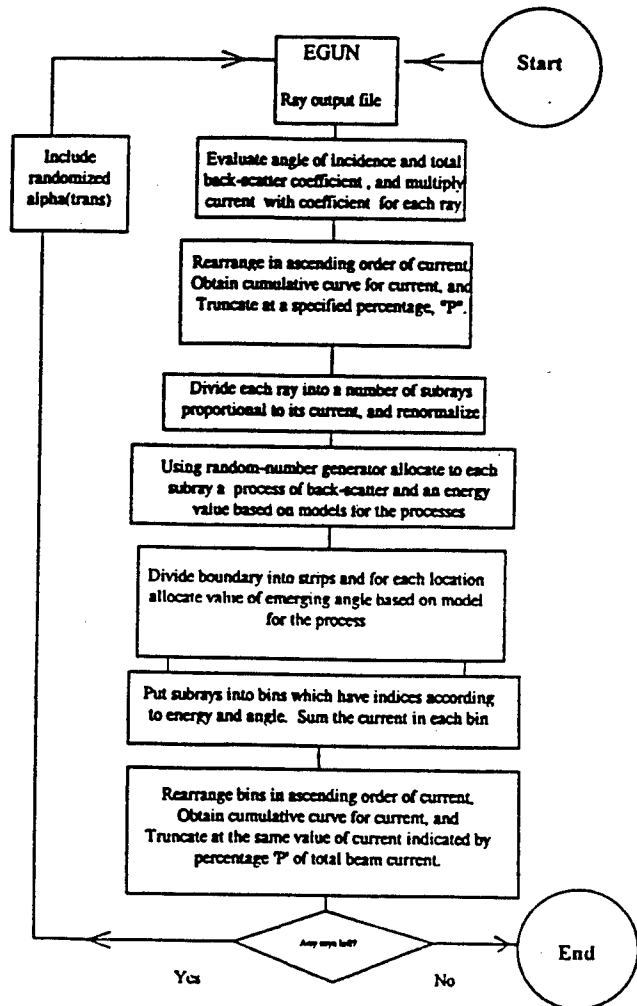


Figure 1. Flow chart for the algorithm for tracing trajectories of backscattered electrons.

# Experimental and Simulation Study of the Thermal Characteristics of a MIG-Type Electron Gun for a 32 GHz, 100 kW Gyrotron

H. Patire Jr. and J.J. Barroso  
Laboratório Associado de Plasma  
Instituto Nacional de Pesquisas Espaciais  
12227-010 - São José dos Campos, SP - Brasil

## Abstract

A thermal study of a MIG-type electron gun has been made to determine the temperature distribution in all the gun elements as a function of the input heater power. Appropriate materials were selected to minimize both the conduction and radiation thermal losses. The gun produces a 5 A50 kV laminar electron beam with the cathode emission ring operating at an average temperature of 1000°C with 346 W input power in the heating filament system. The purpose of the present study is to reduce the input heater power while keeping the required operating cathode temperature and to improve the gun design from a constructional point of view aiming at extending the capabilities of the electron gun. A thermal software has been used by considering the operation conditions taking into account external convection by forced air on the ceramic shells and thermal radiation transfer between the electrodes of the gun.

## Introduction

The INPE gyrotron gun (Fig. 1) is of the magnetron injection type with a triode configuration. Vacuum tight rippled ceramic shells are used to insulate electrodes from the UHV flanges. Since the cathode should operate at a temperature close to 1000°C, the choice of materials for its construction is limited. As for the requirements of mechanical strength and low vapour pressure at high temperature, a material of low emissivity and poor thermal conductivity is needed to reduce heater power losses. The most suitable materials with such properties are the refractory metals. The pure molybdenum on nickel was selected for the emitting band. Titanium was selected for the first anode and flanges as its thermal expansion coefficient is nearly equal to that for ceramic over the range of temperatures to which the seal is exposed during sealing and operation. The heater (Fig. 2) is a toroidal coil made of a 0.5-mm-diameter tungsten wire.

## Thermal Modeling Results

The gun system is azimuthally symmetric with all the elements being sufficiently thin so that one-dimensional heat conduction is assumed. Temperature is calculated at each

point of an irregular finite element mesh having 316 grid points (Fig. 3). In our simulation, heat exchange by forced convection with air from the external surface at a prescribed surrounding temperature and the stipulation of the filament temperature have been used as boundary conditions for the heat-transfer problem<sup>(1)</sup>.

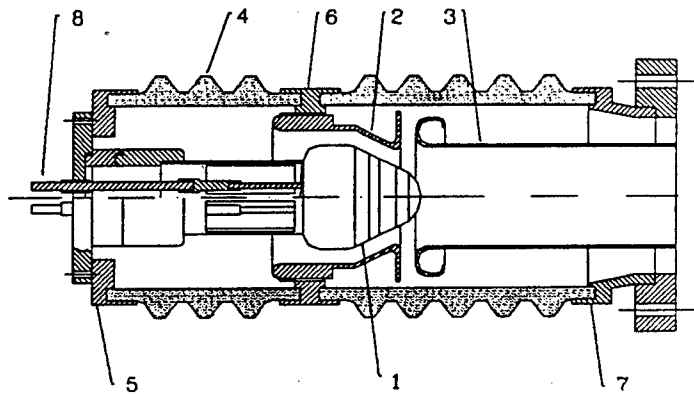


Figure 1: Longitudinal view of the electron gun:  
1-Cathode, 2-First anode, 3-Second anode,  
4-Ceramic shell, 5-Bottom flange,  
6-Intermediate flange, 7-Upper flange,  
8-Filament lead.

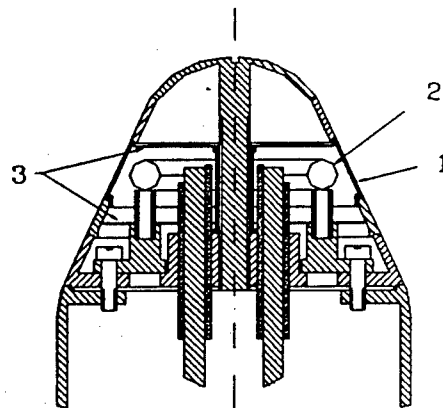


Figure 2: Heater assembly details:  
1-Emitting Band, 2-Toroidally-wound filament,  
3-Reflecting surfaces.

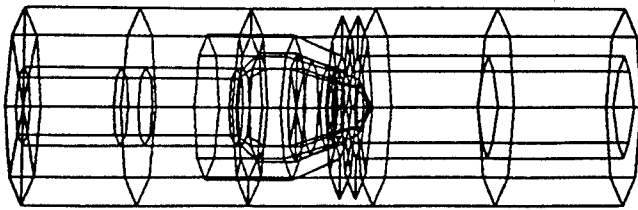


Figure 3: Finite element mesh for simulation of MIG-type gun.

Results of the simulation so far performed are given in Table 1. Columns A and B refer, respectively, to measured and predicted data corresponding to the gun using the molybdenum substrate, while column D lists the predicted temperature of the gun elements taking into account a nickel emitting strip.

Table 1: Measured temperature ( $^{\circ}\text{C}$ ) of the gun elements and numerically predicted temperature in various circumstances

	A	B	C	D	E
Filament	1811	1750	1590	1750	1590
Emission Band	1032	1012	1000	996	1003
First Anode	460	564	485	497	422
Bottom Flanges	69	70	55	64	51
Inter. Flanges	72	71	58	64	52
Upper Flanges	42	51	42	46	39
Surrounding Air	24	24	24	24	24
Input Power (W)	374	350	199	350	199

- A - Experimental data
- B - Simulation using a molybdenum strip
- C - Simulation using a molybdenum strip conductively uncoupled from the cathode body
- D - Simulation using a nickel strip
- E - Simulation using a nickel strip conductively uncoupled from the cathode body

As the thermal conductivity and emissivity coefficients for nickel are both lower than for molybdenum, the energy lost from the emitter to the neighbouring electrodes is reduced accordingly. Thus, as shown in Tab. 1, the replacement of molybdenum by nickel yields a decrease of 10% in the steady-state temperatures of the external flanges, in addition to reducing the temperature of the first anode by a 14% factor.

If any contact area between molybdenum strip and the cathode body is eliminated (column C), then the input heater power is lowered from 350 to 199W while keeping the emitter temperature at around  $1000^{\circ}\text{C}$ . Also, by comparing columns B and C, we observe that the temperature of the inside surface of the first anode is reduced by a 20% factor. If we consider instead a nickel emitting band separated from the cathode by a small gap, we see in column E that the temperature values of the external flanges and the first anode are farther reduced by a 35% factor, leading to a 75% decreasing in the input power.

In conclusion, the thermal and mechanical properties of a MIG-type gun have been examined numerically and also experimentally. The numerical code used was able in handling a problem with complex geometry as numerical predictions are in good agreement with experimentally measured data. Important design features of our gun have been clarified and forthcoming studies will consider unsteady problems by using a higher-density finite element mesh.

## Reference

- [1] H. Patire Jr. "Convective and Conduction Heat Transfer Study of a MIG-Type Electron Gun", (in Portuguese), MSc, Thesis, Aeronautical Technological Institute, S.J. Campos, SP, Brazil, April 1997.



## The First Experiments on an 84GHz Gyrotron with a Single-Stage Depressed Collector

T. Shimozuma, M. Sato, Y. Takita, S. Ito, S. Kubo, H. Idei, K. Ohkubo, T. Watari,  
T. S. Chu<sup>1</sup>, K. Felch<sup>1</sup>, P. Cahalan<sup>1</sup> and C. M. Loring, Jr<sup>1</sup>

National Institute for Fusion Science  
322-6, Oroshi-cho, Toki-shi, Gifu, 509-52, Japan  
1) Communications & Power Industries, Inc.,  
811 Hansen Way, Palo Alto, CA 94303 U.S.A.

### Abstract

We fabricated and tested an 84GHz gyrotron with a single-stage depressed collector. The gyrotron has a high-voltage insulating section made of a low loss silicon nitride composite. In this preliminary experiment in the depressed collector configuration, we obtained 591kW, 41% operation with a depression voltage of 22.5kV. Access to the higher efficiency region was inhibited by an increase in anode current

### Introduction

High power, long pulse gyrotrons have succeeded in stable operation with a single-stage depressed collector[1,2]. The energy recovery of the spent electron beam by the depressed collector leads not only to an improvement in total output efficiency, but a reduction of the power loading and X-ray generation at the collector. When considering of pure CW high power gyrotrons, these merits are very attractive.

We have been developing an 84GHz CW gyrotron in collaboration with CPI for use as the power source in the ECRH system on LHD (Large Helical Device). Based on the previous success of the 84GHz CW gyrotron[3], we newly fabricated a gyrotron which has the same RF circuits, electron gun, and mode converter, but equipped with a depressed collector and larger Vacion pumps.

In this report, we describe the first experimental results of the 84GHz gyrotron in the depressed collector configuration.

### 84GHz gyrotron with a single-stage depressed collector

The 84GHz gyrotron has the same RF circuits, electron gun, built-in mode converter, and output window as the gyrotron which achieved 500kW-2sec., 400kW-10.5sec., 200kW-30sec., and 100kW CW operation. The oscillation mode in the cavity is TE<sub>15,3</sub>, and the built-in mode converter system consists of a modified Vlasov launcher with visor and beam shaping mirrors. The output window is a sapphire double-disk window cooled by FC-75. A photograph of the gyrotron is shown in Fig. 1.

This gyrotron has been improved for high power CW operation: almost all parts of the body and collector sections are water-cooled, and two large 75 liter/second Vacion pumps improve the evacuating speed in

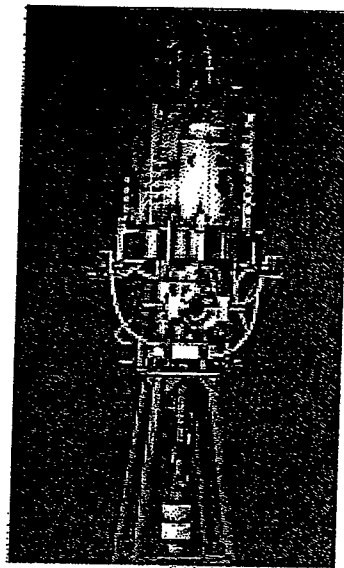


Figure 1 84GHz gyrotron with a depressed collector

the tube. The most remarkable difference is the addition of a high voltage insulating section between the body and the collector to be able to apply the retarding potential for the energy recovery of spent electrons.

The insulating section is made of a silicon nitride composite which has a low loss-tangent in the millimeter wave range[4]. Heat generation in this material can be reduced to less than one-third, compared with the usual alumina material. During CW operation, RF leakage from the insulating section is significant even though it is only a few percent of the output power. So the insulating section includes a cooling jacket which will allow lossy oil flow to cool the ceramic and absorb leaking RF.

### Preliminary depressed collector experiments

Preliminary experiments were performed at the test set at CPI. During the first stage of gyrotron aging (normal operation without the retarding potential) the gyrotron achieved a maximum output power of 639kW and efficiency of 32% at beam voltage of 80kV and beam current of 25A for short pulses. During the normal operation, the insulating section was cooled by pure water so that power from RF leakage could be measured calorimetrically. It was about 0.7-1% of the total output power.

Since the gyrotron test set at CPI is not designed for depressed collector operation, a portable tetrode system was connected between the collector and grounded body to provide

the depressed collector potential[5]. The test circuit is illustrated in Fig. 2. By adjusting the screen grid voltage of the tetrode, we were able to set the collector potential relative to the grounded gyrotron body. This system was only capable of operating at 0.5ms pulsewidth.

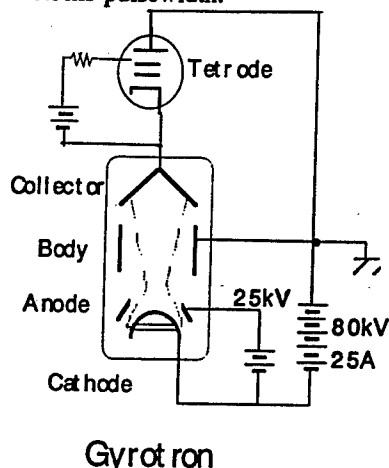


Figure 2 Circuit for depressed collector experiments

Figure 3 shows the dependence of the total oscillation efficiency on the depressed voltage for several beam current operations. At each point, the main accelerating voltage (potential difference between cathode and body) was set at 80kV, and the magnetic field and the anode voltage were optimized. For all beam current values, efficiency gradually increased as depression voltage was increased, until anode current was observed. Increasing the depression voltage beyond this point resulted in a drop in efficiency. Increased efficiency was due to energy recovery; the output power actually remained constant or decreased slightly as voltage depression was increased. The highest efficiency achieved was 41.5% at 25kV of depression and 20A of beam current. At this point, output power was 475kW.

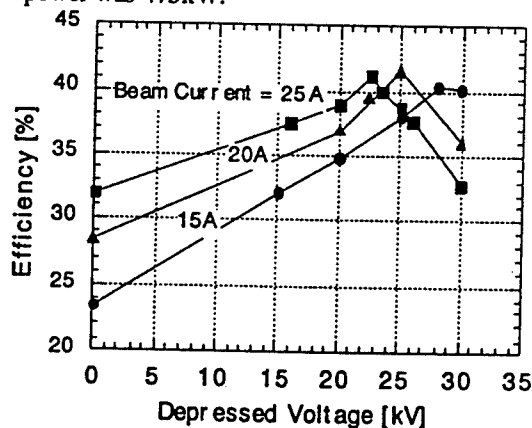


Figure 3 Total output efficiency is plotted as a function of depressed voltage for several beam currents

Figure 4 shows the oscillation mode map for the beam current of 25A. Oscillation regions of the main mode (TE<sub>15,3</sub>) are plotted for values of anode voltage and cavity coil current. In the figure each bounded area corresponds to the oscillation region with the application of the depressed voltage indicated. The maximum output power values obtained for each depressed voltage are also indicated in each region. This map illustrates the degradation of the oscillation efficiency at

higher depressed voltages. When the depressed voltage increases, the anode voltage corresponding to the anode current onset decreases, and the region shrinks to the lower anode voltage and higher magnetic field side. As a result, the gyrotron could not be operated in the higher efficiency region.

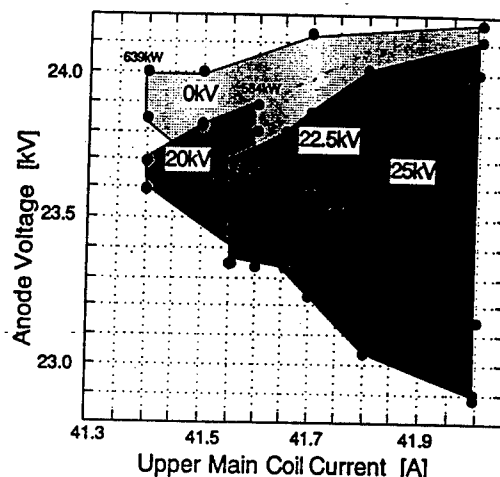


Figure 4 Oscillation mode map for depressed voltage of 0, 20, 22.5, 25kV

This tube is now being aged at the NIFS test set to obtain several hundred kilowatts CW without depression. Long pulse testing in the depressed collector configuration will be conducted in near future.

## Summary

We fabricated and made preliminary tests of an 84GHz gyrotron with a single-stage depressed collector. The gyrotron has a high-voltage insulating section made of a low loss silicon nitride composite. Leakage RF from the insulating section was measured to be 0.7-1% of the output power. In this preliminary experiment in the depressed collector configuration, we obtained 591kW, 41% operation with a depression voltage of 22.5kV at a beam current of 25A, in contrast with 32% without retarding voltage. Access to the higher efficiency region was inhibited by the anode current increase.

## References

- [1] K. Sakamoto, M. Tsuneoka, et al., Phys. Rev. Lett., 73(1994)3532-3535.
- [2] B. Piosczyk, C. T. Iatrou, et al., IEEE Trans. on Plasma Science 24(1996)579-585.
- [3] M. Sato, T. Shimoizuma et al., Conference Digest of the 20th International Conference on Infrared and Millimeter Waves, Orlando, Florida, December 11-14, 1995 T4.3, pp195-196.
- [4] T. Shimoizuma, M. Sato, et al., Conference Digest of the 20th International Conference on Infrared and Millimeter Waves, Orlando, Florida, December 11-14, 1995 T8.3, pp273-274
- [5] R. L. Ives, H. R. Jory, et al., IEEE Trans. on Electron Devices, 40(1993)1316-1321.

# Design of a Multi-Stage Depressed Collector for a 1 MW CW Gyrotrons

R. Lawrence Ives, Y. M. Mizuhara, R.S. Schumacher,  
Calabazas Creek Research, Inc., 20937 Comer Drive, Saratoga, CA, USA

A. Singh, S. Rajapatirana, V. Granatstein,  
Laboratory for Plasma Research, University of Maryland, College Park MD, USA

## Introduction

For a number of current and anticipated fusion experiments, such as ITER, high-efficiency gyrotrons will be required for electron cyclotron heating and current drive[1]. Gyrotron electronic efficiency is typically in the range of 30-35%, which means that the total electrical power required for the electron beam is on the order of 3 MW for 1 MW of RF power. After extraction of microwave power from the beam, the remaining power, approximately 2 MW, is deposited in the collector as thermal energy that must be removed and dissipated using large heat exchangers.

In this paper, we describe a two-stage depressed collector capable of recovering approximately 70% of the incident power in the spent beam. The collector was designed for a 110 GHz gyrotron; however, only minor modifications are required for operation at 170 GHz.

The collector design increases the efficiency of the gyrotron to more than 60%. This increased efficiency results in a 45% reduction in the electrical capacity requirement and power from the grid. As a result, the cost of capital equipment and electrical company resources is substantially reduced. This cost is incurred regardless of how much the tube is operated, and is expected to increase in the next 5-8 years.

With the design described here, the heat dissipation is reduced from 2 MW to 800 kW. This reduction in thermal load reduces the amount of thermal power that must be removed and externally dissipated, thus reducing the cost of pumps, plumbing, cooling towers and/or heat exchangers, and the associated operating costs. It also reduces thermal stress and tube processing, resulting in lower costs and a more robust gyrotron.

## Beam Optics Design

The design of collector electrodes and the magnetic circuit was performed using a library of codes developed at the Institute for Plasma Research[2]. The code ProfileM was employed to design a magnetic field configuration providing a blend of adiabatic and non-adiabatic transitions for the electrons travelling in the collector region. This field, in conjunction with the electrostatic field created by the collector stages, sorts the electrons according to their energy values.

ProfileM also provides contours of effective potential, making it possible to visualize regions of the collector accessible to electrons of specific energy[3]. In this way the electric and magnetic fields are tailored to ensure that no electrons are turning back before reaching a collector stage.

Figure 1 shows a composite diagram of the contours of effective potential, the magnetic flux, and the trajectories against the backdrop of collector geometry. The beam is collected at two electrodes. A third electrode near the axis helps shape the electric field, and is kept at the same potential as the first collector electrode to simplify the power supply requirement.

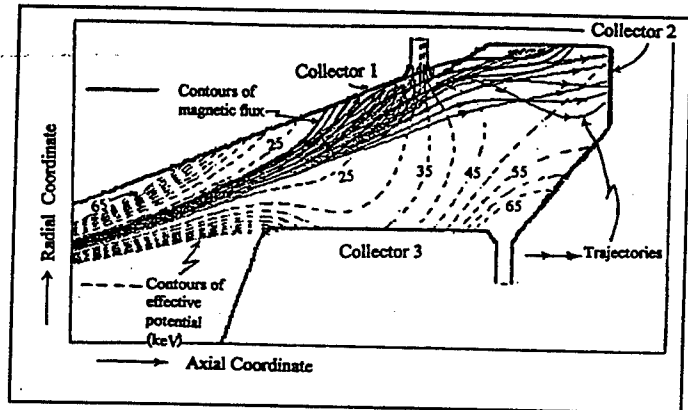


Figure 1. Outline drawing of two-stage 1 MW CW depressed collector

The magnetic field is generated by three external coils and two internal pole pieces. The magnetic flux lines have a sharp bend away from the axis near the mid-point of the collector, thus providing a non-adiabatic transition.

The beamlets of lower energy are selectively deflected toward the first collector electrode, while the lower contours of magnetic flux lead the beamlets of higher energy toward the second collector electrode. The contours of effective potential form "valleys" representing regions accessible to beamlets of energy ranging from 30 keV to 60 keV. The electron trajectories are sorted by these contours and collected without reflection.

The electron distribution on the electrode surfaces is sufficiently dispersed so that the peak heat dissipation density is less than 400 W/cm<sup>2</sup>. The simulation shown in Figure 1 represents collector performance for a gyrotron producing 1 MW of RF output power. Simulations were also performed for the case where no RF is generated, leaving the 'spent' beam with its full initial voltage and power. In this case the peak heat dissipation density was less than 900 W/cm<sup>2</sup>. Thus hot spots on the collector surface can be avoided without sweeping the magnetic field.

## Thermal Design

The collector was thermally analyzed for 1 MW CW RF power operation and for full power, beam-only operation. For

this analysis, the efficiency of the collector was assumed to be 65%, so the results are more conservative than anticipated in actual operation. For 1 MW RF operation with a coolant flow rate of 200 gallons per minute, the maximum temperature reached on the interior (vacuum) wall of the collector is 175°C. The peak temperature on the wet wall (coolant side) of the collector is 103°C. The goal of the thermal design was to ensure that the peak vacuum wall temperature was below 300°C and that the peak wet wall temperature was below 150°C. Both of these goals were achieved with the design shown.

Full power, beam-only operation typically represents an unacceptable operating mode for the gyrotron; however, it is important that the collector be designed to operate under these conditions until the control circuitry can remove power from the tube. Simulations indicate that under these conditions all beam power is deposited in the second stage, with the peak power density approaching 900°C in a small area. Thermal analysis indicates that the peak vacuum wall temperature under these conditions slightly exceeds 282°C, and the wet wall temperature slightly exceeds 145°C. These are within allowable values; however, full-power beam-only operation represents an extremely marginal operation regime, and power should be removed from the tube within 500 ms of the onset of beam-only operation.

### Mechanical Design

Figure 2 shows an outline drawing of the collector. Three external magnetic coils and two internal iron polepieces assist in directing the electrons to the appropriate surface for maximum energy recovery. Large ceramic insulators between collector stages are eliminated by supporting the second electrode of the collector with the coolant feedthroughs located at the top

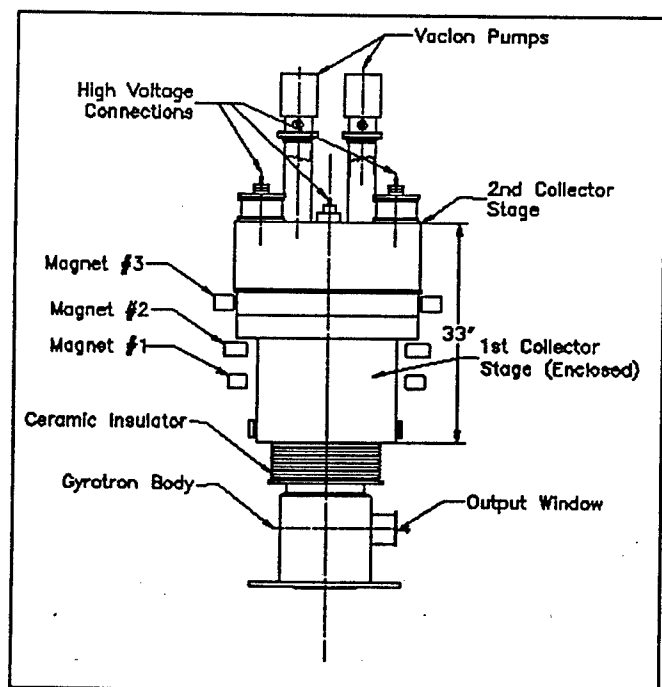


Figure 2. Outline drawing of two-stage 1 MW CW depressed collector

(end) of the structure. In addition, the second electrode is mostly enclosed within the first electrode. In the preferred configuration, the first stage is grounded and the tube body is energized. With the first stage enclosing the second stage and the energized body section located within the superconducting magnet, exposed high voltage surfaces are minimized, and it is not necessary to electrically isolate the collector magnet coils. The collector design shown is applicable to gyrotrons between 110 GHz and 170 GHz.

The applicability of a single depressed collector geometry for gyrotrons between 110 GHz and 170 GHz should result in substantial cost reduction for gyrotrons in this frequency range by standardizing parts, assembly procedures, and processing. The design should be applicable to gyrotrons at other frequencies utilizing electron beams of similar size and power. Calabazas Creek Research, Inc., is also working with a major power supply vendor to develop advanced solid state power supplies capable of meeting all requirements for gyrotron operation. This should significantly reduce system cost while increasing reliability and flexibility.

### Summary

A two-stage depressed collector for high-power gyrotrons outputting microwave power between 110 GHz and 170 GHz in a Gaussian mode was presented. The mechanical design is robust and manufacturable at reasonable cost. The typical requirement for large-diameter ceramic insulators is eliminated by supporting the second stage with coolant feedthroughs. By grounding the first stage of the collector, the need to electrically isolate the magnet coils and surrounding hardware is eliminated, and a safer working environment is established.

The electrical design indicates that approximately 70% of the spent beam energy is recovered, and the total efficiency of the gyrotron is increased from approximately 35% to more than 60%. In addition, the thermal load in the collector is reduced by approximately 1.2 MW, reducing the cost and complexity of the coolant system. Using current electrical usage and capacity costs, the increased efficiency reduces the operating cost for each gyrotron by \$27/hr and capacity cost by approximately \$60,000 per year. For installations requiring numerous tubes, such as ITER, this represents a substantial cost savings for the facility.

### References

1. M. Makowski, "ECRF systems for ITER," *Trans. IEEE Plasma Sci.*, June 1996, pp 1023-1032.
2. A. Singh, D.S. Weile, S. Rajapatirana and V.L. Granatstein, "A library of codes for design of depressed collectors for gyrotrons", *Conference Record-Abstracts IEEE Int. Conf. on Plasma Science*, p. 257 (1996).
3. A. Singh, D.S. Weile, S. Rajapatirana and V. L. Granatstein, "Integrated design of depressed collectors for gyrotrons", *IEEE Trans. Plasma Sc.* June (1997).

# W1.8

## DESIGN OF MAGNETRON INJECTION GUN FOR 94-GHZ GYRO-AMPLIFIERS<sup>®</sup>

198

K. Nguyen\*, B. Danly, B. Levush, and M. Blank

Naval Research Laboratory, Washington D.C. 20375

R. True

Litton Electron Devices, San Carlos, CA 94070

K. Felch and P. Borchard

Communications &amp; Power Industries, Palo Alto, CA 94304

### ABSTRACT

The development of high-average power w-band gyro-amplifiers is currently being pursued by the Naval Research Laboratory, together with Litton Electron Devices and Communication & Power Industries as industrial partners. The gun electrical design were performed with the EGUN code [2], and were independently confirmed with the deformable-mesh gun code, DEMEOS [3]. Excellent agreement between the two codes has been realized.

The magnetron injection gun (MIG) design employs an optimized double-anode geometry and a radical cathode angle of  $50^\circ$  to achieve superior beam optics that are relatively insensitive to electrode misalignments and field errors. Perp. velocity spread of 1.6% at a velocity ratio of 1.52 is obtained for a 6 A, 65 kV beam. The gun is currently under construction.

### 94-GHZ MIG DESIGN

Efficient operation of gyro-devices depends critically on the quality of the electron beam. Consequently, for the current design, special emphasis has been placed not only in obtaining the best point design which exceeds all the requirements of the interaction circuit, but also in identifying and evaluating all factors which may contribute to the beam velocity spreads. Such factors include cathode surface roughness, electrode misalignments, and fabrication tolerances.

Specifically, the MIG design is subjected to the following RF circuit requirements:

Beam Current	5 - 7 Amperes
Beam Voltage	65 - 70 kV
Velocity Ratio	1.3 - 1.8
Perp. Vel. Spread	< 2.5%
Max. Beam Radius	1.25 mm
Guiding Radius	0.8 - 1.1 mm
Oper. Magn. Field	36 - 38 kG

In addition, practical considerations dictate the need to maintain cathode loading,  $J_{\text{cat}}$ , below  $8 \text{ A/cm}^2$  for reasonable cathode lifetime, peak electric field,  $E_{\text{max}}$ , well below  $100 \text{ kV/cm}$  to avoid arcing, and gun magnetic compression ratio,  $B/B_0$ , at or below 25 to minimize electron reflection and beam alignment problems. Moreover, since the gun will be operating at high-repetition rate, the modulating voltage

required for beam pulsing must be minimized to avoid stressing the voltage modulator. It is due in part to this last requirement that the present gun design employs the double-anode geometry. Another key advantage of this geometry is the ability to adjust the beam perpendicular to axial velocity ratio,  $\alpha$ , independent of the magnetic field profile.

Shown in Figure 1 is the MIG geometry and beam trajectory. It is essentially comprised of three regions: the cathode-mod-anode region, the mod-anode-anode region, and the beam tunnel or adiabatic compression region. In performing the design, care has been taken to ensure to the largest extent possible that each region will perform mainly one key function. Such modular approach allows a much more rapid convergence to the final design. Consequently, in the design, the initial beam perpendicular velocity is controlled mainly by the geometry and voltage of the cathode-mod-anode region, the mod-anode-anode region provides mainly axial acceleration to bring the beam up to full potential, and the beam is adiabatically compressed in the beam tunnel region to the final beam velocity ratio. An additional advantage of the modular approach is the ability to locally pinpoint and control beam velocity spread. For instance, the transverse beam spread can be minimized by shaping the cathode and mod-anode geometries.

Key elements of the design include a cathode well-recessed under the mod-anode shroud, a relatively large cathode angle of  $50^\circ$ , and relatively parallel potential contours in the mod-anode-anode region. We shall discuss these key elements in turns. The recessed cathode is critical for three reasons. First, by recessing the cathode deep inside the mod-anode shroud, we essentially shield the cathode from the high anode potential ( $\sim 65 \text{ kV}$  relative to cathode). This design choice reduces the maximum electric field on the cathode tip to less than  $67 \text{ kV/cm}$  (This value has also been independently confirmed with ANSYS [4]), well below the dc breakdown threshold. Second, it allows for the relatively independent control of the beam initial transverse velocity ( $E/B_0$ ) with just the voltage and geometry of the cathode-mod-anode region. Finally, it minimizes the leakage electric field (i.e.,  $V_{\text{mod-anode}} = V_{\text{cathode}}$ ) on the thermionic emitting strip from the anode voltage. This reduces the required negative mod-anode voltage

\* This work is supported by Office of Naval Research, Defense Advanced Research Projects Agency, and in part by grants of HPC time from the Department of Defense HPC centers, NAVO and CEWES.

\* KN Research, Silver Spring, MD 20906

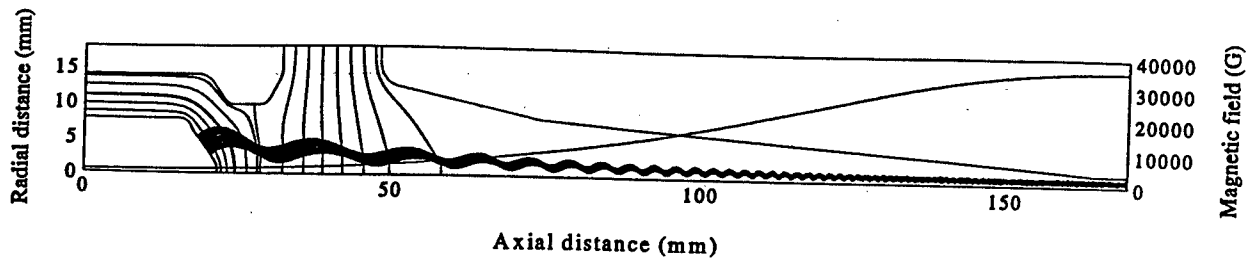


Figure 1: Geometry and beam trajectory of the 94 GHz magnetron injection gun point design

swing relative to the cathode for complete beam shutoff (i.e., less stress on the modulator). For this design, this is -1.7 kV.

The relatively large cathode angle of  $50^\circ$  is a consequence of trading off between various conflicting requirements. Chief among these is the need to maintain the overall coherency of the cyclotron phase for all beam electrons at least until the electric field is primarily axial. This is important because to the lowest order unless all beam electrons picks up the same amount of transverse energy, in their cycloidal motion through the region of substantial radial electric field, serious beam spread will result. For this design, because of the small mean radius of the emitter strip, the relatively high beam current, and cathode loading considerations, the emitter strip width is a substantial fraction of the cyclotron period; thus, the need for large cathode angle to compensate.

In the relatively long region between the mod-anode and anode, it is critical that the electric field is primarily axial. Even though, in principle, for a fixed set of operating parameters, one can shape the potential contours in this region to greatly correct for any initial beam spread. However, due to the fact that the beam can perform more than two cycloidal orbits in this region, any deviation from the operating parameters will also greatly degrade the beam quality; hence, reducing flexibility. Consequently, it is more advantageous to ensure that mainly axial acceleration is performed in this region, consistent with the modular design methodology.

The optimized point design parameters are shown in the table below. Agreement between EGUN and DMEOS is excellent in terms of beam velocity ratio, velocity spreads, position, and size.

Anode Voltage	65 kV
Mod-anode Voltage	17 kV
Beam Current	6.0 A
Velocity Ratio	1.52
Perp. Velocity Sprd.	1.6%
Max. Beam Radius	1.25 mm
Beam Guiding Center	0.82 mm
Circuit Magnetic Fld.	36 kG
Mag. Comp. Ratio	25
Cathode Loading	6.76 A/cm <sup>2</sup>

Additionally, simulations have been performed to explore the gun performance under various operating parameter ranges, i.e., mod-anode voltage, beam current, and beam voltage. This study indicates that the perpendicular

velocity spread does not exceed 2% within the operating range required by the interacting circuit, and that the design is indeed optimized. This is exemplified by Figure 2 which shows the beam velocity and perpendicular velocity spread as a function of mod-anode voltage.

Of the 1.6% final perpendicular velocity spread in the point design, 0.6% of which is a direct result of electron phase-mixing in the present of the beam space-charge in the adiabatic compression region. This is independently confirmed with the Univ. Of Maryland code MAGUN [5].

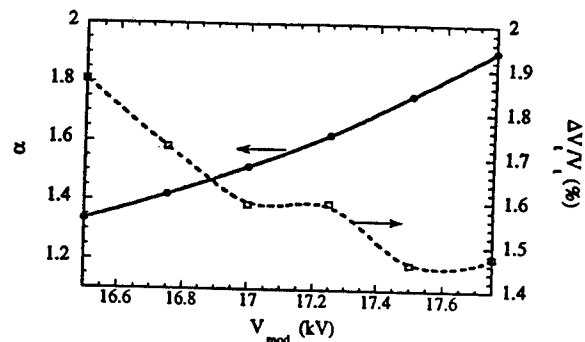


Figure 2: Beam velocity ratio and perp. velocity spread versus mod-anode voltage.

We have also investigated the impact of cathode surface roughness on beam spread [6-7]. Our results indicate an additional 0.7% beam transverse velocity spread can be expected from bumps of 1 microns in height and width.

In addition, an exhaustive study of the resulting beam quality sensitivity with respect to misalignments, fabrication tolerances, and geometric deviations from the design has been performed. Within the fabrication tolerance and alignment specifications, the study indicates that the beam perp. velocity spread does not exceed 2%.

#### REFERENCES

- [1] D. Pershing, K. Nguyen, J. Petillo, J. Calame, B. Danly and B. Levush, in these proceedings.
- [2] W.B. Herrmannsfeldt, AIP Conf. Proc. 177, pp. 45-58, 1988.
- [3] R. True, IEDM Tech. Digest, pp. 257-260, 1975.
- [4] ANSYS/Emag, Ansys Inc..
- [5] T. Antonsen Jr., et al., Conf. Dig. of 20<sup>th</sup> Int. Conf. On Infrared & mm waves, p126 (1995).
- [6] S. E. Tsimring, Izv. Radiofiz. 15, 1247 (1972).
- [7] Y.Y. Lau, J. Appl. Phys. 61, 36 (1987).

## Pseudospark Cathode, Electron Beam and Microwave Production, Theory and Experiments

H.Yin, A.D.R.Phelps, W.He, G.R.M.Robb, P.Aitken, B.W.J.McNeil, A.W.Cross and C.G.Whyte

Department of Physics and Applied Physics, University of Strathclyde, Glasgow, G4 0NG, UK

### Abstract

Experimental investigations have been carried out on single-gap and multi-gap pseudospark discharges[1][2], which include voltage breakdown characteristics and electron beam production. An electron beam of up to 100 A at 10 kV was measured immediately after the anode hole for a single-gap pseudospark. A higher beam current up to 150 A at 20 kV was measured 6 cm from the anode in a three-gap pseudospark with no external focusing magnetic field. The brightness of this pseudospark-based electron beam was measured to be  $10^{11} \text{ Am}^2\text{rad}^{-2}$  with a collimator. The experimental results obtained and some theoretical analysis and prediction make this pseudospark-based electron beam source a potential candidate for applications in high power microwave generation.

### Introduction

A pseudospark discharge[3] is a low pressure, transient hollow cathode gas discharge which occurs in a special geometry in different kinds of gases, i.e., nitrogen, oxygen and hydrogen, etc. The background gas pressure is such that  $pd$ , the product of the gas pressure  $p$  and the distance  $d$  between the front faces of the cathode and anode, is on the left-hand side of the Paschen curve between the Paschen minimum and vacuum breakdown. The pseudospark discharge offers the possibility of producing electron beams of high current density ( $>10^4 \text{ A cm}^{-2}$ ), high brightness (up to  $10^{12} \text{ Am}^2\text{rad}^{-2}$ ), narrow beam diameter ( $<4 \text{ mm}$ ), very low emittance (tens of  $\text{mm mrad}$ ) and variable duration (tens of ns to hundreds of ns)[4][5]. It is therefore very attractive as an electron beam source for high power sources of microwave radiation, such as free electron lasers (FELs), cyclotron autoresonance masers (CARMs) and Cherenkov masers. This paper presents the experimental details and results of pseudospark-based electron beam production. Numerical simulation of a Cherenkov maser based on a multi-gap pseudospark discharge will also be presented.

### Experimental Setup

The experimental setup for the pseudospark-based electron beam production is shown in Fig.1. The discharge

chamber consists of a planar anode, a planar cathode with an adjustable cylindrical hollow cavity, and several sets of Perspex insulators and interelectrodes of 6.5 mm thickness. Both the anode and cathode have an on-axis hole of 3 mm diameter. The centre of the cathode was designed to be an interchangeable structure, which

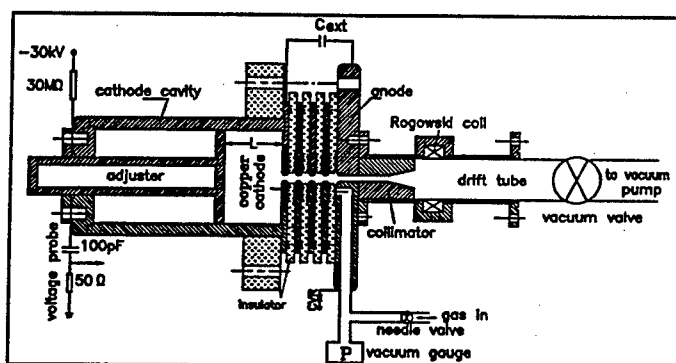


Fig.1 The experimental setup for the pseudospark-based electron beam production

allowed different sizes of cathode core and different kinds of cathode materials to be studied. The hollow cathode cavity made of stainless steel of outer and inner diameters of 63 and 50 mm respectively was length-adjustable through an adjuster. Gas pressure was measured by a digital, active Pirani gauge. The cathode side of the chamber was charged up to 30 kV through a 30 MΩ charging resistor and the charging voltage was measured by a capacitive voltage probe. The discharge current was monitored by a  $0.066 \Omega$  current viewing resistor (CVR). The beam current was measured by a Rogowski coil located 6cm away from the anode and the beam brightness was measured with a 6 cm long cylindrical collimator connected to the anode as shown in Fig.1.

### Experimental Results

The basic investigations of electron beam production were carried on a single-gap pseudospark system for a wide range parameters, including cathode cavity length, cathode hole size, applied voltage, external capacitance and the inductance in the discharge circuit. The experiments showed that the pseudospark discharge phenomenon appeared when the ratio between the cathode cavity length to the cathode hole diameter was

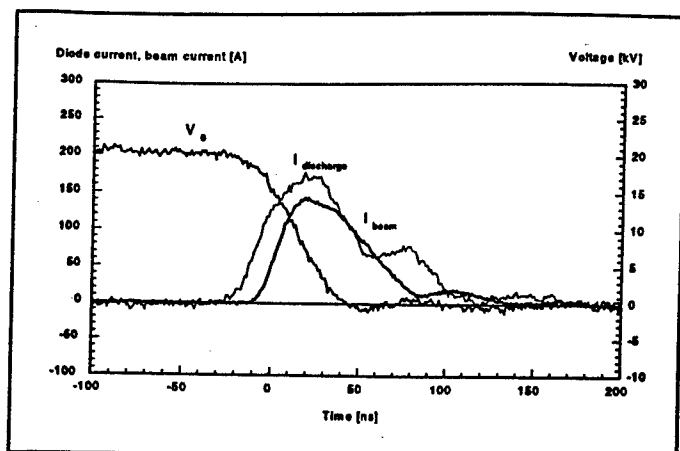


Fig.2 The voltage, diode current and beam current from the 3-gap pseudospark system

greater than 1. The discharge current approximately obeyed the relation  $I_{\text{discharge}} = V_0 (C_{\text{ext}}/L)^{1/2}$ , where  $C_{\text{ext}}$  is the external capacitance,  $V_0$  the applied voltage and  $L$  the total inductance in the discharge circuit. The beam current however had a saturation value when changing the external capacitance. To get maximum beam current the inductance in the discharge circuit should be minimized. The optimum beam current from the single-gap pseudospark discharge chamber was 100 A at 10 kV with  $C_{\text{ext}} = 500$  pF. Higher energy electron beam production was studied from 3-gap pseudospark systems. Fig.2 shows the voltage, diode current and beam current from the 3-gap pseudospark system. The brightness of this beam was measured to be  $\geq 10^{11}$  ( $\text{Am}^2\text{rad}^{-2}$ ) with a 6cm long collimator in contact with the anode[6]. For the 4-gap pseudospark system, a beam of up to 260 A was measured after the collimator with the Rogowski coil.

### Numerical Simulation of the Strathclyde University Cherenkov Maser Amplifier

A Cherenkov maser amplifier experiment is currently under development at the University of Strathclyde. The main aim of the experiment is to demonstrate the suitability of the pseudospark cathode as an electron source for high power microwave generation. In this experiment, an electron beam generated by a multi-gap pseudospark cathode is passed through a section of cylindrical waveguide lined with a layer of dielectric (alumina). The presence of the dielectric allows a resonant interaction to occur between a TM or HE waveguide mode and the electron beam.

A one-dimensional model of the Cherenkov maser amplifier has been developed in an attempt to predict the behaviour of this device both in the linear and nonlinear regime of operation. The model takes into account effects due to electron velocity spread and resonant space charge

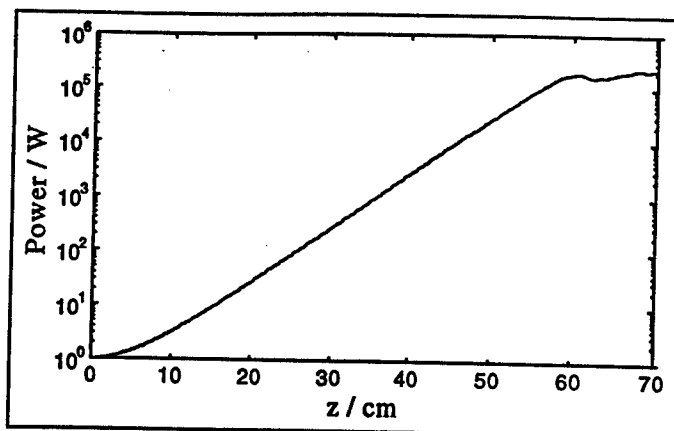


Fig.3 Growth of  $\text{TM}_{01}$  mode power plotted against  $z$  when  $V=70\text{kV}$ ,  $I=50\text{A}$  and  $f=24.5\text{GHz}$ .

forces. A typical example of the results produced by this model is shown in Fig. 3 for interaction involving only a  $\text{TM}_{01}$  mode. The mode power at saturation is  $\approx 220\text{kW}$ , corresponding to an interaction efficiency of  $\approx 11\%$ .

### Conclusions

Electron beam production from a pseudospark-based cathode was experimentally studied using different configurations and external parameters. Measurements of beam voltage, current and brightness were obtained. These results, coupled with computer simulation, suggest that this pseudospark-based electron beam source is a potential candidate for applications in high power microwave generation.

### Acknowledgements

H. Yin would like to thank the Committee of Vice-Chancellors and Principals of the Universities of the United Kingdom and the University of Strathclyde for financial support.

### References

1. H.Yin and A.D.R.Phelps, 22nd Plasma Physics Conference, The Institute of Physics, Oxford, UK, 1995
2. H.Yin, W.He, A.W.Cross and A.D.R.Phelps, 23rd Plasma Physics Conference, The Institute of Physics, Crieff, UK, 1996
3. K.Frank and J.Christiansen, IEEE Trans. Plas. Sci., 17(748), 1989
4. E.Boggasch and M.J.Rhee, Appl. Phys. Lett., 56(18), 1990
5. G.F.Kirkman and M.A.Gunderson, Appl. Phys. Lett., 49(494), 1986
6. W.He, H.Yin, A.W.Cross and A.D.R.Phelps, 24th Plasma Physics Conference, The Institute of Physics, Leeds, UK, 1997



# Millimeter Power Module Performance Review

G. Lednum, T. Ninnis, T. Schoemehl, P. Ballagh  
N. Chiang, J. Shumaker, R. Kopeck

Litton Systems, Inc., Electron Devices Division, San Carlos, CA

Litton Systems, Inc., Solid State Division, Santa Clara, CA

## Abstract

This paper summarizes continuing improvement of the 18 to 40 GHz Millimeter Power Module (MMPM). The MMPM is a complete millimeter wave amplifier which includes a vacuum power booster, a solid-state MMIC driver amplifier, and a high density electronic power conditioner. The three components fit in a variety of packages, but the minimum volume requirement is currently 35 cubic inches. Demonstrated performance is 50 watts CW output power, 50 dB small signal gain, a noise figure of less than 10 dB, and 25% efficiency. Projected performance in the same band is 80 watts CW, and initial test data shows 100 watts CW is possible without significant redesign. Work is also proceeding on a Q-Band version with RF capability to 50 GHz. The entire MMPM is being developed by Litton; the Electron Devices Division is developing the vacuum power booster and electronic power conditioner while the Solid State Division is developing the MMIC amplifier. Applications include radar, electronic countermeasures as well as communications transmitters. For some high power applications, power combining is also possible.

## Background

An MMPM houses three components. The electronic power converter (EPC) is typically a low volume, switching power supply. The solid state MMIC amplifier is a low noise device supplying a drive level signal. A helix traveling wave tube (TWT) is used as the vacuum power booster (VPB). All three major components have been the subject of a multi-year development effort at Litton. Although the EPC design was challenging, the TWT used as the VPB required significant development.

## MMPM Design Goals

The MMPM was designed to meet performance goals well beyond amplifiers available in this size and weight class. Goals were assigned for all normal amplifier performance parameters based on probable applications. These include

electronic countermeasures, radar and communications applications. Table 1 summarizes the most important goals. Figure 1 shows a photograph of the MMPM.

Performance Goal	Value
Bandwidth	18-40 GHz
Output Power	40 Watts
Efficiency	30%
Small Signal Gain	53 dB
Gain at Rated Power	48 dB
Duty Cycle	0 to 100%
Noise Figure	10 dB
Noise Power Density (Beam-on)	-40 dBm/MHz
Phase Tracking	+/- 35 degrees
Spectral Purity	-40 dBc
Size	35 in <sup>3</sup>
Weight	2.5 lb.
Cooling	Conduction
Temperature	-55 to +105 deg C

Table 1. MMPM Design Goals

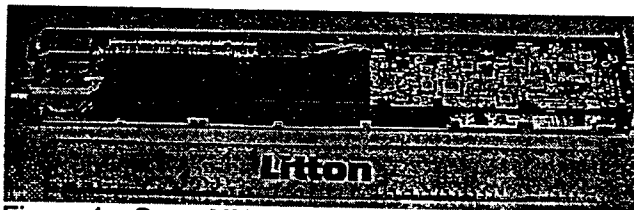


Figure 1. Open MMPM case showing the VPB in the rear left corner, the MMIC amplifier in center rear, the potted high voltage section of the EPC in the front left, and the low voltage and control sections in the front right.

## VPB Electronic Design Parameters

The VPB was mechanically designed as a precision brazed ceramic and metal structure. The device is approximately 7 inches long and 0.65 inches in diameter. It uses a high perveance beam and a three stage depressed collector. The gun design is a stacked ceramic design with a focus electrode for pulsed beam control. The helix is wound tungsten tape supported by four BeO rods. The BeO rods and helix are bound together into a bundle using a tungsten wire overwrap. The resultant circuit bundle is brazed inside the

envelope to maximize thermal transfer. The three stage collector design is a variant of the NASA Lewis Research Center designs, with a single ceramic outer sleeve supporting three, copper electrodes. Electrodes are treated to reduce secondary electron emission. The periodic magnet stack uses Samarium Cobalt magnets having a peak field value of 5000 gauss on axis.

Several pre-production units were built to test manufacturing methods. Currently, the pilot-production VPBs are built and tested using design parameters shown in Table 2.

Parameter	Value
Helix Voltage	6700 V (relative to ground)
Cathode Current	110 mA
Cathode Diameter	0.092 in
Cathode Loading	2.6 A/cm <sup>2</sup>
Helix ID/Pitch	.0255 in / .0177 in
Collector Voltages	35%, 17%, 9%
v/c	0.153 - 0.152
Interaction Impedance	45 - 7 ohms
Gain	21 - 15 dB/in
Noise	-30 dB/MHz (midband)

Table 2. VPB Electronic Design Parameters (Unless otherwise noted, all voltages are relative to cathode)

### MMIC Pre-Driver Amplifier

The pre-driver amplifier is packaged in a 1.8 X 0.7 X 0.5 inch module using MMIC technology to achieve the ultimate size reduction. The design architecture is a cascade, using one driver chip and one power amplifier. The second chip is a MESFET power amplifier MMIC with small signal gain of 31 dB, and output power near 20 dBm at 1dB compression.

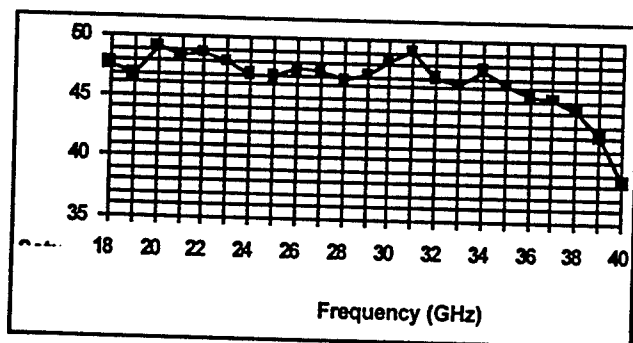


Figure 2. VPB RF Power at 6.7 kV, 110 mA, 100% duty. Design and test values as shown in Table 2.

### Test Data

The MMPM, as pictured in Figure 1, is currently in pilot-production. Detailed testing of these first

production lots is underway. Figure 2 shows saturated RF power for the first VPB. The data shown is for a conduction cooled package running at 100% duty with a microperveance of 0.2. Later units do not show the power drop at the high end of the band. Additionally, some high band test data was taken for VPBs running in pulsed beam test mode (10% duty) at 0.26 microperveance. Power output increased an average of 2 dBm and exceeded 100 W midband (Figure 3). It appears these power output levels are achievable in a CW device.

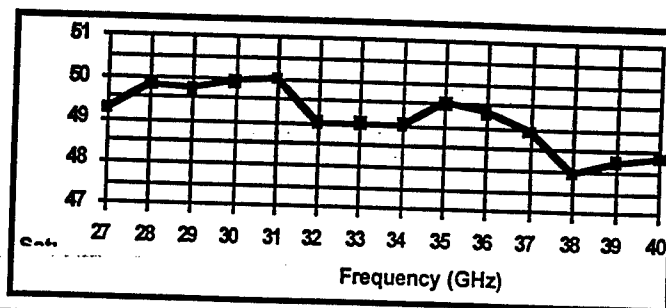


Figure 3. VPB Saturated Output Power at 10% duty and tested at 0.26 microperveance.

### Q-Band MMPM

Work is proceeding on a Q-Band MMPM. This device borrows heavily from the 18-40 GHz device. All major sub-systems are similar, with changes to accommodate the 33-50 GHz frequency design. Initially this device is being designed for narrow band Satellite Communications applications.

### Conclusion

Detailed design parameters for a 50 W, 18-40 GHz MMPM amplifier have been presented. Test data from the pilot production modules shows performance exceeds design goals. Pre-production of a Q-Band (33-50 GHz) variant has begun with deliveries in August 1997. The goals were set to meet the demands of electronic countermeasures, radar, and communications applications.

We would like to acknowledge the encouragement of Dr. Richard Abrams and Mr. Rick Worley and the financial support by Tri-Services/ARPA under contract F33615-94-C-1581. We would also like to acknowledge Army Research Lab and Mr. Cal Bates, Mr. Jacques Wahide and Mr. Bernie Smith and the financial support received under contract DAAL01-96-C-0096.

## Theory of the Clinotron

K. Schünemann<sup>1</sup>, D.M.Vavriv<sup>2</sup>, and K. Yemelyanov<sup>2</sup>

1) Technical University Hamburg-Harburg, Arbeitsbereich Hochfrequenztechnik,  
Wallgraben 55, D-21071 Hamburg, Germany

2) Radio Astronomy Institute of Ukrainian Academy of Sciences,  
4 Chervonopraporna St., 310002 Kharkov, Ukraine

### Abstract

A nonlinear theory of the clinotron, which is a modification of the BWO, is presented. The problem of the electron-wave interaction is treated in terms of the scattering of a wave package of the electromagnetic field on an electron beam. Theoretical results are presented on the start-up scenario, saturation effects, efficiency, and tuning characteristics. The theory predicts a possibility of an essential upgrading of clinotron performance.

### Introduction

The clinotron is an electron tube proposed by Ukrainian scientists [1-2], which is capable of continuous mode of operation in the millimeter and submillimeter wave bands with high output power level. The basic principle of the electron-wave interaction in the clinotron is similar to that in the conventional BWO, but in order to eliminate some drawbacks of the latter, essential modifications in the tube design have been introduced. The principal one is related with the application of a thick electron beam inclined to the surface of a grating, as shown in fig.1. In this case, each layer of the beam can effectively interact with the field. Besides, by varying the tilt angle  $\alpha$  it is easy to optimize the length of the „effective“ interaction space without changing the geometry of the oscillatory circuit. These approaches have resulted in the development of a series of oscillators through the millimeter

and submillimeter wave bands [1,2]. The output power level of these tubes is an order of magnitude larger than that of conventional BWO's [3,4] while small and submillimeter wave bands [1-2]. The physical dimensions and weight, low operating voltages and other advantages of BWO's have been preserved.

In spite of the attractive characteristics of the clinotron obtained in the experiments, this tube has not been adequately studied theoretically. Publications on record deal mainly with some aspects of the clinotron mode of the electron-wave interaction or with properties of the „cold“ oscillatory structures used in the clinotron [1,2, 6,7]. In the meantime, there is a need for a nonlinear self-consistent theory which can be used for a detailed study of the physics of the clinotron and for its simulation and optimization. This paper is intended to make contribute to the development of such a theory.

### Mathematical model

The analysis is based on the solution of self-consistent equations, involving the equations of excitation of coupled forward and backward waves, the motion equation and, the Poisson equation for the space charge field. The effect of an external signal is also included. The electron beam is considered as nonrelativistic and monoenergetic, and the motion of particles is assumed to be straight. To simplify this set of equations, an averaging procedure is applied which eliminates fast-time and fast-space phenomena. This results in the equations of excitation for the complex amplitudes of the waves which slowly vary in time and space. The final mathematical model, depending on specific values of the control parameters, describes various modes of clinotron operation, including self-running oscillations, synchronization, and amplification. In some limits, this system allows further simplifications. One of them corresponds to the case of essential reflections of the waves from the ends of the grating or/and slow values of the beam current. In this limit effects of the beam on the spatial field distribution can be neglected, which gives a possibility to formulate the mathematical model in terms of only time dependent equations and to apply well developed methods [8] for its analysis.

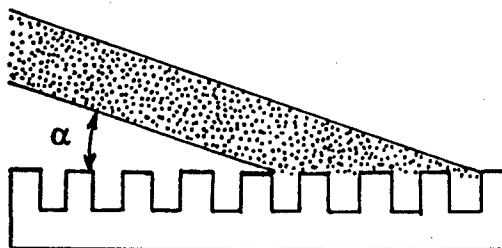


Fig. 1. Configuration of the beam and the grating

## Results

It is convenient to treat the problem of the electron-wave interaction in the clinotron in terms of the scattering of a wave package of the electromagnetic field on an electron beam. In the case of the clinotron, the wave package is characterized by the following spectrum shape function

$$S(k) = [(k - k_s)^2 + k_s^2 \sin^2 \alpha]^{-1}, \quad (1)$$

where  $k_s$  is the propagation constant of a slow wave along the grating. The growth rate of the field in the single-electron interaction regime is proportional to  $dS(k)/dk$  at  $k = \beta_e \equiv \omega / v_0$ , where  $\omega$  is the angular frequency and  $v_0$  the electron velocity. Hence it follows that the minimum starting current ( $I_{st}$ ) value is achieved at  $\beta_e = k_s(1 - \sin \alpha / \sqrt{3})$ , and that  $I_{st} \propto \sin^3 \alpha$ . Thus, there is a strong rise in the starting current with an increase of  $\alpha$ . However, the latter leads also to widening of the spectrum (1), which gives a possibility to considerably increase the efficiency of the energy transfer from the beam under a proper choice of the device control parameters. This conclusion is consistent with the results of experimental investigations [1] and with our computer simulations illustrated in fig. 2. Here the efficiency ( $\eta$ ) is shown as a function of the normalized current  $J \equiv I / I_{st}(\alpha)$  for various values of  $\alpha$ . By increasing the tilt angle (up to  $5^\circ$  or around it), it is possible to essentially upgrade the efficiency provided that the beam current can be made large enough. It should be noted that the efficiency saturates at rather large values of  $J$  compared to those in the conventional BWOs, which is conditioned by a relatively slow decrease of the amplitudes of spatial spectral components of the spectrum (1)

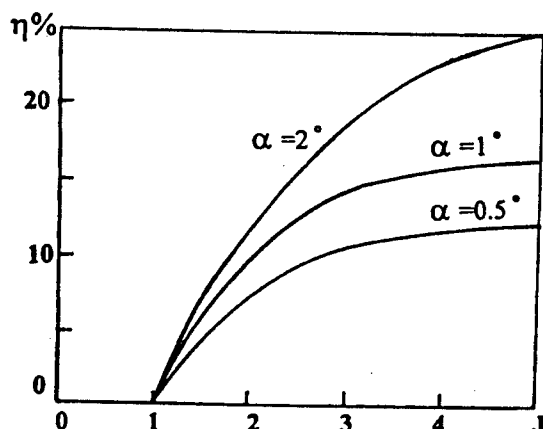


Fig.2. Efficiency versus normalized beam current for different values of the tilt angle.

with an increase of  $(k - k_s)^2$ . In practical clinotron tubes [1], the current value is relatively small, which results in an efficiency of several percent, which is, as is seen from the simulation results, far below the maximum possible values.

The analysis of the space charge field effects has shown that for practically achievable values of the beam current density, they do not impose serious limitations on clinotron performance. In practical devices the maximum value of the current which can be used, and therefore the maximum value of the efficiency, are mainly determined by the possibilities to provide an effective cooling of the grating.

## Conclusions

We have proposed a self-consistent nonlinear model which may be used for the analysis of various regimes of clinotron operation. We have considered main regularities of the electron-wave interaction in the clinotron and have found that they differ in many cases from those in the conventional BWO. The theoretical results predict a large potential of the clinotron interaction mode for the efficiency enhancement.

## Acknowledgement

The authors would like to thank Dr. S. Churilova, V. Zshadan, and Ye. Lysenko for helpful discussions. D. V. and K.Ye. acknowledge support from Technical University Hamburg-Harburg.

## References

1. G. Ya. Levin, A. I. Borodkin, A. Ya. Kirichenko, A. Ya. Usikov, and S. A. Churilova, *The Clinotron*. - Kiev, Naukova Dumka Press (1992), (in Russian).
2. G. Ya. Levin, S. A. Churilova, A. Ya. Kirichenko, L. M. Buzik, and S. N. Terekhin, *Radiotekhnika i Elektronika*, 37, No. 5, pp. 941-943 (1992), (in Russian).
3. M. B. Golant, et al., *Pribory i Tekhnika Eksperimenta*, No 4, pp. 136-139 (1965), (in Russian).
4. G. Kantorowicz and P. Palluel, *Infrared and Millimeter Waves*, vol.4, K. Button, Ed. New York:Academic Press, 1979, ch.1.
5. V.S. Andrushkevich, G.A.Kozlov, and D.I. Trubetskov, *Izv. Vuzov - Radiofizika*, 10, No.1, pp. 105-113 (1967), (in Russian).
6. L. M. Buzik and S. A. Churilova, *Izv. Vuzov - Radioelektronika*, 36, No.6, pp. 35-43 (1993), (in Russian).
7. E. N. Odarenko and A. A. Shmat'ko, *Radiotekhnika i Elektronika*, 37, No. 2, pp. 303-310 (1992), (in Russian).
8. D. M. Vavriv and O. A. Tretyakov, *Radiotekhnika i Elektronika*, 29, No. 8, pp. 1580-1588 (1984), (in Russian).

# Experiments of space harmonic peniotron for cyclotron high harmonic operation

K. Yokoo, T. Ishihara, K. Sagae, H. Shimawaki and N. Sato

Research Institute of Electrical Communication, Tohoku University  
Katahira 2-1-1, Sendai 980-77, Japan

## Abstract

The Paper describes the oscillation characteristics of cyclotron high harmonic peniotrons based on space harmonic interactions in magnetron waveguide resonators. The experimental results showed considerably high efficiencies of 75% for the 3rd harmonic and 6% for the 10th harmonic at 30GHz and 100GHz, respectively.

## 1. Introduction

Peniotron has been theoretically and experimentally recognized to have a very high conversion efficiency for electromagnetic wave generation at a cyclotron high harmonic, as well as a cyclotron fundamental<sup>1-4)</sup>. In addition, we proposed a space harmonic interaction where an axis encircling electron interacts with a space harmonic wave of the respective mode in a magnetron waveguide and pointed out many advantages of the space harmonic interaction using the  $2\pi$  mode in the waveguide for cyclotron high harmonic operations<sup>5)</sup>. The number of corrugations in the waveguide wall is a half of that in a conventional  $\pi$  mode tube. The loss in the resonator is the smallest, because the similar wave of a circularly polarized  $TE_{01}$  wave propagates in the resonator and the output circuit is easier to design than those at other modes in the resonator. The space harmonic peniotrons using the  $2\pi$  mode were fabricated to examine the oscillation characteristics at the cyclotron 3rd and 10th harmonics at the frequency ranges of 30GHz and 100GHz, respectively.

The paper describes fabrication and experiments of the peniotron.

## 2. Experiments

The cyclotron 3rd and 10th harmonic peniotrons were designed and fabricated to examine a 2nd space harmonic interaction at the  $2\pi$  mode in 4 and 11 vanes magnetron waveguide resonators, respectively. Output powers at the  $2\pi$  mode are transmitted into cylindrical waveguides at the  $TE_{01}$  mode through circular coupling holes at the end of the resonators.

First, the paper describes the experimental results obtained in the 3rd harmonic tube. Although many oscillations at cyclotron high harmonics are observed, the highest intensity of oscillation was achieved at the cyclotron 3rd harmonic at the expected operation mode of  $2\pi$  mode. Figure 1 shows the thermo image of the transmitted power in the cylindrical waveguide observed on the liquid crystal sheet. The image indicate clearly that the transmitted mode in the waveguide is  $TE_{01}$  mode, which suggests the operation

mode is  $2\pi$  mode in the 4 vanes magnetron waveguide resonator.

Figure 2 shows the output power and the electronic efficiency at the cyclotron 3rd harmonic operations at the beam voltage of 30kV, as a function of beam current. The solid and half tone symbols are the output powers and the electronic efficiencies of experiments, and the open symbols and their connections are those of design values of the

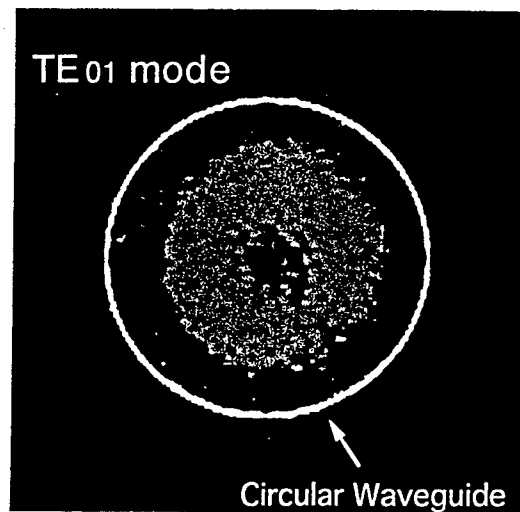


Fig. 1 Mode pattern of output power in the cylindrical waveguide observed on a liquid crystal sheet.

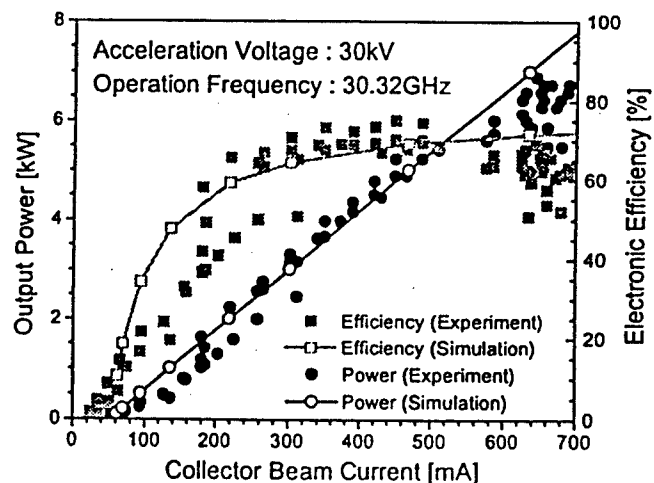


Fig. 2 Output powers and electronic efficiencies of the cyclotron 3rd harmonic tube using the 2nd space harmonic interaction in the  $2\pi$  mode as a function of beam current.

experimental tube, respectively. The highest output power of 6.9kW was obtained at the beam current of 0.65A and the highest conversion efficiency of 39% was achieved at the output power of 5.2kW and at the beam current of 0.45A, respectively. The efficiency corresponds to the electronic efficiency of 75% by estimating the power loss in the resonator and the operation characteristics are very close to the design values, as shown in Fig. 2.

In addition, the collector current and the output power do not change up to the depression potential of nearly 6kV applied on the collector. Then, the highest efficiency of 75% corresponds to the effective efficiency of 92% by the energy recovery of the spent electrons at the depression potential of 5.5kV. However, there is a big difference in the collector current characteristics against the depression potential between the oscillation and without oscillation. Figure 3 shows the changes in the collector current as a function of depression potential on the collector for both cases. The collector current at the oscillation decreases from the potential of nearly 6kV. On the other hand, the current does not change up to the potential of 13kV in the case of without oscillation. The reason of such a difference is explained as follows. The collector is put in the position of 10cm downstream from the end of the resonator and the magnetic flux density decreases gradually along the beam axis. Then, the rotational energy of electron is converted into the axial energy again by the magnetic mirror field. However, electrons without rotational energies by a highly efficient operation of peniotron, such as 75% of efficiency, keep nearly constant axial energies in the down tapered magnetic mirror field. On the other hand, the electrons have large rotational energies in the case of without oscillation, which are converted into the axial energies during electrons travelling in the magnetic mirror field. Therefore, this big difference in the axial energy of spent electrons in a down tapered magnetic mirror field indicates a highly efficient operation of peniotron.

Finally, the paper describes the experimental results of the cyclotron 10th harmonic tube operating at 100GHz. Intense oscillations were achieved at the 10th harmonics as like as the 3rd harmonic operation, suggesting the operation mode of  $2\pi$  mode. Figure 4 shows the output power and the electronic efficiency at the 10th harmonic operation as a function of beam current. The highest efficiency was about 6% at the beam current of 0.35A. Although the efficiency is relatively high for the cyclotron 10th harmonic operation, there are considerably big discrepancies between the experimental results and the design values probably due to the offset of rotating center and the spread of velocity ratio of electrons which affect strongly on the conversion efficiency for cyclotron high harmonic operation.

### 3. Conclusion

The paper described fabrication and experiments of space harmonic peniotrons and showed considerably high

efficiencies of 75% at the cyclotron 3rd harmonic and 6% at the 10th harmonic, respectively.

### References

- [1] K. Yokoo, M. Razeghi, N. Sato and S. Ono, *Int. J. Electron.*, Vol. 67, pp. 485-490, 1989.
- [2] S. Mushoki, K. Sagae, K. Yokoo and S. Ono, *Int. J. Electron.*, vol. 72, pp. 1067-1077, 1992.
- [3] P. Vittello, *IEEE Trans. Microwave Theory Tech.*, vol. MTT-32, pp. 917-921, 1984.
- [4] H. Shimawaki, K. Sagae, N. Sato, K. Yokoo and S. Ono, *Int. J. Electron.*, vol. 76, pp. 143-151, 1994.
- [5] T. Ishihara, H. Tadano, H. Shimawaki, K. Sagae, N. Sato and K. Yokoo, *IEEE Trans. Electron Devices*, vol. 43, pp. 827-833, 1996.

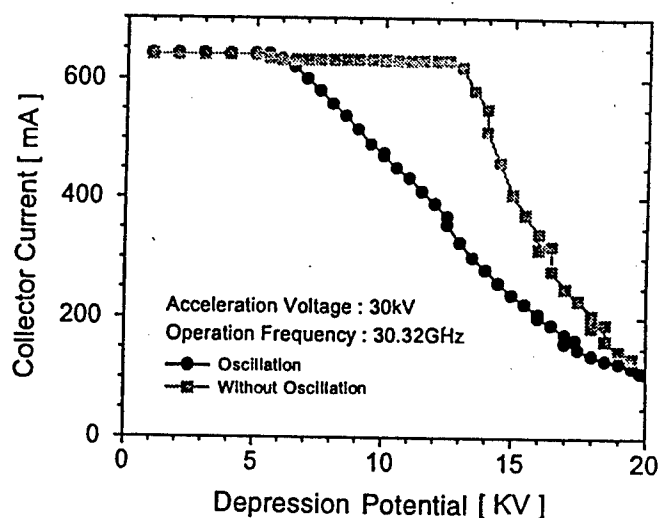


Fig. 3 Collector current as a function of depression potential on the collector. The solids and the half tones are currents with and without oscillations, respectively.

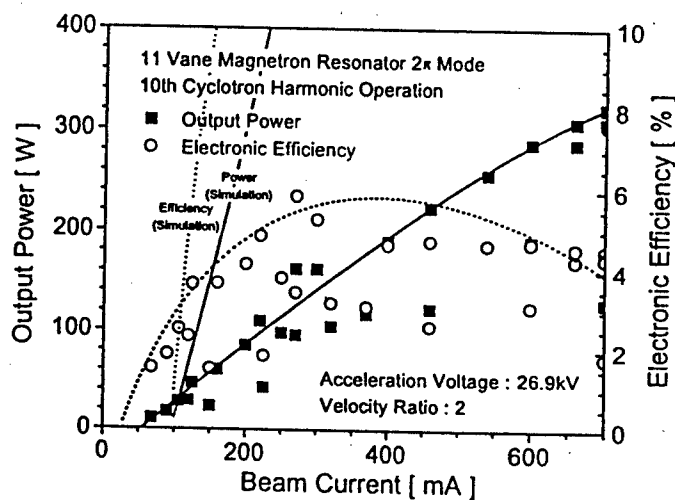


Fig. 4 Output powers and electronic efficiencies at the cyclotron 10th harmonic operation as a function of beam current.

## Hydrazine: the forgotten laser gas

E.C.C. Vasconcellos<sup>1</sup>, S.C. Zerbetto<sup>1</sup>, L.R. Zink<sup>2</sup>, M. Tachikawa<sup>2</sup>, and K.M. Evenson<sup>2</sup>

<sup>1</sup>Instituto de Física "Gleb Wataghin," Departamento de Eletrônica Quântica, State University of Campinas (UNICAMP), 13083-970 Campinas, SP, Brazil.

<sup>2</sup>Time and Frequency Division, National Institute of Standards and Technology, Boulder, Co 80303-3328

### ABSTRACT

Until recently hydrazine ( $N_2H_4$ ) had 35 known far-infrared laser lines when optically pumped by a  $^{12}C^{16}O_2$  cw-laser. We have discovered 127 new lines pumped by regular, sequence, and hot band lines of a  $^{12}C^{16}O_2$  cw-laser. One hundred and one of these new lines have wavelengths less than 200  $\mu m$ , the shortest wavelength line is 49.2  $\mu m$ . Of the 162 known lines, 139 have been frequency measured. We will be presenting the pump line, pump offset, FIR wavelength and frequency, optimum pressure, relative intensity, and relative polarization for each line. Preliminary work has also identified 17 new lines when hydrazine is pumped by an  $N_2O$  laser, and we have also measured most of them in frequency.

Keywords:  $N_2H_4$ , far-infrared lasers, frequency measurement, review.

### 1. INTRODUCTION

For a while it was not paid much attention to hydrazine ( $N_2H_4$ ) as a good far-infrared (FIR) laser medium when pumped by an infrared (IR) laser. However, in the last two years our group has discovered 127 new far-infrared laser lines by optically pumping hydrazine with a cw  $^{12}C^{16}O_2$  laser, and 17 new far-infrared laser lines by optically pumping hydrazine with an  $N_2O$  laser. Unlike the previously known hydrazine laser lines, most of these new lines are less than 200  $\mu m$  in wavelength. We also measured the frequencies of 128 of these new lines as well as 14 previous lines. Optimum pressure, relative polarization, relative strength, and pump offset frequency from line center were also determined for most of the lines. All of this information will be shown at this talk.

Although most of these measurements have been reported before<sup>1-7</sup>, the last summary of hydrazine laser lines<sup>6</sup> listed only 68 lines and did not report the pump offset, polarization, intensity, or pressure. Since we thoroughly examined every  $CO_2$  pump line and we don't anticipate many new FIR lines from hydrazine in the future, this is a good

time to summarize our work. The 17 new  $N_2O$  laser pumped lines quadruples the known hydrazine FIR lines pumped by this source.<sup>8</sup> Jones et al.<sup>8</sup> also reported seven  $N_2H_4$  lines pumped by  $CO_2$  isotope lasers. We have not done any work with these sources and refer the reader to their paper for those FIR wavelengths.

### 2. LASER DESCRIPTION

The  $CO_2$  pump laser uses a 1.5-m long, high-Q Fabry-Perot resonator. The key element in this laser is the high resolution grating. This grating selects the  $CO_2$  laser transition and also couples out the laser radiation in the zeroth order. By using gratings with different coupling percentages we are able to cover the complete range of the normal  $CO_2$  laser bands with up to 40 W of power and also have many sequence band and hot band lines oscillating with up to 20 W of power. A more complete description of this laser design can be found in ref. 9. The  $N_2O$  laser is of the same design as the  $CO_2$  laser, only the cavity and discharge length were extended an extra 0.5 m to increase the power.

Two different FIR lasers were used for these measurements. The first is a 2-m long metal-dielectric waveguide laser. It has two, flat end mirrors.  $CO_2$  pump radiation is coupled into the laser through a hole in one of these end mirrors for longitudinal pumping. A small 45° polished copper mirror near this end couples out a fraction of the FIR radiation. The other end mirror is mounted on a movable micrometer to tune the cavity into resonance with the FIR radiation. A Brewster angle Si output window transmits most of the FIR but blocks any residual  $CO_2$  radiation. The FIR radiation is detected with either a photo diode or a metal-insulator-metal (MIM) diode.

The second FIR laser has a 35-mm diameter, 2-m long Pyrex tube. At the ends of this tube are two mirrors, one a flat copper mirror, the other a 4-m radius gold coated mirror mounted on a movable micrometer. The hydrazine is longitudinally pumped by  $CO_2$  radiation in a V configuration. The  $CO_2$  is focused through a 5 mm hole in the flat mirror that is 16 mm above the mirror center. The pump radiation strikes the curved mirror in the center and is then refocused to strike the flat mirror 16 mm below the center. FIR power

is coupled out and detected in the same way as the waveguide laser. This laser favors short wavelengths. Its calculated loss is less than 0.5 % for wavelengths less than 150  $\mu\text{m}$ . Vasconcellos et al.<sup>10</sup> describe this laser in greater depth.

### 3. MEASUREMENTS

When searching for new laser lines, we first look for absorption of the  $\text{CO}_2$  pump radiation by monitoring the photo-acoustic signal from a microphone mounted inside the FIR laser cavity. Optimum photo-acoustic signals occur at about 650 to 1300 Pa of hydrazine. Once an absorption signal is found, we start a search for FIR emission by lowering the hydrazine pressure and simultaneously tuning the FIR cavity length and the pump offset. Once a FIR laser signal is detected, the pressure, output coupling, and pump offset are adjusted to optimize the signal. Also, for FIR laser two, the polarization relative to the pump polarization is measured. Then a scan of the laser modes is recorded as a function of FIR cavity length. This gives a first measurement of the number of FIR lines that are lasing and their wavelengths. Finally, measuring the difference in cavity length between 20 laser modes ( $10 \lambda$ ) gives a value for the wavelength accurate to about 0.1%. This process is repeated for every  $\text{CO}_2$  or  $\text{N}_2\text{O}$  pump laser line.

#### 3.1. Frequency measurements

The FIR laser frequency is determined by comparing it to a known frequency, in our case the FIR radiation is mixed in a MIM diode with radiation from two reference  $\text{CO}_2$  lasers and a microwave synthesizer. The diode generates frequencies of various mixing orders between these four sources. In the our case

$$\delta\nu = \nu_{\text{FIR}} - n | \nu_1 - \nu_2 | \pm m \nu_m, \quad (1)$$

where  $\delta\nu$  is the frequency generated in the diode,  $\nu_{\text{FIR}}$  is the FIR laser frequency,  $\nu_1$  and  $\nu_2$  are the  $\text{CO}_2$  laser frequencies, and  $\nu_m$  is the microwave frequency. The integers  $n$  and  $m$  are the mixing order of each component. Once  $\delta\nu$  is measured and the values and sign of the mixing components are determined, the FIR laser frequency can be calculated. Inguscio et al. describe this and other frequency measurement techniques in ref. 3.

Amplifying the currents across the MIM diode junction and observing them in a spectrum analyzer displays  $\delta\nu$ . We then tune the FIR laser across its gain curve and map out this change to the beatnote on the spectrum analyzer using a peak hold feature. The center of this beatnote is then measured with a marker frequency. Observing this beatnote as all four frequency mixed components are changed gives the value and sign of  $n$  and  $m$ . For all the measurements here  $n=1$  or 2

and  $m=1$  or 2. The  $\text{CO}_2$  reference frequencies and the microwave frequency are chosen to give a  $\delta\nu$  within the 1.5 GHz bandwidth of our amplifier and spectrum analyzer.

The  $\text{CO}_2$  reference lasers are frequency stabilized to  $\pm 10$  kHz and their frequencies are known to an accuracy of 2.5 kHz. The microwave source is also accurate to better than 10 Hz. Setting the FIR laser to the center of its gain curve determines the accuracy of the FIR laser frequency. We generally measure each frequency five times or more and report the average of these measurements. Our  $1\sigma$  uncertainty is  $2 \times 10^{-7}$  times the frequency.

#### 3.2. Frequency offset measurements

Pump frequency offset measurements are important for assigning these FIR laser transitions. Measuring the offset is a simple matter of setting the pump frequency for maximum FIR power and then mixing, in a MIM diode, some of the pump radiation with a reference laser locked to the appropriate line center. Just as with the FIR frequency measurements, the diode generates a beatnote between the two laser frequencies which is measured in a similar manner as above. Since some residual pump radiation is coupled out of the FIR laser along with the FIR radiation, we remove any  $\text{CO}_2$  filters in front of the FIR measuring MIM and easily perform the measurement. For regular pump lines, the reference laser is set to the same laser transitions as the pump line, for hot band and sequence lines, the closest regular line is used for the reference and the difference made up by a microwave synthesizer. Our pump offset measurements are reproducible to within 2 MHz. Our pump lasers free spectral range is  $\pm 50$  MHz from line center, so any offset measurements  $\geq 38$  MHz are very near the edge of the  $\text{CO}_2$  gain curve. These are probably not accurate measurements of the peak  $\text{N}_2\text{H}_4$  absorption frequency.

### 4. RESULTS

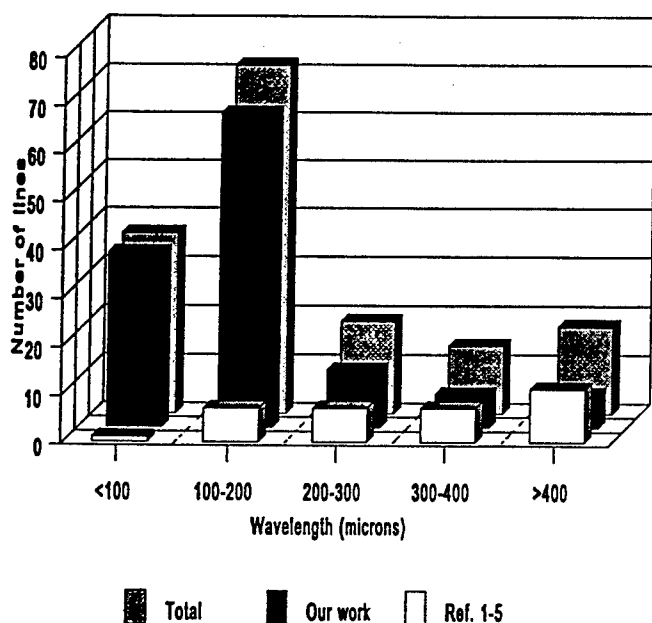
We will present the pump line, FIR frequency and wavelength, optimum pressure, relative strength, relative polarization, pump offset, and reference to the original work for all the 162 known hydrazine FIR laser lines pumped by a cw  $^{12}\text{C}^{16}\text{O}_2$  laser. The 312.027  $\mu\text{m}$  line is pumped by two different  $\text{CO}_2$  lines, 9P(46) and 10R(36). These two pumps populate the same upper lasing level in hydrazine and therefore produce the same FIR lasing line. There are also five doublets from  $\text{CO}_2$  laser pumping and one doublet from  $\text{N}_2\text{O}$  laser pumping. The doublet separations vary from 2.7 to 10 MHz. This doublet structure could be a real property of hydrazine, as noted in ref. 5 for the 533.7  $\mu\text{m}$  line, or it could be an artifact of our longitudinal pumping.

Of the 162 unique FIR laser lines obtained by  $\text{CO}_2$  laser pumping, 139 have been frequency measured. Twelve lines reported in ref. 1 have not been frequency measured, all



but one of these we have never observed oscillating. It could be that our lasers favor the short wavelength lines and have too much loss for these higher wavelengths or else the lines are misassigned. Several other unobserved lines from ref. 1 have been excluded from the table or have been assigned to other pump lines. Of the 17 FIR laser lines obtained by  $N_2O$  laser pumping 12 have been frequency measured. We also measured the frequencies of other three previously reported laser lines.

Figure 1 graphs the wavelength distribution of the  $CO_2$  laser pumped hydrazine lines. One hundred and eight of the 162 lines have wavelengths less than 200  $\mu m$ . This is an important region for spectroscopy and a high density of lines at higher frequencies makes hydrazine an important FIR lasing medium. Of the 108 lines below 200  $\mu m$ , 101 have been discovered in our laboratory. We also pumped hydrazine with an  $N_2O$  laser and discovered 17 new lines to compliment the previously known 6 lines.<sup>8</sup> The 23 total lines will also be presented here, by pump line, wavelength,



frequency measurement, and calculated wavenumber.

Figure 1. Wavelength distribution of  $N_2H_4$  FIR laser lines pumped by  $^{12}C^{16}O_2$ .

## 5. FUTURE WORK

We plan to study the  $N_2O$  pumped  $N_2H_4$  system further, looking for more FIR lines and frequency measuring as many of the lines as possible. Also with so much information on the  $N_2H_4$  FIR laser lines, the next obvious step is assigning the upper and lower laser levels.

## 6. REFERENCES

1. S. F. Dyubko, V. A. Svich, and L. D. Fresenko, "Stimulated emission of submillimeter lines of hydrazine, excited by a  $CO_2$  laser," *J. Appl. Spectrosc.*, Vol. 20, pp. 545-546, 1974.
2. H. E. Radford, F. R. Petersen, D. A. Jennings, and J. A. Mucha, "Heterodyne measurements of submillimeter laser spectrometer frequencies," *IEEE J. Quantum Electron.*, Vol. QE13, pp. 92-94, 1977.
3. M. Inguscio, G. Moruzzi, K. M. Evenson, and D. A. Jennings, "A review of frequency measurements of optically pumped lasers from 0.1 to 8 THz," *J. Appl. Phys.*, Vol. 60, pp. R161-R192, 1986.
4. N. G. Douglas, *Millimeter and Submillimeter Wavelength Lasers*, p. 223, Springer-Verlag, New York, 1989.
5. H. E. Radford, K. M. Evenson, F. Matsushima, L. R. Zink, G. P. Galvão, and T. J. Sears, "Far infrared laser frequencies of  $CH_3OD$  and  $N_2H_4$ ," *Int. J. IR & MM Waves*, Vol. 12, pp. 1161-1166, 1991.
6. E. C. C. Vasconcellos, L. R. Zink, G. P. Galvão, and K. M. Evenson, "New  $N_2H_4$  far infrared laser lines and frequencies," *IEEE J. Quantum Electron.*, Vol. QE-30, pp. 2401-2406, 1994.
7. E. C. C. Vasconcellos, S. C. Zerbetto, K. M. Evenson, and L. R. Zink, "New far-infrared hydrazine laser lines and their frequencies," *J. Opt. Soc. Am. B.*, Vol. 12, pp. 1334-1337, 1995.
8. H. Jones, G. Taubmann, and M. Takami, "The optically pumped hydrazine FIR laser: assignments and new laser lines," *IEEE J. Quantum Electron.*, Vol. QE-18, pp. 1997-1999, 1982.
9. K. M. Evenson, C. Chou, B. W. Bach, and K. G. Bach, "New cw  $CO_2$  laser lines: the 9- $\mu m$  hot band," *IEEE J. Quantum Electron.*, Vol. QE-30, pp. 1187-1188, 1994.
10. E. C. C. Vasconcellos, S. C. Zerbetto, J. C. Holecek, and K. M. Evenson, "Short-wavelength far-infrared laser cavity yielding new lines in methanol," *Op. Lett.*, Vol. 20, pp. 1392-1393, 1995.

Contribution of CNPq and NIST

## Far-Infrared Laser Magnetic Resonance

K.E. Evenson

Time and Frequency Division

National Institute of Standards and Technology

325 Broadway

Boulder, CO 80303

&

J. M. Brown

Oxford University

Oxford, England

### Abstract

Recent developments in the field of far-infrared, FIR, laser magnetic resonance, LMR, are reported. The wavelength range of the techniques have been significantly extended to shorter wavelengths, down to 40  $\mu\text{m}$ . In addition, new methods of generating transient atoms and molecules have been developed. New results on fine structure transitions in atoms and ions will be reported. It has also been possible to detect fine structure transitions in molecules like FeH. In addition, the extended frequency range has made it possible to detect vibration-rotation transitions in an open shell molecule for the first time, namely  $\text{FeD}_2$ .

### Introduction

Laser magnetic resonance (LMR) was first developed in the far-infrared (FIR) in 1968 by Evenson and co-workers [1]. In the experiment, the small mismatch between a FIR laser frequency and a transition in an open shell (hence, paramagnetic) molecule can be tuned by the application of an external magnetic field. A change in laser power at this "resonance" condition is detected. The LMR spectrum is therefore displayed as a function of the magnetic field for a fixed laser frequency. The technique has very high sensitivity, because the sample is located inside the laser cavity. Many novel short-lived free radicals have been detected in the gas phase by this approach [2]. The technique has also been applied very effectively in the mid-infrared region [3].

### Recent Technical Developments

An essential requirement for a successful LMR experiment is that there be a FIR laser line whose frequency is close to that of the molecular transition at zero magnetic field ("close" is generally within 0.3  $\text{cm}^{-1}$  or 15 GHz with currently available magnetic fields). Until 1992, the vast majority of LMR experiments were conducted at wavelengths longer than 100  $\mu\text{m}$ . There was very sparse coverage of the wavelength region to shorter wavelengths by well characterized FIR laser lines [4]. At this time, the design of the transversely-pumped FIR laser in the laboratory at NIST, Boulder, Colorado, was modified to promote the oscillation of short wavelength laser lines. The internally reflecting Cu pump tube, in which the laser gas was pumped with a  $\text{CO}_2$  laser line, was reduced in diameter from 50 mm to 20 mm. With this design, it was much easier to encourage known short wavelength laser lines to oscillate; and many new laser lines were discovered. As a result, there is now reasonable good coverage down to 40  $\mu\text{m}$ . It should be possible to extend this coverage even further down to about 25  $\mu\text{m}$ .

Another important development was the design and construction of a new microwave discharge source [5] which has been used to generate detectable concentrations of many new atomic and molecular free radicals, including ions and molecules in excited electronic states. The discharge has been designed so that the plasma occurs outside the microwave cavity where it can be probed directly with the FIR laser beam. The external magnetic field used in the LMR experiment has the desirable effect of "pinching" the discharge so that it is more energetic within a smaller volume.

### Fine Structure Transitions in Atoms

Atom spin-orbit splittings in the first three rows of the Periodic Table fall mostly in the FIR region. Using the new

microwave discharge source, it has been possible to generate many atomic species, several of them ions, in the FIR LMR spectrometer in sufficient concentration that the magnetic dipole fine structure transitions can be detected. Measurements of the LMR spectra have enabled the values of the fine structure splittings to be measured much more accurately. This is important for astrophysical applications where the transitions are used to probe remote regions of space using heterodyne techniques. In addition, nuclear hyperfine splittings have been measured, many of them for the first time.

### Fine Structure Transitions in Molecules

The spin-orbit splittings observed in molecules reflect the fine structure splittings of their component atoms. Consequently, many molecular fine structure splittings also fall in the FIR region. The fine structure transitions in molecules often acquire significant electric dipole intensity making them stronger than the allowed magnetic dipole transitions, even though they are intrinsically weaker than the pure rotational transitions normally studied in the FIR [6]. The extension of the LMR technique to shorter wavelengths has allowed larger spin-orbit splittings to be measured with greater sensitivity. One example of this is the detection of several fine structure transitions in the FeH radical in its ground  $\Delta$  state [7].

### The Detection of Vibration-Rotation Transitions

The extension of frequency coverage to higher values (up to 6.15 THz or 250  $\text{cm}^{-1}$ ) opens up the possibility of detecting spectroscopic transitions in open-shell molecules which involve low frequency vibrations. These can be of two types: Either bending vibrations of "normal" molecules or stretching vibrations of weakly bound species such as van der Waals complexes. The vibration-rotation transitions involved are weaker than pure rotational transitions but the fact that they occur at higher frequencies increases the instrumental sensitivity so that they are readily detectable. During the last year, we have succeeded in detecting lines in the bending vibrational band  $\nu_2$  of the free radical  $\text{FeD}_2$  at 226  $\text{cm}^{-1}$ . This molecule is linear with a ground  $^3\Delta_g$  state [8].

### References

- [1] K.M. Evenson, H.P. Broida, J.S. Wells, R.J. Mahler and M. Mizushima, Phys. Rev. Lett. **21**, 1038 (1968).
- [2] K.M. Evenson, Faraday Discussions of the Chemical Society **71**, 7 (1981).
- [3] G.W. Hills, Magnetic Resonance Review, **9**, 15 (1984).
- [4] N.G. Douglas, "Millimetre and Submillimetre Wavelength Lasers" (Springer-Verlag, Berlin) 1989.
- [5] T.D. Varberg, J.M. Brown, and K.M. Evenson, J. Chem. Phys. **100**, 2487 (1994).
- [6] J.M. Brown, A.R.H. Cole and F.R. Honey, Mol. Phys. **23**, 287 (1972).
- [7] S.P. Beaton, J.M. Brown and K.M. Evenson, to be published.
- [8] H. Körsgen, K.M. Evenson, and J.M. Brown, J. Chem. Phys., in press.

# Cross-saturated Gains and Dispersion of Optically-pumped Far Infrared Laser Media in a Ring Cavity

N. Sokabe, N. Togawa, M. Hasegawa and S. Yamakawa

*Department of Applied physics, Osaka City University*

*3-3 Sugimoto, Sumiyoshi, Osaka 558, Japan*

Y. Horiuchi

*Department of Liberal Studies, Nara National Institute of Technology*

*22 Yata, Yamato-koriyama, Nara 639-11, Japan*

We report analysis of gains and dispersion of optically pumped far infrared laser media in a ring cavity that allows co-existence of two far infrared radiation fields counter-propagating with each other. The far infrared radiation fields co- and counter-propagating with the infrared pump field in the cavity experience cross-saturated gain depending on the direction of propagation. Results of numerical calculation with relaxation constants as measured with photoacoustic spectroscopy are presented on selected CH<sub>3</sub>OH far infrared laser lines.

## I. INTRODUCTION

Gain and dispersion of a three level system interacting with two resonant radiation fields have attracted much attention [1,2]. A lot of the previous works focused on optically pumped molecular lasers was devoted to analysis of the gain that depends on direction of propagation relative to the pump field. The gain and dispersion of the coupled transitions were analyzed for a radiation field traveling in the same or the opposite direction to the pump field. An analysis of the gain for standing wave was also reported by Feldman [3].

An optical-pumped far infrared laser with a ring cavity was introduced by Heppner [4] and bi-directional output from a ring laser was reported [5]. In general, two far infrared radiation fields counter-propagating with each other may exist in a ring cavity. Vilaseca reported a model that allows two far infrared fields and calculated gains by using matrix continued fraction expansion [6]. We have also reported an alternative treatment that gives an explicit expression for gains and dispersion in the presence of two counter-propagating far infrared fields [7]. In this contribution, we present gains and dispersion including Raman-type double photon transition in the presence of two counter-propagating far infrared fields and results of numerical calculation.

## II. FAR INFRARED SUSCEPTIBILITY AND NUMERICAL CALCULATION

A model with  $\Lambda$ -type level configuration in which two transitions share common upper level 0 is adopted. While a pump laser field couples with 2-0 infrared transition,

two far infrared radiation fields couple with 0-1 transition. Both the transitions are assumed to be inhomogeneously broadened.

The total radiation field is given as

$$E(z, t) = \frac{1}{2} A_p e_p \exp[-i(\Omega_p t - k_p z)] + \frac{1}{2} \sum_{\epsilon=\pm} A^\epsilon e_s^\epsilon \exp[-i(\Omega_s^\epsilon t - \epsilon k^\epsilon z)] + \text{c.c.}, \quad (1)$$

where the first term denotes the pump field propagating along the  $z$ -axis and the second term gives the far infrared fields. The one with  $\epsilon = +1$  is for the co-propagating(forward) field and the other with  $\epsilon = -1$  is for the counter-propagating(backward) field with respect to the pump field. Equation of motion of ensemble averaged population matrix  $\rho$  yields far infrared susceptibility  $\chi^\pm(\Delta_s, \alpha_\pm, \alpha_\mp; \Delta_p, \beta)$  given by

$$\chi^\pm = -\left\langle \frac{N|\mu_{10}^\pm|^2}{\epsilon_0 \hbar D} \left\{ (Y^\pm X^\mp - Z^\pm |\alpha_\pm|^2) r_{10} + Y^\pm |\beta|^2 r_{20} \right\} \right\rangle, \quad (2)$$

in stationary-state where  $r_{i0}$ 's are given by

$$r_{10} = \frac{(1 - J_{22}) r_{10}^e + J_{12} r_{20}^e}{(1 - J_{11})(1 - J_{22}) - J_{12} J_{21}}, \quad (3)$$

$$r_{20} = \frac{(1 - J_{11}) r_{20}^e + J_{21} r_{10}^e}{(1 - J_{11})(1 - J_{22}) - J_{12} J_{21}}, \quad (4)$$

and  $J_{ij} = 2\Im C_{ij}(i, j = 1, 2)$  with  $C_{ij}$ 's defined by

$$C_{11} = \frac{|\alpha_+|^2}{\gamma_0 D} \left\{ \frac{2\eta_1 \gamma_{10}}{\gamma_1} [Y^- X^+ - Z^- |\alpha_-|^2] + Y^- |\beta|^2 \right\} + \frac{|\alpha_-|^2}{\gamma_0 D} \left\{ \frac{2\eta_1 \gamma_{10}}{\gamma_1} [Y^+ X^- - Z^+ |\alpha_+|^2] + Y^+ |\beta|^2 \right\}, \quad (5)$$

$$C_{12} = \frac{|\beta|^2}{\gamma_0 D} \left\{ \frac{2\eta_1 \gamma_{10}}{\gamma_1} [Y^+ |\alpha_-|^2 + Y^- |\alpha_+|^2] + Y^+ Y^- \right\}, \quad (6)$$

$$C_{21} = \frac{|\alpha_+|^2}{\gamma_0 D} \left\{ \frac{2\eta_2 \gamma_{20}}{\gamma_2} Y^- |\beta|^2 + Y^- X^+ \right\}$$

$$-Z^{-}|\alpha_{-}|^2\} + \frac{|\alpha_{-}|^2}{\gamma_0 D} \left\{ \frac{2\eta_2\gamma_{20}}{\gamma_2} Y^{+}|\beta|^2 + Y^{+}X^{-} - Z^{+}|\alpha_{+}|^2 \right\}, \quad (7)$$

$$C_{22} = \frac{|\beta|^2}{\gamma_0 D} \left\{ \frac{2\eta_2\gamma_{20}}{\gamma_2} Y^{+}Y^{-} + Y^{+}|\alpha_{-}|^2 + Y^{-}|\alpha_{+}|^2 \right\}, \quad (8)$$

with  $L^{\pm} = \Delta_s^{\pm} \mp k^{\pm}v + i\gamma_{10}$ ,  $L = -\Delta_p + k_p v + i\gamma_{20}$ ,  $R^{\pm} = -\Delta_p + \Delta_s^{\pm} + (k_p \mp k_s^{\pm})v + i\gamma_{21}$ ,  $D = LY^{+}Y^{-} - L^{+}Y^{-}|\alpha_{+}|^2 - L^{-}Y^{+}|\alpha_{-}|^2$ ,  $X^{\pm} = LR^{\pm} - |\alpha_{\pm}|^2$ ,  $Y^{\pm} = L^{\pm}R^{\pm} - |\beta|^2$ , and  $Z^{\pm} = L^{\pm}R^{\mp} - |\beta|^2$ .

Resonant Rabi frequencies are defined as  $\beta = \mu_{20}A_p^*/2\hbar$  and  $\alpha_{\pm} = \mu_{10}A_s^{\pm}/2\hbar$ , where  $\mu_{10}$ 's are matrix elements of the transition dipole moment,  $r_{i0}(= \rho_{ii} - \rho_{00}, i = 1, 2)$  and  $r_{i0}^e$  are population difference densities in the presence and the absence of the radiation fields, respectively, and  $\eta_i = (\gamma_0 + \gamma_i)/2\gamma_{0i}$ , where  $\gamma_i$  and  $\gamma_{i0}$  are the decay rates of the state  $i$  and of polarization, respectively. The number density of molecules is denoted by  $N$ ,  $\Delta_p$  and  $\Delta_s^{\pm}$  are frequency detunings,  $\epsilon_0$  is the dielectric constant of vacuum,  $\hbar$  is Planck constant, and  $e_p$  and  $e_s^{\pm}$  are polarization vectors. The average denoted by  $\langle \rangle$  is to be taken over the velocity distribution of molecules.

Far infrared gains have been calculated for far infrared laser lines of  $\text{CH}_3\text{OH}$  pumped with  $\text{CO}_2$  laser. Table I lists the parameters relevant to  $70 \mu\text{m}$  line pumped by the  $9 \mu\text{m}$ -band P(34) line. The table contains the decay rates measured with photoacoustic spectroscopy in the optimum pressure range of operation of optically-pumped far infrared laser [8]. Maxwellian distribution at room temperature has been assumed for molecular velocity distribution.

### III. RESULTS AND DISCUSSION

Figure 1 shows calculated far infrared gain of the  $70 \mu\text{m}$  line vs detuning  $\Delta_s/\gamma_0$  for different values of far infrared intensities  $\alpha_{\pm}/\gamma_0$  and pump detunings  $\Delta_p/\gamma_0$ . The directional anisotropy of the gain is due to different velocity distribution of the excited molecules as seen by the two counter-propagating far infrared fields as well as to Raman type double photon transition.

The gain of the backward field experiences stronger

TABLE I. Parameters used in calculation.

$r_{10}^e$	$1.0 \times 10^{-5}$	
$r_{20}^e$	$1.2 \times 10^{-3}$	
$\gamma_0, \gamma_1, \gamma_{10}$	$1.1 \times 10^6 \text{ s}^{-1}$	$(\text{s} \cdot \text{Pa})^{-1}$
$\gamma_2, \gamma_{20}, \gamma_{21}$	$0.9 \times 10^6$	$(\text{s} \cdot \text{Pa})^{-1}$
$ \mu_{10} $	$1.2 \times 10^{-30} \text{ a.u.}$	C · m
$ \mu_{20} $	$3.5 \times 10^{-31} \text{ a.u.}$	C · m

<sup>a</sup>From Ref. [9]

cross saturation than that of the forward one does, and the gain profile becomes more asymmetric as the pump detuning increases. Therefore, it is necessary to take not only the forward wave but also the backward wave into consideration for precise analysis of an optically-pumped far infrared ring laser. Detailed results of calculation including Raman type transition will be reported.

In conclusion, we have derived explicit expressions for far infrared gains of optically pumped far infrared laser transitions in the presence of two counter-propagating far infrared fields. The gain experiences strong cross saturation and its profile becomes more asymmetric for large pump detunings.

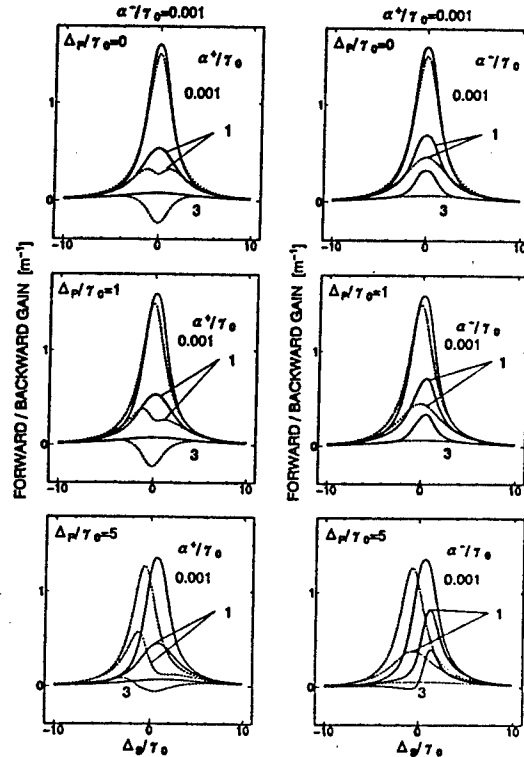


FIG. 1. Forward(solid line curves) and backward(dashed line) gains vs detuning for different pump detuning and intensities.  $\text{CH}_3\text{OH}$   $70 \mu\text{m}$  line. Pressure of 20 Pa and  $\beta/\gamma_0 = 0.7$ .

### REFERENCES

- [1] M.S.Feld and A.Javan, Phys. Rev. 177,540(1969).
- [2] Z.Drozdzowicz, R.J.Termin and B.Lax, IEEE J. Quantum Electron. QE-15,170(1979).
- [3] B.J.Feldman and M.S.Feld, Phys. Rev. A5,899(1972).
- [4] J.Heppner and C.O.Weiss, Appl. Phys. Lett. 33,590(1978).
- [5] P.Wanzen and G.L.Bourdet, IEEE J. Quantum Electron. 27, 152(1991).
- [6] R.Vilasaca, J.Martorell, R.Corbale and P.Laguarta, Opt. Commun. 70, 131(1989)
- [7] K.Matsushima, N.Togawa, Y.Horiuchi and N.Sokabe, Digest of the 19-th Int. Conf. on IR and MM Waves, Sendai 1994, p.167.
- [8] Y.Horiuchi and N.Sokabe, Digest of the 20-th Int. Conf. on IR and MM Waves, Orlando 1995, p.327.
- [9] J.Heppner and C.O.Weiss and U.Hübner and G.Schiin, IEEE J. Quantum Electron. QE-16,392(1980).

# New Far-Infrared Laser Lines from N<sub>2</sub>O Laser pumped Hydrazine and Frequency Measurements

E.C.C. Vasconcellos

Instituto de Física "Gleb Wataghin", Departamento de Eletrônica Quântica, Universidade Estadual de Campinas, 13083-970, Campinas, SP, Brasil

M. Tachikawa, L.R. Zink, and K.M. Evenson

Time and Frequency Division, National Institute of Standards and Technology, Boulder, Co. 80303-3328

## ABSTRACT

We have used an N<sub>2</sub>O laser to optically pump N<sub>2</sub>H<sub>4</sub> molecules in a far-infrared cavity and observed 17 new laser lines in the wavelength range 93.0 to 374.2  $\mu$ m, the 136.791  $\mu$ m line pumped by 10P(16) being a doublet. We also measured the frequencies of the laser lines by heterodyne mixing of the far-infrared radiation with radiation from two frequency-stabilized CO<sub>2</sub> lasers.

Key words: N<sub>2</sub>H<sub>4</sub>, far-infrared laser, frequency measurement, N<sub>2</sub>O pump laser

## 1. Introduction

Until recently hydrazine (N<sub>2</sub>H<sub>4</sub>) had six far-infrared laser lines in the wavelength range 200 to 575  $\mu$ m obtained by optically pumping the molecule with an N<sub>2</sub>O laser [1,2]. We used an improved N<sub>2</sub>O laser with extended coverage of frequencies in the sequence band lines to pump molecules in the 10  $\mu$ m region [3], and found 17 new laser lines in the spectral 93.0 to 374.6  $\mu$ m (3 222 036.901 to 801 069.677 MHz). We measured the wavelengths of the far-infrared laser lines by longitudinally moving one of the mirrors of the laser cavity and counting the laser modes observed, and their frequencies by heterodyne mixing of the far-infrared radiation with radiation from two frequency-stabilized CO<sub>2</sub> lasers.

## 2. Lasers Description

The N<sub>2</sub>O pump laser is a 1.5 m long cavity, described elsewhere [3], with typical powers of about 5-6 W operating in the regular and sequence bands lines. The FIR cavity was a rectangular metal-dielectric waveguide described in detail elsewhere [4].

## 3. Measurements

We determined the far-infrared (FIR) wavelengths by varying the cavity length over about ten wavelengths and measuring the length span with a micrometer. The value thus obtained can be accurate to about 0.05 mm. The FIR frequency measurement was accomplished by heterodyne mixing of two frequency stabilized CO<sub>2</sub> lasers with a microwave frequency and the FIR radiation to be measured [5]. The accuracy in the wavelength estimation is enough to select the CO<sub>2</sub> laser lines for the heterodyne measurement. The radiations are mixed in a metal-insulator-metal diode (MIM) which is also used to detect the FIR radiation when searching for new lines. A beat note is generated in the diode, and the FIR frequency is obtained by the equation

$$\nu_{\text{FIR}} = |\nu_1 - \nu_2| \pm m\nu_{\mu\text{wave}} \pm \nu_{\text{beat}} \quad (1)$$

where  $\nu_1$  and  $\nu_2$  are the CO<sub>2</sub> laser frequencies,  $\nu_{\mu\text{wave}}$

is the frequency of the microwave source,  $\nu_{\text{beat}}$  is the beat note frequency,  $\nu_{\text{FIR}}$  is the laser frequency to be measured, and the integer  $m$  is a harmonic number. The frequencies  $\nu_1$ ,  $\nu_2$  and  $\nu_{\mu\text{wave}}$  are chosen so that

$$0 < |\nu_{\text{beat}}| < 1.5 \text{ GHz} \quad (2)$$

#### 4. Results and Conclusion

Table I shows the observed far-infrared laser lines pumped by an  $\text{N}_2\text{O}$  laser, along with their frequency measurement, calculated wavelength, calculated wavenumber, and  $\text{N}_2\text{O}$  laser pump line.

These preliminary results have shown the potential of this new pumping laser in producing many more far-infrared laser lines, in hydrazine, many with wavelength less than  $150 \mu\text{m}$ .

#### 5. References

1. H. Jones, G. Taubmann, and M. Takami, "The optically pumped hydrazine FIR laser: assignments and new laser lines," *IEEE J. Quantum Electron.*, Vol QE-18, pp. 1997-1999 (1982)
2. N. G. Douglas, *Millimeter and Submillimeter Wavelength Lasers*, p. 223, Springer-Verlag, New York (1989)
3. Maki Tachikawa, Kenneth M. Evenson, Lyndon R. Zink, and Arthur G. Maki, "Frequency Measurements of 9- and 10-  $\mu\text{m}$   $\text{N}_2\text{O}$  Laser Transitions," *IEEE J. Quantum Electron.*, Vol. QE-32, pp. 1732-1736 (1996)
4. M. Inguscio, F. Strumia, K.M. Evenson, D.A. Jennings, A. Scalabrin, S. R. Stein, "Far-Infrared  $\text{CH}_3\text{F}$  Laser," *Opt. Lett.*, vol. 4, pp. 9-11 (1979)
5. F.R. Petersen, K.M. Evenson, D.A. Jennings, J.S. Wells, K. Goto, J.J. Jimenez, "Far-Infrared frequency synthesis with stabilized  $\text{CO}_2$  lasers: accurate measurements of the water vapor and methyl alcohol laser frequencies," *IEEE J. Quantum Electron.*, vol. QE-11, pp 838-843 (1975)

**TABLE I - Frequency Measurements of a  $\text{N}_2\text{H}_4$  far-infrared laser pumped by an  $\text{N}_2\text{O}$  laser**

$\text{N}_2\text{O}$ Line	Measured Frequency	Calculated Wave- length <sup>a</sup>	Calculated Wave- number <sup>a</sup>
	MHz	$\mu\text{m}$	$\text{cm}^{-1}$
10P(32)	3 222 036.901	93.044	107.4756
10R(36)		98.0	
10P(45)	2 823 544.529	106.176	94.1833
10R(25)	2 823 286.972	106.186	94.1747
10P(15)'''	2 631 380.704	113.930	87.7734
10P(26)		114.4	
10P(24)	2 485 511.581	120.616	82.9077
10P(16)	2 191 609.635	136.791	73.1042
	2 191 613.732	136.791	73.1044
10P(30)	1 902 430.289	157.584	63.4582
10P(11)	1 858 872.013	161.277	62.0053
10P(34)	1 426 180.221	210.207	47.5723
10P(07)	1 371 481.504	218.590 <sup>b</sup>	45.7477
10R(04)	1 369 893.297	218.844	45.6947
10P(15)''	1 288 113.660	232.738	42.9668
10P(24)		237.0 <sup>b</sup>	
10P(29)		241.6	
10R(24)		257.5	
10P(34)	1 041 094.216	287.959	34.7272
10R(11)	906 899.814	330.568 <sup>b</sup>	30.2509
10R(38)		339.4	
10P(15)'	801 069.677	374.240 <sup>b</sup>	26.7208
10P(28)		492.4 <sup>b</sup>	

<sup>a</sup> Calculated from  $c = 299\,792\,458 \text{ m/s}$

<sup>b</sup> Previously reported. See reference 1

',' and''' indicate different  $\text{N}_2\text{O}$  laser frequency offsets

Contribution of CNPq and NIST

## Active mode locking of a *p*-Ge hot hole laser

J. N. Hovenier<sup>1</sup>, A. V. Muravjov<sup>2</sup>, S. G. Pavlov<sup>2</sup>,

V. N. Shastin<sup>2</sup>, R. C. Strijbos<sup>1</sup> and W. Th. Wenckebach<sup>1</sup>

<sup>1</sup> Faculty of Applied Physics and Delft Institute for Microelectronics and Submicron Technology,  
Delft University of Technology, P. O. Box 5046, 2600 GA Delft, The Netherlands

<sup>2</sup> Institute for Physics of Microstructures,  
Russian Academy of Sciences, Nizhny Novgorod 603600, Russia

### Abstract.

Active mode locking of a *p*-Ge hot hole laser ( $50 - 140 \text{ cm}^{-1}$ ) has been achieved by electrical intracavity modulation of the gain, that results in the generation of a train of subnanosecond pulses of far-infrared radiation.

The feasibility of generating short pulses of far-infrared radiation is investigated using active mode locking of a hot-hole *p*-Ge laser, operating on light-to-heavy-hole optical transitions in crossed electric and magnetic fields [1]. Due to their broad gain spectrum ( $50 - 140 \text{ cm}^{-1}$ ) and their equidistant set of modes [9], *p*-Ge lasers are expected to be able to generate pulses of far-infrared emission on a picosecond time scale [2]. As a method to achieve active mode locking, it was proposed to use fast modulation of the population inversion of hot holes by applying a radio frequency (RF) burst of a longitudinal electric field [3].

The present experimental study is based on this proposal. The active sample was cut from a single crystal of Ga-doped Ge ( $N_A = 7 \times 10^{13} \text{ cm}^{-3}$ ) in the form of a rectangular parallelepiped of  $5 \times 7 \times 49.5 \text{ mm}^3$ . Two gold mirrors, evaporated on quartz substrates are attached to the polished ends of the sample via  $10 \mu\text{m}$  teflon films. Electric field pulses ( $1.3 \text{ kV/cm}$ ,  $4 \mu\text{s}$ ) are applied to ohmic contacts covering the lateral surfaces of the sample. The entire system is immersed into liquid helium inside an optical cryostat. The magnetic field ( $1.1 \text{ T}$ ) is applied perpendicularly to the long sample axis and perpendicularly to the electric field (Voigt configuration) using a room temperature iron core electromagnet.

To achieve active mode locking the gain is modulated in a local part of the active sample by applying a longitudinal RF electric field  $E_\omega \parallel B$  via small additional electrical contacts close to the output mirror. Our method of gain modulation is based on the strong dependence of the light hole life time on a deviation from orthogonality of the applied electric and magnetic fields. A small electric field component parallel to

the magnetic field  $B$  causes an acceleration of the light holes along  $B$  and their subsequent scattering on optical phonons decreases the population inversion [4, 5, 6]. Because the gain decreases each half period of the RF field, which has a frequency  $\simeq 383 \text{ MHz}$ , the frequency of gain modulation is  $\simeq 767 \text{ MHz}$ , which is chosen to be equal to the cavity roundtrip frequency. Previous experiments using this gain modulation scheme yielded an indirect confirmation of the possibility of actively mode locking the *p*-Ge laser, but lacked the decisive proof in the time- and frequency domain [7, 8].

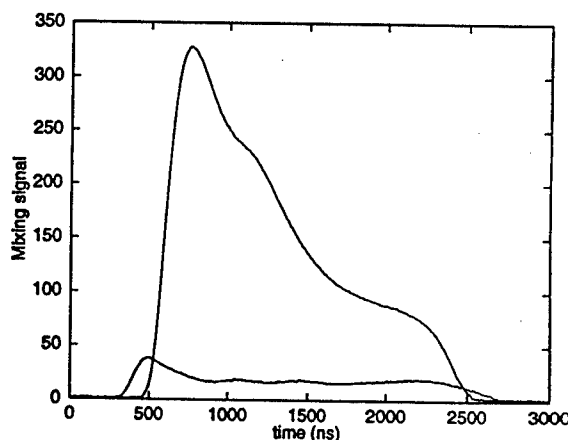


Figure 1: The mixing signal at the frequency  $767 \text{ MHz}$  with and without gain modulation.  $P_{RF} = 180 \text{ W}$ .

In this study, we first used heterodyne spectroscopy [9] to investigate the interference products of the *p*-Ge laser modes with and without external modulation of the gain. As a mixer we used a Schottky diode detector, while a spectrum analyser was used to analyse the output signal of the mixer near the cavity roundtrip frequency ( $767 \text{ MHz}$ ), i.e. the distance between neighbouring longitudinal modes. Without gain modulation the mixing signal is rather weak and instable, because it is the product of random interference of laser modes. With gain modulation we obtain a strong and stable mixing signal, that



demonstrates the synchronisation of the laser mode phases (Fig.1).

This corresponds to the forming of a pulse of electromagnetic field running through the laser cavity, that in a time-resolved measurement (Fig. 2) is observed as a train of subnanosecond pulses of *p*-Ge laser radiation with a repetition rate equal to the cavity roundtrip frequency (767 MHz).

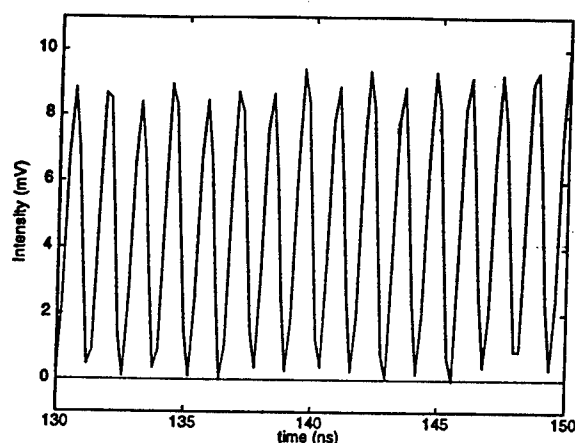


Figure 2: The output of an actively mode-locked *p*-Ge hot hole laser, as detected on the Schottky diode connected to a 1 GHz bandwidth oscilloscope

Authors are thankful to prof. H.-P. Röser's group from the Institute for Space Sensor Technology (DLR) in Berlin for providing a GaAs Schottky diode detector 1T15 [10].

This investigation is partially supported by the Russian Basic Research Foundation (grant # 96-02-19275).

Joint collaboration between IPM RAS and TU Delft is partially supported by International Center for Advanced Studies in Nizhny Novgorod (grant # 97-2-07).

## References

- [1] E. Gornik and A. A. Andronov, Eds., *Opt. Quantum Electron.*, vol. 23, Chapman and Hall, London, 1991, Special Issue Far-infrared Semiconductor Lasers.
- [2] Fritz Keilmann and Rainer Till, *Opt. Quantum Electron.*, vol. 23, pp. S231-S246, 1991.
- [3] R. C. Strijbos, J. G. S. Lok, and W. Th. Wenckebach, *J. Phys. Condens. Matter*, vol. 6, pp. 7461-7468, 1994.
- [4] A. V. Murav'ev, I. M. Nefedov, S. G. Pavlov, and V. N. Shastin, *Quantum Electron.*, vol. 23, no. 2, pp. 119-124, Feb. 1993.
- [5] A. V. Murav'ev, I. M. Nefedov, Yu. N. Nozdrin, and V. N. Shastin, *Sov. Phys.-Semicond.*, vol. 23, no. 10, pp. 1071-1075, Oct. 1989.
- [6] V. N. Shastin, *Opt. Quantum Electron.*, vol. 23, pp. S111-S131, 1991.
- [7] R. C. Strijbos, J. H. Blok, J. N. Hovenier, R. N. Schouten, W. Th. Wenckebach, A. V. Muravjov, S. G. Pavlov, and V. N. Shastin, In K. HESS, J.-P. LEBURTON, AND U. RAVAIOLI, Eds., *Hot Carriers in Semiconductors*, Plenum Press, New York, 1996, pp. 469-471, Proceedings of the 9<sup>th</sup> Int. Conf. on Hot Carriers in Semiconductors, July 31-August 4, 1995, Chicago, Illinois, USA.
- [8] R. C. Strijbos, A. V. Muravjov, J. H. Blok, J. N. Hovenier, J. G. S. Lok, S. G. Pavlov, R. N. Schouten, V. N. Shastin, and W. Th. Wenckebach, In *Conference Digest of 15th Int. Semiconductor Laser Conference, October 13-18, 1996, Haifa, Israel*, 1996, pp 61-62.
- [9] E. Bründermann, H. P. Röser, A. V. Muravjov, S. G. Pavlov, and V. N. Shastin, *Infrared Phys. Technol.*, vol. 36, no. 1, pp. 59-69, 1995.
- [10] H. P. Röser, H.-W. Hübers, T. W. Crowe, and W. C. B. Peatman, *Infrared Phys. Technol.* 35, 451 (1994).

# Problems of Realizing a Long Pulse Length, High Duty Cycle p-Ge Landau Level FIR Laser

Paul D. Coleman and Daniel W. Cronin

Electro-Physics Laboratory  
ECE Department  
University of Illinois  
Urbana, IL 61801

Numerical calculations using analytical solutions of the heat equation subject to heat sink dissipation limits, resonator size and laser temperature cut-off limit of 20°K are presented to determine laser pulse lengths and duty cycles.

A series of detailed graphs point out the problems that are encountered in attempting to realize a CW p-Ge laser system. They also provide design data for future p-Ge lasers and optimization data for existing laser systems. The full version of this paper will be found in the June 1997 issue of *International Journal of Infrared and Millimeter Waves*.

## 1. Introduction

The unique feature of the p-Ge hot-hole laser of being continuously magnetically tunable over a 3-1 range (40-120 cm<sup>-1</sup>) is offset by the short laser pulse (~6 μsec) and small duty cycle (~10<sup>-4</sup>) that are realized in the usual laser configurations. Although research on the p-Ge laser [1] was initiated over 15 years ago, this laser pulse-duty cycle problem has not received any experimental attention until 1996 [2]. To the authors' knowledge, this paper represents the first analytical work on the problem.

The basic problem challenging the realization of a CW p-Ge laser is that of limiting the Ge bar temperature to 20°K [3]. Scattering, which increases with temperature, reduces the laser gain, quenching laser action. Hence the hurdles that need to be addressed to achieve a possible CW p-Ge laser can be readily identified: 1) heat sink dissipation limits, 2) p-Ge bar temperature limits, and 3) laser resonator size limits.

In the interest of obtaining analytical solutions to the heat equation [4], it is assumed that  $C_v$  and  $K$  are constant and that Dirichlet boundary conditions exist. This will lead to the numerical results and conclusions being optimistic in that a CW p-Ge laser will be more difficult to realize than is presented.

## 2. Heat Sink Limitations

Essentially the entire input excitation energy of the p-Ge laser must be dissipated in the heat sinks since the laser is very inefficient. Hence the average power  $P_{AV}$  that must be dissipated can be expressed as

$$P_{AV} = (q N_A vE) VD \leq P_0 \text{ (watts)} \quad (1)$$

Cooling the p-Ge bar with liquid He I limits  $P_0$  to less than 10 watts, while values of the velocity  $v$  and field  $E$  are the order of 10<sup>7</sup> cm/s and 10<sup>3</sup> volts/cm. Hence, the only two parameters for the experimenter to adjust are the doping density  $N_A$  and bar volume  $V$ . Using the values  $P_0 = 4$  watts,  $N_A = 8 \times 10^{13}/\text{cm}^3$ ,  $E = 800$  v/cm and  $V = 0.04$  cm<sup>3</sup>, Bründermann et al. were able to achieve a  $D \approx 10^{-3}$ . Cooling the bar with He II [5] could lead to larger values of  $P_0$ , but it would appear a challenge from the consideration of Eq. (1) that a factor of 10<sup>3</sup> needed to make  $D = 1$  for CW operation could be achieved.

## 3. Bar Temperature Limitation

It does not appear likely that an analytical solution of the well known heat equation

$$\rho C_v \frac{\partial T}{\partial t} = K \nabla^2 T + P \quad (2)$$

can be obtained for a p-Ge bar since  $C_v$  and  $K$  are functions of  $T$  and more importantly cooling the bar surface with LHe I leads to varying boundary conditions for  $T$ .

As a first step in estimating p-Ge bar temperatures, constant values for  $C_v$  and  $K$  and Dirichlet boundary conditions have been assumed which then permit analytical solutions to Eq. (2) to be obtained. Using the formulas for  $T$ , numerous curves can be generated using the p-Ge bar dimensions  $a$ ,  $b$ , peak video pulse power density  $P_0$ , pulse length  $\tau_1$  and cooling time  $\tau_2$ .

If the p-Ge bar center temperature is limited to a maximum temperature of 20°K, then CW operation for  $P_0$  values of 4, 8 and 12 kcal/s-cm<sup>3</sup> can only be realized for bar dimensions  $a = b$  less than 0.42, 0.30, and 0.25 millimeters, assuming Eq. (1) can be satisfied. The obvious price to be paid for possible CW operation by a severe reduction in p-Ge volume is the laser output power.

## 4. Resonator Size Limitations

Two resonator configurations are presently used with the p-Ge laser: 1) a Fabry-Perot, and 2) a dielectric resonator both of which have minimum size constraints for a given frequency. For a Fabry-Perot system, the beam must be kept away from the ohmic contacts to the p-Ge bar to avoid losses and maximize the resonator  $Q$ . This requirement leads to values of  $a = b$  exceeding 0.4 millimeters. In the case of a dielectric slab waveguide [6] resonator model, the guidance condition and/or the conditions that the rays must be trapped, i.e., incident angles greater than the critical angle, lead to  $a = b$  values that can exceed 1 millimeter. Thus the laser resonator poses limitations on realizing a CW p-Ge laser.

## 5. Conclusions

While a CW p-Ge laser cannot be ruled out, the prospects for the near future are not promising. The price to be paid will be for less laser power. Cooling with He II needs to be explored along with possible Landau level heterostructures wherein more specific excitation of the levels might be achieved. Continuous frequency tuning via a magnetic field retains its appeal for a far IR laser in spite of small duty cycles.

## References

- [1] Yu. L. Ivanov and Yu V. Vasilév, *Tech. Phys. Lett.* **9**, 264 (1983).
- [2] E. Bründermann et al., *Appl. Phys. Lett.* **68**, 3075 (1996).
- [3] T. Kielmann et al., *Appl. Phys. Lett.* **58**, 2205 (1991).
- [4] H. S. Carslaw and T. C. Jaeger, "Conduction of Heat in Solids." Oxford Univ. Press, London, 1959.
- [5] "Superfluid Helium Heat Transfer," edited by J. P. Kelly, American Society of Mechanical Engineers, 1990.
- [6] S. L. Chuang, "Physics of Optoelectronic Devices," John Wiley & Sons, Inc., New York, 1995.

# IR spectroscopy of High-Tc Superconductors.

A. Hadni<sup>1</sup>, M. Tazawa<sup>2</sup> & X. Gerbaux<sup>1</sup>

<sup>1</sup>LCM3B, URA - CNRS 809  
Université Henri Poincaré, Nancy 1  
B.P. 239, F-54506 Vandœuvre-lès-Nancy Cedex.

<sup>2</sup>NIRIN, 1, Hirate-cho, Kita-ku, Nagoya 462, Japan

## Abstract

IR spectroscopy of High-Tc Superconductors is highly sensitive to frequency, temperature, magnetic field, and has brought informations useful for both applications and theory.

$\text{cm}^{-1} < \nu < 10,000 \text{ cm}^{-1}$ . A Kramer's Kronig (KK) analysis gives directly the dynamic conductivity  $\sigma = \sigma_1 + j\sigma_2$ . The electric vector of the IR waves can be oriented parallel to  $c$  (smaller dc conductivity), or parallel to the  $ab$ -plane. In that plane  $\sigma_a < \sigma_b$  (additional excitation of chains).

## Introduction

It is well known now that the optical properties of High-Tc Superconductors (HTSC) show large variations in a frequency range extending from microwaves to UV, and also with temperature, and with the magnitude of a magnetic field applied to the HTSC. That is especially appealing for spectroscopists and it is not surprising that so many papers have appeared for ten years since the discovery of these HTSC.

Our purpose is to look at the different spectroscopic domains with a special emphasize at the Far IR where we have some experience, with perhaps more difficult techniques, but an easier modelisation, and we shall give some personal data on YBaCuO, the archetype of HTSC.

## I - Visible, near and Mid-IR [1]

We shall define this domain as the one where bulk reflectivity  $R^*$  is small enough to be measurable, e.g. 200

## I - 1 - Main experimental results

Obviously a simple Drude model cannot work since there is not only free carriers but also IR active lattice vibrations. A generalized Drude model has often been considered where the scattering time  $\tau$  and the effective mass of the carriers  $m^*$  depend on  $\omega$ . In fact, a simple Drude contribution can be determined from the study of the Far IR, and a Mid-IR band added to fit the spectra.

For  $E // c$ , dc conductivity is small, phonons can be seen, and perhaps a gap with  $h\nu_g \approx 3 k \theta_c$ .

For  $E // ab$ ,  $\sigma_1$  exhibits a minimum at  $\nu \approx 435 \text{ cm}^{-1}$  where the gap has been suspected, then at  $\nu \approx 300 \text{ cm}^{-1}$  when the spectral limit of the commercial spectrometers has been extended to smaller frequencies.

## I - 2 - Theoretical models

The origin of the Mid-IR absorption has been much discussed, and also the possibility of an IR active gap.

## II - Far IR (FIR)

### II - 1 - Experimental

If we define the FIR spectral range by  $5 \text{ cm}^{-1} < \nu < 200 \text{ cm}^{-1}$ , we shall have for most HTSC at low temperature,  $R^* > 99\%$ . The KK method is not feasible, and transmission measurements are needed. Very thin films are now available. They are deposited on plates of MgO, Si or LaAlO<sub>3</sub>, which are more or less transparent in the FIR. The film thickness can be as small as  $t = 200 \text{ \AA}$ , and however, for  $\theta < 30 \text{ K}$ , transmission can be smaller than 1%. That is too low to be measurable with conventional FIR spectroscopy. New monochromatic sources, e.g. FIR lasers, have been used. They give a tremendous increase of luminance over the classical mercury source. However interference inside the plate supporting the HTSC film can modify the transmission coefficient by a factor 10 to 20. This difficulty has been solved recently by Prof. Drew. An antireflection coating for internal reflection is possible [2-7], without too much loss of radiative energy.

Another possibility is to keep the broad band mercury source and increase the resolution of the classical Fourier Transform Spectrometer in order to see the fringes as well as possible. It has been shown [3] that the fringes minima can give directly the transmission  $T_{FS}$  of the free standing HTSC film, and the maxima the same transmission amplified by a factor  $n^2$ ,  $n$  being the FIR refractive index of the supporting MgO or Si, or LaAlO<sub>3</sub> plate: the Perot-Fabry is used as an optical amplifier.

### II - 2 - Transmission of a free-standing film

For most of the films we have studied:

- i)  $T_{FS} \propto \nu^2$
- ii)  $T_{FS}$  seems insensitive to  $\theta$  for  $\theta < 30 \text{ K}$  and  $\nu < 40 \text{ cm}^{-1}$

$$\text{It is shown that } T_{FS} = \frac{16 \pi^2 d^4}{\lambda^2 t^2}$$

From the value of  $T_{FS}$ , it is thus possible to get the penetration length  $d$  for wavelength  $\lambda$  and thickness  $t$ . For the YBaCuO films we have studied, the London penetration length seems proportional to  $\theta^2$ .

### II - 3 - A two-fluid model

Different parameters have to be considered: plasma frequency, collision frequency, at least one Mid-IR oscillator, and a law to represent the free carriers condensation vs. temperature. Fortunately they can be fitted separately. A few results:

- i) there is no exponential law as for classical superconductors, but a power law, and it is different for different samples.

There may be a slow condensation with  $f_n \propto \left(\frac{\theta}{\theta_c}\right)^{1.5}$ , or a

faster one with  $f_n \propto \left(\frac{\theta}{\theta_c}\right)^4$ .

- ii) collision frequency decreases rapidly for  $\theta < \theta_c$ , and is around  $\nu_c = 2 \text{ cm}^{-1}$  at liquid helium temperature.
- iii) the contribution of the Mid-IR oscillators to absorptivity is negligible for  $\nu < 10 \text{ cm}^{-1}$ .

### II - 4 - Effect of a magnetic field [2]

At low frequencies, transmission increases. Vortex dynamics and cyclotron resonance of the hole system have been recently observed [2].

## III -Microwaves

Microwaves are used for a long time to get the optical constants  $n$  and  $k$  ( $\bar{n} = n + jk$ ), or the surface

resistance of different materials, with  $R_s^* \approx 100 \text{ A}^*$ ; where

$$A^* = \frac{4n}{(n+1)^2 + k^2} \text{ is the bulk absorptivity. The}$$

measurements are especially difficult for the superconductors, but new methods have recently been used. Kinder et al. in Munich have made a resonant Perot Fabry interferometer with two MgO coated with YBaCuO as we had done for the Far IR. In the case of microwaves, homodyne detection is quite easy at  $\nu = 1 \text{ cm}^{-1}$ , and they have combined the well known elegant methods of optics with the powerful monochromatic microwave sources, and the efficient methods of detection for microwaves. The YBaCuO layers they used are especially thick ( $t = 3000 \text{ }\mu\text{m}$ ), transmission is only 0.3% at its maximum  $T_M$ , but the width,  $\Delta f \approx 350 \text{ kHz}$ , of the observed transmission fringe is very small. From  $T_M$  and  $\Delta f$ ,  $\sigma_1$  and  $\sigma_2$  are directly calculated without any model:  $T_M = \frac{1}{(1 + Z_0 t \sigma_r)^2}$ ;  $Q = \frac{f_0}{\Delta f}$ ;  $Q = \frac{P\pi}{4}(Z_0 t \sigma_i)^2$  where  $P = 1, 2, 3$  etc. is the order of the resonance,  $Z_0$  the impedance of vacuum (377 ohms). Their results are limited to one frequency  $f = 35 \text{ GHz}$ , but the effect of temperature has been accurately measured, and comforts the Far IR measurements. The London penetration length  $\lambda(0) \approx 1500 \text{ }\text{\AA}$  for their film, is smaller than for ours, but a quadratic dependence on temperature is observed as we have. The collision frequency is very low at low temperature (around  $7 \text{ cm}^{-1}$  for  $\theta = 10 \text{ K}$ ). However, surface resistance is not negligible, even at that frequency, and for  $\theta = 10 \text{ K}$ ,  $R_s^* \approx 0.3 \times 10^{-3} \Omega$ , hence  $A^* \approx 0.3 \times 10^{-5}$ . A previous work by Bonn et al. [8] had led to similar results, and also showed that for a single crystal  $R_s$

exhibits a bump at  $\theta \approx 40 \text{ K}$ , and a linear variation of  $\lambda_L$  vs.  $\theta$ , instead of  $\theta^2$  for a film, and no bump.

## Conclusion

The experimental results are just becoming to converge after ten years of research. No definite microscopic theory has really emerged up to now.

## References

- [1] S. Tajima, Superconductivity Review (will appear in 1997).
- [2] S. Wu, S.G. Kaplan, H.T.S. Lihn, H.D. Drew, S.Y. Hou, Julia M. Phillips, J.C. Barbour, E.L. Venturini, Qi Li & D.B. Fenner, Phys. Rev. B, 54, 13343 (1996).
- [3] A. Hadni & X. Gerbaux, Infrared Phys., 34, 327 (1993).
- [4] A.A. Volkov, B.P. Goshunov, G.V. Kozlov, S.I. Krasnosvobodtsev, E.V. Pechen, O.I. Sirotinskii & Ya. Pettselt, Sov. Phys. JETP, 68, 148 (1989).
- [5] A. Hadni, X. Gerbaux, H. Marin Cudraz, M. Tazawa, J.C. Mage, B. Marcilhac, L. Mercandalli & D. Mansart, Physica C, 245, 219 (1995).
- [6] J. Bouvier & J. Bok, Physica C, 249, 117 (1995).
- [7] X. Gerbaux, A. Hadni & M. Tazawa, Int. J. Infrared & Millim. Waves, 17, 693 (1996).
- [8] D.A. Bonn, Ruixing Liang, T.M. Riseman, D.J. Baar, D.C. Morgan, Kuan Zhang, P. Dosanjh, T.L. Duty, A. MacFarlane, G.D. Morris, J.H. Brewer, W.N. Hardy, C. Kallin & A.J. Berlinsky, Phys. Rev. B, 47, 11314 (1993).

# DEVELOPMENT OF W-BAND GYROKLYSTRONS AT NRL

M. Blank, B.G. Danly, P.E. Latham<sup>†</sup>, B. Levush

Code 6843 Naval Research Laboratory  
Washington, D.C. 20375

## Abstract

A four cavity W-band gyrokystron amplifier experiment is currently underway at the Naval Research Laboratory. The gyrokystron has produced 67 kW peak output power and 28% efficiency in the TE<sub>011</sub> mode with a 55 kV, 4.3 A annular electron beam. The full width half maximum (FWHM) bandwidth is greater than 460 MHz. Small signal and saturated gains of 36 dB and 29 dB, respectively, have been observed. Experimental results are in good agreement with theoretical predictions.

## Background

As evidenced in numerous experiments, the gyrokystron amplifier, based on the electron cyclotron maser instability, can reliably and efficiently generate high power, moderate bandwidth electromagnetic radiation at microwave and millimeter wave frequencies. For example, a three cavity C-band gyrokystron amplifier produced 54 kW peak output power and 30% efficiency in the TE<sub>011</sub> at 4.5 GHz [1]. The saturated gain was 30 dB and the FWHM bandwidth was 0.4%. A three cavity X-band gyrokystron achieved 16 kW peak output power 45% efficiency with a 1% bandwidth [2]. Fundamental and second harmonic two cavity gyrokystron amplifiers at 9.87 GHz and 19.7 GHz, designed as drivers for linear colliders, achieved peak output powers of 20 MW and 30 MW, respectively, with efficiencies near 30% [3,4]. A two cavity Ka-band gyrokystron, developed for radar applications, produced 750 kW at 35 GHz in the TE<sub>021</sub> mode at 24 % efficiency [5]. In W-band, a pulsed four cavity gyrokystron amplifier achieved 65 kW peak output power at 26% efficiency with 300 MHz bandwidth [6]. A continuous wave version of this W-band device demonstrated 2.5 kW average output power. The goal of the present work is to enhance the bandwidth of the W-band gyrokystron amplifier while maintaining high efficiency, peak output power, and gain.

## Theory and Design

This paper presents an experimental study of a four cavity W-band gyrokystron amplifier operating in the TE<sub>011</sub> mode near the fundamental cyclotron frequency. The circuit consists of a drive cavity, two idler cavities, and an output cavity. The circuit was designed with a time-dependent version of the nonlinear code MAGYKL [7]. The wave equation is given by

$$\frac{da}{dt} + \left(\frac{1}{2} + i\Delta\right)a = -\frac{QI_b}{2\omega W_{EM}} \int d\xi \frac{c}{\omega} \left\langle \frac{v_{\perp} E_c e^{-i\omega t}}{v_z} \right\rangle,$$

where  $a$  is the complex amplitude of the fields,  $\Delta = Q\{\text{Re}\{\omega_c\} - \omega\}/\omega$  is the normalized frequency shift,  $Q$  is the quality factor of the cavity,  $\omega$  is the drive frequency,  $\omega_c$  is the cold resonant frequency,  $I_b$  is the beam current,  $W_{EM}$  is the stored energy,  $c$  is the speed of light,  $v_{\perp}$  and  $v_z$  are the perpendicular and axial electron velocities,  $E_c$  is the cold cavity electric field, and  $t$  is the normalized time,  $Q/\omega$ .

In the formulation, the cavities are modeled by a series of straight uniform sections with abrupt discontinuities at the boundaries. The fields in each section, expanded as a radial series of TE, TM, and TEM modes, are determined through a scattering matrix solution [8]. Theoretical studies have shown that it is necessary to include many modes in the field description to correctly predict the resonant frequency of the cavity. In order to accurately predict the bandwidth of the amplifier, the formulation detailed in reference [7] was modified to include a frequency dependent drive power, as dictated by the resonant frequency and  $Q$  of in input cavity. The theoretical model was used to design the interaction circuit and determine the parameters of each cavity, which are summarized in Table 1.

	Design			Cold Test	
	L	f <sub>0</sub>	Q	f <sub>0</sub>	Q
cavity 1	0.43	93.00	125	-	-
cavity 2	0.50	93.52	175	93.56	130
cavity 3	0.50	92.89	175	93.02	128
cavity 4	0.80	93.18	300	93.21	299

Table 1 Summary of cavity parameters.

The drive power is coupled into the circuit through a coaxial cavity [9]. A single cylindrical waveguide excites the TE<sub>011</sub> mode of the outer cavity. Power is then coupled from the TE<sub>011</sub> mode in the outer cavity to the TE<sub>011</sub> mode in the inner cavity through four slots positioned symmetrically around the azimuth of the cavity. The coaxial cavity was analyzed with the High Frequency Structure Simulator (HFSS) and found to have a resonant frequency of 93.0 GHz and a diffractive  $Q$  of 150. HFSS simulations also show that 75% of the energy is stored in the TE<sub>011</sub> mode and 25% is stored in the TE<sub>011</sub> inner

cavity mode. Thus, 6 dB of drive power arriving at the input cavity is stored in the outer cavity and is not available for interaction.

Because the second and third cavities are terminated by drift sections that are cut-off for the  $TE_{011}$  mode at 93 GHz, the diffractive Q's are quite large. The design Q's of 175 are achieved through dielectric loading of the cavities. Small annular rings of 80/20 BeO/SiC are placed on one end wall of each idler cavity. The output cavity consists of a 0.8 cm straight section, followed by an iris which is cutoff to the  $TE_{011}$  mode at 93 GHz, and a 5 degree linear uptaper to the collector radius. The wave is coupled out diffractively and there is no ceramic loading the output cavity. The first and second cut-off drift lengths are loaded only by the dielectrics on the upstream end walls of the idler cavities, and the drift length separating the penultimate cavity and output cavity is unloaded.

## Experimental Results

The circuit was built and cold tested on a vector network analyzer. The cavities were excited and sampled through two 0.075 cm diameter holes positioned 180 degrees apart in the side wall. The transmission spectra for the idler and output cavities are shown in Fig. 1 and the measured resonant frequencies and Q's are summarized in Table 1.

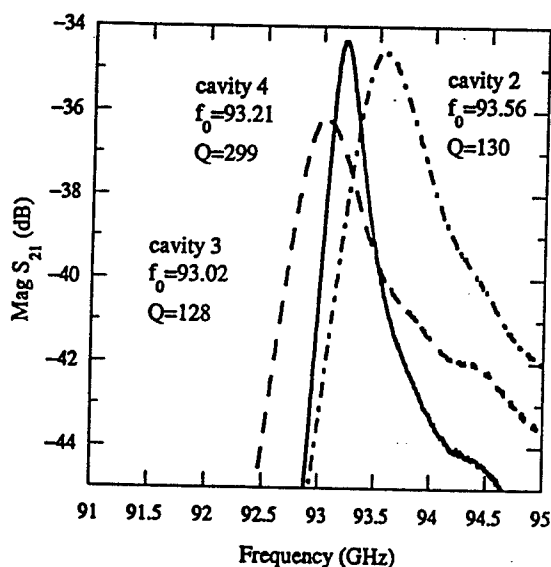


Figure 1 Cold test transmission spectra for cavity 2 (dashed-dot line), cavity 3 (dashed line) and cavity 4 (solid line).

Upon completion of the cold test, the circuit was installed in the test stand. Figure 2 shows a schematic of the gyrokystron amplifier experiment. A 4 A, 55 kV annular electron beam is produced by a double anode magnetron injection gun. The magnetic field at the cathode can be varied with a small gun coil to control the beam velocity ratio,  $\alpha$ . The beam is adiabatically compressed as it enters the region of high magnetic field generated by the 4 T superconducting magnet. The four cavities of the gyrokystron circuit are positioned in a region of constant magnetic field. The output

cavity tapers up to the collector, which is followed by a quartz vacuum window. A conically shaped water load is positioned on the atmosphere side of the vacuum window. The temperature rise of the water is used to measure the average rf power. The frequency of the input and output rf signals are measured with a spectrum analyzer. The drive power is supplied by a 1 kW peak power EIO, which is mechanically tunable from approximately 92.5 GHz to 95.5 GHz. The EIO provides pulses up to 2 microseconds in duration with a duty cycle up to 1%. The beam and EIO are typically pulsed at 250 Hz for an rf duty cycle of 0.05%.

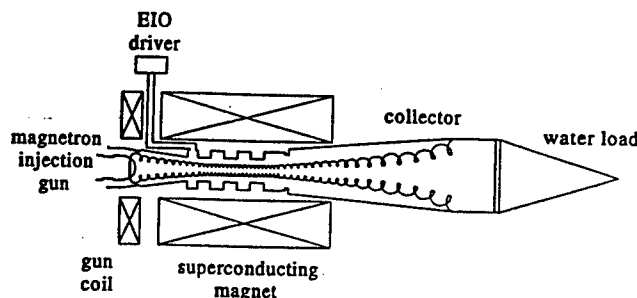


Figure 2 Schematic of the experimental test stand.

Figure 3 shows the measured and predicted output power and efficiency as a function of frequency for the amplified  $TE_{011}$  mode. A peak saturated output power of 67 kW, corresponding to 28% efficiency, was achieved with a 55 kV, 4.3 A electron beam. The FWHM bandwidth is greater than 460 MHz. The input power, measured at the output of the EIO, was 87 W, which gives 29 dB saturated gain. For the theory curve in Fig. 3, the experimentally determined values of cold resonant frequencies and Q's for the idler and output cavities were used. The HFSS predictions of the drive cavity resonant frequency and Q were assumed. The experimental values of beam voltage, beam current, and magnetic field in the interaction circuit were used. The beam  $\alpha$  was taken to be 1.5, and the perpendicular velocity spread was assumed to be 9%, values that were obtained through a combination of modeling and empirical determination. As shown in Fig. 3, the theoretical predictions are in good agreement with experimental data.

The limiting oscillation in the circuit was found to be the  $TE_{011}$  operating mode in the output cavity. The start oscillation current was measured and the results are shown in Fig. 4. The measured data points, indicated by the filled circles, are compared with the theoretical start current, shown with the solid line. In the theory, the measured values of beam current, cold resonant frequency, and cold cavity Q were used. The beam  $\alpha$  was taken to be 1.5, and the perpendicular velocity spread was assumed to be 9%. As shown in Fig. 4, the experimental data and theoretical predictions are in good agreement.



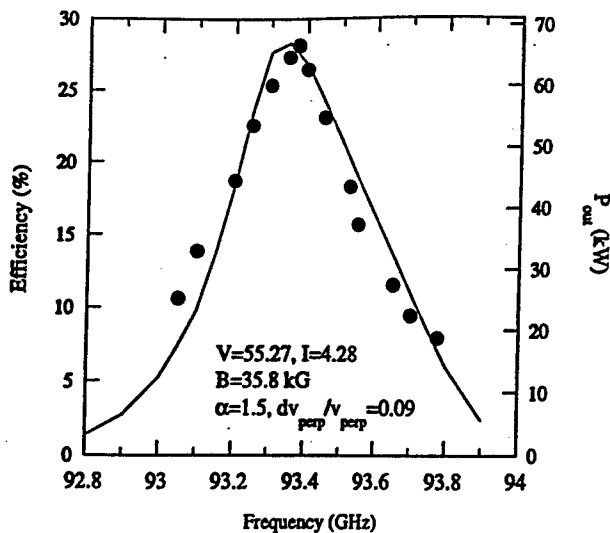


Figure 3 Measured values (filled circles) and theoretical predictions (solid curve) of peak output power and efficiency.

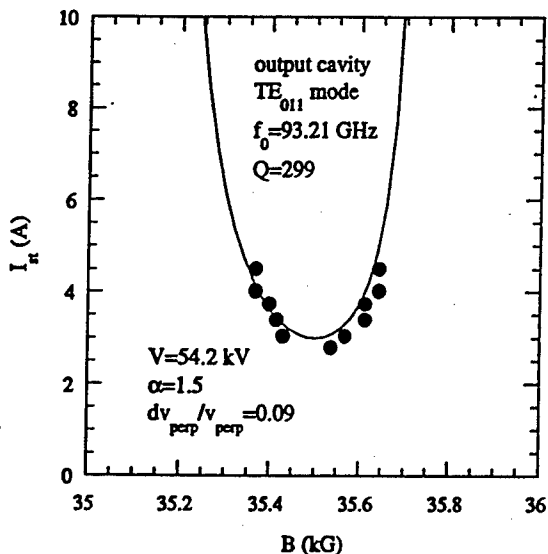


Figure 4 Measured values (filled circles) and theoretical prediction (solid curve) for start oscillation current of the  $TE_{011}$  mode in the output cavity.

## Summary

In summary, a four cavity W-band gyrokystron amplifier circuit was designed, built, and tested. Peak output powers of 67 kW, corresponding to 28% efficiency, were achieved in the  $TE_{011}$  mode with a 55 kV, 4.3 A electron beam. The FWHM bandwidth is greater than 460 MHz. The small signal and saturated gains are 36 dB and 29 dB, respectively. The circuit is zero drive stable and the limiting oscillation is the  $TE_{011}$  operating mode in the output cavity. The experimental data is in good agreement with predictions of theory using calculated values of beam velocity ratio and velocity spread. Future experiments will focus on increasing bandwidth through more aggressive stagger tuning and reduced output cavity Q.

## Acknowledgements

The authors would like to thank M. Barsanti, F. Robertson, B. Sobocinski, and M. Ngo for their technical assistance. This work was supported by the Office of Naval Research. The computational work was supported in part by a grant of HPC time from the DoD HPC Center NAVO.

## References

- † Present Address: Omega P, Inc., New Haven, CT 06520.
- [1] W.M Bollen, A.H. McCurdy, B. Arfin, R.K. Parker, A.K. Ganguly, IEEE Trans. Plasma Sci. 13, 417 (1985).
  - [2] E.V. Zasyrkin, M.A. Moiseev, E.V. Sokolov, V.K. Yulpatov, Int. J. Electron. 78, 423 (1995).
  - [3] W.G. Lawson et al., Phys. Rev. Lett. 67, 520 (1991).
  - [4] H.W. Matthews et al., IEEE Trans. Plasma Sci. 22, 825 (1994).
  - [5] E.V. Zasyrkin, M.A. Moiseev, I.G. Gachev, I. I. Antakov, IEEE Trans. Plasma Sci. 24, 666 (1995).
  - [6] I.I. Antakov, E.V. Zasyrkin, E.V. Sokolov, Conf. Digest of the Eighteenth Intl. Conf. On Infrared and Millimeter Waves, Proc. SPIE 2104, 166 (1993).
  - [7] P.E. Latham, W. Lawson, V. Irwin, IEEE Trans. Plasma Sci. 22, 804 (1994).
  - [8] J.M. Neilson, P.E. Latham, M. Caplan, W. Lawson, IEEE Trans. Microwave Theory Tech. 37, 1165 (1989).
  - [9] G.S. Park, C.M. Armstrong, R.H. Kyser, J.L. Hirshfield, R.K. Parker, Int. J. Electronics 78, 983 (1995).

# Development of a W-Band Gyroklystron for Radar Applications

B.G. Danly, M. Blank, J. Calame<sup>†</sup>, S. Cooke, B. Levush,  
W. Manheimer, A. McCurdy<sup>\*</sup>, K. Nguyen<sup>+</sup>,  
D. Pershing<sup>\*</sup>, J. Petillo<sup>\*</sup>, R.K. Parker  
Vacuum Electronics Branch  
Electronics Science and Technology Division  
U.S. Naval Research Laboratory  
Washington, D.C.

T.A. Hargreaves, A.J. Theiss, R.B. True  
Electron Devices Division  
Litton Systems, Inc.  
San Carlos, CA

K. Felch, T.S. Chu, H. Jory, P. Borchard, W.G. James  
Microwave Power Tube Products Division  
Communications and Power Industries  
Palo Alto, CA

W.G. Lawson and T.M. Antonsen, Jr.  
Electrical Engineering Dept.  
University of Maryland  
College Park, MD

## Abstract

High power millimeter wave radar is of interest for a variety of applications, including high resolution imaging, precision tracking, and cloud physics studies. A focused development effort, led by the Vacuum Electronics Branch of the Naval Research Laboratory, is presently underway with the objective of developing a high average power gyroklystron amplifier for radar applications. This team effort includes members from U.S. industry (CPI and Litton), university researchers (U. of Maryland), and NRL research staff, and is directed towards the development of an 80 kW peak power 94 GHz gyroklystron amplifier capable of operation at an average power of 10 kW. A millimeter wave radar which will utilize this gyroklystron amplifier is presently under construction by the NRL Radar Division.

## Introduction

In wideband coherent radar, where coherent processing times may be from a few to hundreds of milliseconds, the amplifier requirements of high average power, low phase noise, and large instantaneous bandwidth are of paramount concern. For the radar program initiated by the NRL Radar Division, the center frequency of 94 GHz has been chosen over other millimeter wave frequencies, and the requisite average power has been set at 10 kW. The ultimate goal for instantaneous bandwidth is in the 2-3 GHz range; a reduced bandwidth of 600 MHz has been set as the goal for the first amplifier. This goal for power represents a significant increase over the existing capability of coupled-cavity TWT technology. Therefore gyroamplifier technology is the appropriate solution to this requirement.

<sup>†</sup> Omega-P, Inc.

<sup>\*</sup> University of Southern California

<sup>+</sup> KN Research, Inc.

<sup>\*</sup> Mission Research Corp.

<sup>\*</sup> Science Applications International Corp.

## Amplifier Design

The present amplifier is designed to operate at the fundamental of the cyclotron frequency. The advent of cryogen-free superconducting magnet technology will facilitate the application of gyroamplifiers operating at the fundamental of the cyclotron frequency in field deployable systems. Consequently, the large coupling impedance associated with low order modes interacting with the beam at the fundamental cyclotron frequency can be realized, thus yielding high instantaneous bandwidth.

With the emphasis on high average power and moderate bandwidth for the first amplifier, a four-cavity gyrokystron amplifier has been designed. This solution represents the best fastwave amplifier technology for high average power, with the required 600 MHz bandwidth. Higher bandwidth gyroamplifiers, such as the gyrotwyston and the gyro-TWT are attractive options for the subsequent development effort. In gyrokystrons, moderate bandwidths may be obtained by stagger tuning of the cavities. The circuit for the four-cavity gyrokystron has been designed in order to maximize bandwidth. In the present design, a bandwidth of more than 700 MHz is predicted by the MAGYKL computer code. The stagger tuned cold resonant frequencies and Q factors of the cavities are tabulated in Error! Reference source not found.. The beam induced frequency shift is to higher frequency. The drive cavity achieves good excitation of the  $TE_{01}$  mode via a coupling scheme which utilizes an outer  $TE_{41}$  coaxial cavity for uniform excitation of the  $TE_{01}$  through magnetic coupling via four apertures in the common wall of the cavities.

Cavity	Cold Freq.	$Q_T$
Drive Cavity (1)	93.41	126
Cavity (2)	94.21	175
Penultimate (3)	93.28	175
Output Cavity (4)	93.89	162

Fig. 1 Design values for cavity cold resonant frequencies and Q-factors for four-cavity gyrokystron

The electron gun for this amplifier is of the magnetron injection gun type, designed to operate at 65 kV and 6 A peak current. This gun is reported on in detail elsewhere<sup>1</sup>.

The overall amplifier design is summarized in Fig.2. The details of this circuit design, and in

particular the details of the drive cavity design are described in a companion paper in these proceedings<sup>2</sup>. Recent highly successful demonstration of a 67 kW W-Band gyrokystron by NRL<sup>3</sup>, reported in this conference, adds confidence to the design methodology employed in this development.

Parameter	Design Value
Frequency	94 GHz
Operating Mode	$TE_{011}$
Peak Power	80 kW
Average Power	10 kW
Max. Beam Duty Factor	15%
Bandwidth [-3 dB]	> 600 MHz
Drive Power	40 W
Cathode Voltage	- 65 kV
Mod-anode Voltage	-47 kV
Peak Current	6 A

Fig. 2 Design Parameters for 94 GHz Gyrokystron

## Conclusions

A high power W-band gyrokystron amplifier has been designed and is presently being fabricated. High power testing of this amplifier is scheduled to begin in late 1997, with delivery in mid 1998. When successful, the present gyrokystron will represent the highest average power amplifier in existence in this frequency band.

## Acknowledgments

This project is supported by the Office of Naval Research and the Defense Advanced Research Projects Agency under program element PE0602234N. Computational efforts are supported under by grants of computer time from DoD HPC shared resource centers CEWES and NAVO. Litton and CPI are supported by NRL Contract N00014-94-C-2136; University of Maryland is supported by NRL Contract N00014-94-G.

## References

- <sup>1</sup> K. Nguyen, B. Danly, B. Levush, M. Blank, R. True, K. Felch, P. Borchard, "Design of Magnetron Injection Gun for 94-GHz Gyroamplifiers", 22<sup>nd</sup> Int. Conf. IR&MM Waves, 1997. [This Conference]
- <sup>2</sup> D. Pershing, K. Nguyen, J. Petillo, J. Calame, B. Danly, B. Levush, "Circuit Design of the 94 GHz Gyrokystron Amplifier", 22<sup>nd</sup> Int. Conf. IR&MM Waves, 1997. [This Conference]
- <sup>3</sup> M. Blank, et al, This Conf. Proceedings, 1997

## HIGH POWER 35GHz GYROKLYSTRON AMPLIFIERS

J. J. Choi, A. H. McCurdy<sup>§</sup>, F. Wood<sup>&</sup>, R. H. Kyser<sup>&</sup>, J. Calame<sup>¶</sup>, K. Nguyen\*, B. G. Danly, B. Levush, and R. K. Parker

Naval Research Laboratory, Code 6840, Washington, DC 20375

<sup>§</sup>USC, Los Angeles, CA 90089

<sup>&</sup>DynCorp, Rockville, MD 20850

<sup>¶</sup>Omega-P, Inc., New Haven, CT 06520

\*K-N Research, Silver Spring, MD 20906

### Abstract

Experiments on two-cavity and three-cavity gyrokystron amplifiers are underway to demonstrate 140 kW, 35 GHz coherent radiation generation. Initial experiments on the two-cavity gyrokystron show an efficiency of 32% (power = 130 kW), a bandwidth of 0.4%, and a saturated gain of 22dB. Experimental results are moderately in agreement with predictions from nonlinear simulations. Calculations also show that a stagger tuned three cavity circuit increases the bandwidth to more than 0.7%.

### 1. TWO-CAVITY GYROKLYSTRON AMPLIFIER

The two-cavity gyrokystron amplifier is designed using a large signal non-linear time-dependent gyrokystron code, MAGYKL [1]. A high power electron beam is produced from magnetron-injection-gun (CPI) which is optimally designed for TE<sub>01</sub> cylindrical cavity mode coupling at fundamental beam cyclotron mode. The gyrating electron beam is adiabatically compressed through a high magnetic field of 13.2kG which is powered by a 14 coil superconducting magnet. Input and output cavity dimensions and a drift tube length are optimized for maximum efficiency at 70kV, 6A,  $\alpha=1.5$ , and a beam axial velocity spread of 15%. Due to high voltage modulator problems, all the experiments are performed at 60kV and 6.72A. An electron trajectory code, EGUN predicts an axial velocity spread of 10% at 60kV, 6.72A, and  $\alpha=1.5$ .

An input drive signal for beam modulation is injected through a coaxial coupler [2]. The TE<sub>01</sub> mode purity is more than 99% in the central cavity. The coaxial input coupler is also attractive because of a single port excitation through a rectangular TE<sub>10</sub> mode. By the use of a 3-D finite element code, HFSS [3], the coaxial input coupler is designed and fabricated. Cold-test shows Q of 188 and resonant frequency of 34.89GHz.

The output cavity (length=2.75 $\lambda$ ) has a small radial step to control cavity external Q and is followed by a non-linear uptaper section which is a Dolph-Chevychev profile [4].

A TE<sub>01</sub> output vacuum window is designed using HFSS. An 1.5" diameter, half-wavelength thick BeO window which is brazed directly into the conflat flange shows an rf match better than -25dB over 3.7% bandwidth (34.3-35.6GHz). The measured data is in good agreement with the HFSS prediction. The input waveguide vacuum window is a pillbox window which is that used in CPI coupled cavity tubes.

Lossy ceramic rings (80% BeO, 20% SiC) with different radii are inserted in the drift tube between the input cavity and the output cavity in order to avoid oscillations. In addition, a beam tunnel between the input cavity and electron gun is filled with lossy ceramics. A water-cooled beam collector (1.5" diameter) is made of copper for good heat conduction. With a careful magnetic field tapering, an average power density of the electron beam dissipated on the collector is estimated less than 0.5kW/cm<sup>2</sup> at 10% duty operation.

A high average power calorimeter is designed and fabricated to measure the gyrokystron output power. Cold-test shows rf match better than -20dB over the entire operating frequency range. Two different power calibrations are performed; DC heater power and RF power driven by a conventional TWT and a high power EIO. The power calculations obtained from the temperature difference between inlet and outlet thermistors submerged in octanol agree within  $\pm 5\%$  for both calibration methods. A simple thin circular hole on the output waveguide is used to sample the rf signal for frequency measurement and monitoring rf pulse shapes.

Maximum power is obtained with -0.7% downtaper of the magnetic field in the output cavity region. Figure 1 shows a drive curve, efficiency as a function of input drive power, at 34.942GHz. This result is compared with non-linear code (MAGYKL) simulations for various beam axial velocities. The maximum efficiency is measured at 32 $\pm$ 2%, corresponding to amplified radiation power of 130kW. Instantaneous bandwidth is measured and compared with theory as shown in Figure 2. Although the peak efficiency is lower than the predicted value, the measured bandwidth of 0.4% (140MHz) agrees very well with simulations. The discrepancy between the experiments and theory is maybe due to the lack of self-consistent calculation of output cavity field when beam is present and improper modeling of the beam velocity distribution function. The present code assumes a flat-top velocity distribution. The beam loaded frequency upshift is also observed as shown in Figure 2. There is a 70MHz upshift (0.2%) with respect to the cold resonance frequency, which is in good agreement with code prediction. The self consistent gyrotron oscillator code, MAGY [5], has recently been modified for gyro-amplifier

simulations. Differently from the MAGYKL code, MAGY self-consistently solves for the axial field profile in the presence of the electron beam. At  $\Delta v_z/v_z=10\%$  as shown in Figure 1, the experimental drive curve is in excellent agreement with MAGY simulation results.

Rf oscillations in the output cavity are observed when beam current exceeds a threshold current. Measured oscillation frequency is near 34.93GHz which indicates that the oscillation originates from a TE<sub>011</sub> cavity mode. Maximum amplifier efficiency is achieved just below the starting oscillation point which is in the region of negative beam loading in the cavity. From the comparison with calculated threshold currents for different  $\alpha$ , beam  $\alpha$  is estimated to be 1.5, which is consistent with the value obtained from EGUN code simulation.

## 2. THREE-CAVITY GYROKLYSTRON AMPLIFIER

In order to enhance gain and bandwidth, a stagger tuned three-cavity gyroklystron is designed using the non-linear codes and the stability code. The best design parameters result in 30% efficiency, 35dB saturated gain and 0.7% bandwidth at  $\Delta v_z/v_z=15\%$ ,  $Q(1)=130$ ,  $Q(2)=150$ , and  $Q(3)=175$ . The bandwidth increases nearly by a factor of 2 compared with that of the two-cavity gyroklystron. Further increase of gain and bandwidth is possible by adding more buncher cavities at the expense of lower efficiency.

## 3. ACKNOWLEDGMENTS

The work is supported by the Office of Naval Research. The authors would like to acknowledge technical and engineering support from G. Longrie, B. Myers, L. Malsawma, F. Robertson, and B. Sobocinski.

## REFERENCES

- [1] P. Latham, W. Lawson, and V. Irwin, IEEE Trans. Plasma Sc. 22, p. 804, 1994.
- [2] A. H. McCurdy, J. J. Choi, and W. Manheimer, in this conference.
- [3] HP High Frequency Structure Simulator, Version 4.01, Hewlett Packard Co. and Ansoft Co.
- [4] W. G. Lawson, IEEE Trans. MTT, 38(11), pp.1617-1622, 1990.
- [5] S. Y. Cai, et. al., Int. J. Electronics, 72(5-6), pp.759-777, 1992.

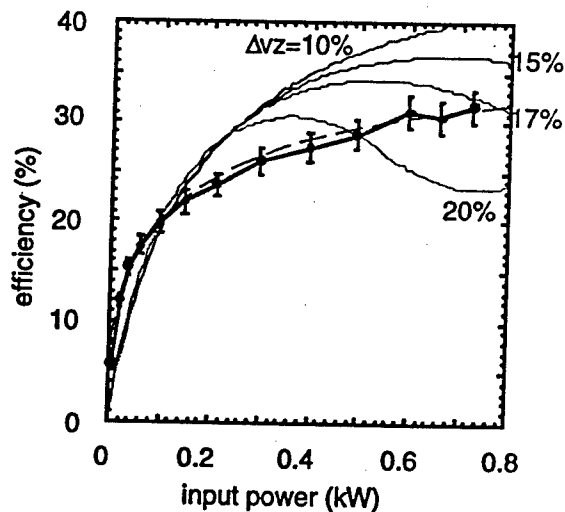


Figure 1. Experimental results on the drive curve. Drive curves from MAGYKL simulations are  $\Delta v_z/v_z=10\%$ , 15%, 17%, and 20%. The dashed line is from MAGY simulations at  $\Delta v_z/v_z=10\%$ .

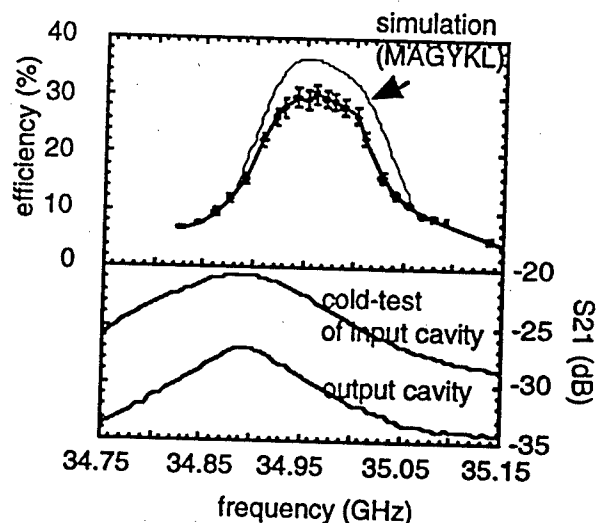


Figure 2. Large signal bandwidth measurement. Note the beam loaded frequency upshift by 70MHz with respect to cold-cavity resonant frequency at 34.89GHz.

# Circuit Design of the NRL/Industrial 94 GHz Gyroklystron Amplifier

D. Pershing

Mission Research Corporation, Newington, VA 22122

K. Nguyen

KN Research, Silver Spring, MD 20906

J. Petillo

Science Applications International Corporation, Burlington, MA 01803

J. Calame

Omega-P, Inc., New Haven, CT 06520

B. Danly, and B. Levush

Naval Research Laboratory, Washington, DC 20375

## Abstract

A wide bandwidth, high average power W-band gyrokystron amplifier is currently under cooperative development by NRL, Litton Electron Devices, and Communication and Power Industries. The amplifier circuit is comprised of 4 stagger-tuned cavities operating in the fundamental  $TE_{011}$  circular cavity mode. The input coupler is the first cavity of the circuit and must exhibit reasonable coupling strength between the  $TE_{10}$  mode in rectangular waveguide and the desired  $TE_{011}$  circular cavity mode over a better than 600 MHz bandwidth centered at 93.4 GHz, with high  $TE_{01}$  mode purity. A single WR-8 rectangular waveguide drives a combined coaxial/cylindrical cavity system. The coaxial cavity resonating in the  $TE_{411}$  mode is tightly coupled to the cylindrical cavity, excited to resonate in the  $TE_{011}$  mode. The rf magnetic field couples the cavities through 4 azimuthally spaced apertures.

## Introduction

Single aperture excitation of the  $TE_{01}$  mode with high mode purity is difficult in a low Q cylindrical cavity. The logical step of splitting the excitation into several azimuthally separated apertures introduces a 'plumbing' complexity to precisely split the source power with the appropriate amplitude and phase. However, the amplitude and phase splitting can be accomplished via an intermediate coaxial cavity [1,2]. In the design discussed below, this coaxial cavity resonates in the  $TE_{411}$  mode, and is tightly magnetically coupled to the cylindrical cavity via 4 rectangular apertures, equally spaced azimuthally. The coupling apertures are oriented  $45^\circ$  with respect to the single WR-8 rectangular drive waveguide.

Generally, a reduced geometry utilizing symmetry considerations, without taper and drift tube dielectric was modeled (see Fig. 1). Modeling tools include HFSS (High Frequency Structures Simulator) from HP [3] and ARGUS from SAIC [4]. HFSS is a finite element code that computes field distributions and S-parameters for passive 3D structures at a driven frequency. Material properties can be included. ARGUS is a 3D, volumetric simulation model for systems involving electric and magnetic fields and

charged particles, including the capability to embed materials in the simulation region, with either time- or frequency-domain operation.

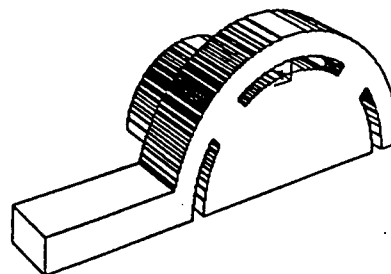


Figure 1: Schematic of one quarter of input coupler geometry. Vacuum regions are shown.

The cylindrical cavity radius and length are approximately set by gyrokystron performance calculations that determine the resonant frequency and Q of all cavities. Additionally, the wall thickness between the cylindrical and coaxial cavities is fixed at 10 mils for mechanical strength. This sets the inner radius of the coaxial cavity. For the initial simulation, the remaining coaxial cavity dimensions are chosen so that the unperturbed resonant frequency is the desired resonant frequency. The aperture width and height, coax cavity length and outer radius are adjusted to achieve the desired (cold) frequency and  $Q_{ext}$ , 93.4 GHz and 150, respectively, with better than 90%  $TE_{01}$  mode purity. Large apertures are used in this design for tight coupling between the cylindrical and coaxial cavities. They are rectangular for simulation and fabrication convenience.

## Simulation Methodology

Both HFSS and ARGUS were used with various methods of solution to model many issues concerning the input coupler, including resonant frequencies, modes, Q's, resistive loading, mode purity, parameterization, and manufacturing tolerance. In particular, ARGUS and HFSS were used to model the Q and resonant frequency for the operating mode of the input coupler, as a means of benchmarking code performance for the coupler

simulations. Excellent agreement was achieved between the two codes, where accuracy exceeding 0.1% was predicted.

Several techniques were employed with HFSS to determine the resonant frequency and  $Q$  of the  $TE_{01}$  mode in the cylindrical cavity. As a first approximation, the stored electric field energy (proportional to  $|E|^2$ ) was integrated over the cavity and drift tube volumes when driven through the drive port at several frequencies. Frequency and  $Q$ , are determined from the peak and 'half-energy' points. A second method 'de-embeds'  $S_{11}$  at the drive port to find the 'detuned short' position. The resonant frequency and  $Q$  are calculated from the phase of the reflection coefficient. HFSS has also been used to model a 'transmission' measurement by launching the  $TE_{01}$  mode in the cylindrical cavity by evanescent coupling through the drift tube and 'receiving' at the rectangular port.

Resonant frequencies and  $Q$ 's in ARGUS are determined from a variation of the 'detuned short' method due to Kroll and Yu [5,6]. Also, both HFSS and ARGUS were used to estimate the mode purity of the  $TE_{011}$  circular cavity mode [7].

### Simulation Results

Performance of the input coupler is found using both HFSS and ARGUS to be quite sensitive to dimensions, in particular slot length and cylindrical cavity radius. Note that a 0.0006 cm change in radius shifts the resonant frequency by ~200 MHz. It is important that the slot angular orientation be within  $\sim 1^\circ$  of  $45^\circ$  with respect to the input waveguide. A  $1^\circ$  slot rotation increases  $f$  by ~20 MHz and reduces  $Q$  by 3%. A  $5^\circ$  slot rotation increases  $f$  by ~36 MHz and reduces  $Q$  by 30%. A frequency and  $Q$  within  $\pm 100$  MHz and  $\pm 50$ , respectively, of the design values are acceptable from overall circuit performance considerations.

For the final design, the best compromise between coupling strength and bandwidth was achieved by 'stagger tuning' the cylindrical and coaxial cavities. The resonant frequency of the coaxial cavity was sufficiently higher than the cylindrical cavity that only ~10% of the combined stored energy is in the coaxial cavity over the nominal operating frequency range. For the final cavity dimensions, including stagger tuning, HFSS and ARGUS are in close agreement, as shown in Table 1.

Simulation	Resonant frequency	Q
HFSS (base case)	93.468 GHz	149
HFSS (w/taper, dielectric)	93.467 GHz	136
ARGUS (base case)	93.477 GHz	157

Table 1. Resonant frequency and  $Q_{ext}$  simulation results.

The calculated  $TE_{01}$  mode purity is shown from both codes to be greater than 96% over a 600 MHz bandwidth. The ohmic  $Q$  for the coupler is about 715, using  $7.6e5$  S/m for the conductivity of stainless steel in W-band. This conductivity is based on cold tests of simple cavities.

### Cold Test Results - Summary

A prototype input coupler was constructed for testing. For the dimensions of this coupler, the calculated  $f$  and  $Q_{ext}$  are approximately 93.14 GHz and 110 GHz, respectively, without wall resistivity. Based on other simulations with resistivity included, we expect  $f$  and  $Q_{ext}$  to be 93.1 GHz and 95, respectively. Note that not all dimensions were available for simulation purposes, so that there is some uncertainty in these values.

The resonant frequency measured with a HP 8510C network analyzer, is 92.98 GHz in transmission mode and 92.96 GHz in reflection mode, in good agreement with predictions, although the test set-up is less than ideal. Power is injected into the drive port and a fraction of the power radiated from the drift tube is sampled with a WR8 waveguide for transmission mode measurements.  $Q_{total}$  measured in transmission mode is 117, which implies  $Q_{ext} \sim 140$  if  $Q_{ohm}$  is 715. More accurate comparisons between simulation and measurement will be made following modifications in the measurement hardware.

### References

- [1] G. S. Park, C. M. Armstrong, R. H. Kyser, J. L. Hirshfield, and R. K. Parker, *Int. J. Electronics* 78, 983 (1995).
- [2] J. J. Choi, A. K. Ganguly, M. Blank, F. Calise, B. G. Danly, R. H. Kyser, B. Levush, P. Latham, A. H. McCurdy, G. S. Park, and R. K. Parker, *Conference Proceedings, 21st International Conference on Infrared and Millimeter Waves, AM15* (1996).
- [3] High Frequency Structures Simulator, Part No. HP 85180A.
- [4] A. Mankofsky, *Linear Accelerator and Beam Optics Codes*, C.R. Eminheizer, ed., A.I.P. Conf. Proc. No. 177 (American Institute of Physics, New York, 1988), p. 137ff.
- [5] N. M Kroll and D. U. L. Yu, *Particle Accelerators* 34, 231 (1990).
- [6] J. Petillo, W. Kreuger, A. Mondelli, and J. Potter, *Proceedings of the 1993 Particle Accelerator Conference*, 2, 1004 (1993).
- [7] A. K. Ganguly, private communication.

# Theory of Extrinsic Noise in Multicavity Gyroklystrons

G.S. Nusinovich<sup>†</sup>, M. Garven<sup>†</sup>, O. Dumbrajs<sup>†</sup>, and B.G. Danly<sup>\*</sup>

<sup>†</sup>Institute for Plasma Research, University of Maryland, College Park, MD 20742, USA

<sup>†</sup>Helsinki University of Technology, Espoo, FIN-02150, Finland

<sup>\*</sup>Naval Research Laboratory, Washington, DC 20375-5000, USA

## Abstract

Phase stability of RF sources is of interest for many applications including radars, communications, and particle accelerators. A study of the effect of fluctuations in gyrotron extrinsic parameters such as beam and mod-anode voltages, beam current and magnetic fields on radiation linewidth has recently been performed for free-running and phase-locked gyrotron oscillators [1, 2]. In the present paper a similar theory is developed for multi-cavity gyrokystrons. A numerical study of this effect is done for a four-cavity, 94 GHz gyrokystron which is under development at the Naval Research Laboratory.

## Introduction

In an ideal microwave tube operating in a steady-state regime the amplitude and phase (frequency in free running oscillators) of radiation are fixed. In real tubes the operating parameters such as beam and mod-anode voltages, beam current and magnetic fields in the interaction and electron gun regions can fluctuate because of the finite stabilization of voltages and other reasons. This slightly affects the interaction between the beam and the microwave field and correspondingly causes some fluctuations in the amplitude and phase near their nominal values. The theory of this effect for free-running and phase-locked gyrotron oscillators has been developed in Refs. 1 and 2. Below, we develop a similar formalism for multi-cavity gyrokystrons. Then we study numerical a four-cavity, 94 GHz gyrokystron which is under development at NRL.

## Formalism

Our formalism is based on the equations describing the amplitude and phase fluctuations of the output cavity field as functions of fluctuations in the susceptibility  $\chi$  of an electron beam with respect to

this field. This susceptibility  $\chi$  depends on a number of normalized parameters  $u_j$  adopted in the gyrokystron theory, which, in their turn, depend on the extrinsic parameters  $\xi_i$ . (In Refs. 1 and 2  $\xi_1$  is the beam current,  $\xi_2$  is the modulating anode voltage,  $\xi_3$  is the beam voltage,  $\xi_4$  and  $\xi_5$  are magnetic fields, respectively, in the interaction and electron gun regions.) Correspondingly, for fluctuations in  $\chi = I_0 \hat{\chi}$  (where  $I_0$  is the normalized beam current parameter) one can derive the following equation (cf. [1, 2])

$$\delta\chi = \frac{1}{4\pi Q} \sum_i \left[ \beta_i \hat{\chi} / \hat{\chi}'' + \sum_j d_j \alpha_{ij} \right] \frac{\delta\xi_i}{\xi_{i0}}, \quad (1)$$

where  $Q$  is the Q-factor of the last cavity,

$$\beta_i = \frac{\xi_{i0}}{I_0} \frac{\partial I_0}{\partial \xi_i} \Big|_{\xi_{i0}}, \quad d_j = \frac{u_{j0}}{\hat{\chi}''} \frac{\partial \hat{\chi}}{\partial u_j} \Big|_{u_{j0}}, \quad \text{and}$$

$$\alpha_{ij} = \frac{\xi_{i0}}{u_{j0}} \frac{\partial u_j}{\partial \xi_i} \Big|_{\xi_{i0}}.$$

From equations for amplitude and phase fluctuations written for different instants of time, one can derive the equations for the correlation functions for amplitude and phase fluctuations [1, 2]. The Fourier transformation of these equations allows one to express the spectral densities of the amplitude-, phase-, and amplitude-phase noise via spectral densities of fluctuations in extrinsic parameters  $\xi_i$ . The transmission coefficients between these spectral densities are determined by the expression given in square brackets in Eq. (1). The coefficients  $\beta_i$  and  $\alpha_{ij}$  there can be found analytically (cf. [1, 2]) while  $d_j$  and  $\hat{\chi} = \hat{\chi}' + i\hat{\chi}''$  should be found numerically. Note that for an  $M$ -cavity gyrokystron with a constant magnetic field in the interaction region, short cavities and long drift sections a total number of normalized parameters  $u_j$  is  $2M$  ( $1 \leq j \leq 2M$ ). This is because we have  $M$  amplitudes of fields excited in  $M$  cavities, the cyclotron resonance mismatch  $\Delta$ , and  $M - 1$



phases (phases  $\phi_m$  for  $m \geq 2$  can be referred to  $\phi_1$ , i.e. one can have to deal with  $\phi_m - \phi_1$  for  $m \geq 2$ ). Below, we will consider a four-cavity gyrokystron and assume that  $u_1 = F_4$ ,  $u_2 = \Delta$ ,  $u_3 = q_1$ ,  $u_4 = q_2$ ,  $u_5 = q_3$ ,  $u_6 = \phi_2$ ,  $u_7 = \phi_3$ ,  $u_8 = \phi_4$  where  $F_4$  is the field amplitude in the last cavity, and  $q_1$ ,  $q_2$  and  $q_3$  are bunching parameters proportional to the corresponding field amplitudes in preceding cavities. We will also assume that for phase deviations the most important are fluctuations in electron transit angles through long drift sections.

### Results

First, we studied the 94 GHz NRL gyrokystron in the absence of fluctuations. It was assumed that the device is driven by a 55 kV, 6 A electron beam with an orbital-to-axial velocity ratio  $\alpha = 1.5$ , the magnetic field is 3.68 T, the operating mode is TE<sub>01</sub>, and all cavities operate at the fundamental cyclotron resonance. The dependence of the amplitudes and phases of the fields in all cavities on the signal frequency was calculated. The cold-cavity frequencies of the cavities were taken as  $f_1 = 93.4$  GHz,  $f_2 = 94.2$  GHz,  $f_3 = 93.28$  GHz, and  $f_4 = 93.887$  GHz.

We then calculated the coefficients  $\alpha_{ij}$  and  $d_j$ , which are presented in Eq. (1). Since the NRL gyrokystron operates in a cryogenically cooled solenoid providing stable magnetic fields we studied only the effect of the beam and mod-anode voltage fluctuations. Corresponding coefficients  $\alpha_{ij}$  are:  $\alpha_{1,j} = 0$ ,  $\alpha_{2,1} = -3$ ,  $\alpha_{3,1} = 2(\gamma_0 - 1)/\gamma_0 = 0.194$ ,  $\alpha_{2,2} = 2 + \alpha^2 = 4.25$ ,  $\alpha_{3,2} = [1 - \gamma_0^2(2 + \alpha^2)]/\gamma_0(\gamma_0 + 1) = -1.805$ ,  $\alpha_{2,3} = \alpha_{2,4} = \alpha_{2,5} = 1 + 2\alpha^2 = 5.5$ ,  $\alpha_{3,3} = \alpha_{3,4} = \alpha_{3,5} = -2\gamma_0(\alpha^2 + 1)/(\gamma_0 + 1) = -3.416$ ,  $\alpha_{2,6} = r_{1,1}\alpha_{2,8}$ ,  $\alpha_{2,7} = r_{1,2}\alpha_{2,8}$ ,  $\alpha_{2,8} = \alpha^2\theta_{dr}$ ,  $\alpha_{3,6} = r_{1,1}\alpha_{3,8}$ ,  $\alpha_{3,7} = r_{1,2}\alpha_{3,8}$ , and  $\alpha_{3,8} = [\gamma_0/(\gamma_0 + 1)](\alpha^2 + 1)(2/\Delta\alpha^2 - 1) = \theta_{dr}$ , where  $\gamma_0$  is the initial electron energy normalized to the rest energy,  $\theta_{dr}$  is the transit angle through the all drift space of length  $L_{dr,\Sigma}$ , and coefficients  $r_{1,1}$  and  $r_{1,2}$  determine the positions of intermediate cavities:  $r_{1,1} = L_{dr,1}/L_{dr,\Sigma}$ ,  $r_{1,2} = (L_{dr,1} + L_{dr,2})/L_{dr,\Sigma}$  (here,  $L_{dr,1,2}$  are lengths of corresponding drift sections).

The dependences of real and imaginary parts of coefficients  $d_j$  on the signal frequency are shown in Figs. 1a and 1b. Corresponding dependences of the coefficients  $\bar{A}_{2,3}$  and  $\bar{B}_{2,3}$  which denote, respectively, the imaginary and real parts of the expressions given in Eq. (1) in square brackets are shown in Fig. 2. As follows from Fig. 2, the effect of fluctuations in the

mod-anode ( $i = 2$ ) and beam ( $i = 3$ ) voltages on the spectrum of the amplitude and phase fluctuations is much stronger at large signal frequencies than at small ones and in the middle of the bandwidth.

The work has been sponsored by the Naval Research Laboratory and the Office of Naval Research.

### References

1. O. Dumbrajs and G. S. Nusinovich, Phys. Plasmas, vol. 5, 1413, (1997).
2. G. S. Nusinovich and O. Dumbrajs, Phys. Plasmas, vol. 5, 1424 (1997).

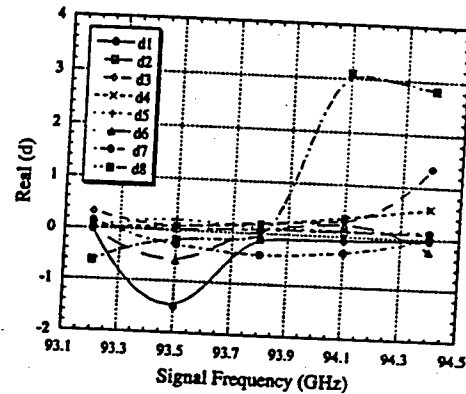


Figure 1a

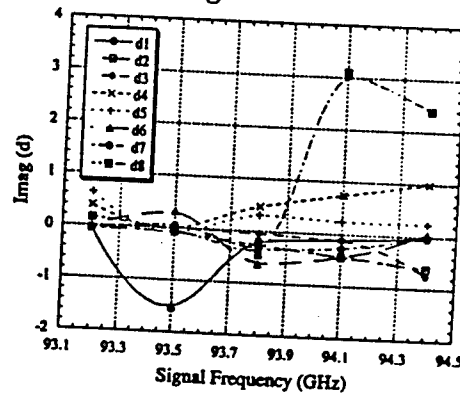


Figure 1b

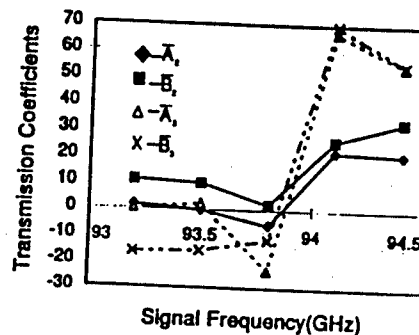


Figure 2

# PHASE STABILITY MEASUREMENTS OF GYROKLYSTRON AMPLIFIERS

M. Garven\*, B.G. Danly, M. Blank and M.J. Siegert

Naval Research Laboratory  
Washington, D.C. 20375, U.S.A

\*Institute for Plasma Research, University of Maryland,  
College Park, MD 20742, U.S.A

## Abstract

An experimental study of phase stability in a four-cavity, 94 GHz gyroklystron amplifier is underway. To date, the phase shift as a function of beam voltage has been measured. The experimental data is in good agreement with theoretical predictions.

## Introduction

Phase stability of RF sources is of interest for many applications, including radar, communications and particle accelerators. The spurious response of any amplifier tube used in a radar system is of importance; measurement of this response is critical for power supply specification as well as for determination of system design tradeoffs.

A high average power gyroklystron amplifier is currently being developed as the driver for a W-band radar. The performance goals are 80-100 kW peak output power, 10 kW average power, and 600 MHz full width half maximum instantaneous bandwidth. A low duty prototype of this gyroklystron amplifier has been constructed and tested at the Naval Research Laboratory [1]. The amplifier has produced 67 kW peak output power and 28% efficiency in the  $TE_{011}$  mode with a 55 kV, 4.3 A annular electron beam. Preliminary phase stability measurements have been performed on this gyroklystron. A similar study of the phase stability of a lower frequency gyroklystron has been performed by Park *et al* [2]. Phase stability measurements of gyroklystron amplifiers have also been discussed by McAdoo *et al* [3] and Park *et al* [4].

## Experimental Set-up

A schematic of the gyroklystron amplifier experiment is shown in figure 1 and is discussed in more detail by Blank *et al* at this conference [1]. A 4.3 A, 55 kV annular electron beam is produced by a double anode magnetron injection gun. The drive power is supplied by a 1 kW peak power extended interaction oscillator (EIO), which is mechanically tunable from approximately 92.5GHz to 95.5GHz. The EIO provides pulses up to 2 microseconds in duration. The beam and EIO are typically pulsed at 250 Hz for an rf duty cycle of 0.05%.

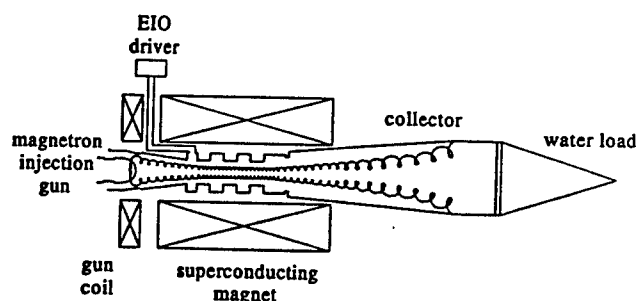


Figure 1 Schematic of the 4-cavity, W-band gyroklystron.

Figure 2 shows the microwave circuit used to measure the phase linearity of the gyroklystron. In this measurement a W-band fundamental mixer with a DC coupled IF port was used as a phase detector. The EIO signal was used as the reference signal to the phase detector. The measurement was performed for a constant drive frequency of 93.18 GHz. Variable attenuation was inserted in each arm of the circuit to balance the input power to the mixer.

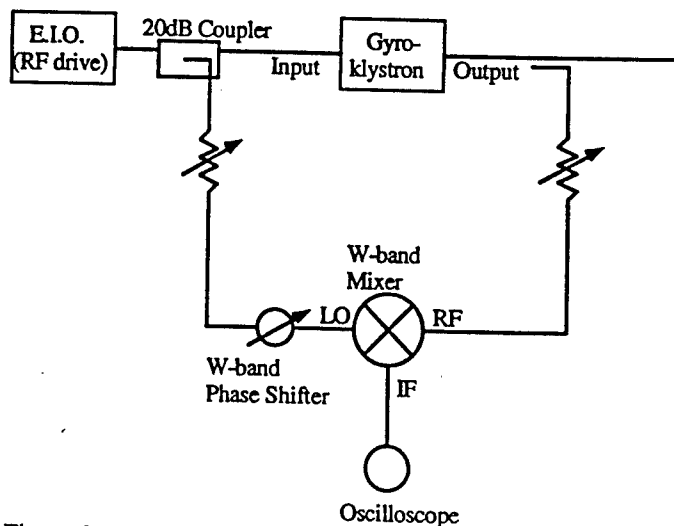


Figure 2 Microwave circuit for measuring the phase linearity of the gyroklystron.

During the experiment the input power was measured to be approximately 3mW peak to both ports. At the mixer, the RF input signal (the output of the gyrokystron) is combined with the local oscillator (LO) signal from the EIO. The nonlinearity of the mixer produces outputs at the sum and difference of the two input signals. The high-frequency component is filtered out and the mixer then produces a dc Intermediate Frequency (IF) signal which is proportional to  $\cos\phi$  if the RF and LO signal frequencies are the same (where  $\phi$  is the phase difference between the RF and LO signals). The system is most sensitive to phase fluctuations when the phase shifter is adjusted to achieve quadrature,  $\phi = \pi/2$  radians.

### Experimental Results

The phase linearity measurement was performed by setting the LO and RF signals in quadrature. This produced an IF of 0V, at an initial value of beam voltage of the gyrokystron. The phase of the gyrokystron signal was then changed by decreasing the beam voltage, causing the IF signal to move out of quadrature. Adjusting the phase shifter compensated for the phase shift of the amplified signal and gave a direct measurement of the phase shift,  $\Delta\phi$ , as shown in figure 3.

To calculate the 'pushing factor' of the amplifier, we fit the experimental data with a line and find that the gradient is 40.6°/kV. For this measured cathode voltage pushing factor, the corresponding spurious response is -63 dBc for a 1V rms ripple on the cathode voltage.

The measured data was then compared to theoretical predictions. EGUN electron trajectory code simulations were used to determine the change in beam velocity ratio,  $\alpha$ , for a given change in cathode voltage. The theoretical phase shift for a change in cathode voltage and the corresponding  $\alpha$  change was determined with a time dependent version of the MAGYKL code [5]. The theoretical prediction of phase shift with cathode voltage variation is also plotted in figure 3. The gradient for the MAGYKL prediction of phase shift was found to be 37.6°/kV which is in good agreement with the 40.6°/kV gradient of the measured data.

### Summary

A preliminary investigation of the phase characteristics of gyrokystron amplifiers has been performed. The phase linearity of an experimental, W-band gyrokystron was measured to be 40.6°/kV. This is in reasonable agreement with the theoretically calculated value of 37.6°/kV. Future experiments are aimed to further investigate phase noise and phase stability in gyro-amplifiers.

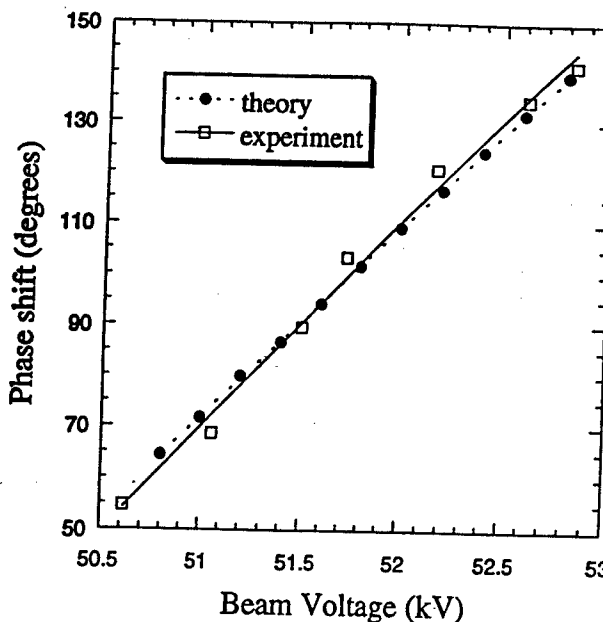


Figure 3 Comparison of experimental results with the theoretical calculation of the phase linearity.

### Acknowledgments

This work was supported by the Office of Naval Research. The authors would also like to thank Dr. V. Gregers-Hansen and M.F. Walder for many useful discussions. The authors are grateful to D. Lohrmann for the loan of the EIO driver and the W-band mixer.

### References

- [1] M. Blank, B.G. Danly, P.E. Latham, B. Levush, presented at this conference.
- [2] G.S. Park, V.L. Granatstein, J. McAdoo, C.M. Armstrong, A.H. McCurdy and S.Y. Park, *Int. J. Electronics* **72**, 909 (1992).
- [3] J. McAdoo, W.M. Bollen, A.H. McCurdy, V.L. Granatstein and R.K. Parker, *Int. J. Electron.* **61**, 1025 (1986).
- [4] G.S. Park, V.L. Granatstein, P.E. Latham, C.M. Armstrong and A.K. Ganguly, *IEEE Trans. Plasma Sci.* **19**(4), 632 (1991).
- [5] P.E. Latham, W. Lawson, V. Irwin, *IEEE Trans. Plasma Sci* **22**, 804 (1994).

# Operation of Two- and Three-Cavity First Harmonic Coaxial X-Band Gyroklystrons

W. Lawson, J. P. Calame, M. Castle, J. Cheng, V. L. Granatstein, B. Hogan, M. Reiser, and G. P. Saraph

Electrical Engineering Department and Institute for Plasma Research  
University of Maryland, College Park, MD 20742 USA

## Abstract

We describe results from the initial operation of our coaxial gyrokylystron experiment, which is being evaluated as a potential driver for future linear colliders. The interaction is designed to occur between a 500 kV, 500 - 700 A beam and a series of coaxial  $TE_{011}$  microwave cavities. Output powers in excess of 100 MW at 8.568 GHz are expected with an efficiency of about 40%.

## Introduction

At the University of Maryland, we have been running a comprehensive program to study the suitability of gyrokylystrons as drivers for linear collider applications [1]. We have previously reported a variety of experimental results, all of which were achieved on a test bed which produced a small-orbit beam with a nominal voltage and current of 450 kV and 200 A, respectively. Published accounts of our effort include an amplified power level of 27 MW at 32% efficiency in a three-cavity first harmonic gyrokylystron near 10 GHz and 32 MW at 29% efficiency in a two-cavity second harmonic gyrokylystron near 20 GHz.

In this paper we present the design details of two coaxial gyrokylystron tubes which are predicted to produce at least 100 MW of output power with an efficiency of nearly 40%. These tubes utilize a fundamental mode  $TE_{011}$  input cavity which is driven by a 150 kW magnetron at 8.568 GHz. The first tube is a two-cavity circuit with an 8.568 GHz  $TE_{011}$  output cavity, whereas the second tube has an 8.568 GHz  $TE_{011}$  buncher cavity in a three-cavity configuration. We present details of the simulated beam properties and the simulated circuit interactions. Cold and hot test results of the first experimental tube are discussed before the project status and a description of our future plans are summarized.

## Theoretical Circuit Performance

A detailed design analysis has been carried out on a number of coaxial, two- and three-cavity gyrokylystron systems with the aid of our partially self-consistent nonlinear code. The input cavity in all tubes is in resonance with the signal frequency at 8.568 GHz and the output cavity is resonant with either the first (8.568 GHz) or the second harmonic (17.136 GHz) frequency. In a three-cavity system, an additional buncher cavity is introduced which is resonant at either the first or second harmonic frequency. In the following sections, we describe only the two-cavity first harmonic tube which has

been hot-tested and the three-cavity first harmonic tube which is scheduled to undergo hot testing in the near future.

### A. Two-Cavity First Harmonic Tube

The first harmonic tube consists of an input cavity and an output cavity separated by a drift section as shown in Fig. 1. The input cavity is defined by a decrease in the inner conductor radius only and the quality factor is brought down to  $Q \approx 70$  by loading the cavity with a thin ring of carbonized aluminum-silicate placed at one end of the cavity. The inner radius is 1.05 cm and the length is 2.29 cm. Power is injected through two radial coupling ports which are separated by  $180^\circ$  and excited in-phase. Our start-oscillation code predicts that the input cavity is completely stable up to a current of 800 A.

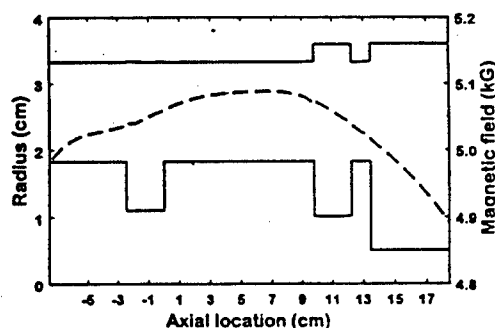


Fig. 1. The first-harmonic two-cavity tube and the optimal magnetic field profile.

The drift section has inner and outer radii of 1.825 cm and 3.325 cm, respectively. The inner conductor is required so that the drift tube is cutoff to the operating mode. The regions adjacent to each cavity are made of copper, but lossy ceramics line the majority of the drift tube to eliminate spurious modes. The total length of the drift region is 9.1 cm. Lossy ceramics are also used in the downtaper between the gun and the input cavity.

The output cavity is defined by changes in both radii and has a length of 1.70 cm. Power is extracted axially into the output waveguide via a coupling aperture. The aperture has the same radii as the drift tube and has a length of 0.9 cm. The diffractive quality factor is 122. The start-oscillation code also predicts the output cavity to be stable at the nominal current, which is given in Table I along with the other operating

parameters. The efficiency is nearly 40% and the output power is about 95 MW. The dependence of tube efficiency on axial velocity spread is plotted in Fig. 2 with the solid line. The simulated velocity spread of the electron gun is 6.4% at the nominal current. The curve shows a slow but steady decrease in efficiency with increasing spread and indicates that an efficiency of 37% is still possible if the spread is as high as 10%.

Table 1. Two cavity design parameters.

Parameters	Two-cavity
Voltage	500 kV
Current	480 A
Velocity ratio	1.508
Input Cavity Q	50
Output Cavity Q	122
Gain	21 dB
Efficiency	39.4%
Output Power	94.6 MW

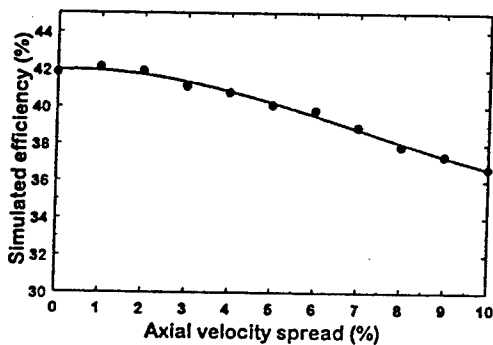


Fig. 2. Efficiency of the two-cavity first harmonic tube vs. velocity spread.

#### B. Three-Cavity First Harmonic Tube

The three-cavity system is similar to the first tube, except that the drift region has been split in two nearly equal sections and a buncher cavity is inserted inbetween. The buncher cavity is nearly identical in shape to the drive cavity and has the same resonant frequency and Q. The efficiency is predicted to be similar to the two-cavity system, but the gain is expected to improve by an additional 20 dB. We expect this tube to go on-line early in June 1997.

#### COLD AND HOT TEST RESULTS

The construction, cold testing, and hot testing of the first experimental tube has been completed. Cold-testing yielded the final dimensions of the input cavity required to achieve the frequency of 8.568 GHz and a quality factor of 70. They are quite near the theoretical estimates given in the previous section. Cold-test drift tube attenuation measurements have

indicated adequate isolation. The results for the output cavity were also quite close to the predicted values.

The performance of the microwave amplification experiment was limited by an input power coupling problem that developed after the tube was installed on the test bed. The net result was that we were only able to inject about 5 kW of power into the input cavity. The two cavity system had a predicted gain slightly above 20 dB, so the tube was severely gain limited. The best amplification results yielded a peak power of about 600 kW with a pulse width of over 1.5  $\mu$ s at a beam voltage of 270 kV and a current of 290 A. The performance at this reduced operating point was consistent with our simulations. While some instabilities were observed in the output waveguide, performance of the tube at these beam parameters was not limited by spurious modes.

#### PROJECT STATUS AND FUTURE PLANS

We continue to work on improving our simulation capabilities. Time-dependent capability has been added to our nonlinear (single-mode) code by researchers from the Naval Research Laboratory and initial results have confirmed the steady-state code predictions. We hope in the future to add multi-mode capability to our time dependent code.

We are also constructing a three-cavity second-harmonic tube which utilizes the same input cavity as the first-harmonic system. The buncher and output cavities resonate at 17.136 GHz in the  $TE_{021}$  mode, but are otherwise similar in shape to the first harmonic cavities. The cold-testing of these cavities is nearly complete and we expect to hot test this tube as soon as the first harmonic studies are completed.

We are also looking at advanced cavity concepts for future tubes. For the input cavity, we are using the High Frequency Structure Simulator code, HFSS, to simulate a single waveguide injection scheme which couples to the input cavity via an outer coaxial cavity. Furthermore, we are investigating an output cavity which couples through the inner radial wall to a circular waveguide, thereby decoupling the microwaves and the beam beyond the output cavity and enabling the use of additional tube stabilization schemes. Preliminary HFSS simulations of this output cavity scheme have been successful. Both concepts promise to improve performance of the gyroklystron tubes beyond the current predictions.

#### Acknowledgements

This work was supported by the US Department of Energy.

#### Reference

- [1] Granatstein, V. L. and W. Lawson, "Gyro-Amplifiers as Candidate RF Drivers for TeV Linear Colliders," *IEEE Trans. Plasma Sci.* 24, 648 - 665 (1996).

# Scaling Law for Ballistic Bunching in Multicavity Gyrokystrons

G. S. Nusinovich, G. P. Saraph, and V. L. Granatstein

Institute for Plasma Research, University of Maryland, College Park, MD 20742, USA

## Abstract

It is shown that the ballistic bunching in multicavity gyrokystrons, in which different cavities operate at different cyclotron harmonics, depends only on the ratios of these harmonics but not on their absolute values. Therefore the efficiency of the bunching process is the same for all schemes of multicavity gyrokystrons with identical ratios of resonant cyclotron harmonics. Predictions based on this scaling law agree well with the results of detailed optimization of design parameters for relativistic gyrokystrons which are under development for driving future linear colliders.

For many applications the operation of gyrokystrons (GKL's) at cyclotron harmonics is of great interest since it allows one to reduce the magnetic field required for providing the cyclotron resonance between gyrating electrons and EM field. In some cases this reduction eliminates the necessity of using superconducting solenoids and even makes the use of permanent magnets possible.

A number of multicavity GKL's in which different cavities operate at different harmonics  $s_i$  was analyzed in [1], [2]. The purpose of our paper is to show that the ballistic bunching in multicavity harmonic GKL's have some common features which allow us to establish the scaling law for studying different operating schemes. This scaling law allows one to estimate the efficiency of a number of schemes when only some of them are studied without making detailed optimization of design for other schemes.

Our consideration is based on the analysis of orbital ballistic bunching of electrons in GKL's which proceeds similar to the axial ballistic bunching of electrons in klystrons. In general, the changes in the electron energy  $w$  and gyrophase  $\theta$  under the action of the EM fields in the  $i$ -th cavity can be described by two equations (see, [1], [2])

$$\frac{dw_i}{d\zeta} = 2w_i^{s_i/2} \operatorname{Re}(F_i e^{i\psi_i} f_i e^{is_i\theta}) \quad (1)$$

$$\frac{d\theta_i}{d\zeta} - \Delta_i - w_i + 1 = -w_i^{s_i/2-1} \operatorname{Im}(F_i e^{i\psi_i} f_i e^{is_i\theta}) \quad (2)$$

In a 'point-gap' model which consists of very short cavities separated by long drift sections the changes in the phase  $\theta$  inside the cavities can be neglected, while the changes in the energy are equal to

$$\Delta w_i = 2w_i^{s_i/2}(0) \operatorname{Re}(F_i e^{i\psi_i} e^{is_i\theta(0)}) \quad (3)$$

Here the index (0) denotes the value at the entrance of the  $i$ -th cavity. These changes in energy lead to the phase bunching as beam passes through the drift sections. The phase after the  $i$ -th drift section of length  $\zeta_{dr,i}$  can be written using Eq. (2) as,

$$\theta_i = \theta_i(0) + \Delta_i \zeta_{dr,i} + (w_i - 1) \zeta_{dr,i} \quad (4)$$

When the device consists of  $M$  cavities we can introduce the bunching parameter  $q_{m,j}$  which gives the contribution of the normalized field amplitude  $F_m$  in the  $m$ -th cavity to the bunching at the entrance of the  $j$ -th cavity,

$$q_{m,j} = 2F_m \sum_{j'=m}^{j-1} \zeta_{dr,j'} \quad \text{where } m+1 \leq j \leq M \quad (5)$$

and determine the phase at the entrance to the  $m$ -th cavity by recurrent relation,

$$\theta_m = \psi_m + \frac{s_m}{s_1} \theta_0 - \sum_{m'=1}^{m-1} \frac{s_m}{s_{m'}} q_{m',m-1} \sin \theta_{m'} \quad (6)$$

Here  $\theta_0$  is the initial phase at the entrance of the first cavity which is homogeneously distributed from 0 to  $2\pi$ . Correspondingly, the amplitude of the  $s$ -th harmonic in the electron current density,  $j_s = (1/2\pi) \int_0^{2\pi} j \exp(-is\theta) d\theta_0$ , at the entrance of the last,  $M$ -th, cavity is equal to

$$F_{s,M} = \frac{1}{2\pi} \int_0^{2\pi} \exp \left( -i \frac{s_M}{s_1} \theta_0 + i \sum_{m=1}^{M-1} \frac{s_M}{s_m} q_{m,M} \sin \theta_m \right) d\theta_0 \quad (7)$$

where  $q_{m,M}$  and  $\theta_m$  are determined by Eqs. (5) and (6), respectively. As follows from Eq. (7), the function  $\mathcal{F}$  depends only on the ratios of resonant harmonics but not on their absolute values. This means that in the absence of electron velocity spread the bunching process in, for instance, a three-cavity GKL with all cavities operating at the second harmonic (so-called '2-2-2' scheme where each number is the resonant harmonic in a corresponding cavity) is the same as in a three-cavity GKL with all cavities operating at the fundamental ('1-1-1' scheme); '2-4-4' scheme is similar to '1-2-2' scheme, and so on.

This rule can also be understood from consideration of the EM field rotating synchronously with the electron gyration. This field is the field of the  $s$ -th order multipole which rotates azimuthally around the axis of electron gyration as shown in Fig. 1 [3]. The field of such a multipole has identical structure in each sector with an angular width  $2\pi/s$ . When the electron beam having uniform distribution in gyrophases at the entrance interacts with the first cavity field at the fundamental resonance only one bunch (in gyrophases) is formed in the rotating dipole field. Correspondingly, when the beam interacting with the first cavity field at the second harmonic (rotating quadrupole field) two bunches are formed separated by  $\pi$  radians. Therefore, when the electron beam prebunched at the fundamental enters the second cavity operating at the  $s$ -th harmonic the electrons will be affected by the second cavity field in the manner similar to the case when the pre-bunching is at the second harmonic followed by the second

cavity at the  $2s$ -th harmonic. Of course, as the harmonic number grows the angular width of a region with decelerating phase becomes more narrow. Correspondingly, the bunching process becomes more sensitive to the electron velocity spread.

This process can be described by the bunching efficiency  $\eta_b = |\mathcal{F}_{sM}|^2$  which relates to the maximum perpendicular efficiency  $\eta_{\perp, \max}$  as  $\eta_{\perp, \max} = \eta_b / s_M$  (as follows from Eq. (1)). The harmonic number  $s_M$  here shows that at higher harmonics the smaller slippage of the bunch with respect to the multipole moves this bunch from the decelerating phase to the accelerating one.

The bunching efficiency plots of several possible schemes of three-cavity GKL's are shown in Fig. 2 in the parameter space defined by  $q_1$  and  $q_2$  (which in notations of Eqs. (5)-(7) are  $q_{1,3}$  and  $q_{2,3}$ , respectively). We did calculations for three positions of the penultimate cavity when the ratio  $r$  of the first drift section length to the total drift length equals  $1/4$ ,  $1/2$ , and  $3/4$ . The contour plots in Fig. 2 correspond to the optimum position of the penultimate cavity in each configuration. These results are also optimized with respect to the phase  $\psi_2$  of the second cavity.

Comparison of 1-1-1 and 1-2-1 schemes shows that operation of the penultimate cavity at the second harmonic in GKL with the output cavity at the fundamental slightly improves the bunching efficiency. Comparison of two schemes with frequency doubling, 1-2-2 and 1-1-2, shows that the 1-2-2 scheme is preferable. Among the schemes with the frequency quadrupling, 1-2-4, 1-4-4, and 1-1-4, the best bunching efficiency can be realized in the 1-2-4 scheme studied in Ref. 1.

Results of these simple calculations agree well with the data of detailed design optimization studies presented in Ref. 2. It was found that in the absence of velocity spread the electronic efficiency of 1-1-1 and 1-2-2 schemes can reach 43 %. The efficiency of the 1-2-1 was reported to be smaller (39 %) due to design constraints ( $r \sim 1/2$  and gain  $\geq 15$  dB between successive cavities). The efficiencies for the optimized designs based on the quadrupling schemes, 1-2-4 and 1-4-4, were reported to be 16 % and 18 %, respectively (for  $r \sim 1/2$ ) [2]. From our scaling law the bunching efficiency of the 2-4-4 scheme is equivalent to that of the 1-2-2 scheme which is higher than the previous two quadrupling schemes. We designed a 2-4-4 type relativistic GKL with similar parameters and optimized it. As expected from the bunching efficiency, this design had 22 % efficiency. Thus, the efficiency predictions based on the scaling law described above are in good agreement with the detailed design optimization results.

### Acknowledgments

This work was supported by the U.S. Dept. of Energy.

### References

1. G. S. Nusinovich and O. Dumbrajs, *Phys. Plasmas*, 2, 568 (1995).
2. G. P. Saraph, et.al., *IEEE Trans. Plasma Sc.*, 24, 671 (1996).
3. V. A. Flyagin, A. V. Gaponov, M. I. Petelin, and V. K. Yulpatov, *IEEE-MTT*, MTT-25, 514 (1977).

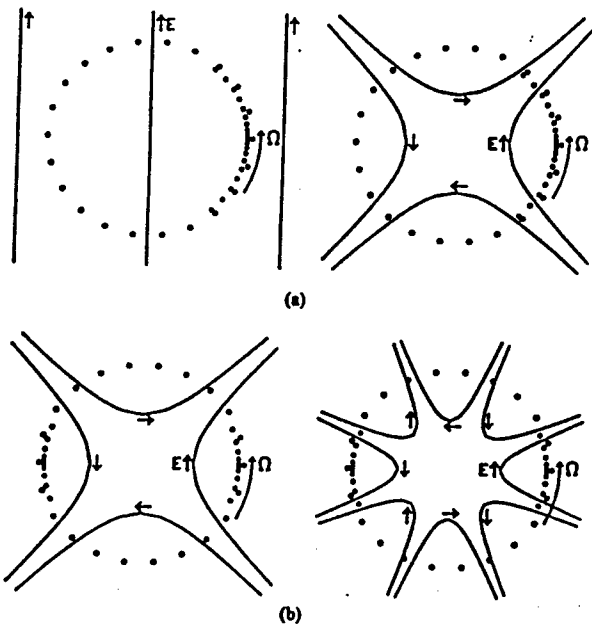


FIG. 1.

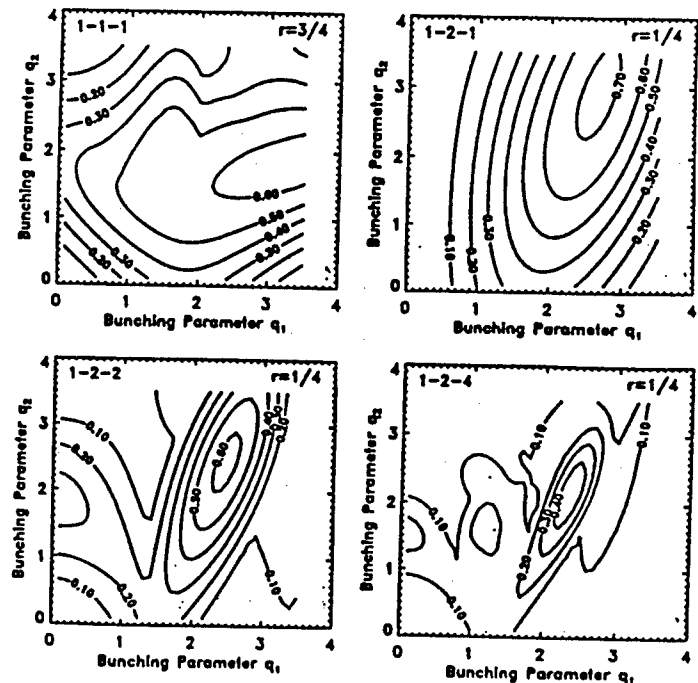


FIG. 2.

# HFSS Simulations of an Advanced Concept Gyroklystron

G. P. Saraph, J. P. Anderson, and W. Lawson

Institute for Plasma Research

University of Maryland, College Park, MD 20742, USA

## Abstract

A three-cavity, relativistic gyrokystron amplifier incorporating special design features is simulated using the High Frequency Structure Simulator (HFSS) code. The advanced features analyzed here include coaxial symmetric injection system for the input cavity, dielectric loading of the buncher cavity, and radial extraction of power from the output cavity through an inner coaxial waveguide. The finite element code, HFSS, is very useful in designing such complex cavities. The advantages of this design include better coupling and mode purity in the input cavity, stable second harmonic operation in  $TE_{021}$  mode in the buncher and output cavities, and radial extraction of microwave power in  $TE_{01}$  mode through the inner coaxial waveguide.

Parameters	Ku band 1-2-2 design
Beam voltage ( $V_b$ )	500 kV
Beam current ( $I_b$ )	770 A
Pitch-angle ( $\alpha_0$ )	1.508
Axial Velocity spread	6.4 %
Avg. magnetic field ( $B_0$ )	4.85 kG
Input frequency	8.568 GHz
Output frequency	17.136 GHz
Input cavity Q	50
Buncher cavity Q	389
Output cavity Q	320
Gain	49 dB
Efficiency	41.1 %
Output power	158 MW

Table 1:

High power, pulsed, relativistic gyrokystron amplifiers are being developed at the University of Maryland for driving future linear colliders. The current experiments are based on the 100-150 MW designs in X and Ku bands with over 40 % efficiencies operating at the fundamental and second harmonic of the cyclotron frequency, respectively [1]. The main advantage of the second harmonic operation in Ku-band is to eliminate the necessity of using cryogenically cooled solenoids. Early experiments have demonstrated 30 MW output power and 28 % efficiency for the second harmonic operation [2]. The current experiments are designed for higher beam power employing coaxial microwave circuits. We refer to the two and three cavity gyrokystron designs based on the resonant cyclotron harmonics in each cavity. The operating parameters of the three cavity 1-2-2 design are tabulated in Table 1.

This paper improves on the basic 1-2-2 design by using complex cavities with advanced features. The advanced

features analyzed here include coaxial symmetric injection system for the input cavity, dielectric loading of the buncher cavity, and radial extraction of power from the output cavity through an inner coaxial waveguide. The three cavity microwave circuit is shown in Fig. 1. Due to the complex geometries the cold cavity fields cannot be solved by simple scattering matrix formulation ([3],[4]). We have used a finite element code HFSS to design these cavities.

The input power is injected into an outer coaxial cavity which resonates in  $TE_{411}$  mode at the injection frequency of 8.568 GHz. The power is then coupled into the input cavity (in  $TE_{011}$ ) symmetrically through four slots which are  $\pi/2$  radians apart. The HFSS simulation results for the input cavity and the coupling scheme are shown in Fig. 2. This design has coupling efficiency and higher mode purity.

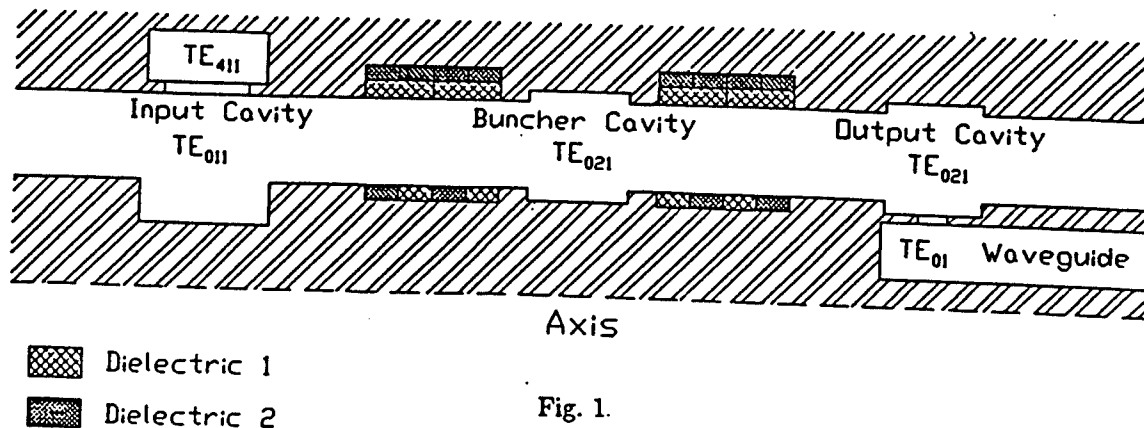


Fig. 1.



The buncher cavity has cut-off drift sections on both sides and the required quality factor of 389 for the operating mode ( $TE_{021}$ ) is achieved by introducing lossy dielectrics. However, the position of the dielectric material can be chosen to improve the stability of the cavity. The competing mode  $TE_{011}$  which resonates at 9.3 GHz is potentially dangerous due to beam interaction at the fundamental cyclotron frequency. Since the frequency of  $TE_{011}$  mode is closer to its cut-off frequency in the drift section the field tapers off slowly. By positioning lossy dielectrics in the drift section (near the cavity) this mode can be selectively loaded. The variations of quality factors for each mode as functions of the dielectric position are plotted in Fig. 3. The results are compared with the approximate solutions using CASCADE code based on scattering matrix formulation. Based on HFSS simulations the dielectrics should be placed at 6 mm from the buncher cavity which gives the Q-values of 389 and 35 for the  $TE_{021}$  and  $TE_{011}$  modes. At these Q-values the cavity is completely stable.

The earlier coaxial output cavity design had a small cut-off lip before the outlet taper for field confinement. The output radiation and the spent electron beam both travelled together in the axial direction in the outlet section. In the present design the output cavity has cut-off sections on either sides and the microwave power is extracted radially through eight coupling slots into an inner coaxial waveguide in  $TE_{01}$  mode. The inner waveguide has a quarter wavelength termination along the negative  $z$  (axial) direction. The dimensions of the coupling slots are adjusted to get the required Q-value of 320 for the operating mode ( $TE_{021}$ ). The results obtained from the HFSS simulations are shown in Fig. 4. This configuration has several advantages, viz. natural separation of radiation and the electron beam, extraction of power in  $TE_{01}$  mode, easier implementation of cooling, support, and energy recovery schemes, likely better performance under the dynamic load conditions, and better stability.

The interaction efficiency of this advanced concept gyrokystron is 38 % (slightly lower than the original design), but further improvement is possible by optimizing the cavity designs and operating parameters.

#### Acknowledgments

This work was supported by the U.S. Dept. of Energy.

#### References

1. G. P. Saraph, et.al., *IEEE Trans. Plasma Sc.*, 24, 671 (1996).
2. H. W. Matthews, W. Lawson, et.al., *IEEE Trans. Plasma Sc.*, 22, 825 (1994).

3. J. M. Neilson, P. E. Latham, et.al., *IEEE Trans. Microwave Theory Tech.*, 37, 1165 (1989).
4. W. Lawson and P. E. Latham, *IEEE Trans. Microwave Theory Tech.*, 40, 1973 (1992).

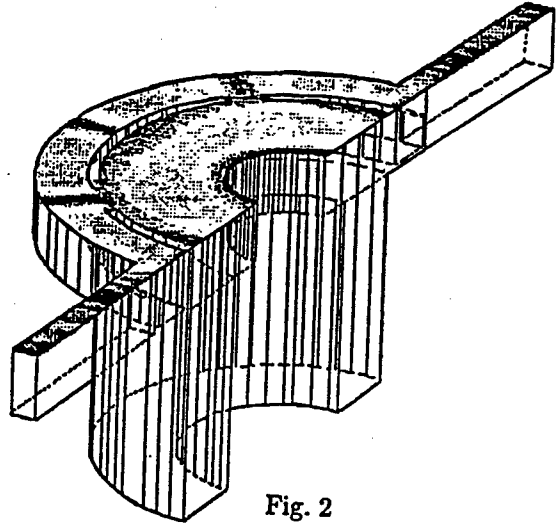


Fig. 2

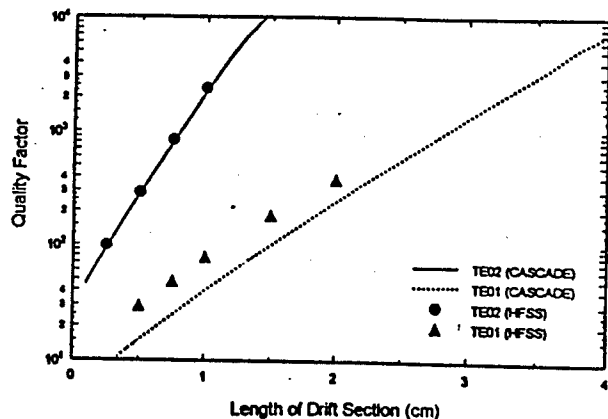


Fig. 3

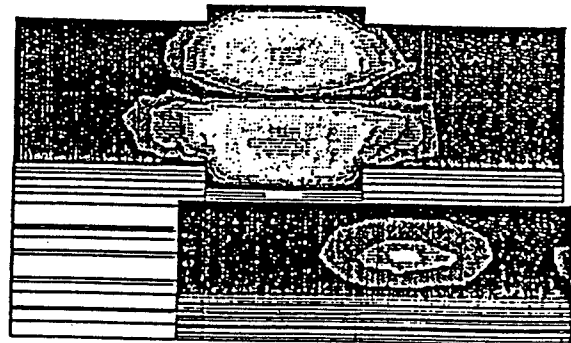


Fig. 4

# Theory of Multi-Beam Stagger-Tuned Gyroklystrons

G.S. Nusinovich

Institute for Plasma Research, University of Maryland, College Park, MD 20742, USA

B. Levush and B.G. Danly

Naval Research Laboratory, Washington, DC 20375-5000, USA

## Abstract

The concept of multi-beam microwave tubes is motivated by the tendency to produce high-power microwaves at low operating voltages. In such devices electron beamlets propagate through individual drift channels and prebunching cavities and then can load either individual output cavities or the common output cavity. The bandwidth of these devices can be increased by stagger-tuning of prebunching cavities. In the present paper a theory of multi-beam gyroklystrons with stagger-tuned prebunching cavities is developed and the trade-off in the gain and bandwidth is analyzed.

## Introduction

Multi-beam gyroklystrons as well as multi-beam conventional klystrons offer a number of advantages over their single-beam counterparts. In these devices the required microwave power can be produced at much lower voltages, which reduces the weight of the tube and high-voltage supply. Also, when one multi-beam tube can be used instead of many single-beam tubes the weight of magnet systems can be reduced drastically. Since the total perveance of multi-beam tubes can be much larger than that of a single-beam device the bandwidth can be significantly increased. It can be increased even further by stagger tuning the cavities driven by individual beamlets. The theory of such multi-beam, stagger-tuned gyroklystrons is developed below.

## Formalism

Our formalism is based on the theory of stagger-tuned single-beam gyroklystrons (GKLs) developed in Ref. 1 which is generalized for the case of multi-beam GKLs. A schematic of the multi-beam GKL with the common output cavity is shown in Fig. 1.

In the same way, one can consider multi-beam GKLs with individual output cavities, however at short wavelengths and high average power levels the microwave Ohmic losses in these cavities can be too high.

The analytical treatment of these devices operating in both small- and large-signal regimes can be done for a "point-gap" model. In such a model one assumes that the device consists of short cavities separated by long drift sections. Correspondingly, in cavities we account only for changes in the electron energy which lead to the orbital electron bunching in long drift sections. Although we developed a general formalism for an  $N$ -stage,  $K$ -beam GKL (see Fig. 1) operating in a large-signal regime, we studied only two-stage, two-, three- and four-beam GKLs operating in small-signal regimes.

## Results

We analyzed two strategies of stagger-tuning for the bandwidth enlargement. The first one is to detune the eigenfrequencies of the input cavities near the eigenfrequency of the input cavity of a single-beam device. The second strategy is to detune the eigenfrequencies of these cavities at about the eigenfrequency of a common output cavity.

The first strategy is illustrated by Figs. 2 and 3, in which the variable part of the gain,  $G_{var}$ , describing the gain degradation due to stagger tuning, is shown as a function of the normalized frequency detuning for different values of the stagger-tuning parameter  $\xi$ . Figure 2 shows the variable gain in a single-beam, two-stage GKL. (This figure is given for the sake of comparison.) In Fig. 3 the variable gain in two-beam GKL is shown for parameters  $\xi$  providing the flatness of the gain curves about 3 dB within the bandwidth.

The second strategy is illustrated by Figs. 4 and 5, which show the variable gain in, respectively, two- and four-beam GKLs.

The results of the study are summarized in Fig. 6 where the increase in bandwidth and the degradation in gain,  $\Delta G$ , are shown as functions of the number of beamlets for both strategies considered above. (In Fig. 6 the results related to these strategies are marked, respectively, I and II;  $BW_{sb}$  is the bandwidth of a single-beam GKL.) As follows from Fig. 6, when we have four or more beamlets the second strategy provides a larger bandwidth and a smaller degradation in gain.

Note that from Figs. 2-5 one can find only the normalized bandwidth, which is  $2Q_2 \cdot BW$ , where  $Q_2$  is the Q-factor of the output cavity. This Q-factor can be different for single- and multi-beam GKLs. Also it depends on whether we have to deal with one common output cavity or individual cavities, as well as on the filling factor of these cavities with electron beams.

The theory developed and the results obtained allow one to analyze the trade-off in gain and bandwidth in multi-beam stagger-tuned GKLs.

This work has been supported by the Naval Research Laboratory and the U.S. Office of Naval Research.

### References

1. G.S. Nusinovich, B.G. Danly, and B. Levush, Phys. Plasmas 4, 469 (1997).

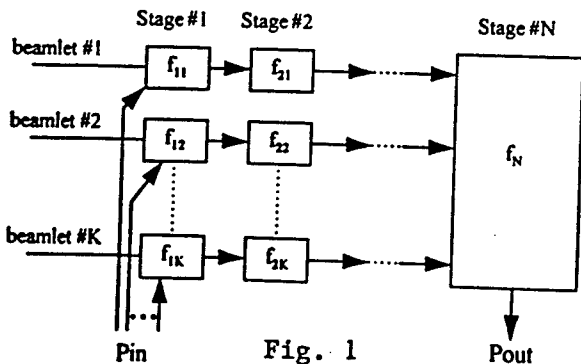


Fig. 1

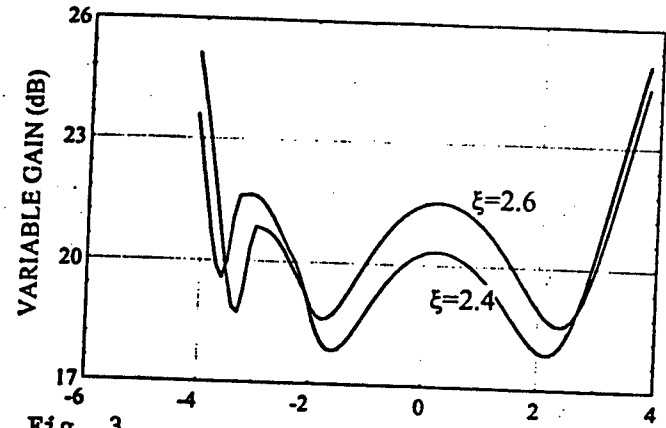
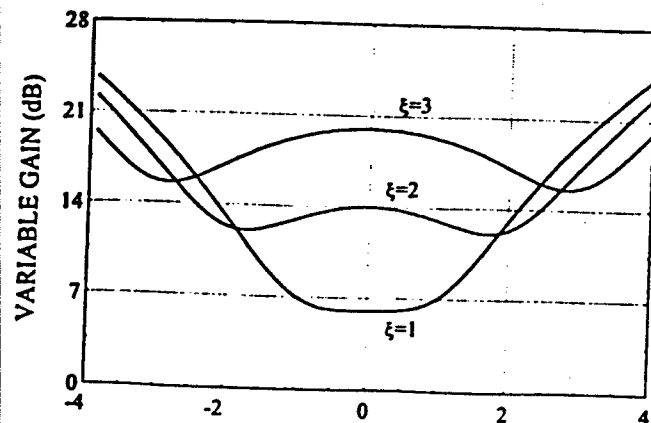


Fig. 3

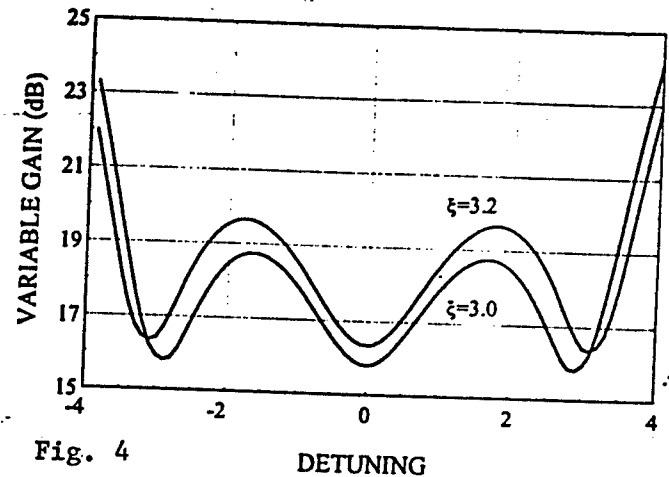


Fig. 4

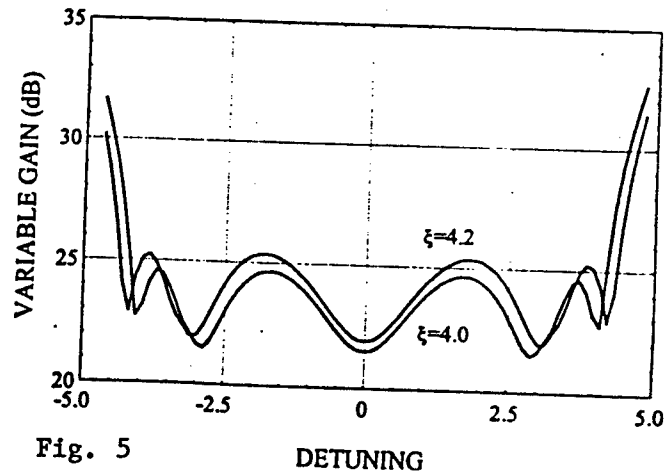
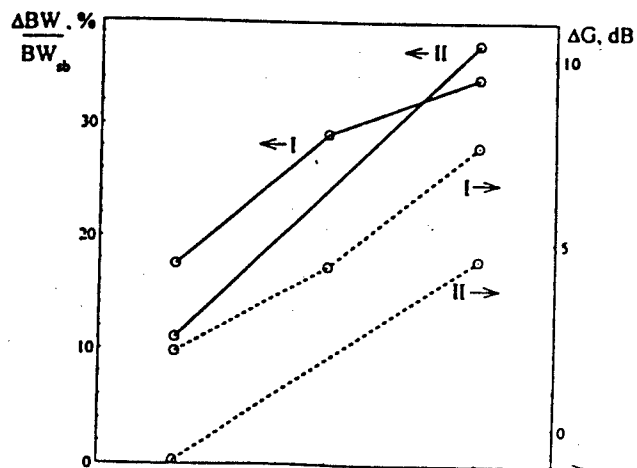


Fig. 5



# Frequency Tunability and Phase Stability of Relativistic Gyroklystron Amplifiers

G. P. Saraph

Institute for Plasma Research

University of Maryland, College Park, MD 20742, USA

## Abstract

High power, pulsed, relativistic gyrokystron amplifiers are being developed for driving future linear colliders. Detailed analysis is performed to determine frequency tunability and phase stability of these devices. Nonlinear, time-dependent simulations are carried out using two designs of X and Ku band gyrokystrons operating at the fundamental and second harmonic frequencies, respectively. It is shown that the second harmonic design is rather sensitive to the variation in cold cavity frequency of the output cavity. However, a significant level of frequency tunability can be achieved by making small changes in the magnetic field strength. Studies of time variations of efficiency and output phase under a typical beam voltage pulse are presented. It is shown that the shape of the pulse and its noise level play important roles in determining the phase stability of the device.

Efficient, 100 MW RF sources in the X and Ku frequency bands with pulse-lengths of 1  $\mu$ s are being developed for future electron-positron colliders with proposed center of mass energies of 1 TeV and more. The relativistic gyrokystron is one of the prime candidates being considered to fulfill these requirements. Early gyrokystron experiments at Maryland have achieved 27-32 MW power levels and about 30 % efficiency at frequencies near 10 and 20 GHz [1]-[3]. The current experiments are based on the 100-150 MW designs in X and Ku bands with over 40 % efficiencies [4]. In addition to the power and efficiency requirements, gyrokystrons should also meet the synchronization criteria to be suitable for driving large accelerators. Hundreds of these RF drivers would have to be synchronized in frequency and output phases.

This paper deals with the synchronization study of relativistic gyrokystron amplifiers using nonlinear, time-dependent simulations. The study is conducted for two specific designs of two-cavity, coaxial gyrokystron amplifiers operating in the X and Ku bands (presented in Ref. 4). We refer to the two designs as 1-1 and 1-2 systems, respectively, based on the resonant cyclotron harmonics in each cavity. These designs were optimized using a stationary, nonlinear gyrokystron code [5]. The operating parameters are tabulated in Table 1. The nonlinear code was later modified to include partial time derivatives of the electromagnetic field amplitudes in order to carry out time-dependent analysis [6].

One of the issues important for synchronization is to

account for manufacturing tolerances which may cause spread in the cold cavity frequencies of gyrokystron cavities about their design values. Typically, 1 mil (1/1000 inch) tolerance in radial dimensions could lead to 10-20 MHz changes in the cold cavity frequency of the X and Ku band cavities. In order to achieve efficient operation at a fixed output frequency the operation of the device should not be sensitive to these changes. Otherwise some sort of frequency tunability should be introduced to compensate for these changes.

It is assumed that the input cavity, which is dielectrically loaded (to lower its Q value), can be tuned to the exact operating frequency. Hence, the sensitivity analysis is carried out with respect to the cold cavity frequency of the output cavity for each design. It is found that the X band design is rather insensitive to the variation in cold cavity frequency as shown in Fig. 1. However, the second harmonic 1-2 design is found to be very sensitive and has a small bandwidth. Some sort of frequency tunability is necessary to compensate for any changes in the cold cavity frequency. One possible option to achieve tunability is to use a mechanically movable part such as a plunger, but it may not be suitable due to high field values in the output cavity.

Another technique to achieve frequency tunability is by varying the strength of the axial magnetic field. The optimum axial profile of the magnetic field is kept the same. However, the amplitude of the field is changed by 1 or 2 % to get the required tunability. The variation of efficiency versus the cold cavity frequency for a small change in the magnetic field strength,  $\Delta B$ , is shown in Fig. 2 for different values of  $\Delta B$ . It shows that the high efficiency operating regime can be moved to higher or lower values of cold cavity frequency by decreasing or increasing the magnetic field strength, respectively. Thus, the operating bandwidth of the design can be increased by a factor of 4 by using this technique.

Another important synchronization criterion is phase stability of the output radiation. Since the output phase is sensitive to the beam voltage we have carried out time-dependent analysis for the voltage pulse. In order to determine the effect of the voltage pulse on the efficiency and output phase we use a simple model of symmetric pulse with exponential rise time of 100 ns and flat top of about 1  $\mu$ s. It is found that the phase saturates much more slowly to its flat-top value (as shown in Fig. 3) as compared to the field amplitude. In order to achieve phase stability of 0.1 rad (or about 6 deg) only about a 300 nsec portion of the pulse can be used. Better results are obtained if an abso-

lutely constant value of the flat-top voltage is used rather than the exponential saturation. Thus, an accurate shape of the voltage pulse is necessary to determine the phase stability characteristics of the device. Since this phase variation is systematic, a pre-programmed phase variation on the gyrokystron drive could in principle counteract this effect.

During the actual voltage pulse there are random fluctuations in voltage level even at the flat-top portion due to noise. We estimate the effect of noise by adding a small perturbation to the original voltage pulse. The time variation of the output phase is plotted in Fig. 4 for a voltage pulse with 1 % perturbation introduced after 600 nsec from the start. The output phase shows a significant change (of about 0.6 rad or 34 deg) due to this perturbation. Thus, in order to achieve phase stability of 0.1 rad the slow time-scale noise level in the beam voltage should be less than 0.2 % or less than 1 kV. Thus, phase stability puts a very stringent requirement on the constancy of the flat-top voltage unless some feedback system is incorporated.

Parameters	X band 1-1 design	Ku band 1-2 design
Beam voltage ( $V_b$ )	500 kV	500 kV
Beam current ( $I_b$ )	480 A	700 A
Pitch-angle ( $\alpha_0$ )	1.508	1.508
Avg. magnetic field ( $B_0$ )	5.0 kG	4.9 kG
Input frequency	8.568 GHz	8.568 GHz
Output frequency	8.568 GHz	17.136 GHz
Input cavity Q	50	50
Output cavity Q	122	320
Gain	21 dB	26 dB
Efficiency	39.4 %	30.2 %
Output power	94.6 MW	105.7 MW

Table 1

### Acknowledgments

This work was supported by the U.S. Dept. of Energy.

### References

1. W. Lawson, et.al., *IEEE Trans. Plasma Sc.*, 20, 216 (1992).
2. S. G. Tantawi, et.al., *IEEE Trans. Plasma Sc.*, 20, 205 (1992).
3. H. W. Matthews, et.al., *IEEE Trans. Plasma Sc.*, 22, 825 (1994).
4. G. P. Saraph, et.al., *IEEE Trans. Plasma Sc.*, 24, 671 (1996).
5. P. E. Latham, et.al., *IEEE Trans. Plasma Sc.*, 22, 818 (1994).
6. B. Levush, *Private Communication*, (1996).

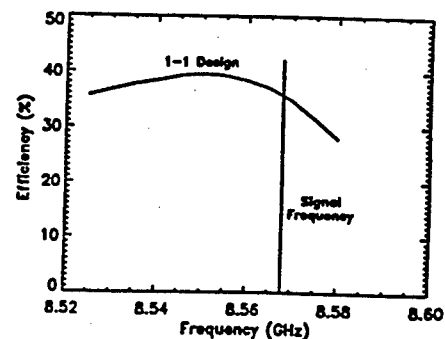


Fig. 1

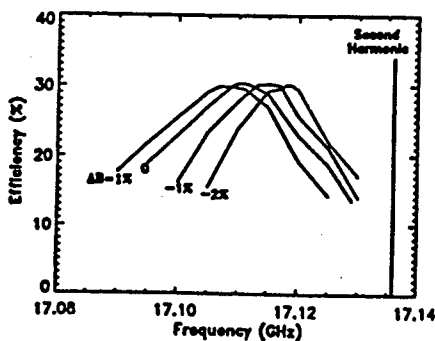


Fig. 2

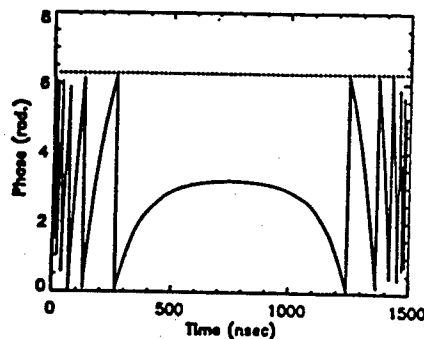


Fig. 3

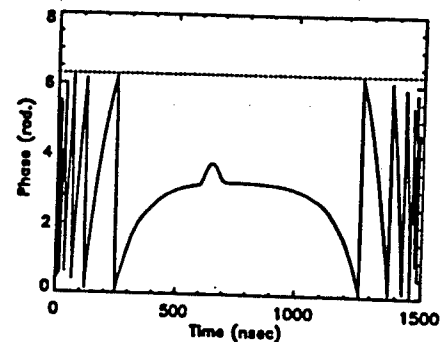


Fig. 4

# A Horn Antenna Coupled Quasi-Optical Oscillator with Gunn Diodes at Millimeter Wavelengths

Jongsuck Bae<sup>††</sup>, Takanori Uno<sup>†</sup>, Hiroyuki Mazaki<sup>†</sup>, Tetsu Fujii<sup>†</sup>, Fumikazu Takei<sup>†</sup>, and Koji Mizuno<sup>††</sup>

<sup>†</sup>*Research Institute of Electrical Communication, Tohoku University,  
2-1-1 Katahira, Aoba-ku, Sendai 980-77, Japan*

<sup>††</sup>*Photodynamics Research Center, The Institute of Physical and Chemical Research,  
19-1399 Aza-Koeji, Nagamachi, Aoba-ku, Sendai 980, Japan*

## Abstract

A quasi-optical oscillator which has a horn antenna array with Gunn diodes placed in a Fabry-Perot resonator, has been developed as a spatial power combiner with high output power at millimeter wavelengths. Experimental results performed at frequencies around 61 GHz have shown that nine Gunn diodes in the oscillator with a 3x3 horn antenna array can oscillate with a total output power of 1 W and a C/N ratio of about 80 dB/Hz at 100 kHz offset.

## Introduction

Coherent power combining of solid-state devices using a quasi-optical resonator is a promising technique to produce intense millimeter and submillimeter waves with a high carrier to noise ratio (C/N) [1]. Two-terminal devices such as Gunn and IMPATT diodes have high capability for radiation power greater than several tens of mW, even at frequencies above 100 GHz. Thus combining power from only twenty diodes or less would produce enough rf-power in practical use for many applications. In conventional quasi-optical resonators [2], the diodes are arrayed two dimensionally with a pitch of less than a wavelength. In that case, a small number of the diodes radiate a strongly diffracted beam in the resonator due to its small radiation area, consequently causing a large rf loss [3]. A horn antenna coupled quasi-optical resonator has been proposed as an efficient power combiner using a small number of diode devices. In this paper, 1 W operation of a horn coupled oscillator with nine Gunn diodes at frequencies around 60 GHz is presented.

## Resonator Configuration

The experimental configuration of the horn coupled resonator with nine Gunn diodes is shown in Fig. 1. The Gunn diode is mounted in a metal V-band waveguide with pyramidal horns at both ends. Both horns have the same square aperture with a size of 15 mm x 15 mm. The waveguides are arrayed by 3x3 and are placed in a Fabry-Perot resonator which consists of a concave mirror and a tunable output coupler. This configuration of the resonator allows nine diodes to generate a well collimated radiation beam which efficiently couples to the fundamental resonator TEM<sub>00</sub> mode. In addition, the metal waveguides provide a large heat sink for the Gunn diodes, which have a low dc-rf conversion efficiency.

In this experiment, the output coupler was not used. The InP-Gunn diodes used in the experiment have a maximum output power of about 160 mW in a well tuned waveguide resonator. The concave mirror has a radii of curvature of 600 mm and a diameter of 120 mm. The metal waveguide has a total length  $L_w$  of 80 mm. Total output power for the oscillator was estimated from power detected through a receiving V-band standard horn (Gain 24 dB at 60 GHz) placed at a distance of 720 mm from the oscillator.

## Experimental Results

Figure 2 shows the measured frequency spectrum for the horn coupled oscillator. The C/N ratio at a 100 kHz offset was -80 dB, compared to -68 dB measured for the oscillator having only a single diode. This experimental result shows that radiation power from the nine Gunn diodes has been successfully combined coherently in the resonator at the center frequency of 61 GHz.

Figure 3 shows the measured E- and H-plane patterns of the output beam from the oscillator at 61.3 GHz. The solid curve is the theoretical directivity of the 3x3 horn antenna array. The agreement between the theoretical and experimental beam patterns implies that the oscillation mode in the resonator is the fundamental TEM<sub>00</sub> mode. It should be noted that the main beam in Fig. 3 corresponds to a Gaussian beam with a spot size of 19.5 mm at the output side of the horn array, which is somewhat smaller than half of the array size of 45 mm. In the experiment, power detected through the receiving horn was 60 mW which corresponds to the total output power of about 1 W. Since the power ratio of the main beam to the sidelobes in Fig. 3 is 6.6:3.4, power contained in the main beam is 660 mW.

For the same output beam patterns shown in Fig. 3, oscillation frequencies in the horn coupled oscillator were measured as a function of the spacing,  $L_w$ , between the concave mirror and horn array and are shown in Fig. 4. The solid lines are the theoretically calculated frequencies using an equivalent circuit for the horn coupled oscillator. The equivalent circuit was constructed by using a simple transmission line model containing a single waveguide as a unit cell. In Fig. 4, the measured tuning frequency range for the oscillator is about 0.56 GHz at a center frequency of 61.2 GHz. This frequency tunability is limited by the free spectral range allowed for a resonator with a length of about 284 mm.

### Conclusion

A horn antenna coupled quasi-optical oscillator has been developed as an efficient power combiner for a small number of diode devices at millimeter wave frequencies. Theoretical and experimental results have shown that the oscillator can produce a fundamental Gaussian output beam with a high power of 660 mW and a small diffraction angle of  $6^\circ$  by using only nine Gunn diodes at frequencies around 61 GHz. These results indicate that the horn coupled oscillator could be a practical source for many applications at millimeter wavelengths.

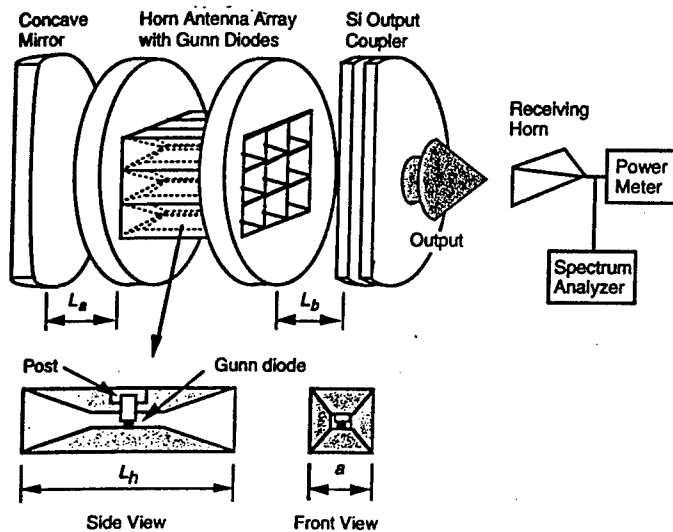


Fig. 1 Experimental configuration of the horn antenna coupled quasi-optical oscillator with Gunn diodes.

This work was partially supported by a Grant-in-Aid of Scientific Research from the Ministry of Education, Science, Sports and Culture of Japan.

### References

- [1] H. Kondo *et al.*, IEEE Trans. Microwave Theory Tech., vol. 40, no. 5, pp. 857-863, 1992.
- [2] R. M. Weikle II *et al.*, Proc. IEEE, vol. 80, no. 11, pp. 1800-1809, 1992.
- [3] J. Mink, IEEE Trans. Microwave Theory Tech., vol. MTT-34, no. 2, pp. 273-279, 1986.

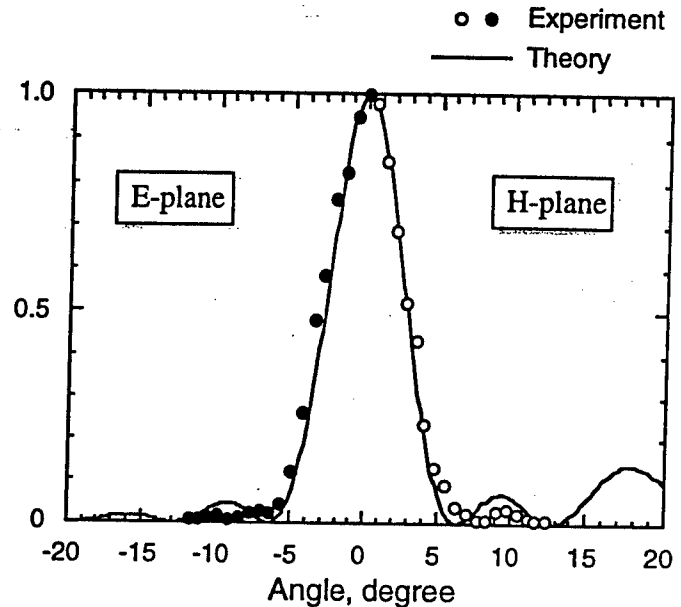


Fig. 3 Measured E- (left) and H- (right) plane patterns of the output beam in the horn antenna coupled oscillator at 61.3 GHz. The radiation angles were measured from the center of the surface of the horn antenna array at the output side of the oscillator.

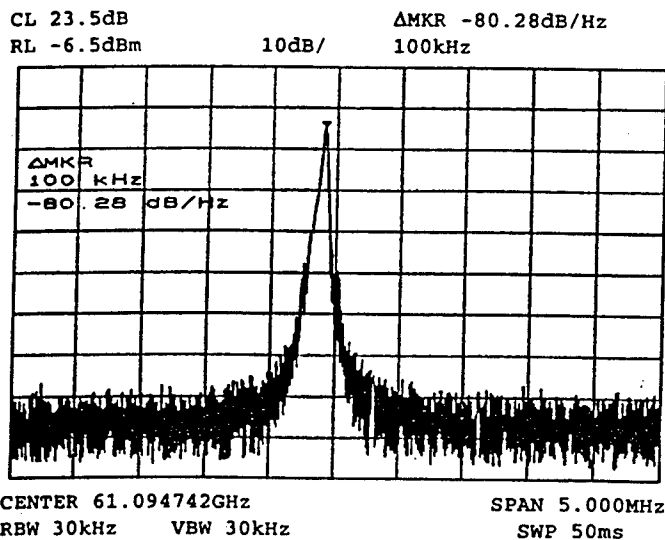


Fig. 2 Measured frequency spectrum of the horn antenna coupled oscillator.

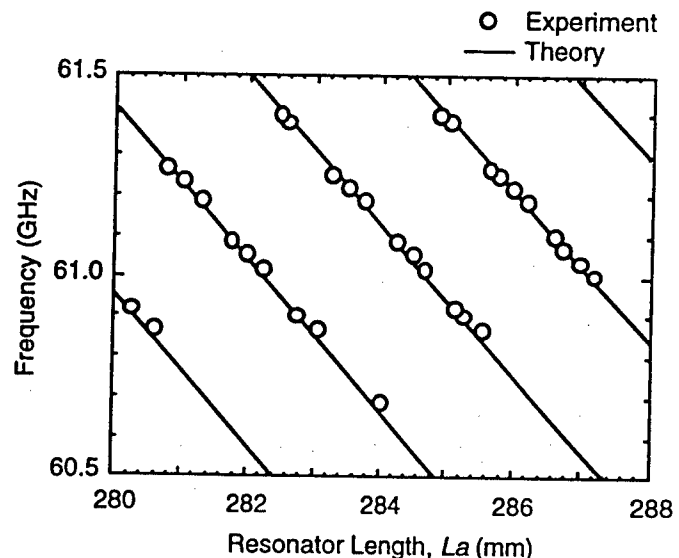


Fig. 4 Measured (a) oscillation frequencies and (b) detection power for the horn antenna coupled oscillators as a function of the resonator length  $L_a$ .

## Design of New Millimeter Wave Sources using Electrically Thick Monolithic Substrate Mode Resonant Combiners

Donald W. Griffin and Ali Afkari Sayyah,

Department of Electrical & Electronic Engineering,  
University of Adelaide, South Australia 5005.

### Abstract

A new design for millimeter wave power sources is presented. A monolithic array of transistor oscillators, designed in shielded inverted microstrip form on an electrically thick substrate is synchronised, phased and power combined in the resonant substrate with efficient output to a single mode waveguide or to an aperture type antenna.

### Introduction - monolithic substrate limitations

The development of transistors that have useful gain at frequencies up to 100GHz has created new prospects in the search for millimeter wave power sources that are more efficient and less expensive than existing sources based on IMPATT and Gunn diodes. The power output capability of transistors decreases with increasing frequency making it necessary to combine the outputs from several oscillators to satisfy systems requirements. Monolithic fabrication of all the transistors and passive components to form an array on a single wafer is the cost-effective solution but a design has yet to be found that is compatible with all of the practical limitations of the technology in current use.

Gallium arsenide (GaAs) wafers of sufficient area to accommodate an array of oscillators need to be 200 microns thick to be mechanically strong enough for processing. With a dielectric constant of 12.8 these wafers are almost  $\lambda_d/4$  thick at 100GHz, where  $\lambda_d$  is the wavelength in the dielectric medium. Conventional microstrip circuit design is not possible on such a thick substrate. Transistor grid oscillators on GaAs wafers as millimeter wave quasi-optical power combined sources [1, 2] exhibit substrate mode power combining and radiation of power from the edges. Consequently monolithic millimeter wave normal mode quasi-optical sources do not appear to be possible whereas there is a natural tendency for substrate mode power combining to occur.

Research has led to a design that exploits substrate mode power combining and is compatible with standard monolithic fabrication limitations for making high electron mobility (HEMT) transistors. The design can be implemented at either microwave or millimeter wave frequencies and it avoids the anomalously high losses in electrically thin GaAs substrates on metal ground planes [3].

### Design principles

A metal strip from the HEMT source provides common source series feedback, one from the gate is terminated in an open circuit and a matching strip connects the drain to the load as in Figure 1. Referring to Figure 2 all designs are on the basis of shielded inverted microstrip circuitry. The transistors and metal strips are formed on the surface of an electrically thick dielectric slab that is separated by air or a low dielectric constant medium from a ground plane. The reverse side of the dielectric slab is covered with a shielding plane that extends over the edges to join the ground plane so that a partially filled rectangular cavity resonator is formed. The required oscillation frequency and the number of transistors in the array together with the dielectric slab and air space determine the internal dimensions of the cavity resonator, the resonant LSM-mode for oscillation throughout the cavity and the electric field distribution on the surface of the dielectric slab associated with that LSM-mode.

Each transistor and its associated metal strip circuitry must be positioned precisely relative to the surface electric field as shown in Figure 3.[4] There should be no coupling between each oscillator circuit and the cavity resonance except via a coupling probe that is fed by the drain in each oscillator. Transistors are placed at zero surface electric field positions that have the additional feature that the metal strips connected

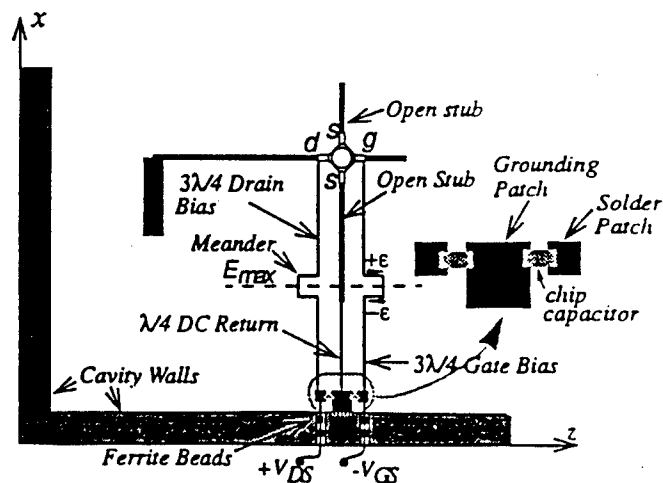


Fig. 1. The oscillator design test circuit for 3.5 GHz.



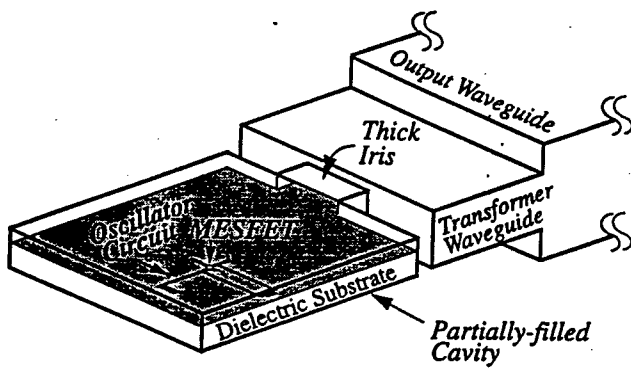


Fig. 2. Outline view of substrate mode power combiner.

to the transistor pass through electric fields that are transverse. DC bias connections are also positioned in transverse surface electric fields.

### Output

The combined output may be coupled from the resonator by means of a partially-filled aperture to air-filled waveguide or a partially-filled aperture to radiating aperture for use as an active antenna. Output coupling affects resonant cavity operation and oscillator loading and is incorporated in design by mode matching analysis.

### Mode stabilisation features[4]

The design has additional features that may be incorporated depending on the required oscillation frequency and the most

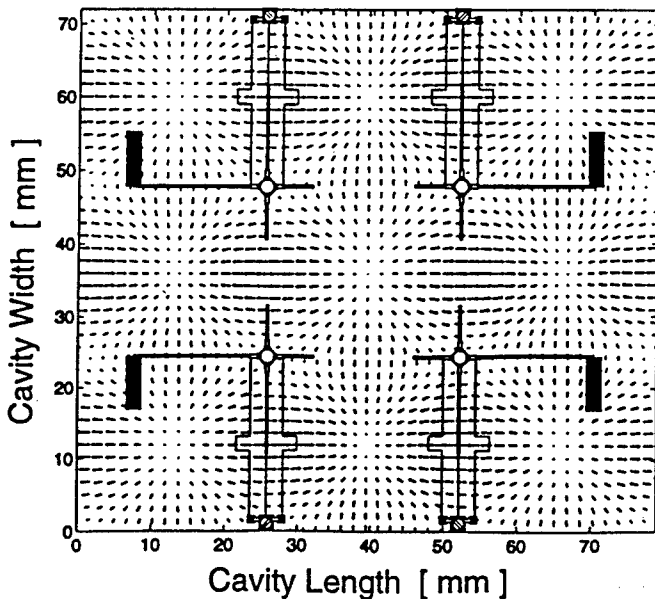


Fig. 3. Placement for an LSM<sub>303</sub> resonance

appropriate technology (packaged, chip or monolithic transistors). Each oscillator may be non-invasively adjusted in frequency by means of a metal screw that reduces the air gap above the metal strip connected to the gate. The oscillator frequency can be increased by as much as 5 percent. The resonant frequency of the cavity can be reduced by as much as 3 percent by moving the end wall opposite the output coupling. The evanescent fields that extend into the airgap that is created effectively add inductive reactance to that face of the dielectric slab. Unwanted LSM mode resonances can be suppressed by means of metal probes and resistive probes that project through the dielectric slab and air space at positions where the desired mode has zero electric field. The oscillators are coupled to each other via the cavity LSM mode resonance. This gives rise to high level injection locking over a range that is determined by the external Q of the oscillators which is typically from 30 to 50. Non-invasive tuning is only needed to bring the oscillators within a range of 1 percent or so. External injection locking is easily arranged via coupling to the resonator.

### Design testing and conclusion

Design testing has been limited by locally available technology to microwave hybrid fabrication of assemblies on dielectric plates with dielectric constant 10.8. Oscillation frequency within 1% and a power efficiency of 20% has been measured for the array of Figure 3. The substrate combining resonator is effectively a tank circuit in each transistor drain path. The potential for classical high efficiency class C operation exists. However transistor transconductance delay may limit the frequency of oscillation at which class C operation may be realised and non-linear design methods appear not to have been extended to class C conditions.

### References

1. M. Kim, E.A. Sovero, R.M. Weikle II, J.B. Hacker, P.M. de Lisio and D.B. Rutledge, "A 35GHz HBT monolithic grid oscillator", Proc. SPIE 17th Int. Conf. on Infrared and Millimeter Waves, R.J. Temkin, ed., pp402-403, 1992.
2. D.W. Griffin, A. Torabi, H.M. Harris, R.W. McMillan, S.P. Halpern, J.C. Wiltse and C.J. Sommers, "Millimeter wave substrate mode transistor grid oscillator power combining", Proc. Workshop on MM Power Gen., Univ. of Alabama in Huntsville, USA, pp219-227, 1993.
3. A. Vilcot and S. Tedjini, "Ground plane effects in monolithic millimeter-wave integrated circuits", IEEE Microwave and Guided Wave Letters, vol.3, pp32-34, Feb.1993.
4. Patent filed 18 December 1996, Adelaide, South Australia.

# Modeling of InGaN-GaN Modulation-Doped Field-Effect Transistors for 60 GHz Operation

S.K. Islam<sup>1</sup> and F.C. Jain<sup>2</sup>

<sup>1</sup>Department of Electrical Engineering  
University of North Florida, Jacksonville, FL 32224

<sup>2</sup>Electrical and Systems Engineering  
University of Connecticut, Storrs, CT 06269

## Abstract

An analytical model, matching the experimental transport characteristics of InGaN-GaN/AlGaIn-GaN Modulation-Doped Field-Effect Transistors (MODFETs) at 18 GHz, predicts that 0.25  $\mu\text{m}$  channel length (and 50  $\mu\text{m}$  gate width) devices will extend the use of InGaN-GaN MODFETs to about 60 GHz. Calculations also show operation at elevated temperatures.

## Introduction

Wide energy gap semiconductors such as GaN and SiC are very attractive for high-power and high-temperature electronic device applications due to their excellent thermal conductivities, large breakdown field and their ability to resist chemical attack [1]. Transistors have been fabricated using SiC and GaN-based materials for microwave operation and high-temperature applications [2,3]. This paper focuses on design and analysis of Modulation-Doped Field-Effect Transistor (MODFET) structures for microwave applications. A Modulation-Doped Field-Effect Transistor (MODFET) structure realized in InGaN-GaN material system is presented [4]. An analytical model predicting the transport characteristics of the proposed MODFET device is also presented. Electron energy levels inside and outside the quantum well channel are evaluated. The two-dimensional electron gas (2DEG) density in the channel is calculated by self-consistently solving Schrödinger and Poisson's equations. The unity-current gain cutoff frequency ( $f_T$ ) of the InGaN-GaN MODFET is computed as a function of the gate voltage  $V_G$ . The analytical model is also used to calculate  $f_T$  of an AlGaIn-GaN MODFET device. The results are compared with experimental  $f_T$  value of a GaN/AlGaIn HFET device [3].

## Device Structure

Figure 1 shows the cross-sectional schematic of the InGaN-GaN MODFET structure. The device structure consists of 150 Å thick  $\text{In}_{0.22}\text{Ga}_{0.78}\text{N}$  quantum well channel separated by 50 Å of undoped  $\text{In}_{0.06}\text{Ga}_{0.94}\text{N}$  spacer layer from 300 Å thick n-type  $\text{In}_{0.06}\text{Ga}_{0.94}\text{N}$  supply layer. The function of the undoped spacer layer is to reduce impurity ion scattering. Thus the mobility of two-dimensional electron gas (2DEG) in the quantum well channel is extremely high as a result of modulation doping. The

MODFET structure is realized by implementing source and drain contacts, as shown in figure 1.

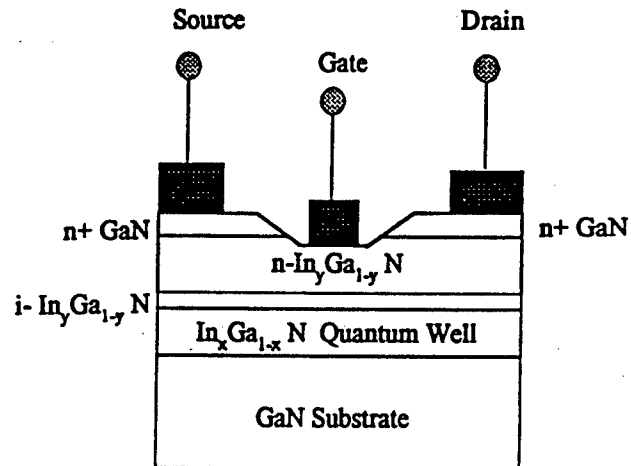


Figure 1. Cross-sectional schematic of the MODFET

## Device Modeling

The energy levels in the quantum well channel and the electron wave function inside and outside the quantum well are evaluated by self-consistently solving Schrödinger and Poisson's equations. The density of two-dimensional electron gas (2DEG) is expressed as a function of the gate voltage  $V_G$  as [5],

$$n_s(x) = \frac{\epsilon_2}{q(d_s + d_i + \Delta d)} [V_G - V(x) - V_{th}] \quad (1)$$

where,  $\epsilon_2$  is the permittivity of the  $\text{In}_{0.06}\text{Ga}_{0.94}\text{N}$  supply and spacer layers,  $d_s$  and  $d_i$  are the thicknesses of the supply and spacer layers respectively and  $\Delta d$  is the average distance of the electron gas from the heterointerface [6], and  $V_{th}$  is the threshold voltage [5].

The current-voltage, the transconductance and the unity current gain cut-off frequency  $f_T$  are obtained by following Chang and Fetterman's analytical model [5].

## RESULTS

The parameter used in the calculations are listed in Table I. Figure 2 shows the  $I_D$ - $V_G$  and  $g_m$ - $V_G$  characteristics. The unity current-gain cut-off frequency is calculated for the device at 300 °K as shown in figure 3. Figure 3 also compares the  $f_T$  values of InGaN-GaN MODFET and an AlGaIn-GaN MODFET. The AlGaIn-GaN MODFET structure is similar to the InGaIn-GaN MODFET with the supply and spacer layers are being replaced by  $Al_{0.15}Ga_{0.85}N$ . The  $f_T$  value of these devices compare very well with that of GaN/AlGaIn-Doped HFET fabricated by Khan *et al* [3]. Table II shows the comparison between the experimental  $f_T$  value of the GaN/AlGaIn-Doped HFET with theoretical  $f_T$  value calculated for the InGaIn-GaN MODFET and the AlGaIn-GaN MODFET device. Based on the experimental data, as well as our computed characteristics, we project the usage of the wide gap semiconductors in the realization of 18-30 GHz power amplifiers and other devices in near future. Using the analytical model we also predict that the InGaIn-GaN MODFET with a 0.25  $\mu m$  channel length and 50  $\mu m$  gate width will extend the operation of these devices to about 60 GHz as shown in figure 4. The calculations also show operation at elevated temperatures ( $\sim 400$  °K). Thus these devices can be driven harder and can be operated at higher temperatures.

Table I. Parameters Used For Calculations

Quantum Well Thickness	150 Å	Channel Length(L)	1.00 $\mu m$
Schottky Barrier Height ( $\phi_b$ )	1.1 V	Channel Width (Z)	150 $\mu m$
Supply Layer Thickness (d)	300 Å	Threshold Voltage( $V_{th}$ )	-2.32 Volts
Spacer Layer Thickness(d)	50 Å	Saturation Velocity( $v_s$ )	$10^7$ cm/sec
Supply Layer Doping ( $N_d$ )	$10^{18}$ cm $^{-3}$	Band Offset ( $\Delta E_c$ )	0.1775 eV
Dielectric Constant of Supply Layer ( $In_{0.5}Ga_{0.5}N$ ) $\gamma=0.06$	2.5 $\epsilon_0$	Electron mobility ( $\mu_n$ )	864 cm $^2$ /V-sec @300°K
Dielectric Constant of Quantum Well Material ( $In_{0.5}Ga_{0.5}N$ ) $x=.22$	2.832 $\epsilon_0$	Electron mobility ( $\mu_n$ )	714 cm $^2$ /V-sec @400°K

Table II. Comparison between GaN/AlGaIn HFET [3] and Proposed MODFET devices

	InGaIn-GaN MODFET	AlGaIn-GaN MODFET	GaN/AlGaIn HFET[4]
$f_T$ (GHz)	15.03	15.11	18.3

## REFERENCES

1. H. Morkoc, S. Strite, G.B. Gao, M.E. Lin, B. Sverdlov, and M. Burns, J. Appl. Phys., 76(3), 1363, 1994.
2. J.W. Palmour, J.A. Edmond, H.S. Kong, and C.H. Carter Jr., Physica B, 185, 461, 1993.

3. M.A. Khan, Q. Chen, J.W. Yang, M.S. Shur, B.T. Dermott, and J.A. Higgins, IEEE Electron Dev. Lett., 17, 325, 1996.
4. S.K. Islam and F.C. Jain, Proc. Connecticut Symposium on Microelectronics and Optoelectronics, P-15, New Haven, 1997.
5. C-S. Chang, and H.R. Fetterman, IEEE Trans. Electron Dev., ED-34, 1456, 1987.
6. T.J. Drummond, H. Morkoc, K. Lee, and M.S. Shur, IEEE Electron Dev. Lett., EDL-3, 338, 1982.

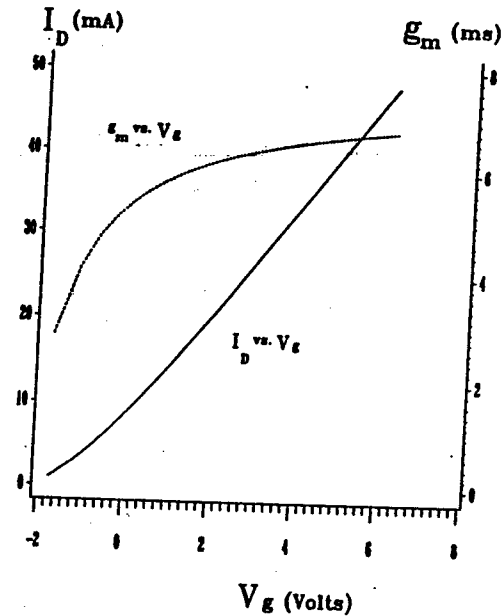


Figure 2.  $I_D$ - $V_G$  and  $g_m$ - $V_G$  Characteristics

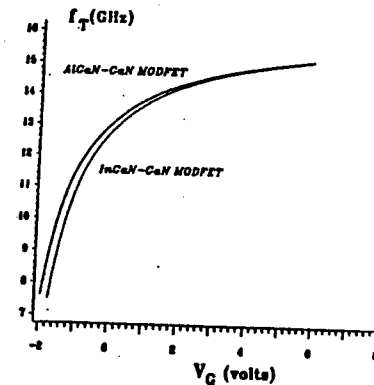


Figure 3.  $f_T$ - $V_G$  characteristics of InGaIn-GaN and AlGaIn-GaN MODFETs

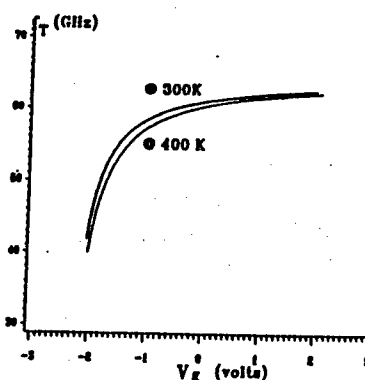


Figure 4.  $f_T$ - $V_G$  characteristics of InGaIn-GaN MODFET

## A High-Power, Millimeter-Wave Balanced Doubler

David W. Porterfield,<sup>†</sup> Thomas W. Crowe,<sup>†</sup> Richard F. Bradley,<sup>\*</sup> Neal R. Erickson<sup>&</sup>

University of Virginia<sup>†</sup>  
Dept. Electrical Eng.  
Charlottesville, VA, 22903

National Radio Astronomy Obs.<sup>\*</sup>  
Central Development Laboratory  
Charlottesville, VA, 22903

Five College Radio Astronomy Obs.<sup>&</sup>  
University of Massachusetts  
Amherst, MA, 01003

### Abstract

We report on the development of high-power, millimeter-wave, fixed-tuned balanced doublers. The initial design is for a 40-80 GHz doubler using a linear array of six planar Schottky barrier varactor diodes. Each diode is designed to handle an input power of 34 mW for a total input power capability of approximately 200 mW. The design is optimized for large bandwidth with the constraint that no mechanical tuners are employed. Emphasis has been placed on making the design easy to fabricate and scalable to higher frequencies.

### Introduction

There is a demand for sources of millimeter-wave and submillimeter-wave power, primarily for use as local oscillators in heterodyne receivers for remote sensing, atmospheric physics, radio astronomy and a variety of laboratory measurements. An ideal source for most of these applications, and particularly for those which involve space qualification, would exhibit high output power and efficiency, large electronically tuned bandwidth (fixed mechanical tuning), high tolerance to mechanical and thermal stress, low noise, low mass and low maintenance.

Systems using frequency multipliers based on GaAs Schottky varactors and a fundamental oscillator, such as a Gunn diode, have long been used to achieve these goals. However, there is typically an important trade-off between bandwidth and power. Multipliers operating in a purely varactor mode exhibit a relatively high Q and therefore tend to be bandwidth limited, while varistor mode multipliers have a potentially large bandwidth as a result of predominantly real embedding impedances, but suffer from low power handling due to high power dissipation.

Until very recently, the most successful millimeter-wave multipliers relied on whisker contacted GaAs diodes to minimize shunt capacitances and therefore allow high frequency operation [1]. However, high quality planar diodes have recently become available [2], and several successful millimeter-wave multipliers have been developed [3,4]. These systems are mechanically very reliable and have exhibited high efficiency and power handling. Unfortunately, these systems have had rather limited fixed-tuned bandwidth. In this research we will use modern analysis software to design the multiplier circuit in an attempt to increase the bandwidth while maintaining both power handling ability, efficiency and ease of fabrication.

### The Balanced Multiplier

Distributed filters are often employed in multiplier circuits to separate and direct the various harmonic components. However, resistive circuit losses in these filters seriously limit performance at high frequencies. For this reason, we selected a balanced doubler based on the design developed by Erickson [1,3,4]. This approach eliminates the need for distributed filters since harmonic separation is achieved by placing the diodes at the junction between balanced and unbalanced transmission lines, as shown in Fig. 1.

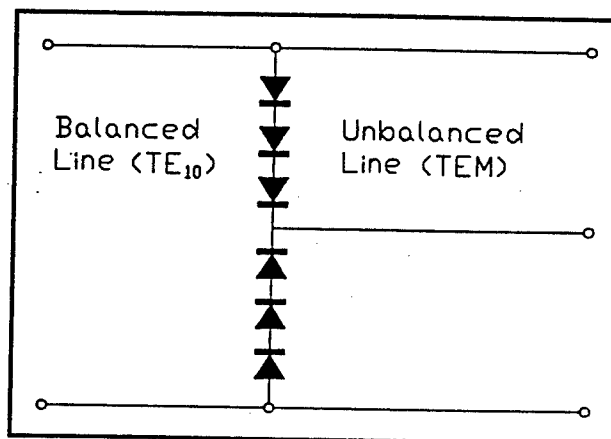


Fig. 1. Balanced doubler schematic.

The fundamental frequency is incident on the diode array in a  $TE_{10}$  mode (balanced), while the second harmonic is generated in an unbalanced (TEM) mode. If the input waveguide height is sufficiently reduced (typically  $\frac{1}{2}$  height or less), the  $TM_{11}$  mode for the second harmonic is suppressed in the input waveguide. At some point along the TEM line, the waveguide width is reduced sufficiently to cut off propagation of the fundamental frequency in the  $TE_{10}$  mode, thus creating an effective fundamental frequency backshort.

Since multiple diodes are used in the balanced design, the potential exists for relatively high power handling. Series-stacking of the varactor diodes has the added benefit of reducing the net capacitance presented to the external circuit.

### Multiplier Design

Erickson's original design incorporated two whisker contacted diodes mounted on a metal post which acted as the center conductor for the TEM line [1]. He later made a slight modification to this design to allow for a planar diode

package [3,4]. However, the design was never fully optimized for planar diodes.

We will replace the metal post in Erickson's design with a quartz substrate. The center conductor for the TEM line, output waveguide probe and hammer-head RF blocking filter for the DC biasing network will be photolithographically formed on the quartz substrate. This design allows for a high degree of flexibility and control of the center conductor dimensions and therefore substantial control over the second harmonic embedding impedance.

Concern over heat dissipation has prompted us to consider three basic variations of this design. In the first variation, the diode package will be soldered to gold pads on a fused quartz substrate. Gold ribbons will extend from the pads to the waveguide block for electrical and heat conduction. Although the diodes will be operated in varactor mode, we predict significant power dissipation in the series resistance of the diode package. Using an active layer doping of  $10^{17} \text{ cm}^{-3}$ , buffer doping of  $4 \times 10^{18} \text{ cm}^{-3}$  and an anode radius of  $13 \mu\text{m}$ , we calculate a series resistance on the order of  $1 \Omega$ . Harmonic balance simulations indicate that each of the six anodes will dissipate approximately 5 mW in the series resistance.

We performed a first order heat analysis for this arrangement where we modeled all heat generated in the series resistance as a heat source located in the active region (anode). In an attempt to simulate a worst case scenario, we used a figure of 7 mW dissipated per anode and treated the center conductor and fused quartz substrate as thermally non-conducting. This resulted in an estimated temperature of nearly  $90^\circ\text{C}$  at the anodes closest to the center conductor. We repeated the heat analysis, but treated the center pad of the diode package as connected to a heat sink at  $27^\circ\text{C}$ . The hottest points, at  $35^\circ\text{C}$ , were the middle anodes between the block and center conductor. This clearly showed the importance of providing a good heat conduction path at the center pad of the diode package.

In the second design variation, the fused quartz substrate is replaced with a z-cut crystalline quartz substrate. The thermal conductivities for fused silica and z-cut crystalline quartz are approximately  $1.4 \text{ W}\cdot\text{m}^{-1}\cdot\text{K}^{-1}$  and  $14 \text{ W}\cdot\text{m}^{-1}\cdot\text{K}^{-1}$  respectively. As a result, the z-cut quartz offers an improved heat dissipation path at the center pad of the diode package.

In the third design variation, a larger diode package will extend across the input waveguide and will be soldered directly to the block for maximum heat dissipation. A gold ribbon will connect the center pad of the diode package to the center conductor on the quartz substrate. All three variations will utilize the same waveguide block.

We have used Hewlett-Packard's High Frequency Structure Simulator (HFSS) to model all parts of the waveguide block, quartz circuit and diode package. Harmonic balance

simulations using the embedding impedances calculated by HFSS indicate a 3 dB bandwidth of approximately 10-15%. HFSS simulations of the output waveguide probe, hammer-head filter, fixed backshort and a linear output waveguide transition to full height E-band show excellent coupling over a 30% bandwidth.

### Conclusion

We have developed a high-power, 40-80 GHz balanced doubler. The doubler uses a linear array of 6 planar varactor diodes and is designed for an input power level of 200 mW. The basic design is modeled after the balanced doubler developed by Erickson [1,3,4]. We have simplified the doubler fabrication by replacing the metal pin in Erickson's original design with a photolithographically formed gold conductor on a quartz substrate. This modification also allows improved fixed-tuned bandwidth due to the increased flexibility in the center conductor geometry. Our design will be scalable to higher frequencies.

At the time of this report, the waveguide block was being machined and the Schottky barrier varactor diodes were in the early stages of production at the University of Virginia Semiconductor Device Laboratory. We expect to have test results available for the conference.

### References

- [1] Neal Erickson, "High Efficiency Submillimeter Frequency Multipliers," IEEE/MTT-S Intl Microwave Symp. Digest, pp. 1301-1304, 1990.
- [2] W.L. Bishop, T.W. Crowe and R.J. Mattauch, "Planar GaAs Schottky Diode Fabrication: Progress and Challenges," Fourth Int. Space THz Tech. Symp., Los Angeles, CA, March 1993.
- [3] Neal Erickson, Brian Rizzi, Thomas Crowe, "A High Power Doubler for 174 GHz Using a Planar Diode Array," Proc. Fourth Intl. Symp. on Space THz Tech., pp. 287-296, March 1993.
- [4] Neal Erickson, Jussi Tuovinen, Brian Rizzi, Thomas Crowe, "A Balanced Doubler Using a Planar Diode Array for 270 GHz," Proc. Fifth Intl. Symp. on Space THz Tech., pp. 409-413, May 1994.

### Acknowledgments

This work was funded by the United States Army National Ground Intelligence Center, contract number DAHC90-96-C-0010 and NASA grants NAGW-4007 and NGT-51326.

# A Frequency Doubler for 200 GHz with a Planar Schottky Varactor

Jyrki T. Louhi, Antti V. Räisänen

Helsinki University of Technology, Radio Laboratory,  
P.O.Box 3000, FIN-02015 HUT, Finland

## Abstract

A frequency doubler for 200 GHz utilizing a planar surface channel Schottky varactor is presented. The doubler employs novel split-waveguide mount design with two tunable backshorts at both input and output waveguides. The measured maximum efficiency is 7.1 % and the maximum output power is 2.6 mW.

## 1. Introduction

One of the biggest challenges of the terahertz community is to develop a reliable all-solid-state power source with reasonable dc and rf efficiency [1]. The aim of this work was to design, construct, and test a planar Schottky varactor frequency doubler for 200 GHz in order to study design methods, multiplier structures and fabrication techniques applicable for frequency multipliers at millimeter and submillimeter wavelengths.

The doubler utilizes a split-waveguide mount design [2], which offers excellent tuning features with two sliding backshorts at both input and output (see Figure 1). The nonlinear element of the doubler is a UVa SC6T5-S50 planar surface channel Schottky varactor, parameters of which are designed to be similar to those of the widely used whisker contacted UVa 6P4 Schottky varactor.

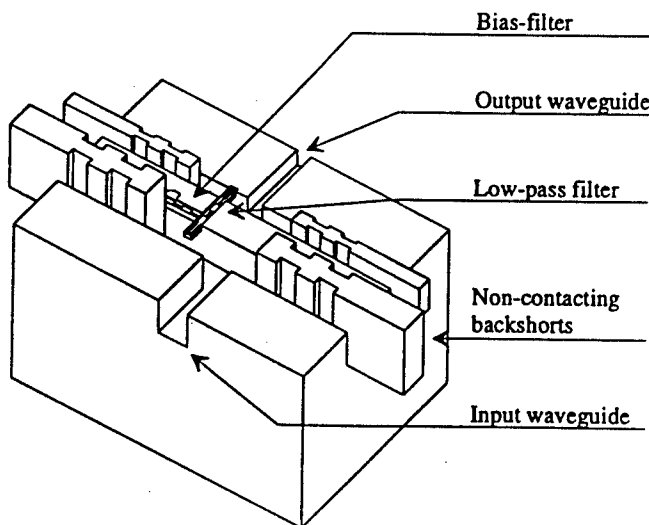


Figure 1. Split-waveguide doubler mount.

## 2. Performance simulations

The performance of the doubler has been analyzed by using the multiple reflections technique [3]. The original computer program presented by Siegel *et al.* has been further developed in the Radio Laboratory. Compared to the original program, the developed program includes an optimization routine so that the optimum embedding impedances can be found for each operation point. The new model of the electron velocity saturation has also been included in the program [4].

As shown in Figure 2, the theoretical maximum efficiency of the doubler is 44.0 %, which is achieved with an input power level of 32 mW and embedding impedances of  $(15 + j95)\Omega$  and  $(30 + j50)\Omega$  at input and output frequencies, respectively. In the majority of practical cases the maximum output power is a more interesting figure of merit than the maximum efficiency. In our case, the maximum available input power is about 50 mW. Thus, the theoretical maximum output power of the doubler is 16.5 mW with an efficiency of 33.0 %, which is achieved with the same impedance levels as the maximum efficiency.

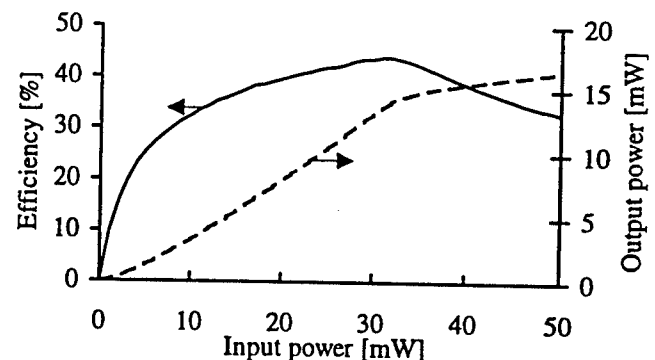


Figure 2. Theoretical efficiency (solid line) and output power (dashed line).

## 3. Doubler mount

The schematic of the split-waveguide doubler mount is shown in Figure 1. The input power is fed through an input waveguide (WR-10) and a quartz microstrip low-pass filter to the planar Schottky varactor. The planar Schottky varactor is soldered on the microstrip filter substrate. The second harmonic frequency generated by the nonlinearity of the varactor is transmitted by the output waveguide

includes also E-plane arms to provide an in-line input and output waveguide flanges. Furthermore, the mount includes a bias filter, through which the applied bias voltage is fed to the varactor. The bias filter is designed to prevent the input power from propagating to the coaxial bias line.

The most important advance provided by the novel split-waveguide mount, is the better tuning possibility. While in the case of only one tuning element only impedances on a circle at the Smith chart can be matched, in the case of two tuning elements, impedances over a very large range can be matched. By studying the equivalent circuit of the mount, it can be seen that in order to realize a good matching property the most important factor is to select a proper value for the length of the waveguide between the E-plane arm and microstrip terminal. In the original design the length is  $\lambda/2$  [2], which, however, does not provide as good performance as that of  $\lambda/2+\lambda/5$  or  $\lambda/2-\lambda/5$ .

#### 4. Measurements

The measured output power and efficiency versus input frequency are shown in Figure 3. The input power level at the doubler input port is measured by using a calorimeter and the output power is measured by using Tektronix spectrum analyzer with an external harmonic mixer (calibrated by using a calorimeter). During the measurements the input and output matching as well as the bias voltage are carefully optimized.

According to the measurements, the doubler works fairly well at input frequencies from 90–95 GHz with an efficiency better than 6 % and output power level greater than 0 dBm. The maximum measured output power is 4.2 dBm at 190 GHz with an input power of 15.7 dBm, while the measured maximum efficiency is 7.1 % at 190 GHz with an input power of 13.5 dBm. At these frequencies the input matching circuit works well with a measured return loss better than 20 dB. The optimum bias point is reached by employing a bias voltage of about -4.0 V.

At input frequencies above 100 GHz the doubler does not work well. The measured efficiency is smaller than 1.5 % and the output power level is only about -10 dBm. The main reason for the poor results is the input matching at these frequencies. According to the measurements, the return loss of the doubler input port is only about 2–3 dB. The bad matching combined with the low maximum output power of the available Gunn oscillator decreases the power delivered to the varactor and, thus, decreases the efficiency and output power level significantly. Due to the low power level delivered to the varactor, the optimum bias point differs from that used at lower frequencies.

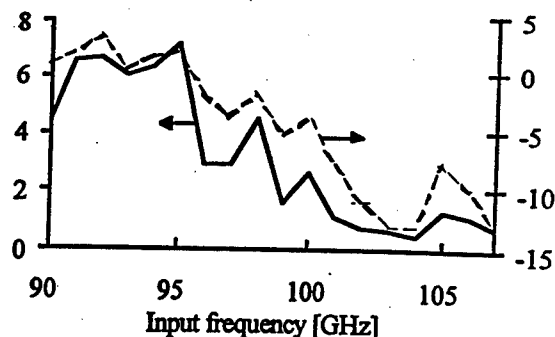


Figure 3. Measured output power (dashed line) and efficiency (solid line).

#### 5. Conclusion

In this work, a frequency doubler for 200 GHz has been designed, constructed, and tested. The measured maximum output is 4.2 dBm at 190 GHz, while the measured maximum efficiency is 7.1 %. However, the experimental results are below the theoretical values, especially at frequencies above 200 GHz. One possible reason is that the parasitic components due to the planar chip are not yet understood well enough.

#### Acknowledgments

The authors would like to thank the chaps in the workshop, Mr. Erkki Laine and Mr. Kauko Herold for careful machining of the multiplier mount.

#### References

- [1] A.V. Räsänen: "Frequency multipliers for millimeter and submillimeter wavelengths," *Proceedings of the IEEE*, vol. 80, no.11, pp. 1842–1852, 1992.
- [2] A. V. Räsänen, D. Choudhury, R. J. Dengler, J. E. Oswald, and P. H. Siegel, "A novel split-waveguide mount design for millimeter- and submillimeter-wave frequency multipliers and harmonic mixers," *IEEE Microwave and Guided Wave Letters*, vol. 3, no 10, 1993, pp. 369–371.
- [3] P. H. Siegel, A. R. Kerr, and W. Hwang, "Topics in the optimization of millimeter-wave mixers," *NASA Technical paper 2287*, 1984, 512 p.
- [4] J.T. Louhi and A.V. Räsänen: "On the modeling and optimization of Schottky varactor frequency multipliers at submillimeter wavelengths," *IEEE Transactions on Microwave Theory and Techniques*, vol. 43, no. 4, pp. 922–926, 1995.

# A 300 GHz QUASIOPTICAL SCHOTTKY FREQUENCY DOUBLER

M. Shaalan<sup>1</sup>, K. Beilenhoff<sup>1</sup>, J. Weinzierl<sup>2</sup>, D. Steup<sup>2</sup>, M. Bozzi<sup>3</sup>, A. Vogt<sup>1</sup>, A. Berkenkamp<sup>1</sup>,  
M. Kiesow<sup>1</sup>, J. Weber<sup>1</sup>, H. Fischer<sup>1</sup>, G. Conciauro<sup>3</sup>, H.L. Hartnagel<sup>1</sup>, and H. Brand<sup>2</sup>

<sup>1</sup> Technical University of Darmstadt, Inst. of Microwave Electronics, Merckstr. 25, 64283 Darmstadt, Germany

<sup>2</sup> University of Erlangen, Laboratories for High Frequency Technology, Cauerstr. 9, 91058 Erlangen, Germany

<sup>3</sup> University of Pavia, Department of Electronics, Via Ferrata 1, 27100 Pavia, Italy

## Abstract

An integrated quasioptical frequency multiplier based on a new antenna concept was realized and measured at 300 GHz. Each circuit comprises a Schottky varactor, slot antenna, MIM-capacitor and microstrip bias feed. The technological approach and the RF performance will be addressed.

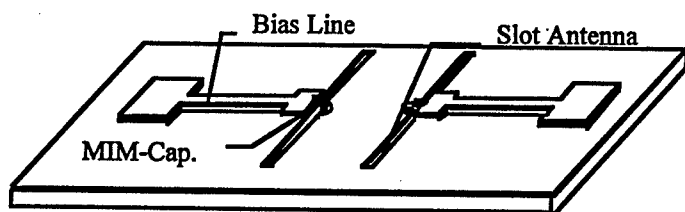


Fig. 1 Schematic of the quasioptical monolithically integrated 300 GHz frequency doubler with the new antenna concept.

## Introduction

Quasioptical submillimeter-wave frequency multipliers have increasingly been subject to research towards an alternative to the established waveguide frequency multipliers in the submillimeter-wave regime [1].

Each of the two frequency multiplier elements shown in fig. 1 integrates a Schottky varactor diode together with a slot antenna, an MIM capacitor and a bias feed. The MIM-capacitor allows for external biasing of the Schottky diode, and suppresses the propagation of the RF along the bias feed. Moreover, a short-circuit must be provided in order to ensure the required input impedance of the antenna.

The substrate thickness together with the antenna dimensions were taken as design parameters to optimize the input impedance of the slot antenna as seen by the diode terminals at the frequencies of interest.

The design approach described in the paper additionally demonstrates a bi-directional radiation pattern [2] of this new antenna approach. This property is aimed at applications, in which the output power must propagate in the direction as the received one. It can also be used to separate between the pump side and the signal side.

Polyimide was extensively used for two main reasons. On the one hand, it serves as an isolation layer for the MIM-capacitor. And on the other hand, it was used to smooth the surface after

the mesa etch. The fabrication and technological aspects are described in detail in this paper.

## Design

The design of the quasioptical frequency doubler chip was based on a new planar bi-directional antenna [2]. At the fundamental frequency, the antenna supplies the Schottky diode with pump power. At the first upper harmonic, on the other hand, the Schottky diode feeds the same antenna with output power. The antenna input impedance resembles the internal impedance of the power source at the fundamental and - simultaneously - the upper harmonics.

Here we differentiate between three distinct loss mechanisms. The input and output gaussian coupling efficiency  $\eta_{in}$  [3] is an indicator of the matching between the antenna and the gaussian waveguide at the fundamental and first upper harmonic, respectively. The circuit conversion efficiency  $\eta_c$  from the fundamental into the first upper harmonic denotes the percentage of power delivered to the antenna by the Schottky diode at the output frequency. The radiation efficiency  $\eta_{rad}$  quantifies the loss due to substrate wave at the input and output frequencies.

With the dimensions of  $300 \times 15 \mu\text{m}^2$  on a  $100 \mu\text{m}$  thick GaAs substrate, the slot provides the following calculated impedances ( $f_0 = 145 \text{ GHz}$ ):

$$\begin{aligned} Z_A(f_0) &= (17.9 + j96.4)\Omega \\ Z_A(2f_0) &= (19.6 + j13.3)\Omega \\ Z_A(3f_0) &= (18.1 + j37.8)\Omega \end{aligned} \quad (1)$$

leading to a circuit conversion efficiency of  $\eta_c = 17.1\%$  (-7.7 dB). The spacing between the two elements was chosen to give the optimal input and output coupling efficiencies to a gaussian waveguide system with a half beam width  $\theta_0$  of  $18^\circ$ . Based on the back side illumination of pump power, the input and output coupling efficiencies were calculated at  $\eta_{in} = 24.2\%$  (-6.2 dB) and  $\eta_{out} = 11.3\%$  (-9.5 dB), respectively. The radiation efficiency is  $\eta_{rad} = 13.8\%$  (-8.6 dB) [2]. Thus, the overall theoretically expected conversion efficiency of the doubler is -32 dB, without the use of external quasioptical filters. The use of external filters, however, influences the antenna input impedance, especially when placing them near the chip. Nonetheless, they can be a useful tool to improve the overall efficiency.



### Fabrication

Fig. 2 shows the photograph of the antenna region. The airbridge is contacted to the anode with 5  $\mu\text{m}$  diameter.

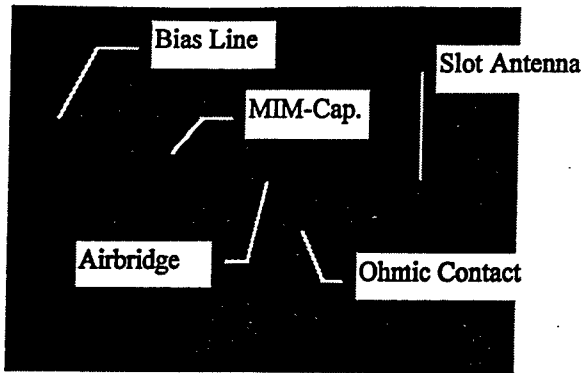


Fig. 2 SEM photograph of the antenna region of the 300 GHz quasi-optical frequency doubler chip.

In the lower part of the photograph the ohmic contact area is depicted, whereas the MIM-capacitor is indicated in the upper part. The slot antenna and bias line are also shown. It can be shown that the ohmic contact is below the surface metallization due to the polyimide filling step.

### RF Performance

The RF performance of the chip was characterized using the measurement system shown in fig. 3. The BWO delivered the pump power to the quasi-optical frequency doubler chip at a level of 150 mW (21.8 dBm) at 144 GHz. This input power was focused to the back side of the doubler chip. The output beam was found at a tilt angle of  $26.5^\circ$  measured from the center axis of the horn in the E-plane at 288 GHz. At this angle, however, the horn antenna receives 15 dB less power compared to the main lobe direction. The power coupled into the mixer at the indicated tilt angle of  $26.5^\circ$  in the E-plane was 1  $\mu\text{W}$  (-30 dBm). The actual output power of the multiplier is, therefore, 35  $\mu\text{W}$  (-15 dBm), corresponding to an overall conversion efficiency of -36.8 dB compared to the theoretically calculated -32 dB indicated in the design.

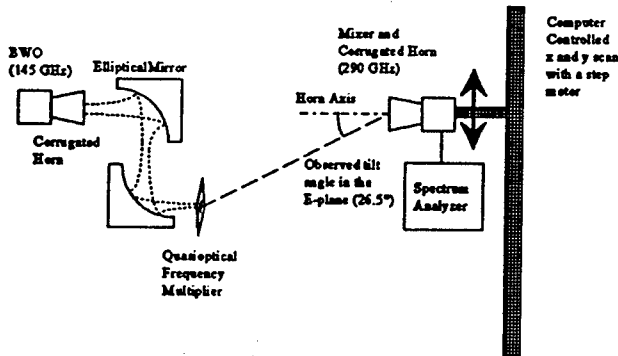


Fig. 3 Measurement setup of the 300 GHz doubler.

The deviation of the output main lobe from the z-axis is an indication of a phase difference between the two radiating elements. The chromium mask set showed an inaccuracy in the size of one of the two anodes. As a consequence, the two

diodes were not identical. This inaccuracy is assumed to be the primary cause of the direction change of the output main lobe.

There are also other second order effects to be considered. The actual substrate thickness of the measured device was 90  $\mu\text{m}$ . This led to an improved radiation efficiency, while the impedance matching was deteriorated compared to the theoretically computed circuit conversion efficiency. Additionally, the edge effects of the finite substrate and chip mount were not considered in the theoretical calculation. The higher-than-expected series resistance of the Schottky diode also led to a decrease of output power. Besides, the conductance of the polyimide film of the MIM capacitor was not taken into account. Unlike in the design, the output power was measured under far-field condition. This also decreased the output coupling efficiency at 290 GHz.

### Conclusion

A quasi-optical monolithically integrated submillimeter-wave frequency doubler circuit based on a new antenna concept is presented. Besides the versatility of its design, the employed antenna results in a significant miniaturization of the chip size. This is mainly due to its direct impedance matching to the Schottky diode at its terminals, avoiding complex matching circuitry at two frequencies.

The bi-directionality of the antenna can be suitable for new applications, notably for subharmonic mixers (or mixer arrays). The observed deviation of the output beam is assumed to be a direct result of the inaccuracies in the fabrication.

The different loss mechanisms were identified, and the overall conversion efficiency was experimentally verified. We obtained good agreement between the theoretical and measured output to input power ratio.

### Acknowledgements

This work is supported by the European Commission under the TMR program contract number ERBFMRXCT960050 and the German Science Foundation (DFG) under the contract number Ha1132/25-2 and Br522/16-2.

### References

- [1] D. Steup, A. Simon, M. Shaalan, A. Grüb, C.I. Lin, "A Quasi-optical Doubler-Array," *International Journal of Infrared and Millimeter Waves*, vol. 17, no. 5, May 1996.
- [2] M. Shaalan *et al.*, "An Antenna Array for Quasi-optical Frequency Multiplier Applications," *Proc. 20th ESTEC Antenna Workshop*, ESTEC, Noordwijk, The Netherlands, 18-20 June 1997.
- [3] G. Rebeiz, "Millimeter-Wave and Terahertz Integrated Circuit Antennas," *Proc. IEEE*, vol. 80, no. 11, November 1992, pp. 1748-1770.

# A Novel Fabrication Process for Refractory Metal/n-GaAs Schottky Diodes

Benjamin K. Sarpong, Thomas W. Crowe, William L. Bishop, Phillip J. Koh  
Department of Electrical Engineering  
University of Virginia  
Charlottesville, VA 22903

**Abstract-** GaAs Schottky barrier multiplier diodes generate local oscillator power at frequencies up to one terahertz. This paper will discuss the development of a fabrication process to create refractory metal Schottky diodes with improved reliability and lifetime for high power, high frequency applications.

## I. INTRODUCTION

Many scientific research fields rely on heterodyne receivers for measurements in the millimeter and submillimeter wavelength regions (30-3000 GHz)[1]. The heterodyne receiver translates the received high frequency signal to a lower frequency where it is easily amplified and analyzed. To achieve this, a local oscillator (LO) source which provides a signal, whose frequency is close to that of the received signal is required. Up to about 140 GHz, Gunn diodes are commonly used as the LO sources. But as the radio frequency approaches the terahertz range, Gunn diodes can no longer provide the necessary power. Therefore, for high frequency sources, frequency multiplier diodes are used. These diodes can generate sufficient output power without degrading the sensitivity or spectral resolution of the receiver.

At high operating powers, reliability is a fundamental concern. The lifetime of the diode is vulnerable to chemical and physical changes that are accelerated by electrical current and high temperatures [2]. Therefore, there is a need for thermally stable GaAs Schottky barriers that can maintain device characteristics at high temperatures with little or no degradation. Present Schottky contact metals, such as platinum (Pt), have demonstrated high operation lifetimes and reliability. However, when these diodes failed, the primary failure mechanism was interdiffusion of metal into the GaAs [3]. Therefore, to create even more efficient and reliable diodes the investigation of improved Schottky contacts is necessary.

In this paper, we report a new fabrication process that produces high quality titanium Schottky contacts. This process enhances reliability, simplifies fabrication and maintains the high quality of the diode. We selected titanium (Ti) as the Schottky contact metal because of its high thermal stability and relative nonreactivity with GaAs [4]. The anode metallization also incorporates a platinum (Pt) diffusion barrier and a soft gold (Au) cap. To demonstrate this new fabrication process, a prototype diode with the same parameters as the UVa-6P4 [6], a very successful doubler to 200 GHz, is being fabricated. This prototype has  $C_{jo}$  of 20fF, anode diameter of 5 microns, and epitaxial doping and thickness of  $1 \times 10^{17} \text{cm}^{-3}$  and 0.4 microns, respectively. The GaAs substrate is doped as high as possible ( $\sim 5 \times 10^{18} \text{cm}^{-3}$ ) and is 100 microns thick.

## II. "TRADITIONAL" DIODE DESIGN AND FABRICATION

Our new fabrication process is a derivative of the traditional electroplated Pt/GaAs process which has produced successful diodes in our laboratory for over twenty years. A cross section of a whisker contacted diode is sketched in Fig. 1. The primary design parameters are the epitaxial layer doping density and thickness and the anode diameter. By varying these parameters the junction capacitance,  $C_{jo}$ , series resistance,  $R_s$ , and the breakdown voltage,  $V_{br}$ , can be controlled [5].

After the growth of the epitaxial layers, the GaAs wafer is diced into 0.2" x 0.2" process wafers. The surface of the wafer is thoroughly cleaned in ethanol, trichloroethane and methanol, followed by an oxygen plasma. About 500 nm of silicon dioxide ( $\text{SiO}_2$ ) is then deposited on the surface of the wafer by chemical vapor deposition.

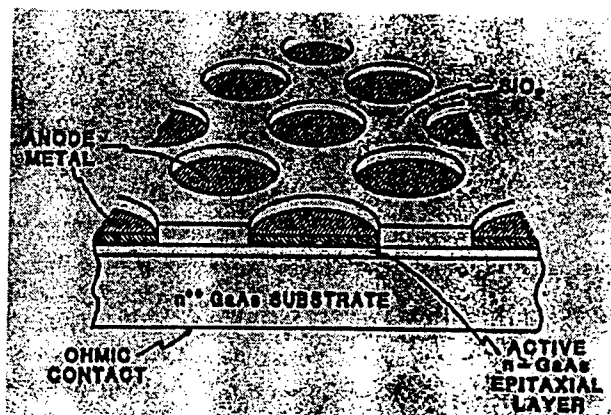


Fig. 1: A schematic view of the Schottky diode chip.

A positive photoresist (PR) is spun on the  $\text{SiO}_2$  and the anodes are defined in the resist by standard UV lithography. The wafer is then etched in a reactive ion etcher (RIE) to transfer the anode pattern into the  $\text{SiO}_2$ . About 50 nm of oxide is left in the bottom of the anode wells to protect the GaAs surface during subsequent processing steps. After PR removal, the wafer is lapped to about 100 microns and an ohmic contact is formed on the substrate using plated SnNi/Ni/Au (alloyed at 400C). The wafer is then diced into 10 mil x 10 mil chips and each chip is mounted onto a metal post for anode plating. The plating process involves carefully wet etching the protective  $\text{SiO}_2$  layer in BOE (buffered oxide etch) and electroplating platinum and gold onto the exposed GaAs surfaces. We have used this process for many years because it consistently yields the highest quality contact as determined by the diode ideality factor and reverse breakdown characteristics.

### III. THE NEW FABRICATION PROCESS

Traditional e-beam processes rely on lift-off to remove deposited metals from the areas between the anodes. However, the presence of PR during the deposition process creates the possibility of contaminating the Schottky interface. Our new process eliminates this problem through the use of a planarization technique to remove the unwanted metals [7].

The initial wafer preparation, cleaning, SiO<sub>2</sub> deposition, lithography, RIE and ohmic contact formation are the same as outlined in the above process. Prior to loading into the electron-beam evaporator, the protective SiO<sub>2</sub> layer is etched in BOE and the wafer is dipped in a solution of 1:25 NH<sub>4</sub>OH:DI in an attempt to remove any surface contamination. After attaining a vacuum of 10<sup>-7</sup> Torr, the Schottky contact (Ti:50 nm), diffusion barrier (Pt:30nm) and the soft top metal (Au:200nm) are evaporated over the entire wafer.

The wafer surface is then planarized with a layer of photoresist. This resist is then etched in an oxygen plasma to expose the "field" metallization between the anodes. The field metals are then removed with a combination of Argon sputter etching and wet chemical etching, thus isolating the anodes and exposing the underlying SiO<sub>2</sub>. Any remaining PR in the anodes is removed with oxygen plasma and acetone. The wafer is then diced into 10 mil x 10 mil chips and the fabrication process is complete.

### VI. SUMMARY

We have developed a new Ti/GaAs Schottky diode fabrication process which eliminates the possibility of photoresist contamination of the Schottky interface. The process is much simpler than electroplating and should yield more robust anodes without any loss of anode quality. Initial prototype devices have shown promising characteristics and we expect to have complete diode characteristics and initial accelerated life-test results for the conference.

### ACKNOWLEDGMENT

This research is supported by NSF grant # ECS-9412931.

### REFERENCES

- [1] R. Blundell and C.-Y. E. Tong, "Submillimeter receivers for radio astronomy", *Proc. IEEE* vol. 80, no. 11, p.1702-1720, Nov. 1992
- [2] H. Sharda, "High-temperature aging studies on Ru/n-GaAs Schottky contacts," *Semicond. Sci. Technol.*, vol. 11, p.221-225, 1996.
- [3] J. L. Bowers, Masters Thesis, University of Virginia, May 1993.
- [4] K. Prasad, L. Faraone, A. G. Nassibian, "Rapid thermal annealing of Ti Schottky contacts to n-GaAs," *J. Mat. Sci.: Materials in Electronics*, vol. 2 p.227-229, 1991.
- [5] T. W. Crowe, R. J. Matlack, R. M. Weikle, U. V. Bhaskar, "Terahertz GaAs devices and circuits for heterodyne receiver applications", *Int. J. High Sp. Elect. Sys.*, vol 6(1) pp125-161 1995.
- [6] T.W. Crowe, W.C.B. Peatman, R. Zimmermann and R. Zimmermann, "Consideration of velocity saturation in the design of GaAs varactor diodes," *IEEE Microwave and Guided Wave Letters*, Vol. 3, No. 6, pp. 161-163, June 1993.
- [7] W.L. Bishop, B.K. Sarpong, and T.W. Crowe, "An improved method for the formation of electrical contacts used in the manufacture of whisker-contacted Schottky diodes," UVA patent disclosure May 1997.

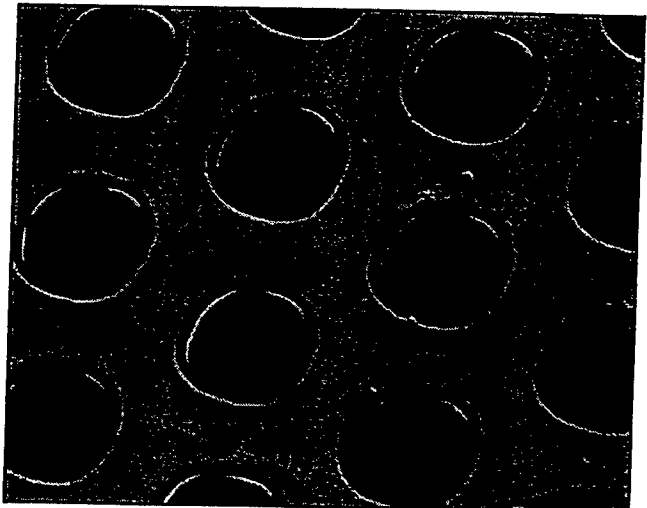


Fig. 2: A planarized wafer surface with PR remaining in anode well and the field metals exposed.

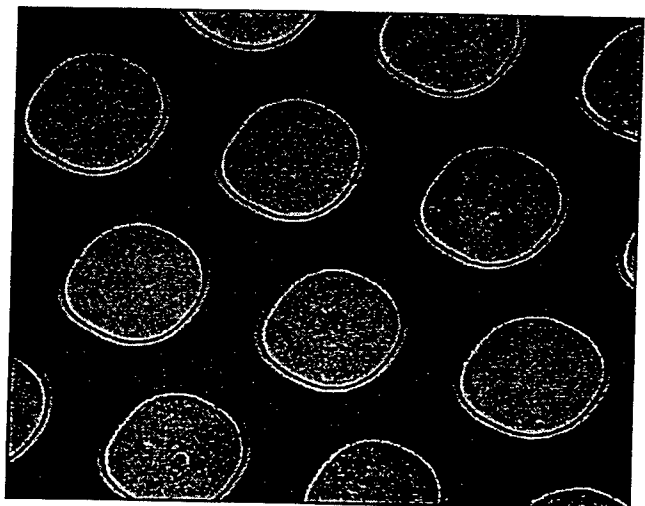


Fig.3: A completed Schottky diode chip.

# Generation of Submillimeter-Wave Pulses of Variable Duration Using Optically Excited Silicon Plates

Hiroaki Minamide<sup>†</sup>, Tatsuo Nozokido<sup>††</sup>, and Koji Mizuno<sup>†,††</sup>

<sup>†</sup>Research Institute of Electrical Communication, Tohoku University,  
2-1-1 Katahira, Aoba-Ku, Sendai 980-77, Japan

<sup>††</sup>Photodynamics Research Center, The Institute of Physical and Chemical Research(RIKEN)  
19-1399 Aza-Koeji, Naga-Machi, Aoba-Ku, Sendai 980, Japan

## Abstract

Submillimeter wave (SMMW) pulses of variable duration have been successfully generated using photo-excited intrinsic Si plates as SMMW switches. SMMW (214.6 $\mu$ m) pulses with durations ranging from 4ns to 20ns have been observed.

## Introduction

Generation of free carriers (electron-hole pairs) in semiconductors irradiated with short laser pulses leads to a rapid change in the complex refractive index of semiconductors, if the photon energy exceeds the band gap energy. By controlling the laser-produced free carrier density, reflection and transmission of electromagnetic waves in a wide spectral range from infrared to microwave, can be varied[1]. In the SMMW region, we have investigated a technique for a modulation using this effect[2]. In this paper, the generation of SMMW pulses of variable duration ranging from 4ns to 20ns using both a reflector and a shutter as switches[3], is presented.

## Experimental Set-Up

The experimental set-up is illustrated in Figure.1. The optically excited Si plates had a high DC resistivity of 15k $\Omega$ ·cm and a thickness of 800 $\mu$ m. The parallel surface of each Si plate acts as an etalon. The angle of incidence for the SMMW signal was set at about 45 degrees to achieve the maximum transmittance (98%). The 214.6 $\mu$ m radiation from a cw SMMW laser was directed onto a Si switch, SW<sub>1</sub>, which was excited (E<sub>1</sub>) by nanosecond pulses from a Q-switched Nd:YAG laser (Wavelength is 532nm:SHG). The pulses had a duration time of 7.5ns and a repetition rate of 10Hz. The SMMW radiation was reflected by dense free carriers generated in the switch, and directed onto another switch, SW<sub>2</sub>, which was excited (E<sub>2</sub>) by the same YAG laser after a variable delay time. SW<sub>2</sub> acted as a SMMW shutter and the delay time could be adjusted by changing the path difference between SW<sub>1</sub> and SW<sub>2</sub> from the YAG laser. The energy densities of the E1 and E2 pulses irradiated

onto Si plates were 2.93mJ/cm<sup>2</sup> and 1.61mJ/cm<sup>2</sup>, respectively. The resulting SMMW pulses were monitored by a Pt/GaAs Schottky barrier diode (SBD) detector[4]. The detection system consisted of a SBD, a bias tee, and an AC amplifier with a 3dB band width from 3Hz to 980MHz. The rapid response of this system was measured to be about 1ns by irradiating Si plate with a 300fs pulse of duration.

## Experimental Results

Figure.2 shows an oscilloscope trace demonstrating the switching action of a single element. The switching time was measured to be about 7ns. The reflectivity and the transmittance of the Si plates could be changed from a few % up to 96%, and from 98% down to less than 1% respectively[2]. The decrease in the reflectivity after photo-excitation is mainly caused by diffusion of excess carriers into the bulk semiconductor. Figure.3 shows the measured temporal evolution of SMMW pulses when the width of the transmission "window" of the switch is varied. The width of the transmission is deter-

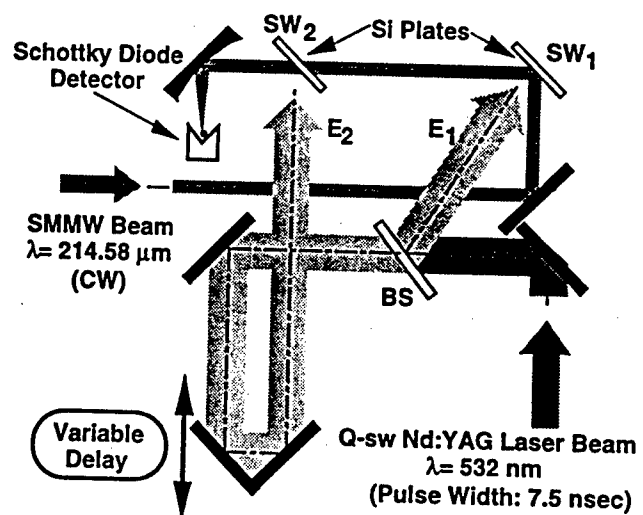


Fig.1 Optical arrangement for generating SMMW pulses of variable duration.

mined by the delay time at  $SW_2$  between the SMMW pulse reflected at  $SW_1$  and the delayed portion of the YAG beam,  $E_2$ . As the delay time is decreased, the duration time of the SMMW pulse becomes shorter. The shortest duration time was measured to be about 4ns. As the delay time is shorter than 10ns, the peak intensity of the SMMW pulses decreases, because it takes 10ns to switch. The peak intensity of the pulses is determined by the duration time of the pulses exciting the Si plates. Pulses with shorter duration time and higher peak intensity can be generated by using a picosecond or femtosecond optical laser.

Calculated temporal evolution of the SMMW pulses is shown in Figure.4. The method of calculation is outlined in.[5] The temporal and the spatial distributions of free carrier density in the Si plate are obtained by solving a one-dimensional carrier continuity equation which takes the free carrier generation, the recombination, and the diffusion processes in account. This yields the complex refractive index distribution by Drude's theory. The temporal change of the SMMW optical properties is then calculated by using the matrix formalism of the theory of stratified media.

By comparing measured and calculated results, the temporal behaviors are in fair qualitative agreement.

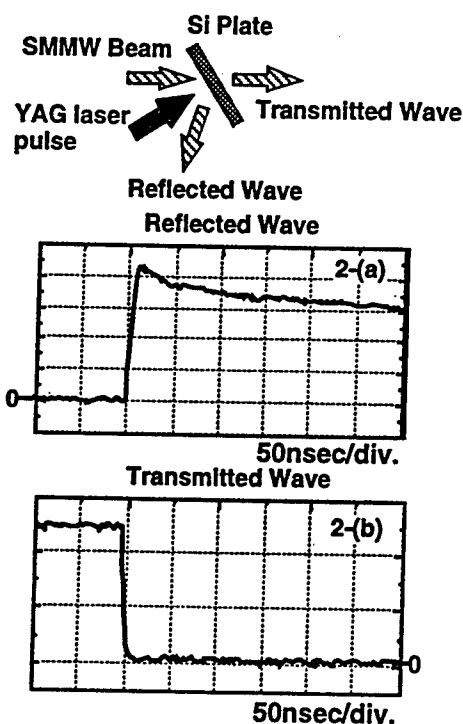


Fig.2 SMMW signals measured in reflection and transmission after 532nm excitation.

## Conclusion

SMMW (214.6 $\mu$ m) pulses of variable duration have been successfully generated using two Si plates irradiated with Q-switched Nd:YAG laser pulses. The shortest duration time obtained was 4ns. Measured and calculated temporal evolution of SMMW pulses were found to agree fairly well. Such pulses might have applications in time-resolved spectroscopy for the SMMW region.

## References

- [1] A. M. Johnson and D. H. Auston, *IEEE J. Quantum Electron.*, vol.11, pp.283-287,1975
- [2] T. Nozokido, H. Minamide, and K. Mizuno, *Technical Report of IEICE*, vol. 96, No.314, pp.9-16, 1996
- [3] S. A. Jamison and A. V. Nurmikko, *Appl. Phys. Lett.*, vol.33, pp.598-600, 1978
- [4] K. Mizuno, T. Suzuki, S. Ono, and K. Sagae, *Int. J. Infrared and Millimeter Waves*, vol.4, pp.321-325, 1983
- [5] T. Vogel, G. Dodel, E. Holzhauere, H. Salzmann, and A.Theurer, *Appl. Optics*, vol.31. No.3, pp.329-337, 1992

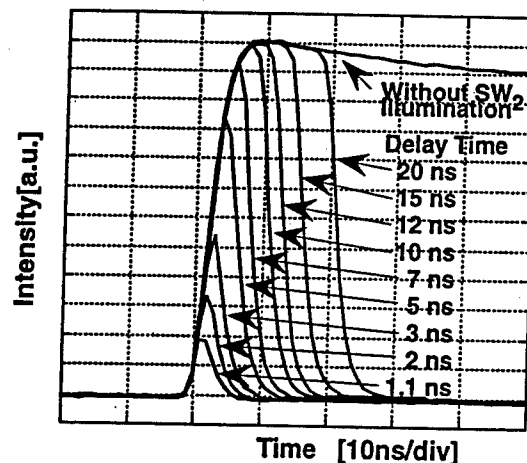


Fig.3 Measured temporal evolution of SMMW pulses when the width of transmission "window" is varied.

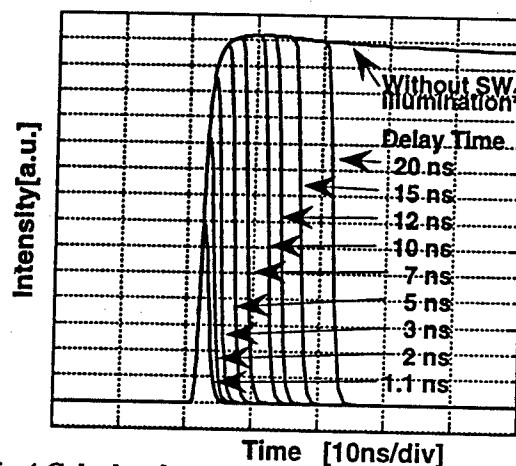


Fig.4 Calculated temporal evolution of SMMW pulses

## GaAs Schottky Diodes for THz Applications

P. Gleeson, P. Maaskant, J. Pike, W.M. Kelly, A. Simon<sup>#</sup>, C. I. Lin<sup>#</sup>, H. L. Hartnagel<sup>#</sup>

National Microelectronics Research Centre, UCC, Lee Maltings, Prospect Row, Cork, Ireland

<sup>#</sup>Institut für Hochfrequenztechnik, Merckstr. 25, 64283 Darmstadt, Germany

### Abstract

GaAs Schottky barrier diodes are used as multipliers and mixers in the THz frequency range. Whisker contacted devices with anode diameters below  $0.4\mu\text{m}$  have been fabricated for this region. In order to enhance the integration potential of these devices, some low capacitance ( $0.25\text{fF}$ ) cylindrical devices are also under development.

Up to about  $300\text{GHz}$ , the integration difficulties associated with whisker contacted devices has led to the development of the quasi vertical approach, which offers a route to competitive planar diodes[1].

### Whisker Diode Fabrication

A standard configuration ( $100\mu\text{m}$  cubic) chip featuring sub- $0.5\text{fF}$  capacitance has been fabricated using direct-write electron beam lithography to define sub  $0.4\mu\text{m}$  anodes[2].



Fig. 1: Micrograph showing sub  $0.5\text{fF}$  diodes

These diodes shown in fig.1, feature the following DC characteristics, and will be tested in a  $1000\text{GHz}$  corner cube system:

$C_{j0}$	$<0.5\text{fF}$
$\eta$	1.59
$R_s @ 1\text{mA}$	$16\ \Omega$
$\phi_B$	$0.6\text{V}$
$V_{bb} @ 10\mu\text{A}$	$-3.5\text{V}$

In addition, we have successfully defined a honeycomb array of  $220\text{nm}$  diameter anodes in oxide on top of  $30\mu\text{m}$  deep cylinders[3], as shown in fig.2. It is intended that these low capacitance diodes (expected to be around  $0.25\text{fF}$ ) will be tested in a  $1000\text{GHz}$  waveguide system.

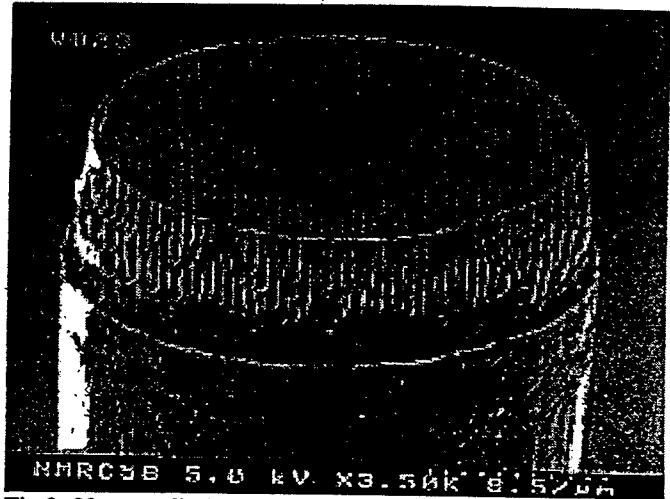


Fig.2:  $30\mu\text{m}$  cylinder featuring array of  $220\text{nm}$  anodes defined in oxide

### Planar Diode Design

The main idea of the quasi-vertical approach is to transfer the optimum geometry of the substrateless whiskered Schottky diode [4] to a planar device. Figure 3 shows the main features.

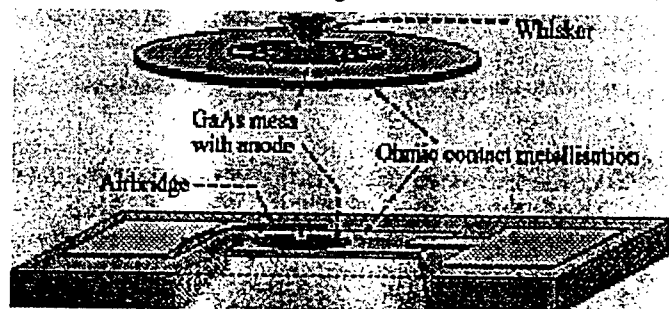


Fig. 3: Structure of the substrateless whiskered Schottky diode and quasi-vertical planar Schottky diode

The benefits [5] of the substrateless Schottky diodes are (a) minimum series resistance, (b) little affected by the skin effect and (c) excellent power handling capabilities. These benefits are mainly caused by a reduction of the GaAs dimensions. For example, the reduction in lateral dimensions (down to  $20 - 30\mu\text{m}$ ) reduces the series resistance caused by the skin effect. The thickness reduction ( $2 - 3\mu\text{m}$ ) reduces heating at high power levels, thus enhancing the power handling capacity. Also, the reduced dimensions minimise the substrate contribution to the series resistance. In the design of planar devices, reducing stray capacitances that limit the performance is important. There are two major sources of parasitic capacitance. The main contribution arises from the contact pads which typically cause a parasitic capacitance of  $10\text{fF}$  on GaAs substrates. In a properly designed integration, this

contribution vanishes. Therefore, the main contribution that has to be reduced is the parasitic capacitance of the airbridge. Using a finite-difference technique, we have investigated the influence of the airbridge parameters on the parasitic capacitance. The most effective reduction was achieved with a high airbridge (at least two microns higher than the diode mesa). Even with an airbridge width of 4 microns, the contributions do not exceed 2 fF.

### Fabrication Technology & Results

The main fabrication issues associated with the quasi vertical planar diode have now been overcome. These include the formation of small contacts from the backside of the wafer using a new two-stage spray etching technique (fig. 4). Furthermore, modification of the airbridge technology to fabricate the reduced dimensions shown in fig. 5, was also achieved.

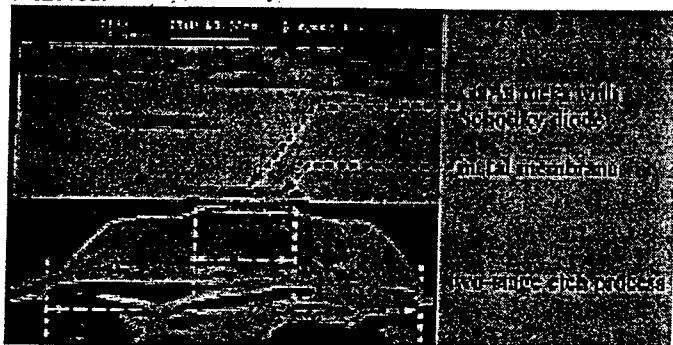


Fig. 4: Two-stage etching technique for contact structure

The characteristic parameters of different planar diodes are given in the table below. The results achieved with these diodes are not markedly different from those of the substrateless whisker diodes with the same diode parameters.

	DAP 0308	DAP 0312	DAP 0320	DAPV 3015	DAP 0715
$n_{epi} [cm^{-3}]$	$3 \cdot 10^{17}$	$3 \cdot 10^{17}$	$3 \cdot 10^{17}$	$8 \cdot 10^{16}$	$8 \cdot 10^{16}$
$d_{epi} [nm]$	70	100	100	560	560
$d_a [\mu m]$	0.8	1.2	2	6-7	2-2.5
$R_S [W]$	15-20	9.2	5	10	20
$C_{jo} [fF]$	1.1	2.2	5.8	30	5-7
$h$	1.13	1.1	1.08	1.03	1.03
$V_{br} [V]$	5-5.8	5-5.8	4.9-5.1	15	15
$f_c [THz]$	9	7.9	5.5	-	-
$C_{min}/C_{jo}$	-	-	-	3	3

The parasitic capacitance of single devices is 9-10 fF (this value has been subtracted from  $C_{jo}$  and  $C_{min}$  to make a reasonable comparison with whiskered diodes possible). The

parasitic capacitance is mainly due to the contribution of the contact pads ( $>8fF$ ).

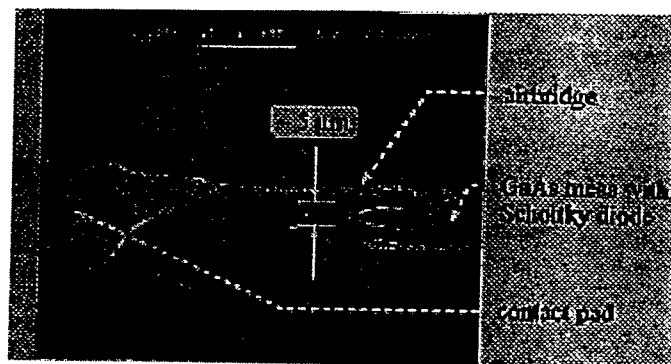


Fig. 5: SEM-picture of quasi vertical diode

### Conclusion

The fabrication process for producing sub 0.5fF capacitance devices has been demonstrated, and a batch of 30  $\mu m$  cylindrical devices featuring  $\sim 0.25$  fF capacitance is near completion. These devices are geared towards operation in the THz range in both open structure and waveguide systems. In addition, the technology for quasi-vertical planar Schottky diodes has been established. Several improvements in the technology have made planar quasi-vertical mixer diodes available with anode diameters of 0.8  $\mu m$ -2  $\mu m$ , and varactor diodes with a very high breakdown voltage and an excellent capacitance modulation ratio.

### Acknowledgments

The authors would like to express their acknowledgements to Dr. H. Grothe and Dr J. Freyer, both from the Technical University of Munich, Germany, for supplying the high-quality epitaxial material for the planar diodes. The support of the European Space Agency through the "Schottky Diode Technology Development for Submillimetre Heterodyne Receivers" project is acknowledged.

### References

- [1] A. Simon, A. Grüb, V. Krozer, K. Beilenhoff, H.L. Hartnagel 1993, Planar THz Schottky Diode Based on a Quasi-Vertical Diode Structure, 4<sup>th</sup> Int. Symp. on Space Terahertz Technology, pp 392-403.
- [2] P. Gleeson, J. Pike, P. Maaskant, W.M. Kelly, 1996, THz Schottky Diodes at the NMRC, 21<sup>st</sup> Int. Conf. on Infrared and Millimeter Waves, Berlin
- [3] W.M. Kelly, S. Mackenzie, P. Maaskant 1994, Novel Chip Geometries For THz Schottky Diodes, 5<sup>th</sup> Int. Symp. on Space Terahertz Technology, pp.404-408
- [4] A. Simon, A. Grüb, M. Rodriguez-Girones, H.L. Hartnagel 1995, A Novel Micron-Thick Whisker Contacted Schottky Diode Chip, 6<sup>th</sup> Int. Symp. on Space Terahertz Technology, pp 5-12.
- [5] C. I. Lin, A. Simon, M. Rodriguez-Girones, H.L. Hartnagel, P. Zimmermann, R. Zimmermann 1997, Substrateless Schottky Diodes for THz Applications, 8<sup>th</sup> Int.

## Millimeter Wave Evanescent Mode Gunn Oscillator in Suspended Stripline Configuration

A.K. Poddar, S.K. Koul, and B. Bhat

Centre for Applied Research in Electronics  
Indian Institute of Technology, New Delhi 110 016

### Abstract

A new millimeter wave Gunn diode oscillator employing a combination of suspended stripline and evanescent mode resonator is developed. With a 35 GHz diode rated at 100 mW, stable power output of more than 75 mW is achieved over a tuning range of about 3.5 GHz. The oscillator is simple in fabrication, cost effective and is amenable for integration with other planar circuits.

### Introduction

Millimeter wave oscillators in MIC form offer advantages in terms of small size and ease of integration with other planar circuits. Since an oscillator forms an essential part of a millimeter wave receiver front end, its development leading to simplicity of fabrication and lower circuit losses while retaining the advantages of MIC fabrication is of considerable importance.

Most millimeter-wave Gunn diode oscillators reported in MIC form employ microstrip medium with varactor tuning [1,2]. For applications not requiring electronic tuning, microstrip oscillator employing evanescent mode resonator offers an attractive cost-effective solution [3]. In the circuit reported [3], the Gunn diode is mounted inside a section of evanescent mode waveguide and the output is taken through a microstrip coupled to the evanescent mode guide. It is well known that in the millimeter wave band, the microstrip tends to be excessively lossy. A low loss planar transmission line which overcomes this problem is the suspended stripline. In the present paper, the low loss feature of the suspended stripline and the inductive property of the evanescent mode guide are utilized to realize a simple, Ka-band oscillator, with broadband performance.

### Oscillator Configuration

As illustrated in Figure 1, the oscillator employs a suspended stripline terminated in an evanescent mode waveguide section.

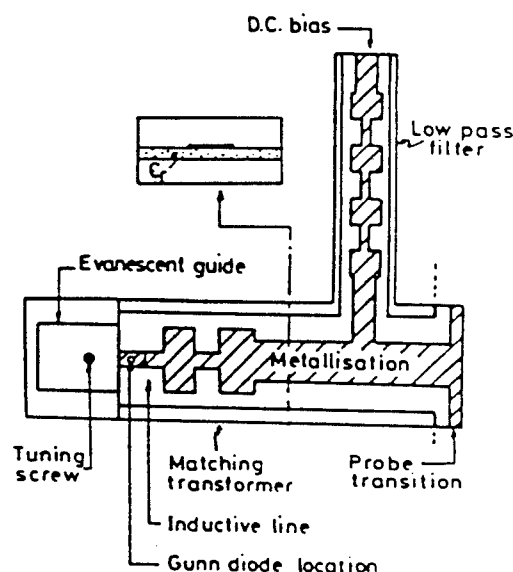


Fig.1 Layout of evanescent mode Gunn diode oscillator in suspended stripline.

The evanescent mode guide is formed by simply extending the suspended stripline channel (without the substrate) with reduced dimensions. The Gunn diode is shunt mounted at the end of the suspended stripline. A dielectric screw is inserted from the opposite side of the substrate so that the diode makes firm contact with the strip conductor. Unlike in [3] where biasing the diode requires bonding a wire to the anode, in this configuration DC bias is easily provided through a low pass filter printed as part of the suspended stripline circuit. The evanescent guide section located immediately next to the diode presents an inductive load to the Gunn diode. Additional tuning screw is provided in the vicinity of the diode to facilitate tuning. The output can be taken either through a K-type coaxial connector connected to the suspended stripline or through a Ka-band rectangular waveguide via a suspended stripline probe transition. The latter arrangement is shown in Figure 1.



## Equivalent Circuit and Design

Figure 2 shows the equivalent circuit of the oscillator.

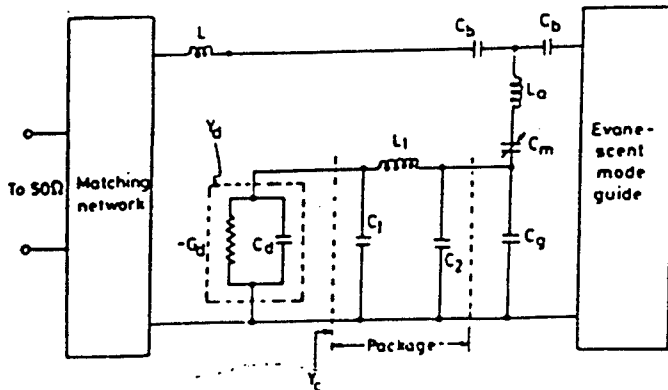


Fig. 2 Equivalent circuit of oscillator

The circuit elements  $L_1$ ,  $C_1$  and  $C_2$  constitute a  $\pi$ - equivalent circuit for the encapsulation of the diode. The diode is supported in the channel by means of a brass-metallic post. This post is represented by a T-network composed of a capacitance  $C_s$  in series and a shunt reactance consisting of the series combination of an inductance  $L_s$  and a capacitance  $C_s$ .  $L$  is due to an inductive line printed as part of the matching network. The capacitance due to the tuning screw is represented as  $C_m$ . The capacitive reactance due to  $C_s$  accounts for the phase variation of the field across the post in the direction of propagation, due to its finite diameter.

The oscillator is designed at 35 GHz by considering the following main aspects: (i) accurate modelling of the resonant region taking into account the equivalent circuit of the Gunn diode, admittance due to the mount and the load presented by the evanescent mode waveguide, (ii) computation of the overall impedance of the above network and establishing resonance condition, (iii) arrangement for dc biasing the diode through a low pass filter and bias-suppressor and (iv) transition from suspended stripline to Ka-band output waveguide.

The device admittance  $Y_d$  is a strong function of the frequency and DC bias current and a weak function of the RF current and temperature. The circuit admittance  $Y_c$  is a function of only the frequency. The criteria for circuit-controlled steady-state oscillation are given by,  $\text{Im}(Y_d + Y_c) = 0$  and  $|\text{Re}(Y_d)| \geq |\text{Re}(Y_c)|$ , where  $Y_c = G_c + jB_c$ , is the load admittance transferred to the diode plane.

## Experimental Results

The oscillator as configured in Figure 1 is fabricated using a MDT diode (MG 1018-16) rated at 100 mW. The output is

taken from a Ka-band waveguide via a suspended stripline probe transition. Figure 3 shows a graph of the measured output power versus the bias voltage. The oscillator offers more than 75 mW of power output at 20°C. With a variable short provided at one end of the output Ka-band waveguide the oscillator could be tuned over a frequency range of about 3.5 GHz around 35 GHz. For oscillator requiring coaxial output, this tuning is provided by the tuning screw in the evanescent guide.

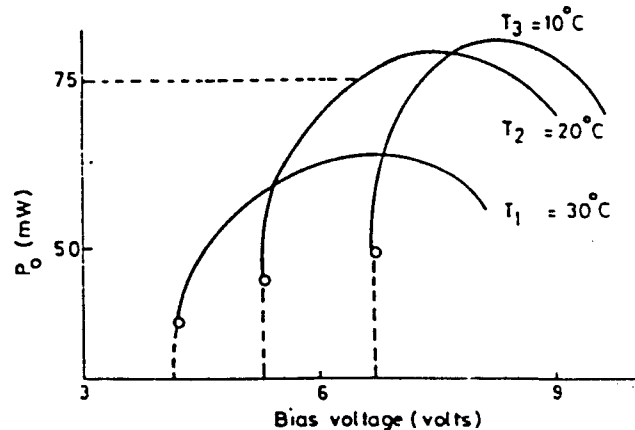


Fig.3 Oscillator power output as a function of bias voltage

## Conclusion

A new configuration of a suspended stripline Ka-band Gunn oscillator employing evanescent guide section as part of the resonant circuit is reported. The oscillator permits easy tunability over a bandwidth of about 3.5 GHz, in addition to offering advantages in terms of ease of biasing, small circuit losses and ease of integration with other planar components.

## Acknowledgement

The authors thank Lt. K. G. Ramkumar for the initial experimentation on the oscillator circuit and to the Directorate of Training and Sponsored Research, DRDO, for funding the project activity.

## References

1. R. Tahim, G.M. Hayashibara and K. Chang, High performance millimeter-wave suspended stripline varactor-tuned Gunn VCO, *Electronics Lett.*, Vol.22, No.20, pp.1057-1059, Sept. 1986
2. D. Rubin, Varactor-tuned millimeter wave MIC oscillator, *IEEE Trans. Microwave Theory and Tech.*, Vol. MTT-24, pp. 866-867, Nov. 1976.
3. S. Bharj, MM-Wave evanescent mode oscillator, *Microwave Journal*, Vol.28, pp. 313-317, May 1985.

# INFRARED MEGAGAUSS-SPECTROSCOPY: A CHALLENGE IN SOLID STATE PHYSICS

by

Nik Puhlmann,

O. Portugall, M. Barczewski, I. Stolpe, H.-U. Müller, and M. von Ortenberg

Humboldt-University Berlin, Institute of Physics (MGT)  
Invalidenstrasse 110, D-10115 Berlin, Germany

## Abstract

*The paper presents the megagauss generator installed recently at the Humboldt-High-Magnetic-Field-Center in Berlin and its application to solid state physics. For the first time magnetic fields above 200 T are routinely available for reproducible series of infrared transmission experiments employing CO<sub>2</sub>-laser radiation. New experimental results on several semiconductors prove impressively the efficiency of our experimental setup for infrared megagauss-magneto-spectroscopy.*

## Introduction

The combination of high magnetic fields as a tuning parameter and monochromatic infrared radiation as a fixed energy probe has established as one of the most powerful tools in solid state research. Especially in semiconductor physics extremely high magnetic fields are well appreciated, because new interesting phenomena are expected due to the strong quantizing effects on spin systems and orbital motion of quasi free as well as bound carriers. The magnetic field provides not only the tuning of electronic energy levels, but defines also via the magnetic length  $\ell = \sqrt{\hbar / eB}$  a probe for the investigation of spatial variation of any potential. For megagauss fields, i.e.  $B \geq 100$  T, the magnetic length gets smaller than 2.5 nm, so that magnetic fields exceeding this limit are most suitable for probing the potential variation of nanostructured materials. The recent progress in pulsed high magnetic field technology, giving access to higher and higher fields, opens various new possibilities in infrared and submillimeter spectroscopy.

## Semidestructive Generation of Megagauss Fields

The generation of stationary magnetic fields by the use of resistive or superconducting coils is nowadays limited to the order of 30 T by Joule heating and the critical field strength, respectively. Recently 36.5 T have been achieved using a hybrid magnet [1]. Higher fields are routinely available by use of nondestructive pulsed magnets, generating peak fields

around 70 T [2]. For megagauss fields in reasonably sized laboratory magnets the Lorentz force exceeds the limit given by the mechanical strength of all materials known nowadays, resulting in inevitable coil destruction. This calls for extreme experimental techniques. The highest fields generated for experimental application by electromagnetic or explosive driven flux compression are of the order 600 to 800 T [3].

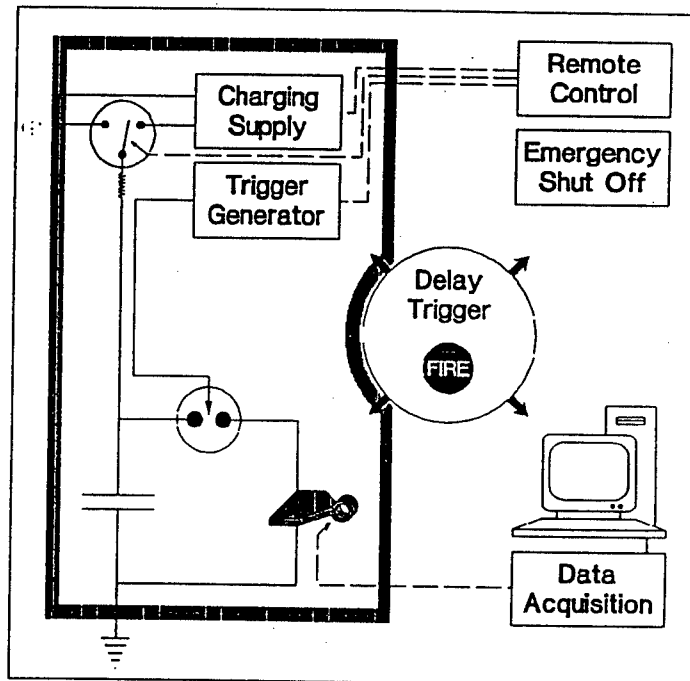


Figure 1: Schematic view of the megagauss generator. The shaded frame indicates the Faraday cage.

Somewhat smaller fields can be achieved by a discharge of a fast capacitor bank into a small single turn coil [4],[5],[6]. Despite the violent explosion of the coil, the sample space remains unharmed, since the Lorentz force causes a motion of the coil fragments away from the field center. This enables the experimentalist to perform reproducible series of investigations without sample destruction, in contrast to the flux compression technique.

Megagauss techniques are so far as well sophisticated as expensive and are therefore available in a few specialized laboratories in the world only [7]. To overcome this

shortcoming we have designed and built a megagauss generator which produces fields above 200 T within a pulse length of  $5\mu\text{s}$  in a single turn coil with a useful volume of about  $1\text{ cm}^3$  [6]. Higher fields up to 300 T are achievable by reducing the coil diameter. However, the tremendous shock wave resulting in a trial of strength of all parts of the experimental environment, is not the only difficulty of a single turn coil experiment. The conditions of very tiny space for the experimental set-up, short time duration and the presence of a strong electromagnetic pulse during the field generation require sophisticated experimental techniques. Figure 1 shows a schematic view of the generator. The facility features a new 60 kV 225 kJ capacitor bank design with low-inductance strip-line connections and a vertical arrangement of the coil. For reasons of safety and noise reduction a Faraday cage in conjunction with optical links is used for consequent galvanic separation of the field generator and both, recording and control equipment, respectively. All units are synchronized by the delay trigger unit. For spectroscopic applications the  $5\mu\text{s}$  pulses are adequately resolved by 10 bit, 1 GSa/s data recording systems [8].

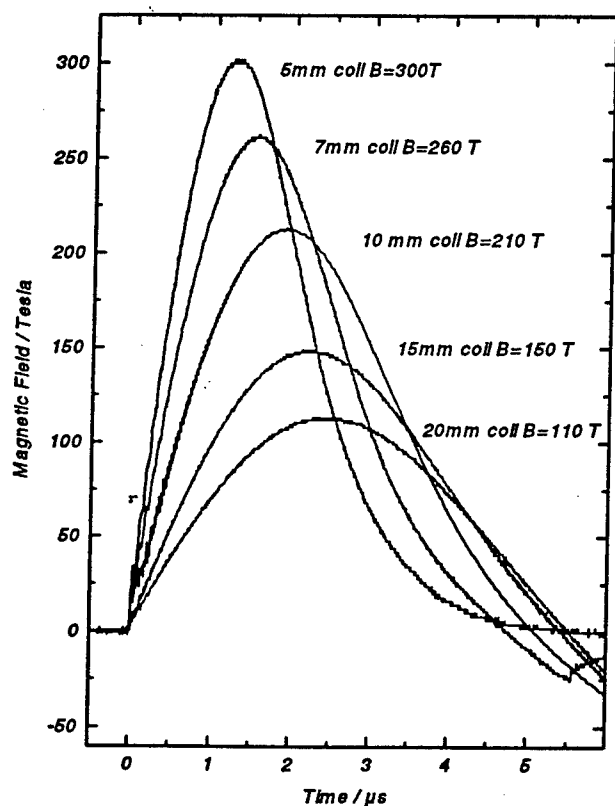


Figure 2: Magnetic Field pulses for 55kV (150 kJ) capacitor discharges into single turn coils with different inner diameters

Figure 2 shows the time dependence of the magnetic field generated by capacitor discharge into coils with inner diameters ranging from 5 to 20 mm at a reduced energy of 150 kJ. For field measurements by use of calibrated pick up coils under the extreme conditions of the high voltage area an

integrated system was designed which combines the functions of RC-integration, attenuation, digitizing, intermediate storage, and electro-optical conversion in a single, well shielded box. The precision of the field data was proved to be better than 2% by Faraday rotation experiments.

The peak field of 210 Tesla obtained in a  $10\times 10\times 3\text{ mm}$  coil (inner diameter  $\times$  axial width  $\times$  conductor thickness) is of particular interest. For this coil size helium flow cryostats can be used for sample cooling [9]. For room temperature investigations, where the requirements concerning the useful experimental volume are less restrictive, smaller coils can be used, thus extending the available field range to 300 T.

### Cyclotron Resonance

Cyclotron resonance (CR) is one of the most powerful and well established tools in solid state physics. CR in megagauss fields in particular offers a couple of interesting possibilities as for example the investigation of the energy band structure

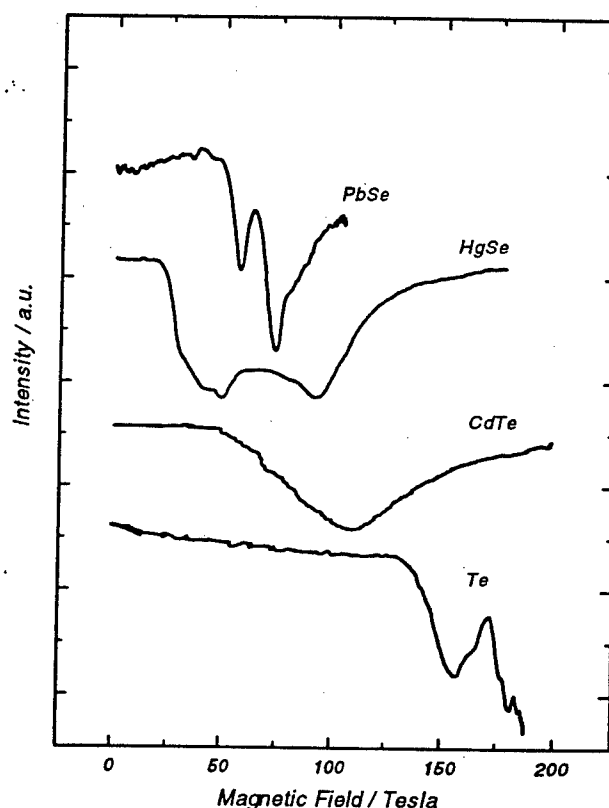


Figure 3: Infrared Transmission vs magnetic Field for PbSe, HgSe, CdTe and Te.

of charge carriers far away from the band extrema. Moreover, the necessary condition for the observation of cyclotron resonance  $\omega_c \tau \gg 1$ , where  $\omega_c$  is the cyclotron frequency and  $\tau$  the mean collision time, is more easily to fulfill at higher fields even for samples with low carrier mobility.

N-type PbSe, epitaxially grown on a BaF<sub>2</sub> substrate is used to check the suitability of our megagauss equipment for magneto-optical investigations. The experiment is performed in Faraday geometry with the magnetic field oriented along the (111)-direction perpendicular to the epitaxial layer. The 10.8  $\mu\text{m}$  line of a CO<sub>2</sub>-laser is used as radiation source. The radiation is focused on the sample by means of mirror optics. A fast HgCdTe detector located in an additionally shielded box outside the Faraday cage is used for the detection of the transmitted radiation intensity. From the receiver module the data are transferred to a 10 bit, 500 MSA/s transient recorder, by the use of a 100 MHz analogue optical system. The temperature of the sample is lowered to T=60 K by a special liquid helium flow cryostat, similar to that, described in [9].

Like all IV-VI semiconductors PbSe features a direct energy gap at the L-point of the Brillouin zone. This results in a nearly elliptical Fermi surface oriented along the (111)-direction. Therefore one can expect contributions due to two different cyclotron orbits if the magnetic field is oriented parallel to the (111)-direction. The upper curve in figure 3 shows two pronounced resonances at magnetic field strengths of B=57 T and B=73.5 T, corresponding to effective cyclotron masses of  $m^*=0.059m_e$  and  $m^*=0.075m_e$ , respectively. The excellent agreement of these values with previous experimental results [10] prove impressively the efficiency of our experimental setup for infrared megagauss-magnetspectroscopy.

A fan of materials has been investigated in the same way as explained above, using different CO<sub>2</sub>-laser lines. The second curve from the top in figure 3 shows the field dependence of the transmission of 10.6  $\mu\text{m}$  radiation through an epitaxially grown HgSe-layer at T=90 K. The resonances at B=49 T and B=92 T correspond to effective masses of  $m^*=0.048m_e$  and  $m^*=0.091m_e$ . The low field resonance is evidently due to ordinary bulk states in HgSe, whereas the origin of the second resonance peak is not completely understood. We attribute this high field resonance to energy states of an additional two-dimensional electron gas caused by the strong lattice mismatch between epitaxial layer and substrate. The shoulder in the low field region of the first resonance peak may be due to the spin splitting of the cyclotron resonance of quasi free conduction band electrons.

The cyclotron resonance of conduction band electrons in a epitaxially grown J-doped CdTe layer is shown in the third curve of figure 3. The experiment was performed at T=65 K using a wavelength of 10.22  $\mu\text{m}$ . The relatively broad resonance peak at B=110 T corresponds to an effective electron mass of  $m^*=0.105m_e$  in good agreement to low field results.

The lower curve in figure 3 shows the transmission of CO<sub>2</sub>-laser radiation ( $\lambda=10.6 \mu\text{m}$ ) through an unintentionally doped Bridgman grown Te- sample with a thickness of 0.5mm at room temperature. The magnetic field was oriented perpendicularly to the c-axis of the crystal. A distinct resonance line is observed at a magnetic field of B=156 T, which can be attributed to electron cyclotron resonance. The

effective mass deduced from the resonance position amounts to  $m^*=0.15m_e$ , in good agreement with former results [11]. The transmission curve suggests, that additional resonance peaks will occur at higher fields.

#### Acknowledgement

The authors are grateful to F. Herlach and N. Miura for many valuable advices concerning the single turn coil technique. Special thanks to H. Scholz and the Humboldt machine shop staff for the realisation of the machinery. One of the authors (N.P.) is obliged to the Deutsche Forschungsgemeinschaft for sponsoring the trip to Wintergreen.

#### References

- [1] G. Kido et al, Proc. 12th Intern. Conf. on the Appl. of High Magnetic Fields, Würzburg (1996)
- [2] G.S. Boebinger et al, Physica B 201, 560 (1994)  
T. Asano et al, IEEE Trans. on Magn. 30, 2106 (1994)  
L. Li, F. Herlach, Meas. Sci. Technol. 6, 1035 (1995)
- [3] N. Miura, H. Nojiri, Y. Imanaka: Proc. 22th Intl. Conf. on the Physics of Semiconductors, Vol.2, p. 1111, ed. D.J. Lockwood, World Scientific, Singapore (1995)  
A.I. Pavlovskii, in: Proc. 5th Int. Conf. on Megagauss Magnetic Field Generation and Related Topics (Novosibirsk, July 1989), p.1(Nova Science, New York, 1994)  
G.A. Shvetsov, Physica B 155, 33 (1989)
- [4] F. Herlach, R. McBroom, T. Erber, IEEE NS-18, 809 (1971)
- [5] K. Nakao, F. Herlach, T. Goto, S. Takeyama, T. Sakakibara, N. Miura, J.Phys E: Sci. Instr., 18, 1018 (1985)  
J.S. Brooks et al., Proc. 12th Int. Conf. on the Appl. of High Magnetic Fields (Würzburg, July 1996)
- [6] N. Puhlmann, I. Stolpe, M. von Ortenberg,  
O. Portugall, M. Barczewski, H.-U. Müller in: European Workshop: "Construction of a 100 Tesla Prototype Magnet", Toulouse (1996)  
M. von Ortenberg, Proc. 12th Intern. Conf. on the Appl. of High Magnetic Fields, Würzburg (1996)
- [7] F. Herlach, J.A.A.J. Perenboom, Physica B 211, 1 (1995)
- [8] N. Puhlmann, O. Portugall, H.-U. Müller,  
M. Barczewski, I. Stolpe, M. von Ortenberg,  
J.Phys.D: Appl.Phys in press
- [9] S. Takeyama, M. Kobayashi, A. Matsui, K. Mizuno, N. Miura, in: „High Magnetic Fields in Semiconductor Physics“ Vol. 71 (Berlin: Springer, ed. G. Landwehr 1987)
- [10] O. Portugall, N. Miura, G. Bauer, R. Schönfeld, M. von Ortenberg, Physica B 201, 280 (1994)
- [11] N. Miura, G. Kido, S. Chikazumi: Springer Series in Solid State Sciences 13, 110 (1980)

# Determination of the anisotropy of the effective masses of electrons and holes in doped GaN epilayers by far infrared spectroscopy

G Mirjalili<sup>1,3</sup>, R A Levett<sup>1</sup>, T J Parker<sup>1</sup>, T S Cheng<sup>2</sup> and C T Foxon<sup>2</sup>

<sup>1</sup>Department of Physics, University of Essex, Wivenhoe Park, Colchester CO4 3SQ, UK

<sup>2</sup>Department of Physics, University of Nottingham, University Park, Nottingham NG7 2RD, UK

<sup>3</sup>Present address: Department of Physics, University of Yazd, P.O. Box 891195-714, Iran

## Abstract

We have used far infrared spectroscopy to obtain measurements of the effective masses,  $m_e$ , of electrons and  $m_h$ , of holes in GaN epilayers with the cubic and wurtzite structure. In cubic structure epilayers we find that the effective masses are isotropic as expected, with  $m_e = 0.2 m_0$ , and  $m_h = 0.8 m_0$ , where  $m_0$  is the mass of the free electron. In wurtzite structure epilayers we find that the effective masses normal,  $\perp$ , and parallel,  $\parallel$ , to the crystallographic c-axis are unequal, with  $m_{\perp} < m_{\parallel}$  for both electrons and holes.

## A. Introduction

GaN has attracted much interest as a promising material for optical devices in the blue and ultraviolet (UV) regions of the spectrum [1-3], but control of the electronic properties continues to be a major challenge to crystal growers. Unintentionally doped GaN has in all cases been observed to be n-type [4], and undoped GaN films grown with GaN buffer layers still have carrier concentrations of about  $10^{16} \text{ cm}^{-3}$  [5,6].

Because of the large background electron concentration, high quality GaN, including p-type material, has been difficult to grow, but there has been much effort aimed at doping GaN p-type by introducing group II and group IV elements [4]. Nakamura et al [6,7] grew high quality p-type Mg-doped GaN films on GaN buffer layers with hole concentrations of about  $3 \times 10^{18} \text{ cm}^{-3}$  by metalorganic chemical vapour deposition (MOCVD). Wang et al [8] and Kim et al [9] have grown Mg-doped p-type GaN films by molecular beam epitaxy (MBE) with carrier concentrations of up to  $10^{18} \text{ cm}^{-3}$ , and  $4.5 \times 10^{17} \text{ cm}^{-3}$ , respectively. Even so, the experimental data on many fundamental properties of GaN are still incomplete, including information on the anisotropy of the effective masses of the free carriers in doped  $\alpha$ -GaN (wurtzite structure) material. Barker and Ilegems used polarised oblique incidence far infrared spectroscopy to investigate plasmon-phonon coupling in highly conducting n-type single crystals of GaN many years ago [10], and reported that the plasma frequency was isotropic within experimental precision, but

investigation of the plasmon properties of high quality doped  $\alpha$ - and  $\beta$ -GaN epilayers has received little attention in the literature so far.

In this paper we describe measurements by polarised far infrared oblique incidence reflection spectroscopy on a selection of doped and undoped GaN samples on GaAs and GaP substrates. The technique enables us to investigate the vibrational (phonon) and collective free carrier (plasmon) modes and their coupling in these systems. Measurements in s-polarisation probe the component of the dielectric response parallel to the plane of the epilayer; measurements in p-polarisation probe both the component parallel and the component normal to the plane of the epilayer, the relative proportions being determined by the angle of incidence.

We observe so-called Brewster and Berreman interface modes [11,12] in these structures and show how they can be used as probes of the structure and electronic properties of the epilayers. Dips in the p-polarisation reflectivity, described as Brewster modes [11], are observed when the numerator of the Fresnel reflection coefficient passes through zero due to impedance matching in the two media; a Berreman interface mode [11,12] occurs in the vicinity of an LO phonon mode if there is a zero-crossing of the real part,  $\epsilon$ , of the dielectric function in one of the media in a frequency range in which  $\epsilon < 0$  in the second medium. We show how assignments of these modes can be made by calculating dispersion curves and profiles of the electromagnetic field intensities throughout the structure.

A Brewster-type mode [11] is observed in the p-polarisation spectra of all samples at a frequency close to the GaN LO phonon frequency; this mode couples strongly to plasmons propagating in the growth direction, so it can be used to determine the plasmon response parallel to the c-axis in  $\alpha$ -GaN. We have previously reported [13] that p-polarisation spectra obtained from epilayers with cubic structure also contain a Berreman-type interface mode which implies the existence of a highly disordered GaN boundary layer with a much reduced LO phonon frequency. The temperature dependence of this mode has been explained in terms of a shallow donor level probably corresponding to nitrogen vacancies [14,15].

Wurtzite structure epilayers are deposited with the crystallographic c-axis along the growth direction, so

careful analysis of both s- and p-polarisation spectra enables the components of the dielectric tensor of  $\alpha$ -GaN for both phonons and plasmons normal and parallel to the crystallographic c-axis to be determined. We also show that in the case of doped wurtzite structure epilayers the spectroscopic results, taken in conjunction with Hall effect measurements of the carrier concentration, can be used to obtain estimates of the effective masses of the free carriers for propagation in the directions normal and parallel to the crystallographic c-axis.

### B. Experimental method

The samples were grown by molecular beam epitaxy (MBE) on GaAs or GaP substrates. The epilayers were grown in the wurtzite ( $\alpha$ -GaN) and cubic ( $\beta$ -GaN) structure with thicknesses in the range of 0.4 to 2.0  $\mu\text{m}$ . The n-doped epilayers were doped with Si and the p-doped epilayers were doped with Be or Mg. Details of the growth procedures are given elsewhere [16]. Far infrared measurements were made at oblique incidence at an angle of  $45^\circ$  at 300 and near 77 K using a modified NPL cube interferometer as described in detail elsewhere [17].

### C. Theoretical analysis

Calculated spectra were obtained by standard multilayer computational techniques [17], the "layers" being vacuum for the medium of incidence, the GaN epilayer, and the substrate; in cubic samples it is also necessary to include in the model an additional thin ( $\sim 15$  nm) highly disordered layer at the base of the epilayer to account for the presence of an unexpected Berreman-type interface mode in the measured spectra [13]. The dielectric function for the substrate (GaAs or GaP) must take account of the fundamental lattice response, and for the epilayer it must include both the free carrier response and the GaN phonons, in the case of wurtzite epilayers including the effects of anisotropy.

### D. Results and discussion

Lack of space prohibits the presentation of detailed results here, so we shall show the measured p-polarisation spectra for three  $\alpha$ -GaN epilayer structures together with their associated calculated dispersion curves and summarise the most important results. Full details will be published elsewhere [18].

In the case of cubic epilayers, the conventional plasma response is observed in the s-polarisation spectrum and it can be analysed to determine the plasma frequency for propagation in the plane of the epilayers. Free carrier propagation in the growth direction produces a plasma response which couples strongly to the Brewster and Berreman modes mentioned above, shifting their frequencies. Analysis of the Brewster mode reveals that there is no observable anisotropy in the effective mass of  $\beta$ -GaN (cubic), as expected. Analysis of plasmon-phonon coupling in the Berreman mode gives information on the free carrier concentration in the GaN boundary layer. The temperature dependence of the mode is explained by a shallow donor level about 30 meV below the conduction

band; similar behaviour is not observed in the temperature dependence of the Brewster mode, so it is concluded that the shallow donor level is associated with the high concentration of defects in the boundary layer, and it probably corresponds to nitrogen vacancies [15] as already mentioned.

It proved impossible to make Hall effect measurements on a Be-doped p-type cubic GaN sample, and this was attributed to loss of electrical continuity across the surface

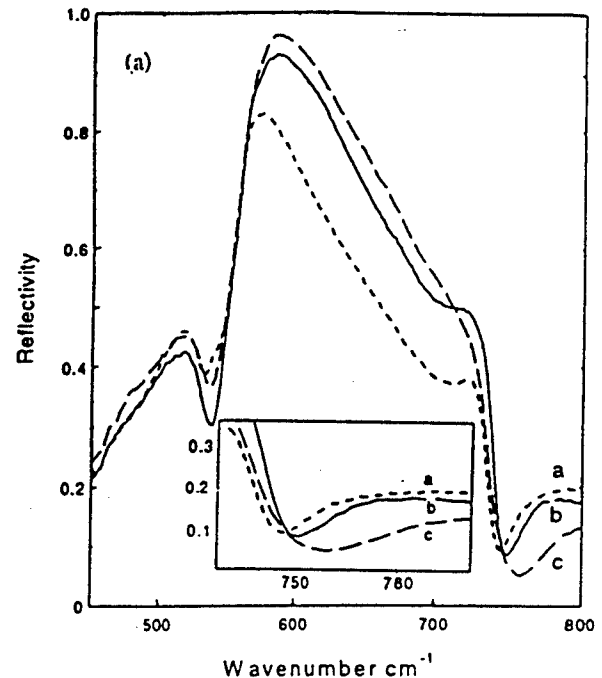


Figure 1. Measured p-polarisation reflection spectra of three  $\alpha$ -GaN (wurtzite) epilayers on GaAs substrates in the GaN reststrahl region. Curve a corresponds to an undoped epilayer. Curves b and c correspond to Si-doped n-type epilayers with carrier concentrations of  $8.7 \times 10^{16}$  and  $5.3 \times 10^{17} \text{ cm}^{-3}$ , respectively. Inset: enlargement of the dip due to the Brewster mode near  $750 \text{ cm}^{-1}$ .

due to the columnar structure of the epilayer. However, far infrared measurements on this sample revealed the plasma response in the usual way, demonstrating that far infrared spectroscopy can be a useful non-contact method for investigating free carrier properties when more conventional methods fail. The most likely explanation is that the amplitude of the oscillations of the free carriers due to the far infrared beam at frequencies in the range of the plasmon frequency is too small to be impeded by any discontinuities due to the columnar structure.

In  $\alpha$ -GaN (wurtzite) epilayers, the s- and p-polarisation reflection spectra probe the two orthogonal components of the plasma response in a similar way. The results reveal anisotropy of the plasma frequency, and hence of the electron and hole effective masses. However, no Berreman mode is observed, mainly due to the phonon damping

parameter being significantly larger in  $\alpha$ -GaN epilayers than in  $\beta$ -GaN, so that in this case attenuation of the far infrared beam in the GaN epilayer prevents coupling to the Berreman mode which propagates along the interface between the GaN and the boundary layer.

In Fig. 1 we show the measured p-polarisation reflection spectra of three  $\alpha$ -GaN epilayers in the GaN reststrahl region of the spectrum. The dips at  $535\text{ cm}^{-1}$  arise from interference between the rays reflected off the top and bottom surface of the epilayer. The frequency of this feature is a useful probe of epilayer thickness, indicating here that

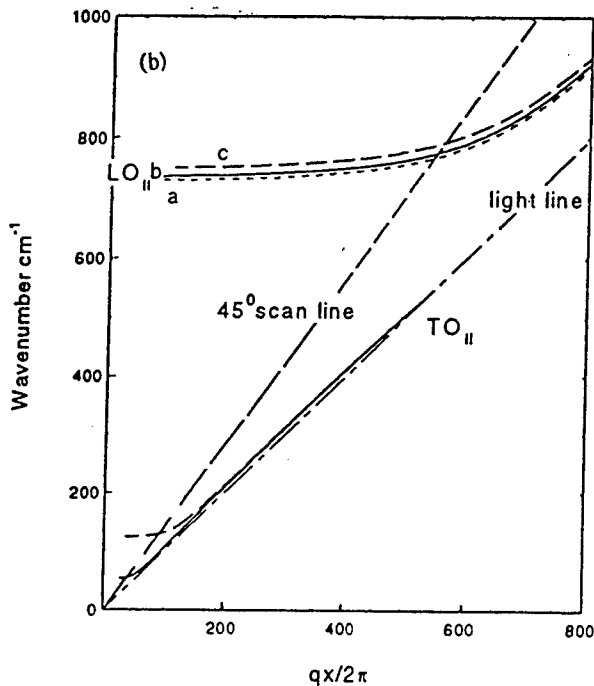


Figure 2. Calculated dispersion curves, a, b, c, for the Brewster modes of the three samples shown in Fig. 1.

the three epilayers have the same thickness. It can be seen that the frequency of the minimum near  $750\text{ cm}^{-1}$  (the Brewster mode) shifts in position due to plasmon-LO phonon coupling according to the concentration of free carriers. Fig. 2 shows calculated dispersion curves showing the shifts in frequency of the Brewster mode corresponding to the three spectra shown in Fig. 1.

### E. Conclusions

We find that the effective masses in  $\beta$ -GaN are isotropic, as expected, with  $m_e = 0.2 m_0$ , and  $m_h = 0.8 m_0$ , where  $m_0$  is the mass of the free electron. In  $\alpha$ -GaN epilayers we find that the effective masses normal,  $\perp$ , and parallel,  $\parallel$ , to the crystallographic c-axis are unequal, with  $m_{e\perp} \sim 0.73 m_0$ ,  $m_{e\parallel} \sim 0.28 m_0$  and  $m_{h\perp} \sim 0.81 m_0$ ,  $m_{h\parallel} \sim 0.88 m_0$ . These values of the electron effective masses are slightly larger than previously reported [10,19].

### F. Acknowledgements

We wish to thank EPSRC for financial support, and G Mirjalili wishes to acknowledge the award of a scholarship by the Islamic Republic of Iran and the University of Yazd.

### G. References

1. N. Koide, H. Kato, M. Sassa, S. Yamasaki, K. Manabe, M. Hashimoto, K. Amano, K. H. Iramatsu, and I. Akasaki, *J. Crystal Growth*, 115, 639 (1991).
2. M. A. Khan, J. N. Vanhove, N. Pan, and J. Carter, *Appl. Phys. Lett.*, 60, 3027 (1992).
3. H. Morkoc and S. Strite, *J. Appl. Phys.*, 76, 1363 (1994).
4. S. Strite, M. E. Lin, and H. Morkoc, *Thin Solid Films*, 231, 197 (1993).
5. H. Amano, I. Akasaki, K. Hirimatsu, and N. Koide, *Thin Solid Films*, 163, 415 (1988).
6. S. Nakamura, *Jpn. J. Appl. Phys.*, 30, L1705 (1991).
7. S. Nakamura, M. Senoh, and T. Mukai, *Jpn. J. Appl. Phys.*, 30, L1708 (1991).
8. C. Wang and R. F. Davis, *Appl. Phys. Lett.*, 63, 990 (1993).
9. W. Kim, A. Salvador, A. E. Botchkarev, O. Aktas, S. N. Mohammad, and H. Morkoc, *Appl. Phys. Lett.* 69, 559 (1996).
10. A. S. Barker and M. Ilegems, *Phys. Rev. B*, 7, 743 (1973).
11. T. Dumelow and D. R. Tilley, *J. Opt. Soc. Am.*, 10, 633 (1993).
12. D. W. Berreman, *Phys. Rev.*, 130, 2193 (1963).
13. G. Mirjalili, T. J. Parker, S. Farjami Shayesteh, T. S. Cheng, C. T. Foxon, L. C. Jenkins, and J. W. Orton, *Proc. 20th Int. Conf., on Infrared and Mm. Waves*, Orlando (1995), p. 377.
14. G. Mirjalili, T. J. Parker, S. Farjami Shayesteh, S. F. Cheng, and J. W. Orton, *Proc. 21st Int. Conf. on Infrared and Mm. Waves*, Berlin (1996), Eds. M. von Ortenberg and H.-U. Mueller, ISBN 3-00-000800-4.
15. E. R. Glaser, T. A. Kennedy, K. Doverspike, L. B. Rowland, and D. K. Gaskill, *The American Phys. Society*, 51, 133326 (1995).
16. C. T. Foxon, T. S. Cheng, S. V. Novikov, D. E. Lacklinson, L. C. Jenkins, D. Johnston, J. W. Orton, S. E. Hooper, N. Baba-Ali, T. L. Tansley, and V. V. Tretyakov, *J. Cryst. Growth*, 150, 892 (1995).
17. T. Dumelow, T. J. Parker, S. R. P. Smith, and D. R. Tilley, *Surface Science Reports*, 17, 151 (1993).
18. G. Mirjalili, R. A. Levett, T. J. Parker, T. S. Cheng, and C. T. Foxon, to be submitted to *Phys. Rev. B*.
19. M. Suzuki and T. Uenoyama, *Jpn. J. Appl. Phys.*, 34, 3442 (1995).

# A Compact Coherent THz Source by Photomixing Diode Lasers in a Photoconductive Antenna for High-Resolution Spectroscopy

H. Abe, S. Matsuura, M. Tani, and K. Sakai

Kansai Advanced Research Center, Communications Research Laboratory, M.P.T.  
588-2 Iwaoka, Nishi-ku, Kobe 651-24, Japan

H. Ozeki and S. Saito

Department of Molecular Structure, Institute for Molecular Science  
Myodaiji, Okazaki 444, Japan

## Abstract

We report generation of continuous-wave terahertz radiation and its application to molecular spectroscopy. The THz radiation is generated by the photomixing of two grating-stabilized diode-lasers in a photoconductive antenna based on low-temperature-grown GaAs. An output power beyond 10 nW at frequencies around 1 THz and the long-term stability of about 5 MHz was achieved. This source is used to the transmission spectroscopy of CO and CH<sub>3</sub>CN molecules, and lines with 1% level absorption were clearly resolved with a simple amplitude modulation technique. The experimental results indicate the potential power of this source for the high-resolution spectroscopy at THz frequencies.

## 1. Introduction

The recent development of ultrafast optoelectronic devices has enabled us to generate coherent terahertz (THz) radiation by photomixing two lasers in photoconductive devices [1-3]. Very recently, the application of such a THz source to molecular spectroscopy by using two stabilized (one for fixed and another for tunable) dye lasers was reported.[4] Although dye lasers have advantages in power and wavelength tunability, diode lasers are preferred for their compactness in practical use. In this paper we report the generation of continuous-wave THz radiation by photomixing of two stabilized diode lasers in a dipole photoconductive antenna made with low-temperature-grown GaAs (abbreviated hereafter as LT-GaAs), and results of transmission spectroscopy for gaseous molecules (CO and CH<sub>3</sub>CN), as a demonstration of THz radiation source in high-resolution spectroscopy.

## 2. Experiment

Figure 1 shows the experimental setup for the transmission measurement. The laser sources were two diode lasers stabilized by optical feed-back with gratings in external cavities, providing an output power of about 100 mW each. The lasing frequency was centered approximately at 820 nm and 830 nm, respectively, and could be tuned over  $\pm 5$  nm by rotating the gating for each laser. The fine tuning and the sweep of the laser frequency was done by using the PZTs attached on the backside of the gratings. The sweeping range of about 10 GHz was available without the mode hopping. The two laser beams were combined with a beamsplitter cube and then focused onto the gap of a 30  $\mu$ m-long photoconductive dipole antenna fabricated

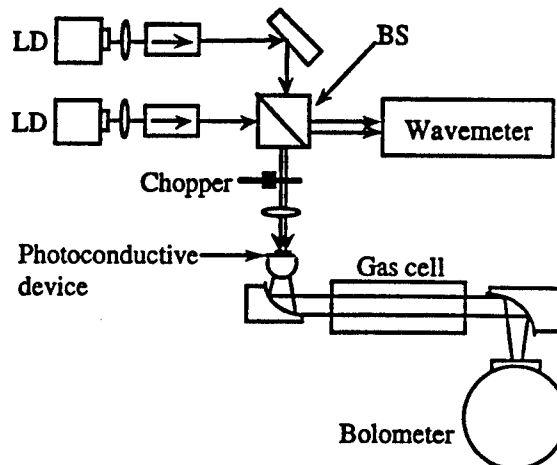


Fig. 1 Schematic view of the experimental set up for the transmission measurement.

on a LT-GaAs [3] after passing through a mechanical chopper for the lock-in detection. The LT-GaAs was a 1.5  $\mu$ m-thick GaAs layer grown by MBE at 250°C on a semi-insulating GaAs and annealed at 600 °C after the growth. The carrier lifetime measured in a time-resolved reflectance measurement was about 0.5 ps [5]. A DC bias voltage of 20 V was applied to the 3  $\mu$ m-gap of the dipole antenna and the incident laser power on the gap was 30 mW. A 3-mm-diameter high-resistivity silicon hemispherical lens was attached on the back side of the GaAs substrate to avoid reflection loss at the substrate-air interface. The difference frequency of the two lasers was measured by a wavemeter with an accuracy less than 100 MHz. The electromagnetic wave emitted from the photoconductive antenna was collimated with a F/0.8 paraboloidal mirror. The THz beam passed through a gas cell with 28-mm diameter windows made of Teflon, in which the sample gases to be measured were contained, and was focused into a 4.2 K silicon composite bolometer with a F/1.6 paraboloidal mirror. For spectroscopic measurements we swept the frequency of one laser with a rate of about 1 scan/min, fixing the frequency of another laser.

## 3. Results and discussion

With the 30-mW laser excitation we obtained an output power of about 14 nW at frequencies of about 1 THz. The long-term (~1 sec) frequency stability of the radiation measured at 40 GHz with a RF spectrum analyzer was about 5 MHz (FWHM).



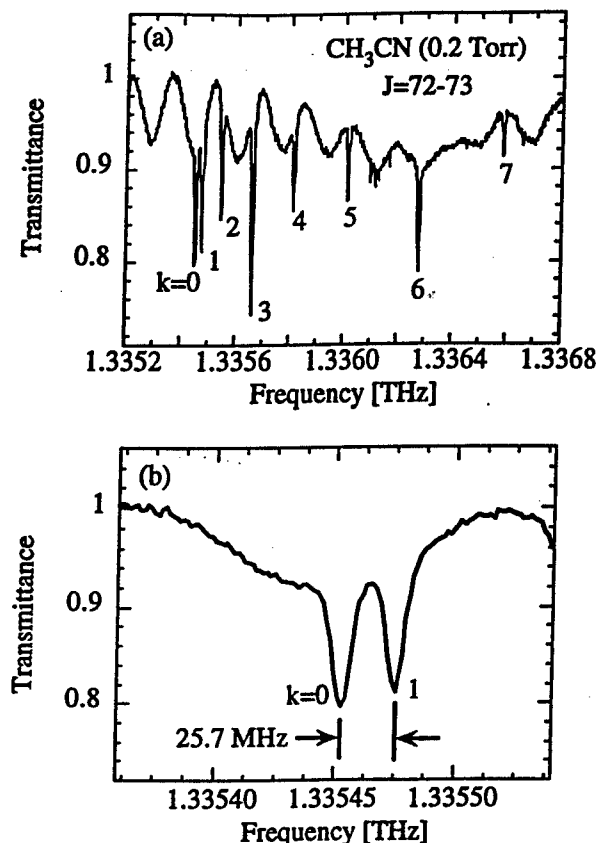


Fig. 2 (a) Transmission spectra for  $\text{CH}_3\text{CN}$  with the fine structure for the lines with  $J=72-73$ ,  $K=0-7$ , and (b) the expanded spectra for  $K=0$  and 1.

Figure 2(a) shows the measured transmission spectrum for  $\text{CH}_3\text{CN}$  at a pressure of 0.2 Torr. With a 1.5 GHz scan at around 1.336 THz, the fine structure of the lines corresponding to the pure rotational transition of  $J=72-73$  with  $K=0-7$  was clearly observed. The base-line fluctuation of several percent was caused by optical fringes. The fringes with the period of about 150 MHz arise from the standing-wave in the spacing between the source and the detector ( $\sim 1$  m). Figure 2(b) shows the detailed spectrum for  $K=0$  and 1 obtained by setting the scan range to about 200 MHz. The two lines with a separation of 25.7 MHz were clearly resolved. The measured linewidth was approximately 10 MHz, and is consistent with the total line broadening estimated from the source linewidth of  $\sim 5$  MHz, the Doppler width of  $\sim 1.5$  MHz, and the pressure broadening of  $\sim 1$  MHz.

The CO gas includes isotopes of  $^{13}\text{CO}$  and  $\text{C}^{18}\text{O}$  with fractions of  $\sim 1\%$  and  $\sim 0.2\%$  in their natural abundance, respectively. We tried to observe the lines of these isotopes with the present spectrometer. Figure 3(a), (b), and (c) show the measured spectra for the pure rotational transitions of  $J=12-13$  for  $^{12}\text{CO}$ ,  $^{13}\text{CO}$  and  $\text{C}^{18}\text{O}$ , respectively. The gas pressure was about 2 Torr, and the absorbance of the isotopes was estimated to be  $\sim 100\%$  for  $^{12}\text{CO}$ ,  $\sim 5\%$  for  $^{13}\text{CO}$  and  $\sim 1\%$  for  $\text{C}^{18}\text{O}$ . The measured absorbance showed good agreement with the prediction.

In conclusion, a transmission spectroscopy for  $\text{CH}_3\text{CN}$  and CO gases was successfully carried out using the photomixer pumped with two stabilized diode, and the results indicate that this system is promising as a compact THz radiation source for the high-resolution spectroscopy.

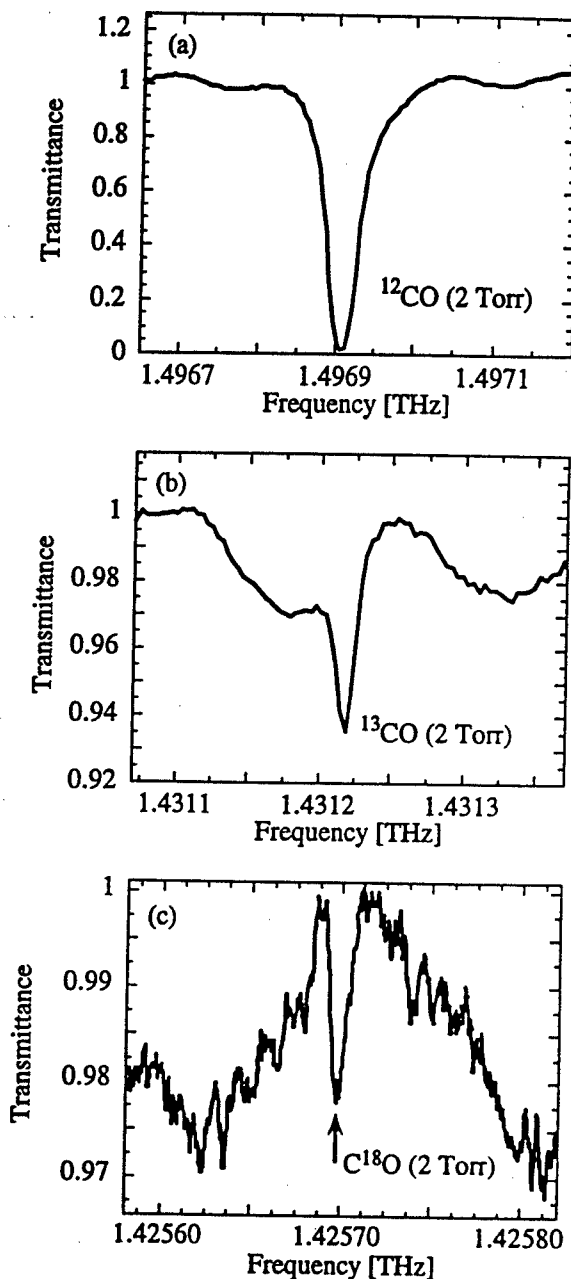


Fig. 3 Transmission spectra for CO gas at a pressure of 2 Torr; (a) spectrum for  $^{12}\text{CO}$ , (b) for  $^{13}\text{CO}$ , and (c) for  $\text{C}^{18}\text{O}$ .

## References

- [1] E. R. Brown *et al.*, Appl. Phys. Lett. 66, 285 (1995).
- [2] K. A. McIntosh *et al.*, Appl. Phys. Lett. 67, 3844 (1995).
- [3] S. Matsuura *et al.*, Appl. Phys. Lett. 70, 3844 (1997).
- [4] A. S. Pine *et al.*, J. Mol. Spectrosc. 175, 37 (1996).
- [5] M. Tani *et al.*, Jpn. J. Appl. Phys. 33, 4807 (1994).

# Tunable Far-Infrared Spectroscopy in the 6 to 8 THz Region

Hitoshi Odashima

Department of Physics, Toyama University, Gofuku 3190, Toyama 930, Japan

Maki Tachikawa, Lyndon R. Zink, and Kenneth M. Evenson

Time and Frequency Division, National Institute of Standards and Technology,  
325 Broadway, Boulder, Colorado 80303

## Abstract

Tunable far-infrared radiation in the 6 to 8 THz region was generated by mixing CO<sub>2</sub> laser, <sup>15</sup>NH<sub>3</sub> laser, and microwave radiations in a W-Co metal-insulator-metal diode. This far-infrared radiation was used to accurately measure torsion-rotation transitions of CH<sub>3</sub>OH.

## Introduction

High-resolution spectroscopy is difficult in the 5-10 THz region of the far-infrared (FIR), because tunable, coherent radiation is difficult to produce. Fourier transform spectroscopy (FTS) covers this region, but its typical resolution is about 50 MHz, and its accuracy is limited to about 3 MHz. A tunable far-infrared (TuFIR) spectrometer based on the difference frequency of two CO<sub>2</sub> lasers generated in a metal-insulator-metal (MIM) diode [1] provides tunable, coherent FIR radiation up to 6.5 THz [2] with a frequency uncertainty of 14 kHz [3]; however, the maximum FIR frequency is limited by the maximum frequency difference between two CO<sub>2</sub> lasers. To generate tunable, coherent radiation above 6.5 THz, we replaced one of the two CO<sub>2</sub> lasers in a traditional TuFIR spectrometer with an optically pumped, mid-infrared <sup>15</sup>NH<sub>3</sub> laser which has several lines at lower frequency than the CO<sub>2</sub> laser.

## Experimental Details

A block diagram of the spectrometer is shown in Fig. 1. The ammonia laser is optically pumped by a CO<sub>2</sub> laser with a power of about 18 W. A grating selects one of five <sup>15</sup>NH<sub>3</sub> laser lines,  $\nu(4,0)$ ,  $\nu(4,3)$ ,  $\nu(5,3)$ ,  $\nu(6,0)$ , or  $\nu(6,3)$ , with typical power of 300-600 mW. More details of this laser are described elsewhere [4]. A CH<sub>3</sub>OH absorption cell blocks

any residual CO<sub>2</sub> laser radiation superposed on the ammonia laser beam. The ammonia laser is stabilized to the center of the saturated-absorption dip in low pressure ammonia, using its third-derivative signal as an error signal [5]. Frequency accuracy is 100-150 kHz. The <sup>15</sup>NH<sub>3</sub> laser frequencies are reported in Ref. 6.

The ammonia laser radiation (frequency,  $\nu_1$ ) is mixed with CO<sub>2</sub> laser radiation ( $\nu_2$ ) in a W-Co MIM diode. This CO<sub>2</sub> laser is stabilized to the saturation dip in a 4.3  $\mu$ m fluorescence signal of CO<sub>2</sub> with the traditional 1f servo technique. The CO<sub>2</sub> reference frequencies are reported in Ref. 7. Typical incident powers are 150 mW for the CO<sub>2</sub> laser and 100-150 mW for the <sup>15</sup>NH<sub>3</sub> laser. Several milliwatts of microwave radiation from the synthesized sweeper ( $1 \leq \nu_{MW} \leq 20$  GHz) is also coupled onto the diode. The W-Co MIM diode generates two tunable FIR frequencies equal to  $\nu_{FIR} = |\nu_1 - \nu_2| \pm \nu_{MW}$ . The synthesized FIR frequency is changed by tuning the

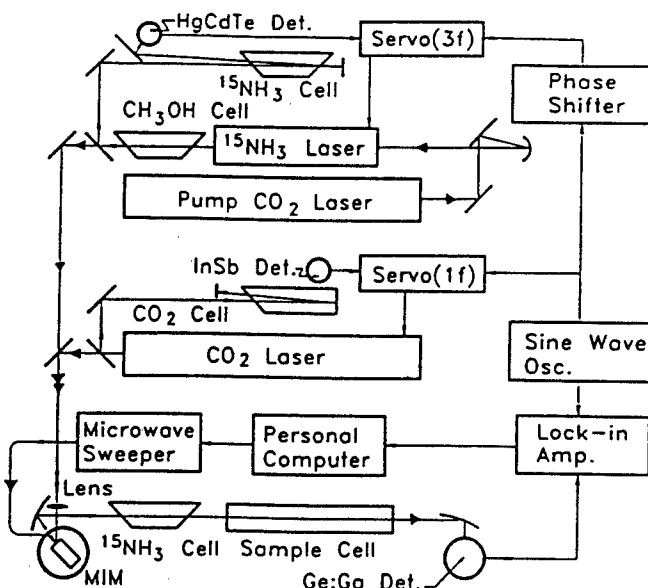


Fig.1. Block diagram of the TuFIR spectrometer based on the difference frequency of <sup>15</sup>NH<sub>3</sub> and CO<sub>2</sub> lasers.

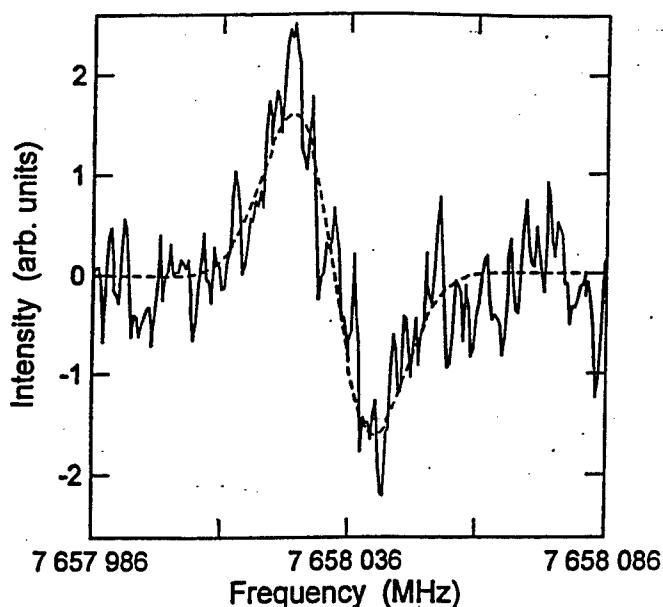


Fig. 2. Observed spectral line of the A,  $(n, K, J) = (1,5,12) \leftarrow (0,4,11)$  transition of  $\text{CH}_3\text{OH}$  at 7.6 THz. The measured spectrum is the solid line and the fitted spectrum is the dashed line.

microwave source. The generated FIR radiation is collimated with an off-axis parabola and sent through a 1.1 m long sample cell. It is then detected by a gallium-doped germanium (Ge:Ga) photoconductive detector with an 8-16  $\mu\text{m}$  diamond scatter filter used to reduce the infrared radiation for  $\lambda < 14 \mu\text{m}$ . A 20 cm long cell of  $^{15}\text{NH}_3$  at 133 Pa is placed in front of the sample cell to eliminate any residual  $^{15}\text{NH}_3$  laser radiation. The frequencies of both lasers are modulated at 450 Hz with opposite phases for frequency stabilization; hence, the generated FIR frequency is also modulated with an amplitude of a few megahertz. The detected signal is demodulated by a lock-in amplifier operated in the 1f mode. Both the microwave sweeper and the lock-in amplifier are computer controlled, and the first-derivative curve of the absorption is recorded on the computer.

### Results and Discussion

$\text{CH}_3\text{OH}$  was chosen as a sample gas because of its rich torsion-rotation spectrum over 6 THz.  $\text{CH}_3\text{OH}$  pressure was around 1.3 Pa and five transitions from 6 THz to 8 THz were measured. A plot of the observed absorption from the A,  $(n,K,J)=(1,5,12) \leftarrow (0,4,11)$  transition at 7.6 THz is shown in Fig. 2, where  $n$  is the torsional quantum number. The measured transition frequencies are reported together with their  $1\sigma$  uncertainties in Table 1. The frequency uncertainties ( $\leq 1$  MHz) are much less than those of FTS. Both reduced

Table 1. Observed Frequencies of  $\text{CH}_3\text{OH}$

transition	observed frequency
symm., $(n',K',J') \leftarrow (n'',K'',J'')$	(MHz)
A, $(2, 8, 18) \leftarrow (1, 7, 17)$	6 567 405.01(32) <sup>a</sup>
A, $(3, 6, 6) \leftarrow (2, 5, 5)$	7 134 675.03(73)
E, $(1, -4, 9) \leftarrow (0, -3, 9)$	7 134 730.84(117)
A, $(1, 5, 12) \leftarrow (0, 4, 11)$	7 658 033.06(76)
E, $(1, -4, 15) \leftarrow (0, -3, 14)$	7 851 003.94(75)

<sup>a</sup> The numbers in parentheses are the estimated  $1\sigma$  uncertainties in units of the last quoted digits.

MIM diode efficiency and reduced detector sensitivity are responsible for the larger frequency uncertainty above 7 THz. We used third-order generation, in which tunable FIR radiation is obtained with two  $\text{CO}_2$  lasers plus microwave sidebands, because of its wide tuning range ( $\pm 20$  GHz). However, second-order generation, in which tunable FIR radiation is obtained with a tunable waveguide  $\text{CO}_2$  laser without microwave sidebands, may provide higher frequency operation because it produces several times as much FIR power. Furthermore, a Ge:Be photoconductive detector is more sensitive than a Ge:Ga detector in the 6-10 THz region. With second-order generation and a Ge:Be detector, this TuFIR technique should be applicable up to  $\sim 10$  THz.

### Acknowledgment

The authors thank Lew Mullen for his technical support. This work was supported by NASA contract W-18, 913. M.T. thanks to the Telecommunication Advancement Foundation for providing the funds for his study at NIST.

### References

1. K. M. Evenson, D. A. Jennings, and F. R. Petersen, *Appl. Phys. Lett.* **44**, 576 (1984).
2. T. D. Verberg and K. M. Evenson, *IEEE Trans. Instrum. Meas.* **42**, 412 (1993).
3. F. Matsushima, K. M. Evenson, and L. R. Zink, *J. Mol. Spectrosc.* **164**, 517 (1994).
4. M. Tachikawa and K. M. Evenson, *Opt. Lett.* **21**, 1247 (1996).
5. L. R. Zink, F. S. Pavoné, R. Meucci, M. Prevedelli, and M. Inguscio, *Opt. Comm.* **77**, 41 (1990).
6. H. Odashima, M. Tachikawa, L. R. Zink, and K. M. Evenson, submitted to *J. Mol. Spectrosc.*
7. A. G. Maki, C.-C. Chou, K. M. Evenson, L. R. Zink, and J.-T. Shy, *J. Mol. Spectrosc.* **167**, 211 (1994).

## Millimeter-wave Radars for Atmospheric Remote Sensing

James B. Mead  
Quadrant Engineering Inc.  
107 Sunderland Rd.  
Amherst, MA 01002 USA

Phone: (413) 549-4402 FAX: 413 549-5203  
email:mead@quad-eng.com

### Abstract

In recent years, a number of millimeter-wave cloud radars have been built and are being used in both ground-based and airborne applications. These instruments take advantage of several major technological developments that have only recently become commercially available: 1) Compact, high-power Extended Interaction Klystron Amplifiers suitable for operation in the 35 and 95 GHz atmospheric transmission windows, 2) Millimeter-wave LNAs improving noise performance by several dB, and 3) solid-state, low-loss switches, allowing pulse-to-pulse polarization agility. Cloud radars operating in the atmospheric transmission windows at 35 and 95 GHz benefit from the strong frequency dependence ( $f^4$ ) of backscattering cross-section for small cloud particles. Thus, millimeter-wave cloud radars with 1-2 m diameter antennas and kW level transmitters achieve similar sensitivity to microwave radars with large antennas and MW level transmitters. These advantages are crucial for airborne and mobile applications: millimeter-wave cloud radars are now being used in a number of small aircraft and may someday be used for monitoring the global distribution of clouds from space.

### Overview of Millimeter-wave Cloud Radars

Since the early 1950s, millimeter-wave radars have been used for scientific studies of non precipitating clouds [1]-[4]. These instruments were more sensitive to small cloud particles than conventional microwave radars and provided new insights into the rich small-scale structure of clouds and precipitation. However, there were several drawbacks to these early millimeter-wave radar systems that prevented their widespread use. These problems included: lack of solid-state, low-noise millimeter-wave components, such as sources, mixers and amplifiers, which resulted in noisy and unreliable receivers; 2) scarcity of other millimeter-wave componentry, such as antennas, switches, and circulators; 3) the lack of devices and techniques for achieving phase coherence, which limited cloud radars to backscattered power measurements; and 4) limited understanding of propagation and scattering at millimeter-wavelengths. These limitations persisted through the 1970s, and prevented millimeter-wave

cloud radars from filling operational needs such as providing information on cloud top and base height, melting layer height, and number of cloud layers.

Modern millimeter-wave cloud radars resemble their predecessors in many respects, but their performance and reliability are considerably enhanced by advances in millimeter-wave and digital technology during the past two decades. Solid-state low phase noise sources, low-noise mixers, and amplifiers are now widely available from commercial sources, as well as power tubes, including compact Extended Interaction Klystron Amplifiers (EIAs) operating at up to 15 percent duty cycle and providing more than 50 dB gain and 1.5 kW peak power output at 35 and 95 GHz. The availability of low-loss switches and latching circulators has made pulse-to-pulse polarization agility practical, which now permits the study of cloud particle shape, orientation and angular distribution through polarimetric techniques.

### Cloud Radar Development at Quadrant Engineering

Quadrant Engineering has recently developed a number of ground-based and airborne millimeter-wave cloud radars for customers in the US and abroad. Based on a polarimetric design developed at the University of Massachusetts, these instruments measure the complex scattering matrix of the scene by transmitting a pair of orthogonally polarized pulses in rapid succession. Covariances of the individual terms of the scattering matrix are then used to compute meteorological radar parameters that give insight into cloud-particle orientation, shape, degree of randomness and anisotropy.

#### *GKSS 95 GHz Miracle Radar*

A photograph of a 95 GHz system, developed for GKSS Research Center in Geesthacht, Germany, is shown in Figure 1. Parameters for this radar are presented in Table I. The radar employs a VKB246IT5 grid modulated EIA built by CPI-Canada (formerly Varian-Canada). The receiver front-end employs a balanced mixer followed by microwave LNA to achieve a noise figure of 8.5 dB, excluding front-end losses. HEMT LNAs, used in subsequent systems built by Quadrant, were just coming on the market at the time and were not included. Commercially-available HEMT LNAs delivered in 1996 exhibited noise

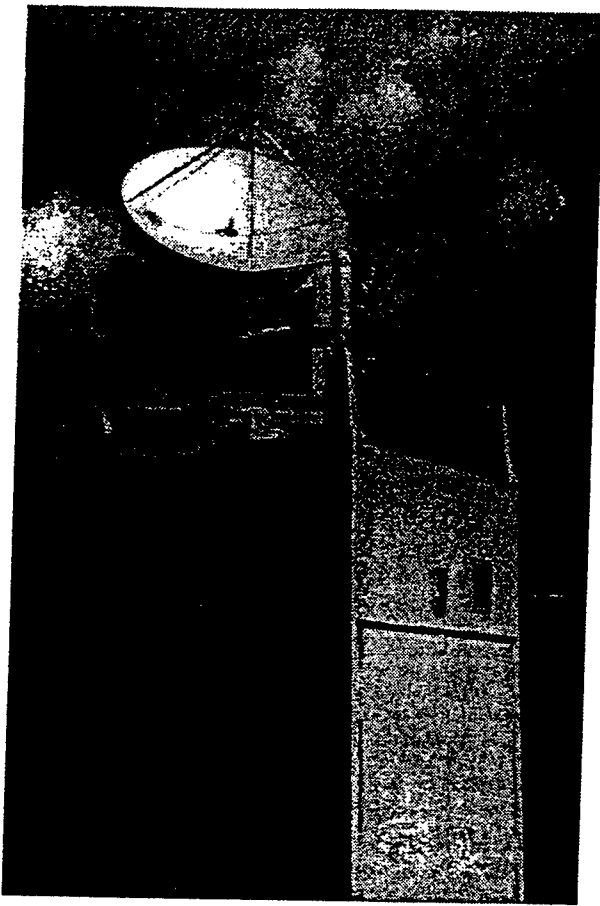


Fig. 1. Photograph of the GKSS Miracle system built by Quadrant Engineering (Photo: courtesy: GKSS Research Institute).

figures of 5.0–5.5 dB at 95 GHz. More information regarding the radar system can be found at the Miracle web site: <http://w3.gkss.de/deutsch/Radar/miracle.html>

Figure 2 shows a time-height cross-section of radar reflectivity in dB,  $dBZ_e$ , where  $Z_e$  is the sixth moment of the drop-size distribution as estimated from the radar power return, assuming scattering in the Rayleigh region. This frontal system, from Feb. 12, 1997, consists of ice clouds above the melting layer at 1.6 km and rain below this height after 1345 GMT. Figure 3 displays linear depolarization ratio, the ratio of cross polarized to co-polarized backscattered power, showing enhanced depolarization at the melting layer.

### 35 GHz cloud radar development

Quadrant is currently building a 35 GHz cloud radar for the Air Force using a high duty cycle (5 percent), water cooled EIA with peak power output of 1.7 kW. Specifications for this radar are given in Table II. Pulse compression must be employed to take full advantage of the added duty cycle, since the pulse repetition rate is limited to 10 kHz for typical vertically-pointed cloud sensing applications (15 km unambiguous range). Conventional pulse-expansion/compression using surface acoustic wave devices, yield peak range sidelobes of no better than -40 to -45 dB below the peak response. Given the impor-

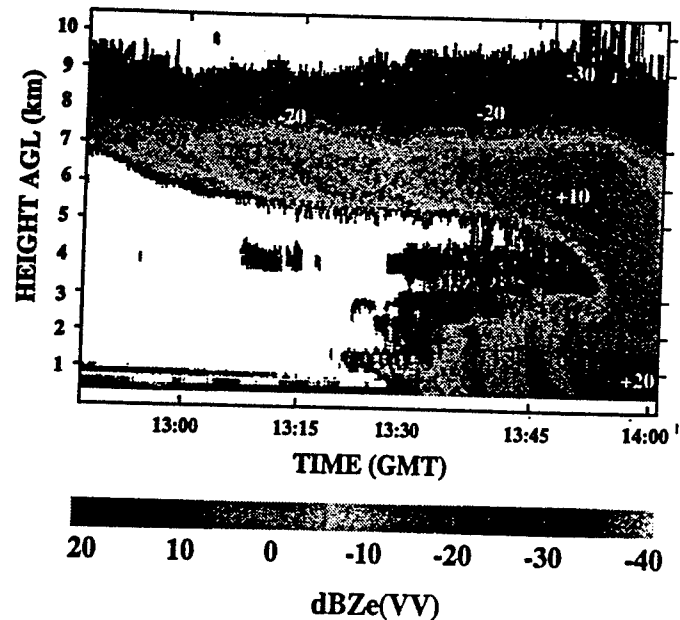


Fig. 2. Radar reflectivity of a frontal system measured on February 12, 1997 with the GKSS 95 GHz cloud radar (data courtesy: GKSS Research Institute.)

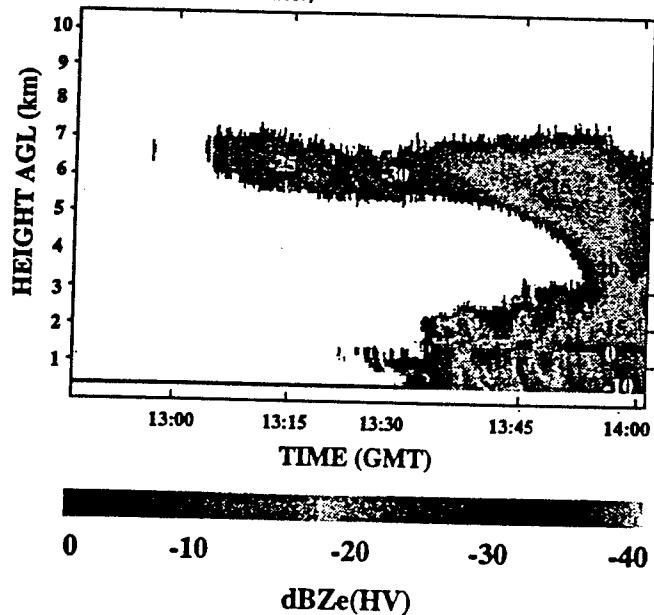


Fig. 3. Cross-polarized reflectivity for the same frontal system (data courtesy: GKSS Research Institute.)

tance of detecting weakly scattering cloud regions, such as cloud edges or thin cloud layers, it is important to reduce peak and integrated sidelobe levels as low as possible to avoid image degradation from strongly reflecting cloud regions. Fully digital pulse compression techniques recently implement for meteorological radars [5] exhibit peak range sidelobe levels of -55 to -60 dB. Combining digital pulse expansion with analog pulse compression appears to yield excellent results, since the expanded pulse can compensate for the non ideal transfer function of the pulse compressor [6].

Data Acquisition One of the most important technolog-

TABLE I  
95 GHz CLOUD RADAR SPECIFICATIONS (GKSS MIRACLE SYSTEM)

parameter	value
Transmit Frequency:	95 GHz
Peak Power:	1.7 kW
Pulse Duration:	100 - 2,000 ns
Duty cycle:	1.2 %
Antenna Diameter:	1.2 m
Antenna Gain:	60 dBi
Antenna Beamwidth:	.17°
Polarization:	V and H
Cross-Polarization Isolation:	26 dB
Receiver Noise Figure: (w/o LNA)	11 dB
(including front-end loss)	
Receiver Dynamic Range:	70 dB
Receiver Channels:	$\log  V , I_v, Q_v$ $\log  H , I_h, Q_h$

TABLE II  
35 GHz CLOUD RADAR SPECIFICATIONS

parameter	value
Transmit Frequency:	35.03 GHz
Peak Power:	1.7 kW
Chirp Pulse Length:	12.8 $\mu$ s
Compressed Pulse Length:	500 ns
Duty Cycle:	5 %
Antenna Diameter:	1.8 m
Antenna Gain:	53 dBi
Antenna Beamwidth:	.33°
Polarization:	V and H
Receiver Noise Figure (w/LNA):	4.7 dB
(including front-end loss)	
Receiver Channels:	$\log  V , I_v, Q_v$ $\log  H , I_h, Q_h$

ical advance affecting the utility of all cloud radars has been the development of programmable digital signal processors (DSPs). Processor boards are now commercially available for a variety of standard buses, including ISA, VME, VXI, Multi-bus, and others. These boards have as many as five independent floating-point processors, each of which can be configured to execute one or more real-time algorithms. Because cloud radars can easily generate data rates of more than 40 MByte·s<sup>-1</sup> it is usually desirable to use real-time processing to reduce data rates to a manageable level. Complete data acquisition systems, including analog-to-digital converters, processor boards, radar timing generators, and host computer, are now available for the VXI-bus. VXI's hierarchical architecture greatly simplifies system configuration, programming and debugging. All of these developments have resulted in a substantial reduction in the engineering effort necessary to develop a custom data acquisition and pro-

cessing system.

## Future Applications

### *Solid-state cloud radar for use on Unmanned Aerial Vehicles*

The University of Massachusetts is currently developing a compact, solid-state 95 GHz cloud radar intended for use on an unmanned aerial vehicle (UAV). This system incorporates a 40 W peak-power IMPATT amplifier, a compact lens antenna utilizing folded optics, and a 95 GHz HEMT LNA to achieve sensitivity of approximately -20 dBZ noise-equivalent reflectivity at 1 km range. When completed, the entire system will weigh less than 30 kg and will consume approximately 150 W prime power.

Further size and power reduction of cloud radars intended for use on UAVs is necessary to allow multiple instruments to be flown simultaneously. Quadrant Engineering is currently working with researchers from the Five College Radio Astronomy Observatory at the University of Massachusetts to develop a low-noise homodyne receiver that will reduce the overall component count in the RF unit by over 50 percent, yielding a significant power and weight reduction. This receiver will use MMIC technology to implement receiver protection, low noise amplification, a W-band I/Q detection and internal calibration functions.

### *Ultra-high sensitivity cloud radars*

Several cloud types are difficult to observe on a regular basis with existing observational tools. These clouds include low-reflectivity boundary layer convective-, mid- and upper-level clouds. Such clouds are often too attenuating to be observed with lidar systems but still exhibit low radar reflectivity, due to the predominance of small droplets. A comparison of optical extinction coefficient and radar reflectivity is presented in Figure 4, where the shaded region indicates a cloud which cannot be readily probed (Assumptions: mono-disperse drop-size distribution; Rayleigh scattering for radar; optical limit extinction for lidar).

Gyrotron oscillators, capable of producing power levels in excess of 1 MW at frequencies exceeding 100 GHz, have been proposed for very high sensitivity atmospheric measurements [7]. MW-level gyrotron oscillators or 100 kW level high duty cycle gyro-klystron amplifiers, will allow cloud measurements down to the -75 dBZ level at 1 km range. Gyrotrons have not been used extensively for radar applications, because the high order waveguide modes used in gyrotrons are poorly suited for radiating a well-defined beam. However, efficient mode converters have been recently developed that can generate Gaussian beams suitable for illuminating lens or reflector antennas [8]. Other problems associated with gyrotrons are the difficulty of generating stable, single mode output, and the need to provide very high magnetic fields, necessitating the use of cryogenic magnets.

### *Cloud remote sensing from space*

The low power consumption and high sensitivity of

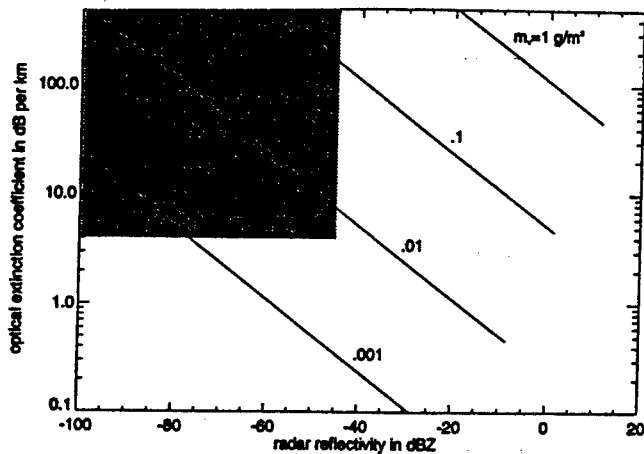


Fig. 4. Optical extinction coefficient as a function of radar reflectivity. Shaded region indicates optically thick clouds that are undetectable by existing cloud radars.

millimeter-wave radars make them well-suited for satellite applications. A recent workshop, held under the auspices of the Global Energy and Water Cycle Experiment (GEWEX), [9], assessed the potential for a spaceborne millimeter-wave radar to measure cloud vertical structure over large regions of the atmosphere. The distribution of ice and liquid water in clouds is a critical parameter in understanding the earth's radiation budget but no existing spaceborne instruments are currently available to measure the vertical structure of clouds.

A nadir-looking 95 GHz pulsed radar with a 2 m diameter antenna and 500 m range resolution could detect clouds of approximately -30 dBZ reflectivity from an altitude of 200 km. Such a system would not be able to detect weakly scattering liquid water clouds such as cumulus, stratocumulus and altocumulus but would be capable of detecting a substantial percentage of ice clouds and liquid clouds having larger drop sizes.

### Bibliography

1. J.B. Mead, A.L. Pazmany, S.M. Sekelsky, R.E. McIntosh, "Millimeter-Wave Radars for Remotely Sensing Clouds and Precipitation", *Proc. IEEE*, 82(12), Dec. 1994, 1891-1906.
2. A.L. Pazmany, R.E. McIntosh, R.D. Kelly, G. Vali, "An Airborne 95 GHz Dual-Polarized Radar for Cloud Studies", *IEEE Trans. Geos. Remote Sens.*, 32(4), July, 1994, 731-739.
3. S.M. Sekelsky and R.E. McIntosh, "Cloud Observations with a Polarimetric 33 GHz and 95 GHz Radar", *J. Meteor. and Atmos. Physics*, 58, Jan. 1996, 123-140.
4. H.B. Bluestein, A.L. Pazmany, J.C. Galloway, and R.E. McIntosh, "Studies of the Substructure of Severe Convective Storms Using a Mobile 3-mm-Wavelength Doppler Radar", *Bulletin American Met. Soc.*, 76(11), Nov. 1995, 2155-2169.
5. A. Tanner, S.L. Durden, R. Denning, E. Im, F.K. Li, W. Ricketts, and W. Wilson, "Pulse Compression

with Very Low Sidelobes in an Airborne Rain Mapping Radar", *IEEE Trans. Geosci. Remote Sens.*, 32, Jan. 1994, 211-213.

6. K. Sato, H. Hanado, and H. Kumagai, "A Low Range-sidelobe Pulse Compression Technique for Spaceborne Rain Radar", *Int. Geosci. Remote Sens. Society Symposium Digest*, Lincoln, NE, 1996.
7. W.M. Manheimer, "On the Possibility of Gyrotrons for Super Range Resolution Radar and Atmospheric Applications", NRL Memo. Rep. 6830, 1991.
8. M. Blank, J.A. Casey, K.E. Kreischer, R.J. Temkin and T. Price, "Experimental Study of a High Efficiency Quasi-optical Mode Converter for Whispering Gallery Mode Gyrotrons", *Int. J. Electronics*, v. 72, pp. 1093-1102, 1992.
9. *Report of the GEWEX Workshop on the Utility and Feasibility of a Cloud Profiling Radar* (Pasadena, CA, June 1993).

# Study of X-band Three-Stage Gyrotwyston Amplifier

E. V. Zasyupkin, B. Levush\*, M. Blank\*, E.V.Sokolov and I.I.Antakov

Institute of Applied Physics, Russian Academy of Science

46 Uljanov Str. 603600 Nizhny Novgorod, Russia

\* Naval Research Laboratory, Vacuum Electronic Branch  
Washington, DC 20375, USA

## Introduction

Gyroklystron is capable of high-efficiency, stable and high-gain amplification of millimeter waves in a rather narrow bandwidth restricted mainly by a high  $Q$ -factor of the output cavity [1], [2]. On the contrary, mm-wave gyro-travelling wave tube amplifier has demonstrated broadband performance at moderate power level and relatively low efficiency [3], [4]. The gyrotwyston configuration cooperating inside one or more buncher cavities together with a travelling wave output section has demonstrated the instantaneous bandwidth capability substantially greater than that for gyroklystron with comparable efficiency and gain [5], [6]. This paper presents the detailed study of several versions of three-stage X-band gyrotwyston and comparison their performance characteristics with those for X-band gyroklystron having the same buncher. Simulations results are compared with the experimental data.

## Results

The performance characteristics of gyroklystron (GK) and three gyrotwyston (GT) versions distinguished by the output section radius have been simulated and tested. The objective of these tests was a direct comparison of the efficiency, gain and bandwidth of both devices. Both tubes utilized a diode magnetron injection gun produced electron beam with a current up to 3 A and a voltage of 16 kV. Gyroklystron RF circuit was comprised of three cylindrical cavities operating in the  $TE_{011}$  mode. The  $Q$ -factors of these cavities were 300, 250, 210 for cavities 1, 2, and 3. The diameter and length of the first cavity were 40.6 mm and 43 mm, respectively. Gyrotwyston used the same buncher cavities, and also the same operating mode. Other RF circuit dimensions of both amplifiers are presented in Table 1.

TABLE 1. RF CIRCUIT DIMENSIONS

Version	$D_2$	$L_2$	$D_3$	$L_3$	$L_{12}$	$L_{23}$
GK	41.7	42-52	40.4	73	89	80
GT1	41.7	42-55	40.8	130	94	30
GT2	41.7	43-54	41.6	143	70	41
GT3	41.7	43-52	42.5	150	72	30

Here  $D$ , and  $L$ , are diameters and lengths of the cavities ( $s=2,3$ ) and output section ( $s=3$ ),  $L_{12}$  and  $L_{23}$  are the first and second drift tube lengths, respectively. As a GT output section diameter is increased, the ratio of the cut-off frequency to the operating that  $\omega_{cut}/\omega$  is diminished. All dimensions in Table 1 are given in millimeter.

Fig.1 compares the measured and calculated efficiency versus drive frequency for gyroklystron and GT1 gyrotwyston. Simulations were performed for 16-kV, 1-A electron beam with  $\alpha=1.6$  and  $\Delta\alpha/\alpha=0.15$ . A good fit between theory and experiment is observed for gyroklystron in Fig.1a. Comparison of calculated and experimental curves in Fig.1b obtained for GT1 shows a reasonable agreement, however the measured bandwidth exceeds predicted that by a factor of 1.5. To diminish the divergence, we plan to modify the existing gyrotwyston code.

In Fig.2, the measured efficiency and half-maximum bandwidth of gyroklystron (GK) and gyrotwyston (GT) as a function of a beam current are presented. The strong dependence of gyrotwyston efficiency and bandwidth on the ratio  $\omega_{cut}/\omega$  at small beam current ( $\approx 1$  A) is observed in Fig.2b. As  $\omega_{cut}/\omega$  is varied from 0.97 for GT1 to 0.93 for GT3, the bandwidth is broaden from 1% to 1.6%. A two-fold improvement in bandwidth over the gyroklystron was demonstrated by the GT3. However, bandwidth broadening is accompanied by the essential efficiency drop: from 43% for GK versus 19% for GT3. The efficiency reduction can be explained by a deterioration of the wave-beam interaction in the travelling wave output section. In the range of large beam current ( $\approx 3$  A), the bandwidth broadening and efficiency reduction at the transit from GK to GT3 are substantially smaller than those observed at 1-A beam current. It may be attributed to the effect of a velocity spread.

## References

- [1] I.I. Antakov et al., 18th International Conference on Infrared and Millimetre Waves, Conference Digest, pp.338-339, 1993.
- I.I. Antakov et al., 18th International Conference on Infrared and Millimetre Waves, Conference Digest, pp.466-467, 1993.



5, pp. 536-543, 1994.

K.R. Chu et al., IEDM Technical Digest, pp. 669-702, 1990.

P.M. Malouf et al., IEEE Trans. on Electr. Dev., Vol. 42, No. 9, pp. 1681-1685, 1995.

W. Lawson et al., IEDM Technical Digest, pp. 247-250, 1994.

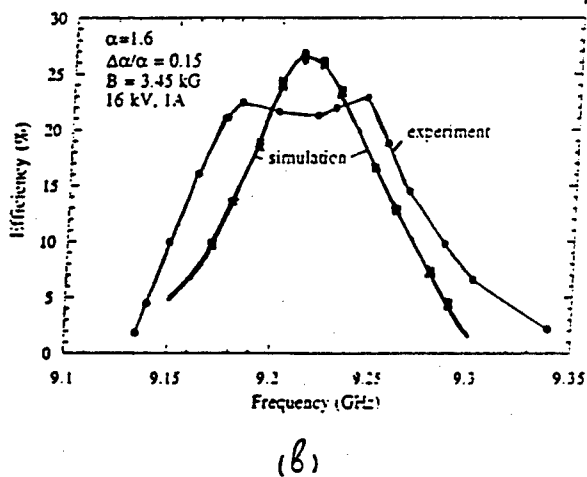
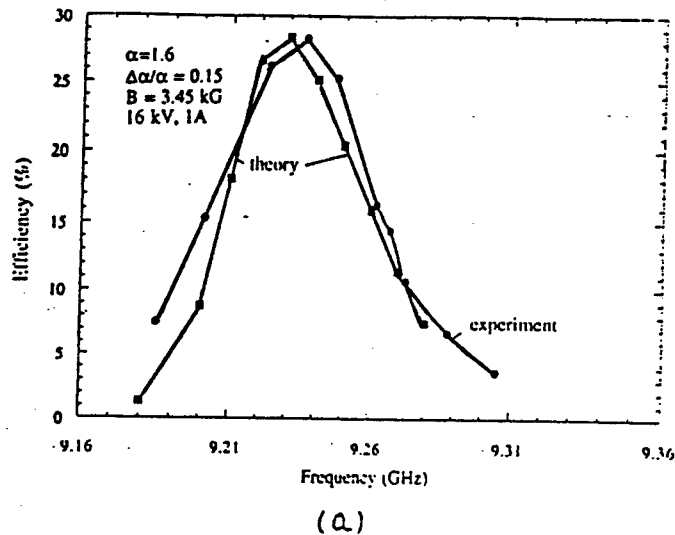


Figure 1: Comparison between measured and calculated efficiency versus drive frequency for (a) gyrokystron (b) gyrotwystron

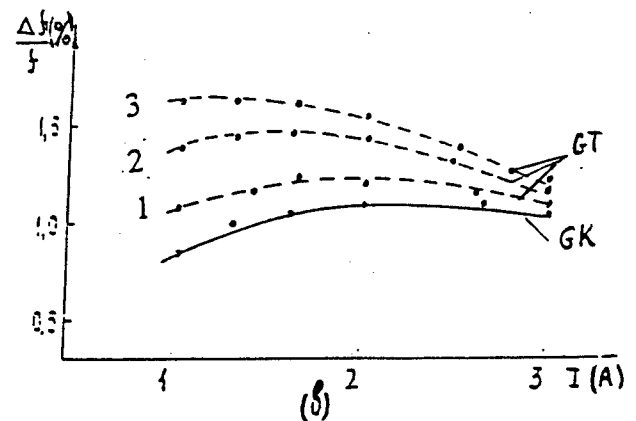
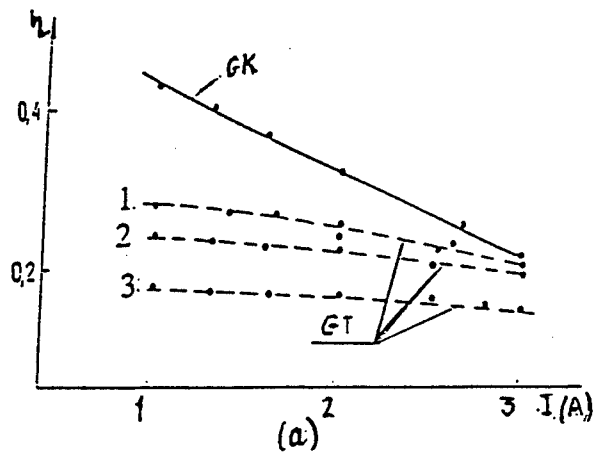


Figure 2: Comparison of measured efficiency (a) and bandwidth (b) for gyrokystron and three gyrotwystron versions

# Linear Theory of the Gyrotwystron with Stagger-Tuned Cavities

G.S. Nusinovich, W. Chen, and V.K. Tripathi\*

Institute for Plasma Research

University of Maryland, College Park, MD 20742-3511, USA

## Abstract

Gyrotwystrons with a large number of stagger-tuned prebunching cavities are promising wide-band, high-gain millimeter-wave amplifiers. In the present paper a small-signal theory describing the trade-off in the gain and bandwidth in these devices is developed. The results of a study of one- and two-cavity gyrotwystrons are presented which show a significant increase in the bandwidth due to the stagger-tuning.

The gyrotwystron, like the conventional twystron, consists of an input cavity and an output waveguide separated by a drift region. The gain in gyrotwystrons can be increased by using a set of prebunching cavities instead of one cavity. The bandwidth in devices with the multi-cavity prebunching can be increased by stagger-tuning the cavities' eigenfrequencies. However, when the stagger-tuning increases the bandwidth it simultaneously decreases the gain. This trade-off between the bandwidth and gain in multi-cavity, stagger-tuned gyroklystrons has been studied [1]. In the present paper we develop a theory which describes the same effect in gyrotwystrons.

In the frame of the small-signal theory the effect of the electromagnetic (EM) field on the electron motion can be considered as a small perturbation. Correspondingly, the self-consistent set of equations describing the interaction between electrons and the EM wave in the output waveguide (see, e.g. Ref. 2) can be linearized and reduced to the following dispersion equation known in the theory of conventional traveling-wave tube [3]

$$\lambda^3 - \Delta\lambda^2 + 1 = 0. \quad (1)$$

Here  $\lambda$  and  $\Delta$  are, respectively, the propagation constant and the cyclotron resonance mismatch normalized to the Pierce parameter. At  $\Delta = 0$  (see e.g. Ref. 3)  $\lambda_1 = -1$  and  $\lambda_{2,3} = (1 \pm i\sqrt{3})/2$ , so the third

partial wave ( $\sim \exp(i\lambda\zeta)$  where  $\zeta$  is the normalized axial coordinate) is a growing one. When the waveguide length is long enough only this growing wave is important. Correspondingly, the normalized wave intensity at the exit can be determined as

$$|F(\zeta_{out})|^2 = |\lambda_3 D_3 / D|^2 \exp \{2\text{Im}\lambda_3 \cdot \zeta_{out}\}. \quad (2)$$

Here  $D$  is the determinant for the linearized self-consistent set of equations which depends on  $\lambda_{1,2,3}$  and

$$D_3 = (\lambda_2 - \lambda_1) \{i\theta(0) + p(0)[1 - 2(\lambda_1 + \lambda_2)/\lambda_1\lambda_2]\}.$$

Here  $\theta(0)$  and  $p(0)$  are the boundary conditions for the electron gyrophase and normalized orbital momentum, respectively, averaged over initial gyrophases. These values ( $\theta(0)$  and  $p(0)$ ), which contain information about electron prebunching in a set of stagger-tuned cavities, have been analyzed [1, 4].

We have analyzed the function,  $G$ , determined as the ratio of the wave intensity at the waveguide exit,  $|F(\zeta_{out})|^2$ , to the intensity of the field exciting the first cavity. Using the balance equations for each cavity, which are given in Ref. 1, and assuming that in each successive cavity the field amplitude is larger than in the previous one, this gain function can be presented as the superposition of two terms:  $G = G_{(c)} - G_{(var)}$ . Here the constant term

$$G_{(c)} = 10 \log \left\{ \Phi_0 \prod_{m=2}^M \left( \frac{2I_{0,m}\zeta_{dr,m-1}}{1 + I_{0,m}} \right)^2 \frac{1}{(1 + I_{0,1})^2} \right\} \quad (3)$$

does not depend on  $\Delta$ , while the variable term

$$G_{(var)} = G_w + \sum_{m=1}^M G_m \quad (4)$$

does. In Eq (3)  $\Phi_0$  is the function

$$\Phi = |F(\zeta_{out})/F_M|^2 = |[i\zeta_{dr,M} + (\lambda_1 + \lambda_2)/\lambda_1\lambda_2] \times \lambda_3(\lambda_2 - \lambda_1/D) \exp \{2\text{Im}\lambda_3 \cdot \zeta_{out}\}|$$

\*Permanent address: Department of Physics, Indian Institute of Technology, New Delhi - 110016, India

at  $\Delta = 0$  ( $F_M$  here is the normalized field amplitude in the last cavity),  $I_{0,m}$  is the normalized current parameter for the  $m$ -th cavity, and  $\zeta_{dr,m-1}$  is the length of the corresponding drift section. In Eq. (4)

$$G_w = 10 \log(\Phi_0/\Phi) \quad (5)$$

describes the amplification in the waveguide and

$$G_m = 10 \log [1 + \bar{Q}_m^2 (\Delta - \Delta_m)^2] \quad (6)$$

describes the effect of the  $m$ -th cavity. These functions are normalized in such a way that in the case of the exact resonance ( $\Delta = \Delta_m = 0$ ),  $G_{(var)} = 0$ . In Eq. (6) the detuning between the signal frequency  $\omega$  and the eigenfrequency of the  $m$ -th cavity,  $\omega_m$ , is expressed via the normalized cyclotron resonance mismatch  $\Delta \sim \omega - k_z v_{z0} - \Omega_0$  and  $\Delta_m \sim \omega_m - k_z v_{z0} - \Omega_0$  (here  $k_z$  is the axial wave number and  $v_{z0}$  and  $\Omega_0$  are, respectively, the electron axial velocity and gyrofrequency). Correspondingly,  $\bar{Q}_m = \beta_{10}^2 I^{1/3} Q_m / (1 + I_{0,m})$ , where  $Q_m$  is the  $Q$ -factor of the  $m$ -th cavity and  $I$  is the normalized current parameter for the output waveguide [2]. (In our theory,  $I^{1/3}$  plays the role of the Pierce parameter.)

The waveguide gain  $G_w$  is shown as a function of  $\Delta$  in Fig. 1 for  $\zeta_{out} = 6$  and two values of  $\zeta_{dr,M}$  (at smaller  $\zeta_{out}$ 's this curve is wider). When  $Q$ -factors of cavities are small enough ( $\bar{Q}_m^2 \ll 1$ ) just this function determines the bandwidth. The variable gain in a one-cavity gyrotwyston with  $\zeta_{out} = 6$ ,  $\zeta_{dr} = 4$  and optimal  $\Delta_1 = -3.7$  and  $\bar{Q}_1 = 1.85$  is shown in Fig. 2. As follows from a comparison of these figures, the bandwidth becomes 2.9 times larger due to stagger tuning while the gain is about 18 dB smaller.

The variable gain for a two-cavity gyrotwyston with  $\zeta_{out} = 6$ ,  $\zeta_{dr,2} = 4$  and optimal parameters ( $\Delta_1 = -3.4$ ,  $\Delta_2 = -5.1$ ,  $\bar{Q}_1 = 1.5$ , and  $\bar{Q}_2 = 3.4$ ) is shown in Fig. 3. In this case the bandwidth is more than 3.5 times larger than in Fig. 1, while the gain is about 40 dB smaller. Note that the constant gain,  $G_{(c)}$ , in a two-cavity gyrotwyston, as follows from Eq. (3), can be much larger than in a one-cavity device.

For a single-cavity gyrotwyston driven by a 60 kV, 5 A electron beam with an orbital-to-axial velocity ratio of 1.5 in the case when the operating wave is the  $TE_{01}$  wave, which propagates with an axial wavenumber of  $k_z \sim 0.1\omega/c$ , the bandwidth shown in Fig. 2 is about 14%. Correspondingly, in

the case shown in Fig. 3 for the same beam and wave parameters the bandwidth is about 20%.

The formalism developed allows one to estimate the small-signal gain and bandwidth in multicavity stagger-tuned gyrotwystons.

This work has been sponsored by the Naval Research Laboratory.

### References

1. G.S. Nusinovich, B.G. Danly, and B. Levush, *Phys. Plasmas* 4, 469 (1997).
2. G.S. Nusinovich and H. Li, *Int. J. Elect.* 72, 895 (1992).
3. J.R. Pierce, *Traveling-Wave Tubes*, D. Van Nostrand Co., NY, 1950.
4. G.S. Nusinovich, G.P. Saraph, and V.L. Granatstein, *Phys. Rev. Lett.* 78, 1815 (1997).

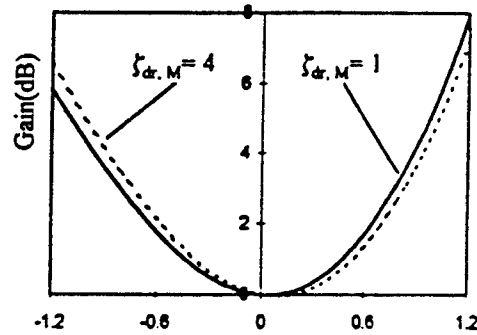


Figure 1.

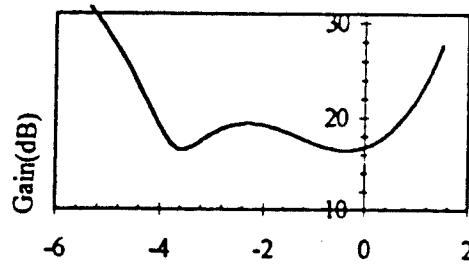


Figure 2.

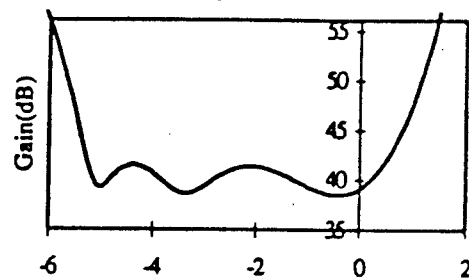


Figure 3.

## A High Performance, Frequency Doubling, Inverted Gyrotwystron

H. Guo, S.H. Chen, V.L. Granatstein, J. Rodgers, G. Nusinovich,  
B. Levush, M. Walter, and W.J. Chen

Institute for Plasma Research  
University of Maryland, College Park, MD 20742-3511, USA

### Abstract

Experimental results of a phase-coherent, harmonic multiplying inverted gyrotwystron (phigtron) are presented. Measured amplifier performance (30 dB, 1.3% bandwidth, 160 kW peak power, 25% maximum efficiency, Ku-band input and Ka-band output) implies that this gyrotron concept merits consideration for advanced radar applications.

### Introduction

This paper reports on the experimental study of a novel type of gyrotron amplifier which is a hybrid of a gyrotron traveling-wave tube (gyro-TWT) and a phase-locked gyroklystron oscillator with subharmonic injection [1] in a configuration of inverted gyrotwystron. Compared to the gyroklystron, it may have significantly wider bandwidth while maintaining a large gain due to replacing the input cavity with a traveling-wave interaction structure. The product of gain and bandwidth is an index of vital importance especially for radar applications.

### Description of the Device

The configuration of the inverted gyrotwystron is shown schematically in Fig. 1. The device uses a magnetron injection gun (MIG) to produce its electron beam. The drive signal is applied via a Ku-band (14-20 GHz) input coupler. By amplification of the drive wave through fundamental harmonic ( $s = 1$ ) cyclotron maser interaction in the TE<sub>22</sub> gyro-TWT section, the signal at harmonics of the drive frequency is nonlinearly generated in the electron beam. The amplified wave is absorbed in a matched load at the end of the gyro-TWT section, but all harmonic components in the beam current continue through into the drift section and further develop by ballistic bunching. Tuning is such that the second harmonic component reaches an optimum value

when the beam reaches the output cavity; there a cavity mode TE<sub>42 $\ell$</sub>  (axial eigennumber  $\ell = 1, 2, 3, 4, \dots$ ) is excited that is resonant at twice the frequency of the driving signal. This cavity mode rapidly grows through the second harmonic ( $s = 2$ ) cyclotron maser interaction. The Ka-band (28-40 GHz) output power is axially extracted and travels to the vacuum window while the spent beam dumps in the collector region. The growth process of harmonic components in the beam current is a nonlinear aspect of cyclotron maser bunching, and provides the basis for harmonic multiplication. This nonlinear behavior has been predicted by both particle-in-cell simulation and analysis to be published elsewhere [2, 3].

By simple nonlinear arguments, we obtained a relation between the drive signal phase,  $\phi_d$ , and the output signal phase,  $\phi_{out}$ , given by

$$\Delta\phi = \phi_{out} - 2\phi_d = \text{const.}$$

Thus, the output radiation of the phigtron can be phase-controlled by the drive source. When operating conditions are tuned below start oscillation, the device operates as a frequency multiplying amplifier, otherwise it is a phase-locked oscillator.

### Experimental Results

Although the inverted gyrotwystron was initially designed as a phase-locked oscillator, it can be operated as an amplifier by modifying the magnetic field profile so that the output cavity is detuned below the threshold of oscillation in the absence of an input signal. Measured saturated output power is plotted as a function of output frequency at the applied voltage of 58 kV and beam current of 9.2 in Fig. 2a. Measurements give ~33 dB gain and 1.3% continuous bandwidth (410 MHz) around 31.8 GHz as well as an amplification range of 820 MHz, from 31.33 GHz to 32.15 GHz, but with two narrow gaps

each about 50 MHz. Measured power is also plotted as a function of beam current at the same operating voltage of 58 kV for the sharp, high power spectral peak at 31,525 GHz, giving a value of 160 kW with corresponding efficiency of 25% and gain of 35 dB, as shown in Fig. 2b.

The input frequency of the amplifier is at exactly half of the output frequency, and the phase of the output signal was observed to be locked to twice the phase of input signal.

No spurious oscillation was observed, a fact we attribute to the merits of using both a relatively low order mode combined with the  $s = 1$  interaction in the input section and a vane mode filter in the output section. Based on the analytical theory [3], simulations using a smooth waveguide interaction circuit were performed. The main computational results for an ideal electron beam without velocity spread are shown in Fig. 2b for comparison with the measured data. The agreement between measured and theoretical amplifier efficiency is reasonable.

### Summary

In summary, we have demonstrated experimentally a highly overmoded, millimeter wave source in an inverted gyrotwistron configuration with frequency/harmonic multiplication and internal mode filters for stable operation. Amplifier peak power of 160 kW is achieved in the  $TE_{42}$  mode in a narrow peak around 31.525 GHz. Stable amplification is observed with a bandwidth of 1.3% and gain of 33 dB around 31.8 GHz. The measured gain-bandwidth performance is the state-of-the-art for a highly overmoded gyrotron amplifier operating at either the fundamental cyclotron frequency or the second harmonic of the cyclotron frequency. Future studies will look into the average power that can be achieved around 35 GHz and 94 GHz and into third and fourth harmonic operation.

### Acknowledgments

The authors thank D.S. Wu, Y.H. Mio, D. Cohen, and J. Pyle for their technical assistance, and acknowledge helpful scientific discussions with K.R. Chu, B. Danly, T. Antonsen, Jr., and A.T. Lin. This work has been supported by the DoD MURI program under AFOSR grant F4962001528306.

### References

1. H. Guo, Y. Carmel, and V.L. Granatstein, "Compact phase-locked harmonic gyrotron for modern millimeter wave radars," Conf. Digest, 15th Int. Conf. Infrared and Millimeter Waves, Orlando, FL, 1990, SPIE 1514, pp. 4-6.
2. K.R. Chu, H. Guo, and V.L. Granatstein, "Theory of the harmonic multiplying gyrotron traveling wave amplifier," to be published in Phys. Rev. Lett.
3. G.S. Nusinovich and M. Walter, "Theory of the Inverted Gyrotwistron," to be published in Phys. Plasmas.

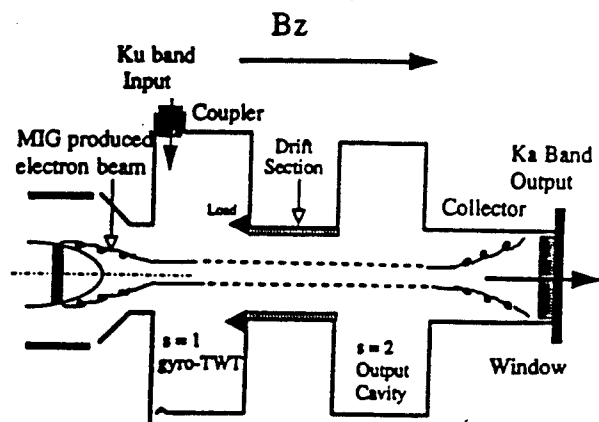


Fig. 1. Configuration of the phigtron.

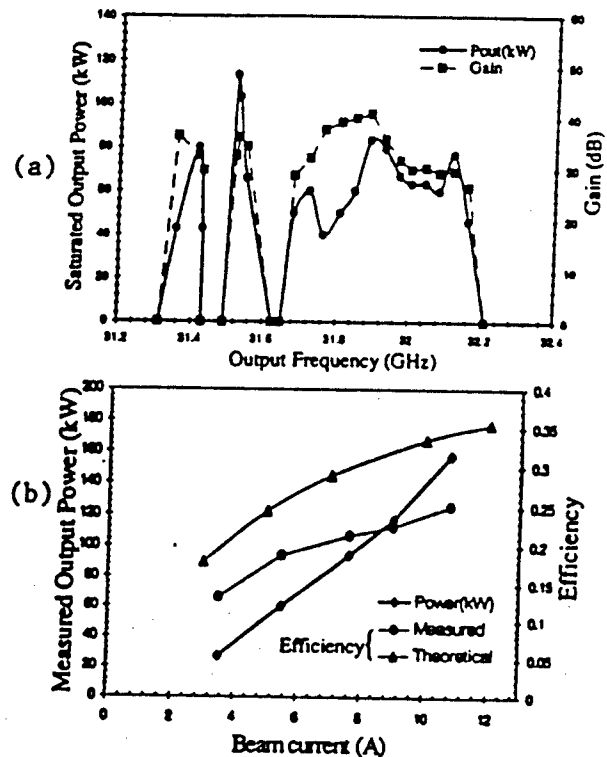


Fig. 2. Experimental and theoretical results of phigtron amplifier with  $TE_{42}$  mode output.

## Theory of the Inverted Gyrotwystron

G. Nusinovich, M. Walter, and V. Granatstein, IPR,  
University of Maryland, College Park, MD 20742

**Abstract:** The inverted gyrotwystron is a device consisting of the input waveguide, drift section, and output cavity. The traveling signal wave in the waveguide may induce a high harmonic content in the electron current density. Then the prebunched electron beam can excite phase-locked oscillations in the cavity at a harmonic of the signal frequency.

We have developed the formalism describing the operation of the inverted gyrotwystron at arbitrary harmonics. The operation of the input waveguide at the fundamental and the output cavity at the second harmonic was studied. It was shown that the electron prebunching in the input waveguide provides a better harmonic content than the ballistic prebunching in gyroklystrons. It was also shown that the dependence of the locking bandwidth on the input power is in qualitative agreement with the Adler's relation while quantitatively the bandwidth in our device is much larger due to prebunching. Degradation of efficiency and bandwidth by the electron velocity spread is dependent on the input waveguide and drift section lengths.

**General Formalism:** Within the input waveguide we can describe the interaction of electrons gyrating in a constant external magnetic field by three equations [1] characterizing the normalized energy, the phase of gyration which varies slowly with respect to the phase of the traveling wave, and the normalized wave amplitude.

In the drift region the electron energy remains constant because we assume that there are no microwaves, but ballistic phase bunching of electrons continues through the drift region due to the adjustments in energy which occurred in the input waveguide.

Finally, in the output cavity we have similar equations for the particles' energy and phase[2]. After integrating these equations one can calculate the susceptibility of the electron beam with respect to the resonator field. The time dependent amplitude and phase of the oscillations may be calculated once the susceptibility is known. For our simulations we assumed that the field distribution within the cavity was a Gaussian.

**Numerical Results:** We began our study by finding the optimal set of parameters which maximize the harmonic content in the electron current density,  $J_{1,2}$ . For an ideal beam the maximum growth rate of harmonics in the current density occurs at the exact cyclotron resonance.

The dependence of the first and second harmonics on the length of the input waveguide was then examined. Results are shown in Fig. 1. The maximum amplitude of

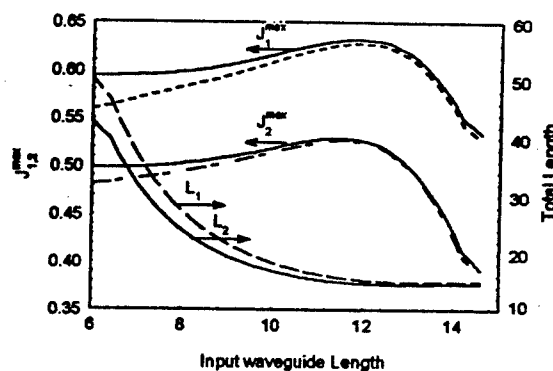


Figure 1. Harmonic current density,  $J_1$  and  $J_2$ , and total length as a function of input waveguide length.

the first and second harmonic of electron current density and the total length,  $L$ , required to reach that maximum are given as a function of the normalized input waveguide length. Dashed lines on the current density indicate the effect placing a lossy dielectric at the end of the input waveguide. From this it can be seen that the input waveguide may provide better maximum harmonic content (0.63 vs. 0.58 for  $J_1$ , and 0.53 vs. 0.49 for  $J_2$ ) than an input cavity. We determined that the second harmonic in current density degrades more quickly than the fundamental harmonic with velocity spread. Also the total optimum length decreases because of the strong effects of velocity spread on bunch formation.

In the output cavity we studied the temporal evolution of oscillations to determine the range of parameters for which stable phase-locked oscillations may be realized. Figures 2a and 2b show the temporal

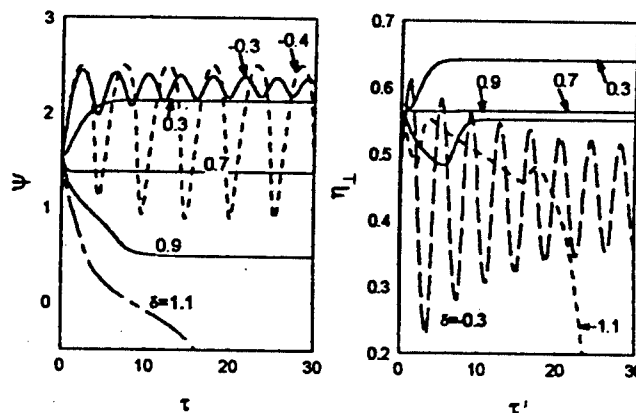


Figure 2a and 2b. Phase and orbital efficiency of oscillations in the output cavity for several values of frequency detuning,  $\delta$ .

evolution of the phase,  $\psi$ , and orbital efficiency,  $\eta_L$  for several values of frequency detuning,  $\delta$ , from the cold cavity eigenfrequency. A beating effect is seen at  $\delta = -0.4$  on the low end of the locking band. At  $\delta = 1.1$  oscillations decay at the upper end of the locking band resulting in a locking bandwidth from -0.3 to 1.0.

Figure 3 shows the dependence of the efficiency,  $\eta_L$ , on the input wave amplitude,  $F_0$ . The locking bandwidth

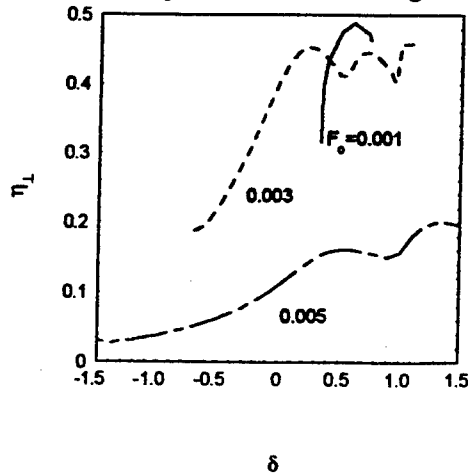


Figure 3. Dependence of the efficiency,  $\eta_L$ , on the input wave amplitude,  $F_0$ .

is characterized by the range of  $\delta$ 's plotted for each  $F_0$ . For this particular fixed value of input waveguide and drift section lengths  $F_0 = 0.001$  provides the maximum efficiency while larger input wave amplitude increases bandwidth and degrades efficiency due to electron overbunching.

The effects of input waveguide,  $L_{in}$ , and drift section,  $L_d$ , length on bandwidth and efficiency are shown in Figure 4. In this example the input wave amplitude is

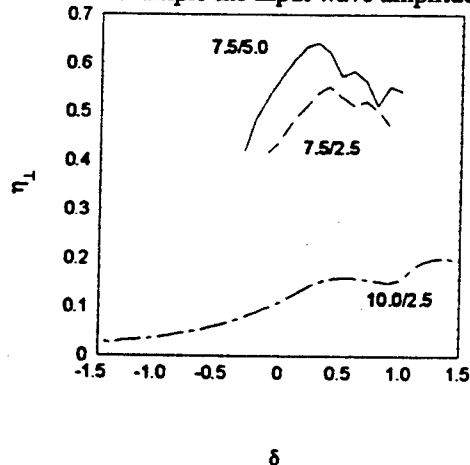


Figure 4. Effect of normalized input waveguide/drift section length on bandwidth and efficiency.

fixed at  $F_0 = 0.005$ . The choice of  $L_{in} = 7.5$  and  $L_d = 5.0$  produce the highest efficiency ( $\eta_L > 60\%$ ) and relatively large bandwidth. The maximum orbital efficiency of a

free-running oscillator with the same parameters of the resonator is only 45% [3,4].

Figure 5 presents the results of studies of the effect of velocity spread on efficiency and locking bandwidth. In

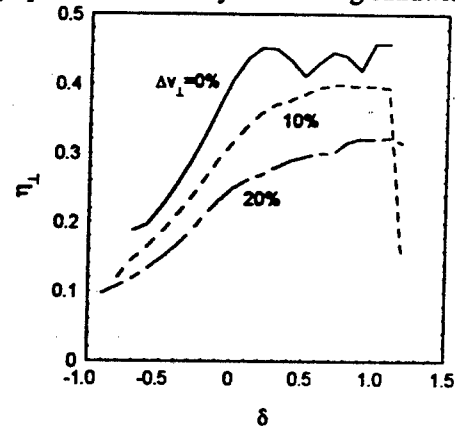


Figure 5. Effect of velocity spread on locking bandwidth and efficiency.

this example the velocity spread,  $\Delta v_L$ , relates to the RMS value,  $\sigma$ , by  $\Delta v_L = 2\sqrt{6}\sigma$ . In simulations with long input waveguides the velocity spread degrades efficiency to a greater extent than bandwidth as seen in Fig. 5. However, calculations done for shorter input waveguide lengths show small effects on efficiency and reductions in bandwidth by as much as a factor of two.

**Summary:** It has been shown that the electron prebunching in the input waveguide provides better harmonic content in the electron current density than the ballistic bunching which occurs in a short input cavity followed by a long drift region. It has also been shown that the efficiency and bandwidth are strongly dependent on the length of the input waveguide and drift section. Degradation of efficiency and bandwidth by the electron velocity spread is dependent on the input waveguide and drift section lengths.

**Acknowledgments:** This work was supported by the DoD MURI program under grant F49620-92-J-0152 and by the Vacuum Electronics Initiative under grant N0014941G036.

## References

- <sup>1</sup> G.S. Nusinovich and H. Li, IEEE Trans. Plasma Sci. 20, 170 (1992).
- <sup>2</sup> P.E. Latham, B. Levush, G. S. Nusinovich, and S. Parikh, IEEE Trans. Plasma Sci. 22, 818 (1994).
- <sup>3</sup> G.S. Nusinovich and R.E. Erm, Elektron Tekh., Ser. I, Elektron. SVCh, 55 (1972).
- <sup>4</sup> B.G. Danly and R.J. Temkin, Phys Fluids 29, 561 (1986).

# Gyro-TWT with a Helical Operating Waveguide: New Possibilities to Enhance Efficiency and Frequency Bandwidth

G.G.Denisov<sup>1)</sup>, V.L.Bratman<sup>1)</sup>, A.D.R.Phelps<sup>2)</sup>, and S.V.Samsonov<sup>1)</sup>

<sup>1)</sup>Institute of Applied Physics, Russian Academy of Sciences  
46 Ulyanov St., Nizhny Novgorod, 603600, Russia

<sup>2)</sup>Department of Physics and Applied Physics, University of Strathclyde,  
John Anderson Bldg., 107 Rottenrow, Glasgow, G4 ONG, U.K.

## Abstract

There is a possibility of providing almost constant group velocity and close to zero longitudinal wavenumber of a particular wave of a helical waveguide for a very broad frequency band. The use of such a waveguide as an operating section of the gyrotron traveling wave tube (gyro-TWT) allows significant widening of its bandwidth and increase in the efficiency at very large particle velocity spreads.

## Introduction

Numerous attempts to realize a gyro-TWT, combining a high efficiency (like the gyrotron-oscillators) with a high gain in a broad frequency band, meet a number of known difficulties (see, e.g. [1]). The most serious problems are linked with the fact that the longitudinal wavenumber of the operating mode and, correspondingly, the wave group velocity in gyro-TWT are significantly larger than those in the gyrotron. Correspondingly, the gyro-TWTs are sensitive to the spurious mode excitation at cutoff frequencies and to particle velocity spread causing large drop in the efficiency. According to Ref.[2] these problems can be avoided when using as a microwave system for a gyro-TWT an oversized waveguide with a special helical corrugation of the inner walls instead of a circular cylindrical waveguide. This helical corrugation couples two partial waves of a regular waveguide with the cutoff frequencies near and far below the operating frequency and makes a specific eigenwave dispersion. The first partial wave resonantly interacts with electrons and the admixture of the second wave makes the group velocity of the eigenwave non-zero. Changing the geometrical parameters of the corrugation one can control the eigenwave group velocity and adjust it to the longitudinal velocity of an electron beam for a rather broad frequency band around the point where the longitudinal wavenumber is equal to zero. These features allow very attractive regimes of gyro-TWT operation to be realized.

## Calculation and measurement of the helical waveguide dispersion

For a relatively small corrugation depth dispersion characteristics of the waveguide described above can be calculated from the coupled waves equations with the coupling coefficient found using perturbation theory. This

method was applied for the design of a second harmonic gyro-TWT driven by a thin solid electron beam encircling the axis of the operating waveguide. In such an amplifier the operating eigenwave is formed by the mutual scattering of counter-rotating  $TE_{2,1}$  and  $TE_{1,1}$  partial waves on the three-fold helical corrugation (Fig.1). The non-axisymmetrical corrugation strongly changes dispersion of the  $TE_{1,1}$  partial wave with a particular direction of rotation. Thus, a linearly polarized  $TE_{1,1}$  wave propagating through such a waveguide changes the direction of its polarization. This fact was used for measurement of the dispersion of the operating eigenwave (curve 1 in Fig.1). The dispersion of another eigenmode (curve 2 in Fig.1) was compared to the theoretical one by measuring eigenfrequencies of different longitudinal modes of a waveguide section. The calculated and measured dispersions are in good agreement.

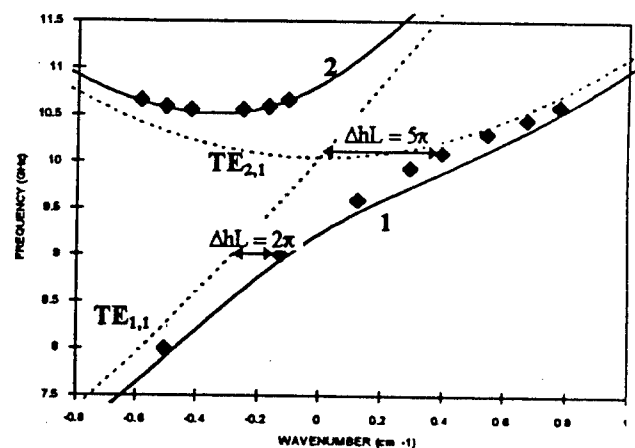


Fig.1. Dispersion of partial waves i.e. modes of a smooth waveguide (dotted line) and eigenmodes of the spiral waveguide (solid line); ◆ - results of measurement.

## Non-linear analysis for the second-harmonic gyro-TWT

The first calculations performed of efficiency and frequency band are encouraging. They show the possibility of high-efficiency and high-gain operation in a broad frequency band, even for very low electron beam quality. It is important to emphasize that at a relatively large coupling coefficient (corrugation depth) the operating eigenmode and the most



dangerous eigenmode for spurious excitation (curves 1,2 in Fig.2) are strongly separated. This allow an optimal interaction length to be chosen, and high efficiency and gain to be obtained simultaneously.

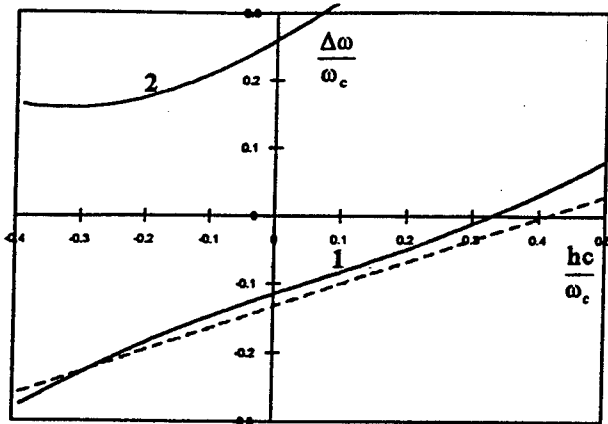
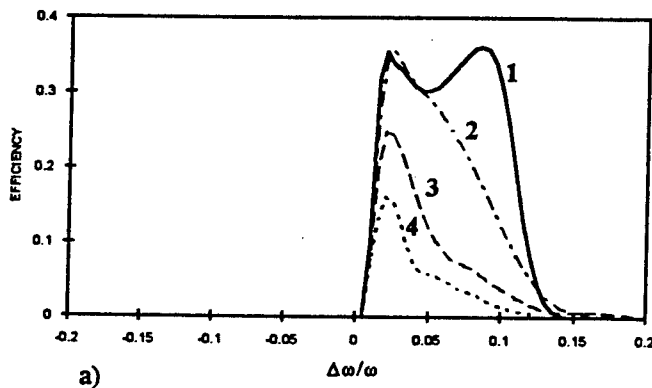
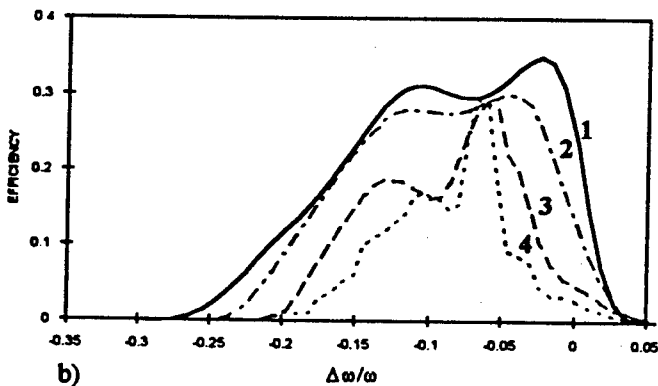


Fig.2 Dispersion of eigenwaves of the microwave system (solid line) and the electron beam (dashed line) for design of 80-keV gyro-TWT.

For subrelativistic electron energy (80 keV) the frequency band of the "helical" gyro-TWT can be significantly (almost two times) wider than that for the "smooth" gyro-TWT (Fig.3) which is provided by optimal adjustment of the



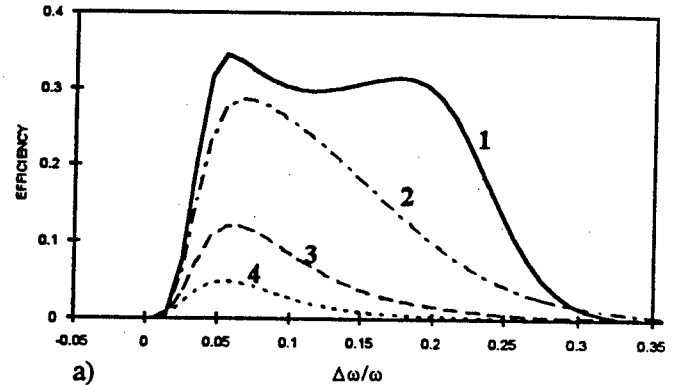
a)



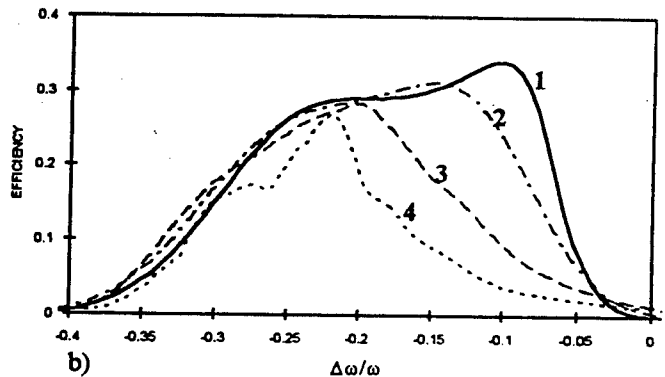
b)

Fig.3. Simulated bandwidths of gyro-TWTs with smooth (a) and helical (b) waveguides driven by a 80-keV, 20-A electron beam with the velocity ratio  $V_L/V_T=1.2$  for different transverse velocity spreads: 1 - 0%, 2 - 18%, 3 - 38%, 4 - 53%.

dispersion curves of the eigenwave and electron beam (Fig.2). For higher particle energy (300 keV) the main advantage of the "helical" gyro-TWT is a very weak sensitivity to the particle velocity spread (Fig.4). In the regime of maximal efficiency the calculated gain is 30 dB for 80-keV and 38 dB for 300-keV gyro-TWTs.



a)



b)

Fig.4. Simulated bandwidths of gyro-TWTs with smooth (a) and helical (b) waveguides driven by a 300-keV, 80-A electron beam with the velocity ratio  $V_L/V_T=1.2$  for different transverse velocity spreads: 1 - 0%, 2 - 18%, 3 - 38%, 4 - 53%.

## References

1. Wang Q.S., McDermott D.B., Luhmann N.C. Operation of a Stable 200-kW Second-Harmonic Gyro-TWT Amplifier, *IEEE Trans. on Plasma Science*, 1996, vol.24, No3, pp.700-706.
2. Denisov G.G., Cooke S.J. New Microwave System For Gyro-TWT. The 21st Int. Conf. on IR and MM Waves. Berlin, 1996. Conf. Proc. AT2.

# Design of an Efficient Broadband 250 kW Ka-Band Amplifier

W. Lawson, M. R. Arjona, and G. P. Saraph

Electrical Engineering Department and Institute for Plasma Research  
University of Maryland, College Park, MD 20742 USA.

## Abstract

We detail the stability and large signal properties of a hybrid slow wave / fast wave, second harmonic amplifier which utilizes a 75 kV, 8 A beam to produce a peak power in excess of 250 kW with an efficiency above 40%, a gain of 26 dB, and a bandwidth of over 5%.

## Introduction

There is currently considerable interest in broadband high power sources for radar applications near 35 and 95 GHz. At these millimeter wave frequencies, applications which require medium-to-high duty factors and peak powers above 50 kW can benefit greatly from the overmoded microwave circuits that are utilized in gyrotrons. In this paper we introduce a hybrid broadband amplifier which uses a slow wave circuit to bunch a linearly-streaming annular beam and then a tapered circular waveguide to extract the power. This device has many potential advantages over both conventional TWTs and gyro-TWTs. The hybrid device should be able to significantly exceed the maximum peak power performance of linear TWTs due to its overmoded output waveguide circuit. The electronic efficiencies simulated for the hybrid device are also typically much better than that achieved in moderate power linear TWTs. The bandwidth of the hybrid device should normally be higher than that which can be achieved in gyro-TWTs because the bunching process depends only on the dispersion relation of the slow-wave structure (SWS) and not on the relative detuning from the cyclotron frequency. Stability of the hybrid device should be considerably better than that of the gyro-TWT in the input section.

A schematic of this device is shown in Fig. 1. For simplicity, we assume the slow wave structure is an ideal sheath helix. The lowest-order axially-symmetric hybrid mode ( $HEM_{01}$ ) is assumed to be launched down the helix near the first cyclotron harmonic. At the end of the slow wave structure there is a drift section where additional ballistic bunching will occur. This region should be loaded with lossy material to isolate the two parts of the microwave circuit and serve as a well-matched termination to the SWS. The drift region is followed by a non-adiabatic magnetic transition which converts most of the axial momentum to rotational momentum. The transition width is typically minimized via the introduction of an iron pole piece. The magnetic field is not reversed, so the transition produces a small-orbit beam. This beam travels through a simple right circular waveguide with a modest taper in the wall radius and interacts with a

$TE_{02}$  traveling wave near the second harmonic. The output waveguide may also have a short sever region immediately following the pole piece to improve stability. In the following sections we describe the design method and results for a tube centered at 34 GHz.

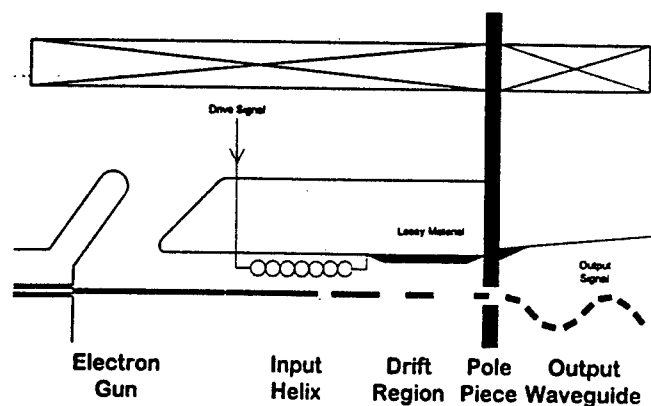


Fig. 1. Schematic of the hybrid system.

## Computer modeling

A single particle code is used to simulate the motion of the beam through the helix circuit, the drift region, and the non-adiabatic magnetic transition region. The magnetic field in this "bunching" code is assumed to be constant in the first two regions and to vary linearly in the transition region. The EM fields are given by the sheath helix approximation inside the helix and are assumed to be zero outside the helix region. Particles are "injected" over the relevant ranges in time and radial location. A predictor-corrector method is used to integrate the particles through the circuit.

The code used to model the output waveguide section is a gyrotwyston code that was modified to accept the angular phase distribution of particles that results from the bunching code. This efficiency code calculates the evolution of the amplified wave's phase self-consistently, includes the effect of the backward wave which arises from reflections at the end of the interaction region, and can take into account the deleterious effect of a single spurious mode that may exist in the output waveguide.

Finally, the start-oscillation code calculates the threshold reflection coefficient for the onset of instabilities as a function of frequency and beam current. The code utilizes the same magnetic field profile and waveguide geometry as the large signal code. Reflection coefficients below this threshold will

be zero drive stable; coefficients above the threshold may still result in stable operation when the drive signal is applied.

### Design results

The parameters of the design are given in Table 1. The average radius is given before the magnetic transition and the velocity ratio after the transition. The total length of the input section is 20 cm. The total beam power is 600 kW. Most of the simulations were performed with an ideal beam, but effects of beam thickness and velocity spread were investigated in the bandwidth studies.

The stability of the output waveguide, assuming the drive power is turned off, is given in Fig. 2. The left curve shows the threshold for the reflection coefficient as a function of frequency for the operating mode and indicates that it must be below about 1.5% near 33.2 GHz. A similar restriction is placed near 31.7 GHz for the nearest competing mode, though slotting the output waveguide should help suppress this mode by interrupting wall currents without interfering with the operating mode.

The optimal results are indicated in Table 2. A peak power of over 250 kW was achieved at 34.2 GHz. The dependence of efficiency on drive frequency is indicated in Fig. 3 for several beam widths. Bandwidth and efficiency performance are seen to degrade only slowly with beam thickness.

Table 1. System design parameters.

Beam Parameters	
Voltage (kV)	75
Current (A)	8
Average radius (cm)	0.55
Beam thickness (mm)	0.00
Velocity ratio ( $v_{\perp}/v_z$ )	2.00
Magnetic Field Parameters	
Input circuit field (kG)	3.30
Drift tube (sever) length (cm)	11.0
Magnetic transition width (mm)	2.0
Output circuit field (kG)	6.62
Output field taper (%)	-9.4
Input Circuit	
Center frequency (GHz)	17.1
Operating mode	HEM <sub>01</sub>
Helix radius (cm)	1.75
Wall radius (cm)	2.00
Length (cm)	9.0
Pitch angle (degrees)	29.0
Output circuit	
Initial wall radius (cm)	1.01
Final wall radius (cm)	1.025
Waveguide length (cm)	17.50
Output waveguide mode	TE <sub>02</sub>
Taper angle (degrees)	0.05

Table 2. Predicted output performance for the ideal beam.

Input circuit result	
Input drive power (W)	540
Drift region results	
Total $\Delta v_z$ (%)	4.99
Total $\Delta v_{\perp}$ (%)	0.09
Energy spread (%)	2.40
Output circuit results	
Center frequency (GHz)	34.2
Instantaneous bandwidth (%)	5.7
Maximum power (kW)	253
Peak efficiency (%)	42.1
Peak gain (dB)	26.7

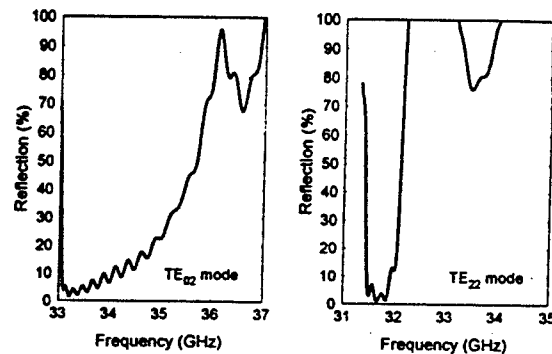


Fig. 2. Output waveguide stability curves.

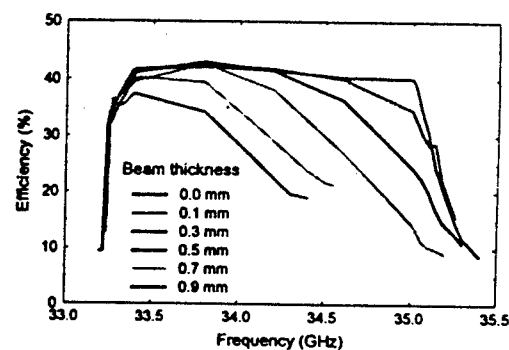


Fig. 3. Output efficiency curves as a function of beam thickness. The perpendicular velocity spread is 4% at a beam thickness of 0.9 mm.

### Acknowledgements

This work was supported by the Tri-Services Program.

# Study of Transient Effects in Injection-Locked Gyrotrons

J. Jelonnek and K. Schünemann

Technische Universität Hamburg-Harburg  
Arbeitsbereich Hochfrequenztechnik, D-21071 Hamburg, Germany

## Abstract

A self-consistent time-domain analysis which rigorously describes the transient response is applied to study transient effects in injection-locked gyrotrons. The stable locking range, the transient response, and the steady-state multi-frequency operation are studied. Simulated results for a 35 GHz gyrotron are compared with well-known Adler theory and with measured data. Variations in the design parameters of the gyrotron are simulated and their influence on the transient response and the locking range is presented.

## Introduction

In addition to plasma heating, gyrotrons can be applied in high-power radar transmitters and for particle acceleration [1], [2]. These applications require coherent, phase controlled radiation what can be achieved by injection locking [3], [4]. For injection locking, important system parameters are the stable locking range, the transient response, and the steady-state phase shift between the injected and the oscillator output signal. Furthermore, the influence of fluctuations of the beam voltage during operation [4], [5] on the dynamic behaviour and on the locking range should be known.

Fundamental theoretical work on injection locking has been published by Adler [6] who modeled a general nonlinear oscillator circuit with lumped elements and calculated the stable locking range. An equation for the transient response of the phase shift  $\Delta\phi(t)$  between the injected signal and the output signal has been presented in [7] for the lumped oscillator model. Application of the results of [6] and [7] to gyrotrons may give a first estimate on their limits on locking range and on the possible modulation rate.

A self-consistent multi-mode time-domain analysis [8] is extended here to the calculation of phase locking by direct injection in order to describe the locking process accurately in time-domain. This analysis, whose basic principle has been presented in [9], is based on an expansion of the electromagnetic field with respect to the solenoidal and irrotational eigenfunctions of the corresponding completely shielded resonator.

## Numerical Results

Simulations have been performed for a 35 GHz single cavity gyrotron presented in [3] with a direct injection signal at the output port. This signal is supposed as  $TE_{01}$  waveguide mode entering the interaction space. Fig. 1 shows the stable locking range

$\Delta f = f_i - f_0$  versus injected power. Results agree even quantitatively with those from Adler's theory and with measured data presented in [3]. The frequency spectrum of the unlocked driven gyrotron has the same characteristics as that of an unlocked-driven oscillator presented in [10]. Details encompass the asymmetry in the frequency response with respect to  $f_0$ , the lack of the line at  $f_0$ , as well as the dependence of  $\Delta f'$  defined as distance between neighbouring frequency lines, on  $\Delta f$  and on the maximum  $\Delta f$  for which locking still occurs.

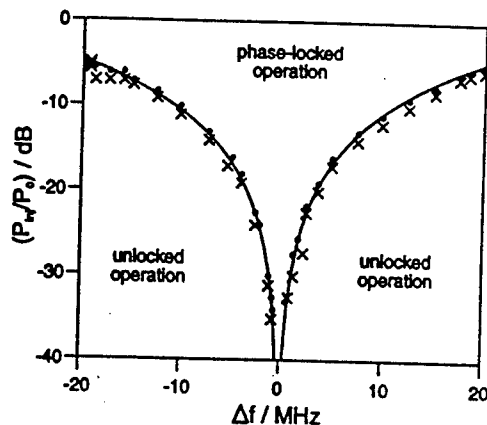


Fig. 1: Stable locking range of the 35 GHz gyrotron [3]

- : Predicted by Adler's theory
  - x : Unlocked operation
  - : Phase-locked operation
- } Simulation

Fig. 2 shows a simulated transient response of amplitude and phase shift of the excited  $TE_{01}$ -waveguide mode at the output port of the gyrotron when an injection signal is switched-on and switched-off after 600 ns. The transients allow to determine the transit times. Furthermore, Fig. 3 shows transient responses of  $\Delta\phi(t)$  for different initial phase shifts  $\Delta\phi_0$ . The steady-state phase shift  $\Delta\phi_\infty$  is independent from the initial phase-shift  $\Delta\phi_0$  what agrees with experimental observations made in [3]. Other simulation results show that  $\Delta\phi$  strongly depends on the amplitude of the injected signal and on  $\Delta f$ . The range of  $\Delta\phi$  is within  $\pm 90^\circ$ , depending on whether  $\Delta f$  is positive or negative what has also been predicted from the lumped oscillator model [6]. Fig. 3 also contains transient responses which have been derived from the heuristic equations given in [7]. These responses agree well with our rigorous calculations in particular for lower  $\Delta\phi_0$ . The main difference is a small shift in the predicted  $\Delta\phi_\infty$ . Hence it is possible to use [7] for both a fast estimate of the maximum modulation rate and of the steady-state phase shift of a phase-locked gyrotron.

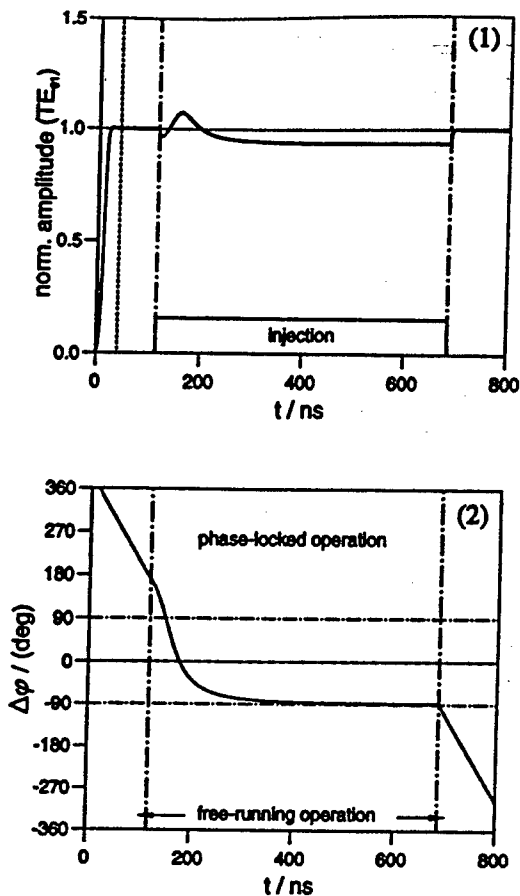


Fig. 2: Transients of amplitude and phase shift  $\Delta\phi$  of outgoing  $TE_{01}$ -waveguide mode for switching on injection after 100 ns and switching it off after 600 ns. ( $\Delta f \approx +5$  MHz,  $P_i/P_0 = -16$  dB)  
(1) : Amplitude, (2) : Phase shift  $\Delta\phi$

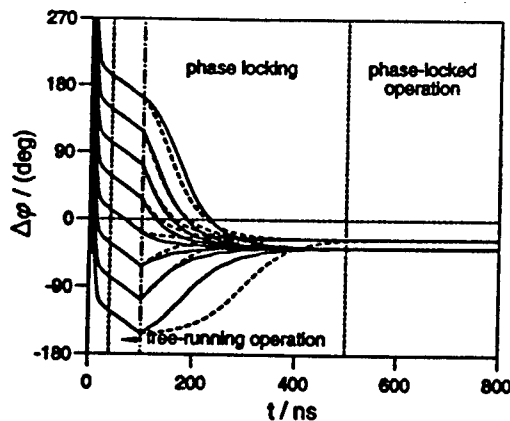


Fig. 3 : Transients of  $\Delta\phi$  for different initial phase shifts  $\Delta\phi_0$ . ( $\Delta f \approx +1.5$  MHz,  $P_i/P_0 = -20$  dB)  
— : Simulation  
-- : Lumped oscillator approximation [7]

Fig. 4 shows the transient response of  $\Delta\phi(t)$  for varying the beam voltage and at different locking gain. The beam voltage is assumed to vary in a typical range of  $\pm 1\%$ . The transient response, the steady-state phase shift, and the locking range can be obtained from such calculations.

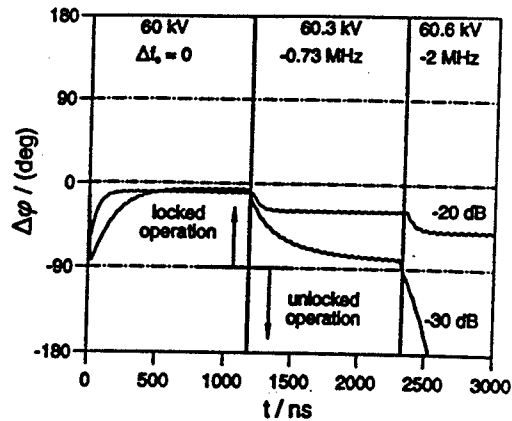


Fig. 4: Transient of  $\Delta\phi$  for a detuned beam voltage. ( $\Delta f = f_i - f_0|_{60kV} \approx +50$  kHz)  
 $\Delta f_0$  : Change of  $f_0$  for detuned beam voltage  
Parameter is the locking gain

## Conclusions

In this contribution, a self-consistent multi-mode time-domain analysis is applied to simulate injection locking of a gyrotron. Transient response, non-locked state, steady-state phase shift, and stable locking range are extensively studied and a good agreement to results is found, which can be derived from Adler's lumped oscillator model. The results also agree with measured data. Fluctuations or variations in the design parameters of the gyrotron are also treated.

## Acknowledgement

The authors are indebted to the Deutsche Forschungsgemeinschaft for financial support.

## References

- [1] Granatstein V. L., *Int. J. Electronics*, vol. 57, no. 6, 1984, pp. 787-799.
- [2] Gaponov-Grekhov A., Granatstein V. L., Pittsburgh, PA.: Artech House, 1994.
- [3] Read, M. E., Seeley R., Manheimer W. M., *IEEE Trans. Plasma Science*, vol. PS-13, no. 6, 1985, pp. 398-403.
- [4] Guo H., et al., *IEEE Trans. Plasma Science*, vol. PS-23, no. 5, 1995, pp. 822-832.
- [5] Latham P. E., Granatstein V. L., Carmel Y., *Int. J. Infrared Millimeter Waves*, vol. 14, no. 6, 1993, pp. 822-832.
- [6] Adler R., *Proc. Inst. Radio Engrs.*, vol. 34, pp. 351-357, 1946, pp. 822-832.
- [7] Mackey R., *IRE Trans. Microwave Theory Techniques*, vol. MTT-34, 1962, pp. 228-235.
- [8] Jöstingmeier A., Rieckmann C., Omar A. S., *Proc. IEEE MTT-S Symp. (Orlando)*, 1995, pp. 821-824.
- [9] Jelonnek J., Schünemann K., *Proc. 21st Int. Conf. Infrared Millimeter Waves (Berlin)*, 1996, p. AM-7.
- [10] Dekleva, J., *Proc. IEEE*, vol. 60, 1972, pp. 135-136.

# The Microwave Sintering of Ceramics: New Insights, Models, and Applications Based on Realistic Ceramic Microstructures

J.P. Calame, Y. Carmel, D. Gershon, and E. Pert

Institute for Plasma Research  
University of Maryland, College Park, MD, 20742

## Abstract

The distribution and intensity of electric fields within a ceramic undergoing microwave sintering are computed using finite difference electromagnetic modeling of realistic ceramic microstructures. The fields in the air-filled pores adjacent to interparticle contact zones are found to be 10-60 times higher than the applied fields by virtue of focusing effects within the microstructure. The high fields are postulated to be capable of creating discharge phenomena within the pores, which could cause enhanced sintering by altering the material defect chemistry.

## Introduction

The use of microwave radiation for the processing of advanced ceramic materials is emerging as a viable alternative to conventional methods. The direct, volumetric nature of the microwave heating scheme allows the achievement of extremely high heating rates (150 to perhaps 1000 °C/min) or selective heating in multiphase systems, which can lead to novel ceramic materials with compositions and microstructures not achievable by other means. This would include nanograin materials, tailored microstructures, and new types of composites. The thermal, mechanical, and electrical properties of the unique ceramics produced by microwave sintering should find application in areas of commercial interest, such as high temperature, toughened, or lightweight structural and wear resistant components, transparent polycrystalline ceramic armor, and tailored grain-boundary electronic materials such as chemical sensors.

During microwave sintering, the electric field distribution within a ceramic body on a macroscopic scale is determined by a combination of the operating frequency, the sample and applicator shape, the manner in which the electromagnetic waves illuminate the sample, and the sample permittivity and permeability. Within the sample, the spatial variation of the electric field occurs on length scales comparable to the wavelength or skin depth of the electromagnetic waves within the ceramic. However, this is only true if one is considering the variation of fields over volumes much larger than the characteristic feature sizes of the microstructure (i.e. grain sizes, rough surfaces of grains, and inter particle contact zones). Within the microstructure itself the electric field exhibits violent variation in magnitude and direction. Furthermore, the electric field in certain areas of the pores in a realistic microstructure can be orders of magnitude stronger

than the spatially averaged electric field. Such field enhancements could create ionization and discharge phenomena in the pores at atmospheric pressure [1], leading to unexpected changes in the material chemistry.

In this paper, calculations of electric field distributions within ensembles of ceramic particles interconnected by spherical necks will be presented and used to justify the claim that discharges could form in localized areas within the pores during ordinary microwave sintering. Implications of this localized discharge/ionization hypothesis on sintering dynamics will also be discussed, based on studies in the literature.

## Average vs. Local Fields in Porous Ceramics

In a volume of material undergoing microwave sintering, the electric field present within a volume  $V$  can be expressed in terms of a rate of energy absorption and thus an experimentally observable temperature rise  $dT/dt$ . The governing relation is

$$c\rho_m V \frac{dT}{dt} = \frac{1}{2} \omega \epsilon_0 \int_V \epsilon'' |E_l|^2 dV \xrightarrow{V \text{ large}} = \frac{1}{2} V \omega \epsilon_0 \epsilon_m'' |E|^2 \quad (1)$$

where  $\rho_m$  is the mass density,  $c$  is the specific heat,  $\omega$  is the frequency,  $\epsilon_0$  is the permittivity of free space,  $\epsilon''$  is the imaginary part of the relative permittivity of the differential integration volume  $dV$ , and  $E_l$  is the electric field inside  $dV$ . If the volume of interest is considerably larger than the size scale of the individual microstructure elements, then one can recast the RHS in terms of  $\epsilon_m''$ , an effective imaginary permittivity of the heterogeneous mixture consisting of ceramic and air, and a spatially averaged electric field amplitude  $E$ . To determine the local electric field  $E_l$  within a microstructure characterized by average field  $E$ , in general it is necessary to examine the electromagnetic behavior on scales much smaller than that of the macroscopic ceramic and perform a finite difference or element simulation of a realistic microstructure. In some cases an analytic solution is possible for the relation between the ceramic fields and the pore (air) fields on these very small scales. For example, if layers of air and ceramic are oriented in planes perpendicular to the applied field, the field inside the ceramic is  $1/\epsilon$  lower than the field in the air due to continuity of normal electric displacement.

However, in some very common microstructures the fields inside certain regions of the ceramic grains can become essentially equal to the highest fields in the pores, and both of these quantities can greatly exceed even the applied electric field. This occurs when the geometry is such that the continuity of tangential electric field is more relevant, such as in a thin ceramic rod oriented parallel to the applied field. Similarly, the nearby dielectric geometry can also act to focus the field, as sort of an electrostatic lens. Such configurations occur naturally in ceramics, such as in the joining of two or more ceramic spheres by spherical contact necks shown in Fig. 1. This is the characteristic microstructure present in a ceramic undergoing any form of sintering. The neck radius of curvature  $\rho$  is given by  $x^2/(2R)$ , where  $x$  and  $R$  are neck and sphere radii.

We have performed finite quasi-electrostatic difference simulations of the structure in Fig. 1 in three dimensions for a variety of angles  $\theta$ , where  $\theta$  is the angle between the principle axis joining the spheres and the direction of the applied field  $E_a$  [2]. In this finite difference procedure a model space is created from simulation cells that are filled with either air or ceramic to form the desired microstructure, and appropriate permittivities are assigned to cells. Quasi electrostatic simulations are justified since at frequencies in the 1-30 GHz range, the wavelengths and skin depths in typical dielectrics are of the order of millimeters compared to microstructure elements on the scale of microns. The non-zero frequency regime is handled through the use of complex permittivities and potentials. An applied electric field is created by assigning a potential of zero on the bottom of the model space, and a potential of one at the top (opposite face). Mirror boundary conditions are applied to the other four sides. Internal potentials are found at the vertices that define each cell by iteration, and electric fields are computed afterwards from potential gradients.

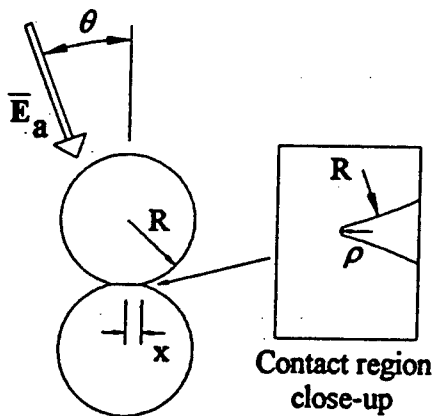


Figure 1. Diagram of the spherical neck geometry

In these simulations uniform cubical mesh cells were used, and the model space was composed of  $32 \times 64 \times 64$  ( $x, y, z$ ) cells. The geometry was constructed such that the center of the contact region was located at the model space center ( $x=16$ ,  $y=32$ ,  $z=32$ ), the applied field was directed along the  $z$  axis,

and the axis of joining was located in the  $y-z$  plane (making an angle of  $\theta$  with respect to the  $z$ -axis). Spheres of radius  $R = 14$  were used, and the inter-sphere separation was chosen to give a neck radius  $x$  equal to  $0.26R$ . To study two representative materials, dielectric permittivities representative of either hot  $\text{Al}_2\text{O}_3$  at 35 GHz ( $\epsilon = 10 - 1.0j$ ) or hot  $\text{ZnO}$  at 2.45 GHz ( $\epsilon = 40 - 20j$ ) were used for the ceramic cells. For  $\theta = 0^\circ$ , intensified fields inside the ceramic are found throughout the circular inter-particle contact zone, with the highest fields located directly adjacent to the outer circumference of the neck. The peak internal fields are significantly greater than the applied field. Lesser peak intensities, with a similar spatial pattern within the neck, are found for other values of  $\theta$ . A plot of this effect for the neck region in two materials is shown in Fig. 2. For the case with  $\theta = 90^\circ$ , the peak field in the neck region is less than the applied field and less than the spatially averaged field throughout the volume of ceramic. The peak external field (in air-filled pores) follows a similar pattern as a function of  $\theta$ , but the intensification values are about twice as large.

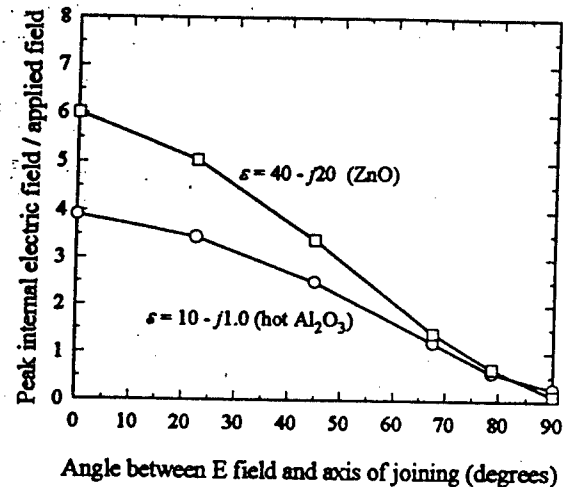


Figure 2. Results of simulations for internal fields

For the case with  $\theta = 0^\circ$ , a variable mesh, 2D axis-symmetric simulation of high accuracy was performed, and the results are shown in Fig. 3. The simulations typically used 230 radial cells by 170 axial cells, with a great concentration of cells in the neck region to accurately model the radius of curvature  $\rho$  in Fig. 1. The agreement between these more accurate simulations and the 3D versions is quite good at  $x/R = 0.26$ . At smaller ratios of  $x/R$  the field intensification increases dramatically. For  $\text{Al}_2\text{O}_3$ , peak internal fields for relevant values of  $x/R$  are 3-8 times larger than the applied field, and in  $\text{ZnO}$  the intensification factor is 10-30 times. The ratio of the deposited power density (proportional to  $\epsilon'' E^2$ ) at the peak field location divided by the average power density in the entire ceramic portion of the model is also plotted in Fig. 3. This is an important curve, since the spatially averaged  $E^2$  in the ceramic grains by themselves is directly related to the average power density and thus the heating rate, and it can be calculated from

experiments. Knowing this, the peak field in the ceramic due to intensification can be determined from the plots, as well as the peak external field. For  $\text{Al}_2\text{O}_3$  local power densities can be 100 times greater than the average value, and in ZnO the factor is over 4000. These factors far exceed previous estimates [1, 3]. Corresponding peak external fields were found to be in the range of 10-15 higher than the applied field for  $\text{Al}_2\text{O}_3$  and 30-60 for ZnO.

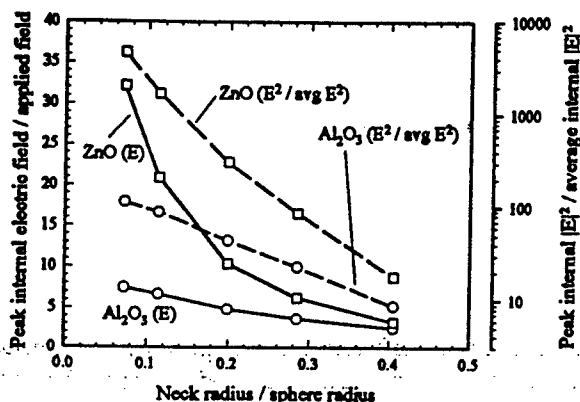


Figure 3. Results of variable mesh simulations for  $\theta = 0$ .

### Possible Effects of Localized Field Intensification

One of the advantages of microwave heating is rapid processing, made possible by the direct, volumetric nature of the absorption process. Microwave sintered materials are typically heated at rates ranging from a modest  $20^\circ\text{C}/\text{min}$  to  $150^\circ\text{C}/\text{min}$  or more. Even at high temperatures, many materials that have been processed with microwaves, such as relatively high purity  $\text{Al}_2\text{O}_3$  or  $\text{AlN}$ , have relatively small absorption ( $\epsilon''$  in the range of 0.01 to 0.1). Applying Eq. 1 to typical ceramic bodies indicates that average fields within the ceramic body are in the range 0.5 to 1.0 kV/cm for a  $50^\circ\text{C}/\text{min}$  heating rate. Under these same conditions, the field intensification calculations outlined above indicate that peak fields in the regions of the pores closest to the interparticle contact necks (the peak external field in the above discussion) can easily be as high as 10-50 kV/cm. These fields are in the general range required to trigger unintentional electrical discharges and ionization in the ambient atmospheric-pressure processing gas present in the pores inside the object being processed [1], without any external breakdown in the processing chamber. As a result of these calculations, we hypothesize that atmospheric-pressure microwave sintering at modest to high heating rates involves plasma-ceramic interactions which are not apparent from the macroscopic conditions surrounding the sample during processing.

Deliberate, macroscopic-scale microwave-induced plasma sintering of ceramics at reduced pressures has been shown to exhibit altered sintering characteristics compared to conventional sintering, including athermal effects [4]. Such effects have been carefully documented in aluminum oxide processed in an oxygen plasma, and include enhancement in

the sintering rate associated with differences in the pre-exponential term of the diffusion coefficient [4]. The researchers involved in this  $\text{Al}_2\text{O}_3$  study proposed that the enhancement results from an increased concentration of aluminum interstitials by the stripping of  $\text{O}^{2-}$  from the surface by bombardment by  $\text{O}^+$  from the plasma. Higher sintering rates were observed at lower gas pressures, which is consistent with the  $\text{O}^+$  induced stripping hypothesis since there is a greater ratio of  $\text{O}^+$  to  $\text{O}_2$  in the plasma as the total pressure drops. The results are quite dramatic; an order of magnitude increase in the sintering rate was observed as the pressure dropped from 2.4 to 1.1 kPa. The sintering rate of  $\text{Al}_2\text{O}_3$  in conventional furnaces is also known to have a dependence on the partial pressure of oxygen in the process gas, but the effect is only a factor of 2.25 over seven orders of magnitude change in partial pressure. In summary, the microwave plasma-sintering process offers the possibility of much more rapid sintering compared to conventional means, and apparently the only role of the microwaves is to create the plasma rather than cause mysterious "microwave effects" by unknown means.

When one considers the possibility of localized discharges within the pores of a ceramic undergoing ordinary (atmospheric pressure) microwave sintering, caused by electric field intensification, one can argue that some of the reported changes in sintering and grain-growth kinetics in microwave processing [5] could actually be caused by plasma effects. Since the electric field intensification in a porous ceramic is at its maximum when the spheres are in poor contact with each other (early in the sintering process when values of  $x/R$  for the necks are small), one would expect reports of enhanced sintering in microwave processed ceramics to occur at the early and intermediate stages of sintering, rather than near full density. This is exactly what is reported in the literature [6]. Furthermore, there is often poor reproducibility of such "microwave effects", which could conceivably be linked to variability in discharge conditions related to surface roughness of the particles, grain size, and the exact values of applied field created by the applicator.

This work was supported by the AFOSR/MURI program on high power microwaves and an ARO STIR.

### References

- [1] T. Saji, *Mat. Res. Soc. Proc.* 430, 15 (1996).
- [2] J.P. Calame, K. Rybakov, Y. Carmel, and D. Gershon, *Ceramic Trans.* 80, to be published (1997).
- [3] T.T. Meek, *J. Mat. Sci. Lett.* 6, 638 (1987).
- [4] D.L. Johnson and H. Su, *Mat. Res. Soc. Proc.* 430, 629 (1996).
- [5] T.T. Meek et. al, *J. Mater. Sci. Lett.* 7, 928 (1988)
- [6] M.A. Janney and H.D. Kimrey, *Ceramic Trans.* 1, 919 (1988).



# Millimeter-Wave Sintering of Ceramic Compacts

A. W. Fliflet, R. W. Bruce, R. P. Fischer, and A. K. Kinhead  
Plasma Physics Division

D. Lewis, III, B. A. Bender, G.-M. Chow and R. J. Rayne  
Materials Science and Technology Division

L. K. Kurihara and P. E. Schoen

Center for Biomolecular Science and Engineering

Naval Research Laboratory

Washington, DC 20375-5000 U.S.A

## Abstract

Millimeter waves couple more strongly than conventional microwaves to low-absorption ceramics such as pure oxides, eliminating the need for auxiliary heating at low temperatures. This paper presents 35 GHz sintering data obtained at NRL, using a gyrotron-powered furnace, for fine-grain (submicron) alumina compacts and compares our data with results from other high frequency microwave and conventional sintering studies.

## Introduction

The use of microwaves for heating, sintering/densification, and annealing of ceramic powders and compacts has several advantages, particularly the ability to deposit energy volumetrically in the sample, and the possibility of rapid heating and cooling profiles. The possibility of more rapid densification compared to conventional methods is expected to result in reduced grain growth and improved material properties [1]. The development of powerful gyrotrons has opened up the millimeter-wave regime ( $\geq 24$  GHz) for processing ceramic materials. Millimeter waves couple more strongly than conventional microwaves to low-absorption ceramics such as pure oxides, eliminating the need for auxiliary heating at low temperatures, and highly uniform fields intensities can be achieved in compact overmoded cavity applicators. A number of low and high frequency microwave sintering studies have been reported [2-4], and the results have generally indicated that sintering proceeds much faster in microwave furnaces when compared to conventional furnaces, and that densification may occur at lower temperatures. Lower sintering temperatures are desirable for minimizing grain growth that usually has a negative effect on the mechanical properties of ceramics. The significant temperature differences observed between conventional and microwave sintering in some studies [2] has motivated the search for a non-thermal microwave enhancement effect that could preferentially drive the sintering process [5]. To assess the potential of high frequency microwave sintering, and to investigate the possibility of a specific microwave mechanism, the Naval Research Laboratory (NRL) has recently undertaken a systematic study focused on alumina because of

its industrial importance, large data base, and challenging microwave properties. This paper presents 35 GHz sintering data obtained at NRL for fine-grain (submicron) alumina compacts and compares our data for densification as a function of temperature with results from other high frequency microwave and conventional furnace sintering studies.

## 35 GHz Pulsed Gyrotron-Powered Furnace

A schematic of the pulsed 35 GHz gyrotron-powered furnace and diagnostic system is shown in Fig. 1. A high pulse repetition rate gyrotron of standard design operates in the  $TE_{01}$  circular waveguide mode at a voltage of 70 kV, currents up to 10 A, and pulse lengths up to 15  $\mu$ s. The gyrotron system was originally developed for high power microwave effects testing at NRL and has been modified for material processing applications. The peak pulsed power of the gyrotron is about 80 kW and the maximum duty factor is 0.5% corresponding to a maximum average output power of 400 W. The gyrotron output efficiency is 20-30% and the average power is controlled by varying the PRF.

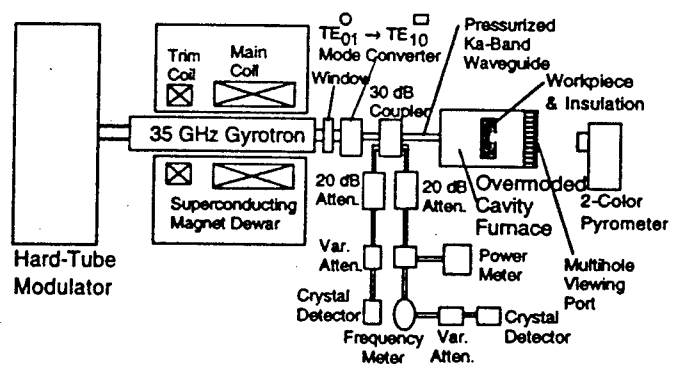


Figure 1: Schematic of 35 GHz pulsed gyrotron with multimode resonator furnace.

After exiting an alumina output window, the microwave power passes through a mode converter that transforms the  $TE_{01}$  circular waveguide mode into the  $TE_{10}$  mode in rectangular Ka-Band waveguide. The power is then

transported to the cavity applicator and monitored using standard Ka-band waveguide components pressurized with  $\text{SF}_6$  or  $\text{N}_2$  gas to  $\sim 2$  atm. to avoid microwave breakdown. The cylindrical, highly overmoded cavity applicator (18 cm dia., 21 cm height) may be isolated from the rest of the waveguide system, allowing a choice of sintering atmospheres. As shown in Fig. 1, the system is operated without a circulator to absorb power reflected from the applicator; however, this power does not significantly impact the operation of the gyrotron at the present power levels. In any case, the reflected power is quite low at sintering temperatures. Typical measured power reflection coefficients include:  $R \sim 0.13$  for the empty cavity,  $R \sim 0.05$  when the cavity contains a casket and compact at room temperature, and  $R \sim 0.01$  when the compact is hot.

### Experimental Results

Results for high frequency microwave sintering of compacts pressed from Sumitomo AKP-50 alumina, a sub-micron grain-size  $\alpha$ -phase powder, are shown in Fig. 2, which compares our 35 GHz results with the 28 GHz data obtained at Oak Ridge National Laboratory (ORNL) [2], and the 60 GHz data obtained by Meek et al. [3] in a collaboration between Los Alamos National Laboratory and Varian (LASL/Varian). For comparison, the figure also shows conventional furnace sintering data for 60 minute hold time obtained at ORNL and NRL. All the NRL compacts underwent rapid heating and cooling without cracking. The NRL microwave results include 5 and 60 minute hold time data, and the LANL/Varian hold times at high temperature were 1–5 minutes. The ORNL hold time was 60 minutes. The NRL and LASL/Varian compacts contained no additives, while the ORNL compacts contained 0.1% wt. MgO, a grain growth inhibitor. The ORNL and LASL/Varian compacts were processed in vacuum, while the NRL compacts were processed in pressurized air or nitrogen.

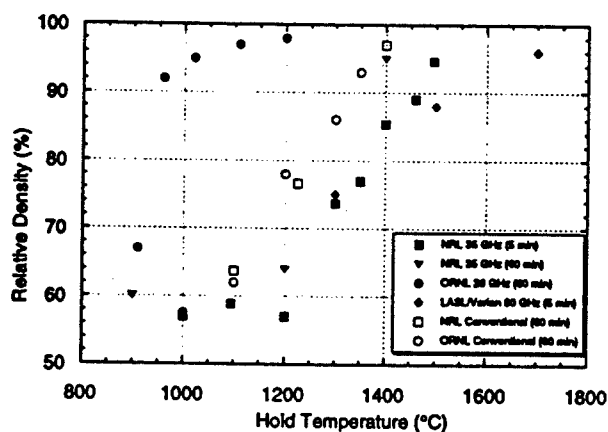


Figure 2: Densification of Sumitomo AKP-50 alumina compacts by millimeter-wave and conventional pressure-free sintering.

As shown in Fig. 2, there is good agreement between the NRL and ORNL conventionally sintered compacts, in-

dicating that the sintering atmosphere and additives have little effect on the temperature dependence of sintering. Conventional sintering is shown to achieve 95% of the theoretical density at about 1400°C. The NRL microwave data for a 5 min. hold time is shifted to about 100°C higher temperature than the conventional data. The NRL 60 min. hold time data shows increased densification, as expected, and is in fairly good agreement with the conventional data. There is also good agreement between the NRL short hold time and the LASL/Varian data. In contrast, the ORNL microwave data shows densification at much lower temperatures than obtained by the conventional furnace. Densification to 95% of the theoretical density is achieved by 1000°C, a shift of about 400°C. The reason for the difference between the ORNL and NRL microwave data is not currently understood. An analysis of possible errors in our temperature measurements suggests that our pyrometer data underestimates the workpiece temperature by up to a few tens of degrees because we are making a surface measurement whereas microwave heating usually produces hotter temperatures in the interior, and because of radiative losses due to the pyrometer view hole. Thus errors in our temperature measurement are unlikely to account for the difference in the results.

The present results suggest that microwave processing of Sumitomo AKP-50 alumina does not lead to sintering at significantly lower temperatures than obtained in conventional furnaces. This has implications for the effect of microwave fields on the activation enthalpy for sintering. From an applications standpoint, the faster processing possible in a microwave furnace does appear to be helpful in reducing grain growth. Data will be presented that shows very little grain growth occurring during microwave sintering except, as expected, at densities over 90%. The final grain size is about 1  $\mu\text{m}$  which compares favorably with conventional furnace sintering.

### Acknowledgement

This work is supported by the Office of Naval Research.

### References

- [1] D. E. Clark, D. C. Folz, R.L. Schulz, Z. Fathi and A.D. Cozzi, *MRS Bulletin* 18, 41-46 (1993).
- [2] M. A. Janney and H. D. Kimrey, "Microwave sintering of alumina at 28 GHz," in *Ceramic Powder Science II*, G. L. Messing, E. R. Fuller, and H. Hausner, editors, American Ceramic Society, Westville, Ohio, 919 (1988).
- [3] T. T. Meek, R. D. Blake, and J. J. Petrovic, "Microwave sintering of  $\text{Al}_2\text{O}_3$  and  $\text{Al}_2\text{O}_3$ -SiC whisker composites," *Ceram. Eng. Sci. Proc.* 8, 861 (1987).
- [4] Y. V. Bykov and V. E. Semenov, "Processing of material using microwave radiation" in *Applications of High-Power Microwaves*, A.V. Gaponov-Grekhov and V.L. Granatstein, editors, (Artech House, Boston, 1994), 319.
- [5] K. I. Rybakov and V. E. Semenov, "Plastic deformation of an ionic crystal due to ponderomotive action of high-frequency electric field," *Phys. Rev. B* 49, 64-68 (1994).

# Initial Testing of a CW Quasioptical Gyrotron for Material Processing

R. P. Fischer and A. W. Fliflet  
 Beam Physics Branch  
 Plasma Physics Division  
 U.S. Naval Research Laboratory  
 Washington, D.C. 20375-5000 U.S.A.

## Abstract

The quasioptical gyrotron (QOG) is under development at the Naval Research Laboratory as a tunable, high power source of millimeter-wave radiation[1]. A new application of the QOG is in the rapid sintering of high-strength ceramic materials and other heating processes. Millimeter-wave radiation is expected to heat samples much more uniformly and rapidly than conventional furnaces, resulting in improved material properties[2]. This paper describes the experimental set-up of the gyrotron and *in situ* cold tests of the asymmetric quasioptical resonator.

## Experimental Set-Up

A schematic diagram of the experiment is shown in Figure 1, where a 20 kV, 1.5 A dc power supply energizes the magnetron injection gun (MIG). The MIG produces an annular electron beam where the pitch angle  $\alpha$  is varied by adjusting the intermediate anode voltage and/or the electron gun trim coil. The magnetic field is produced by a cold bore superconducting magnet with a magnetic compression ratio of 26.8 in the absence of the trim field. The electron beam is collected above the magnet dewar in a water-cooled collector. A pair of asymmetric mirrors comprise the quasioptical resonator, where radiation is collected from one side only. An elliptical reflector is used to focus the radiation beam into an overmoded cavity to heat the workpiece.

The MIG used in the experiment was originally designed for 80 kV, 35 A, a magnetic compression of 30, and  $\alpha = 1.9$ . Electron trajectory simulations of the MIG are shown in Figure 2 as the mod anode voltage divider is varied. The beam voltage is 20 kV and the current is 1.5 A. For the case with no trim field, a voltage divider setting of approximately 60% yields  $\alpha = 2.0$  and  $\Delta\alpha = 30\%$ . By applying a trim coil current of 65 A, the velocity spread drops to  $\Delta\alpha = 10\%$  for the same pitch angle. Capacitive probes in the drift tube will measure the average pitch angle of the electron beam.

Asymmetric mirrors 6.8/13.6 cm in diameter form the quasioptical resonator with 3% output coupling at 85 GHz. Approximately 80% of the resonator round-trip losses diffract around the small mirror, which simplifies the required waveguide system. The mirrors are placed near the vacuum flanges of the crossbore at a separation of approximately 62 cm. The mirror radius of curvature is

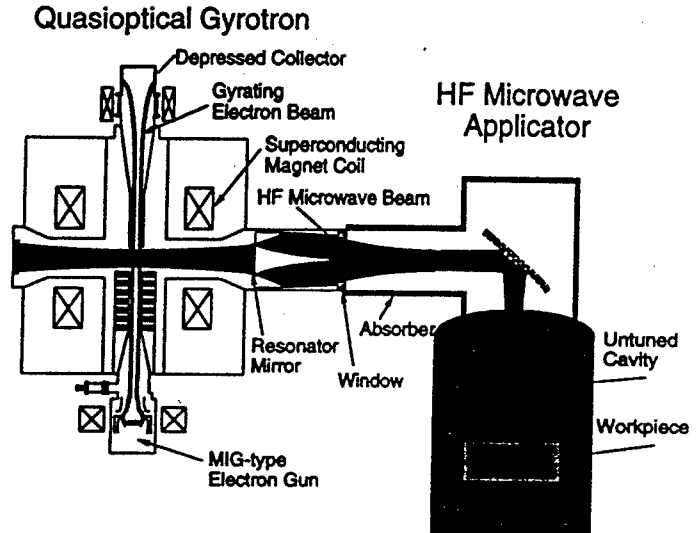


Figure 1: Schematic diagram of the quasioptical gyrotron and high frequency microwave applicator.

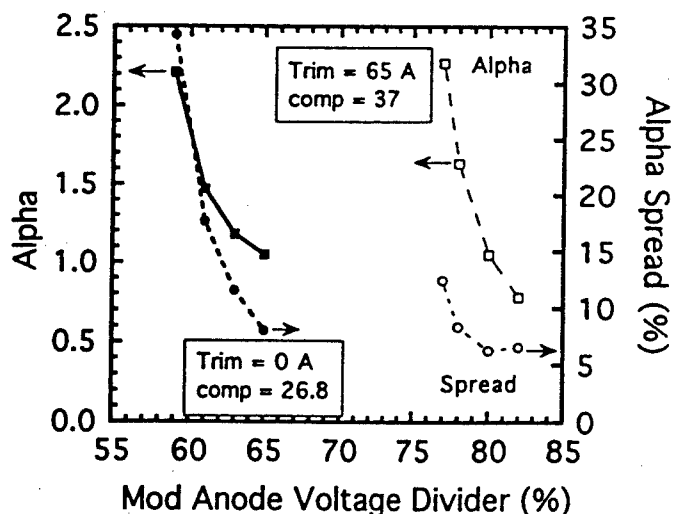


Figure 2: Electron trajectory simulations of the electron gun.

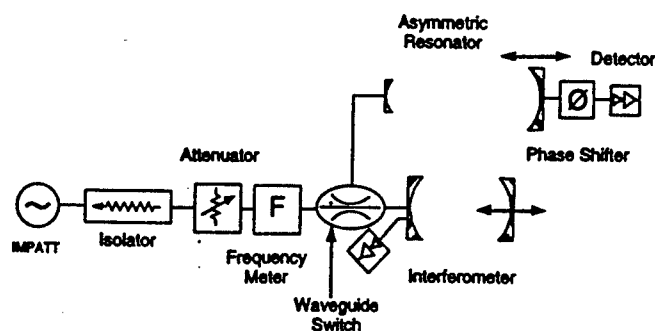


Figure 3: Schematic diagram of the cold test set-up.

chosen to be 65 cm so that the transverse radiation profile fits inside the magnet crossbore. Moving the large mirror by  $\pm 2.5$  cm results in the calculated output coupling varying from 1.6 to 4.9% at 85 GHz. The movable mirror also allows for the optimization of the output coupling when the gyrotron frequency is tuned.

### Cold Test Results

Cold tests of the asymmetric resonator have been performed *in situ* to measure the quality factor ( $Q$ ) and sensitivity to alignment. A schematic diagram of the cold test set-up is shown in Figure 3. An IMPATT oscillator at 95 GHz is used to excite the resonator through a coupling hole in the small mirror. The rf frequency is swept by applying a small voltage ramp to the fm port on the oscillator. The IMPATT produces a small amount of power at a frequency of  $1.5 \times f_0 = 142.5$  GHz, which is also used in the measurements. In the experiment, the small mirror is fixed while the large mirror is mounted using 3 precision micrometers so that mirror separation and tilt can be varied. The initial alignment of the mirrors is optimized using a HeNe laser.

Figure 4 shows measured and calculated values of  $Q$  as the mirror separation is varied. A computer code is used to solve the integral equations of the open resonator and calculate the mode pattern and diffraction losses. The measured values of  $Q$  are consistently lower than the calculations, with the largest discrepancy occurring near confocal separation. However, this effect has also been observed by other researchers [3]. Cold tests at 142.5 GHz yield similar trends and results. Tilting the large mirror by  $0.5^\circ$  reduces the quality factor by approximately 30%. The signal transmitted to the far coupling hole is reduced by 5 dB under these conditions, which allows for a convenient check on the alignment. These tests provide valuable information on the properties of the quasioptical resonator.

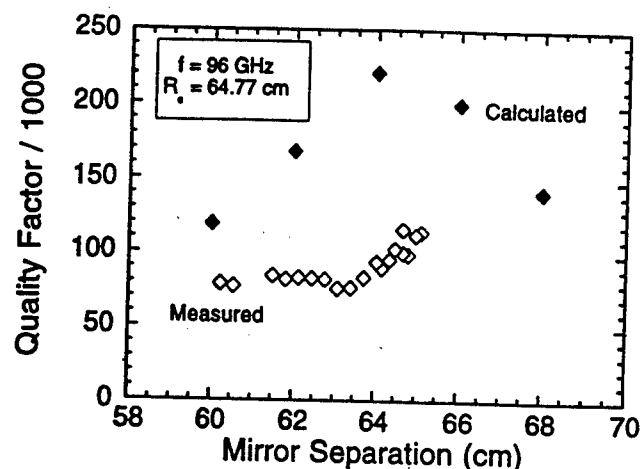


Figure 4:  $Q$  as a function of mirror separation.

### Conclusions

A cw quasioptical gyrotron has been designed to operate from 75–95 GHz with 4 kW average power. Electron trajectory simulations indicate that reasonable pitch angles are achievable with relatively low velocity spread by using a trim coil. Cold test measurements have been performed at 95 and 142 GHz, yielding important information on the quality factor and alignment sensitivity of the asymmetric quasioptical resonator. The experiment has been assembled, the electron gun activated, and high voltage pulsed testing is underway. This gyrotron will complement existing material processing experiments at 2.45 and 35 GHz [4].

### Acknowledgment

This work is supported by the Office of Naval Research.

### References

- [1] R.P. Fischer, A.W. Fliflet, W.M. Manheimer, B. Levush, T.M. Antonsen, Jr., and V.L. Granatstein, "Phase locking, amplification, and mode selection in an 85 GHz quasioptical gyrokystron," *Phys. Rev. Letters*, vol. 72, no. 15, pp. 2395–2398, 11 Apr. 1994.
- [2] *Microwave Processing of Materials*, W.H. Sutton, Guest Editor, *MRS Bulletin*, vol. 23, no. 11, Nov. 1993.
- [3] A. Perrenoud *et al.*, "Low power measurements of the quality factor of an open resonator with stepped mirrors," *Int. J. Infrared and Millimeter Waves*, vol. 7, pp. 1813–1822, 1986.
- [4] A.W. Fliflet, R.P. Fischer, A.K. Kinkead, and R.W. Bruce, "Pulsed 35 GHz gyrotron with overmoded applicator for sintering experiments," *Microwave Processing of Materials V*, vol. 430, pp. 527–532, 1996.

## Scanning Near-Field Millimeter-Wave Microscopy Using a Metal Slit as a Scanning Probe

Tatsuo Nozokido <sup>†</sup>, Jongsuck Bae <sup>†,††</sup>, Tetsu Fujii <sup>†,††</sup>, Masatoshi Ito <sup>††</sup>,  
and Koji Mizuno <sup>†,††</sup>

<sup>†</sup>Photodynamics Research Center, The Institute of Physical and Chemical Research (RIKEN)  
19-1399 Aza-Koeji, Naga-Machi, Aoba-Ku, Sendai 980, Japan.

e-mail: nozokido@postman.riken.go.jp.

<sup>††</sup>Research Institute of Electrical Communication, Tohoku University,  
2-1-1 Katahira, Aoba-Ku, Sendai 980-77, Japan.

### Abstract

We propose a novel type of scanning near-field millimeter-wave microscopy that achieves sub-wavelength resolution by using a metal slit as a scanning probe and an image reconstruction algorithm based on computerized tomographic imaging. In experiments at 60GHz ( $\lambda = 5\text{mm}$ ) with slit dimensions of  $0.1\text{mm} \times 4.8\text{mm}$ , we have demonstrated an image resolution better than  $0.25\text{mm}$ .

### Introduction

Diffraction limits the resolution of a conventional microscope to approximately  $\lambda/2$ . Resolution down to  $\lambda/20$  have been demonstrated with scanning near-field optical microscopes which force incident light through a submicroscopic aperture [1-3]. Similar results had previously been demonstrated in the microwave region [4]. Unfortunately, even in the ideal case of an infinitely thin and perfectly conducting screen, the total flux transmitted through a small hole drops with the sixth power of the radius. In reality, the finite thickness of the conductor and the chosen conical shape of the scanning probe create a hollow waveguide operating below its cutoff frequency, so that much of the incident radiation field is reflected before it reaches the aperture. As a result, sensitive photon counting and very slow scan-speeds have had to be used in these microscopes and improvements in resolution or sensitivity appear difficult. Similar problems are encountered when operating an aperture microscope in the reflection mode [5]. To circumvent these problems, transmission line microscopes using a coaxial cable as a probe have been developed with some success [6,7].

Here we propose and demonstrate a new type of scanning near-field millimeter-wave microscopy (SNMM) using a metal slit at the end of a rectangular waveguide as a scanning probe. Figure 1 shows the waveguide probe used in our experiments, and also the dimensions of a slit and the frequency used. A reduced-height waveguide forms the slit; the wide dimension of the slit and that of the waveguide are identical but the waveguide height is reduced down to  $\lambda/60$ . The probe can be operated above the cutoff frequency imposed by the wide dimension and thus provide stronger signals than point-type probes, resulting in improvements in resolution or sensitivity.

### Experimental technique and results

To achieve sub-wavelength resolution with a slit as a scan-

ning probe, we adopted an image reconstruction algorithm based on computerized tomographic imaging (such as that used in x-ray CT imaging) [8]. Figure 2 is a sketch of our experimental setup. The waveguide probe and a receiving horn are both mounted on fixed stages and are connected to a WILTRON 360B vector network analyzer (VNA). The object to be imaged is mounted on a motor-driven rotational stage, which is attached to another motor-driven linear stage. These two motor-driven stages and VNA are controlled by a computer. The object is scanned linearly for different object-rotation angles,  $\theta$ . This scan method is quite different from the raster-scanning technique used in the other conventional scanning near-field microscopes. The signals from the probe and the horn are obtained in reflection and/or transmission modes through VNA. Since VNA executes phase-sensitive heterodyne detection, the signals ( $S_{11}$ ,  $S_{21}$ ) reflect the sum or line integral of the electric field along the slit

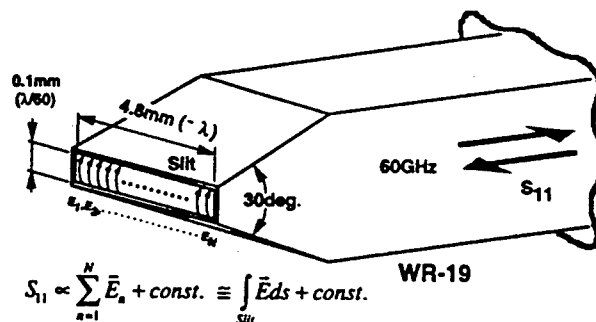


Fig.1 Schematic drawing of the waveguide probe (not to scale).

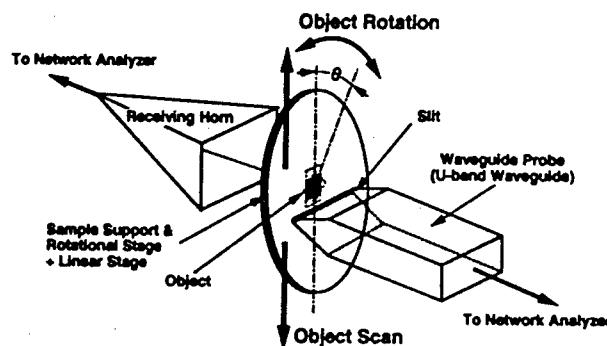


Fig.2 Experimental scheme for SNMM in reflection and transmission modes.

(see Fig.1), so that an image reconstruction code for parallel projections[8] can be used to display the near-field distribution in close proximity to the object.

The object used in our experiment is a 0.9mm x 0.75mm metal patch supported by a quartz plate ( $n=2.12$ ,  $t=1.87$ mm). Figure 3 is an optical image of the object. Figure 4 shows the measured raw-data in reflection mode ( $S_{11}$  signals in linear mag & phase) obtained by linearly scanning the waveguide probe over the object. The edges of a metal patch can be clearly distinguished with a resolution better than 0.16 mm, which is better than  $4/125$  of the wavelength. Figure 5 shows the reconstructed SNMM images. They were obtained for the following conditions:

Field of view (FOV)	: 2100 $\mu$ m
Sampling interval for linear motion	: 48 $\mu$ m
Total sampling points for linear motion	: 63 pt.
Sampling interval for rotational motion	: 5.81 deg.
Total sampling points for rotational motion	: 31 pt.
Probe-to-Object separation	: 20 $\mu$ m.

Intensity and phase images in both reflection and transmission modes are shown in this figure. These images have a matrix size of 128 x 128, and a pixel size of 16.5 $\mu$ m x 16.5 $\mu$ m. Figure 5 (e) shows the one-dimensional intensity variation along the line c-c' in Fig.5 (c), indicating an image resolution better than 0.25mm. These results indicate the advantage of this technique that, due to high-sensitivity, simultaneous acquisition of both intensity and phase images in both reflection and transmission modes is possible.

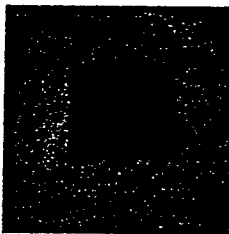


Fig.3 Optical image of the object.

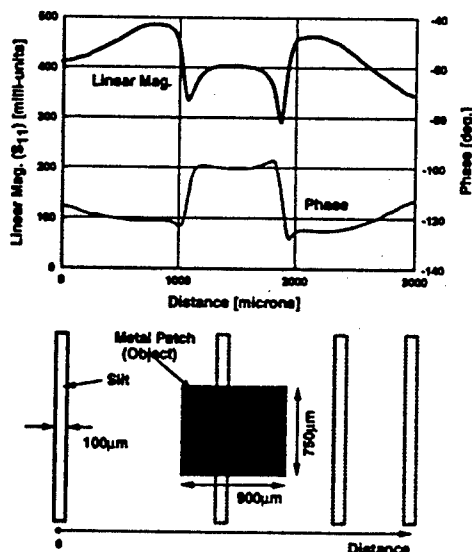


Fig.4 Measured raw-data in reflection mode ( $S_{11}$  signals) at 60GHz obtained by scanning the waveguide probe over the object ( $\theta=0$  in Fig.1).

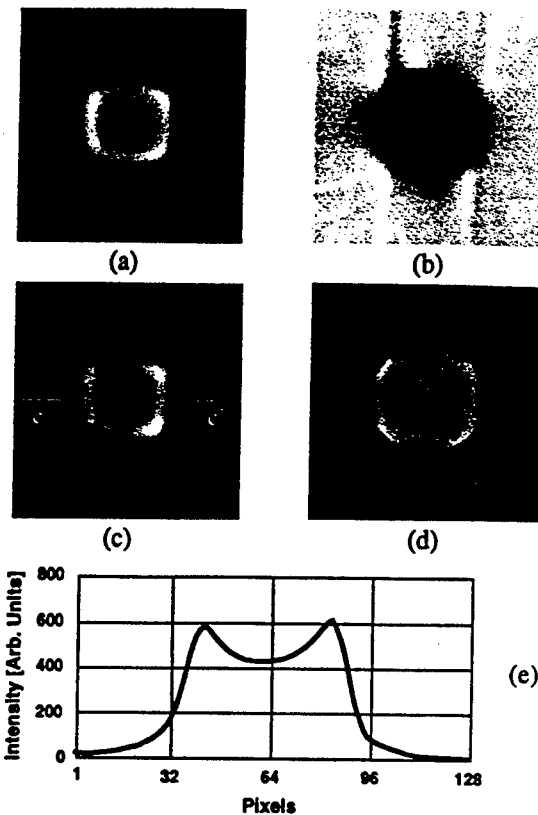


Fig.5 SNMM images of a metal patch at 60GHz: (a) intensity image in reflection mode, (b) phase image in reflection mode, (c) intensity image in transmission mode, (d) phase image in transmission mode, and (e) one-dimensional intensity variation along the line c-c' in (c).

### Summary

A new type of scanning near-field millimeter-wave microscopy has been successfully demonstrated using a metal slit as a scanning probe and an image reconstruction algorithm based on computerized tomographic imaging. We believe the method presented here have a potential to achieve high-speed spectroscopic imaging with sub-wavelength resolution in the millimeter and submillimeter-wave regions.

### Acknowledgment

We thank Dr K. Sekihara, Central Research Lab., Hitachi Ltd., for helpful discussions about the image reconstruction algorithm used in this work.

### References

- [1] D. W. Pohl, W. Denk and M. Lanz, Appl. Phys. Lett. 44, 651 (1984).
- [2] U. Dürig, D. W. Pohl and F. Rohner, J. Appl. Phys. 59, 3318 (1986).
- [3] E. Betzig and J. K. Trautman, Science 257, 189 (1992).
- [4] E. A. Ash and G. Nichols, Nature 237, 510 (1972).
- [5] U. C. Fischer, U. Dürig and D. W. Pohl, Appl. Phys. Lett. 52, 249 (1988).
- [6] M. Fee, S. Chu and T. W. Hansch, Optics comm. 69, 219 (1989).
- [7] F. Keilmann, Infrared Phys. Technol. 36, 217 (1995).
- [8] A. C. Kak and M. Stanly, in Principles of Computerized Tomographic Imaging, Chapter 3, IEEE Press, New York (1988).

# Application of W-Band Gyrotron for Superconducting Magnetic Fusion\*

Saeyoung Ahn<sup>1</sup> and Richard J. Temkin<sup>2</sup>

<sup>1</sup>US Naval Research Laboratory, Washington, DC 20375, and

<sup>2</sup>Plasma Fusion Center, MIT, Cambridge, MA 02139, USA

## Abstract

The electron cyclotron heating and startup will require gyrotron for the Korean Superconducting Tokamak Advanced Research (KSTAR) project. Initial studies on gyrotron is reported to downscale the MIT gyrotron to W-band(75-110 GHz).

## Background

The KSTAR project [1] will develop a steady-state capable advanced superconducting tokamak to establish the scientific and technological basis for an attractive fusion reactor as a future energy source. It aims to extend present stability and performance boundaries of tokamak operation through active control of profiles and transport, and explores methods to achieve steady state operation for tokamak fusion reactors using non-inductive current drive.

Physics design issues address magnetic field requirements of two-point ripple criterion for 16 TF coils and low voltage start-up capability using ECH-assisted and good field-null quality start-up, possibly LHH-assisted. Flexible features of operating boundary and plasma shape control include wide range of  $\kappa$  and  $\delta$  values for PF coils in double and single null configurations with two-pairs of fast position control coils. Profile control of  $J(r)$ ,  $n(r)$  and  $P(r)$  is achieved by NBI, FWCD and LHCD with NBI stacked horizontally.

Four heating and current drive systems mentioned in the above will function to control profile and to drive plasma rotation and initiation; (1) neutral beam injection of 120 keV ~300 sec with baseline of 8 MW in 1 co to an upgrade of 24 MW in 2 co 1 ctr, (2) ICRF/FWCD of 30-80 MHz ~300 sec with 6 MW in 1 launcher to 12 MW in 2 launchers, (3) LHCD of 3.7 GHz ~300 sec with 1.5 MW to 4.5 MW, and (4) ECH of 80 GHz start-up ~0.5 sec with 0.5 MW.

Important parameters for the KSTAR project are as follows; major radius 1.8 m, minor radius 0.5 m, toroidal field 3.5 tesla, plasma current 2.0 MA, elongation 2.0, triangularity 0.8, and pulse length of current drive between 20 and 300 sec. The plasma species are H and D, and to be heated and driven by NBI, ICRH/FWCD, LHCD and ECH/ECCD.

Diagnostics systems, magnet systems, wall facing components, and power supply and control systems are subcontracted to major institutions in collaboration with US, Japan and other countries.

## Gyrotrons for ECRH

### A. MIT design of gyrotron

The MIT gyrotron research resulted in a successful design and experiment for heating fusion plasmas at frequencies between 107 and 151 GHz in order to achieve the required power over 1 MW[2][3]. The parameters used in the 110 GHz experiment for the  $TE_{22,6,1}$  mode were 83 KV beam voltage, 34 amp current, 1.63  $\alpha$ , 1.01 cm beam radius, 1.98 cm wall radius, 6.5 L/ $\lambda$ , 850 diffractive Q, 1.7 Q/Q<sub>min</sub>, and 0.7 KW/cm<sup>2</sup> average loss. The efficiency was 40% and voltage depression 5.2 KV.

### B. KSTAR requirement

The startup and heating for the KSTAR project will be done around at 3.5 tesla of the toroidal magnetic field. The corresponding gyrotron frequency can be between 84-110 GHz. Our aim is to perform the down scalability from the MIT design in 107-151 GHz without losing its efficiency.

### C. Gyrotron design for KSTAR

We will show some initial result of gyrotron design done in MIT at 110 GHz for this efforts using the same mode  $TE_{22,6,1}$ . The cavity ohmic loss is lowered conservatively below 1 KW/cm<sup>2</sup>. The cavity consists of the 4° input linear taper, output nonlinear uptaper, and axial rf profile of 6.6 L/ $\lambda$ .

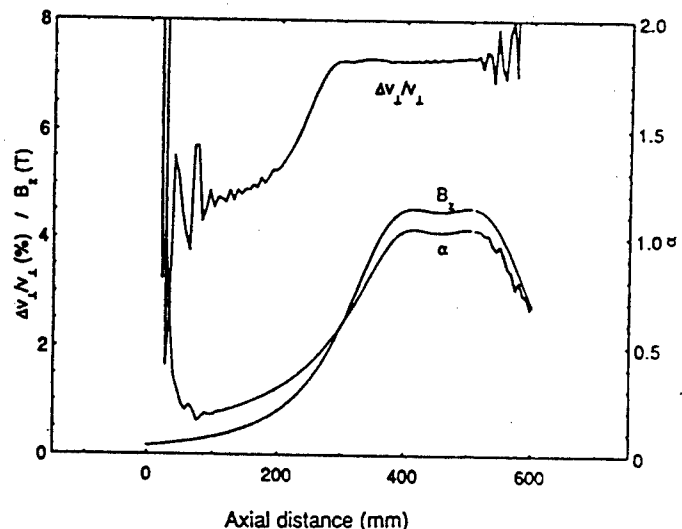


Fig 1. 110 GHz MIG gun run :  $\Delta v/v_p$ ,  $B_z$ , and  $\alpha = v_p/v$ .

The MIG gun run shows 6.5% perpendicular velocity spread at  $\alpha=1.62$  as in Fig.1. The E-gun trajectory is shown in Fig. 2. The magnified cavity dimension (a) along the radial direction is shown in Fig. 3 together with the parameters;  $f=110.287$  GHz,  $Q=785.46$ ,  $L/\lambda=6.6$ ,  $\Omega_{\text{peak}}=0.81$ ,  $\text{Leak}=0\%$ ,  $F=0.1$ ,  $\mu=13.96$ . The initial gaussian wave is plotted in (b).

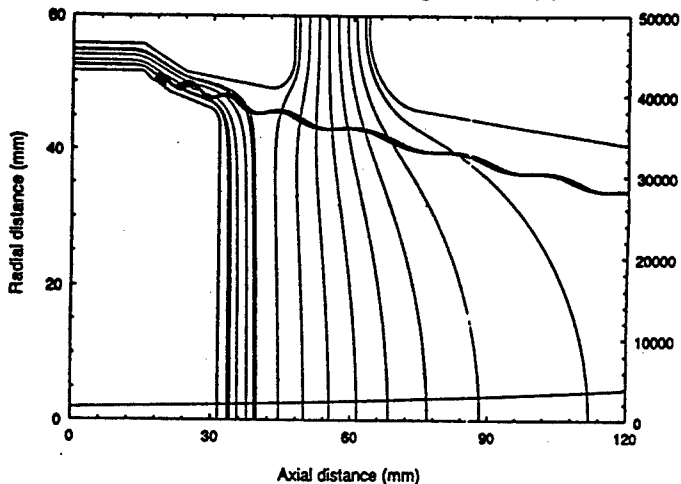


Fig. 2. E-gun trajectories for 110 GHz MIG gun.

The MIT gyrotron code produces the efficiency, beam radius, and rf profile along the cavity of the mode for 77 KV and 34 amp. The maximum efficiency is 42.8%.

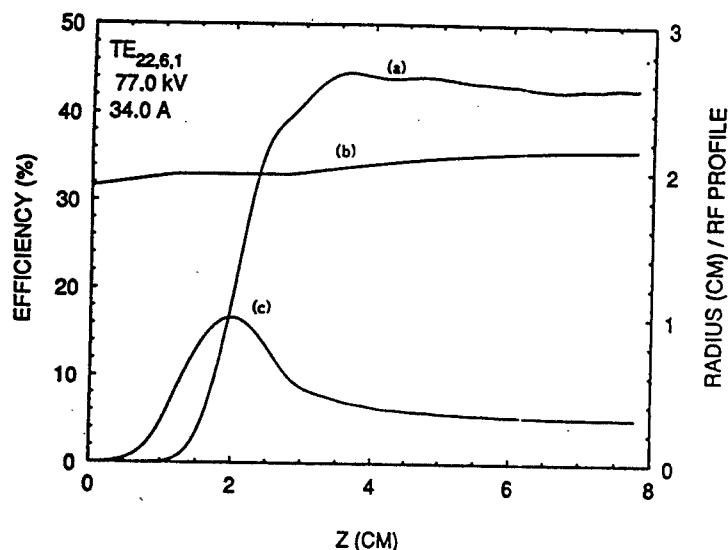


Fig. 4. The efficiency of 110 GHz Gyrotron : (a) efficiency, (b) radius (cm), and (c) rf profile for self-consistent cavity simulation.

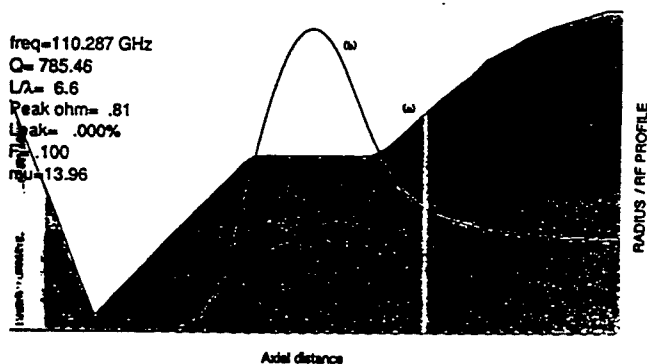


Fig. 3. Profile of the cavity dimension magnified along the radial direction and rf wave amplitude.

The diffractive Q has the value of 723 with ohmic loss of 0.54 KW/cm<sup>2</sup>. Its power at maximum peaks to 1.2 MW.

## Future Research Plan

Based upon the MIT results, further study will continue for the downward scalability of gyrotron performance. Related studies on ECRH/ECCD are also being carried out.

## References

- [1] Choi, Duk-In, "The KSTAR Project Second Year Mid Report," KBSI Report, Korea Basic Science Institute, 2 April, 1997.
- [2] Kreischer, K.E., Blank, M., Danly, B.G., Kimura, T., Mizuno, T., Temkin, R.J., "Operation of a Megawatt Gyrotron at 110 GHz", The 19th Int'l Conf. on IR & mm Waves Sendai, pp. 61-62, 1995.
- [3] Kevin Felch, Monica Blank, Philipp Borchard, Tak Sum Chu, Joseph Feinstein, Howard R. Jory, Jeffrey A. Lorbeck, C. Marshall Loring, Yosuke Maxwell Mizuhara, Jeffrey M. Neilson, Richard Schumacher, Richard J. Temkin, "Long-Pulse and CW Tests of a 110-GHz Gyrotron with an Internal, Quasi-Optical Converter", IEEE Transactions on Plasma Science, v. 24, no. 3, pp.558-569, June 1996.

\* Work supported by the KBSI Korean National Fusion Initiative and Korea Atomic Energy Research Institute (KAERI) and carried out on the first author's (S.A.) sabbatical leave at IAE and Ajou University in Korea. Gyrotron run was done by S. Ahn and T. Kimura of MIT.



# Generation of Ultrashort Millimeter-wave Pulses Based on Superradiance

N.S. Ginzburg,

Institute of Applied Physics, Russian Academy of Science, 603600, Nizhny Novgorod, Russia

A.D.R. Phelps,

Department Physics and Applied Physics University of Strathclyde, Glasgow, G4 ONG, UK

M.I. Yalandin,

Institute of Electrophysics, Russian Academy of Science, 620049 Ekaterinburg, Russia

## Abstract

The first experimental results of the observation of superradiance from a single subnanosecond electron bunch are presented. Superradiance was associated with different varieties of stimulated emission (bremsstrahlung, cyclotron, Cherenkov, etc). Unique megawatt power level microwave pulses of short duration (0.3-0.5 ns) have been obtained.

## Introduction

In recent years much attention has been given to theoretical considerations of superradiance (SR) from space-localized non-equilibrium ensembles of electrons [1-10]. This phenomena includes features of present in both stimulated (selfbunching and coherence) as well as spontaneous processes (absence of threshold). It is reasonable to consider SR in a specific situation when the electron pulse duration essentially exceeds the operating wavelength (otherwise it is effectively traditional spontaneous emission) while at the same time is less or comparable with the interaction length (in contrast with traditional mechanisms of stimulated emission of quasi-continuous electron beams which are used extensively in microwave electronics - FEL, TWT, BWO, CRM, etc). Coherent emission from the entire electron pulse can only occur when a selfbunching mechanism typical for stimulated emission develops. Another natural condition of coherent emission is the mutual influence of different fractions of the electron beam pulse. In the absence of external feedback such influences can be caused by slippage of the wave with respect to the electrons due to a difference between the electron drift velocity and electromagnetic wave group velocity.

## Superradiance and Mechanisms of Stimulated Emissions

Superradiance can be related with different mechanisms of stimulated emission: bremsstrahlung, cyclotron, Cherenkov, etc. In this report we present results of the experimental observation of different types of SR from isolated electron bunch in the  $K_u$  frequency band. The SR pulses have been observed from a bunch of electrons moving along helical as well as rectilinear trajectories. The first type of trajectory was realized when electrons started to rotate in a uniform magnetic

field after passing through a kicker (cyclotron emission) or oscillated in a combined undulator and guiding magnetic field (undulator emission). The corresponding resonance condition can be presented in the form

$$\omega - kv_{\parallel} = \Omega$$

where  $\Omega$  is gyrofrequency  $\omega_H$  for cyclotron SR and  $\Omega = 2\pi v_{\parallel}/\lambda_u$  is the bounce frequency for undulator SR, and  $\lambda_u$  is undulator period. It is important to note that the additional condition of group synchronism has been explored. Under such condition the electron bunch longitudinal velocity coincides with the wave group velocity propagating in a regular waveguide. It has been shown theoretically [9] that this regime gives the possibility of increasing the growth rate of the SR instability and also of reducing the sensitivity of the interaction to the spread of electrons parameters.

In the case of a bunch of electrons moving along rectilinear trajectories in a guiding magnetic field Cherenkov type SR has been studied for two types of slow-wave structures. The first was a periodically corrugated metallic waveguide where a bunch radiates under synchronism with the slow spatial harmonic of the backward wave

$$\omega = (-k + k_c)v_{\parallel}$$

where  $k_c = 2\pi/\lambda_c$ ,  $\lambda_c$  is the corrugation period. The second used a dielectric loaded waveguide where forward wave radiation occurred under synchronism

$$\omega = kv_{\parallel}$$

## Experimental results

A RADAN 303 accelerator with a subnanosecond slicer was used to inject typically 0.3-0.5 ns, 0.2-1 kA, 250 keV single electron pulses [13, 14]. These electron pulses were generated from a magnetically insulated coaxial diode which utilized a cold explosive emission cathode. An oscillogram of the electron bunch current is presented in Fig. 1a. The fast rising e-beam current and accelerating voltage pulses were measured using a Faraday cage strip line current probe and an in-line capacitive voltage probe respectively, with both signals recorded using a 7 GHz Tektronix 7250 digitizing oscilloscope. High current electron pulses were transported

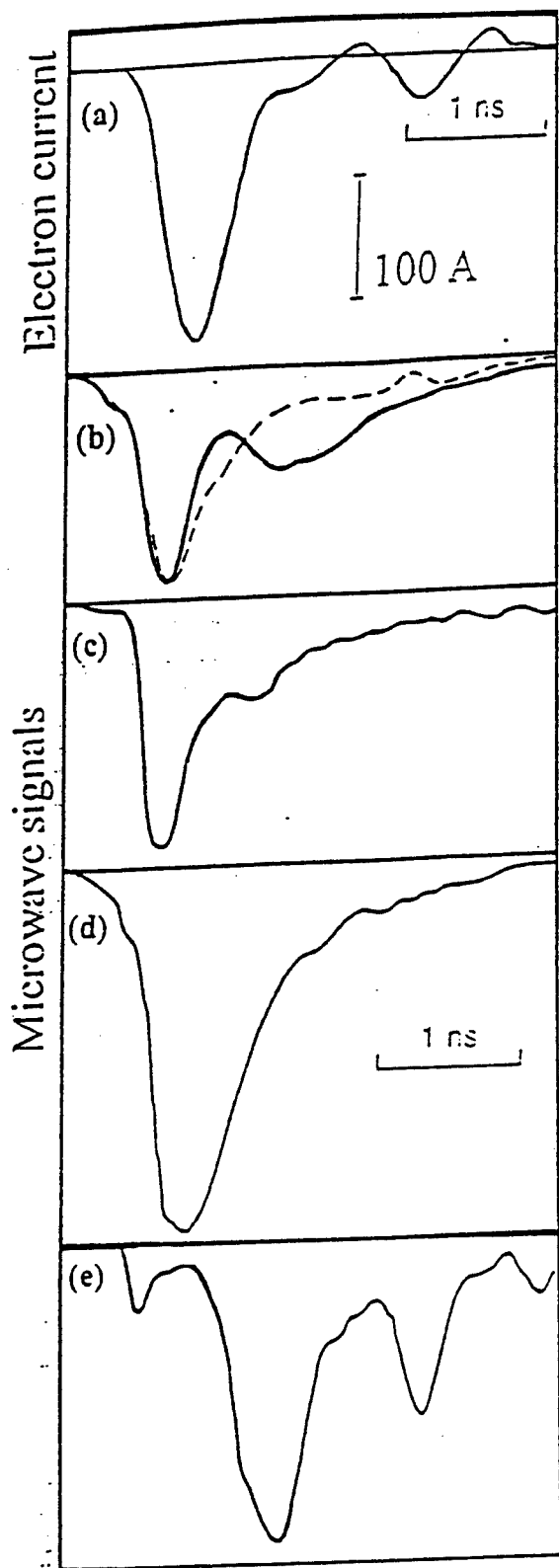


**Fig.1 Oscillograms:** (a) - electron bunch current, (b-e) - microwave pulses for different types of superradiance: (b) - cyclotron SR, (c) - undulator SR, (d) - Cherenkov SR in the case of periodical waveguide, (e) - Cherenkov SR in the case of dielectric-loaded waveguide. Dashed line in Fig 1(b) corresponds to signal passing through the cut-off filter.

through the interaction space over a total length of up to 30 cm in a longitudinal guiding magnetic field of up to 2 T. For measurement of the radiation a hot-carrier germanium detector which had a transient characteristic of 200 ps was used. Oscillograms of microwave SR pulses for different mechanisms of emission are presented in Fig.1 b-e. The typical main pulse duration was 0.3-0.5 ns. The maximum peak power was several hundreds of kilowatts for cyclotron and undulator emission and about 1-2 MW for Cherenkov emission.

Note that the microwave signal in the case of a periodical slow-wave structure (Fig.1 d) consisted of several peaks. The first small peak corresponded to the high frequency radiation propagating in the same direction as the electron beam (TWT mechanism), while the second larger peak corresponded to the designed counter-propagating emission mechanism. Subsequent bursts are related with reflection of radiation from the edges of the slow-wave system.

In the case of cyclotron SR ([13, 14]) the emission appears as a set of two pulses (Fig.1 b) related with more fundamental physics. In fact, under group synchronism condition in the comoving reference frame electrons radiate isotropically at the quasi-cutoff frequencies in the both  $\pm z$  directions. But in laboratory frame both components of the radiation propagate towards the bunch at the longitudinal velocity. So, the first pulse is created by photons emitted in the  $K'$  frame in the  $+z$  direction, while the second one is by photons emitted in the opposite direction. Naturally due to the Doppler effect the frequency in the first pulse exceeds the frequency in the second pulse. For the same reason the peak power of the first pulse is significantly greater than that in the following pulse and the duration of the first pulse is less than the duration of the second pulse. To prove that the frequency in the first pulse exceeds that of the second pulse a set of cut-off waveguides have been used. The dash line in oscillogram Fig. 1(b) illustrates the evident suppression of second low frequency pulse by a high pass filter of cut-off frequency 33.3 GHz. In general, measurements showed a very broad radiation spectrum width which covered the band 28.5-36.5 GHz. Thus, the relative spectrum width amounted to 20%. Note also that SR was observed in a rather narrow range of detuning of the uniform magnetic fields corresponding to grazing conditions with  $TE_{21}$  and  $TE_{01}$  modes. It was thus proven that the regime of group synchronism is optimal for cyclotron emission.

In the case of a bunch passing through an undulator SR has also been registered under grazing conditions with the designed  $TE_{11}$  mode. Adiabatic tapering of undulator entrance was used to provide excitation of bounce-oscillations. The SR was registered for both group I and group II stationary orbits [15]. The first group of orbits corresponds to the so called reverse guide magnetic field regime at a magnetic field strength of  $\sim 1$  T while the second group of orbits was obtained at a direct magnetic field of strength  $\sim 1.3$  T which slightly exceeded the cyclotron resonance value. The maximum peak power was observed for the second case for the amplitude of undulator field  $\sim 0.2$  T. Typical oscillogram for this case is presented in Fig.1 c.

The important confirmation of the stimulated nature of the observed radiation is the dependence of the peak power on

interaction length. The typical dependence is shown in Fig.2 for the case of Cherenkov SR. This figure clearly demonstrates that the radiation power is very small for short interaction lengths and increases drastically as the interaction length is increased. This means that in the initial stage selfbunching of electrons developed and the radiation power exceeded the threshold of the detector's sensitivity only after formation of the electron bunches. The squared dependence of the power of Cherenkov radiation with respect to the number of electrons also confirms the coherent nature of observed radiation. Note that a hybrid system with a BWO section as a prebuncher and a Cherenkov section as an amplifier was tested in recent experiments. As a result microwave pulses were obtained with peak power up to 2 MW with high stability typical of BWO systems.

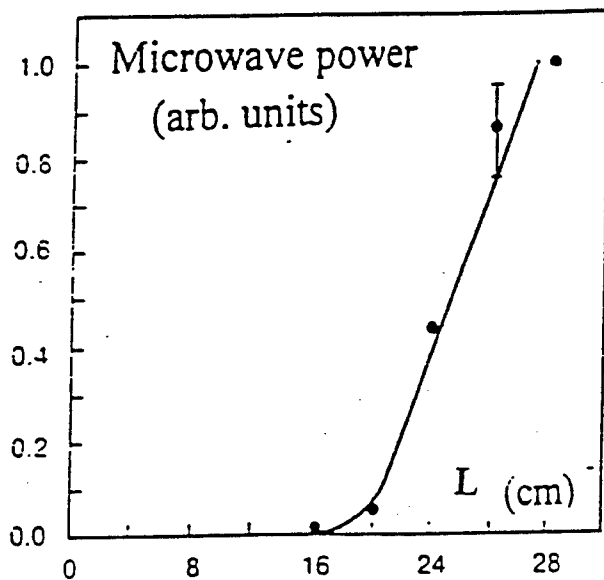


Fig.2 Dependence of peak microwave power on interaction length, in the case of dielectric-loaded waveguide.

### Conclusion.

Summarizing the experimental results presented we believe that the radiation observed was related with a novel mechanism of stimulated coherent emission of short electron bunches, namely superradiance. We should emphasize here that coherent emission occurs from an isolated subnanosecond electron bunch. Of course, the results discussed here give only a rather general physical picture of superradiance, which needs further investigation, which would specifically concentrate on more accurate measurements and comparison with theoretical simulations. However even at this early stage it must be emphasized that the radiation especially in the case of BWO-like regimes was characterized by a high level of stability and reproducibility from pulse to pulse. The efficiency of energy transformation amounted to 3% for the Cherenkov mechanism. The unique characteristic of microwave pulses such as

duration (0.3-0.5ns) in combination with Megawatt power levels is encouraging for future applications in areas such as novel diagnostics and the studying of nonlinear phenomena in plasmas. Another advantage of the RADAN subnanosecond accelerator and consequently any associated experiments is that the whole system is in the form of a table-top system. In addition this accelerator is capable of operation in the repetitive, up to 100 pps regime.

This work was supported by the Russian Fund of Fundamental Research, grant 95-02-04791 and by the United Kingdom DRA and EPSRC.

### References.

- [1] R. Bonifacio, C. Maroli and N. Piovela, Opt. Comm. 68 (1988) 369.
- [2] R. Bonifacio, N. Piovela and B. W. J. McNeil, Phys. Rev. 44 (1991) 3441.
- [3] R. Bonifacio et al. Riv. Nuovo Cimento 13 (1990) N9.
- [4] N. Piovela, et al., Phys. Rev. E 52 (1995) 5470.
- [5] V. V. Zheleznyakov, V. V. Kocharovskiy and V. V. Kocharovskiy, Usp. Fiz. Nauk 159 (1989) 194.
- [6] N. S. Ginzburg, Sov. Tech. Phys. Lett. 14 (1988) 197.
- [7] N. S. Ginzburg and A. S. Sergeev, Sov. Phys. JETP Lett. 54 (1991) 446.
- [8] N. S. Ginzburg and A. S. Sergeev, Opt. Comm. 91 (1992) 140.
- [9] N. S. Ginzburg, I. V. Zotova and A. S. Sergeev Sov. Phys. JETP Lett. 60 (1994) 513.
- [10] G.R.M.Robb, B.W.J. McNeil and A.D.R.Phelps, Proc. 19th Int. Conf. on Inf. and MM Waves, Sendai, Japan, p.155 (1994).
- [11] G.A.Mesyats, et al. Proc. 8th Int. Pulsed Power Conf., USA, San-Diego, p.73 (1991).
- [12] V.G.Shpak, et al. Prib. Tekh. Eksp. 1 (1993) 149.
- [13] N. S. Ginzburg et al. Sov. Phys., JETP Lett. 63 (1996) 331.
- [14] N.S.Ginzburg et al. Phys.Rev.Lett. 78 (1997) 2365
- [15] H.P.Freund Phys.Rev.A 27 (1983) 1977

# Development of a 50 MW Magnicon Amplifier at 11.4 GHz

Steven H. Gold and Arne W. Fliflet  
Beam Physics Branch, Plasma Physics Division,  
Naval Research Laboratory, Washington, DC 20375-5346

Allen K. Kinhead  
Sachs/Freeman Associates, Inc., Landover, MD 20785

B. Hafizi  
Icarus Research, Inc., P.O. Box 30780, Bethesda, MD 20824-0780

Oleg A. Nezhevenko,<sup>†</sup> Viacheslav P. Yakovlev,<sup>†</sup> and Jay L. Hirshfield  
Omega-P, Inc., 202008 Yale Station, New Haven, CT 06520

<sup>†</sup>Permanent Address: Budker Institute of Nuclear Physics, Novosibirsk, Russia 630090

Richard True and Robert J. Hansen  
Litton Systems, Inc., Electron Devices Division, San Carlos, CA 94070

## Abstract

The magnicon is a scanning-beam microwave amplifier that is being developed as a high power, highly efficient microwave source for use in powering the next generation of high gradient electron linear accelerators. In this paper, we present a progress report on a new thermionic magnicon experiment designed to produce more than 50 MW at 11.4 GHz, using a 210 A, 500 kV beam from an ultrahigh convergence thermionic electron gun.

## 1 Introduction

The magnicon [1] is a scanning-beam microwave amplifier tube that is under development to power future high gradient electron accelerators such as the proposed TeV Next Linear Collider (NLC). It uses rotating TM modes to spin up a pencil electron beam to high transverse momentum in a series of deflection cavities, the first externally driven, and then a synchronously rotating RF mode of the output cavity is used to extract the transverse momentum as microwave power at the drive frequency or one of its harmonics.

The Naval Research Laboratory (NRL) has been investigating magnicon physics for the past five years with the goal of building a high power 11.4 GHz magnicon tube. Our initial experiment used a 5.5-mm-diam. beam from a cold-cathode diode on the NRL Long Pulse Accelerator Facility. It demonstrated high power operation ( $14 \text{ MW} \pm 3 \text{ dB}$ ) at  $\sim 10\%$  efficiency in the synchronous magnicon mode at 11.120 GHz, but a plasma loading problem prevented true amplifier operation. Nevertheless, good agreement was found with predictions of a simulation based on the actual experimental parameters [3,4].

The Budker Institute of Nuclear Physics (INP) is carrying out thermionic magnicon experiments at 7 GHz [5]. They recently reported 46 MW at 49% efficiency in a 1  $\mu\text{sec}$  pulse. Some members of the INP magnicon team are collaborators in the present work.

In this paper, we present a progress report on a new high power thermionic magnicon amplifier that is under construc-

tion at NRL in collaboration with Omega-P, Inc. It is designed to produce  $>60 \text{ MW}$  at 11.4 GHz with  $>50\%$  efficiency. Its essential components are a high power modulator, an ultrahigh convergence electron gun, a matched magnet system, and a set of cavities designed for high vacuum, high temperature bakeout, and high efficiency operation. The circuit consists of a drive cavity, three simple gain cavities, and a redesigned penultimate cavity, all operating in the  $\text{TM}_{110}$  mode at 5.712 GHz, followed by a new output cavity operating in the  $\text{TM}_{210}$  mode at 11.424 GHz (see Fig. 1).

## 2 The Electron Gun

The magnicon amplifier design requires a 500 kV, 210 A, 1.5-mm-diam. electron beam, with a 1.5  $\mu\text{sec}$  pulse width and a 10 Hz repetition rate. (The Brillouin diameter is  $\sim 1.3 \text{ mm}$  at 6.5 kG.) The electron gun is a novel ultrahigh convergence relativistic Pierce gun using a dispenser cathode (see Fig. 2 and Table I). A key feature of the gun is an electrically isolated focus electrode that is biased negatively by a few hundred volts with respect to the cathode in order to reduce beam halo. This gun is being built by Litton Systems, Inc., with delivery expected in July of this year, and a matching magnet has been built by the INP.

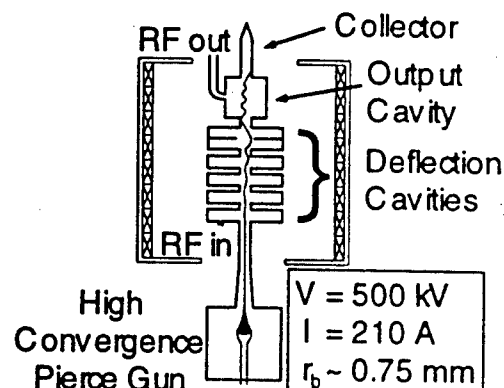


Figure 1: Thermionic magnicon schematic.

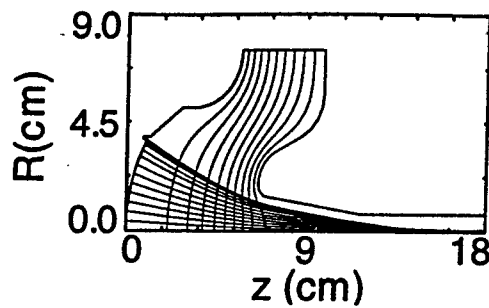


Figure 2: Electron gun design.

TABLE I. Electron gun design parameters

Current	210 A
Voltage	500 kV
Microperveance	0.59
Cathode radius	3.77 cm
Beam radius	0.75 mm
Compression ratio	2500:1
Current density	12 kA/cm <sup>2</sup>
Mean cathode loading	4.5 A/cm <sup>2</sup>

### 3 The Magnicon Circuit

The drive and gain cavities are identical to those in the previous NRL design [2]. The penultimate cavity is an iris-coupled TM<sub>110</sub>  $\pi$ -mode two-section cavity that carries out the final stage of beam spin up. As a result, it contains very high RF fields, creating the danger of RF breakdown. The objective of the new design was to optimize the beam spin-up, while minimizing the surface RF fields. The redesign involved adjusting the beam pipe diameter, rounding of the beam tunnel and the iris, and reducing the length of the first cavity section. These changes reduced the maximum surface electric field from 670 kV/cm in the original design to 572 kV/cm, comparable to values employed in high power X-band klystrons at SLAC.

The output cavity was also redesigned for higher efficiency and lower fields by reducing the beam tunnel diameter, increasing the rounding of the apertures, and shortening the cavity from 5 cm to 4 cm. This is discussed in greater detail in Ref. 6. The second goal is to redesign the cavity for side coupling rather than end coupling, in order to extract the output power directly into X-band waveguide. The INP 7 GHz magnicon employs two rectangular waveguides separated by 135°, and uses additional wall perturbations to restore the quadrupole symmetry [5]. This is the approach that we have adopted.

Figure 3 shows a simulation of the complete magnicon circuit for a 1.5-mm-diam. electron beam. Notice that large energy excursions occur in the region of the penultimate cavity, but that the energy loss in the output cavity is remarkably uniform. The result is 66 MW at 63% efficiency. The magnicon design parameters are shown in Table II. Our simulations show a loss in efficiency of only a few

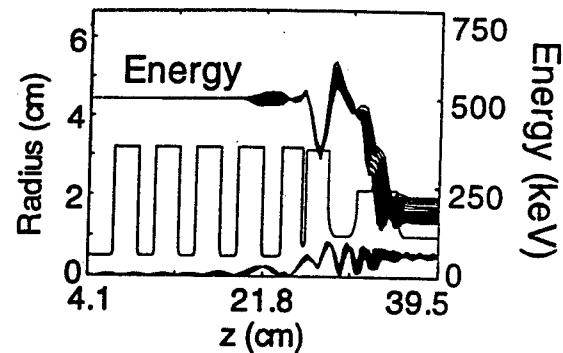


Figure 3: Steady-state simulation for a 1.5-mm-diam. beam.

TABLE II. Thermionic magnicon design parameters

Frequency	11.424 GHz
Power	66 MW
Efficiency	63%
Pulse width	1.5 $\mu$ sec
Repetition rate	10 Hz
Drive frequency	5.712 GHz
Drive power	100 W
Gain	58 dB

percent at beam diameters up to 2.5 mm.

### 4 Summary

We have designed an electron gun and circuit for a high gain, high efficiency 11.424 GHz frequency-doubling magnicon amplifier. The beam parameters are 500 kV, 210 A, and 1.5-mm beam diameter. The electron gun will be driven by a 1.5  $\mu$ sec, 10 Hz modulator. The predicted power is 66 MW at 63% efficiency. This design is the basis of a new thermionic magnicon experiment, which we plan to assemble and test in 1997.

### Acknowledgments

This work was supported by the U.S. Department of Energy (DoE) and the Office of Naval Research under Interagency Agreement DE-AI02-94ER40861, and by a DoE SBIR grant to Omega-P, Inc. It was carried out under a CRADA between NRL and Omega-P.

### References

- [1] O.A. Nezhevenko, *IEEE Trans. Plasma Sci.* **22**, 765 (1994).
- [2] O.A. Nezhevenko *et al.*, *IEEE Trans. Plasma Sci.* **22**, 785 (1994).
- [3] S.H. Gold *et al.*, *IEEE Trans. Plasma Sci.* **24**, 947 (1996).
- [4] S.H. Gold *et al.*, *Phys. Plasmas*, May 1997, in press.
- [5] E.V. Kozyrev *et al.*, *Proc. 1997 Particle Accelerator Conf.* (in press).
- [6] S.H. Gold *et al.*, *NRL Memo Report 7857* (1996).

# Oscillation of TE<sub>11</sub> Mode from a High Power Backward Wave Oscillator

K.Minami\*, K.Tanaka\*, X.D.Zheng\*, Y.Carmel\*\*, A.N.Vlasov\*\*\* and V.L.Granatstein\*\*

\* Graduate school of Sci. and Tech., Niigata University, 950-21, Japan

\*\* Institute for Plasma Research, University of Maryland, College Park, MD 20742, USA

\*\*\* Dept. of Physics, Moscow State University, Moscow, 119899, Russia

## Abstract

Oscillation of TE<sub>11</sub> mode from a high power backward wave oscillator (BWO) is studied experimentally as well as analytically. The TE<sub>11</sub> mode is observed for operation of the BWO far from upper cutoff ( $\pi$  mode), when the beam currents are less than the starting current of conventional TM<sub>01</sub> mode. The conversion efficiencies of 13% and 11% are observed for TE<sub>11</sub> and TM<sub>01</sub> modes, respectively. This may indicate a possibility of further improving the performance of BWO's by choosing the operation regimes.

## Introduction

In conventional high power backward wave oscillator (BWO) studies, axisymmetric TM<sub>01</sub> mode has been exclusively measured and analyzed by many authors[1]. This fact may be reasonable because the electron beam and the slow wave structure (SWS) are arranged to be axisymmetric. The energy source of the radiation is longitudinal space charge mode in the beam in a strong axial magnetic field. The resultant generated microwaves are assumed to be axisymmetric accordingly. However, non-axisymmetric TE modes may be generated if the cyclotron motion of electrons contributes to the oscillation as was in the case of gyrotrons.

In conventional BWO's, the TM<sub>01</sub> mode is generated effectively by the operation near the upper cutoff of the transmission band ( $\pi$  mode). The starting current usually has the lowest value in this case. However, when the beam currents are much larger than the starting current, operation in a multi-frequency regime may result[2]. Because a single-frequency regime is desired, high power BWO's should be operated not only by large beam currents but also by a large starting current so that their ratio does not exceed 3-4. For that purpose, an operation regime far from  $\pi$  mode may be available, if the efficiency of oscillation is not low.

In our experiments far from  $\pi$  mode, it is found that the dominant mode of oscillation is switched from TM<sub>01</sub> mode to TE<sub>11</sub> mode, when beam current is decreased keeping beam energy unchanged. In the present paper, we analyze and measure the TE<sub>11</sub> mode from a high power BWO.

## Dispersion Relation

We consider an infinitely long vacuum axisymmetric SWS with metal wall radius  $R(z)$  expressed as

$$R(z) = R_0 + h \cos K_0 z, \quad K_0 = 2\pi / z_0$$

where  $R_0$  is mean radius,  $h$  and  $z_0$  are, respectively, the amplitude and periodic length of corrugation. Maxwell equations are solved under the boundary conditions  $E_{\parallel} \propto E_z + E_r (dR/dz) = 0$  at  $r=R(z)$  and  $E_{\theta}(r=R(z)) = 0$ . The resultant dispersion relation of TE<sub>11</sub> modes is

$$\det \begin{bmatrix} p_{mn} & q_{mn} \\ r_{mn} & s_{mn} \end{bmatrix} = 0,$$

$$p_{mn} = \frac{2}{K_0} [1 + (n-m)Q_n] J_{m,n},$$

$$q_{mn} = \frac{\omega}{\beta_n c} \left[ \frac{2}{\beta_n} (n-m) J_{m,n} + h(I_{m-1,n} - I_{m+1,n}) \right],$$

$$r_{mn} = \frac{k_n}{\beta_n} (I_{m,n} + K_{m,n}),$$

$$s_{mn} = \frac{\omega}{\beta_n c} (K_{m,n} - I_{m,n}),$$

$$I_{m,n} = \int_0^{\pi} J_0(\beta_n R) \cos(n-m)u du,$$

$$J_{m,n} = \int_0^{\pi} J_1(\beta_n R) \cos(n-m)u du,$$

$$K_{m,n} = \int_0^{\pi} J_2(\beta_n R) \cos(n-m)u du,$$

where  $Q_n = K_0 k_n / \beta_n^2$ ,  $\beta_n^2 = \omega^2 / c^2 - k_n^2$ ,  $k_n = k + nK_0$ ,  $m$  and  $n$  are integers from  $-\infty$  to  $\infty$ . Other notations are standard.

The dispersion relation for the first four TE<sub>11</sub> modes is shown in Fig.1, where  $R_0=1.445$  cm,  $h=0.445$  cm and  $z_0=1.67$  cm that have been used in the University of Maryland. The dispersion curve for TM<sub>01</sub> mode is shown by dashed-and-dotted line for comparison. The frequency versus wavenumber for the first three TE<sub>11</sub> modes are measured by a vector network analyzer (HP-8720D) using a sample SWS. The measured values coincide with the calculated ones in Fig.1 within errors of 1%.

## Experimental Results

Experimental setup is identical to that described in [3]. We varied the beam energy from 70 to 130 keV, with a beam pulse duration 150 ns. In order to study the effect of beam current with identical cathode voltage, two types, A and B, of beam

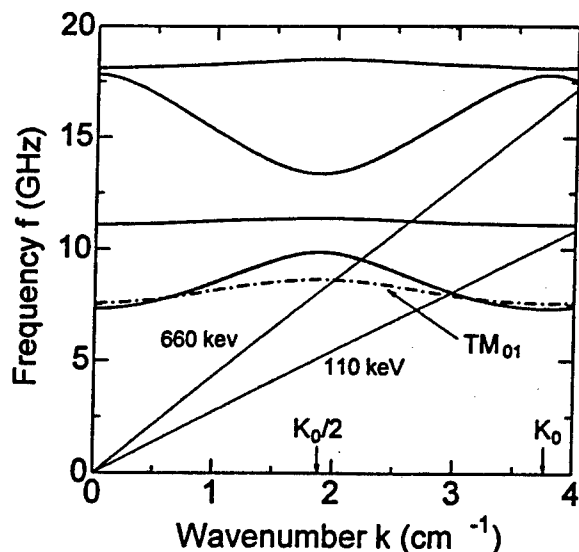


Fig.1 The calculated dispersion diagram for first four  $TE_{1n}$  modes in an infinitely long, spatially periodic structure ( $R_0=1.445$ ,  $z_0=1.67$  cm and  $h=0.445$  cm).

diode are used. The beam diode B allows that a part of current is bypassed by the surface of isolating block. The voltage-current characteristics of the beam diodes A and B are shown in Fig.2. The currents in the former are roughly twice those of the latter for a given cathode voltage. In case (a) of the diode A, typical beam parameters are 110 keV, 540 A and duration of microwave pulse is 60 ns. The peak power is 6.8 MW, and frequency is 8.5 GHz. The peak conversion efficiency is 11%. In case (b) of the diode B, on the other hand, typical beam parameters are 110 keV, 380 A and duration of microwave pulse is 50 ns. The peak power is 5.3 MW at 7.2 GHz. The peak conversion efficiency is 13 %. It should be noted that both cases (a) and (b) are carried out in the operation regime far from  $\pi$  mode. Nevertheless, efficiencies are not inferior to those of conventional regime near  $\pi$  mode.

In order to clarify the mode of oscillation, power directivities are measured for both cases (a) and (b) as are shown in Fig.3 (a) and (b). The results mean that the oscillating modes are  $TM_{01}$  and  $TE_{11}$  modes for the cases (a) and (b), respectively. The calculated radiation patterns for both modes are shown, respectively, in Fig.3(a) and (b). The beam current 380 A in the case (b) is found to be insufficient to start the oscillation of  $TM_{01}$  mode. The  $TE_{11}$  mode then takes turn to oscillate instead of  $TM_{01}$  mode. A question arises here : whether the direction of polarization of the  $TE_{11}$  mode is random from shot to shot, or reproducible in every shot ? Figure 3(b) is observed to be reproducible. It is estimated accordingly that two  $TE_{11}$  modes with different directions of polarization are present as is in the case of a waveguide with elliptical cross section.

### Conclusion

A mode switching from  $TM_{01}$  to  $TE_{11}$  modes is demonstrated as the beam current decreases. The  $TE_{11}$  mode in the SWS is analyzed in some detail. Our finding of the  $TE_{11}$  mode

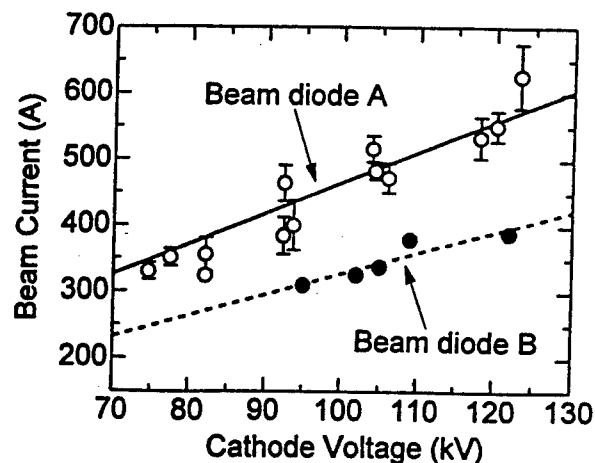


Fig.2 Beam current vs. cathode voltage for type A and B beam diodes.

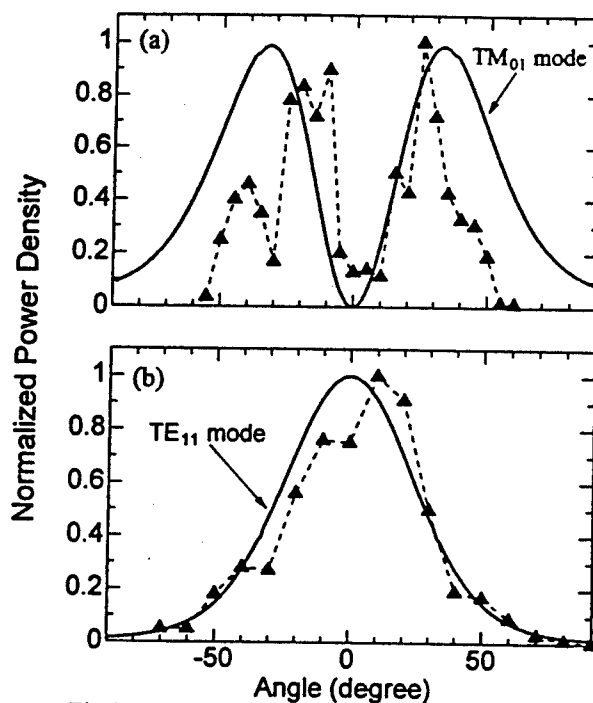


Fig.3 Measured and calculated radiation patterns.

oscillation in the regime far from  $\pi$  mode suggests a possibility to improve further the performance of high power BWO's.

### Acknowledgment

We would like to acknowledge profoundly Professor T.M.Antonsen, Jr., the University of Maryland, for his valuable discussion and suggestion.

### References

- [1] J.A.Swedge et al., Phys. Fluids **28**, (1985) 2882.
- [2] B.Levush et al., IEEE Trans. Plasma Sci. **20**, (1992) 263.
- [3] K.Ogura et al., Phys. Rev. **E53**, (1996) 2726.

## The Angular Distribution of the Power Produced by Smith-Purcell Radiation

J H Brownell,\* G Doucas,+ M F. Kimmitt,†  
J H Mulvey,+ M Omori,+ and J E Walsh,\*

\*Department of Physics and Astronomy, Dartmouth College, Hanover NH 03755-3528, USA

+Department of Physics, University of Oxford, Oxford OX1 3RH, UK

†Department of Physics, University of Essex, Colchester CO4 3SQ, UK

### Abstract

The radiation produced by the interaction of an electron beam with a metallic grating, the Smith-Purcell radiation, can be described in terms of a theory based on the acceleration of the surface charges induced on the grating surface by the passing electrons. The calculated spectral distribution of the emitted power is compared to recent experimental results, the agreement between the two being found to be satisfactory.

The wavelength,  $\lambda$ , of the emitted radiation is related to emission angle  $\Theta$  by the well-established Smith-Purcell dispersion relationship which, for first order emission, is given by

$$\lambda = \lambda_0 (1/\beta) - \cos\Theta$$

where  $\lambda$  is the grating period and  $\beta$  is the electron velocity in units of  $c$ , the velocity of light.

### 1. Introduction

The interaction of an electron beam with a metal grating and the emission of radiation was first reported by Smith and Purcell [1] in 1953 and has received renewed attention in the last few years [2],[3] because it offers the attractive prospect of a compact and efficient method of generating a high-power tunable source of radiation, particularly in the far infrared, where suitable sources are sparse. We have recently developed a theory [4] describing this effect in terms of the surface charges induced on the grating by the passing electron and "dragged" along by it. The source of the emitted radiation is the acceleration imposed on this moving charge by the grooves of the grating. This approach, which is described in detail in ref [4], has the advantage of being relatively transparent in terms of physics and manageable in its mathematics. The calculation leads, eventually, to a formula describing the expected spectral distribution of the emitted incoherent power with wavelength in terms of beam and grating parameters.

The formula takes into account such parameters as the current and diameter of the beam, its height above the grating, its interaction length on the grating, the electron energy and the period of the grating. The most difficult term in the formula relates to the detailed shape of the grating grooves. In a number of experiments we have observed that Smith-Purcell radiation does depend very strongly on the grating profile.

### 2. Experimental Arrangement

We have compared our formula to experimental results obtained at Oxford. Since this experiment has already been described in the literature [2], [5], we summarise briefly the main parameters. A beam of 3.5MeV electrons in a pulse of about 6 $\mu$ s duration was passed over an 'echelle' type grating with a blaze angle  $\alpha = 30^\circ$  mounted on a movable platform, together with a rotatable plane mirror for collecting the emitted light and reflecting it on to a paraboloidal mirror. This, in turn, focused the light at the entrance of an evacuated copper tube which transmitted it to a Czerny-Turner monochromator. A liquid helium-cooled InSb electron bolometer, capable of detecting peak powers of less than 10nW in the wavelength range 400-2500 $\mu$ m, was placed at the exit of the spectrometer. The selection of emission angle  $\Theta$ , and hence of the wavelength  $\lambda$ , was achieved by means of a 36mm wide flat mirror which could be tilted over the grating. Rotation of this mirror enabled observations at emission angles in the range 25-94 $^\circ$  from the direction of the electron beam. Angles in the backward direction could be reached by dismounting the plate of the grating and the mirrors, rotating it by 180 $^\circ$  and using a periscope to carry the light to the entrance of the copper pipe. The angular range explored was between 56 $^\circ$  and 150 $^\circ$  and was defined by the spectral response of the InSb detector, which drops sharply below 350 $\mu$ m.



Most of the measurements were carried out with gratings having periods of 0.762 or 1.016mm; three measurements were taken with a grating of 0.457mm period. The electron beam current varied from 50-200mA. The beam size over the grating was measured at 3mm (transverse to the grating) by 6mm, so the current densities were in the range  $0.35\text{A}/\text{cm}^2$ . The beam size is consistent with a normalised emittance of about  $30\pi\text{mm.mrad}$ .

### 3. Calibration

The calibration of the output power was done by comparison with the black-body radiation of a mercury lamp of approximately the same effective area, placed in the grating position. This allowed for a direct calibration of the complete system, including collection, transport, spectral analysis and detection. The effective source area was found to be  $1.5\text{cm}^2$  and the effective grating length 2cm. The mercury vapour lamp was the well-documented Philips HPK125 [6]. The relationship between mirror angle and emission angle was established by direct calibration with a HeNe laser. It should be noted that the accuracy in the calibration of the emission angle is of the order of  $\pm 1^\circ$ .

### 4. Results

Experimental results were obtained over a spectral range from 350-1800 $\mu\text{m}$ . These have been compared with the formula describing the expected spectral distribution and good agreement has been obtained. Details of the results will be shown at the Conference. The theory predicts that the spontaneously-emitted power for the gratings used should drop quite rapidly at shallow emission angles. Unfortunately this is a range that we did not explore experimentally because not only did the response of the detector fall below 350nm but the optical path was not evacuated and atmospheric water absorption is severe at shorter wavelengths.

The accelerator at Oxford has been closed down but we hope to obtain further data from an experiment that we are at present carrying out in Munich [7]. This experiment uses a photocathode, excited by the output from a quadrupled frequency Q-switched Nd:YAG laser, and a Van der Graaff accelerator to produce electron energies similar to those employed at Oxford. The normalised emittance is much improved and current densities are also considerably higher. However, as the pulse length is much shorter (20ns compared to 6 $\mu\text{s}$  at Oxford), we are unable to use the InSb electron bolometer, which has a response time of  $\sim 500\text{ns}$ . For this reason the experiment has been designed for the 50-140 $\mu\text{m}$  range and the detector is a gallium-doped germanium photoconductor with a response time of  $\sim 25\text{ns}$ . The entire

optical path, including the Czerny-Turner monochromator, is evacuated to avoid absorption by water vapour.

### 5. Summary and Conclusions

The description of the Smith-Purcell radiation in terms of currents induced on the grating surface and accelerated by the grooves of the grating is relatively easy in its mathematical treatment and offers a good physical insight into the emission process. Experimental results obtained at an electron energy of 3.6MeV have been compared to the predictions of the theory for the angular distribution of the spontaneously-emitted power. Good agreement between the two has been obtained. However, more experimental points, over a wider range of parameters, are needed before reaching the final verdict on the validity of this theoretical treatment of a phenomenon that could have an important role in the design of compact tunable sources of coherent radiation. We expect to obtain more data points from the Munich experiment and from Smith-Purcell studies that are being performed/planned by our own group as well as at other laboratories. The very reliable compact microtron accelerator at ENEA, Frascati, with electron energies of 3-5MeV [8] would be an ideal source and we understand that grating experiments are envisaged at that laboratory.

### 6. References

- [1] S J Smith and E M Purcell, *Phys Rev* **92**, 1069 (1953)
- [2] G Doucas, J H Mulvey, M Omori, J E Walsh and M F Kimmitt, *Phys Rev Lett* **69**, 1761 (1992)
- [3] M J Moran, *Phys Rev Lett* **69**, 2523 (1992)
- [4] J H Brownell, G Doucas and J E Walsh, submitted to *Phys Rev E*
- [5] G Doucas, J H Mulvey, M Omori, J E Walsh and M F Kimmitt, *Nucl Instr Meth in Phys Res A*, **331**, 609 (1993)
- [6] M F Kimmitt, *Far-Infrared Techniques*, Pion (London), 50-52 (1970)
- [7] T Kormann, G Korschinek, C Stan-Sion, M Dumitru, G Doucas and M F Kimmitt, *Proc EPAC '96 Barcelona*, vol 1, 748 (1996)
- [8] F Ciocci, R Bartolini, A Doria, G P Gallerano, E Giovanale, M F Kimmitt, G Messina and A Renieri, *Phys Rev Lett* **70**, 928 (1993)

# High Power Microwave Emission of Large and Small Orbit Rectangular Cross Section Gyrotrons

J. M. Hochman<sup>#</sup>, R. M. Gilgenbach, R. L. Jaynes, J. I. Rintamaki<sup>a</sup>, Y. Y. Lau, and T. A. Spencer<sup>+</sup>

Intense Energy Beam Interaction Laboratory  
Nuclear Engineering and Radiological Sciences Department  
The University of Michigan  
Ann Arbor, MI 48109-2104

## Abstract

We summarize the results of experiments on a gyrotron utilizing rectangular-cross-section (RCS) interaction cavities. Current issues under investigation include polarization control as a function of magnetic field, power versus pulselength of microwave emission, and mode competition. The Michigan Electron Long Beam Accelerator (MELBA) produces an annular electron beam at parameters:  $V = -0.7$  to  $-1.0$  MV,  $I_{diode} = 1-10$  kA,  $I_{tube} = 0.1-3$  kA, and  $\tau_{e-beam} = 0.4-1.0$   $\mu$ s. Experimental results from the RCS gyrotron will be compared for large orbit and small orbit beams. MAGIC code simulations using various magnetic fields will be presented.

## Introduction

Efficient, high power microwave sources have significant applications to radar systems, propulsion, and plasma heating, and gyrotron devices have been shown to be one such source [1-5]. Research on gyrotron devices has concentrated on small orbit devices, however, large orbit (or axis encircling) devices offer several advantages including larger azimuthal velocity components at lower magnetic fields and high-harmonic capabilities [6-7].

One challenge for launching high power microwaves is polarization control. A theoretical study of the active-circulator-gyrotron, where a TE01 signal is input but a TE10 signal is amplified and output, was previously performed [8]. The rectangular-cross-section (RCS) gyrotron, which does not require a mode converter, is another approach to polarization control [9]. Experiments at the U of M utilize an RCS gyrotron oscillator, operating in the S-band (2-4 GHz). Polarization control, mode competition, and pulse shortening are under investigation using both small orbit and large orbit e-beams. We have shown the ability to shift high power radiation between the TE10 mode and the TE01 mode by controlling the magnetic fields of an asymmetric magnetic cusp for large orbit measurements.

In this paper we describe the results of RCS gyrotron measurements for both small orbit and large orbit experiments. MAGIC code studies are discussed

## Experimental Configuration

The experimental configuration is shown in Figure 1. The Michigan Electron Long Beam Accelerator (MELBA) produces an annular electron beam by explosive emission at a radius of  $2.25 \pm 0.25$  cm with the following parameters:  $V = -0.7$  to  $-1.0$  MV,  $I_{diode} = 1-10$  kA,  $I_{tube} = 0.1-3$  kA, and  $\tau_{e-beam} = 0.4-1.0$   $\mu$ s. The graphite anode has a 4.55 cm radius aperture for small orbit measurements and an annular, 3-slotted aperture of radius  $2.2 \pm 0.2$  cm for large orbit measurements.

Large, magnetic field coils generate approximately 1kGauss on the diode. The e-beam is extracted through the anode into a stainless-steel tube, which is wound with a solenoid. For the small orbit case, the e-beam is adiabatically compressed in the solenoidal region, but for the large orbit case, the solenoidal field is reversed, creating a magnetic cusp. The beam interacts in the RCS cavity with dimensions of 7.2 by 5.4 cm. A Rogowski coil measures current prior to entering the cavity. The exit of the interaction region has copper strips (1x7.2 cm) at 21 cm downstream, which are used to vary the cavity Q. The beam is then dumped to one side, and microwave output is directed through waveguide of the same transverse dimensions to a chamber lined with microwave absorber. High power microwave emission is collected with two S-band waveguides perpendicular to each other and placed at the end of the chamber. Power measurements are completed in a Faraday cage via coaxial cable. Frequency is diagnosed by a four channel microstrip filter system (2-2.5, 2.5-3, 3-3.5, 3.5-4 GHz filters) and by superheterodyne mixer measurements. Radiation darkened patterns on glass witness plates are used for beam  $\alpha(V_{perp}/V_{par})$  diagnostics [10].

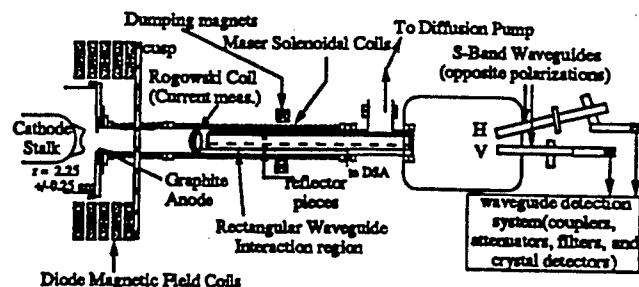


Figure 1. Experimental Configuration

## Experimental Results

Results from small and large orbit gyrotron measurements are shown figures 2 and 3. Figure 2 shows the measured total power in each waveguide versus magnetic field for the small orbit RCS gyrotron case, and figure 3 shows the measured power in the large orbit case.

The small orbit experiment achieves powers of 20MW in the horizontally polarized mode. This corresponds to the 2nd order mode (TE01). The maximum power radiated in the vertically polarized mode was 4MW, and this was due to higher order modes, as frequency measurements showed the fundamental mode was not measured. In almost all cases the power polarization ratio (V/H) was less than 1. The maximum electronic efficiency measured in the small orbit experiments was on the order of 1%. The horizontally

polarized mode dominated in all cases, and polarization control was not achieved.

The large orbit experiment achieved powers of 12 MW in the horizontally polarized mode at a field of 1.7 kGauss, and this corresponds to the TE01 mode. Powers of up to 7 MW were radiated in the fundamental mode (TE10) at a field of 1.5 kGauss. The maximum efficiency generated in these large orbit measurements was 5%. The polarization power ratio (V/H) clearly shows a shift from the fundamental TE10 mode to the next order TE01 mode as a function of magnetic field. Superheterodyne mixer frequency measurements confirm this interpretation. At a field of 1.5 kGauss the polarization power ratio was around 10, while at a field of 1.7 kGauss it dropped to as low as 0.02.

Radiation darkened patterns on glass witness plates (in place of the microwave cavity) were made from eight 1mm diameter pin hole beamlets in the anode aperture and were used to determine the beam alpha ( $V_{\text{perp}}/V_{\text{par}}$ ). For the small orbit experiment a beam alpha of 0.3 was determined, while a beam alpha of 1.0 was measured for the large orbit case. E-gun simulations produced similar results, obtaining 0.24 and 1.6 respectively.

MAGIC code models of an RCS cavity with four beamlets placed at a radius of 2.25 cm were used to simulate the interaction of the annular beam in the cavity. The small orbit model uses an alpha of 0.3 and the large orbit model uses an alpha of 1.0. Both cases assume  $k_z=0$ . The large orbit case assumes a current of 200A while the small orbit case uses 1kA for beam current. For both cases MAGIC results show a shift from the fundamental TE10 mode to the next order TE01 mode. In small orbit simulations the polarization flip occurs around 2.2 kGauss, and 1.8 kGauss in large orbit simulations. While the small orbit experiment shows more of emission power is horizontally polarized, the large orbit experiment shows the shift between modes similar to MAGIC results although the shift occurs at a lower field.

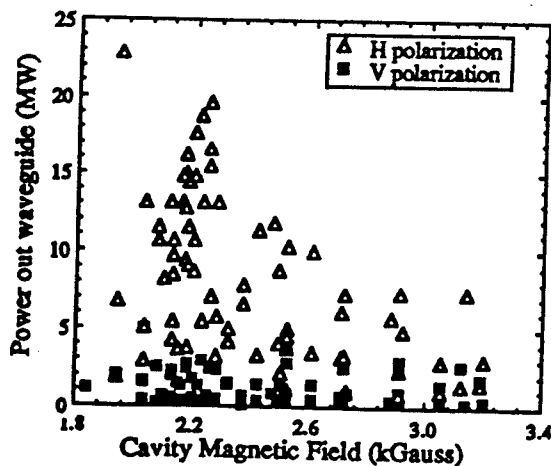


Figure 2. Polarized power measurements for the small orbit gyrotron experiment.

The large orbit RCS gyrotron experiments have demonstrated polarization control, allowing output radiation to be shifted from the fundamental TE10 mode to the TE01.

This occurs as the magnetic field on the interaction cavity is raised from 1.5 to 1.7 kGauss while the diode field is maintained constant. The small orbit case did not create the desired results. Mode competition appeared to have a significant effect in the small orbit results. Furthermore, the microwave electronic efficiency of the axis encircling beam is significantly better (5%) than the small orbit gyrotron (under 1%).

Future experiments will continue to explore the large orbit RCS gyrotron, observing polarization control and effects of mode competition and pulse shortening.

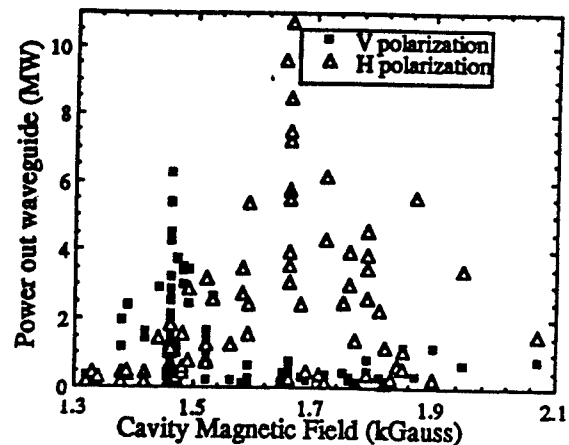


Figure 3. Polarized power measurements for the large orbit gyrotron experiment.

### Acknowledgments

This research is supported by the Air Force Office of Scientific Research, Multidisciplinary University Research Initiative (MURI) through Texas Tech University contract, Phillips Lab, Northrop Grumman Corp., and the AFOSR-sponsored MAGIC Code User's Group, administered by Mission Research Corp.

#AFOSR Augmentation Award for Science and Engineering Research Training

<sup>a</sup>DoE MFET Graduate Fellowship

\*Permanent Address: Air Force Phillips Lab, PL/WSR, Kirtland AFB, NM, 87117-5776

### References

- [1] J. Benford, SPIE OE/LASE conference, LA, CA, Jan(1993).
- [2] J. Benford, R. Dickinson, SPIE 2557, San Diego, CA, July (1995).
- [3] R. M. Gilgenbach, M. E. Read, et al., Phys. Rev. Lett., vol 44, 647 (1980).
- [4] V. L. Granatstein, *High Power Microwave Sources*, Chap. 5, 185 (1987).
- [5] W. Lawson, and W.W. Destler, IEEE Trans. Plasma Sci. PS-22, 895 (1994)
- [6] W. Lawson, P.E. Latham, J. Appl. Phys. 61, 519(1987).
- [7] W. W. Destler, et al., J. Appl. Phys. 66, 4089 (1989).
- [8] Y. Y. Lau, L. R. Barnett, IEEE Trans. Electron Devices, 30, 908 (1983).
- [9] D. J. Radack, et. al, J. Appl. Phys. 73, 8139 (1993).
- [10] J. J. Choi, R. M. Gilgenbach, et al., Rev. Sci. Inst. 63(2), 1671 (1992).

## NONLINEAR THEORY OF THE RELATIVISTIC OROTRON

E.Odarenko, V.Chursin, A.Shmat'ko  
 Dept. of Radiophysics, Kharkov State University  
 Svobody Sq., 4, 310077, Kharkov, Ukraine

## ABSTRACT

The three-dimensional model of millimeter wave resonant O-type oscillator with a relativistic electron beam is analyzed. The selfconsistent nonlinear equations set has been obtained for the arbitrary space distribution of the focusing dc magnetic field<sup>1</sup>. The oscillator efficiency is investigated under steady-state conditions with numerical solution taken for the case of uniform magnetic field. The analysis of nonlinear physical processes for the nonrelativistic case was carried out earlier<sup>2</sup>.

## THEORETICAL MODEL

A sheet relativistic electron beam passes over a reflecting diffraction grating, which is imbedded in a mirror which, along with another mirror, forms an open resonator. The rf field is assumed to have fixed space structure and to change weakly in the scale of the electron transit time through the resonator. It is possible if the oscillatory system has big value of the quality factor  $Q$ . The magnetic displacement vector  $\vec{B}$  is assumed to have two static ( $B_y, B_z$ ) and one rf  $B_x$  components ( $H_x$  polarized wave is exited in the resonator).

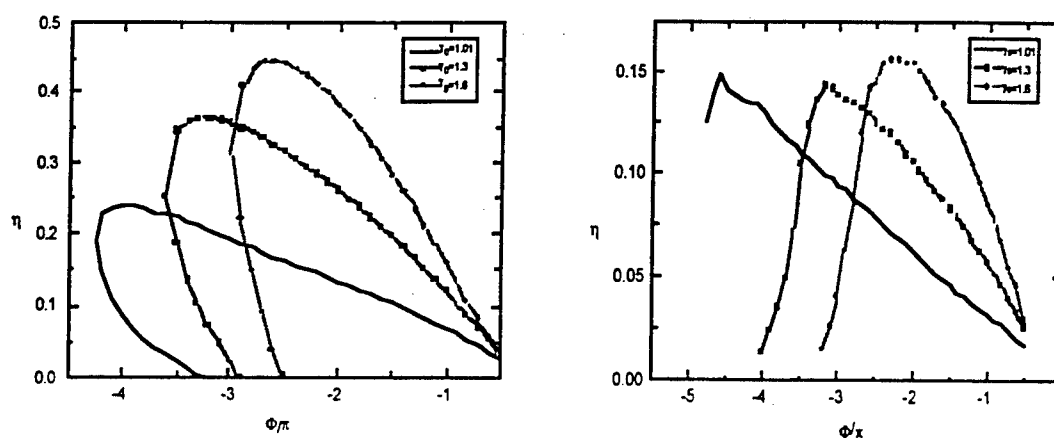
The displacement of the magnetic focusing field can be varied. Hence, the numerical solution of the input equations should be carried out with the settling of electrons onto the slow-wave structure (grating) taken into account.

## DISCUSSION

Results of numerical calculations of the electron-wave interaction efficiency  $\eta$  are shown in Fig. 1, 2. Here  $\Phi$  is the relative synchronism mismatch parameter;  $\gamma_o$  is the relativistic mass factor. Curves in Fig. 1 are obtained at  $\omega_o/\omega = 0.4$ , where  $\omega_o$  is the cyclotron frequency and  $\omega$  is the oscillations frequency. Furthermore the beam current is assumed to be fixed. The solid and dashed curves give the stable and unstable solutions of the governing equations respectively. It is seen that the increase of the relativistic factor  $\gamma_o$  results in the efficiency enhancement and contraction of the generation zone. The similar results were obtained in the one-dimensional theory of the relativistic resonant oscillators.

Hence regularities of the physical processes at  $\omega_0/\omega=0.4$  are retained when the model dimension is varied. It should be noted that the settling of electrons onto the grating is negligible in this case.

Curves in Fig. 2 are obtained at  $\omega_c/\omega=0.1$ . It is seen that the maximum efficiency is weakly varied when the relativistic factor increases. Furthermore hysteretic phenomena are absent in this case. Therefore the decrease of the focusing field displacement results in appearance of new phenomena in the model at issue in comparison with one-dimensional model. It can be explained by settling of electrons onto the grating. This phenomenon results in the variation of electrons distribution in phase of the slow wave. On the other hand in this case the transverse shifts of electrons trajectories increase and transverse electron-wave interaction played a significant role.



#### REFERENCES

1. Chursin V.S., Odarenko E.N., Shmat'ko A.A. Theory of Resonant Relativistic Oscillator with Nonuniform Focusing Field // Int. J. of Infrared and Millimeter Waves.- 1996.- V.17.- N7.
2. Odarenko E.N., Shmat'ko A.A. Nonlinear Theory of O-type Microwave Oscillators with Nonuniform Magnetostatic Field (Two-Dimensional Model) // J. of Communications Techn. and Electronics.- 1994.- 39(9).- p.1 -8.

## Biological Effect of Coherent Radiation of Hyperhigh Frequency When Irradiating Acupunctural Zone

V.K. Kiseliyov, E.M. Kuleshov, Yu.Yu. Kamenev, \*  
V.I. Makolinets, O.P. Timoshenko, B.N. Shevtsov \*\*

\* Institute of Radiophysics and Electronics of the National Academy of Sciences,  
12, Ac. Proskura St., 310085 Kharkov, Ukraine. E-mail: kiseliyov@ire.kharkov.ua

\*\* Institute of Orthopedics and Traumatology named after M.I. Sitenko, Kharkov, Ukraine

### Abstract

The work presents the results of the experimental study and biological effect of submillimetric wave range laser radiation on laboratory animals when irradiating biologically active zones (BAZ) of the body surface and zones with a minimum number of biologically active points (BAP).

### Introduction

Biological aspects of hyperhigh frequency (HHF) radiation have not been sufficiently studied so far. The few facts cited in literature rather state certain phenomena without trying to get closer to understanding the pathogenetic mechanisms of this new and, from our point of view, perspective kind of laser radiation, as regards its employment in medicine. With the aim of filling up this gap to some extent the authors of the work studied experimentally the influence of HHF radiation on the organism of laboratory animals when irradiating various parts of their bodies.

### The Essence of the Problem

A special HHF laser installation was developed and made for immunological research at the Institute of Radio-Electronics of National Academy of Sciences of Ukraine (IRE NAS) and used for the experiments. A gaseous discharge HCN laser of waveguide type with a high frequency pump was the source of linearly polarized coherent HHF radiation with a wave-length of  $337 \mu\text{m}$ . The power of radiation was approximately 5 mW. As components of quasi-optical (QO) waveguiding means there was used a round hollow dielectrical waveguide (HDW) of 20mm diameter and QO element, made on its basis. Required initial power level of HHF radiation was fixed with the help of QO grid polarizing attenuator, and dividing of this power among irradiating channels in necessary proportion was fulfilled by QO power dividers with change dividing elements. Laboratory animals were fixed on special supports and the irradiated zone was located at a 10 cm distance (i.e. within the Frenel zone limits) from the open end of the HDW, used as an irradiator. 3 animals underwent irradiation simultaneously via three parallel channels.

Biological effect of irradiation was assessed by the following tests: mass of body, adrenals, spleen and thymus mass, total protein, glycoproteins,  $\beta$ -lipoproteins, cholesterol, alanine aminotransferase and aspartate aminotransferase levels, chondroitin sulphate concentration in blood serum and 11-oxycorticosteroid concentration in blood plasma of the animals.

For comparing HHF irradiation effect on various body surfaces there were used 2 areas: the plantar surface of the right foot with a lot of BAP and the zone on the right side of the animal between the arch of the last rid and paravertebral muscles, with a lower density of BAP.

The objects of the study were 87 white rats of 3 months. The irradiation was performed twice with a 3 day's interval (power density was  $400 \mu\text{W}/\text{cm}^2$ , exposition time was 15 min). The rats were taken out from the experiment 7 days after the irradiation.

Summing up our study findings we can state that foot irradiation (the zone rich in BAP) resulted in an increase of the test parameters in 70% of cases, decrease of the parameters was observed in 14% of cases. When irradiating the right side of the animal (the zone with a lower density of BAP) an increase of the test readings was observed in 57% of cases, and no decrease was registered. When irradiating the bodies of the animals with HHF radiation certain changes of some biochemical components were observed, whose character depended on individual peculiarities of the animals, and on their sex in particular. In male animals the findings of albumino-carbohydrate metabolism changed significantly, in female animals significant changes in lipid metabolism were registered. The changes were observed in most cases when irradiating the foot as a zone rich in BAP.

### Conclusion

The results obtained during the experiments allow to make a conclusion about the expressed biological effect of the coherent HHF radiation when irradiating BAZ, which testifies to the possibility and perspective of employing HHF radiation of low intensity in medicine as well as to the necessity to continue the research with the aim of elaborating the methods and techniques of non-medicamentous HHF radiation therapy.

## THE POSSIBILITY OF EMPLOYING LASER RADIATION OF HYPERHIGH FREQUENCY IN ORTHOPEDICS AND TRAUMATOLOGY

V.K. Kiseliyov, E.M. Kuleshov, Yu.Yu. Kamenev, \*

V.I. Makolynets, O.P. Timoshenko, S.D. Shevchenko \*\*

\* Institute of Radiophysics and Electronics of National Academy of Sciences,  
Ukraine, Kharkov. E-mail: kiseliyov@ire.kharkov.ua

\*\* Institute of Orthopedics and Traumatology named after M.I. Sitenko  
(Ministry of Health of Ukraine), Kharkov

### ABSTRACT

The results presented are obtained when the effect of laser radiation of low intensity and hyperhigh frequency on the hole defect of the femur of experimental animals being investigated, the radiation being used as an external physical therapeutic factor at different stages of the recovering process.

### INTRODUCTION

Coherent electromagnetic radiation of non-thermal intensity is used at present in medicine as an effective physiotherapeutic means [1-3]. Well mastered sections of electromagnetic spectrum such as optical range, including ultraviolet, visible and infra-red ranges as well as the ranges of super-high frequencies (SHF) and extremely-high frequencies (EHF) are used as a rule for this purpose. The study of physiotherapeutic effect of coherent hyperhigh frequency (HHF) radiation of submillimetric range wave-length ( $0.1 \leq \lambda \leq 1 \text{ mm}$ ) on the course of pathological processes in organs during irradiating bioactive zones (BAZ) with low power density laser radiation ( $\leq 10 \text{ mW/cm}^2$ ) is a matter of no little interest. In our work [4] we experimented with the aim of studying the possibility of employing HHF laser radiation of low intensity in immunology with the use of HCN - laser ( $\lambda = 337 \mu\text{m}$ ) and quasi-optical devices of submillimetric range, created at the Institute of Radiophysics and Electronics of National Academy of Sciences of Ukraine (IRE NAS) [5]. It was shown that such radiation under certain conditions displays expressed therapeutic properties: it results in intensified production of antibodies by immunocompetent cells in particular. The objective of our research was to study the influence of HHF laser radiation of low intensity, employed as an external physiotherapeutic means on various stages of the healing process in defects of femur in white rats in order to determine the possibility of employing said radiation in orthopedics and traumatology.

### THE ESSENCE OF THE PROBLEM

In our experiments we used the improved HHF laser installation, developed at IRE NAS for immunological research [4]. To modernize the installation a HCN-laser with high frequency pump (HFP) was developed having higher stability and a low level of noise as compared with the laser with

direct current pump. Quasi-optical waveguide tract of the installation was modified for irradiating laboratory animals. The animals (white rats of Wistar line) were fixed on special supports and irradiated zone was located at a 10cm distance from the open end of the waveguide used as an irradiator. 3 animals underwent irradiation simultaneously at the installation with equal exposition and at different levels of irradiated power. 45 animals underwent treatment after an operation for producing perforation defect in their femurs. BAZ - the plantar foot surface of traumatized extremity - was subjected to irradiation (wave-length was  $337\mu\text{m}$ , interval of power density was equal to  $400-800\mu\text{W}/\text{cm}^2$ , exposure time was 15 min. and number of irradiation sessions amounted from 1 to 3). Treatment sessions began on the 7<sup>th</sup> day after the surgery, the animals were taken out from the experiment on the 14<sup>th</sup>, 21<sup>st</sup> and 28<sup>th</sup> day after surgery. The levels of 11-oxicorticosteroids, total protein, cholesterol,  $\beta$ -lipoproteins, glycoproteins, chondroitinsulphates were defined in blood, thymul and iodine tests were made, alkaline phosphates activity, AST and ALT were defined. A fragment of femur with perforation defect was studied hystologically.

Analyzing the results obtained we came to the conclusion that the action of HHF laser radiation of low intensity with a wavelength of  $337\mu\text{m}$  on reparative osteogenesis depended on two factors: the power density of irradiation and the terms of application (i.e. the stage of reparative process). The results of the analysis show that laser irradiation of foot BAZ, employed at an early stage (on the 7<sup>th</sup> day), with power density of  $400\mu\text{W}/\text{cm}^2$  renders a stimulating effect on reparative osteogenesis.

### CONCLUSION

Thus, laser irradiation of submillimetric range possesses biostimulating properties and can be used in orthopedics and traumatology as a physiotherapeutic means for the treatment of lesions of locomotor apparatus bone structures.



# A Generalized FDTD Computation Method

ZHANG Zhaofeng HE Liquean

State Key Lab of Millimeter Waves, Southeast University, Nanjing 210096, P.R.China

## Abstract

In this paper, a generalized FDTD computation method is presented, which can extract parameters of various microwave discontinuities. The programming time will be saved greatly. At the same time, a kind of new excitation method is adopted in our general software. With this method, S parameters of microstrip discontinuities and some MMIC structures are given and the results show good agreement with published data.

## Introduction

Finite Difference Time Domain method (FDTD) is very popular to solve electromagnetic problems so far because of its simplicity, flexibility and high adaptability to various sophisticated structures. However, one program can only solve one problem traditionally. Source code must be rewritten and debugged again when the calculated structure changes. It will spend much of our time in programming and debugging, and at the same time, it will eliminate the advantage of FDTD method, especially its high adaptability. In this paper, we come up with a new idea to realize the FDTD algorithm, which is very general and can calculate various microwave structures with only a little memory increased.

## Principle

The limit of traditional method lies on only considering boundary condition of the whole structure when programming, i.e., only the lattices near the boundary of the object are done specially. In order to overcome the disadvantage, the idea of "breaking up the whole into parts" is adopted in this paper. Six surfaces of every unit lattice are given the boundary condition separately. This can be done automatically in the program. It's enough to solve the fields in every unit lattice. Based on this minimum unit, program will be independent of specific structure. If only arbitrary microwave structure is input, program will mesh the structure automatically and give boundary conditions of every lattice and then solve it. It will increase only about 1/32 memory more.

In addition, a new excitation method is introduced. The excitation surface is added several lattices inside and do not need to switch the absorbing surface, which excites very naturally and can not introduce DC leading to divergence. At the same time, it can be very near the discontinuity and save the memory greatly. At the back surface absorbing boundary condition is placed. If we adopt Yee's lattice<sup>[1]</sup>, the excitation formula is given as follows:

$$H_z^{n+1/2}(i+\frac{1}{2}, j, k_{in}-\frac{1}{2}) = H_z^{n-1/2}(i+\frac{1}{2}, j, k_{in}-\frac{1}{2}) + \frac{\Delta t}{\mu} \left[ \frac{E_x^n(i+1, j, k_{in}-\frac{1}{2}) - E_x^n(i, j, k_{in}-\frac{1}{2})}{\Delta x} - \frac{(E_z^n(i+\frac{1}{2}, j, k_{in}) - E_{exc}^n(i+\frac{1}{2}, j, k_{in})) - E_z^n(i+\frac{1}{2}, j, k_{in}-1))}{\Delta z} \right]$$

where  $k_{in}$  is the position of excitation surface in propagation direction.  $E_{exc}$  is the excitation pulse.

## Results

With this new method, a generalized FDTD software package to extract parameters of various microwave discontinuities is developed. Here, some results of microstrip discontinuities and MMIC structures are given, which show good agreement with references. From the results, we can see the efficiency and general of our new FDTD realization approach.

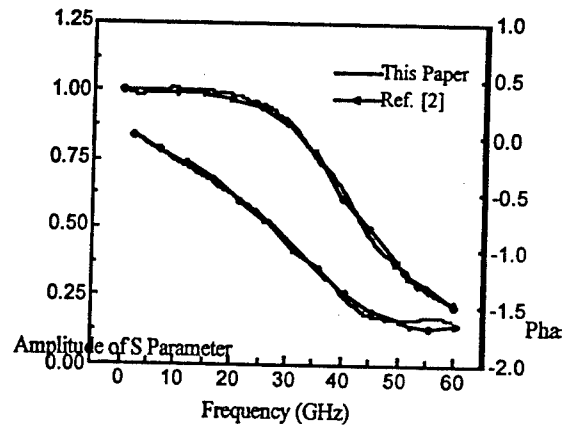


Fig. 1 Open End<sup>[2]</sup>

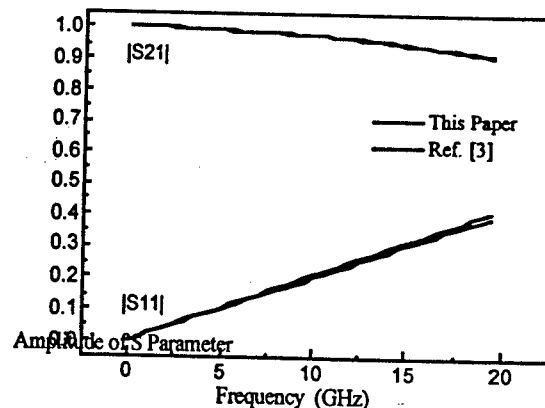


Fig. 2 Air Bridge<sup>[3]</sup>

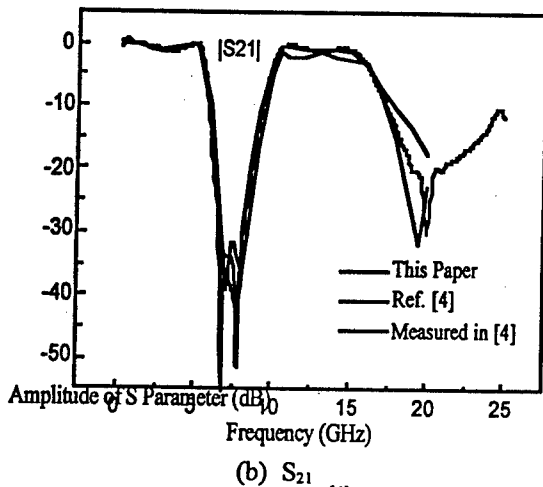
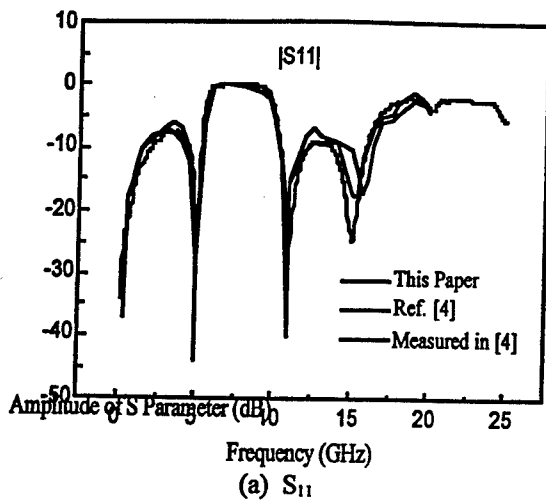
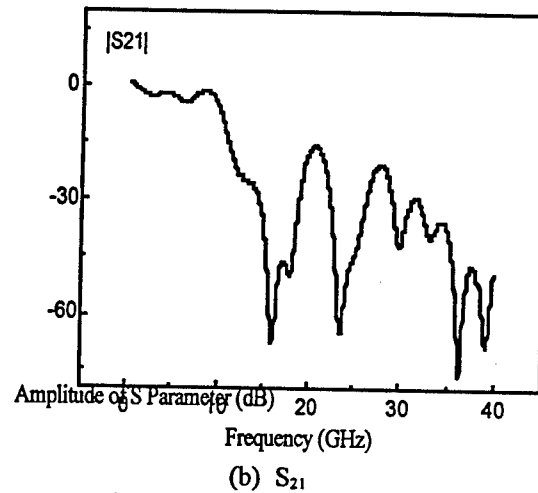
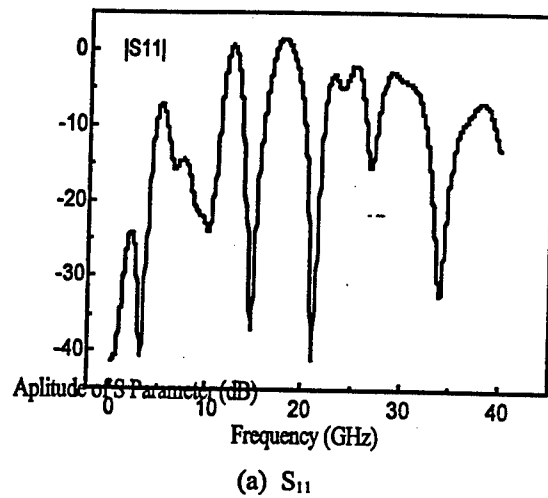
Fig. 3 Stub<sup>[4]</sup>

Fig. 5 Result of Spiral Inductor

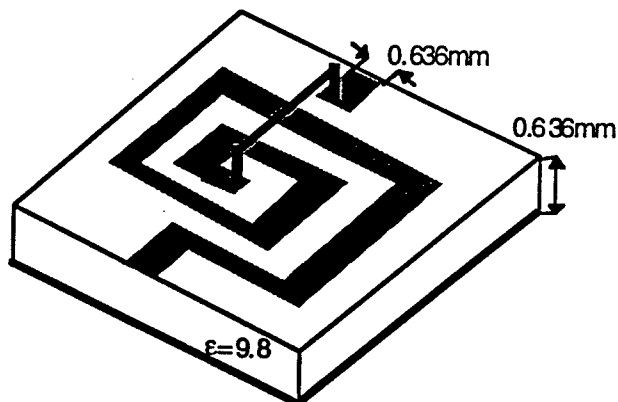


Fig. 4 Spiral Inductor  
( Air Bridge: 0.424×0.424×0.318mm  
Inductor Gap: 0.318mm )

### References

- [1] K.S.Yee, "Numerical solution of initial boundary value problems involving Maxwell's equations in isotropic media," *IEEE Trans. AP*, vol. AP-14, pp.302-307, 1966.
- [2] X.Zhang and K.K.Mei, "Time domain finite difference approach to the calculation of the frequency dependent characteristics of microstrip discontinuities," *IEEE Trans. MTT*, vol. MTT-36, pp.1775-1787, 1988.
- [3] Shuoqi Chen and Ruediger Vahldieck, "A new hybrid symmetrical condensed node for the frequency-domain TLM method," *IEEE MTT-S*, vol.2, pp.427-430, 1996.
- [4] D.M.Sheen, S.M.Ali, *et al.*, "Application of the three-dimensional finite-difference time-domain method to the analysis of planar Microstrip circuits," *IEEE Trans. MTT*, vol. MTT-38, pp849-857, 1990.

# CAD-Oriented Numerical Analysis of Surface-Wave Filters

Svetlana V. Boriskina and Alexander I. Nosich\*

Radiophysics Department, Kharkov State University, Kharkov, 310077, Ukraine

\*Institute of Radiophysics and Electronics National Academy of Sciences, Kharkov, 310085, Ukraine

## Abstract

Grounded dielectric slab surface-wave filters based on a whispering-gallery-mode dielectric resonator and a slitted metal cavity are analyzed. Due to the analytical regularization, solutions are equally accurate off and near resonances. Modes of resonators investigated are suitable for their utilization in millimeter wavelength devices.

## Introduction

Localized discontinuities are known as important components of many optical and millimeter wave electronic systems that are based on the surface wave propagation. They are used as elements of integrated couplers, low-profile leaky-wave antennas, filters, resonators, etc. Design and manufacturing of such devices is a complicated technical task. To reduce their cost and improve the electromagnetic performance, a preceding CAD simulation, by using a reliable method and a moderate computer hardware, is highly desirable. So far simulations of relevant metal and dielectric discontinuities have been based mainly on approximate theories. Further theoretical and experimental work was necessary to reveal the potentials and optimize the performance of prism and grating couplers, filters, and other passive devices. A more accurate analysis is especially important if studying the millimeter-wave applications, instead of optical ones, because here the device dimensions are comparable to the wavelength. However, it was only recently that adequate mathematical methods have been proposed, enabling one to attack the problem in correct full-wave manner.

The work on the problems related to the presented study has been started several years ago. A few regular papers have been published in the major international journals such as IEEE Transactions on Microwave Theory and Techniques [1], to outline the essentials of proposed approaches. However, they did not study specific applications such as filtering and coupling. This CAD-oriented analysis has been started in our recently published paper [2], for the circularly-shaped dielectric and metal-cavity filters in the single-mode open waveguide.

## Problem Formulation

The purpose of this study is to develop a method to modeling the localized dielectric and metal discontinuities in the

grounded dielectric waveguide (Fig. 1), and take account of the leaky and surface-wave effects.

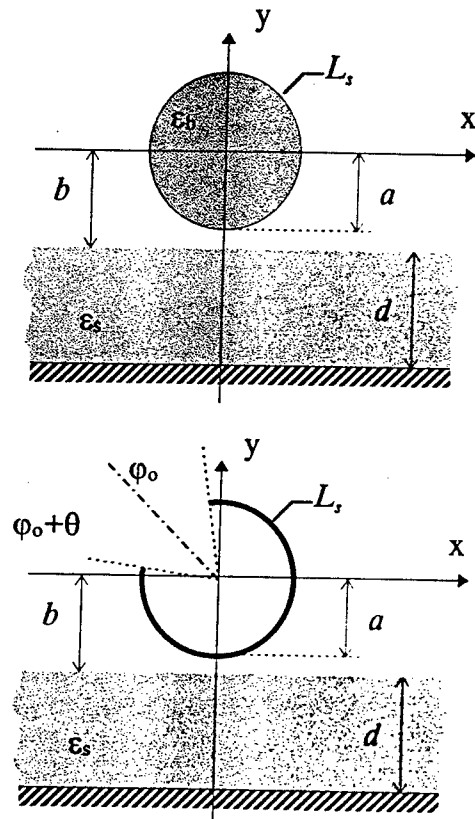


Figure 1. The geometry of the scattering problem.

Based on this method we simulated two types of surface-wave filters. For the filter based on the whispering-gallery-mode dielectric resonator we studied its acting on TE and TM modes of the grounded dielectric waveguide. For the filter based on the slitted metal cavity we considered only the case of TM-polarization because the most interesting low-frequency resonance does not exist in the TE one.

## Method of Analysis

To achieve the objectives, it was supposed to use advanced mathematical methods of electromagnetic theory of wave scattering. The first is the Green's function method which implies that the full Green's function (TE or TM-type) of a homogeneous dielectric slab is obtained analytically, and further used to derive the integral equation governing the

field. Hence, the satisfying of the slab-interface continuity conditions is guaranteed, as well as the accounting of guided and leaky modes of the waveguide. The second is the family of techniques which may be collectively named as Method of Regularization (MoR) to treat the wave scattering problems in mathematically accurate manner. It starts from a surface Integral Equation (IE) well known in electromagnetics. However, unlike MoM, here it is partly inverted analytically, that results in the infinite matrix equation of the Fredholm 2-nd kind, thus giving a proof of existence of unique solution. This procedure is equivalent to a judicious choice of basis/testing functions in MoM, so that they form a set of orthogonal eigenfunctions of the inverted part of IE. The numerical solution of such a matrix equation is always stable and efficient in terms of memory and CPU time expenses. To study the localized dielectric discontinuities, it was supposed to use the surface potentials method, extracting out and analytically inverting the free-space-circular-cylinder part of the IE. To analyze metallic curved-strip scatterer, the static part of the electric field IE was inverted.

### Efficiency and Numerical Results

The efficiency, in terms of the CPU time and memory, of the numerical algorithms, which are based on the regularization, is normally some hundred times better than those operating with direct MoM solutions. Furthermore, the former are uniformly accurate near and far from resonances. All this enables one to use them as a highly reliable instrument in CAD of the surface-wave millimeter-band circuits. Sample numerical results obtained by using the method proposed are presented in Figs. 2, 3. Transmitted ( $P_T$ ) and reflected ( $P_R$ ) power fractions as well as radiation ( $P_{sc}$ ) and dissipation ( $P_{abs}$ ) losses in such a structure were studied. In Fig. 3  $\sigma_{T(R)}$  denotes the total power carried by all right left moving waves, respectively.

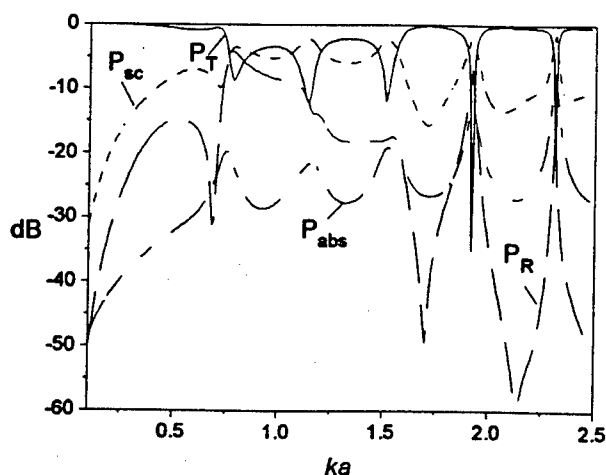


Fig. 2. Far-field scattering characteristics versus  $ka$  for a dielectric resonator. TM-polarization.  $\epsilon_b = 10 + 0.01i$ ,  $w/a = 0.01$ ,  $d/a = 1$ ,  $\epsilon_a = 2.25$

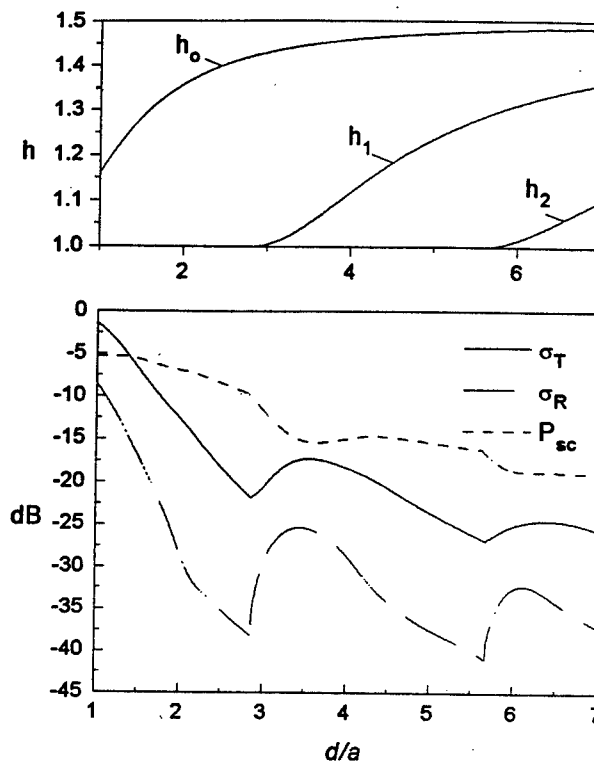


Fig. 3. Far-field scattering characteristics versus  $d/a$  for a dielectric resonator. TM-polarization.  $ka = 1$ ,  $\epsilon_b = 10$ ,  $w/a = 0.01$ ,  $d/a = 1$ ,  $\epsilon_a = 2.25$

### Conclusions

We have proposed a full-wave approach to the analysis of surface-wave bandstop filters. Based on this approach the efficient numerical techniques were developed, and rejection, transmission and radiated-field characteristics were calculated for both TE and TM-polarizations. Sharp resonant phenomena were observed for the scattering from dielectric cylinders and metal cavities. These effects can be used for the design of bandstop filters in surface-wave guides. However, to expand the research, e.g., to extend the MoR analysis to arbitrary-shaped dielectric cylinders, to metal cylinders and curved strips, and also to make a comparison of various realistic couplers and filters more studies are necessary.

### References

- [1]. A. I. Nosich, A. S. Andrenko, Scattering and mode conversion by a screen-like inhomogeneity in dielectric-slab waveguide, IEEE Trans. Microwave Theory and Techniques, vol. MTT-42, no 2, pp. 298-307, 1994.
- [2]. S. V. Boriskina, A. I. Nosich, Numerical analysis of surface-wave band-stop filters, Microwave and Optical Technology Letters, vol. 13, no 3, pp. 169-173, 1996.

**ABSTRACTS**  
**FOR**  
**NON-SUBMITTED,**  
**LATE SUBMITTED,**  
**OR**  
**NON-CONFORMING**  
**DIGEST CONTRIBUTIONS**

## FREE ELECTRON LASER WITH CROSSED MAGNETIC AND VORTEX ELECTRIC UNDULATED FIELDS OF PUMPING

Victor V. Kulish, Oleh B. Krutko, Alexander G. Kailuyk

Theoretical Physics Department, Sumy State University,  
2, Rymski-Korsakov Street, Sumy, 244007, UKRAINE

The model of FEL with crossed magnetic and vortex electric fields of pumping is considered as a convenient example for illustration of essence and possibility of application of the hierarchic theory. Besides that, a number of the interesting physical results are obtained. In particular, possibility of the isochronous states of system realization is shown, the new type of klystron schemes of FEL implementation is proposed and analyzed.

### About plasma heating by high frequency fields.

Khizhnyak N.A., Yatsenko E.A., Yatsenko N.M.  
Department of Radiophysics, Kharkov State University,  
Svoboda sq., 4, Kharkov 310077, Ukraine  
Email: khizh@khizh.kharkov.ua

The problem of excitation of the thin impedance antenna placed in anisotropic plasma was solved. The expressions for current, fields of radiation, conditions of effective energy transmission from antenna into plasma in any frequency region where one of the components of permittivity tensor was negative were obtained.

## Groove Diplexer for millimeter wave applications

A.S.Aydınlık<sup>(1)</sup>, A.A.Vertiy<sup>(1,2,3)</sup>, S.P.Gavrilov<sup>(1,2,3)</sup>, S.R.Samedov<sup>(1)</sup>

1.TÜBİTAK, Marmara Research Center, Space Technologies Department, 41470, Gebze, Kocaeli, TÜRKİYE.

Phone: 090 262 641 23 00; E-Mail: sevinc @ yunus.mam.tr

2.IRE, National Academy of Science of Ukraine, 12 Acad. Proskura st. Kharkov, UKRAINE.

3.State Research Center, FONON, 37, Pobedy Ave. 252056 Kiev, UKRAINE.

### Abstract

The Semi-Symmetrical Circular Groove Guide Resonator was suggested for different goals in millimeter wave region [1]. The main goal was the creation of a Groove Diplexer for millimeter wave receivers. For this goal, the spectral characteristics (resonance spectrum, transmission coefficient) of the Groove Diplexer are calculated and measured in  $\Delta f=30-40$  GHz frequency range .

In this study, the transmission characteristics of the Groove Diplexer are investigated by changing distance between Groove Diplexer mirrors in  $\Delta f=30-40$  GHz frequency range. If we have large distance(3-5mm) between mirrors, the resonance spectrum can be seen at low frequency range. If we have small distance (1-3mm) between mirrors, the resonance spectrum can be seen at high frequency range.

As a conclusion, Groove Diplexer can be used for millimeter wave band receivers. Also, by changing distance between mirrors, Groove Diplexer can be used for different LO and RF frequencies.

### References

- [1]. "Circular Groove Shaped Resonator for Millimeter Waves", A.A.Vertiy, S.P. Gavrilov, A.S. Aydınlık, S. Samedov, International Journal of Infrared and Millimeter Waves, pp: 1613-1637, Vol:17, No: 10, 1996.



### **Waveguide Model of Quasi-optic Resonator with Small-dimension Corner-echelette Mirror.**

O.I. Belous, A.I. Fisun, A.A. Kirilenko, V.I. Tkachenko.

Institute of Radiophysics and Electronics Ukrainian Academy of Science.

12.Ac.Proskura st., Kharkov, 310085, Ukraine.

tel: (0572)-44-87-41, fax: (0572)-44-11-05, e-mail: ire@ire.kharkov.ua

The results of the investigation of the 2-D waveguide model of the corner-echelette open resonator are presented. The corner-echelette mirror consists of two rectangular echelettes where are located symmetric to the OR axis. The theoretical research of the OR was been accomplished by generalized scattering matrix method. The quasifundamental modes are discovered with high Q-quality. This modes are specific only for the OR with corner-echelette mirror. The conception of the small-dimension OR is due to proposed.

## **Super-Resolution in Millimeter-Wave Radiovision**

Yuri A. Pirogov\*, Magdy F. Attia\*\*, Valeri V. Gladun\*,  
Andrei I Dubina\*, Dmitri A. Tischenko\*, Eugene N. Terent'ev\*

\* Faculty of Physics, M.V. Lomonosov University,  
119899 Vorob'evy Gory, Moscow, Russia

\*\* Johnson C. Smith University, 100 Beatties Ford Road,  
Charlotte, N.C. 28216, USA

**Abstract** - The possibility of passive millimeter wave radiovision is discussed. Super-resolution algorithms are developed for image enhancement in the case of 1-D and 2-D images. Electronically scanned phased array antenna systems have been used for the scanning of the observed 2-D scenes. The effect of noise, accuracy in measuring the antenna angular positions and the atmospheric effects on the resolved images have been studied. An experimental system has been developed using phased array antenna and a sensor array system in the focal plane is being proposed.

### **I. INTRODUCTION**

The possibility of utilizing millimeter waves in passive imagers has been discussed by several authors during the last decade. The basic idea of such systems is to collect the millimeter wave range thermal radiation from the scenes to form a clear image. The millimeter wave thermal radiation of the scenes is received by a specially designed scanning antenna system and then processed in the system to display the image of on the system's monitor. It is a very complicated, scientifically and technically challenging process to produce high quality images for the following reasons:

- ♦ Physical limitations on image resolution due to electromagnetic diffraction by the antenna system, the Rayleigh level.
- ♦ The thermal radiation from the scene is incoherent and the signal to noise ratio is low.
- ♦ The required high sampling, image collection and signal processing rates for real time applications.
- ♦ The need for new sophisticated mathematical and numerical techniques to control the antenna scanning, the computer controlled multi-channel system and image restoration.

Passive millimeter wave imaging systems are very attractive because millimeter waves have much less attenuation in the fog, clouds, snow, dust and rain than visible light and infrared. For this reason passive millimeter wave imaging is more efficient in poor weather conditions. Passive millimeter wave imaging systems have strong

ON POSSIBILITY OF REDUCTION OF MUTUAL INFLUENCE  
OF CLOUDY ATMOSPHERE TO PROBLEM OF RADIOMAPPING

N.V.Ruzhentsev and Yu.A.Kuznenko

Radio Astronomy Institute  
4 Krasnoznamennaya Str..310002 Kharkov,Ukraine  
E-mail: rai@ira.kharkov.ua

The differences of space period and its space orientation between earth cover and atmosphere contrasted formations are discussing in this paper. At that notes a possibility to build an algorithmic base of secondary processing of millimeter wave band airspace radioimages using mentioned differences.

# THE ALGORITHM OF RADIO IMAGES QUALITY IMPROVEMENT AT MM WAVES

N.V.Ruzhentsev, Yu.A.Kuznenko and V.P.Churilov

Radio Astronomy Institute  
4 Krasnoznamennaya Str..310002 Kharkov,Ukraine  
E-mail: rai@ira.kharkov.ua

The results of testing of two-frequency (100 GHz and 39 GHz) aircraft radiomapping system of environment are discussing. A main part of report is dedicated to examination of radioimages quality improvement with using of different filtration methods and methods of nature formation boundaries separation.

## **The dispersion equation of the half-circular helical-groove structure**

**Yu Guofen   Wang Wenxiang   Wei Yanyu   Liu Shenggang**

**The Institute of High Energy of Electronics  
University of Science and Technology of China**

### **Abstract**

The helical-groove waveguides as a slow-wave circuit have high heat capacity. The half-circular helical-groove structure has wider bandwidth than that of rectangular helical-groove structure and higher interaction impedance than that of tape helix. Those advantages make it especially suitable to be used as RF structure for high power, moderate wide-bandwidth microwave amplifier.

The dispersion equation of the half-circular helical-groove circuit is obtained making use of much simpler match-field method than that presented in early work. The calculation shows that the results obtained by both method are well agreement and verifies above superiority of half-circular helical-groove waveguide.

## BROADSIDE COUPLED DIELECTRIC IMAGE GUIDE AT MILLIMETER WAVE FREQUENCIES

A. K. RASTOGI, S. MISHRA

*Department of Physics*  
*Govt. MVAM, Bhopal (M.P.), INDIA*

### ABSTRACT

Proposed broadside coupled image guide when excited with the electric field parallel to the image planes should find potential applications in the design of low loss millimeter wave components, specially for couplers and filters. Dispersion characteristics and wave impedance for even and odd modes of the broad side coupled dielectric image guides are computed by using mode matching techniques. Dispersion curves for broadside image guide are plotted for various dielectric materials and dimensional parameters as a function of frequency. Since this structure is symmetrical, this configuration can be analysed in terms of even and odd mode phase velocities. The difference in these even and odd mode phase velocities can be used to determine the coupling between coupled dielectric slab. Various couplers in this configuration can be realised. The superiority of such couplers is also discussed.

## Enhancement of the Quality of Shielded Dielectric Resonator by Grooving of Inside Shield Wall

Yuri A. Pirogov, Evgeniya V. Misiuriyeva

Faculty of Physics  
M.V. Lomonosov Moscow State University  
Vorob'evy Gory, Moscow 119899, Russia

### Introduction

Disk dielectric resonators (DDR) [1-3] are compact and high-quality devices which are used for generators frequency stabilization and narrow-band filtering of microwave oscillations. To exclude radiation losses and irregular reactive connection of resonator with surrounding elements, smooth-wall metallic shields are used which reduce, however, high proper quality of resonator. Possibility to remove the shield on large distance from DDR is almost absent in real cases and the problem to keep high resonator quality is appeared. Here it was shown that in difference of metallic shield with smooth walls, azimuthally corrugated shield gives on the order larger quality of shielded DDR. Phenomenon of enhancement of quality of shielded DDR as a result of fulfilment of longitudinal grooves (azimuth corrugation) on inside wall of cylindrical axis-symmetric shield is due to revealed during digital modelling electrodynamics phenomenon of pushing away of electromagnetic fields from corrugated wall. As a result, effective surface of interaction of metallic wall with leaked field of whispered gallery wave of DDR is significantly reduced sharply decreasing ohmic losses on the shield.

## DISPERSION CHARACTERISTICS OF COPLANAR WAVEGUIDE WITH THICK METAL COATING

A. K. RASTOGI

*Department of Physics*

*Govt. MVAM, Bhopal, (MP), INDIA-462008*

### ABSTRACT

Approximate conformal mapping techniques have been used for analysing the effect of finite substrate thickness on coplanar wave guide (CPW) theoretically. Calculations for impedance and effective dielectric constant are presented for CPW's with finite substrate thickness. Network analytical methods of electromagnetic fields are employed to evaluate the effect of thick metal coating of CPW. Dispersion characteristics of CPW have been plotted for various metallisation thickness. Effect of strip width on total attenuation have also realised.



**Free oscillations spectrum in resonator on evanescent waveguide with two-layer magnetodielectric.**

Belous R.I., Makeev Yu.G., Motornenko A.P.

Institute of Radiophysics and Electronics Ukrainian Academy of Science.

12.Ac.Proskura st., Kharkov, 310085, Ukraine.

tel: (0572)-44-87-41, fax: (0572)-44-11-05, e-mail: ire@ire.kharkov.ua

The results of solving of electrodynamic problem for spectrum of free oscillations of resonator on evanescent modes (waveguide-dielectric resonator) with partial magnetodielectric filling were given. It was shown, that for case of axial-asymmetrical waves the solving exists as  $HE_{mnp}(EH_{mnp})$  hybrid modes. The calculated values and experimentally obtained data for  $HE_{111}$  and  $E_{011}$ -oscillations were compared.

The results obtained may be used for a creation of new microwave filters, for a measurement of different dielectric and magnetic materials including both rods and sleeves and as contour system of microwave generators.

**Micromachining Technology for Terahertz Applications****S.R. Davies, H. Kazemi, J.G. Partridge, S.T.G. Wootton and N.J. Cronin****School of Physics, University of Bath, Bath BA2 7AY, United Kingdom**

The development of micromachined waveguide components for operation at terahertz frequencies will be described. These include passive waveguide components, such as filters, directional couplers and tees, and components with integrated active devices, such as frequency multipliers.

## **Complex Propagation Results in 3-D of the Generic Arbitrary Bilateral Finlines**

**Humberto César Chaves Fernandes and Jarbas de Albuquerque Sales Neto**  
Department of Electrical Engineering - Technological Center  
Federal University of Rio Grande do Norte - PO Box: 1583  
Tel/Fax: +55 84 2153731, e-mail: humbeccf@ncc.ufrn.br  
59.072-970 - Natal - RN - Brazil

### **ABSTRACT**

An electromagnetic application is developed to obtain the complex propagation of the arbitrary bilateral finlines with semiconductor substrate and conductor thickness, simultaneity at the first time, using the concise and efficient Transverse Transmission Line method. These results are in according with that of previous works, and are good to expand the applications possibility in millimeter waves frequencies.

**Dielectric loss measurements with a confocal Fabry-Perot resonator****J. M. Dutta and C. R. Jones****Department of Physics****North Carolina Central University, Durham, NC 27707 USA**

A measurement method which combines coherent optical resonance techniques with conventional microwave techniques, has been optimized to investigate the dielectric loss properties of materials under investigation for the gyrotron window applications. The theory of the method applied is reviewed and preliminary results of some of the candidate materials are presented.

## ANALYSIS OF TWO-DIMENSIONAL DIELECTRIC GRATINGS FOR THE DESIGN OF DICHROIC STRUCTURES

IVAN TORRES LIMA JR. and ATTILIO JOSE GIAROLA\*

School of Electrical and Computer Engineering

State University of Campinas (UNICAMP)

Campinas, SP, Brazil 13083-970

### ABSTRACT

The electromagnetic wave propagation in an array of rectangular dielectric waveguides is examined here using the moment method with an adequate expansion of the electric field. The dyadic Green's function is obtained using the volume equivalence theorem. The frequency selective characteristic of a layer made up of this geometry is obtained from the boundary conditions applied at the interfaces between the dielectric grating layer and the homogeneous regions existing above and below the periodic layer.

**COUPLED SUPERCONDUCTIVITY IN OPENED AND CLOSED MICROSTRIP  
WITH VARIOUS SEMICONDUCTOR SUBSTRATS**

**Humberto César Chaves Fernandes and Gustavo Adolfo B. Lima**  
**Department of Electrical Engineering - Technological Center**  
**Federal University of Rio Grande do Norte - PO Box: 1583**  
**Tel/Fax: +55 84 2153731, e-mail: humbeccf@ncc.ufrn.br**  
**59.072-970 - Natal - RN - Brazil**

**Abstract**

It's analyzed the coupled superconductivity in opened and closed microstrip with three semiconductor substrate. This structure is applied in integrates circuits to high frequency. It's utilized in the analysis the transverse transmission line method (TTI). The results obtained show the effective dielectric constant and attenuation constant changes in function of operation frequency for the superconductor structure, with the development of one coherent theory and numeric and graphics surveys by means of one computational routine in the analysis of structure. (CNPQ).

## ELECTRON GUN DEVELOPMENT FOR HIGH POWER LOW VELOCITY-SPREAD AXIS-ENCIRCLING BEAM<sup>1</sup>

D. Gallagher, J. Richards, F. Scafuri, C. Armstrong

Northrop Grumman Corporation  
Electronics & Systems Integration Division  
Electronic Systems  
600 Hicks Road, M/S H6402  
Rolling Meadows, IL 60008  
Tel (847) 259 9600

Presented is the status of the development of a low velocity spread, 70 kV electron gun for gyro-device research. The design retains the simplicity of the Northrop Grumman (NG) novel gun concept where possible. The main design goals are: beam current = 3.5 A, magnetic focussing field = 6.5 kG, beam alpha = 1.5, beam ripple <  $\pm 10\%$ , and axial velocity spread less than 5%. Preliminary design candidates were obtained by the code NOVGUN developed at NG. This code calculates the single electron trajectories in the electric and magnetic fields calculated by solving Laplace's equation for the electric and magnetic scalar potentials. The gun electrodes and magnetic pole piece electrodes were varied systematically and automatically through hundreds of iterations until the beam ripple (guiding center spread) and axial velocity spread were minimized. To achieve both low ripple and low velocity spread, it was necessary to incorporate a magnetic ring (floating pole piece) around the cathode to deflect the magnetic field lines away from the cathode. After a preliminary design candidate was found through NOVGUN, the gun was modeled by the Herrmannsfeldt code with the magnetics accurately simulated by the MAXWELL code. Cathode surface roughness and the temperature of the cathode ring were taken into account, and the cathode was recessed to reduce edge emission. After fine tuning the design, particularly the shape of the cathode ring, the final simulations indicate all the goal specifications being met. The mechanical design of the gun was completed, all parts and fixtures were fabricated, and all gun subassemblies have been brazed and made ready for final welding.

To test the gun, a beam tester using a cerium glass scintillator witness plate, capacitive probes, and a retarded field analyzer (to measure the average axial and transverse beam velocities as well as the velocity spreads) has been designed, and its fabrication is nearly complete. The gun will be tested at reduced voltage, 24 kV, with the magnetic field and frequency scaled accordingly. Testing could begin as early as the beginning of May. Peniotron circuits have been designed for RF testing after beam testing is complete.

---

<sup>1</sup>Work supported in part by NRL and MURI.

Theory of Electron Beam --Wave Interaction in Waveguide Filled  
With Plasma in Axial Magnetic Field \*

Liu Shenggang etc

University of Electronic Science and Technology of China

Chengdu, P.R.China, 610054

FAX: 0086,28 3334131

Tel : 0086,28 3323974

e-mail: liusg@uestc.edu.cn

Abstract

General formulations of electron beam --wave interaction in waveguide filled with plasma in axial magnetic field were worked out. General interaction equations and dispersion equations have been derived and the equations of the instability criteria were obtained. It shows in the paper that these equations may cover almost all kinds of electron beam --wave interactions, such as the longitudinal interactions (TWT, BWO, Cherenkov Radiation, etc), the transverse interactions, such as ECRM (Gyrotrons). Two examples of the applications of the theory worked out in the paper are presented: the electron cyclotron resonance maser and the cherenkov radiation. Both of them are treated by means of kinetic theory. Detailed discussions are given in the paper.

\*work supported by Chinese National Natural Science Foundation

t



## EFFECTIVE MILLIMETRIC NOISE SOURCES WITH CONTROLLED CHARACTERISTICS

Vladimir A. Rakityansky

Institute of Radiophysics and Electronics

National Academy of Sciences of Ukraine

12, Acad. Proskura St., 310085 Kharkov, Ukraine

E-mail: rakit@ire.kharkov.ua; Fax: 38 0572 441 105; Tel: 38 0572 448 371

The millimetric Noise Sources (NSs) with mean output power level find the wide application in Noise Radars and various measurement systems. Approach / 1,2 /, using dynamical properties of Backward Wave Oscillators (BWOs), allows to excite millimetric Chaotic Oscillations and to develop the effective NSs with continuous and wide enough power spectrum. The NSs developed provide the oscillation frequency and power spectrum width control. The characteristic property of the method is the necessity to provide the great values of operating current to threshold current ratio in result of the oscillators operate in regimes near to limit.

To have an opportunity to increase the NSs output power and operating frequency the application of the slow-wave structures with developed interaction space is proposed to use. With this end in view the  $K_a$ -band packaged NS on BWO with modified vane-type circuit has been designed.

The new NS has efficiency more than twice as many as earlier one and provides CW output power up to  $P = 18W$  with magnetic field value of 3000G in center of samarium-cobalt system gap. Application of system with  $B=4000G$  allows to generate Noise with  $P \geq 32W$ .

Moreover the modified circuit has a lower dispersion and offers electronic tunability of Noise frequency of 8-12% in the range 33,5-38GHz. Power spectrum width depends on the operating current values and can be varied from several to 250-300MHz.

The NS characteristics, listed above, only partially show the possibilities of the method. Its application allows to excite the Noise of microwave and higher frequency of millimeter wave range. The NS combines, in essence, the functions of the modulator and oscillation source. It should be particularly emphasized, that the source is powered by DC voltage only.

At present time the Noise Sources designed are applied for development of the Noise Radars with crosscorrelation signal processing / 3 /, Noise Reflectometers / 4 / for fusion plasma diagnostic and self-mixing measurement systems and sensors with signal power spectrum processing / 5 /.

1. V.A.Rakityansky. Sources of intensive Noise Signals of millimeter wave band, International Journal of Infrared and Millimeter Waves, Vol. 16, No. 12, 1995, pp. 2085-2096.

2. V.A. Rakityansky, K.A. Lukin, Excitation of the chaotic oscillations in millimeter BWO, International Journal of Infrared and Millimeter Waves, Vol.16, No. 6, 1995, pp. 1037-1050.

3. K.A. Lukin, Y.A. Alexandrov, V.V. Kulik, V.A.Rakityansky, A.A.Mogila, Broadband millimeter noise radar, International Conference on Modern Radars, Kiev, Ukraine, 1994, pp. 30-31 (in Russian).

4. V.S. Korosteljev, K.A. Lukin, O.S. Pavlichenko, R.O. Pavlichenko, V.A. Rakityansky, V.P. Shestopalov, Correlation reflectometry via Noise Signals, Proc. of IAEA Tech. Meeting on Microwave Reflectometry, Abingdon, England, 1992.

5. V.V.Kulik, K.A. Lukin, V.A. Rakityansky, Autodyne effect in BWO operating in chaotic behavior, Int. Conf. on MM and Submm. Waves Applications. M.N. Afsar, Editor, Proc. SPIE 2250, 1994, pp. 207-208.

## DESIGNING OF MM-WAVE LNA.

I. and K. Sunduchkov\*, B. Shelkovnikov\*\*

\*) Joint-Stock Company "Saturn", 252148, Kyiv-148,

Pr. 50-Let Oktyabrya, 2b

\*\*) National Technical University ("KPI"), 252056, Kyiv-56,

Pr. Peremogy, 37

The result of development of mm-wave low noise amplifier are given in this paper. The method of designing have been described. The layouts of amplifier stages have been shown.

Characteristics of amplifiers operating in 18GHz, 37GHz and 50GHz frequency band have been presented.

**MILLIMETER WAVE COLD-CATHODE COAXIAL TWT**

Victor D. Yeremka, Maxim O. Khorunzhiy

The Usikov Institute of Radiophysics & Electronics of the National Academy  
of Sciences, 12, Acad. Proskura st., 310085, Kharkiv, Ukraine  
Telephone: 38-0572-448-519. Fax: 38-0572-441-105. E-mail: [eremka@ire.kharkov.ua](mailto:eremka@ire.kharkov.ua)

**ABSTRACT**

The first results of the investigations into the characteristics of MMW coaxial TWT with an electron-optical system comprising an autoelectronic emission cathode in the form of edge-type emitters are presented. A unique slow-wave system is described. The use of the computer model shows that the pulse-operated amplifier is capable of ensuring high-power performance characteristics.

### Phase-Locking Microwave Oscillator with Profiled DC Magnetic Field

E.Odarenko, A.Shmat'ko

Dept. of Radiophysics, Kharkov State University,  
Svobody Sq.,4, 310077, Kharkov, Ukraine

The phase locking of the resonant O-type microwave oscillator by an external signal is theoretically investigated. The signal is introduced directly onto the cavity output. Nonlinear resonant characteristics of the oscillator are calculated with two-dimensional motion of electrons taken into account. The effect of the magnetic nonuniformity on the output characteristics of the phase-locking oscillator is considered.

**MILLIMETER AND SUBMILLIMETER CW CLINOTRONS**

S. Churilova, Ye. Lysenko

Institute of Radio Astronomy  
National Academy of Sciences of Ukraine  
n 4, Chervonopraporna St., Kharkiv 310002, UKRAINE  
Phone: +380 (572) 448 564; Email: lysenko@rian.kharkov.ua

Presented are the recent results of working out CW clinotrons for millimeter and submillimeter wave band. These oscillators are characterized by an enhanced output power as compare with BWO's and carcinotrons. General performances of packaged clinotrons with water cooling and cooling system on the basis of a heat pipe are discribed.

## MILLIMETER WAVE PENIOMAGNETRON

Victor D. Yermka

The Usikov Institute of Radiophysics & Electronics of the National Academy  
of Sciences, 12, Acad. Proskura st., 310085, Kharkiv, Ukraine  
Telephone: 38-0572-448-519. Fax: 38-0572-441-105. E-mail: [eremka@ire.kharkov.ua](mailto:eremka@ire.kharkov.ua)

A description is given of the MMW peniotron oscillator with interaction space in the form of the magnetron waveguide with a spike positioned along the axis. The interaction between the large-orbit tubular electron beam and the High-frequency field occurs in static crossed electric and magnetic fields. The peniomagnetron output signal frequency change is shown to be achieved with no power being consumed in the control circuit

**INFLUENCE OF NON-RESONANCE STANDING WAVE FIELD  
COMPONENTS ON THE POWER PERFORMANCE CHARACTERISTICS  
OF MMW AUTORESONANCE PENIOTRON - OSCILLATOR**

**Victor D. Yeremka**

The Usikov Institute of Radiophysics & Electronics of the National Academy  
of Sciences, 12, Acad. Proskura st., 310085, Kharkiv, Ukraine  
Telephone: 38-0572-448-519. Fax: 38-0572-441-105. E-mail: [eremka@ire.kharkov.ua](mailto:eremka@ire.kharkov.ua)

The results of computer simulation of the MMW autoresonance peniotron-oscillator are presented. It is found that the sinusoidal and Gaussian distribution of the HF-field amplitude profile along the oscillator interaction space results in the attenuated effect of the field non-resonance harmonics on the electron and wave power exchange, thereby increasing the electronic efficiency.

## **OPTICALLY PUMPED FAR INFRARED MOLECULAR LASERS: MOLECULAR AND EXPERIMENTAL ASPECTS**

**Indranath Mukhopadhyay<sup>§</sup> and Shyam Singh<sup>\*</sup>**

**Laser Programme, Centre for Advanced Technology  
Indore 452 013, India**

<sup>§</sup> E-mail: [indra@cat.ernet.in](mailto:indra@cat.ernet.in)

<sup>\*</sup> Visiting Scientist from  
Department of Physics, University of Zambia  
P. O. Box 32379, Lusaka, Zambia.

### **ABSTRACT**

This paper will discuss extensively the optically pumped far infrared molecular lasers particularly the characteristics of the active media and their applications in various fields in science and technology. Various other experimental aspects and problems will be described in detail.



## **New Optically Pumped FIR Laser Lines from CD<sub>3</sub>OH**

**Edjar M. Telles<sup>1</sup>, Lyndon R. Zink, Kenneth M. Evenson**

*Time and Frequency Division*  
*National Institute of Standards and Technology-NIST*  
**325 Broadway, Boulder, CO 80303-3328, U.S.A.**

### **Abstract**

The CO<sub>2</sub> and N<sub>2</sub>O lasers were used as optical source to pump CD<sub>3</sub>OH. As a consequence, thirteen new far-infrared (FIR) laser lines were discovered in the range 46.8 μm to 172.6 μm.

---

<sup>1</sup>Postdoctoral fellow from CNPq-Brasilia-Brasil

## **Accurate Frequency Measurements of Optically Pumped FIR Laser Lines**

**Edjar M. Telles<sup>1</sup>, Lyndon R. Zink, Kenneth M. Evenson**

*Time and Frequency Division*  
*National Institute of Standards and Technology-NIST*  
**325 Broadway, Boulder, CO 80303-3328, U.S.A.**

### **Abstract**

A sub-Doppler signal from the gain curve of a transversally-pumped laser was used to stabilize the frequency of far-infrared (FIR) laser lines. The locked lasers have the frequency reproducibility of parts in  $10^8$  and the accuracy smaller than 30 kHz.

---

<sup>1</sup>Postdoctoral fellow from CNPq-Brasilia-Brasil.

## ABSTRACT

## Transitional Processes in HCN-laser Plasma

Kamenev Yu.Yu.

A stepwise growth in conductivity of HCN-laser gas-discharge plasma has been observed in 100 Hz impulsing discharge on emergence of the laser radiation. No effect of laser resonator re-tuning on this phenomenon is found.

## **Active Conformable Microstrip Antenna Array**

**JunXiang Ge YuXing Li**

**Department of Electronic Engineering**

**Beijing University of Aeronautics and Astronautics**

**Beijing 100083, P. R. China**

### **ABSTRACT:**

Active conformable antenna array develop from active antenna array. It can realize to conform with stuck body, and the spatial power combining from large numbers of microwave and millimeter wave solid-state low power devices. A  $2 \times 1$  active cylindrical microstrip antenna array at X band is designed.

### **KEY WORDS:**

Active Conformable Antenna Array, Power Combining, Millimeter Waves

**THE CYCLOTRON RESONANCE MASER INTERACTION  
IN A LONG NONUNIFORM SYSTEM:  
APPLICATION TO THE GYROTRON BEAM TUNNEL\***

**J. L. Vomvouridis**

National Technical University of Athens,  
Department of Electrical and Computer Engineering

**I. G. Tigelis**

University of Athens, Department of Physics

The Cyclotron Resonance Maser interaction has been extended to study the interaction of a monochromatic electron beam with a propagating TE wave in a long system with axial nonuniformity, approximated by constant gradients. The single-particle response of the system has been found to depend on two gain functions in two variables (length and frequency mis-match, both weighted by the nonuniformity), with behavior similar to the standard results of the uniform case. An exhaustive search in the two variables has identified the conditions of maximum gain. The results have been applied to typical gyrotron-beam-tunnel geometries.

\*Work supported in part by the Fusion Programme of the European Union.

**DENSITY AND ENERGY MODULATION  
OF A GYROTRON ELECTRON BEAM  
IN A PERIODICALLY CORRUGATED BEAM TUNNEL\***

A. Lazaros and J. L. Vomvoridis  
National Technical University of Athens,  
Department of Electrical and Computer Engineering

The equilibrium distribution of an electron beam, under the action of its self and image fields is studied in a periodically corrugated beam tunnel with dielectric lining of the indentations. The Poisson and beam equations are solved self-consistently in terms of the Fourier components of the electrostatic potential and the beam density and velocity. Superposition is applied to reduce the number of unknown coefficients. The system is solved numerically, to give the amplitude of the density and energy modulations for each harmonic. The results are extended to a weakly nonuniform system, to assess the behavior in a gyrotron beam tunnel.

\*Work supported in part by the Fusion Programme of the European Union.

# **HIGH-FREQUENCY NON-CYLINDRICAL MODES IN A DIELECTRICALLY LOADED CORRUGATED GYROTRON BEAM TUNNEL\***

S. Tzima and I. G. Tigelis  
University of Athens, Department of Physics

J. L. Vomvoridis  
National Technical University of Athens,  
Department of Electrical and Computer Engineering

A numerical code (*PERIODIC HE EH*) is developed for the calculation of the dispersion relation, the electromagnetic field components and the quality factor of a dielectrically loaded periodically corrugated gyrotron beam tunnel. The Floquet theorem is used to express the fields in the vacuum region and an eigenfunction expansion is employed in each dielectric indentation. The boundary conditions imposed at the interface lead to a linear system of equations, which is appropriately truncated for the numerical implementation. The results are compared with established code (*CASCADE*).

\*Work supported in part by the Fusion Programme of the European Union.

## Tomography System at Millimeter Waveband

Vertiy A.<sup>(1,2,3)</sup>, Gavrilov S.<sup>(1,2,3)</sup>, Armağan D.S.<sup>(1)</sup>, Samedov S.R.<sup>(1)</sup>

1. TÜBİTAK, Marmara Research Center, Space Technologies Department, 41470,  
Gebze, Kocaeli, TÜRKİYE.

Phone: 090 262 641 23 00; e-mail: demet@mam.gov.tr; Fax: 090 262 641 23 09

2. IRE, National Academy of Science of Ukraine, 12 Acad., Proskura St., Kharkov,  
UKRAINE

3. STATE Research Center, FONON, 37, Pobedy Ave. 252056, Kiev, UKRAINE

### Abstract

The electrodynamical system for tomographic imaging operating in millimeter wave band has been created. The tomographic process is directly applied to microwave imaging of the object which is characterized by complex dielectric permittivity [1-3].

The reconstruction of the cross-section of circular dielectric cylinder with small an absorption (the axial-symmetry function of coordinates) carried out by using Fourier-Bessel transformation. The same reconstruction in the case an absorption is uniaxial-symmetry function of coordinates is used the Fourier transform method. The results of calculation are compared with experimental data.

### References:

- [1] D. L. Mensa, *High Resolution Radar Cross-Section Imaging*, Norwood, MA, Artech House, 1991.
- [2] F. Natterer, *The Mathematics of Computerized Tomography*, B.G. Teubner, Stuttgart, John Wiley & Sons Ltd., 1986.
- [3] Mamel Nieto-Vesperinas, *Scattering and Diffraction in Physical Optics*, a Wiley-Interscience Publication, John Wiley&Sons, Inc., NewYork/ Chichester, Brisbane/ Toronto/ Singapore.



THE INFLUENCE OF IONIZATION AND STRICTION NONLINEARITIES ON  
THE SURFACE WAVES SELF-INTERACTION IN MICROWAVE GAS DISCHARGE  
PLASMAS.

K.N.Ostrikov

Kharkov State University and Kharkov Fire Safety Institute,  
2 Novgorodskaya, # 93, 310145, Kharkov, UKRAINE

The studies of the conditions of production and self-sustainment of RF and microwave gas discharges are actual because of a wide use of such discharges in many low-temperature plasma technologies. The surface waves ( SW ) which sustain the discharge are usually undergo the nonlinear behaviour. Here the influence of ionization and striction nonlinearities on the SW propagation in microwave gas discharge plasmas is studied. The propagation of the SW at the plasma-metal interface across an external magnetic field is considered. The impact of both nonlinear self-interaction mechanisms on the SW propagation as well as on the discharge structure is investigated. The obtained results can be also applied for diagnostics of low-temperature gas discharge plasmas.

SURFACE MAGNETOPLASMA WAVES IN THE SEMICONDUCTOR-SEMICONDUCTOR  
STRUCTURE WITH A NON-UNIFORM TRANSIENT LAYER

N.A.Azarenkov, A.V.Gapon

Kharkov State University, 310077, Kharkov, UKRAINE

K.N.Ostrikov

Kharkov State University and Kharkov Fire Safety Institute,  
2 Novgorodskaya, # 93, 310145, Kharkov, UKRAINE

The wave properties of the semiconductor-semiconductor two-layer structure are considered. The presence of two near-interface transient layers with the non-uniform medium density distributions is assumed. The surface magnetoplasma waves (SW) propagation across an external magnetic field ( the latter is parallel to the interface ) in the Voigt geometry is investigated. It is shown that the presence of the transient layers leads to the rise of the SW resonant damping caused by the excitation of the local hybrid resonances. The quantitative characteristics of this process are obtained as well.

## **HIERARCHIC THEORY OF OSCILLATIONS AND WAVES AND ITS APPLICATION FOR PROBLEMS OF RELATIVISTIC ELECTRONICS**

**Victor V. Kulish, Oleh B. Krutko**

**Theoretical Physics Department, Sumy State University,  
2, Rymski-Korsakov Street, Sumy, 244007, UKRAINE**

The new version of the general nonlinear theory of relativistic electronic devices with long-time interaction is elaborated. Hierarchic principle was considered as a base of this version. The Bogolubov's method of averaging, methods of averaged quasi hydrodynamic and kinetic equations and hierarchic method of asymptotic integration of Maxwell's equation are used for parametrization of the hierarchic principle.

**APPLICATION OF THE THEORY OF HIERARCHIC OSCILLATIONS  
AND WAVES FOR  
INVESTIGATION OF NONLINEAR PROCESSES IN THE  
HYDRORESONANCE SYSTEMS**

**Victor V. Kulish, Oleh B. Krutko, Alexander G. Kailuyk**

**Theoretical Physics Department, Sumy State University,  
2, Rymyski-Korsakov Street, Sumy, 244007, UKRAINE**

The peculiarities of application of the hierarchic oscillations and waves theory for the hydroresonance system nonlinear analysis are illustrated. A number of nontrivial effects that can take place here are shown and investigated. For instance, the subharmonics and fraction harmonics excitation effects, generation of quasi stationary electric field effects and others can be realized in such systems.

**EFFECT OF RELATIVISTIC ELECTRON BEAM COOLING IN THE  
ACCELERATING SYSTEM WITH CROSSED MAGNETIC AND  
VORTEX ELECTRIC UNDULATED FIELD.**

**Victor V. Kulish, \*Peter B. Kosel, Oleh B. Krutko, Ihor V. Gubanov**

**Theoretical Physics Department, Sumy State University,  
2, Rymski-Korsakov Street, Sumy, 244007, UKRAINE**

**\*Department of Electrical And Computer Engineering and Computer Science,  
University of Cincinnati, Cincinnati, OH 45221-0030**

The possibility of realization of the relativistic electron beam cooling effect is shown. The theory of hierarchic oscillations and waves is used as the methodical base. It is ascertained that the effects of acceleration and compression of the beam can occur in the same time. These are illustrated by a number of results of analytical and numerical analysis.

LOW - ENERGETIC PICOSECOND PULSE ELECTROMAGNETIC  
FIELDS OF EHF/ INTERACTIONS WITH TISSUE: ANALYTICAL  
DESCRIPTIONS OF ULTRASHORT OPTICAL PULSE PROPAGATION  
IN AN HETEROGENEOUSLY BROADENED BIOMEDIUM.

1

CHOVNJUK Y.V.

1

Kiev State Technical University of Construction &  
Architecture, 252040, KIEV, P.O.BOX 34, UKRAINE.

This work is devoted to the problems of modeling  
prophylaxis and treatment of some cancer tumour's interactions  
with a low-energetic picosecond pulse electromagnetic fields of  
EHF. We used G.L. LAMB's analytical descriptions of ultrashort  
optical pulse propagation in an heterogeneously broadened  
biomedium. We think that this is a unified survey of various  
theoretical approaches that have been developed to account for  
the novel propagation effects and influence which may take place  
when extremely short pulses of coherent millimeter waves  
interact with tissue (cancer tumour).

"NOISE INDUCED TRANSITIONS IN TISSUE" INTERACTIONS  
WITH WEAK ELECTROMAGNETIC FIELDS OF EXTRA HIGH  
FREQUENCY (EHF)"

<sup>1</sup>  
CHOVNJUK Y.V.

1.  
Kiev State Technical University of Construction &  
Architecture, 252040, KIEV, P.O.BOX 34, UKRAINE.

This work is devoted to the problem of treatment, analysis and modelling of tissue interactions with weak electromagnetic fields of the extra high frequency (EHF). We make an attempt to systematize the existing idea of possible mechanisms of millimeter waves effects on the tissues and human functional state with the help of noise induced transitions model.

"INFORMATIONAL-ENTROPY CONCEPTION IN ANALYSIS AND MODELLING OF THE MAIN PROBLEMS OF THE INTERACTION BETWEEN MILLIMETER WAVES AND TISSUE: STOCHASTIC DIFFERENTIAL EQUATIONS, MARKOVIAN AND DIFFUSIONAL PROCESSES AND THEIR TRAJECTORIES"

Chovnjuk Y.V., Tjurchaninova L.I.

Kiev State Technical University of Construction & Architecture  
252040, KIEV, P.O. BOX 34, UKRAINE

This work is devoted to the problems of treatment of the millimeter waves' interaction with a tissue. We make an attempt to sistematyze the existing ideas of possible mechanisms of extra high frequencies (EHF) electromagnetic waves' effect on the man's functional state with the help of the informational-entropy conception and mathematical modelling (stochastic differential equations, Marcovian and diffusional processes and their trajectories).



## 1.2

2.

7

1



This work is devoted to the problems of phenomenological analysis and treatment of millimeter waves' interaction and absorption by the bioobjects with chiral properties. We used the models for the complex dielectrical permittivity and volume model's polarization.

# THE TTL METHOD APPLIED TO THE FINLINE COUPLER

Humberto C. Chaves Fernandes, Sidney Alexandre P. Silva and Luiz C. de Freitas Júnior  
Department of Electrical Engineering, Technological Center PO Box 1583  
Federal University of Rio Grande do Norte, 59072-970-Natal-RN-BRAZIL  
Tel/Fax +55 84 2153731 , E-mail: humbeccf@ncc.ufrn.br

## ABSTRACT

The direct and concise method of the Transverse Transmission Line (TTL) is applied for the unilateral fin line coupler asymmetric in the plane-E , with semiconductor substrates. The effective dielectric constant, the attenuation constant, and the characteristic impedance are developed. Computer programs are developed in FORTRAN 77 language, and the results in 2-D and 3-D are obtained using a Pentium microcomputer, of the effective dielectric constant and the attenuation constant, with parameters such as the operating frequency, the thickness of the semiconductor substrate and its conductivity, and the slots widths and their location. These results are compared with references and the agreement is quite good. News results are also present.

Analysis of electromagnetic waves scattering by a dielectric cylinder  
in rectangular waveguide

V. Kalesinskas, A. Konstantinov, V. Shugurov

Scattering by a cylinder of any radius and any height is considered. Electromagnetic field is presented by eigenfunctions of the dielectric medium and boundary conditions problem is solved strictly. The algorithm can be used for measurement purposes and development of microwave devices.

Generalized Fourier Series Expansion Method for  
Determining Vco of Elliptical Optical Waveguides

Y.H.Wang, X.Zhang

Shanghai Transmission Lines Research Institute  
P.O.Box 437-833  
Shanghai, 200437  
P.R.China

Abstract

Separation of variables is applied in the elliptical coordinates without using Mathieu function. Numerical results for  $a/b=1.1; \ll 1000$  solve the disputation since 1979 about the disarrangement of Vco and demonstrate the availability of the traditional mode classification.

## AUTHOR INDEX

- Abe, H. 176, 273  
 Abend, S. 91  
 Agapova, M.V. 102  
 Agrawal, D. 1  
 Ahn, S. 304  
 Aitken, P. 200  
 Alberti, S. 104  
 Alikae, V.V. 102, 108  
 Anderson, D.T. 27  
 Anderson, J.P. 241  
 Antakov, I.I. 281  
 Antonsen, Jr., T.M. 162, 184, 227  
 Arjona, M.R. 291  
 Armagan, D.S. 361  
 Armstrong, C. 344  
 Arnold, A. 21  
 Attia, M.F. 331  
 Austin, R.H. 5  
 Aydinlik, A.S. 329  
 Azarenkov, N.A. 363
- Bae, J. 136, 247, 302  
 Ballagh, P. 202  
 Barczewski, M. 267  
 Barroso, J.J. 118, 120, 192  
 Beilenhoff, K. 257  
 Belous, R.I. 330, 338  
 Bender, B.A. 298  
 Berce, T. 33  
 Berkenkamp, A. 257  
 Bhat, B. 265  
 Bigelow, T.S. 75  
 Bishop, W.L. 259  
 Blank, M. 198, 224, 227, 235, 281  
 Bliznyuk, N.Yu. 52  
 Bluem, H.P. 5  
 Bocquet, R. 48  
 Bogdashov, A.A. 102  
 Bongers, W.A. 3  
 Borchard, P. 198, 227  
 Boriskina, S.V. 324  
 Borschegovsky, A.A. 102  
 Botton, M. 162  
 Boucher, D. 48, 93  
 Bozzi, M. 257  
 Bradley, R.F. 253  
 Brand, H. 257  
 Bratman, V.L. 3, 186, 289  
 Braz, O. 21, 29, 114, 144, 148, 150  
 Briceño, G. 140  
 Brown, J.M. 210  
 Brownell, J.H. 313  
 Bruce, R.W. 298  
 Burie, J. 93
- Calame, J. 227, 229, 231, 237, 295  
 Campman, K. 140  
 Caplan, M. 3  
 Carmel, Y. 295, 311  
 Castle, M. 237  
 Castro, P.J. 118, 120  
 Cates, C. 140  
 Ceperley, P.H. 69  
 Chance, K. 89  
 Chang, Y. 44  
 Chen, S.H. 285  
 Chen, W. 48, 93, 287  
 Chen, W.J. 285  
 Cheng, J. 237  
 Cheng, T.S. 270  
 Chiang, N. 202  
 Chirkov, A.V. 31  
 Choi, J.J. 35, 229  
 Chovnjuk, Y.V. 367, 368, 369, 370  
 Chow, G.-M. 298  
 Chu, T.S. 194, 227  
 Churilov, V.P. 333  
 Churilova, S.A. 350  
 Chursin, V. 317  
 Coleman, P.D. 219  
 Conciauro, G. 257  
 Cooke, S. 227  
 Cooke, S.J. 73, 160  
 Correa, R.A. 118, 120  
 Couperus, J. 11, 13  
 Cronin, D.W. 219  
 Cronin, N.J. 132, 339  
 Cross, A.W. 17, 63, 73  
 Crowe, T.W. 253, 259
- Dammertz, G. 114, 148, 150  
 Danly, B.G. 15, 198, 224, 233, 235, 227, 229, 231, 243  
 Davies, S.R. 132, 339  
 de Freitas, L.C. 371  
 de Kroon, S.W.T. 3  
 del Rio, C. 83  
 Denison, D.R. 81  
 Denisov, G.G. 3, 31, 102, 108, 289  
 deWolf, D. 95  
 Dikhtiar, V. 65  
 Doucas, G. 313  
 Drori, R. 67  
 Dubina, A.I. 331  
 Dumbrajs, O. 233  
 Dutta, J.M. 341  
 Eecen, P.J. 3  
 Elzendoorn, B.S.Q. 3  
 Empacher, L. 77  
 Erickson, N.R. 253
- Cahalan, P. 194

Evenson, K.M. 208, 211, 215, 275,  
354,

355

Feiven, S.A. 172  
Felch, K. 194, 198, 227  
Fernandes, H.C.C. 340, 343, 371  
Fetterman, H.R. 44  
Fischer, H. 257  
Fischer, R.P. 298, 300  
Fisun, A.I. 330  
Fix, A.Sh. 108  
Fliflet, A.W. 298, 300, 309  
Flyagin, V.A. 102, 108, 112  
Foxon, C.T. 270  
Freund, H.P. 7, 15  
Fujii, T. 136, 247, 302  
Fujiwara, M. 50  
Fukasawa, R. 176

Gallagher, D. 344  
Ganichev, S.D. 178  
Gantenbein, G. 77, 156  
Gapon, A.V. 363  
Garin, P. 104  
Garven, M. 233, 235  
Gavrilov, S. 361  
Gavrilov, S.P. 329  
Ge, J.X. 357  
Gebbie, H.A. 91  
Gerbaaux, X. 221  
Gershon, D. 295  
Giarola, A.J. 342  
Gigl, P.D. 1  
Giguët, E. 104  
Gilgenbach, R.M. 315  
Ginzburg, N.S. 17, 63, 306  
Gladun, V.V. 331  
Gleeson, P. 263  
Gleim, Th. 178  
Glyavin, M.Yu. 186  
Gold, S.H. 309  
Goldenberg, A.L. 186  
Gonzalo, R. 83  
Gossard, A.C. 140  
Goy, P. 174  
Granatstein, V.L. 7, 190, 196, 237,  
239, 285, 287, 311  
Griffin, D.W. 249  
Gross, M. 174  
Gubanov, I.V. 366  
Guo, H. 285  
Guofen, Y. 334

Hadni, A. 221  
Hafizi, B. 309  
Hagiwara, M. 174  
Haldeman, G.S. 152  
Hansen, R.J. 309

Hargreaves, T.A. 227  
Harper, B.M. 79  
Hartley, R.A. 5  
Hartnagel, H.L. 257, 263  
Hasegawa, M. 213  
Hayashi, K. 19  
He, L. 322  
He, W. 17, 73, 200  
Heidinger, R. 142  
Hirata, Y. 19  
Hiromoto, N. 50  
Hochman, J.M. 315  
Hogan, B. 237  
Hovenier, J.N. 217  
Hu, W. 116

Iatrou, C.T. 114  
Idehara, T. 110, 118, 156  
Idei, H. 146, 194  
Ikeda, Y. 106  
Ilchenko, M.E. 126, 128  
Ilyin, V.I. 102  
Ilyin, V.N. 102  
Imai, T. 19, 106, 144  
Ishihara, T. 206  
Islam, S.K. 251  
Ito, M. 302  
Ito, S. 146, 192  
Itoh, Y. 19  
Ivanchenko, I.A. 370  
Ives, R.L. 196

Jackson, R.H. 7, 15, 164  
Jain, F.C. 251  
James, W.G. 227  
Jaroszynski, D.A. 17  
Jaynes, R.L. 315  
Jelonnek, J. 166, 293  
Jerby, E. 61, 65, 67, 71  
Jones, C.R. 341  
Jory, H. 227

Kailyuk, A.G. 327, 365  
Kalynov, Yu. K. 58  
Kamenev, Yu.Yu. 319, 320, 356  
Kanai, Y. 23  
Kasigai, A. 19  
Kasperek, W. 77, 156  
Kasugai, A. 106, 144  
Katsumata, K. 174  
Kazemi, H. 339  
Kelly, W.M. 263  
Kern, S. 114  
Khizhnyak, N.A. 328  
Khizhnyak, V.I. 112  
Khmara, D.V. 102  
Khmara, V.A. 102  
Khorunzhiy, M.O. 348  
Kiesow, M. 257

- Kimmitt, M. 9, 178, 313  
 Kimura, T. 81  
 Kinhead, A.K. 298, 309  
 Kirilenko, A.A. 330  
 Kiseliiov, V.K. 85, 87  
 Kiseliiov, V.K. 319, 320  
 Koh, P.J. 259  
 Konoplev, I.V. 63  
 Kontogeorgakis, C. 95  
 Kopeck, R. 202  
 Korol, M. 61, 65  
 Korving, J. 138  
 Kosel, P.B. 366  
 Kostyna, A.N. 102  
 Koul, S.K. 265  
 Kreischer, K.E. 116  
 Krishnaswamy, J. 5  
 Krowne, C.M. 168, 170  
 Krutko, O.B. 327, 364  
 Kubo, S. 23, 146, 194  
 Kuftin, A.N. 108, 112, 186, 188  
 Kuleshov, E.M. 319, 320  
 Kulish, V.V. 327, 364, 365, 366  
 Kunkel, H.-R. 21  
 Kuntze, M. 114, 148, 150  
 Kurbatov, V.I. 108  
 Kurihara, L.K. 298  
 Kushta, T.M. 85, 87  
 Kuzikov, S.V. 31  
 Kuzmenko, Yu.A. 332, 333  
 Kyser, R.H. 229  
  
 Latham, P.E. 224  
 Lau, Y.Y. 315  
 Lawson, W. 237, 241, 291, 227  
 Lazaros, A. 359  
 Lazaryev, O.M. 124  
 Lednum, G. 202  
 Lehrman, I.S. 5  
 Lei, L. 65  
 Leibovich, Y. 71  
 Levett, R.A. 270  
 Levush, B. 15, 160, 162, 198, 224,  
 227, 229, 231, 243, 281,  
 285  
 Lewis III, D. 298  
 Li, Y.X. 357  
 Lima, G.A.B. 343  
 Lima, I.T. 342  
 Lin, C.I. 263  
 Lippens, D. 48  
 Liu, C.B. 184  
 Liu, Y. 122  
 Lohrmann, D. 39  
 Loring, Jr., C.M. 194  
 Louhi, J.T. 134, 255  
 Lygin, V.K. 188  
 Lysenko, Ye. 350  
  
 Maaskant, P. 263  
 Maezaki, K. 136  
 Makeev, Yu.G. 338  
 Makolnets, V.I. 319, 320  
 Manheimer, W.M. 35, 227  
 Manintveld, P. 3  
 Manuilov, V.N. 112, 188  
 Maranowski, K.D. 140  
 Marshall, R.E. 95  
 Masalmeh, S.K. 138  
 Mastovsky, I. 65  
 Matsuura, S. 176, 273  
 Mazaki, H. 247  
 McCurdy, A.H. 35, 229, 227  
 McNeil, B.W.J. 200  
 Mead, J.B. 277  
 Michel, G. 25, 114  
 Miller, P.F. 91  
 Milo, R. 65  
 Minami, K. 311  
 Minamide, H. 261  
 Mirjalili, G. 270  
 Mishra, S. 335  
 Misiuriayeva, E.V. 336  
 Mitsunaka, Y. 19  
 Mizuhara, Y.M. 196  
 Mizuno, K. 136, 247, 261, 302  
 Möbius, A. 29, 114  
 Moiseev, M.A. 154  
 Morimoto, S. 146  
 Motorenko, A.P. 338  
 Mottonen, V.S. 134  
 Mounaix, P. 48  
 Mouret, G. 48  
 Mukhopadhyay, I. 353  
 Muley, J.H. 313  
 Müller, H.-U. 267  
 Muravjov, A.V. 217  
 Myasnikov, V.E. 102, 108  
  
 Nakashima, S. 176  
 Naumenko, V.D. 42  
 Naumov, A. 9  
 Nemirovskaya, L.L. 154  
 Neto, J.A.S. 340  
 Newberg, I.L. 44  
 Nguyen, K. 198, 227, 229, 231  
 Nichiporenko, V.O. 102  
 Ninnis, T. 202  
 Nishida, N. 110  
 Nosich, A.I. 52, 324  
 Nozokido, T. 261, 302  
 Nusinovich, G.S. 61, 233, 239, 243,  
 285, 287  
  
 Odarenko, E. 317, 349  
 Odashima, H. 275  
 Ofitserov, M.M. 58  
 Ogawa, I. 110, 118

- Ohkubo, K. 23, 146, 194  
 Omori, M. 313  
 Ostrikov, K.N. 362, 363  
 Ozeki, H. 273  
  
 Pain, M. 104  
 Panaretos, S.K. 44  
 Parker, R.K. 227, 229  
 Parker, T.J. 172, 270  
 Partridge, J.G. 339  
 Patire, Jr., H. 192  
 Pavelyev, A.B. 112  
 Pavelyev, V.G. 112  
 Pavlov, S.G. 217  
 Pereyaslavets, M. 110  
 Pershing, D. 7, 227, 231  
 Pert, E. 295  
 Peskov, N. Yu. 17, 63  
 Petelin, M.I. 101  
 Petillo, J. 227, 231  
 Phelps, A.D.R. 17, 63, 73, 200, 289, 306  
  
 Pike, J. 263  
 Pimenta, A.A. 118  
 Piosczyk, B. 114, 150  
 Pirogov, Y.A. 331, 336  
 Platt, C. 9  
 Pluygers, J. 3  
 Poddar, A.K. 265  
 Poelman, A. 3  
 Popov, L.G. 102  
 Porterfield, D.W. 253  
 Portugall, O. 267  
 Pratman, V.L. 58  
 Prettl, W. 178  
 Prins, P.R. 3  
 Puhlmann, N. 267  
  
 Raguin, J.-Y. 158  
 Raisanen, A.V. 255  
 Rajapatirana, S. 190, 196  
 Rakityansky 346  
 Rastogi, A.K. 335, 337  
 Rayne, R.J. 298  
 Reiser, M. 237  
 Reiter, Gy. 33  
 Richards, J. 344  
 Richards, P.L. 97  
 Rintamaki, J.I. 315  
 Robb, G.R.M. 63, 200  
 Rodgers, J. 285  
 Rosenman, G. 67  
 Roy, R. 1  
 Ruzhentsev, N.V. 332, 333  
  
 Sagae, K. 206  
 Saito, S. 273  
 Sakai, K. 176, 273  
 Sakamoto, K. 19, 106, 144  
  
 Samedov, S.R. 361  
 Samsonov, S.V. 58, 289  
 Saraph, G.P. 237, 239, 241, 245, 291  
 Sarpong, B.K. 259  
 Sasaki, S. 23  
 Sato, M. 23, 146, 192  
 Sato, N. 206  
 Savilov, A.V. 58, 186  
 Sayyah, A.A. 249  
 Scafuri, F. 344  
 Schoemehl, T. 202  
 Schoen, P.E. 298  
 Schumacher, R.S. 196  
 Schunemann, K. 42, 204, 158, 166, 293  
  
 Schwab, R. 142  
 Sergeev, A.S. 63  
 Sh. Fix, A. 102  
 Shaalan, M. 257  
 Shafii, J. 27  
 Shahadi, A. 71  
 Shapiro, M.A. 81, 116  
 Shastin, V.N. 217  
 Shelkovnikov, B. 347  
 Shenggang, L. 334, 345  
 Sherwin, M.S. 140  
 Shevchenko, S.D. 320  
 Shevtsov, B.N. 319  
 Shibalkin, S.F. 126  
 Shimawaki, H. 206  
 Shimosuma, T. 23, 146, 192  
 Shmat'ko, A. 317, 349  
 Shmelyov, M.Yu. 3  
 Shugurov, V. 372  
 Shumaker, J. 202  
 Shur, D. 67  
 Siegert, M.J. 235  
 Silva, S.A.P. 371  
 Simon, A. 263  
 Singh, A. 190, 196  
 Singh, S. 353  
 Smeets, P.H.M. 3  
 Smith, S.R.P. 172  
 Sokabe, N. 213  
 Sokolov, E.V. 281  
 Sorolla, M. 83  
 Spassov, V.A. 118  
 Spencer, T.A. 315  
 Spörl, R. 142  
 Sterk, A.B. 3  
 Steup, D. 257  
 Stolpe, I. 267  
 Strijbos, R.C. 217  
 Strizhachenko, A.V. 124  
 Sunduchkov, I. 347  
 Sunduchkov, K. 347  
 Sveshnicova, L.V. 370  
 Svezhentsev, A. 130



- Taccetti, J.M. 7  
 Tachikawa, M. 208, 215, 275  
 Takahashi, K. 19, 106, 144  
 Takei, F. 136, 247  
 Takita, Y. 23, 146, 192  
 Talmadge, J.N. 27  
 Tanaka, K. 311  
 Tani, M. 176, 273  
 Tatsukawa, T. 110  
 Tazawa, M. 221  
 Telles, E.M. 354, 355  
 Temkin, R.J. 81, 116, 304  
 Teren'ev, E.N. 331  
 Theiss, A.J. 227  
 Theron, D. 48  
 Thouvenin, Ph. 104  
 Thumm, M. 21, 25, 104, 114, 142, 144, 148, 150, 156  
 Tigelis, I.G. 358, 360  
 Timoshenko, O.P. 319, 320  
 Tischenko, D.A. 331  
 Tjurchaninova, L.I. 369  
 Tkachenko, V.I. 330  
 Togawa, N. 213  
 Tokunaga, M. 174  
 Tolkachev, A.A. 37  
 Tran, C. 104  
 Tran, M.Q. 104  
 Tripathi, V.K. 287  
 True, R. 198, 309  
 True, R.B. 227  
 Tsimring, Sh. E. 188  
 Tsuneoka, M. 106, 144  
 Turullols, P. 83  
 Tzima, S. 360  
  
 Uno, T. 136, 247  
 Urata, J. 9  
 Urbanus, W.H. 3  
  
 Valentini, M. 3  
 van der Slot, P.J.M. 11, 13  
 van der Wiel, M.J. 3  
 van Dijk, G. 3  
 Vasconcellos, E.C.C. 208, 215  
 Vavriv, D.M. 42, 204  
 Velazco, J.E. 69  
 ven der Geer, C.A.J. 3  
 Venediktov, N.P. 186  
 Verhoeven, A.G.A. 3  
 Vernon, R.J. 27, 79  
 Vertiy, A. 361  
 Vertiy, A.A. 329  
 Veszely, Gy. 33  
 Vinogradov, D.V. 31  
 Vlasov, A.N. 311  
 Vogt, A. 257  
 Volgyi, F. 33  
 Volkov, V.A. 42  
  
 Vomvroidis, J.L. 358, 359, 360  
 von Ortenberg, M. 267  
  
 Wagner, D. 25, 156  
 Walsh, J. 9  
 Walsh, J.E. 313  
 Walter, M. 285, 287  
 Wang, Y.H. 373  
 Watari, T. 23, 146, 194  
 Weber, J. 257  
 Weinzierl, J. 257  
 Wenckebach, W.Th. 217  
 Wenxiang, W. 334  
 Whittum, D.H. 54  
 Whyte, C. 17  
 Whyte, C.G. 200  
 Wieland, J. 11, 13  
 Williams, J.B. 140  
 Wiltse, J.C. 46  
 Witteman, W.J. 11, 13  
 Wood, F. 229  
 Wootton, S.T.G. 132, 339  
  
 Xu, Y. 122  
  
 Yalandin, M.I. 306  
 Yamada, I. 174  
 Yamaguchi, H. 174  
 Yamakawa, S. 213  
 Yang, H. 122  
 Yanyu, W. 334  
 Yassievich, I.N. 178  
 Yatsenko, E.A. 328  
 Yatsenko, N.M. 328  
 Ye, V. 42  
 Yemelyanov, K. 204  
 Yeremka, V.D. 348, 351, 352  
 Yin, H. 198  
 Yokoo, K. 206  
 Yoshida, K. 110  
 Young, A.R. 73  
 Yushchenko, A.G. 126, 128  
  
 Zapevalov, V.E. 102, 108, 112, 154, 186, 188  
 Zasyppkin, E.V. 281  
 Zavolsky, N.A. 154  
 Zerbetto, S.C. 208  
 Zhang, J. 134  
 Zhang, X. 373  
 Zhang, Z. 322  
 Zheng, X.D. 311  
 Ziemann, E. 178  
 Zink, L.R. 208, 215, 275, 354, 355  
 Zorkin, A.F. 128  
 Zvyagintsev, A.A. 124

# **LATE SUBMISSIONS**

# Development of Output Windows for High-Power Long-Pulse Gyrotrons

Manfred Thumm

Forschungszentrum Karlsruhe, ITP, Association FZK-Euratom  
Postfach 3640, D-76021 Karlsruhe, Germany  
and Universität Karlsruhe, Institut für Höchstfrequenztechnik und Elektronik,  
Kaiserstr. 12, D-76128 Karlsruhe, Germany

## Abstract

Electron cyclotron heating (ECH) is one of the most important schemes for heating and current drive on ITER (170 GHz) and W7-X (140 GHz). High unit power (1 MW or greater) and high efficiency single-mode continuous-wave (CW) gyrotrons are being developed in order to reduce significantly the systems costs. Face-cooled double-disk sapphire and silicon nitride windows (FC-75 liquid cooling), cryogenically edge-cooled single-disk sapphire (liquid nitrogen (LN<sub>2</sub>), liquid neon (LNe) or liquid helium (LHe) cooling) and silicon (230 K refrigerator cooling) windows, water-edge-cooled single-disk CVD-diamond windows and water cooled distributed windows are being investigated in order to solve the window problem. A water-cooled window has two very important advantages, it is employing a cheap and effective coolant and it is compact and probably more reliable than other solutions and thus can also easily be used as torus window. The present paper summarizes the development status of high-power mm-wave windows with emphasis on CVD-diamond.

## Introduction

ECH is one of the major candidates for heating, current drive (170 GHz, 50 MW, CW) and start-up (90 - 140 GHz, 3 MW, 5s) on the ITER tokamak [1,2] and will be the main start-up and heating scheme on the stellarator W7-X (140 GHz, 10 MW, CW) [2] at IPP Greifswald, Germany. ECH is extremely attractive from a fusion reactor engineering point of view, offering compact launch structures, high injected power density and a simple interface with the shield/blanket. Gyrotrons with an output power of at least 1 MW per unit are under development for economical use of such heating systems. The requirement of CW operation results in extremely high demands on the material properties of the dielectric vacuum barrier windows that serve as both the primary tritium containment boundary at the torus and as the output windows of the gyrotrons. The former application is technically more demanding because a torus window must withstand a static 0.5 MPa pressure during off-normal events for safety requirement. It should use a fusion-reactor compatible cooling liquid and, in addition, its performance, both mechanical and mm-wave, must not be severely degraded by modest neutron and  $\gamma$  irradiation.

The most important aspect of high-power window development are the dielectric characteristics of the window materials i.e., loss factor  $\tan\delta$  and permittivity  $\epsilon'$ , because they affect power absorption and reflection. The thickness  $d$  of a window disk is designed so that the power reflection is minimized:

$d = N\lambda/(2\epsilon_r'^{1/2})$ , where  $N$  is an integer and  $\lambda$  is the free-space wavelength. It is evident that a temperature dependence of  $\epsilon_r'$  complicates the choice of  $d$  and that once  $d$  is fixed, maximum transmission occurs at the series of frequencies  $f_i$  for which  $N_i\lambda_i = 2d\epsilon_r'^{1/2}$  (multi-passband window). Possible solutions for broadband windows are multi-layer windows (variation of permittivity for "anti-reflection coating") or "moth-eye-type" windows providing a tapering of the permittivity. However, the ultimate solution for an ultra broadband window is the Brewster window. The Brewster angle for reflection-free broadband transmission of linearly polarized mm-waves through a window disk is given by  $\theta_{\text{Brewster}} = \arctan \epsilon_r'^{1/2}$ .

## Types of High-Power Windows

Four general classes of high-power long-pulse capable windows are being developed: distributed, liquid-edge-cooled and gas-surface-cooled single-disk, and liquid-surface-cooled double-disk [3,4]. A variety of low loss-tangent dielectric materials, i.e. boron nitride, silicon nitride, sapphire, Au-doped silicon and CVD diamond, are either in use or under active development [3].

The distributed window consists of a planar slotted structure of alternating thin bars of dielectric material between microchannel cooled metal ribs. Disadvantages are its complicated and expensive mechanical structure due to the large number of window elements, the high losses, the danger of arcing, even in an evacuated waveguide and that it transmits a single polarization. Cryogenically edge-cooled single-disk windows are an attractive option. For a number of materials including sapphire, it is found that the thermal conductivity increases and the loss tangent decreases as the temperature is reduced. Operating points are usually found between LHe and LN<sub>2</sub> temperatures, depending on material. The advantages of this type of window are that they are low loss and generally not polarization dependent. Disadvantages are that they are large (use of cryogenics implies dewars and insulation surrounding them), the operating point is subject to thermal runaway and they must be prevented by a cold trap from cryo-pumping of the dust in the antenna waveguide. Liquid-surface-cooled double-disk windows have the disadvantages that two disks are required per barrier, instead of one as in the above concepts, and the use of dielectric fluids whose properties generally conflict with safety requirements (free fluorine readily reacts with tritium, decanes are flammable, etc.). Use as a torus window is thus excluded. Several methods exist for increasing the power capability of

Table 1: Experimental parameters of present high-power mm-wave vacuum windows [3]

Material	Type	Power (kW)	Frequency (GHz)	Pulse Length (s)	Institution
water-free fused silica	single disk inertially cooled	200	60	5.0	UKAEA/Culham
boron nitride	single disk water edge cooled	930 550	110 140	2.0 3.0	GYCOM (TORIY) GYCOM (TORIY)
silicon nitride	single disk gas face and water edge cooled	130	84	30.0	NIFS/CPI
sapphire	single disk LN <sub>2</sub> edge cooled	530 285* 500 370	118 140 140 140	5.0 3.0 0.5 1.3	CEA/CRPP/FZK/TTE IAP/INFK FZK/IAP/IPF/TPP FZK/IAP/IPF/TPP
sapphire	single disk LHe edge cooled	410 500	110 110	1.0 0.5	JAERI/TOSHIBA JAERI/GA
sapphire	double disk FC75 face cooled	200 400 350 350 200 500	60 84 110 110 140 170	CW 10.5 10.0 5.0 CW 0.6	CPI NIFS/CPI CPI JAERI/TOSHIBA CPI JAERI/TOSHIBA
sapphire	distributed water cooled	65** 200*	110 110	0.3 0.7	GA/JAERI GA/CPI
diamond	single disk water edge cooled	300** 50 110	110 110 170	1 CW 3	CPI/FOM CPI/FOM JAERI/FZK

Note: \* and \*\* indicates that the power corresponds to that of a 1 MW (\*) and 0.8 MW (\*\*) HE<sub>11</sub> mode

the window without fundamentally altering the design. One is by optimizing the beam profile. Flat, non-Gaussian profiles increase the power handling capability by as much as 50 %, and annular profiles by as much as 100 %. The disadvantage of these methods is that they require the use of waveguide mode converters or non-quadratic profile mode-converting mirrors. Alternatively, high-aspect-ratio elliptical (or rectangular) windows can be used to reduce the thermal path length in one dimension. However, unless the transmission remains in an elliptical (or rectangular) guide, rather long mode converters or profile-transforming mirrors are required.

### Present State-of-the-Art

The present experimental development status of high-power mm-wave windows is summarized in Table 1. As can be seen, no windows for CW application at the MW power level have been tested up to now.

### Material Selection and Options for 1 MW, CW

In order to define the appropriate concepts for the development of 1 MW, CW mm-wave windows one has to compare the thermophysical, mechanical and dielectrical parameters of possible window materials related to the load-failure resistance  $R'$  and the power-transmission capacity  $P_T$  at different temperatures [3]. The comparison of  $R'$  and  $P_T$  for the three materials BN, Si<sub>3</sub>N<sub>4</sub> and sapphire clearly shows that there is no chance to use these dielectrics in an edge-cooled, single-disk window at room temperatures. Experiments at CPI in the US

and NIFS and JAERI in JA confirmed that even a double-disk FC75-face-cooled sapphire window has a CW-power limit of around 0.3-0.4 MW.

Using the available material parameters and employing various beam profiles, finite element computations revealed the options for 170 GHz, 1 MW, CW operation given in Table 2 [3]. Options 1 to 3, being water cooled, are preferred for their simplicity, in particular for use as a torus window. Irradiation tests with neutrons ( $3 \cdot 10^{20}$ - $10^{21}$  n/m<sup>2</sup>) and  $\gamma$ -rays (0.75 Gy/s) show no change of the loss tangent and permittivity of CVD-diamond, sapphire and high-resistivity (HR) silicon [3,5].

The ITER partners distributed the R&D for a 1 MW, CW ECH window among themselves in the following way:

- water-cooled distributed sapphire window (US)
- water-edge-cooled diamond window (EU,JA)
- 230 K-cryo-cooled Au-doped silicon window (RF)
- LNe- or LHe-cryo-cooled sapphire window (EU,JA,RF).

### CVD-Diamond Windows

As a potential new material for simple water-edge-cooled single-disk windows, diamond is attractive due to its good mechanical properties, modest dielectric constant, relatively low loss and excellent thermal conductivity. The temperature dependence of the loss tangent of CVD-diamond (DeBeers, diameter = 40 mm, thickness = 1.1 mm) at 145 GHz is presented in Fig. 1 together with sapphire (HEMEX grade) and Au-doped HR-silicon. Current CVD capabilities have allowed for tests with diamond disks of up to 100 mm diameter and

Table 2: Options for 1 MW, CW, 170 GHz ECH Windows [3]

#	Material	Type	RF-Profile	Cross-Section	Cooling
①	Sapphire/ Metal	distributed	flattened Gaussian	rectangular (100 x 100 mm <sup>2</sup> )	internally water cooled (300 K) $\tan\delta = 2.5 \cdot 10^{-4}$ , $k = 40$ W/mK
②	Diamond	single disk	Gaussian	circular ( $\varnothing = 80$ mm)	water edge cooled (300 K) $\tan\delta = 2 \cdot 10^{-5}$ , $k = 1900$ W/mK
③	Diamond	Brewster	Gaussian	elliptical (152 x 63.5 mm <sup>2</sup> )	water edge cooled (300 K) $\tan\delta = 2 \cdot 10^{-5}$ , $k = 1900$ W/mK
④	Silicon Au-doped	single disk	Gaussian	circular ( $\varnothing = 80$ mm)	edge cooled (230 K), $\tan\delta = 2.5 \cdot 10^{-6}$ , $k = 230$ W/mK
⑤	Silicon Au-doped	single disk	Gaussian	circular ( $\varnothing = 80$ mm)	LN <sub>2</sub> edge cooled (77 K) $\tan\delta = 4 \cdot 10^{-6}$ , $k = 1500$ W/mK
⑥	Sapphire	single disk	flattened Gaussian	elliptical (285 x 35 mm <sup>2</sup> )	LN <sub>2</sub> edge cooled (77 K) $\tan\delta = 6.7 \cdot 10^{-6}$ , $k = 1000$ W/mK
⑦	Sapphire	single disk	Gaussian	circular ( $\varnothing = 80$ mm)	LNe or LHe edge cooled (27 K) $\tan\delta = 1.9 \cdot 10^{-6}$ , $k = 2000$ W/mK

Note that the power capability of options ②, ③, ⑤ and ⑦ is even 2 MW.

2.5 mm thickness. In the temperature range 200-370 K the loss tangent and the permittivity of diamond are nearly constant [5]. This is not the case for sapphire and silicon. The frequency dependence of the loss tangent of sapphire, diamond and silicon is proportional to  $f$ ,  $1/f^{1/2}$  and  $1/f$ , so that the absorbed power is proportional to  $f^2$ ,  $f^{1/2}$  and constant, respectively. The loss tangent values of the large diameter CVD-diamond disks are approximately  $10^{-4}$  ( $5 \cdot 10^{-5}$  for 0.6 mm thickness) with a tendency to decrease, so that we consider a value of around  $2 \cdot 10^{-5}$  as feasible. Manufacturers (DeBeers) claim that they also can produce disks with up to 160 mm diameter which could be used as Brewster windows.

In order to validate the low-power loss tangent measurements on large-size CVD-diamond disks, a first series of experiments using a 170 GHz, 0.2 MW, 10 s JAERI/Toshiba gyrotron have been performed [6]. The dielectric loss tangent has been determined to be  $\tan\delta = 1.3 \cdot 10^{-4}$  which is in good agreement with the low power value. By comparing the experimental results with numerical simulations the thermal conductivity was estimated to be about  $k \approx 1800$  W/mK. Finite element calculations showed that the peak temperatures for CVD-diamond disks with a wide range of  $\tan\delta$  and ratio of window aperture to disk diameter are acceptable (central temperature below 300°C). The window disk in corrugated HE<sub>11</sub> wave-guide with 57.5 mm inner diameter should have an outer diameter of approximately 85-90 mm. In collaboration with the DeBeers Company, FZK is performing metallization and brazing tests on cheap (gray) diamond samples with up to 100 mm diameter and 1 mm thickness. Thermomechanical cycling at temperatures up to 450 °C did not lead to diffusion degradation of the brazing and no leaks occurred. Finite element stress calculations including brazing/ bonding stress show that the maximum principal stress is located at the window brazing (205 MPa) and is always present. During a 0.5 MPa overpressure event the stress increases to 290 MPa and the transmission of 1 MW micro-wave power finally increases the stress to 300 MPa. All these stress values are upper limits since a rigid connection between brazing collar and window disk was assumed. Because the ultimate bending

strength of CVD diamond is 600-900 MPa all stresses are well below the admissible limits.

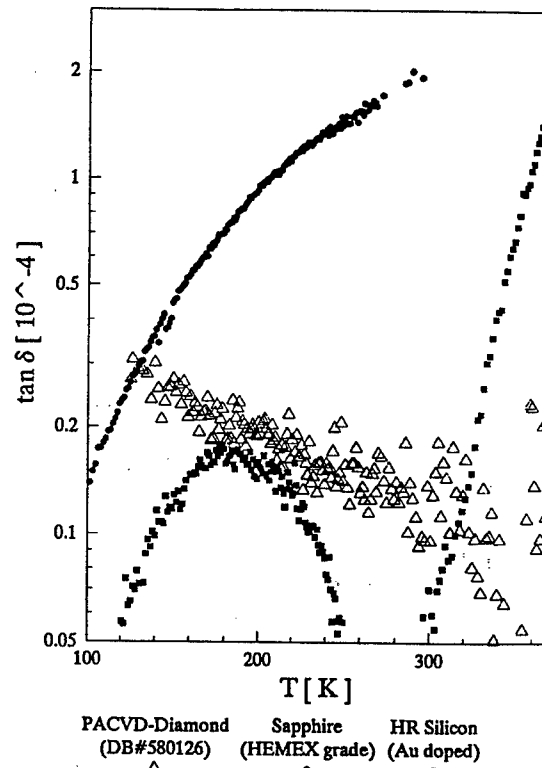


Fig. 1: Temperature dependence of  $\tan\delta$  at 145 GHz [3]

### References

- [1] Makowski, M., IEEE Trans. PS24, 1023-1032 (1996).
- [2] Thumm, M., Fusion Eng. and Design 30, 139-170 (1995).
- [3] Thumm, M., et al., Reports FZKA 5808 and 5909, 1996 and references given there.
- [4] Shimozuma, T., et al., Proc. 20<sup>th</sup> Int. Conf. on IR&MM Waves, Orlando, 273-274 (1995).
- [5] Heidinger, R., private communication, 1997.
- [6] Braz, O., et al., High power millimeter wave transmission through CVD diamond, this conference.

# ELECTRON GUN DEVELOPMENT FOR HIGH POWER, LOW VELOCITY-SPREAD, AXIS-ENCIRCLING BEAM[1]

D. Gallagher, J. Richards, M. Barsanti, F. Scafuri, C.M. Armstrong

Northrop Grumman Corporation  
Electronics & Systems Integration Division  
600 Hicks Road, Rolling Meadows, IL 60008 (847) 259-9600

## Abstract

This paper describes the status of the development of a novel, 70 kV electron gun to generate an axis-encircling beam with low axial velocity spread ( $< 5\%$ ). The gun is almost built and has applications for gyrotron and peniotron experiments at several laboratories in the United States.

## Introduction

In contrast to the high power gyrotron, which uses the MIG gun, some moderate power gyrotron-type devices require an axis encircling electron beam. These devices include harmonic gyrotrons and peniotrons and require substantially less magnetic field. For such devices to become practical, it is necessary to develop a gun to generate a high quality, axis-encircling beam with low velocity spread. The main design goals of the gun under development are: beam current = 3.5 A, with 70 kV beam voltage, magnetic focusing field = 6.5 kG, beam alpha ( $\alpha$ ) (transverse to axial velocity ratio) = 1.5, beam ripple less than  $\pm 10\%$ , and axial velocity spread  $< 5\%$ .

Another goal is to retain the simplicity of the Northrop Grumman novel gun concept[2] where possible. The traditional approach to generate an axis encircling beam is to form a hollow, nonrotating beam in a convergent Pierce gun with a spherical, annular cathode, with the magnetic field being shaped so that the field lines follow the beam trajectory. A field reversal then causes the beam to rotate at the cyclotron frequency, but with substantial ripple. Illustrated in Figure 1, the novel gun, a modification to the traditional approach, is able to generate a rotating hollow beam with little ripple, since the beam passes through a field reversal while it is still converging. By properly choosing the axial location for the field reversal, the convergence of the beam cancels the normal shift in the guiding center experienced when passing through a field reversal.

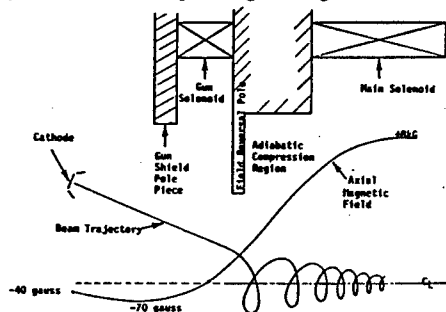


Fig. 1 Illustration of novel gun approach

However, with either approach, there is a large transverse velocity spread due to the spread in cyclotron radius,  $\Delta r$ , from the inner to the outer beam electrons. The relative velocity spread is equal to  $\Delta r/r_0$ , where  $r_0$  is the mean beam radius. By conservation of kinetic energy, the relative axial velocity spread is given by  $\Delta v_z/v_z = (\Delta r/r_0)\alpha^2$ . The solution to this problem is to reduce the magnetic field at the surface of the cathode, so that the outer electrons receive the same transverse impulse as the inner electrons. One way to reduce the magnetic field at the cathode is to divert the field lines away from the cathode surface by placing a magnetic ring (floating pole piece) either around the outside or the inside of the cathode.

## Design

The computer code, NOVGUN, developed at Northrop Grumman, was used to obtain preliminary designs for the electron gun with magnetics. The code uses simplifying assumptions, and quickly calculates electron trajectories, ripple and velocity spread. The gun electrodes and magnetic pole piece electrodes were varied systematically through hundreds of iterations until the axial velocity spread was minimized and the ripple was reasonably small. Without cathode rings, either the velocity spread or the ripple could be made small (under 5%), but the other variable would be very large ( $> 35\%$ ). With the cathode rings, the inner ring had little effect and was therefore eliminated, but the outer ring, if placed correctly, could lead to a design exhibiting low values for both attributes. The best design candidate indicated  $\pm 9\%$  ripple and 3% velocity spread. A tolerance analysis showed that pole piece dimensions are not critical. Considering the field reversal pole radius, the distance from the cathode to the field reversal pole, and the thickness and radius of the main pole piece, each value could be varied over a range of no less than 4.3 mm without causing the velocity spread to increase by more than 5%.

After completing the NOVGUN design, the next steps were: 1) to model the electrostatic gun design by the Herrmannsfeldt code and fine tune it to provide a beam with the correct perveance, shape and position with good laminarity, 2) to model the magnetics from NOVGUN by MAXWELL, 3) to adjust the currents in the coils until MAXWELL predicted the same on-axis magnetic field shape, 4) to enter the fields into the Herrmannsfeldt code and calculate the electron trajectories, and 5) to iterate the pole piece dimensions and coil currents to achieve low velocity spread with reasonable beam ripple. Velocity spread was decreased to 4% by simply shaping the

magnetic cathode ring to suppress the field along the cathode. The ring had to be the same as the outer focus electrode. Thermal calculations show that the magnetic material will be well below the Curie temperature if proper shielding is used.

After these simulations, the cathode was recessed 0.005 inch to suppress edge emission, beam temperature was included, the beam temperature was increased to 20,000° K to simulate surface roughness, and the magnetic properties for iron at 700° C (worse case scenario close to Curie temperature) were entered into MAXWELL for the cathode ring. Upon introducing these more realistic conditions to the simulations, the axial velocity spread increased only to 5%. The beam itself looks very good, having the correct size and velocity ratio (1.5). Also the beam is relatively thin and free of ripple: the total beam envelope thickness, including ripple, is about  $\pm 10\%$ . Figure 2 shows the electron trajectories and magnetic field for the final design. An important feature of this gun design is that the velocity ratio can easily be adjusted (without degrading the focusing) by varying the current on the gun coil.

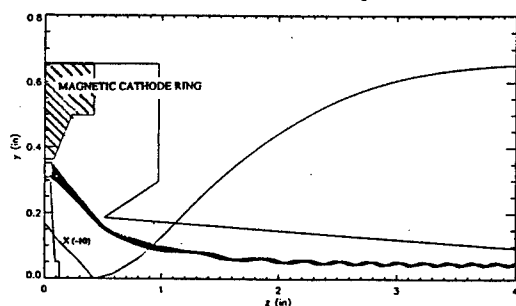


Fig. 2 Herrmannsfeldt plot for final design

## Mechanical Design and Fabrication

The gun design layout is shown in Figure 3. Fabrication is nearly complete. Figure 4 (left) shows a photograph of the gun assembly (without cathode). To test the gun, a beam tester,[3] using a cerium glass scintillator plate to form an image of the beam, capacitive probes, and a retarded field analyzer (to measure the average axial and transverse beam velocities as well as the velocity spreads) has been designed (Figure 5) and its construction is nearly complete. It includes an optical system to view the beam either by the eye or on a monitor and to print a hard copy of the image. Figures 4 (right), 6, and 7 show photographs of the capacitive probes, the movable probe and bellows assembly, and the entire gun and beam-tester assembly.

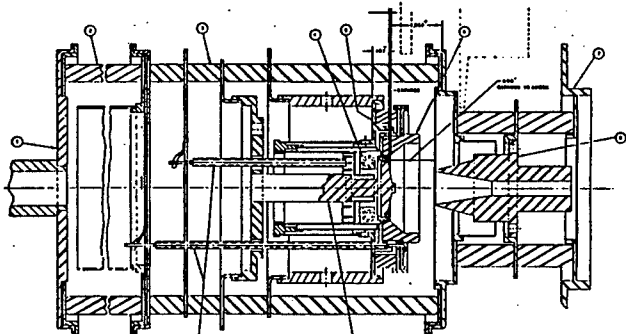


Fig. 3 Mechanical gun design layout

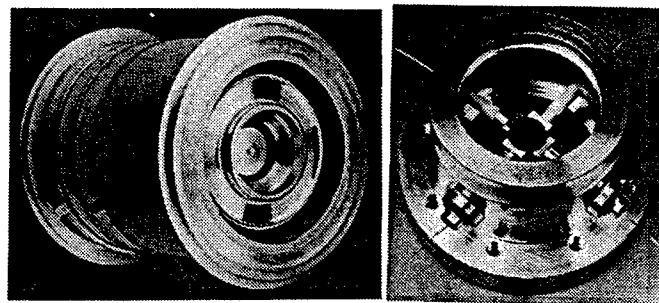


Fig. 4 Gun assembly and capacitive probe assembly

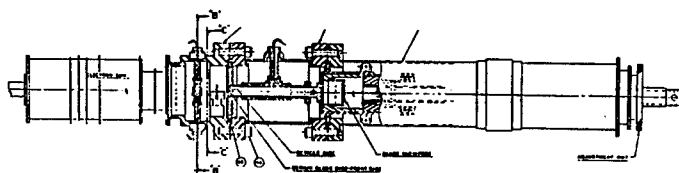


Fig. 5 Mechanical beam tester design layout



Fig. 6 Photograph of movable probe and bellows



Fig. 7 Photograph of gun and beam-tester assembly

## Conclusions

The design of a low velocity spread axis encircling beam electron gun has been completed, and simulations indicate all goal specifications being met, including 5% axial velocity spread. Fabrication of the gun along with a beam tester is nearly complete, and test results (scaled to lower voltage, 24 kV) should be available for the conference. A low velocity spread electron gun is necessary to advance from achieving proof of principal to developing practical and efficient devices such as high harmonic gyrotrons and peniotrons. After successful testing of the gun, the gun will be tested in a peniotron oscillator with a ten-vane, rising-sun magnetron-type waveguide circuit.

## References

1. Work supported in part by NRL, Contract No. N00014-94-C-2194, and by the MURI program (subcontract through the University of California - Davis, Prof. N. C. Luhmann), Main Contract No. F49620-95-1-0253.
2. G. Dohler, D. Gallagher, R. Moats and F. Scafuri, "Recent Peniotron Results at 45 GHz" International Electron Devices Meeting (IEDM) Technical Digest, 1987, pp 311-314.
3. D. Gallagher, J. Richards, F. Scafuri, and G. Dohler, "Update of Harmonic High Power 95 GHz Peniotron Development," Vacuum Electronics Annual Review Abstracts, May 1994, pp. 3-65 to 3-71.

### Gyro-Traveling-Wave Tubes

K. R. Chu  
Department of Physics  
National Tsing Hua University  
Hsinchu, Taiwan, ROC

High power and broad bandwidth capability of the gyrotron in the millimeter and sub-millimeter wavelength range makes it an attractive source for various applications. In particular, the gyrotron traveling wave amplifier is a promising candidate for such applications as radar and electronic counter measures which require broad bandwidth. In contrast to conventional linear beam devices, the electron beam employed in the gyrotron has a purposeful transverse motion at the electron cyclotron frequency. It is this property that allows the beam to selectively interact with a high order mode at a high cyclotron harmonic by properly matching the resonance conditions. However, the extra degree of freedom provided by the multitude of cyclotron harmonics can also generate numerous spurious interactions. Mode competition thus constitutes the principal physics and technology issues common to high power and high harmonic gyrotron research and development. Studies of multi-mode interaction processes under various conditions have shed much light on the physics of mode competition and major advances in high power and high harmonic gyrotrons have been reported by our colleagues in the international community.

In this talk, we report two aspects of the gyro-TWT research and development. The first is a series of theoretical and experimental studies at the National Tsing Hua University which investigates the interplay between the absolute instability, circuit losses, reflective feedback, and the amplifying wave, resulting in the suppression of spurious oscillations and the demonstration of a high power (65 kW), broadband (10%), and high gain (50 db) Ka-band gyro-TWT. The second aspect concerns the theoretical investigation of a novel type of harmonic gyro-TWT which provides frequency multiplication as well as power amplification. In collaboration with the University of Maryland group, we analyze physical properties of importance to the harmonic multiplying gyro-TWT. It is shown that interference from lower harmonic perturbations can significantly affect the interaction efficiency. The power/gain scaling and the phase relation between the drive and output waves are found



# The Cyclotron Resonance Maser in a Long Nonuniform System (Beam Tunnel)\*

J. L. Vomvoridis<sup>(1)</sup> and I. G. Tigelis<sup>(2)</sup>

<sup>(1)</sup> National Technical University of Athens, Dept. of Electrical and Computer Engineering

<sup>(2)</sup> University of Athens, Department of Physics

## Abstract

The Cyclotron Resonance Maser interaction has been studied for a long system with axial nonuniformity (the beam tunnel), approximated by constant gradients. The single-particle response of the beam has been found to depend on two gain functions in two natural variables, with behavior similar to the standard results of the uniform case. An exhaustive search in the two variables has identified the conditions of maximum gain and an approximation has been obtained for the starting current.

## 1. Introduction

In a gyrotron beam tunnel, the increasing magnetostatic field (hence the relativistic gyrofrequency  $\tilde{\omega}(z)/\tilde{a}$ ) can be compensated both by the decreasing parallel velocity  $v_z(z)$  and the decreasing axial wavenumber  $k(z)$  (as the tunnel converges), the result being that the resonance condition  $\tilde{\omega} = \tilde{\omega}/\tilde{a} + kv_z$  can be maintained over respectable axial distances. This potentially causes a premature excitation of the cyclotron resonance interaction inside the beam tunnel (rather than in the gyrotron cavity), with consequences as regards the beam quality and the performance of the system. This has been possibly the case in the quasi-optical gyrotron of CRPP and the observation of accompanying parasitic oscillations [1]. In addition, it has been found [2] that the beam tunnel can support propagating modes, which are largely unaffected by the presence of the absorbing dielectric material inside the corrugations.

In order to obtain background information, useful for the design of a gyrotron beam tunnel, we have studied the cyclotron resonance maser interaction in a system, in which all quantities of relevance are approximated by linear functions in the axial distance  $z$ . Since the typical beam tunnel is rather long, a decomposition of any oscillation into a forward (resonant) and a backward (nonresonant) wave is possible, while at the radial position of any element of the monoenergetic annular beam the wave fields can be locally decomposed into two counter-rotating circular polarizations, of which only one is resonant with the electrons. Expecting low-gain conditions to prevail, the linear (small-signal) analysis is performed in Sec. 2, where the electrons are treated as test particles, whose trajectories are integrated up to the second order in the wave-field amplitude. This process identifies the natural dimensionless parameters of

the interaction (length  $x$  and frequency mis-match  $A$ , both normalized to the nonuniformity). In Sec. 3 the ensemble average over the electron beam distribution is performed, to give the beam response, expressed by the linear (small-signal) efficiency. This is expressed in terms of two resonance functions  $F_1$  and  $F_2$ , both of which depend on the quantities  $A$  and  $x$ . Finally, in Sec. 4 the frequency mis-match parameter is scanned to identify the conditions of highest linear gain and the equation for energy conservation is used to give the starting current for the (undesired) growth of the cyclotron resonance maser inside the nonuniform beam tunnel.

## 2. Electron trajectories

According to the model described in Sec. 1, the variation with the normalized axial distance  $\alpha = iz/c$  of the axial magnetostatic field  $B$ , the refractive index  $n = kc/\tilde{\omega}$  and the normalized wave-field amplitude  $E = eE_0/mc\tilde{\omega}$  at the electron position is taken to be

$$B(\alpha) = B_0(1 + \tilde{a}_1\alpha), \quad n(\alpha) = n_0(1 + \tilde{a}_2\alpha) \quad \text{and} \quad E(\alpha) = E_0(1 + \tilde{a}_3\alpha)$$

the latter giving the fields felt by each electron as

$$\vec{E}_\perp = E_0(z) [\vec{e}_x \cos(\varphi) + \vec{e}_y \sin(\varphi)], \quad \vec{B}_\perp = (k/\omega) \vec{e}_z \times \vec{E}_\perp$$

The dynamics of the electrons are described in terms of the polar components of the dimensionless momentum ( $u_\perp, \dot{\alpha} + \tilde{a}$ ,  $u_\parallel$ ) and the relativistic factor  $\tilde{a}$ . On the assumption of a weak field amplitude, each of these quantities is assumed to be described by an expansion of the type  $\tilde{a} = \tilde{a}^{(0)} + \tilde{a}^{(1)} + \dots$  where  $\tilde{a}^{(n)} \propto E^n$ . Introducing such expansion in the equations of motion yields at first the trajectories to zero order in the wave field amplitude, which describe simply adiabatic cyclotron motion. Of particular mention is the zero-order expression for the phase angle,  $\theta^{(0)} = \theta_0 + \Delta_0\zeta + \Delta_1\zeta^2$ , where the linear term involves the frequency mismatch  $\tilde{A}_0 = (c/v_{z0})(k_0v_{z0} - \tilde{\omega} + \tilde{\omega}/\tilde{a}_0)/\tilde{\omega}$ , while the quadratic term

$$\Delta_1 = \left( -\frac{\gamma_0 u_{\perp 0}^2}{4u_{\parallel 0}^3} + \frac{\Omega_0}{2\alpha u_{\parallel 0}} + \frac{\Omega_0 u_{\perp 0}^2}{4\alpha u_{\parallel 0}^3} \right) \delta_1 + \frac{n_0}{2} \delta_2$$

involves a weighted balance of the gradients of  $B$  and  $k$ . Consequences of this term are (a) the appearance of Fresnel integrals  $S$  and  $C$  in the terms of order one or higher and (b)

the associated introduction of the natural parameters  $x$  and  $A$ , which are defined by

$$a = \sqrt{(2/\pi)|\Delta_1|}, \quad A = (\Delta_0/\pi a) \operatorname{sgn}(\Delta_1) \quad \text{and} \quad x = a\bar{x}$$

and represent the dimensionless distance and frequency mis-match. By subsequent integrations the expressions are obtained for the corrections to first and second order. These expressions are too lengthy to be presented here.

### 3. Small-signal efficiency

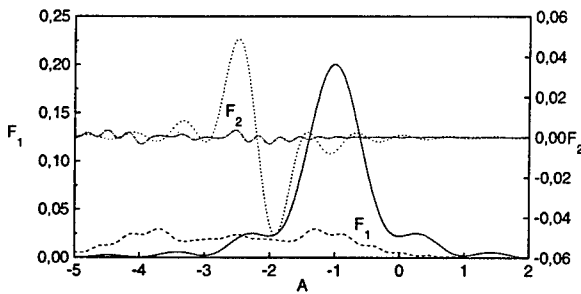
In the expressions obtained in the previous section and for our model of a thin annular monoenergetic beam, individual electrons are distinguished by the initial value of the relative phase angle  $\phi_0$  and (when the azimuthal index is  $m \neq 0$ ) the value of the field amplitude felt by each electron, hence the normalized quantity  $E$ . Performing to the second-order energy  $\bar{a}^{(2)}$  an average over these quantities yields the small-signal efficiency of the interaction,

$$-\langle \gamma^{(2)} \rangle_{\phi_0} = (\gamma_0 - 1)\eta = (1 + \delta_{m0}) \frac{E_0^2 \zeta^2}{2u_{10}} (-S_1 F_1 + \zeta S_2 F_2)$$

where the gain functions  $F_1$  and  $F_2$  are given by

$$F_1(x, A) = \frac{1}{4x^2} \left\{ [S(x+A) - S(A)]^2 + [C(x+A) - C(A)]^2 \right\}$$

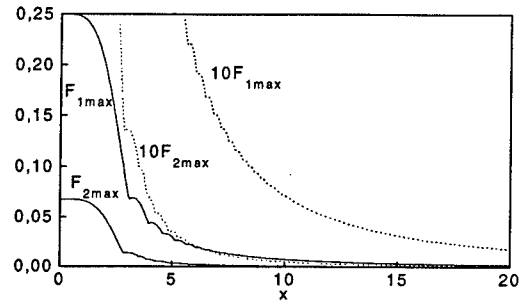
and  $\partial F_2 = \partial F_1 / \partial A$ , while  $S_1 = 2\bar{a}_0/u_{10} - n_0[2 + (u_{10}/u_{10})^2]$  and  $S_2 = [1 - n_0/u_{10}(\bar{a}_0 \cdot \bar{u}_0/\bar{u})](u_{10}/u_{10})^2$ . These functions represent the extension to a nonuniform system of the corresponding functions in a system with no axial gradients. In particular, it can be immediately seen that  $-F_1$  is always negative, representing a stabilizing term, while  $F_2$  may be positive, thus producing instability. Their variation is seen in the following figure, which gives  $F_1$  and  $F_2$  as functions of  $A$  for  $x=2$  and  $x=5$ .



For values up to  $x \approx 3$  both functions behave largely similar to the uniform case. Beyond  $x \approx 3$  the function  $F_1$  is characterized by a broad positive plateau, while  $F_2$  by spikes, competing for the overall maximum. Both functions attain there substantially smaller values than when  $x < 3$ .

### 4. Starting current

The efficiency obtained in the previous section can be used in the energy equation,  $\partial W_{em}/\partial t = \rho I_b V_b - (i\omega/Q)W_{em}$ . Requiring that  $\partial W_{em}/\partial t < 0$  and since both  $\rho$  and  $W_{em}$  are proportional to  $E^2$ , gives the starting current, as function of the two natural parameters  $x$  and  $A$ . Since typically the frequency spectrum of the beam tunnel is very dense and in addition the location of the  $F_2$ -maxima is a very sensitive function of the design parameters, it does not appear to be practical to select design parameters, which avoid the potentially unstable regime (the values of  $A$  for which  $F_2 > 0$ ). A safer procedure is to require, that the system be stable for any value of the frequency mis-match, hence of  $A$ . Scanning the curves  $F_1$  and  $F_2$  over  $A$ , gives the maxima independently for each function, as is shown in the following figure.



Of course, the maximum of the efficiency  $\eta$  depends also on the coefficient to  $F_2$ . However, for values  $x > 3$  of the natural length it has been observed that at the spikes of  $F_{2max}$  the corresponding value is  $F_1 \approx 0.5F_{1max}$ . Furthermore, for  $x > 3$  one can use simple inverse-power approximations for  $F_{1max}$  and  $F_{2max}$  giving the final result for the starting current  $I_{st}$

$$QKI_{st} = 680A[2/(1 + \bar{a}_{m0})](\bar{u}/c)^3 Va^2 u_{10}/(-0.38S_1 + 0.44S_2/a)$$

where the quality factor  $Q$  and the coupling coefficient  $K(= \bar{a}_0 E_0^2 V / 2W_{em})$  depend only on the resonant propagating mode of the beam tunnel and can be obtained e.g. using the procedure of [2]. This equation (which is applicable only when  $x > 3$ ) brings out the significance of axial gradients in suppressing the cyclotron resonance interaction: It indicates a starting current proportional to  $a^2$ , that is, to the gradient, while in addition the unstable effects are also reduced by a factor  $a$ , that is the square root of the gradient.

[1] M. Pedrozzi, These No. 1608, Ecole Polytechnique Federale de Lausanne (1997).

[2] I. G. Tigelis, J. L. Vomvoridis and S. Tzima, paper #118, this conference (1997).

\*Work supported in part by the Fusion Programme of the European Union under contract ERB 5004 CT 96 0060.

# Density and Energy Modulation of a Gyrotron Electron Beam in a Periodically Corrugated Beam Tunnel\*

A. Lazaros and J. L. Vomvoridis

National Technical University of Athens, Dept. of Electrical and Computer Engineering

## Abstract

The equilibrium distribution of an electron beam is studied in a periodically corrugated beam tunnel with dielectric rings. The Poisson and beam equations are solved in terms of the Fourier components of the relevant quantities. Superposition is applied to reduce the number of unknown coefficients. The system is solved numerically, to give the amplitude of the density and energy modulations.

## 1. Introduction

In a gyrotron beam tunnel, the use of alternating dielectric and conducting rings may introduce modulations in the electrostatic potential, as well as the energy, velocity and density of the electron beam. These modulations may (a) shift the threshold for beam penetration through the beam tunnel, possibly resulting in the reflection or trapping of electrons, (b) increase the energy spread, during transition from laminar to turbulent flow, and (c) develop some parametric instability, due to plasma frequency modulation.

To study these effects, in Sec. 2 all quantities of relevance are expanded in Fourier series, with the coefficients interrelated by the appropriate conservation laws. In order to avoid two interfaces in Laplace's equation, superposition is used, reducing the number of coefficients needed for the electrostatic potential by a factor of two. The system of equations is solved in Secs. 3 and 4, to obtain the dependence on the beam current in a uniform and a mildly nonuniform system, respectively.

## 2. Formulation

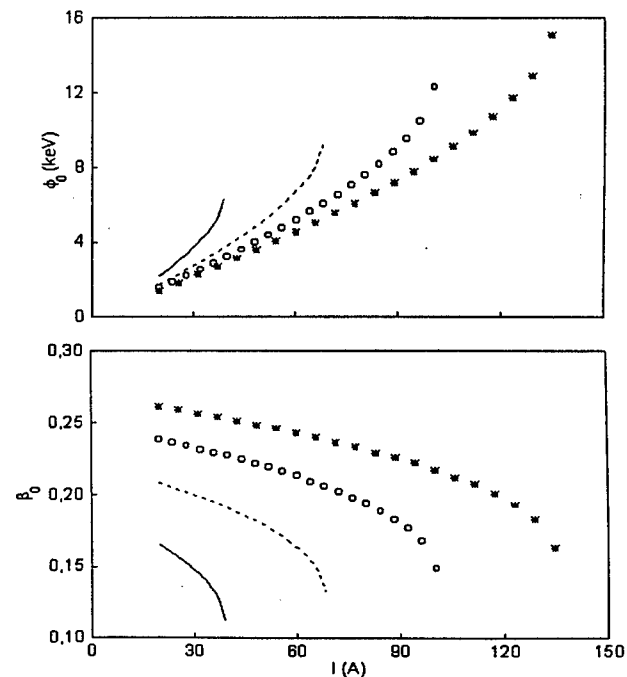
In a periodically corrugated system, but otherwise uniform along the axis (or, in the sense of a WKB approximation, with mild axial variations), the periodicity of length  $L$  allows for the surface charge density  $\phi$ , the normalized parallel velocity  $\hat{a}_z$ , and the relativistic factor  $\hat{a}$  to be represented by Fourier series, with coefficients interrelated by the law of continuity (involving the beam current  $I$ ), the conservation of energy (involving the total energy  $W_{tot} = (\hat{a}_{ref} I) mc^2$ ) and the definition of  $\hat{a}$ . The fourth equation is Laplace's equation for the electrostatic potential  $\bar{\phi}$ , along with the standard boundary ( $\bar{\phi}=0$  at conductor,  $\bar{\phi}=finite$  on axis) and interface conditions ( $\hat{a}\bar{\phi}=0$  and  $\hat{a}(\partial\bar{\phi}/\partial r)=0$  at the

dielectric-vacuum interface at  $r=a$  and  $\hat{a}\bar{\phi}=0$  and  $\hat{a}(\partial\bar{\phi}/\partial r)=-\phi/\hat{a}_0$  across the electron beam at  $r=r_b$ ).

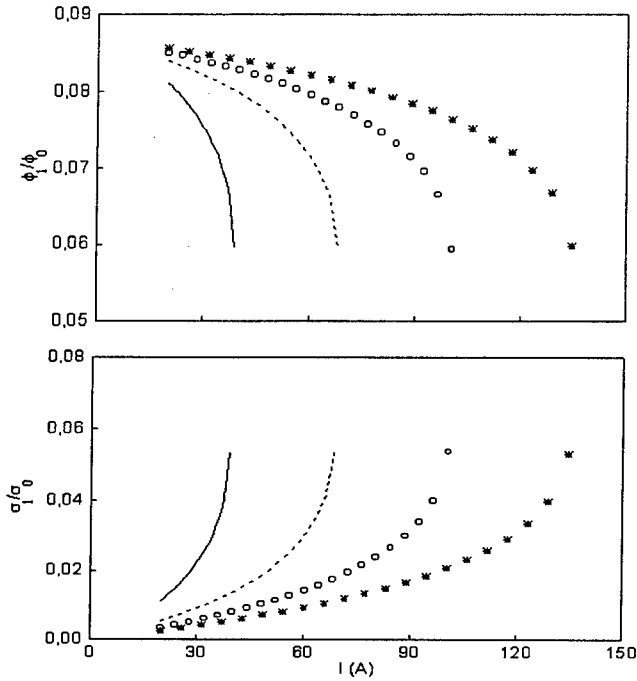
Two intermediate interfaces normally require partitioning of the system in three regions, with result a large number of Fourier coefficients to be determined. This can be avoided by using superposition,  $\bar{\phi}=\bar{\phi}_1+\bar{\phi}_2$ . The term  $\bar{\phi}_1$  is the solution in the presence the electron beam at  $r=r_b$ , when at the radius at  $r=a$  there is a conducting wall, and its Fourier coefficients can be obtained in closed form (in terms of the coefficients of the surface density  $\phi$ ). The term  $\bar{\phi}_2$  is therefore fully continuous at  $r=r_b$ , thus  $\nabla^2\bar{\phi}_2=0$  requires partitioning in two regions only. Although the interface conditions for  $\bar{\phi}_2$  at  $r=a$  are somewhat more complicated (involving  $\partial\bar{\phi}_1/\partial r$  too), this procedure reduces the number of unknown expansion coefficients by a factor of two.

## 3. Modulation of a beam in a uniform system

The system of equations outlined in Sec. 2 is first solved for the constant terms. The dependence on the current is shown in the following figures, for a pitch-angle ratio  $\hat{a}=2$  and permittivity  $\hat{a}=5$ , with  $\hat{a}_{ref}$  ranging from 1.10 to 1.25.



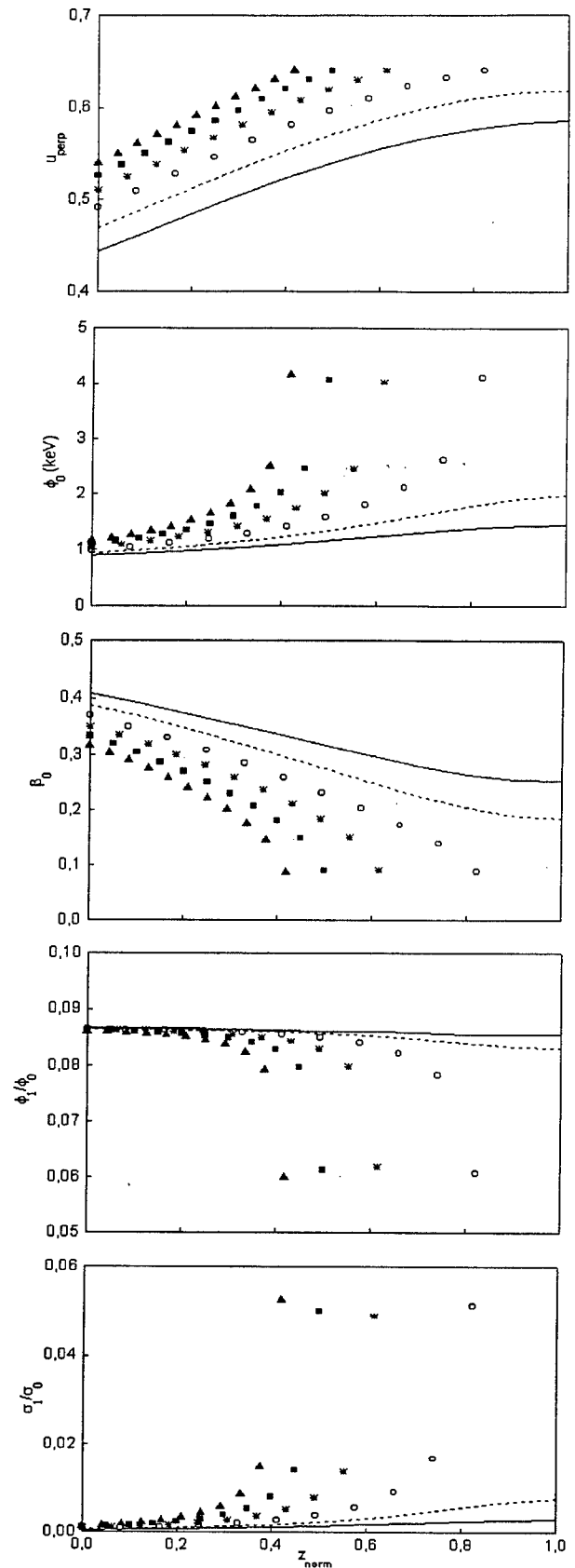
A clear cut-off current is indicated in these figures, by the very steep variation of the unmodulated parameters. At current cut-off the beam is reflected and the analysis breaks-down. The relative amplitude of the first harmonic is a decreasing function of the current for the electrostatic potential and an increasing one for the surface charge density, as is seen in the next figure.



It is also seen that although the fractional fluctuation levels depend on the electron energy, their minimum and maximum values occurring at cut-off current, are independent of the electron energy but depend only on the geometry of the system and the dielectric constant of the absorbing material.

#### 4. Modulations in a nonuniform system

The additional equation in the case of a nonuniform system is the conservation of the electron magnetic moment. The variation of the equilibrium parameters and of the relative amplitude of the modulations along the axis of a converging system with  $B(z=1)/B(z=0)=16/9$  is illustrated in the next figure, for  $\tilde{a}_{ref}=1.2$ ,  $I=20$  A and with the pitch angle ratio ranging from  $\tilde{a}=0.9$  to  $1.4$ . It is seen that electron beams with sufficiently low initial pitch-angle ratios could always pass through the channel, with the maximum transmitted initial pitch-angle ratio decreasing with the current (for  $I=20$  A transmission is allowed up to  $\tilde{a}=1.1$ ); otherwise the beam is reflected somewhere inside the channel.



\*Work supported in part by the Fusion Programme of the European Union under contract ERB 5004 CT 96 0060.

## High-Frequency Modes in a Dielectrically Loaded Corrugated Gyrotron Beam Tunnel\*

I. G. Tigelis<sup>(1)</sup>, J. L. Vomvoridis<sup>(2)</sup> and S. Tzima<sup>(1)</sup>

<sup>(1)</sup> University of Athens, Department of Physics

<sup>(2)</sup> National Technical University of Athens, Dept. of Electrical and Computer Engineering

### Abstract

A numerical code (*HYBRID*) is developed to calculate the dispersion relation, the electro-magnetic field components and the quality factor of a dielectrically loaded periodically corrugated gyrotron beam tunnel. The results are interpreted as the result of coupling between cavity and waveguide modes.

### 1. Introduction

In order to obtain information on beam-wave interactions potentially taking place inside a gyrotron beam tunnel, the information typically needed includes at first the dispersion relation  $\omega(k)$ , in order to identify possible resonances with the electron beam, and subsequently, for the resonances identified, the quality factor  $Q$  and the field structure, in order to assess the coupling to the electron beam. In Sec.2 the Floquet theorem is used to express the fields in the vacuum region and an eigenfunction expansion is employed in each dielectric indentation. The boundary conditions at the interface lead to a linear system of equations, which is appropriately truncated for the numerical implementation of Sec.3. From the discussion of the sample results in Sec. 4, the behavior reveals a coupling between strongly damped cavity modes (controlled almost exclusively by the geometry of the corrugations) and propagating waveguide modes (dependent only on the inner diameter of the tunnel), largely unaffected by the presence of the lossy dielectric.

### 2. Analysis

In a gyrotron beam tunnel, because of its length, the precise type of boundary conditions at its ends is of no particular significance. Thus, in view of the periodicity, Floquet's theorem can be used. In addition, the axial variation is mild enough to permit a quasi-adiabatic WKB approximation.

Accordingly, following standard procedures, the axial field components  $E_z$  and  $H_z$  in the inner (vacuum) region (with axial periodicity  $L$ ) are expressed as sums of Bloch components, each with variation  $\exp[j(m\delta - k_n z)]$ , multiplied by the appropriate Bessel function  $J_m$  or  $I_m$ , with  $k_n = k + 2\pi n/L$ . Similarly, in each dielectric ring (with width  $b$ ) the same field components are expressed as trigonometric series of  $\cos(l\delta/b)$ , or  $\sin(l\delta/b)$ , multiplied by  $\exp[jm\delta]$  and

the appropriate linear combinations of Bessel functions (to satisfy the required boundary conditions at the outer radius). The transverse fields in either region are then expressed as sums involving the derivatives of  $E_z$  and  $H_z$ , as dictated by Maxwell's equations.

Thus, all field components are described in terms of infinite sums, with the coefficients to be specified. The last step is to apply the orthogonality of  $\exp(-jk_n z)$  in  $0 < z < L$  to the continuity conditions for  $E_z$  and  $E_\theta$  and of  $\cos(l\delta/b)$  and  $\sin(l\delta/b)$  in  $0 < z < b$  to the continuity of  $H_z$  and  $H_\theta$ , yields an infinite linear system in the expansion coefficients. The vanishing of the determinant gives the dispersion relation  $D(\omega, k) = 0$ , and subsequently the linear system is solved to give all coefficients in terms of one, thus constructing all field components in each region.

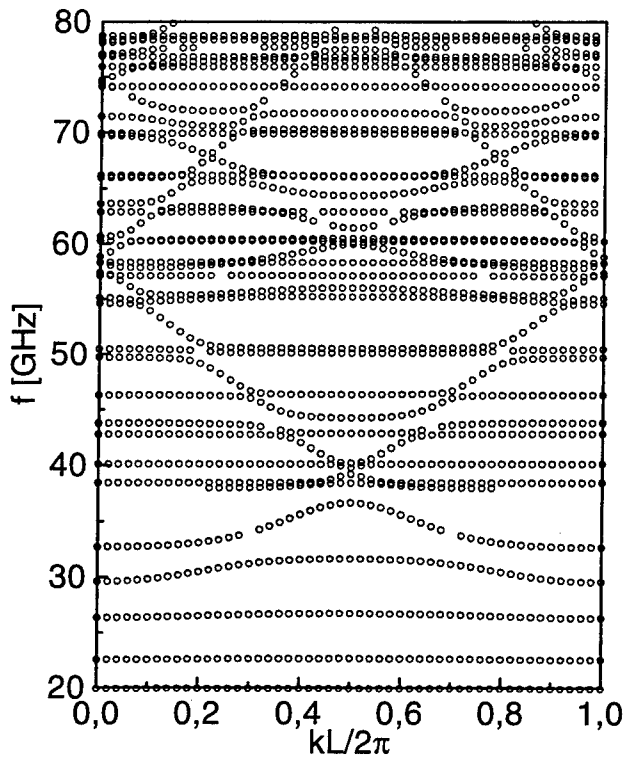
### 3. Numerical Implementation

For its numerical implementation, the analysis of Sec. 2 is simplified in two ways: (a) The infinite summations are truncated, typically beyond  $n_{max}=8$  in the vacuum and  $l_{max}=3$  in the dielectric, and (b) The imaginary part of the permittivity  $\tilde{\epsilon}$  is neglected. The latter simplification has been seen not to affect the field structure, or the frequency, even for values of the loss-tangent as high as 0.1.

Once the frequency and the field structure are obtained, the quality factor  $Q = \omega W_{em} / P$  is calculated by considering the contributions of diffraction and of dissipation. For an open-ended tunnel the diffracted power  $P_{diff}$  is the integral of Poynting's vector over the cross-section of the vacuum region, and since  $W_{em}$  is calculated just for one periodicity length, the resulting quality factor is to be multiplied by the number  $n_d$  of dielectric rings. The power  $P_{diss}$  dissipated inside the dielectric material is calculated by assigning a conductivity  $\tilde{\sigma}$  to the absorbing dielectric material, hence  $Q_{diss} = 2(\tilde{\sigma}/\tilde{\epsilon}) (W_{e,d}/W_{em})$ , where  $W_{e,d}$  is the electric power in each dielectric ring. Thus, the total quality factor is given by  $1/Q_{tot} = 1/n_d Q_{diff} + 1/Q_{diss}$ .

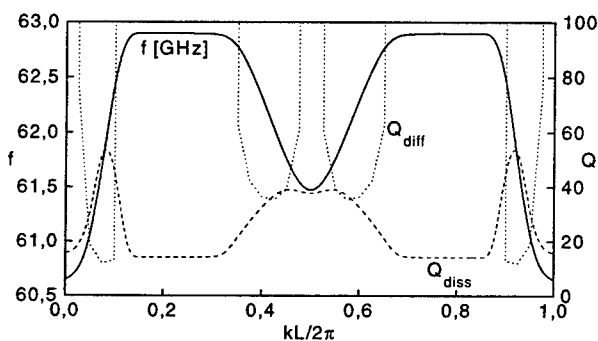
### 4. Results

Using the numerical code *HYBRID* in a typical beam tunnel geometry for azimuthally symmetric TE modes has given a frequency spectrum with horizontal straight lines and with hyperbolic segments, as is presented in the following figure.



The straight lines represent cavity modes and can be associated with the oscillation frequencies of individual cavities, consisting of the dielectric rings (and the inner vacuum bore), fully enclosed by a conducting wall: Each cavity can oscillate at its resonance frequencies, almost independently of the adjacent ones, hence the lines  $\omega(k) = \omega_{cav} = \text{const.}$  The hyperbolic segments represent the Bloch components of propagating waveguide modes, which depend practically only on the inner diameter of the conducting rings and ignore the presence of the dielectric.

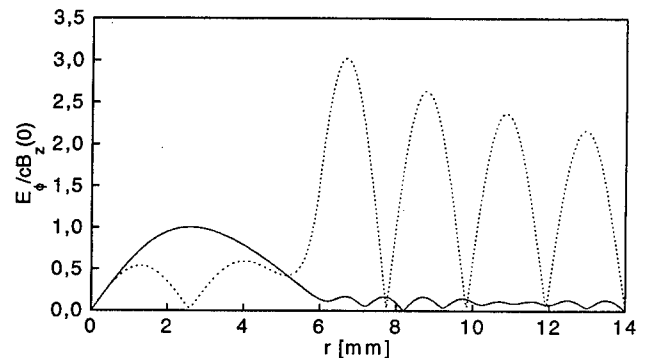
Additional features related to the coupling between the cavity oscillations and the waveguide modes can be seen in the following figure, which amplifies  $\omega(k)$  of mode TE<sub>22,0</sub> and also presents the quality factors  $Q_{diff}$  and  $Q_{diss}$ .



This mode contains two cavity oscillations (at 60.6 and at 62.9 GHz, which correspond to the TE<sub>7,0,2</sub> and TE<sub>4,0,3</sub> cavity modes) and four Bloch components (near the edges of the figure, the harmonics  $n=-1$  and  $n=+2$  of the fundamental, with cutoff frequency at 30.5 GHz, and near the center of the figure the  $n=0$  and  $n=+1$  ones of the first radial harmonic, with cutoff frequency at 55.8 GHz).

In a cavity oscillation, the fields are expected to be concentrated inside the dielectric material, while a propagating mode, which practically ignores the presence of the dielectric, has its fields concentrated inside the inner vacuum bore. As a consequence, the quality factor attains specific limiting values, seen in the previous figure: A cavity mode has practically no diffraction losses,  $Q_{diff} = \infty$ , but significant dissipation losses, for which, in view of equi-partition of energy, the value  $Q_{diss} = \hat{a}_r / \hat{a}_i$  is approached ( $=14$  in the example), giving a total  $Q_{tot} = \hat{a}_r / \hat{a}_i$ . On the other hand, in a propagating mode the fields do not penetrate the dielectric material, hence  $Q_{diss} = \infty$  and  $Q_{tot} = Q_{diff} = n_d \hat{u} L / v_g$ , where  $v_g$  is the group velocity.

Finally, the differentiation between cavity and waveguide modes can be seen indeed in the radial variation of the field component  $E_z$  shown in the next figure for  $kL/2\delta = 0.075$  (waveguide mode) and 0.200 (cavity oscillation).



The threshold in any beam-wave interaction is controlled by the product of  $Q$  with the beam current  $I_b$  and a coupling coefficient, hence a small value of  $Q$  is needed, in order to allow for the beam to propagate unaffected by such an interaction. The existence in a gyrotron beam tunnel of propagating waveguide modes, which may have high  $Q$ -values (diffraction limited only) has therefore to be taken into consideration in the design. This can be accomplished by a combination of (a) a short beam tunnel, which reduces  $Q_{diff}$ , and (b) selecting the parameters of the dielectric rings, so that, in the vicinity of the intersection between the beam mode and a waveguide mode with strong coupling to the beam, the spectrum of the cavity modes is dense enough to suppress the dominance of the waveguide mode.

\*Work supported in part by the Fusion Programme of the European Union under contract ERB 5004 CT 96 0060.